SMALL SCALE SPATIAL AND TEMPORAL PATTERNS IN PARTICLES, PLANKTON, AND OTHER ORGANISMS

EDITED BY: Aditya R. Nayak, Houshuo Jiang, Lee Karp-Boss, James Michael Sullivan, David Murphy, Margaret Byron and Malcolm McFarland

PUBLISHED IN: Frontiers in Marine Science

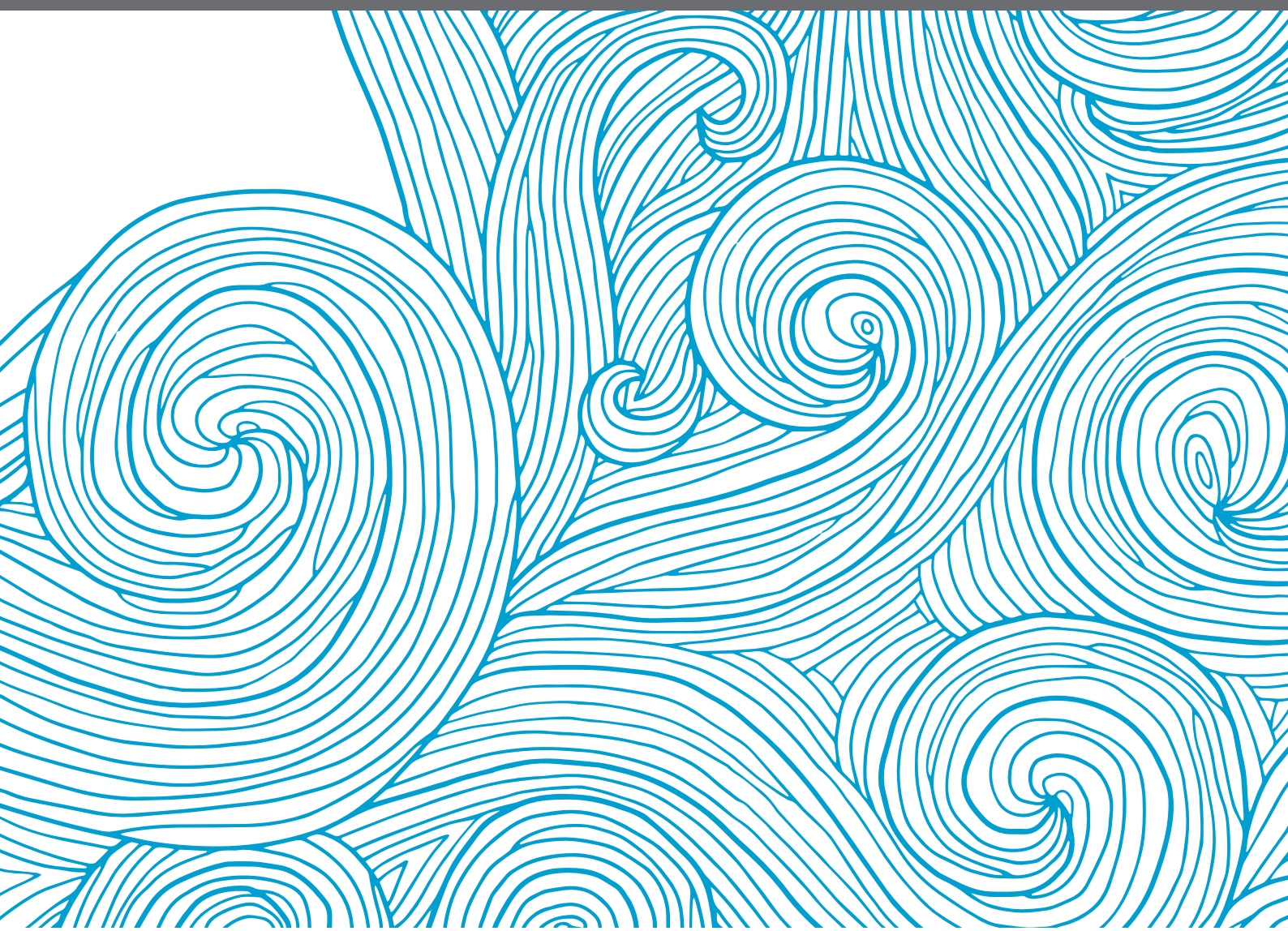

frontiers Research Topics

Frontiers eBook Copyright Statement

The copyright in the text of individual articles in this eBook is the property of their respective authors or their respective institutions or funders. The copyright in graphics and images within each article may be subject to copyright of other parties. In both cases this is subject to a license granted to Frontiers.

The compilation of articles constituting this eBook is the property of Frontiers.

Each article within this eBook, and the eBook itself, are published under the most recent version of the Creative Commons CC-BY licence. The version current at the date of publication of this eBook is CC-BY 4.0. If the CC-BY licence is updated, the licence granted by Frontiers is automatically updated to the new version.

When exercising any right under the CC-BY licence, Frontiers must be attributed as the original publisher of the article or eBook, as applicable.

Authors have the responsibility of ensuring that any graphics or other materials which are the property of others may be included in the CC-BY licence, but this should be checked before relying on the CC-BY licence to reproduce those materials. Any copyright notices relating to those materials must be complied with.

Copyright and source acknowledgement notices may not be removed and must be displayed in any copy, derivative work or partial copy which includes the elements in question.

All copyright, and all rights therein, are protected by national and international copyright laws. The above represents a summary only. For further information please read Frontiers' Conditions for Website Use and Copyright Statement, and the applicable CC-BY licence.

ISSN 1664-8714
ISBN 978-2-88966-769-7
DOI 10.3389/978-2-88966-769-7

About Frontiers

Frontiers is more than just an open-access publisher of scholarly articles: it is a pioneering approach to the world of academia, radically improving the way scholarly research is managed. The grand vision of Frontiers is a world where all people have an equal opportunity to seek, share and generate knowledge. Frontiers provides immediate and permanent online open access to all its publications, but this alone is not enough to realize our grand goals.

Frontiers Journal Series

The Frontiers Journal Series is a multi-tier and interdisciplinary set of open-access, online journals, promising a paradigm shift from the current review, selection and dissemination processes in academic publishing. All Frontiers journals are driven by researchers for researchers; therefore, they constitute a service to the scholarly community. At the same time, the Frontiers Journal Series operates on a revolutionary invention, the tiered publishing system, initially addressing specific communities of scholars, and gradually climbing up to broader public understanding, thus serving the interests of the lay society, too.

Dedication to Quality

Each Frontiers article is a landmark of the highest quality, thanks to genuinely collaborative interactions between authors and review editors, who include some of the world's best academicians. Research must be certified by peers before entering a stream of knowledge that may eventually reach the public - and shape society; therefore, Frontiers only applies the most rigorous and unbiased reviews.
Frontiers revolutionizes research publishing by freely delivering the most outstanding research, evaluated with no bias from both the academic and social point of view. By applying the most advanced information technologies, Frontiers is catapulting scholarly publishing into a new generation.

What are Frontiers Research Topics?

Frontiers Research Topics are very popular trademarks of the Frontiers Journals Series: they are collections of at least ten articles, all centered on a particular subject. With their unique mix of varied contributions from Original Research to Review Articles, Frontiers Research Topics unify the most influential researchers, the latest key findings and historical advances in a hot research area! Find out more on how to host your own Frontiers Research Topic or contribute to one as an author by contacting the Frontiers Editorial Office: frontiersin.org/about/contact

SMALL SCALE SPATIAL AND TEMPORAL PATTERNS IN PARTICLES, PLANKTON, AND OTHER ORGANISMS

Topic Editors:
Aditya R. Nayak, Florida Atlantic University, United States
Houshuo Jiang, Woods Hole Oceanographic Institution, United States
Lee Karp-Boss, University of Maine, United States
James Michael Sullivan, Florida Atlantic University, United States
David Murphy, University of South Florida, United States
Margaret Byron, Pennsylvania State University (PSU), United States
Malcolm McFarland, Florida Atlantic University, United States

Citation: Nayak, A. R., Jiang, H., Karp-Boss, L., Sullivan, J. M., Murphy, D., Byron, M., McFarland, M., eds. (2021). Small Scale Spatial and Temporal Patterns in Particles, Plankton, and Other Organisms. Lausanne: Frontiers Media SA.
doi: 10.3389/978-2-88966-769-7

Table of Contents

05 ***Editorial: Small Scale Spatial and Temporal Patterns in Particles, Plankton, and Other Organisms***
Aditya R. Nayak, Houshuo Jiang, Margaret L. Byron, James M. Sullivan, Malcolm N. McFarland and David W. Murphy

09 ***Nighttime Swimming Behavior of a Mesopelagic Fish***
Svenja Christiansen, Josefin Titelman and Stein Kaartvedt

21 ***Non-breaking Wave Effects on Buoyant Particle Distributions***
Michelle H. DiBenedetto

32 ***Phytoplankton Orientation in a Turbulent Ocean: A Microscale Perspective***
G. Basterretxea, J. S. Font-Muñoz and I. Tuval

40 ***Multi-Instrument Assessment of Phytoplankton Abundance and Cell Sizes in Mono-Specific Laboratory Cultures and Whole Plankton Community Composition in the North Atlantic***
Susanne Menden-Deuer, Françoise Morison, Amanda L. Montalbano, Gayantonia Franzè, Jacob Strock, Ewelina Rubin, Heather McNair, Colleen Mouw and Pierre Marrec

54 ***Hydrodynamics of a Rising Oil Droplet With Bacterial Extracellular Polymeric Substance (EPS) Streamers Using a Microfluidic Microcosm***
Andrew R. White, Maryam Jalali and Jian Sheng

68 ***Copepod Behavior Responses Around Internal Waves***
Mohammad Mohaghar, Seongyu Jung, Kevin A. Haas and Donald R. Webster

83 ***Lagrangian Time Scale of Passive Rotation for Mesoscale Particles in Turbulence***
Ankur D. Bordoloi, Evan Variano and Gautier Verhille

91 ***Enhanced Light Absorption by Horizontally Oriented Diatom Colonies***
Malcolm McFarland, Aditya R. Nayak, Nicole Stockley, Michael Twardowski and James Sullivan

101 ***Ubiquitous Patchiness in Chlorophyll a Concentration in Coastal Archipelago of Baltic Sea***
Matias Scheinin and Eero Asmala

113 ***Biophysical Control on Variability in Phytoplankton Production and Composition in the South-Western Tropical Indian Ocean During Monsoon 2014***
Sarat C. Tripathy, P. Sabu, Sivaji Patra, Ravidas K. Naik, Amit Sarkar, Vankara Venkataramana, Anvita U. Kerkar and Pandi Sudarsanarao

131 ***Spatial Patterns of Particles and Plankton in the Warming Arctic Fjord (Isfjorden, West Spitsbergen) in Seven Consecutive Mid-Summers (2013–2019)***
Marlena Szeligowska, Emilia Trudnowska, Rafał Boehnke, Anna Maria Dąbrowska, Józef Maria Wiktor, Sławomir Sagan and Katarzyna Błachowiak-Samołyk

149 ***Cutting Through the Noise: Bacterial Chemotaxis in Marine Microenvironments***
Douglas R. Brumley, Francesco Carrara, Andrew M. Hein, George I. Hagstrom, Simon A. Levin and Roman Stocker

158 ***Planktonic Protists of the Eastern Nordic Seas and the Fram Strait: Spatial Changes Related to Hydrography During Early Summer***
Anna Maria Dąbrowska, Józef Mikołaj Wiktor Jr, Małgorzata Merchel and Józef Maria Wiktor

172 ***Comparing Vertical Distributions of Chl-a Fluorescence, Marine Snow, and Taxon-Specific Zooplankton in Relation to Density Using High-Resolution Optical Measurements***
Christian Briseño-Avena, Jennifer C. Prairie, Peter J. S. Franks and Jules S. Jaffe

187 ***Persistent Hydrodynamic Cues Elicit Orientation-Specific Behavioral Sensitivities and Kinematic Responses in Dispersed Crab Larvae***
Aaron C. True, Donald R. Webster, Marc J. Weissburg and Jeannette Yen

209 ***Monsoonal Influence and Variability of Water Quality, Phytoplankton Biomass in the Tropical Coastal Waters – A Multivariate Statistical Approach***
Subrat Naik, Rajani Kanta Mishra, K. C. Sahu, Aneesh A. Lotliker, U. S. Panda and Pravakar Mishra

223 ***Drivers of Plankton Distribution Across Mesoscale Eddies at Submesoscale Range***
Nauzet Hernández-Hernández, Javier Arístegui, María F. Montero, Esther Velasco-Senovilla, Federico Baltar, Ángeles Marrero-Díaz, Antonio Martínez-Marrero and Ángel Rodríguez-Santana

236 ***Stirring, Mixing, Growing: Microscale Processes Change Larger Scale Phytoplankton Dynamics***
Francesco Paparella and Marcello Vichi

253 ***Monitoring of Plankton Spatial and Temporal Characteristics With the Use of a Submersible Digital Holographic Camera***
Victor Dyomin, Alexandra Davydova, Sergey Morgalev, Nikolay Kirillov, Alexey Olshukov, Igor Polovtsev and Sergey Davydov

262 ***Swimming and Sinking Behavior of Warm Water Pelagic Snails***
Ferhat Karakas, Jordan Wingate, Leocadio Blanco-Bercial, Amy E. Maas and David W. Murphy

284 ***Three-Dimensional Imaging Lidar for Characterizing Particle Fields and Organisms in the Mesopelagic Zone***
Trevor McKenzie, Michael Twardowski, Nathan Briggs, Aditya R. Nayak, Kevin M. Boswell and Fraser Dalgleish

299 ***High-Resolution Sampling of a Broad Marine Life Size Spectrum Reveals Differing Size- and Composition-Based Associations With Physical Oceanographic Structure***
Adam T. Greer, John C. Lehrter, Benjamin M. Binder, Aditya R. Nayak, Ranjoy Barua, Ana E. Rice, Jonathan H. Cohen, Malcolm N. McFarland, Alexis Hagemeyer, Nicole D. Stockley, Kevin M. Boswell, Igor Shulman, Sergio deRada and Bradley Penta

321 ***A Review of Holography in the Aquatic Sciences:* In situ *Characterization of Particles, Plankton, and Small Scale Biophysical Interactions***
Aditya R. Nayak, Ed Malkiel, Malcolm N. McFarland, Michael S. Twardowski and James M. Sullivan

frontiers in Marine Science

EDITORIAL
published: 22 March 2021
doi: 10.3389/fmars.2021.669530

Editorial: Small Scale Spatial and Temporal Patterns in Particles, Plankton, and Other Organisms

Aditya R. Nayak[1,2], Houshuo Jiang[3], Margaret L. Byron[4], James M. Sullivan[2], Malcolm N. McFarland[2] and David W. Murphy[5]*

[1] Department of Ocean and Mechanical Engineering, Florida Atlantic University, Boca Raton, FL, United States, [2] Harbor Branch Oceanographic Institute, Florida Atlantic University, Fort Pierce, FL, United States, [3] Department of Applied Ocean Physics and Engineering, Woods Hole Oceanographic Institution, Woods Hole, MA, United States, [4] Department of Mechanical Engineering, Pennsylvania State University, University Park, PA, United States, [5] Department of Mechanical Engineering, University of South Florida, Tampa, FL, United States

Keywords: marine particles, plankton, spatial patterns, ocean microscale biophysics, small-scale processes, oceanic instrumentation

Editorial on the Research Topic

Small Scale Spatial and Temporal Patterns in Particles, Plankton, and Other Organisms

INTRODUCTION

Scientists have long known that small-scale interactions of aquatic particles, plankton, and other organisms with their immediate environment play an important role in diverse research areas, including marine ecology, ocean optics, and climate change (Guasto et al., 2012; Prairie et al., 2012). Typically, the distribution of particles and other organisms in the water column tends to be quite "patchy," i.e., non-homogeneous, both spatially and temporally (Durham and Stocker, 2012). Patchiness can manifest itself through well-known phenomena such as harmful algal blooms (HABs), phytoplankton and zooplankton "thin layers," deep scattering layers, and schooling of marine organisms such as krill and fish. This non-homogeneous distribution can significantly influence predator-prey encounters and outcomes, export fluxes, marine ecosystem health, and biological productivity (Sullivan et al., 2010; Durham et al., 2013). Thus, there is a continuing need to study and characterize the small-scale biological-physical interactions between particles/organisms and their local environment, as well as the scaled-up effects of these small-scale interactions on larger-scale dynamics. These studies are also directly linked to broader research topics listed as part of the future "grand challenges" in marine ecosystem ecology, as outlined in Borja et al. (2020).

This Research Topic aims to bring together research efforts from a diverse set of authors across different disciplines, generally focused on the overarching theme of characterizing small-scale interactions of particles, plankton, and organisms through different investigatory lenses. The resulting collection is diverse in its approach to this important and timely problem, and includes field and laboratory studies, theoretical and modeling methods, as well as the development of novel and innovative technologies. A total of 23 articles, including Original Research, Perspectives, Brief Research Reports, Mini-Reviews, and Reviews, are included as part of this Research Topic. While these articles span substantially different areas under this broad topic, they can be roughly grouped based on their primary focus on the type of particle/organism being studied (e.g., general aquatic particles, phytoplankton, zooplankton, bacteria, and fish) or on methodology/technology development geared toward enhancing research in these areas. Below, an overview of these articles

OPEN ACCESS

Edited and reviewed by:
Angel Borja, Technological Center Expert in Marine and Food Innovation (AZTI), Spain

****Correspondence:***
Aditya R. Nayak
anayak@fau.edu

Specialty section:
This article was submitted to Marine Ecosystem Ecology, a section of the journal Frontiers in Marine Science

Received: *19 February 2021*
Accepted: *25 February 2021*
Published: *22 March 2021*

Citation:
Nayak AR, Jiang H, Byron ML, Sullivan JM, McFarland MN and Murphy DW (2021) Editorial: Small Scale Spatial and Temporal Patterns in Particles, Plankton, and Other Organisms. Front. Mar. Sci. 8:669530. doi: 10.3389/fmars.2021.669530

is provided. The organization is as follows: we start with topics ranging from the smallest (bacteria) to the largest organisms (fish), followed by articles related to general aquatic particles and those focusing on methodologies.

FOCUS AREAS

Bacteria

Microscale bacterial interactions with their aquatic micro-environment have important consequences to particle transport, nutrient cycling, and marine biogeochemical models. Brumley et al. present a perspective on bacterial chemotaxis, uptake kinetics, and associated noise sources that these microbes have to deal with in realistic micro-environments in the ocean. It is also known that bacteria can produce extracellular polymeric substance (EPS), constituted of proteins and other secretions. White et al. describe the hydrodynamic interactions of an oil droplet with EPS filaments, with their results indicating that EPS streamers reduce the rising velocity of oil droplets within the water column, potentially impacting the dispersion from oil spill plumes in the ocean.

Phytoplankton

Several articles within the Research Topic focused on phytoplankton distribution, patchiness, and fluid interactions at different scales in the ocean. Paparella and Vichi describe a novel Lagrangian model that clearly distinguishes between irreversible mixing and turbulent stirring to better incorporate the effects of microscale patchiness in plankton on larger-scale processes. This model allows for the interaction between different scales of relevance across a large size range (lacking in many currently used numerical models) and underscores the importance of considering how the microscale can affect large-scale dynamics. Hernandez-Hernandez et al. characterize plankton distributions across mesoscale eddies using *in situ* measurements. Their observations help explain the biophysical interactions between mesoscale structures and the plankton community, including variations in nutrient and chlorophyll *a* concentration.

Previous theoretical and laboratory studies as well as recent field observations have outlined the potential effect of fluid flow on the orientation of phytoplankton in the water column. The orientation of single celled or colonial phytoplankton can have significant implications for different functions including locomotion, reproduction, and metabolism. Furthermore, non-random alignment of elongate particles and phytoplankton (e.g., colonial diatoms) can modulate underwater light propagation in the ocean. Basterretxea et al. provide a brief summary of the currently existing literature and future opportunities in this area of research in their mini-review article. Through a combination of field observations and the development of a geometric optics model, McFarland et al. found significant enhancement in the absorption of downwelling irradiance in the presence of horizontally aligned diatom colonies as opposed to randomly oriented populations.

Five articles focused on the spatial patterns in particles, plankton, and chlorophyll concentrations in aquatic environments in specific geographical regions around the world. Scheinin and Asmala collected and analyzed chlorophyll *a* data, identifying distinct phytoplankton patches over a sampling transect of several hundreds of kilometers in the coastal Baltic Sea. Their observations showed that phytoplankton patches were more abundant and larger in size in areas with higher phytoplankton biomass. Szeligowska et al. carry out a detailed characterization of spatial distributions of particles and plankton across a wide size range in an Arctic fjord over several summer seasons. The results shed light on variations in planktonic community composition with potential associations to large-scale processes and seasonal variations in a rapidly warming Arctic environment. Similarly, Dabrowska et al. report observations of protist community composition and spatial distributions within the Fram Strait and the Norwegian and Greenland seas. It is hypothesized that in warmer years, enhanced phytoplankton concentrations lead to faster nutrient depletion, which in turn leads to a faster shift in the post bloom community composition. Tripathy et al. present a short time series of physical and biological parameters in the Southwest Indian Ocean during the monsoon season, providing information about phytoplankton biomass variability and carbon uptake efficiency. Naik et al. report on the influence of monsoons on water quality variability and phytoplankton community composition just off a highly biodiverse estuarine ecosystem in eastern coastal India.

Zooplankton and Fish

Four articles within the Research Topic focused on different zooplankton including copepods, crab larvae, and sea snails, to characterize associated behavioral patterns, animal-flow interactions, and spatial distributions; a single article focused on swimming patterns of a fish species. Mohaghar et al. utilize a lab-based internal wave generation apparatus to characterize behavioral responses of copepods in the presence of internal waves. Results indicate that the swimming trajectories of the organisms in the vicinity of the internal waves were significantly influenced by their behavioral responses. True et al. characterize the kinematic responses of crab larvae in the presence of a persistent shear layer, a feature typical of the estuarine regions critical to the life-history of such organisms (but under-investigated compared to more spatiotemporally transient cues, such as turbulence). Larval swimming behavior in specific shear flow orientations (upwelling, downwelling, or horizontal shear flows) was strongly directionally dependent, indicating that the overall dispersal patterns of marine larvae may differ significantly between fronts vs. clines—which may in turn affect the extent and character of observed patchiness. Similarly, swimming and sinking behavioral responses of several marine pteropod species have been described in Karakas et al. Their results indicate that size and shell shape play an important role in how these organisms are vertically distributed and that swimming speeds are not necessarily correlated with vertical migration ranges. Briseño-Avena et al. study night-time predator-prey interactions

in a stratified water column off the coast of California using an integrated *in situ* optical instrumentation package. Results elucidated how different predator/prey zooplankton species were located relative to each other as well as relative to the subsurface chlorophyll maximum (SCM) or fluorescent particle maximum zones. Christiansen et al. describe the swimming behavior of *Maurolicus muelleri*, a fish species inhabiting mesopelagic zones in different geographical areas, including Norwegian fjords. High resolution data from an echosounder were used to study swimming behavioral patterns of several individuals during nocturnal migration.

Marine Particles

Bordoloi et al. report experiments on inertial fibers in homogeneous isotropic turbulence, while also developing a model predicting correlation time and tumbling rate variance. Their results can contribute to the better understanding of zooplankton-flow interactions in the ocean by separating the passive rotation of an organism from active locomotion. DiBenedetto develops an analytical model to characterize the effects of non-breaking waves of the spatial distribution of buoyant particles. Results indicated that higher concentration of particles were found under wave crests than troughs. This observation has several implications, including a better understanding of microplastics hotspots in upper waters of coastal regions where wave effects can play a significant role.

Methodology and Instrumentation

Five papers within the Research Topic were focused on discussing development of novel instrumentation and/or assessment and comparison of different instrumentation toward the characterization of marine particles, plankton, and organismal size and distributions. Menden-Deuer et al. utilize different imaging instrumentation and particle counters to assess the impact of instrument/method choice on quantification of phytoplankton species abundance and cell sizes using laboratory cultures. The study highlighted the pros and cons of using each of these different approaches, providing useful information about trade-offs and suitability of a particular instrument toward specific applications. In a review article, Nayak et al. provide a historical perspective of the application of holography in the aquatic sciences and report on previous literature where the technique was used toward the characterization of particles, plankton, and biophysical interactions. Drawbacks of the technique, current efforts to improve the technology and data processing, and future fields of application where holography could be used as a valuable tool by the aquatic sciences community are also outlined. In a related paper, Dyomin et al. report on the development of a novel *in situ* holographic imaging system to monitor the spatial and temporal distributions of plankton. Greer et al. discuss a multi-disciplinary field effort to characterize the particle and plankton field across a broad size spectrum, through a variety of approaches, including conventional net sampling, acoustics and multiple *in situ* imaging systems. Their results highlight how different methods and instruments can complement measurements and enhance the understanding of biological particle fields, over a size range of several microns to several centimeters. Finally, McKenzie et al. outline the development of a three-dimensional imaging lidar system to characterize particles in the millimeter to centimeter size range. Field observations carried out with this novel instrument toward imaging particles and organisms in the mesopelagic zone are presented.

SUMMARY AND CONTRIBUTION TO THE FIELD

In summary, this Research Topic has successfully assimilated a compendium of research related to characterizing and understanding small-scale interactions between particles/organisms and their environment. These articles include a balanced combination of laboratory and field-based experiments, theoretical and modeling approaches, and novel methodologies, all of which bring into sharp focus the importance of pushing the envelope to advance research in these areas. A notable common theme across these diverse topics is the relevance of these small-scale interactions to processes that take place on the order of meters, kilometers, or tens to hundreds of kilometers. For example, the local interactions of particles or plankton with instantaneous flow features can lead to preferential concentration, aggregation, or layer formation, which has strong repercussions across trophic levels and across spatial scales. The aggregated behavior of millimeter-scale organisms in response to similarly sized flow features can impact long-term migration and dispersal patterns, leading to substantial impact over long timescales and large spatial extents. Measurements at small scales—of productivity, particle size distribution, or species abundance—can equip us to make inferences about what is happening at much larger scales. These results further emphasize the overall importance of the microscale, and the need for integrative approaches to uncover potential lines of influence to the macroscale. The editors therefore hope that these publications will be of interest and utility to not only the specialized group of researchers focused on microscale aquatic studies, but to the entire oceanographic community in general.

AUTHOR CONTRIBUTIONS

All authors listed have made a substantial, direct and intellectual contribution to the work, and approved it for publication.

FUNDING

AN was supported through a National Academy of Sciences, Engineering, and Medicine (NASEM) Gulf Research Program (GRP) Early Career Research Fellowship and a faculty start-up grant at Florida Atlantic University. HJ was supported by

US National Science Foundation awards (OCE-1559062 and IOS-1353937). MB was supported by a faculty start-up grant at Penn State University. AN, JS, and MM were supported by US National Science Foundation awards (OCE-1634053 and OCE-1657332). DM was supported by the US National Science Foundation (CBET-1846925).

ACKNOWLEDGMENTS

We would like to thank all the authors, reviewers, and external editors for their substantial contributions toward this Research Topic. We are also grateful to the Frontiers editorial team for their help and support during this entire effort.

REFERENCES

Borja, A., Andersen, J. H., Arvanitidis, C. D., Basset, A., Buhl-Mortensen, L., Carvalho, S., et al. (2020). Past and future grand challenges in marine ecosystem ecology. *Front. Mar. Sci.* 7:362. doi: 10.3389/fmars.2020.00362

Durham, W. M., Climent, E., Barry, M., De Lillo, F., Boffetta, G., Cencini, M., et al. (2013). Turbulence drives microscale patches of motile phytoplankton. *Nat. Commun.* 4:2148. doi: 10.1038/ncomms3148

Durham, W. M., and Stocker, R. (2012). Thin phytoplankton layers: characteristics, mechanisms, and consequences. *Annu. Rev. Mar. Sci.* 4, 177–207. doi: 10.1146/annurev-marine-120710-100957

Guasto, J. S., Rusconi, R., and Stocker, R. (2012). Fluid mechanics of planktonic microorganisms. *Annu. Rev. Flu. Mech.* 44, 373–400. doi: 10.1146/annurev-fluid-120710-101156

Prairie, J. C., Sutherland, K. R., Nickols, K. J., and Kaltenberg, A. M. (2012). Biophysical interactions in the plankton: a cross-scale review. *Limnol. Oceanogr. Fluids Environ.* 2, 121–145. doi: 10.1215/21573689-1964713

Sullivan, J. M., Van Holliday, D., McFarland, M., McManus, M. A., Cheriton, O. M., Benoit-Bird, K. J., et al. (2010). Layered organization in the coastal ocean: an introduction to planktonic thin layers and the loco project. *Cont. Shelf Res.* 30:1. doi: 10.1016/j.csr.2009.09.001

Disclaimer: The content is solely the responsibility of the authors and does not necessarily represent the official views of the Gulf Research Program of the National Academies of Sciences, Engineering, and Medicine.

Conflict of Interest: The authors declare that the research was conducted in the absence of any commercial or financial relationships that could be construed as a potential conflict of interest.

Copyright © 2021 Nayak, Jiang, Byron, Sullivan, McFarland and Murphy. This is an open-access article distributed under the terms of the Creative Commons Attribution License (CC BY). The use, distribution or reproduction in other forums is permitted, provided the original author(s) and the copyright owner(s) are credited and that the original publication in this journal is cited, in accordance with accepted academic practice. No use, distribution or reproduction is permitted which does not comply with these terms.

frontiers in Marine Science

ORIGINAL RESEARCH
published: 20 December 2019
doi: 10.3389/fmars.2019.00787

Nighttime Swimming Behavior of a Mesopelagic Fish

Svenja Christiansen, Josefin Titelman and Stein Kaartvedt*

Department of Biosciences, University of Oslo, Oslo, Norway

Nocturnal migration of mesopelagic fish into surface waters is well-documented. Yet, although there is increasing evidence of individual-based deviations from average population migrations and of the importance of small-scale individual behavior for predator-prey interactions and energetic cycling, little is known about what mesopelagic animals do when in upper waters. Using high-resolution data from an upward-facing, moored, split-beam echosounder we analyzed the night-time individual vertical swimming behavior of pearlsides (*Maurolicus muelleri*) over one winter. The population behavior is characterized by migration to the surface after sunset, "midnight-sinking" and another migration to the surface in the morning, followed by return to the daytime habitat. Focusing on individuals unveiled diverse behavioral patterns during different phases of the migration. After ascending to upper layers at dusk, *M. muelleri* leaves the surface waters, not by sinking, but by actively swimming in a step-wise pattern characterized by relocations alternated by pauses. Following the descent, vertical swimming is sustained at lower levels. Around midnight, the vertical swimming direction changes from predominantly downward to upward. Several hours before dawn, the fish start ascending toward the surface in a step-wise pattern. During population ascent in the afternoon and descent in the morning, some individuals at the fringes of schools migrate without intermittent pauses. This study documents the feasibility of using submerged, stationary echosounders in unveiling the individual behavior of mesopelagic fish.

Keywords: individual behavior, nocturnal, target tracking, diel vertical migration, *Maurolicus muelleri*

OPEN ACCESS

Edited by:
James Michael Sullivan, Florida Atlantic University, United States

Reviewed by:
Mike Jech, Northeast Fisheries Science Center (NOAA), United States
Samuel S. Urmy, Monterey Bay Aquarium Research Institute (MBARI), United States

****Correspondence:***
Svenja Christiansen
svenja.christiansen@ibv.uio.no

Specialty section:
This article was submitted to Marine Ecosystem Ecology, a section of the journal Frontiers in Marine Science

Received: *09 October 2019*
Accepted: *06 December 2019*
Published: *20 December 2019*

Citation:
Christiansen S, Titelman J and Kaartvedt S (2019) Nighttime Swimming Behavior of a Mesopelagic Fish. Front. Mar. Sci. 6:787. doi: 10.3389/fmars.2019.00787

INTRODUCTION

Large scale phenomena, such as diel vertical migration, are normally studied at the population and community level, and *in situ* studies of individual behavior are still scarce among plankton and micronekton (Pearre, 2003). Yet, populations consist of individuals of different states doing different things, many of which may or may not deviate from the average (Torgersen, 2001; Solberg and Kaartvedt, 2017). Understanding the behavior of individuals may improve our understanding of metabolic demands (Treberg et al., 2016), predator-prey interactions (O'Brien et al., 1990), and ultimately carbon flux (Pearre, 2003).

Animals engage in a range of behaviors related to foraging, mating, migrations, or resting. To date, especially the night time behavior of marine animals, such as fish, remains largely elusive, mostly due to methodological restrictions (Hammerschlag et al., 2017). Mesopelagic fish

and other diel vertical migrants are usually expected to feed near the surface at night. How the organisms actually spend the night, though, varies between species (Simard et al., 1985; Giske et al., 1990; Balino and Aksnes, 1993; Pearre, 2003), seasons (Staby and Aksnes, 2011; Prihartato et al., 2015), and states (Simard et al., 1985; Pearre, 2003; Staby et al., 2012). Despite studies indicating this variability among mesopelagic fish (Torgersen, 2001; Kaartvedt et al., 2008; Olivar et al., 2017; Solberg and Kaartvedt, 2017), quantitative data of their individual behavior is largely lacking. We know next to nothing about what these fish do at night.

Twilight migrations, where animals ascend to the ocean surface around dusk and dawn, but return to intermediate depths during night (midnight sinking) are common among pelagic taxa and repeatedly documented for acoustic scattering layers (Tarling et al., 2002; Staby et al., 2011; Valle-Levinson et al., 2014). Potential reasons for such behavior are manifold, but include reduced activity after satiation (Cushing, 1951; Rudjakov, 1970), temperature selection for energy optimization (Giske and Aksnes, 1992), prey distribution (Torgersen et al., 1997; Valle-Levinson et al., 2014) and predator avoidance (Torgersen et al., 1997; Staby, 2010; Staby and Aksnes, 2011; Prihartato et al., 2015). Still, we know very little about the individual behavior and activities resulting in such commonly observed population distribution patterns.

One mesopelagic fish that is known for its twilight migrations is the small (<6 cm standard length; (Rasmussen and Giske, 1994; Goodson et al., 1995) Mueller's pearlside (*Maurolicus muelleri*, Sternoptychidae). It forms the shallowmost mesopelagic scattering layers in Norwegian fjords (e.g., Giske et al., 1990; Staby and Aksnes, 2011). In winter, adult *M. muelleri* reside in a scattering layer at around 150–200 m depth throughout the diel cycle (Staby et al., 2011). The adult fish may rely on lipids built up over the summer and autumn (Falk-Petersen et al., 1986), but may also forage on overwintering *Calanus* during daytime (Bagøien et al., 2001). Juveniles (<1 year) instead maximize growth by feeding on plankton in shallower waters during twilight (Giske et al., 1990; Bagøien et al., 2001). The juveniles form a shallow scattering layer with a strong diel migration pattern with ascent to the surface in the afternoon, subsequent midnight-sinking during a non-feeding period at night (Giske and Aksnes, 1992; Bagøien et al., 2001) and a dawn ascent in the morning before returning to daytime depth (Staby and Aksnes, 2011; Prihartato et al., 2015). Juveniles are a main prey for e.g., blue whiting and saithe (Giske et al., 1990).

Here we explore the night-time behavior of juvenile Mueller's pearlside throughout the winter (December 2010–March 2011) in a well-studied fjord system (e.g., Kaartvedt et al., 1988; Giske et al., 1990; Staby et al., 2011). We applied an upward-looking echosounder floating in an anchored rig enabling studies of individuals with a temporal resolution of 2 records s^{-1} throughout the study period. Based on their population averages (e.g., Staby et al., 2012; Prihartato et al., 2015), we hypothesized that activity of juveniles changes during the night, yet with higher variability in individual behavior than that predicted from average diel vertical migration patterns.

MATERIALS AND METHODS

Location and Target Species

Masfjorden is a 20 km long fjord at the west coast of Norway (∼60°50' N, ∼005°30' E). It has a maximum depth of 494 m and a sill depth of 75 m bordering to Fensfjorden, which is connected to the coastal ocean (details in Kaartvedt et al., 1988). In Masfjorden, scattering layers shallower than 200 m are almost entirely formed by *M. muelleri* with juvenile fish in a shallow scattering layer (<100 m at night and ∼100 m during the day) and the adults in a deeper scattering layer (around 200 m) during autumn and winter (Giske et al., 1990; Staby et al., 2011). The two layers merge in spring (Staby et al., 2011). The glacier lanternfish *Benthosema glaciale* prevails below ∼200 m, with limited diel vertical migration in winter (Giske et al., 1990; Kaartvedt et al., 2009).

Dataset

Three upward facing stationary split-beam echosounders (EK60, Simrad) were deployed in Masfjorden between October 5–7, 2010 and recovered on August 17, 2011. Echosounders were moored at ∼370 m (38 kHz), ∼250 m (120 kHz), and ∼90 m depth (200 kHz) to enable high resolution of acoustic signals throughout the water column. The deepest echosounder was located at the bottom, the two shallower mounted in floating, anchored rigs in the same part of the fjord. The echosounders were cabled to shore and, with the exception of short periods of power failures, continuous recordings are available from all three frequencies for the entire study period. For further details about the setup of the echosounders see Prihartato et al. (2015). Here, we use data from the 200 kHz echosounder for the analysis of scattering layer depth and individual behavior. In addition, we consulted data from the deeper located 120 kHz echosounder for an overall assessment of the population behavior. This allowed to monitor the full diel migrating cycle including when juveniles migrated to below the 200 kHz echosounder (**Figure 1**), and also the largely non-migrating adults.

We analyzed data from December 2010 to March 2011, which enabled detailed analysis of individual swimming behavior of juvenile *M. muelleri* without the inclusion of deeper-living targets that only to a limited degree migrated vertically during this period (see e.g., Prihartato et al., 2015). Echosounder data with a temporal resolution of ∼2 s^{-1} were available from 98 days. Surface light levels (2 m above water) were measured continuously after the end of December 2010, yet the sensitivity of the light meter was too low for winter night-time measurements (see Prihartato et al., 2015).

For information on approximate nocturnal light levels during the study period, we obtained cloud cover and precipitation data from the nearby (∼20 km) weather station Takle from https://seklima.met.no/observations/ (download on November 12, 2019) and moon phases from https://www.timeanddate.com/moon/phases/ (accessed on November 12, 2019). Night time cloud cover and precipitation were calculated by averaging data collected within 0.3 days around midnight on each day. Time of sunrise and sunset were calculated for each day using the function

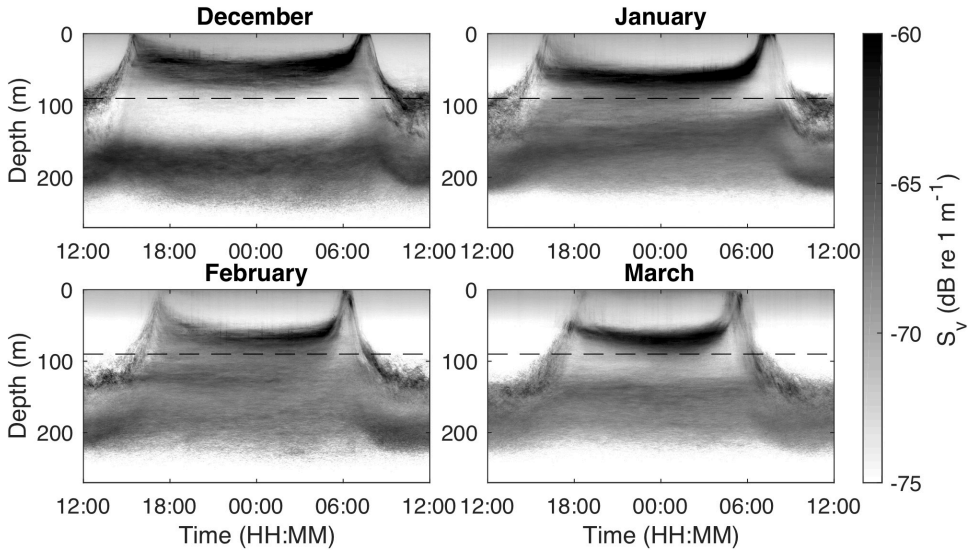

FIGURE 1 | Monthly median echograms for December 2010–March 2011 from an upward-looking, stationary 120 kHz echosounder in Masfjorden, Norway, showing scattering layer movements in the upper 300 m. The shallow scattering layer (<150 m depth) consists mainly of juvenile *Maurolicus muelleri*, the targets of this study, while the deeper scattering layer (>150 m depth) is mainly composed of adult *M. muelleri*. The dashed horizontal line indicates the depth of the 200 kHz echosounder that was used for the tracking analysis.

sunRiseSet[1]. All dates and times are presented in UTC (local time -1 h; maximum deviation from apparent solar time about 33 min on December 1, 2010).

Population Analysis

One aim of the study was to relate individual behavior to that of the *M. muelleri* population. Therefore, the location and migration velocity of the scattering layer formed by juvenile *M. muelleri* were determined. The raw EK60 data were reorganized into a three-dimensional grid, with a daytime (resolution of 90 s), depth (resolution of 0.3 m) and date dimension, in order to improve computation times and data accessibility. Each grid cell contained the average (calculated in the linear domain) volume backscattering strength (S_v, dB re 1 m^{-1} (MacLennan, 2002), in the following referred to as backscatter), calculated from the raw data of the given depth and time interval. The gridded backscatter data were used in all of the following population analyses. We calculated monthly median backscatter from the 120 kHz data by computing the median backscatter for each depth and daytime interval over all dates in the respective month.

Properties of Scattering Layers

The depth of the scattering layer was determined for each day of the study period using night time data (between sunset and sunrise) between 2 and 84 m depth. Data closer to the transducer could not be used due to noise (ping interference) at about 86 m depth. Between 0.1 day (144 min) after sunset and before sunrise, all values with depths < 19 m were excluded to reduce the inclusion of night time surface signals (**Supplementary Figure S1**). Backscatter values > −53 dB re 1 m^{-1} usually occurred due to extended surface signals or strong individual targets (potentially larger fish). These high backscatter values were thus not representative for the *M. muelleri* population and therefore excluded from the analysis. The thresholds for these data exclusions were determined empirically from the echograms. The remaining backscatter data were linearized to s_v (m^{-1}), the volume backscattering coefficient (MacLennan, 2002). For each time point, the cumulative s_v over depth was calculated and the depth where the cumulative s_v reached 50% of its maximum value was defined as the midpoint of the scattering layer. In some cases, the *M. muelleri* scattering layer could not be clearly identified due to low fish densities, which we defined as a cumulative $s_v < 5 \times 10^{-6}$ m^{-1}. Periods where the cumulative s_v fell below this threshold were excluded from the scattering layer analysis. We calculated the vertical velocity of the scattering layer by applying a moving slope approach[2] with a time window of 0.05 decimal days (72 min) on the scattering layer depth.

Delineating Dusk Descent and Dawn Ascent

Individual targets could not be resolved when in surface waters at dusk and dawn, and we here focus on the nocturnal behavior in-between these timepoints. The midnight sinking period was marked by the population starting to descend from the surface to deeper layers in the evening (from now on referred to as dusk descent) and the ascent to the surface in the morning (from now on dawn ascent). We used the location of the scattering layer to determine the start of the dusk descent and the end of the dawn

[1]https://se.mathworks.com/matlabcentral/fileexchange/62180-sunriseset-lat-lng-utcoff-date-plot; downloaded on January 15, 2019.

[2]https://se.mathworks.com/matlabcentral/fileexchange/16997-movingslope; downloaded on April 5, 2018.

ascent of the population (**Figure 2**). We chose the first time-point when the center of the scattering layer was at its shallowest depth in the afternoon and morning, respectively, as criteria. We also calculated the time spent in near-surface waters < 20 m depth at dusk and dawn for each day.

Identification of *Maurolicus muelleri* and Description of Swimming Behavior

The proximity of the *M. muelleri* scattering layer to the 200 kHz transducer at night enabled the identification of night-time individual swimming behavior. Densities of fish in the core of the scattering layer were too high for separating individuals during some parts of the night and at long distance from the transducer (i.e., shallow depth), while individuals outside the core and during periods of lower density could be distinguished successfully. Types of swimming patterns were first visually identified from echograms in the Sonar5-Pro software (Balk and Lindem, 2017) on separate days and thereafter quantified using target tracking.

Target Tracking

Successive echoes of individual targets can be combined and thus the path of individuals over depth, time and in along and athwart direction can be followed (target tracking; Brede et al., 1990). We used target tracking to assess the individual vertical swimming of *M. muelleri* over the entire study period. Target tracking was performed in the software Sonar5-Pro (Version 6.0.4, Balk and Lindem, 2000, 2017). Prior to the tracking, the files were pre-processed by cross-filter detection (Balk and Lindem, 2001, 2017), a procedure which improves the detection of individual tracks in single echo detection mode. Default settings were selected for the cross-filter detection. The thus modified single echo detection echograms were then analyzed by automatic target tracking. We optimized the parameters for the target tracking (**Table 1**) beforehand by comparing manual and automatic tracking at different time points of the study period. We adjusted the tracking parameters depending on distance from the transducer (range), which reduces the uncertainties at longer ranges compared to when using a single set of parameters. Individuals were tracked between 5 and 85 m range (i.e., ∼9–89 m depth). The use of cross-filter detection introduces uncertainties. While enabling tracking at increased ranges and at higher densities (Balk and Lindem, 2002), it also increases the risk of multiple detections, increases ping gaps and introduces noise into the target strength (MacLennan, 2002) of tracks. Yet, we decided to accept these uncertainties to be able to analyze individual movements throughout most of the water column and with longer track durations that enabled the differentiation between behaviors. Only few individuals (∼3%) were tracked at ranges > 60 m (shallower than 34 m depth; **Supplementary Figure S2**). While these few individuals have limited influence on the overall results, they contribute information about processes and behavior in the upper water column.

High population densities hamper individual tracking detection (Handegard, 2007). Correspondingly, individuals close to the transducer are tracked more effectively due to the higher resolution of targets. Differences in population densities over time, e.g., lower densities during the dusk descent, and distances to the transducer, e.g., shorter distances in the morning when many individuals already started descending, thus led to a higher number of descending tracks. Nevertheless, a visual comparison of the tracks and echograms indicated that the tracks' position information and thus behavior of the individuals were represented well. This also makes us confident that we are not assessing the behavior of outliers with deviating behavior and that the large-scale picture of the behavioral repertoire observed here is representative.

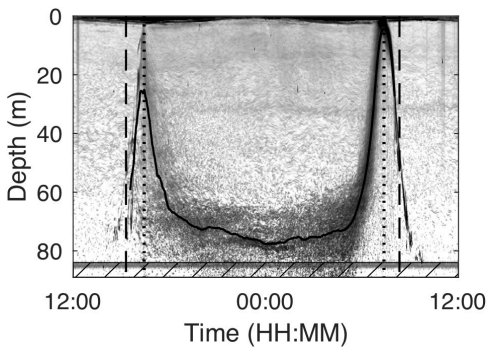

FIGURE 2 | Example echogram from January 22, 2011 as recorded by a 200 kHz echosounder deployed at around 92 m depth in Masfjorden with annotations showing the results of the scattering layer description. The solid line indicates the depth of the middle of the scattering layer. Dashed lines indicate the start of the dusk descent (beginning of midnight sinking) and the end of the dawn ascent (end of midnight sinking). Interrupted lines show the time of sunset and sunrise on that day. The line at around 84 m depth is noise. Data in the hatched box in the lowest part of the echogram were not included in the scattering layer description due to that noise, but were included during target tracking.

Quantification of Tracks and Behavior

The workflow during track processing and filter criteria as outlined below are summarized in the **Supplementary Figure S3**. The data were processed and analyzed in Matlab (Mathworks; R2017b). We first applied a filter to exclude potential other targets than *M. muelleri*. This identity filter included a threshold in mean TS (**Figure 3**) and excluded daytime tracks from after sunrise and before sunset. We determined the TS thresholds by manually tracking *M. muelleri* individuals on one randomly selected day of each of the 4 months (about 800 tracks per day) and then identifying the TS range that included about 90% of the tracked individuals on these 4 days. Tracks with a mean TS outside the defined range were excluded from further analysis. This procedure allowed identification of *M. muelleri* with a reduced influence of tilt angles (Miyashita et al., 1996) as fish in all different angles were included during the manual tracking. A minimum track duration of 30 s was used. The first time-point of each track determined whether the tracks were within the defined night-time hours.

After applying the identity filter, 613003 tracks remained and were further processed. Depth outliers of each individual track

TABLE 1 | Settings used in the automatic target tracking analysis in Sonar5-Pro (Balk and Lindem, 2017).

	Range (m)								
Track properties	**10**	**20**	**30**	**40**	**50**	**60**	**70**	**80**	**90**
Minimum track length (Nr. of echoes)	10	20	20	30	40	30	30	30	30
Maximum ping gap (Nr. of echoes)	3	5	5	5	10	10	5	5	0
Gating	**Ping**		**Range (m)**		**Ath (°)**		**Alo (°)**		
Initial size	1		0.1		5		5		
Increase with missing ping			0.01		0.1		0.1		
Association	**Ping**		**Range (m)**		**Ath (°)**		**Alo (°)**		**TS (dB)**
Distance weights	50		10		1		1		1
Prediction	**A**		**B**						
Alpha Beta	0.5		0.5						

Note that names in the table reflect those in the program. Range (m) represents distance from the transducer, where a range of 10 m is at about 84 m depth and a range of 90 m is at ∼4 m depth. Gating describes the process where the location of the next echo of a track is estimated. The association unit evaluates different track predictions based on user-defined weights. Gating and weights for association are defined for ping distance, range (m), along (Alo (°)), and athwart (Ath (°)) angles. Association also includes a weight on TS (target strength, dB). Alpha Beta is a prediction method. See Balk and Lindem (2017) for further information.

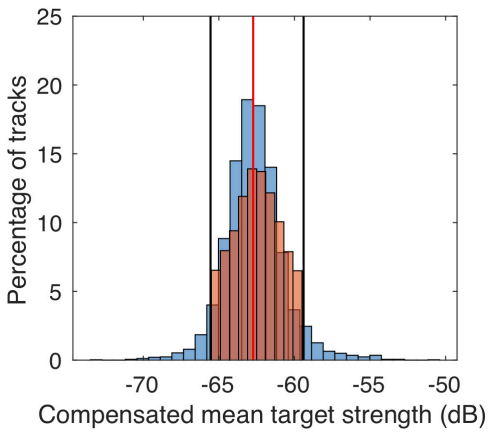

FIGURE 3 | Comparison of target strengths of manually (blue bars) and automatically (orange bars) tracked individuals on four randomly selected dates (one from each month; December 10, 2010, January 8, 2011, February 24, 2011, and March 1, 2011). The red vertical line indicates the median target strength and the black lines the limits of the 90% distribution of target strengths which were used to filter automatically tracked *M. muelleri* tracks.

were removed by first calculating a running median as well as a running median absolute deviation (MAD) (each with a window of 10 echoes) of the track's depths and then replacing depth values that deviated from the running median by more than the MAD × 10 by the running median. In the next step, a running mean (window size of 10 echoes) was applied to the depth values of each such treated track. We calculated net vertical displacement (m), track duration (s) and vertical velocity (vertical displacement divided by track duration; cm s^{-1}) of each track. Each track was also examined for patterns of alternations between segments of active vertical ascent or descent, and pauses in which fish maintained a constant depth, although they might have been active in the horizontal plane (**Supplementary Figure S4**). We determined and subsequently counted the pauses in each track using thresholds. We defined parts of the tracks with depth changes < 0.01 m between at least four subsequent echoes, as pauses and those with larger depth changes as active phases. Single values of pauses or active phases were filled by the surrounding values. For example, when in the vector x = [0,0,0,1,0,0,1,1,1,1,0,0], the digit 1 stands for "pause" and 0 for "active phase," then the resulting index vector of which echoes should be regarded as pause would look like this: y = [0,0,0,0,0,0,1,1,1,1,0,0]. The first and last segments (i.e., the first and last ascent, descent or pause) of each accepted track with more than two pauses were excluded in order to reduce errors from the target tracking, stemming from potentially overlapping tracks. Tracks with < 60 echoes were considered fragments and were therefore excluded from further analysis. The remaining 272290 tracks were used for behavioral analysis.

Based on net vertical displacement, number of pauses and track duration, the tracks were assigned to either of three main swimming patterns (**Supplementary Figure S3**):

1. Step-wise swimming: targets change depth by alternating active upward/downward swimming and pauses (**Supplementary Figure S4**).
2. Stationary: targets maintain a constant depth throughout the track.
3. Direct swimming: targets change depth without pauses.

We then calculated the average active swimming speed (swimming speed, cm s^{-1}), i.e., the vertical velocity during active segments of each step-wise track. In stationary and direct tracks, the swimming speed equals the vertical velocity. Furthermore, we determined the proportion of the three different swimming patterns in relation to time from the start of the dusk descent and time to the end of the dawn ascent, in order to account for seasonal changes. We also calculated the proportion of ascending

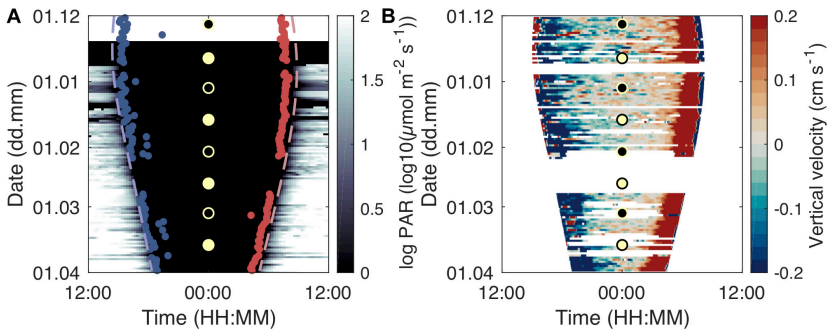

FIGURE 4 | Development of migration timing and velocity over daytime and season. Light intensity and start of dusk descent (beginning of midnight sinking; blue dots) and end of morning ascent (end of midnight sinking; red dots) over the study period and daytime **(A)**. The dashed lines indicate sunset (blue) and sunrise (red). Development of scattering layer vertical velocity over daytime and the study period **(B)**. Warm colors denote upward movement of the scattering layer while cold colors show a downward movement. The circles indicate full moon (yellow fill) and new moon (black fill).

and descending step-wise tracks, as well as their average vertical velocities in relation to daytime and depth using data binned by depth (3 m intervals) and time (72 min). The proportion of ascending tracks for each bin was determined when more than five tracks were found in the respective bin.

RESULTS

Population Migration

The vertical distribution of the scattering layer ascribed to juvenile *M. muelleri* differed distinctly between day and night and was characterized by short-term migrations to the surface at dusk and dawn (**Figure 1**). After the dusk ascent, the population returned to intermediate depths, deepening from an average of 60 m in December to 70 to 75 m in February and March. From mid-January, the vertical distribution changed continuously throughout the night, with the scattering layer moving deeper before midnight and reversing direction after midnight (**Figure 4**). The daytime distribution was generally deeper and below 100 m. The deeper scattering layer ascribed to the adults mostly stayed below 120 m depth throughout the diel cycle, but a small proportion of this adult population sometimes migrated to shallower depths at night (**Figure 1**).

The timing of the dusk descent and dawn ascent of the juveniles changed over the study period in accordance with seasonal changes in sunrise and sunset (**Figure 4A**). The dusk descent from near-surface waters started about 20–70 min after sunset after the fish had spent around 20–40 min in waters shallower than 20 m. The dawn ascent ended around 40–70 min before sunrise on most days and the fish stayed in near-surface waters (<20 m) for about 40–60 min. The duration between these migrations and sunset/sunrise shortened over the study period (**Figure 4A**). On darker, foul weather days (e.g., March 20–25, 2011; **Figure 4A**), dusk descent started earlier and dawn ascent ended later. We did not find a clear relationship of population movement with moon phases (see **Supplementary Figure S5** for a combination of **Figure 4** with cloud cover and moon phase data). Interrupted upward migrations in the afternoon, where the majority of the population started descending again before reaching the surface, were observed on 39 out of 98 analyzed diel echograms.

Population descent velocities were highest ∼30 min after the start of the dusk descent, while ascent velocities were highest 30–40 min before reaching the surface layers in the morning (**Figure 4B**). The maximum velocity of the scattering layer during the dusk descent increased from ∼0.5 cm s^{-1} in December to ∼0.8 cm s^{-1} in March. The maximum velocity during the dawn ascent increased from ∼1 cm s^{-1} in December to ∼1.5 cm s^{-1} in March. On most days, the dawn ascent was faster than the dusk descent.

Individual Swimming Behavior

Of the 272290 tracks, 142547 were classified as step-wise swimming, with 56744 tracks ascending and 85803 descending (**Table 2**). In total 127221 tracks displayed no or little vertical movement and were classified as stationary. An additional 2522 tracks were directly ascending/descending without steps. Duration and net vertical displacement of individuals depended on the respective swimming pattern (**Table 2** and **Figure 5**).

Step-wise swimming was especially prominent during the dusk and dawn migrations (**Figures 6**, **7**). Around 75% of the fish swam step-wise around the start of the dusk descent. Although descending step-wise tracks dominated throughout this period of population descent, some ascending individuals were also recorded. During the latter part of the night, the proportion of step-wise swimming behavior increased (**Figure 7**), reaching a maximum of 87% at the end of the dawn ascent, but then also with a high proportion (>25%) of step-wise descending individuals. The net vertical relocation speed was ∼0.9 cm s^{-1}, while the actual swimming speed during the vertical steps was ∼2–3 cm s^{-1} (**Table 2**).

Vertically stationary tracks dominated (>50%) the nocturnal records throughout most of the night. These tracks usually lasted for > 1 min, with the track duration being restricted by the number of co-occurring tracks (**Figure 6C**). In most of the cases where *M. muelleri* relocated vertically, they moved step-wise (**Figures 6**, **7**). Additional vertical displacement was caused by

TABLE 2 | Major track parameters obtained by automatic target tracking for the whole study period from December 1, 2010 to March 31, 2011 (92 days with tracking data).

	Number	Duration (s)	Net vertical displacement (m)	Vertical velocity (cm s^{-1})	Swimming speed (cm s^{-1})
Step-wise	142547	150 ± 220	0.91 ± 0.5	0.89 ± 0.7	2.54 ± 1.6
Ascending	56744	145 ± 237	0.94 ± 0.56	0.94 ± 0.8	2.93 ± 1.7
Descending	85803	152 ± 208	0.9 ± 0.46	0.86 ± 0.7	2.28 ± 1.4
Stationary	127221	79 ± 46	0.1 ± 0.09	0.14 ± 0.1	0.14 ± 0.1
Direct	2522	149 ± 103	1.1 ± 0.93	1.57 ± 2.0	1.58 ± 2.1
Ascending	770	162 ± 95	0.88 ± 0.7	1.03 ± 1.6	1.04 ± 1.6
Descending	1752	143 ± 106	1.22 ± 1	1.81 ± 2.2	1.81 ± 2.2
Total	272290	117 ± 166	0.54 ± 0.56	0.55 ± 0.7	1.41 ± 1.7

Data are mean ± standard deviation. Vertical velocity is the net vertical displacement over time, including pauses, while swimming speed is the average velocity during active phases.

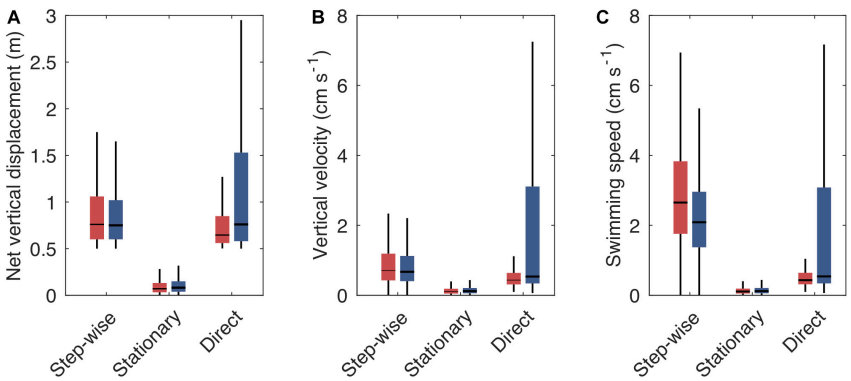

FIGURE 5 | Boxplot showing the vertical swimming characteristics [net vertical displacement **(A)**, vertical velocity **(B)**, and swimming speed **(C)**] of step-wise, stationary and direct tracks when ascending (red boxes) or descending (blue boxes). Vertical velocity is the net vertical displacement over time, including pauses, while swimming speed is the average velocity during active phases. Boxes indicate the interquartile range, horizontal lines the median, vertical lines the first and fourth quartile. Outliers are not shown. For number of tracks with the respective swimming pattern see **Table 2**.

apparent internal waves. In a subsample of randomly selected days, internal wave amplitudes were around 0.7 m (range 0–1.8 m) and periods about 10 min (range 0–30 min). Internal waves led to vertical transitions of up to 0.6 cm s^{-1}, but usually around 0.2 cm s^{-1}, in otherwise stationary animals.

Even though there were main migration periods at dusk and dawn and dominance of stationary tracks at night, there was a clear pattern of the majority of step-wise relocating individuals descending before midnight and ascending after midnight (**Figure 8**). This pattern was accentuated toward the end of the study period (**Figure 8A**). The proportion of descending and ascending tracks depended on depth (**Figure 8B**). During the first half of the night, descending tracks dominated at all depths, nevertheless we observed the highest proportion of descending tracks in shallow layers of 20–40 m depth. In layers between 70 and 80 m, there always was a strong majority of ascending tracks subsequent to midnight. Correspondingly, the average displacement was downward before midnight and upward after midnight. Individual velocities reached > 1 cm s^{-1} during the dusk and dawn migrations, while velocities in the middle of the night were mostly lower. Maximum velocities increased over winter.

The individual behavior during the overall population's upward migration in the afternoon and descent in the morning, differed from that observed at night. During these main migration periods, most pearlsides schooled and individuals could not be resolved. However, individuals could occasionally be detected close to these schools. The pause duration in these individuals was short and some of these individuals refrained from pausing altogether and either ascended or descended directly (**Figure 8**). The highest vertical velocities were achieved in such direct tracks, with means of 1.0 and 1.8 cm s^{-1} in ascending and descending tracks, respectively (**Table 2**).

DISCUSSION

Our approach allowed for unique observations of the individual behavior of a mesopelagic fish. The long-term records, combined with high temporal resolution generated representative data for a whole winter period. We are confident in allocating the observed behavior to juvenile *M. muelleri* due to their well established and distinct vertical distribution pattern in this location (Giske et al., 1990; Staby and Aksnes, 2011;

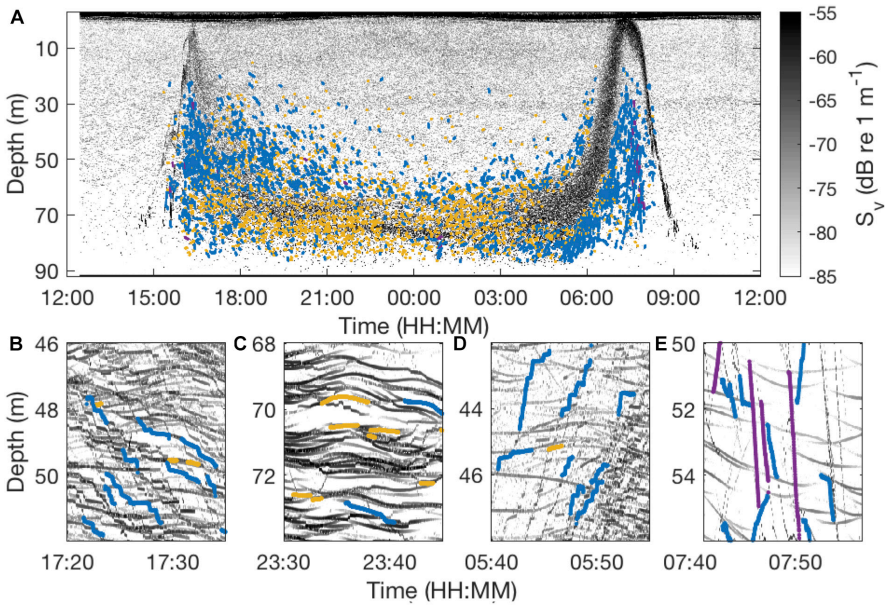

FIGURE 6 | Echogram from January 22, 2011 recorded with a 200 kHz EK60 Echosounder **(A)** and zoomed into 15-min snapshots representing different periods of nocturnal behavior: the dusk descent **(B)**, the middle of the night **(C)**, the dawn ascent **(D)**, and the dawn descent **(E)**. Tracks representing different types of behaviors are depicted in colored lines with blue lines indicating step-wise swimming, yellow lines stationary behavior and purple lines direct ascents/descents.

Staby et al., 2012; Prihartato et al., 2015) that was also confirmed by trawling at the initiation and termination of our campaign (own unpublished results). **Figure 9** summarizes the typical population movement and the dominant individual swimming patterns of the juvenile *M. muelleri* population in Masfjorden during the winter of 2010/2011.

Also earlier short-term acoustic studies have revealed step-wise swimming in individual mesopelagic fish and preliminarily assigned the behavior to *M. muelleri* and *B. glaciale* (Torgersen, 2001; Kaartvedt et al., 2008). Our study using hundreds of thousands of tracks from a period of 4 months shows that *M. muelleri* juveniles consistently swim step-wise when changing depth at night. The dominance of step-wise swimming during the dusk descent – roughly mirroring the dawn ascent – indicates that midnight sinking is not "sinking," but rather encompasses active behavior in *M. muelleri*. The fishes may have been slightly negatively buoyant during the descent as secretion of gas into the swim bladder takes time (Strand et al., 2005), and juveniles often seemed to slowly sink during pauses of their step-wise descent (average 0.25 cm s^{-1}; preliminary results). Nevertheless, swimming speeds during active relocation were almost 10-fold higher.

To what extent midnight sinking represents sinking or an active behavior is often unknown (Pearre, 2003). The consistent active choice of deeper night-time distribution by *M. muelleri* underscores the biological significance of such behavior. Some visual predators are capable of nocturnal feeding also in low light levels (Ryer and Olla, 1999; Kaartvedt et al., 2019). This includes gadoids, which are main predators of *M. muelleri* in Masfjorden (Giske et al., 1990; Staby, 2010), and which indeed migrate to surface waters during winter nights (Staby, 2010).

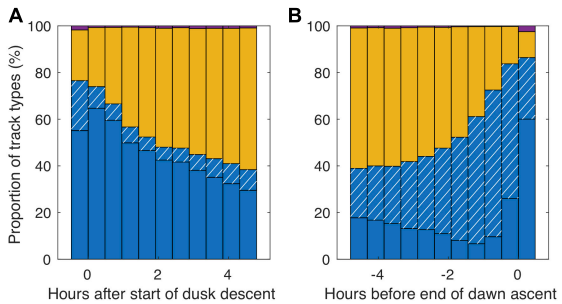

FIGURE 7 | Proportion of different swimming patterns in relation to the start of the dusk descent (beginning of midnight sinking; **A**) and the end of the dawn ascent (end of midnight sinking; **B**). Blue (descending) and blue hatched (ascending) bars indicate staircasing behavior, yellow bars stationary swimming and purple bars direct ascent/descent behavior.

The predator distribution indicates that deeper would be safer. It also suggests that descending in a step-wise pattern may reflect some anti-predatory behavior (see below). Although the increase of the population's night-time depth over winter could agree with a deepening of the temperature maximum in Masfjorden (c.f. Prihartato et al., 2015), the continuous relocation of individuals throughout the night indicates no particular temperature preference. This suggests that other factors than growth optimization in warmer temperatures (Wurtsbaugh and Neverman, 1988; Giske and Aksnes, 1992; Staby et al., 2011; Prihartato et al., 2015), play a role for nocturnal descent in *M. muelleri*.

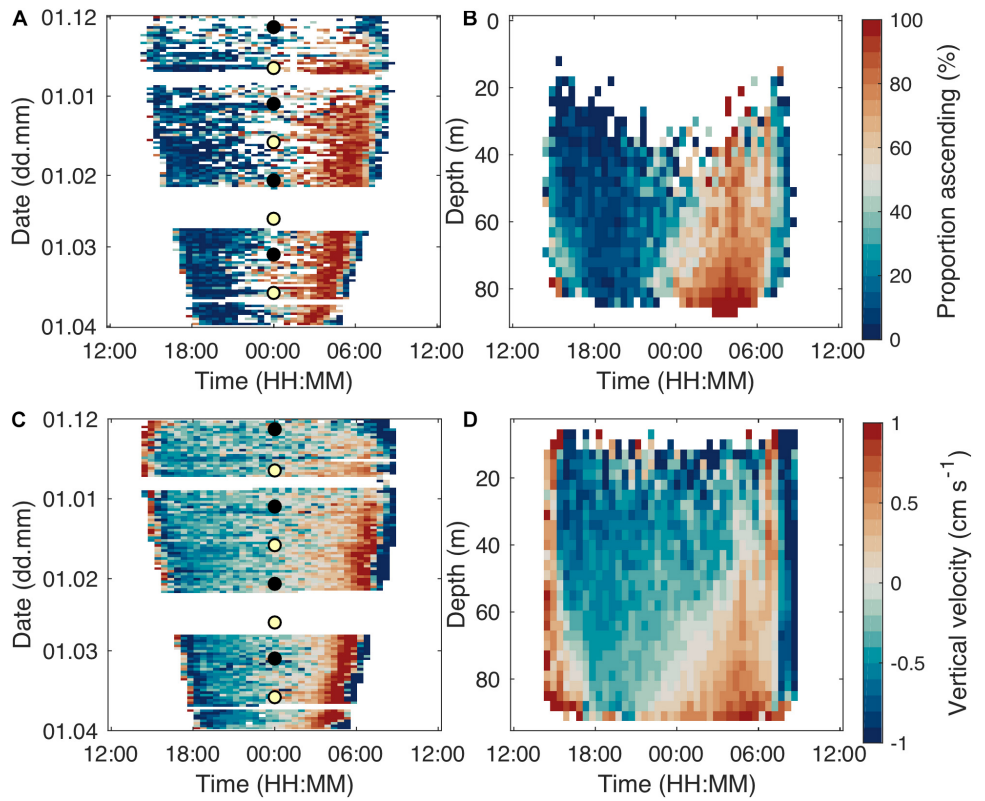

FIGURE 8 | Proportion of (step-wise swimming) ascending tracks, integrated over the whole water column, over daytime and study period **(A)**. Mean image of proportion of ascending stepping tracks over depth and daytime with data from the whole study period **(B)**. Warm colors indicate a higher proportion of ascending individuals. Each bin contains data from at least five tracks. Average vertical velocity of step-wise swimming individuals integrated over depth **(C)** and study period **(D)**. The circles in **(A,C)** indicate full moon (yellow fill) and new moon (black fill).

After the dusk descent and through most of the night, the majority of the fish appeared to be neutrally buoyant, remaining relatively stationary, with short vertical relocations intermitted by long pauses. Such behavior may both save energy (Videler and Weihs, 1982; Torgersen, 2001) and reduce conspicuousness (O'Brien et al., 1990). Nevertheless, there was a small percentage of relocating individuals at all times, which is also reflected in the scattering layer not reaching a constant depth at night. It is intriguing that the shift from predominantly downward to upward swimming on most days took place many hours before dawn during the long winter nights (cf. **Figures 4**, **8**; Staby et al., 2011). This suggests that internal processes, e.g., an internal clock determine the start of the ascent (Cohen and Forward, 2005; Sloman et al., 2005; Tosches et al., 2014; Häfker et al., 2017), while only the speed of the ascent is regulated by the change in light hours later.

The dawn ascent was usually faster than the dusk descent, both on population and individual levels. Although reflecting apparently similar behavior, dusk descent and dawn ascent occur under vitally different environmental conditions. During the dusk descent, the fish swim into darkening water after light levels at the surface have become too low for foraging (de Busserolles et al., 2017), so that the fish merely retreat to more favorable conditions to spend the hours of darkness. In contrast, the step-wise swimming toward increasing light during the dawn ascent initiates a foraging period.

The step-wise behavior observed for both situations, i.e., with and without foraging, contrasts suggestions that stepwise relocation in mesopelagic fish represents saltatory search for prey (Kaartvedt et al., 2008). The similar behavior at descent and ascent is probably also unrelated to swim-bladder adjustment (Mehner, 2006; Fujino et al., 2009), as filling the swim-bladder during descent is a considerably slower process than emptying it during ascent (ascent; Strand et al., 2005). Also, some individuals at the fringes of the schools swam without stepping, i.e., without apparent need for swim-bladder adjustment. Being relatively safe in the vicinity of a school of conspecifics may elicit a different swimming behavior than when swimming solitary, in concordance with a hypothesis of predator-avoidance by step-wise swimming (O'Brien et al., 1990).

Motility represents a balance between maximizing encounter with prey and mates and minimizing encounter with predators. The probability of detection by a predator is higher when moving (O'Brien et al., 1990), and the pauses during step-wise swimming can reduce detection by both visual (De Robertis, 2003; Kaartvedt et al., 2008) and tactile predators (Sørnes and Aksnes, 2004). Moreover, for *M. muelleri,* the intermittent stepping behavior may minimize periods of reduced protection associated with

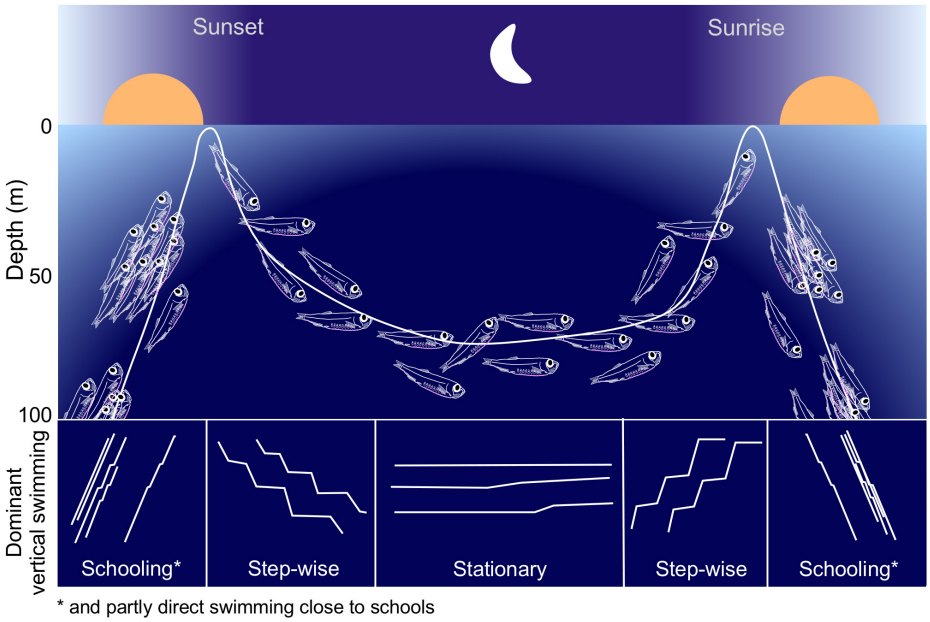

FIGURE 9 | Schematic showing a typical night time distribution and behavior of *M. muelleri* juveniles in Masfjorden. The lower part of the figure indicates the dominant vertical swimming patterns during different parts of the night.

change in tilt. The pearlside is particularly well equipped with ventral photophores for counter illumination (Cavallaro et al., 2004), which are less effective at tilted angles, i.e., when moving vertically (Janssen and Harbison, 1986).

Individual behavior generally, but not always, concurred with the behavior of the scattering layer. For example, at times of fast, continuous scattering layer movements, we also recorded a high proportion of step-wise swimming. Similarly, mostly stationary fish made up the very slow population movements in the middle of the night. On the other hand, we demonstrate that actual swimming speeds during relocations cannot be inferred from the average population movement. Active swimming speeds reached about 1 body length s^{-1} (assuming a body length of about 2.6 cm; Goodson et al., 1995), while scattering layer and individual net velocities always remained well below this value. This may have implications for understanding the energetics of these fish (Giske and Aksnes, 1992; Staby et al., 2012), as energetic costs typically assume a non-linear dependency on speed (e.g., McKenzie, 2011), and energetic models often assume a speed of 1 body length s^{-1} (Staby et al., 2012). Furthermore, there were always individuals swimming in opposite direction to that of the main population, documenting a more diverse behavioral repertoire than that expressed by the main population results.

While the population behavior by necessity results from the cumulative of the individual behaviors, we document that it is not possible to infer individual behavior from the behavior of the average population. We observed intraspecific variability in swimming behavior, both on population level, e.g., in migration timing, and on individual level, e.g., vertical directionality and swimming pattern. Probably, variability in population behavior may best be explained by external factors generating reliable large-scale interpretable signals, as for example light conditions (Prihartato et al., 2015). Water column light levels depend strongly on weather and mesopelagic fish react directly to e.g., darkening caused by rainfall (Kaartvedt et al., 2017) or to moon light (Last et al., 2016; Prihartato et al., 2016). Moon light may deepen night time scattering layer depths (Prihartato et al., 2016) and delay vertical migrations. However, in the typically cloudy and rainy Western Norway and Masfjorden, clear full moon nights are rare, suggesting limited if any influence of moonlight on the behavioral variability in our study (s.a. **Supplementary Figure S5**).

The behavioral options of each individual are manifold, and reflect responses to a whole suite of more local sensory cues, e.g., from predators, prey and conspecifics, and behavior obviously also depends on individual state (Pearre, 2003; Sih et al., 2015). The observed variability in individual behavior suggests that although the vertical migration in *M. muelleri* is generally synchronized, the fishes may behave independent of the group. Whether these differently behaving individuals differ in size, metabolic demands or are otherwise distinguishable from the rest of the population remains unknown for now.

While we can still only speculate about why mesopelagic fish behave as they do, our study documents the feasibility of using a submerged, stationary echosounder in unveiling the individual behavior responsible for the large scale, more easily observed, scattering layer movements of mesopelagic fish. We demonstrate that midnight sinking is not sinking, but an active behavior. The behavioral repertoire of these fish changes not only during the crepuscular migrations, but also during the night at large, with consistent patterns throughout the winter, and

with variations between the individuals within the population. Only with an increased understanding of what these fish actually do can we begin to estimate the ecological interactions involving the enormous amounts of small mesopelagic fish in the world's oceans.

DATA AVAILABILITY STATEMENT

All data supporting the conclusion of this manuscript will be made available upon request, to any qualified researcher.

ETHICS STATEMENT

The acoustic studies did not involve any animal treatment, handling, or experiments. Data and results were only obtained by remote, unobtrusive observation.

AUTHOR CONTRIBUTIONS

SK designed the study and obtained the field data. SC organized and analyzed the data and wrote the manuscript. JT and SK contributed to the improvement of the analysis and writing of the manuscript. All authors contributed to manuscript revision.

FUNDING

The fieldwork was funded by the King Abdullah University of Science and Technology, Saudi Arabia.

ACKNOWLEDGMENTS

We thank Anders Røstad and Thor A. Klevjer for invaluable logistic help with the acoustic studies. We would like to thank Helge Balk for assistance with the Sonar5-Pro software. Comments from the two reviewers helped to improve the manuscript.

SUPPLEMENTARY MATERIAL

The Supplementary Material for this article can be found online at: https://www.frontiersin.org/articles/10.3389/fmars.2019.00787/full#supplementary-material

REFERENCES

Bagøien, E., Kaartvedt, S., Aksnes, D. L., and Eiane, K. (2001). Vertical distribution and mortality of overwintering *Calanus*. *Limnol. Oceanogr.* 46, 1494–1510. doi: 10.4319/lo.2001.46.6.1494

Balino, B. M., and Aksnes, D. L. (1993). Winter distribution and migration of the sound scattering layers, zooplankton and micronekton in Masfjorden, western Norway. *Mar. Ecol. Prog. Ser.* 95, 35–50. doi: 10.3354/meps095035

Balk, H., and Lindem, T. (2000). Improved fish detection in data from split-beam sonar. *Aquat. Living Resour.* 13, 297–303. doi: 10.1016/S0990-7440(00)01079-1072

Balk, H., and Lindem, T. (2001). *Inventors; Bryns Patentkontor A/S P.O. Box 765, Sentrum N-0106*. Patent No. PCT/NO2000/000288. Oslo, NO: University of Oslo.

Balk, H., and Lindem, T. (2002). "A new method for single target detection," in *Proceedings of the ICES 6th Symposium on Acoustics in Fisheries and Aquatic Ecology*, Montpellier.

Balk, H., and Lindem, T. (2017). *Sonar4 and Sonar5-Pro Post Processing Systems, Operator Manual Version 604*. Oslo: CageEye AS.

Brede, R., Kristensen, F. H., Solli, H., and Ona, E. (1990). Target tracking with a split-beam echo sounder. *Rapp. PV Reùn. Cons. Int. Explor. Mer.* 189, 254–263.

Cavallaro, M., Mammola, C. L., and Verdiglione, R. (2004). Structural and ultrastructural comparison of photophores of two species of deep-sea fishes: *Argyropelecus hemigymnus* and *Maurolicus muelleri*. *J. Fish Biol.* 64, 1552–1567. doi: 10.1111/j.0022-1112.2004.00410.x

Cohen, J. H., and Forward, R. B. (2005). Diel vertical migration of the marine copepod *Calanopia americana*. II. Proximate role of exogenous light cues and endogenous rhythms. *Mar. Biol.* 147, 399–410. doi: 10.1007/s00227-005-1570-1574

Cushing, D. H. (1951). The vertical migration of planktonic Crustacea. *Biol. Rev.* 26, 158–192. doi: 10.1111/j.1469-185x.1951.tb00645.x

de Busserolles, F., Cortesi, F., Helvik, J. V., Davies, W. I. L., Templin, R. M., Sullivan, R. K. P., et al. (2017). Pushing the limits of photoreception in twilight conditions: the rod-like cone retina of the deep-sea pearlsides. *Sci. Adv.* 3:eaao4709. doi: 10.1126/sciadv.aao4709

De Robertis, A. (2003). Acoustic observations of the swimming behavior of the euphausiid *Euphausia pacifica* hansen. *ICES J. Mar. Sci.* 60, 885–898. doi: 10.1016/S1054-3139(03)00070-75

Falk-Petersen, I. B., Falk-Petersen, S., and Sargent, J. R. (1986). Nature, origin and possible roles of lipid deposits in *Maurolicus muelleri* (Gmelin) and *Benthosema glaciale* (Reinhart) from Ullsfjorden, Northern Norway. *Polar Biol.* 5, 235–240. doi: 10.1007/BF00446091

Fujino, T., Sadayasu, K., Abe, K., Kidokoro, H., Tian, Y., Yasuma, H., et al. (2009). swimbladder morphology and target strength of a mesopelagic fish, *Maurolicus japonicus*. *J. Mar. Acoust. Soc. Jpn.* 36, 241–249. doi: 10.3135/jmasj.36.241

Giske, J., and Aksnes, D. L. (1992). Ontogeny, season and trade-offs: vertical distribution of the mesopelagic fish *Maurolicus muelleri*. *Sarsia* 77, 253–261. doi: 10.1080/00364827.1992.10413510

Giske, J., Aksnes, D. L., Baliño, B. M., Kaartvedt, S., Lie, U., Nordeide, J. T., et al. (1990). Vertical distribution and trophic interactions of zooplankton and fish in Masfjorden, Norway. *Sarsia* 75, 65–81. doi: 10.1080/00364827.1990.10413442

Goodson, M. S., Giske, J., and Rosland, R. (1995). Growth and ovarian development of *Maurolicus muelleri* during spring. *Mar. Biol.* 124, 185–195. doi: 10.1007/BF00347122

Häfker, N. S., Meyer, B., Last, K. S., Pond, D. W., Hüppe, L., and Teschke, M. (2017). Circadian clock involvement in zooplankton diel vertical migration. *Curr. Biol.* 27, 2194–2201.e3. doi: 10.1016/j.cub.2017.06.025

Hammerschlag, N., Meyer, C. G., Grace, M., Kessel, S., Sutton, T., Harvey, E., et al. (2017). Shining a light on fish at night: an overview of fish and fisheries in the dark of night, and in deep and polar seas. *BMS* 93, 253–284. doi: 10.5343/bms.2016.1082

Handegard, N. O. (2007). Observing individual fish behavior in fish aggregations: tracking in dense fish aggregations using a split-beam echosounder. *J. Acoust. Soc. Am.* 122, 177–187. doi: 10.1121/1.2739421

Janssen, J., and Harbison, G. R. (1986). Hatchetfishes hold horizontal attitudes during diagonal descents. *J. Mar. Biol. Ass.* 66, 825–833. doi: 10.1017/S0025315400048451

Kaartvedt, S., Aksnes, D. L., and Aadnesen, A. (1988). Winter distribution of macroplankton and micronekton in Masfjorden, western Norway. *Mar. Ecol. Prog. Ser.* 45, 45–55. doi: 10.3354/meps045045

Kaartvedt, S., Langbehn, T. J., and Aksnes, D. L. (2019). Enlightening the ocean's twilight zone. *ICES J. Mar. Sci.* 76, 803–812. doi: 10.1093/icesjms/fsz010

Kaartvedt, S., Røstad, A., and Aksnes, D. L. (2017). Changing weather causes behavioral responses in the lower mesopelagic. *Mar. Ecol. Prog. Ser.* 574, 259–263. doi: 10.3354/meps12185

Kaartvedt, S., Røstad, A., Klevjer, T. A., and Staby, A. (2009). Use of bottom-mounted echo sounders in exploring behavior of mesopelagic fishes. *Mar. Ecol. Prog. Ser.* 395, 109–118. doi: 10.3354/meps08174

Kaartvedt, S., Torgersen, T., Klevjer, T. A., Røstad, A., and Devine, J. A. (2008). Behavior of individual mesopelagic fish in acoustic scattering layers of Norwegian fjords. *Mar. Ecol. Prog. Ser.* 360, 201–209. doi: 10.3354/meps07364

Last, K. S., Hobbs, L., Berge, J., Brierley, A. S., and Cottier, F. (2016). Moonlight drives ocean-scale mass vertical migration of zooplankton during the arctic winter. *Curr. Biol.* 26, 244–251. doi: 10.1016/j.cub.2015.11.038

MacLennan, D. (2002). A consistent approach to definitions and symbols in fisheries acoustics. *ICES J. Mar. Sci.* 59, 365–369. doi: 10.1006/jmsc.2001.1158

McKenzie, D. J. (2011). *Energetics of Fish Swimming*. Amsterdam: Elsevier Inc.

Mehner, T. (2006). Individual variability of diel vertical migrations in European vendace (Coregonus albula) explored by stationary vertical hydroacoustics. *Ecol. Freshw. Fish* 15, 146–153. doi: 10.1111/j.1600-0633.2006.00137.x

Miyashita, K., Aoki, I., and Inagaki, T. (1996). Swimming behavior and target strength of isada krill (*Euphausia pacifica*). *ICES J. Mar. Sci.* 53, 303–308. doi: 10.1006/jmsc.1996.0039

O'Brien, W. J., Browman, H. I., and Evans, B. I. (1990). Search strategies of foraging animals. *Am. Sci.* 78, 152–160.

Olivar, M. P., Hulley, P. A., Castellón, A., Emelianov, M., López, C., Tuset, V. M., et al. (2017). Mesopelagic fishes across the tropical and equatorial Atlantic: biogeographical and vertical patterns. *Prog. Oceanogr.* 151, 116–137. doi: 10.1016/j.pocean.2016.12.001

Pearre, S. (2003). Eat and run? The hunger/satiation hypothesis in vertical migration: history, evidence and consequences. *Biol. Rev. Camb. Philos. Soc.* 78, 1–79. doi: 10.1017/S146479310200595X

Prihartato, P. K., Aksnes, D. L., and Kaartvedt, S. (2015). Seasonal patterns in the nocturnal distribution and behavior of the mesopelagic fish *Maurolicus muelleri* at high latitudes. *Mar. Ecol. Prog. Ser.* 521, 189–200. doi: 10.3354/meps11139

Prihartato, P. K., Irigoien, X., Genton, M. G., and Kaartvedt, S. (2016). Global effects of moon phase on nocturnal acoustic scattering layers. *Mar. Ecol. Prog. Ser.* 544, 65–75. doi: 10.3354/meps11612

Rasmussen, O. I., and Giske, J. (1994). Life-history parameters and vertical distribution of *Maurolicus muelleri* in Masfjorden in summer. *Mar. Biol.* 120, 649–664. doi: 10.1007/BF00350086

Rudjakov, J. A. (1970). The possible causes of diel vertical migrations of planktonic animals. *Mar. Biol.* 6, 98–105. doi: 10.1007/BF00347238

Ryer, C. H., and Olla, B. L. (1999). Light-induced changes in the prey consumption and behavior of two juvenile planktivorous fish. *Mar. Ecol. Prog. Ser.* 181, 41–51. doi: 10.3354/meps181041

Sih, A., Mathot, K. J., Moirón, M., Montiglio, P.-O., Wolf, M., and Dingemanse, N. J. (2015). Animal personality and state–behaviour feedbacks: a review and guide for empiricists. *Trends Ecol. Evol.* 30, 50–60. doi: 10.1016/j.tree.2014.11.004

Simard, Y., Lacroix, G., and Legendre, L. (1985). In situ twilight grazing rhythm during diel vertical migrations of a scattering layer of *Calanus finmarchicus*. *Limnol. Oceanogr.* 30, 598–606. doi: 10.4319/lo.1985.30.3.0598

Sloman, K. A., Balshine, S., and Wilson, R. W. (2005). *Fish Physiology: Behaviour and Physiology of Fish*. Cambridge, MA: Academic Press.

Solberg, I., and Kaartvedt, S. (2017). The diel vertical migration patterns and individual swimming behavior of overwintering sprat Sprattus sprattus. *Prog. Oceanogr.* 151, 49–61. doi: 10.1016/j.pocean.2016.11.003

Sørnes, T. A., and Aksnes, D. L. (2004). Predation efficiency in visual and tactile zooplanktivores. *Limnol. Oceanogr.* 49, 69–75. doi: 10.4319/lo.2004.49.1.0069

Staby, A. (2010). *Seasonal Dynamics of the Vertical Migration Behavior of Mesopelagic Fish*. Ph.D. thesis, University of Bergen, Bergen.

Staby, A., and Aksnes, D. L. (2011). Follow the light–diurnal and seasonal variations in vertical distribution of the mesopelagic fish *Maurolicus muelleri*. *Mar. Ecol. Prog. Ser.* 422, 265–273. doi: 10.3354/meps08938

Staby, A., Røstad, A., and Kaartvedt, S. (2011). Long-term acoustical observations of the mesopelagic fish *Maurolicus muelleri* reveal novel and varied vertical migration patterns. *Mar. Ecol. Prog. Ser.* 441, 241–255. doi: 10.3354/meps09363

Staby, A., Srisomwong, J., and Rosland, R. (2012). Variation in DVM behavior of juvenile and adult pearlside (*Maurolicus muelleri*) linked to feeding strategies and related predation risk. *Fish. Oceanogr.* 22, 90–101. doi: 10.1111/fog.12012

Strand, E., Jørgensen, C., and Huse, G. (2005). Modelling buoyancy regulation in fishes with swimbladders: bioenergetics and behavior. *Ecol. Model.* 185, 309–327. doi: 10.1016/j.ecolmodel.2004.12.013

Tarling, G. A., Jarvis, T., Emsley, S. M., and Matthews, J. (2002). Midnight sinking behavior in *Calanus finmarchicus*: a response to satiation or krill predation? *Mar. Ecol. Prog. Ser.* 240, 183–194. doi: 10.3354/meps240183

Torgersen, T. (2001). In situ swimming behavior of individual mesopelagic fish studied by split-beam echo target tracking. *ICES J. Mar. Sci.* 58, 346–354. doi: 10.1006/jmsc.2000.1016

Torgersen, T., Kaartvedt, S., Melle, W., and Knutsen, T. (1997). Large scale distribution of acoustical scattering layers at the Norwegian continental shelf and the Eastern Norwegian Sea. *Sarsia* 82, 87–96. doi: 10.1080/00364827.1997.10413642

Tosches, M. A., Bucher, D., Vopalensky, P., and Arendt, D. (2014). Melatonin signaling controls circadian swimming behavior in marine zooplankton. *Cell* 159, 46–57. doi: 10.1016/j.cell.2014.07.042

Treberg, J. R., Killen, S. S., MacCormack, T. J., Lamarre, S. G., and Enders, E. C. (2016). Estimates of metabolic rate and major constituents of metabolic demand in fishes under field conditions: methods, proxies, and new perspectives. *Comp. Biochem. Physiol. Part A* 202, 10–22. doi: 10.1016/j.cbpa.2016.04.022

Valle-Levinson, A., Castro, L., Cáceres, M., and Pizarro, O. (2014). Twilight vertical migrations of zooplankton in a Chilean fjord. *Prog. Oceanogr.* 129, 114–124. doi: 10.1016/j.pocean.2014.03.008

Videler, J. J., and Weihs, D. (1982). Energetic advantages of burst-and-coast swimming of fish at high speeds. *J. Exp. Biol.* 97, 169–178.

Wurtsbaugh, W. A., and Neverman, D. (1988). Post-feeding thermotaxis and daily vertical migration in a larval fish. *Nature* 333, 846–848. doi: 10.1038/333846a0

Conflict of Interest: The authors declare that the research was conducted in the absence of any commercial or financial relationships that could be construed as a potential conflict of interest.

Copyright © 2019 Christiansen, Titelman and Kaartvedt. This is an open-access article distributed under the terms of the Creative Commons Attribution License (CC BY). The use, distribution or reproduction in other forums is permitted, provided the original author(s) and the copyright owner(s) are credited and that the original publication in this journal is cited, in accordance with accepted academic practice. No use, distribution or reproduction is permitted which does not comply with these terms.

frontiers in Marine Science

ORIGINAL RESEARCH
published: 19 March 2020
doi: 10.3389/fmars.2020.00148

Non-breaking Wave Effects on Buoyant Particle Distributions

*Michelle H. DiBenedetto**

Woods Hole Oceanographic Institution, Woods Hole, MA, United States

The dispersal of buoyant particles in the ocean mixed layer is influenced by a variety of physical factors including wind, waves, and turbulence. Microplastics observations are often made at the free surface, which is strongly forced by surface gravity waves. Many studies have used numerical simulations to examine how turbulence and wave effects (e.g., breaking waves, Langmuir circulation) control buoyant particle dispersal at the ocean surface. However these simulations are not wave phase-resolving. Therefore, the effects of an unsteady free surface due to surface gravity waves remain unknown in this context. To address this, we develop an analytical model for the distribution of buoyant particles as a function of wave-phase under wind-wave conditions in deep-water. Using this analytical model and complementary numerical simulations, we quantify the effects of a nonbreaking, monochromatic, progressive wave train on the equilibrium vertical and horizontal distributions of buoyant particles. We find that waves result in non-uniform horizontal distributions of particles with more particles under the wave crests than the troughs. We also find that the waves can stretch or compress the equilibrium vertical distribution. Finally, we consider the effects of waves on the sampling of microplastics with a towed net, and we show that waves have the ability to lower the measured concentrations relative to nets sampling without the influence of waves.

Keywords: ocean waves, microplastics, particle distributions, sampling error, particle-laden flows, neuston nets

OPEN ACCESS

Edited by:
Aditya R. Nayak,
Florida Atlantic University,
United States

Reviewed by:
Erik Van Sebille,
Utrecht University, Netherlands
Junhong Liang,
Louisiana State University,
United States

****Correspondence:***
Michelle H. DiBenedetto
mdibenedetto@whoi.edu

Specialty section:
This article was submitted to Marine Ecosystem Ecology, a section of the journal Frontiers in Marine Science

Received: *09 January 2020*
Accepted: *26 February 2020*
Published: *19 March 2020*

Citation:
DiBenedetto MH (2020) Non-breaking Wave Effects on Buoyant Particle Distributions. Front. Mar. Sci. 7:148. doi: 10.3389/fmars.2020.00148

1. INTRODUCTION

Plastic pollution in the ocean is ubiquitous. It is found across ocean basins, in the deep-sea, and along our coasts. The estimated sources of plastic into the ocean exceed the current amount of plastic measured in the ocean (Jambeck et al., 2015; Geyer et al., 2017); this discrepancy has become a subject of interest in the scientific community. Solving this question of "missing plastic" requires both accurate measurements and a thorough understanding of oceanic microplastics sources and sinks.

Because a large fraction of plastic in the ocean is buoyant, microplastics measurements are frequently conducted at the surface of the ocean. Direct observations are representative of the microplastic concentration at the time of sampling. However, concentrations are a function of the local conditions: on a calm day, the buoyant plastic can aggregate at the surface, but strong winds can disperse plastic throughout the mixed layer. To address this variability, large-eddy simulations of buoyant particles at the ocean surface have been conducted to show how microplastics can redistribute due to turbulent mixing by wind, currents, breaking waves, and Langmuir circulation (Brunner et al., 2015; Kukulka and Brunner, 2015; Liang et al., 2018). While these studies have provided valuable insight into how particles distribute throughout the ocean mixed layer, they are

not wave-phase or free surface resolving; rather, they rely on parameterizations to include wave-averaged effects (see Chamecki et al., 2019 for a review). In reality, observations at the surface of the ocean are taken by a sampling apparatus that experiences individual wave events and an unsteady free surface. If waves induce phase variability in microplastics concentrations, and waves are not sampled uniformly, bias in the observations can result. Therefore, by studying buoyant particle distributions without wave-averaging, we are able to see important phenomena that may affect how we interpret data from free-surface net tow sampling.

A large body of work has studied the numerous ways in which waves affect surface transport and mixing processes. Waves induce a net drift in the direction of the waves, referred to as Stokes drift (see van den Bremer and Breivik, 2018 for a review); this drift is known to be important for microplastics transport from coastal shelf to oceanic scales (Isobe et al., 2014; Onink et al., 2019). Furthermore, the properties of the particles, such as inertia and shape, have also been shown to be relevant to their transport in waves (Eames, 2008; DiBenedetto et al., 2018). The ability of a wave field to disperse horizontal tracer particles has been studied as well (Herterich and Hasselmann, 1982). With regard to buoyant particles in waves, simulations similar to the ones reported here were conducted by Boufadel et al. (2006), who demonstrated how waves affect oil droplet plumes. Waves have also been studied in relation to ocean mixing through turbulence induced by wave orbital motion (Babanin, 2006). However, the effects of waves on the equilibrium distributions of buoyant particles has to our knowledge, not yet been reported.

In addition to hydrodynamic conditions, observations can be affected by the microplastic sampling method, e.g., net tows, grab samples, or filtering pumps (Hidalgo-Ruz et al., 2012; Prata et al., 2019). Some work has been done to address variability in measurements across methods (e.g., Setälä et al., 2016; Barrows et al., 2017; Karlsson et al., 2019); these studies have demonstrated that net tows can both under-sample and over-sample relative to other measurement techniques. While net tows are ideally conducted under calm conditions (e.g., sea states with Beaufort scales of 0–2) (Viršek et al., 2016), microplastics observations have been reported from conditions with Beaufort scales up to 5 (Eriksen et al., 2014; Kooi et al., 2016; Poulain et al., 2019). Therefore, moderate waves are often encountered during net tows.

Neuston (surface) net tows are conducted by trawling a net over a transect at the surface of the ocean. Captured particles are identified and counted in order to monitor microplastics surface concentrations. As sampling methods evolve and improve, understanding the variability and uncertainty in historic datasets is still necessary when analyzing temporal trends of microplastic pollution. Many longterm datasets are from observations taken with surface net tows (Law, 2010; Eriksen et al., 2014; van Sebille et al., 2015). Therefore, this study's discussion focuses on the influence of waves on the net tow sampling method.

This work describes and quantifies the effects of nonbreaking surface gravity waves on both the vertical and horizontal distributions of buoyant particles at the free surface, and relates these results to microplastics sampling. In section 2, current models used for interpreting microplastics measurements at the free surface are reported. Next, in section 3.1, an analytical description for the distribution of particles at the free surface including wave effects is developed, and in section 3.2, the numerical simulation methodology is described. The results of the models are shown in section 4. These results are considered in the context of microplastics sampling efforts in section 5. Finally, the article finishes with a discussion and summary of the major findings in sections 6 and 7. The purpose of this work is to inform current and past microplastics observations, as well as to provide context for the design of new microplastic sampling procedures. This study is only a first step in fully understanding how to interpret microplastics data, and wave-resolving direct numerical simulations and controlled laboratory experiments are recommended as future steps.

2. BACKGROUND

The ocean surface concentration of microplastics is both a function of the baseline average contamination level and the instantaneous hydrodynamics. Transient local forcing, such as wind and waves, introduce temporal and spatial variability to microplastics measurements. This variance disrupts the ability to directly compare observations. To account for this variance, specialized vertical mixing models have been developed; these models allow surface measurements to be extrapolated to total water column concentrations based on knowledge of local conditions. This process most often uses a one-dimensional model which we will refer to as the *wind-mixing model* as presented by Kukulka et al. (2012).

The wind-mixing model assumes a balance between the upward buoyancy flux and the downward turbulent flux of particles (Kukulka et al., 2012). This is represented as a horizontally-averaged concentration of microplastics c that is a function of vertical position z. At equilibrium, the total flux of particles is equal to zero. Following Kukulka et al. (2012), we assume an eddy dispersivity model for the turbulent flux, where κ_t is the eddy dispersivity of the particles and w_p is the particle's rise velocity. Setting the buoyancy flux equal to the turbulence flux of particles gives:

$$-w_p c = \kappa_t \frac{dc}{dz}. \tag{1}$$

The ratio of the eddy viscosity to the eddy dispersivity, ν_t/κ_t, also known as the turbulent Schmidt number Sc_t, is assumed to be unity. Further assuming that the particle rise velocity w_p and the turbulent eddy dispersivity κ_t are constant, Equation 1 can be directly integrated. Thus, the mean concentration of particles as a function of z follows an exponential curve with the surface concentration c_0 at the surface ($z = 0$):

$$c(z) = c_0 \exp(z/L_m). \tag{2}$$

The decay length scale, or mixing scale L_m, is defined as $L_m = \kappa_t/w_p$. This scale represents the relative depth over which particles are dispersed. Kukulka et al. (2012) assumes that

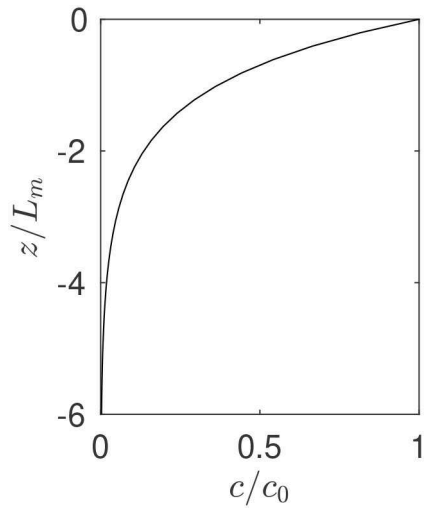

FIGURE 1 | Depth profile of normalized concentration of buoyant particles c/c_0 as a function of z/L_m according to the wind-mixing model as described by Equation (2).

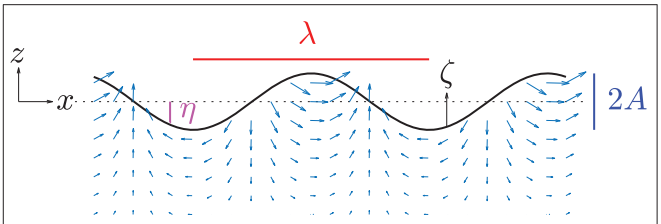

FIGURE 2 | Example of the wave geometry and the wave induced velocity field shown as scaled vectors. The wave is traveling in the postive x direction, with wavelength λ and wave amplitude A. The free surface is denoted by η, and ζ is the coordinate representing distance from the instantaneous free surface.

the depth of the mixed layer is much larger than L_m for the assumption of a constant κ_t to be valid. **Figure 1** shows the relationship described by Equation (2).

One common use of this model is to extrapolate surface measurements to total water column concentrations (e.g., Cozar et al., 2014; Kooi et al., 2016; Lebreton et al., 2018; Poulain et al., 2019). This extrapolation can be done by reconfiguring the model as a correction factor f defined as

$$f = \frac{N}{N_{tow}} = \frac{\int_{-\infty}^{0} c(z)dz}{\int_{z_0}^{0} c(z)dz} = \frac{1}{1 - \exp(z_0/L_m)}, \qquad (3)$$

where N is the predicted total count of microplastics in the water column, and N_{tow} is the number of microplastics captured in the towed net (Kukulka et al., 2012). The parameter z_0 represents the depth over which plastic was measured, or the average submergence of the towed net.

3. METHODS

The *wind-mixing model* is the current standard used to correct surface microplastic measurements, so we start with the assumptions within this model to examine the effects of surface gravity waves. This model includes only uniform turbulence and particle buoyancy. The assumption of constant eddy viscosity is only valid very close to the surface.

In addition, this model assumes that particle inertia effects are negligible. The relative importance of particle inertia can be defined by the particle's Stokes number St, which is a ratio between the particle relaxation timescale and the relevant flow timescale. A small Stokes number implies that the particle behaves as a flow tracer with little to no particle inertia effects. In this case, we assume the particle relaxation time τ_p is defined as $\tau_p = w_p/g$, and the relevant flow time scales are the wave period T and the Kolmogorov timescale of the turbulence τ_η. Thus, we can construct a wave Stokes number St_w and a turbulence Stokes number St_η. A common measured rise velocity for microplastics is $w_p = 1$ cm/s (Kukulka et al., 2012), which corresponds to buoyant microplastics of about 1 cm according to Figure 2 in Poulain et al. (2019). Using $\tau_p = w_p/g$, we find $\tau_p \approx 0.001$ s. Wind wave periods are on the order of seconds, so $St_w = \mathcal{O}(10^{-3}) \ll 1$ and the assumption of no particle inertia is valid. In terms of the turbulence, a conservative estimate using a high dissipation rate at the ocean surface boundary layer of 10^{-3} m^2/s^3 corresponds to $\tau_\eta \approx 0.03$ s (Zippel et al., 2018). In this case, $St_\eta = \mathcal{O}(10^{-2}) \ll 1$ as well. While the assumption of negligible particle inertia theoretically holds in this case for microplastic particles up to approximately 1 cm, finite-size effects may be important for particles at this size and should be studied further.

In order to isolate the wave effects, we consider a progressive train of surface gravity waves in deep-water. We start with linear wave theory which assumes that the wave-induced flow is irrotational, incompressible, and 2-dimensional. It also assumes small amplitude waves with a free surface deflection η, where $\eta = A\cos\theta$ and $\theta = kx - \omega t$ is the wave phase. In this system t represents time, x is the horizontal coordinate, and z is the vertical coordinate where $z = 0$ is the free surface. We further assume that the waves are traveling over an infinite depth H such that $kH \gg 1$, referred to as the deep-water wave limit. The waves are controlled by the wave number k, related to the wave length λ where $k = 2\pi/\lambda$; the wave frequency ω, related to the wave period T where $\omega = 2\pi/T$; and the wave amplitude A. These parameters are not independent as the deep-water dispersion relationship states $\omega = \sqrt{gk}$ where g is the acceleration due to gravity. We will refer to the vertical coordinate relative to the instantaneous free surface as $\zeta = z - \eta$. A schematic of the wave's geometry, its induced velocity field, and the coordinate system is shown in **Figure 2**.

In this model, without waves, the particles are mixed solely due to turbulence and vertically transported due to buoyancy, and the only length scale in the problem is the mixing scale L_m. With the addition of waves, new length scales are introduced. The waves are controlled by $\epsilon = kA$ which is the relative wave steepness. Linear wave theory assumes $\epsilon \ll 1$, and physically $\epsilon < 0.44$ or the waves will break (Stokes, 1880; Perlin et al.,

2013). To relate the mixing to the waves, we use the ratios A/L_m and kL_m.

The exact values of A/L_m and ϵ in the ocean will vary considerably. Kukulka et al. (2012) considered a range of L_m from about 0.4–4 m. The most extreme sea state that samples are conducted under is Beaufort 5 which can have wave amplitudes on the order of 1.5 m. Therefore, we report findings using A/L_m values of 1/3, 1, and 3 across a range of ϵ from 0 to 0.4 to demonstrate the variability of scenarios potentially encountered during sampling.

3.1. Analytical Model

3.1.1. Wave-Averaged Distribution

Surface gravity waves induce wave-orbital motions and deflect the free surface, both of which can affect buoyant particle distributions. We first address the distortion of the free surface; we model this effect by considering a superposition of the wind-mixing model shifted to the instantaneous free surface and averaged over a wave period. We assume a linear wave $\eta = A\cos\theta$, and we denote the phase-dependent concentration as $\widetilde{c}$, where in this case

$$\widetilde{c}(\theta, z) = \begin{cases} c_0 \exp\left(\frac{z-\eta(\theta)}{L_m}\right) & z \leq \eta(\theta) \\ 0 & z > \eta(\theta). \end{cases} \tag{4}$$

We average this concentration over a wave-period, where $\overline{\widetilde{c}}$ is a wave-period averaged quantity,

$$\overline{\widetilde{c}}(z) = \frac{1}{2\pi}\int_0^{2\pi} \widetilde{c}(\theta, z)\mathrm{d}\theta. \tag{5}$$

This expression is evaluated exactly for all points under the wave trough, and above the wave trough the integration range is a function of z/A, which can be integrated numerically. The full expression is:

$$\overline{\widetilde{c}}(z) = \begin{cases} c(z)\, I_0\left(\frac{A}{L_m}\right) & z \leq -A \\ c(z)\, \frac{1}{2\pi}\int_{\cos^{-1}(-z/A)}^{2\pi-\cos^{-1}(-z/A)} \exp\left(-\frac{A}{L_m}\cos\theta\right) d\theta - A < & z < A \end{cases} \tag{6}$$

where I_0 is an elliptic integral of the first kind. From inspection, we see that the wave-averaged vertical distribution $\overline{\widetilde{c}}(z)$ is a function of the original solution without waves, $c(z)$, and a factor dependent on the ratio A/L_m. As $A/L_m \to 0$, the wave solution approaches the no-wave solution, or $\overline{\widetilde{c}}(z) \to c(z)$.

3.1.2. Wave-Phase Variability

Waves also alter the vertical and horizontal particle distributions as a function of wave phase. These effects are largely due to the wave-orbital motion of the particles. We begin our analysis with a study of how the wave kinematics affect the horizontal distribution of particles. At one point in time, horizontal position maps onto wave phase. Thus, we use wave phase distribution as a proxy for the horizontal distribution. We approximate wave phase as a function of time by linearizing the particle equations of motion. Under linear wave theory in deep-water, the horizontal and vertical wave-orbital velocities, respectively, are:

$$u_w = A\omega\, \mathrm{e}^{kz}\cos\theta \tag{7a}$$

$$w_w = A\omega\, \mathrm{e}^{kz}\sin\theta. \tag{7b}$$

Next, we approximate the horizontal particle motion as ξ where $\dot{\xi} = u_w(x_0, z, t)$, and x_0 is a constant value that refers to the center of the particle's horizontal motion. By integration, $\xi(t) = -A\exp kz\sin(kx_0 - \omega t)$. Assuming $x \approx \xi(t)$, we plug this into our expression for $\theta(t)$ leaving:

$$\theta(t) \approx -\epsilon \mathrm{e}^{kz}\sin(kx_0 - \omega t) - \omega t. \tag{8}$$

To obtain the probability distribution function (p.d.f.) of θ over t, we use a Jacobian transformation where $p(\theta) = |dt/d\theta|p(t)$ for a uniform probability of t over one wave period. We then further approximate $\theta \approx kx_0 - \omega t$ to obtain a closed form solution. At this level of approximation, we find the p.d.f. of θ given a value of z to be

$$p(\theta \mid z) = \frac{1}{2\pi}\left(1 - \epsilon \mathrm{e}^{kz}\cos(\theta)\right)^{-1}. \tag{9}$$

We account for the phase variations over the vertical distribution of particles by weighting Equation 9 with the no-wave vertical particle distribution from Equation (2), vertically integrating from $z = -\infty$ to $z = 0$, and normalizing the resultant equation:

$$p(\theta) = \frac{1}{L_m 2\pi}\int_{-\infty}^{0} \frac{\mathrm{e}^{z/L_m}}{\epsilon \mathrm{e}^{kz}\cos(\theta) - 1} dz. \tag{10}$$

This integration is solved numerically to find the vertically-averaged wave-phase p.d.f. of buoyant particles. Note that the p.d.f. of particles over wave phase is controlled by the parameters k, L_m and ϵ. For large kL_m or small ϵ, the p.d.f. becomes uniform over a wave.

While Equation 10 describes how waves affect the total amount of particles under each wave phase, we also find that waves can change the shape of the distributions under a wave. They do this through vertical stretching and compression which has been studied previously in relation to vortical structures and turbulence (Phillips, 1961; Guo and Shen, 2013). The stretching of the distribution is controlled by the vertical divergence of the flow: $dw/dz = \omega\epsilon \exp kz\sin\theta$. To quantify these effects, we calculate L_m as a function of wave phase and account for the vertical stretching with the following relationship, approximating the stretching effect by integrating in time:

$$\widetilde{L_m}(\theta) = \left(1 + \int \frac{dw}{dz} dt\right) L_m \tag{11}$$

After integrating and evaluating at $z = \eta - L_m$, we are left with

$$\widetilde{L_m}(\theta) = (1 + \epsilon \mathrm{e}^{\epsilon\cos\theta - kL_m}\cos\theta)L_m. \tag{12}$$

In this case, $\widetilde{L_m}$ is measured from the instantaneous free surface. The waves' effects on L_m are strongest for large ϵ and small kL_m.

We synthesize our results from Equations (10) and (12) and find an expression for the vertical distribution of particles under waves and turbulence:

$$\frac{\widetilde{c}(\theta,\zeta)}{c_0} = p(\theta)\exp(\zeta/\widetilde{L_m}(\theta)) \mid \zeta \leq 0 \tag{13}$$

This equation is similar to Equation (4), but it now accounts both for the wave-orbital motion effects as well as the effects of the unsteady free surface. It is also a function of ζ, which is the vertical coordinate relative to the instantaneous free surface. In order to both validate this model and expand on its theory, we also conducted complementary numerical simulations.

3.2. Numerical Simulations

To complement the analytical model, we use simple numerical simulations with Lagrangian particle tracking. The turbulent dispersion is modeled using a random walk, which allows us to track individual particles. These Lagrangian simulations contrast the Eulerian analytical model of the concentration field. They also allow for a more accurate representation of the wave field without the approximations made in the derivations.

In the simulations, the wave field is imposed using the analytical form of Stokes third order deep-water waves. Because we are interested in particle behavior near the free surface, we use Stokes third order waves to minimize the errors between the trajectories of particles at the free surface, and the free surface itself. This error is $\mathcal{O}(\varepsilon^2)$ for linear wave theory, but $\mathcal{O}(\varepsilon^4)$ for Stokes waves. At this level of approximation, the free surface η is defined as

$$\eta = A\left(\left[1-\frac{1}{16}\epsilon^2\right]\cos\theta + \frac{1}{2}\epsilon\cos 2\theta + \frac{3}{8}\epsilon^2\cos 3\theta\right), \tag{14}$$

with wave phase $\theta = kx - \omega' t$ where $\omega' = (1+\frac{1}{2}\epsilon^2)\omega$. The wave-induced velocity field described in Equation (7) is extrapolated to the wave crests due to the agreement seen in Baldock et al. (1996) and as summarized in Smit et al. (2017).

The particle trajectories are simulated using a fourth order Runge Kutta integration which calculates particle velocity based on the superposition of the analytical wave velocity field (see Equation 7) and a constant rise velocity w_p. After the velocity is calculated, a random walk perturbation in the vertical and horizontal directions is applied based on the time-step Δt and κ_t:

$$\frac{dx_p}{dt} = u_w(x,z,t) + \frac{X\sqrt{2\kappa_t\Delta t}}{\Delta t}, \tag{15a}$$

$$\frac{dz_p}{dt} = w_w(x,z,t) + \frac{Y\sqrt{2\kappa_t\Delta t}}{\Delta t} + w_p, \tag{15b}$$

with normally distributed random variables $X, Y \sim \mathcal{N}(0,1)$. Particles were constrained to not go above the free surface by setting $z = \eta$ for all particles with $z > \eta$ after each integration step using Equation (14).

The ratio A/L_m and ϵ were varied for a total of 42 unique scenarios. The values of A/L_m were varied from 1/10 to 10, and the values of ϵ were varied from 0 to 0.3. Due to similarities among the trials, we only report results from a subset of the runs.

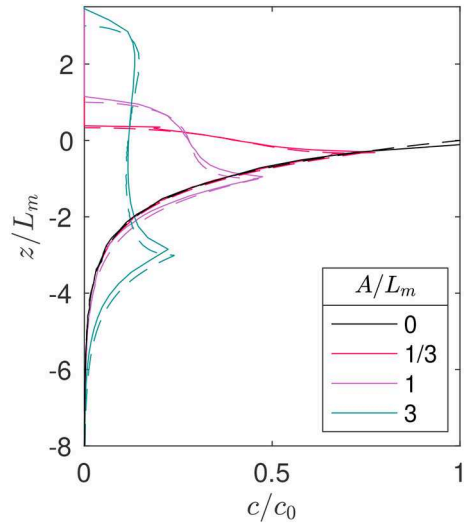

FIGURE 3 | Wave-averaged concentration of particles over the water column. The ratio A/L_m was varied with constant $\epsilon = 0.15$. The solid lines denote the results from numerical simulations, and the dashed lines denote Equation (6).

The simulations were run in MATLAB and started with 1,000 particles at the surface distributed evenly over one wave period, defined by the range $\{x \mid 0 \leq x \leq 2\pi/k\}$, and run until the vertical distribution and wave phase distribution reached equilibrium. Once at equilibrium, the simulations were run for at least an additional 1,000 wave cycles, at which point the data was sampled periodically resulting in 1,000,000 data points for each run.

4. MODEL RESULTS

Both the numerical simulations and the analytical model demonstrate how the unsteady free surface associated with surface gravity waves fundamentally alters the equilibrium vertical and horizontal distributions of buoyant particles. This can be seen in **Figure 3**, where we plot $\widetilde{c}(z)$, the wave-period averaged concentration in the fixed coordinate system for different A/L_m values from both the numerical simulations and the analytical model. For each case, the peak concentration is at the level of the wave trough (when $z/L_m = -A/L_m$), and below this depth the distribution resembles an exponentially decaying curve. However, above this depth, the distribution deviates from the exponential curve. This is due to the fact that there is an unsteady free surface wetting and drying, and thus there are fewer total particles on average when compared to the case without waves. As A/L_m increases, the distribution above the trough level becomes more uniform, and as A/L_m decreases, the distribution approaches the case without waves.

The wave-orbital motion of the particles also introduces phase variation in the distributions. In **Figure 4** we plot the phase-averaged p.d.f. of particles from both the numerical simulations and the theory using Equation 10. In this figure, we see that on average, particle concentration is enhanced under the wave crests ($\theta = 0, 2\pi$) and reduced below the troughs ($\theta = \pi$). For the

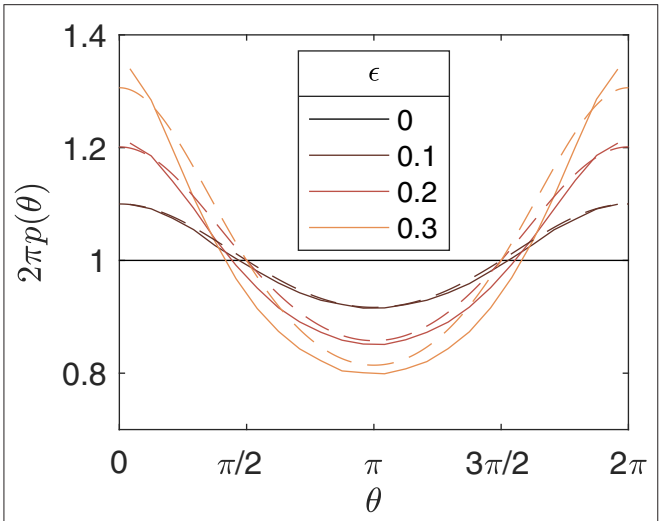

FIGURE 4 | Normalized probability density function $2\pi p(\theta)$ of particles in the water column as a function of wave phase. The ratio $A/L_m = 1$ and ϵ is varied from 0 (no waves) to 0.3. The solid line shows results calculated from numerical simulations and the dashed line shows Equation (10).

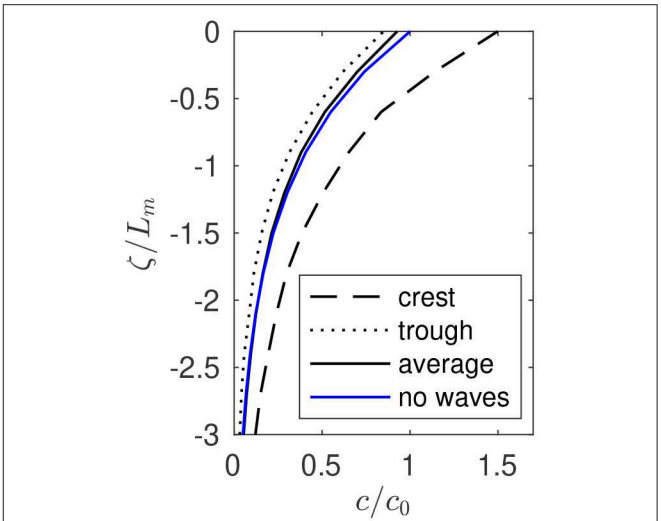

FIGURE 5 | Vertical distribution of relative concentration of buoyant particles under waves as a function of wave phase from numerical simulations. Data comes from a simulation with $A/L_m = 3$ and $\epsilon = 0.2$. The wave phase was subdivided where the crest is the region defined by $\theta < 0.04\pi$ or $\theta > 2\pi - 0.04\pi$ and the trough is defined by $\pi - 0.04\pi < \theta < \pi + 0.04\pi$. The no waves line shows the distribution from Equation (2), and the average line shows the wave-period averaged distribution.

steepest waves, the number of particles under the wave crest can be up to 50% larger than under the wave trough.

The total concentration of particles is phase-dependent, and so is the shape of their vertical distribution. In **Figure 5**, we plot the concentration of particles over depth, relative to the instantaneous free surface. The data are from numerical simulations with $\epsilon = 0.2$ and $A/L_m = 3$, and are subdivided into the concentration under the wave trough, wave crest, the average profile over the wave, and the no-waves case for reference. As expected, the wave crest has higher concentrations than the wave trough. The largest difference in concentrations is near the surface, and the concentration profiles approach each other at depth. The surface concentration at the crest can be up to 50% larger than the average surface concentration across the wave. We also see that the average vertical profile, when adjusted to the instantaneous free surface, recovers a similar profile to the no-wave case.

Another way to visualize the phase-dependence of the particle distributions is with a 2-dimensional p.d.f. of particles over wave-phase and relative depth as plotted in **Figure 6**. In this figure, we again see that the peak concentration at the surface is largest under the wave crests. To characterize the shape of the distribution, we calculate the exponential decay length scale, or mixing length scale $\widetilde{L_m}$, which is plotted as a solid line from the numerical simulations and a dashed line using Equation (12). The two solutions agree with each other. The value of $\widetilde{L_m}$ is smaller under the troughs than it is under the crests, indicating that the vertical distribution is compressed under the troughs and stretched under the crests.

The results from both the analytical model and the numerical simulations demonstrate that waves can affect the distribution of buoyant particles near the free surface. The benefit of the numerical simulations is that they are more accurate, however

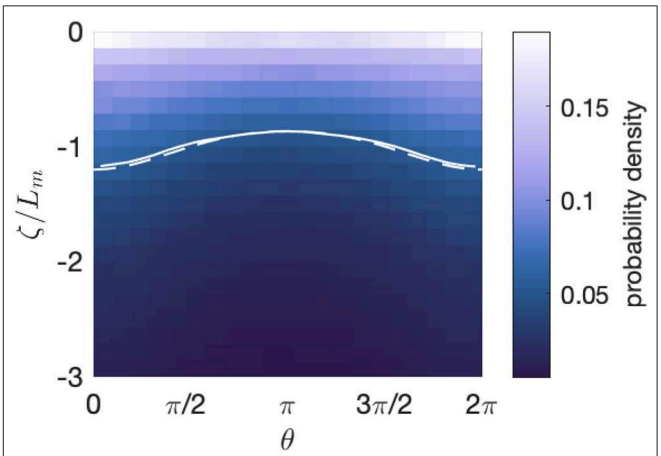

FIGURE 6 | Two-dimensional probability density function of $\widetilde{c}(\theta, \zeta)$ for $\epsilon = 0.2$ and $A/L_m = 1$. The solid line shows the effective $\widetilde{L_m}(\theta)$ calculated from the numerical simulations, and the dashed line shows $\widetilde{L_m}(\theta)$ calculated from Equation (12).

they have a higher computational cost associated with them. Nevertheless, the numerical simulation results largely agree with the theory described in section 3.1, but they differ in a few distinct ways. The waves considered in the theory are from linear wave theory, but the numerical simulations use higher order harmonics. These non-linear wave effects result in waves with taller crests and shallower troughs, the effects of which can be seen in **Figure 3** where the microplastics reach higher in the water column in the numerical simulations when compared with the analytical model. The surface boundary condition combined with the discrete random walk used in the simulations also results in

a concentration discontinuity at the free surface; this is a small effect only seen when analyzing the results very close to the free surface, which is done in the following section. However, the close agreement between the two methods show that the assumptions behind our analytical model capture the major effects of waves in these scenarios.

5. SAMPLING IMPLICATIONS

In this section we consider how the waves may affect the sampling of microplastics at the ocean surface. Under the *wind-mixing model*, a constant free surface profile at $z = 0$ is assumed. If the free surface is deflected due to waves, the total surface area between two fixed points increases. A net trawled over a wavy free surface will not sample around $z = 0$, but rather around $z = \eta$. The waves may also cause the net to sample less effectively; if the net lags the waves, it will not exactly track the free surface with a constant sample volume and the assumption of a single z_0 value may break down. We consider how these effects may alter the particles sampled under various scenarios.

If we let δ be the submerged height of the net opening (where δ corresponds to a varying z_0), W be the width of the net opening, and d be the distance the net traveled over the free surface, then the total sampled volume of water is $V = d\delta W$. Let the total number of particles counted in the net be N_{tow}. Thus, the measured concentration is $c_{tow} = N_{tow}/V$. While W should be constant, d is a function of the free surface deflection, and δ can vary due to the net moving relative to the water surface. We apply this framework to our wave-phase distribution results to discern the possible effects of waves on sampling.

5.1. Surface Tow Length

A net following a deflected free surface will sample a larger volume than if trawled over a flat free surface. The total distance trawled is a function of the free surface deflections, where d from $x = x_a$ to $x = x_b$ is defined using the arc-length formula as

$$d = \int_{x_a}^{x_b} \sqrt{1 + \frac{d\eta}{dx}^2}\, dx. \tag{16}$$

Over one wave length λ, we integrate Equation (16) for a linear wave which results in an expression using an elliptic integral of the second kind $E(m)$:

$$d = \int_0^{2\pi/k} \sqrt{1 + (\epsilon \sin kx)^2} dx = \frac{4}{k}\sqrt{1+\epsilon^2} E\left(\frac{\epsilon^2}{1+\epsilon^2}\right). \tag{17}$$

The effective increase in the length of free surface due to the wave can be defined by the ratio d/λ which is only a function of the wave steepness ϵ:

$$\frac{d}{\lambda} = \frac{2}{\pi}\sqrt{1+\epsilon^2} E\left(\frac{\epsilon^2}{1+\epsilon^2}\right). \tag{18}$$

For a very steep wave where $\epsilon = 0.3$, we find $d/\lambda = 1.022$ for a linear wave and 1.024 for a 3rd order Stokes wave. These are small differences in total tow length that are not necessarily larger than other sources of error during the sampling processes. However, this analysis assumes that as the sample volume travels one linear distance λ, it samples exactly one wave. In reality, the sample volume and the wave are both traveling. Under a traveling wave, d is a function of the relative speed between the sampler and the wave. For simplicity, we will assume that the wave and the sampler are traveling in the same plane. (This is often the case, as sampling vessels will align into the wind direction in order to minimize net destabilization from cross-winds.) If the sampler travels at speed U, then the free surface at the sampler as a function of time is

$$\eta = A\cos([kU - \omega]t). \tag{19}$$

This relationship yields a new effective wave steepness ϵ':

$$\epsilon' = \left(k - \frac{\omega}{U}\right) A = \epsilon\left(1 - \frac{c_p}{U}\right), \tag{20}$$

where $c_p = \omega/k$ is the wave phase speed. Larger values of ϵ result in larger values of d/λ. Thus, the expression for ϵ' suggests that the effective wave steepness is very sensitive to the relative speed of the boat and the waves. Even moderate waves traveling against the direction of the boat can dramatically increase the effective surface area trawled. For example, a boat traveling at 2 knots in the opposite direction of a 50 cm, 5 s deep-water wave where $\epsilon = 0.08$ has $\epsilon' = 0.69$ and $d/\lambda = 1.11$.

The wave-enhanced tow length effect is relevant to the way in which concentrations are calculated from net trawls. The volume of water sampled is sometimes measured directly using a flow meter attached to the net (Isobe et al., 2014; Kooi et al., 2016), but it can also be estimated by using the linear distance of the trawl (often calculated using GPS coordinates) (Law, 2010; Lebreton et al., 2018). The former method may better capture the free surface deflections due to waves as compared to the latter. Let the concentration calculated using the total arc-length of the free surface be c_{tow}, and c^0_{tow} be the concentration calculated using only the linear distance traveled. To assess the sensitivity of these two concentration measurement techniques to waves, c_{tow}/c^0_{tow} is plotted in **Figure 7** as a function of c_p/U and ϵ. In this case, $c_{tow}/c^0_{tow} = \lambda/d$ assuming constant N_{tow}, δ, and W values. As seen in the figure, waves can reduce the measured concentration by up to 50% in the most extreme cases. This difference could potentially account for some of the discrepancies across different measurement techniques in wavy conditions.

5.2. Non-uniform Sampling Effects

The ideal trawling scenario has a net that samples at a constant depth below the free surface. If the free surface is unsteady, then the depth of the trawl relative to mean water level is $\eta - \delta$. In many cases, the net does not necessarily sample at a constant depth. We consider the effects of non-uniform net sampling by assuming that the net lags the free surface resulting in an oscillation with a smaller amplitude:

$$\delta(t) = (1-\alpha)\eta + \overline{\delta}, \tag{21}$$

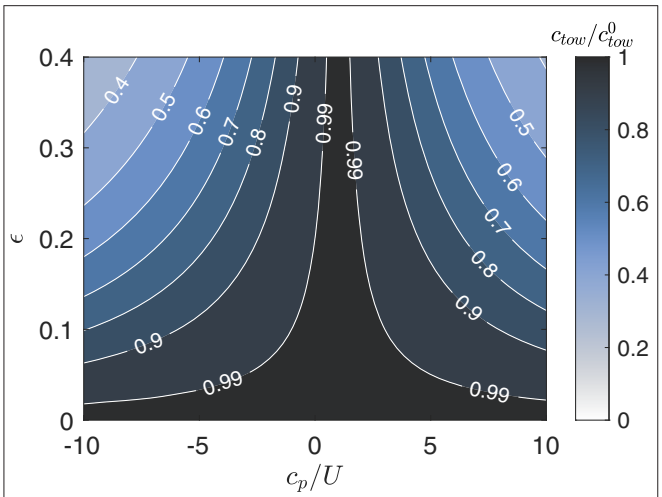

FIGURE 7 | Contour plot of relative concentration calculated using total arc length in waves vs. no waves c_{tow}/c^0_{tow}, plotted as a function of wave steepness ϵ and relative wave speed c_p/U. The values were calculated using Equations (18) and (19).

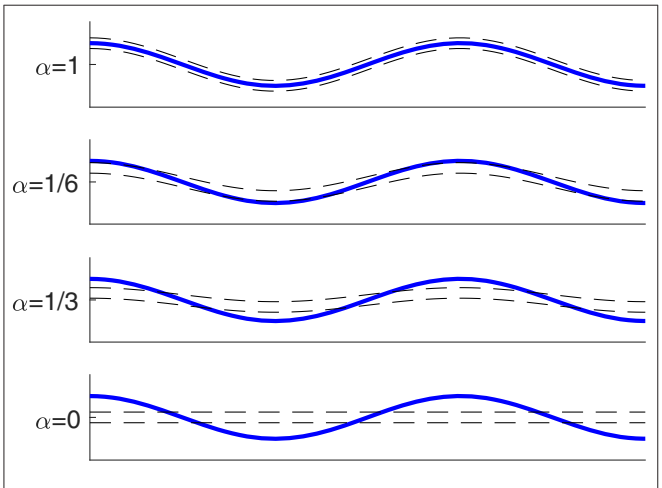

FIGURE 8 | Schematic showing the virtual net sampling volume δ over a wave for different α values as described by Equation (21). The net sampling volume is denoted by the area between the two black dashed lines, and the free surface is shown with the solid blue line. In this case, $\overline{\delta}/A = 0.2$. The wave-averaged sampled volume is constant for all α.

where α is the amplitude reduction factor. Ideal sampling results in a constant δ value with $\alpha = 1$. A sampler that never moves vertically and constantly samples around $z = 0$ corresponds to $\alpha = 0$. The sample volume over a wave as a function of α is shown schematically in **Figure 8**. To assess the effects for $\alpha \neq 1$, we also assume that the net never leaves the water surface such that $\overline{\delta} > (1-\alpha)A$. Finally, we only consider $\alpha \leq 1$ where the troughs are sampled less than the crests. We argue that this corresponds to the more relevant scenario where the net lags the free surface, rather than leads it.

We apply Equation (21) to the numerical simulation results and the distribution modeled by Equation 13 to evaluate how a non-uniform sampler affects the measured number of particles. We assume the net is twice the height of $\overline{\delta}$; this means on-average the net is halfway submerged. Over a wave cycle, the particles above δ and below the top of the net are integrated to determine the effective N_{tow}. The value N_{tow} is then normalized by the reference N^0_{tow} which is calculated using Equation (3). The value of N^0_{tow} represents the number of measured particles using the wind-mixing model with no waves. Assuming a constant volume sampled in both scenarios, the resultant c_{tow}/c^0_{tow} values are plotted against α for various wave scenarios in **Figure 9**. We also consider two different net sizes by varying the ratio $\overline{\delta}/A$.

In **Figure 9**, we see that as α decreases, the amount of particles sampled decreases relative to the no-wave prediction. The effect is the strongest for large A/L_m. The concentrations show the most decrease after the net starts to dip below the free surface for part of the wave cycle, denoted by the vertical lines. In **Figure 9A**, $\overline{\delta}/A = 0.2$, and in **Figure 9B**, $\overline{\delta}/A = 0.5$; by comparing these figures we see that the larger the net is relative to the wave amplitude, the less sensitivity there is to α. However, once the net goes under water in both scenarios, we see a decrease in sampled concentrations. An increase in c_{tow}/c^0_{tow} is seen in the numerical simulations for α values close to 1 in **Figure 9A**. This is due to a slight enhancement of particles at the free surface in the simulations as a result of the surface boundary condition.

6. DISCUSSION

Using a phase-resolving approach, we have analyzed the effects of waves on the equilibrium distribution of buoyant particles in the ocean mixed layer, demonstrating that waves introduce concentration differences across a wave cycle. This work implies that if a towed net does not sample each wave phase equally, the resulting observations will be biased.

The phase variability in the distributions is controlled by the wave kinematics. A tracer particle under a linear wave field spends more time under the crests than the trough. One way to conceptualize this phenomena is by considering a particle traveling under a trough and under a crest. The particle under the trough moves in the opposite direction of the wave, so it is leaving the trough more quickly than if the wave was not traveling. However, under the wave crest, the particle is moving in the direction of the wave, so it has a longer residence time in its relative wave phase. In other words, $d\theta/dt$ has a higher magnitude under the troughs than under the crests. This translates to particles on-average, non-uniformly distributed in wave-phase, with more particles under the crests than the troughs.

Another major focus of this study is how waves stretch and compress the particle distributions as a function of wave phase. While these processes have been studied in relation to turbulence and vortices, this work centers on particle distributions. The wave-induced velocities have non-zero vertical divergence. This results in the distribution of particles being maximally stretched under the crests, i.e., having the maximum $\widetilde{L_m}$ value, and being maximally compressed under the troughs, i.e., having the minimum $\widetilde{L_m}$ value. Because the time-averaged vertical divergence in the wave field is zero, there is no net effect, and this

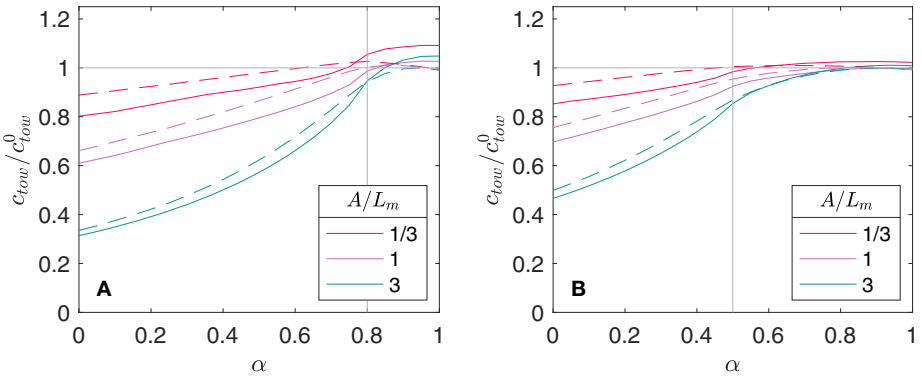

FIGURE 9 | Modeled captured particles as a function of net lag parameter α for various A/L_m. The total number of particles captured in a net tow per volume c_{tow} is normalized by c^0_{tow} which represents the predicted amount without waves. The solid lines denote the results from numerical simulations, and the dashed line denote the results using the analytically modeled concentration as described by Equation (13). The vertical gray line denotes the α value when the net drops below the free surface for part of the wave cycle. In these data, $\epsilon = 0.1$ in both cases, and $\overline{\delta}/A = 0.2$ **(A)** and $\overline{\delta}/A = 0.5$ **(B)**.

stretching is only seen as a function of wave phase. These findings demonstrate that particles are distributed the deepest relative to the free surface under the crests, whereas they are closest to the surface under the troughs. This result is illustrated in **Figure 6**.

Because particles preferentially accumulate under the crests relative to the troughs, if a towed net over-samples the wave crests, it can over-sample the particles. However if the net tends to go under water at the crests, it can under-sample the particles because it will miss the peak concentration at the surface. Another common assumption during net tow sampling is that a net that is on-average halfway submerged will sample the same particles as a net that has constant halfway submergence. A net that comes out of water half the time and submerges underwater half the time, is on-average halfway submerged and corresponds to small α values; we have shown that small α values consistently lead to the under-sampling of particles. Therefore, if waves cause the towed net's submergence to vary over time, under-sampling can result. These effects should be studied more carefully during the time of sampling to further discern any bias in the measurements.

One can imagine there is a range of frequencies to which the sampling net can respond. At the low frequency limit for long waves, i.e., waves which are much longer than the net, the net should be able to effectively track the free surface. In that case, the wind-mixing model is still an appropriate measure to use. However, if the net tends to sample at a constant z-level and move through the waves, which may occur with short-period waves, i.e., waves with higher frequencies than the net's natural response frequency, then the modified wave-period-averaged wind-mixing model presented here may be more appropriate. In that scenario, the net will also under-sample the assumed concentration estimated by the wind-mixing model as seen in **Figure 3**.

When compared to other sampling methods, there is some evidence that net tows can under-sample. For example, grab samples of microplastics measurements have been reported with high values relative to the net tows at the same location (Barrows et al., 2017). This effect is also due to the ability for grab samples to capture particles smaller than the net's mesh size. However, this does not necessarily explain all the discrepancy in observed concentrations, and non-uniform sampling due to waves could be partly responsible. An advantage of net tows in this scenario is that they encompass average concentrations over large distances which lowers sensitivity and variability to patchiness, whereas grab samples are very sensitive to patchiness. Microplastics patchiness can occur due to Langmuir circulation and other hydrodynamic features (van Sebille et al., 2020).

We find that the accumulation of particles under the wave crests is most extreme under the steepest waves. Therefore, as waves steepen before they break, they will accumulate particles under them. The turbulence due to breaking waves is also strongest under the crests of waves (Rapp and Melville, 1990), and thus enhanced turbulent mixing will occur at the point with the highest concentration of particles at the time of breaking. This coupling could result in greater transport of particles away from the surface and should be studied further.

The ocean surface boundary layer is subjected to a multitude of unsteady forcings. Understanding how they each can bias measurements is important to accurately interpreting data, and this study represents only one mechanism: non-breaking surface gravity waves. In this work, we have only considered a monochromatic wave train aligned with the sampler, and therefore future work should include a wave field with a broadband spectrum as well as scenarios in which waves travel obliquely to the sampling apparatus. We have also neglected the effects of Langmuir turbulence, which has been shown to be extremely important in both controlling patchiness and transporting particles to depth. Finally, understanding the limits of the wind-mixing model is important. When L_m is greater than the mixed layer depth, the model's underlying assumption of a constant eddy viscosity no longer holds (Kukulka et al., 2012). Large L_m values can result from small particle rise velocities, and thus this model may not be appropriate for the smallest microplastic particles. A more general model that can account for the smallest particles as well as the effects of waves is therefore needed.

7. CONCLUSIONS

Using both numerical simulations and an analytical model, we have demonstrated how waves affect the vertical and horizontal distributions of buoyant particles at the free surface. In the fixed frame, waves change the wave-period-averaged vertical distribution of particles by lowering the peak concentration of particles to the level of the wave trough. Over a wave cycle, the wave orbital motion redistributes the particles so that on average, more particles are under the wave crest than under the wave trough. Waves also stretch the vertical distribution resulting in a smaller mixing length under the wave trough and a larger mixing length under the wave crest. The free surface is stretched due to waves, and when a sampling volume is traveling relative to the waves, the effective length of the trawl can increase dramatically. Finally, we find that non-uniform sampling of a wave can result in reduced measured particle concentrations relative to predictions based on the wind-mixing model (Kukulka et al., 2012).

While we have shown how a train of monochromatic progressive waves distort buoyant particle distributions, the real ocean surface is subjected to a spectrum of waves. The turbulent mixing at the ocean surface is not necessarily constant nor isotropic. It is also not independent from the waves. Particle inertia can also be important for large particles and low turbulence forcing. However, this work shows the possible range of effects of surface gravity waves on buoyant particle distributions. We recommend a more detailed study of how the trawling process can bias the concentrations observed, and how our findings change under more complicated scenarios.

DATA AVAILABILITY STATEMENT

The datasets generated for this study are available on request to the corresponding author.

AUTHOR CONTRIBUTIONS

MD conceived and designed the study, developed and analyzed the models, interpreted results, and wrote the manuscript.

FUNDING

This work was supported by the Postdoctoral Scholar Program at the Woods Hole Oceanographic Institution, and by the US National Science Foundation under grant no. CBET-1706586.

ACKNOWLEDGMENTS

The author would like to acknowledge Nicholas T. Ouellette and Jeffery R. Koseff for helpful discussions and support over the course of this work.

REFERENCES

Babanin, A. V. (2006). On a wave-induced turbulence and a wave-mixed upper ocean layer. *Geophys. Res. Lett.* 33, 1–6. doi: 10.1029/2006GL027308

Baldock, T. E., Swan, C., and Taylor, P. H. (1996). A laboratory study of nonlinear surface waves on water. *Philos. Trans. R. Soc. A Math. Phys. Eng. Sci.* 354, 649–676. doi: 10.1098/rsta.1996.0022

Barrows, A. P., Neumann, C. A., Berger, M. L., and Shaw, S. D. (2017). Grab: vs. neuston tow net: a microplastic sampling performance comparison and possible advances in the field. *Anal. Methods* 9, 1446–1453. doi: 10.1039/C6AY02387H

Boufadel, M. C., Bechtel, R. D., and Weaver, J. (2006). The movement of oil under non-breaking waves. *Mar. Pollut. Bull.* 52, 1056–1065. doi: 10.1016/j.marpolbul.2006.01.012

Brunner, K., Kukulka, T., Proskurowski, G., and Law, K. L. (2015). Passive buoyant tracers in the ocean surface boundary layer: 2. Observations and simulations of microplastic marine debris. *J. Geophys. Res. Oceans* 120, 7559–7573. doi: 10.1002/2015JC010840

Chamecki, M., Chor, T., Yang, D., and Meneveau, C. (2019). Material transport in the ocean mixed layer: recent developments enabled by large eddy simulations. *Rev. Geophys.* 57, 1338–1371. doi: 10.1029/2019RG000655

Cozar, A., Echevarria, F., Gonzalez-Gordillo, J. I., Irigoien, X., Ubeda, B., Hernandez-Leon, S., et al. (2014). Plastic debris in the open ocean. *Proc. Natl. Acad. Sci. U.S.A.* 111, 10239–10244. doi: 10.1073/pnas.1314705111

DiBenedetto, M. H., Ouellette, N. T., and Koseff, J. R. (2018). Transport of anisotropic particles under waves. *J. Fluid Mech.* 837, 320–340. doi: 10.1017/jfm.2017.853

Eames, I. (2008). Settling of particles beneath water waves. *J. Phys. Oceanogr.* 38, 2846–2853. doi: 10.1175/2008JPO3793.1

Eriksen, M., Lebreton, L. C., Carson, H. S., Thiel, M., Moore, C. J., Borerro, J. C., et al. (2014). Plastic pollution in the world's oceans: more than 5 trillion plastic pieces weighing over 250,000 tons afloat at sea. *PLoS ONE* 9:e111913. doi: 10.1371/journal.pone.0111913

Geyer, R., Jambeck, J. R., and Law, K. L. (2017). Production, uses, and fate of all plastics ever made. *Sci. Adv.* 3:5. doi: 10.1126/sciadv.1700782

Guo, X., and Shen, L. (2013). Numerical study of the effect of surface waves on turbulence underneath. Part 1. Mean flow and turbulence vorticity. *J. Fluid Mech.* 733, 558–587. doi: 10.1017/jfm.2013.451

Herterich, K., and Hasselmann, K. (1982). The horizontal diffusion of tracers by surface waves. *J. Phys. Oceanogr.* 12, 704–711. doi: 10.1175/1520-0485(1982)012<0704:THDOTB>2.0.CO;2

Hidalgo-Ruz, V., Gutow, L., Thompson, R. C., and Thiel, M. (2012). Microplastics in the marine environment: a review of the methods used for identification and quantification. *Environ. Sci. Technol.* 46, 3060–3075. doi: 10.1021/es2031505

Isobe, A., Kubo, K., Tamura, Y., Kako, S., Nakashima, E., and Fujii, N. (2014). Selective transport of microplastics and mesoplastics by drifting in coastal waters. *Mar. Pollut. Bull.* 89, 324–330. doi: 10.1016/j.marpolbul.2014.09.041

Jambeck, J. R., Geyer, R., Wilcox, C., Siegler, T. R., Perryman, M., Andrady, A., et al. (2015). Plastic waste inputs from land into the ocean. *Science* 347, 768–771. doi: 10.1126/science.1260352

Karlsson, T. M., Kärrman, A., Rotander, A., and Hassellöv, M. (2019). Comparison between manta trawl and *in situ* pump filtration methods, and guidance for visual identification of microplastics in surface waters. *Environ. Sci. Pollut. Res.* 27, 5559–5571. doi: 10.1007/s11356-019-07274-5

Kooi, M., Reisser, J., Slat, B., Ferrari, F. F., Schmid, M. S., Cunsolo, S., et al. (2016). The effect of particle properties on the depth profile of buoyant plastics in the ocean. *Sci. Rep.* 6, 1–10. doi: 10.1038/srep33882

Kukulka, T., and Brunner, K. (2015). Passive buoyant tracers in the ocea surface boundary layer: 1. Influence of equilibirum wind-waves on vertical distributions. *J. Geophys. Res. Oceans* 120, 3837–3858. doi: 10.1002/2014JC010487

Kukulka, T., Proskurowski, G., Morét-Ferguson, S., Meyer, D. W., and Law, K. L. (2012). The effect of wind mixing on the vertical distribution of buoyant plastic debris. *Geophys. Res. Lett.* 39:L07601. doi: 10.1029/2012GL051116

Law, K. L. (2010). Plastic accumulation in the North Atlantic subtropical gyre. *Science* 329, 1185–1188. doi: 10.1126/science.1192321

Lebreton, L., Slat, B., Ferrari, F., Sainte-Rose, B., Aitken, J., Marthouse, R., et al. (2018). Evidence that the Great Pacific Garbage Patch is rapidly accumulating plastic. *Sci. Rep*. 8, 1–15. doi: 10.1038/s41598-018-22939-w

Liang, J.-H., Wan, X., Rose, K. A., Sullivan, P. P., and McWilliams, J. C. (2018). Horizontal dispersion of buoyant materials in the ocean surface boundary layer. *J. Phys. Oceanogr*. 48, 2103–2125. doi: 10.1175/JPO-D-18-0020.1

Onink, V., Wichmann, D., Delandmeter, P., and Van Sebille, E. (2019). The role of Ekman currents, geostrophy and Stokes drift in the accumulation of floating microplastic. *J. Geophys. Res. Oceans* 124, 1474–1490. doi: 10.1029/2018JC014547

Perlin, M., Choi, W., and Tian, Z. (2013). Breaking waves in deep and intermediate waters. *Annu. Rev. Fluid Mech*. 45, 115–145. doi: 10.1146/annurev-fluid-011212-140721

Phillips, O. (1961). A note on the turbulence generated by gravity waves. *J. Geophys. Res*. 66, 2889–2893. doi: 10.1029/JZ066i009p02889

Poulain, M., Mercier, M. J., Brach, L., Martignac, M., Routaboul, C., Perez, E., et al. (2019). Small microplastics as a main contributor to plastic mass balance in the North Atlantic subtropical gyre. *Environ. Sci. Technol*. 53, 1157–1164. doi: 10.1021/acs.est.8b05458

Prata, J. C., da Costa, J. P., Duarte, A. C., and Rocha-Santos, T. (2019). Methods for sampling and detection of microplastics in water and sediment: a critical review. *Trends Anal. Chem*. 110, 150–159. doi: 10.1016/j.trac.2018.10.029

Rapp, R. J., and Melville, W. K. (1990). Laboratory measurements of deep-water breaking waves. *Philos. Trans. R. Soc. Lond. A Math. Phys. Sci*. 331, 735–800. doi: 10.1098/rsta.1990.0098

Setälä, O., Magnusson, K., Lehtiniemi, M., and Norén, F. (2016). Distribution and abundance of surface water microlitter in the Baltic Sea: a comparison of two sampling methods. *Mar. Pollut. Bull*. 110, 177–183. doi: 10.1016/j.marpolbul.2016.06.065

Smit, P. B., Janssen, T. T., and Herbers, T. H. C. (2017). Nonlinear wave kinematics near the ocean surface. *J. Phys. Oceanogr*. 47, 1657–1673. doi: 10.1175/JPO-D-16-0281.1

Stokes, G. G. (1880). Supplement to a paper on the theory of oscillatory waves. *Math. Phys. Papers* 1:14.

van den Bremer, T. S., and Breivik, Ø. (2018). Stokes drift. *Philos. Trans. R. Soc. A Math. Phys. Eng. Sci*. 376:20170104. doi: 10.1098/rsta.2017.0104

van Sebille, E., Aliani, S., Law, K. L., Maximenko, N., Alsina, J. M., Bagaev, A., et al. (2020). The physical oceanography of the transport of floating marine debris. *Environ. Res. Lett*. 15:023003. doi: 10.1088/1748-9326/ab6d7d

van Sebille, E., Wilcox, C., Lebreton, L., Maximenko, N., Hardesty, B. D., van Franeker, J. A., et al. (2015). A global inventory of small floating plastic debris. *Environ. Res. Lett*. 10:124006. doi: 10.1088/1748-9326/10/12/124006

Viršek, M. K., Palatinus, A., Koren, Š., Peterlin, M., Horvat, P., and Kržan, A. (2016). Protocol for microplastics sampling on the sea surface and sample analysis. *J. Vis. Exp*. 2016:e55161. doi: 10.3791/55161

Zippel, S. F., Thomson, J., and Farquharson, G. (2018). Turbulence from breaking surface waves at a river mouth. *J. Phys. Oceanogr*. 48, 435–453. doi: 10.1175/JPO-D-17-0122.1

Conflict of Interest: The author declares that the research was conducted in the absence of any commercial or financial relationships that could be construed as a potential conflict of interest.

Copyright © 2020 DiBenedetto. This is an open-access article distributed under the terms of the Creative Commons Attribution License (CC BY). The use, distribution or reproduction in other forums is permitted, provided the original author(s) and the copyright owner(s) are credited and that the original publication in this journal is cited, in accordance with accepted academic practice. No use, distribution or reproduction is permitted which does not comply with these terms.

frontiers in Marine Science

MINI REVIEW
published: 25 March 2020
doi: 10.3389/fmars.2020.00185

Phytoplankton Orientation in a Turbulent Ocean: A Microscale Perspective

G. Basterretxea[1], J. S. Font-Muñoz[2,3]* and I. Tuval[1,4]**

[1] Department of Marine Ecology, Mediterranean Institute for Advanced Studies, University of the Balearic Islands and Spanish National Research Council, Esporles, Spain, [2] Université de Brest – Université de Bretagne Occidentale/Centre National de la Recherche Scientifique/French Research Institute for Exploitation of the Sea/Institut de Recherche pour le Développement, Brest, France, [3] French Research Institute for Exploitation of the Sea, French Institute for Sea Research, Dynamiques des Ecosystèmes Côtiers Laboratoire d'Ecologie Pélagique, Plouzané, France, [4] Department of Physics, University of the Balearic Islands, Palma, Spain

Phytoplankton are by definition autotrophic microorganisms that passively drift with fluid motion. Accordingly, the traditional view of a turbulence-homogenized phytoplankton distribution in the ocean, where cells randomly organize and interact, is deeply rooted in biological oceanography studies. However, increasing understanding of microscopic processes in the ocean is revealing a world of microscale patterns resulting from cell behaviors and fluid-cell interactions that challenges this vision. Autotrophic cells have developed active (i.e., flagella) and passive (i.e., morphological structures and vesicles) motility mechanisms that allow them different degrees of spatial control. Their complex interaction with the ocean physicochemical landscape commonly results in small-scale spatial heterogeneities and non-isotropic orientations that can strongly influence ecosystem level processes. Cell orientation, in particular, is fundamental for key biological functions such as sensing, metabolism, locomotion, chain formation, or sexual reproduction. Moreover, preferential alignment of elongated cells can modulate the propagation of light through the ocean and is fundamental for accurate interpretation of remote sensing data. Innovative observational and experimental techniques (e.g., *in situ* holography, laser diffractometry, etc.) allowing the subtle analysis of cell-fluid interactions are revealing that, at the microscopic level, organisms present well defined orientation and interaction patterns under prevalent conditions in the sea. Thus, the interplay of biology, fluid dynamics, and optics may shape, by means of anisotropic cell distributions, pivotal cross-scale aspects of phytoplankton ecology.

Keywords: phytoplankton, microscale, turbulence, orientation, shear

OPEN ACCESS

Edited by:
Aditya R. Nayak, Florida Atlantic University, United States

Reviewed by:
Jun Sun, Tianjin University of Science and Technology, China
Jennifer Prairie, University of San Diego, United States

****Correspondence:***
G. Basterretxea
gotzon@imedea.uib-csic.es
J. S. Font-Muñoz
Joan.Salvador.Font.Munoz@ifremer.fr
I. Tuval
ituval@imedea.uib-csic.es

Specialty section:
This article was submitted to Marine Ecosystem Ecology, a section of the journal Frontiers in Marine Science

Received: *23 December 2019*
Accepted: *10 March 2020*
Published: *25 March 2020*

Citation:
Basterretxea G, Font-Muñoz JS and Tuval I (2020) Phytoplankton Orientation in a Turbulent Ocean: A Microscale Perspective. Front. Mar. Sci. 7:185. doi: 10.3389/fmars.2020.00185

INTRODUCTION

Each process occurring in the marine environment has an associated fundamental temporal and spatial scale, but cross-scale links exist conforming the full complexity of ocean ecosystem dynamics. For a long time, the microscale structure of the ocean (<1 mm), which is relevant to understanding many phytoplankton related processes, has been overlooked in the framework of biological oceanography. There are technical and conceptual historical reasons for this dissociation between studies of the seemingly chaotic microscopic habitat where algal cells grow and interact with their congeners and with other organisms, and research on larger scale processes determining

the fate of marine phytoplankton. In this review, we contribute to conciliate these two worlds, with the conviction that understanding the interaction among processes occurring at the micro- and macroscopic scales can enhance our understanding of phytoplankton and ocean ecosystem dynamics. Here, we particularly aim at exploring the importance of preferential cell orientation in the ocean; a ubiquitous example of a microscale process for which large scale implications are anticipated.

A BRIEF HISTORICAL REVIEW

Early studies assumed that pelagic phytoplankton spent most of their life cycle freely suspended in the water column and that, despite the motile ability of some species, movements were too weak to overcome fluid motion. Pioneering botanist and zoologist Hensen (1887) inferred that, if the environment was uniform, plankton should be uniformly distributed freely drifting passively in the sea. Implicitly, plankton were believed to be poorly structured and organized at small scales where microbial organisms were randomly oriented by shear and turbulence. Only conspicuous larger scale space and time variations generally associated with changes in hydrographic properties and seasonality were recognized. Highly influential Hensen's theories were eagerly confronted by contemporary studies by Haeckel (1891) who defended an irregular distribution of plankton both in time and space. Although Haeckels's criticisms were initially overlooked, subsequent investigations revealed non-homogeneous organism distributions that early researchers ascribed to small scale fluid patterns driven by unequal heat distribution (Sachs, 1876). To the eyes of the microscopist, cells often showed active orientation and movement in a definite direction (Schwarz, 1884) and field observations revealed that some phytoplankton species even presented marked diurnal and seasonal migration patterns, as well as aggregation behavior (Wager, 1910). Nevertheless, the idea of homogeneously and isotropically mixed plankton organisms persisted until the 50s when new concepts and theories arose showing the importance of small-scale plankton processes (Barnes and Marshall, 1951; Bainbridge, 1957; Cassie, 1959, 1963).

The mid-20th century was an important epoch for the development of physical and biological oceanography. Advances were made by introducing mathematical foundations in the study of plankton ecology which opened new possibilities for the understanding of the fundamental processes controlling plankton (see Russel, 1950). In this context, Harvey (1942) analyzed the interactions between different components of plankton (phyto- and zooplankton) and the relationships between these and the surrounding water. Riley (1942) and Riley et al. (1949) described the impact of water column stability on spring blooms, Sverdrup (1953) postulated the conditions for vernal phytoplankton blooms and Margalef (1967, 1978) provided a holistic perspective to phytoplankton organization. Also, a conceptual framework was proposed analyzing plankton variability over various spatial scales together with the physical factors contributing to this variation (Haury et al., 1978). These and other studies made evident that the apparent uniformity of the oceans was simply "an illusion generated by the original need for widely spaced sampling both horizontally and vertically" (Steele, 1959). Small scale heterogeneities and individual interactions in which cell orientation plays a fundamental role were still ignored but as part of these simplified large biological compartments.

With the advent of new continuously sampling instrumentation like fluorometers (Lorenzen, 1966) and particle counters (Sheldon et al., 1972), marine scientists were able to address the patterns of spatial variability of phytoplankton and to determine its structure. These features where crucial for the understanding of its role as a food source for marine life (see Steele, 1978 and review by Vance and Doel, 2010). The ocean was now conceived as a mixture of process spanning from length scales of centimeters to thousands of kilometers and associated timescales ranging from seconds to centuries (Stommel, 1963; Haury et al., 1978). Progress was made in the measurements of turbulence in the ocean and in the development of a turbulence theory that was rapidly assimilated into physical oceanography (Grant et al., 1962; Levich, 1962). Nevertheless, a preconception that phytoplankton behaved like passive particles immersed in the flow field and, thus, their distribution was driven by turbulence, was the general consensus (see Platt, 1972, 1978). The "red noise" power spectra for physical and biological properties depicted from continuous underway measurements demonstrated that the effects of physical forces dissipated effectively during the cascade of energy transfer to scales on the order of meters (Powell et al., 1975; Denman and Platt, 1976). Spatial scales below this level were seldom considered either because of lack of technology for the observation of the sea at these scales, or because adding sampling detail was assumed irrelevant for the scientific challenges of the time (i.e., seasonal variations, mesoscale processes, regional the productivity of the ocean). As a consequence, biologists and ecologists observing the complexity of the microscopic world (mostly restricted to taxonomists and microbiologists) diverged in aims from a rapidly developing community of biological oceanographers interested in the more evident and predictable changes in phytoplankton at larger scales.

It was not until the last quarter of the century, with the focus in microbial motility, feeding mechanisms, and encounter rates, that interest on understanding phytoplankton related processes at the microscale, including cell orientation, was renewed (Holwill, 1974; Lighthill, 1976; Lehman and Scavia, 1982; Rothschild and Osborn, 1988; Fenchel, 1993; Kiørboe, 1993). The study of patchiness acquired importance because it affected cell densities and thus regulated encounter rates among organisms. It became apparent that interactions were not only ruled by mixing rates. Also, it was speculated that small planktivores survived where their food rations appeared too low by making use of adequate food patches too small to detect (Owen, 1989). Improved bio-optical instrumentation showed the existence of persistent thin layers with high phytoplankton abundance spanning over large horizontal distances (e.g., Cowles et al., 1998; Dekshenieks et al., 2001). While estimates of many microscale processes (e.g., encounter rates, competition) were implicitly based on a random distribution of plankton, a number of key works in the field of microbiology showed a

rich physical and biochemical heterogeneity at submillimetric scales (Derenbach et al., 1979; Gregg, 1980); however, recent studies have shown that these submillimetric patches often may represent single large phytoplankton cells, chains, or aggregates (Doubell et al., 2014). Biological studies at the microscale remained considered a separate discipline and were seldom integrated in mainstream oceanography perspectives. This led to some long-standing ecological misconceptions. For example, it is remarkable that the concept that phytoplankton orientations and spatial distributions along with environmental parameters such as heat and nutrients are passively homogenized by turbulence has persisted through time (e.g., Siegel, 1998; Currie and Roff, 2006). This inherited scale-biased vision in which small scale processes average out at larger scales and can therefore be considered irrelevant, contrasts with the viewpoint of other disciplines, like physics, where the continuum between the subatomic processes and astrophysics and the necessity of understanding all spatial scales is well established. It also contraposes ecological theories about system behavior based on hierarchical interactions among processes at different scales (i.e., self-organization or resilience; Holling, 1992; Rietkerk et al., 2004).

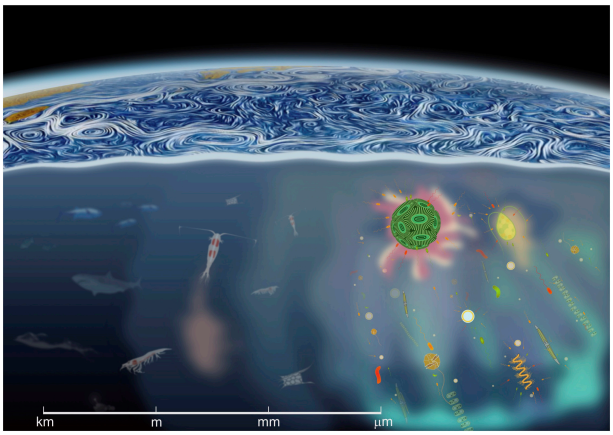

FIGURE 1 | A cross-scale view of the ocean spanning from linear gradients and microscale interactions (right), to top predators and mammals and regional circulation patterns (left and top). The scale at the bottom provides a reference of the spatial dimension in which the interactions between distinct organisms occur. The linear microbial landscape is embedded in a world of turbulent motions and progressively larger swirls.

UPSCALING EFFECTS OF THE MICROSCOPIC WORLD

Microscale and single cells studies are nowadays acknowledged as the cutting-edge of plankton research (e.g., Seymour et al., 2010; Rusconi et al., 2014). The concept that plankton displaces where the water transports it remains broadly valid and turbulence is the dominant physical process redistributing small organisms. But, as we begin to understand the processes occurring at the smaller scales, the importance of interfacing this microhabitat with larger scale dynamics is evidenced (Prairie et al., 2012). As in other ecological fields, to fully understand phytoplankton dynamics we must decipher first how information is transferred between scales: from fine to broad, and vice versa (Levin, 1992).

The oceanic flow fields and their interaction with phytoplankton entail a nearly continuous spectrum of motions and associated processes which range from global scale circulation to the smaller molecular adjustments and from ecosystems to individual cells (**Figure 1**). The appearance and effects of flow change dramatically as one moves from the human scale, at which our intuition is trained, to the microscale, at which microorganisms experience flow (Kiørboe, 2008; Wheeler et al., 2019). Because the majority of phytoplankton are smaller than the smallest eddy size by one or two orders in magnitude, processes affecting individual cells develop in the viscous non-inertial realm where they displace with no turbulent drag (Purcell, 1977). This microscopic environment may be envisioned as a universe of viscous packets that are transported rapidly through a turbulence field (Reynolds, 2006). At this scale, turbulent energy dissipates as heat while water motion can be characterized as laminar shear. Phytoplankton experience turbulence as an instantaneous, linearly varying fluid velocity across the cell body (Jumars et al., 2009; Barry et al., 2015) and interactions with the surrounding environment are effective at defining anisotropic organism orientations.

Contrarily to common view, stirring strengthens linear gradients at the microscale level therefore generating a landscape full of gradients, as determined by the Bachelor scale. Variability in cell microhabitats is fundamental to the way organisms exploit the resources and interact with other organisms, either mates, parasites, or predators. Considering that most pelagic environments are extremely dilute, insofar as the supply of the spectrum of the cells' chemical requirements is concerned (Reynolds, 1997), this heterogeneity provides opportunity for coexistence of species despite their differential fitness, therefore favoring diversity.

Whenever individual cells are important, the linear world under the Kolmogorov scale (Kolmogorov, 1941, 1962) must be considered. According to Stocker (2012), the spatial scale that is relevant for a single cell depends on behavior and time. At day scales, small non-motile cells restrict their universe to a micrometric environment defined by their Brownian motion, whereas swimming organisms evolve in a horizon of centimeters. It is the behavior of phytoplankton relative to its most immediate fluid layer and the transport of this microenvironment within larger scale flows which determines some relevant patterns of phytoplankton (**Figure 2**). Movement is a necessity for phytoplankton cells that would otherwise become rapidly nutrient limited by the inefficient molecular diffusion. If the phytoplankton cell is sinking or is able to move, the microzone of nutrient-depleted water surrounding the cell will be replaced faster than if the cell remains motionless; in effect the steepness of the nutrient gradient and, hence, the nutrient uptake rate will increase due to this advective transport of nutrients toward the cell surface.

Some motile phytoplankton can vertically orient and swim over tens of meters of the water column per day vertically varying

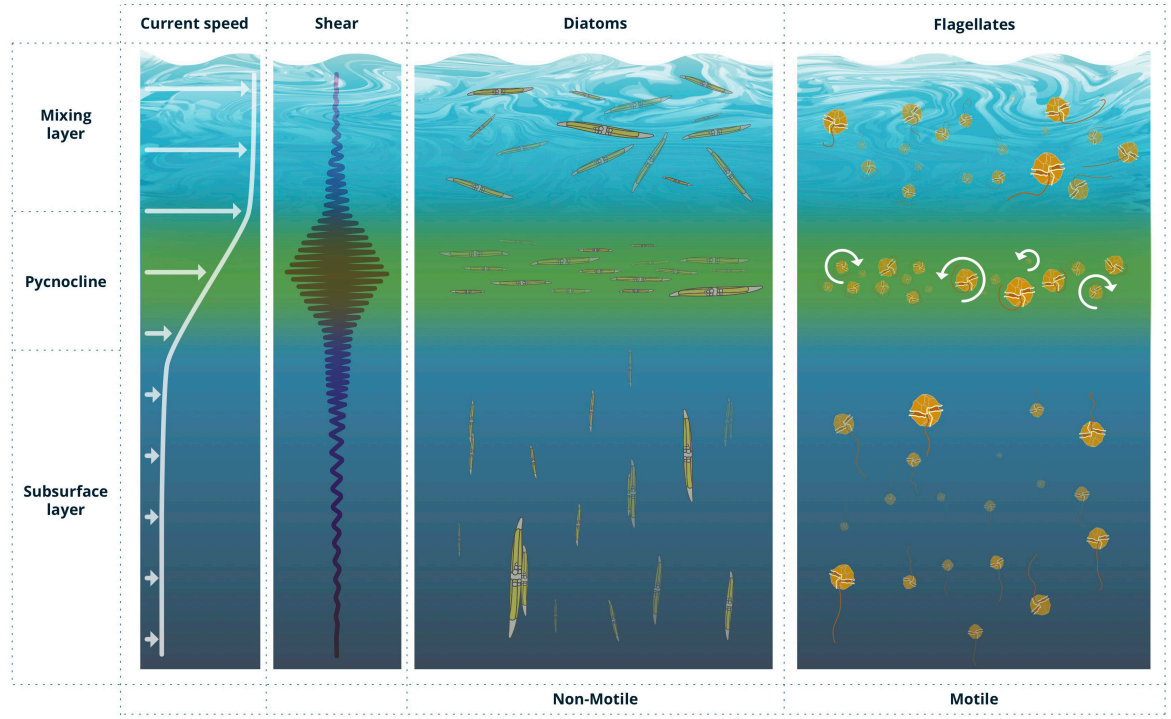

FIGURE 2 | Idealized profiles of current speed and shear in the ocean and corresponding preferential cell orientation of non-motile and motile phytoplankton cells, including the formation of thin layers, in response to varying shear conditions.

the biomass distribution (e.g., Jeong et al., 2015). Likewise, non-motile phytoplankton –e.g., some diatom and cyanobacteria species- orient in hydrodynamically favorable directions to displace over large distances (e.g., Eppley et al., 1968) by either positively or negatively varying their buoyancy through different mechanisms such as gas vesicles, lipid storage, the exchange of heavy ions with their surroundings or by forming chains that modify their sinking rates (Gross and Zheuten, 1948; Anderson and Sweeney, 1978; Walsby, 1994). These directionally oriented patterns often respond to collective behaviors common to many planktonic organisms, which favor cell to cell interactions at the population level and may produce far reaching effects at larger scales, for instance by contributing to the vertical transport of carbon and nutrients (e.g., Cullen and Horrigan, 1981; Schofield et al., 2006; Hall and Paerl, 2011). Physical coagulation, facilitated by secretion of viscous extracellular polysaccharides, is a fundamental part of marine snow formation and carbon recycling processes (Passow, 2002).

PHYTOPLANKTON ORIENTATION IN THE SEA

Cell orientation, widely believed to be homogenized by the effect of turbulence, is a prime example of erroneous preconceptions in phytoplankton ecology. In fact, and on the contrary, the interaction between cell shape, motility, and fluid flows establishes a plethora of non-uniform orientational distributions. These, in turn, affect a rich variety of key biological functions epitomizing the relevance of mechanisms occurring at the scale of microns to centimeters for the correct interpretation of larger scale processes. These include sensing, nutrient uptake, parasite and predator avoidance, competition for resources, reproduction, the quest for optimal light conditions for growth or aggregation of phytoplankton into marine snow (Eppley et al., 1968; Smayda, 1980; Denny, 1993; Reynolds, 2006; Kiørboe, 2008; Burd and Jackson, 2009).

For motile organisms, whose orientation is mainly driven by body asymmetry that favors directed swimming, preferential orientation occurs in a variety of forms: as active responses to locally anisotropic environmental stimuli, such as photo- or chemotaxis, and as passive responses to the incessantly moving fluid environment (e.g., gyro- or rheotaxis). These oriented responses or "taxes" are the result of the necessity of the organism to react to specific gradients or stimuli and are greatly facilitated by cell motility. Even though it is energetically demanding, motility is advantageous in a world where resources (i.e., nutrients) are heterogeneously distributed (Stocker et al., 2008). The majority of the phytoplankton classes are flagellated and, therefore, motile. Since velocities generated by flagellar movement (50–500 μm s^{-1}; Sournia, 1982 and references therein) are commonly larger than the Kolmogorov velocity microscale[1], $V_K = (\nu\varepsilon)^{1/4}$, motility allows for a reasonable

[1]Where ν is the kinematic viscosity of the water ($\sim 10^{-6}$ m^2 s^{-1} for sea water) and ε is the mean dissipation rate of turbulent kinetic energy ($\varepsilon \approx 10^{-10}$ to 10^{-5} m^2 s^3).

control of orientation. Cells move to new locations to seek more favorable environments or to interact with other organisms.

Among the variety of phytoplankton response cues (hydrodynamics, nutrient availability, predator and/or parasite avoidance, etc.), most commonly observed taxes are the positive phototaxis triggering migration to the sea surface during daylight hours and negative gravitaxis driving cell descent at night. This oriented swimming determines, for instance, marked circadian patterns in several dinoflagellate species. However, most importantly, movement also allows phytoplankton cells to cross unfavorable microenvironments and to access microscale nutrient maxima (Guasto et al., 2012).

Studies on microorganism motility under distinct flow conditions further evidence how coupling between swimming and fluid flow can result in non-random cell orientations, and consequently, non-uniform cell accumulation. Paradigmatic examples include laboratory experiments and modeling on gyrotaxis, where local shear flow couples to motility to induce cell focusing in localized streams (Kessler, 1985; Pedley and Kessler, 1992), dynamic aggregation regimes (Durham et al., 2011) and intense patchiness in turbulent flows far exceeding that of randomly distributed, non-motile populations (Durham et al., 2013); or rheotaxis, where swimming cells (whether bacteria, heterotrophs, sperm cells, or phytoplankton) reorient with respect to gradients in the flow velocity to successfully migrate in the local upstream direction (Marcos et al., 2012; Bukatin et al., 2015; Mathijssen et al., 2019).

Likewise, vertical gradients in horizontal velocity in the water column ($S = \partial u/\partial z$) can disrupt vertical migration of gyrotactic phytoplankton. When vertically swimming cells encounter regions of strong horizontal shear flows, their orientation can be dramatically altered, causing them to tumble continuously and triggering sharply peaked cell accumulations in localized layers and regions of enhanced shear (Durham et al., 2009; Durham and Stocker, 2012). This trapping effect arising from shear flow has been proposed to be a plausible mechanism for the formation of the frequently observed thin layers of phytoplankton in aquatic systems (**Figure 2**).

Non-motile phytoplankton can also exhibit preferential orientation and movement under the influence of gravity, at least in the case of the larger microplanktonic cells such as diatoms. Cell orientation influences displacement trajectories, sinking velocities and cell concentrations. A growing number of studies have advanced our understanding of the translation, rotation, and orientation of dilute suspensions of small spheroids and fibers in turbulence, highlighting the rich dynamics of interactions (Metzger et al., 2005; Botte et al., 2013). Insight on the behavior of particles in these flow regimes mainly emanates from experiments and theory developed for dilute suspensions of fibers and spheroids (see Voth and Soldati, 2017) yet, most studies in this field corresponds to inertial particles above Kolmogorov length scales and, therefore, not directly transposable to phytoplankton. The interplay between cell buoyancy regulated displacements and their entrainment by turbulence leads, under general conditions, to even more acute non-homogeneous distributions (Arrieta et al., 2015; Borgnino et al., 2019) and greater social complexity amongst planktonic species is predicted in regions of large shear (Breier et al., 2018; Uppal and Vural, 2018).

The fact that shear generates changes in velocity in the proximity of the organisms results in forces and torques that depend on cell orientation. Torque favors the rotation of cells with an angular speed which leads to preferential alignment with the flow. Rotation is proportional to the velocity gradient and depends on shape (Barry et al., 2015). Two different behaviors can be approximated depending on cell shape; prolate shapes (cells with the apical to transapical ratio $\lambda > 1$) that approximate the rod-like morphology of pennate diatoms and oblate shapes ($\lambda < 1$), similar to disk-shaped centric diatoms. Non-spherical cells describe periodic orbits as they sink in Couette (laminar) flows. According to Jeffery (1922), prolate cells tend to set their apical axis perpendicular to the plane of the undisturbed fluid motion describing steady periodic orbits. Oblate cells tend to set themselves with an equatorial diameter perpendicular to the plane of undisturbed motion of the fluid while rotating periodic but not steadily. In unsteady shear and turbulent flows, this reorientation dynamics becomes far more complex.

Certain cells can counteract rotation by actively varying the distribution of mass inside the cell or passively using morphological structures such as with protuberances and spines, or certain body shapes. Others are able to form chains and aggregations increasing even further their vertical displacements (Lovecchio et al., 2019). The evolutive solutions to this problem have resulted in a remarkable diversity of phytoplankton morphologies. For example, spines in non-motile phytoplankton have been suggested to decrease settling rates by enhancing drag and elongated morphologies may alter the organisms' orientational distribution in flow. These structures may be biologically important since they produce cell tumbling that increases cell encounter probabilities with nutrient and infochemical micro-patches and with neighboring cells and grazers (Karp-Boss et al., 1996; Kiørboe, 2008). In contrast, in the presence of intense shear, cells are preferentially aligned with the flow which limits their ability to migrate in other (e.g., perpendicular to the flow) directions, inexorably producing cell accumulations (see **Figure 2**). Shear induced preferential orientation of sinking spheroidal cells also drift them out of their prominently vertical motion to oversample downwelling regions of a turbulent flow which affects their average settling speed and modulates their escape time to the deep ocean (Ruiz et al., 2004; Arrieta et al., 2015; Ardekani et al., 2017; Borgnino et al., 2019). Moreover, and under quiescent flow environments, the coupling between orientation and sinking drift direction induces large scale hydrodynamic instabilities (Koch and Shaqfeh, 1989), facilitating cell encounters even under dilute conditions (Font-Muñoz et al., 2019).

Patterns of preferential orientation of motile and non-motile phytoplankton has been by now amply shown in laboratory studies (e.g., Karp-Boss and Jumars, 1998; Karp-Boss et al., 2000; Guasto et al., 2012). However, and despite noticeable technological progress over the last decades, direct observations of phytoplankton cells in their natural environment are still scarce. Most evidences of preferential cell orientation in the ocean have been obtained using digital holography.

Talapatra et al. (2013), using a submersible holographic imaging system, analyzed diatom chain orientation and its relationship with mean shear rate in East Sound (WA, EEUU). More recently, also using holography, Nayak et al. (2018) observed preferential cell alignment at horizontal angles coinciding with regions of low velocity shear and weak turbulent dissipation rates. A different process related with preferential cell orientation of diatoms was inferred from *in situ* laser transmissometry (LISST-100×) by Font-Muñoz et al. (2019). In this case, a progressive increase in vertical cell alignment was observed under the pycnocline during a *Pesudo-nitzschia* sp. bloom. This preferential cell orientation was paralleled by an increase in the number of paired cells (up to 19% of the population) providing the first *in situ* link between orientational order and crucial intercellular interactions in the population dynamics of a cosmopolitan pennate diatom.

CONCLUSION

With the scientific advances carried out in the last century, our vision of marine phytoplankton and its interaction with the surrounding environment has expanded significantly. As we nosedive into the microscale, with the aid of new technology (and renew use of old technology), emerging insights reveal a highly structured, dynamic and organized realm. Phytoplankton interactions at this scale between congeners, competitors and with their immediate physico-chemical landscape, directly impinge on large scale oceanographic and ecosystem level processes.

Cell orientation, in particular, is a rarely assessed example of the relevance of these cross-scale interactions. Beyond its importance for key cell physiological processes, preferential cell orientation impacts the formation of thin phytoplankton layers, the absorption and transmission of light in the ocean (Marcos et al., 2011), its spectral characteristics (Goessling et al., 2018) and fundamental ecological interactions between organisms. Still, much remains to be explored both in terms of thorough field observations and detailed analysis of experimental conditions to fully appreciate the role of non-random phytoplankton cell orientations and its link with larger scales dynamics. Technological advances are also needed in order to intensify *in situ* observations.

Finally, we still need further understanding and full integration into mainstream biological oceanography of the governing laws and detailed mechanisms ruling in this microscale kingdom.

AUTHOR CONTRIBUTIONS

GB, JF-M, and IT conceived and wrote the manuscript.

FUNDING

This work was partially funded by the SIFOMED grant (CTM2017-83774-P) and INTERDIBIO (FIS2016-77692-C2-1-P) from Ministerio de Ciencia, Innovación y Universidades (MICINN), the Agencia Estatal de Investigación (AEI) and the Fondo Europeo de Desarrollo Regional (FEDER, UE). This work benefited from the French state aid managed by the National Research Agency under the ISblue program (ANR-17-EURE-0015).

REFERENCES

Anderson, L. W. J., and Sweeney, B. M. (1978). Role of inorganic ions in controlling sedimentation rate of a marine centric diatom Ditylum Brightwelli. *J. Phycol.* 14, 204–214. doi: 10.1111/j.1529-8817.1978.tb02450.x

Ardekani, M. N., Sardina, G., Brandt, L., Karp-Boss, L., Bearon, R., and Variano, E. (2017). Sedimentation of inertia-less prolate spheroids in homogenous isotropic turbulence with application to non-motile phytoplankton. *J. Fluid Mech.* 831, 655–674. doi: 10.1017/jfm.2017.670

Arrieta, J., Barreira, A., and Tuval, I. (2015). Microscale patches of nonmotile phytoplankton. *Phys. Rev. Lett.* 114:128102.

Bainbridge, R. (1957). The size, shape and density of marine phytoplankton concentrations. *Biol. Rev.* 32, 91–115. doi: 10.1111/j.1469-185x.1957.tb01577.x

Barnes, H., and Marshall, S. M. (1951). On the variability of replicate plankton samples and some application of 'contagious' series to the statistical distribution of catches over restricted periods. *J. Mar. Biol. Assoc. U. K.* 30, 233–263. doi: 10.1017/s002531540001273x

Barry, M. T., Rusconi, R., Guasto, J. S., and Stocker, R. (2015). Shear-induced orientational dynamics and spatial heterogeneity in suspensions of motile phytoplankton. *J. R. Soc. Interface* 12:20150791. doi: 10.1098/rsif.2015.0791

Borgnino, M., Arrieta, J., Boffetta, G., De Lillo, F., and Tuval, I. (2019). Turbulence induces clustering and segregation of non-motile, buoyancy-regulating phytoplankton. *J. R. Soc. Interface* 16:20190324. doi: 10.1098/rsif.2019.0324

Botte, V., D'Alcalaİ, M. R., and Montresor, M. (2013). Hydrodynamic interactions at low Reynolds number: an overlooked mechanism favouring diatom encounters. *J. Plankton Res.* 35, 914–918. doi: 10.1093/plankt/fbt033

Breier, R. E., Lalescu, C. C., Waas, D., Wilczek, M., and Mazza, M. G. (2018). Emergence of phytoplankton patchiness at small scales in mild turbulence. *Proc. Natl. Acad. Sci. U.S.A.* 115, 12112–12117. doi: 10.1073/pnas.1808711115

Bukatin, A., Kukhtevich, I., Stoop, N., Dunkel, J., and Kantsler, V. (2015). Bimodal rheotactic behavior reflects flagellar beat asymmetry in human sperm cells. *Proc. Natl. Acad. Sci. U.S.A.* 112, 15904–15909. doi: 10.1073/pnas.1515159112

Burd, A. B., and Jackson, G. A. (2009). Particle aggregation. *Annu. Rev. Mar. Sci.* 1, 65–90.

Cassie, R. M. (1959). Micro-distribution of plankton. *N. Z. J. Sci.* 2, 398–409.

Cassie, R. M. (1963). Microdistribution of plankton. *Oceanogr. Mar. Biol. Ann. Rev.* 1, 223–252.

Cowles, T. J., Desiderio, R. A., and Carr, M. E. (1998). Small-scale planktonic structure: persistence and trophic consequences. *Oceanography* 11, 4–9. doi: 10.5670/oceanog.1998.08

Cullen, J. J., and Horrigan, S. G. (1981). Effects of nitrate on the diurnal vertical migration, carbon to nitrogen ratio, and the photosynthetic capacity of the dinoflagellate *Gymnodinium splendens*. *Mar. Biol.* 62, 81–89. doi: 10.1007/bf00388169

Currie, W. J. S., and Roff, J. C. (2006). Plankton are not passive tracers: plankton in a turbulent environment. *J. Geophys. Res.* 111:C05S07.

Dekshenieks, M. M., Donaghay, P. L., Sullivan, J. M., Rines, J. E. B., Osborn, T. R., and Twardowski, M. S. (2001). Temporal and spatial occurrence of thin phytoplankton layers in relation to physical processes. *Mar. Ecol. Prog. Ser.* 223, 61–71. doi: 10.3354/meps223061

Denman, K. L., and Platt, T. (1976). The variance spectrum of phytoplankton in a turbulent ocean. *J. Mar. Res.* 34, 593–601.

Denny, M. W. (1993). *Air and Water: The Biology and Physics of Life's Media*. Princeton, NJ: Princeton University Press.

Derenbach, J. B., Astheimer, H., Hansen, H. P., and Leach, H. (1979). Vertical microscale distribution of phytoplankton in relation to the thermocline. *Mar. Ecol. Prog. Ser.* 1, 187–193. doi: 10.3354/meps001187

Doubell, M. J., Prairie, J. C., and Yamazaki, H. (2014). Millimeter scale profiles of chlorophyll fluorescence: deciphering the microscale spatial structure of phytoplankton. *Deep-Sea Res. II* 101, 207–205.

Durham, W., Climent, E., Barry, M., De Lillo, F., Boffetta, G., Cencini, M., et al. (2013). Turbulence drives microscale patches of motile phytoplankton. *Nat. Commun.* 4:2148.

Durham, W., Kessler, J. O., and Stocker, R. (2009). Disruption of vertical motility by shear triggers formation of thin phytoplankton layers. *Science* 323, 1067–1070. doi: 10.1126/science.1167334

Durham, W. M., Climent, E., and Stocker, R. (2011). Gyrotaxis in a steady vortical flow. *Phys. Rev. Lett.* 106:238102.

Durham, W. M., and Stocker, R. (2012). Thin phytoplankton layers: characteristics, mechanisms, and consequences. *Ann. Rev. Mar. Sci.* 4, 177–207. doi: 10.1146/annurev-marine-120710-100957

Eppley, R. W., Holm-Harisen, O., and Strickland, J. D. H. (1968). Some observations of the vertical migration of marine dinoflagellates. *J. Phycol.* 4, 333–340.

Fenchel, T. (1993). There are more small than large species? *Oikos* 68, 375–378.

Font-Muñoz, J. S., Jeanneret, R., Arrieta, J., Anglès, S., Jordi, A., Tuval, I., et al. (2019). Collective sinking promotes selective cell pairing in planktonic pennate diatoms. *Proc. Natl. Acad. Sci. U.S.A.* 116, 15997–16002. doi: 10.1073/pnas.1904837116

Goessling, J. W., Su, Y., Maibohm, C., Ellegaard, M., and Kühl, M. (2018). Differences in the optical properties of valve and girdle band in a centric diatom. *Interface Focus* 9, 20180031. doi: 10.1098/rsfs.2018.0031

Grant, H., Stewart, R., and Moilliet, A. (1962). Turbulence spectra from a tidal channel. *J. Fluid Mech.* 12, 241–268.

Gregg, M. C. (1980). Microstructure patches in the thermocline. *Journal of Physical Oceanography* 10, 915–943. doi: 10.1175/1520-0485(1980)010<0915:mpitt>2.0.co;2

Gross, F., and Zheuten, E. (1948). The buoyancy of plankton diatoms: a problem of cell physiology. *Proc. R. Soc. Lond. B* 135, 382–389. doi: 10.1098/rspb.1948.0017

Guasto, J. S., Rusconi, R., and Stocker, R. (2012). Fluid mechanics of planktonic microorganisms. *Annu. Rev. Fluid Mech.* 44, 373e400.

Haeckel, E. (1891). Plankton studien. *Jena Z. Naturwis.* 25, 232–336.

Hall, N. S., and Paerl, H. W. (2011). Vertical migration patterns of phytoflagellates in relation to light and nutrient availability in a shallow microtidal estuary. *Mar. Ecol. Prog. Ser.* 425, 1–19. doi: 10.3354/meps09031

Harvey, H. W. (1942). Production of life in the sea. *Biol. Rev.* 17, 221–246. doi: 10.1111/j.1469-185x.1942.tb00438.x

Haury, L. R., McGowan, J. A., and Wiebe, P. H. (1978). "Patterns and processes in the time-space scales of plankton distribution," in *Spatial Pattern in Plankton Communities*, ed. J. H. Steele (New York, NY: Plenum Press), 277–327. doi: 10.1007/978-1-4899-2195-6_12

Hensen, V. (1887). "Über die bestimmung des plankton's oder des im meere treibenden materials an pflanzen und thieren," in *Berichte Kommss. wissenschaftlichen Untersuchung der deutschen Meere* eds Schmidt and Klaunig (Kiel: Berlin Parey) 5, 1–107.

Holling, C. S. (1992). Cross-scale morphology, geometry, and dynamics of ecosystems. *Ecol. Monogr.* 62, 447–502. doi: 10.2307/2937313

Holwill, M. E. J. (1974). "Hydrodynamic aspects of ciliary and flagellar movement," in *Cilia and Flagella*, ed. M. A. Sleigh (London: Academic Press), 43.

Jeffery, G. B. (1922). The motion of ellipsoidal particles immersed in a viscous fluid. *Proc. R. Soc. Lond. A.* 102, 161–179. doi: 10.1098/rspa.1922.0078

Jeong, H. J., Lim, A. S., Franks, P. J. S., Lee, K. H., Kim, J. H., Kang, N. S., et al. (2015). A hierarchy of conceptual models of red-tide generation: nutrition, behavior, and biological interactions. *Harmful Algae* 47, 97–115. doi: 10.1016/j.hal.2015.06.004

Jumars, P. A., Trowbridge, J. H., Boss, E., and Karp-Boss, L. (2009). Turbulence-plankton interactions: a new cartoon. *Mar. Ecol.* 30, 133–150. doi: 10.1111/j.1439-0485.2009.00288.x

Karp-Boss, L., Boss, E., and Jumars, P. A. (1996). Nutrient fluxes to planktonic osmotrophs in the presence of fluid motion. *Oceanogr. Mar. Biol. Annu. Rev.* 34, 71–107.

Karp-Boss, L., Boss, E., and Jumars, P. A. (2000). Motion of dinoflagellates in a simple shear flow. *Limnol. Oceanogr.* 45, 1594–1602. doi: 10.4319/lo.2000.45.7.1594

Karp-Boss, L., and Jumars, P. A. (1998). Motion of diatom chains in steady shear flow. *Limnol. Oceanogr.* 43, 1767–1773. doi: 10.4319/lo.1998.43.8.1767

Kessler, J. O. (1985). Hydrodynamic focusing of motile algal cells. *Nature* 313, 218–220. doi: 10.1038/313218a0

Kiørboe, T. (1993). Turbulence, phytoplankton cell size, and the structure of pelagic food webs. *Adv. Mar. Biol.* 29, 1–72. doi: 10.1016/s0065-2881(08)60129-7

Kiørboe, T. A. (2008). *Mechanistic Approach to Plankton Ecology*. Princeton, NJ: Princeton University Press.

Koch, D. L., and Shaqfeh, E. S. G. (1989). The instability of a dispersion of sedimenting spheroids. *J. Fluid Mech.* 209, 521–542. doi: 10.1017/s0022112089003204

Kolmogorov, A. N. (1941). The local structure of turbulence in incompressible viscous fluid for very large Reynolds numbers. *Dokl. Akad. Nauk SSSR* 30, 301–305.

Kolmogorov, A. N. (1962). A refinement of previous hypotheses concerning the local structure of turbulence in a viscous incompressible fluid at high Reynolds number. *J. Fluid Mech.* 13, 82–85. doi: 10.1017/s0022112062000518

Lehman, J. T., and Scavia, D. (1982). Microscale patchiness of nutrients in plankton communities. *Science* 216, 729–730. doi: 10.1126/science.216.4547.729

Levich, V. G. (1962). *Physicochemical Hydrodynamics*. Upper Saddle River, NJ: Prentice Hall, 163.

Levin, S. A. (1992). The problem of pattern and scale in ecology. *Ecology* 73, 1943–1967. doi: 10.2307/1941447

Lighthill, J. (1976). Flagellar hydrodynamics. *SIAM Rev.* 18, 161–230. doi: 10.1137/1018040

Lorenzen, C. J. (1966). A method for the continuous measurement of in rive chlorophyll concentration. *Deep-Sea Res.* 13, 223–227. doi: 10.1016/0011-7471(66)91102-8

Lovecchio, S., Climent, E., Stocker, R., and Durham, W. M. (2019). Chain formation can enhance the vertical migration of phytoplankton through turbulence. *Sci. Adv.* 5:EAAW7879.

Marcos, Fu, H. C., Powers, T. R., and Stocker, R. (2012). Bacterial rheotaxis. *Proc. Natl. Acad. Sci. U.S.A.* 109, 4780–4785. doi: 10.1073/pnas.1120955109

Marcos, Seymour, J. R., Luhar, M., Durham, W. M., Mitchell, J. G., Macke, A., et al. (2011). Microbial alignment in flow changes ocean light climate. *Proc. Natl. Acad. Sci. U.S.A.* 108, 3860–3864. doi: 10.1073/pnas.1014576108

Margalef, R. M. (1967). Some concepts relative to the organization of plankton. *Oceanogr. Mar. Biol. Ann. Rev.* 5, 257–289.

Margalef, R. M. (1978). Life forms of phytoplankton as survival alternatives in an unstable environment. *Oceanol. Acta* 1, 493–509.

Mathijssen, A. J. T. M., Figueroa-Morales, N., Junot, G., Clément, E., Lindner, A., and Zöttl, A. (2019). Oscillatory surface rheotaxis of swimming E. *coli bacteria*. *Nat. Commun.* 10:3434.

Metzger, B., Guazzelli, E., and Butler, J. E. (2005). Large-scale streamers in the sedimentation of a dilute fiber suspension. *Phys. Rev. Lett.* 95:164506.

Nayak, A. R., McFarland, M. N., Sullivan, J. M., and Twardowski, M. S. (2018). Evidence for ubiquitous preferential particle orientation in representative oceanic shear flows. *Limnol. Oceanogr.* 63, 122–143. doi: 10.1002/lno.10618

Owen, R. W. (1989). Microscale and finescale variations of small plankton in coastal and pelagic environments. *J. Mar. Res.* 47, 197–240. doi: 10.1357/002224089785076415

Passow, U. (2002). Transparent exopolymer particles (TEP) in aquatic environments. *Prog. Oceanogr.* 55, 287–333. doi: 10.1016/s0079-6611(02)00138-6

Pedley, T. J., and Kessler, J. O. (1992). Hydrodynamic phenomena in suspensions of swimming microorganisms. *Annu. Rev. Fluid Mech.* 24, 313–358. doi: 10.1146/annurev.fl.24.010192.001525

Platt, T. (1972). Local phytoplankton abundance and turbulence. *Deep-Sea Res.* 19, 183–187. doi: 10.1016/0011-7471(72)90029-0

Platt, T. (1978). "Spectral analysis of spatial structure in phytoplankton populations," in *Spatial Patterns in Plankton Communities*, ed. J. H. Steele (Brussels: NATO conference Series), 73–84. doi: 10.1007/978-1-4899-2195-6_4

Powell, T. M., Richardson, P. J., Dillon, T. M., Agee, B. A., Dozier, B. J., Godden, D. A., et al. (1975). Spatial scales of current speed and phytoplankton biomass

fluctuations in Lake Tahoe. *Science* 189, 1088–1090. doi: 10.1126/science.189.4208.1088

Prairie, J. C., Sutherland, K. R., Nickols, K. J., and Kaltenberg, A. M. (2012). Biophysical interactions in the plankton: a cross-scale review. *Limnol. Oceanogr. Fluids Environ.* 2, 121–145. doi: 10.1215/21573689-1964713

Purcell, E. M. (1977). Life at low Reynolds number. *Am. J. Phys.* 45, 3–11.

Reynolds, C. S. (1997). *Vegetation Processes in the Pelagic: A Model for Ecosystem Theory. xxvii,* Oldendorf/Luhe. Berlin: Ecology Institute, 371.

Reynolds, C. S. (2006). *The Ecology of Phytoplankton*. Cambridge: Cambridge University Press.

Rietkerk, M., Dekker, S. C., de Ruiter, P. C., and van de Koppel, J. (2004). Self-organized patchiness and catastrophic shifts in ecosystems. *Science* 305, 1926–1929. doi: 10.1126/science.1101867

Riley, G. A. (1942). The relationship of vertical turbulence and spring diatom flowering. *J. Mar. Res.* 5, 67–87.

Riley, G. A., Stommel, H. M., and Bumpus, D. (1949). Quantitative ecology of the plankton of the Western North Atlantic. *B. Bingham Oceanogr. C.* 12, 1–169.

Rothschild, B. J., and Osborn, T. R. (1988). Small-scale turbulence and plankton contact rates. *J. Plankton Res.* 10, 465–474. doi: 10.1093/plankt/10.3.465

Ruiz, J., Macìas, D., and Peters, F. (2004). Turbulence increases the average settling velocity of phytoplankton cells. *Proc. Natl. Acad. Sci. U.S.A.* 101, 17720–17724. doi: 10.1073/pnas.0401539101

Rusconi, R., Guasto, J. S., and Stocker, R. (2014). Bacterial transport is suppressed by fluid shear. *Nat. Phys.* 10, 212–217. doi: 10.1038/nphys2883

Russel, F. S. (1950). Quantitative ecology of plankton. *Nature* 165, 559–560. doi: 10.1038/165559a0

Sachs, J. (1876). Ueber Emulsionsfiguren und Gruppirung der Schwarmsporen im Wasser. *Flora* 59, 273–275.

Schofield, O., Kerfoot, J., Mahoney, K., Moline, M., Oliver, M., Lohrenz, S., et al. (2006). Vertical migration of the toxic dinoflagellate Karenia brevis and the impact on ocean optical properties. *J. Geophys. Res. Oceans* 111:C06009.

Schwarz, F. (1884). Der einfluss der schwerkraft auf die bewegungsrichtung von chlamidomonas und euglena ber. *Deutsch. Bot. Ges.* 2, 51–72.

Seymour, J. R., Simó, R., Ahmed, T., and Stocker, R. (2010). Chemoattraction to dimethyl-sulfoniopropionate throughout the marine microbial food web. *Science* 329, 342–345. doi: 10.1126/science.1188418

Sheldon, R. W., Prakash, A., and Sutcliffe, W. H. Jr. (1972). The size distribution of particles in the ocean. *Limnol. and Oceanogr.* 17, 327–340. doi: 10.4319/lo.1972.17.3.0327

Siegel, D. A. (1998). Resource competition in a discrete environment: why are plankton distributions paradoxical? *Limnol. Oceanogr.* 43, 1133–1146. doi: 10.4319/lo.1998.43.6.1133

Smayda, T. J. (1980). "Phytoplankton species succession," in *The Physiological Ecology of Phytoplankton*, ed. I. Morris (Oxford: Blackwell Scientific Publications), 493–570.

Sournia, A. (1982). Form and function in marine phytoplankton. *Biol. Rev.* 57, 347–394. doi: 10.1111/j.1469-185x.1982.tb00702.x

Steele, J. H. (1959). The quantitative ecology of marine phytoplankton. *Biol. Rev.* 34, 129–158. doi: 10.1111/j.1469-185x.1959.tb01287.x

Steele, J. H. (1978). *Spatial Pattern in Plankton Communities*. Plenum Press, NY: NATO Conference Series. IV.

Stocker, R. (2012). Marine microbes see a sea of gradients. *Science* 338, 628–633. doi: 10.1126/science.1208929

Stocker, R., Seymour, J. R., Samadani, A., Hunt, D. E., and Polz, M. F. (2008). Rapid chemotactic response enables marine bacteria to exploit ephemeral microscale nutrient patches. *Proc. Natl. Acad. Sci. U.S.A.* 105, 4209–4214. doi: 10.1073/pnas.0709765105

Stommel, H. (1963). Varieties of oceanographic experience. *Science* 139, 572–576. doi: 10.1126/science.139.3555.572

Sverdrup, H. U. (1953). On conditions for the vernal blooming of phytoplankton. *ICES J. Mar. Sci.* 18, 287–295. doi: 10.1093/icesjms/18.3.287

Talapatra, S., Hong, J., McFarland, M., Nayak, A. R., Zhang, C., Katz, J., et al. (2013). Characterization of biophysical interactions in the water column using in situ digital holography. *Mar. Ecol. Prog. Ser.* 473, 29–51. doi: 10.3354/meps10049

Uppal, G., and Vural, D. C. (2018). Shearing in flow environment promotes evolution of social behavior in microbial populations. *eLife* 7:e34862.

Vance, T. C., and Doel, R. E. (2010). Graphical methods and cold war scientific practice: the stommel diagram's intriguing journey from the physical to the biological environmental sciences. *Hist. Stud. Nat. Sci.* 40, 1–47. doi: 10.1525/hsns.2010.40.1.1

Voth, G. A., and Soldati, A. (2017). Anisotropic Particles in Turbulence. *Annu. Rev. Fluid Mech.* 49, 249–276. doi: 10.1146/annurev-fluid-010816-060135

Wager, H. W. T. (1910). The effect of gravity upon the movements and aggregation of euglena viridis, ehrb., and other micro-organisms. *Proc. R. Soc. Lond. B.* 83.

Walsby, A. E. (1994). Gas vesicles. *Microbiol. Rev.* 58, 94–144. doi: 10.1128/mmbr.58.1.94-144.1994

Wheeler, J. D., Secchi, E., Rusconi, R., and Stocker, R. (2019). Not just going with the flow: the effects of fluid flow on bacteria and plankton. *Annu. Rev. Cell Dev. Biol.* 35, 213–237. doi: 10.1146/annurev-cellbio-100818-125119

Conflict of Interest: The authors declare that the research was conducted in the absence of any commercial or financial relationships that could be construed as a potential conflict of interest.

Copyright © 2020 Basterretxea, Font-Muñoz and Tuval. This is an open-access article distributed under the terms of the Creative Commons Attribution License (CC BY). The use, distribution or reproduction in other forums is permitted, provided the original author(s) and the copyright owner(s) are credited and that the original publication in this journal is cited, in accordance with accepted academic practice. No use, distribution or reproduction is permitted which does not comply with these terms.

frontiers in Marine Science

ORIGINAL RESEARCH
published: 24 April 2020
doi: 10.3389/fmars.2020.00254

Multi-Instrument Assessment of Phytoplankton Abundance and Cell Sizes in Mono-Specific Laboratory Cultures and Whole Plankton Community Composition in the North Atlantic

Susanne Menden-Deuer[1], Françoise Morison[1], Amanda L. Montalbano[1], Gayantonia Franzè[1,2†], Jacob Strock[1], Ewelina Rubin[1], Heather McNair[1], Colleen Mouw[1] and Pierre Marrec[1]*

[1] Graduate School of Oceanography, University of Rhode Island, Narragansett, RI, United States, [2] Norwegian Institute of Marine Research (IMR), Bergen, Norway

OPEN ACCESS

Edited by:
Malcolm McFarland, Florida Atlantic University, United States

Reviewed by:
Nicole J. Poulton, Bigelow Laboratory for Ocean Sciences, United States
Abdiel E. Laureano-Rosario, Florida Atlantic University, United States

***Correspondence:**
Susanne Menden-Deuer
smenden@uri.edu

†Present address:
Gayantonia Franzè, Institute of Marine Research, Flødevigen, Norway

Specialty section:
This article was submitted to Marine Ecosystem Ecology, a section of the journal Frontiers in Marine Science

Received: *26 September 2019*
Accepted: *30 March 2020*
Published: *24 April 2020*

Citation:
Menden-Deuer S, Morison F, Montalbano AL, Franzè G, Strock J, Rubin E, McNair H, Mouw C and Marrec P (2020) Multi-Instrument Assessment of Phytoplankton Abundance and Cell Sizes in Mono-Specific Laboratory Cultures and Whole Plankton Community Composition in the North Atlantic. Front. Mar. Sci. 7:254. doi: 10.3389/fmars.2020.00254

The abundance and size distribution of plankton in the surface ocean are key metrics to understanding primary and export production, food web dynamics, and the optical properties of the water column. Here we quantified cell size and abundance of phytoplankton species from mono-specific laboratory cultures, using optical, electrical, and image-based benchtop instrumentation. Moreover, we combined particle size distribution and size fractionated chlorophyll a (Chl a) analysis with image analysis to estimate phytoplankton community composition and abundance comparing a high and low biomass station in the North Atlantic during springtime. In laboratory cultures, we found generally good agreement in estimates of both particle concentration and particle size among instruments. Image-based approaches (e.g., microscopy, FlowCam) delivered somewhat lower cell abundance estimates, because image-based instruments distinguish cells from non-target particles. Image-based approaches also measured 10–20% greater cell sizes, because measurements were based only on in-focus images of the target species. Compared to image-based instruments, particle counters delivered indistinguishable estimates of size and abundance with much lower effort and technical expertise required; maximum coefficient of variation for cell abundance and size did not exceed 10 and 15%, respectively. Measurement precision was consistent across instrument type and across a cell size spectrum from 3 to >40 μm equivalent spherical diameter (ESD). For whole plankton community analyses from the North Atlantic, combined estimation of Chl a concentration and image-based diversity assessments resolved the dominant phytoplankton species and spatial differences in the size structure of the plankton community. These results provide strong support for using particle counters, that can rapidly process large volumes of samples, to quantify particle size and abundance, including rarer, larger particles. Species identities and community composition can be revealed by supplemental,

image-based approaches. Application of this coupled approach can help identify fundamental ecosystem characteristics such as particle size spectra that affect primary production, trophic transfer, and export. Ultimately, the tremendous species diversity of plankton can be leveraged as particle tracking and identification keys, such as near-real time identification of coherent water masses.

Keywords: plankton, marine particles, particle counter, BD Influx, FlowCam, microscope, NAAMES, EXPORTS

INTRODUCTION

The abundance and size distribution of particles in the surface ocean, including plankton, are critical determinants of the optical properties of aquatic primary and export production, food web structure, and biogeochemistry (Reynolds et al., 2010; Maranon, 2015). Marine particulates including plankton span orders of magnitude in size, from nanometers to centimeters (10^{-9} to 10^{-2} m), which has made their characterization challenging. No one instrument is currently optimized to characterize particle abundance and sizes across this vast size range (Stemmann and Boss, 2011). This mismatch results in limited predictive capacity of important metrics, such as particle sinking rates and thus export production of organic matter from the surface ocean (Siegel et al., 2016). Many phytoplankton have complex shapes that are difficult to express in simple geometric terms, yet size and shape of particles are key properties that affect light absorption and scattering, which are important metrics for satellite measurements and remote sensing of ocean ecosystem properties (Kostadinov et al., 2009; Mouw and Yoder, 2010). This problem is exacerbated by the diverse, taxon-specific cell surface coverings characteristic of phytoplankton (e.g., silica frustules, coccoliths).

Adding to the challenge of quantifying characteristics of individual particles is the fact that particles are embedded in a complex mixture of living, detrital, and abiotic material. The living component, the plankton community composition and its fine scale distribution, is increasingly recognized as important for understanding food web dynamics and large scale ecosystem function (Menden-Deuer and Fredrickson, 2010; Durham and Stocker, 2011; Levy et al., 2015), but our ability to quantify plankton community composition and variability therein is subject to a substantial technological challenge. Overcoming this challenge, however, is critical for a holistic understanding of ocean-atmosphere processes, which rely on near real time assessment of the fine-scale spatial and temporal trends in plankton community structure that can be leveraged for adaptive sampling by an inter-disciplinary team of investigators.

Recent advances in benchtop, in-line, and *in situ* instrumentation have vastly increased the sampling power and resolution of measurements of surface ocean particle size distributions (PSD). There are several excellent reviews of major instrumentation, which include diverse measurement approaches, including electrical impedance (e.g., Beckman Multisizer), optical (e.g., flow cytometers), and image-based instruments (e.g., FlowCam), some of which can be used on autonomous or remotely operated *in situ* instrumentation (Reynolds et al., 2010; Lombard et al., 2019). Each instrument type measures different particle properties (e.g., resistivity, fluorescence, light scattering), which result in instrument-specific advantages and disadvantages. For example, measurements of resistivity process samples with densities of 10^5 particles ml^{-1} or more within <1 min, but fail to detect key properties, such as distinguishing living from non-living particles.

For decades, analysis of microscope samples by highly trained individuals was necessary to characterize the species composition and abundance of particles in water samples. This approach yields high quality data, but it is labor-intensive and time consuming and thus results in considerable limitations with respect to spatial and temporal resolution. There is also high potential for operator-dependence of the results (Culverhouse et al., 2003). A major breakthrough was the development of image-based particle analyzers that can be operated in *in situ* or benchtop mode (Sieracki et al., 1998; Olson and Sosik, 2007; Sosik and Olson, 2007; Thyssen et al., 2015). These image-based approaches are further supported by the development of automated classification methods aided by machine-learning tools (e.g., neural networks), which are trained to recognize specific phytoplankton species, and permit extensive quantification of particle characteristics (Luo et al., 2018). Such instruments provide powerful tools to examine the optical and morphological details of particles and species in the surface ocean by distinguishing individual particles with respect to their characteristics such as detritus, lithogenic matter, biological species or fabricated materials (e.g., plastics). One caution to the utility of the image-based approaches is that recent molecular analyses suggest limited utility with respect to morphologically based identification, given that even dominant and keystone taxa are not distinguishable by visual inspection alone and can contain "cryptic species" (Canesi and Rynearson, 2016). Moreover, image-based approaches are most suitable for specimen with sizes $>\sim$5 μm diameter, thus image analysis cannot adequately address important components of the pico- and nanoplankton. Thus, analysis has to be supplemented by additional characteristics, such as optical properties, including scatter and fluorescence.

Many instruments aim to characterize whole seawater PSD, irrespective of their specific characteristics, as these PSD can yield important environmental insights, such as magnitude of ecosystem production (e.g., Kim and Menden-Deuer, 2013 and references therein). A common challenge is the mathematical description of these PSD and the appropriate quantification of the slope of often non-linear PSD distributions (Reynolds et al., 2010 and references therein). For mono-specific laboratory cultures,

TABLE 1 | Species analyzed in this study.

Species	Strain ID	Size (ESD, μm)
Dinoflagellates		
Akashiwo sanguinea (Hirasaka) G. Hansen and Moestrup	PA280909	42
Ceratium lineatum (Ehrenberg) Cleve	PA230210	15
Heterocapsa triquetra (Ehrenberg) Stein	CCMP448	25
Prorocentrum concavum Fukuyo	PA081009	32
Chlorophytes		
Dunaliella tertiolecta Butcher	CCMP1320	6.4
Prymnesiophyte		
Isochrysis galbana Parke	CCMP1323	4
Raphidophyte		
Heterosigma akashiwo (Hada) Sournia	CCMP3374	9
Picocyanobacteria		
Synechococcus Nägeli	PA_DJ34_D6	2.5

PA, Narragansett Bay Long Term Time Series; CCMP, now National Center for Marine Algae and Microbiota.

instrument software provides analysis tools, but these tools are often user selected and not always supported by establishment of a standard operating procedure.

To address these challenges and establish particle characterization tools for the quantification of plankton, we present an instrument inter-comparison by evaluating measurements of cell abundance and cell size, along with reproducible, operator-independent analysis protocols that minimize user-induced biases in selection of the size ranges or particle types to include in analyses. Furthermore, these protocols can be standardized and subjected to sensitivity analyses. Our goal was to compare the precision and size range of each instrument using a best-case scenario of mono-specific phytoplankton cultures that are characterized by uniformity in size (i.e., at most a 2-fold variation) as well as a lack of detrital and non-biogenic particles. Finally, we use data collected at two open-ocean stations from the North Atlantic to demonstrate how combining image-based analyses with automated particle enumeration as well as measurements of size-fractionated Chl a concentration can provide a rapid assessment of whole plankton community composition.

MATERIALS AND METHODS

Phytoplankton Culture Conditions

Eight phytoplankton species were selected as targets for cross-instrument comparisons. These species were chosen because they represent a size range from pico- to microplankton and vary in their surface properties, including thecate dinoflagellates covered by cellulose plates. All phytoplankton cultures (**Table 1**) were grown exponentially in F/2-Si medium (Guillard, 1975) and maintained in 250–500 ml PC bottles on a 12:12 light: dark cycle at 15°C, salinity of ∼30 psu, and a light intensity of 70–80 μmol photons m^{-2} s^{-1}. All species were pigmented and grown phototrophically but not axenically.

Laboratory Inter-comparison of Instruments

For the laboratory inter-instrument comparison, special emphasis was placed on three species: *Isochrysis galbana*, *Dunaliella tertiolecta,* and *Prorocentrum concavum*, which were measured with all instruments (**Table 2**). These three species represent differences in size and surface properties. Additional measurements of species listed in **Table 1** were made as possible (**Table 2**). Constraints included the fact that not all species could be analyzed on all instruments. For example, picoplankton could not be imaged with the FlowCam. Moreover, we restricted the time frame of observation to 3 h, and instrument preparation and sample handling for some instruments was longer, limiting the number of species imaged. Measurements were acquired within 3 h, to ensure comparability of results and avoid changes in the properties of the phytoplankton cultures. Cultures were kept at room temperature and at low ambient light.

Instruments used in the inter-comparison of counts and sizing included a microscope, two models of Coulter Counter (MIII and MIV), a FlowCam, and a BD Influx flow cytometer. These instruments were chosen to represent different measurement approaches, including optical and electrical. Details on each instrument and the measurements are given below.

Microscopy analyses

To determine cell counts and cell volume, 5 ml samples were preserved in acid Lugol (2% final conc.) and analyzed using 1 ml aliquots on a Sedgwick-Rafter counting chamber and a Nikon Eclipse E800 light microscope. For low concentration samples with $<$500 cells ml^{-1}, all cells within the chamber were counted, while a minimum number of 500 cells or those in 20 grids in a Sedgwick-Rafter were counted for high concentration samples ($>$500 cells ml^{-1}). Microscope counts were not replicated but count variation for the two smaller species was estimated as among field of view abundances. Species-specific cell volume was calculated based on linear dimensions measured from 30 to 100 cells, using an image analysis system consisting of a high-resolution digital camera (Allied Vision, F45) and ImageJ software v1.5i. Both length and width were measured on cells in planar view using a magnification between 100× and 200×.

Coulter Counter Analysis

A Multisizer III (MS3) and a Multisizer IV (MS4) (Beckman Coulter Counter, CC) were used to measure particle numbers and size distribution. Triplicate 10 ml aliquots were withdrawn from each phytoplankton culture and 1 ml of each aliquot was counted using a 100 μm aperture. Aperture diameter determines the theoretical size range of the measurable particle size spectrum, which is 3–65% of the aperture diameter. Data blanks were generated with 0.2 μm Parker string-wound cartridge filtered sterile seawater and used to verify the reliability of the theoretical range. The instrument was regularly calibrated with manufacturer supplied beads of a nominal diameter of 10 μm. The particle size spectrum produced number of counts per size bin between 3 and 65 μm with a bin width of 0.2 μm, the

TABLE 2 | Overview of instruments included, their general characteristics and our assessment of instrument utility for size, abundance and particle size distribution estimates.

Method	Instrument	Type of measurement	Size range	Volume analyzed	Sample processing time	Abundance accuracy	Taxonomy	Size accuracy	Resolution of PSD	Operator independence	Immediacy of results	Species analyzed	Advantage	Disadvantage
Microscopy	Nikon Eclipse E800	Image	2–200 μm	5 ml	+++	+++	+++	+++	-	+	++	l.g., D.t., P.c.	High Quality Data, Taxonomic information	Time Consuming, Operator expertise
Size fractionated Chl-a	Turner 10AU	Filtration and Chl a fluorescence	>0.2 μm	180 ml	++	NA	-	+	+	++	+	Field samples	Simplicity, biomass proxy, link to *in situ* measurements	Limited information about size distribution and taxonomy
Flow cytometry	BD Influx	Optics	0.5–50 μm	0.05 ml	+	+++	+	++	++	++	+++	Syn, l.g., D.t., P.c.	Excells at picoplankton, high sample sizes, multiple cell characteristics	Small sample volumes can exclude large and rare specimen. Complex size calibration.
Imaging system	FlowCAM	Image	6–200 μm	0.5 ml	+	++	+++	++	++	++	++	l.g., D.t., H.a., P.c.	Taxonomic information, wide size range, multiple cell characteristics, reproducible	Data processing of images, excludes picophytoplankton, dilute samples require concentration
Particle counter	Beckman coulter MS3 and MS4	Resistivity	0.2–200 μm	1–5 ml	+	+++	-	+++	+++	+++	+++	l.g., D.t., H.a.,H.t., P.c., C.l., A.s.	Rapid, full size spectrum > 2 μm, operator independent	Can't distinguish non-biological or live or dead cells, no taxonomic information

Species abbreviations follow species listed in ***Table 1****. Plus signs indicate relative assessment from less (+) to more (+++). Minus signs indicate not available.*

CC default. Coulter counter sizes are expressed as equivalent spherical diameter (ESD).

BD Influx

Cell abundances for four of the phytoplankton cultures (*Synechococcus* sp., *D. tertiolecta, I. galbana, and P. concavum*, **Table 1**) were determined using the BD Influx flow cytometer (BD Biosciences). This flow cytometer is equipped with multiple lasers and photomultiplier tubes for optical signal collection. We used optical pulse shape signals from a blue laser beam (488 nm) and forward scatter (FSC), sideward scatter, orange (580/30 nm) and red (692/40 nm) fluorescence optical parameters to assess culture abundances. Flow rate and analyzed sample volume were calculated from the difference in sample weight between the start and the end of the analysis. Event acquisition and recording times were at least 125 and at most 225 s. The mean flow rate during the analyses was 0.60 μl s^{-1}. Cell abundance was determined from the number of events in a gate for a given cell population divided by the volume of the sample that passed through the instrument during acquisition. SpheroAccuCount^{TM} (7.3 μm, Spherotech) calibration beads, with certified concentration, were analyzed before and after the measurements to monitor the instrument stability and to confirm the calculation of the volume analyzed by the instrument. Ultra Rainbow beads (3 μm, Spherotech) were also analyzed to monitor the instrument stability. Data were collected using the BD FACS Software to acquire, record data and pick gates, and then reanalyzed in Flowing Software[1] to obtain the abundances of each culture. Flow cytometry was used as a reference approach to estimate the abundance of phytoplankton species based on their fluorescence emissions. Phytoplankton cell size was estimated from mean single-cell FSC. We used an iterative linear regression approach including both beads and the cultured phytoplankton species of known size (**Table 1**), and assuming a 0 intercept. The iterative linear regression approach included the mean FSC of the two different beads and mean FSC of three phytoplankton species of known size (Sieracki and Poulton, 2011; Cetinic et al., 2015). The analysis excluded the species under investigation. This approach resulted in significant relationships between size and FSC with r^2-values of 0.99, except for *Prorocentrum*, the largest cells, with a r^2 of 0.89. Although we observed reliable linear fits, we caution that prior reports observed a polynomial relationship (Shalapyonok et al., 2001) or a power law function (Jacquet et al., 2001). Future applications of this approach need to resolve the effects of the optical properties of beads and cells on cell size estimates with flow cytometers and determine when linear relationships can be applied.

FlowCam

Samples were analyzed using a benchtop B3 Series FlowCam (Fluid Imaging) with a 50 μm standard flow cell at a 20× magnification. Samples were analyzed in triplicate for all species except *Heterosigma* sp., for which only one sample could be analyzed within the allotted 3 h time frame. The FlowCam offers three working modes: auto-image, fluorescence or side-scatter trigger modes. In auto-image, images are taken at a constant frame rate, whereas in either trigger modes, the camera is triggered only when particle fluorescence or scattering exceeds a default threshold that can be adjusted. For phytoplankton analyses, the use of the fluorescence trigger mode is the more frequently used mode due to the pigment composition of phototrophic cells. We used the fluorescence trigger mode to support comparison to the BD influx measurement. Samples were run for ∼3 min, corresponding to a processed volume of ∼0.3 ml. In trigger mode, ideally the particle per used image (PPUI) should be kept at <1.2, i.e., only one cell should be present in the field of view when the camera is triggered. Due to the elevated density of the laboratory cultures, average PPUI of triplicates values were 2.2 and 1.37 for *I. galbana* and *D. tertiolecta* cultures, respectively. This implies coincident observations of cells and inaccurate estimates of cell concentrations as automatically generated by the instrument software. To overcome the inaccuracy of the system supplied concentration estimates, final concentrations were re-calculated manually (see below in section "Data Analysis"). Cell density for *P. concavum* was low and auto-image mode was used to avoid potential loss of cells due to low fluorescence. The number of *P. concavum* cells analyzed was further maximized by running the sample for 10 min, corresponding to a volume of ∼1 ml. After analysis, FlowCam images were processed twice: first to generate abundance estimates after removing non-target species particles (e.g., detrital material), and second to generate size estimates after removing target-species images that were not in planar view or not in focus. Cell abundance and cell ESD of the target species were retrieved using the instrument software. ESD was estimated as the mean value of 36 Feret measurements, i.e. perpendicular distances between parallel tangents across opposite sides of the particle, made at 5° each between −90° and +90°.

Whole Plankton Community Analysis

Source water was collected in May 2016 during the NAAMES second field campaign aboard the R/V Atlantis along a north to south transect (54–44°N, ∼40°W) in the North Atlantic Ocean (Behrenfeld et al., 2019). Here we focus on two stations that represented the extremes of the range of Chl a concentrations encountered during the campaign, Station 3 (50.24°N, 43.86°W) and Station 4 (47.35°N, 38.31°W). The station numbers are identical to the numbering used during the NAAMES cruise to facilitate comparisons with other reports from that campaign. Water for plankton community analyses was collected from a depth of 5 m using a Niskin rosette with 10 L bottles equipped with a SBE911plus (Seabird Electronics) CTD (Conductivity, Temperature and Depth) profiler and gently strained through a 200 μm mesh (see Morison et al., 2019).

Particle counts and size distribution were analyzed onboard using a Coulter Counter Model III, following the protocol described above for the analysis of mono-specific laboratory cultures. Chl a analysis followed the procedure regularly used by our laboratory for Chl a extraction (e.g., Morison et al., 2019). In brief, Chl a concentration was determined from triplicate 180 ml subsamples taken from the same Niskin bottle after filtration on GF/F filters and extraction followed Graff and Rynearson (2011),

[1] http://flowingsoftware.btk.fi/

except that extraction took place in the dark at room temperature for 12 h in 96% ethanol (Jespersen and Christoffersen, 1987). Size fractionated Chl a concentration was also measured on 5, 10, and 20 μm filters. Comparison of extracted Chl a concentration with those obtained from High Performance Liquid Chromatography (HPLC) analysis showed an excellent agreement ($r^2 =$ 0.98, $p <$ 0.0001). Based on the good agreement between <200 μm extracted Chl a and unfiltered HPLC Chl a we conclude that the pre-filtering step through 200 μm did not result in any notable loss of phytoplankton cells. HPLC data were obtained from the NASA data repository SeaBASS (Behrenfeld et al., 2019).

FlowCam Analysis largely followed the methods outlined above. Due to generally low abundance of cells within a size range appropriate for the instrument, 2 L volumes were concentrated approximately 3-fold, by gently pouring seawater into a tall 5 μm mesh strainer. Concentration factors were specified before analysis to be taken into account in the software retrieval of cell concentrations. Sample volumes processed varied from 3 to 5 ml and, depending on concentration and size of the target species, were analyzed using either 50 or 100 μm flow cells and corresponding magnifications of 20× and 10×, specifying a minimum FlowCam size filter of 3 and 6 μm (Area Based Diameter), respectively.

Data Analysis

Abundance per species and instrument was averaged across triplicate measurements (where available) to calculate standard deviations and determine instrument specific coefficients of variation (CV = standard deviation/mean, %). Due to the high density of two of the laboratory cultures, the FlowCam analyses performed in trigger-mode resulted in high Particles per used Image and high frame-rates. When this is the case, the instrument functions as if in auto-image mode, and particle concentration can be manually calculated applying the algorithm used in auto-image mode, an approach that has been tested to yield accurate estimates (Fluid Imaging, pers. comm.). Particle concentrations were thus calculated by dividing the counts obtained after removal of unwanted particles (see above) by the volume imaged, the latter retrieved from the software generated run summary.

For microscopy measurements, which provided separate length and width measurements, cell volume was determined using appropriate geometric formulae (e.g., Sun and Liu, 2003). Here we compare plankton mean size based on instrument estimates of ESD. We recognize that estimation of the ESD varies with instrument type, e.g., the Coulter Counter estimates an equivalent volume based on the impedance of the sensing field. Comparison of the type of ESD estimate was not subject to further analysis, since the estimation of ESD was not subject to user selection.

To estimate total particle abundance, the CC requires selection of an operator-defined range of particle sizes, which affects estimates of particle abundance and size distribution. To examine the effect of operator-choice and possible bias, and to develop operator-independent means to estimate the size distribution, we compared particle abundance and mean cell size estimated from a subset of the CC measurements. The comparison was made by determining the mode of the particle size frequency distribution and choosing a series of percentile ranges about the mode that varied from including 20% to 80% of the distribution. Abundance and size estimates derived from these specified percentile ranges were compared to user-selected ranges based on visual inspection of the frequency distribution of counts across particle sizes. The latter is the procedure necessary when using the CC provided software to analyze data. Cell abundance was then calculated as the sum of particles within the included range. Cell size and standard deviation thereof was calculated as the weighted mean across the included range of discrete size bins of 0.2 μm.

RESULTS AND DISCUSSION

Abundance

There was generally good agreement (within 2-fold differences) in the abundance measurements generated with the different instrument types, despite the vastly different measurement approaches (**Figure 1**, left panels). There was no difference in abundance by the two types of CC and counts were similar to those generated by the BD Influx. FlowCam counts tended to be comparable but lower than the other instruments, especially for *Prorocentrum concavum*. Microscope counts for the three focal species were inconsistent relative to the other methods, including higher, comparable, and lower estimates than the other instruments delivered. It is noteworthy that the use of exponentially growing phytoplankton cultures represents a best case scenario, in which the occurrence of non-target particles is minimized, but co-occurrence of detrital material, precipitate, and other non-biological and biologically derived particulates, which can be species dependent (see below), can lead to contamination of the sample. Thus, even in laboratory cultures there will be some non-target species that will elevate the counts of passive assessments that do not distinguish living cells from other particles. However, such contaminants will be much reduced compared to whole water samples.

For all instruments and particle concentrations of up to 20,000 particles ml^{-1} the variation in count estimates across replicates averaged <10% and did not vary systematically with concentration or instrument. Thus we do not see an instrument specific bias in the precision. Counts in excess of 400,000 cells ml^{-1} had a lower CV (1–3%). Variation among triplicate abundance counts on the same instrument was <10% for species whose abundance ranged from 10^2 to 10^5 cells (or particles for CC) ml^{-1} (**Figure 2**, top panel). Replication of microscope counts was not possible due to the restricted time frame of analysis, but replication is of course highly desirable and should be performed if at all possible. To get a sense of variation of microscope counts we estimated among field of view variation for *I. galbana* and *D. tertiolecta*, which were 7 and 11%, respectively, and prior examination of among replicate variability for microscope counts in our lab yields about 10% variation. This variation is modest and comparable to all other instrument count variation. One exception was *H. triquetra* analyzed with the CC (data not shown), which had highly variable replicate abundance measurements and a CV of 37%. The CC has

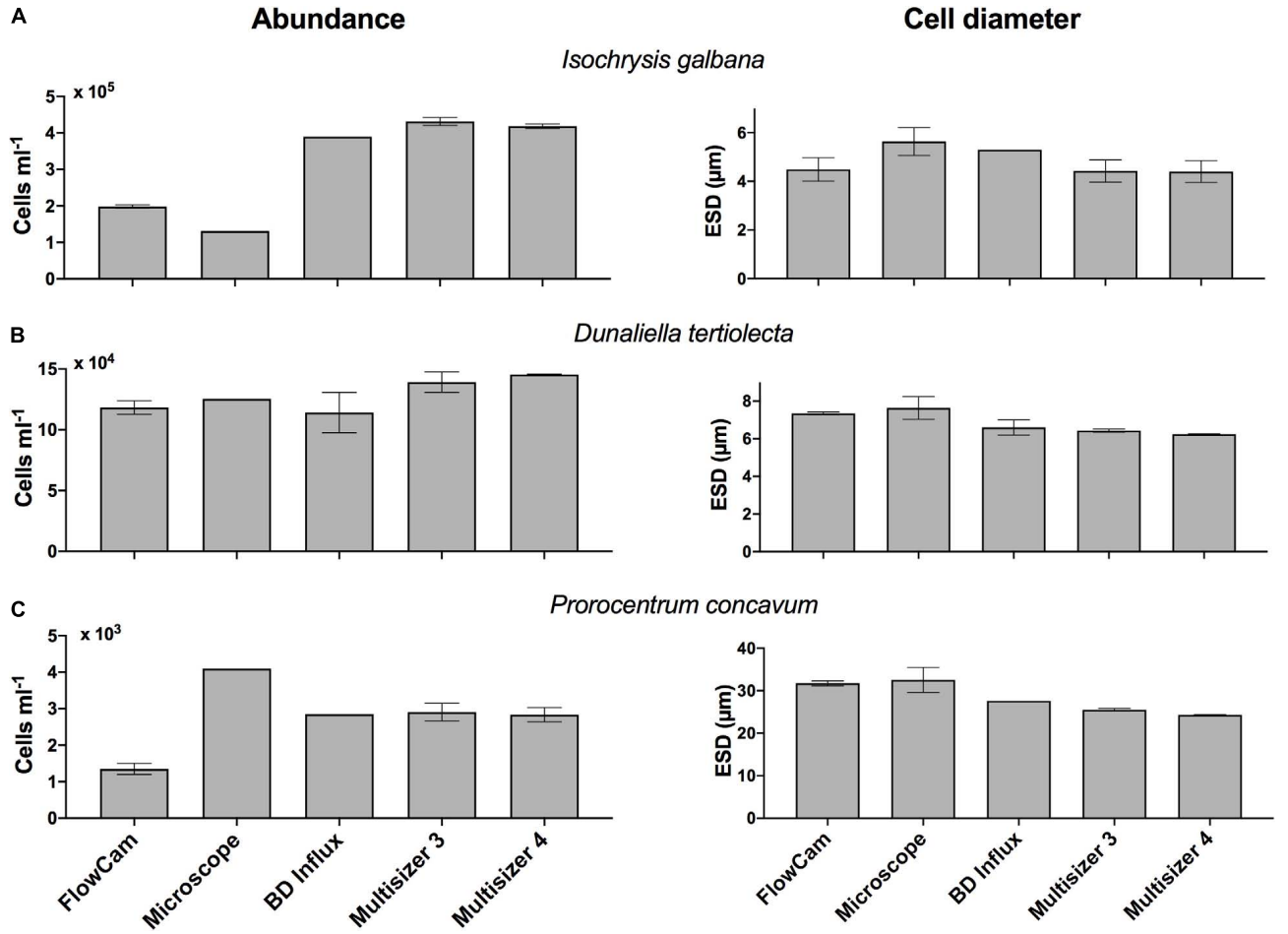

FIGURE 1 | Abundance (cells ml^{-1}, left panels) and cell diameter (ESD, right panels) measured with the FlowCam, Micrscocope, BD Influx, Coulter MultiSizer III and IV, for (top row, **A**) *Isochrysis galbana*, (middle row, **B**) *Dunaliella tertiolecta*, and (bottom row, **C**) *Prorocentrum concavum*. Error bars indicate one standard deviation of the mean.

previously been shown to deliver poor abundance estimates of *H. triquetra* (Kim and Menden-Deuer, 2013), but the reason remains unknown. The BD Influx counts were comparable to the particle counters (**Figure 1**, left panels). The flow cytometer was the only instrument used to count *Synechococcus* sp. Although counts could have been obtained on the microscope, the other instruments could not acquire measurements for this pico-cyanobacterium due to non-compatible size ranges measured (see below).

Abundance estimates for I. *galbana* where lower for both microscopy and FlowCam compared to all other instruments (**Figure 1**). We suspect that the passive particle counters may be including non-target species events in the total count, but we did not evaluate the contribution of non-cells to the total count with FlowCam or microscopy. Counts for D. *tertiolecta* were consistent across instrument types, which may be due to the suitability of this particular size of organism across instruments (**Figure 1**).

Counts for FlowCam were lower than the other methods for *P. concavum*. The FlowCam data presented were subjected to post-acquisition analyses that included removal of particles, including biologically derived particles that did not represent the target species. Moreover, *P. concavum* culture contained empty thecae (**Figure 3**) that were not included in the abundance estimates. In contrast, counts from the particle counters undoubtedly included non-target species particles, including empty thecae, which would elevate the particle counter abundance results. However, the number of empty thecae and other particles that were removed through post-acquisition modifications was 200 particles ml^{-1}, and therefore this analysis step alone would be insufficient to close the gap between the FlowCam and particle counter counts. The reason for the difference is unknown. *P. concavum* microscopy counts exceeded estimates from all other instruments. The reason why microscopy counts for this species exceeded estimates from all other instruments is unknown but was verified, and counts did not include empty thecae. It suggests that even expert usage of the different instruments can yield substantial differences in abundance estimates and makes establishment of a superior method difficult. Instead, we suggest balancing the method taken

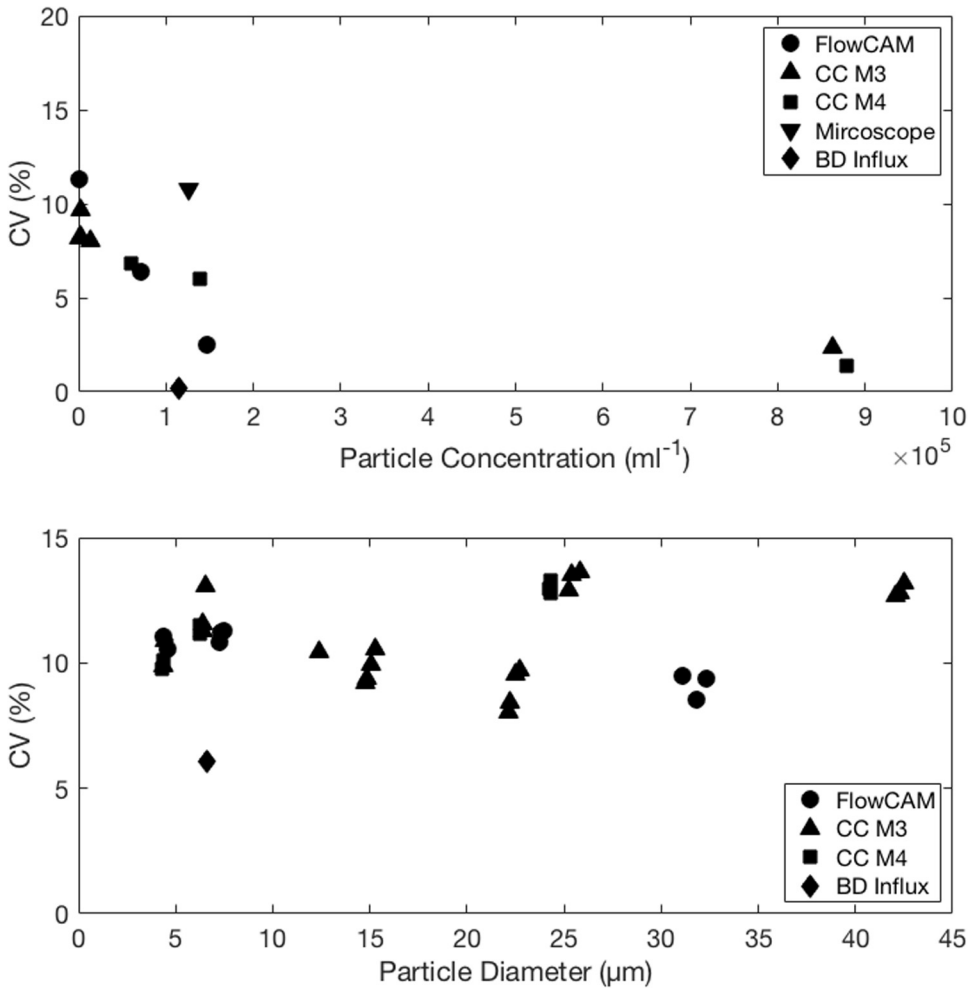

FIGURE 2 | Consistent coefficient of varition (CV, %) among (top) concentration and (bottom) particle size measurements for phytoplankton ranging from <5 to >40 µm in diameter measured with five different instruments. Coefficient of variation did not exceed 10 and 15%, respectively, of the abundance or size measurement and was independent of instrument and particle size. Particle counts in excess of 400,000 ml^{-1} did have a lower CV but are measured at the risk of high conincident particle passages.

with trade-offs of time, accuracy and if possible, to gather multi-instrument measurements (**Table 2**). Additionally, in order to ensure proper capture of particles in fluorescence-trigger mode, it is important that when a size filter is applied, it is chosen to be broad enough to span the variability of the cells analyzed. A broad, if any, filter avoids scenarios where

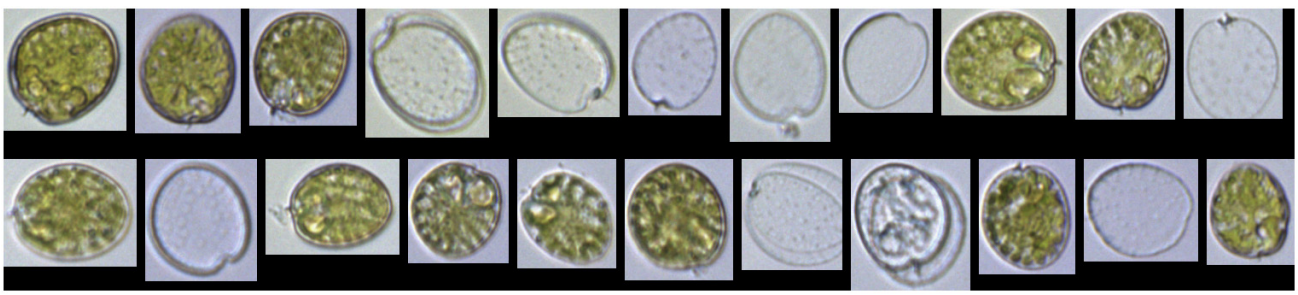

FIGURE 3 | FlowCam collage of *P. concavum*, which illustrates that even an exponentially growing laboratory culture contains both live cells and accumulated, empty thecae.

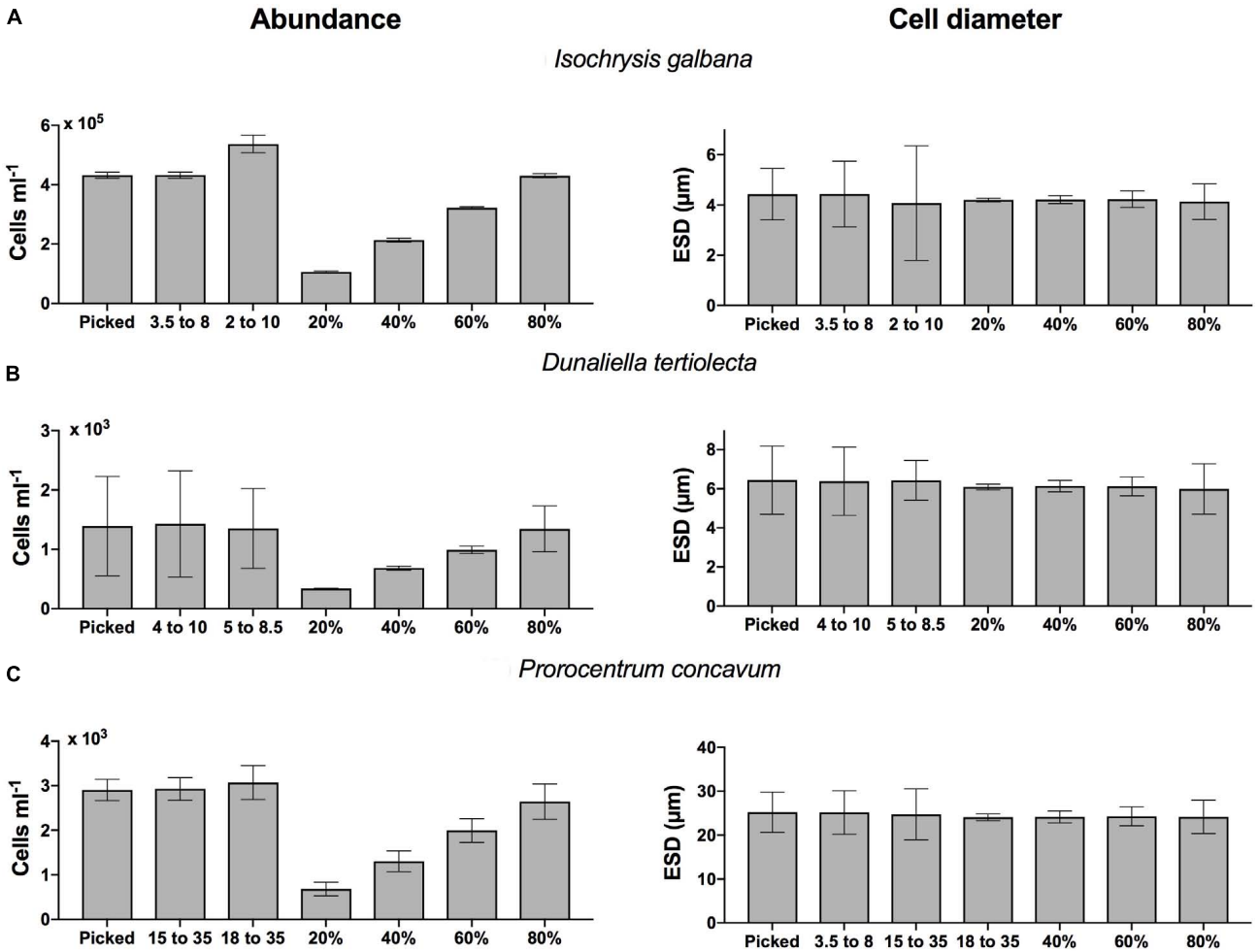

FIGURE 4 | (A–C) Abundance estimates (left panels) and size estimates (right panels) for the three focal phytoplankton species, (top **A**) *Isochrysis galbana,* (middle **B**) *Dunaliella tertiolecta*, and (bottom **C**) *Prorocentrum concavum*, from an electronic particle analyzer (Coulter Counter), based on inclusion of different distribution ranges of the total particle size distributions, as indicated on the x-axis. "Picked" indicates a range as would be operator chosen using the CC software. Units are in µm size range or fractions of the percentile ranges.

particles falling outside filter specifications trigger the camera, but are not be included in the counts. It may also be necessary to lower the specified fluorescence threshold. Cells with low pigment concentration and fluorescing at values below the threshold will not trigger the camera, which may result in underestimates of cell abundance. For motile species, samples need to be processed rapidly, ideally including the entire volume of sample inserted in the instrument or applying a continuous mixing of the sample in the intake funnel, unless the sample can be preserved before analysis. Preservation, however, may induce biases both in the cell size and in the types of species preserved (e.g., Menden-Deuer et al., 2001). Overall, given the typically high variability of abundance estimates of plankton, the abundance measurements agreed well across instruments, and positive identification of the target species afforded by microscopy and image based FlowCam analyses may be a useful addition to the analysis.

Cell Size

There was generally good agreement in the size measurements generated with the four different instrument types, with the image-based approaches delivering the largest ESD estimates (**Figure 1**, right panels). In case of *D. tertiolecta*, the ESD for the FlowCam was 1 µm larger than for the particle counters and the FlowCam estimate for *P. concavum* was 6 µm greater than ESD estimates from the particle counters; a difference of 12–20% in ESD delivered by different instruments. The larger ESD estimates from the FlowCam, which agreed with the microscope except for I. *galbana,* suggest that an image-based approach that allows processing of images and measurements based on only in focus cells delivers a substantially higher estimate of mean cell size and thus volume. ESD estimates from the BD Influx were in close agreement with the size estimates obtained by the particle counters, despite the limitation of our size estimate approach with the BD Influx, which imposed a linear assumption on the

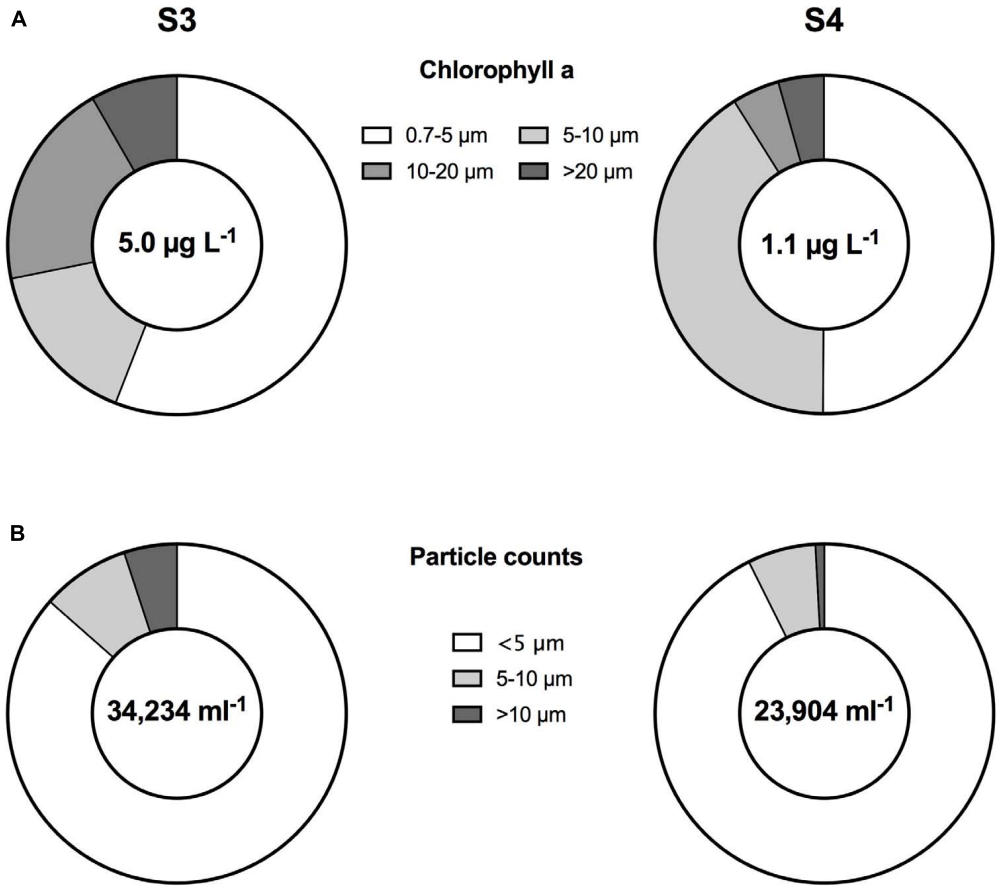

FIGURE 5 | Community structure from size-fractionated Chl a concentration (top, **A**) and particle counter (bottom, **B**) at two stations (S3 and S4) in the North Atlantic during May 2016. The dominance of small (<10 µm) particles is revealed, as are shifts in the relative contribution of different size classes. Total Chl a and particle concentration at each station is shown at the center of the pie charts.

FSC size relationship. Remarkably, measurement variation of ESD, expressed as the coefficient of variation (CV, %), did not show any instrument or size specific bias (**Figure 2**, bottom panel). This suggests that across the size spectrum from 3 to 45 µm ESD measured here, the instruments delivered, similarly, variable results and that precision was independent of the instrument used. While count data uncertainties were based on triplicate count values, the sample sizes for ESD measurements were vastly greater because ESD variation could be estimated across thousands of cells within a sample. Thus, the ESD variation represents the intrinsic variability in the sizes within the population and the measurement variation represents the achievable technical limit.

Cell-Size and Abundance Estimation

For mono-specific laboratory cultures there appears to be no standard, published, operator-independent analysis to determine mean cell size and total abundance. Standard CC software for example requires users to select the particle size range to include for abundance and size measurements. User bias in selecting a particular size range may alter estimates. To examine the magnitude of that potential bias and quantify the effect of analysis parameters on abundance and size measurement, we subjected the PSD of the mono-specific laboratory cultures measured with the Coulter Counter MultiSizer III to a sensitivity analysis. For all phytoplankton species, particle size distribution was analyzed for abundance and size using either a user defined ("picked") size range, two *a priori* chosen size ranges that encompass the mode, as well as four user independent percentile ranges that include increasing fractions of the distribution from 20 to 80% around the mode. None of the species size abundance distributions conformed to normality. For all species (with the exception of the smallest species measured with the CC, *I. galbana*) a similar picture emerges: Abundance estimates based on user selected size ranges were indistinguishable from one another (**Figure 4**, left panels). This suggests that even relatively large differences (e.g., 3–5 µm) in the PSD cut-offs do not alter the ultimate concentration estimate. The deviation of *I. galbana* from the general result is likely due to the fact that small particulates accumulate in the culture medium and were not distinguished from the cells themselves. This is also evident in the difference in FlowCam and microscopy counts relative to the particle counters.

The passively selected percentile ranges delivered increasing abundances with increasing percentile ranges considered, with

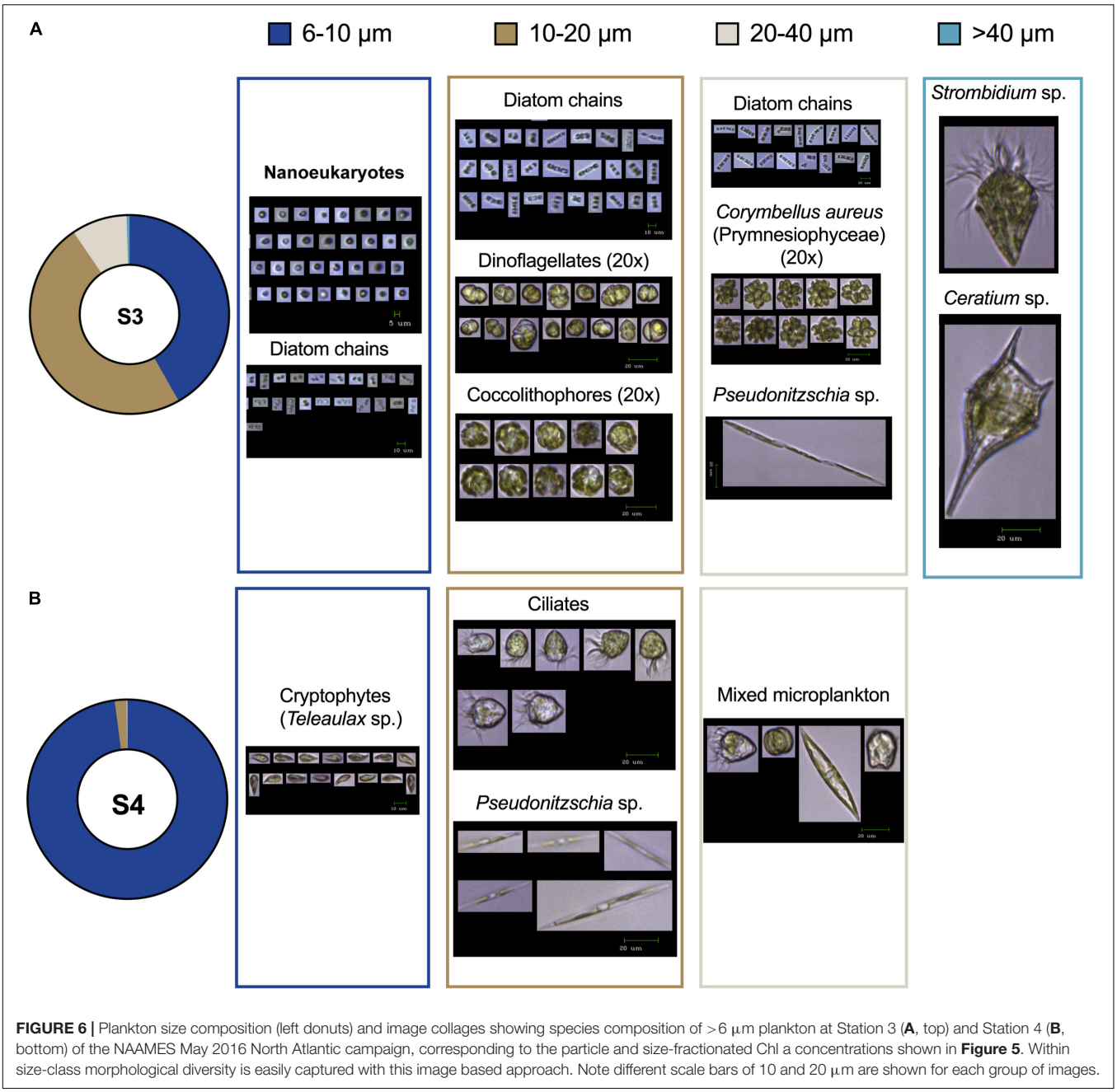

FIGURE 6 | Plankton size composition (left donuts) and image collages showing species composition of >6 µm plankton at Station 3 (**A**, top) and Station 4 (**B**, bottom) of the NAAMES May 2016 North Atlantic campaign, corresponding to the particle and size-fractionated Chl a concentrations shown in **Figure 5**. Within size-class morphological diversity is easily captured with this image based approach. Note different scale bars of 10 and 20 µm are shown for each group of images.

the 80% range delivering the best estimate on total abundance compared to the user selected ranges. One exception to the ideal 80% range was *A. sanguinea,* which had the largest size range and the lowest blank counts among the species selected (not shown). Thus, nearly the entire signal resulted from cells of this species and excluding 20% of the counts lead to an undercount for that species only; using a passively selected range of the distribution may introduce bias in undercounting larger microplankton.

Mean size estimates based on user selected size ranges were indistinguishable from one another, suggesting that even large differences (e.g., 3–5 µm) in the size cut-offs do not alter the ultimate mean size estimate (**Figure 4**, right panels). This is likely because the averages were calculated as weighted averages and thus the most frequent observations dominate the results. This result persisted, irrespective if the weighted mean was based on an arithmetic or geometric mean estimation. Moreover, even considerable changes in size distribution range selection by users had no effect on the ultimate estimate. The central fraction (20%) can deliver a similar estimate of mean size, if an entirely user independent approach is desired.

Overall, to achieve a user-independent, reproducible approach to select the particle size distribution to estimate mean cell size and total abundance, the central 20% fraction delivers the best

estimate of the mean ESD and the 80% range of the distribution provides the best estimate of the total abundance of cells.

Whole Plankton Community Analysis

We conducted an examination of whole community plankton composition in the <200 μm size range from samples collected during the May 2016 cruise of the NAAMES campaign (Behrenfeld et al., 2019; Morison et al., 2019; Saliba et al., 2019). Particle counts, size-fractionated Chl a, and an image-based approach resolved the dominant species, thus spatial shifts in plankton community composition and particle size distribution could rapidly be identified. The relative duration of data acquisition for the three methods were completed within minutes for the particle counter, 1–2 h for the imaging system, and within 12 h for the Chl a extraction. All three approaches clearly identified communities dominated by small particles (<10 μm). Instrument-specific estimates differ in measurement units, with Chl a extraction delivering a proxy for biomass, whereas the particle counters provide an approximation of particle abundance without positively identifying cells, that can then be converted to biomass, using assumptions of C density, for example. The relative contribution of Chl a < 10 μm (72% at S3 and 91% at S4) and the size distributions of this same size fraction measured by the particle counter (95% at S3 and 99% at S4) were similar (**Figure 5**). Discrepancy between Chl a size fractions and particle sizes is likely due to smaller particles to be captured on larger pore-sized filters when concentrations are high, or large volumes are filtered and differences in size estimations for the two methods. FlowCam's lower size limit in our application was 5–6 μm and thus FlowCam did not capture the quantitative contribution of small cells to total abundance. This gap in estimation of the whole particle size spectrum of whole plankton communities would be filled by flow cytometric methods that can deliver excellent, group specific estimation of cell size, fluorescence and scattering properties and abundance, particularly for pico- and nanophytoplankton (Cetinic et al., 2015).

Each of the three coupled size/abundance measurements of the whole plankton community provided information that, in combination, created a detailed view of the phytoplankton community. Size fractionated Chl a provided broad characterization of phytoplankton biomass distribution in four size classes. The CC generated a higher resolution distribution of particle abundance and ESD from 2 to 63 μm sized particles. However, the CC distribution is not specific to phytoplankton. While the particles captured by the FlowCam fall within a limited range of the entire size spectrum, imaging of single cells provides a valuable layer of taxonomic information in combination with cell size. By shedding light on the identity of species, particle imaging can expand information gained from molecular analyses of species diversity, where taxonomic resolution is often limited to the class level (e.g., Bolaños et al., 2020). This is exemplified at S3 (**Figure 6**), where images show that both coccolithophores and the colonial species *Corymbellus aureus* likely contributed to the molecularly detected Prymnesiophyceae (Bolaños et al., 2020).

Particles imaged by FlowCam cover the ecologically important size range of microplankton, that despite low numerical abundance often contribute a substantial fraction of total biomass and are important components of marine microbial food webs (Steinberg and Landry, 2017) production and export processes (Siegel et al., 2016) and whose identity is tied to ecosystem states (e.g., Margalef, 1978). FlowCam derived assessment of the species composition reveals that a diverse set of species contributed to the microplankton community composition (**Figure 6**). Further advantages of the image-based approach are revealed in the within-size-class information that clearly distinguishes pigmented nanoeukaryotes and Cryptophytes in the 6–10 μm size range or shifts in the abundance of dinoflagellates or the species of diatoms, all within the 20–40 μm size range (**Figure 6**). The combination of Chl a, CC, and FlowCam measurements provides a three-tiered resolution of whole phytoplankton communities. With the coarsest resolution (i.e., Chl a) measurement delivering information and bulk metrics useful for biogeochemical processes, the finer scale assessments (CC and FlowCam) provide critical details for understanding and mapping shifts in community structure.

CONCLUSION AND RECOMMENDATIONS

The instruments included here provide excellent opportunities for the rapid quantification of mono-specific laboratory cultures and characterization of whole plankton communities at sea in terms of particle sizes, abundance and relative contributions of size fractions. Image-based approaches deliver higher quality data on individual particles, as images show particle characteristics that allow elimination of non-living and detrital material and identify species- and cell-cycle specific properties (e.g., parasite infection, Peacock et al., 2014). For field applications, size structure and abundance are revealed through rapid, operator independent methods while image-based approaches provide key information on within-size class morphological diversity that can have ramifications for ecological processes, including food web structure and production. Moreover, image-based estimates were conservative, avoiding false positives, but relative to the particle counter estimates, are far more labor intensive and require greater operator skill and expertise than particle counting techniques. We anticipate that machine learning techniques will advance automated image analysis and reduction in manual classification in coming years (Zheng et al., 2017; González et al., 2019). Image-based classification will also be a fruitful tool to discover non-biogenic particles, including pervasive microplastics (Law, 2017).

Particle counters have the distinct advantage in that they can enumerate large volumes, to reveal the presence and frequency of larger particles. Although particle abundance decreases exponentially with size, ecological and ecosystem importance does not. Large particles may contribute a relatively larger component of the total biomass, where a large diatom (e.g., *Coscinodiscus* sp.) can hold equivalent biomass of one million picoplankton cells, for example. The strengths and weaknesses

of the different measurement approaches are quantified here, which provides users with diverse instrumentation for specific applications. The fundamental challenge of diminishing abundance of particles with increasing size will always require a trade-off between the particle size range accurately represented and the number of particles captured. As measurement variability inversely scales with particle abundance (i.e., sample size), measurement confidence diminishes with increasing particle size for any one instrument. The precision of measurements was remarkably consistent for all instruments, across the entirety of the cell sizes, from pico to microplankton, and concentrations measured here. Larger, rarer particles require either instruments that process larger sampling volumes or concentration of sample volumes during which smaller particles are lost.

Operator independent analyses approaches for plankton characterization and quantification are highly desirable and can enhance reproducibility of results and will be necessary as autonomous and *in situ* instrumentation is tasked with these types of analyses. Having established the reliability of a common suite of particle counters relative to more labor-intensive approaches opens possibilities for their *in situ* application, including in conjunction with other instrumentation, such as gliders and floats. Species identities and their abundances can provide near real time information on coherent water masses (e.g., Smetacek et al., 2002; Marrec et al., 2018) transitions in functional groups, or other metrics that would enable a synoptic sampling plan. Such adaptive strategies are essential to enhance spatio-temporal resolution of particle and plankton composition analyses to adequately characterize the importance of environmental and biological heterogeneity that can persist to the meter scale or less. This type of information also aids in post-cruise efforts of optimizing sample analysis. As discussed in a recent review (Lombard et al., 2019) the challenge remains to parse together the strength (i.e., size range covered) of different instruments to provide a holistic and continuous assessment of whole plankton communities. This assessment will need to include often non-pigmented, heterotrophic forms as well as identification of the trophic mode of mixotrophic species. Based on the evidence delivered here, *in situ* application of large volume particle counters supplemented with image-based approaches can illuminate the relative contribution of pico- to microplankton to overall particle abundance and derived processes. While far from a holistic assessment, the pico- to microplankton size range covers much of the ecologically relevant drivers of marine production processes and thus provides an important near-term goal.

DATA AVAILABILITY STATEMENT

The datasets generated for this study can be found in the SeaBASS at https://seabass.gsfc.nasa.gov/archive/URI/menden-deuer/NAAMES/naames_2/archive.

AUTHOR CONTRIBUTIONS

SM-D designed this study and conducted the data analysis. SM-D, FM, AM, GF, JS, ER, HM, and PM contributed to the laboratory measurements and data analysis. SM-D and FM conducted the whole plankton community analysis at sea. SM-D wrote the manuscript with input and approval from all co-authors.

FUNDING

This research was supported by the National Atmospheric and Space Administration, through funding of the field campaigns addressing EXport Processes in the global Ocean from RemoTe Sensing (EXPORTS, grant 80NSSC17K0716 to SM-D and Tatiana Rynearson) and the North Atlantic Aerosol and Marine Ecosystems Study (NAAMES, grant NNX15AL2G to SM-D) and in part through the National Science Foundation under EPSCoR Research Infrastructure Improvement Award OIA-1655221.

ACKNOWLEDGMENTS

This work was motivated by prior discussions with the Particle Size discussion group within the NASA EXPORTS Campaign. Harry Nelson of FluidImaging Technologies kindly provided advise on the FlowCam analysis. SM-D appreciates discussion with Melissa Omand (URI).

REFERENCES

Behrenfeld, M. J., Moore, R. H., Hostetler, C. A., Graff, J. R., Gaube, P., Chen, S. C., et al. (2019). The North Atlantic aerosol and marine ecosystem study (NAAMES): science motive and mission overview. *Front. Mar. Sci.* 6:122. doi: 10.3389/fmars.2019.00122

Bolaños, L. M., Karp-Boss, L., Choi, C. J., Worden, A. Z., Graff, J. R., Haëntjens, N., et al. (2020). Small phytoplankton dominate western North Atlantic biomass. *ISME J.* doi: 10.1038/s41396-020-0636-0 [Epub of ahead print].

Canesi, K. L., and Rynearson, T. A. (2016). Temporal variation of *Skeletonema* community composition from a long-term time series in Narragansett Bay identified using high-throughput DNA sequencing. *Mar. Ecol. Prog. Ser.* 556, 1–16. doi: 10.3354/meps11843

Cetinic, I., Perry, M. J., Asaro, E. D., Briggs, N., Poulton, M. E., Sieracki, C., et al. (2015). A simple optical index shows spatial and temporal heterogeneity in phytoplankton community composition during the 2008 North Atlantic bloom experiment. *Biogeosciences* 12, 2179–2194. doi: 10.5194/bg-12-2179-2015

Culverhouse, P., Williams, R., Reguera, B., Herry, V., and González-Gil, S. (2003). Do experts make mistakes? A comparison of human and machine identification of dinoflagellates. *Mar. Ecol. Prog. Series* 247, 17–25. doi: 10.3354/meps247017

Durham, W. M., and Stocker, R. (2011). Thin phytoplankton layers: characteristics, mechanisms, and consequences. *Annu. Rev. Mar. Sci.* 4, 177–207. doi: 10.1146/annurev-marine-120710-100957

González, P., Castaño, A., Peacock, E. E., Díez, J., Del Coz, J. J., and Sosik, H. M. (2019). Automatic plankton quantification using deep features. *J. Plankton Res.* 41, 449–463. doi: 10.1093/plankt/fbz023

Graff, J. R., and Rynearson, T. A. (2011). Extraction method influences the recovery of phytoplankton pigments from natural assemblages. *Limnol. Oceanogr. Methods* 9, 129–139. doi: 10.4319/lom.2011.9.129

Guillard, R. R. L. (1975). "Culture of phytoplankton for feeding marine invertebrates," in *Culture of Marine Invertebrate Animals*, eds W. L. Smith and M. H. Chanley (Boston, MA: Springer).

Jacquet, S., Partensky, F., Lennon, J.-F., and Vaulot, D. (2001). Diel patterns of growth and division in marine picoplankton in culture. *J. Phycol.* 37, 357–369.

Jespersen, A. M., and Christoffersen, K. (1987). Measurements of chlorophyll-a from phytoplankton using ethanol as extraction solvent. *Arch. Hydrobiol.* 109, 445–454.

Kim, H., and Menden-Deuer, S. (2013). Reliability of rapid, semi-automated assessment of plankton abundance, biomass, and growth rate estimates: coulter counter versus light microscope measurements. *Limnol. Oceanogr. Methods* 11, 382–393. doi: 10.4319/lom.2013.11.382

Kostadinov, T. S., Siegel, D. A., and Maritorena, S. (2009). Retrieval of the particle size distribution from satellite ocean color observations. *J. Geophys. Res. Oceans* 114:C09015.

Law, K. L. (2017). Plastics in the marine environment. *Annu. Rev. Mar. Sci.* 9, 205–229. doi: 10.1146/annurev-marine-010816-060409

Levy, M., Jahn, O., Dutkiewicz, S., Follows, M. J., and d'Ovidio, F. (2015). The dynamical landscape of marine phytoplankton diversity. *J. R. Soc. Interface* 12:20150481. doi: 10.1098/rsif.2015.0481

Lombard, F., Boss, E., Waite, A. M., Vogt, M., Uitz, J., Stemmann, L., et al. (2019). Globally consistent quantitative observations of planktonic ecosystems. *Front. Mar. Sci.* 6:196. doi: 10.3389/fmars.2019.00196

Luo, J. Y., Irisson, J.-O., Graham, B., Guigand, C., Sarafraz, A., Mader, C., et al. (2018). Automated plankton image analysis using convolutional neural networks. *Limnol. Oceanogr. Methods* 16, 814–827. doi: 10.1002/lom3.10285

Maranon, E. (2015). Cell size as a key determinant of phytoplankton metabolism and community structure. *Annu. Rev. Mar. Sci.* 7, 241–264. doi: 10.1146/annurev-marine-010814-015955

Margalef, R. (1978). Life-forms of phytoplankton as survival alternatives in an unstable environment. *Oceanol. Acta* 1, 493–509.

Marrec, P., Grégori, G., Doglioli, A. M., Dugenne, M., Della Penna, A., Bhairy, N., et al. (2018). Coupling physics and biogeochemistry thanks to high-resolution observations of the phytoplankton community structure in the northwestern Mediterranean Sea. *Biogeosciences* 15, 1579–1606. doi: 10.5194/bg-15-1579-2018

Menden-Deuer, S., and Fredrickson, K. (2010). Structure-dependent, protistan grazing and its implication for the formation, maintenance and decline of plankton patches. *Mar. Ecol. Prog. Ser.* 420, 57–71. doi: 10.3354/meps08855

Menden-Deuer, S., Lessard, E. J., and Satterberg, J. (2001). Effect of preservation on dinoflagellate and diatom cell volume and consequences for carbon biomass predictions. *Mar. Ecol. Prog. Ser.* 222, 41–50. doi: 10.3354/meps222041

Morison, F., Harvey, E., Franzè, G., and Menden-Deuer, S. (2019). Storm-induced predator-prey decoupling promotes springtime accumulation of North Atlantic phytoplankton. *Front. Mar. Sci.* 6:608. doi: 10.3389/fmars.2019.00608

Mouw, C. B., and Yoder, J. A. (2010). Optical determination of phytoplankton size composition from global SeaWiFS imagery. *J. Geophys. Res. Oceans* 115:C12018.

Olson, R. J., and Sosik, H. M. (2007). A submersible imaging-in-flow instrument to analyze nano-and microplankton: Imaging FlowCytobot. *Limnol. Oceanogr. Methods* 5, 195–203. doi: 10.4319/lom.2007.5.195

Peacock, E. E., Olson, R. J., and Sosik, H. M. (2014). Parasitic infection of the diatom *Guinardia* delicatula, a recurrent and ecologically important phenomenon on the New England Shelf. *Mar. Ecol. Prog. Ser.* 503, 1–10. doi: 10.3354/meps10784

Reynolds, R. A., Stramski, D., Wright, V. M., and Woźniak, S. B. (2010). Measurements and characterization of particle size distributions in coastal waters. *J. Geophys. Res. Oceans* 115:C08024.

Saliba, G., Chen, C.-L., Lewis, S., Russell, L. M., Rivellini, L.-H., Lee, A. K. Y., et al. (2019). Factors driving the seasonal and hourly variability of sea-spray aerosol number in the North Atlantic. *Proc. Natl. Acad. Sci. U.S.A.* 116:20309. doi: 10.1073/pnas.1907574116

Shalapyonok, A., Olson, R. J., and Shalapyonok, L. S. (2001). Arabian sea phytoplankton during southwest and northeast Monsoons 1995: composition, size structure and biomass from individual cell properties measured by flow cytometry. *Deep Sea Res. II Top. Stud. Oceanogr.* 48, 1231–1261. doi: 10.1016/s0967-0645(00)00137-5

Siegel, D. A., Buesseler, K. O., Behrenfeld, M. J., Benitez-Nelson, C. R., Boss, E., Brzezinski, M. A., et al. (2016). Prediction of the export and fate of global ocean net primary production: the EXPORTS science plan. *Front. Mar. Sci.* 3:22. doi: 10.3389/fmars.2016.00022

Sieracki, C., Sieracki, M. E., and Yentsch, C. (1998). An imaging-in-flow system for automated analysis of marine microplankton. *Mar. Ecol. Prog. Ser.* 168, 285–296. doi: 10.3354/meps168285

Sieracki, M. E., and Poulton, N. (2011). *Phytoplankton_Carbon-NAB08*. Woods Hole, MA: BCO-DMO Office. Available online at: http://osprey.bcodmo.org/project.cfm?flag=view&id=102&sortby=project

Smetacek, V., Klaas, C., Menden-Deuer, S., and Rynearson, T. A. (2002). Mesoscale distribution of dominant diatom species relative to the hydrographical field along the Antarctic Polar Front. *Deep Sea Res. II Top. Stud. Oceanogr.* 49, 3835–3848. doi: 10.1016/s0967-0645(02)00113-3

Sosik, H. M., and Olson, R. J. (2007). Automated taxonomic classification of phytoplankton sampled with imaging-in-flow cytometry. *Limnol. Oceanogr. Methods* 5, 204–216. doi: 10.4319/lom.2007.5.204

Steinberg, D. K., and Landry, M. R. (2017). Zooplankton and the ocean carbon cycle. *Annu. Rev. Mar. Sci.* 9, 413–444. doi: 10.1146/annurev-marine-010814-015924

Stemmann, L., and Boss, E. (2011). Plankton and particle size and packaging: from determining optical properties to driving the biological pump. *Annu. Rev. Mar. Sci.* 4, 263–290. doi: 10.1146/annurev-marine-120710-100853

Sun, J., and Liu, D. (2003). Geometric models for calculating cell biovolume and surface area for phytoplankton. *J. Plankton Res.* 25, 1331–1346. doi: 10.1093/plankt/fbg096

Thyssen, M., Alvain, S., Lefèbvre, A., Dessailly, D., Rijkeboer, M., Guiselin, N., et al. (2015). High-resolution analysis of a North Sea phytoplankton community structure based on in situ flow cytometry observations and potential implication for remote sensing. *Biogeosciences* 12, 4051–4066. doi: 10.5194/bg-12-4051-2015

Zheng, H., Wang, R., Yu, Z., Wang, N., Gu, Z., and Zheng, B. (2017). Automatic plankton image classification combining multiple view features via multiple kernel learning. *BMC Bioinform.* 18:570. doi: 10.1186/s12859-017-1954-8

Conflict of Interest: The authors declare that the research was conducted in the absence of any commercial or financial relationships that could be construed as a potential conflict of interest.

Copyright © 2020 Menden-Deuer, Morison, Montalbano, Franzè, Strock, Rubin, McNair, Mouw and Marrec. This is an open-access article distributed under the terms of the Creative Commons Attribution License (CC BY). The use, distribution or reproduction in other forums is permitted, provided the original author(s) and the copyright owner(s) are credited and that the original publication in this journal is cited, in accordance with accepted academic practice. No use, distribution or reproduction is permitted which does not comply with these terms.

frontiers in Marine Science

ORIGINAL RESEARCH
published: 06 May 2020
doi: 10.3389/fmars.2020.00294

Hydrodynamics of a Rising Oil Droplet With Bacterial Extracellular Polymeric Substance (EPS) Streamers Using a Microfluidic Microcosm

*Andrew R. White, Maryam Jalali and Jian Sheng**

Department of Engineering, Texas A&M University-Corpus Christi, Corpus Christi, TX, United States

During the *Deepwater Horizon* oil spill, the unprecedented injection of millions of liters of chemical dispersant at the wellhead generated large quantities of submillimeter oil droplets that became entrained in a deep sea plume. The unexpected generation of these droplets has resulted in many studies in the last decade aiming to understand their transport and fate during and after the spill. Complicating matters, the plume coincided with a microbial bloom, and in addition to ocean dynamics these droplets were subjected to biological processes such as biodegradation and microbial aggregation. A lack of field observations and laboratory experiments using relevant conditions has left our understanding of these biotic processes and the role they played in the fate of the oil droplets poorly constrained. Furthermore, while biodegradation has been incorporated into drop transport models using available data, the effects of microbial aggregation involving extracellular polymeric substances (EPS) on their transport has seldom been incorporated into modeling efforts particularly due to our lack knowledge of these processes. We use a microfluidic platform to observe bacterial suspensions interacting with a single $\sim$200 μm oil drop in conditions relevant to the drop rising through the microbial bloom. We observe the development of individual, invisible bacterial EPS threads extending from the drop surface which can capture additional passing bacteria and form bacteria-EPS aggregates. Using high speed imaging, we make high resolution flow measurements both with and without EPS threads present and analyze the momentum balance to elucidate the hydrodynamic impact of these filaments. Surprisingly, these thin individual EPS filaments alter significantly the pressure field around the drop and increase the drag, which would drastically reduce the drop's rising velocity in the water column. We demonstrate that this mechanism which plausibly occurred in the deep sea plume would have major impacts on both the drop and bacteria transport during and after the *Deepwater Horizon* oil spill.

Keywords: oil drop hydrodynamics, extracellular polymeric substances, microfluidics, oil drop fate, bacteria oil interactions, marine oil snow, deepwater horizon, bacterial aggregates

OPEN ACCESS

Edited by:
Houshuo Jiang,
Woods Hole Oceanographic Institution, United States

Reviewed by:
Binbin Wang,
University of Missouri, United States
Eleonora Secchi,
ETH Zürich, Switzerland

****Correspondence:***
Jian Sheng
jian.sheng@tamucc.edu

Specialty section:
This article was submitted to Marine Ecosystem Ecology, a section of the journal Frontiers in Marine Science

Received: *28 January 2020*
Accepted: *14 April 2020*
Published: *06 May 2020*

Citation:
White AR, Jalali M and Sheng J (2020) Hydrodynamics of a Rising Oil Droplet With Bacterial Extracellular Polymeric Substance (EPS) Streamers Using a Microfluidic Microcosm. Front. Mar. Sci. 7:294. doi: 10.3389/fmars.2020.00294

INTRODUCTION

The *Deepwater Horizon* (DWH) oil spill was a unique disaster. Other underwater well blowouts have occurred, such as the Ixtoc I spill in 1979–1980 which released three million barrels of oil at a depth of 50 m over 290 days (Jernelöv and Lindén, 1981). However the DWH blowout occurred 1,500 m below the sea surface, released nearly five million barrels of oil (Camilli et al., 2012; Mcnutt et al., 2012; Reddy et al., 2012), and involved an unprecedented injection of 2.9 million liters of chemical dispersant directly at the wellhead (Lehr et al., 2010). The introduction of dispersant caused a reduction in oil-water interfacial tensions by several orders of magnitude, generating additional submillimeter oil droplets that would not have been possible without dispersant (Zhao et al., 2014). In fact, laboratory experiments suggest droplets only several microns in diameter may have been possible in the DWH spill (Gopalan and Katz, 2010). Without dispersant, drop sizes during the DWH would have been limited to several mm to cm-scale (Zhao et al., 2014), similar to drop sizes observed from natural oil seeps in the Gulf of Mexico (Römer et al., 2019).

These submillimeter oil droplets, consisting of sparingly soluble hydrocarbons such as *n*-alkanes, became entrained in a deep-sea plume with other dissolved hydrocarbons between depths of 900 and 1,300 m (Camilli et al., 2010; Reddy et al., 2012; Spier et al., 2013; Valentine et al., 2014; Wade et al., 2016). The transport of these droplets and their ultimate fate have been the subject of numerous studies in the decade since the DWH spill (Paris et al., 2012; North et al., 2015; Socolofsky et al., 2015; Joye et al., 2016; French-Mccay et al., 2019; Perlin et al., 2020). To complicate matters, the deep-sea plume coincided spatially and temporally with a microbial bloom (Camilli et al., 2010; Hazen et al., 2010; Joye et al., 2011; Kessler et al., 2011; Mason et al., 2012; Redmond and Valentine, 2012; Valentine et al., 2012; Dubinsky et al., 2013; Kleindienst et al., 2016; Yang et al., 2016), suggesting the droplets would be subjected to biodegradation as well as other biotic processes such as marine oil snow sedimentation and flocculent accumulation (MOSSFA) (Daly et al., 2016), where sticky planktonic secretions (extracellular polymeric substances or EPS; Alldredge and Silver, 1988; Gutierrez et al., 2013; Quigg et al., 2016) facilitate aggregation with microbes, other debris, and oil (Marine Oil Snow or MOS; Passow et al., 2012; Ziervogel et al., 2012; Fu et al., 2014; Passow, 2016), which can become neutrally or even negatively buoyant and settle to the sea floor.

Incorporating these biological processes in far-field droplet transport modeling is difficult particularly due to the insufficient field or laboratory observations in relevant conditions. Direct measurements of biodegradation rates in the water column during the DWH oil spill are unavailable, and the available hydrocarbon oxidation data leaves many inferences of biodegradation rates poorly constrained (Kostka et al., 2020). Laboratory experiments have provided preliminary estimates of *n*-alkane degradation rates. For example, in experiments using seawater from Logy Bay collected at 8 m depth and weathered European crude oil with 1:15 dispersant to oil ratio (approximate ratio during the DWH response), alkane half-lives were $<$7 d at either 0.1 or 15 MPa (Prince et al., 2016). In (Hu et al., 2017), experiments using seawater sampled from 1,100 to 1,200 m in the Mississippi Canyon containing median 10 μm droplets of Macondo surrogate crude oil (2 ppm) and 1:100 dispersant:oil ratio indicated alkane half-lives of 6–8 d but with an initial lag period of 5–10 d, although these measurements were not performed at elevated pressure. Droplet transport models rely on these studies to estimate changing droplet volumes due to biodegradation among other processes, and incorporating biodegradation can have a drastic impact on results (North et al., 2015).

Even less understood is the role of microbe-mediated oil-containing aggregates, i.e., marine oil snow (MOS), on the transport of these droplets. Despite many laboratory experiments and some field observations near surface oil slicks during the DWH spill, significant knowledge gaps exist (Brakstad et al., 2018). Specifically, there is a lack of observations of microbe-mediated aggregation with oil droplets in relevant hydrodynamic environments. A major barrier is to simultaneously track and image both oil droplets (e.g., $>$100 μm in diameter) and bacteria (e.g., $\sim$1 μm in size) near their vicinities over a sufficiently long time period to allow aggregation to occur (e.g., days or weeks) as well as over a long distance traveled by a rising submillimeter oil droplet during this timeframe (e.g., a fresh 100 μm droplet in 4°C seawater can rise 100 m in about 3 d). Recently, we used microfluidics to provide the first means to observe a submillimeter oil droplet in relevant hydrodynamic environments (White et al., 2019). Briefly, a single oil droplet was pinned in place in a $\sim$10 mm wide microchannel while maintaining a mobile oil-water interface with an oleophobic contact angle to the top and bottom channel walls that are spaced 100 μm apart. The stationary drop was subjected to a flow containing a microbial or other particulate suspension, analogous to the inverse case of the droplet rising through an otherwise quiescent suspension. With the capability of additionally controlling the biological and chemical environment, this "ecology-on-a-chip" platform has the potential to make the most relevant laboratory measurements yet of a droplet rising through a microbial bloom. In particular, we have observed for the first time bacterial aggregates forming directly on the sheared oil-water interface, with the morphology and timescale varying drastically between three bacterial isolates (White et al., 2019).

In this paper, we detail the hydrodynamic impacts of the initiation of a bacteria-mediated aggregate on an oil droplet. Specifically, we observe EPS threads, which is composed of proteins, carbohydrates, lipids, DNA, and other materials secreted by bacteria (Alldredge and Silver, 1988), anchored on the trailing side of the droplet and extending downstream (White et al., 2020). These threads are reminiscent of "streamers" recently observed in other laminar flows using microfluidics (Rusconi et al., 2010). Generally these streamers form either by an established bacterial film that recruits passing suspended bacteria (Rusconi et al., 2010; Marty et al., 2012; Valiei et al., 2012; Drescher et al., 2013; Zarabadi et al., 2017), or by a pre-formed floc from upstream which encounters a surface (Hassanpourfard et al., 2015). In the case of streamers forming on rectangular and circular pillars in a model porous geometry, it has been

demonstrated that streamers initiate as small viscous filaments with sparsely attached bacteria that extrude downstream from the trailing edge of the pillars (Marty et al., 2012; Valiei et al., 2012; Das and Kumar, 2014; Scheidweiler et al., 2019). Here we observe the early initiation of transient EPS threads attached to the trailing side of the liquid droplet and extending downstream. The threads contain sparsely attached bacteria and can capture additional bacteria passing by as they encounter the filament. The flow field around the drop is measured by tracking the position of the bacteria in high speed imaging. Surprisingly, these practically invisible and <1 μm in diameter EPS threads containing sparse bacteria significantly alter the hydrodynamics and would have substantial impacts on the rising velocity and transport of a droplet in the water column.

MATERIALS AND METHODS

Experiment Setup and Procedure

We performed kernel experiments using the ecology-on-a-chip setup described in detail in (White et al., 2019). A schematic of the setup is shown in **Figure 1**. Experiments began by sterilizing all components of the setup by autoclaving at 121°C for 30 min. Components that could not be autoclaved (e.g., the microfluidic channel) were washed with 70% ethanol for 20 min and placed under UV illumination for at least 60 min. The system was then carefully assembled on the stage of an inverted microscope (Nikon Ti-E). The system consisted of a 125 ml flask (reservoir in **Figure 1**) which was initially filled with 50 ml of sterile 8 g/L nutrient broth (Difco, BD catalog no. 234000) dissolved in deionized (DI) water. All the tubing (Tygon and PEEK), two peristaltic pumps (**Figure 1**), and the microfluidic channel (**Figure 1**) were then filled with the broth from the reservoir, with ∼30 ml of broth remaining in the reservoir and 20 ml distributed throughout the flow circuit.

The flow circuit consisted of two loops as shown in **Figure 1**. Liquid drawn from the reservoir approached a T-junction, where liquid could either be rerouted back to the reservoir or sent toward the microfluidic channel for observation. When the peristaltic pump leading to the microfluidic channel (**Figure 1**) is off, this path is closed and the flow is restricted to the "culturing loop" (boxed-in region in **Figure 1**).

The microfluidic channel was fabricated using poly(dimethylsiloxane) (PDMS) (Dow Corning) (White et al., 2019) with a 10:1 ratio of PDMS and crosslinking agent. The PDMS channel and a clean glass microscope slide were exposed to air plasma (Harrick) for 1.5 min, and then the channel was bonded to the glass slide. The channel was then functionalized with a hydrophilic polyelectrolyte multilayer (PEM) deposited using a layer-by-layer technique (Bauer et al., 2010). Shortly after bonding, while the PDMS and glass were still plasma-activated, the channel was filled with 10 μM poly(allylamine hydrochloride) (PAH) (Sigma) in 0.1 M NaCl for 5 min. The channel was then rinsed with 0.5 M NaCl followed by filling with 10 μM poly(sodium 4-styrenesulfonate) (PSS) (Sigma) in 0.1 mM NaCl for 5 min. This procedure of alternating layers of PAH and PSS was continued until 4 PAH-PSS layers were formed. Additional details including a schematic of this process are found in (White et al., 2019). The channel was then rinsed with DI water and sterilized with 70% ethanol for the experiment.

A drop of oil (Macondo surrogate) was generated inside the microfluidic channel using a simple flow focusing junction ("drop dispense" in **Figure 1**). Oil was carefully introduced to the junction using a 1 ml glass syringe (Hamilton) and syringe pump (New Era Pump Systems) while a second syringe pump delivered sterile aqueous buffer to the junction to produce the drop. Once a drop was generated at this junction, the two syringe pumps were turned off and the drop traveled to the observation area of the channel shown in **Figure 1** via flow generated by the peristaltic pump leading to the channel. Once in position, the peristaltic pump was also turned off such that the drop remained stationary. The diameter of the drop in this paper was 240 μm once in the observation area of the channel.

In tandem with setting up the experiment on the microscope, *Pseudomonas* sp. (ATCC 27259) (Vangnai and Klein, 1974) was cultured separately in 8 g/L nutrient broth on a rotary shaker at 120 rpm and room temperature. *Pseudomonas* sp. is an alkane degrader and also a motile bacterium. The culture was grown until saturation, which occurred after about 4 days and the optical density at 600 nm was $OD_{600} > 1$. After the drop was generated as described above and the peristaltic pump leading to the channel was turned off, effectively closing off that loop, the system was inoculated via the access valve (**Figure 1**) with 100 μl of the *Pseudomonas* sp. culture grown outside of the system. The inoculated broth could then continuously recirculate in the culturing loop in **Figure 1**.

The system was left overnight which served three purposes. First, overnight the drop penetrated the PEM and became pinned, i.e., the contact area of the drop was fixed at both the PDMS and glass surfaces of the channel, but the oil-aqueous interface was freely mobile and the oleophobic contact angle between the drop and the channel walls was preserved. Second, by visually inspecting the microfluidic channel the next day, the sterility of the microfluidic channel was verified. Third, the *Pseudomonas* sp. in the culturing loop would grow to the target $OD_{600} = 0.4$ desired for the experiment overnight.

After the culture reached the desired growth in the culturing loop, the peristaltic pump leading to the microchannel as shown in **Figure 1** was turned on, allowing the culture to begin encountering the drop. The incoming velocity of the suspension in the microfluidic channel was 2.2 mm/s. A 20X S Plan Fluor ELWD objective (NA 0.45, depth of field ∼5 μm) and differential interference contrast (DIC) imaging were used for imaging the drop with the inverted microscope. Images were recorded at 1,000 fps using a 1k × 1k CMOS high speed camera (IDT NR4) for 1 s periods spaced 10 min apart. The moment the first bacteria encountered the drop was considered $t = 0$, and thus high speed imaging sequences were taken at 10, 20, 30, etc. min after the first exposure to bacteria.

Flow Measurements

The high speed images are used to obtain flow measurements using micro-particle image velocimetry (μPIV)-assisted particle tracking velocimetry (PTV) (Evans et al., 2016) using the bacteria

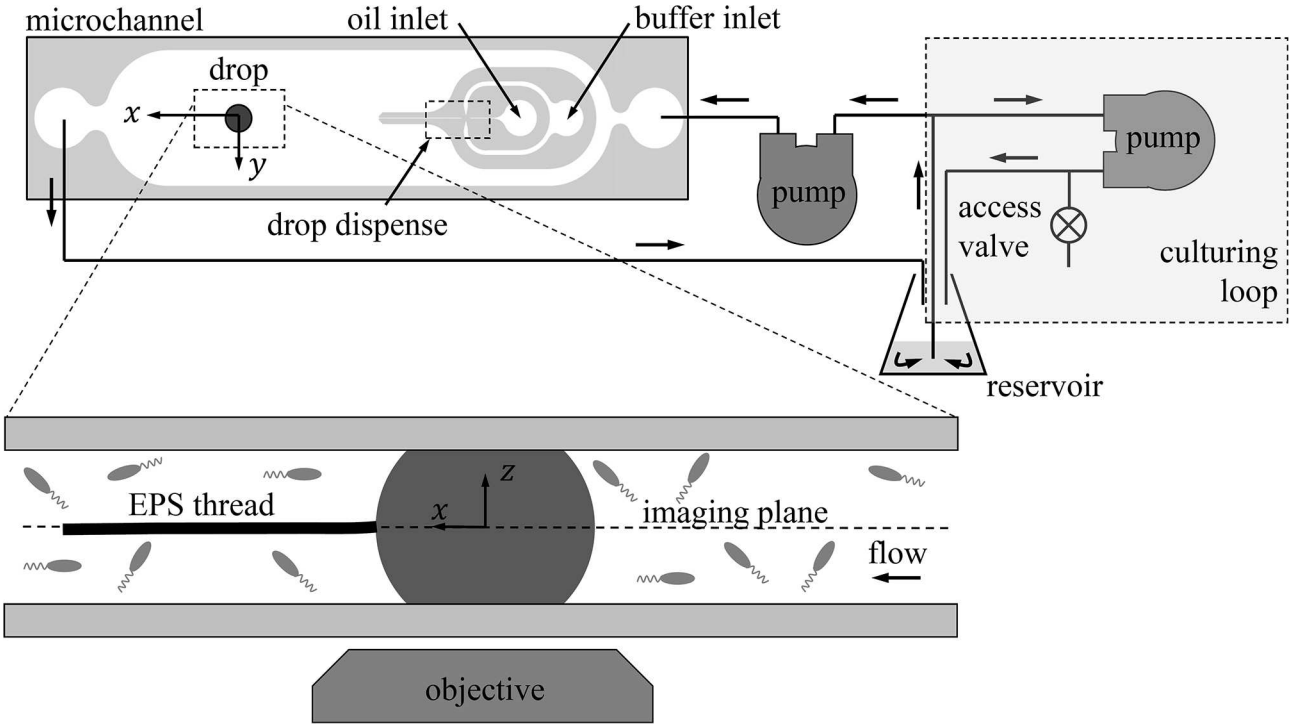

FIGURE 1 | The experimental setup. At the top is the fluidics circuit consisting of the culturing loop (top right) where *Pseudomonas* sp. are cultured *in situ* and the observation loop that includes the microchannel (top left). The drop is generated in the flow focusing region indicated by "drop dispense." The bulk of the bacteria suspension is contained in the reservoir (125 ml flask) during the experiment. A vertical cross section of the channel containing the pinned oil droplet is shown in detail at the bottom of the figure.

as flow tracers. Two quantities provide justification for using the bacteria as flow tracers. First, the Peclet numbers $Pe = D_d\,\mathcal{D}/\left\|\vec{u}\right\|$, where $\left\|\vec{u}\right\|$ is the velocity magnitude and $\mathcal{D}$ is the effective diffusivity of the bacteria including swimming, are $Pe \gg 1$, indicating that bacteria swimming does not significantly influence bacteria transport. Here $\mathcal{D} = 2.26 \times 10^{-9}$ m^2/s with mean bacterial swimming speed of 22 μm/s (White et al., 2020). Second, the Stokes numbers $Stk = 2/9\left(\rho_b/\rho_f\right)\left(d_b/D_d\right)^2 Re_D$, where ρ_b and d_b are the bacteria density ($\sim$1.1 g/cm^3) and characteristic size of the bacteria ($\sim$2 μm), are on the order of 10^{-5}, indicating the bacteria will follow the streamlines. The measurement area was 720×720 pixels, and the depth of field (DOF) is $\sim$5 μm so the flow measurements are averaged over this 5 μm thick slice of the flow. The DOF is approximated by $DOF = \lambda\sqrt{n^2 - NA^2}/NA^2$ where λ is the light wavelength ($\sim$400–700 nm), n is the medium's index of refraction ($\sim$1.34), and NA is the numerical aperture (0.45) (Shillaber, 1944).

The microscope was focused in the center of the 100 μm thick channel. In a given imaging sequence captured at 1,000 fps for 1 s, every two consecutive images underwent a conventional cross-correlation PIV analysis (Roth and Katz, 2001). In a given image the bacteria locations are determined, and with the assistance of the PIV analysis their positions in the next image are found. Therefore, for each bacterium in each frame, a velocity vector is determined based on its position in the previous frame. Approximately 1,000 bacteria cells were identified per frame, providing about 1×10^6 velocity vectors per high speed image period. The flow was averaged over the 1 s period and mapped onto a 4 pixel or 2.7 μm grid using a Taylor expansion scheme (Evans et al., 2016).

Conservation of Momentum

The pinned droplet has a diameter D_d and is subjected to a flow with incoming velocity U_f, density ρ_f and dynamic viscosity μ_f as shown in **Figure 2A**. The x-direction is in the positive flow direction. Assuming the flow is steady, the differential form of the balance of momentum is

$$\rho_f\left(\vec{\boldsymbol{u}}\cdot\vec{\nabla}\right)\vec{\boldsymbol{u}} = \vec{\nabla}p + \mu_f\vec{\nabla}\cdot\vec{\nabla}\vec{\boldsymbol{u}} \tag{1}$$

where $\vec{\boldsymbol{u}}$ is flow velocity vector, $\vec{\nabla}$ is the gradient operator, and $p = P - \rho_f g h$ is a modified pressure (hereafter called simply pressure) i.e., static (P) minus hydrostatic ($\rho_f g h$) pressure where g is gravitational acceleration and h is depth. For analysis, the velocities are scaled by U_f, the lengths are scaled by D_d, and pressure is scaled by $\mu_f U_f/D_d$. Using this scaling, the $\boldsymbol{x}$- and $\boldsymbol{y}$-component, respectively, of the differential form of the

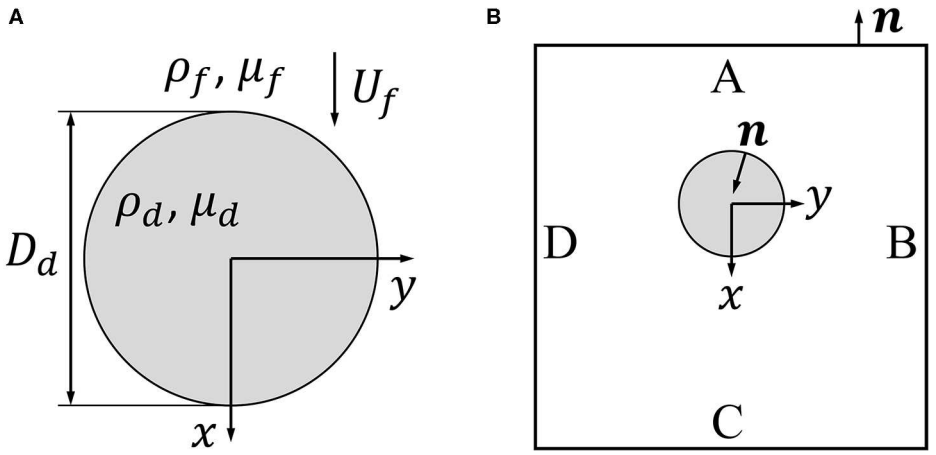

FIGURE 2 | (A) shows a schematic depicting the stationary drop (gray circle) with diameter D_d, density ρ_f and dynamic viscosity μ_d, subjected to a flow with upstream velocity U_f, density ρ_f, and dynamic viscosity μ_f. In **(B)** a control region ABCD is drawn around the drop where the positive x-direction is in the flow direction.

momentum balance is

$$Re_D\left(u_x^*\frac{\partial u_x^*}{\partial x^*}+u_y^*\frac{\partial u_x^*}{\partial y^*}\right)=-\frac{\partial p^*}{\partial x^*}+\left(\frac{\partial^2 u_x^*}{\partial x^{*2}}+\frac{\partial^2 u_x^*}{\partial y^{*2}}\right), \quad (2)$$
$$Re_D\left(u_x^*\frac{\partial u_y^*}{\partial x^*}+u_y^*\frac{\partial u_y^*}{\partial y^*}\right)=-\frac{\partial p^*}{\partial y^*}+\left(\frac{\partial^2 u_y^*}{\partial x^{*2}}+\frac{\partial^2 u_y^*}{\partial y^{*2}}\right)$$

where u_x^* and u_y^* are the x- and y-components of the velocity, and $Re_D = \rho_f U_f D_d/\mu_f$ is the Reynolds number. The superscript "*" indicates a non-dimensionalized parameter. In both rows, the left-hand side contains the advection terms, and on the right-hand side is the pressure gradient followed by the viscous stresses. Using flow measurements from the previous section to obtain u_x^* and u_y^*, each term in both rows of Eq. (2) can be determined directly, including the x- and y-components of the pressure gradient. The derivatives of u^* and v^* are calculated using second order central or forward/backward finite differences. The pressure gradient, if properly integrated, can yield the pressure p, which we will see in the Results section is a crucial part of the force balance on the droplet. In the next section, we describe how the drag force on the drop is estimated.

Control Volume Analysis

A control volume analysis is used to estimate the drag force on the pinned droplet. In this analysis, the droplet pinned between the two walls of the microfluidic channel is assumed to be a cylinder in a 2D flow. A control region ABCD as shown in **Figure 2B** is drawn around the droplet, and the control volume is taken as the area between the ABCD box and the droplet surface extending infinitely into and out of the page. The unit normal vector $\boldsymbol{n}$ points outside the control volume as shown in **Figure 2B**. With this geometry in mind, the integral form of the x-momentum balance is

$$\int_{ABCD}\left[Re_D\left(\vec{\boldsymbol{n}}\cdot\vec{\boldsymbol{u}}^*\right)u_x^*+n_x p^*-\vec{\boldsymbol{n}}\cdot\vec{\vec{\boldsymbol{\tau}}}\cdot\vec{\boldsymbol{e}}_x\right]dS^* \quad (3)$$
$$+F_d^*=0,$$

where $F_d^* = F_d/\mu U_f$ is the dimensionless drag force per length or viscous drag coefficient, $\vec{\vec{\tau}}^* = \vec{\nabla}^*\vec{\boldsymbol{u}}^* + \left(\vec{\nabla}^*\vec{\boldsymbol{u}}^*\right)^T$ is the dimensionless stress tensor, and S^* is the perimeter ABCD. Evaluating each term in Eq. (3) besides F_d^* yields the following form:

$$F_d^* = \int_{A,\,C}\left[Re_D\left(u_{x,A}^{*2}-u_{x,C}^{*2}\right)+\left(p_A^*-p_C^*\right)-\left(\tau_{xx,A}^*-\tau_{xx,C}^*\right)\right]dy^* \quad (4)$$
$$+\ \ldots\int_{B,D}\left[Re_D\left(u_{y,D}^*u_{x,D}^*-u_{y,B}^*u_{x,B}^*\right)-\left(\tau_{yx,D}^*-\tau_{yx,B}^*\right)\right]dx^*.$$

In Eq. (4), the stresses are defined in terms of the x- and y-components of velocity as $\tau_{xx}^* = 2\partial u_x^*/\partial x^*$ and $\tau_{yx}^* = \partial u_x^*/\partial y^* + \partial u_y^*/\partial x^*$. The subscripts A, B, C, and D indicate velocity, pressure or stress profiles over those respective boundaries. Thus, each term can be evaluated using the experimental flow measurements directly except for p_A^* and p_C^*.

Since the pressure gradients are known using Eq. (2), these gradients can be integrated over the region ABCD to estimate the pressure over boundaries A and B. Integration is performed using first order forward/backward finite differences. Beginning at a corner of the control volume, the pressure gradient field is integrated both clockwise and counterclockwise over ABCD. The resulting pressure profiles for both integration directions are averaged to produce p_A^* and p_C^*. Combined with the flow measurements u_x^* and u_y^*, and calculated τ_{xy}^* and τ_{xx}^*, the drag force per length F_d^* is calculated.

RESULTS AND DISCUSSION

EPS Aggregations and the Hydrodynamic Impacts

In **Figure 3** the measured flow field around the stationary droplet prior to any bacterial attachment (20 min after first bacterial encounter) is presented as a series of contour plots. **Figure 3A** shows the u^* and v^* components of the velocity field. Due to the

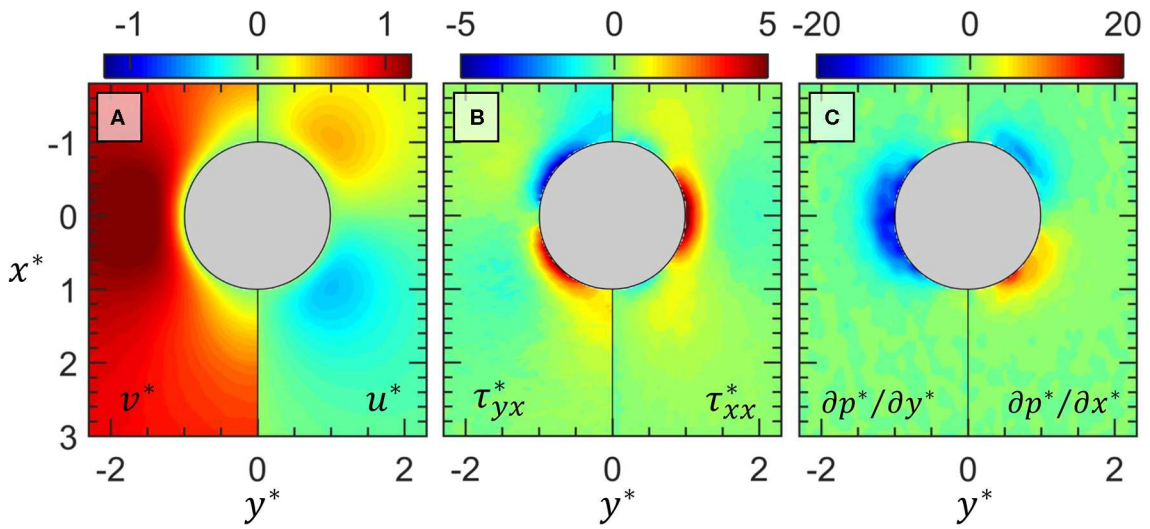

FIGURE 3 | The measured flow field around the oil drop (gray circle) prior to attachment of any bacteria. In **(A)** the *y*-component (left half) and *x*-component (right half) of velocity is shown. In **(B)** the shear (left half) and normal (right half) viscous stresses are shown. In **(C)** the *y*-component (left half) and *x*-component of the pressure gradients are shown. All quantities are normalized as described in the text. The magnitudes correspond to the respective color bar above each plot.

symmetry of the flow field, we plot v^* on the left half and u^* on the right half of **Figure 3A** separated by the vertical black line through $y^* = 0$. Similarly, the viscous shear (τ^*_{xy}) and normal (τ^*_{xx}) stresses are shown in **Figure 3B**, and the two components of the pressure gradient $\partial p^*/\partial y^*$ and $\partial p^*/\partial x^*$ are shown in **Figure 3C**. The pressure gradient fields are calculated using Eq. (2). The flow field shown in **Figure 3** is expected of Stokes flow ($Re_D < 0.5$), which has symmetry both left and right as well as top to bottom in the streamwise direction.

At first glance, raw images from a high speed image sequence captured 50 min after the first bacterial encounter (**Figure 4**) do not appear to show any obvious aggregates or presence of EPS filaments. A video of the sequence of images shown in **Figure 4** is available in the (**Video S1**). In **Figure 4A**, a cropped image 44 ms into the 1 s imaging period appears to show only single distributed bacteria freely flowing past the drop (dark semi-circle in **Figure 4**), or in some cases clusters of 2-3 bacteria can be identified. In **Figure 4A** we have pointed out one particular cluster of ∼3 bacteria (red arrow). A dotted black line is plotted on top of the image representing a streamline passing through this cluster at this instant in **Figure 4A**. This streamline is determined from the measured mean flow field over the entire 1 s imaging period. In **Figure 4B**, 100 ms later, the same cluster is spotted in a new position along the same streamline as expected.

However, in **Figure 4C**, the cluster appears to run into an invisible obstacle, which is confirmed by viewing **Video S1**. As other bacteria seem to flow past freely, this cluster stalls for a moment, and 100 ms later the cluster drifts away from its streamline in **Figure 4D**. In fact, this cluster has encountered an EPS filament, anchored on the drop surface. Since the depth of field in these images is ∼5 μm, and bacteria (1–3 μm) seemingly flow past the same location as the trapped cluster without getting trapped themselves, this suggests the EPS thread is quite thin and localized, perhaps being in the vicinity of 1 μm in diameter or smaller. We stress that we do not directly measure the filament diameter, but rather infer its diameter based on the DOF and the observation that not all bacteria within this DOF encounter the filament. Furthermore, we note that in subsequent drag calculations, the filament diameter is not included in the control volume analysis and has no direct impact on our calculations.

In **Figure 4E**, the same cluster has traveled along the EPS filament a little further downstream. It is unclear if the bacteria cluster is moving through the EPS material in the filament, or if the EPS material itself is moving or deforming, or if both could be happening simultaneously. Another 100 ms later in **Figure 4F**, the bacteria cluster has remained in approximately the same location. In the latter half of this imaging sequence (**Video S1**), the bacterial cluster can be seen traveling further downstream and out of frame.

Figure 4 highlights two important things. First, these early EPS filaments and the attached bacteria are quite transient, with EPS filaments forming and detaching, and bacteria attaching and subsequently moving downstream along the filament. Second, this demonstrates that preformed EPS threads without attached bacteria and attached to a liquid drop are capable of capturing bacteria as they pass by, and in this case this appears to be the primary mode of aggregation in comparison to the mode that bacteria attached to the drop transfer to the EPS filament (Das and Kumar, 2014). The origins of the preformed EPS threads are more difficult to determine. In one scenario, it is plausible that bacteria that are attached to the drop surface are responsible for secreting EPS that is extruded downstream due to flow shear similar to observations by other researchers (Marty et al., 2012; Valiei et al., 2012; Das and Kumar, 2014; Scheidweiler et al., 2019).

The consequences of these apparently short-lived EPS threads and their attached bacteria are twofold. First, the trapped bacteria

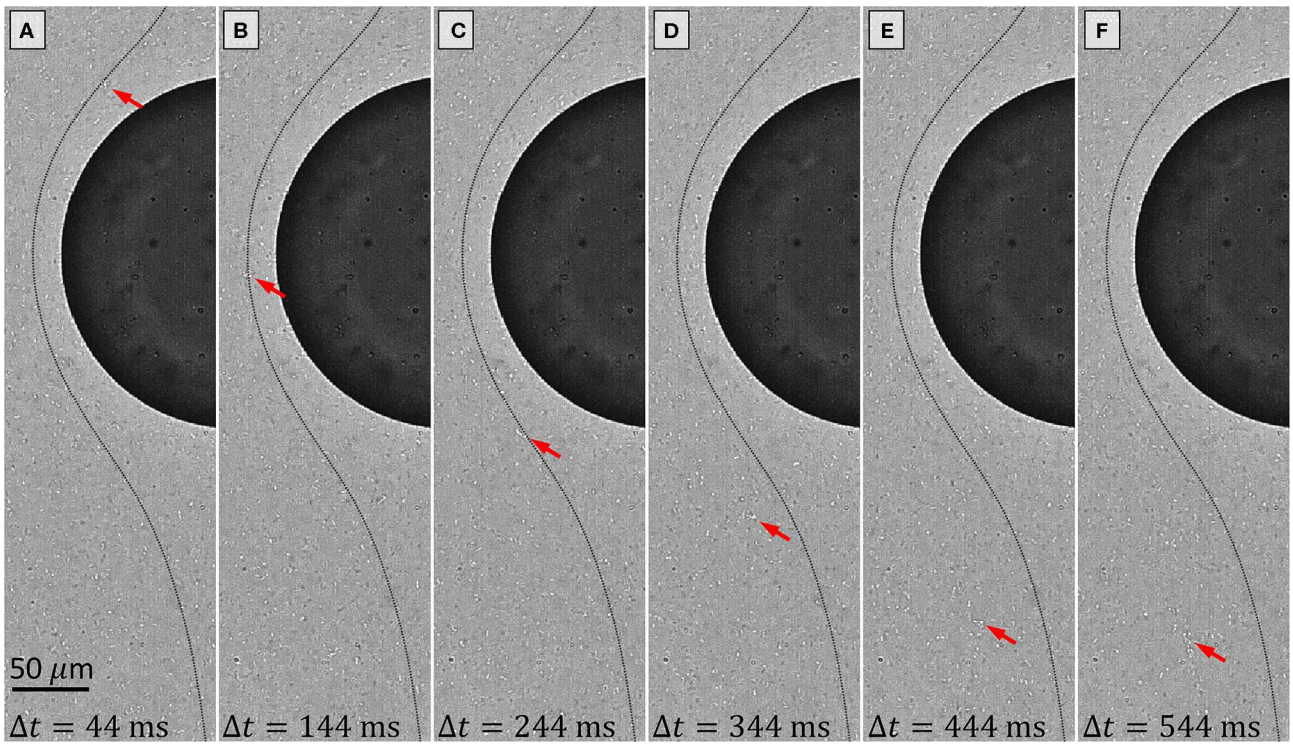

FIGURE 4 | Raw images of a high speed imaging sequence captured 50 min after the first bacteria encounter are shown. The time step for each image during the 1 s imaging sequence is shown at the bottom, and 100 ms separates each image. A video of this sequence is provided in the **Video S1**. In **(A)** a cluster of ∼3 bacteria is indicated by the red arrow. The thin dotted black line is a streamline of the mean flow passing through the current position of the indicated cluster. In **(B)** the cluster has traveled along the streamline. In **(C)** the cluster encounters a transparent EPS filament (confirmed in **Video S1**). In **(D–F)** the cluster has now deviated from the streamline and is trapped in the EPS filament.

effectively "hitch a ride" on the tails of the droplet, affecting the transport of the bacteria. In the water column, one can imagine bacteria stowing away on a rising oil droplet, traveling many meters or perhaps kilometers away from its origin. This would have major implications on marine ecology, influencing microbial distribution and the food web in the water column (Kiørboe et al., 2002). Second, the EPS filament and attached bacteria manipulate the flow around the drop. **Figure 5** depicts the mean flow field around the drop 50 min after first bacterial encounter, the same imaging period shown in **Figure 4**. In **Figures 5A,D**, the $v^*$and u^* fields are clearly disturbed by the presence of EPS filaments present behind the drop. The presence of these threads is even more apparent in the τ^*_{xy} and τ^*_{xx} (**Figures 5B,E**), and $\partial p^*/\partial y^*$ and $\partial p^*/\partial x^*$ (**Figures 5C,F**) fields. In fact, the $\partial p^*/\partial x^*$ field seems to be particularly capable of indicating the positions of otherwise invisible EPS filaments and attached bacteria. In **Figure 5F**, ∼4 distinct EPS threads are distinguished by the steep increase in the pressure gradient. The filament on which the bacteria cluster in **Figure 4** become trapped has the most pronounced signal on the left trailing side of the drop. It is important to note that we are presenting the mean flow field here, and it is apparent in **Figure 4** that attached bacteria and bacteria clusters are not necessarily stationary even over the 1 s imaging period.

It is reasonable to wonder if the disrupted flow around the drop in **Figure 5**, and the apparently reduced velocity behind the drop shown in **Figures 5A,D** compared to the same drop without attached bacteria (**Figure 3**), could enhance bacteria transport to the drop surface due to bacteria motility. That is, will the mobile bacteria swim fast enough relative to the decreased flow that attachment is increased in **Figures 4**, **5** vs. **Figure 3**? To answer this question, we plot the Peclet numbers, $Pe = D_d\,\mathcal{D}/\left\|\vec{u}\right\|$, where $\left\|\vec{u}\right\|$ is the velocity magnitude and $\mathcal{D}$ is the effective diffusivity of the bacteria including swimming. We estimate $\mathcal{D}$ to be 2.26×10^{-9} m^2/s by separately tracking bacteria trajectories in quiescent medium [Supplemental Materials of (White et al., 2020)]. Contours of $Pe(x^*, y^*)$ when no attached bacteria are present (**Figure 3**) are plotted in **Figure 6A**. *Pe* is largely greater than one aside from very close to the drop surface. In **Figure 6B**, $Pe(x^*, y^*)$ is plotted at the instant 50 min after the first bacterial encounter (**Figures 4**, **5**). The Peclet numbers are reduced directly behind the drop in **Figure 6B** (larger green region on the trailing side of the drop) which is a direct consequence of the reduced velocity (**Figures 5A,D**). This lowering of the *Pe* is highlighted in **Figure 6C** where *Pe* from **Figures 6A,B** along $y^* = 0$ are plotted. Still, Peclet numbers are largely $Pe > 1$, and thus flow advection is the dominant transport mechanism for the bacteria and swimming is not

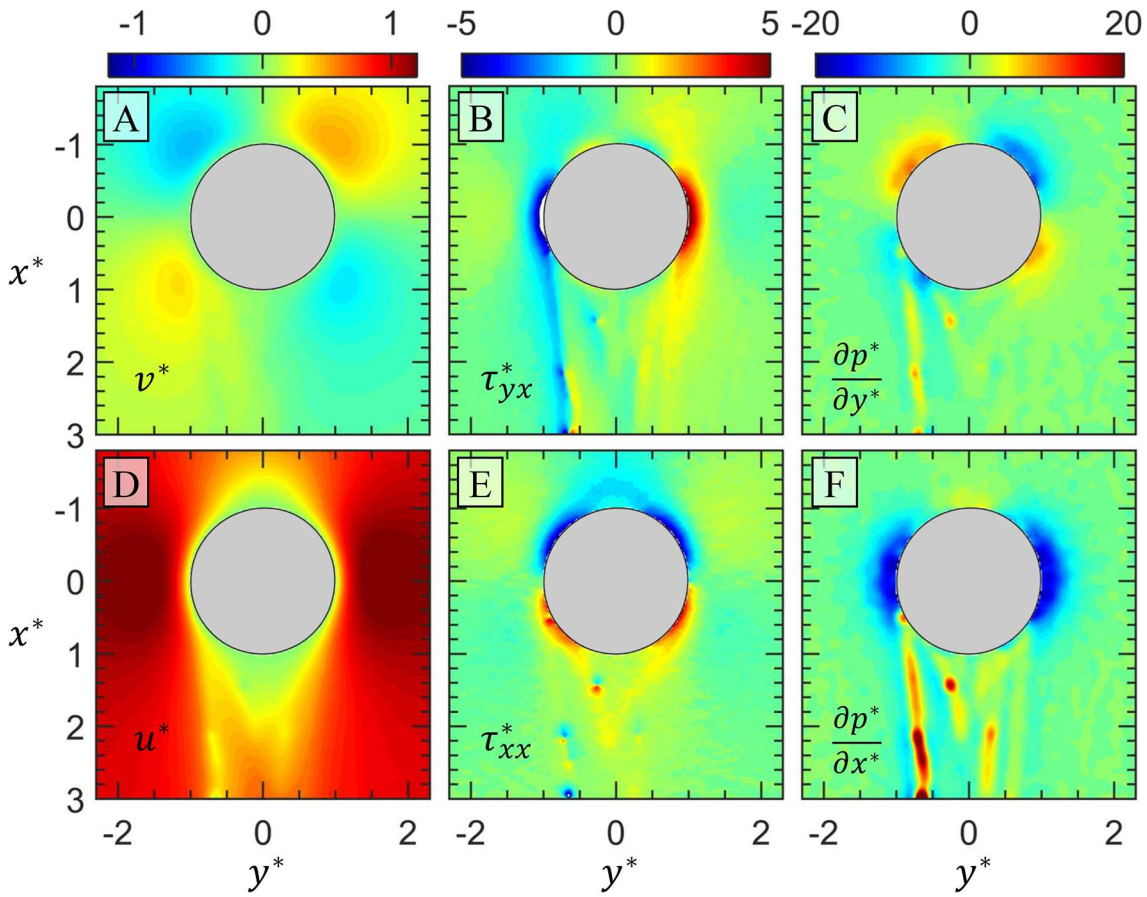

FIGURE 5 | The measured flow field around the oil drop (gray circle) after bacterial streamers have developed on the trailing half of the drop 50 min after the first bacteria encounter (**Figure 4**). In **(A)** the *y*-component and **(D)** *x*-component of velocity is shown. In **(B)** the shear and **(E)** normal viscous stresses are shown. In **(C)** the *y*-component and **(F)** *x*-component of the pressure gradients are shown. All quantities are normalized as described in the text. The magnitudes correspond to the respective color bar above each column of plots.

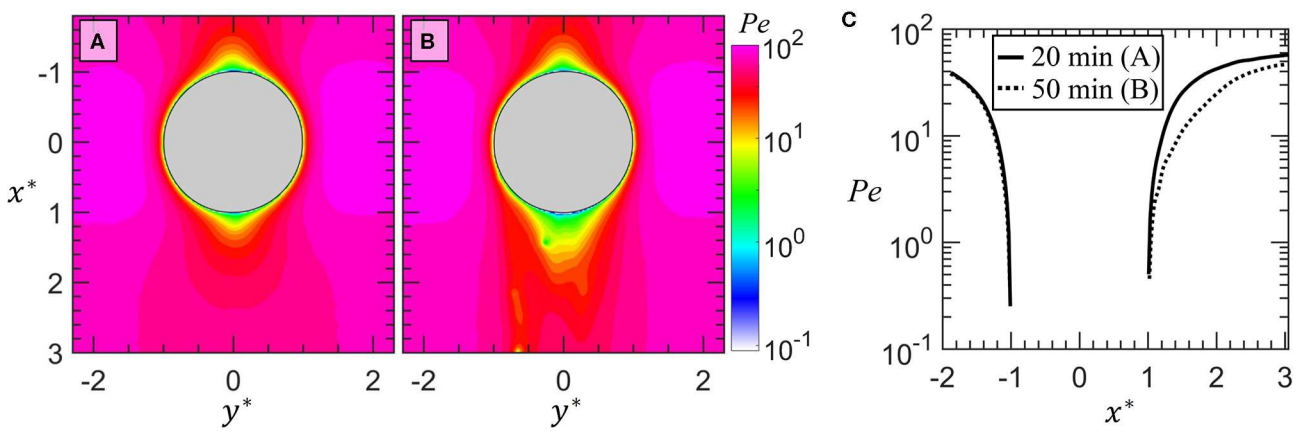

FIGURE 6 | In **(A)**, Peclet numbers are shown for the drop prior to attachment of bacteria at the same instance depicted in **Figure 3**. In **(B)**, Peclet numbers are shown for the same drop after bacterial streams have developed on the trailing half of the drop at the same instance depicted in **Figure 5**. The color contours are on a log scale with magnitudes corresponding to the color bar. In **(C)** a semilog plot of the Peclet numbers along $y^* = 0$ (i.e. through the center of the drop) is shown without attached bacteria (**A** at 20 min) and with streamers (**B** at 50 min).

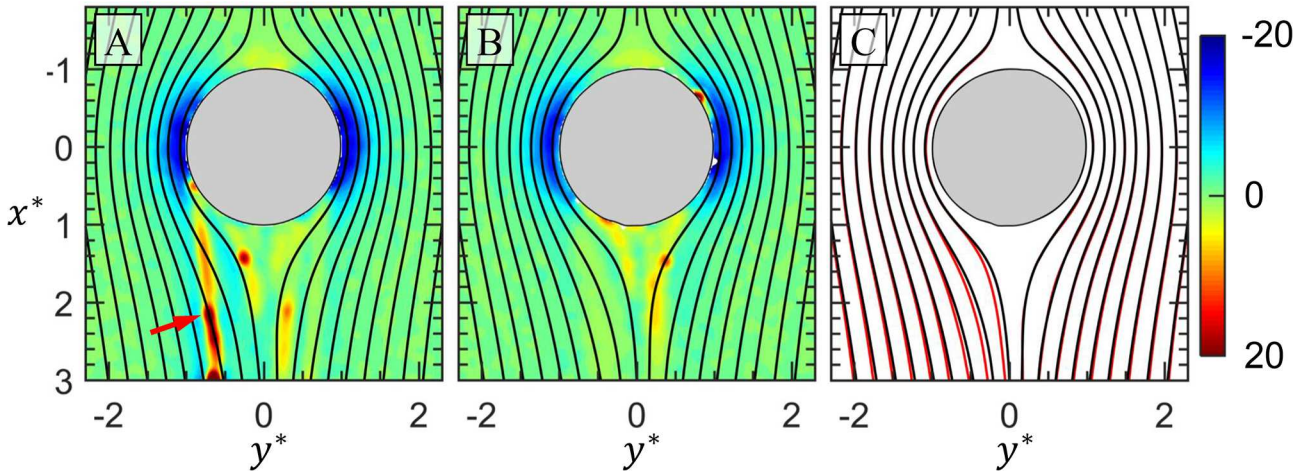

FIGURE 7 | In **(A)** contours of $\partial p^*/\partial x^*$ for the drop at 50 min (**Figure 5F**) is plotted with streamlines overlaid. In **(B)** contours of $\partial p^*/\partial x^*$ around the same drop at 70 min is shown with streamlines overlaid and originating at the same x-coordinates as **(A)**. A streamer indicated by the red arrow in **(A)** has detached in **(B)**. In **(C)** the streamlines from **(B)** (black lines) are plotted on top of the streamlines from **(A)** (red lines) to show the deviation in streamlines caused by the streamer indicated by the red arrow in **(A)**.

expected to have a significant effect on bacteria transport outside of 1-2 bacteria lengths away from the drop surface. Additionally, this provides justification for the use of the suspended bacteria as flow tracers for the purposes of flow measurements (in addition to the low Stokes numbers as described in the Materials and Methods).

Returning to the hydrodynamic impacts of an EPS filament, we plot the $\partial p^*/\partial x^*$ field with streamlines overlaid (black lines) for 50 min after first bacterial encounter (**Figure 7A**) and 70 min after first bacteria encounter (**Figure 7B**). The $\partial p^*/\partial x^*$ field is plotted due to its ability to highlight the presence of the invisible EPS filaments. In **Figure 7A**, the EPS filament discussed in **Figure 4** is indicated by the red arrow. It is clear from this plot that the streamlines cross the EPS filaments, a result that is necessary due to the elastic nature of the filaments (Autrusson et al., 2011). This will have significant hydrodynamic consequences. In **Figure 7B**, after 20 min have elapsed since **Figure 7A**, the EPS filament indicated in **Figure 7A** has disappeared while two remain in similar positions as two EPS filaments in **Figure 7A**. Now in **Figure 7C**, the streamlines from **Figure 7B** (black lines) are plotted on top of the streamlines from **Figure 7A** (red lines) to highlight the differences between them. Specifically, on the left half of the downstream side of the drop, it is clear that the presence of the indicated filament in **Figure 7A** "pushed" the streamlines in the negative y-direction. This demonstrates that a single EPS filament can cause a significant deviation in the streamlines. This widening of the streamlines due to the presence of an EPS filament effectively increases the hydrodynamic profile of the drop, which indicates an increase in "form drag" (in contrast to drag due to increased friction).

The ultimate hydrodynamic impact of these attached EPS filaments is elucidated though an analysis of the momentum balance in the system using Eq. (4). Here, the drag force is the addition of the contribution of five terms: the x-momentum difference across surfaces A and C, $Re_D\left(u^{*2}_{x,A} - u^{*2}_{x,C}\right)$; the x-momentum difference across surfaces D and B, $Re_D\left(u^*_{y,D}u^*_{x,D} - u^*_{y,B}u^*_{x,B}\right)$; the pressure difference across surfaces A and C, $\left(p^*_A - p^*_C\right)$; the viscous normal stress difference across surfaces C and A, $\left(\tau^*_{xx,C} - \tau^*_{xx,A}\right)$; and the viscous shear stress difference across surfaces B and D, $\left(\tau^*_{yx,D} - \tau^*_{yx,B}\right)$. Note the negative signs in front of the viscous terms in Eq. (4) have been distributed here. We designate each of these terms as pieces of the total momentum budget, and by analyzing these five contributions we can further analyze how the presence of these EPS threads and attached bacteria are impacting the hydrodynamics.

Figures 8B–F plots these five terms from Eq. (4) for the drop 20, 50, and 70 min after the first bacterial encounter. The area under the curve of each plot adds up to the total drag force on the drop (note that we plot $\left(\tau^*_{yx,D} - \tau^*_{yx,B}\right)$ and $\left(\tau^*_{xx,C} - \tau^*_{xx,A}\right)$, i.e., the negative signs in front of the viscous terms in Eq. (4) have been distributed through those terms). In **Figures 8B,C**, we see minimal differences when comparing the drop without attached aggregates (20 min) and with attached aggregates (50 and 70 min). In **Figure 8E**, we see clear differences between the three snapshots of the drop. The curve taken at 50 min after the first bacterial encounter has a pronounced peak at $x^* = -0.3$ caused by the EPS filament indicated in **Figure 7A** as well as the smaller filament to its right. Another smaller peak at $x^* = 0.25$ is caused by the EPS filament on the right side of the drop in **Figure 7A**. At 70 min, and the two EPS filaments identifiable in **Figure 7B** cause similar sized peaks in **Figure 8E**. However, it is important to take note of the magnitude of the vertical axis in **Figure 8E**; the $Re_D\left(u^{*2}_{x,A} - u^{*2}_{x,C}\right)$ does not contribute as much to the drag as the viscous stresses, τ^*_{xx} (**Figure 8F**) and τ^*_{xy}

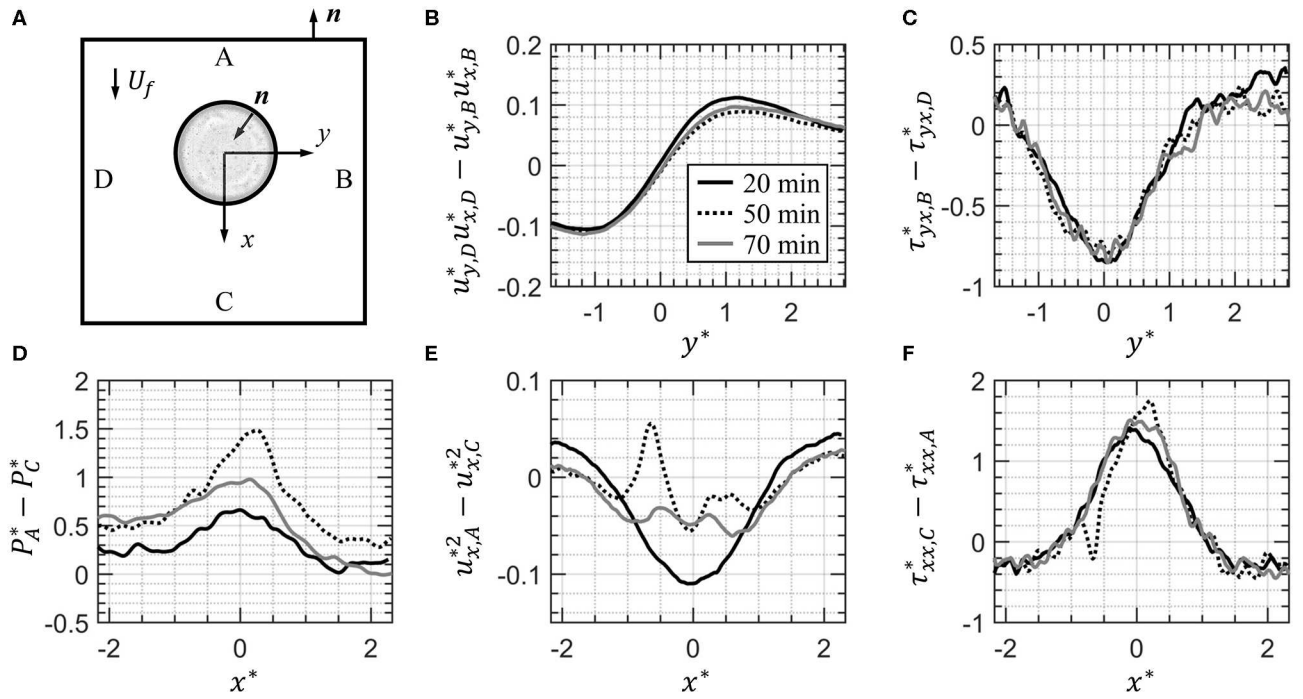

FIGURE 8 | In **(A)** the control region ABCD is shown again for convenience. In **(B–F)** the terms from Eq. (4) contributing to the drag force on the drop are plotted for the drop prior to attached bacteria (20 min, **Figure 3**), after attachment of several streamers on the trailing half of the drop (50 min, **Figure 5**), and after one streamer present at 50 min has detached (70 min, **Figure 7B**). The area under the curve in each plot is added together to determine the drag at each instant in time according to Eq. (4).

(**Figure 8C**), and the pressure p^* (**Figure 8D**). The magnitudes of these terms are an order of magnitude greater than the other two terms. Furthermore, the pressure difference in **Figure 8D** is the term most significantly affected by the presence of the EPS filaments.

In **Table 1**, the magnitudes of the individual terms in Eq. (4) (i.e., area under the curves in **Figure 8**) are tabulated for the drop 20 min after the first bacterial encounter (i.e., no attached EPS filaments or aggregates), 50 min after the first exposure (i.e., with several EPS filaments), and 70 min (i.e., one less filament than at 50 min as shown in **Figure 7**). As seen graphically in **Figure 8**, this table shows that the pressure term is the most affected by the presence of the EPS filaments, more than doubling from 20 to 50 min, and then decreasing some at 70 min after the filament highlighted in **Figure 7** has detached. This is corroborated by the observation of the EPS filaments significantly deviating the streamlines, and indication of the hydrodynamic profile of the drop becoming larger. As a result, the drag increase is due to "form drag" as mentioned earlier, i.e., the drag is increased primarily due to the modulation of the pressure field around the drop.

The sum of each term gives the viscous drag coefficient F^*_d shown in the bottom row of **Table 1** which allows us to quantify the impact of the EPS filaments and attached bacteria on the drag force experienced by the drop. The drag coefficient increases by 85% from the instant at 20 min (no filaments) to 50 min (several filaments). In **Figure 7C**, we showed that the detachment of a single EPS filament produced a noticeable deviation in the streamlines, and this resulted in a 27% reduction in the drag coefficient from 50 min (**Figure 7A**) to 70 min (**Figure 7B**). However, the drag coefficient at 70 min is still 46% greater than the drag coefficient for the clean drop at 20 min.

TABLE 1 | Magnitudes of terms in the momentum balance Eq. (4) and the viscous drag coefficients F^*_d for the drop 20, 50, and 70 min after the first encounter with bacteria.

Term from Eq. (4)	$\Delta t = 20$ min (Figure 3)	$\Delta t = 50$ min (Figures 5, 7A)	$\Delta t = 70$ min (Figure 7B)
$Re_D\left(u^{*2}_{x,A} - u^{*2}_{x,C}\right)$	−0.080	−0.020	−0.065
$\tau^*_{x,x,C} - \tau^*_{x,x,A}$	1.207	1.038	1.285
$\rho^*_A - \rho^*_A$	1.382	3.212	2.355
$Re_D\left(u^*_{y,D}u^*_{x,D} - u^*_{y,B}u^*_{x,B}\right)$	0.067	0.031	0.041
$\tau^*_{y,x,B} - \tau^*_{y,x,D}$	−0.814	−1.001	−1.045
F^*_d	1.762	3.260	2.571

It should be noted here that the EPS filaments extend outside the image frame, and so the full effect of the filaments on the flow field and the drag cannot be realized. In fact, this suggests that the drag measurements reported here are likely conservative, and if the entire manipulated flow field were captured the apparent drag increase may be increased

further. Furthermore, we have only to this point captured these flow fields in the early stages of the EPS filament generation. On the one hand, this importantly shows that the EPS filaments, and as a consequence the drag coefficients, are rather transient in the early period of initial bacteria attachment to the drop. However, in (White et al., 2019) we showed that bacteria can form quite robust aggregates and streamers on an oil drop by three bacterial isolates and six natural assemblages using ecology-on-a-chip microcosm platform, and it is reasonable to expect drastic increases in drag when these larger aggregates develop.

Deviations From the DWH Environment

It is clear that these EPS filaments and their attached bacteria can have a significant impact on the drag of the drop, and ultimately we are interested in knowing how this will impact the transport and fate of the oil droplet in the water column after encountering a microbial bloom, and also how this may in turn affect the microbial community. However, we must stress that caution be taken when interpreting the results in the context of the DWH spill. These laboratory experiments have several deviations from the real environment during the DWH oil spill:

1) We use a bacterial isolate [*Psuedomonas* sp. (ATCC 27259)], albeit an alkane degrader isolated from a marine environment (Vangnai and Klein, 1974). A community of bacteria, and in particular a community representative of the initial deep sea plume including *Oceanospirillales*, *Colwellia*, and *Cycloclasticus* (Hazen et al., 2010; Mason et al., 2012) would provide more relevant results in future work;
2) The aqueous phase contains ample nutrients and these nutrients are not presentative of those leading to the microbial bloom in the DWH deep sea plume;
3) The cell density is estimated to be $\sim 10^8$ cells/ml, which is quite high but allows us to produce high resolution flow measurements. In the deep sea plume, reported cell densities were as high as 1,540,000 cells/ml (Kleindienst et al., 2016), and in localized areas they were perhaps more dense.
4) The measurements were made at room temperature and pressure;
5) The drop is not a sphere but rather more of a disc with 100 μm thickness, 240 μm diameter, and a curved edge with an oleophobic contact angle with the microchannel top and bottom walls.

Therefore, it is important to consider the results presented here in the context of these caveats. For example, in the real environment, time scales for developing bacterial aggregates, as well as the morphology and ultimate hydrodynamic impacts of the aggregates, could be quite different. Nonetheless, we have demonstrated a very important mechanism and its plausible impacts on the drag of a rising oil droplet through a dense microbial bloom that has seldom been considered when predicting the fate of submillimeter oil droplets during the DWH spill. Incorporating these bacteria-mediated EPS filaments, which can grow into large aggregates, into oil droplet transport models could drastically affect our understanding of the distribution and fate of these oil droplets and their impact on the microbial community.

CONCLUSIONS

In this paper we used an ecology-on-a-chip platform (White et al., 2019) to demonstrate the significant hydrodynamic impacts that nearly invisible EPS threads can have on an emulated droplet rising through a bacterial suspension. Instead of observing a droplet rising through the suspension, we have flowed a bacterial suspension past a pinned droplet while periodically recording high speed images used for flow measurements. These threads were observable only by either identifying bacteria and bacteria clusters trapped in the threads (**Figure 4**) or by using anomalies in the flow measurements (**Figure 5**). In fact, we observed a bacteria cluster, which initially follows a mean flow streamline, become captured by an EPS thread (**Video S1**).

These EPS threads have two major consequences. First, the bacteria can hitch a ride on these threads and significantly alter their transport in the water column. Although the threads are initially transient and detach frequently in the time period over which we made our measurements, over time a more stable and robust aggregate or streamer can form (White et al., 2019), allowing the bacterial stowaways to travel much greater distances, potentially greatly affecting their distribution in the water column. Second, these threads immediately and significantly perturb the flow field around the drop, affecting the hydrodynamics and drag experienced by the drop.

By performing a control volume analysis around the drop, the conservation of momentum provided more insight into how the EPS threads affected the drag. Specifically, it was found that modulations in the pressure field were the primary contributor to increasing drag on the drop (**Table 1**), caused by the threads widening the streamlines (**Figure 7C**). These threads, though estimated to be about 1 μm thick or smaller, appear to be effective at deviating the streamlines. Comparing a clean drop without any EPS threads or attached bacteria to the same drop after about four EPS threads appear to be attached, the viscous drag coefficient increased by 85%. To demonstrate the impact of a single EPS thread, when one thread had detached from the drop (**Figures 7A,B**), the drag coefficient decreased by 27%.

There are several caveats to keep in mind when considering these results in the context of the real open ocean as described in the Results and Discussion: the bacteria community, the aqueous phase composition, the temperature and pressure, and the shape of the drop are not the same as the real conditions. However, it is plausible to expect similar EPS threads and bacterial aggregates to form on a real drop rising through a microbial bloom in the water column, and hydrodynamic impacts would be analogous to those quantified in these microfluidic experiments.

With this in mind, we can put an 85% drag coefficient increase on a spherical drop in perspective. Assuming Stokes

flow ($Re_D < 0.5$), the rising velocity of a spherical droplet is inversely proportional to the drag coefficient (i.e., $C_d = 24/Re_D$). Therefore, an 85% increase in the drag coefficient corresponds to a 46% reduction in the rising velocity. We can alternatively put an 85% drag increase in the perspective of biodegradation, where it is common in modeling studies to assume the drop volume decreases with time according to available biodegradation half-life data (North et al., 2015). Since the drop diameter is also inversely proportional to the drag coefficient, to achieve an 85% increase in the drag coefficient would require a 46% reduction in the drop diameter, or about a 10% reduction in the drop volume. Thus, the hydrodynamic impact of several EPS threads (**Figure 5**) attached to a rising droplet is roughly on the same order of magnitude as a 10% reduction in the drop's volume.

While more work needs to be done with more ecologically relevant conditions (bacteria, temperature, and pressure, aqueous phase), the mechanism investigated in this paper and the measurable impacts on the hydrodynamics and the drag experienced by the drop are significant and will drastically affect drop transport and fate predicted by current modeling efforts.

DATA AVAILABILITY STATEMENT

Data are publicly available through the Gulf of Mexico Research Initiative Information & Data Cooperative (GRIIDC) at https://data.gulfresearchinitiative.org (doi: 10.7266/N7N58JTF, doi: 10.7266/N7BV7F6V).

AUTHOR CONTRIBUTIONS

AW and JS designed research and analyzed data. AW, MJ, and JS performed research. AW and MJ contributed new tools. All authors wrote the paper.

FUNDING

This research was partially supported by the grants from the Gulf of Mexico Research Initiative (GoMRI) SA18-17/UTA17-001449 and SA15-19/UTA16-000545 and a grant from ExxonMobile under grant no. A4006200. Microfabrication equipment is partially supported from ONR under grant no. W911NF-17-1-0371.

SUPPLEMENTARY MATERIAL

The Supplementary Material for this article can be found online at: https://www.frontiersin.org/articles/10.3389/fmars.2020.00294/full#supplementary-material

Video S1 | A 700 ms segment of the high speed image sequence captured 50 min after the first bacterial encounter is shown. The playback is at 1/100 real speed. The oil drop (black half circle) has a radius of 120 μm. White dots in the video are suspended bacteria. Initially a cluster of ∼3 bacteria are circled in red. A black dotted line represents the mean flow streamline passing through this bacteria cluster in the initial frame. As the video plays, the cluster can be seen following the streamline until suddenly encountering an EPS thread on the trailing side of the drop. The cluster then deviates from the streamline, following the path of the EPS thread. The bacteria become momentarily trapped in the thread, and toward the end of the clip they again begin to drift downstream along the thread out of the frame.

REFERENCES

Alldredge, A. L., and Silver, M. W. (1988). Characteristics, dynamics, and significance of marine snow. *Prog. Oceanogr.* 20, 41–82. doi: 10.1016/0079-6611(88)90053-5

Autrusson, N., Guglielmini, L., Lecuyer, S., Rusconi, R., and Stone, H. A. (2011). The shape of an elastic filament in a two-dimensional corner flow. *Phys. Fluids* 23:063602. doi: 10.1063/1.3601446

Bauer, W.-A. C., Fischlechner, M., Abell, C., and Huck, W.T. (2010). Hydrophilic PDMS microchannels for high-throughput formation of oil-in-water microdroplets and water-in-oil-in-water double emulsions. *Lab. Chip.* 10, 1814–1819. doi: 10.1039/c004046k

Brakstad, O. G., Lewis, A., and Beegle-Krause, C. (2018). A critical review of marine snow in the context of oil spills and oil spill dispersant treatment with focus on the deepwater horizon oil spill. *Mar. Pollut. Bull.* 135, 346–356. doi: 10.1016/j.marpolbul.2018.07.028

Camilli, R., Di Iorio, D., Bowen, A., Reddy, C. M., Techet, A. H., Yoerger, D. R., et al. (2012). Acoustic measurement of the deepwater horizon macondo well flow rate. *Proc. Natl. Acad. Sci. U. S. A.* 109, 20235–20239. doi: 10.1073/pnas.1100385108

Camilli, R., Reddy, C. M., Yoerger, D. R., Van Mooy, B. A., Jakuba, M. V., Kinsey, J. C., et al. (2010). Tracking hydrocarbon plume transport and biodegradation at deepwater horizon. *Science* 330, 201–204. doi: 10.1126/science.1195223

Daly, K. L., Passow, U., Chanton, J., and Hollander, D. (2016). Assessing the impacts of oil-associated marine snow formation and sedimentation during and after the deepwater horizon oil spill. *Anthropocene* 13, 18–33. doi: 10.1016/j.ancene.2016.01.006

Das, S., and Kumar, A. (2014). Formation and post-formation dynamics of bacterial biofilm streamers as highly viscous liquid jets. *Sci. Rep.* 4:e7126. doi: 10.1038/srep07126

Drescher, K., Shen, Y., Bassler, B. L., and Stone, H. A. (2013). Biofilm streamers cause catastrophic disruption of flow with consequences for environmental and medical systems. *Proc. Natl. Acad. Sci. U. S. A.* 110, 4345–4350. doi: 10.1073/pnas.1300321110

Dubinsky, E. A., Conrad, M. E., Chakraborty, R., Bill, M., Borglin, S. E., Hollibaugh, J. T., et al. (2013). Succession of hydrocarbon-degrading bacteria in the aftermath of the deepwater horizon oil spill in the Gulf of Mexico. *Environ. Sci. Technol.* 47, 10860–10867. doi: 10.1021/es401676y

Evans, H. B., Gorumlu, S., Aksak, B., Castillo, L., and Sheng, J. (2016). Holographic microscopy and microfluidics platform for measuring wall stress and 3D flow over surfaces textured by micro-pillars. *Sci. Rep.* 6:28753. doi: 10.1038/srep28753

French-Mccay, D., Crowley, D., and Mcstay, L. (2019). Sensitivity of modeled oil fate and exposure from a subsea blowout to oil droplet sizes, depth, dispersant use, and degradation rates. *Mar. Pollut. Bull.* 146, 779–793. doi: 10.1016/j.marpolbul.2019.07.038

Fu, J., Gong, Y., Zhao, X., O'reilly, S. E., and Zhao, D. (2014). Effects of oil and dispersant on formation of marine oil snow and transport of oil hydrocarbons. *Environ. Sci. Technol.* 48, 14392–14399. doi: 10.1021/es5042157

Gopalan, B., and Katz, J. (2010). Turbulent shearing of crude oil mixed with dispersants generates long microthreads and microdroplets. *Phys. Rev. Lett.* 104:054501. doi: 10.1103/PhysRevLett.104.054501

Gutierrez, T., Berry, D., Yang, T., Mishamandani, S., Mckay, L., Teske, A., et al. (2013). Role of bacterial exopolysaccharides (EPS) in the fate of the oil released during the deepwater horizon oil spill. *PLoS ONE* 8:e67717. doi: 10.1371/journal.pone.0067717

Hassanpourfard, M., Nikakhtari, Z., Ghosh, R., Das, S., Thundat, T., Liu, Y., et al. (2015). Bacterial floc mediated rapid streamer formation in creeping flows. *Sci. Rep.* 5:13070. doi: 10.1038/srep13070

Hazen, T. C., Dubinsky, E. A., Desantis, T. Z., Andersen, G. L., Piceno, Y. M., Singh, N., et al. (2010). Deep-sea oil plume enriches indigenous oil-degrading bacteria. *Science* 330, 204–208. doi: 10.1126/science.1195979

Hu, P., Dubinsky, E. A., Probst, A. J., Wang, J., Sieber, C. M., Tom, L. M., et al. (2017). Simulation of deepwater horizon oil plume reveals substrate specialization within a complex community of hydrocarbon degraders. *Proc. Natl. Acad. Sci. U.S.A.* 114, 7432–7437. doi: 10.1073/pnas.1703424114

Jernelöv, A., and Lindén, O. (1981). Ixtoc I: a case study of the world's largest oil spill. *Ambio* 10, 299–306.

Joye, S. B., Bracco, A., Kmen, T. M., Chanton, J. P., Grosell, M., Macdonald, I. R., et al. (2016). The Gulf of Mexico ecosystem, six years after the Macondo oil well blowout. *Deep Sea Res. Pt II* 129, 4–19. doi: 10.1016/j.dsr2.2016.04.018

Joye, S. B., Macdonald, I. R., Leifer, I., and Asper, V. (2011). Magnitude and oxidation potential of hydrocarbon gases released from the BP oil well blowout. *Nat. Geosci.* 4, 160–164. doi: 10.1038/ngeo1067

Kessler, J. D., Valentine, D. L., Redmond, M. C., Du, M., Chan, E. W., Mendes, S. D., et al. (2011). A persistent oxygen anomaly reveals the fate of spilled methane in the deep Gulf of Mexico. *Science* 331, 312–315. doi: 10.1126/science.1199697

Kiørboe, T., Grossart, H.-P., Ploug, H., and Tang, K. (2002). Mechanisms and rates of bacterial colonization of sinking aggregates. *Appl. Environ. Microbiol.* 68, 3996–4006. doi: 10.1128/AEM.68.8.3996-4006.2002

Kleindienst, S., Grim, S., Sogin, M., Bracco, A., Crespo-Medina, M., and Joye, S. B. (2016). Diverse, rare microbial taxa responded to the deepwater horizon deep-sea hydrocarbon plume. *ISME J.* 10, 400–415. doi: 10.1038/ismej.2015.121

Kostka, J. E., Joye, S. B., Overholt, W., Bubenheim, P., Hackbusch, S., Larter, S. R., et al. (2020). "Biodegradation of petroleum hydrocarbons in the deep sea," in *Deep Oil Spills*, eds S. A. Murawski, C. H. Ainsworth, S. Gilbert, D. J. Hollander, C. B. Paris, M. Schlüter, and D. L. Wetzel (Cham: Springer), 107–124. doi: 10.1007/978-3-030-11605-7_7

Lehr, B., Bristol, S., and Possolo, A. (2010). *Oil Budget Calculator Deepwater Horizon*. Washington, DC: The Federal Interagency Solutions Group.

Marty, A., Roques, C., Causserand, C., and Bacchin, P. (2012). Formation of bacterial streamers during filtration in microfluidic systems. *Biofouling.* 28, 551–562. doi: 10.1080/08927014.2012.695351

Mason, O. U., Hazen, T. C., Borglin, S., Chain, P. S. G., Dubinsky, E. A., Fortney, J. L., et al. (2012). Metagenome, metatranscriptome and single-cell sequencing reveal microbial response to Deepwater Horizon oil spill. *ISME J.* 6, 1715–1727. doi: 10.1038/ismej.2012.59

Mcnutt, M. K., Camilli, R., Crone, T. J., Guthrie, G. D., Hsieh, P. A., Ryerson, T. B., et al. (2012). Review of flow rate estimates of the deepwater horizon oil spill. *Proc. Natl. Acad. Sci. U. S. A.* 109, 20260–20267. doi: 10.1073/pnas.1112139108

North, E. W., Adams, E. E., Thessen, A. E., Schlag, Z., He, R., Socolofsky, S. A., et al. (2015). The influence of droplet size and biodegradation on the transport of subsurface oil droplets during the Deepwater Horizon spill: a model sensitivity study. *Environ. Res. Lett.* 10:024016. doi: 10.1088/1748-9326/10/2/024016

Paris, C. B., HéNaff, M. L., Aman, Z. M., Subramaniam, A., Helgers, J., Wang, D.-P., et al. (2012). Evolution of the macondo well blowout: simulating the effects of the circulation and synthetic dispersants on the subsea oil transport. *Environ. Sci. Technol.* 46, 13293–13302. doi: 10.1021/es303197h

Passow, U. (2016). Formation of rapidly-sinking, oil-associated marine snow. *Deep Sea Res. Pt II* 129, 232–240. doi: 10.1016/j.dsr2.2014.10.001

Passow, U., Ziervogel, K., Asper, V., and Diercks, A. (2012). Marine snow formation in the aftermath of the deepwater horizon oil spill in the Gulf of Mexico. *Environ. Res. Lett.* 7:035301. doi: 10.1088/1748-9326/7/3/035301

Perlin, N., Paris, C. B., Berenshtein, I., Vaz, A. C., Faillettaz, R., Aman, Z. M., et al. (2020). "Far-field modeling of a deep-sea blowout: sensitivity studies of initial conditions, biodegradation, sedimentation, and subsurface dispersant injection on surface slicks and oil plume concentrations," in *Deep Oil Spills,* eds S. A. Murawski, C. H. Ainsworth, S. Gilbert, D. J. Hollander, C. B. Paris, M. Schlüter, and D. L. Wetzel (Cham: Springer), 170–192. doi: 10.1007/978-3-030-11605-7_11

Prince, R. C., Nash, G. W., and Hill, S. J. (2016). The biodegradation of crude oil in the deep ocean. *Mar. Pollut. Bull.* 111, 354–357. doi: 10.1016/j.marpolbul.2016.06.087

Quigg, A., Passow, U., Chin, W. C., Xu, C., Doyle, S., Bretherton, L., et al. (2016). The role of microbial exopolymers in determining the fate of oil and chemical dispersants in the ocean. *Limnol. Oceanogr. Lett.* 1, 3–26. doi: 10.1002/lol2.10030

Reddy, C. M., Arey, J. S., Seewald, J. S., Sylva, S. P., Lemkau, K. L., Nelson, R. K., et al. (2012). Composition and fate of gas and oil released to the water column during the deepwater horizon oil spill. *Proc. Natl. Acad. Sci. U. S. A.* 109, 20229–20234. doi: 10.1073/pnas.1101242108

Redmond, M. C., and Valentine, D. L. (2012). Natural gas and temperature structured a microbial community response to the deepwater horizon oil spill. *Proc. Natl. Acad. Sci. U. S. A.* 109, 20292–20297. doi: 10.1073/pnas.1108756108

Römer, M., Hsu, C.-W., Loher, M., Macdonald, I., Dos Santos Ferreira, C., Pape, T., et al. (2019). Amount and fate of gas and oil discharged at 3400 m water depth from a natural seep site in the Southern Gulf of Mexico. *Front. Mar. Sci.* 6:700. doi: 10.3389/fmars.2019.00700

Roth, G., and Katz, J. (2001). Five techniques for increasing the speed and accuracy of PIV interrogation. *Meas. Sci. Technol.* 12:238. doi: 10.1088/0957-0233/12/3/302

Rusconi, R., Lecuyer, S., Guglielmini, L., and Stone, H. A. (2010). Laminar flow around corners triggers the formation of biofilm streamers. *J. R. Soc. Interface* 7, 1293–1299. doi: 10.1098/rsif.2010.0096

Scheidweiler, D., Peter, H., Pramateftaki, P., De Anna, P., and Battin, T. J. (2019). Unraveling the biophysical underpinnings to the success of multispecies biofilms in porous environments. *ISME J.* 13, 1700–1710. doi: 10.1038/s41396-019-0381-4

Shillaber, C. P. (1944). *Photomicrography In Theory and Practice.* New York, NY: John Wiley and Sons.

Socolofsky, S. A., Adams, E. E., Boufadel, M. C., Aman, Z. M., Johansen, Ø., Konkel, W. J., et al. (2015). Intercomparison of oil spill prediction models for accidental blowout scenarios with and without subsea chemical dispersant injection. *Mar. Pollut. Bull.* 96, 110–126. doi: 10.1016/j.marpolbul.2015.05.039

Spier, C., Stringfellow, W. T., Hazen, T. C., and Conrad, M. (2013). Distribution of hydrocarbons released during the 2010 MC252 oil spill in deep offshore waters. *Environ. Pollut.* 173, 224–230. doi: 10.1016/j.envpol.2012.10.019

Valentine, D. L., Fisher, G. B., Bagby, S. C., Nelson, R. K., Reddy, C. M., Sylva, S. P., et al. (2014). Fallout plume of submerged oil from deepwater horizon. *Proc. Natl. Acad. Sci. U. S. A.* 111, 15906–15911. doi: 10.1073/pnas.1414873111

Valentine, D. L., Mezić, I., Maćešić, S., Crnjarić-Žic, N., Ivić, S., Hogan, P. J., et al. (2012). Dynamic autoinoculation and the microbial ecology of a deep water hydrocarbon irruption. *Proc. Natl. Acad. Sci. U. S. A.* 109, 20286–20291. doi: 10.1073/pnas.1108820109

Valiei, A., Kumar, A., Mukherjee, P. P., Liu, Y., and Thundat, T. (2012). A web of streamers: biofilm formation in a porous microfluidic device. *Lab. Chip.* 12, 5133–5137. doi: 10.1039/c2lc40815e

Vangnai, S., and Klein, D. (1974). A study of nitrite-dependent dissimilatory micro-organisms isolated from Oregon soils. *Soil Biol. Biochem.* 6, 335–339. doi: 10.1016/0038-0717(74)90040-6

Wade, T. L., Sericano, J. L., Sweet, S. T., Knap, A. H., and Guinasso, N. L. (2016). Spatial and temporal distribution of water column total polycyclic aromatic hydrocarbons (PAH) and total petroleum hydrocarbons (TPH) from the deepwater horizon (Macondo) incident. *Mar. Pollut. Bull.* 103, 286–293. doi: 10.1016/j.marpolbul.2015.12.002

White, A. R., Jalali, M., Boufadel, M. C., and Sheng, J. (2020). Bacteria forming drag-increasing streamers on a drop implicates complementary fates of rising deep-sea oil droplets. *Sci. Rep.* 10, 1–14. doi: 10.1038/s41598-020-61214-9

White, A. R., Jalali, M., and Sheng, J. (2019). A new ecology-on-a-chip microfluidic platform to study interactions of microbes with a rising oil droplet. *Sci. Rep.* 9:13737. doi: 10.1038/s41598-019-50153-9

Yang, T., Nigro, L. M., Gutierrez, T., Joye, S. B., Highsmith, R., and Teske, A. (2016). Pulsed blooms and persistent oil-degrading bacterial populations in the water column during and after the Deepwater Horizon blowout. *Deep Sea Res. Pt II* 129, 282–291. doi: 10.1016/j.dsr2.2014.01.014

Zarabadi, M. P., Paquet-Mercier, F. O., Charette, S. J., and Greener, J. (2017). Hydrodynamic effects on biofilms at the biointerface using a microfluidic

electrochemical cell: case study of pseudomonas sp. *Langmuir.* 33, 2041–2049. doi: 10.1021/acs.langmuir.6b03889

Zhao, L., Boufadel, M. C., Socolofsky, S. A., Adams, E., King, T., and Lee, K. (2014). Evolution of droplets in subsea oil and gas blowouts: development and validation of the numerical model VDROP-J. *Mar. Pollut. Bull.* 83, 58–69. doi: 10.1016/j.marpolbul.2014.04.020

Ziervogel, K., Mckay, L., Rhodes, B., Osburn, C. L., Dickson-Brown, J., Arnosti, C., et al. (2012). Microbial activities and dissolved organic matter dynamics in oil-contaminated surface seawater from the deepwater horizon oil spill site. *PLoS ONE* 7:e34816. doi: 10.1371/journal.pone.0034816

Conflict of Interest: The authors declare that the research was conducted in the absence of any commercial or financial relationships that could be construed as a potential conflict of interest.

Copyright © 2020 White, Jalali and Sheng. This is an open-access article distributed under the terms of the Creative Commons Attribution License (CC BY). The use, distribution or reproduction in other forums is permitted, provided the original author(s) and the copyright owner(s) are credited and that the original publication in this journal is cited, in accordance with accepted academic practice. No use, distribution or reproduction is permitted which does not comply with these terms.

frontiers in Marine Science

ORIGINAL RESEARCH
published: 21 May 2020
doi: 10.3389/fmars.2020.00331

Copepod Behavior Responses Around Internal Waves

*Mohammad Mohaghar, Seongyu Jung, Kevin A. Haas and Donald R. Webster**

School of Civil and Environmental Engineering, Georgia Institute of Technology, Atlanta, GA, United States

Internal waves are ubiquitous features in coastal marine environments and have been observed to mediate vertical distributions of zooplankton. Internal waves possess fine-scale hydrodynamic cues that copepods and other zooplankton are known to sense, such as fluid density gradients and velocity gradients (quantified as shear strain rate). The role of copepod behavior in response to cues associated with internal waves is largely unknown. The objective is to provide insight to the bio-physical interaction and the role of biological vs. physical forcing in mediating organism distributions. A laboratory-scale internal wave apparatus is designed to facilitate fine-scale observations of copepod behavior in flows that replicate *in situ* conditions of internal waves in two-layer stratification. An experimental configuration is presented with a density jump of 1 σ_t. Theoretical analysis of the two-layer system provided guidance to the target forcing frequency needed to generate a standing internal wave with a single dominate frequency of oscillation. Flow visualization and signal processing of the interface location were used to quantify the wave characteristics. The results show a close match to the target wave parameters. Marine copepod (mixed population of *Acartia tonsa*, *Temora longicornis*, and *Eurytemora affinis*) behavior assays were conducted for three different physical arrangements: (1) no density stratification (i.e., control), (2) stagnant two-layer density stratification, and (3) two-layer density stratification with internal wave motion. Digitized trajectories of copepod swimming behavior indicate that in the control (case 1) the animals showed no preferential aggregation. In the stagnant density jump treatment (case 2) copepods preferentially moved horizontally, parallel to the density interface. In the internal wave treatment (case 3) copepods demonstrated loopy, orbital trajectories near the density interface. Analysis of advected trajectories in the internal wave, with and without superimposed copepod swimming, reveal distinct differences with the observed copepod trajectories in the internal wave treatment. These differences and a consideration of the potential hydrodynamic cues indicate that copepod behavior response has a substantial influence on the swimming trajectories in the internal wave region.

Keywords: internal wave, copepod, density stratification, behavior assay, wave dispersion relationship

OPEN ACCESS

Edited by:
Houshuo Jiang, Woods Hole Oceanographic Institution, United States

Reviewed by:
François-Gaël Michalec, UMR5502 Institut de Mecanique des Fluides de Toulouse (IMFT), France
Jessica Garwood, Rutgers, The State University of New Jersey, United States

****Correspondence:***
Donald R. Webster
dwebster@ce.gatech.edu

Specialty section:
This article was submitted to Marine Ecosystem Ecology, a section of the journal Frontiers in Marine Science

Received: *09 January 2020*
Accepted: *22 April 2020*
Published: *21 May 2020*

Citation:
Mohaghar M, Jung S, Haas KA and Webster DR (2020) Copepod Behavior Responses Around Internal Waves. Front. Mar. Sci. 7:331. doi: 10.3389/fmars.2020.00331

1. INTRODUCTION

Internal waves are ubiquitous phenomena that often form in regions of high temperature or salinity variability as the pycnocline oscillates to create the wave (Phillips, 1966). Interests in studying internal waves have varied across a wide spectrum including breaking internal waves, shoaling internal waves, and tidal internal wave packets (e.g., Thorpe, 1999; Troy and Koseff, 2005; Hult et al., 2009).

In addition to interest in the physical aspects of internal waves, studies often are focused on understanding the vertical mixing of nutrients or vertical displacements of plankton distributions (Mann and Lazier, 1996). Zooplankton distributions are also influenced by the presence of internal waves (e.g., Haury et al., 1979; Greer et al., 2014; Sevadjian et al., 2014). In fact, the majority of observations indicate aggregation and increased zooplankton presence in and around the internal wave region (e.g., Haury et al., 1983; McManus et al., 2005; Van Haren, 2014). This phenomenon also has been observed in a fresh-water lake (Rinke et al., 2007). To understand the association of zooplankton population dynamics with internal waves, we must better understand the bio-physical coupling and the role of fine-scale hydrodynamic cues induced by internal waves. The majority of these studies suggest that the zooplankton are advected by the internal wave fluid motion, although there are some indications that behavioral responses may play an important or critical role. In this regard, Macías et al. (2010) reported that the distribution of zooplankton in internal waves in the Strait of Gibraltar appeared to result from a spatial differentiation between weakly-swimming and strong-swimming taxa. Despite this observation, they ultimately concluded that zooplankton distributions result from physical forcing as opposed to migration patterns. Further, Van Haren (2014) noted that zooplankton "gathered" near internal wave structure, which implies a behavioral component. Modeling efforts also suggest that behavior may play an important role. Lennert-Cody and Franks (1999) and Lennert-Cody and Franks (2002) showed that horizontal distributions of phytoplankton in internal wave structure are greatly influenced by their ability to weakly swim. Further, Scotti and Pineda (2007) and Garwood et al. (2020) found that depth-keeping zooplankton in propagated weakly internal wave can form aggregations and enhance cross-shore transport.

In the absence of the oscillations associated with internal waves, there are many observations that the pycnocline is important for the distribution of biomass along the water column. Field observations have shown that thin layers, which are sparse patches of high phytoplankton biomass in the water column (Holliday et al., 2003), are often formed around the pycnocline (Dekshenieks et al., 2001; McManus et al., 2003). Further, copepods and other zooplankton have been observed to aggregate around thin layers (e.g., Cowles et al., 1998; Dekshenieks et al., 2001; Gallager et al., 2004). And, there is evidence that zooplankton sensing and behavioral responses play an important role in the distribution of zooplankton (Woodson et al., 2005, 2007a,b; True et al., 2018). Thus, a relevant question is whether the behavioral component that contributes to aggregations of zooplankton around thin layers is modified by the unsteady, orbital oscillations of internal waves.

The objective of this study is to design and test a laboratory apparatus to study the balance of behavioral vs. physical forcing in the distribution of marine zooplankton in and around internal waves at an individual scale. No study to date has examined the mechanistic link between the fluid motion of internal waves and copepod behavior. However, the oscillations of the internal wave generate dynamic hydrodynamic cues that copepods may be able to sense. Hence, our intent is to provide insight to the mediating factors that dictate organism distributions such as advective transport and swimming behavior responses to velocity and density gradients. The objective is consistent with the statements in Haury et al. (1983) seeking to determine the influence of passive transport vs. the influence of behavior responses to explain the resulting zooplankton distributions. The paper presents a detailed description of the apparatus and a theoretical analysis of the internal wave structure in the laboratory configuration. The wave characteristics are experimentally quantified to compare to the theoretical targets, and finally behavioral trials for a mixed population of copepods are described and interpreted.

2. MATERIALS AND PROCEDURES

A laboratory-scale internal wave apparatus was created to replicate the flow characteristics of a standing internal wave in a two-layer stratified system. It should be noted that internal waves typically propagate in a stratified medium in the ocean, but a standing internal wave can be generated in the special case of a finite trapped region of altitude or depth (Ewing, 1950). A standing wave is preferred in this study in order to avoid traveling waves that reflect in the finite-sized laboratory apparatus. The target parameters were chosen based on the theoretical analysis of a standing internal wave in a two-layer stratified system, presented in the next section. Flow visualization and signal processing were used to quantitatively compare the results to the target parameters. Copepod behavioral assays were conducted to understand their response to hydrodynamic cues (in addition to the inevitable directional cue of the orientation of gravity) associated with internal waves such as fluid density gradients and velocity gradients (quantified as shear strain rate).

2.1. Experimental Apparatus

The main tank (2.438 m × 50 cm × 50 cm) was constructed from clear acrylic sheets with thickness of 1.905 cm. The schematic of the internal wavemaker apparatus is shown in **Figure 1**. A line diffuser (PVC) was installed along the middle of the tank floor to be used to fill the tank.

Following the theory described in Dean and Dalrymple (1991), a half-cylinder plunger-type wavemaker was used to create a perturbation at the pycnocline represented by the interface between the density layers. The PVC plunger had dimensions of 10.16 cm diameter and 50 cm length and was driven by an electric motor. A stainless steel linkage connected the plunger to a disk mounted on the rotating motor shaft. A timing control signal is triggered by a striking tab on

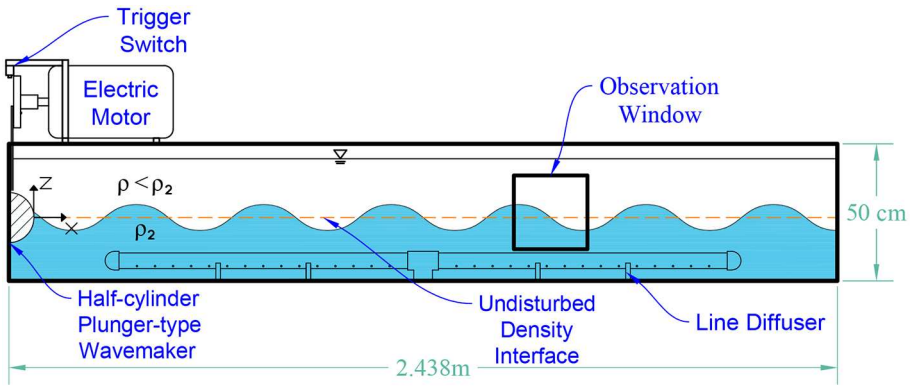

FIGURE 1 | Schematic diagram of the internal wavemaker apparatus.

the disk contacting a switch button. On each revolution, the switch sent a voltage signal to the external trigger port of a pulse generator. By precisely controlling the delay following the external trigger signal, the pulse generator sent a signal to the camera to capture an image at a targeted phase of the standing wave cycle.

2.2. Experimental Parameters

The design parameters for a standing internal wave were chosen in order to mimic the thin layer structures found in highly-stratified coastal environments (Cheriton et al., 2009; Velo-Suárez et al., 2010). In determining the parameters, several constraints were taken into account such as the tank dimensions, the size of the wave with respect to the observation window, and the resolution of the recorded images. The independent variables were: (1) the fluid density jump between the layers, (2) the amplitude of the plunger displacement, (3) the layer thickness, and (4) the seiching mode of the wave. The wave period ($T = 2\pi/\omega$, where ω is the angular frequency of the wave) was calculated from these input variables using the theoretical wave description presented in the next section.

A density jump of 1.0 σ_t was chosen based on previous copepod behavior assays performed by Woodson et al. (2007a). This study showed that based on a regression analysis of the number of individual calanoid copepods *Temora longicornis* and *Acartia tonsa* crossing the interface vs. the magnitude of the density jump, the threshold range was between $\triangle\rho = 0.4$ to 2.0 σ_t. The lower boundary was where the regression curve began to decrease, and the upper boundary was where approximately 75% of the population was not crossing the density interface. The density jump of 1.0 σ_t was also consistent with density interfaces observed *in situ* (e.g., Dekshenieks et al., 2001; Cowles, 2004; Gallager et al., 2004, and Cheriton et al., 2009). The amplitude of the plunger motion was experimentally (i.e., trial and error) set to 3 cm; larger amplitudes produced higher harmonics, evanescent modes, and eventually wave breaking. In the experimental set-up, the layer thicknesses were equal (i.e., $h_1 = h_2 = 22.2$ cm, where h is the layer thickness).

2.3. Stratification Procedure

A two-layer stratified volume was prepared prior to running either the wave characterization or behavior assay experiments. The fluid for each layer was created in separate batches using filtered artificial seawater (Instant Ocean). The lighter density layer (ρ_1 referred to as the "upper layer") was prepared in the experimental tank with a density of 1,025 kg/m^3 (33 ppt). The heavier density layer (ρ_2, the "lower layer") was prepared in a separate reservoir with a density of 1,026 kg/m^3 (34.3 ppt). The salinity levels were chosen to best match natural levels in the ocean where the copepods were harvested. For visual characterization, red food coloring (Kleckner's Tomatoshade) was mixed into the lower layer fluid. The lower layer fluid was slowly introduced to the tank via the line diffuser at the bottom of the tank. The flow rate was initially 1.9 L/min until the depth of the incoming layer was greater than the height of the diffuser. Then the flow was increased to 7.6 L/min. The incoming flow rate was specified to maintain laminar flow in the jet flows exiting the diffuser holes in order to avoid turbulent mixing. The layer structure was assumed to be fixed over the course of the experiments ($\sim$ 2 h) because of the long time scales ($\sim$ days) associated with molecular diffusion.

3. THEORETICAL ANALYSIS

An accurate wave dispersion relationship is needed to identify the target wave and piston motion parameters. The two-layer density stratified system is represented in **Figure 2**. Anticipating that the amplitude of the waves will be significant compared to the wavelength, the third-order solution for internal waves propagating along the interface between two homogeneous incompressible and inviscid fluids, which considers the non-linearity of the internal wave profile, is computed in this work to find the dispersion relationship (Umeyama, 2000, 2002). Since the flow is considered inviscid for analysis purposes, the potential function is a useful parameterization of the velocity field, and it is denoted with the variable ϕ_1 and ϕ_2 in each layer. The position of the instantaneous density interfaces are denoted by η_1 and η_2 as shown in **Figure 2**. The third-order solution for internal waves

may be defined as:

$$\phi_1 = \varepsilon\phi_1^{(1)} + \varepsilon^2\phi_1^{(2)} + \varepsilon^3\phi_1^{(3)} + O(\varepsilon^4) \quad (1)$$

$$\phi_2 = \varepsilon\phi_2^{(1)} + \varepsilon^2\phi_2^{(2)} + \varepsilon^3\phi_2^{(3)} + O(\varepsilon^4) \quad (2)$$

$$\eta_1 = \varepsilon\eta_1^{(1)} + \varepsilon^2\eta_1^{(2)} + \varepsilon^3\eta_1^{(3)} + O(\varepsilon^4) \quad (3)$$

$$\eta_2 = \varepsilon\eta_2^{(1)} + \varepsilon^2\eta_2^{(2)} + \varepsilon^3\eta_2^{(3)} + O(\varepsilon^4) \quad (4)$$

$$\omega = \omega^{(0)} + \varepsilon\omega^{(1)} + \varepsilon^2\omega^{(2)} + O(\varepsilon^3), \quad (5)$$

where ε is the perturbation parameter. The superscripts (1), (2), and (3) indicate quantities that correspond to the first-order, second-order, and third-order perturbation solutions. The governing equations and boundary conditions are

$$\phi_{1,xx} + \phi_{1,zz} = 0 \quad (6)$$

$$\phi_{2,xx} + \phi_{2,zz} = 0 \quad (7)$$

$$g(\eta_1 + h_1) + \phi_{1,t} + \frac{1}{2}(\phi_{1,x}^2 + \phi_{1,z}^2) = 0 \ \ at \ \ z = h_1 + \eta_1 \quad (8)$$

$$\eta_{1,t} + \eta_{1,x}\phi_{1,x} - \phi_{1,z} = 0 \ \ at \ \ z = h_1 + \eta_1 \quad (9)$$

$$\phi_{2,z} = 0 \ \ at \ \ z = -h_2 \quad (10)$$

$$\eta_{2,t} + \eta_{2,x}\phi_{1,x} - \phi_{1,z} = 0 \ \ at \ \ z = \eta_2 \quad (11)$$

$$\eta_{2,t} + \eta_{2,x}\phi_{2,x} - \phi_{2,z} = 0 \ \ at \ \ z = \eta_2 \quad (12)$$

$$\rho_1[g\eta_2 + \phi_{1,t} + \frac{1}{2}(\phi_{1,x}^2 + \phi_{1,z}^2)] = \rho_2[g\eta_2 + \phi_{2,t} + \frac{1}{2}(\phi_{2,x}^2 + \phi_{2,z}^2)] \ \ at \ \ z = \eta_2, \quad (13)$$

where g is acceleration due to gravity, t is time, and the comma notation in the subscript indicates a derivative operation with respect to the subsequent variable. Equations (6) and (7) are the Laplace equations, which describe mass continuity for each layer. Equations (8) and (9) are the kinematic and dynamic boundary conditions at the free surface. Equation (10) is the bottom solid wall boundary condition, and the kinematic and dynamic boundary conditions at the density interface are defined in Equations (11), (12), and (13). Since the vertical velocity of the fluid in both layers at the interface must be equal to the velocity of the interface, Equations (11) and (12) should be satisfied. Furthermore, Equation (13) provides the dynamic boundary condition at the fluid interface, where the normal stress of the fluid must be continuous across the interface (Drazin, 2002). It was shown that the boundary conditions and the governing equations for the first-, second-, and third-order functions can be derived by substituting Equations (1)–(5) into Equations (6)–(13) (Umeyama, 2000, 2002). The first-, second-, and third-order perturbation solutions for the frequency dispersion relation of the wave are

$$\omega^{(0)} = \sqrt{\frac{\rho_2 - \rho_1}{\rho_2}\frac{kg}{coth(kh_1) + coth(kh_2)}}, \quad (14)$$

$$\omega^{(1)} = 0, \quad (15)$$

$$\omega^{(2)} = \frac{k[gk\gamma_1^{(1)} - \omega^{(0)^2}\gamma_2^{(1)}]}{\omega^{(0)}\gamma_1^{(1)} + ga_1^{(1)}}a_1^{(2)} + \frac{3k^2[gk\gamma_2^{(1)} - \omega^{(0)^2}\gamma_1^{(1)}]}{4[\omega^{(0)}\gamma_1^{(1)} + ga_1^{(1)}]}a_1^{(1)^2} + \frac{k[8gk\gamma_1^{(2)} - 16\omega^{(0)^2}\gamma_2^{(2)} + 3\omega^{(0)}k^2\gamma_1^{(1)}\gamma_1^{(2)} - 2\omega^{(0)}k^2\gamma_1^{(1)}\gamma_2^{(1)}]}{4[\omega^{(0)}\gamma_1^{(1)} + ga_1^{(1)}]}a_1^{(1)} - \frac{2\omega^{(0)}k^2[\gamma_1^{(1)}\gamma_1^{(2)} - \gamma_2^{(1)}\gamma_2^{(2)}]}{\omega^{(0)}\gamma_1^{(1)} + ga_1^{(1)}}, \quad (16)$$

where k is the wavenumber, and

$$\gamma_1^{(1)} = A^{(1)}cosh(kh_1) + B^{(1)}sinh(kh_1) \quad (17)$$

$$\gamma_2^{(1)} = A^{(1)}sinh(kh_1) + B^{(1)}cosh(kh_1) \quad (18)$$

$$\gamma_1^{(2)} = A^{(2)}cosh(2kh_1) + B^{(2)}sinh(2kh_1) \quad (19)$$

$$\gamma_2^{(2)} = A^{(2)}sinh(2kh_1) + B^{(2)}cosh(2kh_1) \quad (20)$$

$$A^{(1)} = \alpha_{11}^{(1)}a_2^{(1)} = \frac{1}{\omega^{(0)}}[\frac{\rho_2\omega^{(0)^2}}{k\rho_1}coth(kh_2) - \frac{\rho_2 - \rho_1}{\rho_1}g]a_2^{(1)} \quad (21)$$

$$B^{(1)} = \alpha_{12}^{(1)}a_2^{(1)} = \frac{\omega^{(0)}a_2^{(1)}}{k} \quad (22)$$

$$\alpha_2^{(1)} = \frac{\omega^{(0)}}{ksinh(kh_2)} \quad (23)$$

$$a_1^{(1)} = \beta^{(1)}a_2^{(1)} = \frac{\omega^{(0)}}{g}[\alpha_{11}^{(1)}cosh(kh_1) + \alpha_{12}^{(1)}sinh(kh_1)]a_2^{(1)} \quad (24)$$

$$\alpha_{11}^{(2)} = \frac{\rho_2 - \rho_1}{\rho_1}g - 2\frac{\rho_2\omega^{(0)^2}}{\rho_1 ktanh(2kh_2)} \quad (25)$$

$$\alpha_1^{(2)} = \frac{\rho_2}{\rho_1}\omega^{(0)}k\alpha_2^{(1)}coth(kh_2) - \frac{\rho_2}{\rho_1}\omega^{(0)^2}(1 - \frac{1}{2sinh^2(kh_2)} + \frac{1}{2}[3\omega^{(0)^2} - k^2\alpha_{11}^{(1)^2}] \quad (26)$$

$$\alpha_{12}^{(2)} = \frac{\rho_2}{\rho_1}\omega^{(0)}k\alpha_2^{(1)}\frac{cosh(kh_2)}{tanh(2kh_2)} - \frac{\rho_2}{\rho_1}\omega^{(0)^2}(1 - \frac{1}{2sinh^2(kh_2)} + \frac{1}{2}[3\omega^{(0)^2} - k^2\alpha_{11}^{(1)^2}] \quad (27)$$

$$\alpha_{21}^{(2)} = \alpha_{22}^{(2)} = 2kcosh(2kh_1) - 4\frac{\omega^{(0)^2}}{g}sinh(2kh_1) \quad (28)$$

$$\chi^{(2)} = \frac{2\omega^{(0)^2}\beta^{(1)}k}{g}[\alpha_{11}^{(1)}sinh(kh_1) + \alpha_{12}^{(1)}cosh(kh_1)] \quad (29)$$

$$a_2^{(2)} = \frac{-[\alpha_1^{(2)}\alpha_{21}^{(2)} + 2\omega^{(0)}k\alpha_{11}^{(1)}\alpha_{22}^{(2)} + 2\omega^{(0)}\chi^{(2)}]a_2^{(1)^2}}{\alpha_{11}^{(2)}\alpha_{21}^{(2)} - 2\omega^{(0)}\alpha_{12}^{(1)}\alpha_{22}^{(2)}} \quad (30)$$

$$A^{(2)} = -\frac{1}{2\omega^{(0)}}[\alpha_{11}^{(2)}a_2^{(2)} + \alpha_{12}^{(2)}a_2^{(1)^2}] \quad (31)$$

$$B^{(2)} = \alpha_{12}^{(1)}a_2^{(2)} - k\alpha_{11}^{(1)}a_2^{(1)^2} \quad (32)$$

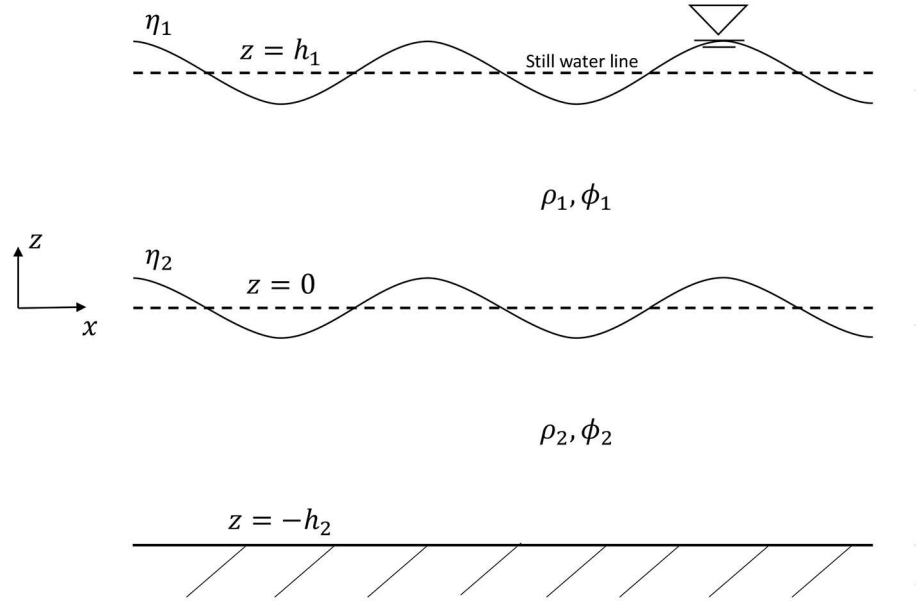

FIGURE 2 | Schematic of the Boundary Value Problem for a two-layer stratified internal wave.

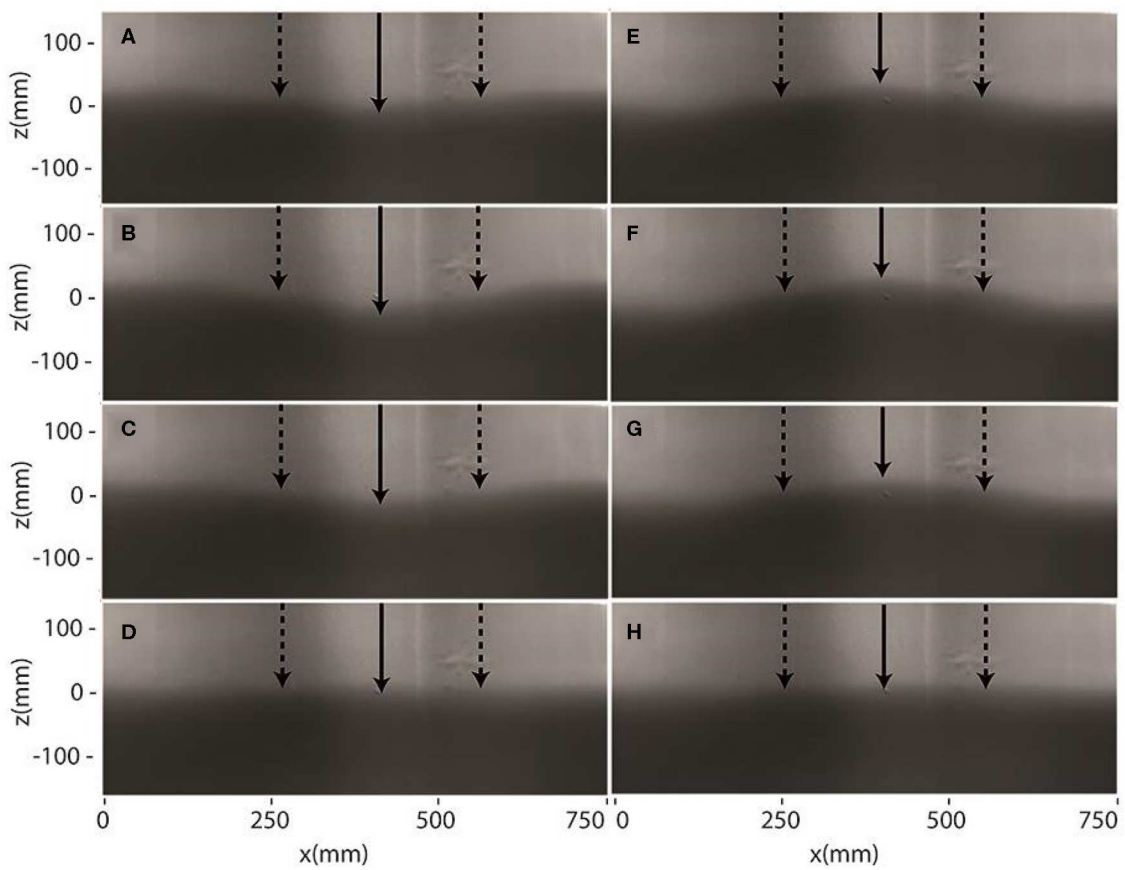

FIGURE 3 | Flow visualization showing eight phases during the wave cycle corresponding to ϕ = **(A)** 0, **(B)** $\frac{\pi}{4}$, **(C)** $\frac{\pi}{2}$, **(D)** $\frac{3\pi}{4}$, **(E)** π, **(F)** $\frac{5\pi}{4}$, **(G)** $\frac{3\pi}{2}$, and **(H)** $\frac{7\pi}{4}$ [radians]. The locations of the nodes are marked by the vertical dotted arrows and the antinodes are marked by the solid arrows.

$$a_1^{(2)} = \frac{2\omega^{(0)}}{g}[A^{(2)}cosh(2kh_1) + B^{(2)}sinh(2kh_1)] + \{\frac{\omega^{(0)}\beta^{(1)}k}{g}[\alpha_{11}^{(1)}sinh(kh_1) + \alpha_{12}^{(1)}cosh(kh_1)] - \frac{k^2}{2g}[\alpha_{11}^{(1)^2} - \alpha_{12}^{(1)^2}]\}a_2^{(1)^2}. \quad (33)$$

The analytical third-order solution is used to calculate the frequency of oscillation of the piston to be used as an operational parameter to achieve the target wave treatment. As noted above, the density jump was 1.0 σ_t, which was selected based on previous observations of copepod behavior in stagnant density interface treatments. The density interface was established in the center of the tank with $h_1 = h_2 = 22.2$ cm. These parameters, combined with the length dimension of the main tank and the wave amplitude [$a_2^{(1)} = 2.5$ cm], were used in the analytical equations presented above to determine the dispersion relationship between the mode of the standing wave and the frequency (i.e., Equation 5). The seiching mode number is equal to the harmonic mode of a standing wave, which dictated the number of full wavelengths in the tank. The target seiching mode is determined by a criteria to capture at least a quarter wavelength in a 30 × 30 cm viewing window during the behavioral trials in order to uniquely pinpoint any location on the wave at a given time and to maintain enough imaging resolution to resolve the wave interface position. In the case presented here, mode 8 was selected to yield a wavelength of 610 mm. Based on these parameters, the third-order dispersion equation yields a targeted frequency of 0.041 Hz, corresponding to a wave period of 24.27 s. As a final note, the value of $ka_2^{(1)}$ for this treatment is 0.26, which indicates the amplitude is not negligible relative to the wavelength and is consistent with the anticipated need to include the non-linear effects in the analysis.

4. FLOW CHARACTERIZATION TECHNIQUES

For the wave characterization trials, the layers were marked by the sharp interface between the red-dyed bottom layer and clear upper layer. After initiating the wavemaker motion, the interface motion took about 30 min (on average) to develop into a standing internal wave due to the long wave period and return time of the transient reflected waves.

A CCD camera (Vision Research Inc. model Phantom v210) with 60 mm focal length lens (Nikon) was used to record the interface location. The resolution of the camera was 1,280 × 800 pixels. The spatial resolution of the images is 0.758 mm/pixel, which provides high resolution of the internal wave interface location. The recorded videos were calibrated for distortion via the camera control software (i.e., Vision Research Phantom Camera Control Application). The exposure was set to 750 μs and f-stop to f/2.8 to get the necessary depth of field and attaining sufficient brightness for the imaging. Five lamps using fluorescent coil bulbs illuminated the tank and fluid volumes.

Two different triggering strategies were required for capturing images for (1) flow visualization, and (2) recording an image sequence for signal processing. First, to capture still images, the triggered pulse generator was used to control the image acquisition with a precise delay to capture an image at the targeted phase in the cycle. Images were captured for eight phases in the cycle for flow visualization purposes. **Figure 3** shows the flow visualization of a complete wave cycle at eight equally-spaced phases. The interface shows a partial standing wave (nodes and antinodes indicated in **Figure 3**) with some wave perturbations being generated.

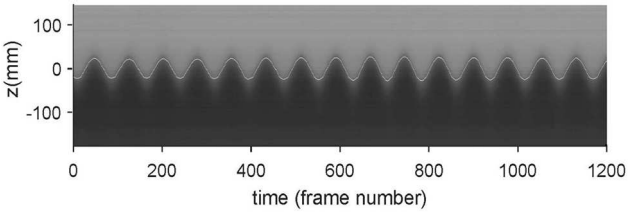

FIGURE 4 | Time stack image at an antinode with the digitally-identified interface location (white line) superimposed.

The camera setup for recording image sequences for signal processing required throttling the frame rate of the camera. In this arrangement, the trigger signal was not phase-locked with the wavemaker motion. The minimum frame rate of the Phantom camera was 24 fps, but the objective was to record at a slower rate in order to increase the total duration of the image sequence and achieve a higher resolution estimate of the dominant frequency during signal processing. The frame rate was lowered to 4 fps by using the camera's trigger mode option and sending a trigger signal for each frame capture. Three sequences of 7,200 images each were captured in this manner.

The generated wave frequencies in the time record of wave height were quantified using signal processing. A time stack image at an anti-node of the wave was created by extracting a vertical line of pixels from a single horizontal location in each image of the recorded sequence and re-arranging them side-by-side to effectively form an image time series at the anti-node location. Two image processing filters, median and sharpen, were used to reduce the noise and sharpen the image in order to use the Sobel edge-detection algorithm, which reliably identified the interface location (and hence the wave height). **Figure 4** shows the detected interface (white line) superimposed on the time-stack image. The detected interface accurately captured the oscillation of the density interface at the anti-node. Both elevation and depression internal waves have been observed under various ocean conditions (Orr and Mignerey, 2003). **Figures 3**, **4** suggest that the apparatus has the potential to investigate zooplankton response to both types of waves.

A fast Fourier transform (FFT) algorithm was used to convert the extracted time record of wave height to the frequency domain. The target parameters for the internal wave were chosen based on the theoretical analysis as explained above, and consisted of $\Delta\rho = 1.0\sigma_t$, seiching mode of 8, and wave period of 24.27 s (i.e., 0.041 Hz). The power spectral density (PSD), which is shown in **Figure 5**, indicates a narrow peak, where the peak is very close

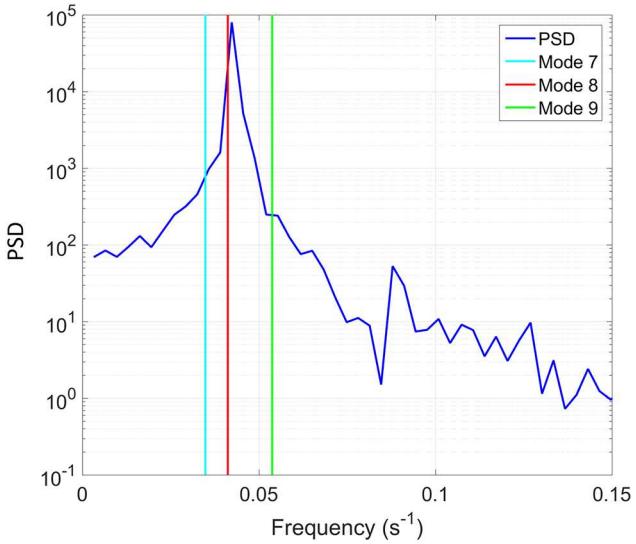

FIGURE 5 | Power spectral density (PSD) of the time record of the interface location shown as function of frequency. In addition, the theoretically-predicted frequencies corresponding to three modes are indicated with the vertical lines.

to the target mode of 8 as indicated by the vertical line. It is apparent that the third-order theory captures the non-linearity of the internal wave profiles and predicts the actual behavior of the internal wave with a high degree of accuracy.

5. BEHAVIORAL ASSAYS AND DATA ANALYSIS TECHNIQUES

For the behavioral assays, a mixed population of three species of copepods was used: *A. tonsa*, *T. longicornis*, and *Eurytemora affinis*. The main goal of the trials is to observe the animals' trajectory paths in the internal wave treatment and gain insight to the influence of biological forcing via their swimming behavior responses.

5.1. Copepod Collection and Maintenance

The copepod specimens were collected in Boothbay, ME, USA (Latitude: 43.860 N, Longitude: 69.582 W). The tow was done during the hours of 12:00–12:30 p.m. using a 153 micron net. The deployment was a surface tow during high tide for 30 min off of the dock at the Bigelow Laboratory for Ocean Sciences. The animals were contained in eight 1 L bottles with food (Rhodomonas) and shipped overnight in a cooler to the Georgia Institute of Technology (Atlanta, GA).

After arrival, the mixed population of copepods were placed into 19 L buckets in a temperature-controlled environmental room. The culture media was artificial seawater (Instant Ocean) at salinity level of 33 ppt, and the ambient temperature was kept at 12°C in order to match natural environment conditions. Copepods were fed Isochrysis and *Tetraselmis* spp. phytoplankton.

5.2. Behavioral Assays

Behavioral assays were conducted in the same internal wave apparatus as the flow characterization experiments. Dye was not present during the copepod trials. All experiments were conducted at constant temperature (12 ± 0.2 °C). In each trial, 200 fresh copepods of mixed population of *A. tonsa*, *T. longicornis*, and *E. affinis* were used. The tested population consisted entirely of adults. The behavioral assays were performed with artificial seawater (Instant Ocean). A 30 × 30 cm window was used to observe the copepod swimming kinematics (**Figure 1**). The observation window was positioned such that the undisturbed density interface was at the mid line.

Two 7-W continuous-wave infrared lasers (CrystaLaser, Inc.) with a wavelength of 808 nm illuminated the tank. The lasers were mounted behind the tank at 45° angles and diffused via 50° circular, top hat diffusers (Thorlabs model ED1-C50-MD) to provide uniform illumination in the observation region. The experiments were conducted in the dark, except for the infrared illumination described. Infrared lighting was chosen because copepods typically cannot sense light at this wavelength; therefore, their swimming behavior was not influenced by the illumination during the observation. The Phantom v210 camera was used with a 60 mm focal length lens (Nikon). The exposure time was set to 2,400 μs and the camera was positioned 0.77 m away from the front wall of the tank. The spatial resolution of the recordings was 0.394 mm/pixel. The frame rate was 15 fps because it provided sufficient temporal resolution to accurately quantify swimming behaviors. The camera was externally triggered to achieve this frame rate as described above, and the image capture was not synced with the motion of the wavemaker.

The behavior assays were conducted for three physical treatments: (1) stagnant fluid with no density stratification (i.e., control), (2) stagnant two-layer density stratification, and (3) two-layer density stratification with standing internal wave motion.

Five 5-min image sequences were recorded for each treatment. The copepod trajectories were manually tracked in DLTdv5, a MATLAB particle tracking software developed by Hedrick (2008). The vertical distribution of the copepod specimens was quantified via a probability density function (PDF) of the copepod position in the z-direction. The distribution of trajectories are analyzed for the regions that the computed absolute value of the shear strain rate in the internal wave treatment (**Figure 10**) is above 80% (−20 to +20 mm of the midline), and 40% (−50 to +50 mm of the midline) of the maximum value. The two-sample Kolmogorov–Smirnov test (2KS-test) is used to measure the agreement between the PDF of vertical position with 100 bins that have at least 100 data points in each bin.

Net-to-gross-displacement-ratio (NGDR), fractal dimension, and turn frequency of swimming trajectories are computed to quantify the degree of morphological complexity of a swimming path. The NGDR represents the ratio of the straight linear distance to the total distance between the beginning and the end

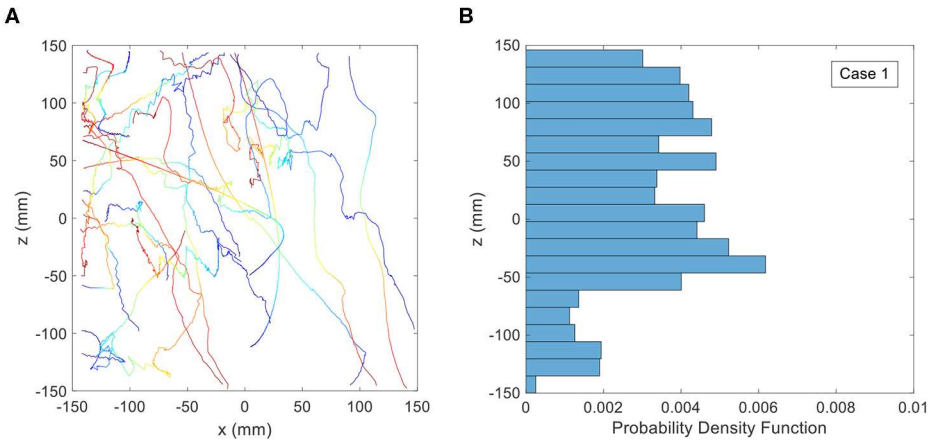

FIGURE 6 | (A) Copepod trajectories for the control treatment with stagnant, uniform density fluid. Color indicates the passage of time with blue corresponding to the beginning of the trajectory and red corresponding to the end. Although shown on the same plot, these trajectories were not collected simultaneously. **(B)** Probability Distribution Function (PDF) of copepod position in the vertical direction for the control treatment.

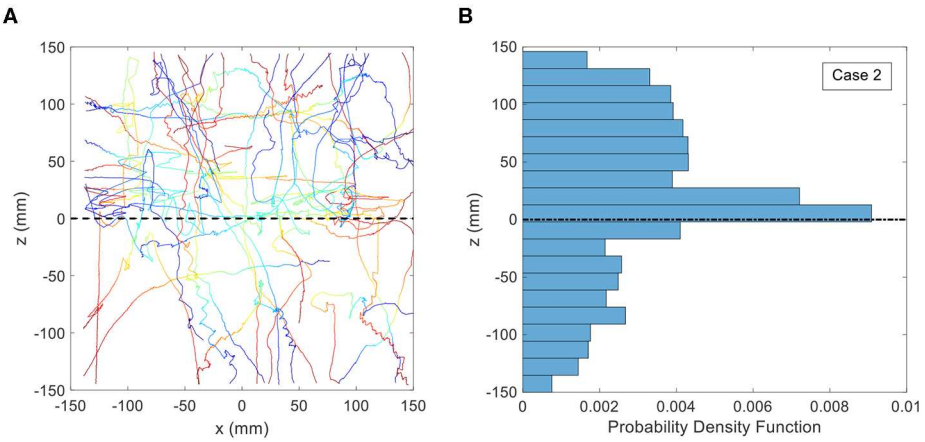

FIGURE 7 | (A) Copepod trajectories for the treatment consisting of a stagnant density jump of 1.0 σ_t. The black dashed line indicates the location of the density interface. Color indicates the passage of time with blue corresponding to the beginning of the trajectory and red corresponding to the end. Although shown on the same plot, these trajectories were not collected simultaneously. **(B)** Probability Distribution Function (PDF) of copepod position in the vertical direction for the treatment consisting of a stagnant density jump of 1.0 σ_t.

points of the path traveled by an organism (Buskey, 1984), which is defined as

$$NGDR = \frac{\sqrt{(x_n - x_0)^2 + (y_n - y_0)^2)}}{\sum_{i=1}^{n} \sqrt{(x_i - x_{i-1})^2 + (y_i - y_{i-1})^2)}}. \quad (34)$$

This parameter ranges from 0, for a circular, sinuous and diffused path, to 1, for a straight ballistic trajectory. However, the scale dependency of this parameter is its limitation, and the NGDR calculation depends on the length of the track (Dodson et al., 1997). Thus, the tracks are divided to the same period (6.0 s in this case) trajectories for the NGDR computation (Tiselius, 1992). In addition to NGDR, the degree of space occupation of copepod trajectories without any scale-dependency is assessed in this study using the fractal dimension (Coughlin et al., 1992; Seuront et al., 2004; Uttieri et al., 2005). Therefore, it should be noted that the sample sizes for fractal dimension analysis and turn frequency computation are equal to the number of trajectories for each case (23, 33, and 25 for control, stagnant density jump and internal wave treatments, respectively), while the sample sizes for NGDR computation are equivalent to the total number of same period segments (98, 187, and 238 for control, stagnant density jump and internal wave treatments, respectively). The fractal dimension is computed using the box counting method to compare the degree of convolution of trajectories between different treatments. In this method, the slope of the power fit of the log-log plot of the number of boxes vs. mesh size is corresponding to the fractal dimension. Furthermore, the number per second of changes in the direction of motion of more than 15 degrees in each trajectory is defined as turn frequency (Woodson et al., 2005).

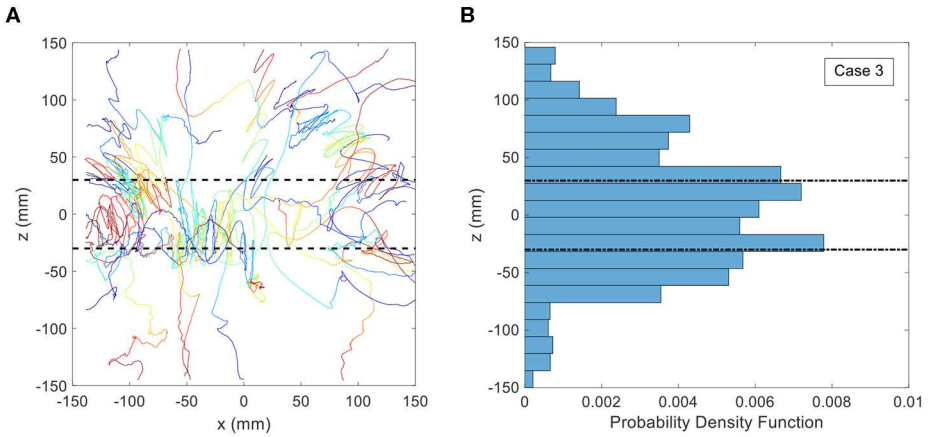

FIGURE 8 | (A) Copepod trajectories for the internal wave treatment with a density jump of 1.0 σ_t. The black dashed lines indicate the boundaries of the internal wave. Color indicates the passage of time with blue corresponding to the beginning of the trajectory and red corresponding to the end. Although shown on the same plot, these trajectories were not collected simultaneously. **(B)** Probability Distribution Function (PDF) of copepod position in the vertical direction for the internal wave treatment with a density jump of 1.0 σ_t.

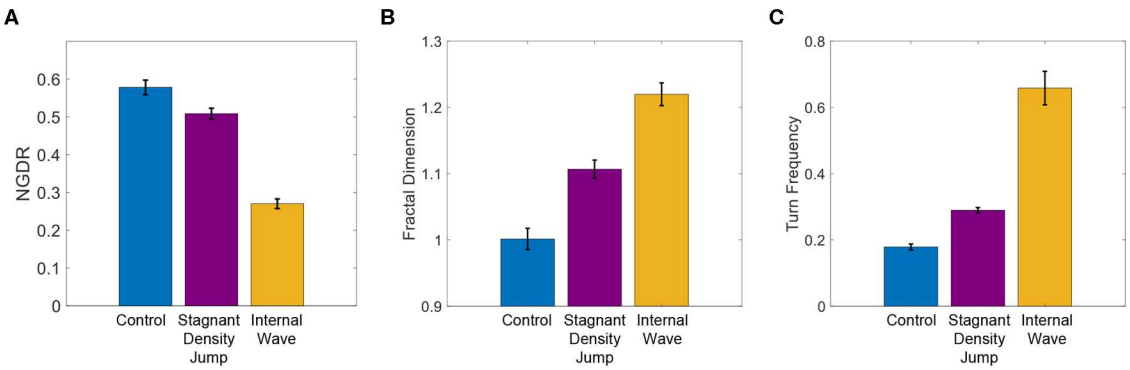

FIGURE 9 | (A) Net-to-gross-displacement-ratio (NGDR), **(B)** fractal dimension, and **(C)** turn frequency (turns per copepod per second) for the swimming trajectories for the control, stagnant density jump, and internal wave treatments. The error bars span ± one standard error.

6. RESULTS

Figure 6 shows the digitized swimming trajectories for a mixed-population of copepods in a body of water with uniform salinity of 33 ppt (the control case). The 25 sample tracks appear to be predominantly directed upward or downward with no obvious restriction for motion in any direction. Also the PDF of vertical position lacks a strong peak at a particular depth, which suggests the copepods are not aggregating (as one would expect for the control treatment). The lack of preferential aggregation in the trajectories was expected since no directionally-oriented hydrodynamic cues were present in the control treatment except for the orientation of gravity. Approximately 18% of the trajectories of copepods are located between −20 to +20 mm of the midline, and ≈ 47% between −50 and +50 mm of the midline. It should be noted that the PDF is not perfectly uniform and it is less dense toward the bottom (i.e., negative z values). This is perhaps due to the mostly vertically aligned trajectories or the effect of a limited number of trajectories.

For the second treatment, the salinity of the lower level water was increased to 34.3 ppt and the salinity of the upper layer was maintained at 33 ppt. The trajectories of copepods and the PDF of the vertical position for this case are shown in **Figure 7**. The black dashed line indicates the position of the density interface. The plunger was not activated, and the fluid volume was therefore stationary. The digitized trajectories show that many of the copepods moved preferentially in the horizontal direction, parallel to the density interface. Quantitative analysis using the PDF indicates that ≈ 31% of the trajectories are located between −20 and + 20 mm and ≈ 49% of the trajectories are located between −50 and + 50 mm in the z-direction. Although the comparison of PDFs for the whole region indicates that there is not a significant difference between the PDF of control and stagnant density jump treatments ($p = 0.347$), the PDF of vertical position for these two treatments are significantly different between −20 and + 20 mm of the midline ($p = 0.016$).

In the third treatment, the copepods were observed in the standing internal wave with density jump properties identical to

TABLE 1 | Tukey–Kramer *post-hoc* test results for NGDR, fractal dimension, and turn frequency between pairs of treatments based on $\alpha = 0.05$.

p	Control-stagnant density jump	Stagnant density jump - IW	Control - IW
NGDR	0.012	$\ll$0.001	$\ll$0.001
Fractal dimension	$\ll$0.001	$\ll$0.001	$\ll$0.001
Turn frequency	0.017	$\ll$0.001	$\ll$0.001

Tests for NGDR ($F = 120.45, p \ll 0.001$), fractal dimension ($F = 47.58, p \ll 0.001$), and turn frequency ($F = 74.25, p \ll 0.001$) indicated significant differences.

the second treatment, where the lower layer salinity is 34.3 ppt and the upper layer salinity is 33 ppt. **Figure 8** shows animal trajectories and the PDF of the vertical position for this case. The dashed lines indicate the upper and lower boundaries of the internal wave as defined by the peak locations of the crests and troughs. In clear contrast to the other treatments, the copepod swimming paths demonstrated more curved trajectories near and inside the boundaries of the internal wave. Some of the trajectories are loopy, orbital motions, whereas a few of the trajectories appear to be zig-zag-like oscillation patterns. Beyond a distance of roughly 75 mm from the resting position of the interface (i.e., $z = 0$), the trajectories were much less likely to show the looping, orbital shape that is observed in the immediate vicinity of the interface location. The probability of copepods positions between −20 and +20 mm in the z-direction is $\approx$ 27%, and in the internal wave region (−50 to + 50 mm) is $\approx$ 65%. Further, according to the 2KS-test, the PDF of vertical position in the internal wave treatment is significantly different from the density jump treatment ($p < 0.001$) as well as the control treatment ($p = 0.008$).

Results of NGDR, fractal dimension, and turn frequency of the swimming trajectories for the different treatments are shown in **Figure 9** and are analyzed using an ANOVA with a Tukey–Kramer *post-hoc* test between treatment pairs. The statistical analysis is summarized in **Table 1**. Clear and consistent trends are observed for NGDR, fractal dimension, and turn frequency (**Figure 9**). The statistical tests (**Table 1**) also verify these significant differences in NGDR, fractal dimension, and turn frequency. There is a significant difference between average values of NGDR (largest value for the control treatment and smallest value for the internal wave treatment), fractal dimension, and turn frequency (smallest value for the control treatment and largest value for the internal wave treatment) in all pairwise comparisons. Therefore, the statistical analysis implies that the copepod swimming trajectories are changed from more linear, straight and ballistic trajectories for the control treatment to more curved, loopy, and diffused ones in the internal wave treatment.

7. DISCUSSION

For the stagnant density interface treatment, the trajectory pattern shows a clear difference from the control treatment. The apparent reluctance of some of the copepod specimens in the current results to cross the density interface is consistent with the previous results for *A. tonsa* and *T. longicornis*, who for a $\Delta\rho$ of 1.0 σ_t showed a decrease in the number of copepods crossing the density jump layer (Woodson et al., 2007a). In contrast, the other member of the tested copepod population, *E. affinis*, previously did not reveal a reluctance to crossing a density jump interface (Woodson et al., 2007b). The trajectories in **Figure 8** are consistent with both variability among individuals and the reported species-specific variability in behavior with some trajectories clearly oriented parallel to the interface (and hence not crossing the interface location) and other trajectories crossing the interface. The results also show elevated population density near the fluid density interface. This is consistent with previous observations of Harder (1968) and Woodson et al. (2007a). Harder (1968), in particular, found that the aggregations were a behavior response to the change in fluid density itself, rather than another cue such as salinity or temperature. The PDF for the stagnant density interface treatment suggests that the copepods preferred to be in the upper layer, possibly due to a preference to remain in the fluid density (and salinity) in which they were acclimated. Thus, for the stagnant density interface treatment, we conclude that the current population behaves in a consistent manner by moving in the horizontal direction along the fluid density interface, limiting the number of interface crossings, and aggregating near the fluid density interface. Further, the trajectories for the stagnant density interface treatment are more convoluted (i.e., decreased NGDR and increased fractal dimension and turn frequency; **Figure 9**) compared to the control treatment due to the increased heading changes associated with the limited crossings of the density interface.

In the internal wave treatment, the copepod trajectory shapes were quite distinct from either the control or the stagnant density jump treatment. The looping, orbital trajectories will be discussed further below. The PDF of the vertical position indicates that the copepods are most commonly found in the internal wave region. The percentage of the trajectories that are in the wave region is roughly double that of a uniform distribution (i.e., 65 vs. 33%). While the length scales are obviously different compared to an *in situ* internal wave, the aggregation reported here for the internal wave treatment suggests that copepod behavior may be an important contribution to explain reported aggregations near internal waves by Haury et al. (1983), McManus et al. (2005), Macías et al. (2010), and Van Haren (2014), and others.

In order to gain insight regarding the looping, orbital copepod trajectories, the trajectory patterns of neutrally-buoyant particles in the theoretical flow field are analyzed. In particular, the authors seek to better understand the balance of physical vs. biological forcing and specifically whether the copepod trajectories resulted from pure advection by the surrounding flow or whether animal behavior was a substantial contributor. The velocity field in the two-layer system is found via the third-order solution, as described in section 3, for the flow conditions matching the experimental treatment. **Figure 10** shows the velocity vectors, the iso-contours of the velocity magnitude, and the shear strain rate for four phases $\phi = \pi/4, \phi = \pi/2, \phi = 3\pi/4$, and $\phi = 3\pi/2$. The velocity fields show the expected sense of motion relative

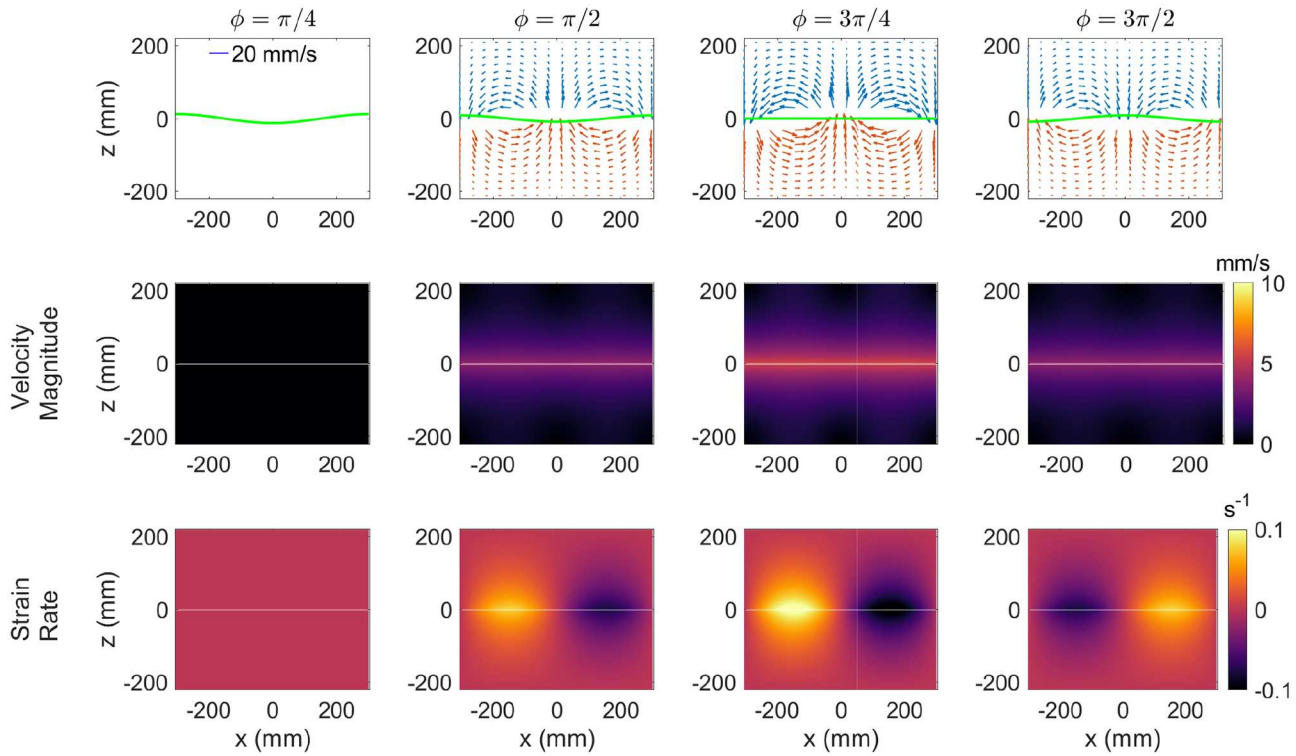

FIGURE 10 | The flow field in the standing internal wave cycle. The velocity field **(Top)**, contours of the velocity magnitude **(Middle)**, and contours of the strain rate **(Bottom)**.

to the dynamic interface. The velocity magnitude is maximum at the interface ($z = 0$) and decreases with distance away from it. The iso-contour plots of velocity magnitude show the variation through the wave cycle. Among the phases shown, the greatest velocity magnitude appears for $\phi = 3\pi/4$ and has a peak value of 5.6 mm/s. As reported in Woodson et al. (2007a), among others, the copepod species tested in this treatment demonstrate swimming velocities in the same range, which suggests an inherent ability to swim relative to even the strongest fluid motion presented in the treatment.

Trajectory analysis for passive, neutrally-buoyant particles was performed in the theoretical flow field, by initiating particles at a grid of locations throughout the two-layer system and tracking their subsequent position due to advection by the time-varying flow field. In **Figure 11A**, the passively advected particles essentially oscillate back-and-forth, which is expected in a standing internal wave. By comparing to the loopy, orbital trajectories exhibited by copepods in the vicinity of the internal wave interface (**Figure 8**), the obvious conclusion is that the observed copepod motions are not explained solely by advection due to the fluid motion.

While passive particle advection is clearly distinct from the observed trajectories, the question remains whether the trajectories are explained by the combination of copepod swimming and advection by the wave motion. To address this question, the copepod trajectories for the stagnant density jump treatment (shown in **Figure 7A**) were combined with advection due to the time-varying theoretical flow field. In this manner, the observed swimming trajectories in the vicinity of the density interface were modified at each time step to include the additional displacement due to advection by the wave. **Figure 11B** reveals that the modification of the trajectories was minimal. A few trajectories show the addition of a zig-zag-like oscillation to the path, but the overall shape is generally distinct compared the actual copepod trajectories in the internal wave treatment (**Figure 8A**). The qualitative conclusion is that the observed copepod motions cannot be explained by the addition of advection due to the fluid motion. The potential differences between the copepod swimming trajectories in the stagnant density jump treatment (**Figure 7A**) and the combined trajectories (**Figure 11B**) are quantified via NGDR, fractal dimension, and turn frequency (**Figure 11C**). There is no significant difference for each variable. The mild influence of flow advection is consistent with the relatively small and time-varying fluid velocities, as quantified in **Figure 10**, compared with copepod swimming velocity. It should be noted that since the copepod trials were not phase-locked with the wave motion, the phase at the start of the trajectory integration and the trajectory start location relative to the wave nodes are independent variables in this analysis. Exploring this parameter space reveals that the mild influence of wave advection on the trajectory shape is not affected by these variables. The trajectory

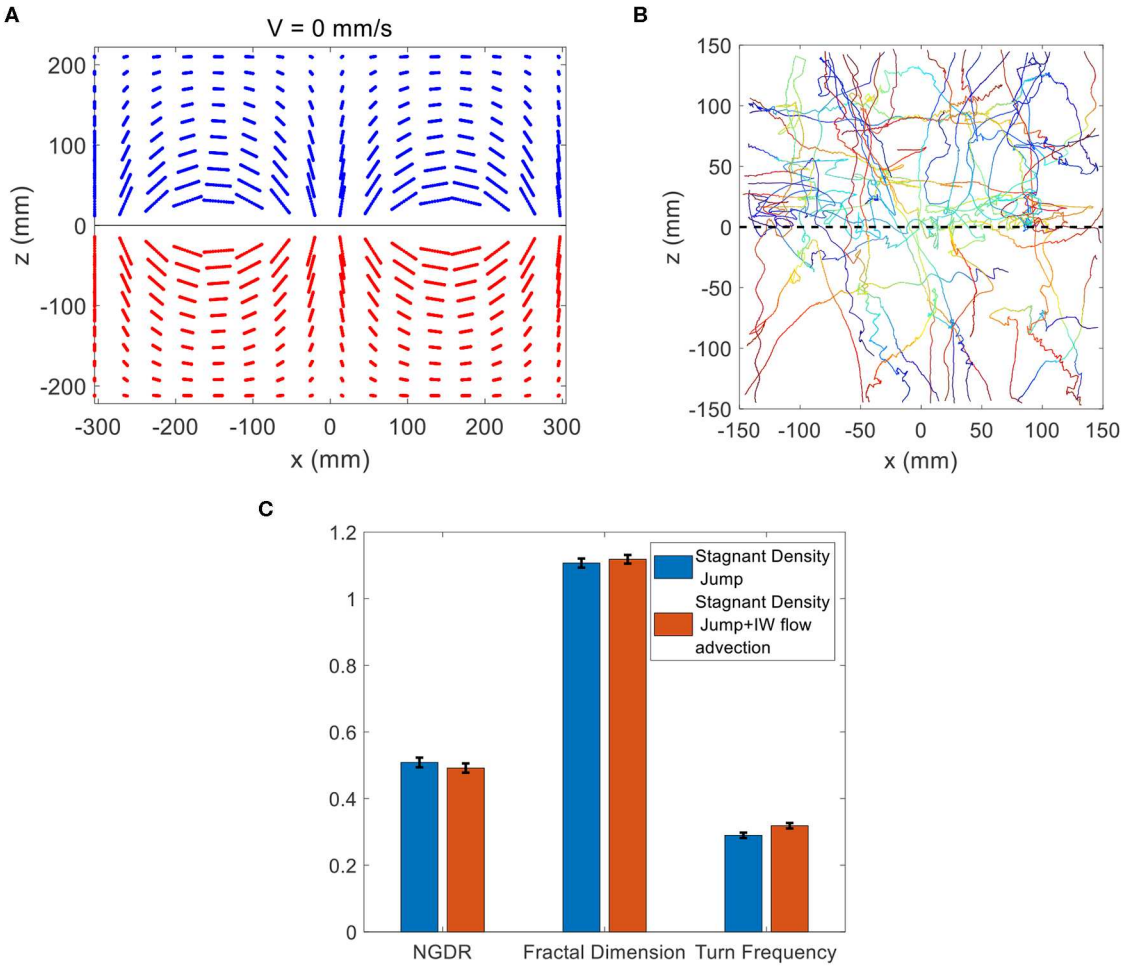

FIGURE 11 | (A) Theoretical trajectories of passive neutrally-buoyant particles in the flow conditions of the internal wave treatment. **(B)** Copepod trajectories observed for the stagnant density jump treatment (**Figure 7A**) with advection due to the internal wave motion added at each time step. The trajectories shown correspond to an initial phase of $\phi = 3\pi/4$, and other initial values for the phase yielded similar results. **(C)** Comparison of NGDR, fractal dimension and turn frequency between the wave-modified trajectories in **(B)** and the observed copepod trajectories for the stagnant density jump treatment in **Figure 7A**. There is no significant difference for any variable.

details change slightly, but they do not change the qualitative and quantitative conclusion that the addition of wave advection is a mild influence.

In order to make a more direct comparison between the copepod and advection-modified trajectories, a few examples of animal trajectories are isolated and shown in **Figure 12**. In a qualitative comparison, several of the copepod trajectories in the internal wave treatment show a similar zig-zag-like oscillation pattern to the stagnant density jump trajectories modified with the addition of wave flow advection. Some of these similar trajectories are shown in **Figure 12A**. However, the superimposed trajectories (**Figure 11B**) are quite distinct in character compared to the loopy, orbital trajectories exhibited by other copepod specimens in the internal wave treatment (**Figures 12B–D**). This suggests animal swimming behavior in response to the hydrodynamic sensory cue was a major contributor to the observed copepod motion. In conclusion, whereas some trajectories may be explained by the addition of wave advection, the majority of trajectories clearly cannot be explained by such a simple response.

While the density jump is clearly an important sensory cue (Harder, 1968; Woodson et al., 2005, 2007a,b), the shear strain rate is also a potential hydrodynamic cue to guide copepod behavior. The shear strain rate (**Figure 10**) shows the maximum value to be at the interface with a peak value of 0.1 s^{-1}. As with the plotted velocity field, there is a strong cyclic temporal variation in the shear strain rate field. The shear strain rate and velocity magnitude are minimum (nearly zero) for phase $\phi = \pi/4$ and at maximum for phase $\phi = 3\pi/4$. To check the consistency with reported internal waves, the wave characteristics reported by Haury et al. (1983) and Greer et al. (2014) were used to estimate the shear strain rates that copepods may encounter *in situ*. In this case, the internal wave parameters $h_{total} = 80$ m, wavelength = 200 m, amplitude = 30 m, and $\Delta\rho$ of 1.0 σ_t

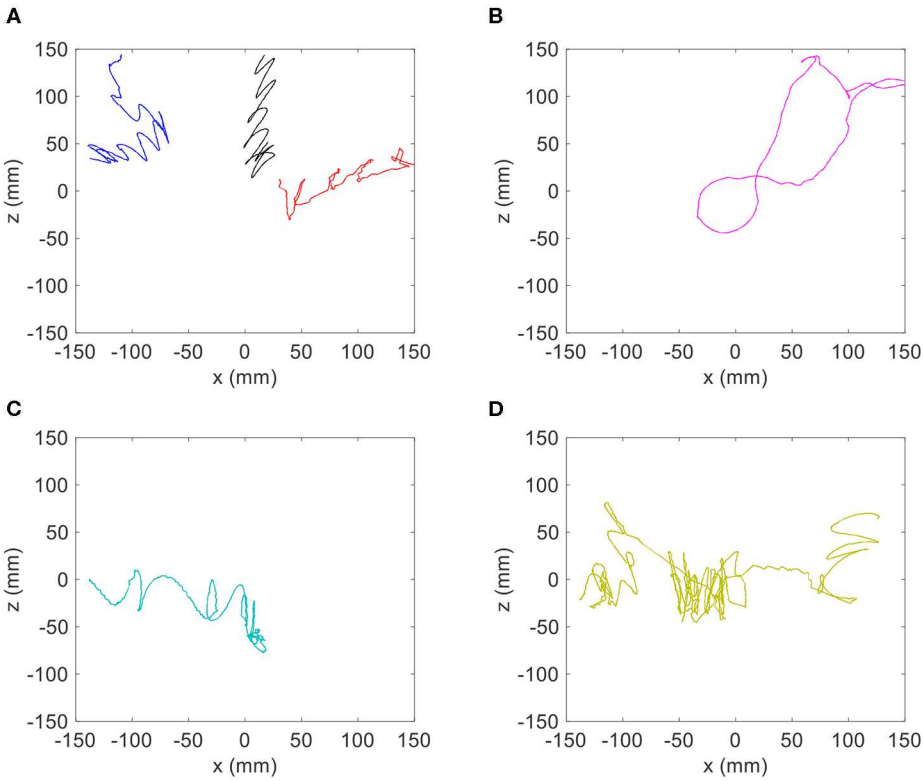

FIGURE 12 | Isolated copepod trajectories for the internal wave treatment with a density jump of 1.0 σ_t to compare with the theoretical trajectories of passive particles. **(A)** Samples of trajectories that have a similar zig-zag motion to passive particles with superimposed horizontal velocity, and **(B–D)** samples of trajectories with loopy, orbital motions.

were input into the theoretical internal wave model. The period resulting from these calculations (i.e., 9.2 min) was consistent with that reported in Haury et al. (1983) (i.e., 8–10 min) therefore providing some assurance of the accuracy of the theoretical model characterization. The maximum shear strain rate in the modeled *in situ* internal wave was 0.015 s^{-1}. This value is roughly 6 times smaller than the maximum shear strain rate in the laboratory arrangement, but it is not radically different in magnitude as one might anticipate from the difference in scales between the laboratory and the ocean. Further, this value is close to the range that copepods have been previously observed to sense and evoke a behavioral response.

The ability of copepods to sense velocity gradients, typically quantified as strain rate, has been extensively documented in recent decades (e.g., Kiørboe et al., 1999). The shear strain rate threshold level to evoke an escape response vary among copepod species ranging from 0.4-26 s^{-1} (summarized in Woodson et al., 2014), which is much greater than the shear strain rates in the internal wave treatment. However, the reported threshold was much smaller, around 0.025 s^{-1} for response of *A. tonsa* and *T. longicornis* to environmental flow structure (i.e., thin layer shear flow) (Woodson et al., 2005, 2007a,b). The response in this case consisted of excited area-restricted search behavior as part of a cue hierarchy in the search for food. For the current internal wave treatment, copepods experience a shear strain rate field that has peak values in a similar range to the threshold reported by Woodson et al. (2005), Woodson et al. (2007a), and Woodson et al. (2007b). The internal wave treatment also was different from the thin layer treatment because the flow is dynamic and time varying including periods in which the shear strain rate is below the sensory threshold (**Figure 10**). Nevertheless, the results here suggest a substantial animal behavior contribution to the trajectory shape and the shear strain rate values are consistent with the previously reported threshold to evoke excited area-restricted search behavior suggesting that it may be an important sensory cue.

8. CONCLUSIONS

A laboratory-scale internal wave apparatus was used to create a standing internal wave for various physical arrangements that mimic conditions observed in the field. This experimental design was motivated by the objective to understand the biophysical forcing in zooplankton transport in and near internal waves, where high levels of zooplankton densities have been observed. The third-order finite-amplitude solution of a standing internal wave inside a two-layer stratification system guided the selection of the operating parameters for the independent variables controlling the wave motion. A boundary value problem was setup assuming incompressible and irrotational flow. A series

of boundary conditions, including bottom, kinetic, and dynamic conditions at the interface between the two layers and the free surface, was applied. The analysis yielded the dispersion relationship between the seiching mode and the wave angular frequency. The internal wave was targeted in the apparatus that correspond to density jump of 1.0 σ_t, seiching mode of 8, and wave period of 24.27 s (i.e., 0.041 Hz). Signal processing of the interface location revealed that the laboratory generated frequency matched accurately the target frequency from the theoretical analysis.

The zooplankton behavioral assays with a mixed population of marine copepods *A. tonsa*, *T. longicornis*, and *E. affinis* were conducted in control (stagnant homogeneous fluid), stagnant density jump interface, and internal wave flow treatments. The results from tracking their swimming trajectories revealed that the animals reacted to the stagnant density jump interface by showing a preferential horizontal motion parallel to the interface. In the internal wave treatment, the copepods showed an acrobatic, orbital-like motion in and around the internal wave region (bounded by the crests and troughs of the waves). Significant differences in the morphology of the trajectories are quantified by the NGDR, fractal dimension, and turn frequency.

The influence of passive advection is investigated by superimposing advection due to the wave motion on the trajectories observed in the stagnant density jump treatment. The results show only mild changes to the trajectories both visually and quantitatively. A few of the modified trajectories showed zig-zag-like oscillation patterns that are consistent with some trajectories of copepods in the internal wave treatment. However, the majority of the trajectories in the internal wave treatment were characterized as loopy, orbital shapes in the region near the internal wave interface. Therefore, although the response of a few copepods to the internal wave interface could be explained by the addition of flow advection, the swimming patterns for other copepods is more complicated. The conclusion is that copepod behavior response is a key contributor to the observed trajectories in and around the internal wave.

DATA AVAILABILITY STATEMENT

All datasets generated for this study are included in the article/supplementary material.

AUTHOR CONTRIBUTIONS

DW and SJ designed the study. SJ performed the experiments and processed the physical and behavioral data. KH and MM performed the theoretical wave analysis. MM and DW analyzed the data and wrote the manuscript. All authors approved the final manuscript.

FUNDING

This research was partially funded by the National Science Foundation (OCE-0728238). Additional funding was provided by the Karen and John Huff Chair endowed funds.

ACKNOWLEDGMENTS

Thanks to Dr. David Fields of the Bigelow Laboratory for Ocean Sciences for collecting and shipping the copepod specimens. Thanks also to Dr. Aaron True for initial design contributions and construction of the tank and to Dr. Jeannette Yen and Dr. Jeff Koseff for helpful discussions and inspiration. A portion of this study was reported in SJ's M.S. Thesis (Jung, 2015).

REFERENCES

Buskey, E. J. (1984). Swimming pattern as an indicator of the roles of copepod sensory systems in the recognition of food. *Mar. Biol.* 79, 165–175. doi: 10.1007/BF00951825

Cheriton, O. M., McManus, M. A., Stacey, M. T., and Steinbuck, J. V. (2009). Physical and biological controls on the maintenance and dissipation of a thin phytoplankton layer. *Mar. Ecol. Prog. Ser.* 378, 55–69. doi: 10.3354/meps07847

Coughlin, D., Strickler, J., and Sanderson, B. (1992). Swimming and search behaviour in clownfish, *Amphiprion perideraion*, larvae. *Anim. Behav.* 44, 427–440. doi: 10.1016/0003-3472(92)90053-C

Cowles, T. J. (2004). "Planktonic layers: physical and biological interactions on the small scale," in *Handbook of Scaling Methods in Aquatic Ecology: Measurements, Analysis, Simulation*, eds L. Seuront and P. G. Strutton (Boca Raton, FL: CRC Press), 31–49. doi: 10.1201/9780203489550.ch3

Cowles, T. J., Desiderio, R. A., and Carr, M.-E. (1998). Small-scale planktonic structure: persistence and trophic consequences. *Oceanography* 11, 4–9. doi: 10.5670/oceanog.1998.08

Dean, R. G., and Dalrymple, R. A. (1991). *Water Wave Mechanics for Engineers and Scientists, Volume 2, Advanced Series on Ocean Egineering*. World Scientific Publishing Company, Singapore. doi: 10.1142/1232

Dekshenieks, M. M., Donaghay, P. L., Sullivan, J. M., Rines, J. E. B., Osborn, T. R., and Twardowski, M. S. (2001). Temporal and spatial occurrence of thin phytoplankton layers in relation to physical processes. *Mar. Ecol. Prog. Ser.* 223, 61–71. doi: 10.3354/meps223061

Dodson, S. I., Ryan, S., Tollrian, R., and Lampert, W. (1997). Individual swimming behavior of *Daphnia*: effects of food, light and container size in four clones. *J. Plankton Res.* 19, 1537–1552. doi: 10.1093/plankt/19.10.1537

Drazin, P. G. (2002). *Introduction to Hydrodynamic Stability, Volume 32, Cambridge Texts in Applied Mathematics*. New York, NY: Cambridge University Press.

Ewing, G. C. (1950). Slicks, surface films and internal waves. *J. Mar. Res.* 9, 161–187.

Gallager, S. M., Yamazaki, H., and Davis, C. S. (2004). Contribution of fine-scale vertical structure and swimming behavior to formation of plankton layers on Georges Bank. *Mar. Ecol. Prog. Ser.* 267, 27–43. doi: 10.3354/meps267027

Garwood, J. C., Lucas, A. J., Naughton, P., Alford, M. H., Roberts, P. L. D., Jaffe, J. S., et al. (2020). A novel cross-shore transport mechanism revealed by subsurface, robotic larval mimics: internal wave deformation of the background velocity field. *Limnol. Oceanogr.* doi: 10.1002/lno.11400

Greer, A. T., Cowen, R. K., Guigand, C. M., Hare, J. A., and Tang, D. (2014). The role of internal waves in larval fish interactions with potential predators and prey. *Prog. Oceanogr.* 127, 47–61. doi: 10.1016/j.pocean.2014.05.010

Harder, W. (1968). Reactions of plankton organisms to water stratification. *Limnol. Oceanogr.* 13, 156–168. doi: 10.4319/lo.1968.13.1.0156

Haury, L. R., Briscoe, M. G., and Orr, M. H. (1979). Tidally generated internal wave packets in Massachusetts Bay. *Nature* 278, 312–317. doi: 10.1038/278312a0

Haury, L. R., Wiebe, P. H., Orr, M. H., and Briscoe, M. G. (1983). Tidally generated high-frequency internal wave packets and their effects on plankton

in Massachusetts Bay. *J. Mar. Res*. 41, 65–112. doi: 10.1357/002224083788223036

Hedrick, T. L. (2008). Software techniques for two-and three-dimensional kinematic measurements of biological and biomimetic systems. *Bioinspir. Biomimet*. 3:034001. doi: 10.1088/1748-3182/3/3/034001

Holliday, D. V., Donaghay, P. L., Greenlaw, C. F., McGehee, D. E., McManus, M. M., Sullivan, J. M., et al. (2003). Advances in defining fine- and micro-scale pattern in marine plankton. *Aquat. Living Resour*. 16, 131–136. doi: 10.1016/S0990-7440(03)00023-8

Hult, E. L., Troy, C. D., and Koseff, J. R. (2009). The breaking of interfacial waves at a submerged bathymetric ridge. *J. Fluid Mech*. 637, 45–71. doi: 10.1017/S0022112009008040

Jung, S. (2015). *Implementation of internal wave apparatus for copepod behavioral assays* (Master's thesis). Atlanta, GA: Georgia Institute of Technology.

Kiørboe, T., Saiz, E., and Visser, A. (1999). Hydrodynamic signal perception in the copepod *Acartia tonsa*. *Mar. Ecol. Prog. Ser*. 179, 97–111. doi: 10.3354/meps179097

Lennert-Cody, C. E., and Franks, P. J. S. (1999). Plankton patchiness in high-frequency internal waves. *Mar. Ecol. Prog. Ser*. 186, 59–66. doi: 10.3354/meps186059

Lennert-Cody, C. E., and Franks, P. J. S. (2002). Fluorescence patches in high-frequency internal waves. *Mar. Ecol. Prog. Ser*. 235, 29–42. doi: 10.3354/meps235029

Macías, D., Somavilla, R., González-Gordillo, J. I., and Echevarría, F. (2010). Physical control of zooplankton distribution at the Strait of Gibraltar during an episode of internal wave generation. *Mar. Ecol. Prog. Ser*. 408, 79–95. doi: 10.3354/meps08566

Mann, K. H., and Lazier, J. R. N. (1996). *Dynamics of Marine Ecosystems: Biological-physical Interactions in the Oceans*, 2nd Edn. Malden, MA: Blackwell Publishing Ltd.

McManus, M. A., Alldredge, A. L., Barnard, A. H., Boss, E., Case, J. F., Cowles, T. J., et al. (2003). Characteristics, distribution and persistence of thin layers over a 48 hour period. *Mar. Ecol. Prog. Ser*. 261, 1–19. doi: 10.3354/meps261001

McManus, M. A., Cheriton, O. M., Drake, P. T., Holliday, D. V., Storlazzi, C. D., Donaghay, P. L., et al. (2005). Effects of physical processes on structure and transport of thin zooplankton layers in the coastal ocean. *Mar. Ecol. Prog. Ser*. 301, 199–215. doi: 10.3354/meps301199

Orr, M. H., and Mignerey, P. C. (2003). Nonlinear internal waves in the South China Sea: observation of the conversion of depression internal waves to elevation internal waves. *J. Geophys. Res. Oceans* 108:3064. doi: 10.1029/2001JC001163

Phillips, O. M. (1966). *The Dynamics of the Upper Ocean*. New York, NY: Cambridge University Press.

Rinke, K., Hübner, I., Petzoldt, T., Rolinski, S., König-Rinke, M., Post, J., et al. (2007). How internal waves influence the vertical distribution of zooplankton. *Freshw. Biol*. 52, 137–144. doi: 10.1111/j.1365-2427.2006.01687.x

Scotti, A., and Pineda, J. (2007). Plankton accumulation and transport in propagating nonlinear internal fronts. *J. Mar. Res*. 65, 117–145. doi: 10.1357/002224007780388702

Seuront, L., Brewer, M. C., and Strickler, J. R. (2004). "Quantifying zooplankton swimming behavior: the question of scale," in *Handbook of Scaling Methods in Aquatic Ecology: Measurement, Analysis, Simulation*, eds L. Seuront and P. G. Strutton (Boca Raton, FL: CRC Press), 333359. doi: 10.1201/9780203489550.ch22

Sevadjian, J. C., McManus, M. A., Ryan, J., Greer, A. T., Cowen, R. K., and Woodson, C. B. (2014). Across-shore variability in plankton layering and abundance associated with physical forcing in Monterey Bay, California. *Continent. Shelf Res*. 72, 138–151. doi: 10.1016/j.csr.2013.09.018

Thorpe, S. A. (1999). On the breaking of internal waves in the ocean. *J. Phys. Oceanogr*. 29, 2433–2441. doi: 10.1175/1520-0485(1999)029<2433:OTBOIW>2.0.CO;2

Tiselius, P. (1992). Behavior of *Acartia tonsa* in patchy food environments. *Limnol. Oceanogr*. 37, 1640–1651. doi: 10.4319/lo.1992.37.8.1640

Troy, C. D., and Koseff, J. R. (2005). The instability and breaking of long internal waves. *J. Fluid Mech*. 543, 107–136. doi: 10.1017/S0022112005006798

True, A. C., Webster, D. R., Weissburg, M. J., and Yen, J. (2018). Copepod avoidance of thin chemical layers of harmful algal compounds. *Limnol. Oceanogr*. 63, 1041–1055. doi: 10.1002/lno.10752

Umeyama, M. (2000). Third-order Stokes internal waves for a density-stratified two-layer fluid. *Mem. Graduate Schl. Eng. Tokyo Metropolit. Univers*. 50, 120–136.

Umeyama, M. (2002). Experimental and theoretical analyses of internal waves of finite amplitude. *J. Waterway Port Coast. Ocean Eng*. 128, 133–141. doi: 10.1061/(ASCE)0733-950X(2002)128:3(133)

Uttieri, M., Zambianchi, E., Strickler, J. R., and Mazzocchi, M. G. (2005). Fractal characterization of three-dimensional zooplankton swimming trajectories. *Ecol. Modell*. 185, 51–63. doi: 10.1016/j.ecolmodel.2004.11.015

Van Haren, H. (2014). Internal wave-zooplankton interactions in the Alboran Sea (W-Mediterranean). *J. Plankton Res*. 36, 1124–1134. doi: 10.1093/plankt/fbu031

Velo-Suárez, L., Fernand, L., Gentien, P., and Reguera, B. (2010). Hydrodynamic conditions associated with the formation, maintenance and dissipation of a phytoplankton thin layer in a coastal upwelling system. *Continent. Shelf Res*. 30, 193–202. doi: 10.1016/j.csr.2009.11.002

Woodson, C. B., Webster, D. R., and True, A. C. (2014). "Copepod behavior: oceanographic cues, distributions and trophic interactions," in *Copepods: Diversity, Habitat and Behavior* (Hauppauge, NY: Nova Publishers), 215–253.

Woodson, C. B., Webster, D. R., Weissburg, M. J., and Yen, J. (2005). Response of copepods to physical gradients associated with structure in the ocean. *Limnol. Oceanogr*. 50, 1552–1564. doi: 10.4319/lo.2005.50.5.1552

Woodson, C. B., Webster, D. R., Weissburg, M. J., and Yen, J. (2007a). Cue hierarchy and foraging in calanoid copepods: ecological implications of oceanographic structure. *Mar. Ecol. Prog. Ser*. 330, 163–177. doi: 10.3354/meps330163

Woodson, C. B., Webster, D. R., Weissburg, M. J., and Yen, J. (2007b). The prevalence and implications of copepod behavioral responses to oceanographic gradients and biological patchiness. *Integr. Comp. Biol*. 47, 831–846. doi: 10.1093/icb/icm091

Conflict of Interest: The authors declare that the research was conducted in the absence of any commercial or financial relationships that could be construed as a potential conflict of interest.

Copyright © 2020 Mohaghar, Jung, Haas and Webster. This is an open-access article distributed under the terms of the Creative Commons Attribution License (CC BY). The use, distribution or reproduction in other forums is permitted, provided the original author(s) and the copyright owner(s) are credited and that the original publication in this journal is cited, in accordance with accepted academic practice. No use, distribution or reproduction is permitted which does not comply with these terms.

frontiers in Marine Science

ORIGINAL RESEARCH
published: 26 June 2020
doi: 10.3389/fmars.2020.00473

Lagrangian Time Scale of Passive Rotation for Mesoscale Particles in Turbulence

Ankur D. Bordoloi[1]*, *Evan Variano*[1] *and Gautier Verhille*[2]

[1] *Department of Civil and Environmental Engineering, University of California Berkeley, Berkeley, CA, United States,* [2] *Aix Marseille Univ, CNRS, Centrale Marseille, IRPHE, Marseille, France*

Turbulence induces rotation in the living and the non-living materials in the ocean. The time scale of rotation for a living organism is important in understanding an organism's feeding efficiency, mating, prey capture rate, etc. This time scale is also crucial for understanding the migration of non-living materials such as microplastics. Herein, we investigate the tumbling motion of mesoscale particles that resemble organisms of intermediate size, such as zooplankton that appear in the ocean. Using time-resolved measurements of the orientation of rigid inertial fibers in a turbulence-tank, we analyze the autocorrelation of their tumbling rate. The correlation time (τ_d) is well-predicted by Kolmogorov inertial-range scaling based on the fiber length (L) when the fiber inertia can be neglected. For inertial fibers, we propose a simple model considering fiber inertia (measured by a tumbling Stokes number) and a viscous torque which accurately predicts both the correlation time and the variance of the tumbling rate. Our measurements and the theoretical model provide a basic understanding of the rotational response of an intermediately sized organism to the surrounding turbulence in its non-active state.

Keywords: fiber in turbulence, Lagrangian turbulence, timescale, microplasitcs, tumbling, marine organism

OPEN ACCESS

Edited by:
David Murphy, University of South Florida, United States

Reviewed by:
Perry Johnson, Stanford University, United States
Gaetano Sardina, Chalmers University of Technology, Sweden

***Correspondence:**
Ankur D. Bordoloi
aerials00@gmail.com

Specialty section:
This article was submitted to Marine Ecosystem Ecology, a section of the journal Frontiers in Marine Science

Received: *08 January 2020*
Accepted: *27 May 2020*
Published: *26 June 2020*

Citation:
Bordoloi AD, Variano E and Verhille G (2020) Lagrangian Time Scale of Passive Rotation for Mesoscale Particles in Turbulence. Front. Mar. Sci. 7:473. doi: 10.3389/fmars.2020.00473

1. INTRODUCTION

Understanding the dynamic response of a particle suspended in turbulent flow is applicable to many small marine organisms. For instance, the rate of prey capture, predator sensitivity, feeding efficiency, and habitat selection of an organism depend on how an organism responds to the varying intensity of turbulence across the ocean (Rothschild and Osborn, 1988; MacKenzie et al., 1994; Gilbert and Buskey, 2005; Reidenbach et al., 2009; Sutherland et al., 2014; Byron, 2015; Michalec et al., 2017). The alignment and rotation of a non-spherical organism may influence its nutrient uptake by influencing the surrounding boundary layer thickness, and hence the biological cycles of the environment at various scales (Pahlow et al., 1997; Nguyen et al., 2011; Byron, 2015). Further, the local distribution of micro-organisms such as phytoplankton relate to their mechanistic response to the turbulence in the ocean (Durham and Stocker, 2012).

Organisms such as phytoplankton are typically smaller than the smallest scale of oceanic turbulence. Orientation and rotation of sub-Kolmogorov particles in turbulence have been widely studied in the past and are relatively well-understood (Jeffery, 1922; Maxey, 1983; Ferrante and Elghobashi, 2003; Lundell and Carlsson, 2010; Pumir and Wilkinson, 2011; Pujara and Variano, 2017). Of particular interest to this research are the mesoscale organisms such as zooplankton; their sizes exceed the Kolmogorov scale but are within the inertial subrange of turbulence. Earlier studies have shown that the orientation of an organism plays a significant role in their gravitaxis,

settlement, and directed swimming (Roberts and Deacon, 2002). Besides, the active swimming characteristics of such organisms add further complexity to the problem (Michalec et al., 2017).

The motion, aggregation and fragmentation of microplastics in the ocean are also affected by turbulence. Such mesoscale particles are also often non-spherical. Besides being an obvious threat to the environment, these particles also act as rafting mechanism in long distance transport for various organisms that influences the ecological connectivity of the ocean (Thiel and Gutow, 2005; Wright et al., 2013). However, the kinematics of rotation of mesoscale particles are complex; because they experience non-linear shear along their size, these organisms respond to the ambient distribution of angular velocities in a non-trivial way.

Several fundamental studies in the past few years have been devoted to the passive rotation induced by turbulence of spheres (Zimmermann et al., 2011; Klein et al., 2013; Mathai et al., 2016), of complex particles (Pujara et al., 2018), and axisymmetric anisotropic particles [Voth and Soldati (2017) and reference therein]. Two important goals related to these inquiries are to understand: (A) how the statistics of rotation relates to the particle size, and (B) once set to motion by the ambient turbulence, how long a particle continues to preserve its rotation. Considering the simple cylindrical shape as analogous to the shape of various oceanic organisms, the first piece of this puzzle has been addressed extensively in the past for both non-inertial (tracer) (Parsa et al., 2012; Marchioli and Soldati, 2013; Pujara and Variano, 2017) and inertial particles (Parsa and Voth, 2014; Bordoloi and Variano, 2017; Sabban et al., 2017; Bounoua et al., 2018; Kuperman et al., 2019). Inertia might arise due to the density difference between the fiber and the fluid, and/or because of the fiber dimensions (length and diameter) being larger than the Kolmogorov length η_K. In the latter category, long fibers with negligible diameter ($d \leq \eta_K$) were shown to obey Kolmogorov inertial-range scaling such that the variance of the tumbling rate, $\langle \dot{p}_i \dot{p}_i \rangle \approx (L/\eta_K)^{-4/3} \tau_K^{-2}$ (Parsa and Voth, 2014). Here, η_K and τ_K are Kolmogorov length and time scales, respectively. For fibers with large diameter ($d \gg \eta_K$) and small aspect ratio (L/d = 1, 4), Bordoloi and Variano (2017) modified this relationship by replacing particle length (L) by the spherical-volume-equivalent diameter $d_{eq} = (Ld^2)^{1/3}$. The d_{eq}-based scaling was also found to be consistent for particles of other complex shapes, such as cubes, cuboids, and cones (Pujara et al., 2018).

In general, the rotation of a rigid fiber can be described by the conservation of angular momentum, written in the frame of the particle as

$$I\dot{\Omega} + \Omega \times (I \cdot \Omega) = \Gamma_f \tag{1}$$

Here, Ω is the total rotation (i.e., spinning and tumbling) rate; I is the moment of inertia tensor of the fiber, and Γ_f is the total torque applied on the fiber by the turbulent flow. Considering a viscous torque (linear in velocity profile), Bounoua et al. (2018) model the torque as $\Gamma_f \sim -4\pi\eta\Omega L^3/3 + 4\pi\eta \int \mathbf{u_f} \times \mathbf{s} ds$. The first term corresponds to the viscous dissipation. The second term is the forcing term which is responsible for the transfer of energy from the fluid to the fiber. The Coriolis term $\Omega \times (I \cdot \Omega)$ is generally neglected for long fibers assuming that the spinning rate is smaller than the relaxation rate of tumbling. This disputable assumption is generally justified by the weak alignment of long fibers with coarse grained vorticity (Pujara et al., 2019). The Equation (1) then reduces to a simplified Langevin equation,

$$\ddot{p}_i + \frac{1}{\tau_r}\dot{p}_i = \frac{1}{\tau_r}\xi. \tag{2}$$

Here, $\tau_r = I/4\pi\eta L^3$ is the rotational response time and $\xi \sim \int \mathbf{u_f} \times \mathbf{s} ds/L^3$ is a colored noise related to the background turbulence. The tumbling rate ($\dot{p}$) is then determined by the nature of the forcing ξ and by the ratio of the response time of the particle (τ_r) and the characteristic time of the forcing $\tau_L \sim L/u_L \sim \epsilon^{-1/3} L^{2/3}$. This ratio defines the tumbling Stokes number $St_{\dot{\mathbf{p}}} \sim \tau_r/\tau_L$ that scales as:

$$St_{\dot{\mathbf{p}}} \sim \frac{1}{48}\frac{\rho}{\rho_f}\left(\frac{d}{\eta_K}\right)^{4/3}\left(\frac{d}{L}\right)^{2/3}\left[1 + \frac{3}{4}\left(\frac{d}{L}\right)^2\right]. \tag{3}$$

for a cylindrical fiber of length L and diameter d.

In a previous letter (Bounoua et al., 2018), we modeled ξ as a Dirac function peaked at fiber length, L. This provided a theoretical basis to understand the influence of the fiber inertia on the variance of the tumbling rate via:

$$\langle \dot{p}_i \dot{p}_i \rangle \sim \frac{1}{1 + St_{\dot{\mathbf{p}}}^2}(L/\eta_K)^{-4/3}\tau_K^{-2}. \tag{4}$$

The model stated in Equation (4) unified results from Parsa and Voth (2014) and Bordoloi and Variano (2017), and our experimental data over a wide range of aspect ratios. This relation has also been verified recently by Kuperman et al. (2019) for long nylon fibers in air.

While the variance of rotation rate has been investigated in detail, few studies have been devoted to the correlation time of rotation. The main results come from numerical simulation, which are limited to either short ($L \approx 10\eta_K$) (Marchioli and Soldati, 2013) or slender ($d < \eta_K$) (Shin and Koch, 2005) fibers. Shin and Koch (2005) showed that in the slender body limit, the correlation time is constant for fiber length smaller than $10\eta_K$ and then increases with fiber length. For fibers smaller than Kolmogorov length but heavier than the carrying fluid, Marchioli and Soldati (2013) showed that the correlation time increases with the Stokes number, so with the fiber inertia. Extrapolating our previous model (Bounoua et al., 2018) to inertial fibers longer than the Kolmogorov length, we find that the correlation time of the tumbling rate scales with the forcing time scale, $\tau_L \sim L^{2/3}$ independent of fiber inertia (see section 3). The correlation time is important in understanding the temporal response of an organism to the surrounding turbulence and its rotational diffusivity. For example, a comparison between the response time of a copepod with the frequency of fluctuating nutrient field can help better understand the nutrient uptake event of the organism (Peters and Marrasé, 2000).

Herein, we take an experimental approach to measure the correlation time of rotation for inertial fibers over a wide range

TABLE 1 | Characteristics of turbulence in the cube tank facility.

Rotation frequency, f	5 Hz	10 Hz	15 Hz
Reynolds number, Re_λ	350	530	610
Kolmogorov lengthscale, η_K	78.3 μm	46.6 μm	34.4 μm
Kolmogorov timescale, τ_K	6.14 ms	2.17 ms	1.18 ms

of length and diameter. We also take the work of Bounoua et al. (2018) a step further and propose a new model that predicts both variance of tumbling rate and the correlation time scale of tumbling. In section 2, we review the experimental setup and describe our data analysis method. In section 3, we present our results and a theoretical model interpreting the results. Finally, we provide concluding remarks with a discussion about future research directions in section 4.

2. EXPERIMENTAL SETUP AND METHOD

The experimental setup consists of a cubic tank (each side = 60 cm) filled with water. We generate homogeneous and isotropic turbulence inside the tank by strategically stirring the water using 8 disks (diameter = 17 cm) with straight blades (height = 5 mm), each mounted on one corner of the tank. Each impeller is set to rotate independently via a 1.5 kW brushless motor at the same frequency but with opposite chirality to its adjacent three nearest neighbors. The turbulence inside the tank, set by the impeller frequency (f = 5, 10, or 15 Hz), is characterized using standard PIV measurements (Xu and Chen, 2013), and is found to be fairly homogeneous and isotropic in the central region (volume $\approx 10 \times 10 \times 10$ cm^3). The relevant characteristics of turbulence in the tank are summarized in **Table 1**. Rigid polystyrene fibers cut to specific length (L = 3.2–40 mm) and diameter (d = 0.5–2.5 mm) are introduced in dilute concentration ($< 0.01\%$ by volume) into the turbulence tank. We perform experiments on 18 different cases with aspect ratio ($\Lambda = L/d$) varying between 1.28 and 80. The details of each experimental case is provided in **Table 2**. The density of polystyrene (ρ_d = 1.04 g/cm^3) makes the fibers near-neutrally buoyant, and the low fiber concentration allows to neglect the interaction between fibers and the retro-action of the fiber on the turbulence.

We image the fibers on two orthogonally arranged 1-MP-high-speed-cameras, all cameras being triggered simultaneously at a frame rate of 0.5–1 kHz. The fibers are backlit onto each camera by an accompanying LED panel with diffuser. Each fiber is reconstructed into the 3D space using a custom MATLAB code. First, the extremities of each fiber are detected in all two images. Then, those extremities are triangulated into the 3D space. Finally, the centroid location ($x_{c,i}$) and the orientation (p_i) of each fiber are optimized such that the difference between the projection of the fiber onto each camera and the actual image is minimized. The measurement volume is that of a cube of $\approx$ 13 cm length centered at the center of the tank. $N \geq 5,000$ individual trajectories are stored and used to compute the rotation statistics for each case.

The characteristic time of the dynamics of a random signal is given by the correlation function. The correlation function of

TABLE 2 | Fiber-dimensions (L, d) normalized by Kolmogorov length scale (η_K), aspect ratio ($\Lambda = L/d$), and rotational Stokes number ($St_{\dot{p}}$) of fibers tested under three specific Reynolds number (Re_λ) of the background turbulence.

Length (L/η_K)	Diameter (d/η)	Aspect ratio (Λ)	Stokes number ($St_{\dot{p}}$)	Reynolds number (Re_λ)	Symbol
510.8	6.4	80	0.014	350	●
858.9	10.7	80	0.027	530	■
255.4	8.2	31	0.035	350	●
127.7	8.2	15	0.056	350	●
429.5	13.7	31	0.071	530	■
40.9	8.2	5	0.123	350	●
127.7	12.8	10	0.138	350	●
429.5	21.5	20	0.172	530	■
81.7	12.8	6	0.187	350	●
255.4	25.5	10	0.347	350	●
137.4	21.5	6	0.375	530	■
127.7	25.5	5	0.563	350	●
429.5	42.9	10	0.694	530	■
51.1	20.4	2	0.722	350	●
127.7	31.9	4	0.894	350	●
214.7	42.9	5	1.126	530	■
85.9	34.4	2	1.443	530	■
214.7	53.7	4	1.788	530	■
291	72.8	4	2.682	610	▲

*Each case is specified by a symbol color-coded in the ascending order of $St_{\dot{p}}$. The three Re_λ (see **Table 1**) are designated by the symbol shape.*

$\dot{p}_i(t)$ is defined as,

$$C_{\dot{p}_i}(t) = \langle \dot{p}_i(t)\dot{p}_i(t+\tau) \rangle. \tag{5}$$

Here there is no summation over i. The angle-bracket $\langle . \rangle$ indicates mean over all temporal lags, $\tau = 0 \rightarrow \infty$. For our calculations, we consider trajectories which are longer than 10 ms. Typically, a fast moving particle remains in the camera frame for a shorter duration compared to a slow moving particle. Hence, the trajectory length is dependent on particle speed. To avoid bias in the mean of $C_{\dot{p}_i}$ due to the correlation between trajectory length and particle speed, we compute the mean weighted on trajectory length, such that

$$\bar{C}_{\dot{p}_i}(\tau) = \frac{\sum_{k=1}^{N} C_{\dot{p}_i}(\tau) T_k}{\sum_{k=1}^{N} T_k}, \tag{6}$$

where T_k is the length of a trajectory and N is the total number of trajectories. The correlation function is normalized by the variance $\langle \dot{p}_i \dot{p}_i \rangle$, such that $\bar{C}_{\dot{p}_i}(0) = 1$. For our analysis, we use the average of the three components of $\bar{C}_{\dot{p}_i}$, which were statistically indistinguishable. We denote the average as $\bar{C}_{\dot{p}}(\tau)$ and use it to compute two time scales of rotation. The first time scale is based on the zero-crossing time (τ_{d1}) of the Lagrangian autocorrelation function $\bar{C}_{\dot{p}}(\tau)$ as described in Shin and Koch (2005). The second time scale is the integral time scale computed as:

$$\tau_{d2} = \int_0^\infty \bar{C}_{\dot{p}}(\tau)^2 d\tau \approx \sum \bar{C}_{\dot{p}}(\tau)^2 \Delta\tau \tag{7}$$

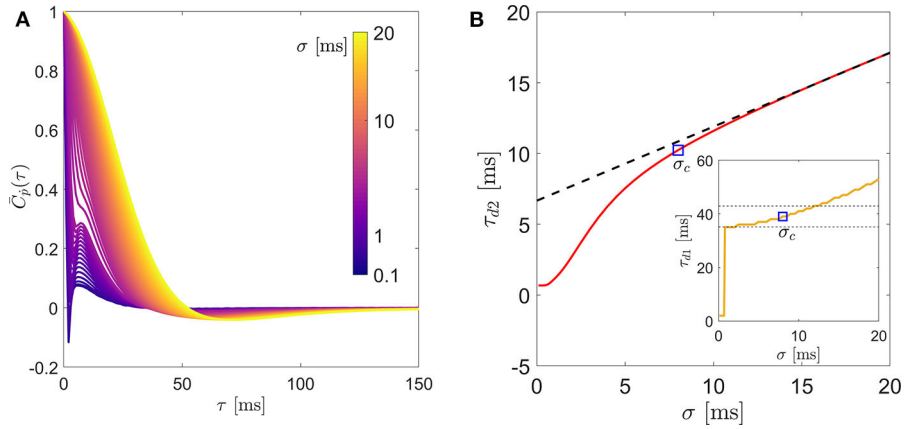

FIGURE 1 | (A) Lagrangian autocorrelation of fiber tumbling rate, **(B)** the integral time scale of rotation (τ_{d2}) and in inset: the zero-crossing time (τ_{d1}) of a representative fiber ($L = 3.2\eta_K$, $d = 0.64\eta_K$) for different filtering window size. The two dashed lines in the inset of **(B)** indicate a range of ±10% of τ_{d1} obtained from the σ_c shown by the square symbol.

which is more tractable theoretically as shown later.

Before computing the statistics of rotation, the experimental noise in $p_i(t)$ is removed by filtering it through a series of one-dimensional Gaussian kernels of window-size $\sigma \leq 20$ ms (Mordant et al., 2004; Volk et al., 2007). The tumbling rate ($\dot{p}_i(t)$) for each σ is then computed using a symmetric second-order central-difference scheme. **Figure 1** demonstrates this method by showing the effect of σ on (a): the mean autocorrelation of tumbling rate $\bar{C}_{\dot{p}}(\tau)$, and (b): the integral time-scale of rotational dispersion (τ_{d2}). Assuming that the experimentally measured $\dot{p}_i(t)$ contains only uncorrelated noise, we extract the noise-free τ_{d2} by fitting a straight line for the linear segment ($\sigma \geq 10$ in this example) of each plot and extrapolating it to $\sigma = 0$ (see **Figure 1B**). We use a critical σ_c to compute the noise-free mean autocorrelation ($\bar{C}_{\dot{p}}(\tau)$) of rotation and the zero-crossing time (τ_{d1}). We choose σ_c to be the smallest σ at which the filtered data deviated from the fit by less than 10%. We tested the sensitivity of this criterion by varying it between 5 and 20% and did not find it to affect our results. This is demonstrated in **Figure 1B** (inset) where we show the evolution of zero-crossing time for the example case.

3. CORRELATION TIME SCALE OF TUMBLING RATE

3.1. Experimental Observation

If we neglect inertia and assume that a fiber of size L is rotated only by eddies of size L, the tumbling rate of the fiber should correlate to a timescale $\tau_L \sim L/u_L \approx (L/\eta_K)^{2/3}\tau_K$, where u_L is the typical velocity at scale L. The mean Lagrangian autocorrelation function $\bar{C}_{\dot{p}}(\tau)$ of tumbling for various fibers are shown in **Figure 2A**. This plot includes our measurements and the longest fiber ($L = 41.7\eta_K$) simulated by Shin and Koch (2005) at $R_\lambda = 39.9$ neglecting fiber inertia ($I = 0$). With the horizontal-axis normalized by τ_L, the measurements of the autocorrelation function for fibers with $St_{\dot{p}} < 0.7$ are independent of $St_{\dot{p}}$ and close to the one obtained by Shin and Koch (2005). In all these cases, the zero-crossing time is $\tau_{d1} = 0.43\tau_L$ with a 95% confidence interval ±0.02. The difference from the slender body approximation appears after the zero-crossing time, such that our measurements decorrelate on a shorter time scale than simulations by Shin and Koch (2005). For fibers with $St_{\dot{p}} > 0.7$, $\bar{C}_{\dot{p}}(\tau)$ becomes sensitive to $St_{\dot{p}}$, such that the zero-crossing time increases with $St_{\dot{p}}$.

In **Figure 2B**, we directly show the evolution of zero-crossing time (τ_{d1}) normalized by the Kolmogorov time scale (τ_K) with respect to normalized fiber length (L/η_K). We also include the zero-crossing time for all slender fibers computed by Shin and Koch (2005). Irrespective of the Reynolds number (Re_λ), a 2/3 power-law scaling qualitatively captures the evolution of τ_{d1} for fibers with $St_{\dot{p}} < 0.7$. Also, the zero-crossing times reported in Shin and Koch (2005) approach this power-law scaling as their length enters the inertial range. A similar plot for the integral time (τ_{d2}) is shown in inset that also demonstrates the 2/3 power-law fit. Shin and Koch (2005) proposed a linear fit for τ_{d1} from their simulations with long fibers ($25\eta < L < 60\eta$); the inertial-range scaling was not obvious there because of the limited range of fiber length they simulated.

Our data agree with the scaling law when $St_{\dot{p}} < 0.7$, but not when $St_{\dot{p}} > 0.7$. To investigate this effect, we propose an improved version of the model proposed in Bounoua et al. (2018) which captures both the evolution of the variance and the tumbling rate for inertial fibers ($L \geq 10\eta_K$).

3.2. Theoretical Model

In Bounoua et al. (2018), we modeled the forcing torque ξ as a Dirac function peaked at the fiber length, L. As we saw, this assumption fails to predict the effect of fiber inertia on the correlation time scale (τ_d) measured from our experiments. Here, we assume that the process of filtering due to the integration of the viscous forces along the fiber length is smoother and can be

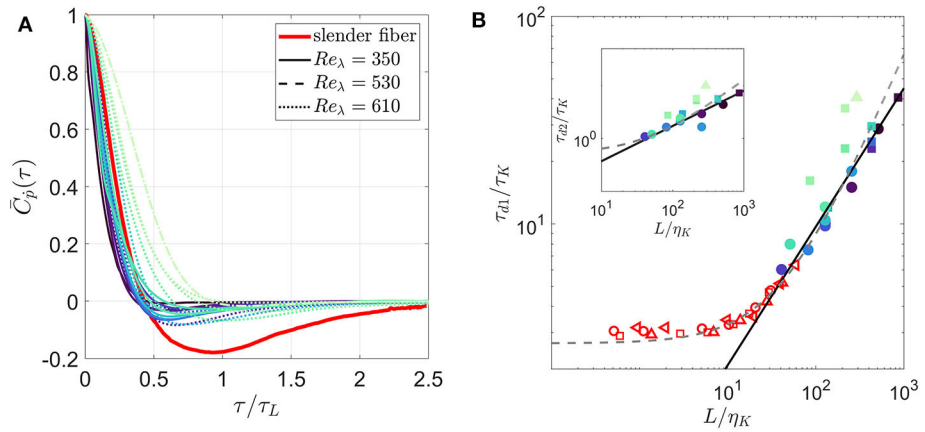

FIGURE 2 | (A) Lagrangian autocorrelation $\bar{C}_{\dot{p}}(\tau)$ of tumbling rate, **(B)** the zero-crossing time τ_{d1} and the integral time scale τ_{d2} (see inset) for inertial fibers. Numerical result from Shin and Koch (2005) for a slender fiber with $L = 41.7\eta_K$, $Re_\lambda = 39.9$ is included in **(A)** and slender fibers at multiple lengths and $Re_\lambda = 16.5$ (□), 30.7 (○), 39.9 (△), and 53.3 (▽) are included in **(B)** for comparison. The dashed lines in **(B)** represent the linear fit ($\tau_d/\tau_K = 2.66 + 0.063L/\eta_K$) suggested in Shin and Koch (2005). This fit is multiplied by the mean ratio of the zero crossing time and the integral time from our data in the inset. Data include particles from very little inertia (●) to those with $St_{\dot{p}} > 0.7$ (● ● ■ ■ ■ ▲).

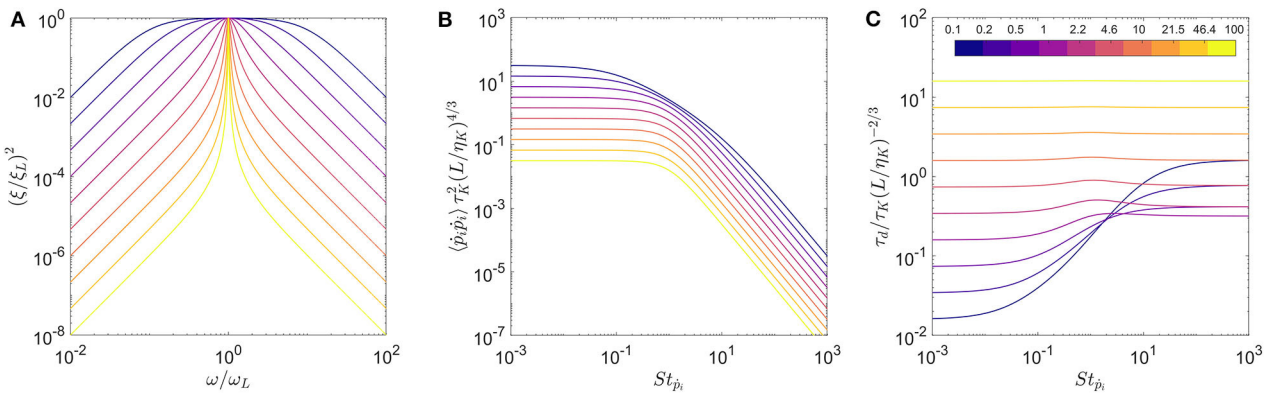

FIGURE 3 | The effect of quality factor (Q) on **(A)** the white noise spectrum, the transfer functions for **(B)** variance of tumbling rate and **(C)** correlation time scale. The colormap indicates the value of Q used for this computation.

described by a bandpass filter peaked on $\omega_L \sim \epsilon^{1/3}L^{-2/3}$. In that case, the forcing torque ξ in Fourier space can be scaled as,

$$\xi(x) \sim \xi_L \frac{1}{1 + \imath Q(x - 1/x)}, \tag{8}$$

with $x = \omega/\omega_L$ and Q is the quality factor of the filter. ξ_L is the amplitude of the turbulent spectrum at scale L, such that $|\xi_L|^2 \sim \tau_K^{-2}(\eta_K/L)^{4/3}$. The quality factor Q determines the width of the band-pass filter as shown on **Figure 3**. The spectrum reduces to the Dirac function when $Q \to \infty$.

The solution of Equation (2) leads to:

$$\dot{p}_i = \frac{\xi(\omega)}{1 + \imath\omega\tau_r}. \tag{9}$$

For a given spectrum of ξ_L, one can determine the variance and the correlation time of tumbling rate from Equation (9). For simplicity, we will assume that ξ_L is a white noise to derive analytical expression for the variance and the tumbling rate. This assumption should hold as long as the quality factor is not too low and that the spectrum is indeed peaked at the frequency ω_L. Further, this assumption will be justified by the agreement between the model and our experimental results (which do not match when the Dirac function selects the amplitude of the spectrum only at the frequency ω_L). Within this framework, the variance of $\dot{p}_i$ is:

$$\langle \dot{p}_i \dot{p}_i \rangle = \xi_L^2 \int \frac{1}{1 + St_{\dot{p}}^2 x^2} \frac{x^2}{x^2 + Q^2(x^2 - 1)^2} dx. \tag{10}$$

In a similar vein, we can derive an analytical expression for the correlation time (τ_d) of the tumbling rate:

$$\tau_d = \int C_{\dot{p}}(t)^2 dt = \int \hat{C}_{\dot{p}}(\omega)\hat{C}^*_{\dot{p}}(\omega) d\omega, \tag{11}$$

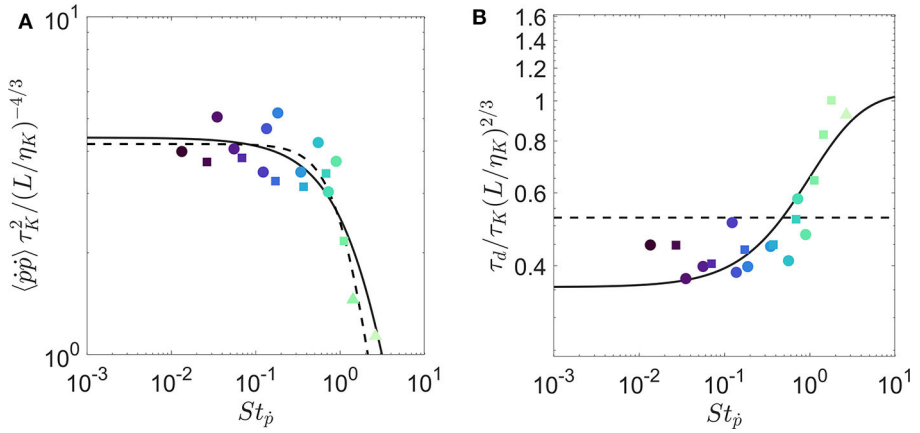

FIGURE 4 | Evolution of transfer functions of **(A)** variance of tumbling rate and **(B)** correlation time-scale of rotation with respect to rotational Stokes number for fibers of various length and diameter.

where, $\hat{C}_{\dot{p}}(\omega)$ is the Fourier transform of the autocorrelation of $\dot{p}_i$. Contrary to the definition of the zero-crossing time, this expression is suitable analytically. From Equations (8) and (9), the modulus of the correlation function $\hat{C}$ can be written:

$$\left|\hat{C}_{\dot{p}}(x)\right|^2 = \frac{1}{\langle \dot{p}_i \dot{p}_i \rangle^2} \left(\frac{\xi_L^4}{1 + St^2 x^2} \frac{x^4}{(x^2 + Q^2(x^2-1)^2)^2} \right). \quad (12)$$

Hence, the correlation time τ_d is,

$$\tau_d = \frac{\xi_L^4}{\langle \dot{p}_i \dot{p}_i \rangle^2} \int \frac{1}{1 + St_{\dot{p}}^2 x^2} \frac{x^4}{(x^2 + Q^2(x^2-1)^2)^2} dx. \quad (13)$$

The solutions for the two transfer functions: $\langle \dot{p}_i \dot{p}_i \rangle \tau_K^{-2} (L/\eta_K)^{4/3}$ and $\tau_d (L/\eta_K)^{-2/3}/\tau_K$ are shown for multiple Q values in **Figures 3B,C**, respectively. The rescaled variance $\langle \dot{p}_i \dot{p}_i \rangle \tau_K^2 (L/\eta_K)^{-4/3}$ for all Q values show similar trends with a plateau for low Stokes number, and its value decreasing as $St_{\dot{p}}^{-2}$ for higher Stokes numbers as observed for the Dirac function approximation in Bounoua et al. (2018). Also, the Stokes number where the transition between these two regimes occurs increases with decreasing Q (see **Figure 3B**). The correlation time for the large values of Q is almost constant irrespective of Stokes number, which is a trend observed for the Dirac function formulation in Bounoua et al. (2018). For smaller values of Q, we observe that the correlation time increases beyond $St_{\dot{p}} \approx 1$ and eventually reaches a plateau.

We test this model on our experimental measurements of $\langle \dot{p}_i \dot{p}_i \rangle$ and τ_{d1} in **Figures 4A,B**, respectively. We fit Equations (10) and (13) simultaneously using two least-squares fits with 3 fitting parameters: besides the quality factor Q, we introduce a parameter α to compensate the scaling in tumbling Stokes number $St_{\dot{p}}$ (see Equation 4), and a parameter β to compensate the scaling in the amplitude of the spectrum ξ (see Equation 8). This last parameter is fully justified to compare our prediction with the measurement of the zero-crossing time τ_{d1} and to compensate the finiteness of the trajectory for the evaluation of the correlation time τ_{d2}. The best fit for τ_{d1} is reached for $Q = 0.72$, $\alpha = 0.41$, and $\beta = 3.12$. A similar fit to the integral time (τ_{d2}) has yielded the same Q and α, but a smaller scaling factor ($\beta = 0.64$) because of the lower magnitude in τ_{d2} seen previously (see **Figure 2B**). The dashed lines in each plot represent the predictions from Bounoua et al. (2018). Results show that although the previous model is able to predict the variance of tumbling rate, it fails to estimate the evolution of the correlation time. The current model predicts both quantities very well. Our fitted results for Q shows that the inertial effects begin for $St_{\dot{p}}$ between 0.1 to 1. This agrees qualitatively with the critical $St_{\dot{p}} = 0.7$ that we chose by eye in **Figure 2**.

4. SUMMARY AND CLOSING COMMENTS

We report experimental measurements of Lagrangian autocorrelation of tumbling rate of inertial fibers in homogeneous isotropic turbulence that is applicable to zooplankton-like organisms in their non-active state. Based on the zero-crossing and the integral of the mean autocorrelation function, we compute two correlation times (τ_{d1} and τ_{d2}) for fibers with a wide range of length and aspect ratio. The inertia of a fiber is quantified using a rotational Stokes number ($St_{\dot{p}}$) that takes into account fiber length, diameter, as well as the relative density. For low $St_{\dot{p}}$, both correlation times from our measurement follow Kolmogorov's inertial range scaling of $(L/\eta_K)^{2/3}$. This scaling is further supported by the numerically computed zero-crossing times for long slender fibers ($L > 10\eta_K$) in Shin and Koch (2005). For fibers with high $St_{\dot{p}}$, the rotation rate escapes this prediction. We find that our previous model (Bounoua et al., 2018) designed for the variance of tumbling rate does not capture the effect of fiber inertia on correlation time. Instead of assuming the spectrum of background excitation to be a simple Dirac function peaked at the fiber length, we model the excitation as a white noise filtered by a bandpass filter (viscous torque). The evolution of the tumbling rate can then be described by a Langevin equation with a response time given by the fiber

inertia. We show that this model recovers the evolution of both the variance and the correlation time of tumbling rate for the range of explored Stokes number.

Recent studies on settling of anisotropic particles in turbulent flows (Lopez and Guazzelli, 2017; Gustavsson et al., 2019; Roy et al., 2019) argue that non-linear torque plays an important role on the orientation dynamics. It can be surprising that our model, which only considers viscous torque, is in very good agreement with our measurements. We attribute this contradiction to two main differences between ours and these studies on settling: (a) the settling speed in our case is negligible compared to turbulent fluctuations, and (b) the size of particles considered in the latter case are generally smaller than the Kolmogorov length. A direct estimation of inertial torque requires measurement of fluid velocity around the particle, which is beyond the scope of this work. Future experiments or DNS study will help better understand the importance of inertial torque in the rotational kinematics of fibers.

Oceanic organisms such as zooplankton are capable of active locomotion in turbulence. Results from this investigation will help in addressing the biological aspect of their locomotion by separating the passive rotation from their active swimming.

Finally, to fully characterize the rotation of an anisotropic inertial particle, it is necessary to investigate also its spinning motion, which is currently underway in our laboratory. This quantity has been shown to be larger than the tumbling for fibers smaller than the Kolmogorov length due to a preferential alignment (Parsa et al., 2012). Measuring spinning along with tumbling will also help estimating the total torque and lift experienced by a fiber.

DATA AVAILABILITY STATEMENT

The datasets generated for this study are available on request to the corresponding author.

AUTHOR CONTRIBUTIONS

GV collected the data. AB and GV analyzed the data. AB, GV, and EV wrote the manuscript. All authors contributed to the article and approved the submitted version.

FUNDING

This work was carried out in the framework of FlexFiT Project (ANR-17-CE30-0005-01) funded by the French National Research Agency (ANR), the Labex MEC Project (No. ANR-10-LABX-0092) and of the A*MIDEX Project (No. ANR-11-IDEX-0001-02), funded by the Investissements d'Avenir French Government program managed by the French National Research Agency (ANR). In addition to NSF, this work and its open-access publication was supported by the University of California.

ACKNOWLEDGMENTS

The authors acknowledge the support of S. Bounoua and G. Bouchet in collection of data used in this manuscript.

REFERENCES

Bordoloi, A. D., and Variano, E. (2017). Rotational kinematics of large cylindrical particles in turbulence. *J. Fluid Mech*. 815, 199–222. doi: 10.1017/jfm.2017.38

Bounoua, S., Bouchet, G., and Verhille, G. (2018). Tumbling of inertial fibers in turbulence. *Phys. Rev. Lett*. 121:124502. doi: 10.1103/PhysRevLett.121.124502

Byron, M. L. (2015). *The rotation and translation of non-spherical particles in homogeneous isotropic turbulence* (Ph.D. thesis). University of California, Berkeley, Berkeley, CA, United States.

Durham, W. M., and Stocker, R. (2012). Thin phytoplankton layers: characteristics, mechanisms, and consequences. *Annu. Rev. Mar. Sci*. 4, 177–207. doi: 10.1146/annurev-marine-120710-100957

Ferrante, A., and Elghobashi, S. (2003). On the physical mechanisms of two-way coupling in particle-laden isotropic turbulence. *Phys. Fluids* 15, 315–329. doi: 10.1063/1.1532731

Gilbert, O. M., and Buskey, E. J. (2005). Turbulence decreases the hydrodynamic predator sensing ability of the calanoid copepod *Acartia tonsa*. *J. Plankton Res*. 27, 1067–1071. doi: 10.1093/plankt/fbi066

Gustavsson, K., Sheikh, M. Z., Lopez, D., Naso, A., Pumir, A., and Mehlig, B. (2019). Effect of fluid inertia on the orientation of a small prolate spheroid settling in turbulence. *N. J. Phys*. 21:083008. doi: 10.1088/1367-2630/ab3062

Jeffery, G. B. (1922). The motion of ellipsoidal particles immersed in a viscous fluid. *Proc. R. Soc. Lond. Ser. A* 102, 161–179. doi: 10.1098/rspa.1922.0078

Klein, S., Gibert, M., Bérut, A., and Bodenschatz, E. (2013). Simultaneous 3d measurement of the translation and rotation of finite size particles and the flow field in a fully developed turbulent water flow. *Meas. Sci. Techol*. 24:024006. doi: 10.1088/0957-0233/24/2/024006

Kuperman, S., Sabban, L., and van Hout, R. (2019). Inertial effects on the dynamics of rigid heavy fibers in isotropic turbulence. *Phys. Rev. Fluids* 4:064301. doi: 10.1103/PhysRevFluids.4.064301

Lopez, D., and Guazzelli, E. (2017). Inertial effects on fibers settling in a vortical flow. *Phys. Rev. Fluids* 2:024306. doi: 10.1103/PhysRevFluids.2.024306

Lundell, F., and Carlsson, A. (2010). Heavy ellipsoids in creeping shear flow: transitions of the particle rotation rate and orbit shape. *Phys. Rev. E* 81:016323. doi: 10.1103/PhysRevE.81.016323

MacKenzie, B. R., Miller, T. J., Cyr, S., and Leggett, W. C. (1994). Evidence for a dome-shaped relationship between turbulence and larval fish ingestion rates. *Limnol. Oceanogr*. 39, 1790–1799. doi: 10.4319/lo.1994.39.8.1790

Marchioli, C., and Soldati, A. (2013). Rotation statistics of fibers in wall shear turbulence. *Acta Mech*. 224, 2311–2329. doi: 10.1007/s00707-013-0933-z

Mathai, V., Neut, N. W. M., van der Poel, E. P., and Sun, C. (2016). Translational and rotational dynamics of a large buoyant sphere in turbulence. *Exp. Fluids* 57:51. doi: 10.1007/s00348-016-2136-6

Maxey, M. R. (1983). Equation of motion for a small rigid sphere in a nonuniform flow. *Phys. Fluids* 26:883. doi: 10.1063/1.864230

Michalec, F.-G., Fouxon, I., Souissi, S., and Holzner, M. (2017). Zooplankton can actively adjust their motility to turbulent flow. *Proc. Natl. Acad. Sci. U.S.A*. 114, E11199–E11207. doi: 10.1073/pnas.1708888114

Mordant, N., Crawford, A., and Bodenschatz, E. (2004). Experimental Lagrangian acceleration probability density function measurement. *Phys. D Nonlinear Phenomena* 193, 245–251. doi: 10.1016/j.physd.2004.01.041

Nguyen, H., Karp-Boss, L., Jumars, P. A., and Fauci, L. (2011). Hydrodynamic effects of spines: a different spin. *Limnol. Oceanogr. Fluids Environ*. 1, 110–119. doi: 10.1215/21573698-1303444

Pahlow, M., Riebesell, U., and Wolf-Gladrow, D. A. (1997). Impact of cell shape and chain formation on nutrient acquisition by marine diatoms. *Limnol. Oceanogr*. 42, 1660–1672. doi: 10.4319/lo.1997.42.8.1660

Parsa, S., Calvazarini, E., Toschi, F., and Voth, G. A. (2012). Rotation rate of rods in turbulent fluid flow. *Phys. Rev. Lett*. 109:134501. doi: 10.1103/PhysRevLett.109.134501

Parsa, S., and Voth, G. A. (2014). Inertial range scaling in rotations of long rods in turbulence. *Phys. Rev. Lett*. 112:024501. doi: 10.1103/PhysRevLett.112.024501

Peters, F., and Marrasé, C. (2000). Effects of turbulence on plankton: an overview of experimental evidence and some theoretical considerations. *Mar. Ecol. Prog. Ser*. 205, 291–306. doi: 10.3354/meps205291

Pujara, N., Oehmke, T. B., Bordoloi, A. D., and Variano, E. A. (2018). Rotations of large inertial cubes, cuboids, cones, and cylinders in turbulence. *Phys. Rev. Fluids* 3:054605. doi: 10.1103/PhysRevFluids.3.054605

Pujara, N., and Variano, E. A. (2017). Rotations of small, inertialess triaxial ellipsoids in isotropic turbulence. *J. Fluid Mech*. 821, 517–538. doi: 10.1017/jfm.2017.256

Pujara, N., Voth, G. A., and Variano, E. A. (2019). Scale-dependent alignment, tumbling and stretching of slender rods in isotropic turbulence. *J. Fluid Mech*. 860, 465–486. doi: 10.1017/jfm.2018.866

Pumir, A., and Wilkinson, M. (2011). Orientation statistics of small particles in turbulence. *N. J. Phys*. 13:093030. doi: 10.1088/1367-2630/13/9/093030

Reidenbach, M. A., Koseff, J. R., and Koehl, M. A. R. (2009). Hydrodynamic forces on larvae affect their settlement on coral reefs in turbulent, wave-driven flow. *Limnol. Oceanogr*. 54, 318–330. doi: 10.4319/lo.2009.54.1.0318

Roberts, A. M., and Deacon, F. M. (2002). Gravitaxis in motile micro-organisms: the role of fore-body asymmetry. *J. Fluid Mech*. 452, 405–423. doi: 10.1017/S0022112001006772

Rothschild, B., and Osborn, T. (1988). Small-scale turbulence and plankton contact rates. *J. Plankton Res*. 10, 465–474. doi: 10.1093/plankt/10.3.465

Roy, A., Hamati, R. J., Tierney, L., Koch, D. L., and Voth, G. A. (2019). Inertial torques and a symmetry breaking orientational transition in the sedimentation of slender fibres. *J. Fluid Mech*. 875, 576–596. doi: 10.1017/jfm.2019.492

Sabban, L., Cohen, A., and van Hout, R. (2017). Temporally resolved measurements of heavy, rigid fibre translation and rotation in nearly homogeneous isotropic turbulence. *J. Fluid Mech*. 814, 42–68. doi: 10.1017/jfm.2017.12

Shin, M., and Koch, D. (2005). Rotational and translational dispersion of fibres in isotropic turbulent flows. *J. Fluid Mech*. 540:143. doi: 10.1017/S0022112005005690

Sutherland, K. R., Costello, J. H., Colin, S. P., and Dabiri, J. O. (2014). Ambient fluid motions influence swimming and feeding by the ctenophore *Mnemiopsis leidyi*. *J. Plankton Res*. 36, 1310–1322. doi: 10.1093/plankt/fbu051

Thiel, M., and Gutow, L. (2005). "The ecology of rafting in the marine environment. II. The rafting organisms and community," in Oceanography and Marine Biology, eds R. N. Gibson, R. J. A. Atkinson, and J. D. M. Gordon (Boca Raton, FL: CRC Press), 279–418. doi: 10.1201/9781420037449.ch7

Volk, R., Mordant, N., Verhille, G., and Pinton, J.-F. (2007). Laser doppler measurement of inertial particle and bubble accelerations in turbulence. *Europhys. Lett*. 81:34002. doi: 10.1209/0295-5075/81/34002

Voth, G., and Soldati, A. (2017). Anisotropic particles in turbulence. *Annu. Rev. Fluid Mech*. 49:249. doi: 10.1146/annurev-fluid-010816-060135

Wright, S. L., Thompson, R. C., and Galloway, T. S. (2013). The physical impacts of microplastics on marine organisms: a review. *Environ. Pollut*. 178, 483–492. doi: 10.1016/j.envpol.2013.02.031

Xu, D., and Chen, J. (2013). Accurate estimate of turbulent dissipation rate using PIV data. *Exp. Thermal Fluid Sci*. 44, 662–672. doi: 10.1016/j.expthermflusci.2012.09.006

Zimmermann, R., Gasteuil, Y., Bourgoin, M., R., B., Pumir, A., and Pinton, J. F. (2011). Rotational intermittency and turbulence induced lift experienced by large particles in a turbulent flow. *Phys. Rev. Lett*. 106:154501. doi: 10.1103/PhysRevLett.106.154501

Conflict of Interest: The authors declare that the research was conducted in the absence of any commercial or financial relationships that could be construed as a potential conflict of interest.

Copyright © 2020 Bordoloi, Variano and Verhille. This is an open-access article distributed under the terms of the Creative Commons Attribution License (CC BY). The use, distribution or reproduction in other forums is permitted, provided the original author(s) and the copyright owner(s) are credited and that the original publication in this journal is cited, in accordance with accepted academic practice. No use, distribution or reproduction is permitted which does not comply with these terms.

frontiers in Marine Science

ORIGINAL RESEARCH
published: 08 July 2020
doi: 10.3389/fmars.2020.00494

Enhanced Light Absorption by Horizontally Oriented Diatom Colonies

Malcolm McFarland[1]*, *Aditya R. Nayak*[1,2], *Nicole Stockley*[1], *Michael Twardowski*[1] and *James Sullivan*[1]

[1] Harbor Branch Oceanographic Institute, Florida Atlantic University, Fort Pierce, FL, United States, [2] Department of Ocean and Mechanical Engineering, Florida Atlantic University, Boca Raton, FL, United States

Through *in situ* holographic imaging of undisturbed water, diatom colonies with high aspect ratios have been found to exhibit preferential horizontal orientation within high biomass subsurface layers. We analyzed holographic video to determine the abundance, size, and orientation of colonies over several vertical profiles from the surface to ∼25 m depth. A geometric optics model based on these measurements was then used to estimate light absorption by phytoplankton throughout the water column. Results show a substantial increase in absorption of downwelling irradiance (up to 24.5%) for horizontally oriented colonies when compared to randomized orientations. The effect can be attributed to maximization of the projected area of colonies when oriented perpendicular to the direction of incident light. Formation of high aspect ratio cells and colonies may represent an adaptation to maximize light harvesting in low light environments through interaction with the low velocity shear fields commonly found along pycnoclines at the base of the surface mixed layer. The effect of orientation on light absorption by large chain forming diatoms could influence their abundance and distribution in the ocean as well as the broader structure and function of marine ecosystems.

Keywords: phytoplankton, orientation, diatoms, absorption, holography, optical model, thin layer, *Ditylum brightwellii*

OPEN ACCESS

Edited by:
Alberto Basset,
University of Salento, Italy

Reviewed by:
Jun Sun,
Tianjin University of Science and Technology, China
Johannes Wilhelm Goessling,
International Iberian Nanotechnology Laboratory (INL), Portugal

***Correspondence:**
Malcolm McFarland
mmcfarland@fau.edu

Specialty section:
This article was submitted to Marine Ecosystem Ecology, a section of the journal Frontiers in Marine Science

Received: *31 January 2020*
Accepted: *03 May 2020*
Published: *08 July 2020*

Citation:
McFarland M, Nayak AR, Stockley N, Twardowski M and Sullivan J (2020) Enhanced Light Absorption by Horizontally Oriented Diatom Colonies. Front. Mar. Sci. 7:494. doi: 10.3389/fmars.2020.00494

1. INTRODUCTION

Marine phytoplankton, responsible for approximately half of global primary production, are fundamental components of marine food webs and play a critical role in biogeochemical cycles linked to climate change (Field et al., 1998). Large phytoplankton (>20 μm) contribute substantially to the downward flux of carbon in the ocean, and large size classes are often dominated by diatoms that form cells or colonies with high aspect ratios (length/width > 10) (Boyd and Newton, 1995, 1999; Smetacek, 1999; Tréguer et al., 2018). It has generally been assumed that these non-spherical phytoplankton are randomly oriented throughout the water column due to turbulence (Basterretxea et al., 2020). However, recent observations using *in situ* holographic imaging suggest that preferential horizontal orientation may be a common occurrence in the ocean (Talapatra et al., 2013; Nayak et al., 2018). Theoretical and laboratory based experimental studies have shown that non-random orientations result from interaction of particles with low velocity shear fields (Jeffery, 1922; Karp-Boss and Jumars, 1998). In the ocean, shear fields capable of orienting particles can occur within the pycnocline, at the base of the surface mixed layer where

phytoplankton biomass is often enhanced (e.g., thin layers or deep chlorophyll maxima, Sullivan et al., 2010b). The resulting orientation can influence light absorption by large phytoplankton and may have important ecological consequences for species-specific growth rates, community structure, and the efficiency of the biological pump (Basterretxea et al., 2020).

To survive in the aquatic environment, phytoplankton require light for photosynthesis and growth. Absorption of light by an individual phytoplankton cell or colony is a function of its size, shape, orientation, and the complex refractive index of its components (Morel and Bricaud, 1986; Bohren and Huffman, 1998). Size, shape, and orientation relative to incident light define the projected area of cells. Light intercepted within this projected area is attenuated exponentially along optical paths through cells by absorption and scattering. Light absorbed by photosynthetic pigments is used to drive the biochemical reactions of photosynthesis, ultimately providing the energy needed for growth. The exponential decrease in intensity results in the self-shading of intracellular photosynthetic pigments, also referred to as the "package effect" (Duysens, 1956; Kirk, 1976; Bricaud et al., 1983, 1995). This self-shading increases with cell size and reduces the total amount of light absorbed by a given amount of pigment (e.g., chlorophyll), cellular volume, or unit of biomass (e.g., carbon).

For non-spherical cells and colonies (most phytoplankton $>20\ \mu$m, Fogg, 1991; Tomas, 1997), both the projected area and optical path lengths through cells change with orientation relative to the incident light direction. Particles with large aspect ratios, such as colonial diatoms, will maximize their projected area and minimize package effects when their major axis is oriented perpendicular to the direction of incident light. In the ocean, light mostly propagates vertically from surface to depth, therefore, horizontal orientation of elongate phytoplankton will tend to maximize light capture efficiency and increase chlorophyll or biomass specific absorption. In deep or turbid water where light is limiting, this may have a significant impact on rates of photosynthesis and growth.

Currently available methods cannot measure absorption by individual phytoplankton in their natural, undisturbed orientation. Bottle samplers and *in situ* absorption meters that require pumping of seawater through a reflective flow cell (e.g., ac meters from Sea-bird Scientific, Bellevue, WA) alter natural orientations and size distributions by subjecting particles, cells, and colonies to induced turbulent shear stress. Alternatively, phytoplankton size, shape, and orientation can be observed directly through imaging and their optical absorption can be subsequently modeled. Over the last two decades digital holographic techniques have been developed that can image phytoplankton *in situ* at video frame rates with minimal disturbance of their natural orientation (Katz et al., 1999; Katz and Sheng, 2010; Talapatra et al., 2013; Nayak et al., 2018). Holography overcomes the narrow depth of field associated with high magnification in standard optical imaging systems and allows for in-focus imaging of particles in a volume of sea water large enough to provide statistically meaningful observations (e.g., several mL). Optically important morphological characteristics of particles such as length, width, projected area, and orientation can be measured directly through automated analysis of reconstructed images.

Measured particle characteristics can be used to calculate optical properties through a variety of modeling techniques (Mishchenko et al., 2000; Kahnert, 2003; Wriedt, 2009). Previous studies have used optical modeling to investigate light scatter by oriented, non-spherical bacterial cells and found that optical backscatter could be enhanced by up to 30% under typical oceanic shear flows (Marcos et al., 2011). Unlike bacteria, however, many large phytoplankton cells and colonies have high aspect ratios (>10) and their Equivalent Spherical Diameter (ESD) is large compared to the wavelengths (λ) of light (size parameters $\pi ESD/\lambda > 150$). This can be problematic for methods that explicitly solve Maxwell's Equations for simple particle geometries (i.e., Lorenz-Mie theory, T-Matrix). Finite difference time domain (FDTD) models can accommodate particles of any shape and orientation but are computationally expensive and impractical to compute for populations of many large particles with distinct characteristics. Although an approximation, geometric optics methods (i.e., ray tracing) are efficient to compute and provide accurate results for particles much larger in size than the wavelengths of incident visible light (Macke et al., 1995; Yang and Liou, 1995).

In this study we assess the effect of orientation on light absorption by natural phytoplankton populations. We measured the concentration, length, width, and vertical orientation of large phytoplankton colonies with a submersible digital holographic microscope and used geometric optics to model their light absorption over several depth profiles. The data was acquired in East Sound, WA (USA), a productive and hydrographically constrained coastal fjord where stratification and thin layers of phytoplankton are common (Dekshenieks et al., 2001; McManus et al., 2003).

2. METHODS

2.1. Study Site

In situ holographic video and optical measurements were acquired from East Sound, WA in September, 2015. East Sound is located at 48.64°N latitude, 122.87°W between the Strait of Juan de Fuca and Strait of Georgia. It is 13 km long, 2 km wide, has a mean depth of 30 m, and is surrounded on the north, east, and west by Orcas Island. The sound is open to the south but flow is restricted by a partial sill. Currents and mixing are primarily driven by wind and tides. Due to its depth and restricted hydrography, the water column is often strongly stratified and thin layers of phytoplankton frequently form along the pycnocline (Dekshenieks et al., 2001; Rines et al., 2002). Multiple profiles were conducted over a 2 week field effort, and a subset of three with the highest particle concentrations and strongest orientation were selected for modeling of particulate absorption. The three profiles presented here were collected near the middle of the sound on the morning of September 22nd.

2.2. *In situ* Holography, Water Column Structure, and Optics

The digital holographic microscope (HOLOCAM) used an in-line configuration to image diffraction patterns produced by

cells, colonies, and other particles over a 4 cm open path. The design consisted of two waterproof housings containing an Imperx digital camera and laser light source connected by a rigid support. The 660 nm nanosecond pulsed laser was spatially filtered, expanded, and collimated to produce a coherent plane wave light source. An objective lens in front of the camera was used to increase magnification and position the holographic imaging plane near the edge of the sample volume. The hologram field of view was 9.39 × 9.39 mm, the resolution was 4.58 μm pixel^{-1}, and the total volume imaged per frame was 3.53 mL. Digital holographic video (2,048 × 2,048 pixels) was acquired and viewed in real time at 15 frames per second as the instrument descended slowly through the water column. Video was recorded on a shipboard disk array connected to the submersible unit by a fiber optic cable. The submersible housings had a smooth, hydrodynamic shape designed to minimize any turbulent shear within the sample volume that could alter natural particle orientations when vertically profiling at 5–10 cm per second (Nayak et al., 2018).

The submersible instrument package also included a Sea-Bird Scientific SBE 49 FastCAT conductivity, temperature, and depth sensor (CTD), a WET Labs ac9 multispectral optical absorption and attenuation meter, a WET Labs bb9 multispectral optical backscatter sensor, a WET Labs DH-4 data logger, and a Nortek Vector acoustic doppler velocimeter (ADV) with an inertial motion unit (IMU). The CTD provided information on package depth, descent rate, and water column structure in real time. Data from the ADV IMU was used to correct for package tilt during deployment. Optical sensors were used to determine chlorophyll and particle distributions throughout the water column with high vertical resolution. The ac9 measured the total absorption coefficient, a_{pg}, including particulate and dissolved water components. The instrument was calibrated and data was corrected according to Twardowski et al. (1999) and Stockley et al. (2017). The bb9 backscatter sensor was calibrated and the backscatter coefficient b_b was determined according to Sullivan et al. (2013). Chlorophyll was calculated from a_{pg} spectra using the line height method and a chlorophyll specific absorption line height of 0.0104 m^2 mg^{-1} at 676 nm (Roesler and Barnard, 2013; Nardelli and Twardowski, 2016). The complete instrument package was slightly negatively buoyant and allowed to freely descend through the water column during data acquisition at a rate of 5–6 cm s^{-1} decoupled from ship motion (Cowles et al., 1998; Rines et al., 2010; Sullivan et al., 2010a). The package was deployed from a 50 foot vessel that remained anchored during data collection to minimize drag on the instrument package. All measurements, including holographic video frames, were associated with a common time stamp that was used to align data points in post processing.

2.3. Phytoplankton Sampling and Identification

Depth integrated net tows using a 20 μm mesh net were conducted in coordination with profiles. The net was lowered by hand from the surface to ∼15 m depth over a period of 5–10 minutes while the research vessel was anchored. Current flow past the ship ensured adequate volumes of water were captured by the net. Contents of the net tow samples were analyzed immediately on board the research vessel with a compound microscope at 100x to 400x magnification. Phytoplankton were identified to the lowest taxonomic level possible in water mounts using phase contrast illumination. Identifications were based on morphological features that could be visualized with light microscopy following published descriptions of taxa (Round et al., 1990; Tomas, 1997; Hoppenrath et al., 2009, and references therein) and extensive previous work conducted in the area (Rines et al., 2002; McManus et al., 2003; Menden-Deuer, 2008; McFarland et al., 2015). Identification of taxa was used to choose appropriate estimates of previously published intracellular chlorophyll concentrations needed for modeling, to provide an ecological context to results, and to better interpret holographic images which were more limited in resolution than standard microscopy.

2.4. Holographic Reconstruction and Analysis

Processing of digital holograms consisted of background subtraction, image reconstruction throughout the sample volume, and formation of an extended depth of field (EDF) image. The subtracted background image was an average of a subset of frames ($\geq$ 50) recorded over each depth profile. Digital holograms were numerically reconstructed using the Kirchhoff-Fresnel convolution kernel (Katz and Sheng, 2010). Reconstruction was performed for 80 focal planes spaced at 500 μm intervals over the 4 cm sample path. The gradient of each reconstructed plane was divided into 32 × 32 pixel windows and a composite, EDF image was generated by selecting the windows from all planes with the greatest number of pixels above a fixed threshold value. The threshold was pre-determined manually for a subset of reconstructed planes and subsequently applied to all holograms. To avoid duplicate imaging of particles and reduce the total computation time, only every third frame from the holographic video was processed resulting in an effective frame rate of 5 per second.

Analysis of EDF images included frequency filtering, segmentation, and region analysis. EDF images were first processed with a band-pass Gaussian frequency filter to reduce high frequency noise and low frequency artifacts (e.g., uneven background intensity). Images were then segmented by thresholding at a fixed, pre-determined intensity value. As for EDF image generation, the intensity threshold was determined manually for a subset of images and later applied to all images. Regions within 10 pixels (45.8 μm) distance from each other were merged to compensate for the fragmentation of regions caused by segmentation. The major axis orientation of each region was determined from the eigenvectors and eigenvalues of the covariance matrix of the segmented region's pixel coordinates (second order central moments). Measured angles ranged from 0–90 degrees. Small angles indicated horizontal orientation while angles close to 90 degrees indicated vertical orientation. The length of each region was defined as the Feret diameter (caliper diameter) along the direction of the major axis. Width was

determined by scanning along the major axis and computing the mean of all scan lengths perpendicular to the major axis. **Figure 1** illustrates the orientation, length, and width measurements for a typical diatom colony. Regions smaller than 100 μm (22 pixels) in length or with an aspect ratio smaller than 3 were ignored to focus only on particles with sizes and shapes capable of measurable orientation in response to small scale shear fields. These criteria effectively isolated long chain forming diatom colonies from other particles in EDF images. The orientation distribution throughout the water column (i.e., the number of particles at a given orientation and depth) was determined using a two dimensional Gaussian kernel density estimator with standard deviations of 2 degrees and 25 cm calculated over 128 bins in each dimension.

2.5. Optical Absorption Modeling

A simplified geometric optics model based on the method of Yang and Liou (1995, 1996) was used to estimate the absorption cross sections of individual diatom colonies at a wavelength of 676 nm, the red chlorophyll absorption peak. This ray tracing approach was selected for its ability to model large, high aspect ratio particles at any orientation relative to incident light with greater computational efficiency than other available methods. To focus exclusively on diatom colonies capable of orientation, the absorption cross section was modeled only for particles in EDF images larger than 100 μm in length and with an aspect ratio greater than 3. Particles were represented as prolate spheroids with major and minor axes lengths determined from image analysis as described above. For each spheroid, the model determined absorptance (the proportion of incident radiant flux absorbed) along ray paths while accounting for external surface reflection, refraction, and internal reflection according to the Fresnel equations (**Figure 2**) (Kirk, 1994; Yang and Liou, 1996; Bohren and Huffman, 1998; Hecht, 2002). All rays originated from above and included 6 internal reflections. Absorptance along intracellular ray paths was calculated from the decrease in intensity according to the Beer-Lambert law using an absorption coefficient for intracellular material (a_{cm}) based on a range of possible intracellular chlorophyll concentrations (C_i). The absorption cross section (S_a) for each spheroid was determined by numerical integration (Shampine, 2008) of absorptance over its projected area (σ). The absorption efficiency (Q_a) was calculated as:

$$Q_a = \frac{S_a}{\sigma}$$

This dimensionless parameter describes the ratio of light absorbed by the particle to the light incident on its projected area in the direction of propagation (Morel and Bricaud, 1981). Vertical profiles of the phytoplankton absorption coefficient (a_{ph} m^{-1}) for the modeled populations were then computed by summing particle absorption cross sections within ~20 cm vertical depth bins and dividing by the volume analyzed (V) in each bin.

$$a_{ph} = \frac{\sum S_a}{V}$$

For all particles, we assumed a real refractive index of 1.035 relative to water (Aas, 1996) and a uniform intracellular chlorophyll distribution. Since C_i can vary substantially but could not be measured directly for modeled phytoplankton, results were computed for three different concentrations including 0.3, 1.0, and 3.0 kg m^{-3} following the range of values for diatoms reported in the literature (Morel and Bricaud, 1986; Haardt and Maske, 1987; Bricaud et al., 1988; Osborne and Geider, 1989; Agustí, 1991; Álvarez et al., 2017). The absorption coefficient of the intracellular material (a_{cm}) was calculated as the product of C_i and a chlorophyll specific absorption coefficient, a^*_{ph}, at 676 nm.

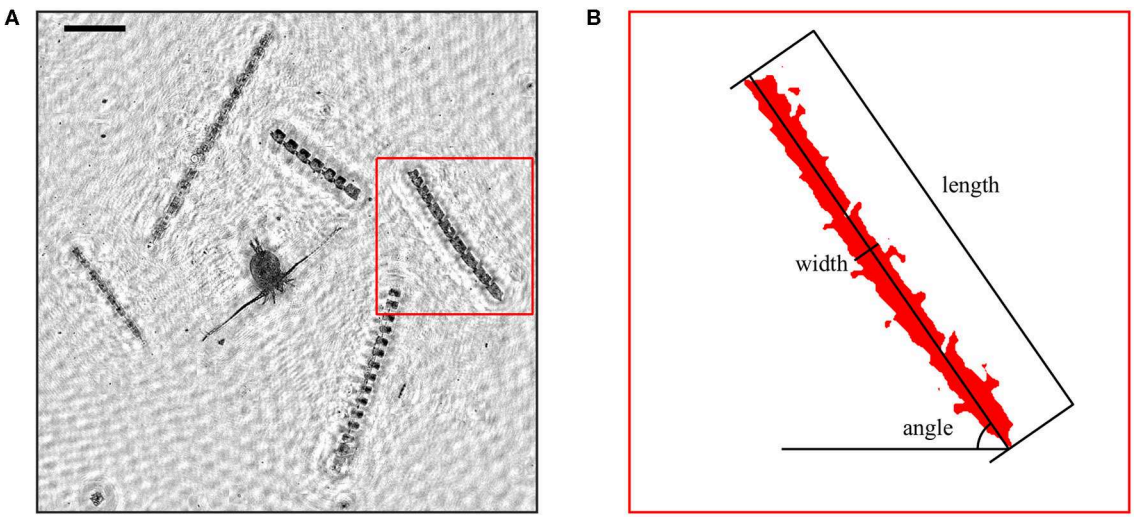

FIGURE 1 | (A) A portion of an extended depth of field (EDF) image obtained after holographic reconstruction showing multiple colonies of *Ditylum brightwellii* and a copepod. Scale bar (upper left) represents 500 μm. **(B)** Illustration of the length, width, and angle measurements from image analysis for one *D. brightwellii* colony.

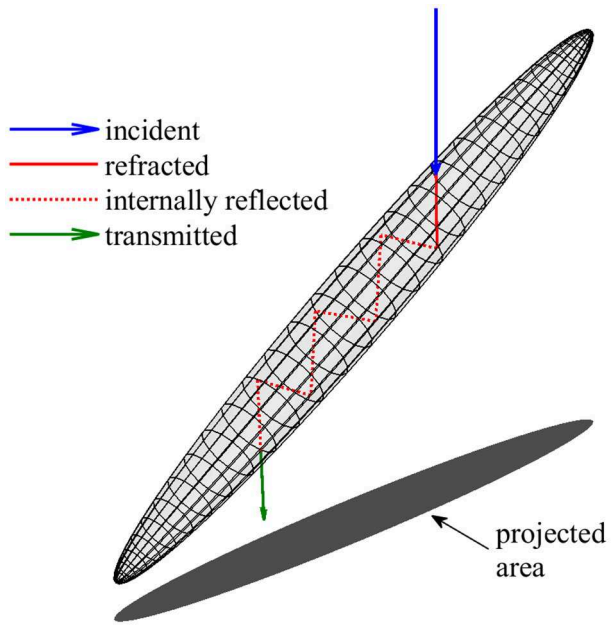

FIGURE 2 | Illustration of the geometric optics model used to estimate absorption by diatom colonies. Cells and colonies are represented by prolate spheroids with major axes, minor axes, and orientation determined from image analysis (**Figure 1**). Modeled ray paths originated from above and included 6 internal reflections. Absorption cross section was determined from the decrease in radiant flux along internal ray paths (shown in red) and integration over the vertically projected area.

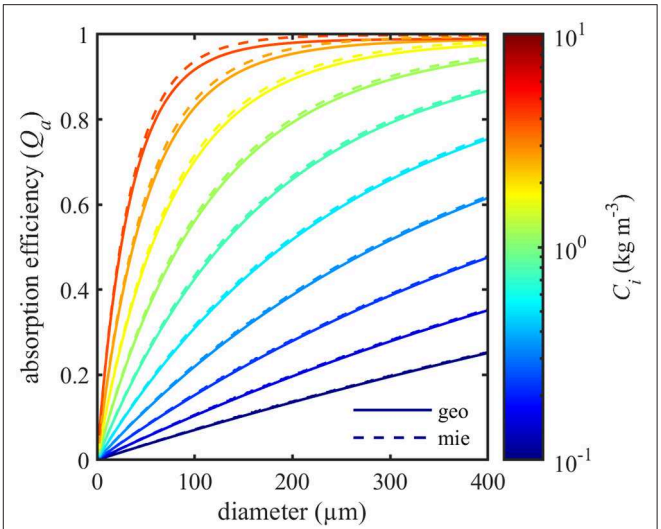

FIGURE 3 | Comparison of absorption efficiencies (Q_a) at 676 nm calculated with geometric optics (geo, solid lines) and Lorenz-Mie theory (mie, dashed lines) for spheres of various size and intracellular chlorophyll content (C_i).

A value of 0.014 m^2 mg^{-1} was used for a^*_{ph}, appropriate for the large coastal phytoplankton found in East Sound (Bricaud et al., 1995; Roesler and Barnard, 2013).

Vertical profiles of a_{ph} at 676 nm were modeled for phytoplankton populations in their measured orientations (a_{ph}) and in simulated random orientations (a^r_{ph}) by assigning randomly generated angles to all spheroids. Random angles were assigned five times and a^r_{ph} was determined as the mean over all randomized orientations. We computed the parameter Δa_{ph} as the difference between a_{ph} and a^r_{ph} ($\Delta a_{ph} = a_{ph} - a^r_{ph}$). Δa_{ph}, therefore, represents the effect of the measured, non-random orientation distribution on absorption. Positive values indicate a net increase in a_{ph} relative to random orientations while negative values indicate a net decrease.

2.6. Model Validation

Accuracy of the geometric optics model was assessed by comparison with Lorenz-Mie theory for homogeneous spheres of various diameter and complex refractive index (Bohren and Huffman, 1998). The imaginary part of the complex refractive index (n') was calculated according to Morel and Bricaud (1986):

$$n' = \frac{a_{cm}\lambda}{4\pi m}$$

Where a_{cm} is the intracellular absorption coefficient at wavelength λ (676 nm) and m is the corresponding refractive index of sea water (1.3368) at a temperature of 12°C and salinity of 30 PSU (Quan and Fry, 1995). Model estimates of Q_a at 676 nm were compared for intracellular chlorophyll concentrations between 0.1 and 4 kg m^{-3} and cell diameters ranging from 2 to 400 μm (**Figure 3**). The geometric optics model produced slightly smaller estimates of absorption than Lorenz-Mie theory. Comparison of model outputs showed that absorption efficiencies varied by less than 2.5% between the two models for this range of sizes and refractive indices. The largest difference between the models was found at high intracellular chlorophyll concentrations for 60 μm diameter spheres. Differences decreased with increasing particle size.

3. RESULTS

Vertical profiles of density, backscatter, and chlorophyll *a* for three separate casts revealed shallow thin layers of high phytoplankton biomass along the pycnocline (**Figure 4**). EDF images reconstructed from *in situ* holographic video showed these thin layers to be composed primarily of the colonial diatom *Ditylum brightwellii* (**Figure 5**). Other less abundant chain forming diatoms included *Eucampia zodiacus*, various species of *Chaetoceros*, *Dactyliosolen fragillisimus*, *Skeletonema* sp., *Stephanopyxis turris*, *Leptocylindrus danicus*, *Cerataulina pelagica*, and *Pseudo-nitzschia* sp. Phytoplankton samples collected with a net tow and examined with a conventional microscope confirmed these identifications. Backscatter profiles also show an increase in non-algal or detrital particles at depths >15 m, most likely due to sinking detrital material and particle flocculation (**Figure 4**, Alldredge et al., 2002; Sullivan et al., 2005; McFarland et al., 2015).

Preferential horizontal orientation of long diatom chains was clearly visible in EDF images acquired within the thin

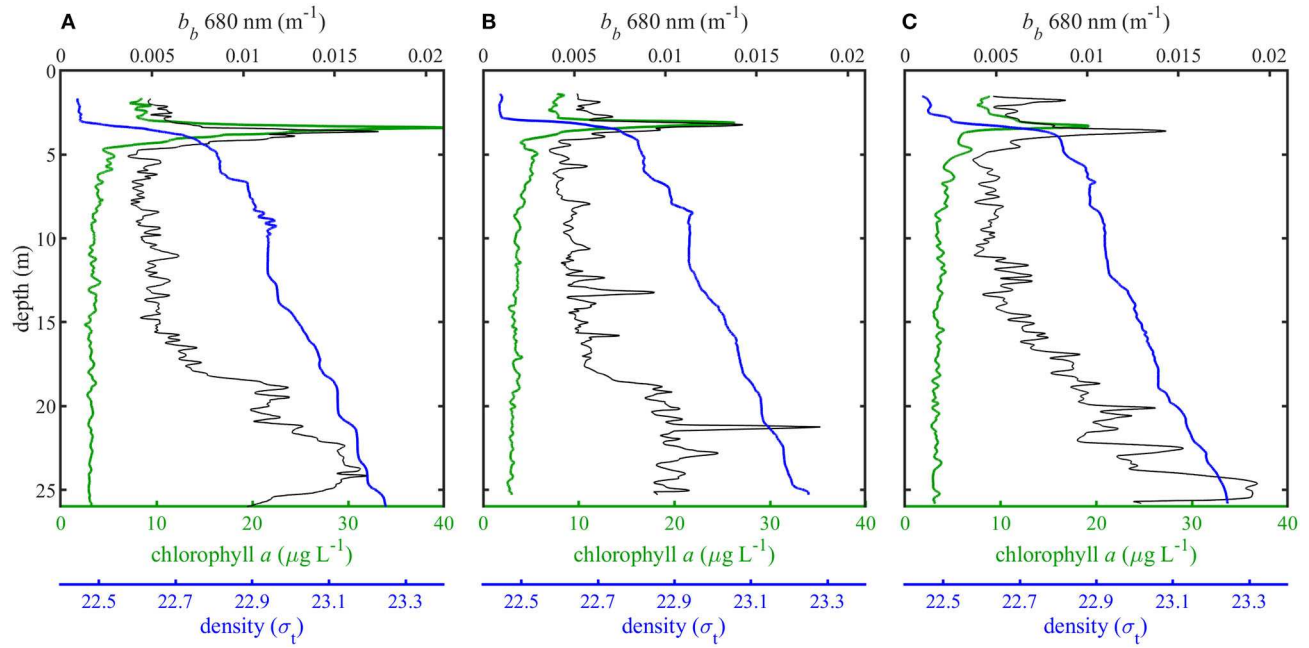

FIGURE 4 | Density (σ_t), chlorophyll *a* concentrations (μg L^{-1}), and backscatter (m^{-1}) for each of three vertical profiles **(A–C)**.

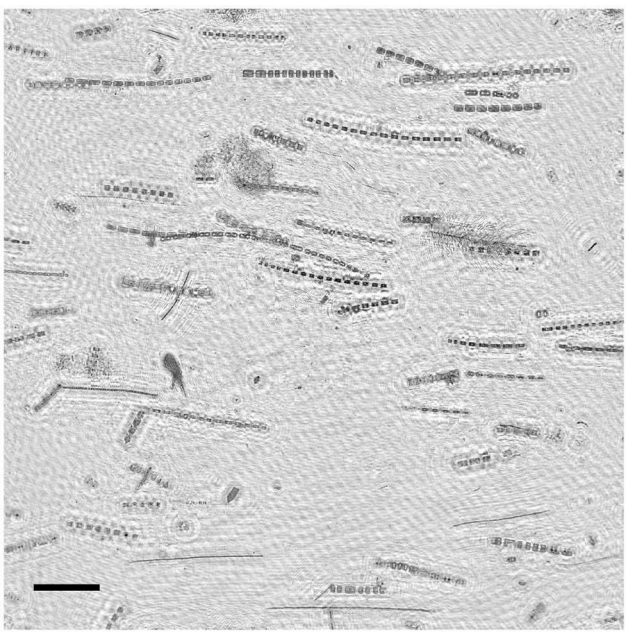

FIGURE 5 | Example extended depth of field image from the phytoplankton thin layer in profile C showing predominantly horizontal orientation of diatom colonies. Scale bar (lower left) represents 1 mm.

layer (**Figure 5**). The orientation distributions for each profile (**Figure 6**) revealed high concentrations of large (>100 µm), horizontally oriented particles at 3–4 m depth with angles below ∼20 degrees. Particle concentrations were lower and orientation distributions were more uniform above and below the thin layer. As seen with backscatter, particle concentrations determined from image analysis were also higher at depths >20 m, especially in profile A (**Figure 6A**), most likely due to sinking and flocculating detritus (Alldredge et al., 2002). Total modeled particle concentrations for all orientations ranged from 5.45 to 22.3 particles mL^{-1}. The mean volume analyzed for estimates of a_{ph} at each depth was 61.2 mL. This varied somewhat with the descent rate of the instrument package (standard deviation of 24.2 mL).

Model results show absorption peaks in vertical profiles corresponding to the depth of the thin layer (**Figure 7**). Modeled a_{ph} (676 nm) at the thin layer peak for each C_i is shown in **Table 1**. Intracellular chlorophyll *a* concentrations had a substantial impact on modeled values of a_{ph} which increased approximately five fold between the lowest and highest values of C_i (0.3 and 3 kg m^{-3}) at the thin layer peak. A slight increase in modeled a_{ph} values at depths >20 m was seen in profile A (**Figure 7**), but no increase was observed in measured a_{pg} at these depths despite higher backscatter (**Figure 4**).

The effect of orientation on absorption, Δa_{ph}, is shown in **Table 1** and in **Figure 6** overlaid on the observed orientation distributions for each profile. We found positive modeled values of Δa_{ph} for colonies within the thin layer. Δa_{ph} also increased with increasing C_i. When compared to modeled and measured absorption (**Table 1**), values of Δa_{ph} ranged from 4.5 to 24.5% of modeled a_{ph} and from 0.7 to 31% of measured a_{pg}. There was no increase in Δa_{ph} at depths >20 m in profile A despite indication of some preferential horizontal orientation.

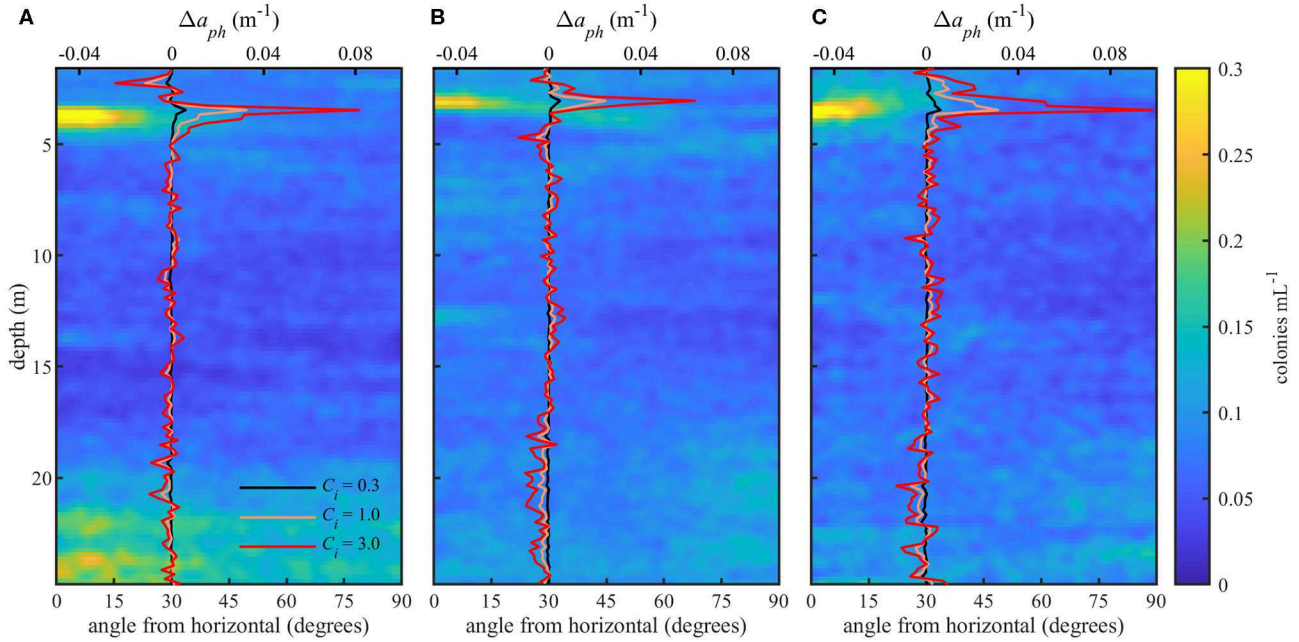

FIGURE 6 | Orientation distributions (bottom x-axis) for three profiles **(A–C)** and modeled change in absorption (Δa_{ph}) due to orientation (top x-axis) at 0.3, 1.0, and 3.0 kg m^{-3} intracellular chlorophyll concentrations (C_i). Color scale shows the concentration of colonies at a particular depth and orientation. Modeled Δa_{ph} values are the difference between measured and simulated random orientations.

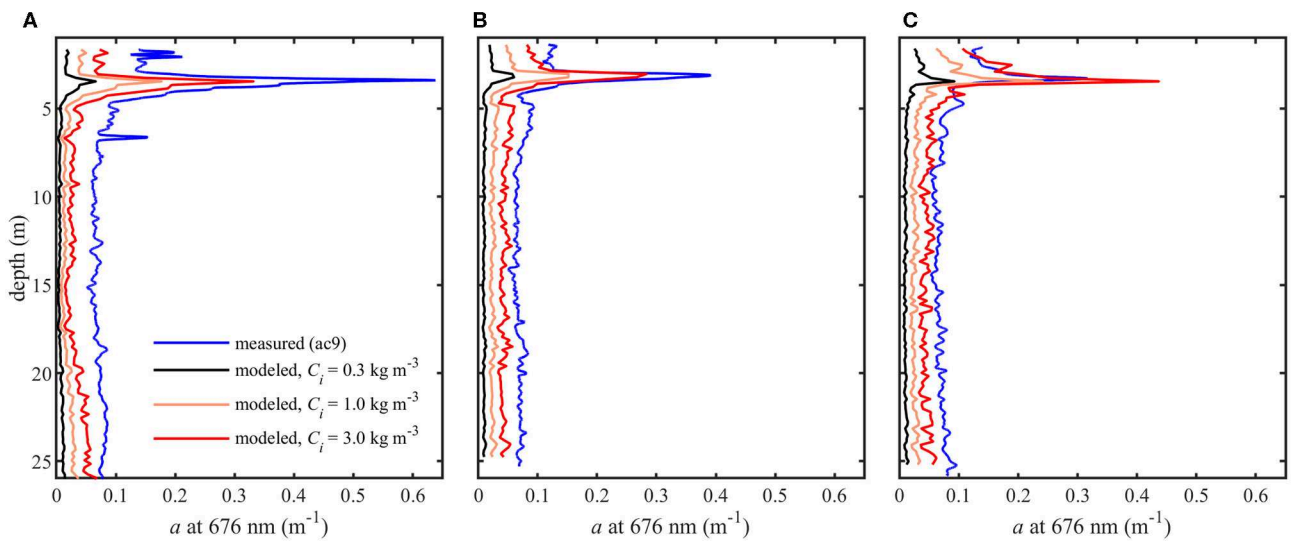

FIGURE 7 | Modeled phytoplankton absorption coefficients (a_{ph}) at 0.3, 1.0, and 3.0 kg m^{-3} intracellular chlorophyll concentrations (C_i) and measured total absorption coefficients (a_{pg}) at 676 nm for three profiles **(A–C)**.

4. DISCUSSION

The optical model used in this study showed an increase in absorption of 4.5–24.5% for populations of horizontally oriented diatom colonies relative to random orientations. Computations were based on the measured orientation and size distribution of a natural phytoplankton community, and the modeled effects were repeated over three separate profiles. Results suggest that horizontal orientation helps maximize light absorption by relatively large (>100 μm length), high aspect ratio (length/width > 3) phytoplankton. This may allow horizontally oriented cells and colonies to achieve higher rates of photosynthesis and growth under light limited conditions.

TABLE 1 | a_{ph} and Δa_{ph} (m^{-1}) at 676 nm modeled for colonial diatoms using three C_i values (0.3, 1.0, and 3.0 kg m^{-3}).

	C_i (kg m^{-3})							
	0.3	1.0	3.0	0.3	1.0	3.0		
Profile	Modeled a_{ph} (m^{-1})			Modeled Δa_{ph} (m^{-1})			Measured a_{pg} (m^{-1})	Chlorophyll *a* (mg m^{-3})
A	0.0661	0.1769	0.3317	0.0061	0.0324	0.0814	0.6381	41.4
B	0.0603	0.1521	0.2832	0.0027	0.0246	0.0634	0.3917	26.3
C	0.0925	0.2413	0.4366	0.0062	0.0312	0.0981	0.3168	19.2

Measured a_{pg} at 676 nm, and total chlorophyll a concentrations (μg L^{-1}) are also shown. All values were obtained within the thin layer peak for each profile.

An increase in modeled values of Δa_{ph} within the thin layer indicated an increase in phytoplankton absorption caused by their horizontal orientation. At depths >20 m, however, the relative proportion of horizontally oriented particles in profile A (**Figure 6**) appeared insufficient to influence values of Δa_{ph}. The increase in Δa_{ph} with increasing C_i showed the effect of orientation on absorption was more pronounced for higher intracellular pigment concentrations. As expected, measured values of a_{pg} were generally higher than modeled values since we modeled a_{ph} for only a portion of the phytoplankton community and measured a_{pg} included some absorption by dissolved organic material. However, modeled a_{ph} exceeded measured values at the thin layer peak in profile C for the highest C_i value (**Table 1**). This may be due to the instruments measuring different parcels of water, or may indicate that a C_i value of 3.0 kg m^{-3} was not representative of these phytoplankton. Alternatively, it may indicate an underestimation of a_{pg} by the ac meter which randomizes particle orientations within the instrument's pumped flow cell.

The increase in absorption can be primarily attributed to an increase in the projected area of colonies as their major axes become perpendicular to the direction of incident light. Assuming incident illumination from above, horizontal orientation results in a net increase in absorption cross section ($S_a = \sigma Q_a$) despite a decrease in Q_a relative to vertical. For a typical *D. brightwellii* colony with a width of 50 μm, length of 800 μm, and C_i of 1.0 kg m^{-3}, Q_a decreases by half while σ increases by a factor of 16 as orientation changes from vertical to horizontal. The effect is especially pronounced for cells with high C_i since Q_a remains high in any orientation. Closer inspection of model output shows almost all absorption occurs over the initial refracted internal ray path and the path of the first internal reflection. These path lengths are longer for vertical orientations resulting in higher Q_a and greater self shading of pigments (i.e., package effects).

In this study, horizontally oriented colonies were found in a shallow (3–4 m deep) thin layer of high phytoplankton biomass along the pycnocline. Previous studies have shown similar particle orientation within regions of low velocity shear and low turbulent dissipation (Talapatra et al., 2013; Nayak et al., 2018). Orientation distributions of these natural particle assemblages closely match those predicted by physical models of spheroidal particle motion in simple shear flow (Jeffery, 1922; Nayak et al., 2018). The low shear conditions that promote horizontal orientation can be found along density gradients and at the base of surface mixed layers throughout the ocean. Such locations likely represent an ecological niche for which elongate, colonial diatoms are well-adapted. Their interaction with small scale shear fields could be considered a form of passive heliotropism, similar to the solar tracking behavior of plant leaves (Niinemets, 2010; Kutschera and Briggs, 2016). Large diatoms may even adjust their buoyancy to remain within layers of low shear to optimize light and nutrient resource acquisition (Moore and Villareal, 1996; Richardson et al., 1996; Cullen and MacIntyre, 1998; Klausmeier and Litchman, 2001).

Enhanced light absorption by horizontally oriented diatom colonies could also have an impact on phytoplankton community structure and the biological pump. Phytoplankton growth is often light limited at the base of surface mixed layers. Even a modest increase in absorption under these light limited conditions is likely to substantially increase rates of photosynthesis and growth (Edwards et al., 2015). Orientation may allow large chain forming diatoms to more effectively compete for available light at depths where shear is low (Litchman and Klausmeier, 2001; Yoshiyama et al., 2009). These large forms also sink more readily, transport carbon more efficiently to depth, and their relative abundance may influence net carbon export from surface layers (Smetacek, 1999; Tréguer et al., 2018).

Although the model incorporated fundamental morphological features of diatom colonies such as length and width, prolate spheroids provided only a coarse approximation of true diatom morphology. The shape and three dimensional structure of actual cells and colonies is considerably more complex (Round et al., 1990). The model also assumes a homogeneous intracellular distribution of chlorophyll. In eukaryotic phytoplankton cells, however, chlorophyll is embedded in thylakoid membranes and packaged within chloroplasts that have a variable and non-uniform distribution throughout the cell. Furthermore, incident light within the model came directly from above and propagated straight down. The actual propagation of light in the ocean is not so simple or uniform, although natural light fields are dominated by downwelling light (Kirk, 1994; Mobley, 1994). Despite lacking these more detailed morphological and optical features, we believe the modeled results reflect a substantial effect of orientation on light harvesting by colonial diatoms and other elongate forms. The effect appears strong enough to have

important ecological consequences to the broader structure and function of marine ecosystems.

DATA AVAILABILITY STATEMENT

The datasets generated for this study are available on request to the corresponding author.

AUTHOR CONTRIBUTIONS

MM was responsible for collection and processing of holograms, analysis of holographic data, optical modeling, and manuscript preparation. AN also participated in holographic data collection, processing, and analysis, and assisted with manuscript preparation. NS assisted with data collection and was responsible for processing of optical data. MT and JS coordinated field data collection and provided project guidance. All authors contributed to the article and approved the submitted version.

FUNDING

Funding for this study was provided by the Office of Naval Research, Coastal Geophysics Program, contract # N00014-15-1-2628 (MT and JS). MM, AN, and JS were also supported by National Science Foundation grants OCE-1657332 and OCE-1634053.

ACKNOWLEDGMENTS

We thank Alan Weidemann, Bradley Penta, and the Naval Research Laboratory for their assistance and participation in the field research for this project.

REFERENCES

Aas, E. (1996). Refractive index of phytoplankton derived from its metabolite composition. *J. Plankton Res.* 18, 2223–2249. doi: 10.1093/plankt/18.12.2223

Agustí, S. (1991). Allometric scaling of light absorption and scattering by phytoplankton cells. *Can. J. Fish. Aquat. Sci.* 48, 763–767. doi: 10.1139/f91-091

Alldredge, A. L., Cowles, T. J., MacIntyre, S., Rines, J. E. B., Donaghay, P. L., Greenlaw, C. F., et al. (2002). Occurrence and mechanisms of formation of a dramatic thin layer of marine snow in a shallow Pacific fjord. *Mar. Ecol. Prog. Ser.* 233, 1–12. doi: 10.3354/meps233001

Álvarez, E., Nogueira, E., and López-Urrutia, N. (2017). *In-vivo* single-cell fluorescence and the size-scaling of phytoplankton chlorophyll content. *Appl. Environ. Microbiol.* 83:e03317-16. doi: 10.1128/AEM.03317-16

Basterretxea, G., Font-Munoz, J. S., and Tuval, I. (2020). Phytoplankton orientation in a turbulent ocean: a microscale perspective. *Front. Mar. Sci.* 7:185. doi: 10.3389/fmars.2020.00185

Bohren, C. F., and Huffman, D. R. (1998). *Absorption and Scattering of Light by Small Particles*. New York, NY: John Wiley & Sons. doi: 10.1002/9783527618156

Boyd, P., and Newton, P. (1995). Evidence of the potential influence of planktonic community structure on the interannual variability of particulate organic carbon flux. *Deep Sea Res. I Oceanogr. Res. Pap.* 42, 619–639. doi: 10.1016/0967-0637(95)00017-Z

Boyd, P. W., and Newton, P. P. (1999). Does planktonic community structure determine downward particulate organic carbon flux in different oceanic provinces? *Deep Sea Res. I Oceanogr. Res. Pap.* 46, 63–91. doi: 10.1016/S0967-0637(98)00066-1

Bricaud, A., Babin, M., Morel, A., and Claustre, H. (1995). Variability in the chlorophyll-specific absorption coefficients of natural phytoplankton: analysis and parameterization. *J. Geophys. Res. Oceans* 100, 13321–13332. doi: 10.1029/95JC00463

Bricaud, A., Bedhomme, A. L., and Morel, A. (1988). Optical properties of diverse phytoplanktonic species: experimental results and theoretical interpretation. *J. Plankton Res.* 10, 851–873. doi: 10.1093/plankt/10.5.851

Bricaud, A., Morel, A., and Prieur, L. (1983). Optical efficiency factors of some phytoplankters. *Limnol. Oceanogr.* 28, 816–832. doi: 10.4319/lo.1983.28.5.0816

Cowles, T. J., Desiderio, R. A., and Carr, M. E. (1998). Small-scale planktonic structure: persistence and trophic consequences. *Oceanography* 11, 4–9. doi: 10.5670/oceanog.1998.08

Cullen, J. J., and MacIntyre, J. G. (1998). Behavior, physiology and the niche of depth-regulating phytoplankton. *Nato ASI Ser. G Ecol. Sci.* 41, 559–580.

Dekshenieks, M. M., Donaghay, P. L., Sullivan, J. M., Rines, J. E. B., Osborn, T. R., and Twardowski, M. S. (2001). Temporal and spatial occurrence of thin phytoplankton layers in relation to physical processes. *Mar. Ecol. Prog. Ser.* 223, 61–71. doi: 10.3354/meps223061

Duysens, L. N. M. (1956). The flattening of the absorption spectrum of suspensions, as compared to that of solutions. *Biochim. Biophys. Acta* 19, 1–12. doi: 10.1016/0006-3002(56)90380-8

Edwards, K. F., Thomas, M. K., Klausmeier, C. A., and Litchman, E. (2015). Light and growth in marine phytoplankton: allometric, taxonomic, and environmental variation. *Limnol. Oceanogr.* 60, 540–552. doi: 10.1002/lno.10033

Field, C. B., Behrenfeld, M. J., Randerson, J. T., and Falkowski, P. (1998). Primary production of the biosphere: Integrating terrestrial and oceanic components. *Science* 281, 237–240. doi: 10.1126/science.281.5374.237

Fogg, G. E. (1991). Tansley review No. 30. The phytoplanktonic ways of life. *N. Phytol.* 118, 191–232. doi: 10.1111/j.1469-8137.1991.tb00974.x

Haardt, H., and Maske, H. (1987). Specific *in vivo* absorption coefficient of chlorophyll a at 675 nm. *Limnol. Oceanogr.* 32, 608–619. doi: 10.4319/lo.1987.32.3.0608

Hecht, E. (2002). *Optics, 4th Edn.* Boston, MA: Addison-Wesley.

Hoppenrath, M., Elbrachter, M., and Drebes, G. (2009). *Marine Phytoplankton*. Stuttgart: Schweizerbart Science Publishers.

Jeffery, G. B. (1922). The Motion of Ellipsoidal Particles Immersed in a Viscous Fluid. *Proc. R. Soc. Lond. Ser. A* 102, 161–179. doi: 10.1098/rspa.1922.0078

Kahnert, F. M. (2003). Numerical methods in electromagnetic scattering theory. *J. Quant. Spectrosc. Radiat. Transfer* 79–80, 775–824. doi: 10.1016/S0022-4073(02)00321-7

Karp-Boss, L., and Jumars, P. A. (1998). Motion of diatom chains in steady shear flow. *Limnol. Oceanogr.* 43, 1767–1773. doi: 10.4319/lo.1998.43.8.1767

Katz, J., Donaghay, P. L., Zhang, J., King, S., and Russell, K. (1999). Submersible holocamera for detection of particle characteristics and motions in the ocean. *Deep Sea Res. I* 46, 1455–1481. doi: 10.1016/S0967-0637(99)00011-4

Katz, J., and Sheng, J. (2010). Applications of holography in fluid mechanics and particle dynamics. *Annu. Rev. Fluid Mech.* 42, 531–555. doi: 10.1146/annurev-fluid-121108-145508

Kirk, J. T. O. (1976). A theoretical analysis of the contribution of algal cells to the attenuation of light within natural waters. III. Cylindrical and spheroidal cells. *N. Phytol.* 77, 341–358. doi: 10.1111/j.1469-8137.1976.tb01524.x

Kirk, J. T. O. (1994). *Light and Photosynthesis in Aquatic Ecosystems, 2nd Edn.* Cambridge: Cambridge University Press. doi: 10.1017/CBO9780511623370

Klausmeier, C. A., and Litchman, E. (2001). Algal games: The vertical distribution of phytoplankton in poorly mixed water columns. *Limnol. Oceanogr.* 46, 1998–2007. doi: 10.4319/lo.2001.46.8.1998

Kutschera, U., and Briggs, W. R. (2016). Phototropic solar tracking in sunflower plants: an integrative perspective. *Ann. Bot.* 117, 1–8. doi: 10.1093/aob/mcv141

Litchman, E., and Klausmeier, C. A. (2001). Competition of phytoplankton under fluctuating light. *Am. Natural*. 157, 170–187. doi: 10.1086/318628

Macke, A., Mishchenko, M. I., Muinonen, K., and Carlson, B. E. (1995). Scattering of light by large nonspherical particles: ray-tracing approximation versus T-matrix method. *Optics Lett*. 20:1934. doi: 10.1364/OL.20.001934

Marcos, Seymour, J. R., Luhar, M., Durham, W. M., Mitchell, J. G., Macke, A., et al. (2011). Microbial alignment in flow changes ocean light climate. *Proc. Natl. Acad. Sci. U.S.A*. 108, 3860–3864. doi: 10.1073/pnas.1014576108

McFarland, M. N., Rines, J., Sullivan, J., and Donaghay, P. (2015). Impact of phytoplankton size and physiology on particulate optical properties determined with scanning flow cytometry. *Mar. Ecol. Prog. Ser*. 531, 43–61. doi: 10.3354/meps11325

McManus, M. A., Alldredge, A. L., Barnard, A. H., Boss, E., Case, J. F., Cowles, T. J., et al. (2003). Characteristics, distribution and persistence of thin layers over a 48 hour period. *Mar. Ecol. Prog. Ser*. 261, 1–19. doi: 10.3354/meps261001

Menden-Deuer, S. (2008). Spatial and temporal characteristics of plankton-rich layers in a shallow, temperate fjord. *Mar. Ecol. Prog. Ser*. 355:21. doi: 10.3354/meps07265

Mishchenko, M. I., Hovenier, J. W., and Travis, L. D. (2000). *Light Scattering by Nonspherical Particles: Theory, Measurements, and Applications*. San Diego, CA: Academic press. doi: 10.1016/B978-012498660-2/50029-X

Mobley, C. D. (1994). *Light and Water: Radiative Transfer in Natural Waters*. San Diego: Academic press.

Moore, J. K., and Villareal, T. A. (1996). Buoyancy and growth characteristics of three positively buoyant marine diatoms. Marine ecology progress series. *Oldendorf* 132, 203–213. doi: 10.3354/meps132203

Morel, A., and Bricaud, A. (1981). Theoretical results concerning light absorption in a discrete medium, and application to specific absorption of phytoplankton. *Deep Sea Res*. 28, 375–1. doi: 10.1016/0198-0149(81)90039-X

Morel, A., and Bricaud, A. (1986). "Inherent optical properties of algal cells including picoplankton: theoretical and experimental results," in *Photosynthetic Picoplankton*, eds T. Platt and W. K. W. Li (Ottawa: Department of Fisheries and Oceans) 521–559.

Nardelli, S. C., and Twardowski, M. S. (2016). Assessing the link between chlorophyll concentration and absorption line height at 676 nm over a broad range of water types. *Optics Exp*. 24, A1374–A1389. doi: 10.1364/OE.24.0A1374

Nayak, A. R., McFarland, M. N., Sullivan, J. M., and Twardowski, M. S. (2018). Evidence for ubiquitous preferential particle orientation in representative oceanic shear flows. *Limnol. Oceanogr*. 63, 122–143. doi: 10.1002/lno.10618

Niinemets, l. (2010). A review of light interception in plant stands from leaf to canopy in different plant functional types and in species with varying shade tolerance. *Ecol. Res*. 25, 693–714. doi: 10.1007/s11284-010-0712-4

Osborne, B. A., and Geider, R. J. (1989). Problems in the assessment of the package effect in five small phytoplankters. *Mar. Biol*. 100, 151–159. doi: 10.1007/BF00391954

Quan, X., and Fry, E. S. (1995). Empirical equation for the index of refraction of seawater. *Appl. Optics* 34, 3477–3480. doi: 10.1364/AO.34.003477

Richardson, T. L., Ciotti, U. M., Cullen, J. J., and Villareal, T. A. (1996). Physiological and optical properties of *Rhizosolenia formosa* (bacillariophyceae) in the context of open-ocean vertical migration. *J. Phycol*. 32, 741–757. doi: 10.1111/j.0022-3646.1996.00741.x

Rines, J., McFarland, M., Donaghay, P., and Sullivan, J. (2010). Thin layers and species-specific characterization of the phytoplankton community in Monterey Bay, California, USA. *Continent. Shelf Res*. 30, 66–80. doi: 10.1016/j.csr.2009.11.001

Rines, J. E. B., Donaghay, P. L., Dekshenieks, M. M., Sullivan, J. M., and Twardowski, M. S. (2002). Thin layers and camouflage: hidden *Pseudo-nitzschia* spp. (Bacillariophyceae) populations in a fjord in the San Juan Islands, Washington, USA. *Mar. Ecol. Prog. Ser*. 225, 123–137. doi: 10.3354/meps225123

Roesler, C. S., and Barnard, A. H. (2013). Optical proxy for phytoplankton biomass in the absence of photophysiology: rethinking the absorption line height. *Methods Oceanogr*. 7, 79–94. doi: 10.1016/j.mio.2013.12.003

Round, F. E., Crawford, R. M., and Mann, D. G. (1990). Diatoms: Biology and Morphology of the Genera. Cambridge: Cambridge University Press.

Shampine, L. F. (2008). Vectorized adaptive quadrature in MATLAB. *J. Comput. Appl. Math*. 211, 131–140. doi: 10.1016/j.cam.2006.11.021

Smetacek, V. (1999). Diatoms and the ocean carbon cycle. *Protist* 150, 25–32. doi: 10.1016/S1434-4610(99)70006-4

Stockley, N. D., Rottgers, R., McKee, D., Lefering, I., Sullivan, J. M., and Twardowski, M. S. (2017). Assessing uncertainties in scattering correction algorithms for reflective tube absorption measurements made with a WET Labs ac-9. *Optics Exp*. 25, A1139–A1153. doi: 10.1364/OE.25.0A1139

Sullivan, J. M., Donaghay, P. L., and Rines, J. E. (2010a). Coastal thin layer dynamics: Consequences to biology and optics. *Continent. Shelf Res*. 30, 50–65. doi: 10.1016/j.csr.2009.07.009

Sullivan, J. M., Twardowski, M. S., Donaghay, P. L., and Freeman, S. A. (2005). Use of optical scattering to discriminate particle types in coastal waters. *Appl. Optics* 44, 1667–1680. doi: 10.1364/AO.44.001667

Sullivan, J. M., Twardowski, M. S., Zaneveld, J., and Moore, C. C. (2013). "Measuring optical backscattering in water," in *Light Scattering Reviews 7, Springer Praxis Books*, ed A. A. Kokhanovsky (Berlin; Heidelberg: Springer), 189–224. doi: 10.1007/978-3-642-21907-8_6

Sullivan, J. M., Van Holliday, D., McFarland, M., McManus, M. A., Cheriton, O. M., Benoit-Bird, K. J., et al. (2010b). Layered organization in the coastal ocean: an introduction to planktonic thin layers and the LOCO project. *Continent. Shelf Res*. 30:1. doi: 10.1016/j.csr.2009.09.001

Talapatra, S., Hong, J., McFarland, M., Nayak, A. R., Zhang, C., Katz, J., et al. (2013). Characterization of biophysical interactions in the water column using in situ digital holography. *Mar. Ecol. Prog. Ser*. 473, 29–51. doi: 10.3354/meps10049

Tomas, C. R. (1997). *Identifying Marine Phytoplankton*. San Diego, CA: Academic Press.

Tréguer, P., Bowler, C., Moriceau, B., Dutkiewicz, S., Gehlen, M., Aumont, O., et al. (2018). Influence of diatom diversity on the ocean biological carbon pump. *Nat. Geosci*. 11:27. doi: 10.1038/s41561-017-0028-x

Twardowski, M. S., Sullivan, J. M., Donaghay, P. L., and Zaneveld, J. R. V. (1999). Microscale quantification of the absorption by dissolved and particulate material in coastal waters with an ac-9. *J. Atmos. Ocean. Technol*. 16, 691–707. doi: 10.1175/1520-0426(1999)016<0691:MQOTAB>2.0.CO;2

Wriedt, T. (2009). Light scattering theories and computer codes. *J. Quant. Spectrosc. Radiat. Transfer* 110, 833–843. doi: 10.1016/j.jqsrt.2009.02.023

Yang, P., and Liou, K. N. (1995). Light scattering by hexagonal ice crystals: comparison of finite-difference time domain and geometric optics models. *JOSA A* 12, 162–176. doi: 10.1364/JOSAA.12.000162

Yang, P., and Liou, K. N. (1996). Geometric-optics-integral-equation method for light scattering by nonspherical ice crystals. *Appl. Optics* 35, 6568–6584. doi: 10.1364/AO.35.006568

Yoshiyama, K., Mellard, J., Litchman, E., and Klausmeier, C. (2009). Phytoplankton competition for nutrients and light in a stratified water column. *Am. Nat*. 174, 190–203. doi: 10.1086/600113

Conflict of Interest: The authors declare that the research was conducted in the absence of any commercial or financial relationships that could be construed as a potential conflict of interest.

Copyright © 2020 McFarland, Nayak, Stockley, Twardowski and Sullivan. This is an open-access article distributed under the terms of the Creative Commons Attribution License (CC BY). The use, distribution or reproduction in other forums is permitted, provided the original author(s) and the copyright owner(s) are credited and that the original publication in this journal is cited, in accordance with accepted academic practice. No use, distribution or reproduction is permitted which does not comply with these terms.

frontiers in Marine Science

ORIGINAL RESEARCH
published: 14 July 2020
doi: 10.3389/fmars.2020.00563

Ubiquitous Patchiness in Chlorophyll *a* Concentration in Coastal Archipelago of Baltic Sea

Matias Scheinin[1,2]* *and Eero Asmala*[3]*

[1] Department of Environmental Protection, Hanko, Finland, [2] Pro Litore Association, Raseborg, Finland, [3] Tvärminne Zoological Station, Faculty of Biological and Environmental Sciences, University of Helsinki, Hanko, Finland

Productivity and trophic status of aquatic systems is traditionally quantified by chlorophyll *a* measurements. Environmental conditions and ecological interactions cause variability in chlorophyll *a* abundance. In coastal ecosystems, shallow and complex bathymetry reduces vertical heterogeneity, but promotes horizontal heterogeneity. However, coastal monitoring programs and scientific surveys are primarily focused on the vertical dimension. Here we demonstrate the spatial patchiness of chlorophyll *a* in coastal waters. We collected horizontally detailed and extensive *in situ* chlorophyll *a* data from the coastal Baltic Sea (SW Finland), covering the ice-free season of an annual cycle. Altogether, more than 200,000 observations were logged by an automated underway measurement system equipped with an optical sensor connected to a flow-through system. We analyzed the spatial heterogeneity of calibrated chlorophyll *a* data by using multiple statistical approaches, and quantified the chlorophyll *a* patches using a rolling average filter. We were able to identify patches and quantify their abundance and size for each of the 11 sampling campaigns. On average, 285 patches, ranging from 0.6 to 3142 m in size, were observed on the 830 km sampling transect. The average size of the patches was 237 (95% CI 226–248) m, most patches being between 10 and 1000 m. Our results show that patches of chlorophyll *a* can be effectively identified and quantified by modern *in situ* optical instrumentation. Such information is both theoretically and practically relevant. First, these results increase our understanding of the overall heterogeneity of the coastal environment. Further, they demonstrate the value of knowing the magnitude and occurrence of chlorophyll *a* patchiness in accurate detection of changes in coastal ecosystems caused by increased inputs of nutrients.

Keywords: estuary, eutrophication, littoral, trophic state, spatial heterogeneity, chlorophyll fluorescence, flow-through measurement, water quality monitoring

OPEN ACCESS

Edited by:
David Murphy, University of South Florida, United States

Reviewed by:
Kalle Olli, University of Tartu, Estonia
Agneta Andersson, Umeå University, Sweden

***Correspondence:**
Matias Scheinin
matias@scheinin.fi
Eero Asmala
eero.asmala@helsinki.fi

Specialty section:
This article was submitted to Marine Ecosystem Ecology, a section of the journal Frontiers in Marine Science

Received: *07 February 2020*
Accepted: *19 June 2020*
Published: *14 July 2020*

Citation:
Scheinin M and Asmala E (2020) Ubiquitous Patchiness in Chlorophyll a Concentration in Coastal Archipelago of Baltic Sea. Front. Mar. Sci. 7:563. doi: 10.3389/fmars.2020.00563

INTRODUCTION

Understanding environmental change is founded on describing, explaining, and predicting ecosystem state. The trophic state of an ecosystem, or the property of energy availability to its food web (Dodds, 2007), is a fundamental manifestation of ecosystem structure (Scheffer et al., 2001), function (Howarth et al., 2011), and services (Antón et al., 2011). It is thus pertinent for

both basic and applied ecology to assess how the trophic state of an ecosystem varies in space and time. Trophic state is typically quantified through total organic carbon, primary producer biomass, or macronutrient availability (Lindeman, 1942; Odum, 1956; Nixon, 1995). Most conventionally, phytoplankton biomass—measured using chlorophyll *a* concentration (hereafter Chl-*a*) as a proxy—has been applied as the prime indicator of trophic state (Carlson, 1977).

Ecosystems vary in their trophic state depending primarily on external and internal nutrient fluxes. While external fluxes determine the level of nutrients in an ecosystem, their distribution among its compartments is regulated by internal fluxes, that thus govern how the nutrient level is expressed in the trophic state of the system. External nutrient loading leads to an increase in the trophic state of the recipient ecosystem, that is, eutrophication. Essentially, nutrient enrichment initiates a shift in species composition, which involves concomitant changes in food web structure and ecological transfer efficiency (Havens, 2014). The concrete manifestations of this depend on the rate and degree of eutrophication as well as on ecosystem-specific characteristics. In coastal ecosystems, eutrophication has diminished water clarity, caused toxic algal blooms, resulted in localized hypoxia, and reduced macrovegetation in nearshore environments (Boesch, 2019). In terms of coastal ecosystem services, eutrophication can alter the functioning of the coastal filter, e.g., carbon storage and cross-ecosystem nutrient transfer (Asmala et al., 2017), erosion and pollution control (Barbier et al., 2011), fisheries and nurseries (Worm et al., 2006), as well as the recreational value and aesthetic quality of the environment (Chung et al., 2015). While nutrient loading from point sources has decreased substantially during the past few decades (e.g., Reusch et al., 2018), inputs from diffuse atmospheric and terrestrial sources are difficult to reduce. This difficulty is compounded by the legacy storage of nutrients in soils, waterways and groundwater (Boesch, 2019). Moreover, diffuse loading is challenging to mitigate because of the spatiotemporal heterogeneity of the sources. Consequently, coastal eutrophication is a globally topical problem (Andersen et al., 2019).

In coastal waters, phytoplankton biomass is prone to be patchy due to a combination of environmental, ecological and physiological drivers. Bathymetry, tides, and currents combine freshwater runoff and marine surface and deeper waters over small spatial scales to create considerable spatial complexity in hydrography, mixed layer depth, and nutrient content, driving spatial complexity in phytoplankton biomass. Furthermore, short temporal variability, similar in timescale with that of phytoplankton physiological variability, is induced by advective currents and wind-driven mixing (Carberry et al., 2019). Hence, disregarding the patchiness of Chl-*a* in assessments of the trophic state of coastal ecosystems is likely to result in spatiotemporally skewed or overgeneralized interpretation of their properties. Robust measurements of Chl-*a* on adequate scales of space and time are also relevant for planning, prioritizing, targeting, and following up management actions that can alter external nutrient loading.

Quantification of Chl-*a* patchiness—including the quantity, extent, prevalence, and intensity of the patches—requires sampling with sufficiently high precision and resolution. Two principal sampling approaches are being used: discrete water sampling and *in situ* observations. Both of these involve their own constraints that complicate the determination of the different patchiness parameters. Discrete water sampling is well suited for the precise quantification of Chl-*a*, since the pigment can be extracted from the cells and measured reliably and accurately by various methods such as high-performance liquid chromatography (HPLC), spectrophotometry or -fluorometry. However, the quantification of small-scale spatiotemporal variation by discrete sampling is virtually impossible due to the labor-intensity of the approach—resulting in high precision but low resolution (Cloern et al., 1989). By contrast, *in situ* observations have fewer limitations regarding spatial and temporal resolution. Chl-*a* can be assessed through *in vivo* fluorescence from different remote sensing vehicles or waterborne platforms. While these approaches allow for high resolution, their precision is significantly lower with raw values than that of the methods based on chlorophyll *a* extraction (e.g., Cullen, 1982). The *in vivo* fluorescence yield per Chl-*a* may vary depending primarily on the size (Alpine and Cloern, 1985) and species (Proctor and Roesler, 2010) of phytoplankton, and the photochemical (Sosik and Mitchell, 1991) and non-photochemical (Misumi et al., 2016) quenching properties of the species. On top of these proximate causes, the optical complexity of coastal waters in the form of other compounds (e.g., DOM and non-living particles) that fluoresce at similar wavelengths as chlorophyll *a* will further distort *in situ* fluorescence measurements. Although *in situ* observations can be calibrated using discrete water samples, the work is often logistically too challenging due to match up issues (Carberry et al., 2019).

Here, we present a cost-efficient methodological framework that enables the quantification of Chl-*a* patchiness and its subsequent decomposition into the basic patchiness parameters in heterogeneous coastal waters. Our overall aim was to identify and quantify the chlorophyll *a* patches, and use these as indicators for patchiness of the coastal environment, in general. The framework builds upon spatially high-frequency Chl-*a* *in situ* observations in a geographically complex coastal archipelago environment. To collect the data, we surveyed Chl-*a* at high resolution in the coastal waters of SW Finland along an 830 km long transect throughout the entire ice-free season of 2019.

MATERIALS AND METHODS

Study Site and General Description of the Area

The study was carried out within a 40 km by 50 km rectangular area around the SW tip of mainland Finland on both sides of the 60th parallel north and the 23rd meridian east, in the northern Baltic Sea. The area encompasses the entire coastal waters of the cities of Hanko and Raseborg, thus covering parts of the Finnish Archipelago Sea in the west and parts of the Gulf of Finland in the East. The climate of the study area is cold and

temperate, or "Dfb" according to the Köppen–Geiger climate classification. The long-term average annual air temperature is 5.3°C, and the average annual rainfall is 603 mm. The sea starts to freeze typically in October, while the ice cover tends to disappear completely in May. However, there are pronounced differences in the prevalence, thickness, and permanence of the ice cover within the area (HELCOM, 2010).

The coastal zone of the northern Baltic Sea exemplifies the heterogeneity of coastal environments, as it is characterized by its vast mosaic-like archipelago consisting of thousands of small islands. Further, littoral zone constitutes a large proportion of these coastal waters due to the planar profile of the region, its fine-scale topographical variability, and the extensive length of the aggregate shoreline. These features translate as comparatively high photic zone coverage as well as strong benthic-pelagic, terrestrial, and atmospheric coupling (McGlathery et al., 2007). While temperature and light modulate phytoplankton dynamics during the ice-free season, primarily nutrient availability and to a lesser extent grazing drive the timing and amount of phytoplankton standing stock biomass, or Chl-*a* (Lyngsgaard et al., 2017). Further, in shallow and intensively mixed waters phytoplankton production can be very high already before the onset of thermal stratification (Sommer and Lengfellner, 2008). Since nutrients are continuously cycled within the well-mixed system, phytoplankton production is more permanently fueled by the dissolved nutrient resources than in pelagic areas.

Sampling Methods

Flow-Through System Including the Chlorophyll *a* Sensor

The spatially detailed and extensive *in situ* Chl-*a* data were collected by an automated underway measurement system equipped with an optical Chlorophyll *a* sensor. The system was constructed by Luode Consulting Inc. and installed in a rigid inflatable boat (RIB) (Brig N610H) with 0.4 m draft. The system consisted of seven sequential components as follows: The water intake was placed at 0.5 m depth, facing forward right below the left-hand stern. Since the water intake was the lowest part of the whole system, its minimum operation depth was also 0.5 m. After passing the pump at 29 L/min, the water was led through a lamellar debubbler before entering a 0.5-L cylindrical chamber enclosing an EXO2 sonde equipped with a dual-channel fluorescence sensor (Xylem Inc., United States) for integrated Chl-*a* detection, incorporating also cyanobacterial contribution by applying two excitation wavelengths; 470 ± 15 and 590 ± 15 nm and one emission detection wavelength at 685 ± 15 nm. From the sonde, the water passed by a faucet for water collection before being led back to the sea from an outflow pipe at the right-hand rail of the boat. Time and GPS position were tracked continuously for geolocating the Chl-*a* measurements by using an EXO Handheld unit (Xylem Inc., United States) connected to the sonde with a data transmission cable.

Data were constantly recorded at 5 s intervals, while the typical traveling speed of the boat was 22.3 knots (12 m/s), resulting in the vast majority of the data being logged at 60-m intervals. As the spatial resolution of the applied method was determined by the traveling speed of the boat, resolution finer than 60 m could only be achieved at velocities lower than the standard traveling speed at the chosen logging interval. Due to, e.g., complex navigation, marine traffic regulations, or very shallow water depth, the speed of the boat was reduced in few locations. In any given location, traveling speed was virtually invariable among the campaigns, allowing for unbiased temporal comparisons of the patchiness data. In order to maximize the geolocation precision, the total response time of the flow-through system was determined according to Crawford et al. (2015) and adjusted to 10 s by altering the length of the water hose between the water intake and the pump. The total response time consists of the hydraulic lag between the water intake and the cylindrical chamber (8 s), the total exchange of the water in the chamber (0.5 s), and the response time (T63) of the sensor (<2 s).

Sampling Schedule

The samples were collected along an 830 km long transect (**Figure 1**), where water depth varied between 0.5 and 80 m. The transect was surveyed with 3-week intervals throughout the entire ice-free season from week 14 at the turn of March and April until week 44 at the turn of October and November 2019. However, only a fraction of the transect could be sampled during the first occasion, since sea ice was still covering most of the transect. During all the later occasions, the transect could be followed in high detail so that both the route and the traveling speeds at different parts of the route were virtually constant. Apart from the first sampling occasion, each sampling campaign was carried out during four consecutive days. During each occasion, the number of data points collected was approximately 20,000, totaling 212,150 observations from the eleven sampling occasions. Eight locations were chosen randomly to represent variation in local Chl-*a* dynamics (**Figure 1**).

Calibration of the *in situ* Chl-*a* Observations

During each sampling occasion, 20 discrete water samples were collected for calibrating the *in situ* Chl-*a* data. To represent maximal variability in terms of phytoplankton composition and biomass, and of the surrounding conditions, the 20 sampling stations were located along three distinctive environmental gradients, each starting from a river mouth and ending at the open sea. Since the gradients were spatially apart from each other, and each gradient was geographically extensive (12, 18, and 38 km), the collected samples also represented different sampling days and contrasting times of each day. During the brief stop at each sampling station, 50 mL of water was collected into a plastic centrifuge tube from the faucet for water collection while logging parallel Chl-*a* data. Each sample was immediately filtered onto a GF/F (Whatman) filter. The filter was submerged in ethanol in a glass scintillation vial. The vials were transported in a dark cool box to the laboratory by the end of each sampling day. In the laboratory, the samples were incubated in the dark in a −20°C freezer for 72 h prior to the analysis. The concentration of the extracted Chlorophyll *a* was determined by fluorometry (Varian Cary Eclipse spectrofluorometer, Agilent, United States) using a plate reader (Simis et al., 2012). Finally,

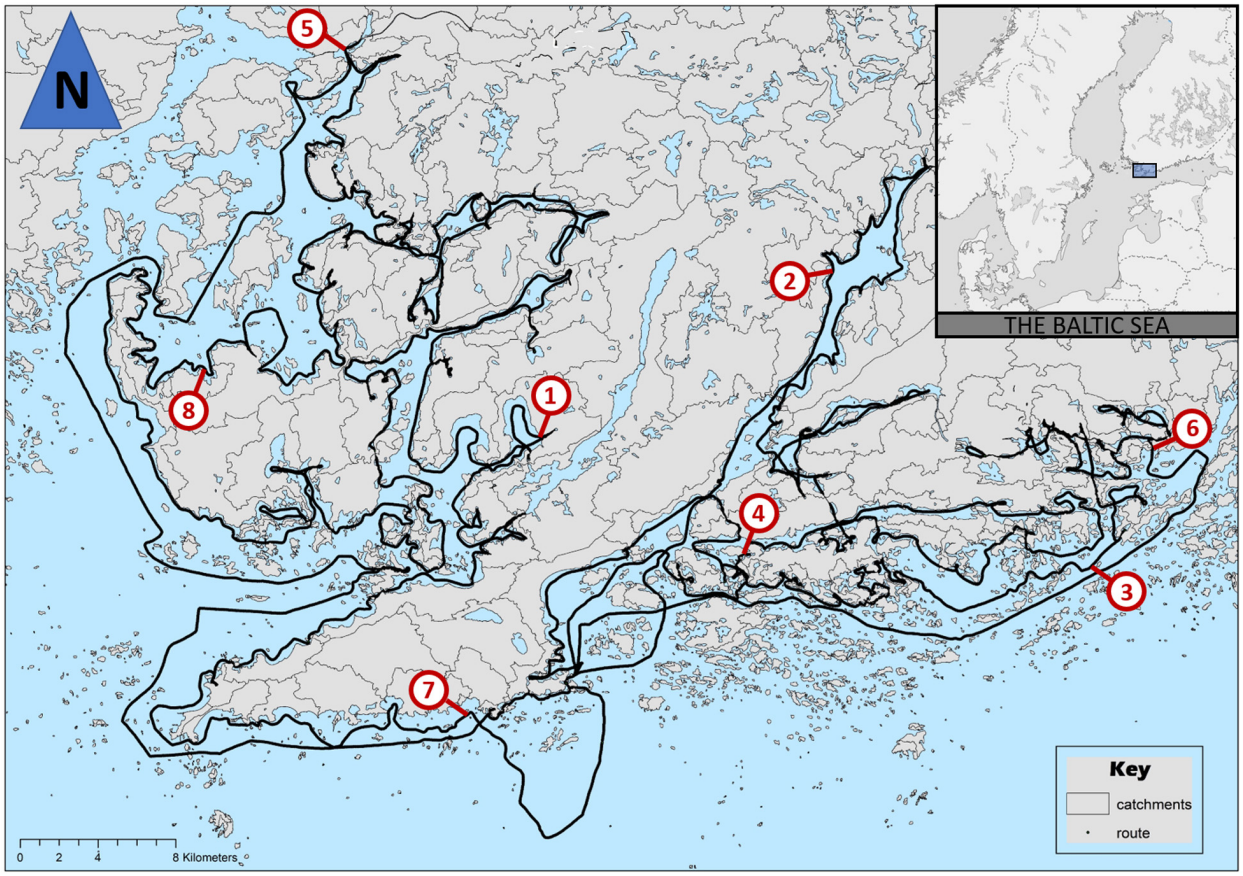

FIGURE 1 | Map of study area with the route of the boat (black solid line) and eight reference stations (1 = Båtviken, 2 = Elimogrundet, 3 = Gästans, 4 = Gyltviken, 5 = Kiskonjoki, 6 = Stakasund, 7 = Stödjekobbarna, 8 = Svärtesviken). Inset figure of the northern Baltic Sea.

the coefficient of determination between the temporally parallel *in situ* and extracted Chl-*a* measurements was calculated by using linear regression with 0 as the intercept (*in situ* data was validly 0-calibrated). Thus, the slope of the model function was used as the correction factor for the *in situ* Chl-*a* data (**Supplementary Figure S1**).

Data Analysis

We used the calibrated values for the analysis of spatial and temporal variation in Chl-*a*. Average values for each sampling campaign were calculated, as well as average values for the eight specific locations indicated in **Figure 1**. Spatial autocorrelation shows the correlation within variables across georeferenced space (Getis, 2008). Although spatial autocorrelation can be used to determine the average size of patches (Sokal and Oden, 1978), autocorrelation occurs over some minimal scale that is dependent on both processes and sampling. Consequently, autocorrelation may not capture patterns smaller than this inherent minimal scale, and other methods to quantify patterns at smaller scales may be needed (Underwood and Chapman, 1996). Autocorrelation (covariance) of the Chl-*a* observations was calculated for each round separately, up to lag value equaling maximum number of observations for each campaign.

We acknowledged the inherent autocorrelation of the high frequency Chl-*a* observations and used it to identify the large-scale patchiness of Chl-*a*. Using the sequence of Chl-*a* observations from each sampling campaign, the difference in Chl-*a* observations between two sampling points with *n* number of observations in between was calculated. The difference was calculated for *n* values of 1–300, which corresponds to 18 km. To complement the autocorrelation analysis and to identify and quantify the local heterogeneity on a smaller scale, we identified patches, i.e., operational units of local heterogeneity by using a rolling mean filter along the sequence of Chl-*a* observations. This approach allows identification and quantification of local heterogeneity beyond autocorrelation analysis (Underwood and Chapman, 1996). We used the *rollapply* function from the R package *zoo* (Zeileis and Grothendieck, 2005) with a rolling bin width of 101 observations (50 observations to both forward and backward from each observation). This corresponded to a distance of 6 m on average, which is approximately four times the size of phytoplankton patches identified by Platt et al. (1970). We applied a threshold of 25%, which means that Chl-*a* values that deviated (either negatively or positively) more than 25% from the rolling mean value, were categorized as patches. The performance of a range of thresholds and bin widths in patch detection was

tested with simulated data, and the combination of threshold value 25% and bin width identified patches from simulated dataset with a 100% accuracy (**Supplementary Figure S2**). Consecutive observations categorized as patches were assigned a unique patch ID, and the spatial extent of each patch was calculated using the geospatial information of each observation using the R package *sf* (Pebesma, 2018). The patch extent was determined as the maximum extent, as the distance between the two farthest points of each patch. Paired relationships between average Chl-*a*, number of patches, and patch extent were analyzed with simple linear regression for each sampling campaign. All statistical analyses were done by using R software (R Core Team, 2014).

RESULTS

The measured Chl-*a* ranged from 0.76 to 195 $\mu g\, l^{-1}$ during the study period from late March to early November (**Figure 2** and **Supplementary Figure S3**). The overall average was 7.65 $\mu g\, l^{-1}$, but the values varied considerably among sampling campaigns and locations. The lowest average values were observed during the first campaign (4.75 $\mu g\, l^{-1}$), and the highest 3 weeks later, during the second campaign (14.24 $\mu g\, l^{-1}$).

Chl-*a* varied considerably among the eight randomly chosen sampling points (**Figure 3**). The lowest values were observed in Stödjekobbarna (3.8 [95% CI 3.6–4.1], range 1.3–7.5 $\mu g\, l^{-1}$), and the highest in Svärtesviken (19.4 [13.9–24.8], 2.2–149.1 $\mu g\, l^{-1}$). The apparent seasonal pattern varied also considerably among the chosen points, and in general, did not follow the overall regional pattern (c.f. **Figure 2**).

Differences in Chl-*a* among sampling points, i.e., patchiness, varied from one sampling campaign to another (**Figure 4**). In general, the mean difference between two sampling points increased in concert with the number of observations in between. This increase was not linear, as the difference increase was steepest in the range of ∼<50 observations in between. During the campaign in week 17, the differences were the highest, reaching on average 3.9 (95% CI 3.8–4.0) $\mu g\, l^{-1}$ between two observations that were 300 observations apart. During week 14, the mean difference at an interval of 300 observations was less than 1 $\mu g\, l^{-1}$, as well as during week 20. After week 20, the mean differences gradually increased toward the autumn, reaching 2.8 (2.7–2.9) $\mu g\, l^{-1}$ in week 44.

For the identification of the potential patches in Chl-*a* observations, we used a rolling mean filter and a deviation threshold, as exemplified in **Supplementary Figure S4**. By using this approach, we were able to identify multiple patches from each sampling day.

The number of patches varied between the sampling campaigns; from 5 in week 14 and 458 in week 17, and the average number of patches was 285 (**Figure 5** and **Table 1**).

The location of individual patches changed from one sampling to another, appearing apparently randomly across the region (**Figure 6**). There was a weak positive relationship with average Chl-*a* and the number of patches during the samplings ($p = 0.07$).

Compared to the number of patches, the size of the patches varied less among the sampling occasions, the average values ranging from 141 m in week 14 to 272 m in week 38 (**Figure 7**). After low patch extent values in week 20 (183 m on average), there was a general increasing trend in patch extents toward autumn. As with the number of patches, patch extent did not have a significant relationship with the average Chl-*a* of each sampling occasion ($p = 0.13$).

The size of the patches (patch extent) ranged from 0.6 to 3142 m (**Figure 8**). Most patches were in the range of 10–1000 m, and the modal values between 50 and 100 m.

Chl-*a* had weak positive relationship with patch extent (**Figure 9A**) and number of patches (**Figure 9B**). The number of patches and the mean patch extent had a significant positive

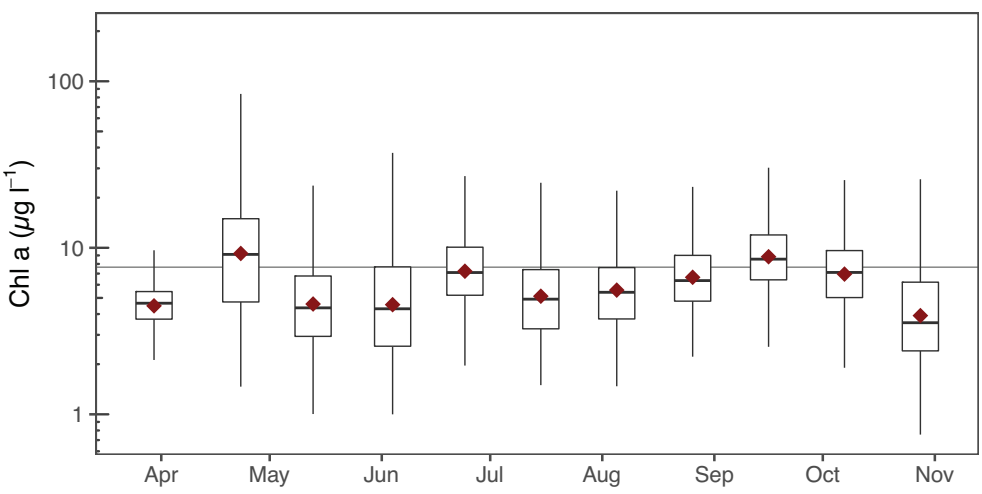

FIGURE 2 | Chl-*a* during each sampling campaign. Lower and upper ends of boxes indicate the interquartile range (Q3–Q1), whiskers the lowest and the highest values within the range of 1.5 IQR, and thick black line indicates median value. Mean values are indicated by red diamonds, and horizontal line represents the overall mean value across all samplings (7.65 $\mu g\, l^{-1}$). On week 14, the number of observations was only 5514 due to ice cover.

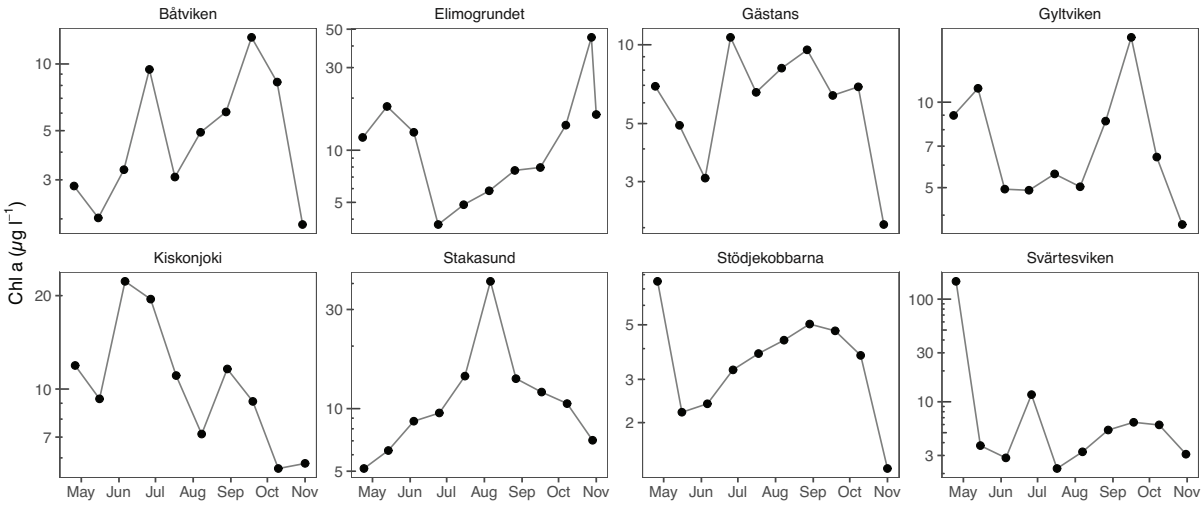

FIGURE 3 | Chl-*a* at eight randomly selected sampling points, whose locations are indicated in **Figure 1**. The first sampling campaign (week 14) was not included due to ice cover in most of the points.

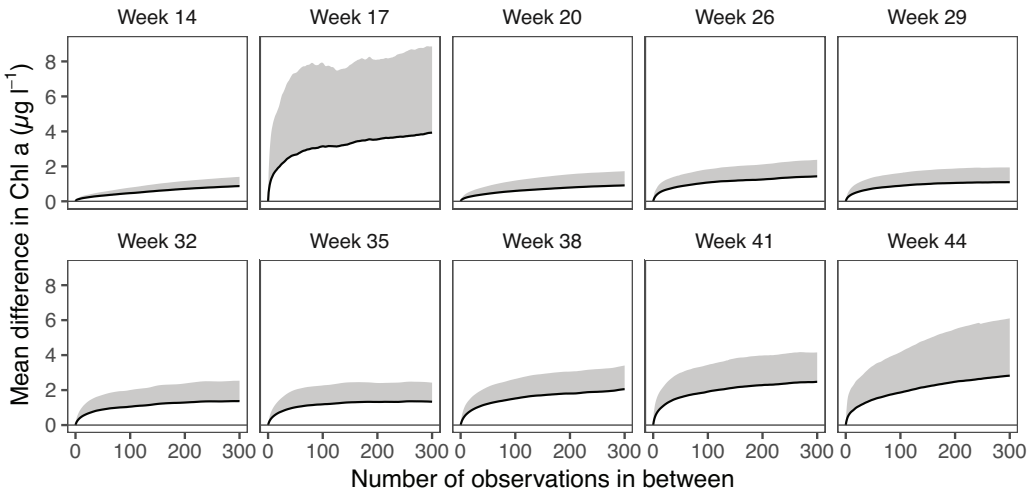

FIGURE 4 | Mean difference in observed Chl-*a* along a lag gradient, i.e., number of observations between the observations being compared. Gray area indicates 0.65 standard deviation, which corresponds to a 50% confidence interval. Note: week 23 not included.

relationship (**Figure 9C**). In other words, the more patches were observed, the larger they were on average.

DISCUSSION

Chlorophyll Concentrations and Phenology

The total average Chl-*a* across all sampling points and campaigns was 7.65 $\mu g\, l^{-1}$ (**Figure 2**), which generalizes the eutrophication status of the sampling area to mesotrophic (Carlson, 1977). We observed weak spring and autumn peaks (in April–May and September–October) typical for temperate, pelagic areas (Cebrián and Valiela, 1999; Gasiûnaitë et al., 2005), as well as an apparent unimodal midsummer maximum (July) characteristic for temperate, littoral areas (Harding et al., 2019) from the overall average dynamics of the whole area. The average dynamics appeared relatively static compared to other temperate coastal areas (Carstensen et al., 2015; Harding et al., 2019), since the coastal sampling route averaged and canceled off the seasonality. In other words, the small difference between minima and maxima was simply a manifestation of average dynamics with high variability due to large spatial differences in Chl-*a* levels and phenology. Annual mean Chl-*a* levels varied substantially among different locations, while the different locations displayed highly different temporal dynamics (**Figure 3**). Both sorts of differences are characteristic for nearshore areas and marginal seas, in general (Song et al., 2019). The phenological differences

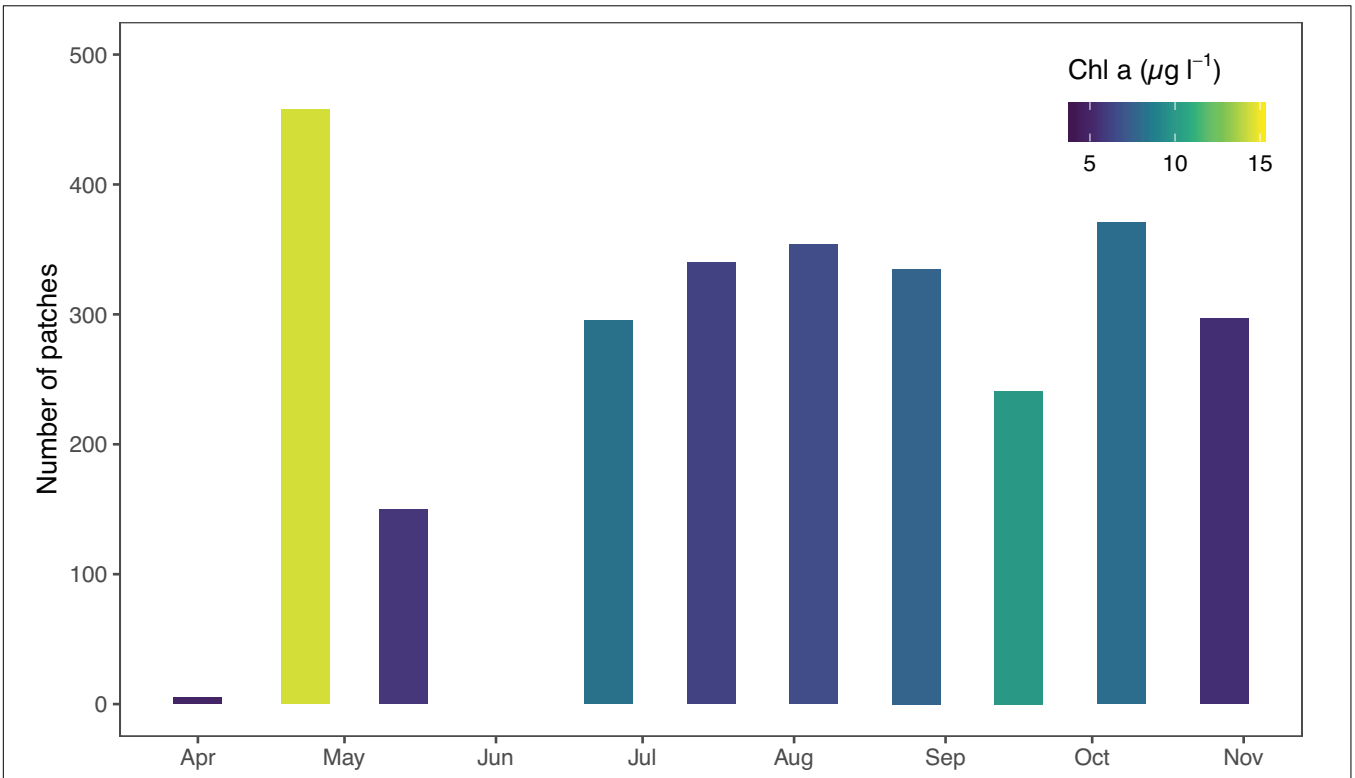

FIGURE 5 | Number of individual patches identified during 10 sampling campaigns. Note that during week 14 the route was limited to offshore areas with only ~5000 observations. Note: week 23 not included.

can result from multiple different factors—including the local overall Chl-*a* level—that affect phytoplankton dynamics. Accordingly, site-specific internal processes, related to their actual trophic state, may change the N:P stoichiometry, overall nutrient availability, or grazing pressure (Sommer et al., 2012). Moreover, especially in the more enclosed areas, temperature and salinity differences are more pronounced and abrupt, driving changes in the temperature- (Yvon-Durocher et al., 2017) or salinity-sensitive (Oseji et al., 2019) parts of the plankton community. Finally, inherent stochasticity can cause spatial heterogeneity in organism and resource distributions, which leads to temporal heterogeneity in resource access for phytoplankton (Anderies and Beisner, 2000).

Chlorophyll Patchiness

Patchiness, here defined as the contrast in Chl-*a* among different observations as a function of the observation sequence, varied across the year (**Figure 4** and **Supplementary Figure S5**). This applied both to the intensity and scale of patchiness, illustrated by the systematic temporal changes in the level (intensity) and slope (scale) of the mean difference in Chl-*a* in relation to the observation sequence (**Figure 4**). The temporal variation in the intensity and scale of patchiness underline that the theoretical and practical implications of patchiness are far from the same around the year. However, the relationship between the intensity and scale of patchiness appeared comparably constant throughout the season, indicating that Chl-*a* patchiness is a ubiquitous characteristic of coastal waters.

The temporal patterns in the intensity and scale of patchiness may partially be attributed to external nutrient loading. Like in other coastal environments, most of the external nutrient loading in the study area originates from diffuse terrestrial sources (Boesch, 2019). In the spring, high transient loading from diffuse sources is likely to promote considerable horizontal heterogeneity in resource availability, leading to high intensity and scale of patchiness in the distribution of phytoplankton biomass in April (**Figure 4**). The subsequent collapse in patchiness may be due to, e.g., patch-targeted top-down control of phytoplankton (Sommer et al., 1986) and stochastic dilution by diffusion of the nutrient resources (Romero et al., 2016). During the following months, the considerably decreased but still substantial level of patchiness was maintained probably by the legacy storage of nutrients in the sediments (Vahtera et al., 2007). These sources of internal loading should reflect the diffuse geography of the external ones, while nutrient resuspension rates in shallow and vertically well-mixed waters tend to be driven by temperature (Harding et al., 2019). The gradual increase of the intensity and scale of Chl-*a* patchiness from the late-spring minimum until the late fall also coincides with the amount of terrestrial runoff in the boreal region. However, the apparent temporal relationship between runoff and patchiness does not lead to predictable appearance of patches to given locations (**Figure 5**). In addition to internal patch dynamics (Denman and Dower, 2008), this relationship

TABLE 1 | Summary statistics of the peak extents during 10 sampling campaigns.

Time	Mean patch extent (m)	Range (m)	Number of patches	Patch coverage (km)
Week 14	141 (0–327)	14.1–377	5	<1 (<1%)
Week 17	245 (214–276)	1.6–2790	458	112 (13.5%)
Week 20	183 (135–231)	3.7–2201	150	27 (3.3%)
Week 26	208 (181–235)	1.2–1955	295	61 (7.4%)
Week 29	209 (181–237)	0.6–1391	340	71 (8.5%)
Week 32	251 (218–284)	1.6–2261	354	89 (10.7%)
Week 35	234 (204–264)	1.2–1998	335	78 (9.4%)
Week 38	272 (230–314)	1.7–3123	241	66 (7.9%)
Week 41	263 (232–294)	3–2669	371	98 (11.7%)
Week 44	240 (204–276)	0.6–3142	297	71 (8.6%)
All weeks	237 (226–248)	0.6–3142	285	68 (8.1%)

Mean value with 95% confidence interval and range of the patch extent is given.

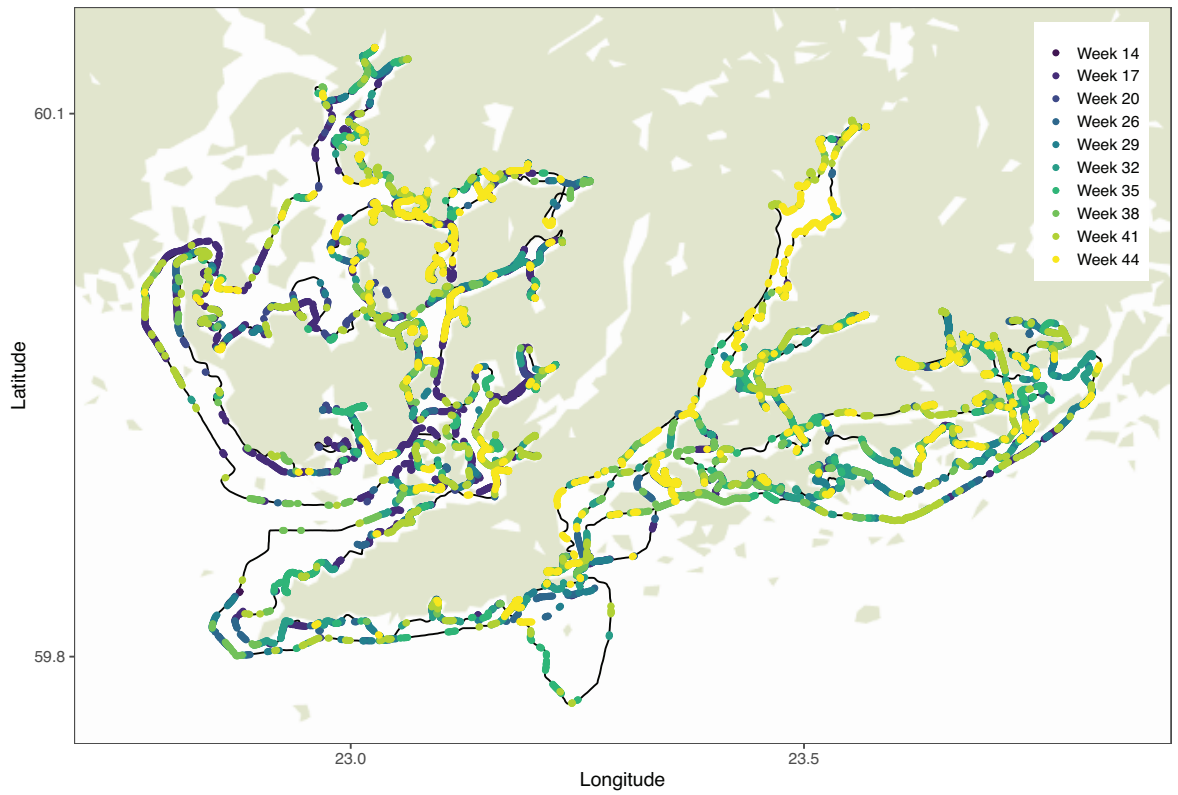

FIGURE 6 | Chl-*a* patches from each round overlaid on map. Route of the boat marked with black solid line.

is distorted by the fact that both the quantity and quality of terrestrial runoff vary substantially depending on local land-use (Delkash et al., 2018).

The chosen method of rolling (moving) average analysis proved to be effective in identifying the patches in the Chl-*a* data (**Supplementary Figure S4**). Essentially, patches were defined as deviations from local average. Sensitivity analysis of the rolling average method revealed that the width of the bin is less important than the threshold in defining the patch characteristics (**Supplementary Figure S6**). With this method, we were able to identify both positive and negative patches (**Supplementary Figure S7**). Positive patches result from phytoplankton growth and immigration locally exceeding the mortality and emigration, and in negative patches mortality exceeds growth (Wroblewski and O'Brien, 1976). In addition to biological factors, abiotic factors may result in spatially varying higher- or lower-than average phytoplankton biomass (Therriault and Platt, 1981). The identified patches did not overlap in general, but appeared

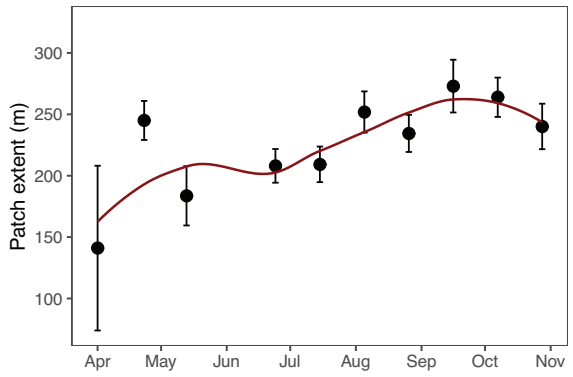

FIGURE 7 | Mean patch extent on each sampling campaign. Error bars indicate ± 1 standard error of mean. Red line indicates locally estimated scatterplot smoothing and gray area 95% confidence interval of the local regression. Note: week 23 not included.

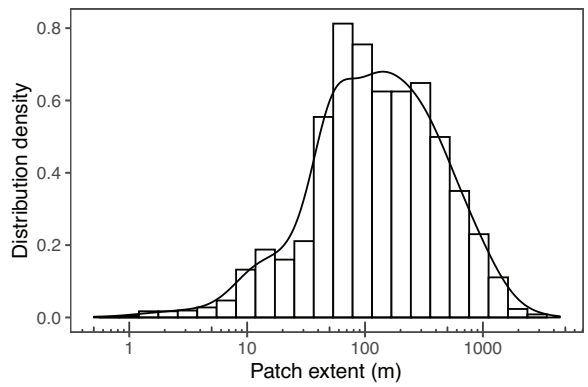

FIGURE 8 | Patch extent distribution density along the size gradient from 0.6 to 3142 m.

to be distributed randomly in the study area (**Figure 5**). This indicates that the processes behind patch formation are not linked with specific locations, but vary spatiotemporally and may occur apparently anywhere in the coastal environment. Most patches were observed during week 17 (**Figure 6**), which coincides with the typical timing of the pelagic spring bloom and the highest overall Chl-*a* during the annual cycle (**Figure 4**). In general, there was a weak positive relationship between the number of patches and Chl-*a* concentrations ($p = 0.07$). This is an indication of relatively higher spatial variability in conditions with high phytoplankton biomass (Maso and Duarte, 1989). The magnitude of changes in patch abundance was similar to the magnitude of the overall Chl-*a* dynamics, both varying by a factor of three over the sampling period.

The patches covered 3–14% of the total passage during sampling campaigns. The size of the individual patches (patch extent) is temporally much less variable than Chl-*a* or number of patches (**Figure 7**). This indicates that the biotic and abiotic processes forming and breaking up patches are similar during the annual cycle (Therriault and Platt, 1981). Most observed patches were between 10 and 1000 m, indicating lower and upper bounds of typical phytoplankton patches (**Figure 8**). Lower bound is strongly related to the spatial sampling frequency, as patches smaller than sampling resolution cannot be detected. Overall, our observed range concurs with previous estimates of phytoplankton patches from different environments, suggesting that there are universal factors determining the typical size of phytoplankton patches (Platt, 1972; Lovejoy et al., 2001; Bulit et al., 2004; Fossum et al., 2019). The largest patches on average were observed in spring, suggesting that the apparent regional spring bloom consists of multiple small and local blooms (Seuront, 2005). We observed patches decreasing in number after spring, but not in size (**Table 1**). Typically, after the spring bloom, the heterogeneity of phytoplankton communities in temperate areas increases, leading to the emergence of relatively short-lived patches dominated by varying species (Cetinić et al., 2015). The number of patches had a significant positive relationship with the average patch extent, but the number varied threefold (150–458), whereas the extent only with a factor of 1.5 (183–272 m). This indicates that the constraints over patch size are more rigid than constraints over their number, which is likely the result of the physical forcing (e.g., wind, turbulence), which are critical in defining the upper bound of the plankton patch sizes (Therriault and Platt, 1981; Blukacz et al., 2009).

Considerations About the Use of High-Frequency Measurements in Coastal Environment

Patchiness has been associated as an inherent property of plankton since the 1800s (Horwood, 1978). From the early estimates ranging from a few feet to hundreds of kilometers (Bainbridge, 1957), today it is thought that this heterogeneity spans many orders of magnitude from planetary down to microscale (Sale et al., 2006). While this general statement is logically true, it is dependent on the very definition of Chl-*a* patchiness. In empirical studies that rely on discrete water sampling, the operational definition of Chl-*a* patchiness and its methods of quantification depend on the objectives of the assessment. Those determine the accuracy and resolution of the sampling. Similar context-dependency applies to the general patch properties; quantity, extent, prevalence, and intensity. Since these basic parameters are inherently interdependent, at least one of them is typically predetermined by the objectives of the assessment in order to deduce the others from observational data. Under the circumstances, direct comparisons of Chl-*a* patchiness and patch characteristics across studies that use different, discrete sampling strategies can yield only a limited amount of generalizable information. In principle, such information can be derived from empirical data by using phenomenological models. While they can deal with the variability of resolution among different geospatial datasets, the accuracy of these approaches is challenged by the complexity and diversity of the underlying processes (Carberry et al., 2019). In short, the observed outcome is a result of physical, chemical and biological interactions (McGillicuddy, 2008). Accordingly, dissolved and suspended matter is continually redistributed by advection and

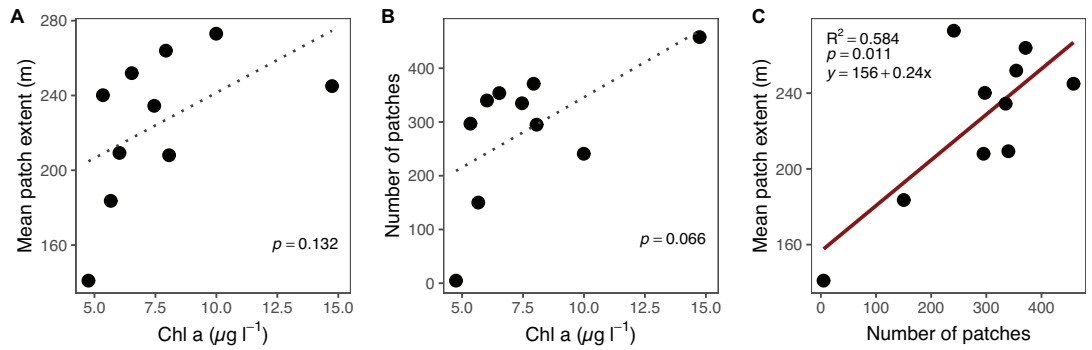

FIGURE 9 | Relationship between **(A)** Chl *a* and mean patch extent, **(B)** Chl *a* and number of patches and **(C)** number of patches and mean patch extent for each sampling occasion (week 23 excluded). Red solid line indicates a significant ($p < 0.05$) linear relationship between variables, and gray dotted line indicates non-significant ($p \geq 0.05$).

convection, while the spatial or temporal alterations in these flows affect the chemical and biological interactions. Moreover, living planktonic organisms actively move in the flow field. Although some of these processes have successfully been incorporated in phenomenological models (Carberry et al., 2019), they still rely on inherent assumptions about the relative contribution of most of the underlying processes.

To overcome the problems of resolution and accuracy, we have presented a methodological framework that enables the identification of Chl-*a* patches and their decomposition into basic patchiness parameters through robustly calibrated, high-frequency *in situ* observations. Further, by defining patches as deviations from their proximate context, our data can yield up patterns that are central from the perspectives of food web dynamics, and consequently, coastal zone management. In complex coastal environments, the detailed composition and relative process rates that drive Chl-*a* vary considerably in space and time. Therefore, Chl-*a* does not reflect only the trophic state of its environment but rather the synergistic effects of all the surrounding conditions. Those other conditions being equal, Chl-*a* patches are principally promoted by increased nutrient input and demoted by trophic transfer. Since both types of ecological interactions depend on their physical context, Chl-*a* patches defined as local deviations from the mean provide specific information about the roles of these processes. This is relevant for understanding food-web dynamics, since the prevalence, extent, and intensity of the local patches are associated with nutrient availability for primary producers, but also with food availability for the higher trophic levels. Correspondingly, the location and the fundamental characteristics of the patches are pertinent for coastal management actions such as the mitigation of nutrient discharges or the identification of conservation hotspots.

CONCLUSION

We documented ubiquitous Chl-*a* patchiness in the heterogeneous coastal environment. Chl-*a* had a positive relationship with both patch number and extent, showing that in conditions with high phytoplankton biomass, patches tend to be more abundant and larger in size. Most patches were between 10 and 1000 m in size across the spatial and temporal range sampled, indicating constraints by common physico-chemical and biological drivers. Knowing the magnitude and occurrence of phytoplankton patchiness is pertinent in understanding the overall heterogeneity of the coastal environment and in accurate detection of changes in coastal ecosystems caused by increased inputs of nutrients.

DATA AVAILABILITY STATEMENT

The dataset generated and analyzed for this study can be found in the open data repository PANGAEA (https://doi.pangaea.de/10.1594/PANGAEA.916204).

AUTHOR CONTRIBUTIONS

MS and EA have together planned the study, done the sampling and analyses, and produced the contents of the manuscript. Both authors contributed to the article and approved the submitted version.

FUNDING

MS and operational costs were supported by Bergsrådinnan Sophie von Julins Stiftelse. EA was supported by the Academy of Finland (Grant No. 309748).

ACKNOWLEDGMENTS

We would like to thank Anna-Karin Almén, Göran Lundberg, and Iris Orizar from the University of Helsinki, Ville Wahteristo from the City of Hanko, and Ruslan Gunko from the University of Turku for support in field, laboratory activities, and data preparation.

SUPPLEMENTARY MATERIAL

The Supplementary Material for this article can be found online at: https://www.frontiersin.org/articles/10.3389/fmars.2020.00563/full#supplementary-material

REFERENCES

Alpine, A. E., and Cloern, J. E. (1985). Differences in *in vivo* fluorescence yield between three phytoplankton size classes. *J. Plankton Res.* 7, 381–390. doi: 10.1093/plankt/7.3.381

Anderies, J. M., and Beisner, B. E. (2000). Fluctuating environments and phytoplankton community structure: a stochastic model. *Am. Nat.* 155, 556–569. doi: 10.1086/303336

Andersen, J. H., Carstensen, J., Holmer, M., Krause-Jensen, D., and Richardson, K. (2019). Editorial: research and management of eutrophication in coastal ecosystems. *Front. Mar. Sci.* 6:768. doi: 10.3389/fmars.2019.00768

Antón, A., Cebrian, J., Heck, K. L., Duarte, C. M., Sheehan, K. L., Miller, M. C., et al. (2011). Decoupled effects (positive to negative) of nutrient enrichment on ecosystem services. *Ecol. Appl.* 21, 991–1009. doi: 10.1890/09-0841.1

Asmala, E., Carstensen, J., Conley, D. J., Slomp, C. P., Stadmark, J., and Voss, M. (2017). Efficiency of the coastal filter: nitrogen and phosphorus removal in the Baltic Sea. *Limnol. Oceanogr.* 62, 222–238.

Bainbridge, R. (1957). The size, shape and density of marine phytoplankton concentrations. *Biol. Rev.* 32, 91–115. doi: 10.1111/j.1469-185x.1957.tb01577.x

Barbier, E. B., Hacker, S. D., Kennedy, C., Koch, E. W., Stier, A. C., and Silliman, B. R. (2011). The value of estuarine and coastal ecosystem services. *Ecol. Monogr.* 81, 169–193.

Blukacz, E. A., Shuter, B. J., and Sprulesc, W. G. (2009). Towards understanding the relationship between wind conditions and plankton patchiness. *Limnol. Oceanogr.* 54, 1530–1540. doi: 10.4319/lo.2009.54.5.1530

Boesch, D. F. (2019). Barriers and bridges in abating coastal eutrophication. *Front. Mar. Sci.* 6:123. doi: 10.3389/fmars.2019.00123

Bulit, C., Díaz-Ávalos, C., and Montagnes, D. J. (2004). Assessing spatial and temporal patchiness of the autotrophic ciliate *Myrionecta rubra*: a case study in a coastal lagoon. *Mar. Ecol. Prog. Ser.* 268, 55–67. doi: 10.3354/meps268055

Carlson, R. E. (1977). A trophic state index for lakes. *Limnol. Oceanogr.* 22, 361–369. doi: 10.4319/lo.1977.22.2.0361

Carberry, L., Roesler, C., and Drapeau, S. (2019). Correcting in situ chlorophyll fluorescence time? series observations for nonphotochemical quenching and tidal variability reveals nonconservative phytoplankton variability in coastal waters. *Limnol. Oceanogr.* 17, 462–473. doi: 10.1002/lom3.10325

Cloern, J. E., Powell, T. M., and Huzzey, L. M. (1989). Spatial and temporal variability in south san francisco bay (USA). II. temporal changes in salinity, suspended sediments, and phytoplankton biomass and productivity over tidal time scales. *Estuar. Coast. Shelf Sci.* 28, 599–613. doi: 10.1016/0272-7714(89)90049-8

Carstensen, J., Klais, R., and Cloern, J. E. (2015). Phytoplankton blooms in estuarine and coastal waters: seasonal patterns and key species. *Est. Coast. Shelf Sci.* 162, 98–109. doi: 10.1016/j.ecss.2015.05.005

Cebrián, J., and Valiela, I. (1999). Seasonal patterns in phytoplankton biomass in coastal ecosystems. *J. Plankton Res.* 21, 429–444. doi: 10.1093/plankt/21.3.429

Cetinić, I., Perry, M. J., D'asaro, E., Briggs, N., Poulton, N., Sieracki, M. E., et al. (2015). A simple optical index shows spatial and temporal heterogeneity in phytoplankton community composition during the 2008 North Atlantic bloom experiment. *Biogeosciences* 12, 2179–2194. doi: 10.5194/bg-12-2179-2015

Chung, M. G., Kang, H., and Choi, S.-U. (2015). Assessment of coastal ecosystem services for conservation strategies in South Korea. *PLoS One* 10:e0133856. doi: 10.1371/journal.pone.0133856

Crawford, J. T., Loken, L. C., Casson, N. J., Smith, C., Stone, A. G., and Winslow, L. A. (2015). High-speed limnology: using advanced sensors to investigate spatial variability in biogeochemistry and hydrology. *Environ. Sci. Technol.* 49, 442–450. doi: 10.1021/es504773x

Cullen, J. J. (1982). The deep chlorophyll maximum: Comparing vertical profiles of chlorophyll *a*. *Can. J. Fish. Aquat. Sci.* 39, 791–803. doi: 10.1139/f82-108

Delkash, M., Al−Faraj, F. A., and Scholz, M. (2018). Impacts of anthropogenic land use changes on nutrient concentrations in surface waterbodies: a review. *Clean Soil Air Water* 46:1800051. doi: 10.1002/clen.201800051

Denman, K. L., and Dower, J. F. (2008). "Patch dynamics," in *Encyclopedia of Ocean Sciences, Second Edition*, ed. J. H. Steele (Cambridge, MA: Academic Press), 2107–2114.

Dodds, W. K. (2007). Trophic state, eutrophication, and nutrient criteria in streams. *Trends Ecol. Evol.* 22, 669–676. doi: 10.1016/j.tree.2007.07.010

Fossum, T. O., Fragoso, G. M., Davies, E. J., Ullgren, J., Mendes, R., Johnsen, G., et al. (2019). Toward adaptive robotic sampling of phytoplankton in the coastal ocean. *Sci. Robotics* 13:eaav3041. doi: 10.1126/scirobotics.aav3041

Gasiûnaitë, Z. R., Cardoso, A. C., Heiskanen, A.-S., Henriksen, P., Kauppila, P., Olenina, I., et al. (2005). Seasonality of coastal phytoplankton in the Baltic Sea: influence of salinity and eutrophication. *Est. Coast. Shelf Sci.* 65, 239–252. doi: 10.1016/j.ecss.2005.05.018

Getis, A. (2008). A history of the concept of spatial autocorrelation: a geographer's perspective. *Geogr. Anal.* 40, 297–309. doi: 10.1111/j.1538-4632.2008.00727.x

Harding, L. W., Jr, Mallonee, M. E., Perry, E. S., Miller, W. D., Adolf, J. E., Gallegos, C. L., et al. (2019). Long-term trends, current status, and transitions of water quality in Chesapeake Bay. *Sci. Rep.* 9:6709. doi: 10.1038/s41598-019-43036-6

Havens, K. (2014). "Lake eutrophication and plankton food webs," in *Eutrophication: Causes, Consequences and Control*, eds A. Ansari and S. Gill (Dordrecht: Springer), 73–80. doi: 10.1007/978-94-007-7814-6_6

HELCOM (2010). Ecosystem health of the baltic sea 2003–2007: HELCOM Initial holistic assessment. *Balt. Sea Environ. Proc.* No. 122.

Horwood, J. (1978). Observations on spatial heterogeneity of surface chlorophyll in one and two dimensions. *J. Mar. Biol. Assoc. U.K.* 58, 487–502. doi: 10.1017/s0025315400028149

Howarth, R., Chan, F., Conley, D. J., Garnier, J., Doney, S., Marino, R., et al. (2011). Coupled biogeochemical cycles: eutrophication and hypoxia in temperate estuaries and coastal marine ecosystems. *Front. Ecol. Environ.* 9, 18–26. doi: 10.1890/100008

Lindeman, R. L. (1942). The trophic-dynamic aspect of ecology. *Ecology* 23, 399–417. doi: 10.2307/1930126

Lovejoy, S., Currie, W. J. S., Tessier, Y., Claereboudt, M. R., Bourget, E., Roff, J. C., et al. (2001). Universal multifractals and ocean patchiness: phytoplankton, physical fields and coastal heterogeneity. *J. Plankton Res.* 23, 117–141. doi: 10.1093/plankt/23.2.117

Lyngsgaard, M. M., Markager, S., Richardson, K., Møller, E. F., and Jakobsen, H. H. (2017). How well does chlorophyll explain the seasonal variation in phytoplankton activity? *Estuar. Coast.* 40, 1263–1275. doi: 10.1007/s12237-017-0215-4

Maso, M., and Duarte, C. M. (1989). The spatial and temporal structure of hydrographic and phytoplankton biomass heterogeneity along the Catalan coast (NW Mediterranean). *J. Mar. Res.* 47, 813–827. doi: 10.1357/002224089785076145

McGlathery, K. J., Sundbäck, K., and Anderson, I. C. (2007). Eutrophication patterns in shallow coastal bays and lagoons: the role of plants in the coastal filter. *Mar. Ecol. Prog. Ser.* 348, 1–18. doi: 10.3354/meps07132

McGillicuddy, D. J. Jr. (2008). "Models of small-scale patchiness," in *Encyclopedia of Ocean Sciences, Second Edition*, ed. J. H. Steele (Cambridge, MA: Academic Press), 474–487. doi: 10.1016/b978-012374473-9.00405-7

Misumi, M., Katoh, H., Tomo, T., and Sonoike, K. (2016). Relationship between photochemical quenching and non-photochemical quenching in six species of cyanobacteria reveals species difference in redox state and species commonality in energy dissipation. *Plant Cell Physiol.* 57, 1510–1517.

Nixon, S. W. (1995). Coastal marine eutrophication: a definition, social causes and future concerns. *Ophelia* 41, 199–219. doi: 10.1080/00785236.1995.10422044

Odum, H. T. (1956). Primary production in flowing waters. *Limnol. Oceanogr.* 1, 102–117.

Oseji, O. F., Fan, C., and Chigbu, P. (2019). Composition and dynamics of phytoplankton in the coastal bays of Maryland, USA, revealed by microscopic counts and diagnostic pigments analyses. *Water* 11:368. doi: 10.3390/w11020368

Pebesma, E. (2018). Simple features for R: standardized support for spatial vector data. *R J.* 10, 439–446.

Platt, T., Dickie, L. M., and Trites, R. W. (1970). Spatial heterogeneity of phytoplankton in a near-shore environment. *J. Fish. Board Can.* 27, 1453–1473. doi: 10.1139/f70-168

Platt, T. (1972). Local phytoplankton abundance and turbulence. *Deep-Sea Res.* 19, 183–188. doi: 10.1016/0011-7471(72)90029-0

Proctor, C. W., and Roesler, C. S. (2010). New insights on obtaining phytoplankton concentration and composition from *in situ* multispectral chlorophyll fluorescence. *Limnol. Oceanogr. Methods* 8, 695–708. doi: 10.4319/lom.2010.8.0695

R Core Team (2014). *R: A Language and Environment for Statistical Computing*. Vienna: R Foundation for Statistical Computing.

Reusch, T. B. H., Dierking, J., Andersson, H. C., Bonsdorff, E., Carstensen, J., Casini, M., et al. (2018). The Baltic Sea as a time machine for the future coastal ocean. *Sci. Adv.* 4:eaar8195. doi: 10.1126/sciadv.aar8195

Romero, L., Siegel, D. A., McWilliams, J. C., Uchiyama, Y., and Jones, C. (2016). Characterizing stormwater dispersion and dilution from small coastal streams. *J. Geophys. Res. Oceans* 121, 3926–3943. doi: 10.1002/2015jc011323

Sale, P. F., Hanski, I., and Kritzer, J. P. (2006). "The merging of metapopulation theory and marine ecology: establishing the historical context," in *Marine Metapopulations*, eds J. P. Kritzer and P. F. Sale (Cambridge, MA: Academic Press), 3–28. doi: 10.1016/b978-012088781-1/50004-2

Scheffer, M., Carpenter, S., Foley, J. A., Folke, C., and Walker, B. (2001). Catastrophic shifts in ecosystems. *Nature* 413, 591–596. doi: 10.1038/35098000

Seuront, L. (2005). Hydrodynamic and tidal controls of small-scale phytoplankton patchiness. *Mar. Ecol. Prog. Ser.* 302, 93–101. doi: 10.3354/meps302093

Simis, S. G. H., Huot, Y., Babin, M., Seppälä, J., and Metsämaa, L. (2012). Optimization of variable fluorescence measurements of phytoplankton communities with cyanobacteria. *Photosynth. Res.* 112, 13–30. doi: 10.1007/s11120-012-9729-6

Sokal, R. R., and Oden, N. L. (1978). Spatial autocorrelation in biology: 1. Methodology. *Biol. J. Linn. Soc.* 10, 199–228. doi: 10.1111/j.1095-8312.1978.tb00013.x

Sommer, U., Gliwicz, Z. M., Lampert, W., and Duncan, A. (1986). The PEG-model of seasonal succession of planktonic events in fresh waters. *Arch. Hydrobiol.* 106, 433–471.

Sommer, U., Adrian, R., De Senerpont Domis, R., Elser, J. J., Gaedke, U., Ibelings, B., et al. (2012). Beyond the plankton ecology group (PEG) model: mechanisms driving plankton succession. *Annu. Rev. Ecol. Evol. Syst.* 43, 429–448. doi: 10.1146/annurev-ecolsys-110411-160251

Sommer, U., and Lengfellner, K. (2008). Climate change and the timing, magnitude, and composition of the phytoplankton spring bloom. *Global Change Biol.* 14, 1199–1208. doi: 10.1111/j.1365-2486.2008.01571.x

Song, H., Ji, R., Xin, M., Liu, P., Zhang, Z., and Wang, Z. (2019). Spatial heterogeneity of seasonal phytoplankton blooms in a marginal sea: physical drivers and biological responses. *ICES J. Mar. Sci.* 77, 408–418.

Sosik, H. M., and Mitchell, B. G. (1991). Absorption, fluorescence, and quantum yield for growth in nitrogen-limited *Dunaliella tertiolecta*. *Limnol. Oceanogr.* 36, 910–921. doi: 10.4319/lo.1991.36.5.0910

Therriault, J. C., and Platt, T. (1981). Environmental control of phytoplankton patchiness. *Can. J. Fish. Aquat. Sci.* 38, 638–641. doi: 10.1139/f81-085

Underwood, A. J., and Chapman, M. G. (1996). Scales of spatial patterns of distribution of intertidal invertebrates. *Oecologia* 107, 212–224. doi: 10.1007/bf00327905

Vahtera, E., Conley, D. J., Gustafsson, B. G., Kuosa, H., Pitkänen, H., Savchuk, O. P., et al. (2007). Internal ecosystem feedbacks enhance nitrogen-fixing cyanobacteria blooms and complicate management in the Baltic Sea. *Ambio* 36, 186–194. doi: 10.1579/0044-7447(2007)36[186:iefenc]2.0.co;2

Worm, B., Barbier, E. B., Beaumont, N., Duffy, J. E., Folke, C., Halpern, B. S., et al. (2006). Impacts of biodiversity loss on ocean ecosystem services. *Science* 314, 787–790.

Wroblewski, J. S., and O'Brien, J. J. (1976). A spatial model of phytoplankton patchiness. *Mar. Biol.* 35, 161–175. doi: 10.1007/bf00390938

Yvon-Durocher, G., Schaum, C.-E., and Trimmer, M. (2017). The temperature dependence of phytoplankton stoichiometry: investigating the roles of species sorting and local adaptation. *Front. Microbiol.* 8:2003. doi: 10.3389/fmicb.2017.02003

Zeileis, A., and Grothendieck, G. (2005). zoo: S3 infrastructure for regular and irregular time series. *arXiv* [Preprint]. doi: 10.18637/jss.v014.i06

Conflict of Interest: The authors declare that the research was conducted in the absence of any commercial or financial relationships that could be construed as a potential conflict of interest.

Copyright © 2020 Scheinin and Asmala. This is an open-access article distributed under the terms of the Creative Commons Attribution License (CC BY). The use, distribution or reproduction in other forums is permitted, provided the original author(s) and the copyright owner(s) are credited and that the original publication in this journal is cited, in accordance with accepted academic practice. No use, distribution or reproduction is permitted which does not comply with these terms.

frontiers in Marine Science

ORIGINAL RESEARCH
published: 16 July 2020
doi: 10.3389/fmars.2020.00515

Biophysical Control on Variability in Phytoplankton Production and Composition in the South-Western Tropical Indian Ocean During Monsoon 2014

Sarat C. Tripathy[1], P. Sabu[1], Sivaji Patra[2], Ravidas K. Naik[1], Amit Sarkar[1,3], Vankara Venkataramana[1], Anvita U. Kerkar[1] and Pandi Sudarsanarao[1]*

[1] National Centre for Polar and Ocean Research (NCPOR), Ministry of Earth Sciences, Vasco da Gama, India, [2] National Centre for Coastal Research (NCCR), Ministry of Earth Sciences, Chennai, India, [3] Environment and Life Sciences Research Centre, Kuwait Institute for Scientific Research Centre, Shuwaikh, Kuwait

OPEN ACCESS

Edited by:
Malcolm McFarland, Florida Atlantic University, United States

Reviewed by:
S. Sai Elangovan, National Institute of Oceanography (CSIR), India
Jelena Godrijan, Rudjer Boskovic Institute, Croatia

***Correspondence:**
Sarat C. Tripathy
sarat@ncpor.res.in

Specialty section:
This article was submitted to Marine Ecosystem Ecology, a section of the journal Frontiers in Marine Science

Received: *07 February 2020*
Accepted: *04 June 2020*
Published: *16 July 2020*

Citation:
Tripathy SC, Sabu P, Patra S, Naik RK, Sarkar A, Venkataramana V, Kerkar AU and Sudarsanarao P (2020) Biophysical Control on Variability in Phytoplankton Production and Composition in the South-Western Tropical Indian Ocean During Monsoon 2014. Front. Mar. Sci. 7:515. doi: 10.3389/fmars.2020.00515

The existing oligotrophic conditions in the southwest tropical Indian Ocean (SWTIO) is believed to be one of the causes for low phytoplankton productivity (PP) observed in this area. Though many remote sensing based studies on PP have been carried out in SWTIO, studies on *in situ* estimation of PP and its cause(s) of variability are scarce. Thus, to understand the controlling environmental forcings on the variability in phytoplankton biomass (chlorophyll-a; Chl-*a*), community structure and productivity, time series (TS; @6 h intervals for 10 days; 1 station), plus point measurements (RT; 3 stations) were carried out in the SWTIO during the southwest monsoon (June) of 2014. Strong thermohaline stratification resulted in shallow (35–40 m) mixed layer (ML). Subsurface Chl-*a* maximum (SCM) was observed to oscillate within 40–60 m with majority of peaks at ∼50 m, and existed just beneath the ML depth. Light availability during sampling period was highly conducive for algal growth; nutrient ratios indicated N- and Si-limitation (N:P $<$ 10; N:Si $<$ 1 and SiO_4 $<$ 5 μM) suggesting unfavorable conditions for diatoms and/or silicoflagellates growth within the ML. Furthermore, HPLC-based pigments analysis confirmed dominance of nano-sized plankton (53%) followed by pico-plankton (25%) and micro-plankton (22%). Column integrated production (IPP) varied from 176 to 268 (241 ± 43 mgC m^{-2} d^{-1}) and was relatively stable during the observation period, except a low value (19.4 E m^{-2} d^{-1}) on 11 June, which was ascribed to the drastic dropdown in the daily incident PAR due to overcast sky. Vertical profiles of PP and Chl-*a* resembled each other and maximum PP usually corresponded with SCM depths. The Chl-*a*-specific PP (P^B) was mostly higher within the ML and showed no surface photoinhibition, due to the dominance of smaller phytoplankton (less prone to pigment packaging effect) in the surface layer. Comparatively, higher P^B within the ML is indicative of phytoplankton healthiness during the sampling time, whereas low P^B below the SCM was due to light limitation. Highest integrated Chl-*a* (39 mg m^{-2})

and IPP (328 mgC m^{-2} d^{-1}) observed at RT-2 was clearly linked to low sea surface height anomaly (SSHA), cyclonic disturbance, and associated positive Ekman suction. Conversely, high SSHA and strong stratification conditions prevailed at TS, RT-4, and RT-6 stations leading to comparatively lower IPP (176-268, 252, and 243 mgC m^{-2} d^{-1}), respectively.

Keywords: chlorophyll maximum, tropical Indian Ocean, phytoplankton productivity, pigment signatures, time series, upwelling

INTRODUCTION

Oceanic phytoplankton, being the base of marine food-web, plays a crucial role in global biogeochemical cycles (Falkowski et al., 1994), regulates the global climate (Sabine et al., 2004), fisheries (Stock et al., 2017), and the condition and variability of life in the oceans. Understanding alterations in global ocean phytoplankton production (PP) is one of the pressing issues in ocean biogeochemistry because it not only provides vital insights to the bio−physical interactions of the ecosystem (Naqvi et al., 2010) but also offer biophysical feedbacks (Murtugudde et al., 1999). Through the process of PP significant drawdown of atmospheric CO_2 occurs which is subsequently transported to the ocean interior through "biological pump" (Longhurst and Harrison, 1989). Thus, it is essential to gain clear perception of the cause(s) responsible for PP variability in the oceanic environment. Basically, PP is a function of four variables viz., photosynthetically active radiation (PAR), nutrients, phytoplankton biomass (chlorophyll-*a*), and water temperature (Behrenfeld and Falkowski, 1997b), and hence any adverse changes in the above variables can have telling effect on PP variability which would cascade through the entire food-web in the region.

The southwest tropical Indian Ocean (SWTIO) situated between 5°S to 10°S and 50°E to 80°E is one of the major upwelling area in the Indian Ocean region due to the presence of Seychelles–Chagos Thermocline Ridge (SCTR) system characterized by a thermocline shallower than the euphotic zone (Murtugudde and Busalacchi, 1999; Wiggert et al., 2005). The SWTIO is influenced by the unique seasonally reversing monsoon wind systems that act as the major physical driver for the prevailing upwelling processes resulting in significant variability in sea surface temperature (SST) in different timescales, in comparison to the other regions of Indian Ocean (Annamalai et al., 2003; Zhou et al., 2008; Jung and Kirtman, 2016). Also, rising SST in this region can enhance surface stratification inhibiting vertical mixing, thereby dwindling supply of nutrients into the well-lit euphotic zone where photosynthesis takes place (Behrenfeld et al., 2006; Roxy et al., 2016). Fluctuations in the vertical mixing process also influences the overall time span of light experienced by the phytoplankton (McCreary et al., 1996) in the water column. Moreover, the variability in bio-physical processes in SWTIO region are mostly controlled by the strength and duration of the monsoon winds and associated nutrient dynamics, and the downward trend in biological production, if any, in these upwelling systems has immense ramification on the marine food-web and economic status of the fishing community of this region (Roxy et al., 2016; Sreeush et al., 2018).

The SWTIO region is climatologically and biologically important because of active upwelling processes and/or the shallow thermocline, which is prone to the atmospheric forcing at different time scales (Wiggert et al., 2006). The vertical turbulence effectively exchanges heat with the thermocline, introducing cooler thermocline waters to the surface. Nevertheless, SST in the SWTIO is much warmer (annual mean is 28°C) than the surface waters from other upwelling tropical regions like eastern equatorial Pacific Ocean and Atlantic Ocean (George et al., 2013). In Northwest Indian Ocean (Arabian Sea) frequent occurrence of phytoplankton blooms was reported (Prasanna Kumar et al., 2001; Wiggert et al., 2005; Naqvi et al., 2010), which was attributed to the strong monsoonal wind forcing in this region that lead to year-round upwelling resultant from coastal divergence of Ekman transport and from Ekman suction (Murtugudde et al., 1996), replenishing nutrients in the surface and supporting higher rates of PP (Wiggert et al., 2005; McCreary et al., 2009; Resplandy et al., 2011). On the other hand, the surface phytoplankton blooms observed in the oligotrophic SCTR region is caused by nutrients entrainment into the mixed layer (ML) and/or the dispersal of phytoplankton from the deep chlorophyll maximum (DCM) layer to the surface layer (Resplandy et al., 2009). Furthermore, Resplandy et al. (2009) opined that SCTR region is typified by local Ekman suction-induced Open Ocean upwelling, which sustains shallow ML throughout the year, and hence responsive to atmospheric forcing. Furthermore, studies have shown that the propagation of internally generated Rossby waves modifies the depth of the thermocline and thus influences the PP because the thermocline is shallower than the euphotic zone in this region (Wiggert et al., 2006, 2009).

George et al. (2013) studied the physical control of the chlorophyll-a distribution during winter and summer monsoon and opined that surface freshening controls the chlorophyll-*a* by modulating static stability and ML depth. Ocean warming induced an alarming decline of up to 20% in phytoplankton over the past 60 years (Roxy et al., 2016), and impact of the Indian Ocean Dipole (IOD) and El Niño Southern Oscillation (ENSO) on significant interannual variation chlorophyll-*a* has been reported (Dilmahamod et al., 2016) in this region. Resplandy et al. (2009) have shown that interannual variability of the

thermocline and its role modulating the response to Madden-Julian Oscillation (MJO) controls the chlorophyll-*a* and export flux of carbon. Further, recent study has shown that Ocean Carbon-Cycle Model Intercomparison Project (OCMIP-II)–based estimated CO_2 flux and pCO_2 underestimated the SCTR variability portraying it as a CO_2 sink region (Sreeush et al., 2018). Studies carried out in the SCTR region either describe the role of physical forcings in modulating the phytoplankton biomass (chlorophyll-a) concentrations (George et al., 2013; Roxy et al., 2016; Dilmahamod et al., 2016) and/or satellite or model-based PP (Resplandy et al., 2009; Sreeush et al., 2018); however, none of the studies have reported any *in situ* measured phytoplankton C-uptake rates (PP), phytoplankton size class/community, and phytoplankton physiological perspective vis-à-vis the physical forcings prevailing in this oligotrophic region. Hence, this study investigates the spatiotemporal variability in sea truth PP and phytoplankton composition with respect to the prevailing environmental forcings. To the best of our comprehension, this is the first report of *in situ* measurements of PP and phytoplankton size class/community from this area, which would enhance our understanding of the existing bio−physical interactions and plug our knowledge gaps.

MATERIALS AND METHODS

Study Area, Sampling Periodicity, and Hydrography

Part of the study area (**Figure 1**) is located in the Seychelles-Chagos Thermocline Ridge (SCTR, 5°S–10°S, 50°E–80°E) in the southwest tropical Indian Ocean (SWTIO) as defined by Hermes and Reason (2008) and part in the equatorial Indian Ocean (EIO) region. Year-round occurrence of upwelling phenomena is one of the salient features of SCTR region (Woodberry et al., 1989; McCreary et al., 1993), nevertheless oligotrophic conditions prevails in this area. Existence of Ekman suction driven upwelling (Spencer et al., 2005) and shallow thermocline signifies this region's importance in the perspective of biological productivity. Due to shallow thermocline the influence of physical forcings on phytoplankton bloom/productivity in this region is clearly discernible (Wiggert et al., 2006, 2009; Resplandy et al., 2009; George et al., 2013).

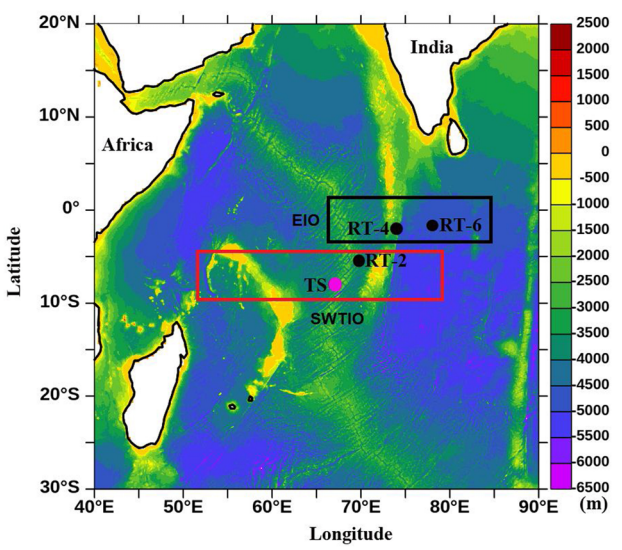

FIGURE 1 | Study area map showing the four sampling locations. The black and pink dots indicate return track (RT) and time series (TS) stations; red and black rectangle denotes the southwest tropical Indian Ocean (SWTIO) and equatorial Indian Ocean (EIO) region, respectively. Background colors indicate the bathymetry derived from ETOPO data.

Sampling was conducted onboard *ORV-Sagar Nidhi* at four stations in the study area during the monsoon season (June 9–23) of 2014. Time series (TS) observations (6-hourly interval over 10 days) were conducted at 08°S and 67°E; on the return track (RT) three discrete stations (RT-2 at 5.58°S and 69.75°E, RT-4 at 1.90°S and 73.88°E, and RT-6 at 1.73°S and 77.97°E) were also sampled (**Table 1**) for assessing same sets of parameters as carried out for TS station. Based on the geographical locations, the TS and RT-2 stations were considered as SCTR stations, whereas RT-4 and RT-6 were considered as the stations located in the EIO region.

The conductivity-temperature-depth (CTD) profiling were conducted using Sea-Bird (SBE-9plus, United States) instrumentation mounted on a Sea-Bird carousel, and the measured vertical profiles were used to determine the water mass properties of the study area. The CTD casts were performed at 6-hourly intervals at the TS station. Salinity measured by the CTD were calibrated against the values obtained from onboard Salinometer (Guildline 8400A). Sea surface temperature (SST) was recorded using a bucket thermometer (Theodor Friedrichs & Co.) with an accuracy of ± 0.2°C. Mixed layer depth (MLD) was determined based on a density (σ_t) change of 0.05 kg m^{-3} at depth compared to near-surface. Water sampling from standard depths (0, 10, 20, 30, 50, 75, 100, 120, 150, and 200 m) were carried out by 5 L Niskin bottles (General Oceanics) attached to the carousel sampler.

Phytoplankton Pigments, Light, and Nutrients

Concentration of phytoplankton biomass (Chl-*a*; mg m^{-3}) was estimated by filtering 3 L of water samples onto 47 mm GF/F filters (Whatman®) under dim light and low suction pressure (<0.1 kPa). The filters were kept frozen at −80°C till further analysis. Quantification of the pigments was carried out fluorometrically (10-AU, Turner Designs, United States) following overnight extraction of the GF/F filters in 10 ml of AR grade 90% acetone in dark and cool condition (Strickland and Parsons, 1972). Chl-*a* values at discrete depths were integrated to obtain column Chl-*a* (Chl_{int}; mg m^{-2}). Furthermore, 3 L of surface water samples at time series (TS) stations were filtered through 2 and 10 μm isopore-membrane filters (47 mm, Merck Millipore) and assayed fluorometrically (as described above) to estimate size-fractionated Chl-*a* contribution by smaller and larger phytoplankton size-classes. Due to logistical limitations we restricted the size-fractionation exercise to the above two

TABLE 1 | Primary productivity and associated variables at sampling station: sea surface temperature (SST), mixed layer depth (MLD), euphotic depth (Z_{eu}), Vertical light attenuation coefficient (k_d), mean photosynthetically active radiation (PAR) level in the mixed layer (E_{ML}), daily surface PAR, surface chlorophyll-*a* (Chl_0), column-integrated chlorophyll-*a* (Chl_{int}), surface primary productivity (PP_0), column-integrated PP (IPP), surface Chl-*a*-specific PP (P^B), and maximum P^B in the water column (P^B_{opt}, in parenthesis).

Station ID	Sampling Date	Latitude (°S)	Longitude (°E)	SST (°C)	MLD (m)	Z_{eu} (m)	k_d (m^{-1})	E_{ML} (E m^{-2} d^{-1})	PAR (E m^{-2} d^{-1})	Chl_0 (mg m^{-3})	Chl_{int} (mg m^{-2})	PP_0 (mgC m^{-3} d^{-1})	IPP (mgC m^{-2} d^{-1})	P^B (P^B_{opt}) (mgC (mgChl a)$^{-1}$ d^{-1})
TS-6	June 09, 2014	8	67	27.9	35	80	0.065	15.8	42.4	0.17	30.2	2.39	268.8	13.5 (15.0)
TS-14	June 11, 2014	8	67	28.0	35	80	0.070	6.7	19.4	0.26	37.9	1.82	176.8	6.8 (8.7)
TS-22	June 13, 2014	8	67	28.2	35	80	0.051	18.4	42.0	0.19	32.6	2.19	265.0	11.1 (13.2)
TS-30	June 15, 2014	8	67	28.4	35	80	0.061	16.6	42.5	0.18	22.7	2.09	253.2	11.6 (16.79)
RT-2	June 19, 2014	5.58	69.75	29.0	42	70	0.068	16.0	46.5	0.22	39.4	3.14	328.1	14.3 (17.8)
RT-4	June 21, 2014	1.90	73.88	29.7	38	80	0.062	19.5	51.0	0.10	28.3	1.84	252.9	17.8 (17.8)
RT-6	June 23, 2014	1.73	77.97	29.9	55	90	0.044	19.5	52.0	0.16	35.1	1.98	243.1	11.7 (11.7)

size classes to approximate the % contribution by small (<2–10 μm) and large (>10 μm) phytoplankton. The above size-fractionation would not account for the picoplankton, and may not give appropriate estimation of the largest fraction (microplankton > 20 μm).

For phytoplankton pigments, 4 L of waters samples were filtered onto 25 mm GF/F filters and the filters were stored at −80°C till further analysis. Pigments analysis was also carried out by high-performance liquid chromatography (HPLC, Agilent Technologies) by means of XDB C8 column. Pigments separation was done by a binary solvent (solvent A-70/30: methanol/0.5M ammonium acetate; solvent B-100% methanol) gradient according to Kurian et al. (2012). Commercially available standards procured from DHI Inc. (Denmark) were used for the identification and quantification of pigments. In general, HPLC allows determining a suite of pigments (usually up to 15). In this study we identified seven pigments (i.e., Fucoxanthin, Peridinin, Alloxanthin, 19'-Hexanoyloxyfucoxanthin [19'HF], 19'-Butanoyloxyfucoxanthin [19'BF], Zeaxanthin, and TChl-b [Chl-b + divinyl chlorophyll-b]) as markers or diagnostic pigments (DP) of phytoplankton taxa as described in Uitz et al. (2006) to construct the "pigment indices" with objective to quantify phytoplankton taxonomic composition (%) with minimum number of pigments. The DP represents the sum of all the seven DP concentrations. Size-fractionated contributions of phytoplankton (f_{micro} [>20 μm], f_{nano} [2–20 μm], f_{pico} [<2 μm]) were calculated using following equations:

$$f_{micro}\% = 100 \times (1.41\,[\text{fucoxanthin}] + 1.41\,[\text{peridinin}])/\Sigma DP \quad (1)$$

$$f_{nano}\% = 100 \times (0.60\,[\text{alloxanthin}] + 0.35\,[19'\text{BF}] + 1.27\,[19'\text{HF}])/\Sigma \text{DP} \quad (2)$$

$$f_{pico}\% = 100 \times (0.86\,[\text{zeaxanthin}] + 1.01\,[\text{TChlb}])/\Sigma \text{DP} \quad (3)$$

Photosynthetically active radiation (PAR, 400–700 nm) at sea surface (E_0, m^{-2} s^{-1}) was measured using a scalar irradiance sensor attached to the automatic weather station (AWS) mounted on the ship. The instantaneous values were integrated over the day length (dawn to dusk) to quantify daily incoming PAR (D_{PAR}; E m^{-2} d^{-1}). Subsurface (E_z) PAR intensity were measured by a sensor (QSP-2200, Biospherical Inc.) attached to the CTD carousel, and the diffuse attenuation coefficient for downwelling PAR (k_d) was calculated according to Kirk (1994) as follows:

$$k_d = \frac{\ln(E_0) - \ln(E_z)}{z} \quad (4)$$

The euphotic depth, Z_{eu} (physical depth receiving 1% of E_0), was calculated as:

$$Z_{eu} = \frac{1}{k_d} \times \ln(100) \quad (5)$$

by substituting k_d in the Beer-Lambert equation (Kirk, 1994). Mean light levels in the mixed layer (E_{ML}) at different stations were calculated as: $E_{ML} = D_{PAR}[1\text{-}\exp(\text{-}k_d.z)]/k_d.z$ (Boyd et al., 2007; Cheah et al., 2013), where z is the depth of the mixed layer. Water samples collected in pre-cleaned polypropylene bottles used for estimating concentrations of the inorganic macronutrients (NO_3, SiO_4, and PO_4) were determined onboard by a continuous flow autoanalyser (SKALAR Inc.).

Primary Productivity Measurements

Apart from the three discrete stations, primary productivity (PP) was also quantified every alternative day between 9 and 17 June 2014 at the time series station (**Table 1**). Water samples (3 L) were collected from five discrete depths corresponding to 100, 50, 25, 10, and 1% of surface irradiance. Samples were sieved through a 200 μm plankton mesh to exclude zooplankton grazers. After adding 1 ml of ^{14}C [$NaH^{14}CO_3$] in each sample (5 μCi per 250 ml of seawater in Nalgene bottles), the samples (in duplicates) were incubated in an on-deck incubation tank for 12 h (dawn to dusk) following standard simulated *in situ* incubation technique (UNESCO-JGOFS, 1994). To achieve the most realistic condition with regard to light quality and temperature during the incubations, the incubation tank temperature was maintained by continuously circulating surface seawater through the incubation tank. One bottle was immediately filtered for a time zero control (initial value), whereas two light and one dark bottle from each depth were incubated using appropriate density filters packets to compensate for light intensity (50, 25, 10, and 1%) for respective depths. Incubation was terminated by filtration of samples onto pre-combusted 25 mm GF/F filters (Whatman®), followed by exposing them to concentrated HCl fumes to remove excess inorganic carbon. The filters were placed in scintillation vials and stored at −20°C until further analysis at shore laboratory. The activity was counted on a liquid scintillation counter (Packard 2500 TR) after adding 10 ml of scintillation cocktail (Lohrenz et al., 1992). Disintegrations per minute (dpm) were converted into daily PP (mgC m^{-3} d^{-1}) at discrete depths (UNESCO-JGOFS, 1994) and the euphotic zone-integrated PP (IPP; mg C m^{-2} d^{-1}) was estimated by trapezoidal integration. Chl-*a*-specific PP, (P^B; mgC [mgChl-*a*]$^{-1}$ d^{-1}) was calculated by normalizing PP with corresponding Chl-*a*. The optimum value of P^B in the water column was considered as P^B_{opt}.

The link between P^B and corresponding PAR in the water column (hereafter, PAR-P^B relationship) was established by curve-fitting. Here, the PAR-P^B relationship does not represent the true photosynthesis-irradiance (P-E) response of the same phytoplankton assemblages; rather, it symbolizes the association between the P^B and the corresponding PAR at discrete depths as described by Sakshaug et al. (1997). For curve fitting, P-E model (Webb et al., 1974) containing only two photosynthetic parameters was used, which can be described by the following equation:

$$P^B = P^B_{opt}\left[1 - exp\left(-E/E_{max}\right)\right] \quad (6)$$

where P^B, P^B_{opt}, E_{max} are Chl *a*-normalized PP (mgC [mgChl-*a*]$^{-1}$ d^{-1}), Chl *a*-normalized optimal PP (mgC [mgChl-*a*]$^{-1}$ d^{-1}) in the water column, irradiance value at the point of inflection between light-limited and light-saturated phases (μE m^{-2} d^{-1}), respectively. Since no photoinhibition was apparent, the above model was chosen for the dataset.

Primary Production Model

The vertically generalized production model (VGPM) proposed by Behrenfeld and Falkowski (1997a) was employed to estimate IPP from the satellite measured variables. This is a depth-integrated model, which relates sea surface Chl-*a* concentration (Chl_0) to Z_{eu}-integrated primary productivity (IPP) and can be expressed as:

$$IPP = 0.66125 \times P^B_{opt} \times \left[\frac{E_0}{(E_0 + 4.1)}\right] \times Z_{eu} \times Chl_0 \times DL \quad (7)$$

where IPP, P^B_{opt}, E_0, Z_{eu}, Chl_0, and DL are Z_{eu}-integrated daily PP (mgC m^{-2} d^{-1}), Chl-*a*-normalized maximum PP in the vertical profile (mgC [mgChl-*a*]$^{-1}$ h^{-1}), PAR at sea surface (E m^{-2} d^{-1}), depth (m) of the euphotic zone estimated from Chl_0 according to Morel and Berthon (1989), sea surface Chl-*a* (mg m^{-3}), and day-length (h) calculated as proposed by Kirk (1994), respectively. The light-dependent function [$E_0/(E_0 + 4.1)$] describes the relative change in the quantum efficiency of depth-integrated PP as a function of E_0; whereas as 0.66125 is a combined scaling factor for Chl-*a* concentration at discrete depth, and relative vertical distribution of C-fixation as a function of optical depth (Behrenfeld and Falkowski, 1997a). The P^B_{opt}, a photo-adaptive parameter necessary to convert the estimated biomass into photosynthetic rate, can be expressed as a 7th order polynomial function of SST as described in Behrenfeld and Falkowski (1997a). Sea surface variables (i.e., SST, Chl_0, and E_0) were derived from Moderate Resolution Imaging Spectroradiometer (MODIS) and used as input for the VGPM to measure satellite estimates of IPP in the study area.

Satellite-Based Observations

Weekly average level-3 chlorophyll was derived from MODIS-Aqua for May and June 2014, whereas daily surface winds were derived from the Advanced Scatterometer (ASCAT). Daily SST was derived from Advanced Very High Resolution Radiometer (AVHRR) and daily sea surface height anomaly (SSHA) information was obtained from the Copernicus Marine Environment Monitoring Service (CMEMS) for the study period. Ekman suction velocity (W_e) was calculated using the equation:

$$W_e = \mathrm{Curl}(\tau/\rho f) \quad (8)$$

where τ, ρ, and f is the surface wind stress, density of the seawater, and Coriolis parameter, respectively.

RESULTS

Hydrographic Variations Observed From CTD Profiling

At time series (TS) station the sea surface temperature (SST) ranged from 27.9–28.4°C (**Table 1**), whereas vertical variation

of temperature laid between 12.0–28.17 (19.52 ± 5.26°C) with minimal variations in the upper 35–40 m compared to the deeper layers, and depicted a shallow thermocline (**Figure 2A**). Depth profile variation of salinity ranged from 34.38–35.31 (34.96 ± 0.20). Compared to temperature, variation of salinity was more prominent in the upper layer (**Figure 2B**). Occurrence of low saline and warm water mass formed a stratified surface layer and restricted the mixed layer depth (MLD) to 35–40 m as evidenced from the vertical profiles of sigma-t (**Figure 2C**) which varied between 21.97–27.42 (25.18 ± 1.77 kg m^{-3}-1000). Fluorescence profiles indicated clear subsurface Chl-*a* maximum (SCM) oscillating within 40–60 m with majority of peaks at ∼50 m, and existed just beneath the MLD (**Figure 2D**). The depth of the euphotic zone (Z_{eu}) was ∼80 m (**Table 1**) and did not vary over the study period. Z_{eu} was deeper than MLD resulting in moderately high Z_{eu}-MLD values (>35 m), implying that light availability during the sampling period was extremely favorable for algal growth within the ML (Sakshaug and Holm-Hansen, 1986; Westwood et al., 2011).

The return track (RT) stations witnessed higher SST compared to TS stations, which varied from 29.0–29.9^{0}C. Likewise, the vertical variation of temperature was also high, ranging between 12.8 and 29.8 (21.27 ± 5.99 ^{0}C). Temperature profile of RT-2 was different (cooler) compared to the other two stations (**Figure 2E**), whereas RT-6 depicted deeper MLD, probably due to the intrusion of low-saline warm water from north EIO region as evidenced by lower salinity values at RT-6 (**Figure 2F**). However, relatively higher salinity was observed at RT stations with vertical profile varying from 34.69–35.55 (35.19 ± 0.20). Decease in water density, deepening of MLD, SCM (**Figure 2H**), and Z_{eu} (**Table 1**) was observed toward the EIO region. Similar to TS station, the MLD was always shallower than the depth of SCM and Z_{eu} signifying favorable light environment for phytoplankton production within the MLD (Westwood et al., 2011). There was a significant positive relationship between SCM and MLD for entire study region ($r = 0.69$, $n = 43$, $p < 0.001$).

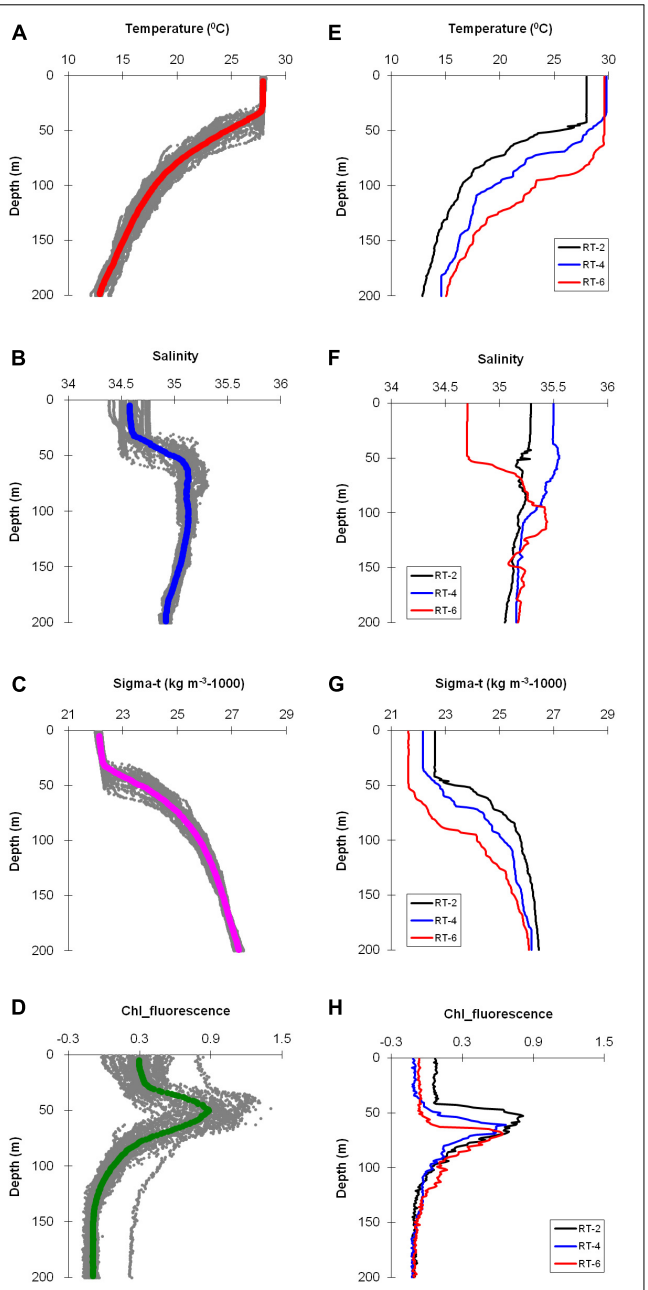

FIGURE 2 | Vertical profiles of hydrographic parameters at TS **(A–D)** and RT **(E–H)** stations measured by CTD profiling. The solid line in time series profiles indicates mean value, whereas the dotted profiles denote all the casts performed. Legends for RT stations are given in respective figures.

Phytoplankton Biomass, Nutrients, and PAR

Vertical profiles of different parameters concurrently collected along with the PP measurements (on 9, 11, 13, and 15 June) are only discussed here. At TS station, surface Chl-*a* (Chl_0) showed minimal variation ranging from 0.17 to 0.26 mg m^{-3} (**Table 1**); whereas vertical variation was more pronounced (**Figure 3A**) with concentrations ranging from not detectable quantity (ND) to 0.54 (0.23 ± 0.15 mg m^{-3}). Disparity in SCM depths was noticed for different days, which varied between 40−60 m as corroborating the Chl-*a* fluorescence data obtained from CTD. The column (up to 120 m)-integrated Chl-*a* (Chl_{int}) was moderately low and varied between 22.7 and 37.9 mg m^{-2} (**Table 1**). Concentrations of macronutrients, i.e., nitrate (NO_3), phosphate (PO_4), and silicic acid or silicate (SiO_4) were nearly stable and low in the mixed layer (ML), showing gradual increase with depth (**Figures 3B–D**). NO_3 was almost ND in the ML, indicating its limitation. However, all nutrient concentrations below the ML were higher than surface waters suggesting that NO_3 and/or Si-limitation for diatoms/silicoflagellates were lesser at deeper depth. In general, the nutrient ratios were lower than the classical Redfield ratio (N:P:Si = 16:1:16) throughout the water column, where the mean N:P, N:Si, and Si:P ratios were 3.74 (±3.86), 0.41 (±0.41), and 6.93 (±3.49), respectively, indicating N-limited conditions (N:P <10 and N:Si <1; Levasseur and Therriault, 1987; Paul et al., 2008), and higher SiO_4 concentrations relative to NO_3 at TS station. Furthermore, data

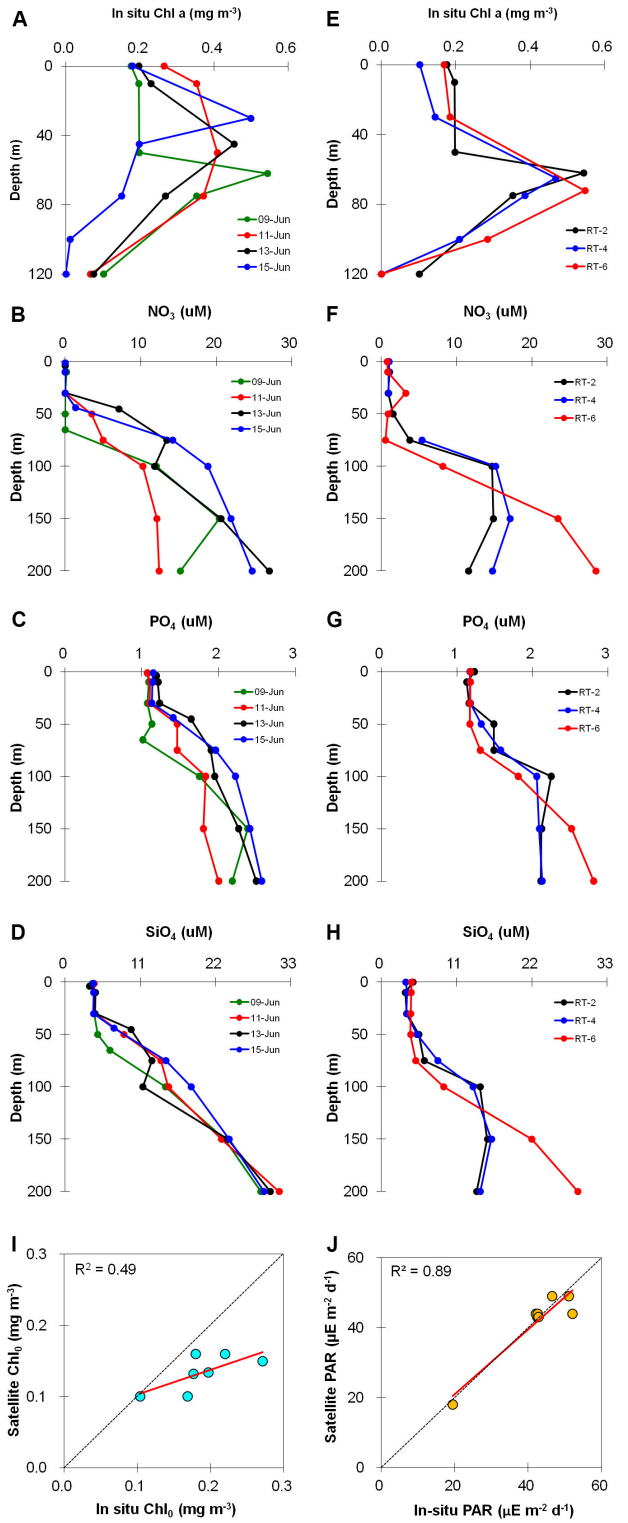

FIGURE 3 | Depth profiles of phytoplankton biomass (only for the locations where primary productivity was measured), and nutrients for TS **(A–D)** and RT **(E–H)** stations. Scatter plots of **(I)** chlorophyll *a* and **(J)** photosynthetically active radiation measured by *in situ* and satellite remote sensing methods. Legends for TS and RT stations are given in respective figures. The dotted diagonal line indicates 1:1 relationship.

suggests that SiO_4 (<5 μM) was highly limited for diatoms and/or silicoflagellates growth (Westwood et al., 2011) and for other phytoplankton groups, whereas NO_3 was limiting, especially in the ML. Nevertheless, Si:P ratio was <3 throughout the water column showing Si-enrichment (Harrison et al., 1977) especially below the MLD. Water column PAR varied from 0–1899 (11.45 ± 60.46 μE m^{-2} s^{-1}). Daily integrated surface PAR (D_{PAR}) was high (∼42 E m^{-2} d^{-1}) during the sampling period; however, low D_{PAR} (∼19.4 E m^{-2} d^{-1}) observed on 11 June (**Table 1**) was ascribed to the prevailing overcast sky condition.

Similar to TS station, Chl_0 variation was insignificant at RT stations (**Table 1**) and showed distinct vertical variation ranging from ND to 0.54 (0.25 ± 0.18 mg m^{-3}). Compared to TS station, SCM was located at deeper depths (**Figure 3E**) coinciding with CTD-based fluorescence measurements. The Chl_{int} was slightly higher and laid between 28.3 and 39.4 mg m^{-2} (**Table 1**). Correlation between Chl_0 and Chl_{int} was weak and insignificant (r = 0.4, p > 0.05) for the entire study area (figure now shown) emphasizing that sub-surface Chl-*a* has more contribution toward magnitude of Chl_{int}. Nutrients concentrations (**Figure 3F–H**) and ratios were virtually identical to TS station indicating depletion of NO_3 and SiO_4 in the ML, and enrichment of N and Si below the MLD. Intensity of D_{PAR} varied between 46.5 and 52.0 E m^{-2} d^{-1} (**Table 1**) and was higher for the stations depending on its proximity to the equator. The vertical light attenuation coefficient (k_d) varied from 0.051–0.070 (avg. 0.061 m^{-1}) and 0.044–0.068 (avg. 0.058 m^{-1}) at TS and RT stations, respectively (**Table 1**). No correlation between k_d and Chl_{int} was observed. Light climate, i.e., the mean PAR levels available to the phytoplankton in the ML (E_{ML}), varied from 6.7–18.4 and 16.0–19.8 E m^{-2} d^{-1} at TS and RT stations, respectively (**Table 1**). Variation in D_{PAR} and E_{ML} between different sampling stations were insignificant (p > 0.05), and E_{ML} corresponded to 36–45% of the D_{PAR} in the study area.

Comparison of Chl_0 obtained from satellite and *in situ* measurements (**Figure 3I**) resulted in underestimation by satellite and showed a moderate (r = 0.49, n = 7), insignificant ($p \leq 0.07$) correlation. Conversely, the observed D_{PAR} values were significantly correlated (r = 0.94, n = 7, $p < 0.001$) with its satellite-based counterparts (**Figure 3J**).

Phytoplankton Pigments Signatures

Fluorometrically measured size-fractionation of surface Chl-*a* data at TS station (**Figure 4A**) revealed dominant contribution from smaller (flagellates, nano- and pico-sized) phytoplankton (0.2−10 μm) representing 55–93% (avg. 72%) of the total Chl-*a*, which ranged from 0.18 to 0.26 mg m^{-3}. Since Chl-*a* size-fraction data was unavailable, the % contribution of smaller and larger phytoplankton to the total Chl-*a* could not be quantified for RT stations. Through, HPLC-based analyses we could segregate different photosynthetically active marker pigments for diatoms (fucoxanthin) and dinoflagellates (peridinin), both signifying micro-plankton (large cells); prymnesiophytes (19'HF) and chrysophytes (19'BF) representing nano-plankton (small cells); and synechococcus (zeaxanthin) and prochlorococcus (divinyl chlorophyll-a and divinyl chlorophyll-b), both characterizing pico-plankton (small cells). Size-fractioned

analysis of phytoplankton pigments showed an average of 22%, 53%, 25% contributions by micro-plankton (f_{micro}), nano-plankton (f_{nano}), and pico-plankton (f_{pico}), respectively, indicating dominance of nano-sized plankton in the TS stations almost throughout the study period (**Figure 4B**). Though the micro-plankton % remained stable during the TS measurements, a sharp decline in nano-plankton was observed on the 8th day (16 June) that coincided with increase in pico-plankton community in the surface layer. Size-fractionated contributions and vertical distribution pattern of plankton in the water column were similar to surface layer (see **Supplementary Material**).

Primary Production Variability

Measured PP in near-surface waters were low (∼2 mgC m^{-3} d^{-1}) and at discrete depths ranged from 5.83 mgC m^{-3} d^{-1} in subsurface waters, down to 0.56 mgC m^{-3} d^{-1} at the Z_{eu} (**Figure 5A**). Column integrated production (IPP) varied from 176–268 (241 ± 43 mgC m^{-2} d^{-1}) and was relatively stable during the observation period, except with low value for TS-14 (**Table 1**), which was ascribed to the drastic dropdown in the available D_{PAR} on that particular day due to overcast sky. Higher PP rates in the subsurface layers were directly related to higher Chl-*a* concentrations (**Figure 3A**). Vertical profiles of PP followed the distribution pattern of Chl-*a* within and below the ML and usually showed maximum values corresponding to SCM depths (∼10% of surface PAR). The assimilation number or Chl *a*-specific PP (P^B) varied from 1.6–16.7 (9.7 ± 4.1 mgC [mgChl-*a*]$^{-1}$ d^{-1}), and was mostly higher within the ML (**Figure 5B**) showing minimal/no surface photoinhibition (**Figure 5C**), which is indicative of probable dominance of smaller cells (Bricaud et al., 1995; Westwood et al., 2011) in the surface layer. Comparatively, higher P^B within the ML indicated that cells within this layer were healthy during the sampling time. Low P^B below the SCM depth could be due to light limitation.

Analogous to TS station, the PP at surface layer of the RT stations (**Figure 5D**) were low and at discrete depths it ranged from 0.09–7.52 (2.9 ± 1.9 mgC m^{-3} d^{-1}). Average IPP was relatively higher (274 mgC m^{-2} d^{-1}) than the TS stations. Like TS station, vertical profiles of PP rates resembled the distribution pattern of Chl-*a*, where the depths of maximum PP were observed below the MLD nearly coinciding with the SCM depths. The P^B (**Figure 5E**) varied from 0.25–17.8 mgC (mgChl-a^{-1} d^{-1}) with higher average (11.4 ± 6.7) compared to TS stations. PAR-P^B relationship indicated minimal/no surface photoinhibition (**Figure 5F**). Unlike TS station, surface P^B maximum was observed at RT-4 and RT-6, whereas subsurface P^B maximum, within the ML, was observed at RT-2. No surface photoinhibition and higher P^B in the surface and ML indicates probable preponderance of smaller phytoplankton communities (Bricaud et al., 1995; Westwood et al., 2011). Chl-*a* at discrete depths yielded in a significant positive and negative linear relationship (see **Supplementary Material**) with PP (r^2 = 0.19, n = 36, p < 0.05) and P^B (r^2 = 0.18, n = 36, p < 0.05), respectively. Inverse relationship between P^B and Chl-*a* implied decreasing photosynthetic efficiency with increasing biomass in the study area.

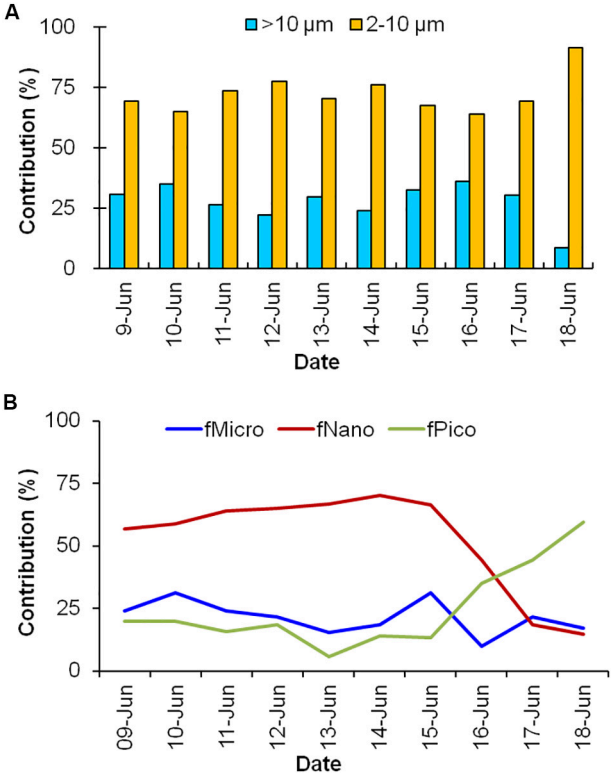

FIGURE 4 | Size-fractionated contribution (%) of phytoplankton community structure measured by **(A)** fluorometric and **(B)** HPLC-based pigment analysis in the surface layer of the TS station.

Comparison of measured and model (VGPM)-based IPP showed insignificant, weak correlation (r^2 = 0.24, n = 6) for the entire study area (**Figure 6**), yet, a close look at the data suggests that the measured and model-based IPP were strongly correlated for the RT stations (3 data points close to 1:1 line), conversely the calculated IPP underestimated (2.6 to 3 times) the measured IPP in TS stations. This underestimation could solely be linked to the difference in satellite-derived and measured Chl_0 concentrations that were fairly matching for the RT stations, whereas reasonably incongruous for the TS stations. Nevertheless, the results showed that a global model VGPM with its original parameterization can be used for precise estimation of IPP in this region. Since IPP on 14 June 2014 could not be calculated, that data has been removed from comparison.

To further understand the observed variability in IPP, relationship measured between IPP, and surface variables (those are embedded in the VGPM model) were investigated. Among the sea surface variables, D_{PAR} showed a moderately linear (r^2 = 0.45, n = 7) but insignificant (p > 0.05) relationship with measured IPP (**Figure 7A**). Furthermore, there was no clear relationship between measured IPP and SST (**Figure 7B**) and Chl_0 (**Figure 7C**). The only significant correlation (r^2 = 0.73, n = 7, p < 0.05) observed was between IPP and P^B_{opt} (**Figure 7D**). The P^B_{opt}, which is a key parameter in satellite-based modeling of

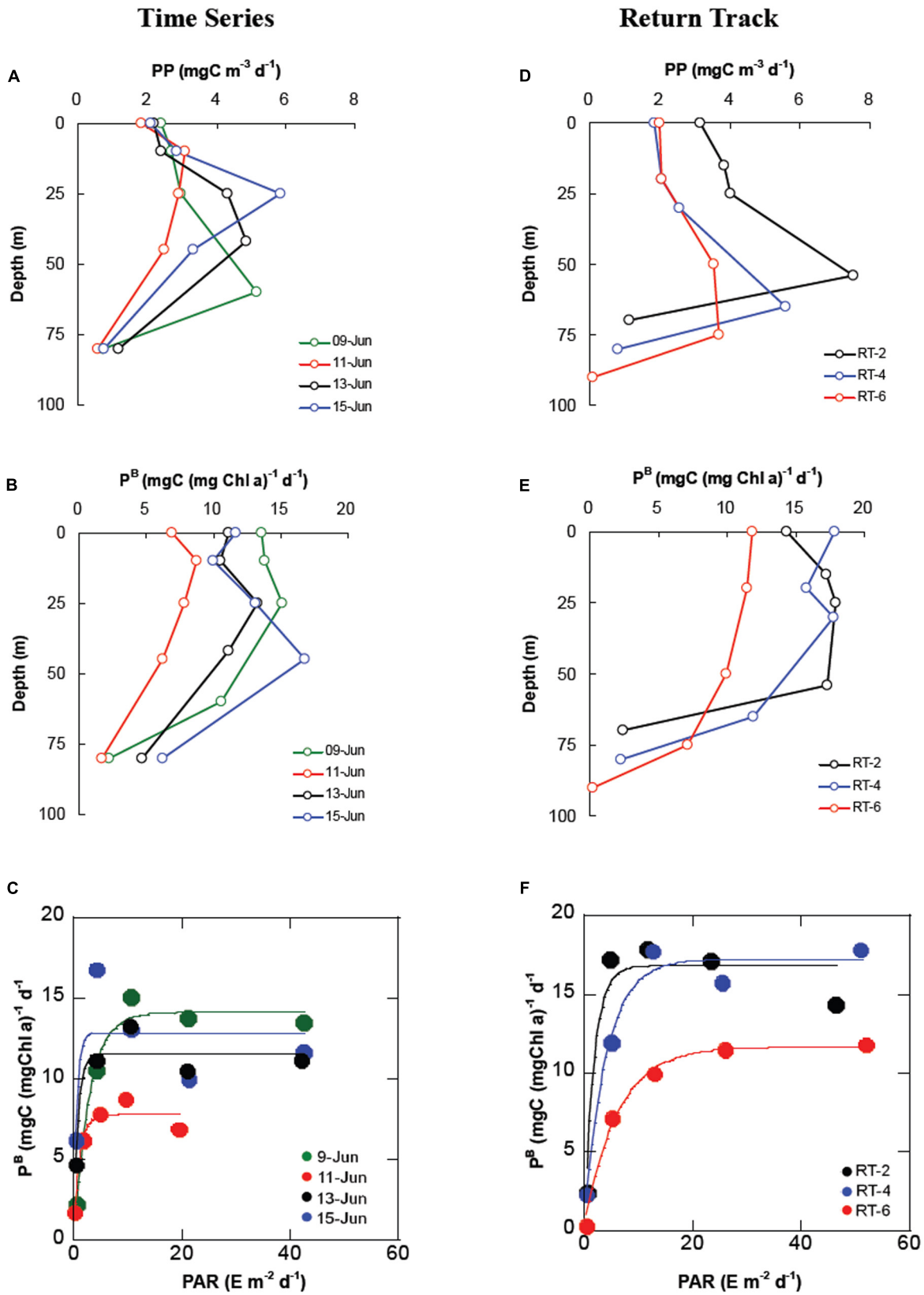

FIGURE 5 | Vertical profiles of primary productivity, chlorophyll a-normalized primary productivity, and daily PAR-P^B relationship in the water column for TS **(A–C)** and RT **(D–F)** stations.

IPP ranged from 8.72 (TS-14) to 17.81 (RT-2) mgC (mgChl-*a*)$^{-1}$ d^{-1} accounting for 73 % of variance in the measured IPP.

DISCUSSION

Factors Governing Phytoplankton Community Composition and Production: Implication on Export Flux and Transfer Efficiency

Phytoplankton are enormously dissimilar in terms of their taxonomy, morphology, and size spanning over 10 orders of magnitude in cell volume (Margalef, 1978; Cullen et al., 2002). Ambient physicochemical factors (i.e., temperature, nutrient, and light availability) are often decisive for regulating growth of a particular phytoplankton species and its relative contributions to community structure (Reynolds and Reynolds, 1985). Thus, phytoplankton community structure can be regarded as an integral response of ambient environmental factors (Claustre et al., 2005). Phytoplankton forms the base of the oceanic food-web and performs a pivotal role in biogeochemical processes (especially influencing the efficiency of the carbon [C] export to the deep ocean through "biological pump"), which is an important component of global ocean C-sequestration and modulation of atmospheric CO_2.

During this study, shallow thermocline was observed with minimal thermohaline variations in the upper 35–40 m (**Figure 2**). Occurrence of low saline and warm water mass formed a stratified surface layer restricting MLD to 35–40 m. The stratification, with its determinant influence on upward nutrients fluxes, restricted the vertical mixing and prevented supply of nutrients from deeper layers resulting in macronutrients depletion in the MLD (**Figure 3**). The vertical position of the maximum Chl-*a* fluorescence (SCM) was located near or below the nitracline (vertical gradient of nitrate availability) in both TS and RT stations (**Figures 2**, **3**) possibly reflecting phytoplankton adaptive strategies. Extremely high Z_{eu}-MLD values (>35 m) indicated that light availability within the ML was highly favorable for growth of phytoplankton (Westwood et al., 2011) during the observation period. The N:P:Si ratios were lower than Redfield values indicating NO_3 and SiO_4-limited conditions (N:P < 10 and N:Si < 1; Levasseur and Therriault, 1987; Paul et al., 2008) for diatoms and/or silicoflagellates growth (Westwood et al., 2011) in the ML throughout the sampling region. Nevertheless, Si:P ratio was <3 throughout the water column showing Si-enrichment (Harrison et al., 1977) especially below the MLD. The nutrient-limited conditions were well reflected in the Chl-*a* size-fractionation and phytoplankton pigment signatures data, which have clearly shown that the study area was dominated (55–93%) by smaller phytoplankton (0.2–10 μm) and the contribution of nano-plankton was highest (53%) followed by pico (25%)- and micro-plankton (22%). The most abundant pigments at TS location were 19′HF, which is used as markers for prymnesiophytes (*Phaeocystis sp.*) (Jeffrey et al., 1997). The next most dominant pigment was alloxanthin (indicating cryptophytes). Fucoxanthin (indicating diatoms)

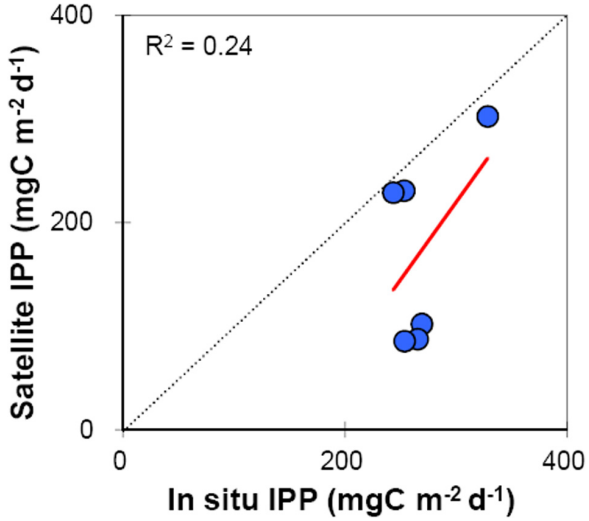

FIGURE 6 | Linear relationship between *in situ* and satellite-derived primary productivity measurements (r^2 = 0.24, n = 6, p > 0.05). The dotted line indicates 1:1 relationship. Data points close to (away from) the 1:1 line belong to RT (TS) stations, respectively.

percentage was comparatively high in the first 8 days but was less/absent during the 9th and 10th days, which witnessed rise in TChl-b and 19′BF concentrations indicative of dominance of pico-plankton (Seeyave et al., 2007). This kind of shift/succession in phytoplankton community structure could be ascribed to the vertical stratification-induced nutrient-stress prevailing in this region, as reported in other tropical and temperate marine ecosystems (Margalef, 1978; Cullen et al., 2002). In other words, the vertical stratification can also determine the intensity and phytoplankton communities of the SCM. Furthermore, the difference between Z_{eu} and nitracline depth can therefore be a useful indicator of phytoplankton communities inhabiting at the SCM depth (Ardyna et al., 2011).

In general, small phytoplankton predominates in stable oligotrophic (open ocean) environments, while larger cells dominate in variable eutrophic (coastal and upwelling) environments (Chisholm, 1992), and their cell size has been shown to regulate the export efficiency of organic matter in the water column (Dunne et al., 2005; Guidi et al., 2009; Mouw et al., 2016). Dominance of smaller plankton in the phytoplankton community of the study area implies that the SWTIO region would experience lower carbon transfer efficiency and high export flux efficiency since the portion exported by small cells is generally less refractory, thus, sinks slower, resulting in lower transfer efficiency. Conversely, larger cells are more vulnerable of being associated with ballasting materials and thus leads to greater transfer efficiency (Klaas and Archer, 2002; Armstrong et al., 2009; Mouw et al., 2016). Previous study shows that the magnitude and export efficacy of carbon flux are dependent on the size of the phytoplankton cells prevailing in the ecosystem (Mouw et al., 2016). As a whole, the carbon export variability in a system is not only regulated by the phytoplankton cell size but also by zooplankton grazing and other components

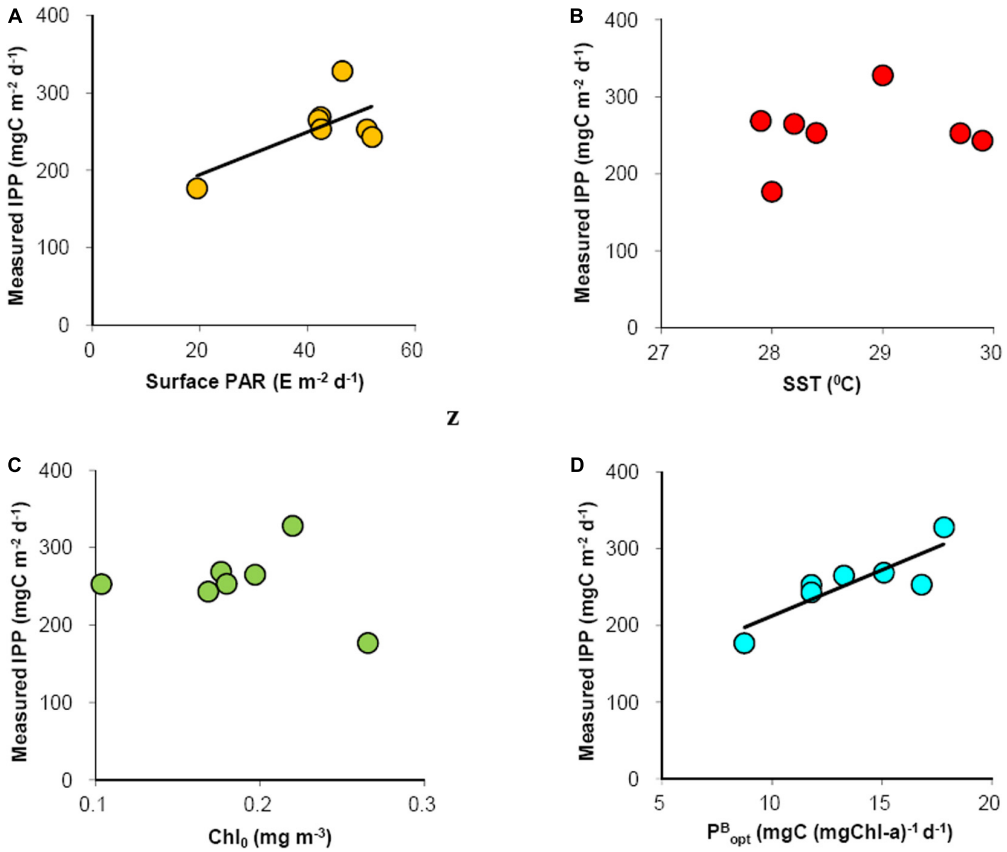

FIGURE 7 | Linear relationships between measured IPP and **(A)** surface PAR ($r^2 = 0.41$, $p < 0.05$), **(B)** SST, **(C)** Chl_0, and **(D)** P^B_{opt} ($r^2 = 0.73$, $p < 0.05$). Trend line for figure b and c are not shown due to absence of any clear trend.

(particle aggregation and feces production) of the food-web (Siegel et al., 2014).

Increase in Chl-*a* concentration is usually associated with an increase in intracellular pigment concentration or cell volume rather than in cell number leading to decrease in phytoplankton light absorption efficiency (due to intracellular overlapping of the chloroplasts) is popularly known as "package effect" (Bricaud et al., 1995). Thus, the observed decrease in Chl-*a*-specific PP (P^B) in the surface layer is hypothesized to be caused by the onset of "package effect" (Bricaud et al., 1995), which is obvious in large (>10 μm) or micro-phytoplankton (diatoms) compared to small size (nano or pico) plankton. We observed minimal or no decrease in the PAR-P^B relationship in the surface layer at TS (**Figure 5C**) and RT (**Figure 5F**), which is indicative of absence of photoinhibition in the study area. Tripathy et al. (2010, 2014) have reported package-effect induced decrease in PP in eutrophic coastal waters of temperate and polar regions, and attributed this to dominance of large-sized phytoplankton. However, low nutrients availability in the ML have shown that the conditions were supportive for the growth of smaller phytoplankton (flagellates, nano- and pico-sized) that can efficiently utilize the low concentrations of nutrients due to their high surface to volume ratio. This canonical hypothesis was supported by the HPLC-based DP analysis corroborating the dominance of nano-sized plankton in the surface as well as in the water column.

Ocean warming-induced decline in the spatial coverage and temporal occurrence of micro-plankton has been observed due to significantly reduced nutrients in the ML in the major biogeochemical provinces of the world ocean (Rousseaux and Gregg, 2015). Recent study pointed out an astounding decrease (up to 20%) in phytoplankton in western tropical Indian Ocean region over the past 60 years (Roxy et al., 2016) caused by warming-induced enhanced ocean stratification that restrains mixing of nutrients from subsurface layers. Gao et al. (2012) have shown that increased CO_2 and light exposure have adverse impacts on the growth of marine phytoplankton causing extensive reduction in oceanic PP and a shift in community structure away from diatoms that are mainly accountable for sustaining higher trophic levels and export of carbon in the ocean. If spatiotemporal dominance of small cells continues, this may result in less but efficient export of materials leading to reduced POC transfer to the deep ocean. This has possible cascading implications for both atmospheric drawdown of CO_2 and C-sequestration in the deep ocean. Yet, there are some small diatoms (such as *Minidiscus*) that can reach the ocean bottom at high sinking rates, hence challenging the classical binary vision of pico- and nanoplanktonic cells supporting the microbial

loop, while micro-plankton sustain secondary trophic levels and carbon export (Leblanc et al., 2018) in the ocean.

Comparison of Measured and Modeled Primary Production: Implications of P^B_{opt} on IPP Variability

The major inaccuracy in VGPM-based estimates of IPP are associated with estimations of P^B_{opt}, which is a key variable in PP modeling, yet is inadequately explained, and its predictability requires further refinement (Behrenfeld and Falkowski, 1997b; Kameda and Ishizaka, 2005; Siswanto et al., 2006; Hyde et al., 2008; Tripathy et al., 2012). Satellite-based estimates of P^B_{opt} can be derived by establishing predictive relationships between P^B_{opt} and one or more environmental variables (e.g., temperature, light, Chl-*a*), which can be measured by satellites (Behrenfeld et al., 2002). The following section elucidates the importance of P^B_{opt} in modeling primary production in the studied region.

Our results showed that VGPM, a global model with its original parameterization, could be used for precise estimation of IPP in the RT stations (3 data points close to 1:1 line); however, the modeled IPP underestimated (2.6 to 3 times) measured IPP at TS stations (**Figure 6**). This underestimation could be attributed to the difference in satellite-derived and measured Chl_0 concentrations that were fairly matching for the RT stations, whereas reasonably incongruous for the TS stations. It has been shown that, next to P^B_{opt}, the Chl_0 has significant contribution toward the errors associated with VGPM-based IPP estimates (Behrenfeld and Falkowski, 1997b). Analysis of measured IPP vs. *in situ* variables (those are embedded in the VGPM model) indicated that only *in situ* P^B_{opt} was significantly correlated ($r^2 = 0.73$, $n = 7$, $p < 0.05$) with IPP (**Figure 7D**) accounting for 73% of variance in measured IPP. Thus, it is presumed that the discrepancies in measured and modeled IPP at TS stations could be due to errors in estimating P^B_{opt}.

In this study, no distinct relationships were observed between the *in situ* P^B_{opt} and SST, PAR, and/or Chl-*a*; thus, a P^B_{opt} model using the above oceanographic variables was not feasible in SWTIO region. Also, due to small *in situ* dataset ($n = 7$), fitting any kind of relationship function between P^B_{opt} and other oceanographic variables was not realistic. Previously attempts to construct SST-dependent P^B_{opt} models (Behrenfeld and Falkowski, 1997b; Gong and Liu, 2003; Kameda and Ishizaka, 2005; Siswanto et al., 2006) have shown varying shapes for the P^B_{opt} function. Our results depicted that the derivation of P^B_{opt} by adopting the above model formulations was not effective (**Figure 8**) in this region. The observed P^B_{opt} and SST relationship of this study resembles the observations at Cariaco station, southeastern Caribbean Sea (Muller-Karger et al., 2004) and in the East China Sea (Siswanto et al., 2006), where consistent increase in P^B_{opt} was noticed even at SST as high as 29°C. Our data show that the P^B_{opt} increased with increasing SST until 29°C and then decreased, which is not in line with the global seventh-order polynomial P^B_{opt} model (Behrenfeld and Falkowski, 1997b), as well as SST and Chl_0 dependent P^B_{opt} model (Kameda and Ishizaka, 2005). Both models showed decline in P^B_{opt} with increasing SST (**Figure 8**), and opined that

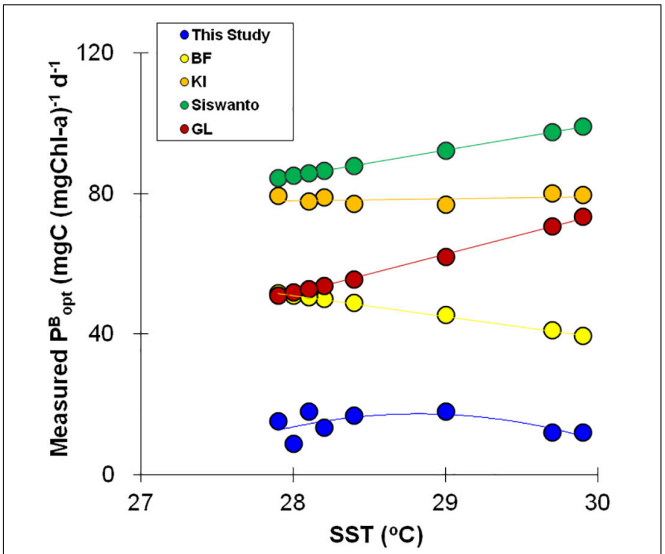

FIGURE 8 | Relationships between measured P^B_{opt} and SST. Circles, stars, diamonds, triangles, and squares indicate P^B_{opt} variations based on datasets of this study, models of Behrenfeld and Falkowski (1997a), Gong and Liu (2003); Kameda and Ishizaka (2005), Siswanto et al. (2006), respectively.

persistent nutrient limitation in the strongly stratified high SST regions lead to decline in P^B_{opt} at higher SST. Such discrepancy could possibly be accountable for the ineffectiveness of VGPM to capture measured IPP variance at TS station.

Temperature exclusively was unable to explain the variation in P^B_{opt}, because P^B_{opt} variation was plausibly influenced by the cumulative effects of nutrient concentrations, total biomass, light history, day-length, phytoplankton composition, and size that are independent of temperature (Cote and Platt, 1983; Behrenfeld and Falkowski, 1997b). Thus, a single-factor, statistical P^B_{opt} model may not capture the physiological adjustments by phytoplankton with respect to the surrounding growth conditions (Behrenfeld and Falkowski, 1997b), and warrant development of a mechanistic model (e.g., Kameda and Ishizaka, 2005). Constant P^B_{opt} values have been used to estimate IPP elsewhere (Dierssen et al., 2000; Hyde et al., 2008) when reliable derivation of P^B_{opt} using environmental variables failed. Developing a P^B_{opt} model was out of scope of this study and hence not attempted because of the small dataset.

The other likely justification for the poor performance of VGPM at TS station is that the optical property of this study region may not be resembling the domain (i.e., Chl-*a* is the major determinant of the water optical properties) in which VGPM was formulated. Absence of correlation between k_d and Chl_{int} implied that the study area was optically complex, where constituents other than Chl-*a* (such as suspended sediments, chromophoric dissolved organic matter) could be playing a main role in determining light attenuation in the water column. Alas, due to lack of data on other optically active constituents we could not verify this. The observed k_d values (**Table 1**) were similar for both TS and RT stations indicating identical optical properties. Thus, observed discrepancies between measured and

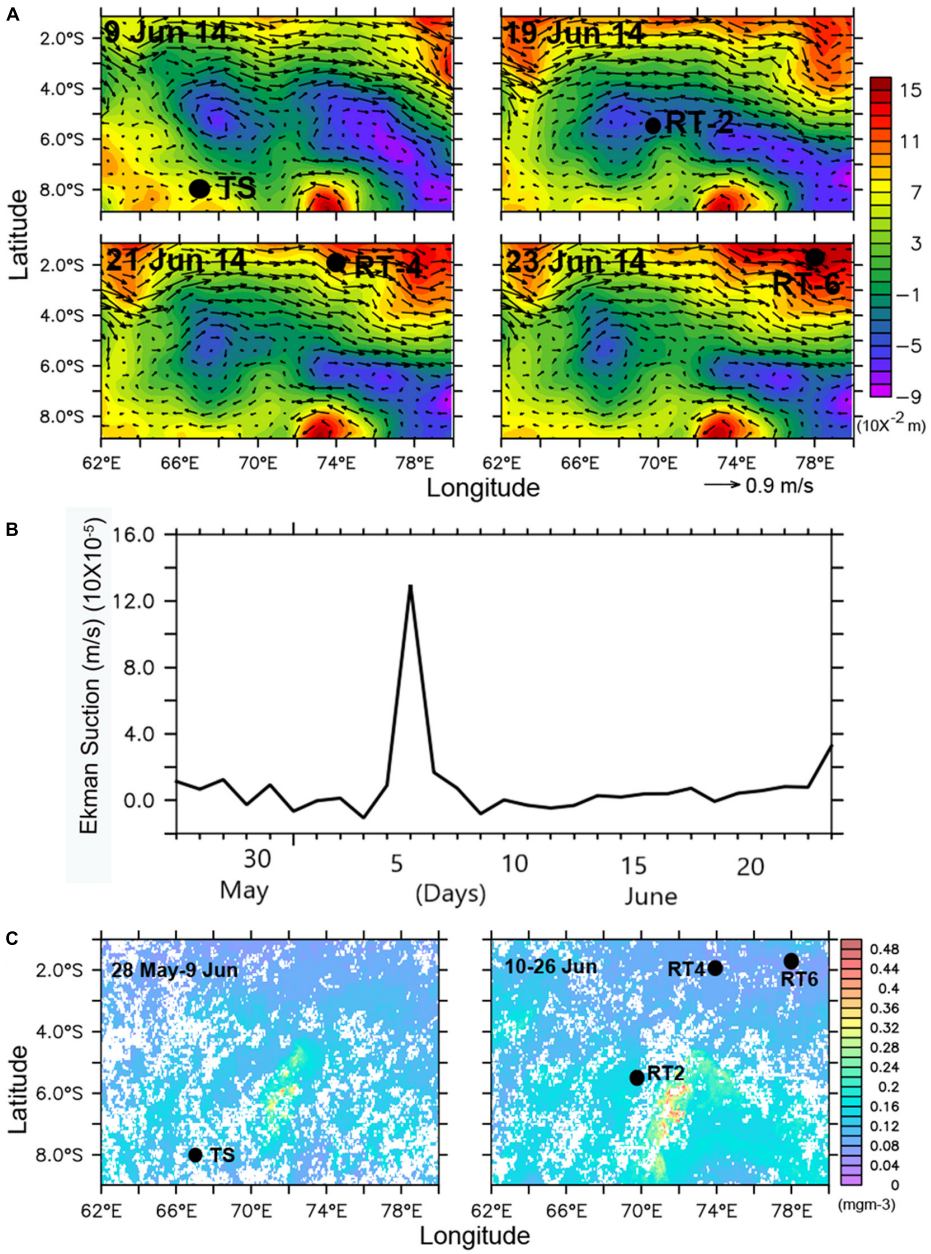

FIGURE 9 | (A) spatial distribution of sea surface height anomaly (SSHA) overlaid on geostrophic wind vectors (top right panel corresponds to RT-2, black dots denote the station locations), **(B)** average Ekman suction velocity at RT-2 region (6S:5S and 69E:70E) during May–June 2014 showing peak on 6 June, and **(C)** MODIS-Aqua derived weekly average level-3 chlorophyll images (black dots symbolizes station locations) indicating high chlorophyll-a patch at RT-2.

modeled IPP at TS and RT stations could only be attributed to the differences in satellite-derived and *in situ* Chl_0.

Physical Forcings Associated With the Observed High Productivity at RT-2

Throughout the year, the SCTR experiences upwelling due to the upward Ekman suction (Murtugudde et al., 1996; Spencer et al., 2005). Previously it was shown that the interannual variability of the thermohaline stratification in the SCTR region is primarily caused by the equatorial zonal wind anomalies caused by the Indian Ocean Dipole (IOD). The IOD induces a strong Ekman suction south of the equator including the eastern and central Indian Ocean, which subsequently move westward under the influence of planetary wave dynamics (Masumoto and Meyers, 1998), thereby modulating the biogeochemistry of the SCTR region.

During the study period highest Chl_{int} (39.4 mg m^{-2}) and IPP (328.1 mgC m^{-2} d^{-1}) was observed at RT-2. To investigate the possible role of physical forcings on the observed high

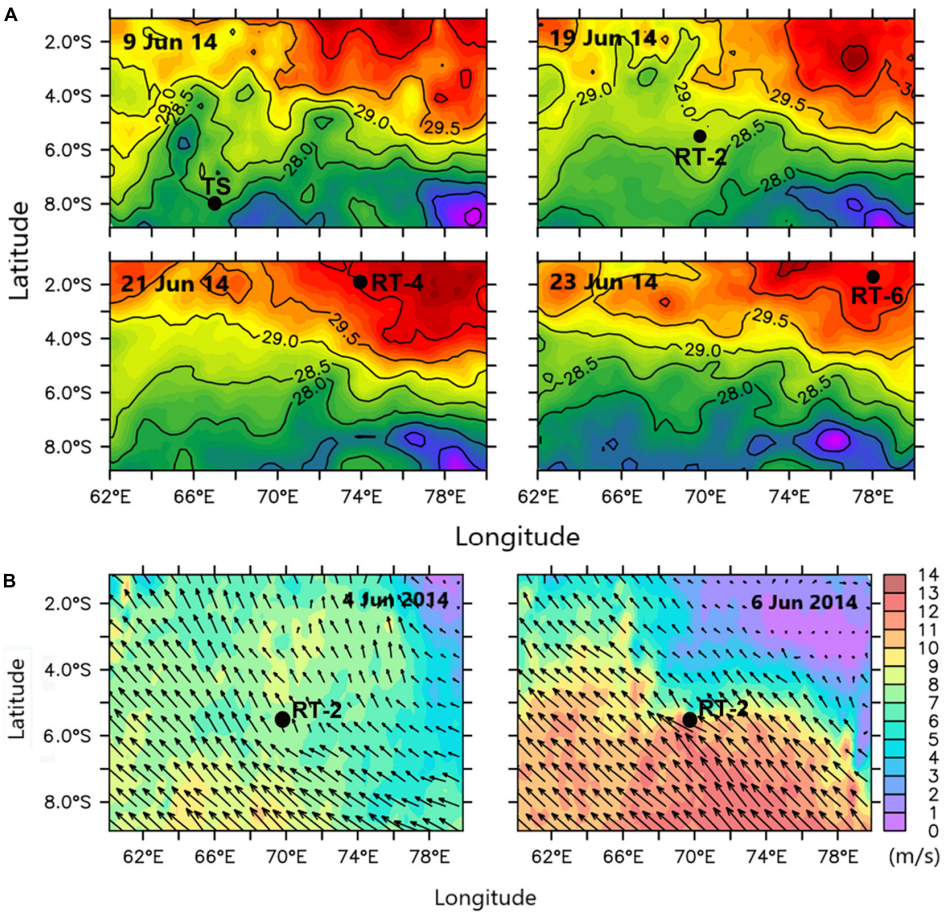

FIGURE 10 | (A) Sea surface temperature (SST) variability during the observation period, and **(B)** surface wind pattern during 4 and 6 June. Black dots signify station locations.

phytoplankton biomass and productivity at RT-2, we analyzed sea surface height anomaly (SSHA) coupled with geostrophic currents during the sampling period. Interestingly, the SSHA plots highlighted that the observed high Chl-*a* region was well inside negative SSHA regions (**Figure 9A**, top right panel) as observed elsewhere (Sabu et al., 2014). Previous study (George et al., 2013) correlated the negative (in SCTR region) and positive (near the equator and south of the SCTR region) SSHA to shallower and deeper thermocline, respectively. The observed negative SSHA could be linked to the Ekman suction velocity calculated for the study area, which showed a surge on 6th June signaling possible upwelling during this period (**Figure 9B**). The elevated Ekman suction velocity could have upwelled nutrient-rich waters thereby enhancing phytoplankton growth. It is well documented that strong Ekman suction deepens the surface ML considerably and Chl peaks when SSHA decreases in SCTR region (Resplandy et al., 2009). MODIS-Aqua-derived Chl-*a* images (**Figure 9C**) confirmed presence of high Chl patch near to RT-2 well before the observation date (28th May to 9th June), which persisted till 26th June. Since the intensity and spatial extension of the Chl increased in the last week of June, the high Chl observed in our study had originated from this high Chl patch. Furthermore, the high surface Chl might have resulted not only from the entrainment of subsurface Chl but also from the influx of nutrients and phytoplankton production in the ML (Resplandy et al., 2009).

Moreover, analysis of SST images indicated that RT-4 and RT-6 were in higher SST region than TS and RT-2 (**Figure 10A**), and SST in the RT-2 was colder on 9th June than on 19th June, indicating upwelling signatures. So the cooler water on 9th June was triggered by the high Ekman suction velocity just 3 days before, corroborating that the SCTR region is significantly influenced by Ekman-suction-induced upwelling, driven by the northward decrease of the southeast trade wind (Vialard et al., 2008). Analysis of surface wind data for this period indicated that the high Ekman suction/low SSHA in the RT-2 region was due to the occurrence/passage of a high wind event on 6th June (**Figure 10B**) that's enhanced Ekman suction and favored entrainment of nutrients to the surface layer, in consequence enhancing phytoplankton growth and photosynthetic activity. Thus, the high Chl_{int} and IPP at RT-2 on 19th June was due to occurrence of an upwelling event before our observation. Previous report (Spencer et al., 2005)

shows that the annual mean upwelling in the SWTIO is associated with wind driven Ekman suction. Our result is consistent with the findings of George et al. (2013), who have revealed Ekman suction-induced variability in MLD and increase in surface Chl by entrainment of nutrients from deeper layers in the SCTR region.

Unlike RT-4 and RT-6, we observed subsurface P^B_{opt} for RT-2 station (**Figure 5F**), which indicates that the reduced phytoplankton photosynthetic efficiency in the surface layer was probably due to the light-shock the plankton experienced when they were transported from deeper to shallower regions. Earlier study documents that vertical displacements of phytoplankton, due to mixing, force phytoplankton to experience fast alterations in underwater light intensity (Shibata et al., 2010), which exposes the phytoplankton cells to higher PAR, causing damages to the photosynthetic apparatus and photoinhibitory decrease in the photosynthetic efficiency (Falkowski et al., 1994). The PAR-P^B relationship showed mild photoinhibition (**Figure 5F**) at RT-2, which could be attributed to the less pigment packaging due to dominance of nano-plankton during the sampling period. Similar observations (Tripathy et al., 2014) were also reported in the offshore waters of Southern Ocean where nutrient-limitation induced predominance of smaller plankton existed.

SUMMARY AND CONCLUSION

To our knowledge, this is the first *in situ* measurement-based study describing the factors modulating phytoplankton productivity and composition in the SCTR region. Our study not only confirmed some of the earlier reports about variability in phytoplankton biomass but also provides first-hand information about the *in situ* variability in phytoplankton pigment signatures and carbon-uptake efficiency. Some of the conclusions drawn from this study are summarized below.

The SCTR region is usually oligotrophic in nature in the month of June. Strong thermohaline stratification resulted in shallow (35–40 m) mixed layer (ML). Subsurface Chl-*a* maximum (SCM) was a prominent feature and observed to oscillate 40–60 m with majority of peaks at 50 m, and existed just beneath the ML depth. Light availability during the sampling period was highly conducive for algal growth, whereas nutrient ratios indicated N- and Si-limitation suggesting unfavorable conditions for diatoms and/or silicoflagellates growth within the ML. Moreover, dominance of nano-sized plankton (53%) followed by pico-plankton (25%) and micro-plankton (22%) could be confirmed by HPLC-based pigments analysis. Drastic dropdown in daily incident light due to overcast sky can severely influence the IPP even though other supporting parameters remain unchanged. In the vertical profiles maximum PP usually coexisted to SCM depths. The Chl-*a*-specific PP (P^B) was higher within the ML and showed no surface photoinhibition, due to the dominance of smaller phytoplankton, which are less prone to pigment packaging effect. Comparatively, higher P^B within the ML is indicative of phytoplankton healthiness during the sampling time, whereas low P^B below the SCM was due to light limitation. The highest column integrated phytoplankton biomass (Chl_{int}) and productivity (IPP) observed at RT-2 could be clearly linked to low sea surface height anomaly (SSHA); cyclonic disturbances and associated positive Ekman suction velocity occurred before our observation period. Conversely, high SSHA and strong stratification conditions prevailed at other stations (TS, RT-4, and RT-6) leading to comparatively low Chl_{int} and IPP. Though dominance of smaller phytoplankton were observed in the study area, future work focusing on grouping of phytoplankton into functional types will have more interest to the biogeochemical community because they are relevant indicators of ecosystem dynamics and functioning vis-à-vis climate change, and may provide vital information about potential impacts on the efficiency of oceanic carbon sequestration which controls global climate change.

DATA AVAILABILITY STATEMENT

The datasets generated for this study are available on request to the corresponding author.

AUTHOR CONTRIBUTIONS

ST collected the primary production data, conceived the study, and wrote the manuscript. PS helped in processing satellite-based observations. SP, RN, AS, VV, AK, and PR contributed in generation of other *in situ* data and analyses. All authors contributed toward interpreting results, discussion, and improvement of this manuscript.

FUNDING

Financial assistance from the Ministry of Earth Sciences, Government of India is highly acknowledged.

ACKNOWLEDGMENTS

The authors are thankful to the Director, NCPOR and Group Director, Ocean Sciences Group for their constant encouragement and support. Exemplary assistance from the Captain, officers, and all crew members onboard *ORV-Sagar Nidhi* is sincerely acknowledged. This is NCPOR contribution number J-13/2020-21.

SUPPLEMENTARY MATERIAL

The Supplementary Material for this article can be found online at: https://www.frontiersin.org/articles/10.3389/fmars.2020.00515/full#supplementary-material

MATERIAL S1 | Size-fractioned contributions (average) of phytoplankton pigments in the water column at the TS station.

MATERIAL S2 | Scatter plots showing linear relationships between Chl *a* and **(A)** PP, and **(B)** P^B for the entire study area.

REFERENCES

Annamalai, H. R., Murtugudde, J., Potemra, S. P., Xie, P. L., and Wang, B. (2003). Coupled dynamics over the Indian Ocean: spring initiation of the zonal mode. *Deep-Sea Res. II* 50, 2305–2330. doi: 10.1016/s0967-0645(03)00058-4

Ardyna, M., Gosselin, M., Michel, C., Poulin, M., and Tremblay, J. E. (2011). Environmental forcing of phytoplankton community structure and function in the Canadian High Arctic: contrasting oligotrophic and eutrophic regions. *Mar. Ecol. Prog. Ser.* 442, 37–57. doi: 10.3354/meps09378

Armstrong, R. A., Peterson, M. L., Lee, C., and Wakeham, S. G. (2009). Settling velocity spectra and the ballast ratio hypothesis. *Deep Sea Res. II* 56, 1470–1478. doi: 10.1016/j.dsr2.2008.11.032

Behrenfeld, M. J., and Falkowski, P. G. (1997a). A consumer's guide to phytoplankton primary productivity models. *Limnol. Oceanogr.* 42, 1479–1491. doi: 10.4319/lo.1997.42.7.1479

Behrenfeld, M. J., and Falkowski, P. G. (1997b). Photosynthetic rates derived from satellite based chlorophyll concentration. *Limnol. Oceanogr.* 42, 1–20. doi: 10.4319/lo.1997.42.1.0001

Behrenfeld, M. J., Maranon, E., Siegel, D. A., and Hooker, S. B. (2002). Photoacclimation and nutrient-based model of light-saturated photosynthesis for quantifying oceanic primary production. *Mar. Ecol. Prog. Ser.* 228, 103–117. doi: 10.3354/meps228103

Behrenfeld, M. J., O'Malley, R. T., Siegel, D. A., McClain, C. R., Sarmiento, J. L., Feldman, G. C., et al. (2006). Climate-driven trends in contemporary ocean productivity. *Nature* 444, 752–755. doi: 10.1038/nature05317

Boyd, P. W., Jickells, T., Law, C. S., Blain, S., Boyle, E. A., Buesseler, K. O., Coale, K. H., et al. (2007). Mesoscale iron enrichment experiments 1993-2005: synthesis and future directions. *Science* 315, 612–617. doi: 10.1126/science.1131669

Bricaud, A., Babin, M., Morel, A., and Claustre, H. (1995). Variability in the chlorophyll-specific absorption coefficients for natural phytoplankton: analysis and parameterization. *J. Geophys. Res.* 100, 13321–13332.

Cheah, W., McMinn, A., Griffiths, F. B., Westwood, K. J., Wright, S. W., et al. (2013). Response of phytoplankton photophysiology to varying environmental conditions in the sub-antarctic and polar frontal zone. *PLoS One* 8:e72165. doi: 10.1371/journal.pone.0072165

Chisholm, S. (1992). "Phytoplankton size," in *Primary Productivity and Biogeochemical Cycles in the Sea*, eds P. G. Falkowski, A. D. Woodhead, and K. Vivirito (Berlin: Springer), 213–237.

Claustre, H., Babin, M., Merien, D., Ras, J., Prieur, L., Dallot, S., et al. (2005). Towards a taxon-specific parameterization of bio-optical models of primary production: a case study in the North Atlantic. *J. Geophys. Res.* 110:C07S12. doi: 10.1029/2004JC002634

Cote, B., and Platt, T. (1983). Day-to-day variations in the spring-summer photosynthetic parameters of coastal marine phytoplankton. *Limnol. Oceanogr.* 28, 320–344. doi: 10.4319/lo.1983.28.2.0320

Cullen, J., Franks, P., Karl, D., and Longhurst, A. (2002). "Physical influences on marine ecosystem dynamics," in *The Sea*, eds A. R. Robinson, J. J. McCarthy, and B. J. Rothschild (New York, NY: John Wiley), 297–336.

Dierssen, H. M., Vernet, M., and Smith, R. C. (2000). Optimizing models for remotely estimating primary production in Antarctic coastal waters. *Antarct. Sci.* 12, 20–32. doi: 10.1017/s0954102000000043

Dilmahamod, A. F., Hermes, J. C., and Reason, C. J. C. (2016). Chlorophyll-a variability in the Seychelles-Chagos Thermocline Ridge: analysis of a coupled biophysical model. *J. Marine Syst.* 154, 220–232. doi: 10.1016/j.jmarsys.2015.10.011

Dunne, J., Armstrong, R., Gnanadesikan, A., and Sarmiento, J. (2005). Empirical and mechanistic models for the particle export ratio. *Global Biogeochem. Cycles* 19:GB4026. doi: 10.1029/2004GB002390

Falkowski, P. G., Greene, R., and Kolber, Z. (1994). "Light utilization and photoinhibition of photosynthesis in marine phytoplankton," in *Photoinhibition of Photosynthesis: From Molecular Mechanisms to the Field*, eds N. R. Baker and J. Bowes (Oxford: Bios Scientific).

Gao, K., Xu, J., Gao, G., Li, Y., Hutchins, D. A., Huang, B. A., et al. (2012). Rising CO2 and increased light exposure synergistically reduce marine primary productivity. *Nat. Clim. Change* 2, 519–523. doi: 10.1038/NCLIMATE1507

George, J. V., Nuncio, M., Chacko, R., Anilkumar, N., Noronha, S. B., Patil, S. M., et al. (2013). Role of physical processes in chlorophyll distribution in the western tropical Indian Ocean. *J. Marine Syst.* 113- 114, 1–12. doi: 10.1016/j.jmarsys.2012.12.001

Gong, G. C., and Liu, G. J. (2003). An empirical primary production model for the ECS. *Cont. Shelf Res.* 23, 213–224. doi: 10.1016/s0278-4343(02)00166-8

Guidi, L., Stemmann, L., Jackson, G. A., Ibanez, F., Claustre, H., Legendre, L., et al. (2009). Effects of phytoplankton community on production, size, and export of large aggregates: a world-ocean analysis. *Limnol. Oceanogr.* 54, 1951–1963. doi: 10.4319/lo.2009.54.6.1951

Harrison, P. J., Conway, H. L., Holmes, R. W., and Davis, C. O. (1977). Marine diatoms in chemostats under silicate or ammonium limitation. III. Cellular chemical composition and morphology of three diatoms. *Mar. Biol.* 43, 19–31. doi: 10.1007/bf00392568

Hermes, J. C., and Reason, C. J. C. (2008). Annual cycle of the South Indian Ocean (Seychelles-Chagos) thermocline ridge in a regional ocean model. 113, C04035. doi: 10.1029/2007JC004363

Hyde, K. J. W., O'Reilly, J. E., and Oviatt, C. A. (2008). Evaluation and application of satellite primary production models in Massachusetts Bay. *Cont. Shelf Res.* 28, 1340–1351. doi: 10.1016/j.csr.2008.03.017

Jeffrey, S. W., Mantoura, R. F. C., and Wright, S. W. (1997). *Phytoplankton Pigments in Oceanography: Guidelines to Modern Methods*. Paris: UNESCO Publishing.

Jung, E., and Kirtman, B. P. (2016). ENSO modulation of tropical Indian ocean subseasonal variability. *Geophys. Res. Lett.* 43, 12634–12642. doi: 10.1002/2016GL071899

Kameda, T., and Ishizaka, J. (2005). Size-fractionated primary production estimated by a two-phytoplankton community model applicable to ocean color remote sensing. *J. Oceanogr.* 61, 663–672. doi: 10.1007/s10872-005-0074-7

Kirk, J. T. O. (1994). *Light and Photosynthesis in Aquatic Ecosystems*. Cambridge: Cambridge University Press, 509.

Klaas, C., and Archer, D. E. (2002). Association of sinking organic matter with various types of mineral ballast in the deep sea: implications for the rain ratio. *Glob. Biogeochem. Cycles* 116:1116. doi: 10.1029/2001GB001765

Kurian, S., Roy, R., Repeta, D. J., Gauns, M., Shenoy, D. M., Suresh, T., et al. (2012). Seasonal occurrence of anoxygenic photosynthesis in Tillari and Selaulim reservoirs, western India. *Biogeosciences* 9, 2485–2495. doi: 10.5194/bg-9-2485-2012

Leblanc, K., Quéguiner, B., Diaz, F., Cornet, V., Michel-Rodriguez, M., Durrieu de Madron, X., et al. (2018). Nanoplanktonic diatoms are globally overlooked but play a role in spring blooms and carbon export. *Nat. Comm.* 9:953. doi: 10.1038/s41467-018-03376

Levasseur, M. E., and Therriault, J. C. (1987). Phytoplankton biomass and nutrient dynamics in a tidally induced upwelling: the role of NO3: SiO4 ratio. *Mar. Ecol. Prog. Ser.* 39, 87–97. doi: 10.3354/meps039087

Lohrenz, S. E., Wiesenburg, D. A., Rein, C. R., Arnone, R. A., Taylor, C. T., Knauer, G. A., et al. (1992). A comparison of in situ and simulated in situ methods for estimating oceanic primary production. *J. Plankton Res.* 14, 201–221. doi: 10.1093/plankt/14.2.201

Longhurst, A. R., and Harrison, W. G. (1989). The biological pump: profiles of plankton production and consumption in the upper ocean. *Prog. Oceanog.* 22, 47–123. doi: 10.1016/0079-6611(89)90010-4

Margalef, R. (1978). Life-forms of phytoplankton as survival alternatives in an unstable environment. *Oceanol. Acta* 1, 493–509.

Masumoto, Y., and Meyers, G. (1998). Forced Rossby waves in the southern tropical Indian Ocean. *J. Geophys. Res.* 103, 27589–27602. doi: 10.1029/98jc02546

McCreary, J. P. Jr., Kundu, P. K., and Molinari, R. L. (1993). A numerical investigation of dynamics, thermodynamics and mixed-layer processes in the Indian Ocean. *Prog. Oceanogr.* 31, 181–244. doi: 10.1016/0079-6611(93)90002-u

McCreary, J. P., Kohler, K. E., Hood, R. R., and Olson, D. B. (1996). A four-component ecosystem model of biological activity in the Arabian Sea. *Prog. Oceanogr.* 37, 193–240. doi: 10.1016/s0079-6611(96)00005-5

McCreary, J. P., Murtugudde, R., Vialard, J., Vinayachandran, P. N., Wiggert, J. D., Hood, R. R., et al. (2009). "Biophysical processes in the Indian Ocean," in *Indian Ocean Biogeochemical Processes and Ecological Variability, Geophysical Monograph Series 185*, eds J. D. Wiggert, R. R. Hood. S. Wajih, A. Naqvi, K. H. Brink and S. L. Smith (Washington, D.C: American Geophysical Union), 9–32. doi: 10.1029/2008gm000768

Morel, A., and Berthon, J. F. (1989). Surface pigments, algal biomass profiles, and potential production of the euphotic layer: relationships reinvestigated in view of remote sensing applications. *Limnol. Oceanogr.* 34, 1545–1562. doi: 10.4319/lo.1989.34.8.1545

Mouw, C. B., Barnett, A., McKinley, G. A., Gloege, L., and Pilcher, D. (2016). Phytoplankton size impact on export flux in the global ocean. *Global Biogeochem. Cycles* 30, 1542–1562. doi: 10.1002/2015GB005355

Muller-Karger, F. R., Varela, R., Thunell, Y., Astor, H. Z., Luerssen, R., and Hu, C. (2004). Processes of coastal upwelling and carbon flux in the Cariaco Basin. *Deep-Sea Res. II.* 51, 927–943. doi: 10.1016/j.dsr2.2003.10.010

Murtugudde, R., and Busalacchi, A. J. (1999). Interannual variability of the dynamics and thermodynamics of the tropical Indian Ocean. *J. Clim.* 12, 2300–2326. doi: 10.1175/1520-1442

Murtugudde, R. G., Seager, R., and Busalacchi, A. J. (1996). Simulation of the tropical oceans with an ocean GCM coupled to an atmospheric mixed-layer model. *J. Clim.* 9, 1795–1815. doi: 10.1175/1520-0442(1996)009<1795:sottow>2.0.co;2

Murtugudde, R. G., Signorini, S. R., Christian, J. R., Busalacchi, A. J., McClain, C. R., and Picaut, J. (1999). Ocean color variability of the tropical Indo-Pacific basin observed by SeaWiFS during 1997–1998. *J. Geophys. Res.* 104, 18351–18366. doi: 10.1029/1999JC900135

Naqvi, S. W. A., Moffett, J. W., Gauns, M. U., Narvekar, P. V., Pratihary, A. K., Naik, H., et al. (2010). The Arabian Sea as a high-nutrient, low-chlorophyll region during the late Southwest Monsoon. *Biogeosciences* 7, 2091–2100. doi: 10.5194/bg-7-2091-2010

Paul, J. T., Ramaiah, N., and Sardessai, S. (2008). Nutrient regimes and their effect on distribution of phytoplankton in the Bay of Bengal. *Mar. Environ. Res.* 66, 337–344. doi: 10.1016/j.marenvres.2008.05.007

Prasanna Kumar, S., Madhupratap, M., Dileepkumar, M., Muraleedharan, P., DeSouza, S., Gauns, M., et al. (2001). High biological productivity in the central Arabian Sea during the summer monsoon driven by Ekman pumping and lateral advection. *Curr. Sci.* 81, 1633–1638.

Resplandy, L., Lévy, M., Madec, G., Pous, S., Aumont, O., and Kumar, D. (2011). Contribution of mesoscale processes to nutrient budgets in the Arabian Sea. *J. Geophys. Res.* 116:C11007. doi: 10.1029/2011JC007006

Resplandy, L., Vialard, J., Lévy, M., Aumont, O., and Dandonneau, Y. (2009). Seasonal and intraseasonal biogeochemical variability in the thermocline ridge of the southern tropical Indian Ocean. *J. Geophys. Res.* 114, C07024. doi: 10.1029/2008JC005246

Reynolds, C. S., and Reynolds, J. B. (1985). The atypical seasonality of phytoplankton in Crose Mere, 1972: an independent test of the hypothesis that variability in the physical environment regulates community dynamics and structure. *Brit. Phycol. J.* 20, 227–242. doi: 10.1080/00071618500650241

Rousseaux, C. S., and Gregg, W. W. (2015). Recent decadal trends in global phytoplankton composition. *Global Biogeochem. Cycles* 29, 1674–1688. doi: 10.1002/2015GB005139

Roxy, M. K., Modi, A., Murtugudde, R., Valsala, V., Panickal, S., Prasanna Kumar, S., et al. (2016). A reduction in marine primary productivity driven by rapid warming over the tropical Indian Ocean. *Geophys. Res. Lett.* 43, 826–833. doi: 10.1002/2015GL066979

Sabine, C. L., Feely, R. A., Gruber, N., Key, R. M., Lee, K., Bullister, J. L., et al. (2004). The oceanic sink for anthropogenic CO2. *Science* 305:367. doi: 10.1126/science.1097403

Sabu, P., Anilkumar, N., George, J. V., Chacko, R., Tripathy, S. C., and Achuthankutty, C. T. (2014). The influence of air-sea-ice interactions on an anomalous phytoplankton bloom in the Indian Ocean sector of the Antarctic Zone of the Southern Ocean during the austral summer, 2011. *Pol. Sci.* 8, 370–384. doi: 10.1016/j.polar.2014.08.001

Sakshaug, E., Bricaud, A., Dandonneau, Y., Falkowski, P. G., Kiefer, D. A., Legendre, L., et al. (1997). Parameters of photosynthesis: definitions, theory and interpretation of results. *J. Plankton Res.* 19, 1637–1670. doi: 10.1093/plankt/19.11.1637

Sakshaug, E., and Holm-Hansen, O. (1986). Photoadaptation in Antarctic phytopfankton: variations in growth rate, chemical composition and P versus I curves. *J. Plankton Res.* 8, 459–473. doi: 10.1093/plankt/8.3.459

Seeyave, S., Lucasa, M. I., Moore, C. M., and Poultona, A. J. (2007). Phytoplankton productivity and community structure in the vicinity of the Crozet Plateau during austral summer 2004/2005. *Deep-Sea Res. II* 54, 2020–2044. doi: 10.1016/j.dsr2.2007.06.010

Shibata, T., Tripathy, S. C., and Ishizaka, J. (2010). Phytoplankton Pigment Change as a Photoadaptive Response to Light Variation Caused by Tidal Cycle in Ariake Bay. *J. Oceanogr.* 66, 831–843. doi: 10.1007/s10872-010-0067-z

Siegel, D. A., Buesseler, K. O., and Doney, S. C. (2014). Global assessment of ocean carbon export by combining satellite observations and foodweb models. *Glob. Biogeochem. Cycles* 28, 181–196. doi: 10.1002/2013GB004743

Siswanto, E., Ishizaka, J., and Yokouchi, K. (2006). Optimal primary production model and parameterization in the eastern East China Sea. *J. Oceanogr.* 62, 361–372. doi: 10.1007/s10872-006-0061-7

Spencer, H., Sutton, R. T., Slingo, J. M., Roberts, M., and Black, E. (2005). Indian Ocean climate and dipole variability in Hadley Centre coupled GCMs. *J. Clim.* 18, 2286–2307. doi: 10.1175/jcli3410.1

Sreeush, M. G., Valsala, V., Pentakota, S., Prasad, K. V. S. R., and Murtugudde, R. (2018). Biological production in the Indian Ocean upwelling zones –Part 1: refined estimation via the use of a variable compensation depth in ocean carbon models. *Biogeosciences* 15, 1895–1918. doi: 10.5194/bg-15-1895-2018

Stock, C. A., John, J. G., Rykaczewski, R. R., Asch, R. G., William, W. L., Cheung, J. P., et al. (2017). Reconciling fisheries catch and ocean productivity. *Proc. Natl Acad. Sci. U.S.A.* 114, 1441–1449. doi: 10.1073/pnas.1610238114

Strickland, J. D. H., and Parsons, T. R. (1972). A practical handbook of seawater analysis. *J. Fish. Res. Board. Can.* 167:310.

Tripathy, S. C., Ishizaka, J., Fujiki, T., Shibata, T., Okamura, K., Hosaka, T., et al. (2010). Assessment of carbon- and fluorescence-based primary productivity in Ariake Bay, southwestern Japan. *Estuar. Coast. Shelf Sci.* 87, 163–173. doi: 10.1016/j.ecss.2010.01.006

Tripathy, S. C., Ishizaka, J., Siswanto, E., Shibata, T., and Mino, Y. (2012). Modification of the vertically generalized production model for the turbid waters of Ariake Bay, southwestern Japan. *Estuar. Coast. Shelf Sci.* 97, 66–77. doi: 10.1016/j.ecss.2011.11.025

Tripathy, S. C., Pavithran, S., Sabu, P., Naik, R. K., Noronha, S. B., Bhaskar, P. V., et al. (2014). Is primary productivity in the Indian Ocean sector of Southern Ocean affected by pigment packaging effect? *Curr. Sci* 107, 1019–1026.

Uitz, J., Claustre, H., Morel, A., and Hooker, S. B. (2006). Vertical distribution of phytoplankton communities in open ocean: an assessment based on surface chlorophyll. *J. Geophys. Res.* 111:C08005. doi: 10.1029/2005JC003207

UNESCO-JGOFS (1994). *Protocols for the Joint Global Ocean Flux Study (JGOFS) Core Measurements. IOC Manual Guides 29*. Paris: UNESCO.

Vialard, J., Foltz, G. R., McPhaden, M. J., Duvel, J. P., and de Boyer, M. C. (2008). Strong Indian Ocean sea surface temperature signals associated with the Madden-Julian Oscillation in late 2007 and early 2008. *Geophys. Res. Lett.* 35:L19608. doi: 10.1029/2008GL035238

Webb, W. L., Newton, M., and Starr, D. (1974). Carbon dioxide exchange of Alnus rubra: a mathematical model. *Oecologia* 17, 281–291. doi: 10.1007/bf00345747

Westwood, K. J., Griffiths, F. B., Webb, J. P., and Wright, S. W. (2011). Primary production in the Sub-Antarctic and Polar Frontal Zones south of Tasmania. Australia; SAZ-Sense survey, 2007. *Deep-Sea Res. II* 58, 2162–2178. doi: 10.1016/j.dsr2.2011.05.017

Wiggert, J. D., Hood, R. R., Banse, K., and Kindle, J. C. (2005). Monsoon-driven biogeochemical processes in the Arabian Sea. *Progr. Oceanogr.* 65, 176–213. doi: 10.1016/j.pocean.2005.03.008

Wiggert, J. D., Murtugudde, R. G., and Christian, J. R. (2006). Annual ecosystem variability in the tropical Indian Ocean: results of a coupled bio-physical ocean general circulation model. *Deep-Sea Res. II* 53, 644–676. doi: 10.1016/j.dsr2.2006.01.027

Wiggert, J. D., Vialard, J., and Behrenfeld, M. (2009). "Basin-wide modification of dynamical and biogeochemical processes by the positive phase of the Indian Ocean Dipole during the SeaWiFS era," in *Indian Ocean BiogeochemicalProcesses and Ecological Variability*, eds J. D. Wiggert, et al. (Washington, D.C: American Geophysical Union), 350.

Woodberry, K. E., Luther, M. E., and O'Brien, J. (1989). The wind-driven seasonal circulation in the southern tropical Indian Ocean. *J. Geophys. Res.* 94, 17985–18002.

Zhou, L., Murtugudde, R., and Jochum, M. (2008). Seasonal influence of Indonesian through flow in the southwestern Indian Ocean. *J. Phys. Oceano.* 38, 1529–1541. doi: 10.1175/2007jpo3851.1

Conflict of Interest: The authors declare that the research was conducted in the absence of any commercial or financial relationships that could be construed as a potential conflict of interest.

Copyright © 2020 Tripathy, Sabu, Patra, Naik, Sarkar, Venkataramana, Kerkar and Sudarsanarao. This is an open-access article distributed under the terms of the Creative Commons Attribution License (CC BY). The use, distribution or reproduction in other forums is permitted, provided the original author(s) and the copyright owner(s) are credited and that the original publication in this journal is cited, in accordance with accepted academic practice. No use, distribution or reproduction is permitted which does not comply with these terms.

frontiers in Marine Science

ORIGINAL RESEARCH
published: 17 July 2020
doi: 10.3389/fmars.2020.00584

Spatial Patterns of Particles and Plankton in the Warming Arctic Fjord (Isfjorden, West Spitsbergen) in Seven Consecutive Mid-Summers (2013–2019)

Marlena Szeligowska[1], Emilia Trudnowska[1], Rafał Boehnke[1], Anna Maria Dąbrowska[2], Józef Maria Wiktor[2], Sławomir Sagan[3] and Katarzyna Błachowiak-Samołyk[1]*

[1] Pelagic Biocenosis Functioning Laboratory, Marine Ecology Department, Institute of Oceanology, Polish Academy of Sciences, Sopot, Poland, [2] Marine Protists Laboratory, Marine Ecology Department, Institute of Oceanology, Polish Academy of Sciences, Sopot, Poland, [3] Remote Sensing Laboratory, Department of Marine Physics, Institute of Oceanology, Polish Academy of Sciences, Sopot, Poland

OPEN ACCESS

Edited by:
David Murphy, University of South Florida, United States

Reviewed by:
Aaron True, University of Michigan, United States
Kusum Komal Karati, Centre for Marine Living Resources and Ecology (CMLRE), India

***Correspondence:**
Marlena Szeligowska
lena@iopan.pl

Specialty section:
This article was submitted to Marine Ecosystem Ecology, a section of the journal Frontiers in Marine Science

Received: *09 February 2020*
Accepted: *23 June 2020*
Published: *17 July 2020*

Citation:
Szeligowska M, Trudnowska E, Boehnke R, Dąbrowska AM, Wiktor JM, Sagan S and Błachowiak-Samołyk K (2020) Spatial Patterns of Particles and Plankton in the Warming Arctic Fjord (Isfjorden, West Spitsbergen) in Seven Consecutive Mid-Summers (2013–2019). Front. Mar. Sci. 7:584. doi: 10.3389/fmars.2020.00584

The restructuring of planktonic communities toward an increasing share of small individuals is not only expected, but also already observed consequence of warming in the rapidly changing Arctic. Here, we demonstrate a simultaneous study on the nano-, micro- and meso plankton (divided into small and large), and corresponding size fractions of particles along a hydrographical gradient in the Isfjorden – the largest Spitsbergen fjord system. The sampling was performed in seven following summers (2013–2019) from the main basin under the influence of Atlantic Waters (ISA station), up to Billefjorden – the innermost part affected by meltwaters from Nordenskiöldbreen (BAB station). Our objective was to elucidate the composition and spatial patterns in distribution of plankton and particles (P&P) under various hydrographical regimes. Combining two laser-based measurements (LOPC and LISST) with standard plankton analysis allowed us to conclude that vertical hydrographical stratification and eddy activity were forcing either layered or patchy distribution of P&P. The concentrations of P&P measured by LISST (nano- and micro-) were lower than the abundance of the corresponding size fractions of protists, but they did not differ significantly among the stations due to different origin of P&P. Nevertheless, the decreasing trend in the abundance of both investigated mesoplankton fractions could be observed between the ISA and BAB stations, whereas the opposite tendency was noted for P&P. Moreover, the abundance of mesoplankton was equal to the concentrations of the corresponding size fractions of P&P at the ISA station and much lower than the LOPC counts at the BAB station, which points toward notable amount of marine aggregates in the glacial bay. Even if some observations alluded to P&P susceptibility to the local processes, the inter-annual variability in P&P distribution surpassed the differences between the sampling stations. It suggests that both the large-scale processes (i.e., intensified inflow of Atlantic Waters) and natural seasonal changes associated with

subtle differences in sampling timing had a stronger influence on investigated plankton than local factors. This pioneering study, which links traditional and advanced methods, clearly demonstrated that such approach is convenient for tracking small-scale spatial patterns and inter-annual variability of P&P in the Arctic pelagial.

Keywords: particles, plankton, spatial patterns, Arctic, Isfjorden, glaciers, Atlantification

INTRODUCTION

The most rapid and substantial climate-related changes in marine ecosystems are observed at high latitudes, particularly in the Arctic. The reduction of sea ice cover, retreat of glaciers and thus an intensified freshwater discharge with suspended sediments are among the most pronounced consequences of climate fluctuations in this polar region. They are expected to result in strengthening of Arctic stratification and weakening of the large-scale ocean circulation (Murray et al., 2012; Straneo and Heimbach, 2013). Svalbard archipelago (74–81°N, 10–35°E), located in the European Arctic, is a unique area to study the aftermaths of warming (Symon et al., 2005; Piechura and Walczowski, 2009; Pavlov et al., 2013). The fjords on the western coast of Spitsbergen, which is the largest island of Svalbard archipelago, are exposed to various and dynamic forces that are driving local ecosystems. Among them, an advection of warm Atlantic Waters (AW) with West Spitsbergen Current - the major contributor to the oceanic heat transport to the Arctic - is essential (Carroll et al., 2011). Since these fjords balance Atlantic, Arctic, saline and freshwater regimes, different habitats exist there over relatively small spatial scales. Therefore, biological components of the west Spitsbergen coastal waters might be extremely vulnerable and potentially sensitive indicators of the environmental changes. However, they are still not fully explored and the knowledge gap is the most apparent for Isfjorden - the largest Svalbard fjord system.

It is only recently that glacier-impacted fjordic waters have been recognized as unique ecosystems being important nurseries and feeding areas for many fish, seabirds and marine mammals (Lydersen et al., 2014; Urbanski et al., 2017), or even as biomes with potential implications for the global carbon cycle (Smith et al., 2015). Since plankton is a key component of the Arctic pelagic food web, pathways and efficiency of energy transfer to the higher trophic levels depend on its structure and dynamics. Despite a few group-specific studies on the fluctuations of either protists or zooplankton (e.g., Gluchowska et al., 2016; Kubiszyn et al., 2017), the nature of the progressing changes in its functioning as an entire planktonic community remains poorly characterized. It is caused by the fact that such investigations require extensive, simultaneous, and interdisciplinary studies on the essential roles which various plankton size fractions play. For planktonic organisms size is a crucial determinant of their predator and prey range, but it is a technical challenge to cover such a wide size spectrum of planktonic individuals. However, resolving their community structure and dynamics is of great importance, since high spatial variability in plankton distribution represented by patches formation have been widely demonstrated to have a substantial role in enhancing trophic transfer (e.g., Wishner et al., 1988; Godø et al., 2012; Majaneva et al., 2013).

Even though the mosaic nature of the plankton distribution pattern is well-known, the phenomenon of plankton patchiness, which has been shown to be a ubiquitous and important feature also in the Arctic (e.g., Trudnowska et al., 2016), is still poorly characterized. Thus, any ability to predict the spatial patterns of plankton would significantly enhance our understanding of the Arctic ecosystems functioning. However, owing to the high variability of physical processes at small spatial scales and their impacts on biological dynamics controlling plankton distribution, high resolution sampling is necessary for further elucidation of such patterns. Recent technical advances in laser-based devices have opened new perspectives in ecological and behavioral studies by significantly improving sampling resolution. For instance, they allowed to describe wide size structure and distribution of particles and plankton in the Fram Strait, which is the main northward passage of AW to the Arctic region (Trudnowska et al., 2018). Nonetheless, even though laser-based systems used in the study measure particles suspended in the seawater in a wide range of sizes and at high frequency (Sprules and Barth, 2016), they do not allow distinguishing between living organisms (protists, zooplankton) and particulate matter. Hence, in areas with high detritus abundances the amounts of plankton might be overestimated (Stemmann and Boss, 2012) and it is important to compare the results obtained by laser-based measurements with complementary dataset to provide qualitative information.

Addressing the evident knowledge gap concerning the simultaneous examination of the relative roles of various size fractions of plankton and particles (P&P), we performed a comprehensive study on the inter-annual changes in distribution of wide range of plankton size fractions (nano-, micro-, small, and large mesoplankton) and the corresponding size fractions of particles. We used two laser-based counters: Laser In Situ Scattering and Transmissometry instrument (LISST-100X) for smaller (3–200 μm), and Laser Optical Plankton Counter (LOPC) for larger size fractions (200–5000 μm). These measurements were conducted simultaneously with standard sampling methods for protists and zooplankton (Niskin bottles and plankton nets, respectively) followed by microscopic analyses of these formations. Due to a strong contribution of marine aggregates to the laser-based counts, throughout this article we refer to P&P collectively while describing results from LISST or LOPC, whereas we refer exclusively to plankton in the case of standard methods. Our objective was to describe small-scale distribution and relative roles of different planktonic groups in relation to the hydrographic structure and various

river/glacier discharge impacts in Isfjorden in seven summer seasons (2013–2019). In this context, our research constitutes the first such comprehensive attempt to present a holistic view on spatio-temporal coupling between particles, aggregates, auto- and heterotrophic protists together with zooplankton divided into small and large size fractions.

MATERIALS AND METHODS

Study Area

Data were collected in Isfjorden (78°70′ N–78°27′ N, 13°–17° E), Spitsbergen (**Figure 1**) during the cruises on the R/V *Oceania* conducted by the Institute of Oceanology of the Polish Academy of Sciences (IO PAN) in the late July – early August surveys (covering the main melting season) in 2013–2019 (24–25 July 2013, 24 July 2014, 10 August 2015, 9–10 August 2016, 12–13 August 2017, 2–3 August 2018, 26–27 July 2019). The continuous, high resolution laser-based measurements were performed within the upper 70 m water column along a 60 km transect crossing Isfjorden, starting from sampling station located at the mouth of the southern branch of Isfjorden – Adventfjorden (ISA), through station in the central part of Isfjorden (ISF3 sampling station) up to the innermost part of Billefjorden (BAB sampling station).

During summer hydrographic conditions in Isfjorden can easily switch from typically Arctic to the Atlantic (Cottier et al., 2005, 2007). Due to the wide (about 10 km) and deep (455 m) mouth, it is open to the seawaters, and thus prone to the influence of AW carried by the West Spitsbergen Current (Nilsen et al., 2008). The hydrographical properties of Isfjorden vary from year to year, depending on the intensity of the advection of AW (Walczowski and Piechura, 2011) and the extent of the mixing (Svendsen et al., 2002) with Arctic Waters from the Sørkapp Current (flowing along West Spitsbergen shelf), local water and additional freshwater input originating from melting glaciers (Saloranta and Svendsen, 2001; Pavlov et al., 2013).

The area of ISA sampling station is influenced by the inflow of AW and three glacial-fed rivers discharging fresh and turbid waters during the main melting season (Leikvin and Evenset, 2009). BAB sampling station was located in Billefjorden - about 30 km long and 5–8 km wide northern branch of Isfjorden. The fjord is relatively shallow - the average depth is 160 m and maximum of approximately 190 m (Nilsen et al., 2008). An outer sill of 70 m and inner one of 50 m divide Billefjorden into outer and inner basins and restrict to some extent the exchange between them (Nilsen et al., 2008). AW advected to Billefjorden, Arctic Waters and/or Transformed AW undergo subsequent transformation through mixing with local waters from fjord and glacial waters (Pavlov et al., 2013). In summer, Billefjorden is supplied with meltwater with sediments load from a large glacier (Nordenskiöldbreen). A distinctive stratification of surface waters develops during this season and a pronounced thermocline and a halocline extend down to sill depth (Daase et al., 2007) covering cold and dense water masses. Due to severely restricted water masses exchange in the inner basin of Billefjorden, it is less affected by inflowing AW (Cottier et al., 2005; Nilsen et al., 2008). Hence, winter water is still present. ISF3 station is located approximately in the middle of the transect. This station was set in order to represent typical conditions of the central part of Isfjorden. Moreover, a cross-fjord location of the sampling station gives a possibility to test if in some years the upper water layer was under higher influence of either the innermost glacial plumes, or the AW advected from the shelf.

Laser-Based Measurements

The high resolution laser-based measurements of size-fractionated P&P distribution were conducted along a 60 km transect from the mouth of Adventfjorden up to Billefjorden (**Figure 1**) in an undulating mode between the surface and 70 m depth. The concentrations of wide size range of P&P (between 3 μm to 5 mm) were measured by means of two optical counters mounted on the same platform: Laser In Situ Scattering and Transmissometry instrument (LISST-100X, type B, Sequoia Scientific, Inc., WA, United States) and a Laser Optical Plankton Counter (LOPC, Brooke Ocean Technology Dartmouth, Canada) equipped with a conductivity-temperature-depth sensors (CTD, SBE 911plus, Seabird Electronics Inc., United States) and a fluorometer (Seapoint Sensors Inc., United States). The details regarding the principles of the LISST and LOPC are presented elsewhere (e.g., Agrawal and Pottsmith, 2000; Herman et al., 2004; Basedow et al., 2010; Trudnowska et al., 2014).

Standard Plankton Sampling and Analysis

Plankton samples were collected at three stations (BAB, ISF3, and ISA) located along a 60 km transect of laser-based measurements. Samples for analysis of the protist community, as well as chlorophyll *a* concentration were collected by means of 8 L Niskin bottles. In 2013 and 2014 sampling was performed in the euphotic zone, defined as layer from 100% (at 0 m) down to 1% of incident photosynthetically active radiation (PAR). In 2015, samples were collected from the arbitrarily chosen depths covering the photic zone: 0 m, 5 m, 15 m, 25 m, 50 m; due to technical problems two depths remained unsampled, i.e., 15 m and 0 m at the ISA and BAB stations, respectively. Starting from 2016 the depths, from which samples were collected, were fixed on 5 m, 15 m, 25 m, and 50 m and immediately physically integrated into one sample (volume of 200 mL) representing the mean community structure (cells in m^3) for the upper 5–50 m water column. For this purpose, samples were mixed in proportion to the vertical extent of water they represent, according to the formulas given in Möller and Bernhard (1974). Regardless of the sampling method, the protists subsamples of 200 mL volume were immediately fixed with an acidic Lugol's solution and, after 24 h, with borax-buffered formaldehyde. Both fixatives were added to a 2% final concentration. In years 2013 to 2016 subsamples of volume 250 mL - 400 mL for chlorophyll *a* concentrations were filtered through GF/F Whatman filters (pore size of 0.7 μm) in triplicates, and immediately frozen at −80°C. Extraction was done in 10 mL methanol for 20–24 h in cold (4°C) and dark place as given in Holm-Hansen and Riemann (1978). Chlorophyll *a* concentration ($mg \cdot m^{-3}$) was measured with a Turner Trilogy

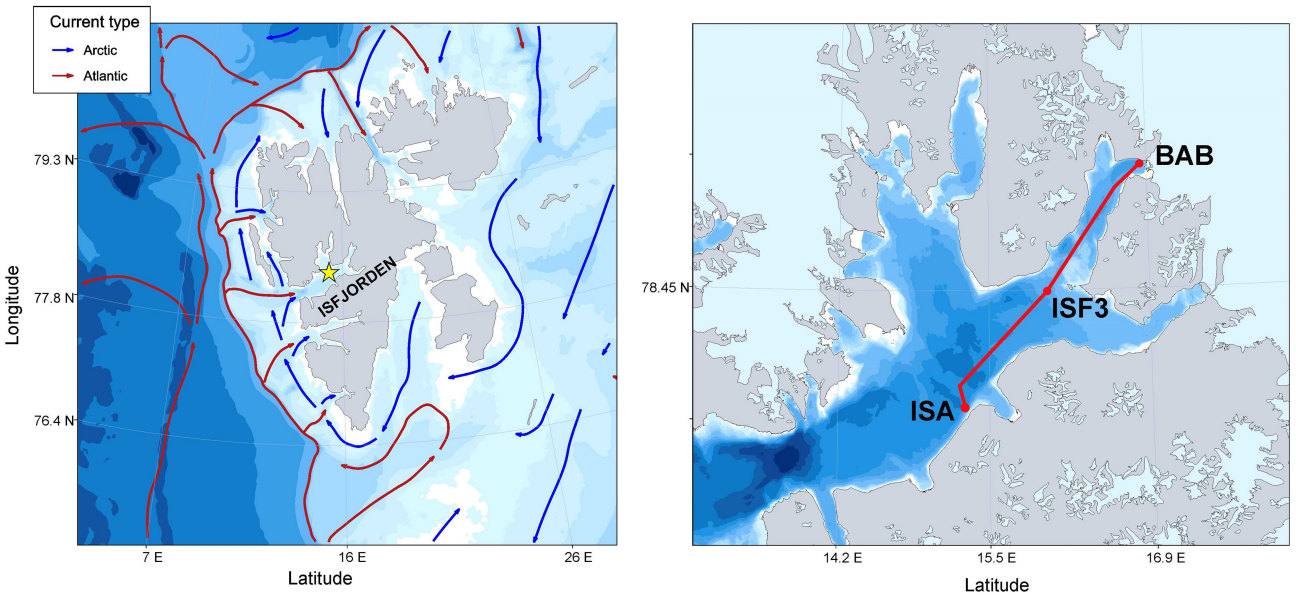

FIGURE 1 | Study area: Map of Svalbard Archipelago with schematic ocean currents circulation (PlotSvalbard R package by Vihtakari (2019); transect of laser-based measurements (LOPC & LISST marked as a red line) and plankton stations (ISA, ISF3 and BAB marked as red dots) in Isfjorden.

fluorometer calibrated with chlorophyll *a* standard (Sigma S6144). Quantitative and qualitative analyses of protists were done following the protocols of Utermöhl (1958) and modified by Edler (1979). Protist samples preparation for microscopic analysis and data processing was performed in accordance with Kubiszyn et al. (2014). As the Lugol's fixative precluded mode of nutrition identification, we used the available literature (Stoecker et al., 1994; Vaqué et al., 1997; Dolan et al., 2002; Gribble et al., 2007; Leadbeater, 2008; Mironova et al., 2009; Gómez and Artigas, 2014) and the Nordic Microalgae web base[1], to distinguish mode of nutrition of the observed taxa. Because mixotrophy cannot be determined in fixed material, taxa were classified as strict phototrophs or heterotrophs as described by Kubiszyn et al. (2014). If taxa could not be identified to the species level, and thus, the mode of nutrition could not be specified (i.e., unidentified small mono- and biflagellates of 3–7 μm) and a few taxa of the *Gymnodinium* and *Gyrodinium* genera), the "undetermined" mode of nutrition was also used.

Zooplankton sampling was performed at the same three stations as protists sampling in a vertical hauls (50–0 m) of WP2 net with a mesh size of 100 μm and an opening of 0.25 m^2. Samples were immediately preserved with 4% borax-buffered formaldehyde-seawater solution. Samples were prepared into appropriate volume depending on their densities and 2 mL subsamples were taken by Henson-Stempel pipette. The analysis was done under the stereomicroscope at 10–40× magnifications. All organisms were enumerated and identified from subsamples until at least 300 individuals were identified. The rest of each sample was analyzed for less abundant stages and rare species. Zooplankton identification was done to the lowest possible taxonomic level. All large and medium-sized calanoids were identified to appropriate species and copepodite stages. *Calanus finmarchicus*, *C. glacialis* and *C. hyperboreus* copepodite stages were distinguished by the comparison of prosome length measurements of all counted individuals with a size table obtained for *Calanus* spp. from Billefjorden by Arnkværn et al. (2005). Identification of *Pseudocalanus* to species level (*P. minutus* and *P. acuspes*) was done only for females because of uncertainties in distinguishing the remaining copepodite stages. Additionally, at least ten individuals representing various macrozooplankton and non-copepod mesozooplankton taxa per sample were measured. For morphometric analysis the total length distance from the top of a head/tip of a rostrum to the end of the body was used in case of longitudinal shape zooplankters (Søreide et al., 2003) or diameter in case of round shape zooplankters (Gannefors et al., 2005). Zooplankton abundances were calculated as a number of individuals in a cubic meter (individuals·m^{-3}) using the volume of cylinder formula where h: layer of sampled water column, surface area: opening of the WP2 net. Filtration efficiency of 100% of the net was assumed. The occasional counts of macrozooplanktonic organisms >5 mm (i.e., euphausiids, amphipods) were not included in the total abundance.

Data Processing and Statistical Analysis

Measurements of LISST and LOPC from the upper 2.5 m were discarded to minimize false counts due to a wave action, stray light or air bubble formation. The concentrations of P&P were calculated as the counts in a cubic meter (counts·m^{-3}), based on the sampled water volume and then averaged over 1 m depth intervals. In order to avoid potential errors at the lower and

[1]http://nordicmicroalgae.org

upper ends of the instrument's detection limits (Blanco et al., 1994; Mikkelsen et al., 2005; Stemmann et al., 2008; Davies et al., 2012), we restricted data to 3–200 μm equivalent spherical diameter (ESD) for the LISST and to 200–5000 μm ESD for the LOPC. Consequently, the size bins were aggregated into commonly used size ranges for nano- (3–20 μm) and micro- (20–200 μm) fractions as well for small- (200–500 μm) and large mesoplankton (500–5000 μm ESD) fractions, which corresponds to the division level between small and large copepods as well as between microaggregates and macroaggregates (>500 μm) (Simon et al., 2002; Trudnowska et al., 2018).

Brunt–Väisälä frequency squared (N^2), which is a measure of the vertical stratification or the static stability of the water column, was calculated from salinity, temperature and pressure using the MATLAB seawater toolbox[2]. If $N^2 > 0$, the water column is hydrostatically stable, and when $N^2 < 0$, it becomes hydrostatically unstable. The level of stratification can be based on the following criteria: $N^2 < 2{\cdot}10^{-5}$ rad^{2}s^{-2} non-stratified, $2{\cdot}10^{-5}$ rad^{2}s^{-2} < N^2 < $5{\cdot}10^{-5}$ rad^{2}s^{-2} weakly stratified and $N^2 > 5{\cdot}10^{-5}$ rad^{2}s^{-2} strongly stratified (Mojica et al., 2015). The sections of temperature, salinity, chlorophyll *a* fluorescence, N^2, and different P&P size fractions distributions were prepared using Ocean Data View Software (Schlitzer, 2018).

The analysis of plankton taxonomic composition (grouped into few dominating categories, corresponding to the ones presented in the results) and share of particular size fractions was performed on log-transformed abundance data to ensure a more balanced view of the community structure by reducing the influence of the most numerous taxa. Bray–Curtis similarity matrixes, which are the most commonly used scaling for biological community analysis, were applied to measure the resemblance among communities found at stations in particular years. To assess the similarities in the taxonomic composition of size fractions a non-metric MDS method was applied. The one-way ANOSIM was used to test if the differences in the relative roles of various plankton size fractions between investigated years and stations were similar ($R = 0$) or statistically different ($R = 1$, when groups of samples are well separated and characterized by the highest dissimilarity). The Spearman rank was used as a correlation method either for years or stations.

The number spectrum, an analog to the widely known particle size distribution (PSD), is one among the most popular approaches to analyze the size spectrum of particles (e.g., Jackson et al., 1997; Stemmann et al., 2008) and here it was calculated by dividing the concentration (abundance) of plankton as well of P&P within the size fractions by a width (difference between size limits) of the size fraction. The slope of the linear log-log dependence between size and a number of P&P reflects the relative importance of smaller (steep slope) or larger (flatter slope) components. The slopes of the size-fractionated concentrations of plankton and P&P were compared and tested using the Kruskal–Wallis test, which is a nonparametric one-way ANOVA based on ranks, used for comparing numerous independent samples. The importance of the effect of year and station was also tested by the Kruskal–Wallis test on abundances of particular size fractions of both plankton and P&P. The statistical analyses were computed in R (R Core Team, 2013), PRIMER v7 & PERMANOVA (Anderson et al., 2008; Clarke and Gorley, 2015), and Matlab v2018b packages (MATLAB, 2018).

[2]http://mooring.ucsd.edu/software/matlab/doc/toolbox/ocean/swstate.html

RESULTS

Hydrography and Chlorophyll *a* Fluorescence

The warmest water was generally found within the upper 20 m (**Figure 2**). In this surface layer, the temperature varied mainly between 4 and 10°C, with the highest temperatures near the BAB station in 2018 and 2019. Seawater temperature was decreasing with depth and toward the innermost station. The coldest water masses (Winter Cooled Water, $T < -0.5$°C, $S > 34.4$) were observed each year behind the sill that separates Billefjorden from the central part of Isfjorden (Nilsen et al., 2008). At ISA and ISF3 stations temperature was usually above 0°C even at 70 m depth. Out of the seven investigated summers, in 2013 the lowest seawater temperatures (below 0°C) were noted at each station in the water layer below 40 m, while opposite temperature pattern was found in the warmest 2014 (up to 40 km of section distance temperature in the 50 m water layer was higher than 4°C). The water stratification differed between the first 20–40 km of the transect and further on, with shallower warm and freshwater layer near the ISA station and deeper and more pronounced freshwater layer closer to Billefjorden (BAB station). At approximately 20 km distance from the ISA station a discontinuity in hydrographic structure was observed in 2016–2018 (marked by arrows in **Figure 2**). It was most probably accompanied by shallow submesoscale eddy with a diameter of a few kilometers, whose core was characterized by local depression of the warmer and fresher water. The fresh surface water layer (10 m) with salinity reduced to around 29 was stretched for around 30 km from the BAB station. The area close to ISA station was also influenced by freshwater input (salinity reduced to 32 in the uppermost 10 m). The salinity was increasing with depth and it was generally between 33 and 34 below 20 m with an exception in 2014 when it reached 35. The fluorescence of chlorophyll *a* along the transect was the highest in the upper 20 m layer, but occasionally its high values reached down to 40 m at the ISA station. The fluorescence of chlorophyll *a* was usually lower and restricted to narrower vertical ranges in Billefjorden. The relative values of chlorophyll *a* fluorescence were the lowest in 2013 and the highest in 2014. The vertical extent of an euphotic zone varied along the transect, e.g., from 10–12 m in the inner Billefjorden (BAB station) to 28–32 m in the southern part of the fjord (ISA) in 2013 and 2014. Low fluorescence of chlorophyll *a* in the surface water layer was observed inside the hydrographical discontinuity in 2016–2018. In 2013–2016, the water column was strongly stratified and hydrostatically stable even down to 40 m, whereas in 2017–2019, a stratification gradient was shallow (upper 5 m) and hydrographic structure of the water column was most probably unstable, especially in the Billefjorden part of the transect (**Figure 2**).

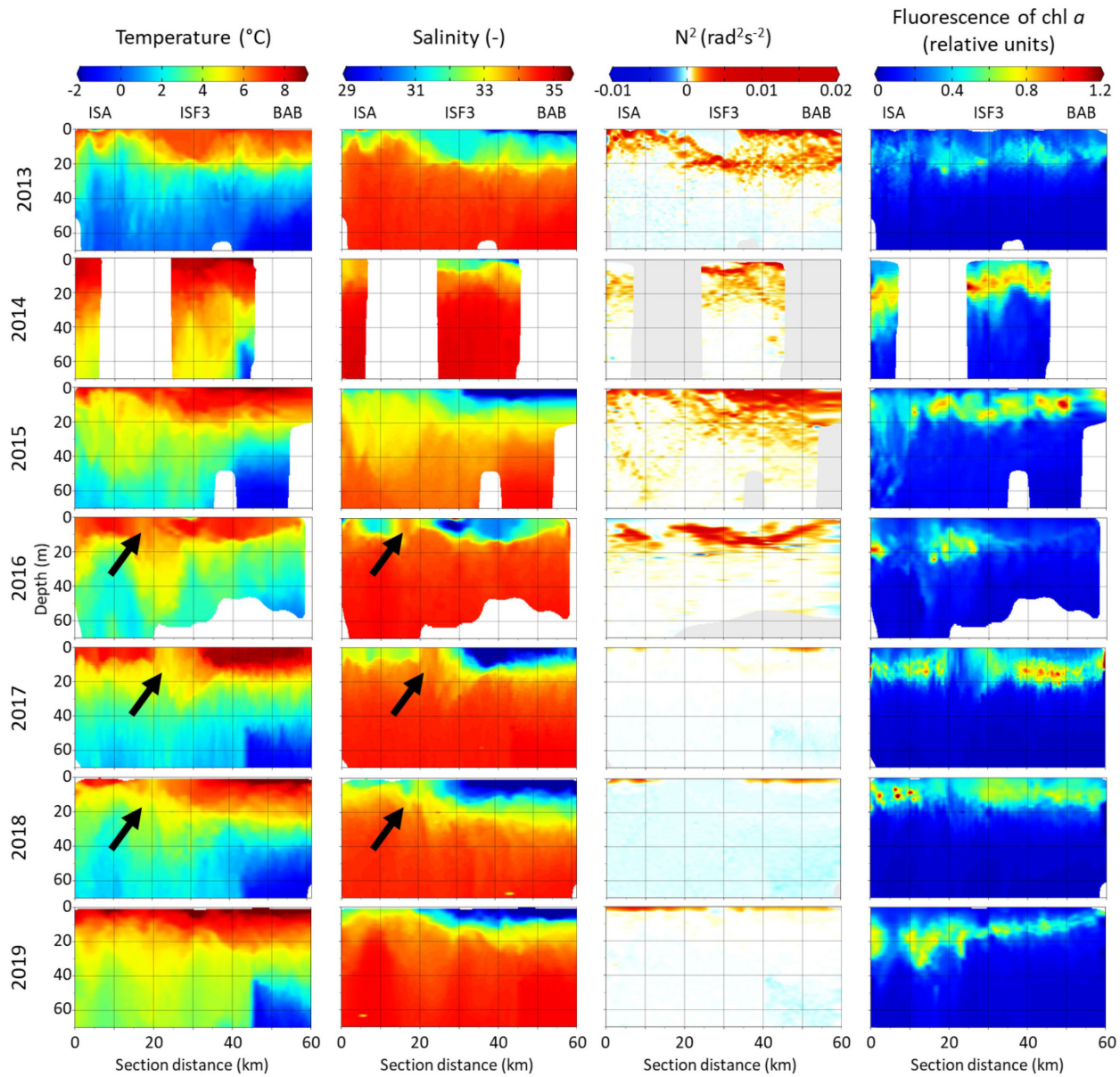

FIGURE 2 | Distribution of temperature (°C), salinity, water column stability (Brunt–Väisälä frequency squared N^2 [$rad^2 s^{-2}$]) and fluorescence of chlorophyll *a* (relative units) along Isfjorden transect from ISA station (left side of each graph) up to BAB station (right side of each graph) in seven consecutive mid-summers (2013–2019). Arrows indicate a hydrographical discontinuity followed by eddy.

Spatial Distribution of P&P Size Fractions Along the Investigated Transect of Laser-Based Measurements

Distribution of P&P evaluated by laser-based devices (LISST and LOPC) of nano- (3–20 μm), micro- (20–200 μm), small meso- (200–500 μm) and large meso- (500–5000 μm) size fractions strongly varied between the investigated summers (**Figure 3**). Apart from 2018, the peaks of all analyzed fractions were mostly concentrated in the upper 20 m layer. Generally, the nano-fraction was almost uniformly concentrated near the surface along the transects. Between 2015 and 2017 the micro- fraction occurred in a form of a few kilometers long surface patches. This fraction was extremely abundant in 2018 (note different scale) and 2019 and expressed a particularly distinguishable distribution pattern in 2019, with the vertical extension of the peaks through the whole investigated water body. The interesting feature of the small meso- fraction distribution was that at the BAB station – the end of the transect – P&P were often (in 2013, 2016, 2018, and 2019) very numerous also in the deeper parts of the water column. The patches of the large meso- fraction were mostly less extended than the ones of the small meso- fraction (except

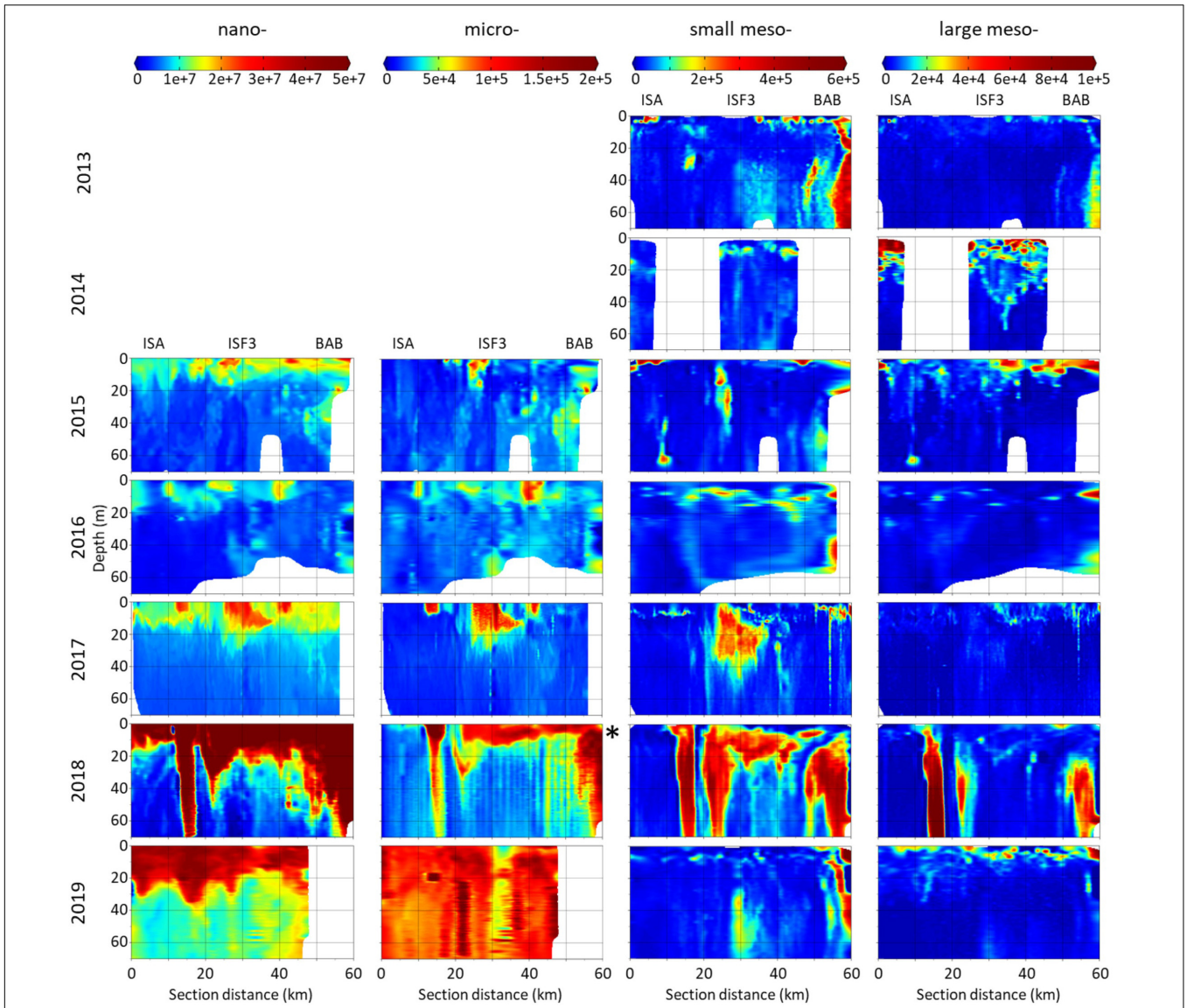

FIGURE 3 | Distribution of abundance (counts·m^{-3}) of P&P classified into four size fractions: nano-, micro-, small meso- and large meso- in the upper water column along Isfjorden transect from ISA station (left side of each graph) up to BAB station (right side of each graph) in seven consecutive mid-summers (2013–2019). Note different scales between size fractions. In 2018 the abundances of micro- fraction were one order of magnitude higher than in other years (*). Data for nano- and micro- fractions (LISST) were not collected in 2013 and 2014.

for 2014). There was a similar vertical pattern of nano-, micro- and small meso- fractions in 2015 and 2016, manifested by their peaks in distribution – the larger the fraction, the deeper it was present in the water column. In 2017 the location of peaks in abundance of nano-, micro- and small fractions was also compatible. The exceptionally high abundance of all size fractions of P&P was observed in 2018 in a form of three corresponding concentration peaks that spread vertically through the whole studied water column (70 m). In 2016–2018 low abundance of P&P in the surface water layer was associated with the observed hydrographical discontinuity. At its edge the P&P accumulation zone was present, which most probably resulted from the eddy formation. In 2019 there were also high numbers of nano- and micro- sized particles accompanied by a peak in abundance of small meso- fraction observed in the deeper waters.

Abundance and Taxonomic Composition of Plankton Divided Into Various Size Fractions

In total, 90 protist taxa with the most diverse Dinophyceae (39), Ciliophora (16), Bacillariophyce (15), and Prymnesiophyceae (5) were identified, whereas in the case of zooplankton we noted 40 taxonomical categories with the highest number of Copepoda (14). The nanoplanktonic fraction, which constituted the most important contributor to the total protists abundance,

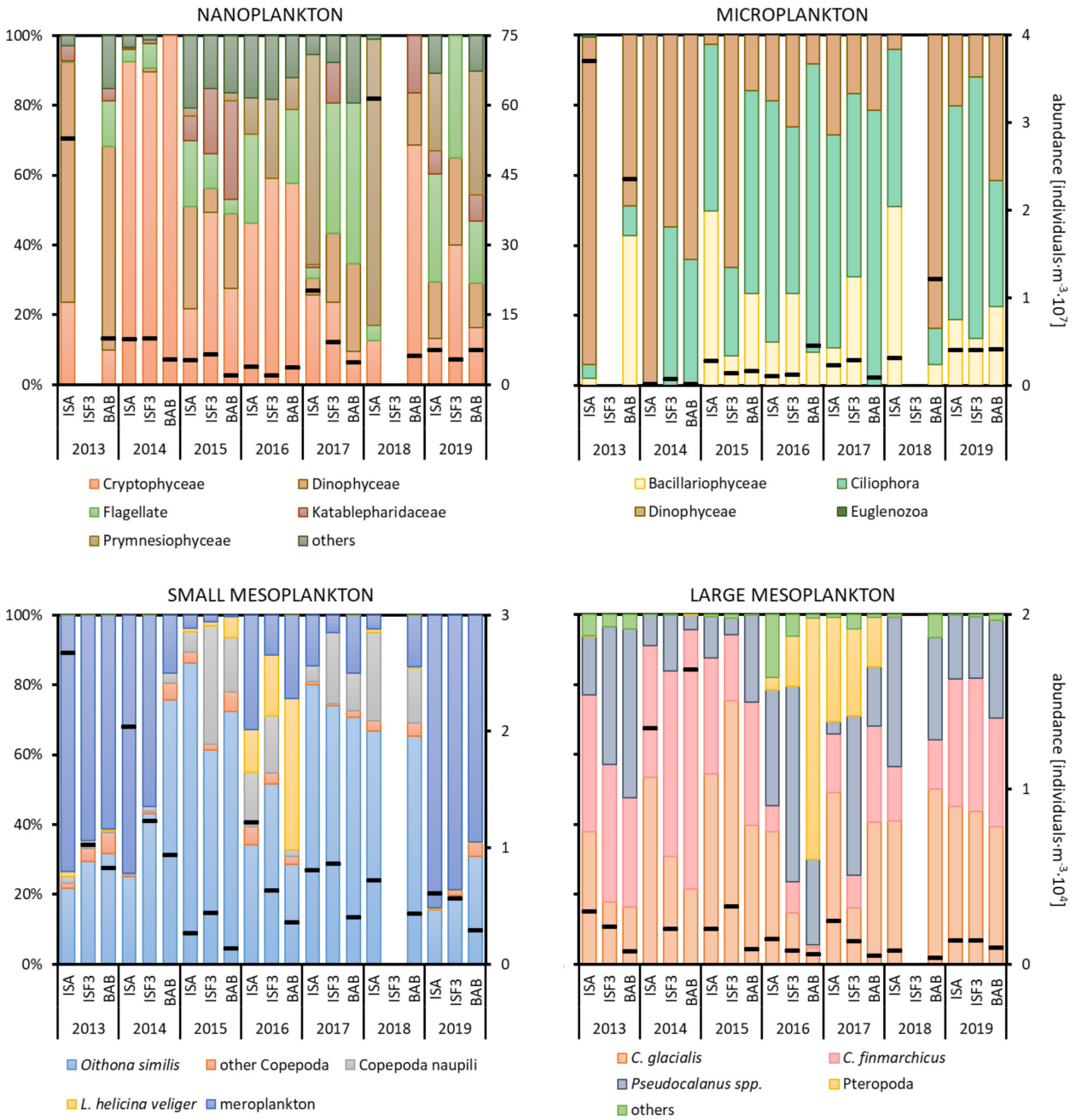

FIGURE 4 | Abundance (black dashes) of various plankton size fractions (individuals·m^{-3}) and relative abundances (%) of the major taxonomic groups at three Isfjorden stations: ISA, ISF3 and BAB in seven consecutive mid-summers (2013–2019). Data for protists at ISF3 station were not collected in 2013 and 2018, whereas for zooplankton in 2018. Note different scales for size fractions.

was predominated by Cryptophyceae (up to 100%) mainly represented by *Teleaulax* spp., whereas the microplanktonic fraction was usually dominated by Ciliophora (up to 82%) with the highest number of *Lohmanniella oviformis* and *Acanthostomella norvegica* (**Figure 4**). Occasionally, there were peaks in abundance associated with Dinophyceae (*Gymnodinium* spp. in 2013) or Prymnesiophyceae (*Phaeocystis pouchetii* in 2017 and 2018) at the ISA station. The high abundance of Dinophyceae (Peridiniales indet. and *Protoperidinium* spp.) was also observed among the microorganisms in 2013 at the ISA station and in 2018 at the BAB station.

The small mesoplankton fraction was primarily represented by *Oithona similis* (15–82% of the total abundance) throughout the entire study period (**Figure 4**). In addition to typical planktonic organisms, larval stages of benthic organisms (Bivalvia, Polychaeta, and Echinodermata) were also abundant,

especially in 2013, 2014, and 2019. Their abundance was the highest at the ISA station and the lowest at the BAB station in most of the investigated mid-summers. Veligers of *Limacina helicina* were observed each year with abundance peak in 2016. High densities of juveniles of *L. helicina* (marked in yellow as Pteropoda in **Figure 4** – large mesoplankton) were found in 2016 and 2017 at all investigated stations. In 2015–2018, a significant number of Copepoda nauplii was also observed. The large mesoplankton fraction was characterized by the domination of both *Calanus* species with prevailing *C. finmarchicus* in 2013 and 2014 and *C. glacialis* in 2015. In 2014 older life stages (CIV–CVI) of *C. glacialis* were especially abundant, but due to high overall abundance of L mesoplankton their relative role was similar to other years.

Taxonomic composition of protists and zooplankton was characterized by large temporal (between 2013 and 2019) and spatial (among ISA, ISF3, and BAB stations) variations. The species composition of the nano- fraction differed between stations especially in 2014, 2018, and 2019 (**Figure 5**). Non-metric MDS scaling (**Figure 5**) showed that microplanktonic community composition was clearly separated at ISA station in 2013 and 2014 (due to the overwhelming dominance of Dinophycae). Even though the differences in the detailed nano- and microplankton species composition between years and stations were tremendous, no significant differences were assigned to coarse taxonomical grouping (a few dominating categories presented in **Figure 4**) used for non-metric MDS scaling and data analyses (**Table 1**). The most year-specific taxonomic composition was found for the small meso- fraction (**Figure 5** and **Table 1**), whereas the composition of the large meso- fraction was relatively similar between 2016 and 2017, but different in other years (due to the prominent presence of pteropods). Abundance of the taxonomical groups within small and large mesoplankton differed more among various years than among stations (**Figure 5** and **Table 1**).

Shares of Various Plankton Size Fractions in Total Abundance

The shares of various plankton size fractions (%) differed more between years (**Supplementary Figure S1**, slopes in **Table 1**) than among stations. At the BAB station the share of microplankton was higher than at the ISA station in 2013, 2016, and 2018, whereas the lowest across all the stations ratio between

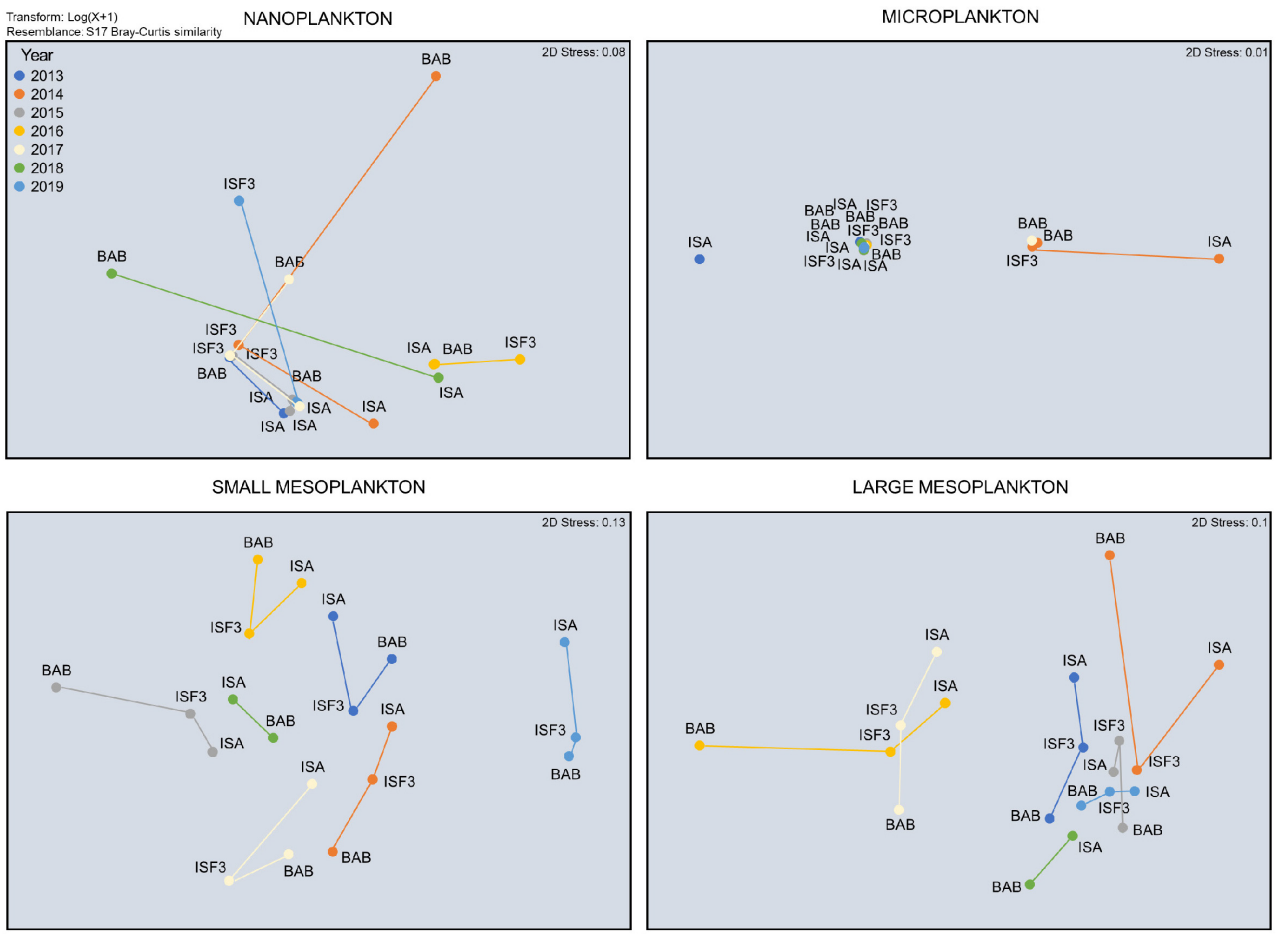

FIGURE 5 | Non-metric MDS scaling of Bray–Curtis resemblance of the composition of dominating taxonomical groups within particular plankton size fractions.

TABLE 1 | The results of ANOSIM and Kruskal–Wallis tests provided for all plankton size fractions and studied years/stations together with the slopes of plankton size spectra derived from LISST and LOPC.

Type	Test	Year	Station
Nanoplankton community	ANOSIM	$R = 0.23$	$R = 0.06$
Microplankton community	ANOSIM	$R = 0.26$	$R < 0$
Small mesoplankton community	ANOSIM	$R = 0.81$	$R < 0$
Large mesoplankton community	ANOSIM	$R = 0.50$	$R < 0$
Nanoplankton abundance	Kruskal–Wallis	$p = 0.08$	$p = 0.21$
Microplankton abundance	Kruskal–Wallis	$p = 0.028$	$p = 0.62$
Small mesoplankton abundance	Kruskal–Wallis	$p = 0.046$	$p = 0.11$
Large mesoplankton abundance	Kruskal–Wallis	$p = 0.16$	$p = 0.07$
Nano- P&P abundance	Kruskal–Wallis	$p = 0.024$	$p = 0.76$
Micro- P&P abundance	Kruskal–Wallis	$p = 0.046$	$p = 0.76$
Small meso- P&P abundance	Kruskal–Wallis	$p = 0.92$	$p = 0.001$
Large meso P&P abundance	Kruskal–Wallis	$p = 0.37$	$p = 0.096$
Plankton size spectra slopes	Kruskal–Wallis	$p = 0.017$	$p = 0.69$
LISST size spectra slopes	Kruskal–Wallis	$p = 0.025$	$p = 0.99$
LOPC size spectra slopes	Kruskal–Wallis	$p = 0.22$	$p = 0.29$

micro- to nanoplankton was observed in 2014 and 2017. The exceptionally high (>25%) importance of large in relation to small mesoplankton was observed in 2014, 2015, and 2019. In general, the ratio between larger size fraction and smaller size fraction (micro- vs. nano-, large- vs. small-) was higher in dataset comprising plankton than in laser-based measurements of P&P (**Supplementary Figure S1**). The abundance of both plankton and P&P decreased from the smallest to the largest size fractions studied (**Figures 6A,B**). The slopes obtained for plankton at each station and year investigated separately ranged from around −2.5 to −4.7, but mostly oscillated around −3 (**Figure 6C**). The slightly increasing trend of the size spectra slopes toward steepness (i.e., the increasing role of smaller fractions) was observed between 2016 through 2017 to 2018 (**Figure 6C**). The variability in the slopes was the highest at the ISA station and the lowest at the ISF3 station with only one exception in 2013 (−4.7) (**Figure 6D**). The BAB station was characterized by rather low variability, except in 2014 (−2.5), but also characterized by more steeper size spectra slopes in comparison with ISF3 station (implying higher contribution of the smallest fractions). Due to the methodological issues discussed below, we could not obtain a smooth transition between the results provided by the two laser-based instruments and thus we decided to consider them separately (**Figure 6B**). The steeper slope was observed for LOPC measurements and ranged from around −5.4 at the ISA station to −6.09 at the ISF3 station. For LISST measurements the slopes were very similar between stations (around −4), but differed significantly among years (**Table 1**).

Regional Comparison Between Standard (Plankton) and Laser-Based (P&P) Abundance Estimates

In general, higher abundance of planktonic organisms was observed at the ISA station and lower at the BAB station, while opposite pattern was noted for P&P (**Figure 7**). This gradient was especially well-pronounced for small mesoplankton fraction (Kruskal–Wallis chi-squared = 13.318, df = 2, p-value = 0.001282), but was also visible for nano- and large meso- fractions. The concentrations measured by LISST were lower than the abundance of the corresponding size fractions of protists collected by standard plankton sampling. The abundances of nano- and micro- fractions assessed by the laser counter did not differ significantly among the stations, while slightly decreasing gradient (from ISA toward BAB) was observed in the abundance of nanoplankton concentrations. Abundance of zooplankton was usually lower than the concentrations of the corresponding size fractions derived from LOPC measurements, with the exception of large meso- fraction at ISA station, where the similar ranges of concentrations were assessed by both methodological approaches. Moreover, the gradient between stations could be observed in the form of decreasing number of small and large mesoplankton along with the increasing number of particles toward BAB station. What is worth noting, the difference between concentrations estimated by the LOPC measurements and zooplankton concentrations estimated from net samples was the highest at BAB station.

DISCUSSION

Environmental Gradients and Their Influence on P&P Distribution

The inflow of freshwater from the glacier in the inner part of the Billefjorden induced strong physical gradients of temperature and salinity along the investigated transect and triggered substantial, typical for summer stratification of the water column (Hop et al., 2002; Cottier et al., 2010). The observed vertical environmental gradients and eddies as well as stratification reflected by the Brunt–Väisälä frequency squared, N^2 (**Figure 2**), enhanced either layered or patchy distribution pattern of P&P, similarly as was shown in several previous studies (Dekshenieks et al., 2001; Möller et al., 2012; Trudnowska et al., 2016). In this study a sharp decrease in P&P numbers with depth was observed in the case of nano- and micro- size fractions of P&P, which were concentrated in the upper 20–30 m depth layer. It seems to be a common pattern observed in various marine environments (e.g., Jackson and Checkley, 2011; Gluchowska et al., 2017b). Such a distribution of the two smallest fractions of P&P could be caused by either the fact that they were entrapped by the stratification gradient or that they were concentrated close to the surface due to the better light conditions for photosynthesis, as their distribution corresponded well with peaks in fluorescence of chlorophyll *a* in the surface water layer (**Figures 2**, **3**). Even though the averaged concentrations of nano- and micro-fractions in the 50 m water column did not differ significantly among the stations along the transect (**Figure 7**), they most likely were of diverse origin. We concluded that in the central part of the Isfjorden there was a high number of primary producers in the surface water layer (down to around 20 m depth), whereas in the Billefjorden the presence of numerous fine inorganic sediments within the whole 50 m water column strongly contributed to the overall abundance of these size fractions. It was

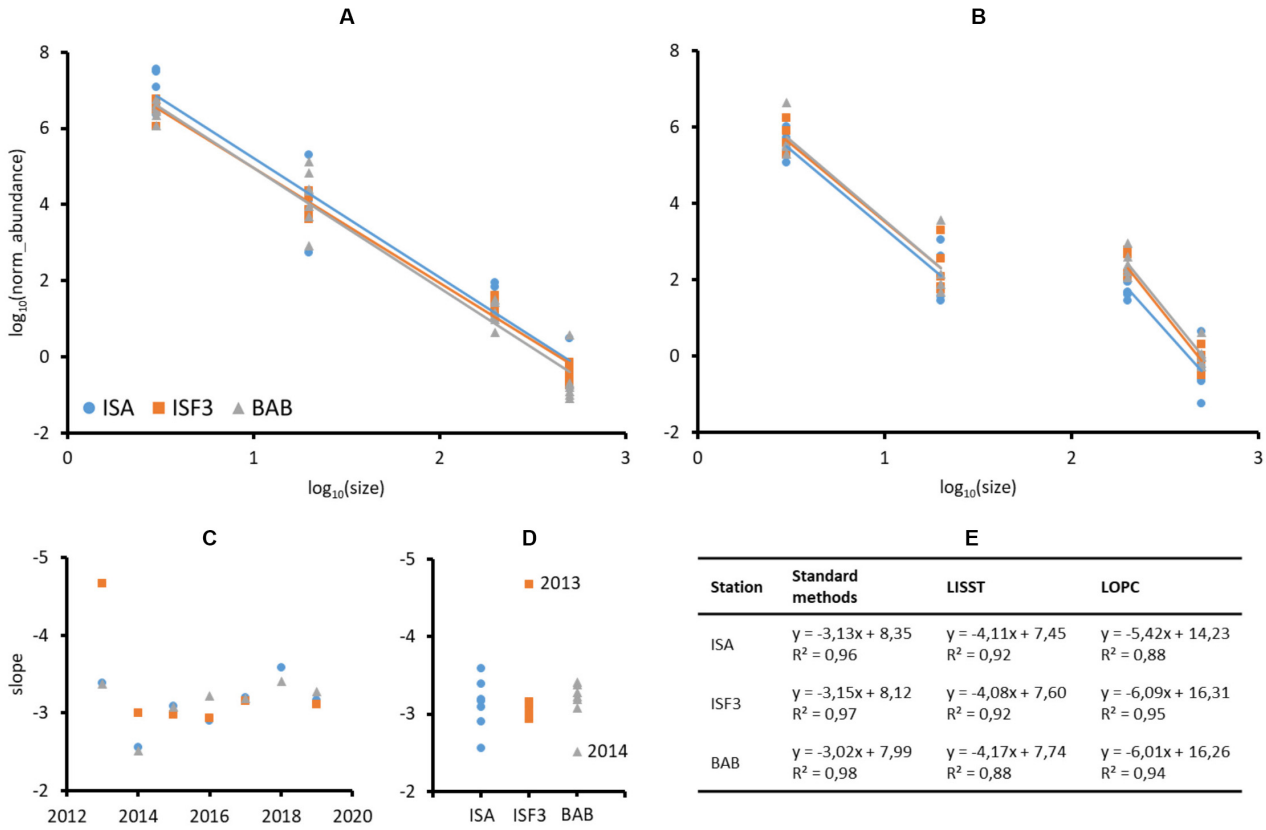

E

Station	Standard methods	LISST	LOPC
ISA	y = -3,13x + 8,35 R^2 = 0,96	y = -4,11x + 7,45 R^2 = 0,92	y = -5,42x + 14,23 R^2 = 0,88
ISF3	y = -3,15x + 8,12 R^2 = 0,97	y = -4,08x + 7,60 R^2 = 0,92	y = -6,09x + 16,31 R^2 = 0,95
BAB	y = -3,02x + 7,99 R^2 = 0,98	y = -4,17x + 7,74 R^2 = 0,88	y = -6,01x + 16,26 R^2 = 0,94

FIGURE 6 | Log-transformed normalized abundances of plankton **(A)** and P&P **(B)** size fractions (individuals·m^{-3} and counts·m^{-3}) at three Isfjorden stations: ISA, ISF3, and BAB in seven consecutive mid-summers (2013–2019). Slopes of the number spectrum fitted to plankton concentrations over years **(C)** and stations **(D)**. Table of linear fit equations and R-squared values obtained for standard methods and laser-based measurements of plankton and P&P abundance **(E)**.

evident in 2015, 2016, and 2019 due to the diminishing signal of chlorophyll *a* fluorescence toward innermost part of the section. The low salinity at the surface – a sign of freshwater discharge with suspended sediments – is associated with an increase in the turbidity of the upper water layer. The high particles loads result in substantial light absorption and consequently reduction of the vertical extent of the euphotic zone (Weslawski et al., 1995; Keck et al., 1999) as was observed in the glacial bay in Billefjorden.

Contrary to the smaller size fractions, we observed well-pronounced gradual increase in number of two meso- fractions of P&P from ISA toward BAB station (**Figures 3**, **7**). It was associated with the opposite trend for planktonic organisms, whose concentrations were generally higher at ISA station and gradually decreased toward the innermost BAB station (**Figures 4**, **7**). The similar horizontal gradient of dominance of zooplankton in relation to marine aggregates concentrations was previously followed along the Hornsund fjord axis and was clearly coupled with hydrographical differences between the outer and innermost parts of the fjord (Trudnowska et al., 2014). The increased number of particles at BAB station within small meso- fraction was probably caused by the same phenomena as recently observed in other fjords, where the glacier meltwater discharge led to increase in the abundance of small and amorphous particles (Trudnowska et al., 2014, 2020a). We also observed lower abundance of larvae of benthic organisms (meroplankton in **Figure 4**) in Billefjorden than outside the Adventfjorden in most of the investigated mid-summers. The survey on benthic communities in an Arctic glacier-fed river estuary in Adventfjorden showed that they are sensitive to sediment instabilities and physical disturbance caused by high sedimentation and frequent sediment gravity flows (Włodarska-Kowalczuk et al., 2007). In 2018 the patches of P&P were spreading along the whole water column and most probably they consisted of sea-bottom sediments resuspended by storm-induced wave action (Zajączkowski and Włodarska-Kowalczuk, 2007). The influence of bottom sediments on the optical seawater properties after storm has been earlier observed in Svalbard coastal waters (Trudnowska et al., 2015).

The accumulation of P&P in the central part of investigated transect (ISF3) was observed by both laser-based (mainly smaller size fractions) and conventional methods (zooplankton), which suggests that a transitional zone between glacial waters and advected AW may constitute a convergence zone for P&P. We observed a specific hydrographical structure in the form of discontinuities in the temperature, salinity and fluorescence of chlorophyll *a* distributions at the entrance to Billefjorden (**Figure 2**), which was followed by the submesoscale eddies localized in the vicinity of the Gåsøyane islands in 2016–2018.

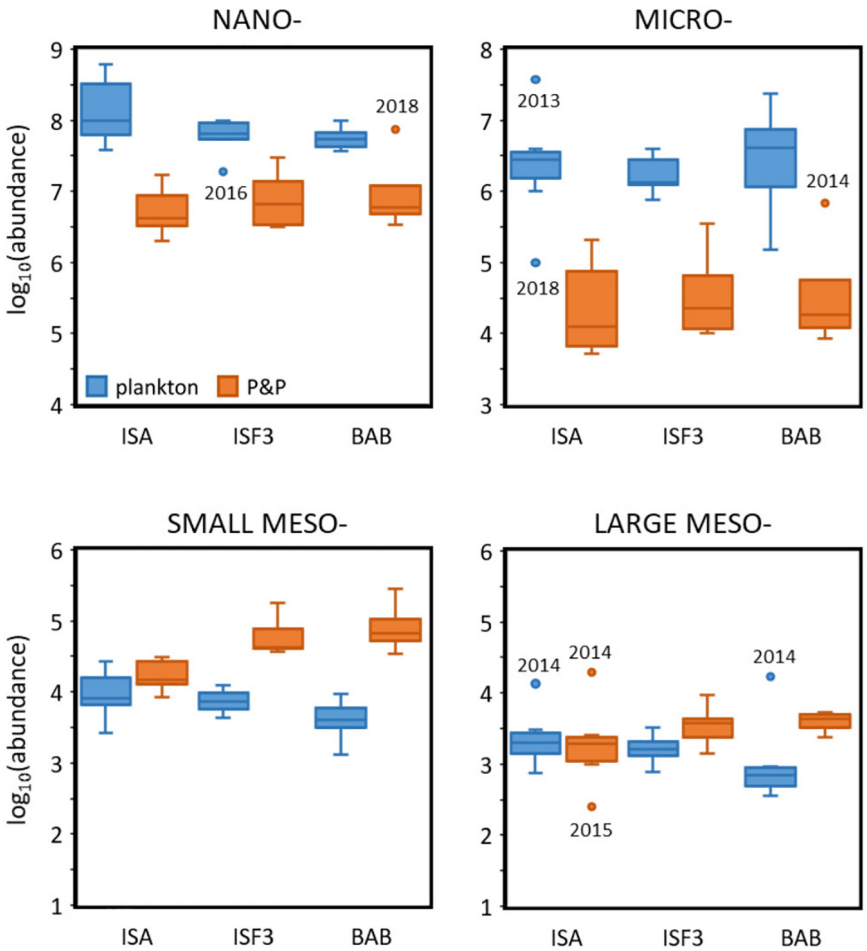

FIGURE 7 | Log-transformed abundances (individuals·m^{-3} and counts·m^{-3}) of plankton (blue) and P&P (orange) within four analyzed size fractions at three Isfjorden stations: ISA, ISF3 and BAB in seven consecutive mid-summers (2013–2019). The start (the lower quartile) and the end of the box (the upper quartile) represent 25% and 75% of the data, respectively. The line in the box represents the median value. The whiskers are defined as 1.5 times the inter-quartile range. Anything outside the whiskers is considered as an outlier (dots).

The formation of eddies in the middle of investigated transect was confirmed by satellite observations (**Supplementary Figure S2**). It is also supported by a numerical model of barotropic tides in the western Svalbard fjords developed by Kowalik et al. (2015), which showed stronger currents in the ISF3 station area and indicated a local depression of water surface as an interesting feature of the tidal eddies. The strong tidal currents, frequently generated in the western fjords of Svalbard (modeled by Kowalik et al., 2015; Nilsen et al., 2016) are responsible for the water exchange in the shallow or narrow subdomains and can cause oscillating motion resulting in P&P entrapment within eddies, which in turn are an additional driving force of the observed patchiness, both in fjords and on the shelf (Trudnowska et al., 2016).

Even though the nano- and micro- fractions of P&P represented mostly layered distribution, both meso- fractions of P&P followed the patchy pattern. Occasionally a tight spatial coupling among peaks in abundance of particular size fractions of P&P was observed (e.g., between micro- and small meso- fractions in 2015; among nano-, micro- and small meso- fractions in 2017). Moreover, the multi-fraction patches were also observed (e.g., in 2016 and 2018, consisting of nano-, micro- and small meso-). Large meso- fraction seemed to be mostly de-coupled in space from the other fractions, which agrees with previous observation that its distribution is independent from basic environmental forcing and biological factors are thought to have a stronger influence on large mesoplankton aggregation processes (Trudnowska et al., 2016). However, it seems that when the strong physical forcing occurs, such as the mixture of storm waving and eddy activity observed in 2018, this fraction is also contributing to the multi-fraction patches. Due to the high overall variability in Isfjorden dataset, most probably caused by the interaction between active (biologically driven) and passive (forced by physical mechanisms) patchiness and seasonal dynamics of P&P in this region, which also differ depending on their origin, it is difficult to indicate specific mechanisms for matching or separation of different P&P fractions' distribution. However, considering the fact that the larger size fractions of P&P tended

to occur slightly deeper in the water column than the smaller ones, they were most likely formed in the process of physical coagulation (McCave, 1984; Jackson, 1990) and/or flocculation of smaller P&P, which is especially intensified by freshwater supply (Zajączkowski and Włodarska-Kowalczuk, 2007; Trudnowska et al., 2020a). The biological process enhancing formation of larger particles with higher sinking velocities is the presence of mucilaginous colonies of phytoplankton, which due to their increased sugar-driven strictness play a 'cleaning' role when passing through the water column. Also zooplankton activity (e.g., grazing) may produce large sinking particles in form of the fecal pellets, molts and dead bodies (Sheldon et al., 1972; Alldredge and Silver, 1988). In addition, many ecological traits such as niche portioning, predator avoidance, population abundance, growth rate and productivity of zooplankton are also responsible for the diverse spatial patterns of P&P (Simon et al., 2002; Norrbin et al., 2009; Lalande et al., 2011).

The Inter-Annual Variability in the Taxonomic Composition of Various Plankton Size Fractions

The observed mid-summer protists community structure (**Figure 4**) was typical for the West Spitsbergen waters (e.g., Piwosz et al., 2009; Hodal et al., 2012; Kubiszyn et al., 2014, 2017). It was characterized by the domination of nanoplanktonic flagellates (especially Dinophyceae and Cryptophyceae), as well as microplanktonic Ciliophora, which, due to active movement ability and a number of nutrition modes, are well adapted to live in turbid fjord waters. The abundances of nano- and microplankton were at a similar level throughout the observational period, except for much higher values of both size fractions recorded in 2013 and 2018. In 2013, it was represented primarily by highly numerous Dinophyceae (mainly *Gymnodinium* of size 5–20 μm), which constitutes an almost year-round component of the West Spitsbergen plankton (Kubiszyn et al., 2017). Unfortunately, due to the plasticity of the naked (athecate) *Gymnodinium* cells and the susceptibility to fixation, most of the taxa are usually (also in the presented study) identified only to the genus level in the light microscopy, by what the determination of their contribution to the total primary production is largely unknown. Due to the fact that most of the protists are mixotrophic and the mode of nutrition of some of them could not be specified, it was not possible to infer about the decrease in primary producers in glacier-influenced waters based on the species composition. In 2018, the exceptionally high nanoplankton abundance was related mainly to the presence of the prymnesiophyte *P. pouchetii*, and most likely resulted from advection of the community along with the AW. The high numbers of *P. pouchetii* at the ISA station were observed, *inter alia*, by Kubiszyn et al. (2017) during spring 2012, after the strong inflow of AW to the shelf. According to recent studies, *Phaeocystis* cells are affiliated with AW (Metfies et al., 2016). However, this species has been regularly noted in the European Arctic waters. Moreover, it is commonly believed that the increase in abundance of small pico- and nanoplankton species in the last two decades is directly related to the warm anomaly in the Fram Strait (Nöthig et al., 2015).

The small mesoplankton was dominated by *O. similis*, which is one of the most abundant mesozooplankton species in the sub-Arctic and Arctic regions (Auel and Hagen, 2002; Hopcroft et al., 2005; Daase and Eiane, 2007; Madsen et al., 2008; Gluchowska et al., 2016), but often underestimated in standard mesozooplankton studies basing on sampling with plankton net with 180 or 200 um mesh size. Thus, in the current investigation, we took an advantage to assess the whole copepodite structure of this species by using WP2 net with 100 μm mesh size. Dominance of this cyclopoid occurred in years 2014 and 2017. It was probably due to the intensified advection of AW since *O. similis* is the most abundant zooplankton transported with the West Spitsbergen Current (Weydmann et al., 2014; Gluchowska et al., 2017a,b) which strongly reshapes the zooplankton size structure (Trudnowska et al., 2020b). Substantially higher abundance of *O. similis* in 2014 noted at BAB sampling station indicates that the strong advection of AW in this year reached even the innermost parts of Isfjorden. It is consistent with the CTD profiles from this survey, which showed the presence of warmer and more saline waters in 2014 in Isfjorden than in the remaining years. Studies from another west Spitsbergen fjord - Hornsund showed that in the summer of 2014 AW was observed for the first time in its main basin and even in Brepollen – the innermost glacial bay (Promińska et al., 2018). In this study, the main contributors to the abundance of large meso- fraction were *Calanus* copepods, which represent the key element of zooplankton communities in Svalbard fjords (Scott et al., 2000; Weslawski et al., 2000; Hop et al., 2002; Kwasniewski et al., 2003) and are of major importance in the Arctic food web (Falk-Petersen et al., 1987, 2002; Scott et al., 1999) due to both their high abundance and high lipid content. A similar pattern in abundance peaks were observed for *C. finmarchicus* as for *O. similis*, since both species are typically advected to the region with AW (Wassmann et al., 2015, 2019; Basedow et al., 2018). Because of the smaller individual size of the local population of *C. glacialis* in Billefjorden (Gabrielsen et al., 2012), the distinction between the two species has to be interpreted with caution. However, the coexistence of these two *Calanus* species in Billefjorden is year-round, despite the lower survival rate of *C. finmarchicus* (Arnkværn et al., 2005). Large meso- fraction represented mainly by *Calanus* spp., which was shown to gather during summer in the surface 20 m water layer either in high (2014, 2015, 2017, and 2019) or low concentrations (2013, 2016, and 2018), suggests oscillation of stronger or weaker advection of AW, respectively (**Figure 3**).

Apart from numerically dominating copepods (*Oithona* spp. and *Calanus* spp.), also pteropods have been found to be significant zooplanktonic group in this study. In 2015 and 2016 we noted high numbers of *L. helicina* veligers (small mesoplankton in **Figure 4**), whereas in 2016 and 2017 there was a high abundance of *L. helicina* post-larval stages (large mesoplankton in **Figure 4**). Since pteropods have their main seasonal abundance peaks in the late summer and/or early autumn (Lischka and Hagen, 2016; Wiedmann et al., 2016), the current results suggest that seasonal development of zooplankton

in Isfjorden was the most advanced in 2015–2017. In a year-round study carried out in Adventfjorden Stübner et al. (2016) detected the higher abundances of juvenile Pteropoda in the early August 2012. In this study the samples were collected in the first half of August in 2015–2018, whereas in 2013, 2014, and 2019 at the end of July. Our results demonstrated that even such small changes in sampling dates as several days (up to 3 weeks) could result in domination of different compositional state of zooplankton as the shifts between peaks of pteropods in 2016 and 2017 and meroplankton in 2013, 2014, and 2019. Potentially, it could affect the observed mid-summer protist community structure as many benthic invertebrate larvae are at their peak abundance in the water column during the summer (Kuklinski et al., 2013) and rely largely on the protist food base (Maloy et al., 2013). Also, the high abundance of Copepoda nauplii in 2015–2018 have been most probably caused by the fact that the present study was not performed at exactly the same time of the summer. Due to the high inter-annual variability in taxonomic structure and abundance of protists and zooplankton in comparison to less pronounced differences between stations, which was illustrated by non-metric MDS scaling, we concluded that large-scale processes and natural seasonal changes had stronger influence on the plankton communities than local factors.

Standard vs. Laser-Based Approach

A size is an important property of P&P affecting their concentration and multiple physical, biogeochemical and ecological traits such as settling speed, coagulation rate, consumption and/or trophic relationships. Thus, it is a convenient ecological indicator that merges many co-varying traits. The typical, negative relation between plankton size and concentrations was observed, with nano- fraction being on average two orders of magnitude more abundant than micro- fraction, which in turn was from two to three orders of magnitude more abundant than mesoplankton. Similarly, small mesoplankton was a few times more abundant than large meso- fraction (**Figure 6A** and **Supplementary Figure S1**). Laser counts showed similar trend for the smallest fractions (nano- two to three orders of magnitude more abundant than micro-), but the numbers of P&P in micro- fraction were only slightly higher than in both meso- fractions combined (**Figure 6B** and **Supplementary Figure S1**). The relations between particular size fractions, assessed by the slopes to their size spectra linear fitting, did not differ among stations (**Figure 6D**), but varied among years in the case of plankton (**Figure 6C**) and the smallest P&P fraction (assessed via LISST). This suggests that seasonal differences in pulses of specific plankton taxa may cause some deviations from theoretical striking regularity of body size distributions within aquatic systems (Platt and Denman, 1978; Stemmann et al., 2008). We conclude that the lack of smooth transition from nano- and micro- to the meso- fractions (**Figure 6B**) was due to the fact that the measurements of LISST and LOPC are based on a different physical property (LISST uses light scattering, whereas LOPC detection is based on light attenuation), which results in their different sensitivity to mineral vs. organic material. Thus, we decided to analyze and interpret the results from these two devices separately. Moreover, the differences between abundance of plankton estimates derived from standard and laser-based approaches showed that abundances of protists were generally higher than those provided for small P&P measured by LISST (**Figure 7**, upper). However, the protists were sampled at a few depth levels up to 50 m, while LISST continuous measurements were averaged over the upper 50 m layer. In case of zooplankton, the net catches were either equal (ISA station) or lower (BAB and ISF3 stations) to those detected by LOPC (**Figure 7**, bottom). This discrepancy in numbers of P&P can partially be explained by the smaller seawater volume sampled by the lasers compared to standard methods. However, according to previous data the difference between zooplankton abundance and LOPC measurements is mainly attributed to fragile aggregates and detritus that are often not analyzed in net catches, but also disaggregated by the net passage and thus not correctly sampled (e.g., González-Quirós and Checkley, 2006). This was the case especially at the BAB station, where the glacier runoff resulted in an increase of small and amorphous particles in the water column (this study), similarly as in other Svalbard glacial bay (Trudnowska et al., 2014, 2020a). However, their role is still seriously underestimated because the marine snow aggregates are so fragile that they can only be observed *in situ* in undisturbed water.

Even though the high resolution measurements of all particles suspended in sampled seawater (Sprules and Barth, 2016) have important advantages, traditional plankton sampling followed by taxonomic analysis is still necessary to recognize living and non-living components of the pelagic environment. By combining these two approaches we were able to show that most of the particles counted by LOPC included biological components (i.e., zooplankton) in the central part of Isfjorden, but suspended matter from a river (Schultes and Lopes, 2009) or a glacier plume (Trudnowska et al., 2014) in Billefjorden was also incorporated. The estimates dealing with the real contribution of plankton and other biota to the overall content of Spitsbergen fjordic waters are lacking, even though the substantial role of marine aggregates in the overall P&P biomass was previously recorded in Hornsund fjord (Trudnowska et al., 2014) as well as in Fram Strait and along West Spitsbergen Shelf (Trudnowska et al., 2018). Furthermore, Sagan and Darecki (2018) have examined a level of correlation between light attenuation at 676 nm and simultaneously measured size fractioned particle content with LISST, in attempt to confer mineral to organic particle proportions between Hornsund and Kongsfjorden waters. This successful combination of independent methods of observation has shown that 'Atlantification' observed in Kongsjorden yielded highest proportion of organic suspensions over the Hornsund waters, while the two fjords are equally under the influence of glacier's meltwater. However, so far only a few studies took an effort to distinguish between plankton and non-living particles by analysis of their optical properties obtained from automatic devices (Mikkelsen et al., 2005; Stemmann et al., 2008; Jackson and Checkley, 2011; Forest et al., 2012).

CONCLUSIONS

1. The environmental gradient, imposed by the advection of saline waters of Atlantic origin to the central part of Isfjorden and turbid freshwater discharge from the glacier in the inner fjord, was consistent among studied years. Together with vertical water stratification and signals of eddies it was forcing either layered (nano- and micro-fractions) or patchy (meso- fractions) distribution of P&P.
2. The nano- and micro- fractions of P&P were mostly confined to the upper water layer and their distribution was interrelated with the highest fluorescence of chlorophyll *a*. Even though their concentrations did not differ significantly between the stations, they most likely were of diverse origin (i.e., primary producers in the central part of Isfjorden vs. fine inorganic particles in the glacial bay).
3. Increasing amount of both meso- fractions of P&P from AW (ISA) toward glacial-influenced turbid waters (BAB) with simultaneous decrease in the zooplankton abundance from the central part of Isfjorden to the glacial bay was observed.
4. Many patches of P&P were observed as 'multi-fractionated,' i.e., the peak concentrations of various size fractions were well matched regarding the position in the water column, while some concentration peaks were located independently for individual size fractions, with large meso- fraction being the most self-governing P&P fraction.
5. Despite the conservative dominants, subtle changes in plankton composition structure were mostly year-specific., e.g., years with the intensified advection of AW were characterized by increased share of *P. pouchetii* and *O. similis*, while years with slightly later sampling dates were characterized by higher contribution of pteropods and benthic larvae.
6. The relations between particular size fractions, assessed by the size spectra slopes, did not differ among stations, but varied among years in the case of plankton and the smallest P&P fractions. The observed inter-station differences in LOPC measurements point toward notable contribution of marine aggregates to total P&P counts in the glacial bay in the Billefjorden.
7. The compatibility between concentrations of zooplankton obtained by traditional nets and optical method (LOPC) in central part of Isfjorden proves the usefulness of this laser counter to map fine-scale zooplankton distribution in clear seawaters in contrast to glacial-influenced waters where the misalignment in concentrations (significantly higher recorded by LOPC) was a common feature.

DATA AVAILABILITY STATEMENT

The datasets generated for this study are available on request to the corresponding author.

AUTHOR CONTRIBUTIONS

MS analyzed the data, prepared the original draft and most of the figures. ET analyzed the laser-based measurements derived from LOPC and then integrated them with LISST data, prepared part of the figures and statistical analysis, and designed the concept of this study. KB-S acquired the funding, designed the field campaign, and the concept of this manuscript. KB-S, AD, ET, and JW collected the samples. AD performed the chlorophyll *a* and protists analysis and substantially contributed to the protistan part of the manuscript. RB performed the zooplankton analysis. SS analyzed the laser-based measurements derived from LISST. All co-authors proof-read the manuscript prior to submission. All authors contributed to the article and approved the submitted version.

FUNDING

This study was funded by two Polish National Science Centre projects (NCN, PicMac 2013/09/B/NZ8/03365, and CoastDark 2018/29/B/NZ8/02463) and partly also by Polish Ministry of Science and Education grant (AREX Project 3547/Norway/2016/2). This survey was additionally supported by the statutory activity of the Institute of Oceanology, Polish Academy of Sciences (IO PAN).

ACKNOWLEDGMENTS

The authors acknowledge the captain and crew of the RV Oceania for their valuable support during field measurements.

SUPPLEMENTARY MATERIAL

The Supplementary Material for this article can be found online at: https://www.frontiersin.org/articles/10.3389/fmars.2020.00584/full#supplementary-material

REFERENCES

Agrawal, Y. C., and Pottsmith, H. C. (2000). Instruments for particle size and settling velocity observations in sediment transport. *Mar. Geol.* 168, 89–114. doi: 10.1016/s0025-3227(00)00044-x

Alldredge, A. L., and Silver, M. W. (1988). Characteristics, dynamics and significance of marine snow. *Prog. Oceanogr.* 20, 41–82. doi: 10.1016/0079-6611(88)90053-5

Anderson, M., Gorley, R. N., and Clarke, K. (2008). *PERMANOVA+ for PRIMER. Guide to Software and Statistical Methods*. Plymouth: PRIMER-E Ltd.

Arnkværn, G., Daase, M., and Eiane, K. (2005). Dynamics of coexisting *Calanus finmarchicus*, *Calanus glacialis* and *Calanus hyperboreus* populations in a high-Arctic fjord. *Polar Biol.* 28, 528–538. doi: 10.1007/s00300-005-0715-8

Auel, H., and Hagen, W. (2002). Mesozooplankton community structure, abundance and biomass in the central Arctic Ocean. *Mar. Biol.* 140, 1013–1021. doi: 10.1007/s00227-001-0775-4

Basedow, S. L., Sundfjord, A., von Appen, W.-J., Halvorsen, E., Kwasniewski, S., and Reigstad, M. (2018). Seasonal variation in transport of zooplankton into the Arctic basin through the Atlantic gateway, Fram Strait. *Front. Mar. Sci.* 5:194. doi: 10.3389/fmars.2018.0

Basedow, S. L., Tande, K. S., and Zhou, M. (2010). Biovolume spectrum theories applied: spatial patterns of trophic levels within a mesozooplankton community at the polar front. *J. Plankton Res.* 32, 1105–1119. doi: 10.1093/plankt/fbp110

Blanco, J. M., Echevarría, F., and García, C. M. (1994). Dealing with size-spectra: some conceptual and mathematical problems. *Sci. Mar.* 58, 17–29.

Carroll, M. L., Ambrose, W. G. Jr., Levin, B. S., Henkes, G. A., Hop, H., and Renaud, P. E. (2011). Pan-Svalbard growth rate variability and environmental regulation in the Arctic bivalve *Serripes groenlandicus*. *J. Mar. Syst.* 88, 239–251. doi: 10.1016/j.jmarsys.2011.04.010

Clarke, K. R., and Gorley, R. N. (2015). *Getting Started with PRIMER v7*. Plymouth: Plymouth Marine Laboratory.

Cottier, F., Tverberg, V., and Inall, M. (2005). Water mass modification in an Arctic fjord through cross−shelf exchange: the seasonal hydrography of Kongsfjorden, Svalbard. *J. Geophys. Res.* 110:C12005.

Cottier, F. R., Nilsen, F., Inall, M. E., Gerland, S., Tverberg, V., and Svendsen, H. (2007). Wintertime warming of an Arctic shelf in response to large-scale atmospheric circulation. *Geophys. Res. Lett.* 34:L18504. doi: 10.1029/2007GL029948

Cottier, F. R., Nilsen, F., Skogseth, R., Tverberg, V., Skarðhamar, J., and Svendsen, H. (2010). Arctic fjords: a review of the oceanographic environment and dominant physical processes. *Geol. Soc. Lond. Special Publ.* 344, 35–50. doi: 10.1144/SP344.4

Daase, M., and Eiane, K. (2007). Mesozooplankton distribution in northern Svalbard waters in relation to hydrography. *Polar Biol.* 30, 969–981. doi: 10.1007/s00300-007-0255-5

Daase, M., Vik, J. O., Bagøien, E., Stenseth, N. C., and Eiane, K. (2007). The influence of advection on Calanus near Svalbard: statistical relations between salinity, temperature and copepod abundance. *J. Plankton Res.* 29, 903–911. doi: 10.1093/plankt/fbm068

Davies, E. J., Nimmo-Smith, W. A. M., Agrawal, Y. C., and Souza, A. J. (2012). LISST-100 response to large particles. *Mar. Geol.* 307, 117–122. doi: 10.1016/j.margeo.2012.03.006

Dekshenieks, M. M., Donaghay, P. L., Sullivan, J. M., Rines, J. E., Osborn, T. R., and Twardowski, M. S. (2001). Temporal and spatial occurrence of thin phytoplankton layers in relation to physical processes. *Mar. Ecol. Prog. Ser.* 223, 61–71. doi: 10.3354/meps223061

Dolan, J. R., Claustre, H., Carlotti, F., Plounevez, S., and Moutin, T. (2002). Microzooplankton diversity: relationships of tintinnid ciliates with resources, competitors and predators from the Atlantic Coast of Morocco to the Eastern Mediterranean. *Deep Sea Res. Part I* 49, 1217–1232. doi: 10.1016/S0967-0637(02)00021-3

Edler, L. (ed.) (1979). *Recommendations on Methods for Marine Biological Studies in the Baltic Sea. Phytoplankton and Chlorophyll*. Sweden: Baltic Marine Biologists BMB.

Falk-Petersen, S., Dahl, T. M., Scott, C. L., Sargent, J. R., Gulliksen, B., Kwasniewski, S., et al. (2002). Lipid biomarkers and trophic linkages between ctenophores and copepods in Svalbard waters. *Mar. Ecol. Prog. Ser.* 227, 187–194. doi: 10.3354/meps227187

Falk-Petersen, S., Sargent, J. R., and Tande, K. S. (1987). Lipid composition of zooplankton in relation to the sub-arctic food web. *Polar Biol.* 8, 115–120. doi: 10.1007/BF00297065

Forest, A., Stemmann, L., Picheral, M., Burdorf, L., Robert, D., Fortier, L., et al. (2012). Size distribution of particles and zooplankton across the shelf-basin system in southeast Beaufort Sea: combined results from an Underwater Vision Profiler and vertical net tows. *Biogeosciences* 9, 1301–1320. doi: 10.5194/bg-9-1301-2012

Gabrielsen, T. M., Merkel, B., Søreide, J. E., Johansson-Karlsson, E., Bailey, A., Vogedes, D., et al. (2012). Potential misidentifications of two climate indicator species of the marine arctic ecosystem: *Calanus glacialis* and *C. finmarchicus*. *Polar Biol.* 35, 1621–1628. doi: 10.1007/s00300-012-1202-7

Gannefors, C., Böer, M., Kattner, G., Graeve, M., Eiane, K., Gulliksen, B., et al. (2005). The Arctic sea butterfly *Limacina helicina*: lipids and life strategy. *Mar. Biol.* 147, 169–177. doi: 10.1007/s00227-004-1544-y

Gluchowska, M., Dalpadado, P., Beszczynska-Möller, A., Olszewska, A., Ingvaldsen, R. B., and Kwasniewski, S. (2017a). Interannual zooplankton variability in the main pathways of the Atlantic water flow into the Arctic Ocean (Fram Strait and Barents Sea branches). *ICES J. Mar. Sci.* 74, 1921–1936. doi: 10.1093/icesjms/fsx033

Gluchowska, M., Kwasniewski, S., Prominska, A., Olszewska, A., Goszczko, I., Falk-Petersen, S., et al. (2016). Zooplankton in Svalbard fjords on the Atlantic–Arctic boundary. *Polar Biol.* 39, 1785–1802. doi: 10.1007/s00300-016-1991-1

Gluchowska, M., Trudnowska, E., Goszczko, I., Kubiszyn, A. M., Blachowiak-Samolyk, K., Walczowski, W., et al. (2017b). Variations in the structural and functional diversity of zooplankton over vertical and horizontal environmental gradients en route to the Arctic Ocean through the Fram Strait. *PLoS One* 12:e0171715. doi: 10.1371/journal.pone.0171715

Godø, O. R., Samuelsen, A., Macaulay, G. J., Patel, R., Hjøllo, S. S., Horne, J., et al. (2012). Mesoscale eddies are oases for higher trophic marine life. *PLoS One* 7:e30161. doi: 10.1371/journal.pone.0030161

Gómez, F., and Artigas, L. F. (2014). High diversity of dinoflagellates in the intertidal sandy sediments of Wimereux (north-east English Channel, France). *J. Mar. Biol. Assoc. U.K.* 94, 443–457. doi: 10.1017/S0025315413001744

González−Quirós, R., and Checkley, D. M. (2006). Occurrence of fragile particles inferred from optical plankton counters used in situ and to analyze net samples collected simultaneously. *J. Geophys. Res. Oceans* 111:C05S06.

Gribble, K. E., Nolan, G., and Anderson, D. M. (2007). Biodiversity, biogeography and potential trophic impact of *Protoperidinium* spp. (Dinophyceae) off the southwestern coast of Ireland. *J. Plankton Res.* 29, 931–947. doi: 10.1093/plankt/fbm070

Herman, A. W., Beanlands, B., and Phillips, E. F. (2004). The next generation of optical plankton counter: the laser-OPC. *J. Plankton Res.* 26, 1135–1145. doi: 10.1093/plankt/fbh095

Hodal, H., Falk-Petersen, S., Hop, H., Kristiansen, S., and Reigstad, M. (2012). Spring bloom dynamics in Kongsfjorden, Svalbard: nutrients, phytoplankton, protozoans and primary production. *Polar Biol.* 35, 191–203. doi: 10.1007/s00300-011-1053-7

Holm-Hansen, O., and Riemann, B. (1978). Chlorophyll a determination: improvements in methodology. *Oikos* 30, 438–447. doi: 10.2307/3543338

Hop, H., Pearson, T., Hegseth, E. N., and Kovacs, K. M. (2002). The marine ecosystem of Kongsfjorden. *Polar Res.* 21, 167–208.

Hopcroft, R. R., Clarke, C., Nelson, R. J., and Raskoff, K. A. (2005). Zooplankton communities of the Arctic's Canada basin: the contribution by smaller taxa. *Polar Biol.* 28, 198–206. doi: 10.1007/s00300-004-0680-7

Jackson, G. A. (1990). A model of the formation of marine algal flocs by physical coagulation processes. *Deep Sea Res. Part A. Oceanogr. Res. Papers* 37, 1197–1211. doi: 10.1016/0198-0149(90)90038-w

Jackson, G. A., and Checkley, D. M. Jr. (2011). Particle size distributions in the upper 100 m water column and their implications for animal feeding in the plankton. *Deep Sea Res. Part I Oceanogr. Res. Papers* 58, 283–297. doi: 10.1016/j.dsr.2010.12.008

Jackson, G. A., Maffione, R., Costello, D. K., Alldredge, A. L., Logan, B. E., and Dam, H. G. (1997). Particle size spectra between 1 pum and 1 cm at Monterey Bay. *Deep Sea Res. I* 11, 1739–1767. doi: 10.1016/s0967-0637(97)00029-0

Keck, A., Wiktor, J., Hapter, R., and Nilsen, R. (1999). Phytoplankton assemblages related to physical gradients in an arctic, glacier-fed fjord in summer. *ICES J. Mar. Sci.* 56, 203–214. doi: 10.1006/jmsc.1999.0631

Kowalik, Z., Marchenko, A., Brazhnikov, D., and Marchenko, N. (2015). Tidal currents in the western Svalbard Fjords. *Oceanologia* 57, 318–327. doi: 10.1016/j.oceano.2015.06.003

Kubiszyn, A. M., Piwosz, K., and Wiktor, J. M. (2014). The effect of inter-annual Atlantic water inflow variability on the planktonic protist community structure in the West Spitsbergen waters during the summer. *J. Plankton Res.* 36, 1190–1203. doi: 10.1093/plankt/fbu044

Kubiszyn, A. M., Wiktor, J. M., Wiktor, J. M. Jr., Griffiths, C., Kristiansen, S., and Gabrielsen, T. M. (2017). The annual planktonic protist community structure in an ice-free high Arctic fjord (Adventfjorden, West Spitsbergen). *J. Mar. Syst.* 169, 61–72. doi: 10.1016/j.jmarsys.2017.01.013

Kuklinski, P., Berge, J., McFadden, L., Dmoch, K., Zajaczkowski, M., Nygård, H., et al. (2013). Seasonality of occurrence and recruitment of Arctic marine benthic invertebrate larvae in relation to environmental variables. *Polar Biol.* 36, 549–560. doi: 10.1007/s00300-012-1283-3

Kwasniewski, S., Hop, H., Falk-Petersen, S., and Pedersen, G. (2003). Distribution of *Calanus* species in Kongsfjorden, a glacial fjord in Svalbard. *J. Plankton Res.* 25, 1–20. doi: 10.1093/plankt/25.1.1

Lalande, C., Bauerfeind, E., and Nöthig, E. M. (2011). Downward particulate organic carbon export at high temporal resolution in the eastern fram strait: influence of Atlantic water on flux composition. *Mar. Ecol. Prog. Ser.* 440, 127–136. doi: 10.3354/meps09385

Leadbeater, B. S. (2008). Choanoflagellate evolution: the morphological perspective 1. *Protistology* 5, 256–267.

Leikvin, Ø, and Evenset, A. (2009). *Avløp fra Longyearbyen til Adventfjorden. Miljøfaglige Vurderinger.* Akvaplan-Niva Report, 4535-1.

Lischka, S., and Hagen, W. (2016). Seasonal dynamics of mesozooplankton in the Arctic Kongsfjord (Svalbard) during year-round observations from August 1998 to July 1999. *Polar Biol.* 39, 1859–1878. doi: 10.1007/s00300-016-2005-z

Lydersen, C., Assmy, P., Falk-Petersen, S., Kohler, J., Kovacs, K. M., Reigstad, M., et al. (2014). The importance of tidewater glaciers for marine mammals and seabirds in Svalbard, Norway. *J. Mar. Syst.* 129, 452–471. doi: 10.1016/j.jmarsys.2013.09.006

Madsen, S. D., Nielsen, T. G., and Hansen, B. W. (2008). Annual population development and production by small copepods in Disko Bay, western Greenland. *Mar. Biol.* 155, 63–77. doi: 10.1007/s00227-008-1007-y

Majaneva, S., Berge, J., Renaud, P. E., Vader, A., Stübner, E., Rao, A. M., et al. (2013). Aggregations of predators and prey affect predation impact of the Arctic ctenophore *Mertensia ovum*. *Mar. Ecol. Prog. Ser.* 476, 87–100. doi: 10.3354/meps10143

Maloy, A. P., Nelle, P., Culloty, S. C., Slater, J. W., and Harrod, C. (2013). Identifying trophic variation in a marine suspension feeder: DNA- and stable isotope-based dietary analysis in *Mytilus* spp. *Mar. Biol.* 160, 479–490. doi: 10.1007/s00227-012-2105-4

MATLAB (2018). *MATLAB VERSION: 9.5.0.944444 (R2018b)*. Natick, MA: The MathWorks Inc.

McCave, I. N. (1984). Size spectra and aggregation of suspended particles in the deep ocean. *Deep Sea Res. Part A. Oceanogr. Res. Papers* 31, 329–352. doi: 10.1016/0198-0149(84)90088-8

Metfies, K., von Appen, W. J., Kilias, E., Nicolaus, A., and Nöthig, E. M. (2016). Biogeography and photosynthetic biomass of arctic marine pico-eukaroytes during summer of the record sea ice minimum 2012. *PLoS One* 11:e0148512. doi: 10.1371/journal.pone.0148512

Mikkelsen, O. A., Hill, P. S., Milligan, T. G., and Chant, R. J. (2005). In situ particle size distributions and volume concentrations from a LISST-100 laser particle sizer and a digital floc camera. *Continent. Shelf Res.* 25, 1959–1978. doi: 10.1016/j.csr.2005.07.001

Mironova, E. I., Telesh, I. V., and Skarlato, S. O. (2009). Planktonic ciliates of the Baltic Sea (a review). *Inland Water Biol.* 2, 13–24. doi: 10.1134/S1995082909010039

Mojica, K. D., van de Poll, W. H., Kehoe, M., Huisman, J., Timmermans, K. R., Buma, A. G., et al. (2015). Phytoplankton community structure in relation to vertical stratification along a north−south gradient in the Northeast Atlantic Ocean. *Limnol. Oceanogr.* 60, 1498–1521. doi: 10.1002/lno.10113

Möller, F., and Bernhard, M. (1974). A sequential approach to the counting of plankton organisms. *J. Exp. Mar. Biol. Ecol.* 15, 49–68. doi: 10.1016/0022-0981(74)90063-x

Möller, K. O., John, M. S., Temming, A., Floeter, J., Sell, A. F., Herrmann, J. P., et al. (2012). Marine snow, zooplankton and thin layers: indications of a trophic link from small-scale sampling with the video plankton recorder. *Mar. Ecol. Prog. Ser.* 468, 57–69. doi: 10.3354/meps09984

Murray, M. S., Eicken, H., Starkweather, S., Gerlach, S. C., Evengard, B., Gearhard, S., et al. (2012). "Responding to Arctic environmental change-translating our growing understanding into a research agenda for action," in *Proceedings of the Workshop Report'Responding to Arctic Environmental Change'International Study for Arctic Change, (IASC)*, Kingston.

Nilsen, F., Cottier, F., Skogseth, R., and Mattsson, S. (2008). Fjord–shelf exchanges controlled by ice and brine production: the interannual variation of Atlantic Water in Isfjorden, Svalbard. *Cont. Shelf Res.* 28, 1838–1853. doi: 10.1016/j.csr.2008.04.015

Nilsen, F., Skogseth, R., Vaardal-Lunde, J., and Inall, M. (2016). A simple shelf circulation model: intrusion of Atlantic water on the west spitsbergen shelf. *J. Phys. Oceanogr.* 46, 1209–1230. doi: 10.1175/JPO-D-15-0058.1

Norrbin, F., Eilertsen, H. C., and Degerlund, M. (2009). Vertical distribution of primary producers and zooplankton grazers during different phases of the Arctic spring bloom. *Deep Sea Res. Part II Top. Stud. Oceanogr.* 56, 1945–1958. doi: 10.1016/j.dsr2.2008.11.006

Nöthig, E. M., Bracher, A., Engel, A., Metfies, K., Niehoff, B., Peeken, I., et al. (2015). Summertime plankton ecology in Fram Strait—a compilation of long-and short-term observations. *Polar Res.* 34:23349. doi: 10.3402/polar.v34.23349

Pavlov, A. K., Tverberg, V., Ivanov, B. V., Nilsen, F., Falk-Petersen, S., and Granskog, M. A. (2013). Warming of Atlantic water in two west Spitsbergen fjords over the last century (1912–2009). *Polar Res.* 32:11206. doi: 10.3402/polar.v32i0.11206

Piechura, J., and Walczowski, W. (2009). Warming of the west Spitsbergen current and sea ice north of Svalbard. *Oceanologia* 51, 147–164. doi: 10.5697/oc.51-2.147

Piwosz, K., Walkusz, W., Hapter, R., Wieczorek, P., Hop, H., and Wiktor, J. (2009). Comparison of productivity and phytoplankton in a warm (Kongsfjorden) and a cold (Hornsund) Spitsbergen fjord in mid-summer 2002. *Polar Biol.* 32, 549–559. doi: 10.1007/s00300-008-0549-2

Platt, T., and Denman, K. (1978). The structure of pelagic ecosystems. *Rapports Proce Verbaux Re'unions Conseil Int. Pour l'Exp. Mer* 173, 60–65.

Promińska, A., Falck, E., and Walczowski, W. (2018). Interannual variability in hydrography and water mass distribution in Hornsund, an Arctic fjord in Svalbard. *Polar Res.* 37:1495546. doi: 10.1080/17518369.2018.1495546

R Core Team (2013). *R: A Language and Environment for Statistical Computing*. Vienna: R Foundation for Statistical Computing.

Sagan, S., and Darecki, M. (2018). Inherent optical properties and particulate matter distribution in summer season in waters of Hornsund and Kongsfjordenen, Spitsbergen. *Oceanologia* 60, 65–75. doi: 10.1016/j.oceano.2017.07.006

Saloranta, T. M., and Svendsen, H. (2001). Across the Arctic front west of Spitsbergen: high-resolution CTD sections from 1998–2000. *Polar Res.* 20, 177–184. doi: 10.3402/polar.v20i2.6515

Schlitzer, R. (2018). *Ocean Data View*. Available online at: https://odv.awi.de (accessed June 3, 2020).

Schultes, S., and Lopes, R. M. (2009). Laser optical plankton counter and zooscan intercomparison in tropical and subtropical marine ecosystems. *Limnol. Oceanogr. Methods* 7, 771–784. doi: 10.4319/lom.2009.7.771

Scott, C. L., Falk-Petersen, S., Sargent, J. R., Hop, H., Lønne, O. J., and Poltermann, M. (1999). Lipids and trophic interactions of ice fauna and pelagic zooplankton in the marginal ice zone of the Barents Sea. *Polar Biol.* 21, 65–70. doi: 10.1007/s003000050335

Scott, C. L., Kwasniewski, S., Falk-Petersen, S., and Sargent, J. R. (2000). Lipids and life strategies of *Calanus finmarchicus*, *Calanus glacialis* and *Calanus hyperboreus* in late autumn, Kongsfjorden, Svalbard. *Polar Biol.* 23, 510–516. doi: 10.1007/s003000000114

Sheldon, R. W., Prakash, A., and Sutcliffe, W. Jr. (1972). The size distribution of particles in the ocean 1. *Limnol. Oceanogr.* 17, 327–340. doi: 10.4319/lo.1972.17.3.0327

Simon, M., Grossart, H. P., Schweitzer, B., and Ploug, H. (2002). Microbial ecology of organic aggregates in aquatic ecosystems. *Aqua. Microb. Ecol.* 28, 175–211. doi: 10.3354/ame028175

Smith, R. W., Bianchi, T. S., Allison, M., Savage, C., and Galy, V. (2015). High rates of organic carbon burial in fjord sediments globally. *Nat. Geosci.* 8, 450–453. doi: 10.1038/ngeo2421

Søreide, J. E., Hop, H., Falk-Petersen, S., Gulliksen, B., and Hansen, E. (2003). Macrozooplankton communities and environmental variables in the Barents Sea marginal ice zone in late winter and spring. *Mar. Ecol. Prog. Ser.* 263, 43–64. doi: 10.3354/meps263043

Sprules, W. G., and Barth, L. E. (2016). Surfing the biomass size spectrum: some remarks on history, theory, and application. *Can. J. Fish. Aqua. Sci.* 73, 477–495. doi: 10.1139/cjfas-2015-0115

Stemmann, L., and Boss, E. (2012). Plankton and particle size and packaging: from determining optical properties to driving the biological pump. *Ann. Rev. Mar. Sci.* 4, 263–290. doi: 10.1146/annurev-marine-120710-100853

Stemmann, L., Eloire, D., Sciandra, A., Jackson, G. A., Guidi, L., Picheral, M., et al. (2008). Volume distribution for particles between 3.5 to 2000 μm in the upper 200 m region of the south pacific gyre. *Biogeosciences* 5, 299–310. doi: 10.5194/bg-5-299-2008

Stoecker, D. K., Sieracki, M. E., Verity, P. G., Michaels, A. E., Haugen, E., Burkill, P. H., et al. (1994). Nanoplankton and protozoan microzooplankton during the JGOFS north Atlantic bloom experiment: 1989 and 1990. *J. Mar. Biol. Assoc. U.K.* 74, 427–443. doi: 10.1017/S0025315400039448

Straneo, F., and Heimbach, P. (2013). North Atlantic warming and the retreat of Greenland's outlet glaciers. *Nature* 504, 36–43. doi: 10.1038/nature12854

Stübner, E. I., Søreide, J. E., Reigstad, M., Marquardt, M., and Błachowiak-Samołyk, K. (2016). Year-round meroplankton dynamics in high-Arctic, Svalbard. *J. Plankton Res.* 38, 522–536. doi: 10.1093/plankt/fbv124

Svendsen, H., Beszczynska-Møller, A., Hagen, J. O., Lefauconnier, B., Tverberg, V., Gerland, S., et al. (2002). The physical environment of Kongsfjorden – Krossfjorden, an Arctic fjord system in Svalbard. *Polar Res.* 21, 133–166. doi: 10.1111/j.1751-8369.2002.tb00072.x

Symon, C., Arris, L., and Heal, B. (2005). *Arctic Climate Impact Assessment: ACIA*. Cambridge: Cambridge University Press.

Trudnowska, E., Basedow, S. L., and Blachowiak-Samolyk, K. (2014). Mid-summer mesozooplankton biomass, its size distribution, and estimated production within a glacial Arctic fjord (Hornsund, Svalbard). *J. Mar. Syst.* 137, 55–66. doi: 10.1016/j.jmarsys.2014.04.010

Trudnowska, E., Dąbrowska, A. M., Boehnke, R., Zajączkowski, M., and Blachowiak-Samolyk, K. (2020a). Particles, protists, and zooplankton in glacier-influenced coastal svalbard waters. *Estuar. Coast. Shelf Sci.* 242:106842. doi: 10.1016/j.ecss.2020.106842

Trudnowska, E., Gluchowska, M., Beszczynska-Möller, A., Blachowiak-Samolyk, K., and Kwasniewski, S. (2016). Plankton patchiness in the polar front region of the west spitsbergen shelf. *Mar. Ecol. Prog. Ser.* 560, 1–18. doi: 10.3354/meps11925

Trudnowska, E., Sagan, S., and Błachowiak-Samołyk, K. (2018). Spatial variability and size structure of particles and plankton in the Fram Strait. *Prog. Oceanogr.* 168, 1–12. doi: 10.1016/j.pocean.2018.09.005

Trudnowska, E., Sagan, S., Kwasniewski, S., Darecki, M., and Blachowiak-Samolyk, K. (2015). Fine-scale zooplankton vertical distribution in relation to hydrographic and optical characteristics of the surface waters on the Arctic shelf. *J. Plankton Res.* 37, 120–133. doi: 10.1093/plankt/fbu087

Trudnowska, E., Stemmann, L., Blachowiak-Samołyk, K., and Kwasniewski, S. (2020b). Taxonomic and size structures of zooplankton communities in the fjords along the Atlantic water passage to the Arctic. *J. Mar. Syst.* 204:103306. doi: 10.1016/j.jmarsys.2020.103306

Urbanski, J. A., Stempniewicz, L., Wêsławski, J. M., Dragańska-Deja, K., Wochna, A., Goc, M., et al. (2017). Subglacial discharges create fluctuating foraging hotspots for sea birds in tidewater glacier bays. *Sci. Rep.* 7:43999. doi: 10.1038/srep43999

Utermöhl, H. (1958). Zur vervollkommnung der quantitativen phytoplankton-methodik. *Mitt. Int. Ver. Theor. Angew. Limnol.* 9, 1–38. doi: 10.1080/05384680.1958.11904091

Vaqué, D., Blough, H. A., and Duarte, C. M. (1997). Dynamics of ciliate abundance, biomass and community composition in an oligotrophic coastal environment (NW Mediterranean). *Aquat. Microb. Ecol.* 12, 71–83. doi: 10.3354/ame012071

Vihtakari, M. (2019). *PlotSvalbard: PlotSvalbard – Plot research data from Svalbard on maps. R Package Version 0.8.5*. Available online at: https://github.com/MikkoVihtakari/PlotSvalbard (accessed February 4, 2020).

Walczowski, W., and Piechura, J. (2011). Influence of the West spitsbergen current on the local climate. *Int. J. Climatol.* 31, 1088–1093. doi: 10.1002/joc.2338

Wassmann, P., Kosobokova, K. N., Slagstad, D., Drinkwater, K. F., Hopcroft, R. R., Moore, S. E., et al. (2015). The contiguous domains of Arctic ocean advection: trails of life and death. *Prog. Oceanogr.* 139, 42–65. doi: 10.1016/j.pocean.2015.06.011

Wassmann, P., Slagstad, D., and Ellingsen, I. H. (2019). *Advection of Mesozooplankton into the Northern Svalbard Shelf Region*. Available online at: https://munin.uit.no/handle/10037/16195 (accessed August 14, 2019).

Weslawski, J. M., Koszteyn, J., Zajaczkowski, M., Wiktor, J., and Kwasniewski, S. (1995). "Fresh water in Svalbard fjord ecosystems," in *Ecology of Fjords and Coastal Waters*, eds H. R. Skjoldal, C. Hopkins, K. E. Erikstad, and H. P. Leinaas (Amsterdam: Elsevier Science), 229–241.

Weslawski, J. M., Pedersen, G., Petersen, S. F., and Porazinski, K. (2000). Entrapment of macroplankton in an Arctic fjord basin, Kongsfjorden, Svalbard. *Oceanologia* 42, 57–69.

Weydmann, A., Carstensen, J., Goszczko, I., Dmoch, K., Olszewska, A., and Kwasniewski, S. (2014). Shift towards the dominance of boreal species in the Arctic: inter-annual and spatial zooplankton variability in the west spitsbergen current. *Mar. Ecol. Prog. Ser.* 501, 41–52. doi: 10.3354/meps10694

Wiedmann, I., Reigstad, M., Marquardt, M., Vader, A., and Gabrielsen, T. M. (2016). Seasonality of vertical flux and sinking particle characteristics in an ice-free high arctic fjord—different from subarctic fjords? *J. Mar. Syst.* 154, 192–205. doi: 10.1016/j.jmarsys.2015.10.003

Wishner, K., Durbin, E., Durbin, A., Macaulay, M., Winn, H., and Kenney, R. (1988). Copepod patches and right whales in the Great South channel off New England. *Bull. Mar. Sci.* 43, 825–844.

Włodarska-Kowalczuk, M., Szymelfenig, M., and Zajączkowski, M. (2007). Dynamic sedimentary environments of an Arctic glacier-fed river estuary (Adventfjorden, Svalbard). II: Meio-and macrobenthic fauna. *Estuar. Coast. Shelf Sci.* 74, 274–284. doi: 10.1016/j.ecss.2007.04.017

Zajączkowski, M., and Włodarska-Kowalczuk, M. (2007). Dynamic sedimentary environments of an Arctic glacier-fed river estuary (Adventfjorden, Svalbard). I. Flux, deposition, and sediment dynamics. *Estuar. Coast. Shelf Sci.* 74, 285–296. doi: 10.1016/j.ecss.2007.04.015

Conflict of Interest: The authors declare that the research was conducted in the absence of any commercial or financial relationships that could be construed as a potential conflict of interest.

Copyright © 2020 Szeligowska, Trudnowska, Boehnke, Dąbrowska, Wiktor, Sagan and Błachowiak-Samołyk. This is an open-access article distributed under the terms of the Creative Commons Attribution License (CC BY). The use, distribution or reproduction in other forums is permitted, provided the original author(s) and the copyright owner(s) are credited and that the original publication in this journal is cited, in accordance with accepted academic practice. No use, distribution or reproduction is permitted which does not comply with these terms.

frontiers in Marine Science

PERSPECTIVE
published: 24 July 2020
doi: 10.3389/fmars.2020.00527

Cutting Through the Noise: Bacterial Chemotaxis in Marine Microenvironments

Douglas R. Brumley[1]*, *Francesco Carrara*[2], *Andrew M. Hein*[3,4], *George I. Hagstrom*[5], *Simon A. Levin*[5] and *Roman Stocker*[2]

[1] School of Mathematics and Statistics, The University of Melbourne, Parkville, VIC, Australia, [2] Department of Civil, Environmental and Geomatic Engineering, Institute of Environmental Engineering, ETH Zurich, Zurich, Switzerland, [3] Institute of Marine Sciences, University of California, Santa Cruz, Santa Cruz, CA, United States, [4] Department of Ecology and Evolutionary Biology, University of California, Santa Cruz, Santa Cruz, CA, United States, [5] Department of Ecology and Evolutionary Biology, Princeton University, Princeton, NJ, United States

The ability of marine microbes to navigate toward chemical hotspots can determine their nutrient uptake and has the potential to affect the cycling of elements in the ocean. The link between bacterial navigation and nutrient cycling highlights the need to understand how chemotaxis functions in the context of marine microenvironments. Chemotaxis hinges on the stochastic binding/unbinding of molecules with surface receptors, the transduction of this information through an intracellular signaling cascade, and the activation and control of flagellar motors. The intrinsic randomness of these processes is a central challenge that cells must deal with in order to navigate, particularly under dilute conditions where noise and signal are similar in magnitude. Such conditions are ubiquitous in the ocean, where nutrient concentrations are often extremely low and subject to rapid variation in space (e.g., particulate matter, nutrient plumes) and time (e.g., diffusing sources, fluid mixing). Stochastic, biophysical models of chemotaxis have the potential to illuminate how bacteria cope with noise to efficiently navigate in such environments. At the same time, new technologies for experimentation allow for continuous interrogation—from milliseconds through to days—of bacterial responses in custom dynamic nutrient landscapes, providing unprecedented access to the behavior of chemotactic cells in microenvironments engineered to mimic those cells navigate in the wild. These recent theoretical and experimental developments have created an opportunity to derive population-level uptake from single-cell motility characteristics in ways that could inform the next generation of marine biogeochemical cycling models.

Keywords: chemotaxis, bacteria, motility, sensing noise, ocean, microbial ecology, navigation, fluctuations

OPEN ACCESS

Edited by:
Aditya R. Nayak,
Florida Atlantic University,
United States

Reviewed by:
Francesca Malfatti,
Istituto Nazionale di Oceanografia e di Geofisica Sperimentale (OGS), Italy
Jian Sheng,
Texas A&M University Corpus Christi, United States
Navish Wadhwa,
Harvard University, United States

***Correspondence:**
Douglas R. Brumley
d.brumley@unimelb.edu.au

Specialty section:
This article was submitted to Marine Ecosystem Ecology, a section of the journal Frontiers in Marine Science

Received: *24 January 2020*
Accepted: *09 June 2020*
Published: *24 July 2020*

Citation:
Brumley DR, Carrara F, Hein AM, Hagstrom GI, Levin SA and Stocker R (2020) Cutting Through the Noise: Bacterial Chemotaxis in Marine Microenvironments. Front. Mar. Sci. 7:527. doi: 10.3389/fmars.2020.00527

1. INTRODUCTION

The fine-scale interactions between marine bacteria and both dissolved and particulate organic matter underpin marine biogeochemistry, thereby supporting productivity and influencing carbon storage and sequestration in the planet's oceans (Azam, 1998). It has been historically very difficult to characterize marine environments on the microscales that are most relevant to individual bacteria. Rather, research efforts have typically sampled much larger volumes of water and made comparisons from one sampling site to another (Karsenti et al., 2011; Bork et al., 2015). However,

at the length scales relevant to individual microbes, the ocean is an intricate and dynamic landscape of nutrient patches, at times too small to be mixed by turbulence (Kiørboe, 2008; Stocker, 2012). The capacity for microbes to actively navigate these structured environments using chemotaxis can strongly influence their nutrient uptake. Although some work has examined time-dependent chemical profiles (Zhu et al., 2012), past investigations of chemotaxis using *Escherichia coli* and other model organisms have routinely examined steady chemical gradients strong enough to elicit a discernible chemotactic response (Sneddon et al., 2012; Salek et al., 2019). However, the typical chemical gradients wild marine bacteria encounter are often very weak, ephemeral in nature, and with low background concentrations (Stocker, 2012). Shallow gradients are relevant for marine bacteria because, in general, gradients become weaker as one moves away from the source. Yet, detecting such gradients at distance has tremendous value, because they point toward nutrient sources. Shallow gradients are important precisely because they can be used to navigate to regions in the vicinity of sources where gradients become steep, concentrations are high, and bacteria can acquire resources at a high rate.

Past experiments have typically been limited in duration to the 1–100 s timescales over which gradient-climbing occurs (Stocker, 2015), but the timescales over which bacteria respond to nutrient uptake—through gene regulation and bacterial reproduction—are much longer. Accurately quantifying the influence of microscale dynamics in oceanic nutrient cycling hinges on (1) interrogating bacterial chemotaxis in realistic microenvironments for extended periods of time and (2) developing mathematical models that capture the essential features of chemotaxis in dilute, dynamic conditions. In this Perspective, we discuss recently developed experimental tools and mathematical frameworks for furthering our understanding of bacterial chemotaxis. We examine the various ways in which noise can enhance or degrade the sensitivity of bacterial navigation, and outline priorities for future research.

2. BRIDGING THE TIMESCALES OF MOTILITY AND METABOLISM

Bacterial chemotaxis is one of the most thoroughly understood behaviors in all of biology (Berg, 2008; Endres, 2013). Many experimental and modeling approaches have been used to investigate chemotaxis in fine detail, from early capillary assays (Adler, 1973; Brown and Berg, 1974) to experiments in controlled microfluidic environments (Mao et al., 2003; Englert et al., 2009; Seymour et al., 2010; Son et al., 2015; Salek et al., 2019) and computational modeling of complete biochemical pathways (Morton-Firth et al., 1999; Jiang et al., 2010; Long et al., 2017). Despite the vast literature on bacterial chemotaxis, unanswered questions still remain. In particular, we still know relatively little about the types of microenvironments bacteria navigate in the wild, and how chemotaxis operates and evolves in such environments (Endres, 2013; Wong-Ng et al., 2016).

The distribution of nutrients in the ocean is highly structured, varying strongly with depth, across the globe (Hansell et al., 2009), and with time (Druffel et al., 1996). Moreover, there is tremendous diversity in the types of organic matter available (Riedel and Dittmar, 2014; Benner and Amon, 2015), and substantial exchange of materials between dissolved, particulate, colloidal and gel phases (Kiørboe, 2001; Verdugo, 2012). Although bulk concentrations of dissolved organic carbon (DOC) typically vary between 35 and 70 μM throughout the ocean (Hansell et al., 2009), the vast majority of DOC exists in forms either difficult or impossible to use by bacteria. Low molecular weight, highly labile molecules such as dissolved sugars, amino acids, or nucleotides, have only nanomolar concentrations in the bulk and residence times under 1 day (Keil and Kirchman, 1999). These molecules can have transiently high concentrations in the aftermath of cell lysis, predation, or nutrient exudation by phytoplankton, but they are not components of more long-lived hotspots such as gels or particles (Verdugo, 2012). The majority of labile or semi-labile organic matter has much higher molecular weight, and consists of biological macromolecules such as proteins or large algal polysacharides (Benner and Amon, 2015). Too large to pass through bacterial cell membranes, bacteria degrade these molecules into monomers or oligomers using ecto- and exo-enzymes, allowing for their uptake, but also creating public goods which feed other bacteria or give them information on the location of nutrient hotspots.

Dissolved organic matter can be redistributed through ubiquitous fluid flows in the ocean, but at the length scale relevant to microbial motion—less than approximately 1 mm—molecular diffusion predominantly drives the redistribution of chemical cues (Batchelor, 1959). The structure and dynamics of chemical gradients in the ocean thus emerge from the interplay of DOC release by living organisms, the aggregation and disaggregation of DOC into gels and particles, the degradation and uptake of DOC by heterotrophic bacteria, and fluid turbulence.

Experiments (Blackburn et al., 1998; Stocker et al., 2008; Smriga et al., 2016) and mathematical theory (Hein et al., 2016a; Mora and Nemenman, 2019) have begun to assess the role of dynamic chemical gradients (Taylor and Stocker, 2012), investigating the interaction between timescales for motility and timescales for changes in the chemoattractant landscape. Experiments have revealed that marine bacteria are capable of rapidly responding to leaking diatoms (Smriga et al., 2016), pulses of phytoplankton exudates (Seymour et al., 2009), model marine particles and sinking aggregates (Kiørboe et al., 2002), exemplifying the importance of chemotaxis throughout the microbial food web. However, previous work has typically been limited to one single unsteady source, and to durations of a few minutes or less. While this may be long compared to the timescales for cell motility and reorientation (seconds), it is still much shorter than the timescales over which bacterial metabolism varies (Lambert and Kussell, 2014) and cell division occurs (hours to days) (Kirchman, 2016). Observations over minute-long timescales cannot detect slow modulations or systematic changes in swimming speed or chemotactic abilities, which could in principle, strongly affect the collective cell dynamics. Chemotaxis assays conducted over short timescales do not necessarily represent the dynamics of wild foraging bacteria

throughout their lifetime. Beyond determining the chemotactic *ability* of wild marine bacteria, it will be critical to assess their *propensity* for performing chemotaxis in realistic environments over extended periods of time.

3. CHEMOTAXIS IN REALISTIC MICROENVIRONMENTS

What constitutes a *realistic* environment varies wildly between different regions of the ocean, from upwelling of nutrient-rich deep water (Lauro et al., 2009) to the nutrient-poor photic zone; and over time with seasons and bloom conditions (Teeling et al., 2012). The chemical microenvironments are sometimes driven predominantly through the action of physical processes (currents, sunlight) whose effects are known *a priori*. However, in many cases, the nutrient dynamics are strongly coupled to the microbial population itself. Moreover, organic matter may be dissolved (DOM, **Figure 1A**i), due to phytoplankton exudation or sloppy feeding (Jackson, 2012); particulate (POM, **Figure 1A**ii) in marine snow and precipitates; or a combination of DOM and POM in, for example, oil droplets and phytoplankton lysis events (Smriga et al., 2016) (**Figure 1A**iii).

The precise values of the chemical gradients depend on many factors, including the quantity of nutrients released, its molecular diffusivity, the time over which release occurs, the rate of background uptake by bacteria, and any mixing by fluid flows. The phycosphere radius, or distance at which bacteria interact with nutrient pulses, therefore varies from $\lesssim 10\,\mu$m through to several millimeters (Seymour et al., 2017). Sources can vary in duration from seconds to minutes in the case of lysis events (Blackburn et al., 1998), or many hours in the case of continuous leakage.

4. GENERATING CONTROLLED, DYNAMIC CHEMICAL LANDSCAPES

A promising method for creating custom dissolved (DOM) nutrient landscapes utilizes the photo-release of caged chemoattractants (McCray and Trentham, 1989; Jasuja et al., 1999; Sagawa et al., 2014; Jikeli et al., 2015). Dissolved organic compounds such as the amino acid glutamate, which naturally occurs in coastal environments and acts as a chemoattractant for marine bacteria (Barbara and Mitchell, 2003; Duursma and Dawson, 2011), can be chemically appended using a "cage" molecule. When bound to the cage, this attractant is undetectable by bacteria. Calibrated exposure to light causes photolysis of the cage, and the precise release of chemoattractant hotspots. Since the illumination can be easily varied in space and time, this method facilitates the creation of custom two-dimensional

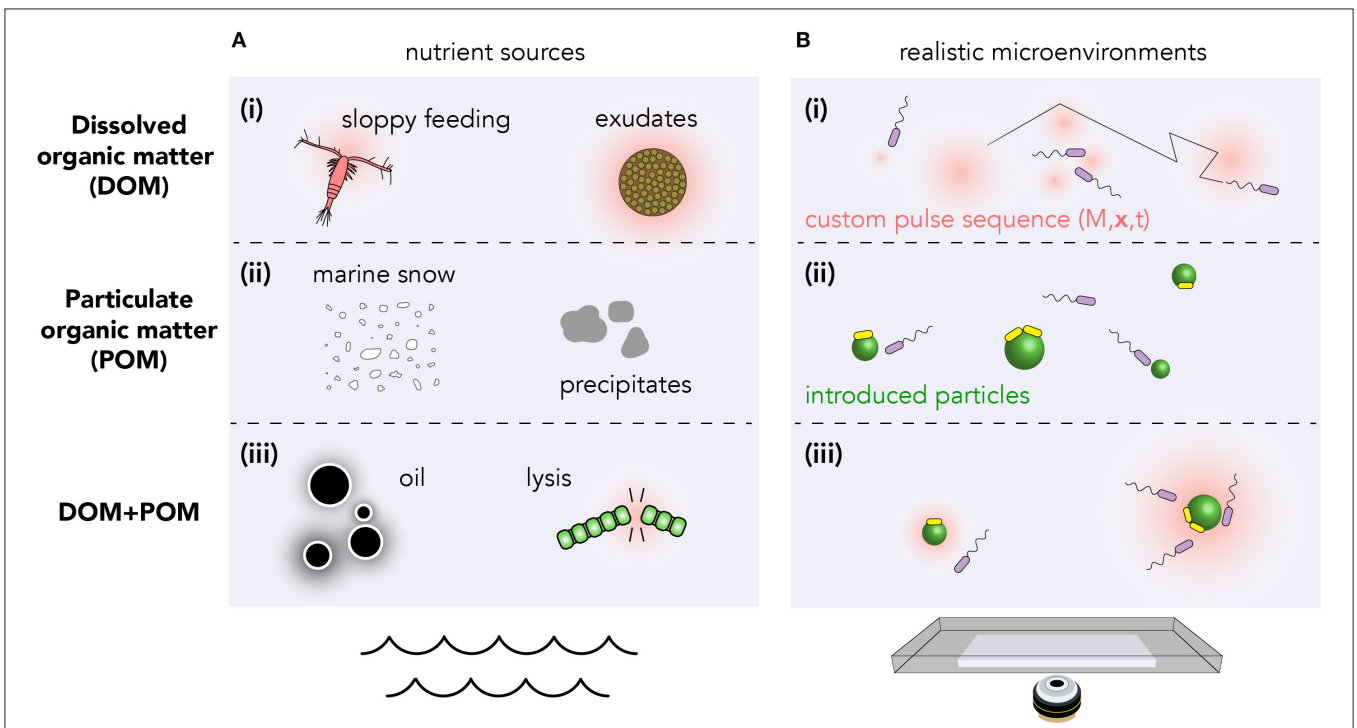

FIGURE 1 | Structured nutrient landscapes found in the ocean can be quantitatively reproduced in laboratory settings using microfluidics, photolysis of caged resources, and discrete nutrient particles. **(A)** Various biological processes produce resources which may be (i) dissolved, (ii) particulate, or (iii) a combination of both. **(B)** Realistic microenvironments can be recreated using (i) photolysis of caged compounds to produce custom DOM landscapes (Brumley et al., 2019; Carrara et al., 2020); (ii) spatial arrays of particles (e.g., chitin or alginate) (Datta et al., 2016); or (iii) both. Within these custom arenas, bacterial chemotaxis and population kinetics can be tracked over timescales from milliseconds to days. Transitions between planktonic (purple) and surface-attached bacteria (yellow) can also be quantified (Yawata et al., 2014).

nutrient landscapes, with exquisite precision (Brumley et al., 2019; Carrara et al., 2020).

Alginate beads (Yawata et al., 2014), chitin particles (Datta et al., 2016) and oil droplets (Desai et al., 2018) can be used to mimic particulate organic matter (POM), investigate bacterial chemotaxis, and study the physics of attachment/detachment dynamics (**Figure 1**). However, controlled sequential introduction of multiple particles can be difficult to achieve experimentally. Moreover, particulate matter in the ocean tends to sediment, making visualization in realistic environments challenging. Microscopy techniques that continuously follow individual marine snow particles for days at a time (Krishnamurthy et al., 2019) have the potential to provide tremendous insight into the long-time dynamics of bacterial chemotaxis and particle colonization. Reconciling the known resource landscape with bacterial trajectories measured using high throughput techniques (Taute et al., 2015; Waite et al., 2016; Brumley et al., 2019), is key to teasing apart the mechanisms bacteria use to navigate their microenvironment.

5. NOISE IN BACTERIAL CHEMOTAXIS

From the stochastic encounters with chemoattractant molecules to the actuation of the flagellar motors, there are many sources of noise that can influence the capacity of microbes to detect and respond to chemical gradients (Sourjik and Wingreen, 2012; Micali and Endres, 2016; Kromer et al., 2018). Individual microbes experience the chemical environment as a sequence of encounters with individual molecules (Berg and Purcell, 1977) (see **Figure 2A**). The randomness in this sequence is particularly important within marine environments, where resource hotspots may be very small ($\lesssim$ 1 pmol) (Blackburn et al., 1998; Davis and Benner, 2007) and short-lived (seconds to minutes) (Smriga et al., 2016). The discrete molecular nature of the chemoattractant means that even in a steady, uniform environment, the number of chemoattractant molecules reaching the surface receptors per unit of time will fluctuate (Endres and Wingreen, 2008; Mora and Wingreen, 2010), and may be as small as a few molecules per second (Brumley et al., 2019). Provided that bacteria rely on temporal signaling to perform chemotaxis (Macnab and Koshland, 1972; Segall et al., 1986), a *gradient* can only ever be defined in an average sense, and requires integration of the arrival sequence over an appropriate timescale, T. If the cell's uncertainty in the gradient estimate is larger in magnitude than the gradient itself, a typical measurement will not be able to resolve the signal. The photo-release of glutamate in sub-picomole quantities—explicitly designed to mimic an individual lysing phytoplankton cell (Blackburn et al., 1998)—was used to assess the role of sensory noise in realistic environments (Brumley et al., 2019). The chemotactic precision of *Vibrio ordalii* was found to be close to the fundamental limit set by this molecule counting noise. While these results assume sampling through discrete time intervals, it will be important for future work to examine the role of continuous integration of ligand binding events (Mora and Nemenman, 2019), determine exactly how cells average measurements, and ascertain how noise propagates through the chemotaxis networks of different model organisms (Micali and Endres, 2019). Phenotypic variation may also influence the collective chemotactic response of many cells (Frankel et al., 2014; Waite et al., 2018).

Intracellular noise can also influence the capacity of bacteria to respond to chemical gradients (Korobkova et al., 2004) (see **Figure 2A**). The discrete nature of signaling molecules places limits on a cell's chemotactic ability in a manner similar to extracellular counting noise (Bialek and Setayeshgar, 2005). Suppressing internal noise in biochemical networks generally requires a cell to produce and maintain an increased number of signaling molecules (Lestas et al., 2010; Govern and ten Wolde, 2014). Depending on the dynamics of the chemical environment, the extra cost in noise suppression (Sartori and Tu, 2015) may exceed the additional resources acquired through greater sensitivity. For systems in which the noise frequency is much higher than that of the signal, it may be possible to filter noise (Andrews et al., 2006). However, for realistic marine environments, the timescales over which chemoattractant concentrations vary and signaling molecules fluctuate may be similar. The conflation of these timescales could thwart the ability for cells to successfully filter the intracellular noise.

While it is intuitive that noise in the incoming chemical signal and the internal signaling pathway can degrade chemotactic performance, there are cases in which cells actually appear to benefit from noise (Flores et al., 2012). For bacteria with multiple flagella such as *E. coli*, stochastic coordination of flagellar motors can reduce the latency below that of an individual motor, which can assist in steep gradients (Sneddon et al., 2012). Random fluctuations in the signal protein CheY-P have also been shown to increase the chemotactic sensitivity of *E. coli* at the level of the flagellar motors (Hu and Tu, 2013; He et al., 2016). Yet, these particular mechanisms are generally not accessible to marine bacteria, which typically possess one flagellum (Xie et al., 2011) and operate in shallow, ephemeral gradients.

Greater chemotactic abilities do not necessarily lead to enhanced resource acquisition or growth (Ni et al., 2020). The level of bacterial chemotaxis which confers the greatest advantage for individual cells depends on the structure of the chemical microenvironment (Celani and Vergassola, 2010). For bacteria in the vicinity of a single isolated nutrient source, a greater chemotactic precision will generally lead to an enhancement in the nutrient exposure and uptake rate (Smriga et al., 2016). However, in an environment with multiple nutrient sources of different magnitude, a cell which perfectly follows the gradient may become trapped in a locally favorable, but globally sub-optimal position (see **Figure 2B**i). Sources of noise which reduce the cell's chemotactic sensitivity may actually improve the overall nutrient acquisition by allowing the cell to more thoroughly explore its environment (see **Figure 2B**ii). The optimal bacterial behavior will therefore be sensitively linked to the precise spatiotemporal dynamics of the chemical microenvironment (Passino, 2002). Theoretical frameworks linking organismal navigation with the overall resource landscape structure (Hein et al., 2016b; Seymour et al., 2017; Hein and Martin, 2019) provide predictions about the optimal strategies for bacterial foraging, which can be explicitly tested, for example using microfluidic platforms.

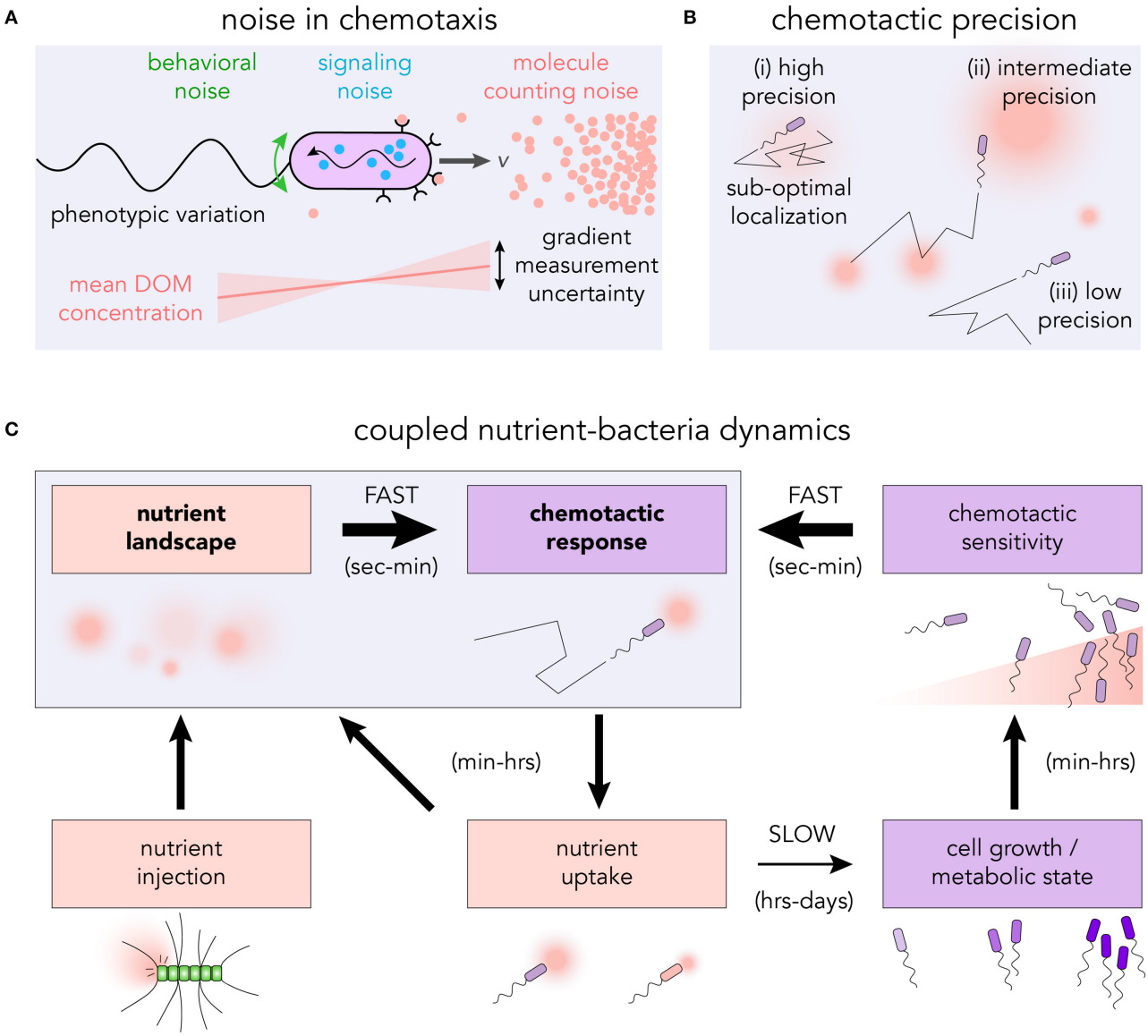

FIGURE 2 | (A) The discrete nature of dissolved chemoattractants introduces molecule counting noise into the bacterium's measurement of the gradient. In conjunction with other sources of noise in the signaling pathway, the flagellar response as well as rotational diffusion, the cell executes an effective chemotactic response. **(B)** The level of chemotactic precision governs the ability of bacteria to navigate toward, and reside at, regions of high DOM concentration. (i) High chemotactic precision may result in sub-optimal localization at local nutrient maxima; (ii) intermediate precision allows for both exploration and exploitation; and (iii) low precision results in undirected motility. **(C)** Highly coupled nutrient-bacteria dynamics in chemotactic foraging cycle. The traditional means of studying chemotaxis is to assess the motility response to prescribed nutrient landscapes (seconds to minutes). However, over timescales of hours to days, feedback loops exist which have the capacity to reshape the nutrient landscape and modify the chemotactic response.

6. BACTERIAL UPTAKE KINETICS IN STRUCTURED MICROENVIRONMENTS

Because of fluctuations in nutrient exposure within the structured microenvironments of the ocean, the generation times, and therefore biomass production, of wild bacteria are likely to be fundamentally different from those measured during experiments in homogenous batch culture (Fenchel, 2002; Azam and Malfatti, 2007). In fact, temporal fluctuations can drive distinct growth physiologies and strategies (Yan et al., 2017), even for environments with the same mean nutrient concentration. Bacterial chemotaxis has the capacity to systematically redistribute the cells, and therefore may provide a feedback loop between the microbial population and the resource landscape (Cremer et al., 2019). In cases where there is strong two-way coupling between the bacterial dynamics and the nutrient field—i.e., nutrient field drives chemotaxis, and bacterial consumption shapes nutrient profile—it is important to study the system for an extended period of time (Carrara et al., 2020). This will provide great utility in determining realistic cell growth

rates that are often very difficult to measure *in situ* (Kirchman, 2016).

Chemotaxis, as well as plasticity in physiology and behavioral strategy, can enhance the ability of bacteria to respond to spatial and temporal variation in resources. This, in turn, has the potential to influence ecosystem level processes such as remineralization rates or carbon export fluxes. Rates of these microbially mediated processes exhibit considerable regional variation (Hansell et al., 2012; Mouw et al., 2016), and they also strongly influence the distribution of carbon throughout the oceans and atmosphere (Kwon et al., 2009). Global-scale biogeochemical models rely on highly simplified, phenomenological parameterizations of remineralization of particulate and dissolved organic matter, which prevents them from detecting carbon-cycle feedbacks induced by the ecological dynamics of marine microbes (Mislan et al., 2014). The ability to assess long-term changes in microbial motility presents a unique opportunity for determining the influence of physiological states in bacterial chemotaxis (Jordan et al., 2013; Cremer et al., 2019), which is a key step to understanding how to link microbes and biogeochemistry.

Following early evidence that aspects of *E. coli* chemotaxis are independent of uptake or metabolism (Adler, 1969), research has largely overlooked the capacity for uptake or physiological states to influence motility. Studies of microbial motion often use highly specific culturing conditions. If the nutrients are too scarce cells may not grow, swim or navigate. Similarly, cell motility and chemotaxis may also be reduced by overly abundant nutrients, since they are not advantageous when resources are plentiful (Ni et al., 2020). Additional work suggests that *E. coli* (Taylor and Zhulin, 1998), *Azospirillum brasilense* (Alexandre et al., 2000) and other species of bacteria (Alexandre and Zhulin, 2001) exhibit metabolism-dependent chemotaxis. Bacteria appear to modulate the way they perform chemotaxis—and indeed whether they even swim at all—based on their metabolic state, which presumably helps cells cope with the conditions they experience in natural environments (Ni et al., 2020). Correlations between cellular motility and other copiotrophic traits (Koch, 2001), such as ribosomal copy number, hydrolytic enzymes, and genes for environmental sensing and signaling (Lauro et al., 2009; Roller et al., 2016) hint at the capacity for motile bacteria to rapidly expand their population, to adapt their behavioral and trophic strategies in response to their environment, and to structure local nutrient fields by being the primary degraders of biological macromolecules. The feedback loop between nutrient exposure, swimming speed (Son et al., 2016) and ultimately chemotactic sensitivity (Hein et al., 2016a; Ni et al., 2020) exemplifies the need to interrogate bacteria in realistic environments for extended periods of time, and investigate temporal variations in motility and chemotactic performance (see **Figure 2C**), within and between successive generations. Since biogeochemical cycling will be driven not only by the spatial distribution of cells with respect to the nutrient field, but also by their metabolic state, modeling both of these processes (Egbert et al., 2010) may prove to be important in predicting nutrient cycling in the ocean.

7. PRIORITIES FOR FUTURE RESEARCH

The capacity to generate controlled, dynamic chemical landscapes, while simultaneously visualizing bacterial responses from milliseconds through to days, represents a uniquely powerful approach to investigating marine microbial processes. An important area for future exploration will be considering multiple interacting species of bacteria and other organisms (Amin et al., 2012; Hol et al., 2016; Raina et al., 2019), where population and community dynamics may depend on the nutrient properties and organismal phenotypes. This will be particularly important in assessing the spatial patterning of metabolic handoffs (Anantharaman et al., 2016), density dependent competition dynamics (Gude et al., 2020), and the role of quorum sensing (Hmelo, 2017).

Investigating the rich interplay between multiple chemoattractants represents another important direction for future research. Except in some simplified domains (Kalinin et al., 2010), bacterial chemotaxis is routinely studied in response to single molecular species. Yet, phytoplankton exudates and other dissolved organic matter exist as complex mixtures of compounds which differ in their abundance, diffusivity and propensity to elicit chemotaxis (Davis and Benner, 2007; Duursma and Dawson, 2011). Emerging analytical methods of characterizing chemical microenvironments, exudation rates and nutrient exchanges (Wessel et al., 2013) will further inform models for microbial motion (Keller and Segel, 1970; Jackson, 1987; Bray et al., 2007; Desai et al., 2019) through to ocean-scale dynamics of microbial populations (Barton et al., 2010; Worden et al., 2015; Kuhn et al., 2019).

AUTHOR CONTRIBUTIONS

DB wrote the first draft of the manuscript. All authors revised the manuscript and approved it for publication.

FUNDING

This work was supported by an Australian Research Council Discovery Early Career Researcher Award DE180100911 (to DB), an NSF IOS Grant 1855956 (to AH), NSF grant OCE-1848576 (to SL and GH), NOAA-AWD1005828 (to GH), a Simons Foundation Grant 395890 (to SL and GH), a grant from the Swiss National Science Foundation (315230_176189) (to RS), and a Simons Foundation Grant 542395 (to RS) as part of the Principles of Microbial Ecosystems Collaborative (PriME).

REFERENCES

Adler, J. (1969). Chemoreceptors in bacteria. *Science* 166, 1588–1597. doi: 10.1126/science.166.3913.1588

Adler, J. (1973). A method for measuring chemotaxis and use of the method to determine optimum conditions for chemotaxis by *Escherichia coli*. *Microbiology* 74, 77–91. doi: 10.1099/00221287-74-1-77

Alexandre, G., Greer, S. E., and Zhulin, I. B. (2000). Energy taxis is the dominant behavior in *Azospirillum brasilense*. *J. Bacteriol.* 182, 6042–6048. doi: 10.1128/JB.182.21.6042-6048.2000

Alexandre, G., and Zhulin, I. B. (2001). More than one way to sense chemicals. *J. Bacteriol.* 183, 4681–4686. doi: 10.1128/JB.183.16.4681-4686.2001

Amin, S. A., Parker, M. S., and Armbrust, E. V. (2012). Interactions between diatoms and bacteria. *Microbiol. Mol. Biol. Rev.* 76, 667–684. doi: 10.1128/MMBR.00007-12

Anantharaman, K., Brown, C. T., Hug, L. A., Sharon, I., Castelle, C. J., Probst, A. J., et al. (2016). Thousands of microbial genomes shed light on interconnected biogeochemical processes in an aquifer system. *Nat. Commun.* 7:13219. doi: 10.1038/ncomms13219

Andrews, B. W., Yi, T.-M., and Iglesias, P. A. (2006). Optimal noise filtering in the chemotactic response of *Escherichia coli*. *PLoS Comput. Biol.* 2:e154. doi: 10.1371/journal.pcbi.0020154

Azam, F. (1998). Microbial control of oceanic carbon flux: the plot thickens. *Science* 280, 694–696. doi: 10.1126/science.280.5364.694

Azam, F., and Malfatti, F. (2007). Microbial structuring of marine ecosystems. *Nat. Rev. Micro* 5, 782–791. doi: 10.1038/nrmicro1747

Barbara, G. M., and Mitchell, J. G. (2003). Marine bacterial organisation around point-like sources of amino acids. *FEMS Microbiol. Ecol.* 43, 99–109. doi: 10.1111/j.1574-6941.2003.tb01049.x

Barton, A. D., Dutkiewicz, S., Flierl, G., Bragg, J., and Follows, M. J. (2010). Patterns of diversity in marine phytoplankton. *Science* 327, 1509–1511. doi: 10.1126/science.1184961

Batchelor, G. K. (1959). Small-scale variation of convected quantities like temperature in turbulent fluid Part 1. General discussion and the case of small conductivity. *J. Fluid Mech.* 5, 113–133. doi: 10.1017/S002211205900009X

Benner, R., and Amon, R. M. W. (2015). The size-reactivity continuum of major bioelements in the ocean. *Annu. Rev. Mar. Sci.* 7, 185–205. doi: 10.1146/annurev-marine-010213-135126

Berg, H. C. (2008). *E. coli in Motion*. Berlin: Springer Science & Business Media.

Berg, H. C., and Purcell, E. M. (1977). Physics of chemoreception. *Biophys. J.* 20, 193–219. doi: 10.1016/S0006-3495(77)85544-6

Bialek, W., and Setayeshgar, S. (2005). Physical limits to biochemical signaling. *Proc. Natl. Acad. Sci. U.S.A.* 102, 10040–10045. doi: 10.1073/pnas.0504321102

Blackburn, N., Fenchel, T., and Mitchell, J. (1998). Microscale nutrient patches in planktonic habitats shown by chemotactic bacteria. *Science* 282, 2254–2256. doi: 10.1126/science.282.5397.2254

Bork, P., Bowler, C., de Vargas, C., Gorsky, G., Karsenti, E., and Wincker, P. (2015). Tara Oceans studies plankton at planetary scale. Science 348, 873–873. doi: 10.1126/science.aac5605

Bray, D., Levin, M. D., and Lipkow, K. (2007). The chemotactic behavior of computer-based surrogate bacteria. *Curr. Biol.* 17, 12–19. doi: 10.1016/j.cub.2006.11.027

Brown, D. A., and Berg, H. C. (1974). Temporal Stimulation of Chemotaxis in *Escherichia coli*. *Proc. Natl. Acad. Sci. U.S.A.* 71, 1388–1392. doi: 10.1073/pnas.71.4.1388

Brumley, D. R., Carrara, F., Hein, A. M., Yawata, Y., Levin, S. A., and Stocker, R. (2019). Bacteria push the limits of chemotactic precision to navigate dynamic chemical gradients. *Proc. Natl. Acad. Sci. U.S.A.* 116, 10792–10797. doi: 10.1073/pnas.1816621116

Carrara, F., Brumley, D. R., Hein, A. M., Yawata, Y., Salek, M. M., Lee, K. S., et al. (2020). Generating controlled, dynamic chemical landscapes to study microbial behavior. *J. Visual. Exp.* e60589. doi: 10.3791/60589

Celani, A., and Vergassola, M. (2010). Bacterial strategies for chemotaxis response. *Proc. Natl. Acad. Sci. U.S.A.* 107, 1391–1396. doi: 10.1073/pnas.0909673107

Cremer, J., Honda, T., Tang, Y., Wong-Ng, J., Vergassola, M., and Hwa, T. (2019). Chemotaxis as a navigation strategy to boost range expansion. *Nature.* 575, 658–663. doi: 10.1038/s41586-019-1733-y

Datta, M. S., Sliwerska, E., Gore, J., Polz, M. F., and Cordero, O. X. (2016). Microbial interactions lead to rapid micro-scale successions on model marine particles. *Nat. Commun.* 7:11965. doi: 10.1038/ncomms11965

Davis, J., and Benner, R. (2007). Quantitative estimates of labile and semi-labile dissolved organic carbon in the western Arctic Ocean: a molecular approach. *Limnol. Oceanogr.* 52, 2434–2444. doi: 10.4319/lo.2007.52.6.2434

Desai, N., Shaik, V. A., and Ardekani, A. M. (2018). Hydrodynamics-mediated trapping of micro-swimmers near drops. *Soft Matter* 14, 264–278. doi: 10.1039/C7SM01615H

Desai, N., Shaik, V. A., and Ardekani, A. M. (2019). Hydrodynamic interaction enhances colonization of sinking nutrient so-urces by motile microorganisms. *Front. Microbiol.* 10:289. doi: 10.3389/fmicb.2019.00289

Druffel, E. R. M., Bauer, J. E., Williams, P. M., Griffin, S., and Wolgast, D. (1996). Seasonal variability of particulate organic radiocarbon in the northeast Pacific Ocean. *J. Geophys. Res. Oceans* 101, 20543–20552. doi: 10.1029/96JC01850

Duursma, E. K., and Dawson, R. (2011). *Marine Organic Chemistry*. Amsterdam: Elsevier.

Egbert, M. D., Barandiaran, X. E., and Di Paolo, E. A. (2010). A minimal model of metabolism-based chemotaxis. *PLoS Comput. Biol.* 6:e1001004. doi: 10.1371/journal.pcbi.1001004

Endres, R. G. (2013). *Physical Principles in Sensing and Signaling: With an Introduction to Modeling in Biology*. Oxford: Oxford University Press.

Endres, R. G., and Wingreen, N. S. (2008). Accuracy of direct gradient sensing by single cells. *Proc. Natl. Acad. Sci. U.S.A.* 105, 15749–15754. doi: 10.1073/pnas.0804688105

Englert, D. L., Manson, M. D., and Jayaraman, A. (2009). Flow-based microfluidic device for quantifying bacterial chemotaxis in stable, competing gradients. *Appl. Environ. Microbiol.* 75, 4557–4564. doi: 10.1128/AEM.02952-08

Fenchel, T. (2002). Microbial behavior in a heterogeneous world. *Science* 296, 1068–1071. doi: 10.1126/science.1070118

Flores, M., Shimizu, T. S., ten Wolde, P. R., and Tostevin, F. (2012). Signaling noise enhances chemotactic drift of *E. coli*. *Phys. Rev. Lett.* 109:148101. doi: 10.1103/PhysRevLett.109.148101

Frankel, N. W., Pontius, W., Dufour, Y. S., Long, J., Hernandez-Nunez, L., and Emonet, T. (2014). Adaptability of non-genetic diversity in bacterial chemotaxis. *eLife* 3:e03526. doi: 10.7554/eLife.03526

Govern, C. C., and ten Wolde, P. R. (2014). Optimal resource allocation in cellular sensing systems. *Proc. Natl. Acad. Sci. U.S.A.* 111, 17486–17491. doi: 10.1073/pnas.1411524111

Gude, S., Pinçe, E., Taute, K. M., Seinen, A.-B., Shimizu, T. S., and Tans, S. J. (2020). Bacterial coexistence driven by motility and spatial competition. *Nature* 578, 588–592. doi: 10.1038/s41586-020-2033-2

Hansell, D. A., Carlson, C. A., Repeta, D. J., and Schlitzer, R. (2009). Dissolved organic matter in the ocean: a controversy stimulates new insights. *Oceanography* 22, 202–211. doi: 10.5670/oceanog.2009.109

Hansell, D. A., Carlson, C. A., and Schlitzer, R. (2012). Net removal of major marine dissolved organic carbon fractions in the subsurface ocean. *Glob. Biogeochem. Cycles* 26. doi: 10.1029/2011GB004069

He, R., Zhang, R., and Yuan, J. (2016). Noise-induced increase of sensitivity in bacterial chemotaxis. *Biophys. J.* 111, 430–437. doi: 10.1016/j.bpj.2016.06.013

Hein, A. M., Brumley, D. R., Carrara, F., Stocker, R., and Levin, S. A. (2016a). Physical limits on bacterial navigation in dynamic environments. *J. R. Soc. Interfac* 13:20150844. doi: 10.1098/rsif.2015.0844

Hein, A. M., Carrara, F., Brumley, D. R., Stocker, R., and Levin, S. A. (2016b). Natural search algorithms as a bridge between organisms, evolution, and ecology. *Proc. Natl Acad. Sci. U.S.A.* 113, 9413–9420. doi: 10.1073/pnas.1606195113

Hein, A. M., and Martin, B. T. (2019). Information limitation and the dynamics of coupled ecological systems. *Nat. Ecol. Evol.* 4, 82–90. doi: 10.1038/s41559-019-1008-x

Hmelo, L. R. (2017). Quorum sensing in marine microbial environments. *Annu. Rev. Mar. Sci.* 9, 257–281. doi: 10.1146/annurev-marine-010816-060656

Hol, F. J. H., Rotem, O., Jurkevitch, E., Dekker, C., and Koster, D. A. (2016). Bacterial predator-prey dynamics in microscale patchy landscapes. *Proc. R. Soc. Lond. B Biol. Sci.* 283:20152154. doi: 10.1098/rspb.2015.2154

Hu, B., and Tu, Y. (2013). Coordinated switching of bacterial flagellar motors: evidence for direct motor-motor coupling? Phys. Rev. Lett. 110:158703. doi: 10.1103/PhysRevLett.110.158703

Jackson, G. A. (1987). Simulating chemosensory responses of marine microorganisms. *Limnol. Oceanogr.* 32, 1253–1266. doi: 10.4319/lo.1987.32.6.1253

Jackson, G. A. (2012). Seascapes: the world of aquatic organisms as determined by their particulate natures. *J. Exp. Biol.* 215, 1017–1030. doi: 10.1242/jeb.059105

Jasuja, R., Keyoung, J., Reid, G. P., Trentham, D. R., and Khan, S. (1999). Chemotactic responses of *Escherichia coli* to small jumps of photoreleased L-aspartate. *Biophys. J.* 76, 1706–1719. doi: 10.1016/S0006-3495(99)77329-7

Jiang, L., Ouyang, Q., and Tu, Y. (2010). Quantitative modeling of *Escherichia coli* chemotactic motion in environments varying in space and time. *PLoS Comput. Biol.* 6:e1000735. doi: 10.1371/journal.pcbi.1000735

Jikeli, J. F., Alvarez, L., Friedrich, B. M., Wilson, L. G., Pascal, R., Colin, R., et al. (2015). Sperm navigation along helical paths in 3D chemoattractant landscapes. *Nat. Commun.* 6:7985. doi: 10.1038/ncomms8985

Jordan, D., Kuehn, S., Katifori, E., and Leibler, S. (2013). Behavioral diversity in microbes and low-dimensional phenotypic spaces. *Proc. Natl. Acad. Sci. U.S.A.* 110, 14018–14023. doi: 10.1073/pnas.1308282110

Kalinin, Y., Neumann, S., Sourjik, V., and Wu, M. (2010). Responses of *Escherichia coli* bacteria to two opposing chemoattractant gradients depend on the chemoreceptor ratio. *J. Bacteriol.* 192, 1796–1800. doi: 10.1128/JB.01507-09

Karsenti, E., Acinas, S. G., Bork, P., Bowler, C., De Vargas, C., Raes, J., et al. (2011). A holistic approach to marine eco-systems biology. *PLoS Biol.* 9:e1001177. doi: 10.1371/journal.pbio.1001177

Keil, R. G., and Kirchman, D. L. (1999). Utilization of dissolved protein and amino acids in the northern sargasso sea. *Aquat. Microb. Ecol.* 18, 293–300. doi: 10.3354/ame018293

Keller, E. F., and Segel, L. A. (1970). Initiation of slime mold aggregation viewed as an instability. *J. Theoret. Biol.* 26, 399–415. doi: 10.1016/0022-5193(70)90092-5

Kiørboe, T. (2001). Formation and fate of marine snow: small-scale processes with large-scale implications. *Sci. Mar.* 65, 57–71. doi: 10.3989/scimar.2001.65s257

Kiørboe, T. (2008). *A Mechanistic Approach to Plankton Ecology*. Princeton University Press. doi: 10.1515/9780691190310

Kiørboe, T., Grossart, H.-P., Ploug, H., and Tang, K. (2002). Mechanisms and rates of bacterial colonization of sinking aggregates. *Appl. Environ. Microbiol.* 68, 3996–4006. doi: 10.1128/AEM.68.8.3996-4006.2002

Kirchman, D. L. (2016). Growth rates of microbes in the oceans. *Annu. Rev. Mar. Sci.* 8, 285–309. doi: 10.1146/annurev-marine-122414-033938

Koch, A. L. (2001). Oligotrophs versus copiotrophs. *Bioessays* 23, 657–661. doi: 10.1002/bies.1091

Korobkova, E., Emonet, T., Vilar, J. M. G., Shimizu, T. S., and Cluzel, P. (2004). From molecular noise to behavioural variability in a single bacterium. *Nature* 428, 574–578. doi: 10.1038/nature02404

Krishnamurthy, D., Li, H., Benoit du Rey, F., Cambournac, P., Larson, A., and Prakash, M. (2019). Scale-free vertical tracking microscopy: towards bridging scales in biological oceanography. *bioRxiv* 610246. 1–44. doi: 10.1101/610246

Kromer, J. A., Märcker, S., Lange, S., Baier, C., and Friedrich, B. M. (2018). Decision making improves sperm chemotaxis in the presence of noise. *PLoS Comput. Biol.* 14:e1006109. doi: 10.1371/journal.pcbi.1006109

Kuhn, A. M., Dutkiewicz, S., Jahn, O., Clayton, S., Rynearson, T. A., Mazloff, M. R., et al. (2019). Temporal and spatial scales of correlation in marine phytoplankton communities. *J. Geophys. Res. Oceans.* 124, 9417–9438. doi: 10.1029/2019JC015331

Kwon, E. Y., Primeau, F., and Sarmiento, J. L. (2009). The impact of remineralization depth on the air-sea carbon balance. *Nat. Geosci.* 2, 630–635. doi: 10.1038/ngeo612

Lambert, G., and Kussell, E. (2014). Memory and fitness optimization of bacteria under fluctuating environments. *PLoS Genet.* 10:e1004556. doi: 10.1371/journal.pgen.1004556

Lauro, F. M., McDougald, D., Thomas, T., Williams, T. J., Egan, S., Rice, S., et al. (2009). The genomic basis of trophic strategy in marine bacteria. *Proc. Natl. Acad. Sci. U.S.A.* 106, 15527–15533. doi: 10.1073/pnas.0903507106

Lestas, I., Vinnicombe, G., and Paulsson, J. (2010). Fundamental limits on the suppression of molecular fluctuations. *Nature* 467, 174–178. doi: 10.1038/nature09333

Long, J., Zucker, S. W., and Emonet, T. (2017). Feedback between motion and sensation provides nonlinear boost in run-and-tumble navigation. *PLoS Comput. Biol.* 13:e1005429. doi: 10.1371/journal.pcbi.1005429

Macnab, R. M., and Koshland, D. E. (1972). The gradient-sensing mechanism in bacterial chemotaxis. *Proc. Natl Acad. Sci. U.S.A.* 69, 2509–2512. doi: 10.1073/pnas.69.9.2509

Mao, H., Cremer, P. S., and Manson, M. D. (2003). A sensitive, versatile microfluidic assay for bacterial chemotaxis. *Proc. Natl Acad. Sci. U.S.A.* 100, 5449–5454. doi: 10.1073/pnas.0931258100

McCray, J. A., and Trentham, D. R. (1989). Properties and uses of photoreactive caged compounds. *Annu. Rev. Biophys. Biophys. Chem.* 18, 239–270. doi: 10.1146/annurev.bb.18.060189.001323

Micali, G., and Endres, R. G. (2016). Bacterial chemotaxis: information processing, thermodynamics, and behavior. *Curr. Opin. Microbiol.* 30, 8–15. doi: 10.1016/j.mib.2015.12.001

Micali, G., and Endres, R. G. (2019). Maximal information transmission is compatible with ultrasensitive biological pathways. *Sci. Rep.* 9:16898. doi: 10.1038/s41598-019-53273-4

Mislan, K. A. S., Stock, C. A., Dunne, J. P., and Sarmiento, J. L. (2014). Group behavior among model bacteria influences particulate carbon remineralization depths. *J. Mar. Res.* 72, 183–218. doi: 10.1357/002224014814901985

Mora, T., and Nemenman, I. (2019). Physical limit to concentration sensing in a changing environment. *Phys. Rev. Lett.* 123:198101. doi: 10.1103/PhysRevLett.123.198101

Mora, T., and Wingreen, N. S. (2010). Limits of sensing temporal concentration changes by single cells. *Phys. Rev. Lett.* 104:248101. doi: 10.1103/PhysRevLett.104.248101

Morton-Firth, C. J., Shimizu, T. S., and Bray, D. (1999). A free-energy-based stochastic simulation of the tar receptor complex1. *J. Mol. Biol.* 286, 1059–1074. doi: 10.1006/jmbi.1999.2535

Mouw, C. B., Barnett, A., McKinley, G. A., Gloege, L., and Pilcher, D. (2016). Phytoplankton size impact on export flux in the global ocean. *Glob. Biogeochem. Cycles* 30, 1542–1562. doi: 10.1002/2015GB005355

Ni, B., Colin, R., Link, H., Endres, R. G., and Sourjik, V. (2020). Growth-rate dependent resource investment in bacterial motile behavior quantitatively follows potential benefit of chemotaxis. *Proc. Natl. Acad. Sci. U.S.A.* 117, 595–601. doi: 10.1073/pnas.1910849117

Passino, K. M. (2002). Biomimicry of bacterial foraging for distributed optimization and control. *IEEE Control Syst.* 22, 52–67. doi: 10.1109/MCS.2002.1004010

Raina, J.-B., Fernandez, V., Lambert, B., Stocker, R., and Seymour, J. R. (2019). The role of microbial motility and chemotaxis in symbiosis. *Nat. Rev. Microbiol.* 17, 284–294. doi: 10.1038/s41579-019-0182-9

Riedel, T., and Dittmar, T. (2014). A method detection limit for the analysis of natural organic matter via Fourier transform ion cyclotron resonance mass spectrometry. *Anal. Chem.* 86, 8376–8382. doi: 10.1021/ac501946m

Roller, B. R. K., Stoddard, S. F., and Schmidt, T. M. (2016). Exploiting rRNA operon copy number to investigate bacterial reproductive strategies. *Nat. Microbiol.* 1:16160. doi: 10.1038/nmicrobiol.2016.160

Sagawa, T., Kikuchi, Y., Inoue, Y., Takahashi, H., Muraoka, T., Kinbara, K., et al. (2014). Single-cell *E. coli* response to an instantaneously applied chemotactic signal. *Biophys. J.* 107, 730–739. doi: 10.1016/j.bpj.2014.06.017

Salek, M. M., Carrara, F., Fernandez, V., Guasto, J. S., and Stocker, R. (2019). Bacterial chemotaxis in a microfluidic T-maze reveals strong phenotypic heterogeneity in chemotactic sensitivity. *Nat. Commun.* 10:1877. doi: 10.1038/s41467-019-09521-2

Sartori, P., and Tu, Y. (2015). Free energy cost of reducing noise while maintaining a high sensitivity. *Phys. Rev. Lett.* 115:118102. doi: 10.1103/PhysRevLett.115.118102

Segall, J. E., Block, S. M., and Berg, H. C. (1986). Temporal comparisons in bacterial chemotaxis. *Proc. Natl Acad. Sci. U.S.A.* 83, 8987–8991. doi: 10.1073/pnas.83.23.8987

Seymour, J. R., Amin, S. A., Raina, J.-B., and Stocker, R. (2017). Zooming in on the phycosphere: the ecological interface for phytoplankton-bacteria relationships. *Nat. Microbiol.* 2:17065. doi: 10.1038/nmicrobiol.2017.65

Seymour, J. R., Marcos, and Stocker, R. (2009). Resource patch formation and exploitation throughout the marine microbial food web. *Am. Natural.* 173, E15–E29. doi: 10.1086/593004

Seymour, J. R., Simó, R., Ahmed, T., and Stocker, R. (2010). Chemoattraction to dimethylsulfoniopropionate throughout the marine microbial food web. *Science* 329, 342–345. doi: 10.1126/science.1188418

Smriga, S., Fernandez, V. I., Mitchell, J. G., and Stocker, R. (2016). Chemotaxis toward phytoplankton drives organic matter partitioning among marine bacteria. *Proc. Natl. Acad. Sci. U.S.A.* 113, 1576–1581. doi: 10.1073/pnas.1512307113

Sneddon, M., Pontius, W., and Emonet, T. (2012). Stochastic coordination of multiple actuators reduces latency and improves chemotactic response in bacteria. *Proc. Natl. Acad. Sci. U.S.A.* 109, 805–810. doi: 10.1073/pnas.1113706109

Son, K., Brumley, D. R., and Stocker, R. (2015). Live from under the lens: exploring microbial motility with dynamic imaging and microfluidics. *Nat. Rev. Microbiol.* 13, 761–775. doi: 10.1038/nrmicro 3567

Son, K., Menolascina, F., and Stocker, R. (2016). Speed-dependent chemotactic precision in marine bacteria. *Proc. Natl. Acad. Sci. U.S.A.* 113, 8624–8629. doi: 10.1073/pnas.1602307113

Sourjik, V., and Wingreen, N. S. (2012). Responding to chemical gradients: bacterial chemotaxis. *Curr. Opin. Cell Biol.* 24, 262–268. doi: 10.1016/j.ceb.2011.11.008

Stocker, R. (2012). Marine microbes see a sea of gradients. *Science* 338, 628–633. doi: 10.1126/science.1208929

Stocker, R. (2015). The 100 a length scale in the microbial ocean. *Aquat. Microb. Ecol.* 76, 189–194. doi: 10.3354/ame01777

Stocker, R., Seymour, J. R., Samadani, A., Hunt, D. E., and Polz, M. F. (2008). Rapid chemotactic response enables marine bacteria to exploit ephemeral microscale nutrient patches. *Proc. Natl. Acad. Sci. U.S.A.* 105, 4209–4214. doi: 10.1073/pnas.0709765105

Taute, K. M., Gude, S., Tans, S. J., and Shimizu, T. S. (2015). High-throughput 3D tracking of bacteria on a standard phase contrast microscope. *Nat. Commun.* 6:8776. doi: 10.1038/ncomms9776

Taylor, B. L., and Zhulin, I. B. (1998). In search of higher energy: metabolism-dependent behaviour in bacteria. *Mol. Microbiol.* 28, 683–690. doi: 10.1046/j.1365-2958.1998.00835.x

Taylor, J. R., and Stocker, R. (2012). Trade-offs of chemotactic foraging in turbulent water. *Science* 338, 675–679. doi: 10.1126/science.12 19417

Teeling, H., Fuchs, B. M., Becher, D., Klockow, C., Gardebrecht, A., Bennke, C. M., et al. (2012). Substrate-controlled succession of marine bacterioplankton populations induced by a phytoplankton bloom. *Science* 336, 608–611. doi: 10.1126/science.1218344

Verdugo, P. (2012). Marine microgels. *Annu. Rev. Mar. Sci.* 4, 375–400. doi: 10.1146/annurev-marine-120709-142759

Waite, A. J., Frankel, N. W., Dufour, Y. S., Johnston, J. F., Long, J., et al. (2016). Non-genetic diversity modulates population performance. *Mol. Syst. Biol.* 12:895. doi: 10.15252/msb.20167044

Waite, A. J., Frankel, N. W., and Emonet, T. (2018). Behavioral variability and phenotypic diversity in bacterial chemotaxis. *Annu. Rev. Biophys.* 47, 595–616. doi: 10.1146/annurev-biophys-062215-010954

Wessel, A. K., Hmelo, L., Parsek, M. R., and Whiteley, M. (2013). Going local: technologies for exploring bacterial microenvironments. *Nat. Rev. Microbiol.* 11, 337–348. doi: 10.1038/nrmicro3010

Wong-Ng, J., Melbinger, A., Celani, A., and Vergassola, M. (2016). The role of adaptation in bacterial speed races. *PLoS Comput. Biol.* 12:e1004974. doi: 10.1371/journal.pcbi.1004974

Worden, A. Z., Follows, M. J., Giovannoni, S. J., Wilken, S., Zimmerman, A. E., and Keeling, P. J. (2015). Rethinking the marine carbon cycle: Factoring in the multifarious lifestyles of microbes. *Science* 347:6223. doi: 10.1126/science.1257594

Xie, L., Altindal, T., Chattopadhyay, S., and Wu, X.-L. (2011). Bacterial flagellum as a propeller and as a rudder for efficient chemotaxis. *Proc. Natl. Acad. Sci. U.S.A.* 108, 2246–2251. doi: 10.1073/pnas.1011953108

Yan, J., Nadell, C. D., and Bassler, B. L. (2017). Environmental fluctuation governs selection for plasticity in biofilm production. *ISME J.* 11, 1569–1577. doi: 10.1038/ismej.2017.33

Yawata, Y., Cordero, O. X., Menolascina, F., Hehemann, J.-H., Polz, M. F., and Stocker, R. (2014). Competition-dispersal tradeoff ecologically differentiates recently speciated marine bacterioplankton populations. *Proc. Natl. Acad. Sci. U.S.A.* 111, 5622–5627. doi: 10.1073/pnas.131894 3111

Zhu, X., Si, G., Deng, N., Ouyang, Q., Wu, T., He, Z., et al. (2012). Frequency-dependent *Escherichia coli* chemotaxis behavior. *Phys. Rev. Lett.* 108:128101. doi: 10.1103/PhysRevLett.108.1 28101

Conflict of Interest: The authors declare that the research was conducted in the absence of any commercial or financial relationships that could be construed as a potential conflict of interest.

Copyright © 2020 Brumley, Carrara, Hein, Hagstrom, Levin and Stocker. This is an open-access article distributed under the terms of the Creative Commons Attribution License (CC BY). The use, distribution or reproduction in other forums is permitted, provided the original author(s) and the copyright owner(s) are credited and that the original publication in this journal is cited, in accordance with accepted academic practice. No use, distribution or reproduction is permitted which does not comply with these terms.

frontiers in Marine Science

ORIGINAL RESEARCH
published: 27 July 2020
doi: 10.3389/fmars.2020.00557

Planktonic Protists of the Eastern Nordic Seas and the Fram Strait: Spatial Changes Related to Hydrography During Early Summer

Anna Maria Dąbrowska[1], Józef Mikołaj Wiktor Jr.[1], Małgorzata Merchel[2] and Józef Maria Wiktor[1]*

[1] Marine Protists Laboratory, Department of Marine Ecology, Institute of Oceanology Polish Academy of Sciences, Sopot, Poland, [2] Observational Oceanography Laboratory, Department of Physical Oceanography, Institute of Oceanology Polish Academy of Sciences, Sopot, Poland

The European Arctic is rapidly changing where increasing water temperatures and rapid loss of sea ice will likely influence the structure and functioning of the entire ecosystem. This study aimed to describe the taxonomic composition and spatial distribution of early summer (2015–2016) nano- and microplanktonic protists in the Nordic (Norwegian, Greenland) Seas and the Fram Strait (70.99°N to 78.84°N; 1.52°E to 19.90°E) and to determine the distribution patterns of the communities from the aspect of hydrography, as deduced from *in situ* measurements. Here we identify some generalized regularity in the protistan distribution, indicating the two separated domains at the 6°C threshold. While *Phaeocystis* seemed to be a fairly conservative representative of the colder area (<6°C), the taxonomic structure of the warmer waters (>6°C) may vary significantly between successive summers: from mostly Bacillariophyceae-dominated communities in 2015 to flagellate-dominated in 2016. Based on our results, we hypothesized that the more intense phototroph development in the area, as deduced from higher remotely sensed chlorophyll *a* concentrations in 2016, i.e., record warm year in the observational period, could lead to faster depletion of nutrients and, thus, an earlier shift into the post-bloom community stage. Taking into account the possible phenological shift toward early summer domination of flagellates in a warmer year, as well as a higher number of heterotrophic protists associated with the warmer domain in two evaluated summers, it is highly likely that climatic warming of this region will have an impact on energy transfer to higher trophic levels. Although generalized patterns could be elucidated, more information is needed to predict and understand how the changing Arctic will alter protistan communities and, thus, higher-order consumers.

Keywords: protists, hydrography, Atlantic water, Nordic Seas, Fram Strait

OPEN ACCESS

Edited by:
Houshuo Jiang, Woods Hole Oceanographic Institution, United States

Reviewed by:
Eva-Maria Nöthig, Alfred Wegener Institute Helmholtz Centre for Polar and Marine Research (AWI), Germany
Elizabeth Harvey, University of New Hampshire, United States

****Correspondence:***
Anna Maria Dąbrowska (Formerly Anna Maria Kubiszyn)
dabrowska@iopan.gda.pl

Specialty section:
This article was submitted to Marine Ecosystem Ecology, a section of the journal Frontiers in Marine Science

Received: *17 December 2019*
Accepted: *17 June 2020*
Published: *27 July 2020*

Citation:
Dąbrowska AM, Wiktor JM Jr, Merchel M and Wiktor JM (2020) Planktonic Protists of the Eastern Nordic Seas and the Fram Strait: Spatial Changes Related to Hydrography During Early Summer. Front. Mar. Sci. 7:557. doi: 10.3389/fmars.2020.00557

INTRODUCTION

The Nordic Seas (Greenland, Iceland, and Norwegian Seas) cover a large area south and north of the Arctic Circle. They play an important role in the climate dynamics of the northern hemisphere, as the major transport route for fresh water and heat between the North Atlantic and the Arctic Ocean. Compared with other areas at its latitudes, this area has the strongest positive sea surface and air temperature anomalies (Drange et al., 2005). Since the 1990s, the temperature and salinity of the

Atlantic water (AW) entering the Nordic Seas have rapidly increased (Holliday et al., 2008; Lauvset et al., 2018), leading to weaker ocean stratification and, in turn, intensified wintertime mixing (Latarius and Quadfasel, 2016; Bosse et al., 2018; Brakstad et al., 2019). The northward advection of warm AW not only affects the thermal conditions (Walczowski et al., 2012; Walczowski, 2014; Bosse et al., 2018) and the sea ice cover (e.g., Hansen et al., 2013) in the area but also determines the structure of pelagic communities (among others, Leu et al., 2011; Nöthig et al., 2015).

Planktonic protists represent the primary trophic level in marine ecosystems through which most of the biological material produced *via* photosynthesis (phototrophic protists) is further channeled through the food web (*inter alia*, by phagotrophic protists) to the higher-level consumers (Calbet, 2008). Due to their short lifetime and high reproductive rates, protists may be considered especially sensitive to environmental changes (Foissner and Hawksworth, 2009). Recent studies of the European Arctic protists have focused on how climate-driven alterations can drive modifications in the communities. So far, however, *in situ* determined relationships between environmental factors and protists are well-documented mainly for the West Spitsbergen fjords and the adjacent waters (e.g., Keck et al., 1999; Wiktor, 1999; Owrid et al., 2000; Piwosz et al., 2009, 2015; Hegseth and Tverberg, 2013; Kubiszyn et al., 2014, 2017; Smoła et al., 2017; Hegseth et al., 2019). Those studies have indicated several potential responses of protist communities to the ongoing environmental changes regarding shifts in species sizes toward pico- and nanoplanktonic organisms, promoting flagellates and reducing the share of microplanktonic primary producers during spring bloom period (Hegseth and Tverberg, 2013; Piwosz et al., 2015; Kubiszyn et al., 2017); functional structure with the prevalence of microplanktonic grazers (especially ciliates and dinoflagellates: Seuthe et al., 2011; Mayzaud et al., 2013; Kubiszyn et al., 2014); biogeographical patterns with the northward expansion of boreal species such as coccolithophores (Hegseth and Sundfjord, 2008; Dylmer et al., 2015); and phenology due to earlier ice breakup and onset of the phytoplankton bloom (Søreide et al., 2010; Hodal et al., 2012). However, more field observations are needed to ground reliable predictions of biotic/abiotic interactions in the age of the progressive Arctic warming. These data are also essential to support findings from previous primary production studies at the Atlantic–Arctic boundary based primarily on ocean color sensors and physically–biologically coupled models. For example, satellite remote sensing of chlorophyll *a* concentration in the Arctic is spatially and temporally limited and sensitive to cloudiness—a common feature of the spring–summer months. Thus, it needs to be supplemented and validated with a significant amount of *in situ* observations. This is all the more important that the recent studies revealed potential climate-generated changes in the productivity of the Atlantic–Arctic sector, including slight trends toward higher productivity in the eastern Fram Strait (Nöthig et al., 2015), a considerable influence of AW advected phytoplankton on the local *in situ* primary production (Vernet et al., 2019), and a shift in the summer months plankton composition from large diatoms toward *Phaeocystis pouchetii* and other small flagellates (e.g., Lalande et al., 2013; Nöthig et al., 2015).

The Arctic Experiment (AREX) cruises, performed during early summers 2015–2016, offered us the opportunity to sample protistan plankton and measure chlorophyll *a* in waters extended from the northern coasts of continental Norway to northwest Svalbard and covered the mainstream of the AW to the Arctic Ocean. This study attempts to provide a detailed insight into the Arctic planktonic protists of the open ocean at a time of warming northward water flow. The specific purposes of this study are (1) to describe the taxonomic composition and spatial distribution of the sizes and trophic (abundance) structures of summer (2015–2016) nano- and microplanktonic protists in the Nordic (Norwegian, Greenland) Seas and the Fram Strait and (2) to determine the distribution patterns of the communities from the aspect of hydrography, as deduced from *in situ* measurements. Due to the high spatial resolution of the research, as well as the investigation of both taxonomical and functional traits, the data presented herein represent an important contribution to the broadening of knowledge of the European Arctic communities.

MATERIALS AND METHODS

Hydrography of the Area

The study site was located in the eastern Nordic Seas and the Fram Strait (70.99°N to 78.84°N; 1.52°E to 19.90°E). This area is open to the North Atlantic in the south and the Arctic Ocean in the north and is connected to the Barents Sea to the east; thus, a cauldron is formed in this area in which various water masses mix and transform (Rudels et al., 2015). Briefly, AW enters the Nordic Seas *via* the northern limb of the North Atlantic Current through the Greenland–Scotland Ridge and travels northward *via* two branches of the Norwegian Atlantic Current (Hansen and Østerhus, 2000); the major pathways of the AW entering the Nordic Seas are illustrated in Walczowski (2010). The colder, less saline western branch (the Faroe branch) of the Norwegian Atlantic Current is topographically guided from the Iceland–Faroe Front toward the Fram Strait (Walczowski, 2013). However, only a part of this joint AW flow between 77°N and 77°30′N continues into the Arctic Ocean; a significant amount recirculates directly within the Fram Strait and returns south to the Nordic Seas (Schauer et al., 2004). The warmer, more saline eastern branch of the AW (the Shetland branch) enters the Nordic Seas through the Faroe–Shetland Channel and continues north along the Norwegian shelf edge as the Norwegian Atlantic Slope Current. After passing northern Norway, this current divides (Beszczynska-Moller et al., 2012). One branch of the AW enters the Barents Sea as the North Cape Current (the Barents Sea Branch) and flows into the Arctic Ocean. The second branch, the West Spitsbergen Current (WSC), continues northward along the continental slope. This flow is also called the eastern branch of the WSC or the core of the WSC; correspondingly, the continuation of the Faroe branch linked with the oceanic frontal system is called the western branch of the WSC (Walczowski, 2013). These two currents and hydrological fronts related to both branches of the WSC create the dynamic borders of the

region occupied by the AW—the Atlantic domain of the Nordic Seas. Both fronts separate the Atlantic-origin waters from the ambient, much colder and fresher water masses. Between Bear Island and Sørkapp, the frontal line is complicated because part of the AW circulates cyclonically and mixes with waters from the Barents Sea (Walczowski, 2013). In this region, the Bjørnøya Current (Barents Current) maintains the front on the right, shallow-water side. The current carrying the cold and less saline waters around the southern Spitsbergen tip, which originates mostly from the East Spitsbergen Current, is often called the Sørkapp Current or the South Cape Current, whereas the flow over the western Spitsbergen shelf is called the Coastal Current (Saloranta and Svendsen, 2001). On the West Spitsbergen Shelf, the freshwater input from the glaciers and rivers makes an additional hydrographic contribution.

Data Collection

Biological and environmental data were collected during two (2015–2016) summer expeditions on the *r/v* Oceania as part of the AREX program led by the Institute of Oceanology Polish Academy of Sciences (IO PAN; **Figure 1**). The sampling stations were distributed along several zonal sections, crossing the continental shelf break and extending toward the deep basin. On the eastern side, the stations were limited by the Barents Sea shelf break and the shelf area west and north of Svalbard, and they covered the eastward flow of AW to the Barents Sea. To the west, the transect crossed the Arctic Front. Sampling was performed at 35 stations in 2015 and 31 stations in 2016 starting from continental Norway and extending toward the north. In both years, the sampling dates were similar and occurred at approximately the same times (June 20, 2015–July 14, 2015; June 22, 2016–July 16, 2016); the coordinates of the stations and the dates of sample collection in individual summers are available online as **Supplementary Data 1**. The seawater sampling was preceded by measuring the temperature and salinity of the upper (50 m) water column using a conductivity, temperature, depth (CTD) probe (Sea-Bird 911+), equipped with *in situ* fluorometer sensor (Seapoint Sensors Inc.). Seawater samples for analysis of the protist community, as well as the chlorophyll *a*, were collected using 10-L Niskin bottles from depths of 5, 15, 25, 35, and 50 m.

Chlorophyll *a* Analysis

Water subsamples (250–400 ml) were analyzed in triplicate, as described by Holm-Hansen and Riemann (1978). The subsamples were filtered through Whatman GF/F filters, folded, wrapped in aluminum foil and immediately frozen at −80°C. Pigment extraction was performed in 10 ml of 90% acetone for 20–24 h in a cool (4°C), dark location no later than 4 months after sampling. The chlorophyll *a* concentrations (mg m^{-3}) were measured with a Trilogy fluorometer (Turner Designs, model no. 7200-000; calibrated with pure chlorophyll *a*, Sigma S6144) and averaged for the upper 50-m water column using a weighted average with weights adjusted to the thickness of the layer.

Protist Community Analysis

Protist samples were collected from discrete depths (5, 15, 25, 35, and 50 m) and immediately physically integrated into one sample (volume of 200 ml) representing the mean community structure (cells in m^3) for the upper 5–50-m water column. For this purpose, samples were mixed in proportion to the vertical extent of water they represent, according to the formulas given in Möller and Bernhard (1974). The integrated samples were fixed with an acidic Lugol's solution and, after 24 h, with glutaraldehyde (Edler and Elbrächter, 2010). The fixatives were added to final concentrations of 2 and 1%, respectively. Samples were qualitatively and quantitatively analyzed according to the protocols described by Utermöhl (1958) and modified by Edler (1979). For this purpose, 10–50-ml subsamples were poured into the sedimentation chambers for 24 h, and then the protists were counted under an inverted microscope equipped with phase and interference contrasts (Nikon Eclipse TE-300). Nanoplanktonic cells (3–20 μm) were counted at 400× magnification by moving the field of view along the length of three transverse transects. For the most numerous taxa, we counted up to 50 specimens, and the number of fields of view was considered individually. Taxa were identified to the lowest possible taxonomic level. The taxonomic system presented in the World Register of Marine Species (WoRMS) was considered. Except for the indeterminate flagellates (Flagellate indet.: classified as mono- and biflagellates, up to 13 μm), each taxon was classified as one major taxonomic group (class or phylum). Thereafter, they were classified into nanoplanktonic and microplanktonic fractions. As Lugol's fixative precluded feeding strategy identification, we use the data available in the literature and the Nordic Microalgae web base[1], which was developed and operated by the Swedish Meteorological and Hydrological Institute (SMHI), to distinguish taxa with different modes of nutrition. Because we could not determine the mixotrophs, taxa were categorized as phototrophs (for which chloroplasts can be reproduced in an individual) and heterotrophs, analogously to the classification provided in Kubiszyn et al. (2014, 2017). When the taxa could not be identified at the species level and the trophic mode was not evident, the contribution from phototrophy or heterotrophy could not be determined. Hence, these taxa were classified into a separate group of unknown feeding mode.

Statistical Analysis of the Community

We used the R statistical environment, version 3.4.3 (R Core Team, 2017), and the Vegan 2.4-3 library: Community Ecology Package for R (Oksanen et al., 2017) for all of the statistical analyses. All plots were created with the ggplot2 package in R (Wickham, 2016), except for the temperature and salinity data, which were analyzed and illustrated using MATLAB. To determine the differences in the variability in protist community composition (2-year abundance data), we used permutational NP-MANOVA (multivariate analysis of variance) (as implemented in the Adonis function in the Vegan package; Oksanen et al., 2017), which is a non-parametric permutational and multidimensional equivalent of ANOVA and uses the Bray–Curtis distance metric, which is interpreted as a dissimilarity measure. To determine the transition temperature for the communities expressing the largest intergroup to intragroup

[1]http://nordicmicroalgae.org

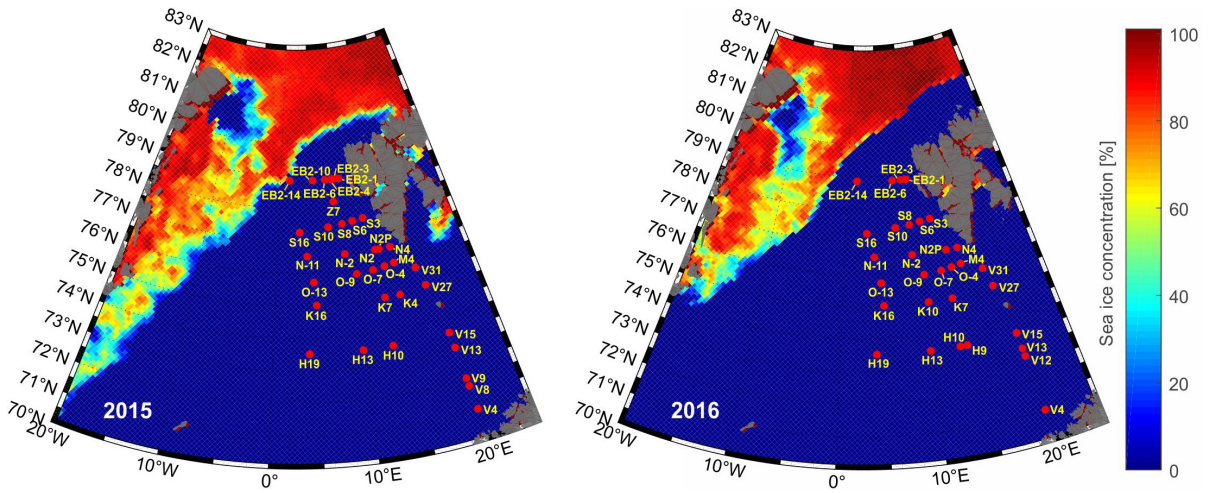

FIGURE 1 | The sampling station locations in the summers of 2015 and 2016. The satellite remote sensing sea ice concentration data (5-day median calculated for a sampling day closest to the ice) were obtained from https://nsidc.org/ (Cavalieri et al., 1996, updated yearly).

variance in the protist community structure, we evaluated the R^2 of the different splitting values ranging from 3 to 7°C with a 0.5°C step; the highest R^2 value marks the best splitting. Community types were determined based on their mutual similarity levels using k-means. The number of groups was estimated by applying the k-means procedure to the data with different *k*-values and determining the goodness of fit (homogeneity of the resulting groups). The *k*-value after which the goodness of fit decreased was selected.

RESULTS

Hydrography

The analysis of the CTD data from the upper (50 m) water layer demonstrated that the mean seawater temperature and salinity for the whole region were slightly higher in 2016 than in 2015 (+0.29°C and +0.045, respectively); the warmer conditions in 2016 were also reflected in the less sea ice concentrations in this area (**Figures 1**, **2A,B**). In both years, the maximum seawater temperature was observed close to northern Norway at an area represented by station V4 (7.47°C in 2015 and 7.80°C in 2016), while the minimum temperature was recorded south of Spitsbergen (at the sampling station V27–1.21°C in 2015 and 3.00°C in 2016). The spatial distributions of water temperature and salinity characterized the AW transformation during its northward flow. In the southern part of the investigated area (south of Bear Island, <74.5°N), the water was warmer and more saline, with mean temperatures of 6.17°C in 2015 and 5.91°C in 2016 and salinities of 34.97 in 2015 and 34.92 in 2016 compared with the values of 4.13 and 4.88°C and 34.69 and 34.87 in the north (>74.5°N) in 2015 and 2016, respectively. Regarding the longitudinal aspect, the water temperature increased from west to east, except the West Spitsbergen Shelf (**Figure 2A**), where colder and less saline waters were observed, especially in 2015. The higher mean temperature and salinity along the western coast of Spitsbergen in 2016 (+1.5°C and +0.3, respectively) likely resulted from the weaker on-shelf advection of the Sørkapp Current, carrying cold and relatively fresh waters from the Barents Sea.

Planktonic Protists

Qualitative Composition

During both campaigns (35 samples in 2015 and 31 in 2016), 153 taxa were detected (109 in 2015, 125 in 2016), and most of them were determined to the species level (**Table 1**; a complete list of taxa is available online as **Supplementary Data 2**). Regarding taxonomic composition, plankton consisted of 12 major groups of which Bacillariophyceae were the most biodiverse (39.87% of all taxa), followed by Dinophyceae (32.03%) and Ciliophora (14.38%). Among the other groups, only Prymnesiophyceae exceeded 5% (**Table 1**). Indeterminate mono- and biflagellates (up to 13 μm) were also found.

Chlorophyll *a* and Fluorescence

We observed substantial spatial variation in the chlorophyll *a* concentrations in both summers (**Figure 3A**). In 2015, the highest chlorophyll values occurred in the eastern and western frontal zones at stations N-11 and V31 (4.67 mg m^{-3} and 3.18 mg m^{-3}, respectively). Relatively high values (>1.24 mg m^{-3}) were noted in the area represented by station M4, as well as the O section and partially (N-11, N-2, N2) the N section. Distinctly low values (0.06–0.79 mg m^{-3}) were observed along the S and EB2 profiles, as well as at stations N2P and N4.

In 2016, the chlorophyll *a* concentrations ranged from 0.23 mg m^{-3} (EB2-1) to 2.26 mg m^{-3} (V31). Generally, high values were observed in the regions of the H, K, and O sections and stations V27 and M4 (72.5–76°N) and in the north throughout the S section. Similar to 2015, low values occurred along the EB2 section.

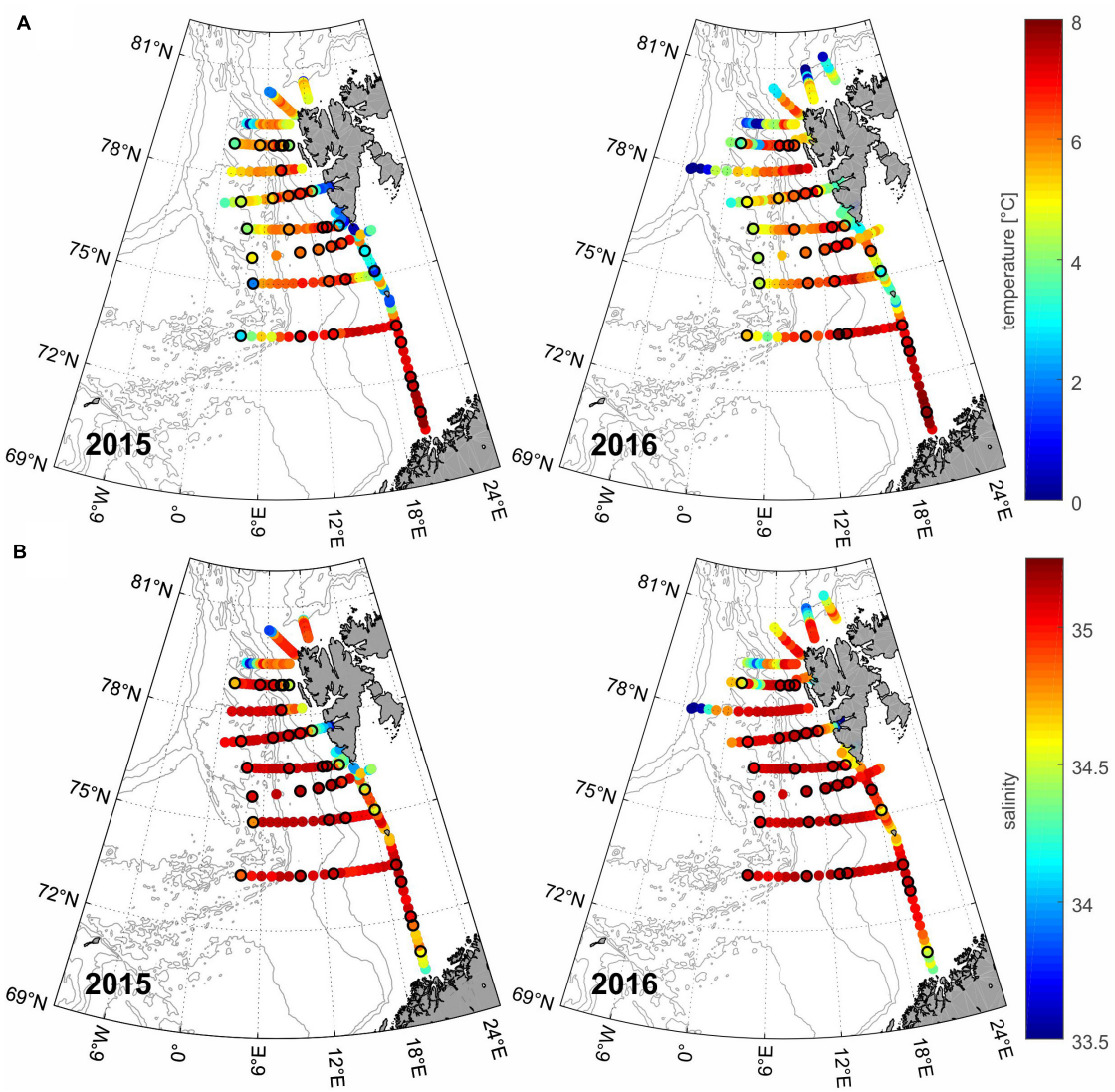

FIGURE 2 | Temperature [°C] **(A)** and salinity **(B)** of seawater (values averaged for the upper 50-m water column) in the area in 2015 and 2016. Colored circles correspond to the conductivity, temperature, depth (CTD) stations of the Arctic Experiment (AREX) cruises; circles with additional black frame indicate the plankton stations.

The *in situ* chlorophyll *a* fluorescence generally corresponded with the values of extracted chlorophyll *a* concentrations (**Supplementary Data 3**). In 2015, the deepest (>35 m) fluorescence maxima were observed in the area represented by stations O-7, N-11, V31, and K16, whereas in 2016, at V27, V15, N2P, and N-2. In 2015, the shallowest (<15 m) chlorophyll *a* maxima were found at stations V13 and V27, while in 2016, they were found at N4, H13, K7, O-7, and V13.

Cell Numbers and Species Distribution

Considering the entire investigated period, there were no significant differences in protist community composition (abundance data) with respect to latitude (NP-MANOVA, $R^2 = 0.021$, $p = 0.085$) even though the communities displayed different patterns of latitudinal variability in both years (interaction term between latitude and year in NP-MANOVA, $R^2 = 0.074$, $p = 0.001$). The largest intergroup to intragroup protist community structure variance occurred at the 6°C threshold (**Figure 4**).

In both summers, the protistan communities, dominated by nanoplankton, were characterized by considerable spatial variability in the qualitative and quantitative (size and trophic) structures (**Figures 3B**, **5A**). While the share of heterotrophs was higher in the warmer domain in both analyzed years, the contribution of phototrophs varied inter-annually (2015 vs 2016). In 2015, phototrophs were more abundant in warmer waters mainly due to numerous (mostly microplanktonic) Bacillariophyceae, while in 2016—in colder waters primarily because of high numbers of nanoplanktonic Prymnesiophyceae (**Figures 5B,C**).

TABLE 1 | The number of taxa of individual protist groups observed in the study according to the different taxonomic classification levels.

Group	Number of taxa in the 2-year dataset	Number of taxa in an individual year	Level of taxonomic classification		
			Species	Genus	Higher taxonomic unit
Bacillariophyceae	61	41 (47)	29 (27)	10 (20)	2 (x)
Chlorophyta	2	2 (2)	1 (1)	1(1)	x (x)
Choanoflagellatea	2	2 (1)	2 (1)	x (x)	x (x)
Chrysophyceae	1	1 (1)	1 (1)	x (x)	x (x)
Ciliophora	22	15 (19)	10 (15)	5 (3)	x (1)
Cryptophyceae	4	4 (3)	1 (1)	1 (1)	2 (1)
Dictyochophyceae	1	1 (1)	1 (1)	x (x)	x (x)
Dinophyceae	49	35 (42)	22 (25)	9 (13)	4 (4)
Katablepharidaceae	1	1 (1)	1 (1)	x (x)	x (x)
Prasinophyceae	1	1 (1)	x (x)	1 (1)	x (x)
Prymnesiophyceae	8	6 (6)	4 (3)	1 (1)	1 (2)
Telonemea	1	x (1)	x (1)	x (x)	x (x)
Total number of taxa	153	109 (125)	72 (77)	28 (40)	9 (8)

The values before the parentheses refer to 2015, while those in parentheses refer to 2016; "x" – no record.

In 2015, the highest abundances were observed at the sampling stations V31 (1.14×10^9 cells m^{-3}) and N-11 (1.13×10^9 cells m^{-3}) mainly due to the numerous indeterminate biflagellates (3–7 μm) of unknown feeding mode (96.84%) and phototrophic *P. pouchetii* (97.78%), respectively (**Figure 3B**; the percent contributions of all taxa to the total abundance at individual sampling stations are available online as **Supplementary Data 2**). The relatively high abundances ($>2.70 \times 10^8$ cells m^{-3}) were also noted in descending order in the regions represented by stations V4, H10, V27, N2P, M4, S10, and K16 (**Figure 3B**). At areas of sampling stations V4, H10, N2P, and M4, the total abundance was dominated by Bacillariophyceae (77.66–97.76%; **Figure 6**), especially *Pseudo-nitzschia* cf. *pseudodelicatissima*, *Thalassiosira* spp. of size class 10–30 μm, and *Eucampia groenlandica*. At station V27, the community was predominated by *P. pouchetii* (79.78% of the overall abundance), whereas further north at station S10, the community was composed of Dinophyceae (mainly *Gymnodinium* sp. 5–10 μm, *Prorocentrum minimum*, and indeterminate thecate species of size 10–20 μm), and Bacillariophyceae (*Pseudo-nitzschia* cf. *pseudodelicatissima*, *Thalassiosira* spp. 10–20 μm) (approximately 36% of each group). In turn, at station K16, the dominant group was Choanoflagellatea (*Monosiga marina*; 71.11%).

In 2016, the highest abundances were recorded at stations S16 (0.83×10^9 cells m^{-3}), O-9 (0.76×10^9 cells m^{-3}), and EB2-14 (0.69×10^9 cells m^{-3}) mainly due to the high share (71.24–91.65%) of *P. pouchetii* (**Figure 3B**; **Supplementary Data 2**). Relatively abundant communities ($>0.31 \times 10^9$ cells m^{-3}) were also found along the Barents Sea Opening at stations V12, V27, and V31, as well as in the eastern Fram Strait (S10). At V12, the community was primarily composed of prymnesiophytes (57.06%; mainly *Chrysochromulina* sp.) and Dinophyceae (31.19%; mostly *Gymnodinium* sp. and Peridiniales indet., both of size 10–20 μm). At V27, indeterminate flagellates predominated (43.17%; especially biflagellates 3–7 μm), Prymnesiophyceae (35.42%; *P. pouchetii*), and Dinophyceae (13.28%; mostly *Gymnodinium* sp. 10–20 μm, *Pronoctiluca pelagica*, *Gymnodinium wulffii*, and *Gymnodinium* sp. 5–10 μm). The abundance of protists at S10 mainly consisted of indeterminate biflagellates (3–7 μm; 49.55%) and *P. pouchetii* (36.71%). At V31, high protist numbers constituted mainly of Bacillariophyceae (54.02%; especially *Thalassiosira* sp. 10–20 μm), *P. pouchetii* (25.85%), and Dinophyceae (17.20%; primarily *Gymnodinium galeatum*, *Gymnodinium* spp. 5–20 μm, and Peridiniales indet. 10–20 μm).

Community Types

Based on 2-year data analysis, we distinguished four types of summer protist communities in the investigated area (**Figure 6A**). The community predominated by Bacillariophyceae, as well as composed of a wide range of flagellated forms (Dinophyceae, Cryptophyceae, Flagellate indet.) and, to a lesser extent, Bacillariophyceae, was recorded mainly in warmer waters (>6°C; **Figures 6B,C**). In turn, the community formed primarily by Prymnesiophyceae (mainly colonial *P. pouchetii*) and those characterized by the dominance of indeterminate nanoplanktonic flagellates was mostly associated with colder waters.

DISCUSSION

Hydrography

Since 1987, oceanographic measurements during the open ocean part of *r/v* Oceania cruise under the AREX program have been collected at the stations presented herein. Collected time series of water properties were studied in the aspect of long-term changes in the ocean climate in the Nordic Seas and the Fram Strait (e.g., Jankowski, 1991; Druet, 1993; Piechura et al., 2002; Schauer et al., 2008; Walczowski and Piechura, 2011; Beszczynska-Moller et al.,

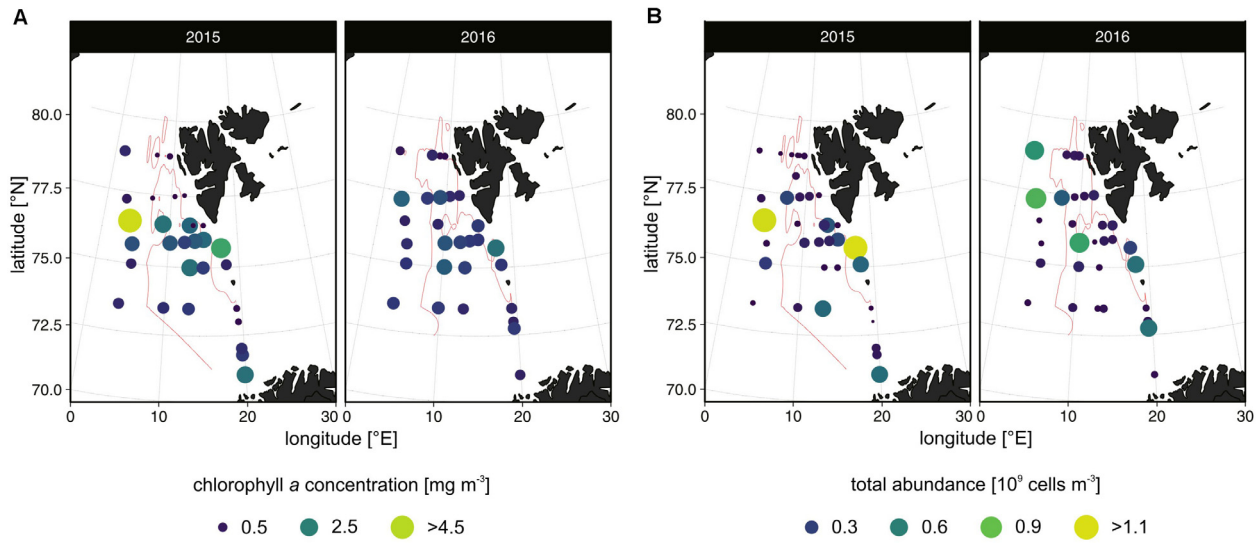

FIGURE 3 | The extracted chlorophyll *a* concentrations [mg m^{-3}] **(A)** and total protist abundance [10^9 cells m^{-3}] **(B)** at the stations in the summers of 2015 and 2016. Only values higher than 0.5 mg m^{-3} and 0.3 × 10^9 cells m^{-3} are included in the legend. The 6°C isotherm is marked with the solid line (also in **Figure 6C**).

2012; Walczowski et al., 2012, 2017). Due to its time resolution, this series is considered as representative for temporal variability of the AW properties in the area. On its basis, it can be assumed that the oceanographic conditions in both summers were in line with the long-term (1997–2016) means (Walczowski et al., 2017) and were consistent with the ongoing Arctic warming trend (Huang et al., 2017).

In both summers, the water masses in the area were characterized by the comparable meridional extent of warm and saline AW and location of the Arctic Front (Walczowski et al., 2017). The major hydrographical feature that distinguished both years was a stronger inflow of colder and less saline Arctic waters from the Barents Sea to the area in 2015, which shaped the hydrographic patterns along the West Spitsbergen Shelf and in waters between Bear Island and Sørkapp. Due to this input, the mean AW temperature throughout the whole studied region was slightly lower than that in 2016, when the recirculation of warmer AW in the northern Fram Strait was recorded. However, if the northern (above 74.5°N) and southern (below 74.5°N) parts are considered independently, the southern region was warmer in 2015. A more detailed description of the hydrological and physical characteristics of the Nordic Seas and the Fram Strait based on simultaneously performed *r/v* Oceania-based measurements is presented in Walczowski et al. (2017).

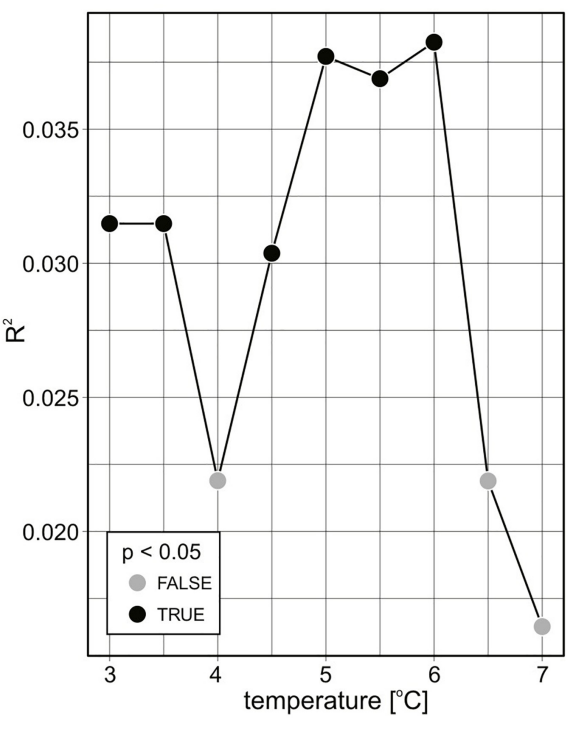

FIGURE 4 | Differences in protist community composition variability (2-year abundance data) in various seawater temperatures [°C] expressed using NP-MANOVA R^2 and *p*-values.

Protistan Plankton Composition

The 153 planktonic protist taxa observed during the present study corresponded to previous investigations in the European Arctic (Markowski and Wiktor, 1998; Owrid et al., 2000). The observed taxa were characteristic of summer Atlantic communities (Weslawski et al., 1993; Hasle and Heimdal, 1998; Hegseth and Sundfjord, 2008), which are commonly observed in both shelf and open-ocean environments over a wide latitudinal range from polar to temperate waters (e.g., Halldal and Halldal, 1973; Eilertsen et al., 1989; Keck et al., 1999; Wiktor and Wojciechowska, 2005; Piwosz et al., 2009; Poulin et al., 2011; Kubiszyn et al., 2014,

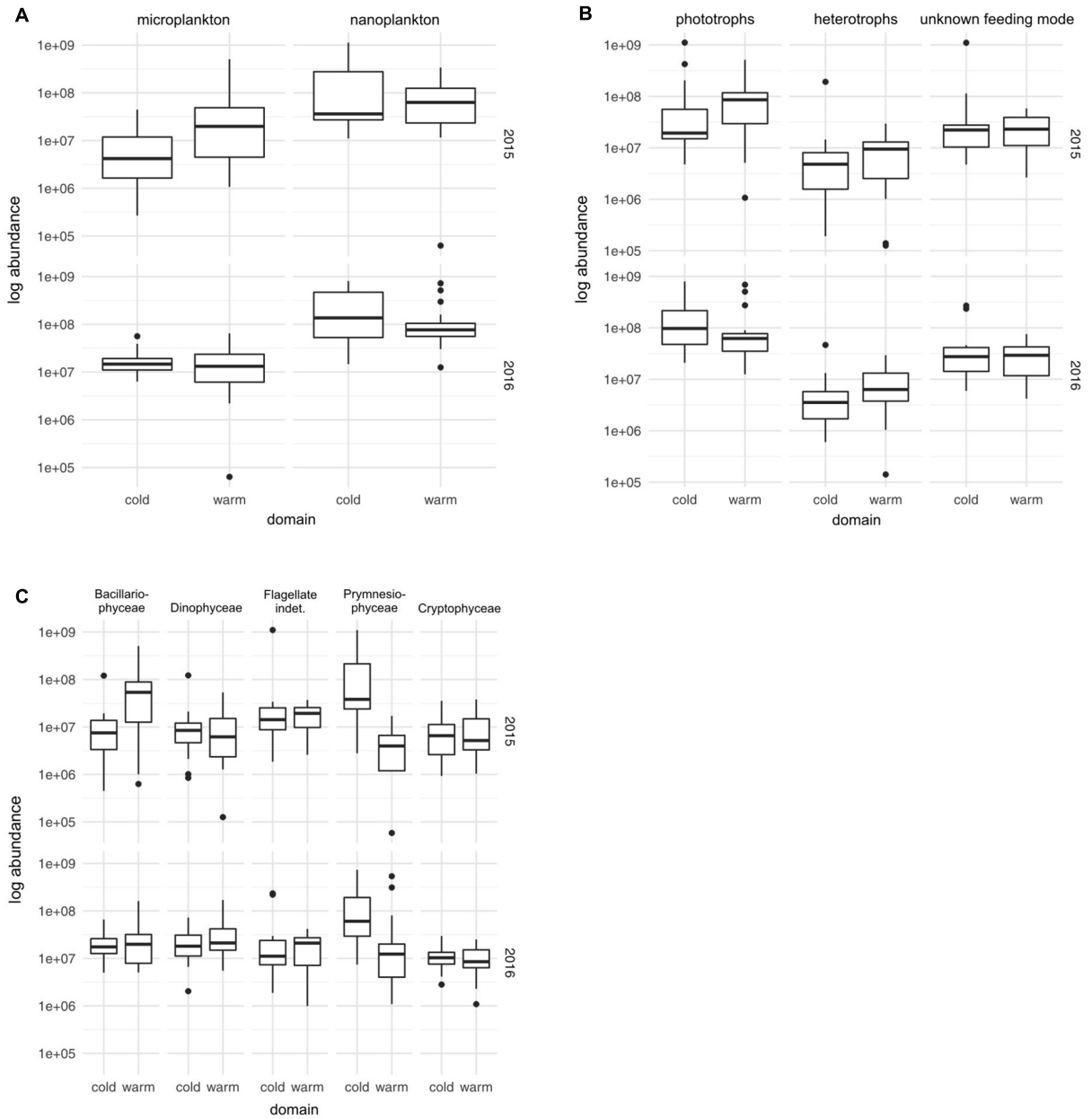

FIGURE 5 | Box plots of the abundance (a log scale) of nanoplanktonic and microplanktonic protists **(A)**, of phototrophs, heterotrophs, and protists with unknown feeding mode **(B)** and of the major protist groups (>5% of the total protist abundance) **(C)** recorded in the colder and warmer water domains (at a 6°C threshold) in the summers of 2015 and 2016.

2017; Piquet et al., 2015). The total protist biodiversity, as well as the biodiversity of the individual groups, was comparable between the two summers but was slightly higher in 2016.

Since our study covered waters through seven degrees of latitude (>700 km), we could expect that different physical and biological processes taking place at every location, through photosynthesis and the interactions of the food web components, will cause large fluctuations in protists' structure. The results showed that the investigated area was indeed characterized by high spatial variability of most of the parameters (chlorophyll *a*, protist abundance, taxonomic composition) probably due to ever-changing environmental conditions, as light and nutrients change, and hydrographic mesoscale processes.

Similar to previous protist studies in the West Spitsbergen area (e.g., Hirche et al., 1991; Owrid et al., 2000; Seuthe et al., 2011; Piwosz et al., 2015), the communities were dominated mainly by nanoplanktonic phototrophs, which, combined with eukaryotic picoplankton (Iversen and Seuthe, 2011), are one

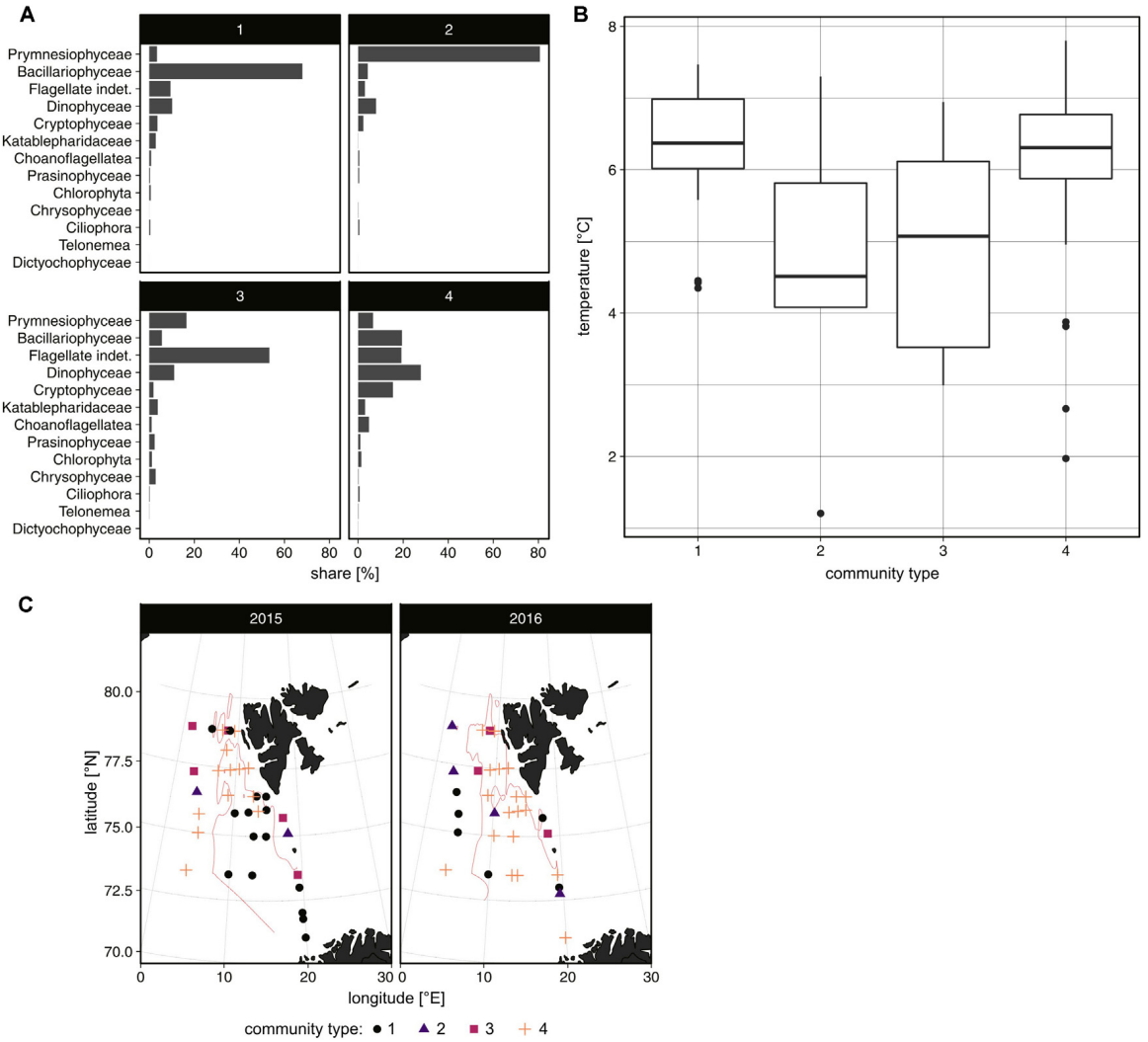

FIGURE 6 | The share [%] of protist groups in individual community types determined by k-means analysis **(A)**, the temperature range in their areas of occurrence **(B)** (both based on 2-year abundance data), and their spatial distribution in the area in the summers of 2015 and 2016 **(C)**.

of the most important contributors to primary production in the eastern Fram Strait (Eilertsen et al., 1989). Based on our data, the highest protist abundances were observed along the frontal zones, which are regions of strong density gradients where the physical and chemical properties of the surface mixed layer enhance protist biomass and productivity (Dylmer et al., 2015). On the eastern side, the hydrographic front was visible on the shelf, separating warm AW carried by the WSC from cold and freshened waters of the Sørkapp Current, whereas the Arctic Front was located west of the WSC at about 7°E (Walczowski et al., 2017). In waters supplied by the Bjørnøya and Sørkapp Currents, exceptionally high protist numbers [mostly the colonies of *P. pouchetii*, as well as mono- and biflagellates of indeterminate taxonomic affinity, which, considering the results of Piwosz et al. (2015), are most probably the flagellated solitary form of *P. pouchetii*] were likely caused by an import of cells together with the outflow of water masses from the Barents Sea and/or massive local growth on "new nutrients"; analogous observations were documented in June 1991 by Markowski and Wiktor (1998) and Owrid et al. (2000).

Implications of Hydrography on Protistan Plankton

While physical processes associated with AW inflow into the Arctic have been the subject of an extensive study, the implications of water hydrography for planktonic protists remain poorly examined (Vernet et al., 2019). In particular, studies on *in situ* high-spatial resolution changes in the community structure from Norway's coast into the Arctic Ocean are especially rare. One of the main problems of plankton research in this area is logistical difficulties with sampling, which are caused by large waves and strong oceanic currents. Considering the frequent incompleteness in plankton sampling

during previous open-ocean AREX cruises, mostly resulting from harsh weather conditions, we state that the protist sample collection presented herein, which practically covers the entire poleward flow of AW in the eastern Nordic Seas and the Fram Strait, is a very good result, which, to the best of our knowledge, has no equivalent in previous protistan *in situ* studies in the area.

Contrary to the expectations, there were no significant differences in protist community composition (abundance data) in terms of latitude (70.99 to 78.84°N); less than 10% of the variability was explained by the north–south extension (based on NP-MANOVA analyses). Our initial assumptions were supported, *inter alia*, by the results of Monti and Minocci (2013), who showed a meridional increase in both the abundance and number of microzooplankton taxa in the waters from northern continental Norway to Svalbard (65°N–78°N). This result, however, was more likely to be obtained because the study was limited to a certain plankton size class (20–200 μm; represented by heterotrophic dinoflagellates, foraminifers, ciliates, micrometazoans) collected along a longitudinally oriented (approximately 7–15°E) transect, where the hydrographic conditions gradient was stronger and more pronounced. In our case, an interplay (mixing and transformation) of various water masses most likely affected protist communities to the degree that prevented the observation of similar geographical patterns.

Interestingly, the results of further MANOVA (NP-MANOVA) between the protist structure and the seawater temperature revealed the division of the communities into two domains related to warmer and colder waters at a 6°C threshold. The communities in the colder water (<6°C) domain were represented primarily by Prymnesiophyceae in both summers, especially the colonial stage of *P. pouchetii* and, presumably, its motile stage (biflagellates indet. 3–7 μm). The quantitative importance of *P. pouchetii*, which is considered a marginal ice species (Gradinger and Baumann, 1991), was previously shown in the North Atlantic and Arctic waters by Owrid et al. (2000); Hegseth and Sundfjord (2008), and Degerlund and Eilertsen (2010), among others. It is commonly believed that the increase in *P. pouchetii* (and other small pico- and nanoplankton species) in the last two decades is directly related to the warm anomaly in the European Arctic (Nöthig et al., 2015). However, it should be noted that high abundances of this species have also been reported in the Fram Strait during the 1980s–1990s (i.e., before warming intensification; Smith et al., 1987). Thus, *Phaeocystis* blooms are not a new feature in this region, but their prevalence certainly deserves further studies. Due to the low bioavailability (cell size is in the lower range of optimum filtration efficiency) and low nutritive value of this species for calanoid copepods (Huntley et al., 1987), investigations on trophic interactions between *Phaeocystis* and zooplankton in the warming Arctic are particularly needed.

Contrary to the colder domain, with the domination of *Phaeocystis* in the two evaluated summers, we observed clear inter-annual differences in community composition of the warmer (>6°C) domain. In 2015, in the largest part of the investigated area (up to the southern tip of Spitsbergen), the protist community was dominated by Bacillariophyceae, while Dinophyceae, Cryptophyceae, and indeterminate nanoflagellates predominated more northward (to the west of Spitsbergen). In turn, in 2016, flagellates dominated the whole domain; a similar situation was reported in the summer of 2012 (Gluchowska et al., 2017).

Does Only Temperature Matter in Differentiating Summer Protist Community?

In our opinion, the aforementioned inter-annual differences in the summer protist community composition in the warmer water domain may be closely related to the variations in the phenology within the growing season. Because the summer protistan community structure depends on processes taking place during the spring bloom (*inter alia*, vertical mixing process, an influx of nutrients to the photic zone, number and efficiency of resting spores and resting cell germination, species competition, and mortality ratio), the observed differences could be predetermined a few months earlier and lasted until summer. Due to the lack of biological *in situ* data allowing us to track the initiation and progression of the spring bloom, we analyzed the satellite-derived 8-day and monthly (March–August) averaged chlorophyll *a* (a proxy for phototrophic protist biomass) satellite grid images derived from the MODIS (Aqua) satellite (resolution of 4 km) for the area between latitudes 70, 80°N, and longitudes 0, 20°E, which were extracted from the NASA's OceanColor Web[2] (data not shown; access date: November 15, 2019). High temporal and spatial resolutions selected for the satellite-based datasets were chosen to minimize the effect of the common heavy cloudy conditions over the Nordic Seas in the summertime. According to these data, the onset of the spring bloom in both investigated years took place at a similar time, i.e., in the first half of April. Driven by the light regime, the bloom started north of Norway (at a latitude of approximately 70°N) and gradually shifted northward with the seasonal lengthening of daylight at the increasingly higher latitudes. Comparing both analyzed years, the remotely sensed chlorophyll *a* concentrations in 2016, when record-high air and sea surface temperatures were observed (González-Pola et al., 2018), were noticeably higher throughout the growing season (spring–summer) in most of the examined area. Considering the recent findings of Mayot et al. (2020), different phytoplankton bloom phenology, driven by the various springtime Arctic ice flux and salinity-based water column stratification, may have substantial consequences on the timing and quantity of biological carbon pump and the production of higher trophic levels. Although we cannot say what hydrographic and atmospheric conditions prevailed in the studied area in the springs of 2015 and 2016 [except that the ice export through the Fram Strait was low in both years; Mayot et al. (2020)], it seems likely that the generally warmer conditions may benefit more intense

[2]http://oceancolour.gsfc.nasa.gov/

phototrophs development, leading to faster depletion of nutrients and, thus, an earlier shift into the post-bloom community stage, which is indicated by the domination of flagellates in the warmer domain (observed in this study). Additionally, it cannot be ruled out that the structure of different taxonomic communities was also a result of the species transport with the inflow of water from distant areas to the north and south of the actual study site and corresponds to the phenology in the places where these water masses originated. However, T-S diagrams for both summers (not shown) did not indicate considerable variability in AW that could support different seeding population scenarios.

We are also mindful that the protist composition, as constituted by the interaction of photo- and heterotrophs, may also be affected by different grazing pressures by micro- and mesozooplankton [as demonstrated, among others, in Hirche et al. (1991) and Owrid et al. (2000)]. Due to rapid doubling rates of microzooplankton (especially ciliates and dinoflagellates), as well as their adaptation to utilize particles one order of magnitude smaller (Sheldon et al., 1972), it is assumed that microzooplankton has more of direct control on protist loss rates than mesozooplankton grazing (Friedland et al., 2016). Nevertheless, mesozooplankton, by having a significant impact on microzooplankton *via* predation, can also disrupt the balance between the gain and loss of protist abundances and produce rapid changes in community dynamics (Behrenfeld and Boss, 2014). Although we did not observe substantial variability in microplanktonic heterotrophic protist abundance within the investigated summers (mostly associated with the warmer domain), we cannot exclude the possibility that these differences would be visible after considering the protists with indeterminate feeding modes (a few taxa of the *Gymnodinium* and *Gyrodinium* genera and the Peridiniales order), as well as mixotrophs, widespread in the marine plankton (Stoecker et al., 2017). Interestingly, the study by Bałazy (2019) presented different copepodite structures of *Calanus* spp. (important protist consumers) in a warm (Atlantified) Kongsfjorden in the summers of 2015 and 2016. In 2016, the *Calanus* population throughout the examined period (early July–mid-August) was predominated by young stages. According to the author, this could have been caused by the influx of juvenile forms with the advection of AW to the shelf and may have suggested very good conditions for zooplankton reproduction and development in the West Spitsbergen area in the summer of 2016. A minor role of Bacillariophyceae in the warmer waters in summer 2016, as well as more numerous zooplankton fecal pellets observed at the time, somehow speaks to the validity of this assumption. Although this result may indicate potentially differentiating impacts on protists by zooplankters, the lack of open-ocean mesozooplankton data prevents us from testing this scenario. Noteworthy, the earlier mesoplankton studies (AREX 2001–2014) suggested that its community structure is subjected to strong year-to-year fluctuations, which are most likely related to the natural 6-year cycle of WSC hydrographical property changes described in Walczowski et al. (2012) (Sławomir Kwaśniewski, personal communication, November 19, 2019). Hence, differences in protistan plankton structure described herein may be associated with this cycle and the aforementioned physical/biological coupling. Further investigations are needed to distinguish whether they are caused by natural variability or climate change in the Nordic Seas and the Fram Strait.

Recommendations for Future Studies

Although we observed relationships between protist distribution and seawater temperature, our results indicate that other factors alone or combined additionally affect the summer communities in the area. To better understand these dependencies, future protist studies should relate to mesoscale phenomena, be supplemented by at least mesozooplankton data and water chemistry, and have an equivalent in springtime. Because recent satellite-derived and bio-optical *in situ* surveys suggested rapid expansion of temperate phototrophic protists (mainly coccolithophores) in the Arctic (e.g., Dylmer et al., 2015; Neukermans et al., 2018; Kowalczuk et al., 2019), it would also be reasonable to confirm these suppositions by microscopic studies. Our research does not support these findings.

CONCLUDING REMARKS AND OUTLOOK

Several interesting conclusions have arisen from this study, indicating significant variability in protist community structures of the studied area in the successive summers, most likely due to different phenologies, supporting the importance of *in situ* studies to determine potential future ecosystem shifts in response to climate change.

Specifically:

(1) differentiation of the protistan plankton structure into two separated domains at the 6°C threshold
(2) domination of *Phaeocystis* (colonial and flagellated cells) in the colder domain in two evaluated summers
(3) higher abundance of heterotrophic protists in the warmer domain in both investigated years
(4) the possible earlier shift of the communities into the post-bloom stage in the warmer 2016, indicated by the domination of flagellates in the early summer

Given the recently demonstrated beneficial effects of warming on picoeukaryotes including *Micromonas pusilla* (Hoppe et al., 2018) and bacteria (Maranger et al., 2015), as well as our findings, we hypothesize that the further climate change of the European Arctic seas (especially the Atlantic domain) will favor the dominance of small, mobile protists. Restructuring of communities toward pico- and nanoplankton will likely lengthen the carbon pathway through the food web by increasing the significance of heterotrophic protists and, thus, will result in increased microbial loop activity. Such a scenario has been already speculated by Vernet et al. (2017) based on the model results. Importantly, these protists due to their small size may not be efficiently utilized by mesozooplankton (Levinsen et al., 2000).

Therefore, the predicted changes in protistan plankton community composition, with the increasing role of microplanktonic grazers and detritus as a source of carbon to higher trophic levels (both pelagic and benthic), may lead to partial energy dissipation in the marine trophic network.

DATA AVAILABILITY STATEMENT

All datasets generated for this study are included in the article/**Supplementary Material**.

AUTHOR CONTRIBUTIONS

AD contributed to obtaining the funding for the research, project coordination, designing the field study, organizing and leading the field investigation, sample collection, analysis of chlorophyll *a* and protist communities, data processing, and manuscript writing. JMiW contributed to statistical data processing/analysis and to the statistical part of the manuscript. MM contributed to temperature and salinity measurements, hydrography data treatment/visualization and to the hydrographic part of the manuscript. JMaW contributed to designing the field study, substantive care over the project implementation, and manuscript editing. All authors contributed to the article and approved the submitted version.

FUNDING

The presented research was carried out as part of the implementation of the IO PAN statutory task (I.5.7) and with financial support from the Ministry of Science and Higher Education (AREX Project, 3547/Norway/2016/2) and the National Science Center (Let's Sea Project, 2015/17/N/NZ8/01642; DWINS Project, 2016/21/N/ST10/02920).

ACKNOWLEDGMENTS

We would like to thank two reviewers and the editor HJ for their thorough review of the manuscript and constructive comments. Also, we wish to express our sincere gratitude to Prof. Waldemar Walczowski (IO PAN) for substantial assistance with the hydrographic data discussion. The assistance of the crew of *r/v* "Oceania," particularly of Roman Obuchowski and Krzysztof Rosiński, specialists in research equipment, and of the scientific staff from the Institute of Oceanology, Polish Academy of Sciences, Sopot, especially Dr. Przemysław Makuch, during the cruise is very much appreciated.

SUPPLEMENTARY MATERIAL

The Supplementary Material for this article can be found online at: https://www.frontiersin.org/articles/10.3389/fmars.2020.00557/full#supplementary-material

REFERENCES

Bałazy, K. (2019). *The Phenology of Key Calanus Species in the Context of Food Demand of Little Auk (Alle Alle) Nesting on Spitsbergen*. PhD Dissertation, Institute of Oceanology Polish Academy of Sciences Sopot.

Behrenfeld, M. J., and Boss, E. S. (2014). Resurrecting the ecological underpinnings of Ocean plankton blooms. *Annu. Rev. Mar. Sci.* 6, 167–194. doi: 10.1146/annurev-marine-052913-021325

Beszczynska-Moller, A., Fahrbach, E., Schauer, U., and Hansen, E. (2012). Variability in Atlantic water temperature and transport at the entrance to the Arctic Ocean, 1997-2010. *ICES J. Mar. Sci.* 69, 852–863. doi: 10.1093/icesjms/fss056

Bosse, A., Fer, I., Søiland, H., and Rossby, T. (2018). Atlantic water transformation along its poleward pathway across the Nordic Seas. *J. Geophys. Res. Oceans* 123, 6428–6448. doi: 10.1029/2018JC014147

Brakstad, A., Våge, K., Håvik, L., and Moore, G. W. K. (2019). Water mass transformation in the Greenland Sea during the period 1986–2016. *J. Phys. Oceanogr.* 49, 121–140. doi: 10.1175/JPO-D-17-0273.1

Calbet, A. (2008). The trophic roles of microzooplankton in marine systems. *ICES J. Mar. Sci.* 65, 325–331. doi: 10.1093/icesjms/fsn013

Cavalieri, D., Parkinson, C., Gloersen, P., and Zwally, H. J. (1996). *Sea Ice Concentrations from Nimbus-7 SMMR and DMSP SSM/I-SSMIS Passive Microwave Data. 19782007. Digital Media. Boulder, CO: National Aeronautics and Space Administration Distributed Active Archive Center at the National Snow and Ice Data Center*. Avaliable at: http://nsidc.org/data/nsidc-0051.html (Accessed 8 April 2020).

Degerlund, M., and Eilertsen, H. C. (2010). Main species characteristics of phytoplankton spring blooms in NE Atlantic and Arctic waters (68–80° N). *Estuaries Coasts* 33, 242–269. doi: 10.1007/s12237-009-9167-7

Drange, H., Dokken, T., Furevik, T., Gerdes, R., Berger, W., Nesje, A., et al. (2005). "The Nordic seas: an overview," in *The Nordic Seas: An Integrated Perspective*, eds H. Drange, T. Dokken, T. Furevik, R. Gerdes, and W. Berger (Washington DC: AGU Monograph 158), 1–10. doi: 10.1029/158gm02

Druet, C. (1993). Polar marine research (2). The results of Polish oceanographic investigations focused on interannual variability of the Greenland sea energoactive zones. Stud. *Mater. Oceanol.* 65, 3–223.

Dylmer, C. V., Giraudeau, J., Hanquiez, V., and Husum, K. (2015). The coccolithophores *Emiliania huxleyi* and *Coccolithus pelagicus*: extant populations from the Norwegian–Iceland seas and Fram Strait. *Deep Sea Res. Part I Oceanogr. Res. Pap.* 98, 1–9. doi: 10.1016/j.dsr.2014.11.012

Edler, L. (1979). Recommendations on methods for marine biological studies in the Baltic sea, Phytoplankton and chlorophyll. *Balt Mar. Biol. Publ.* 5, 1–38.

Edler, L., and Elbrächter, M. (2010). The Utermöhl method for quantitative phytoplankton analysis. Microscopic and molecular methods for quantitative phytoplankton analysis. Manuals and guides 55. *Intergov. Oceanogr. Commun.* 55, 13–20.

Eilertsen, H. C., Tande, K. S., and Taasen, J. P. (1989). Vertical distributions of primary production and grazing by *Calanus glacialis* Jaschnov and *C. hyperboreus* Krøyer in Arctic Waters (Barents Sea). *Polar Biol.* 9, 253–260. doi: 10.1007/bf00263773

Foissner, W., and Hawksworth, D. L. (eds) (2009). "Protist Diversity and Geographical Distribution," in *Topics in Biodiversity and Conservation*. Dordrecht: Springer.

Friedland, K. D., Record, N. R., Asch, R. G., Kristiansen, T., Saba, V. S., Drinkwater, K. F., et al. (2016). Seasonal phytoplankton blooms in the North Atlantic linked to the overwintering strategies of copepods. *Elem. Sci. Anth.* 4:000099. doi: 10.12952/journal.elementa.000099

Gluchowska, M., Trudnowska, E., Goszczko, I., Kubiszyn, A. M., Blachowiak-Samolyk, K., Walczowski, W., et al. (2017). Variations in the structural and functional diversity of zooplankton over vertical and horizontal environmental

gradients en route to the Arctic Ocean through the Fram Strait. *PLoS One* 12:e0171715. doi: 10.1371/journal.pone.0171715

González-Pola, C., Larsen, K. M. H., Fratantoni, P., Beszczynska-Moller, A., and Hughes, S. L. (eds) (2018). *ICES Report on Ocean Climate 2016. ICES Cooperative Research Report No. 339*. Copenhagen: International Council for the Exploration of the Sea, 110.

Gradinger, R. R., and Baumann, M. E. M. (1991). Distribution of phytoplankton communities in relation to the large-scale hydrographical regime in the Fram Strait. *Mar. Biol.* 111, 311–321. doi: 10.1007/bf01319714

Halldal, P., and Halldal, K. (1973). Phytoplankton, chlorophyll, and submarine light conditions in Kings Bay. Spitsbergen, July 1971. *Norw. J. Bot.* 20, 99–108.

Hansen, B., and Østerhus, S. (2000). North Atlantic–Nordic seas exchanges. *Prog. Oceanogr.* 45, 109–208. doi: 10.1016/s0079-6611(99)00052-x

Hansen, E., Gerland, S., Granskog, M. A., Pavlova, O., Renner, A. H. H., Haapala, J., et al. (2013). Thinning of Arctic sea ice observed in Fram Strait: 1990–2011. *J. Geophys. Res. Oceans* 118, 5202–5221. doi: 10.1002/jgrc.20393

Hasle, G. R., and Heimdal, B. R. (1998). The net phytoplankton in Kongsfjorden, Svalbard, July 1988, with general remarks on species composition of Arctic phytoplankton. *Polar Res.* 17, 31–52. doi: 10.3402/polar.v17i1.6605

Hegseth, E. N., Assmy, P., Wiktor, J., Kristiansen, S., Leu, E., Piquet, A. M.-T., et al. (2019). "Phytoplankton seasonal dynamics in Kongsfjorden, Svalbard and the adjacent shelf," in *The Ecosystem of Kongsfjorden, Svalbard, Advances in Polar Ecology 2*, eds H. Hop and C. Wiencke (Cambridge: Springer), 173–228.

Hegseth, E. N., and Sundfjord, A. (2008). Intrusion and blooming of Atlantic phytoplankton species in the high Arctic. *J. Mar. Syst.* 74, 108–119. doi: 10.1016/j.jmarsys.2007.11.011

Hegseth, E. N., and Tverberg, V. (2013). Effect of Atlantic water inflow on timing of the phytoplankton spring bloom in a high Arctic fjord (Kongsfjorden, Svalbard). *J. Mar. Syst.* 11, 94–105. doi: 10.1016/j.jmarsys.2013.01.003

Hirche, H. J., Baumann, M. E. M., Kattner, G., and Gradinger, R. (1991). Plankton distribution and the impact of copepod grazing on primary production in Fram Strait. Greenland sea. *J. Mar. Syst.* 2, 477–494. doi: 10.1016/0924-7963(91)90048-y

Hodal, H., Falk-Petersen, S., Hop, H., Kristiansen, S., and Reigstad, M. (2012). Spring bloom dynamics in Kongsfjorden, Svalbard: nutrients, phytoplankton, protozoans and primary production. *Polar Biol.* 35, 191–203. doi: 10.1007/s00300-011-1053-7

Holliday, N. P., Hughes, S. L., Bacon, S., Beszczynska-Moller, A., Hansen, B., Lavin, A., et al. (2008). Reversal of the 1960s to 1990s freshening trend in the northeast North Atlantic and Nordic Seas. *Geophys. Res. Lett.* 35:L03614. doi: 10.1029/2007GL032675

Holm-Hansen, O., and Riemann, B. (1978). Chlorophyll a determination: improvements in methodology. *Oikos* 30, 438–447. doi: 10.2307/3543338

Hoppe, C. J. M., Flintrop, C. M., and Rost, B. (2018). The Arctic picoeukaryote *Micromonas pusilla* benefits synergistically from warming and ocean acidification. *Biogeosciences* 15, 4353–4365. doi: 10.5194/bg-15-4353-2018

Huang, J., Zhang, X., Zhang, Q., Lin, Y., Hao, M., Luo, Y., et al. (2017). Recently amplified arctic warming has contributed to a continual global warming trend. *Nat. Clim. Chang.* 7, 875–879. doi: 10.1038/s41558-017-0009-5

Huntley, M., Tande, K., and Eilertsen, H. C. (1987). On the trophic fate of Phaeocystis pouchetii (Hariot). II. Grazing rates of Calanus hyperboreus (Krøyer) on diatoms and different size categories of Phaeocystis pouchetii. *J. Exp. Mar. Biol. Ecol.* 110, 197–212. doi: 10.1016/0022-0981(87)90001-3dsew

Iversen, K. R., and Seuthe, L. (2011). Seasonal microbial processes in a high-latitude fjord (Kongsfjorden, Svalbard): I. *Heterotrophic bacteria*, picoplankton and nanoflagellates. *Polar Biol.* 34, 731–749. doi: 10.1007/s00300-010-0929-2

Jankowski, A. (1991). Heat flux and wind momentum flux evaluation in certain regions of the Norwegian Sea in summer 1987 (based on results of AREX–87 cruise). *Stud. Mater. Oceanol.* 58, 77–89.

Keck, A., Wiktor, J., Hapter, R., and Nilsen, R. (1999). Phytoplankton assemblages related to physical gradients in an Arctic, glacier-fed fjord in summer. *ICES J. Mar. Sci.* 56, 203–214. doi: 10.1006/jmsc.1999.0631

Kowalczuk, P., Sagan, S., Makarewicz, A., Meler, J., Borzycka, K., Zabłocka, M., et al. (2019). Bio-optical properties of surface waters in the Atlantic water inflow region off Spitsbergen (Arctic Ocean). *J. Geophys. Res. Ocean* 124, 1964–1987. doi: 10.1029/2018jc014529

Kubiszyn, A. M., Piwosz, K., Wiktor, J. M. Jr., and Wiktor, J. M. (2014). The effect of inter-annual Atlantic water inflow variability on the planktonic protist community structure in the West Spitsbergen waters during the summer. *J. Plankton Res.* 36, 1190–1203. doi: 10.1093/plankt/fbu044

Kubiszyn, A. M., Wiktor, J. M., Wiktor, J. M. Jr., Griffiths, C., Kristiansen, S., and Gabrielsen, T. M. (2017). The annual planktonic protist community structure in an ice-free high Arctic fjord (Adventfjorden, West Spitsbergen). *J. Mar. Syst.* 169, 61–72. doi: 10.1016/j.jmarsys.2017.01.013

Lalande, C., Bauerfeind, E., Nöthig, E. M., and Beszczynska-Moller, A. (2013). Impact of a warm anomaly on export fluxes of biogenic matter in the eastern Fram Strait. *Prog. Oceanogr.* 109, 70–77. doi: 10.1016/j.pocean.2012.09.006

Latarius, K., and Quadfasel, D. (2016). Water mass transformation in the deep basins of the Nordic Seas: analyses of heat and freshwater budgets. *Deep Sea Res. Patt I* 114, 23–42. doi: 10.1016/j.dsr.2016.04.012

Lauvset, S. K., Brakstad, A., Våge, K., Olsen, A., Jeansson, E., and Mork, K. A. (2018). Continued warming, salinification and oxygenation of the Greenland Sea gyre. *Tellus A* 70, 1–9. doi: 10.1080/16000870.2018.1476434

Leu, E., Søreide, J. E., Hessen, D. O., Falk-Petersen, S., and Berge, J. (2011). Consequences of changing sea-ice cover for primary and secondary producers in the European Arctic shelf seas: timing, quantity, and quality. *Prog. Oceanogr.* 90, 18–32. doi: 10.1016/j.pocean.2011.02.004

Levinsen, H., Turner, J. T., Nielsen, T. G., and Hansen, B. W. (2000). On the trophic coupling between protists and copepods in arctic marine ecosystems. *Mar. Ecol. Prog. Ser.* 204, 65–77. doi: 10.3354/meps204065

Maranger, R., Vaqué, D., Nguyen, D., Hébert, M. P., and Lara, E. (2015). Pan-Arctic patterns of planktonic heterotrophic microbial abundance and processes: controlling factors and potential impacts of warming. *Prog. Oceanogr.* 139, 221–232. doi: 10.1016/j.pocean.2015.07.006

Markowski, D., and Wiktor, J. (1998). Phytoplankton and water masses in the European subarctic Polar front zone. *Oceanologia* 40, 51–64.

Mayot, N., Matrai, P. A., Arjona, A., Bélanger, S., Marchese, C., Jaegler, T., et al. (2020). Springtime export of Arctic sea ice influences phytoplankton production in the Greenland Sea. *J. Geophys. Res. Oceans* 125:e2019JC015799. doi: 10.1029/2019JC015799

Mayzaud, P., Boutoute, M., Noyon, M., Narcy, F., and Gasparini, S. (2013). Lipid and fatty acids in naturally occurring particulate matter during spring and summer in a high arctic fjord (Kongsfjorden. *Svalbard). Mar. Biol.* 160, 383–398. doi: 10.1007/s00227-012-2095-2

Möller, F., and Bernhard, M. (1974). A sequential approach to the counting of plankton organisms. *J. Exp. Mar. Biol. Ecol.* 15, 49–68. doi: 10.1016/0022-0981(74)90063-x

Monti, M., and Minocci, M. (2013). Microzooplankton along a transect from northern continental Norway to Svalbard. *Polar Res.* 32:19306. doi: 10.3402/polar.v32i0.19306

Neukermans, G., Oziel, L., and Babin, M. (2018). Increased intrusion of warming Atlantic water leads to rapid expansion of temperate phytoplankton in the Arctic. *Glob. Change Biol.* 24, 2545–2553. doi: 10.1111/gcb.14075

Nöthig, E. M., Bracher, A., Engel, A., Metfies, K., Niehoff, B., Peeken, I., et al. (2015). Summertime plankton ecology in Fram Strait – a compilation of long-and short-term observations. *Polar Res.* 34:23349. doi: 10.3402/polar.v34.23349

Oksanen, J., Blanchet, F. G., Friendly, M., Kindt, R., Legendre, P., McGlinn, D., et al. (2017). *Vegan: Community Ecology Package. R Package Version 2.4-3*. Avaliable at: https://CRAN.R-project.org/package=vegan. (accessed March 12, 2019).

Owrid, G., Socal, G., Civitarese, G., Luchetta, A., Wiktor, J., Nöthig, E. M., et al. (2000). Spatial variability of phytoplankton, nutrients and new production estimates in the waters around Svalbard. *Polar Res.* 19, 155–171. doi: 10.3402/polar.v19i2.6542

Piechura, J., Osiński, R., Petelski, T., and Woźniak, S. B. (2002). Heat and salt fluxes in the West Spitsbergen current area in summer. *Oceanologia* 44, 307–321.

Piquet, A. M. T., Maat, D. S., Confurius-Guns, V., Sintes, E., Herndl, G. J., van de Poll, W. H., et al. (2015). Springtime dynamics, productivity and activity of prokaryotes in two Arctic fjords. *Polar Biol.* 39, 1749–1763. doi: 10.1007/s00300-015-1866-x

Piwosz, K., Spich, K., Całkiewicz, J., Weydmann, A., Kubiszyn, A. M., and Wiktor, J. M. (2015). Distribution of small phytoflagellates along an Arctic fjord transect. *Environ. Microbiol.* 17, 2393–2406. doi: 10.1111/1462-2920.12705

Piwosz, K., Walkusz, W., Hapter, R., Wieczorek, P., Hop, H., and Wiktor, J. (2009). Comparison of productivity and phytoplankton in a warm (Kongsfjorden) and a cold (Hornsund) Spitsbergen fjord in mid-summer 2002. *Polar Biol.* 32, 549–559. doi: 10.1007/s00300-008-0549-2

Poulin, M., Daugbjerg, N., Gradinger, R., Ilyash, L., Ratkova, T., and von Quillfeldt, C. (2011). The pan-Arctic biodiversity of marine pelagic and Sea-ice unicellular eukaryotes: a first-attempt assessment. *Mar. Biodivers.* 41, 13–28. doi: 10.1007/s12526-010-0058-8

R Core Team (2017). *R: A Language and Environment for Statistical Computing*. Vienna: R Foundation for Statistical Computing.

Rudels, B., Korhonen, M., Schauer, U., Pisarev, S., Rabe, B., and Wisotzki, A. (2015). Circulation and transformation of Atlantic water in the Eurasian Basin and the contribution of the Fram Strait inflow branch to the Arctic Ocean heat budget. *Prog. Oceanogr.* 132, 128–152. doi: 10.1016/j.pocean.2014.04.003

Saloranta, T. M., and Svendsen, H. (2001). Across the Arctic front west of Spitsbergen: high-resolution CTD sections from 1998-2000. *Polar Res.* 20, 177–184. doi: 10.1111/j.1751-8369.2001.tb00054.x

Schauer, U., Beszczynska-Moller, A., Walczowski, W., Fahrbach, E., Piechura, J., and Hansen, E. (2008). "Variation of measured heat flow through the Fram Strait between 1997 and 2006, in Arctic-Subarctic Ocean fluxes," in *Defining the role of the Northern Seas in Climate*, eds R. R. Dickson, J. Meincke, and P. Rhines (Dordrecht: Springer), 65–85. doi: 10.1007/978-1-4020-6774-7_4

Schauer, U., Fahrbach, E., Østerhus, S., and Rohardt, G. (2004). Arctic warming through the Fram Strait: oceanic heat transport from 3 years of measurements. *J. Geophys. Res.* 109:C06026. doi: 10.1029/2003JC001823

Seuthe, L., Iversen, K. R., and Narcy, F. (2011). Microbial processes in a high-latitude fjord (Kongsfjorden, Svalbard): II. Ciliates and dinoflagellates. *Polar Biol.* 34, 751–766. doi: 10.1007/s00300-010-0930-9

Sheldon, R. W., Prakash, A., and Sutcliffe, W. H. (1972). The size distribution of particles in the Ocean 1. *Limnol. Oceanogr.* 17, 327–340. doi: 10.4319/lo.1972.17.3.0327

Smith, W. O., Baumann, M. E. M., Wilson, D. L., and Aletsee, L. (1987). Phytoplankton biomass and productivity in the marginal ice zone of the Fram Strait during summer 1984. *J. Geophys. Res.* 92, 6777–6786. doi: 10.1029/JC092iC07p06777

Smoła, Z. T., Tatarek, A., Wiktor, J. M., Wiktor, J. M., Kubiszyn, A. M., and Wêsławski, J. M. (2017). Primary producers and production in Hornsund and Kongsfjorden – comparison of two fjord systems. *Pol. Polar Res.* 38, 351–373. doi: 10.1515/popore-2017-0013

Søreide, J. E., Leu, E., Berge, J., Graeve, M., and Falk-Petersen, S. (2010).). Timing of blooms, algal food quality and *Calanus glacialis* reproduction and growth in a changing Arctic. *Glob. Change Biol.* 16, 3154–3163. doi: 10.1111/j.1365-2486.2010.02175.x

Stoecker, D. K., Hansen, P. J., Caron, D. A., and Mitra, A. (2017). Mixotrophy in the marine plankton. *Annu. Rev. Mar. Sci.* 9, 311–335. doi: 10.1146/annurev-marine-010816-060617

Utermöhl, H. (1958). Zur vervollkommnung der quantitativen phytoplankton-methodik. *Mitt. Int. Ver. Theor. Angew. Limnol.* 9, 1–38. doi: 10.1080/05384680.1958.11904091

Vernet, M., Ellingsen, I. H., Seuthe, L., Slagstad, D., Cape, M. R., and Matrai, P. A. (2019). Influence of phytoplankton advection on the productivity along the Atlantic Water Inflow to the Arctic Ocean. *Front. Mar. Sci.* 6:583. doi: 10.3389/fmars.2019.00583

Vernet, M., Richardson, T. L., Metfies, K., Nöthig, E. M., and Peeken, I. (2017). Models of plankton community changes during a warm water anomaly in arctic waters show altered trophic pathways with minimal changes in carbon export. *Front. Mar. Sci.* 4:160. doi: 10.3389/fmars.2017.00160

Walczowski, W. (2010). Atlantic water in the Nordic Seas - properties, variability, climatic significance. *Oceanologia* 52, 319–324. doi: 10.5697/oc.52-2.325

Walczowski, W. (2013). Frontal structures in the West Spitsbergen current margins. *Ocean Sci.* 9, 957–975. doi: 10.5194/os-9-957-2013

Walczowski, W., Beszczynska-Moller, A., Wieczorek, P., Merchel, M., and Grynczel, A. (2017). Oceanographic observations in the Nordic Sea and Fram Strait in 2016 under the IO PAN long-term monitoring program AREX. *Oceanologia* 59, 187–194. doi: 10.1016/j.oceano.2016.12.003

Walczowski, W., and Piechura, J. (2011). Influence of the West Spitsbergen current on the local climate. *Int. J. Climatol.* 31, 1088–1093. doi: 10.1002/joc.2338

Walczowski, W., Piechura, J., Goszczko, I., and Wieczorek, P. (2012). Changes in Atlantic water properties: an important factor in the European Arctic marine climate. *ICES J. Mar. Sci.* 69, 864–869. doi: 10.1093/icesjms/fss068

Walczowski, W. (2014). "Atlantic water in the nordic seas," in *Properties, Variability, Climatic Importance, GeoPlanet: Earth and Planetary Sciences* (Berlin: Springer International Publishing), 174.

Walczowski, W. (2014). *Atlantic Water in the Nordic Seas. Properties, Variability, Climatic Importance*. Dordrecht: Springer International Publishing. doi: 10.1007/978-3-319-01279-7

Wickham, H. (2016). *ggplot2: Elegant Graphics for Data Analysis*. New York, NY: Springer.

Wiktor, J. (1999). Early spring microplankton development under fast ice covered fjords of Svalbard. Arctic. *Oceanologia* 41, 51–72.

Wiktor, J., and Wojciechowska, K. (2005). Differences in taxonomic composition of summer phytoplankton in two fjords of West Spitsbergen. *Svalbard. Pol. Polar Res.* 26, 259–268.

Conflict of Interest: The authors declare that the research was conducted in the absence of any commercial or financial relationships that could be construed as a potential conflict of interest.

Copyright © 2020 Dąbrowska, Wiktor, Merchel and Wiktor. This is an open-access article distributed under the terms of the Creative Commons Attribution License (CC BY). The use, distribution or reproduction in other forums is permitted, provided the original author(s) and the copyright owner(s) are credited and that the original publication in this journal is cited, in accordance with accepted academic practice. No use, distribution or reproduction is permitted which does not comply with these terms.

frontiers in Marine Science

ORIGINAL RESEARCH
published: 28 July 2020
doi: 10.3389/fmars.2020.00602

Comparing Vertical Distributions of Chl-*a* Fluorescence, Marine Snow, and Taxon-Specific Zooplankton in Relation to Density Using High-Resolution Optical Measurements

Christian Briseño-Avena[1,2†], Jennifer C. Prairie[1†], Peter J. S. Franks[2†] and Jules S. Jaffe[2†]*

[1] Department of Environmental and Ocean Sciences, University of San Diego, San Diego, CA, United States, [2] Scripps Institution of Oceanography, University of California, San Diego, San Diego, CA, United States

OPEN ACCESS

Edited by:
Aditya R. Nayak,
Florida Atlantic University,
United States

Reviewed by:
Emilia Trudnowska,
Institute of Oceanology (PAN), Poland
Kevin T. Du Clos,
University of South Florida,
United States
Marsh J. Youngbluth,
Florida Atlantic University,
United States

***Correspondence:**
Christian Briseño-Avena
cbriseno@ucsd.edu;
cbrisenosio@gmail.com

†ORCID:
Christian Briseño-Avena
orcid.org/0000-0003-0806-1046
Jennifer C. Prairie
orcid.org/0000-0001-8637-5345
Peter J.S. Franks
orcid.org/0000-0003-1862-0171
Jules S. Jaffe
orcid.org/0000-0002-5407-0448

Specialty section:
This article was submitted to Marine Ecosystem Ecology, a section of the journal Frontiers in Marine Science

Received: 24 January 2020
Accepted: 30 June 2020
Published: 28 July 2020

Citation:
Briseño-Avena C, Prairie JC, Franks PJS and Jaffe JS (2020) Comparing Vertical Distributions of Chl-a Fluorescence, Marine Snow, and Taxon-Specific Zooplankton in Relation to Density Using High-Resolution Optical Measurements. Front. Mar. Sci. 7:602. doi: 10.3389/fmars.2020.00602

Interactions between predators and their prey are important in shaping planktonic ecosystems. However, these interactions are difficult to assess *in situ* at the spatial scales relevant to the organisms. This work presents high spatial resolution observations of the nighttime vertical distributions of individual zooplankton, chlorophyll-*a* fluorescence, and marine snow in stratified coastal waters of the Southern California Bight. Data were obtained using a planar laser imaging fluorometer (PLIF) augmented with a shadowgraph zooplankton imaging system (O-Cam) mounted along with ancillary sensors on a free-descent platform. Fluorometer and PLIF sensors detected two well-defined and distinct peaks: the subsurface chlorophyll maximum (SCM) and a fluorescent particle maximum (FPM) dominated by large marine snow. The O-Cam imaging system allows reliable estimates of concentrations of crustacean and gelatinous zooplankton groups; we found that grazers and their predators had well-structured nighttime distributions in and around the SCM and FPM in ways that suggested potential predator avoidance at the peak of the SCM and immediately above the FPM (where predatory hydromedusae, and to some degree euphausiids, were primarily located). Calanoid copepods were found above the SCM while cyclopoids were associated with the FPM. The locations of predator and grazer concentration peaks suggest that their dynamics may control the vertical gradients defining the SCM and FPM.

Keywords: marine snow, subsurface chlorophyll maximum, zooplankton, density coordinates, *in situ*

INTRODUCTION

Planktonic organisms are at the base of pelagic food webs, driving the transfer of energy from primary producers to higher trophic levels. Although these interactions occur throughout the water column, the sun-lit epipelagic region is of special interest, as it contains the ubiquitous subsurface chlorophyll maxima (SCMs) (Cullen, 2015 and references therein). These features are biologically active regions that directly affect the biological pump (Turner, 2015), which is driven by interactions between organisms grazing on phytoplankton and being eaten by their predators.

Observations on the relationships between SCMs and the primary consumers they sustain have been conflicting. Harris (1988) described how different studies showed a direct relationship between the location and intensities of SCMs and zooplankton concentrations, while others concluded that zooplankton peaks occurred mainly above SCMs; Harris' own study focused mainly on copepods and explained some of these discrepancies by invoking Diel Vertical Migration (DVM). More recently, Schmid and Fortier (2019) found similar discrepancies in the location of the SCM in relation to two species of arctic calanoid copepods, which they attributed to predator avoidance due to observed DVM behavior. In addition to the fact that all of these studies (and the work they reference) used different sampling methods that ranged from pumps, optical counters, nets, to *in situ* imaging devices, an important limitation was that they focused on herbivorous zooplankton, and specifically copepods.

Overall, studying SCM-zooplankton dynamics *in situ* at the spatial scales at which these interactions occur is difficult. To understand the dynamics shaping the vertical structure of planktonic ecosystems, from primary producers to grazers and their carnivorous consumers, it is necessary to sample as many assemblage components as possible *simultaneously* on the spatial scales relevant to their individual interactions. Nets are incapable of making these measurements as they integrate observations over tens of meters vertically and filter hundreds of cubic meters of water. Although multiple net systems exist (e.g., MOCNESS, Wiebe et al., 1976, 1985, 2016; Coupled Asymmetrical MOCNESS, Guigand et al., 2005; Mininess, Reid et al., 1987), stratified sampling by net systems is usually performed relative to depth. Vertical displacements of isopycnals and organisms due to internal waves are aliased by such sampling methods, and relationships of the organism distributions to other variables such as density are lost (Banse, 1964).

The use of imaging devices to observe individual plankton *in situ* has created opportunities to quantify their fine-scale distributions concurrent with environmental parameters (Wiebe and Benfield, 2003). While standard *in situ* fluorometers can resolve the fine-scale vertical distributions of phytoplankton (via their chl-*a* fluorescence), quantifying the spatial distributions of individual phytoplankton and other fluorescent particles requires technologies such as the planar laser imaging fluorometer (e.g., Franks and Jaffe, 2008; Prairie et al., 2010; Jaffe et al., 2013). In the case of zooplankton, observations of fine-scale distributions can be obtained via the use of underwater imaging devices. Examples include the Video Plankton Recorder (VPR; Davis et al., 1996), the *In Situ* Ichthyoplankton Imaging System (*IS*IIS; Cowen and Guigand, 2008), the Underwater Vision Profiler (UVP; Picheral et al., 2010), the lightframe on-sight keyspecies investigation system (LOKI; Schulz et al., 2010; Schmid and Fortier, 2019), the ZooCam (Ohman et al., 2018), and various holographic imaging systems (e.g., Katz et al., 1999; Malkiel et al., 2006; Pfitsch et al., 2007; Talapatra et al., 2013). A comprehensive recent review of these and others is contained in Wiebe et al. (2017). In addition to quantifying a diversity of taxa, these imaging systems are advancing the understanding of distributions of fragile organisms (e.g., cnidarians and pelagic hemichordates), which are often under sampled or destroyed by nets (e.g., Benfield et al., 1996; Remsen et al., 2004). Importantly, imaging systems produce accurate estimates of taxa such as the cosmopolitan cyclopoid copepod *Oithona* spp., which is severely undersampled by coarse nets (Galliene and Robins, 2001). Nevertheless, imaging devices have limitations because they lack final taxonomic resolution of diverse zooplankton assemblages, which varies by both system and species composition (Benfield et al., 2007; Lombard et al., 2019).

To resolve the relationships among nighttime vertical distributions of chlorophyll-*a* fluorescence and marine snow, and the vertical structure of five zooplankton groups in the coastal Southern California Bight (SCB), we used the Free-falling Imaging Device for Observing Plankton (FIDO-Φ, **Figure 1A**; Franks and Jaffe, 2008). This platform is a quasi-Lagrangian, slowly descending vehicle, equipped with a planar laser imaging fluorometer (PLIF), a zooplankton-imaging device (O-Cam) and ancillary sensors (CTD, fluorometer). We use a water-density frame of reference, rather than depth, allowing the removal of vertical displacements of organisms due to physical effects such as internal waves.

In spite of taxonomic limitations, in this study we explore the relationships between the fine-scale vertical distributions of chl-*a* fluorescence, marine snow, and zooplankton. Our analysis puts our observations into the context of functional ecology traits such as feeding preferences. Functional groups, like trait-based ecology, can be used to reduce the complexity of food web analyses imposed by individual species ecological complexities (e.g., Barnett et al., 2007; Pomerleau et al., 2015; Ohman, 2019, and references therein). Here, we provide evidence that the spatial relationships among the nighttime vertical distributions of phytoplankton (measured by chl-*a* fluorescence), marine snow (quantified as large fluorescent particles), zooplankton grazers, detritivores, carnivores, and omnivores can be explained to a first degree by these generalized functional groups.

MATERIALS AND METHODS

The FIDO-Φ/O-Cam System

The O-cam was mounted on a slow descent, self-ballasted platform named FIDO that was combined with a planar laser imaging fluorometer (PLIF). Together, the system was named the Free-falling Imaging Device for Observing phytoplankton and zooplankton, or FIDO-Φ/O-Cam. The O-Cam was placed immediately above the PLIF imaging volume (**Figure 1B**). In addition, SBE25 and SB49 CTDs (Sea-Bird Electronics, United States) were placed on the platform; the SBE25 also included an ECO FL fluorometer (Wet Labs). In operation, and by adjusting ballast, the FIDO-Φ/O-Cam system was programmed to maintain a descent rate of approximately 10 cm/s.

The PLIF has been extensively described (Franks and Jaffe, 2001, 2008; Prairie et al., 2010). However, briefly, it consists of a CCD camera (Cooke Sensicam) equipped with a 50 mm Nikor lens (f/1.4 aperture) that images a 6.5 mm thick sheet of light that is parallel to the image plane of the camera (**Figure 1B**).

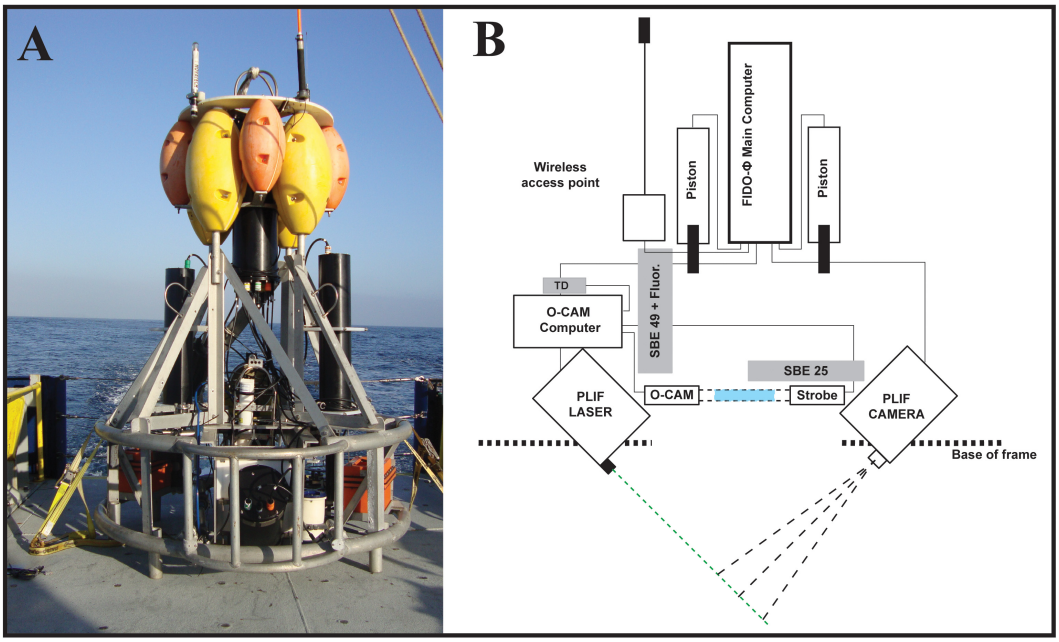

FIGURE 1 | (A) FIDO-Φ/O-Cam on the deck of R/V *New Horizon* during the August 2011 cruise. **(B)** Modified schematic from Prairie et al. (2011) to reflect the sensors used for this work. Notice the relative position of the imaging volumes for the PLIF (Intersection of camera and laser dashed lines) and O-Cam (blue rectangle) systems, as well as the location of the imaging volumes with respect to CTD (SBE 25 and SBE 49) and Temperature Depth (TD) sensors.

The light was produced by a 3-W, 532-nm diode-pumped solid-state laser (CVI Melles Griot). The field of view of the camera was approximately 9.8 × 13 cm with a spatial sampling resolution slightly smaller than 100 × 100 μm per pixel that was approximately equal to the true system optical resolution. The camera acquired images at a rate of 1 Hz with an exposure time of 20 ms. Observations were made through a band pass light filter that transmitted light at wavelengths of 670–690 nm, identical to those used by the fluorometer to measure chl-*a* fluorescence.

The O-Cam imaging system was described in detail in Briseño-Avena et al. (2015), however a brief description is provided here. Designed as a self-contained shadowgraph camera to capture undisturbed images of zooplankton *in situ*, the system consists of two separate underwater cylindrical housings, one containing a strobing LED light (LedEngine LZ74 2 × 2 Diode Array) and the other a camera (AVT GX1910 × 1080, 5.5-micron pixels, 14 bits). The view ports face each other with the collimated light beam aimed directly into the camera (Settles, 2012). The 71 cm space between the housings' view ports contains the imaged volume. The O-Cam's sampling volume, estimated by measuring the distance in which a transparent resolution target is in focus (15 cm) and multiplying by the circular area of the field of view (7.0686 cm^2), was 0.106 L per frame. The O-cam was positioned near the bottom of the profiling vehicle and, as such, only O-Cam data from downcasts were analyzed.

PLIF and O-Cam Image Processing

PLIF bulk chl-*a* fluorescence was obtained by integrating the intensity of fluorescence in the images as it is linearly correlated with chl-*a* fluorescence intensity measured by commercial fluorometers (Franks and Jaffe, 2001; Prairie et al., 2010). Fluorescent particle concentrations were obtained from the fluorescence images following the protocol of Prairie et al. (2010). Images were first corrected for spatial variations in the fluorescence intensity of the incident laser sheet and a fluorescence intensity threshold was then used to define "fluorescent particles" as one or more contiguous pixels with fluorescence intensities greater than the threshold value. The threshold was determined separately for each profile prior to processing. Since the imaging pixel size was ∼100 × 100 μm, and most particles observed had an area of more than one pixel, fluorescent particles here are considered to be primarily marine snow (*sensu* Alldredge and Silver, 1988). However, we note that they may also include some large individual phytoplankton and chains. Single-pixel fluorescence could be created by particles as small as 20–50 μm in diameter (Zawada, 2002), although their sizes cannot be resolved. A total of 5,906 fluorescence images from nine profiles were analyzed.

O-cam images were manually annotated using a custom-made graphical user interface in Matlab. Every image for all profiles presented here was visually inspected for the presence of zooplankton. In total, 6,116 O-Cam images, spanning nine vertical profiles, were annotated. The annotation consisted of drawing a box around the identified organism and then assigning it to one of 22 predetermined taxonomic categories. These categories were created based on the most common zooplankton observed in early test deployments of the O-Cam. Images were classified at the lowest taxonomic level possible. For this work, the most abundant categories were: hydromedusae, euphausiids, calanoid copepods, cyclopoid copepods, and appendicularians

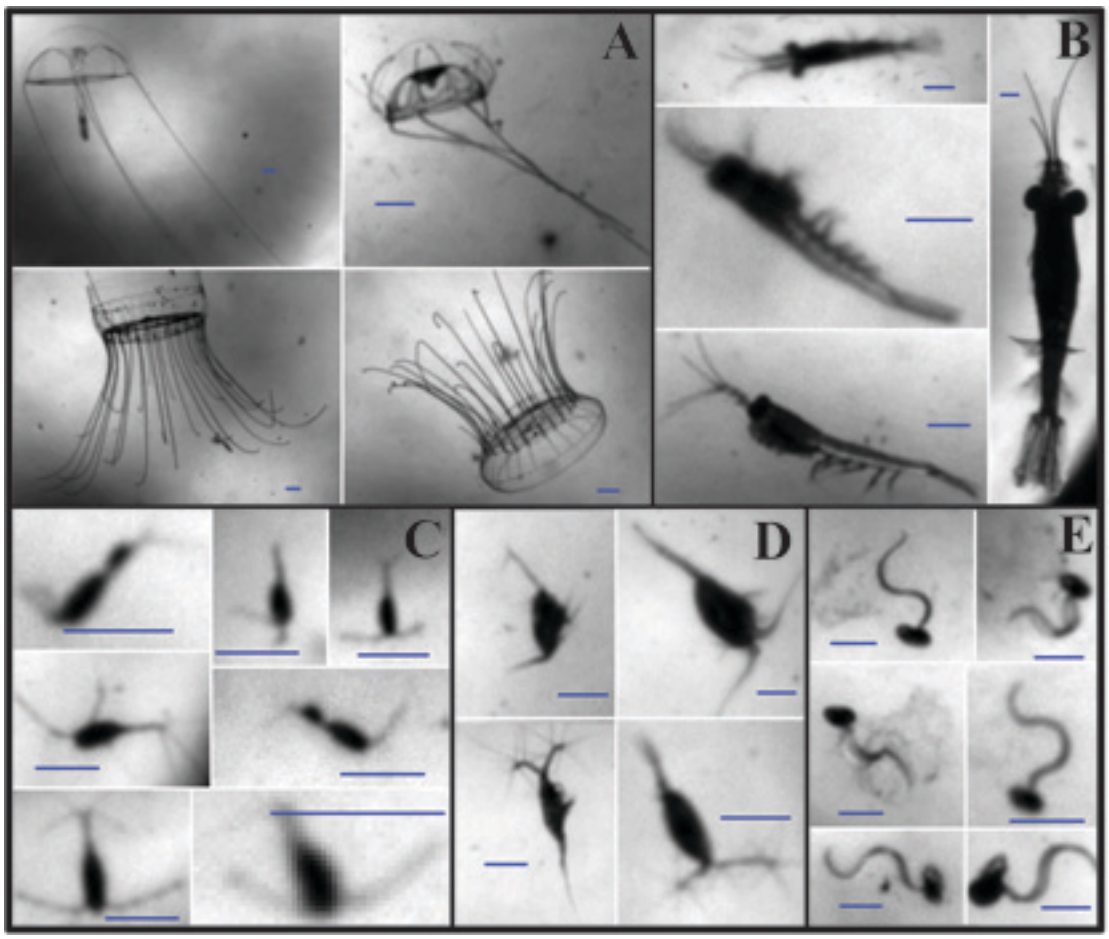

FIGURE 2 | Examples of zooplankton images from the O-Cam system. **(A)** Hydromedusae; **(B)** Euphausiids; **(C)** Cyclopoid copepods; **(D)** Calanoid copepods; **(E)** Appendicularians. All the scale bars are 1 mm long.

(**Figure 2**). Concentration estimates (individuals per liter) were obtained by dividing the number of observations in each frame by the volume sampled per frame (0.106 L). To test the quantitative capabilities of the O-Cam, the image-derived zooplankton concentration (Individuals L^{-1}) estimates were previously compared to those obtained from net samples collected with a 1 m^2, 202 μm mesh size MOCNESS (**Supplementary Material**).

Description of the FIDO-Φ/O-Cam 2011 Cruise

The FIDO-Φ/O-Cam cruise was conducted near the head of a submarine canyon at the northern end of the Santa Catalina Basin aboard the R/V New Horizon during August 18–23, 2011 (triangle symbol in **Figure 3**). This region was chosen because SCM layers and zooplankton grazers have been extensively studied here (Cullen, 1982; Napp et al., 1988) thereby enhancing our chances of capturing these features. Hence, fine-scale nighttime vertical distributions of zooplankton and phytoplankton were resolved using the FIDO-Φ/O-Cam. These data were used to reconstruct the *in situ* concurrent distributions of chl-*a* fluorescence, fluorescent particles (consisting primarily of marine snow), and zooplankton, along with hydrographic properties.

Over successive nights, the FIDO-Φ/O-Cam platform was deployed in the same general location. Deployments were limited to nighttime to avoid contamination of the PLIF images by ambient sunlight (Franks and Jaffe, 2008). Furthermore, higher zooplankton biomass in this region tend to coincide with the SCM at night, when diel vertical migrators have reached their nighttime locations (Napp et al., 1988). Nighttime profiling also enhanced the chances of imaging a depth-dependent diverse group of zooplankters, given the relatively small imaged volume of the O-Cam system. Each FIDO-Φ/O-Cam deployment was composed of three consecutive vertical profiles; data were acquired during the downcasts to a maximum depth of 75 m. After each drop cycle was completed, the platform was recovered for data download and system updates, such as battery recharging or replacement. Because the platform drifted with the water currents, the ship was repositioned to the original drop location centered at 33° 33′N and 118° 54′W before the FIDO-Φ/O-Cam was re-deployed for a new cycle. While

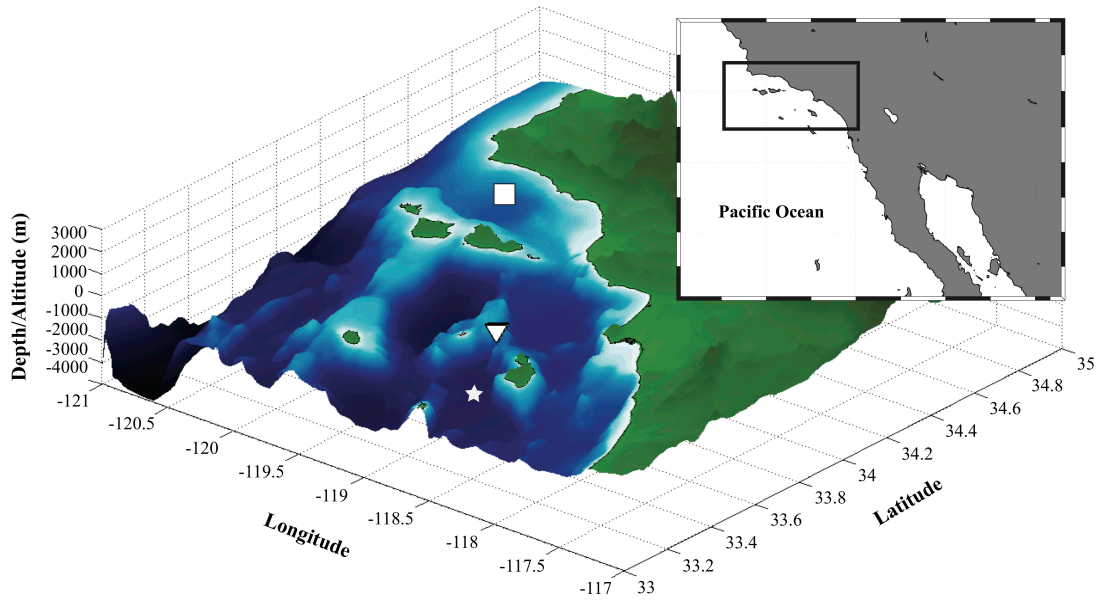

FIGURE 3 | Bathymetry of the study region (area bounded by the solid black rectangle in the inset map). White square indicates the general location of the Santa Barbara Channel sampling sites for the CalEchoes cruise aboard R/V Melville from September 26–October 1, 2010 (see **Supplementary Materials**). Inverted triangle represents the site occupied during the FIDO-Φ/O-Cam cruise aboard R/V New Horizon from August 18–23, 2011. White star indicates the location of the Santa Catalina Basin.

TABLE 1 | FIDO-Φ/O-Cam cruise "Drop_Profile" information.

Drop_Profile Number	Location of Deployment	Deployment date and time (PST)	Usable Depth Range (m)	PLIF: total images (from chl-*a* filter)	O-cam: total images
05_1	33.57 N 118.91 W	21-Aug-2011, 21:44	10–70	584	589
05_2	33.56 N 118.91 W	21-Aug-2011, 22:15	10–70	614	654
06_1	33.55 N 118.91 W	22-Aug-2011, 02:14	10–70	671	672
06_2	33.55 N 118.92 W	22-Aug-2011, 03:03	10–70	937	971
06_3	33.56 N 118.93 W	22-Aug-2011, 04:02	10–60	569	610
07_1	33.57 N 118.92 W	22-Aug-2011, 20:33	10–70	573	584
07_2	33.57 N 118.92 W	22-Aug-2011, 21:04	10–70	610	649
07_3	33.57 N 118.92 W	22-Aug-2011, 21:32	10–70	706	750
08_1	33.56 N 118.93 W	23-Aug-2011, 00:26	10–70	642	637

this repositioning can be counter-intuitive for a self-contained, free-descent platform, we were not seeking to conduct a Lagrangian experiment, but rather we wanted to observe potential changes in zooplankton assemblage distributions as internal waves passed through the same sampling region. Nine profiles from four cycles collected over two consecutive nights (each one labeled by its "Drop_Profile" identifying number) when all the sensors were fully functional were chosen for the present analysis (**Table 1**).

Sensor Data Merging and Data Analyses

As most instruments had their own pressure sensors, all data from a given profile were merged based on depth. The PLIF imaging volume was 0.8 m below the depth sensor and this offset was incorporated into the analysis before merging with the other data. Because the O-Cam was self-contained and had its own temperature-pressure (TP) sensor, no depth corrections were necessary. After data merging, each variable was independently binned by depth using a 0.3 m bin size and then smoothed over 1.5 m using LOWESS to remove small-spatial-scale noise. The result was a fixed-size data vector for each variable, giving profiles that could be compared to each other using regular depth coordinates. In addition, data from the PLIF, SBE 25-ECO FL, SBE 49 and O-Cam were binned in density coordinates using a density bin size of 0.09 kg/m^3. This bin size was found empirically to be the minimum size that would allow adequate observations per bin, given the density range of 1023.8 to 1026.1 kg/m^3.

All biological profile concentrations were normalized in depth and density coordinates by dividing all the values in a given profile by its maximum. The normalized values thus ranged between zero and one. Normalization allowed comparisons across all profiles, particularly when profiles were dominated by a data point of particularly high intensity. Then, canonical profiles were estimated by averaging the individual normalized profiles in

density coordinates over time. This time averaging was justifiable given the spatial and temporal proximity of drops and profiles (**Table 1**), and the consistent distributions of properties among different normalized profiles. In the case of CTD fluorescence intensity and PLIF fluorescent particles, this data processing step resulted in the normalized Fluorescence Intensity (FI_n) and Fluorescent Particles (FP_n; primarily composed of marine snow) variables. Both, non-normalized and normalized data are reported here.

A cross-correlation analysis was done to determine the vertical offset (i.e., decoupling, in density coordinates) between the FI_n and FP_n canonical profiles. Cross-correlation analyses were similarly conducted to determine the vertical offset between zooplankton canonical profiles and the FI_n and FP_n canonical profiles. The spatial lags for all cross-correlation analysis outputs were reported as vertical density offsets in density units (kg/m^3) while retaining the sign ($\pm$) of the signal lag. Finally, we also calculated the absolute differences between FI_n and FP_n offsets (i.e., $|FI_{n\ offset} - FP_{n\ offset}|$) for each taxon to examine the decoupling magnitude from each taxon and both fluorescence parameters combined.

FI_n, FP_n, Their Gradients and Zooplankton Peaks

Vertical gradients of the FI_n and FP_n canonical profiles in density coordinates were calculated using the following equations:

$$FI_{\text{gradient}} = \Delta FI_n / \Delta \rho$$

$$FP_{\text{gradient}} = \Delta FP_n / \Delta \rho$$

where $\Delta\rho$ = 0.09 kg/m^3 in both cases, and FI_n and FP_n denote normalized, time-averaged fluorescence intensity and PLIF fluorescent particle concentration, respectively (referred to as canonical profiles for these variables).

Zooplankton peaks were identified in the raw, time-averaged counts for each zooplankton group (**Supplementary Figure 2**). Briefly, we defined a peak of the vertical distribution of each zooplankton group to be those values having a greater than 95% probability of being higher than the background (mean) count in any given density bin (0.09 kg/m^3 per bin).

RESULTS

CTD, PLIF, and O-Cam Profiles in a Depth Frame of Reference

The slow descent of the FIDO platform and the high sampling rate of the sensors yielded fine-scale (cm) distributions of physical and biological data, uncontaminated by ship heave motions. During our field work, salinity did not vary substantially (**Figure 4A**); the water column was thermally stratified, with the thermocline occurring between 25 and 30 m depth (**Figure 4B**). A fluorescence intensity maximum was located within the thermocline in all profiles (**Figure 4C**). Fluorescent particles (marine snow) were found below the thermocline, and one profile (6_3) had more than twice the concentration of particles than any other profile during the deployment cycles (**Figure 4D**). Total zooplankton concentrations were located in the warm surface waters, above the thermocline and the fluorescence intensity maximum; furthermore, total zooplankton was patchily distributed both with depth and over time (**Figure 4E**). Hydromedusae, appendicularians, and calanoid copepods were found in warmer waters (**Figures 4F–H**). Cyclopoid copepods showed higher concentrations in colder waters, below the thermocline and fluorescence intensity maximum (**Figure 4I**). Euphausiids were widely distributed throughout the water column but were located in warmer waters in the first half of the profiles and deeper in colder waters in the second half (**Figure 4J**).

CTD, PLIF, and O-Cam Non-normalized Profiles in Density Coordinates

The vertical displacements of the fluorescence intensity maximum evident in the fluorescence versus depth profiles (**Figure 4C**) followed the displacements of isotherms (**Figure 4B**) – temperature being the main determinant of density during our study, as evidenced by the larger variations in temperature than salinity in surface waters (**Figures 4A,B**). While there could be other potential contributors, we attributed such vertical displacements to passing internal waves and/or the internal tide. Tide charts (data not shown) for the nearest location to our sampling site (Catalina Harbor, Santa Catalina Island; 33° 25.8′ N, 118° 30′ W) showed that the vertical displacement of the isotherms (**Figure 4B**) were synchronous with the local tide during the cruise sampling dates (**Table 1**). The density-binned data (**Figure 5**) showed that the vertical displacements visible among depth profiles disappeared when using density coordinates, confirming that fluorescence intensity followed isopycnals rather than pressure surfaces (i.e., depth layers). Not obvious in **Figures 4**, **5** are vertical displacements of the fluorescent particle concentration profiles due to the substantially higher signal in profile 6_3 than the profiles before and after. This inter-profile variability in total concentration was removed by normalizing each variable by its maximum value in a given profile (see "Materials and Methods section"). These normalized vertical distributions of each variable now range between zero and one in each profile (**Figure 6**).

CTD, PLIF, and O-Cam Normalized Profiles in Density Coordinates

Once data plotted in density coordinates were normalized, patterns that were obscured in the depth and density/non-normalized plots became strikingly evident (**Figure 6**). In this concentration-normalized, density-coordinate frame of reference, two maxima were identified: a subsurface chlorophyll maximum (SCM; **Figure 6C**) and a fluorescent particle concentration maximum, from here on referred to as the fluorescent particle maximum (FPM; **Figure 6D**), which was composed primarily of marine snow. While the FPM overlaps with the SCM, the peak intensities of the features were offset from one another, with the FPM peak being located in denser (deeper) waters than the SCM (**Figures 6C,D**).

The normalized total zooplankton concentrations distributions were found mostly above both the SCM and FPM (**Figure 6E**). However, different taxa showed distinct

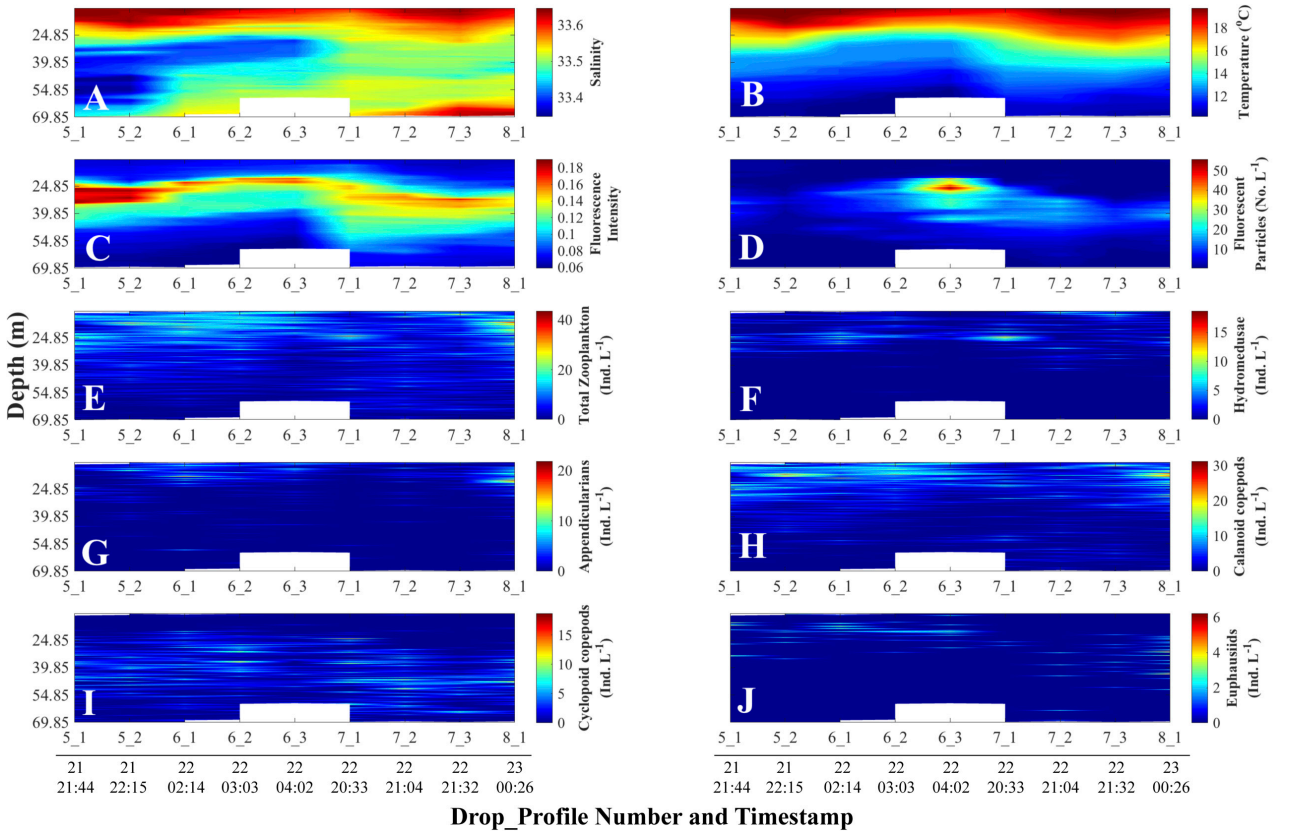

FIGURE 4 | Depth-time distributions of physical and non-normalized biological data. Day and time (all in August 2011, Pacific Standard Time) are at the bottom of each column and apply to all the panels above the line of timestamps. Full details on each Drop_Profile can be found in **Table 1**. **(A)** Salinity; **(B)** Temperature (°C); **(C)** Fluorescence Intensity (SBE 25 fluorometer); **(D)** Planar Laser Imaging Fluorometer (PLIF) fluorescent particle concentration (Numbers L^{-1}); Panels **(E)** through **(J)** represent O-Cam zooplankton concentrations (Individuals L^{-1}): **(E)** Total zooplankton; **(F)** Hydromedusae; **(G)** Appendicularians; **(H)** Calanoid copepods; **(I)** Cyclopoid copepods; and **(J)** Euphausiids.

distributions with respect to the maxima, and no individual zooplankton taxon was found exclusively within either the SCM or the FPM. Hydromedusae showed some overlap with the SCM but were mostly located above the FPM (**Figure 6F**). Similarly, appendicularians and calanoid copepods (**Figures 6G,H**) were mainly located above both the SCM and FPM. Cyclopoid copepods were mainly concentrated at the lower boundary of the FPM (**Figure 6I**). Euphausiids showed a more even vertical distribution, with some located above the FPM at the beginning of the cruise and within it toward the end (**Figure 6J**).

Canonical Profiles and Cross-Correlation Analyses

The time-averaged profiles (canonical profiles) for each variable revealed different relationships among FI_n and FP_n, and the zooplankton canonical distributions in relation to each of the two fluorescent variables (**Figure 7**) as quantified by the cross-correlation analyses are described below.

The cross-correlation of FI_n and FP_n showed a peak correlation at a vertical displacement in density coordinates of -0.18 kg/m^3 (i.e., the FP_n main signal peak was deeper than the FI_n main signal peak by two density bins, recalling that each density bin was 0.09 kg/m^3 wide) as shown in **Figure 7A**. These peaks in the FI_n and FP_n represent the core of the SCM and FPM shown in **Figures 6C,D**. The peak cross-correlations between zooplankton canonical profiles and FI_n, and FP_n all occurred at non-zero vertical offsets (**Table 2**), confirming that the main signal peak in each zooplankton group fell above or below the main signal peaks in both FI_n, and FP_n, although to varying degrees, indicating different degrees of decoupling between taxa and the SCM and FPM. With the exception of cyclopoid copepods, all zooplankton groups showed consistently larger vertical density offsets with respect to FI_n than to FP_n, although the magnitude of this offset varied among zooplankton groups (**Table 2**). The differences in vertical offsets were directly affected by the shape of the canonical profile of each taxa (**Figure 7B**). Cyclopoid copepods were the only group whose canonical profile peaked deeper than both the SCM and the FPM, as indicated by negative vertical density offsets relative to FI_n (-0.36 kg/m^3) and FP_n (-0.18 kg/m^3). Yet their offset difference (0.18 kg/m^3) indicate some degree of coupling with the SCM and FPM (**Figure 7**, gray line). Calanoid copepods and appendicularians, with consistent higher relative abundances in the upper water column, had the largest vertical density offsets of all zooplankton groups with respect to FI_n (0.63, 0.72 kg/m^3, respectively) and FP_n (0.90, 0.99 kg/m^3, respectively) but, interestingly the same

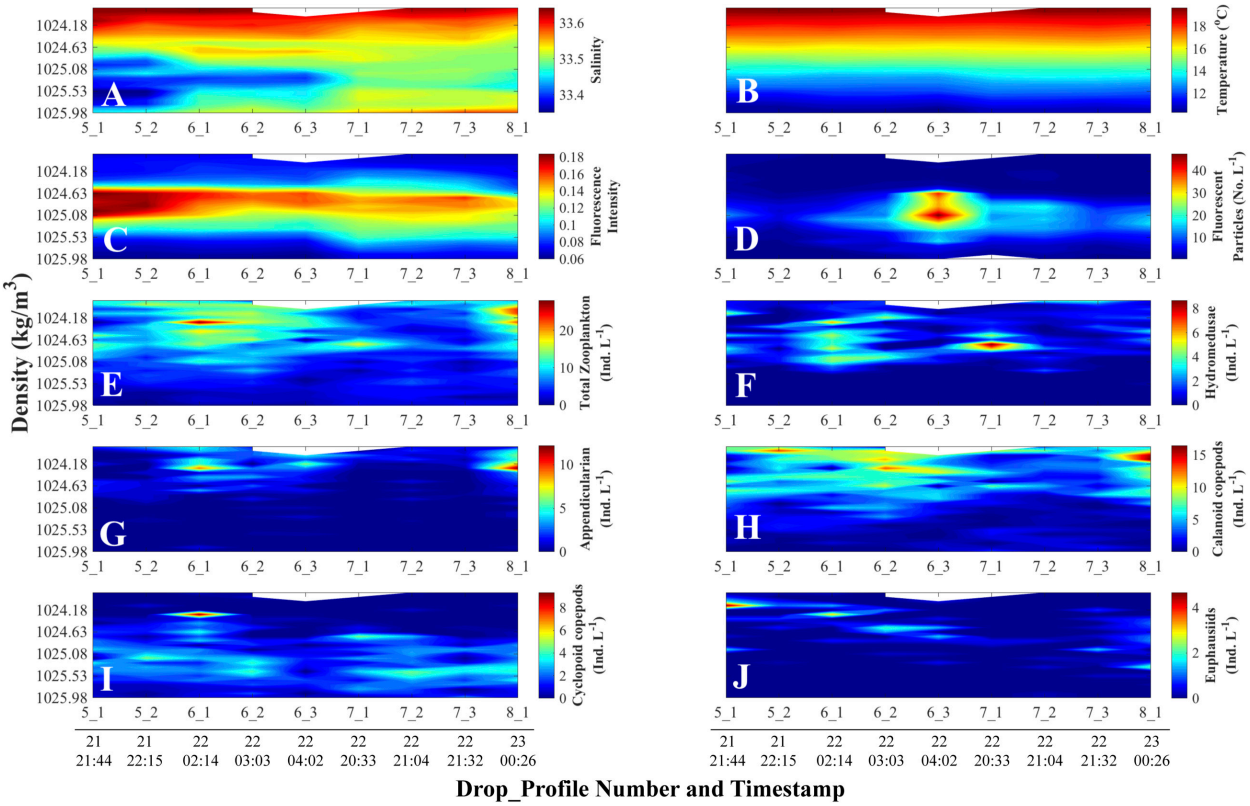

FIGURE 5 | Density-time distributions of physical and non-normalized biological data. Day and time (all in August 2011, Pacific Standard Time) are at the bottom of each column and apply to all the panels above the line of timestamps. Full details on each Drop_Profile can be found in **Table 1**. **(A)** Salinity; **(B)** Temperature (°C); **(C)** Fluorescence Intensity (SBE 25 fluorometer); **(D)** Planar Laser Imaging Fluorometer (PLIF) fluorescent particle concentration (Numbers L^{-1}); Panels **(E)** through **(J)** represent O-Cam zooplankton concentrations (Individuals L^{-1}) data: **(E)** Total zooplankton concentration; **(F)** Hydromedusae; **(G)** Appendicularians; **(H)** Calanoid copepods; **(I)** Cyclopoid copepods; and **(J)** Euphausiids.

offset difference value of 0.27 kg/m^3, showing a similar degree of decoupling with respect to the SCM and FPM (**Figures 7A,B**, black and dark blue lines). Hydromedusae had vertical density offsets of 0.36 and 0.45 kg/m^3 with respect to FI_n and FP_n, respectively, and smaller differences between offsets (0.09 kg/m^3) than all other groups (**Table 2**), indicating a close coupling with the SCM and FPM (**Figure 7**, red line). Euphausiids had a smaller vertical density offset with respect to FI_n (0.18 kg/m^3) than with FP_n (0.54 kg/m^3) and was the group with the largest vertical density offset difference (0.36 kg/m^3) of all the zooplankton groups, and therefore the group that showed the highest degree of decoupling from both SCM and FPM (**Figure 7**, light blue line). However, the canonical profile of the euphausiids may reflect that their vertical distributions changed over the duration of the study, unlike the other zooplankton groups.

FI_n, FP_n Profiles, Their Gradient, and Zooplankton Peaks

The shape of the SCM and the FPM differed with regard to the sharpness of their upper and lower gradients. The SCM was characteristically asymmetric, with one distinct, sharp gradient forming its upper boundary, and a gradient about half the magnitude of the upper, forming its lower boundary (**Figure 8A**). The FPM, on the other hand, was symmetric, bounded by two vertical gradients of similar magnitudes (**Figure 8B**). Peaks in the zooplankton vertical distributions showed different associations with the SCM, the FPM, and their vertical gradients (**Figure 8**). Hydromedusae (carnivorous) peaks were distinctly associated with the SCM, with only one peak (of minor relative intensity) within the upper SCM gradient. No hydromedusae peaks were found within the deeper SCM gradient (**Figure 8A**; red stars). At the same time, hydromedusae peaks were associated with the FPM upper gradient (**Figure 8B**; red stars), but not with the FPM itself. Euphausiids (carnivores/omnivores) had two peaks, the largest of which was associated only with the upper SCM gradient, but not the SCM itself (**Figure 8**; light blue diamonds). Calanoid copepods (considered herbivores here although the group potentially includes omnivores) were found mostly above the upper SCM gradient and SCM, with only one calanoid peak (of medium relative intensity) located within the SCM (and by extension within the decaying slope of the upper gradient; **Figure 8A**; black squares). Calanoid copepods had no association with the FPM, with one notable exception: one of the medium-intensity peaks occurred in the steeper slope of the upper FPM gradient (**Figure 8B**; black squares).

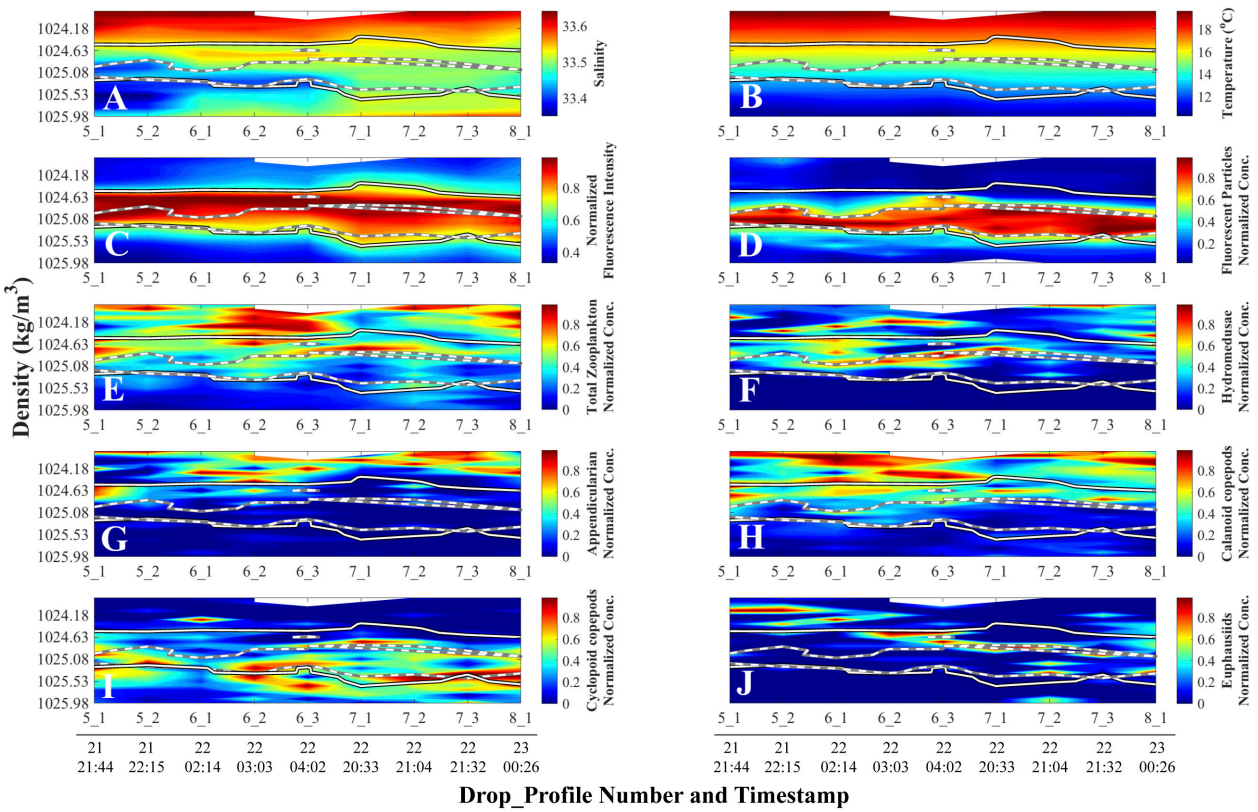

FIGURE 6 | Density-time distributions of physical and normalized biological data. Day and time (all in August 2011, Pacific Standard Time) are at the bottom of each column and apply to all the panels above the line of timestamps. Full details on each Drop_Profile can be found in **Table 1**. **(A)** Salinity; **(B)** Temperature (°C); **(C)** Fluorescence Intensity (SBE 25 fluorometer); **(D)** Planar Laser Imaging Fluorometer (PLIF) fluorescent particle normalized concentration. Panels **(E)** through **(F)** represent O-Cam zooplankton normalized concentrations: **(E)** Total zooplankton; **(F)** Hydromedusae; **(G)** Appendicularians; **(H)** Calanoid copepods; **(I)** Cyclopoid copepods; and **(J)** Euphausiids. Solid lines superimposed on panels represent the 70% threshold normalized Fluorescence Intensity from panel **(C)**, and white-on-black lines superimposed on panels represent the 70% threshold fluorescent particle normalized concentration contour from panel **(D)**.

Cyclopoid copepods (herbivores and detritivores) were not fully associated with the SCM or the FPM. However, the cyclopoid copepods' most intense peak was co-located within the deeper gradients of these features, with two minor cyclopoid peaks above (but within the FPM; **Figure 8B**; gray triangles) and five peaks of medium, but decreasing in intensity, below the deeper SCM/FPM gradients. Finally, appendicularians (filter-feeders) were not clearly associated with either the SCM, the FPM, or their gradients. However, their higher concentrations were consistently located above the SCM and FPM (**Figure 8**; dark blue circles), and were closely associated with the strongest calanoid copepod concentration peaks.

DISCUSSION

Relationships Between the SCM and FPM

Subsurface chlorophyll maxima (SCM) are ubiquitous features of marine and freshwater ecosystems (Cullen, 2015), and considerable research has explored the roles of bottom-up controls, including light, thermal stratification, and nutrients in shaping the SCM (e.g., Cullen, 2015; Leach et al., 2018). Thus, the persistent peak in FI_n observed throughout this study (representative of a SCM) is not surprising, particularly in our stratified coastal region study site. More recently, studies have found that marine snow can also form layers, which are often ubiquitous features of stratified systems (MacIntyre et al., 1995; Alldredge et al., 2002, Prairie and White, 2017). The fluorescent particle maximum (FPM) we observed similarly represents a peak in marine snow concentration, although the vertical scale, while narrower than the SCM, was substantially wider than the vertical scale of thin layers as they are typically classified (Dekshenieks et al., 2001).

In our data, the FPM was distinct from the SCM (with the FPM sitting deeper in denser waters, albeit with apparent overlap. **Figure 7A**), which is consistent with Prairie et al. (2010) who observed (also with the FIDO-Φ) cryptic peaks containing large fluorescent particles (primarily marine snow) that sat below the sub-surface chlorophyll maximum. This pattern confirms that the profiles of bulk chl-*a* fluorescence and fluorescent particles detected by the PLIF have different compositions; while the bulk chl-*a* fluorescence is dominated by individual phytoplankton representing a wide range of sizes,

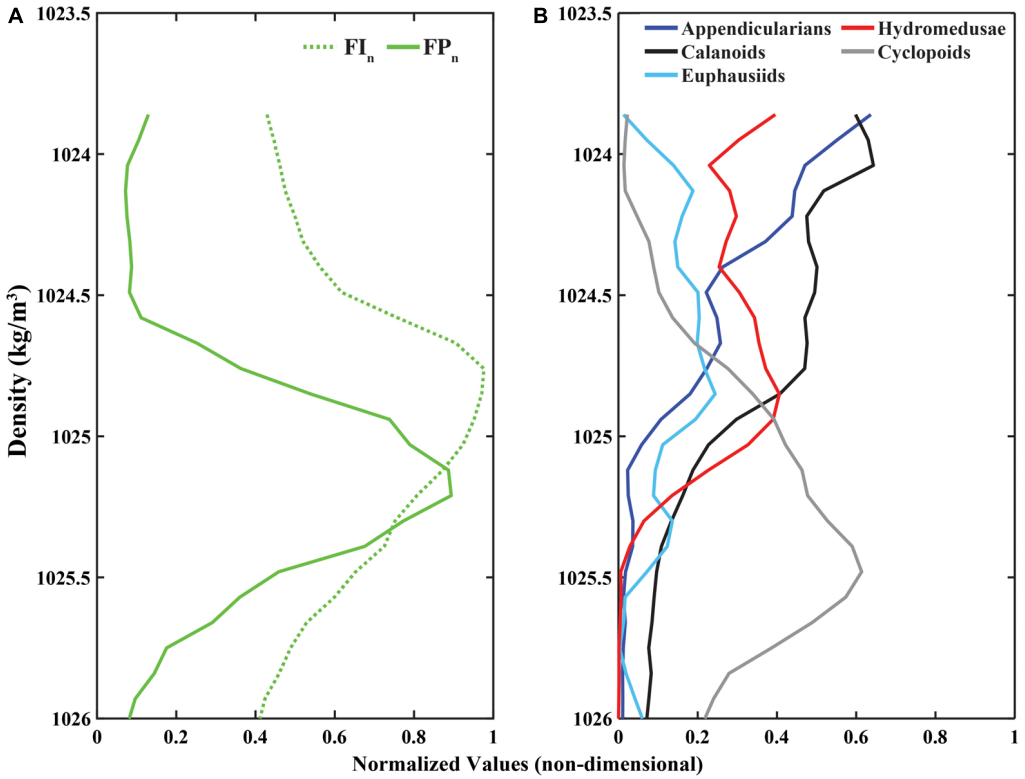

FIGURE 7 | Canonical profiles (time-averaged normalized values in density coordinates) for **(A)** Fluorescence Intensity (FI_n; green dotted line) and Fluorescent Particles (FP_n; green solid line), and **(B)** appendicularians, calanoid copepods, cyclopoid copepods, euphausiids, and hydromedusae.

the fluorescent particles are large and likely composed primarily of marine snow. The relationship between the SCM and the FPM observed here (**Figure 7A**) is reminiscent of a marine snow layer observed forming 1–2 m below a diatom bloom (Alldredge et al., 2002). Similarly, isolated layers or diatom flocs formed by *Pseudo-nitzschia* off Monterey Bay, California were detected by an imaging system, but not by standard fluorometers (Timmerman et al., 2014). Although our data cannot distinguish between detritus of phytoplanktonic origin and that derived from other organic material (e.g., discarded appendicularian houses, decomposing plankton, fecal pellets), the difference in the depths of the SCM and the FPM is notable, considering that they may represent different food sources for different zooplankton grazers. This observation is not trivial, especially given laboratory observations of food selectivity (live phytoplankton vs. detritus) by the copepod genera most likely present in our imagery: *Pseudocalanus*, *Acartia*, and *Temora* (DeMott, 1988).

TABLE 2 | Cross-correlation lag/vertical offset values in density (kg/m^3) coordinates between FI_n, FP_n, and each canonical profile for zooplankton groups.

	FI_n	*Offset magnitude*	FP_n	*Offset diff.*
Cyclopoid copepods	−0.36	>	−0.18	0.18
Calanoid copepods	0.63	<	0.9	0.27
Appendicularians	0.72	<	0.99	0.27
Hydromedusae	0.36	<	0.45	0.09
Euphausiids	0.18	<	0.54	0.36

Positive (negative) values indicate main signal peak of the zooplankton canonical profile lies above (below) the main signal peak in either FI_n or FP_n. The offset magnitude comparison column uses the absolute value of the vertical offsets (i.e., signal lag). The fourth column is the difference between the offsets ($|FI_{n\ offset}$-$FP_{n\ offset}|$) for each group.

Relationships Between the SCM, FPM, and Zooplankton Distributions

In most cases, the SCM is thought to be a region of intense biological activity, including remineralization, primary production, grazing, predation, sexual reproduction, and infection (Cullen, 2015 and references therein). Similarly, marine snow accumulations have been suggested as potential hotspots for feeding by zooplankton (e.g., Alldredge et al., 2002; Möller et al., 2012). However, the impacts of higher trophic-level processes on the SCM have rarely been studied. Only recently global biogeochemical models have revealed the potential of top-down microzooplankton control of the SCM, for example (Moeller et al., 2019). Quantifying the effects of larger heterotrophic grazers, however, has been difficult. This knowledge gap is partially because sampling these organisms at the spatio-temporal scales of the SCM is difficult in the field – a problem obviated by the recent introduction of *in situ* imaging technologies. Still, relatively little is known about how *in situ*

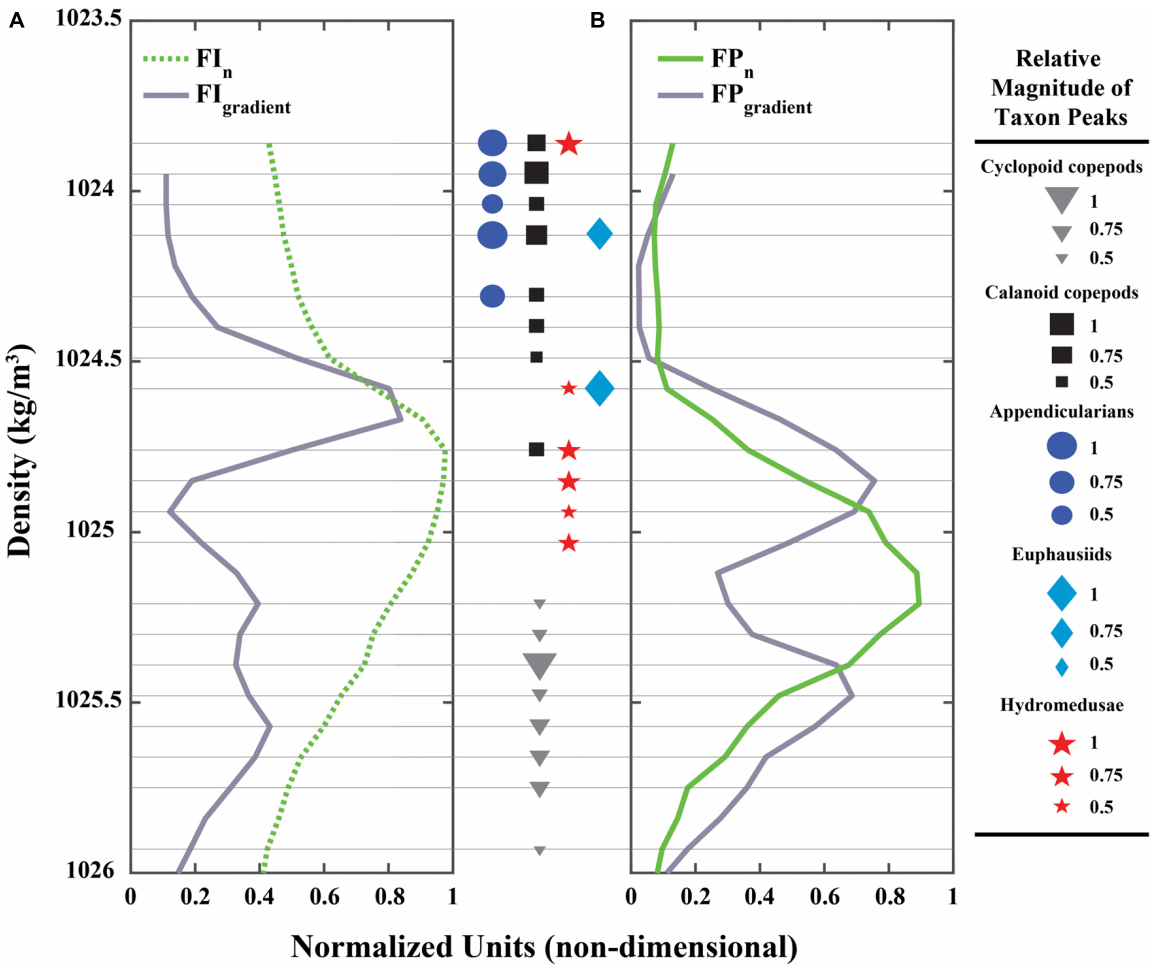

FIGURE 8 | (A) Normalized, time-averaged Fluorescence Intensity (FI_n) profile (green dotted line) and its vertical gradient ($FI_{gradient}$; gray solid line). **(B)** Normalized, time-averaged PLIF Fluoresence Particles (FP_n) profile (green solid line) and its vertical gradient ($FP_{gradient}$; gray solid line) in water density space. Markers (sizes are relative magnitude of raw counts of the peak) between **(A,B)** represent zooplankton peaks (95% probability of being higher than background values; see **Supplementary Figure 2**) and are the thin gray horizontal lines show their vertical position in relation to **(A,B)**. Colors are the same as in **Figure 7B** for each zooplankton group: calanoid copepods (black squares), cyclopoid copepods (gray triangles), appendicularians (dark blue circles), euphausiids (light blue diamonds), and hydromedusae (red stars).

distributions of various zooplankton taxa relate to those of marine snow and the SCM simultaneously.

Despite the known strong trophic links between zooplankton grazers and both phytoplankton and marine snow, we were surprised to find a spatial *mismatch* between the vertical distributions of all zooplankton taxa and these two potential food sources. As revealed by the cross-correlation analyses, the main peaks of all groups of zooplankton were vertically offset from the main peaks of both fluorescence intensity (representing phytoplankton) and fluorescent particles (representing marine snow). The direction and extent of this vertical offset, however, depended on taxon, with cyclopoid copepods being found below both the SCM and FPM, and the other zooplankton (calanoid copepods, appendicularians, and euphausiids) found either slightly or substantially above both the SCM and FPM. Offsets between copepods and the SCM were observed by Harris (1988) in the stratified summer waters of the English Channel. Harris, however, found the calanoid copepods *Paracalanus parvus* and *Centropages typicus* peaked above the SCM, whereas the cyclopoids *Oncaea subtilis* and *Oithona similis* were located immediately above and within the SCM, respectively. Other calanoid copepods in the same study showed a bi-modal distribution, where some peaks were co-located with the SCM or below in deeper waters. Interestingly, the SCM in that work and this one occurred at about the same depth (20–25 m). However, we observed quite different distributions of copepods relative to the SCM.

Not much could be inferred from our current data on appendicularians, which were observed mainly in the upper water column, and not associated with either the SCM or the FPM. In a location close to our sampling area, Alldredge (1982) found that a shallow aggregation of *Oikopleura longicaudata* was due to a spawning event – she observed sexually mature individuals (free swimming; that is, without "houses"), as well as juveniles and

eggs. Our observations included numerous free-swimming (no houses attached), potentially sexually mature appendicularians mainly from the genus *Oikopleura*. Appendicularians are filter feeders, capable of preying on bacterioplankton and phytoplankton, including ciliates (Lombard et al., 2010). An alternative hypothesis to their presence in the region above both SCM and FPM would be that they were feeding on high concentrations of bacteria or organisms not sampled by our devices, neither of which can be tested using our data.

Our observations of hydromedusae distributions suggest that these predators may have affected how herbivorous grazers interacted with their food sources. Gaps in our understanding of this predator-prey relationship stem from gelatinous organisms, including hydromedusae, being severely damaged by nets (Ohman, 2019), making it difficult to identify and quantify them, let alone observe their fine-scale distributions with respect to physical and biological factors *in situ*. One of the most striking examples that emerged from this analysis was the distribution of hydromedusae, which are considered primarily carnivorous, within the SCM (**Figure 8A**; red stars) and above the FPM (**Figure 8B**; red stars). Another distinct peak of high relative hydromedusae concentration is also located in the lowest density values at the top of the water column, and not associated with either the SCM or FPM (**Figure 8**). Interestingly, Napp et al. (1988) did not find any relationship between medusae (although no details were provided on what types of medusae were quantified in their work) and the SCM in a study conducted in the same region where our field work took place.

Hydromedusae are known to feed on copepods and appendicularians (e.g., Fulton and Wear, 1985; Costello and Colin, 2002). In our data, the hydromedusae group was composed of at least 6 different body types, and most likely different species, all present in every FIDO-Φ/O-Cam profile: the narcomedusae *Solmaris* sp. and *Solmundella bitentaculata*; the trachymedusae *Liriope tetraphylla*, *Crossota* sp., and at least two other unknown species. Some of these species (*L. tetraphylla*) are known to cause regime shifts in crustacean zooplankton assemblages (Yilmaz, 2015) and some species (including narcomedusae) have been observed feeding on appendicularians and crustaceans (among other prey), especially at night (Madin, 1988). In micro-scale (cm) laboratory experiments, Frost et al. (2010) found that hydromedusae tended to aggregate at density discontinuities where phytoplankton and calanoid copepod layers were located at the beginning of the experiment. In addition, they also noted that while hydromedusae (*Nemopsis bachei*) remained in these layers, the calanoid copepods (*Acartia tonsa*) dispersed during the same period, avoiding their predators. In our work, high-concentration peaks of calanoid copepods and appendicularians occurred above the SCM (black squares and blue circles in **Figure 8A**). These distributions are interesting because the largest peaks of hydromedusae seemed to bracket all major peaks observed for calanoid copepods and appendicularians. We believe that this pattern may indicate predator avoidance by the latter groups, a particularly interesting pattern given the fact that these relationships persisted over the two consecutive nights of our fieldwork.

An additional, but not necessarily mutually exclusive, hypothesis is that hydromedusae were feeding on phytoplankton and marine snow during this field work, as their largest peaks were associated with both the SCM and FPM (**Figure 8**). Although there is plenty of evidence that hydromedusae benthic stages can consume bacteria, protozoa, phytoplankton, detritus, and even dissolved organic matter (Gili and Hughes, 1995, cited in Bouillon et al., 2004), fewer reports exist for the free-swimming hydromedusa stages. Working on a species not found in our imagery (*Blackfordia virginica*), Morais et al. (2015) were surprised to find diatoms and dinoflagellates in the guts of these field collected hydromedusae. Colin et al. (2005) found that the trachymedusa *Aglaura hemistoma* effectively fed on chlorophyll-bearing protists, in addition to copepods and nauplii, effectively labeling this hydromedusa as an omnivore. It is possible that the trachymedusae and narcomedusae found in this study, generally recognized as primarily carnivorous, were feeding on primary producers, and potentially on marine snow. While our data cannot answer this question, the position of these hydromedusae within both the SCM and FPM, in addition to the limited but conclusive evidence in the above-mentioned studies, support this hypothesis.

Zooplankton Dynamics and Physical Factors Driving the Shape of the SCM and FPM

Several studies have suggested that peaks in food abundance may not be the most important determinant of grazer distribution, but rather the *gradients* in food abundance (Leising et al., 2005; Prairie et al., 2011). The presence of high-density aggregations of zooplankton immediately above or below thin layers of phytoplankton and marine snow has been observed in stratified systems, in both shallow and deep waters (e.g., Benoit-Bird et al., 2009; Möller et al., 2012; Greer et al., 2013, 2020). In many cases, previous studies concluded that the sharp vertical gradients in the concentrations of phytoplankton and marine snow were caused by their consumers (Alldredge et al., 2002; Benoit-Bird et al., 2009; Möller et al., 2012). Here we examine how the distributions of herbivorous zooplankton taxa and their potential responses to predators might explain the shape of the distributions of their food sources.

The upper boundary (and sharpest gradient) of the SCM coincides with a peak in euphausiids and overlaps with peaks in calanoid copepods. The interplay of the predatory hydromedusae located at the SCM, potentially driving their (herbivorous grazer) prey upward may help explain the shape of this upper boundary. While it is recognized that copepods have been found above the SCM grazing on higher-quality food sources within the region of maximum primary productivity – a common mechanism invoked to explain the formation and maintenance of SCM layers (Cullen, 2015 and references therein) – it may also be possible that predator avoidance may drive herbivorous grazers upward, enhancing the grazing on the phytoplankton above the SCM, which in turn could shape the phytoplankton gradients forming the SCM. It is harder to interpret the location of euphausiids in relation to the SCM given their widely known diel vertical migration behavior (e.g., De Robertis, 2002; Werner and Buchholz, 2013) and the fact that their vertical distribution changed over the duration of our study.

The dynamics shaping the lower SCM boundary are more difficult to discern, because the bulk fluorescence signal includes some marine snow. This overlap in signal sources is perhaps evident in the secondary, less-sharp gradient (that is, below the SCM) in the bulk fluorescence signal (gray line in **Figure 8A**), which aligns with the FPM. Alldredge et al. (2002) observed the *in situ* formation of a marine snow layer, deriving from growth and subsequent sinking of phytoplankton two meters above that layer. Because the FPM in this work was primarily composed of fluorescence particles, it is reasonable to hypothesize that the FPM could be maintained by aggregation and sinking of phytoplankton from the SCM above.

Marine snow layers form by sinking particles, which can slow down when passing through sharp density gradients, providing an explanation for why marine snow layers are often found associated with density transitions (Prairie et al., 2015; Prairie and White, 2017). This mechanism may also apply to the FPM observed in the present work, despite the fact that the peak we observed is wider (∼5–10 m; **Figure 4D**) than many of the marine snow layers previously observed by others (10 s of cm; e.g., Alldredge et al., 2002). The shape of the FPM we observed was roughly symmetrical, with two sharp gradients of similar magnitude above and below the maximum (**Figure 8B**; gray line). Layers formed solely by decreases in settling velocity are predicted to have sharper gradients at the upper boundary (Prairie and White, 2017), which may indicate that different mechanisms generated the upper and lower boundaries of the FPM observed here. A decrease in sinking velocity may explain the sharp gradient above the maximum, and the sharp gradient below it may be explained by a combination of losses to sinking and consumption by cyclopoid copepods, which were found immediately below the FPM in its lower boundary (**Figure 8B**; gray triangles). The same predator-prey argument invoked above for calanoid copepods and appendicularians could be made in the case of the FPM and cyclopoid copepods – that is, cyclopoids were located where their potential predators were not. However, another possibility stems from the complex feeding ecology of cyclopoid copepods, which, in addition to being ambush predators (Paffenhöfer, 1993; Saiz et al., 2014; Kiørboe et al., 2015), are also known to feed on marine snow and fecal pellets of calanoid copepods (Turner, 1986; González and Smetacek, 1994). The fact that cyclopoid copepods have been observed to repackage larger particles into smaller, potentially slowly sinking marine snow (González and Smetacek, 1994) these copepods may have contributed to the symmetrical shape of the FPM feature studied here. These observations are also consistent with the "coprophagous filter" hypothesis; metazooplankton activities in the epipelagic reduce the vertical fluxes of large marine snow (González and Smetacek, 1994; Turner, 2015 and references therein). Unfortunately, we cannot conclusively say that cyclopoids were feeding on marine snow, as no grazing measurements or gut content analyses were conducted. Neither can we rule out other biological processes taking place, including grazing on marine snow by other organisms.

Significance to Plankton Ecology

Our fine-scale observations of the vertical distributions of chl-*a*, marine snow, and zooplankton with different feeding preferences allowed us to infer the trophic drivers underlying the observed spatial distribution patterns of the SCM and FPM. These inferences were possible through the combined deployments of new *in situ* technologies developed for this purpose. Even though the "enduring enigma" of SCM dynamics has been deemed a mystery solved (Cullen, 2015), the observations presented in our work open new avenues of scientific inquiry, allowing us to develop new hypotheses that could be tested using models of the dynamics of top-down controls on subsurface chlorophyll maxima and marine snow distributions in a variety of aquatic environments, and to evaluate how climate change might alter these dynamics. With the sophistication of *in situ* sensors, sampling methods, and mathematical models, these approaches could inform each other (Everett et al., 2017), so in future studies, measurements of diel biological rates (primary production, grazing, predation), and measurements of bacterial growth and distribution patterns, along with fine-scale *in situ* imaging will be important in further elucidating the trophic interactions that we hypothesized, based on our data. Evaluating these hypotheses might be possible with the development and potential availability of new *in situ* molecular systems (e.g., Spanbauer et al., 2019) especially when they are deployed on multi-sensor platforms.

DATA AVAILABILITY STATEMENT

The datasets generated for this study are available on request to the corresponding author.

AUTHOR CONTRIBUTIONS

JJ, PF, and CB-A contributed to the conception, design, and execution of the study. JP processed PLIF imagery. CB-A processed O-Cam, MOCNESS and Zooscan data, and performed the data analyses. CB-A wrote the first draft of the manuscript. All authors contributed to manuscript revision, read and approved the submitted version.

FUNDING

The bulk of this work is the result of CB-A Ph.D. dissertation work, which was supported by the Mexican agency CONACyT and its UC system partner UC MEXUS.

ACKNOWLEDGMENTS

CB-A would like to thank UC Ship Funds for funding the CalEchoes cruise and the CCE-LTER program for the generous support to conduct MOCNESS tows and for providing materials and equipment necessary to process the zooplankton samples. Thanks to Jesse Powell who helped sort zooplankton net samples with the Zooscan. We are thankful to the members, past and present, of the Jaffe Lab who worked hard in setting up the FIDO-Φ platform, especially Paul Roberts, Fernando Simonet, and Fred Uhlman. We thank Michael Ford (NOAA) for providing

taxonomic identification of selected hydromedusae images. The fieldwork would not have been possible without the help of the captains and crew of the R/V New Horizon and the now retired R/V Melville. We are thankful to three reviewers, whose constructive criticism greatly helped improve this manuscript.

SUPPLEMENTARY MATERIAL

The Supplementary Material for this article can be found online at: https://www.frontiersin.org/articles/10.3389/fmars.2020.00602/full#supplementary-material

REFERENCES

Alldredge, A. L. (1982). Aggregation of spawning appendicularians in surface windrows. *Bull. Mar. Sci.* 32, 250–254.

Alldredge, A. L., Cowles, T. J., MacIntyre, S., Rines, J. E. B., Donaghay, P. L., Greenlaw, C. F., et al. (2002). Occurrence and mechanisms of formation of a dramatic thin layer of marine snow in a shallow Pacific fjord. *Mar. Ecol. Prog. Ser.* 233, 1–12. doi: 10.3354/meps233001

Alldredge, A. L., and Silver, M. W. (1988). Characteristics, dynamics, and significance of marine snow. *Prog. Oceanogr.* 20, 41–82. doi: 10.1016/0079-6611(88)90053-5

Banse, K. (1964). On the vertical distribution of zooplankton in the sea. *Prog. Oceanogr.* 2, 53–125. doi: 10.1016/0079-6611(64)90003-5

Barnett, A. J., Finlay, K., and Beisner, B. E. (2007). Functional diversity of crustacean zooplankton communities: towards a trait-based classification. *Freshw. Biol.* 52, 796–813. doi: 10.1111/j.1365-2427.2007.01733.x

Benfield, M. C., Davis, C. S., Wiebe, P. H., Gallager, S. M., Lough, R. G., and Copley, N. J. (1996). Video Plankton Recorder estimates of copepod, pteropod and larvacean distributions from a stratified region of Georges Bank with comparative measurements from a MOCNESS sampler. *Deep Sea Res. Part II Top. Stud. Oceanogr.* 43, 1925–1945. doi: 10.1016/S0967-0645(96)00044-6

Benfield, M. C., Grosjean, P., Culverhouse, P. F., Irigoien, X., Sieracki, M. E., Lopez-Urrutia, A., et al. (2007). RAPID: research on automated plankton identification. *Oceanography* 20, 172–187. doi: 10.5670/oceanog.2007.63

Benoit-Bird, K. J., Cowles, T. J., and Wingard, C. E. (2009). Edge gradients provide evidence of ecological interactions in planktonic thin layers. *Limnol. Oceanogr.* 54, 1382–1392. doi: 10.4319/lo.2009.54.4.1382

Bouillon, J., Medel, M. D., Pagès, F., Gili, J.-P., Boero, F., and Gravili, C. (2004). Fauna of the mediterranean hydrozoa. *Sci. Mar.* 68, 5–438. doi: 10.3989/scimar.2004.68s25

Briseño-Avena, C., Roberts, P. L. D., Franks, P. J. S., and Jaffe, J. S. (2015). ZOOPS-O2: a broadband echosounder with coordinated stereo optical imaging for observing plankton in situ. *Methods Oceanogr.* 12, 36–54. doi: 10.1016/j.mio.2015.07.001

Colin, S. P., Costello, J. H., Graham, W. M., and Higgins, J. I. I. I. (2005). Omnivory by the small cosmopolitan hydromedusa *Aglaura hemistoma*. *Limnol. Oceanogr.* 50, 1264–1268. doi: 10.4319/lo.2005.50.4.1264

Costello, J. H., and Colin, S. P. (2002). Prey resource use by coexistent hydromedusae from Friday Harbor, Washington. *Limnol. Oceanogr.* 47, 934–942. doi: 10.4319/lo.2002.47.4.0934

Cowen, R. K., and Guigand, C. M. (2008). *In situ* ichthyoplankton imaging system (ISIIS): system design and preliminary results. *Limnol. Oceanogr. Methods* 6, 126–132. doi: 10.4319/lom.2008.6.126

Cullen, J. J. (1982). The deep chlorophyll maximum: comparing vertical profiles of chlorophyll *a*. *Can. J. Fish. Aquat. Sci.* 39, 791–803. doi: 10.1139/f82-108

Cullen, J. J. (2015). Subsurface chlorophyll maximum layers: enduring enigma or mystery solved? *Annu. Rev. Mar. Sci.* 7, 207–239. doi: 10.1146/annurev-marine-010213-135111

Davis, C. S., Gallager, S. M., Marra, M., and Sewart, W. K. (1996). Rapid visualization of plankton abundance and taxonomic composition using the Video Plankton Recorder. *Deep Sea Res. Part II Top. Stud. Oceanogr.* 43, 1947–1970. doi: 10.1016/S0967-0645(96)00051-3

De Robertis, A. (2002). Small-scale spatial distribution of the euphausiid *Euphausia pacifica* and overlap with planktivorous fishes. *J. Plankton Res.* 24, 1207–1220. doi: 10.1093/plankt/24.11.1207

Dekshenieks, M. M., Donaghay, P. L., Sullivan, J. M., Rines, J. E. B., Osborn, T. R., and Twardowski, M. S. (2001). Temporal and spatial occurrence of thin phytoplankton layers in relation to physical processes. *Mar. Ecol. Prog. Ser.* 223, 61–71. doi: 10.3354/meps223061

DeMott, W. R. (1988). Discrimination between algae and detritus by freshwater and marine zooplankton. *Bull. Mar. Sci.* 43, 486–499.

Everett, J. D., Baird, M. E., Buchanan, P., Bulman, C., Davies, C., Downie, R., et al. (2017). Modeling what we sample and sampling what we model: challenges for zooplankton model assessment. *Front. Mar. Sci.* 4:77. doi: 10.3389/fmars.2017.00077

Franks, P. J. S., and Jaffe, J. S. (2001). Microscale distributions of phytoplankton: initial results from a two-dimensional imaging fluorometer, OSST. *Mar. Ecol. Prog. Ser.* 220, 59–72. doi: 10.3354/meps220059

Franks, P. J. S., and Jaffe, J. S. (2008). Microscale variability in the distributions of large fluorescent particles observed in situ with a planar laser imaging fluorometer. *J. Mar. Syst.* 69, 254–270. doi: 10.1016/j.jmarsys.2006.03.027

Frost, J. R., Jacoby, C. A., and Youngbluth, M. J. (2010). Behavior of *Nemopsis bachei* L. Agassiz, 1849 medusae in the presence of physical gradients and biological thin layers. *Hydrobiologia* 645, 97–111. doi: 10.1007/s10750-010-0213-z

Fulton, R. S., and Wear, R. G. (1985). Predatory feeding of the nydromedusae Obelia geniculata and Phialella quadrata. *Mar. Biol.* 87, 47–54. doi: 10.1007/bf00397004

Galliene, C. P., and Robins, D. B. (2001). Is Oithona the most important copepod in the world's oceans? *J. Plankton Res.* 23, 1421–1432. doi: 10.1093/plankt/23.12.1421

Gili, J. M., and Hughes, R. G. (1995). The Ecology of marine benthic hydroids. *Oceanogr. Mar. Biol. Annu. Rev.* 33, 351–426.

González, H. E., and Smetacek, V. (1994). The possible role of the cyclopoid copepod Oithona in retarding the vertical flux of zooplankton faecal material. *Mar. Ecol. Prog. Ser.* 113, 233–246. doi: 10.3354/meps113233

Greer, A. T., Boyette, A. D., Cruz, V. J., Cambazoglu, M. K., Dzwonkowski, B., Chiaverano, L. M., et al. (2020). Contrasting fine-scale distributional patterns of zooplankton driven by the formation of a diatom-dominated thin layer. *Limnol. Oceanogr.* (in press). doi: 10.1002/lno.11450

Greer, A. T., Cowen, R. K., Guigand, C. M., Mcmanus, M. A., Sevadjian, J. C., and Timmerman, A. H. V. (2013). Relationships between phytoplankton thin layers and the fine-scale vertical distributions of two trophic levels of zooplankton. *J. Plankton Res.* 35, 939–956. doi: 10.1093/plankt/fbt056

Guigand, C. M., Cowen, R. K., Llopiz, J. K., and Richardson, D. E. (2005). A coupled asymmetrical multiple opening closing net with environmental sampling system. *Mar. Technol. Soc. J.* 39, 22–24. doi: 10.4031/002533205787444042

Harris, R. P. (1988). Interactions between diel vertical migratory behavior of marine zooplankton and the subsurface chlorophyll maximum. *Bull. Mar. Sci.* 43, 663–674.

Jaffe, J. S., Franks, P. J. S., Briseño-Avena, C., Roberts, P. L. D., and Laxton, B. (2013). "Advances in underwater fluorometry: from bulk fluorescence to planar laser imaging," in *Subsea Optics and Imaging*, 1st Edn, eds J. Watson, and O. Zieliski (Sawston: Woodhead Publishing), 536–549. doi: 10.1533/9780857093523.3.536

Katz, J., Donaghay, P. L., Zhang, J., King, S., and Russell, K. (1999). Submersible holocamera for detection of particle characteristics and motions in the ocean. *Deep Sea Res. Part I Oceanogr. Res. Pap.* 46, 1455–1481. doi: 10.1016/S0967-0637(99)00011-4

Kiørboe, T., Jian, H., and Colin, S. P. (2015). Danger of zooplankton feeding: the fluid signal generated by ambush-feeding copepods. *Proc. Biol. Sci.* 277, 3229–3237. doi: 10.1098/rspb.2010.0629

Leach, T. H., Beisner, B. E., Carey, C. C., Pernica, P., Rose, K. C., Huot, Y., et al. (2018). Patterns and drivers of deep chlorophyll maxima structure in 100 lakes: the relative importance of light and thermal stratification. *Limnol. Oceanogr.* 63, 628–646. doi: 10.1002/lno.10656

Leising, A. W., Pierson, J. J., Cary, S., and Frost, B. W. (2005). Copepod foraging and predation risk within the surface layer during night-time feeding forays. *J. Plankton Res.* 27, 987–1001. doi: 10.1093/plankt/fbi084

Lombard, F., Boss, E., Waite, A. M., Uitz, J., Stemmann, L., Sosik, H. M., et al. (2019). Globally consistent quantitative observations of planktonic ecosystems. *Front. Mar. Sci.* 6:196. doi: 10.3389/fmars.2019.00196

Lombard, F., Eloire, D., Gobet, A., Stemmann, L., Dolan, J. R., Sciandra, A., et al. (2010). Experimental and modeling evidence of appendicularian-ciliate interactions. *Limnol. Oceanogr.* 55, 77–90. doi: 10.4319/lo.2010.55.1.0077

MacIntyre, S., Alldredge, A. L., and Gotschalk, C. C. (1995). Accumulation of marine snow at density discontinuities in the water column. *Limnol. Oceanogr.* 40, 449–468. doi: 10.4319/lo.1995.40.3.0449

Madin, L. P. (1988). Feeding behavior of tentaculate predators: in situ observations and a conceptual model. *Bull. Mar. Sci.* 43, 413–429.

Malkiel, E., Abras, J. N., Widder, E. A., and Katz, J. (2006). On the spatial distribution and nearest neighbor distance between particles in the water column determined from in situ holographic measurements. *J. Plankton Res.* 28, 149–170. doi: 10.1093/plankt/fbi107

Moeller, H. V., Laufkötter, C., Sweeney, E. M., and Johnson, M. D. (2019). Light-dependent grazing can drive formation and deepening of deep chlorophyll maxima. *Nat. Commun.* 10:1978. doi: 10.1038/s41467-019-09591-2

Möller, K. O., St John, M., Temming, A., Floeter, J., Sell, A. F., Herrmann, J. P., et al. (2012). Marine snow, zooplankton and thin layers: indications of a trophic link from small-scale sampling with the Video Plankton Recorder. *Mar. Ecol. Prog. Ser.* 468, 57–69. doi: 10.3354/meps09984

Morais, P., Parra, M. P., Marques, R., Cruz, J., Angélico, M. M., Chainho, P., et al. (2015). What are jellyish really eating to support high ecophysiological condition. *J. Plankton Res.* 37, 1036–1041. doi: 10.1093/plankt/fbv044

Napp, J. M., Brooks, E. R., Matrai, P., and Mullin, M. M. (1988). Vertical distribution of marine particles and grazers II. Relation of grazer distribution to food quality and quantity. *Mar. Ecol. Prog. Ser.* 50, 59–72. doi: 10.3354/meps050059

Ohman, M. D. (2019). A sea of tentacles: optically discernible traits resolved from planktonic organisms *in situ*. *ICES J. Mar. Sci.* 76, 1959–1972. doi: 10.1093/icesjms/fsz184

Ohman, M. D., Davis, R. E., Sherman, J. T., Grindley, K. R., Whitmore, B. M., Nickels, C. F., et al. (2018). Zooglider: an autonomous vehicle for optical and acoustic sensing of zooplankton. *Limnol. Oceanogr. Methods* 17, 69–86. doi: 10.1002/lom3.10301

Paffenhöfer, G. (1993). On the ecology of marine cyclopoid copepods (Crustacea, Copepoda). *J. Plankton Res.* 15, 37–55. doi: 10.1093/plankt/15.1.37

Pfitsch, D. W., Malkiel, E., Takagi, M., Ronzhes, Y., King, S., Sheng, J., et al. (2007). "Analysis of in-situ microscopic organism behavior in data acquired using a free-drifting submersible holographic imaging system," in *Proceedings of the IEEE Conference 2007 Oceans* (Vancouver: IEEE), 1–8. doi: 10.1109/OCEANS.2007.4449197

Picheral, M., Guidi, L., Stemman, L., Karl, D. M., Iddaoud, G., and Gorsky, G. (2010). The underwater vision profiler 5: an advanced instrument for high spatial resolution studies of particle size spectra and zooplankton. *Limnol. Oceanogr. Methods* 8, 462–473. doi: 10.4319/lom.2010.8.462

Pomerleau, C., Sastri, A. R., and Beisner, B. E. (2015). Evaluation of functional trait diversity for marine zooplankton communities in the Northeast subarctic Pacific Ocean. *J. Plankton Res.* 37, 712–726. doi: 10.1093/plankt/fbv045

Prairie, J. C., Franks, P. J. S., and Jaffe, J. S. (2010). Cryptic peaks: invisible vertical structure in fluorescent particles revealed using a planar laser imaging Fluorometer. *Limnol. Oceanogr.* 55, 1943–1958. doi: 10.4319/lo.2010.55.5.1943

Prairie, J. C., Franks, P. J. S., Jaffe, J. S., Doubell, M. J., and Yamazaki, H. (2011). Physical and biological controls of vertical gradients in phytoplankton. *Limnol. Oceanogr. Fluids Environ.* 1, 75–90. doi: 10.1215/21573698-1267403

Prairie, J. C., and White, B. L. (2017). A model for thin layer formation by delayed particle settling at sharp density gradients. *Cont. Shelf Res.* 133, 37–46. doi: 10.1016/j.csr.2016.12.007

Prairie, J. C., Ziervogel, K., Camassa, R., McLaughlin, R. M., White, B. L., Dewald, C., et al. (2015). Delayed settling of marine snow: effects of density gradient and particle properties and implications for carbon cycling. *Mar. Chem.* 175, 28–38. doi: 10.1016/j.marchem.2015.04.006

Reid, J. G. G., Hurley, P. C. F., and O'Boyle, R. N. (1987). "Mininess: a self-trimming multiple openening and closing plankton net frame design," in *Proceedings of the IEEE Conference On Oceans '87*, Halifax, NS, 466–471.

Remsen, A., Hopkins, T. L., and Samson, S. (2004). What you see is not what you catch: a comparison of concurrently collected net, optical plankton counter, and shadowed image particle profiling evaluation recorder data from the northeast Gulf of Mexico. *Deep Sea Res. Part I Oceanogr. Res. Pap.* 51, 129–151. doi: 10.1016/j.dsr.2003.09.008

Saiz, E., Griffell, K., Calbet, A., and Isari, S. (2014). Feeding rates and prey: predator size ratios of the nauplii and adult females of the marine cyclopoid copepod Oithona davisae. *Limnol. Oceanogr.* 59, 2077–2088. doi: 10.4319/lo.2014.59.6.2077

Schmid, M. S., and Fortier, L. (2019). The intriguing co-distribution of the copepods *Calanus hyperboreus* and *Calanus glacialis* in the subsurface chlorophyll maximum of Arctic seas. *Elementa Sci. Anthropocene* 7:20. doi: 10.1525/elementa.388

Schulz, J., Barz, K., Ayon, P., Lüdke, A., Zielinski, O., Mengedoht, D., et al. (2010). Imaging of plankton specimens with the lightframe on-sight keyspecies investigation (LOKI) system. *J. Eur. Opt. Soc. Rapid Publ.* 5, 1–9. doi: 10.2971/jeos.2010.10017s

Settles, G. S. (2012). *Schlieren and Shadowgraph Techniques: Visualizing Phenomena in Transparent Media*. Berlin: Springer.

Spanbauer, T. L., Briseño-Avena, C., Pitz, K. J., and Suter, E. (2019). Salty sensors, fresh ideas: the use of molecular and imaging sensors in understanding plankton dynamics across marine and freshwater ecosystems. *Limnol. Oceanogr. Lett.* 5, 169–184. doi: 10.1002/lol2.10128

Talapatra, S., Hong, J., McFarland, M., Nayak, A. R., Zhang, C., Katz, J., et al. (2013). Characterization of biophysical interactions in the water column using *in situ* digital holography. *Mar. Ecol. Prog. Ser.* 473, 29–51. doi: 10.3354/meps1s0049

Timmerman, A. H. V., McManus, M. A., Cheriton, O. M., Cowen, R. K., Greer, A. T., Kudela, R. M., et al. (2014). Hidden thin layers of toxic diatoms in a coastal bay. *Deep Sea Res. Part II Top. Stud. Oceanogr.* 101, 129–140. doi: 10.1016/j.dsr2.2013.05.030

Turner, J. T. (1986). Zooplankton feeding ecology: contents of fecal pellets of the cyclopoid copepods *Oncaea venusta*, *Corycaeus amazonicus*, *Oithona plumifera*, and *O. simplex* from the northern Gulf of Mexico. *Mar. Ecol.* 7, 289–302. doi: 10.1111/j.1439-0485.1986.tb00165.x

Turner, J. T. (2015). Zooplankton fecal pellets, marine snow, phytodetritus and the ocean's biological pump. *Prog. Oceanogr.* 130, 205–248. doi: 10.1016/j.pocean.2014.08.005

Werner, T., and Buchholz, F. (2013). Diel vertical migration behaviour in Euphausiids of the northern Benguela current: seasonal adaptations to food availability and strong gradients of temperature and oxygen. *J. Plankton Res.* 35, 792–812. doi: 10.1093/plankt/fbt030

Wiebe, P. H., and Benfield, M. C. (2003). From the Hansen net towards four-dimensional biological oceanography. *Prog. Oceanogr.* 56, 7–136. doi: 10.1016/S0079-6611(02)00140-4

Wiebe, P. H., Bucklin, A., and Benfield, M. (2017). "Sampling, preservation and counting II: zooplankton," in *Marine Plankton: A Practical Guide to Ecology, Methodology, and Taxonomy*, eds C. Castellani and M. Edwards (Oxford: Oxford University Press), 104–135. doi: 10.1093/oso/9780199233267.003.0010

Wiebe, P. H., Burt, K. H., Boyd, S. H., and Morton, A. W. (1976). A multiple opening/closing net and environmental sensing system for sampling zooplankton. *J. Mar. Res.* 34, 313–326.

Wiebe, P. H., Harris, R., Gislason, A., Margonski, P., Skjoldal, H. R., Benfield, M., et al. (2016). The ICES working group on zooplankton ecology: accomplishments of the first 25 years. *Prog. Oceanogr.* 141, 179–201. doi: 10.1016/j.pocean.2015.12.009

Wiebe, P. H., Morton, A. W., Bradley, A. M., Backus, R. H., Craddock, J. E., Barber, V., et al. (1985). New developments in the MOCNESS, an apparatus for sampling zooplankton and micronekton. *Mar. Biol.* 87, 313–323. doi: 10.1007/bf00397811

Yilmaz, I. N. (2015). Collapse of zooplankton stocks during *Liriope tetraphylla* (Hydromedusa) blooms and dense mucilaginous aggregations in a thermohaline stratified basin. *Mar. Ecol.* 36, 595–610. doi: 10.1111/maec.12166

Zawada, D. G. (2002). *The Application of a Novel Multispectral Imaging System to the in vivo Study of Fluorescent Compounds in Selected Marine Organisms*. Ph.D. dissertation, University of California, San Diego, CA.

Conflict of Interest: The authors declare that the research was conducted in the absence of any commercial or financial relationships that could be construed as a potential conflict of interest.

Copyright © 2020 Briseño-Avena, Prairie, Franks and Jaffe. This is an open-access article distributed under the terms of the Creative Commons Attribution License (CC BY). The use, distribution or reproduction in other forums is permitted, provided the original author(s) and the copyright owner(s) are credited and that the original publication in this journal is cited, in accordance with accepted academic practice. No use, distribution or reproduction is permitted which does not comply with these terms.

frontiers in Marine Science

ORIGINAL RESEARCH
published: 06 August 2020
doi: 10.3389/fmars.2020.00603

Persistent Hydrodynamic Cues Elicit Orientation-Specific Behavioral Sensitivities and Kinematic Responses in Dispersed Crab Larvae

Aaron C. True[1]*, *Donald R. Webster*[1], *Marc J. Weissburg*[2] and *Jeannette Yen*[2]

[1] Civil and Environmental Engineering, Georgia Institute of Technology, Atlanta, GA, United States, [2] Biological Sciences, Georgia Institute of Technology, Atlanta, GA, United States

The estuarine mud crab *Panopeus herbstii* navigates a complex, but structured, hydrodynamic environment throughout its life history. The effects of hydrodynamic cues associated with turbulent flows on larval behavior are relatively well understood in the context of selective tidal stream transport (STST) phenomena during the dispersed (pelagic) larval stages preceding benthic settlement. In contrast, the potential relevance of hydrodynamic cues associated with spatiotemporally persistent flow features, which are typical of estuarine regions of enhanced productivity such as fronts and clines, remains much less certain. To investigate the behavioral relevance of persistent hydrodynamic cues, larval assays were conducted in a flume system that uses a laminar slot jet to produce steady fluid shear layers. Further, to ascertain whether or not the spatial orientation of the shear layers relative to gravity significantly affected larval behavior, assays were conducted in upwelling, downwelling, and horizontal shear flows, corresponding to the direction of the bulk flow produced by the jet. The flow was quantified using particle image velocimetry (PIV) and tuned to produce ecologically-relevant hydrodynamic conditions for larval assays. Changes in larval swimming kinematics show a distinct response to shear flows in all orientations relative to no-flow conditions, and the macro effect of these changes is to enhance depth-keeping and induce area-restricted search behaviors. Furthermore, the specifics of larval behavioral responses depend on the directional orientation of the shear flow, and the statistical properties of the strength of the hydrodynamic cue (vorticity) eliciting these responses are also shown to be shear flow orientation-specific. Orientation-specific hydrodynamic sensitivity and behavioral response strategies in the presence of persistent hydrodynamic cues may enable larvae to effectively forage and sample to locate and exploit nearby resource patches, while also inducing dispersal trajectories toward favorable benthic settlement habitats through depth-regulation and effective STST. In this regard, hydrodynamic cues associated with spatiotemporally persistent flow features are likely fundamental drivers of decapod crab larvae behavior and may act as another mechanism of larval patchiness by directly impacting finescale population distributions and resultant dispersal trajectories.

Keywords: hydrodynamic cue, shear flow, decapod larvae, larval behavior, larval dispersal

OPEN ACCESS

Edited by:
Margaret Byron, Pennsylvania State University (PSU), United States

Reviewed by:
Michelle Heather DiBenedetto, Woods Hole Oceanographic Institution, United States
Kelly Sutherland, University of Oregon, United States

***Correspondence:**
Aaron C. True
aaron.true@gatech.edu

Specialty section:
This article was submitted to Marine Ecosystem Ecology, a section of the journal Frontiers in Marine Science

Received: *10 February 2020*
Accepted: *30 June 2020*
Published: *06 August 2020*

Citation:
True AC, Webster DR, Weissburg MJ and Yen J (2020) Persistent Hydrodynamic Cues Elicit Orientation-Specific Behavioral Sensitivities and Kinematic Responses in Dispersed Crab Larvae. Front. Mar. Sci. 7:603. doi: 10.3389/fmars.2020.00603

1. INTRODUCTION

Dispersal trajectories of pelagic zooplankton are fundamentally influenced by both individual behavior and physical forcing (Woodson and McManus, 2007). For Brachyuran crabs whose life history includes a dispersed larval stage preceding benthic settlement, a predominant behavioral mode is depth-regulation that enables diel, tidal (endogenous), and ontogenetic (larval stage-specific) vertical migrations. Well-timed vertical migrations allow larvae to exploit vertical gradients of horizontal velocity, typical in nearshore and estuarine hydrodynamics (**Figure 1**), in order to selectively induce horizontal transport and improve fitness through favorable habitat selection. For example, larvae can gain net transport shoreward by swimming vertically down during ebb tide and up during flood tide. Or, depending on the goals of the particular larval stage, they can gain net transport seaward with the opposite behavior. These behavioral adaptations are collectively referred to as selective tidal stream transport (STST), and they strongly affect dispersal trajectories and population connectivity (Cronin and Forward, 1986; Eggleston et al., 1998; Forward et al., 2001, 2004).

There are a number of environmental cues that strongly affect larval swimming behaviors throughout dispersal (Ott and Forward, 1976; Queiroga and Blanton, 2005; Lecchini et al., 2010). Vertical migratory behaviors and depth-regulation are predominant behavioral responses driven by combined geotaxis, phototaxis, and barokinesis (Forward, 1974; Sulkin, 1975, 1984; Sulkin et al., 1980). Other larval behavioral responses to environmental cues are strongly dependent on larval stage (Shanks, 1986; Jamieson and Phillips, 1988; Hobbs and Botsford, 1992) and the particular combination of cues present (Queiroga and Blanton, 2005), as well as their intensities (Tankersley et al., 1995) and rates of change (Forward, 1989a). Nonetheless, some larval stage-specific behavioral patterns emerge. For example, megalopae (the post-larval stage directly preceding benthic settlement) respond to increasing pressure (Forward, 1990), salinity (Queiroga and Blanton, 2005), and turbulent kinetic energy (Welch et al., 1999) associated with flood tide by swimming vertically upward to induce shoreward transport toward favorable benthic settlement habitats (flood tide transport, FTT). However, these typical behavioral responses may be confounded by finescale foraging and sampling behaviors induced by chemical and hydrodynamic cues indicative of nearby resource patches. The intermittent presence of a dominant sensory cue that induces localized foraging and sampling may cause temporary departures from typical behavioral modes such as FTT and significantly influence larval dispersal trajectories (Woodson and McManus, 2007).

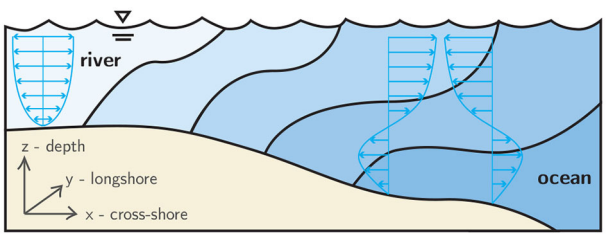

FIGURE 1 | Conceptual schematic of estuarine hydrodynamics. Shades of blue indicate water masses of differing salinity in a weakly-stratified estuary, and the blue arrows indicate tidally-modulated, oscillating flow structure.

Effective foraging and sampling behaviors in competent larval stages are enabled by highly-developed morphologies suitable for detecting and exploiting ambient chemical and hydrodynamic cues (Anger, 2001; Queiroga and Blanton, 2005). Chemical cues can induce or delay larval metamorphoses (Rodriguez and Epifanio, 2000; Andrews et al., 2001), inform habitat selection (Forward et al., 2001; Lecchini et al., 2010; Tapia-Lewin and Pardo, 2014), and affect swimming behaviors (Forward et al., 2003a; Houser and Epifanio, 2009). Further, hydrodynamic cues associated with fluid velocity gradients fundamentally structure complex estuarine and nearshore environments. Hydrodynamic cues that mechanosensitive larvae may respond to, in any flow of interest, include rotation (vorticity), deformation (strain), and acceleration, which follows directly from the total or material derivative of the fluid velocity field in the Navier-Stokes equations that govern fluid motion. The material derivative includes the temporal (unsteady) acceleration term as well as the spatial (convective) acceleration terms resulting from the dot product of the velocity vector and the velocity gradient tensor; the decomposition of this tensor, in turn, yields the fluid deformation rate and rotation rate tensors (Kundu et al., 2011). Larvae may respond to all or any of these hydrodynamic cues, for example, when exposed to turbulent flow. Changing turbulent kinetic energy (TKE) levels elicits excited swimming (Welch et al., 1999) that enhances effective STST (Criales et al., 2013), one of the most distinctive behavioral modes of dispersed larvae.

While it is well-understood that turbulence, with its characteristic unsteadiness and rapidly fluctuating hydrodynamic cues, plays an important role in larval behavior (Queiroga and Blanton, 2005), the potential relevance of hydrodynamic cues associated with spatiotemporally persistent flow features remains largely unknown, despite the fact that such cues are likely to be ecologically relevant. Finescale hydrographic structure in the water column is often associated with enhanced productivity and high-density resource patches, such as the regions around fronts and clines (Largier, 1993; McManus et al., 2003). This suggests that spatiotemporally persistent hydrodynamic cues, such as rotation and deformation in a steady fluid shear layer (**Figure 2**), may also play a fundamental role in larval behavior, particularly in the context of foraging and sampling. While turbulence acts to homogenize a larva's environment by dissipating hydrodynamic and chemical gradients, persistent hydrodynamic features indicative of nearby resource patches offer an opportunity to improve fitness through area-restricted search behaviors and resource exploitation.

There are two primary questions the present study seeks to answer. First, do hydrodynamic cues associated with spatiotemporally persistent flow features affect individual behavioral processes of dispersed decapod crab larvae? And second, given that regions of enhanced productivity *in situ* are often characterized by strong hydrographic gradients both

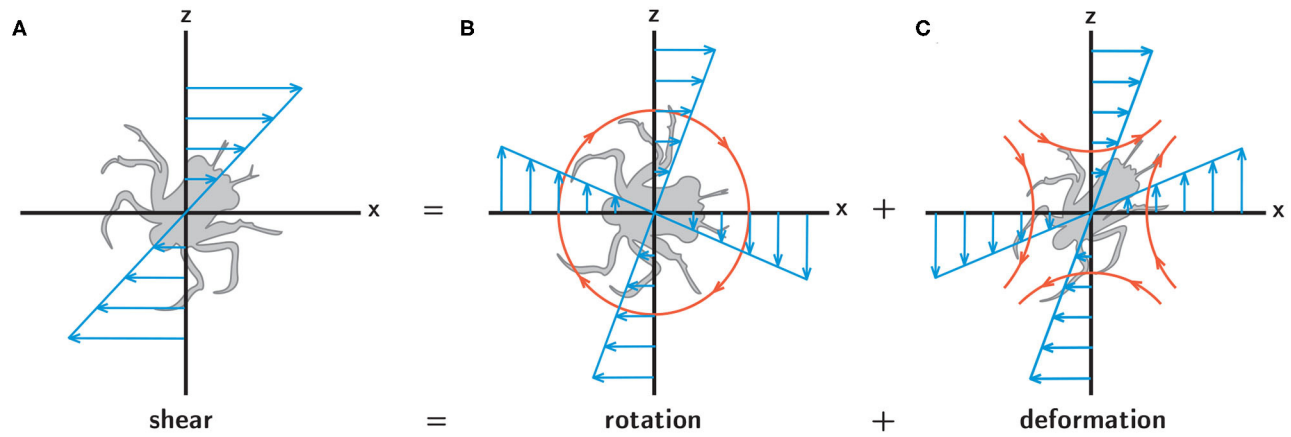

FIGURE 2 | A simple shear flow **(A)** can be decomposed into fluid rotation **(B)** and deformation **(C)**. In each panel the blue arrows indicate the spatial structure of the corresponding flow components, and in **(B,C)** the orange lines and arrows indicate the resultant rotation **(B)** and stretching **(C)** experienced by larvae.

vertically and horizontally, do differing spatial orientations of persistent hydrodynamic cues relative to gravity produce differential behavioral responses? To differentiate among spatial orientations, we use the terms "front" and "cline" generally to denote regions of enhanced spatial gradients of fluid velocity (or shear), temperature, salinity, nutrients, or other associated hydrographic variables, in which the predominant gradient (direction of most rapid change) is in the horizontal (front) and vertical (cline) directions (Woodson and McManus, 2007; McManus and Woodson, 2012; Woodson et al., 2012).

2. MATERIALS AND METHODS

To investigate the relevance of spatiotemporally persistent hydrodynamic cues on larval behavior, free-swimming behavioral assays were conducted with megalopae of the common Atlantic mud crab *Panopeus herbstii* (**Figure 3**) in a laboratory flume system that uses a laminar slot jet to produce steady fluid shear layers (**Figure 4A**). To investigate the importance of the directional orientation of the hydrodynamic cue relative to gravity, the main test section could be rotated into three different flow configurations, corresponding to the direction of the bulk flow produced by the jet: upwelling, downwelling, and horizontal. The flow fields were quantified and tuned to produce ecologically-relevant hydrodynamic conditions for larval assays. Larval swimming kinematics were quantified and analyzed under each shear flow orientation in addition to a no-flow control condition. Flow measurements and larval swimming kinematics were observed in a 10 × 10 cm window in a 25 L experimental volume, beginning 5 cm downstream of the jet nozzle opening and centered with respect to the jet centerline (**Figures 4B,C**).

FIGURE 3 | Megalopa of the common Atlantic mud crab *Panopeus herbstii*.

2.1. Shear Layer Flume

The shear layer flume is a recirculating flow system that uses a laminar slot jet (the Bickley jet) to produce steady fluid shear layers with tunable hydrodynamic characteristics. The main flume section is constructed of clear acrylic for optical access and can be rotated into upwelling, downwelling, or horizontal flow configurations (**Figure 4A**). An elevated constant head tank (28 L, US Plastics) with a free surface overflow drives flow with adjustable volumetric flowrate (Dwyer Instruments rotameter) through a slot jet nozzle (316 SS, jet opening 1 × 25 cm), creating a steady fluid shear layer in the main test section due to the dynamics of the laminar, planar free jet downstream of the nozzle opening. A 12:1 area ratio contraction was employed with a 5th-order polynomial contraction to prevent flow separation and to minimize turbulent fluctuations in the upstream section. Stainless steel mesh (50% open area) and a layer of high porosity polypropylene sponge inside the main body of the nozzle further dampen turbulent fluctuations and distribute fluid momentum across the width of the nozzle opening. These design features ensure a uniform (top-hat) velocity profile at the nozzle exit and produce a laminar, steady match to the analytical velocity field immediately downstream in the observation section (Bickley, 1937; Mehta and Bradshaw, 1979; Hussein, 1994; Woodson et al.,

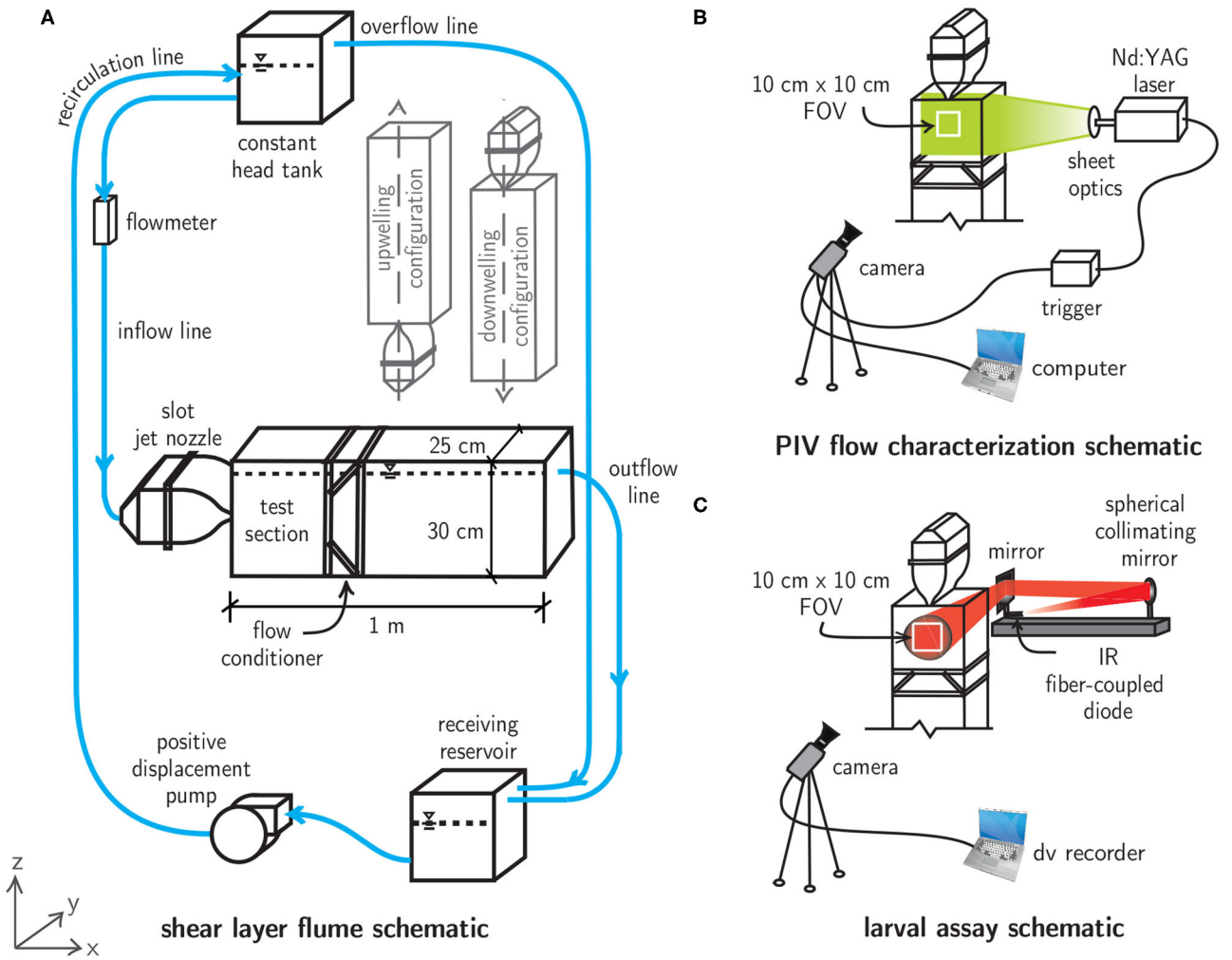

FIGURE 4 | (A) Shear layer flume schematic featuring a main flume section that can be oriented in upwelling, downwelling, or horizontal flow configurations. The water levels in the main flume, constant head tank, and receiving reservoir are indicated by dashed lines and the free surface symbols. **(B)** Particle image velocimetry (PIV) schematic for flow characterization. **(C)** Collimated, infrared (IR) shadowgraph system for larval shear layer behavioral assays.

2005). The jet flow in the main test section continues through a custom flow conditioner which prevents recirculation, flow instability, and exit geometry effects. Finally, the flow continues via either a free-surface overflow or intermediate constant head reservoir (horizontal or vertical flow configurations, respectively) into a receiving reservoir (28 L, US Plastics). From there, it is pumped through a positive displacement pump (JABSCO Model 31801-1305) to the constant head tank in a closed loop.

The shear layer flume employed here, and previously (Woodson et al., 2005, 2007; True et al., 2015), is noteworthy in that it is tunable and therefore capable of matching hydrodynamic characteristics for a range of ecologically-relevant oceanographic shear flow features. This is advantageous for studying the interactions of free-swimming plankters of various species and life stages with persistent shear flow features in varying ecological contexts. Another advantageous feature is the existence of a known analytical solution for the steady shear flow produced by the laminar slot jet (Bickley, 1937), which provides a useful benchmark for assessing the steadiness and repeatability of the flow conditions produced in the apparatus. The analytical solution also provides *a priori* knowledge about the hydrodynamic conditions a laminar slot jet will produce under given operational parameters. Bickley (1937) considers a steady, incompressible, two-dimensional flow generated by a viscous fluid issuing from a long narrow orifice into a body of the same fluid at rest. Assuming the Prandtl boundary layer equations provide a good description of the free jet and noting that the dynamic pressure is invariant in both the streamwise (x for horizontal flows or z for vertical flows) and transverse (z for horizontal flows or x for vertical flows) directions, the flow is governed by the continuity equation,

$$\frac{\partial u}{\partial x} + \frac{\partial w}{\partial z} = 0, \tag{1}$$

and the streamwise momentum equation. For example, the x-momentum equation for the horizontal flow configuration (**Figure 4**) is

$$u\frac{\partial u}{\partial x} + w\frac{\partial u}{\partial z} = \nu\frac{\partial^2 u}{\partial z^2}, \quad (2)$$

where u and w are the x- and z-components of velocity, respectively, and ν is the kinematic viscosity. For simplicity, the focus below is on the horizontal flow case. The flow is subject to the following three boundary conditions: symmetry about the jet centerline and boundedness in the transverse direction,

$$\frac{\partial u}{\partial z} = 0 \; at \; z = 0 \, , \quad (3)$$

$$w = 0 \; at \; z = 0 \, , \quad (4)$$

$$u \to 0 \; as \; z \to \pm\infty \, . \quad (5)$$

Further, the total streamwise momentum, M, is conserved such that

$$M = \rho \int_{-\infty}^{\infty} u^2 dz = initial \; streamwise \; momentum \; flux \, . \quad (6)$$

Following the solution method of Schlichting (1933), Sato and Sakao (1964) give the following self-similar form of the nondimensional velocity profile

$$\frac{u}{u_o} = \mathrm{sech}^2\left(\frac{az}{\delta_j}\right), \quad (7)$$

where a = 0.88136. The maximum (centerline) velocity, u_o, deceases with distance downstream due to lateral entrainment of low momentum fluid as

$$u_o = \left(\frac{3M^2}{32\nu x}\right)^{1/3} \quad (8)$$

and the jet half-width δ_j, i.e., the transverse location at which the local velocity is half the centerline velocity at a given streamwise location, is

$$\delta_j = a\left(\frac{48\nu^2 x^2}{M}\right)^{1/3} \, . \quad (9)$$

The centerline velocity is mathematically singular at $x = 0$ (the physical location of the slot jet orifice), which has given rise to the idea of a virtual origin as the streamwise location of a point source of momentum a small distance upstream of the orifice from which the jet can be considered to emanate (Andrade, 1939; Sato and Sakao, 1964; Revuelta et al., 2002; Peacock et al., 2004). The virtual origin correction accounts for the non-zero nozzle width; for all shear flows here with nozzle width $d_j = 1$ cm and jet Reynolds number $Re_j = 52$, described in detail below, the virtual origin correction is not necessary to obtain a satisfactory match between the measured and predicted velocity fields. Up to jet Reynolds numbers of about 50, irregular velocity fluctuations near the orifice dampen out in the streamwise direction and the flow is steady and laminar within a few nozzle widths downstream (Sato and Sakao, 1964).

2.2. Flow Characterization

The fluid velocity and associated gradient (vorticity, shear strain rate) fields were quantified using time-resolved particle image velocimetry (PIV) for each shear flow configuration (**Figure 4B**). The flow was seeded with low Stokes number titanium dioxide particles (diameter 5 μm) and illuminated with a sheet of laser light from a dual-cavity, pulsed Nd:YAG laser (New Wave Research Gemini, 532 nm, 125 mJ/pulse). The laser beam was focused with a spherical lens (focal length f = 1 m) and then expanded into a thin sheet with a cylindrical lens (f = −12.6 mm), illuminating the shear layer flow in the observation window. Double-frame images were captured at 15 Hz using an eight-channel pulse generator (Berkeley Nucleonics Model 500D), which triggered synchronized laser pulses and image acquisition (CCD, Kodak Megaplus ES 1.0, 1 MP, 8-bit monochrome). The camera was equipped with a 105 mm lens (Nikon AF Micro Nikkor). Images were processed and analyzed using DaVis software (LaVision GmbH). PIV best practices (Raffel et al., 2018) were utilized to maximize measurement quality, including optimal particle seeding densities of 8-10 particles per correlation window, particle displacements of 5–10 px between successive frames ("1/4 rule"), 2–3 px particle image diameters, and multi-pass (iterative) cross-correlation schemes with overlapping subwindows (50–75 %) of decreasing sizes (64–16 px).

2.3. Larval Collection and Care

Panopeus herbstii larvae were collected from Wassaw Sound at Priest Landing (Skidaway Institute of Oceanography) on Skidaway Island near Savannah, GA, USA. Larvae were collected in late spring (end of May/early June) when planktonic (dispersed) megalopae exhibited predictable, high-density surface aggregations during nighttime slack tides. A light trap was deployed from the dock between 10 pm and midnight (on slack tide). The trap consisted of a plastic jar (5 L Nalgene) with an inverted funnel designed to increase retention of larvae drawn in by a dive light secured to the bottom of the jar. The assembly was suspended horizontally between a weighted mooring device on the bed and a float on the water surface and was retrieved after a 2 h deployment. Larvae were sorted and kept in recirculating seawater, while being fed copepod nauplii (*Acartia tonsa*), before being transported to the Environmental Fluid Mechanics Laboratory at the Georgia Institute of Technology for shear layer behavioral assays. Larvae were kept in well-oxygenated artificial seawater (Instant Ocean) at estuarine conditions (30 ppt, 28°C) and fed copepod nauplii (*A. tonsa*) and brine shrimp nauplii (*Artemia* spp.) over the 1 week duration in which all behavioral assays were conducted. Larvae were not fed in the 24 h prior to behavioral assays.

2.4. Shear Layer Behavioral Assays

Two-hour shear layer assays were conducted between 8 p.m. and midnight under horizontal, upwelling, and downwelling flow configurations (separately). Assays were run within this time window to reduce variability in larval behavior among shear layer assays since decapod larvae exhibit variability in ontogenetic, diel, and tidally-modulated swimming behaviors, both among

and within larval stages (Shanks, 1986; Jamieson and Phillips, 1988; Hobbs and Botsford, 1992; Queiroga and Blanton, 2005). Two replicates were conducted for each flow configuration, in addition to a 1-h control (no-flow). For each assay, a group of 50–60 mixed-sex, stage-specific (megalopa) larvae were introduced to the main test section and allowed to acclimate for a one-hour period prior to the experiment. During this period, the shear layer flow was started and allowed to reach steady state while larvae were aggregated away from the flow with a white fiber-optic light. At the start of the assay, the white light was turned off and free-swimming larval swimming trajectories were observed under infrared (IR) illumination via a shadowgraph system (**Figure 4C**). An IR fiber-coupled diode (CVI Melles Griot, 57 PNL 054/P4/S, 660 nm, 22 mW) was collimated with a spherical mirror (Edmunds Optics, NT32-845, $f = 1{,}524$ mm) and reflected off a planar mirror toward the rear of the tank. This method provided uniform illumination throughout the experimental volume and projected larval silhouettes onto a sheet of film paper on the front surface of the tank. The shadowgraph trajectories produced over the course of each two hour behavioral assay were recorded in the observation window with a CCD camera (Pulnix, 745i, 768 × 494 px) linked to a digital video recorder. Because the three-dimensional swimming trajectories are projected onto a plane with the shadowgraph system used here, all swimming kinematic and gross path parameters (discussed below) correspond to projected two dimensional trajectories (**Figure 4**).

For larval assays in all flow configurations, a volumetric flowrate of 16.8 cm^3/s was selected to produce ecologically-relevant hydrodynamic conditions. This flowrate for the given nozzle geometry (slot width $d_j = 1$ cm) results in a maximum jet exit velocity, U_j, of 6.7 mm/s and a jet Reynolds number ($Re_j = U_j d_j/\nu$) of 52, which is in a transitionally stable, laminar flow regime (Sato, 1960). The resulting velocity field is steady in time and features smooth gradients throughout the observation window. The corresponding hydrodynamic cue fields (shear strain rate and vorticity) feature large, steep gradients in the transverse direction (z for the horizontal configuration or x for the vertical configurations) and small, gradual gradients in the streamwise direction (x or z depending on the flow configuration). For all flow configurations, there are no gradients in the y-direction as a result of the slot jet used here (large aspect ratio rectangular nozzle opening), justifying the use of two-dimensional flow characterization and larval swimming kinematic analyses.

2.5. Kinematic Analysis

Raw trajectory data were digitized using LabTrack (BioRAS) software with a temporal resolution of 66.67 ms (15 Hz), sufficient to accurately resolve larval swimming kinematics. For example, larvae exhibited typical maximum relative swimming speeds up to 2 cm/s. For an image magnification of 0.2 mm/pixel and a typical larval carapace length of 2 mm, this maximum relative swimming speed results in a displacement of 10 body lengths per second, or 2/3 body length per frame. The kinematics of the resulting raw swimming trajectories (x, z, t, **Figure 5**) were analyzed using a suite of custom MATLAB codes to compute path kinematics including relative swimming speed [mm/s], relative swimming acceleration [mm/s^2], directional heading relative to the bulk flow direction [°, ranging from 0 to 360, where 0 is aligned with the bulk flow direction], change in directional heading [°, difference in directional heading between successive displacement vectors], and turn frequency [turns/larva/s]. For relative swimming speed and acceleration, the local fluid velocity computed from the PIV data is subtracted to isolate the larval motion relative to the local flow. For turn frequency, a "turn" event is universally defined as a change in directional heading of 15° or more between successive displacement vectors.

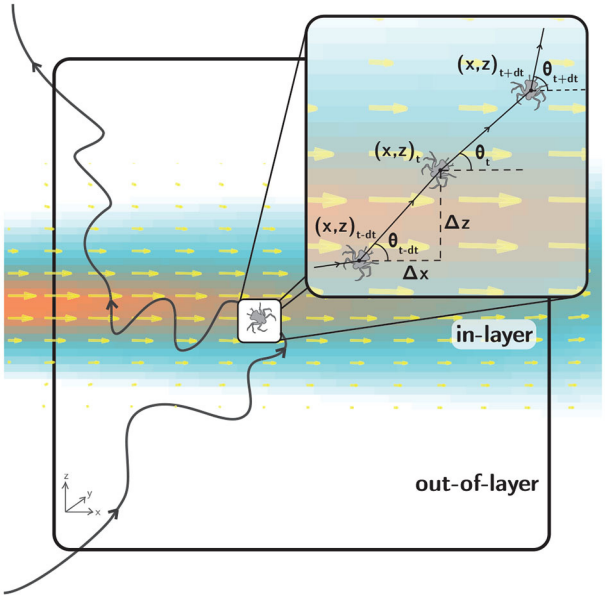

FIGURE 5 | A hypothetical larval swimming trajectory (black line) in the observation window (large black rectangle). The fluid shear layer is denoted by the velocity vectors (yellow) and velocity magnitude contours (orange to blue). The inset (small black rectangle) shows a detailed view of kinematic parameters used to quantify swimming behavior during shear layer assays. The two-dimensional swimming trajectory projections are characterized by larval positions at each time step [$x(t)$, $z(t)$] and displacement vectors of varying magnitude with directional headings $\theta(t)$ relative to the bulk flow direction.

Figure 5 shows a hypothetical larval trajectory in the 10 cm x 10 cm observation window that encompasses both in-shear layer and out-of-shear layer regions ("in-layer" and "out-of-layer," respectively), as delineated by a threshold hydrodynamic value. For example, for a vorticity delineation (contour) of 0.2 s^{-1} (corresponding to the light blue edge of the layer in **Figure 5**), the fluid shear layer occupies approximately 40% of the observation window. Segmenting the observation window into in-layer and out-of-layer regions provides a useful context for kinematic analyses comparing larval swimming behavior as a function of location relative to the shear layer (in-layer vs. out-of-layer) or historical exposure to the shear layer (pre-first-contact vs. post-first-contact). Analyzing larval swimming kinematics by location and exposure provides complementary insights into behavioral response trends associated with the spatial scale of the layer itself and short time scales (by location) as well as the relatively larger scale of the vicinity of the layer (the encompassing volume) and longer time scales (by exposure).

In addition to analyzing swimming kinematics, gross trajectory parameters were computed to examine the net effect of kinematic changes on macroscale trajectory characteristics. These include the following: net-to-gross-displacement ratio (*ngdr* = net displacement/gross displacement), the vertical net-to-gross-displacement ratio (*vngdr* = net vertical displacement/gross vertical displacement), and the proportional residence time (*prt* = time spent in-layer/total time in observation window). *ngdr* ranges from 0 to 1, with small values (→ 0) indicating more diffuse trajectories (curved, loopy), and large values (→ 1) indicating more ballistic trajectories (straight). *vngdr* also ranges from 0 to 1 and describes the *vertical* diffusivity of the swimming trajectory, and thus can be viewed as a spectrum of depth-keeping behaviors. Small *vngdr* values (→ 0) indicate swimming behavior that counteracts sinking or vertical advection with the flow (in vertical flows), resulting in small net vertical displacement (e.g., u-shaped or c-shaped trajectories) and hence strong depth-keeping behavior. Similarly, large *vngdr* values (→ 1) indicate trajectories with large net vertical displacement, and thus weak depth-keeping behavior at the scale of the observation. Displacement ratio parameters were computed consistently for 4 s periods of a given trajectory and averaged over the entire trajectory to alleviate potential dependence on the trajectory duration (Tiselius, 1992). This computation period, being long relative to the imaging period and short relative to the total trajectory duration, was found to yield displacement ratio values that were relatively insensitive to small changes in the computation period (True et al., 2015).

The swimming kinematic and gross path parameters detailed above were selected for analysis as they are well-suited to address the core questions of this study: do hydrodynamic cues associated with spatiotemporally persistent flow features affect individual behavioral processes of dispersed decapod crab larvae, and do differing cue spatial orientations relative to gravity produce differential responses? These parameters also take into account the inherent limitations of our experimental apparatus and design. For example, the analysis examines the effects of flow-induced changes in swimming kinematics when possible (e.g., subtracting local fluid velocity to analyze the relative swimming speed). However, the spatial resolution of our system (larval carapace size on the order of 10 px) prohibits a full accounting of the instantaneous effects of shear flow-induced advection and rotation, which would require resolution of the larval body orientation vector and high-resolution PIV measurements in the surrounding volume. Although advection and rotation may influence other observed trajectory parameters (turn frequency, *ngdr*, etc.), our analysis (see below) provides compelling evidence that the results are consistent with behavioral effects, and not flow forcing, as the primary driver.

2.6. Statistical Analysis

Statistical analyses of larval shear layer behavioral responses were performed using JMP Pro 11 (2013, SAS Institute). Path kinematic responses were investigated using a single factor, nested, repeated measures ANOVA by location (in-layer vs. out-of-layer) or exposure (pre-contact vs. post-contact). The single factor (or treatment) was the flow configuration, which has four levels: control, upwelling, downwelling, and horizontal. The repeated measures aspect of the design specifies that kinematic values by location and exposure were examined and compared for individual larva. A general linear model (GLM) was used because of the unbalanced design, whereas the nested aspect accounted for potential variability across replicates (data were pooled if replicate effects were insignificant, and the pooled error variance was used). Changes in gross path parameters were evaluated using a single factor, nested ANOVA of the arcsine-transformed data sets between control and flow (upwelling, downwelling, horizontal) values. Dunnett's control tests were used for *post-hoc* evaluation of differences among control and flow groups. Arcsine transformation of proportional data (gross path parameters) was required to satisfy ANOVA assumptions of normality and homoscedasticity (Zar, 1999). For some proportional data types (binomial) the logit transform is superior in satisfying linear modeling assumptions, statistical power, and reduced potential for Type I statistical error (Warton and Hui, 2011); however, in the present study there is no reason to prefer the logit over the arcsine transform since the data were proportional, but not binomial (True et al., 2015). All data sets were examined and tested for normality (Shapiro-Wilk goodness-of-fit) and homoscedasticity (examination of fit-by-residual plots for fan or funnel shapes) prior to statistical analyses, revealing no significant departures.

Significant efforts were made to reduce the possibility of pseudo-replication and to ensure statistical independence of larval swimming trajectories such that they could be treated as independent samples. For example, for all assays the number of digitized swimming trajectories was less than the number of larvae introduced to the test section in order to minimize the possibility of repeated sampling of a given larva (pseudo-replication). Larvae typically had only one sustained interaction with the shear layer and aggregated downstream at the end of the test section, both of which suggest a low likelihood of larval resampling. The potential for larva-larva interactions was also minimized to alleviate unwanted modifications to swimming behavior by using a low population density in the test section of approximately 2 larvae/L; this resulted in rare observations of more than two larvae in the observation window at any time.

3. RESULTS

3.1. Flow Characterization

Planar PIV measurements of the flow field produced by the laminar, planar free jet in the shear layer flume are shown in **Figure 6** for horizontal (**Figures 6A,B**), upwelling (**Figures 6C,D**) and downwelling (**Figures 6E,F**) flow configurations. In the left column, the fluid velocity (vectors) and vorticity magnitude (contours) fields show steady (time-invariant) and near-identical spatiotemporal structure among the different flow configurations, with the obvious exception of the bulk flow direction. The peak streamwise velocity along the jet centerline (u_o or w_o, depending on flow configuration) varies in the streamwise direction (x for the horizontal configuration or z for the vertical configuration, Equation 8) from approximately 6.5 to 4.5 mm/s, and the streamwise velocity (u or w, depending

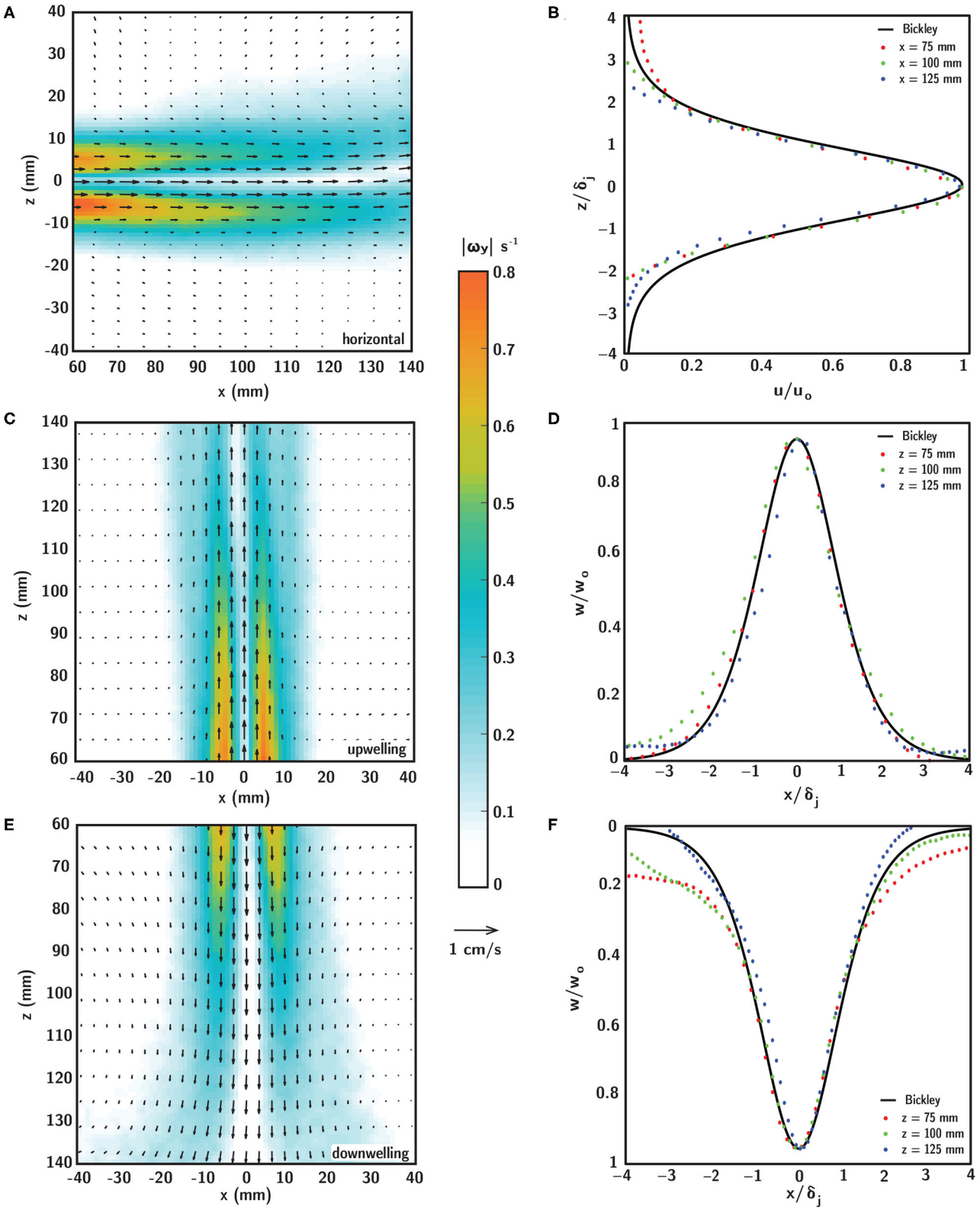

FIGURE 6 | Time-averaged fluid velocity (black vectors) and vorticity magnitude (contours) fields in **(A)** horizontal, **(C)** upwelling, and **(E)** downwelling shear layers generated by a laminar, planar free jet at $Re_j = 52$. Comparison of analytical (Bickley) and experimental (PIV) self-similar velocity profiles extracted at various streamwise locations for the **(B)** horizontal, **(D)** upwelling, and **(F)** downwelling shear layers. Scaling parameters for the velocity profiles in **(B,D,F)** are defined in Equation (7).

on flow configuration) decays smoothly in the transverse direction (z or x, depending on the flow configuration) from a peak at the centerline. Strong, steep velocity gradients in the transverse direction become gradually smoother with streamwise distance from the jet exit as lateral fluid entrainment causes gradual broadening of the velocity profile due to transverse diffusion of fluid momentum. Vorticity reaches a maximum near 0.8 s^{-1} in two symmetric peaks off of the jet centerline that decay rapidly in the transverse direction and gradually in the streamwise direction. The vorticity peak locations correspond to the strongest velocity gradients at the edges of the jet, and there is a local vorticity minimum on the jet centerline where the transverse velocity gradient goes to zero. The steep vorticity gradients at the edges of the jet provide a well-defined demarcation of the fluid shear layer and corresponding in-layer and out-of-layer regions of the observation window (**Figure 5**). The gradual broadening of the velocity profile in the streamwise direction causes the layer half-width, as defined by the 0.2 s^{-1} vorticity isocontours, to grow from approximately 10.25 to 21.25 mm over the streamwise extent of the observation window. This follows readily by taking the derivative of Equation (7) with respect to the transverse direction (z or x, depending on the flow configuration) and solving for the transverse location of the vorticity isocontour, and the half-widths so defined agree well with the measured vorticity fields (**Figures 6A,C,E**). Given the satisfactory agreement between the analytical and measured flow conditions, the analytical vorticity-based half-width was used to define a common in-layer region for the ANOVAs to mitigate small differences in layer definitions among different shear flow orientations (discussed more below). The shear strain rate field is not presented here, but is structurally identical to and spatially coincident with the vorticity field, with magnitude reduced by 1/2.

In all flow configurations, the experimental (PIV) fluid velocity field agrees well with the steady analytical solution of Bickley given in Equation (7) (Bickley, 1937) as shown in the self-similar velocity profiles for each shear flow orientation in **Figures 6B,D,F**. Experimental transverse profiles of streamwise velocity (u or w, depending on flow configuration) taken at various streamwise locations (colored symbols) are scaled by the local jet half-width δ_j (Equation 9) and centerline velocity u_o (Equation 8) and collapse well onto the self-similar solution of Bickley (black line). Thus, there is good agreement between the analytical and experimental flow fields throughout the observation window, with negligible differences among the different flow configurations. Note that small differences in flow conditions among the different shear flow orientations, such as the more rapid decay in the transverse direction of the analytical velocity profile relative to the downwelling profile in **Figure 6E**, are unlikely to significantly affect results since the strong velocity gradients are well-confined to the in-layer region and both velocity magnitudes and gradients are near-zero out-of-layer. Collectively, the PIV flow characterizations confirm that all shear layer flows i. are self-consistent and repeatable, ii. are steady (time-invariant), and iii. agree well with the theoretical description, producing a steady fluid shear layer, well-defined by steep transverse gradients and smooth streamwise gradients.

The PIV results in **Figure 6** were used to tune the flow system and to confirm that the shear flows presented here are ecologically-relevant for larval behavioral assays. That is, to confirm that the velocity gradients (vorticity or shear strain rate) are consistent with those that dispersed decapod larvae are likely to encounter *in situ* in estuarine and nearshore environments. Across a variety of estuarine systems, typical total shear (composed of steady and periodic tidal components) ranges from 0.02 to 0.1 s^{-1} (reviewed by Whitney et al., 2012). Similarly, maximum shear values reported around nearshore thin plankton layers (e.g., in a fjord system) are on the order of 0.1 s^{-1} (Dekshenieks et al., 2001). It is useful to note that these values of oceanographic shear are defined as the change in horizontal velocity over some vertical distance ($\partial u/\partial z$), which is closely related to, but distinct from, the fluid dynamic shear strain rate (i.e., $1/2[\partial u/\partial z + \partial w/\partial x]$) or vorticity (i.e., $\partial w/\partial x - \partial u/\partial z$). For the two-dimensional simple shear flows presented here, the $\partial u/\partial z$ term dominates the $\partial w/\partial x$ term for horizontal shear layers and vice versa for vertical layers, such that the magnitude of vorticity corresponds to the definition of oceanographic shear whereas the shear strain rate is reduced by a factor of 1/2. The maximum vorticity values achieved here approach 0.8 s^{-1}; however these values are confined to small patches symmetrically located about the jet centerline at the upstream end of the observation window, with more representative in-layer vorticity values ranging from 0.1 to 0.2 $^{-1}$ (**Figure 6**). In this context, and considering also resolution limitations in measurements that might lead to underestimation of measured shear values *in situ* (e.g., Woodson et al., 2005), the velocity gradients and corresponding vorticity (or shear strain rate) values presented in laboratory shear flows are comparable to reported shear values in estuarine and nearshore environments.

3.2. Hydrodynamics and Larval Swimming Kinematics

This section seeks to answer two fundamental questions: do larvae behaviorally respond to shear layers, and if so, does the response depend on the directional orientation of the layer? These questions are addressed via a detailed look at how swimming kinematics (relative swimming acceleration and change in directional heading) vary among different flow configurations (shear flow and no-flow) and examination of corresponding differences in how larvae respond to a relevant hydrodynamic cue (fluid vorticity).

Representative larval swimming trajectories for each flow configuration are shown in **Figure 7** relative to the fluid shear layer indicated by the velocity vectors (yellow) and velocity magnitude contours (orange to blue). Qualitative visual comparison of larval swimming trajectories under no-flow (**Figure 7A**) and shear flow (**Figures 7B–D**) configurations suggests a more complex spatial structure (more diffuse) in the shear flow conditions. Larval swimming trajectories in shear layers exhibit more pronounced multiscale structure, potentially reflective of more variable swimming kinematics during interaction with the layer.

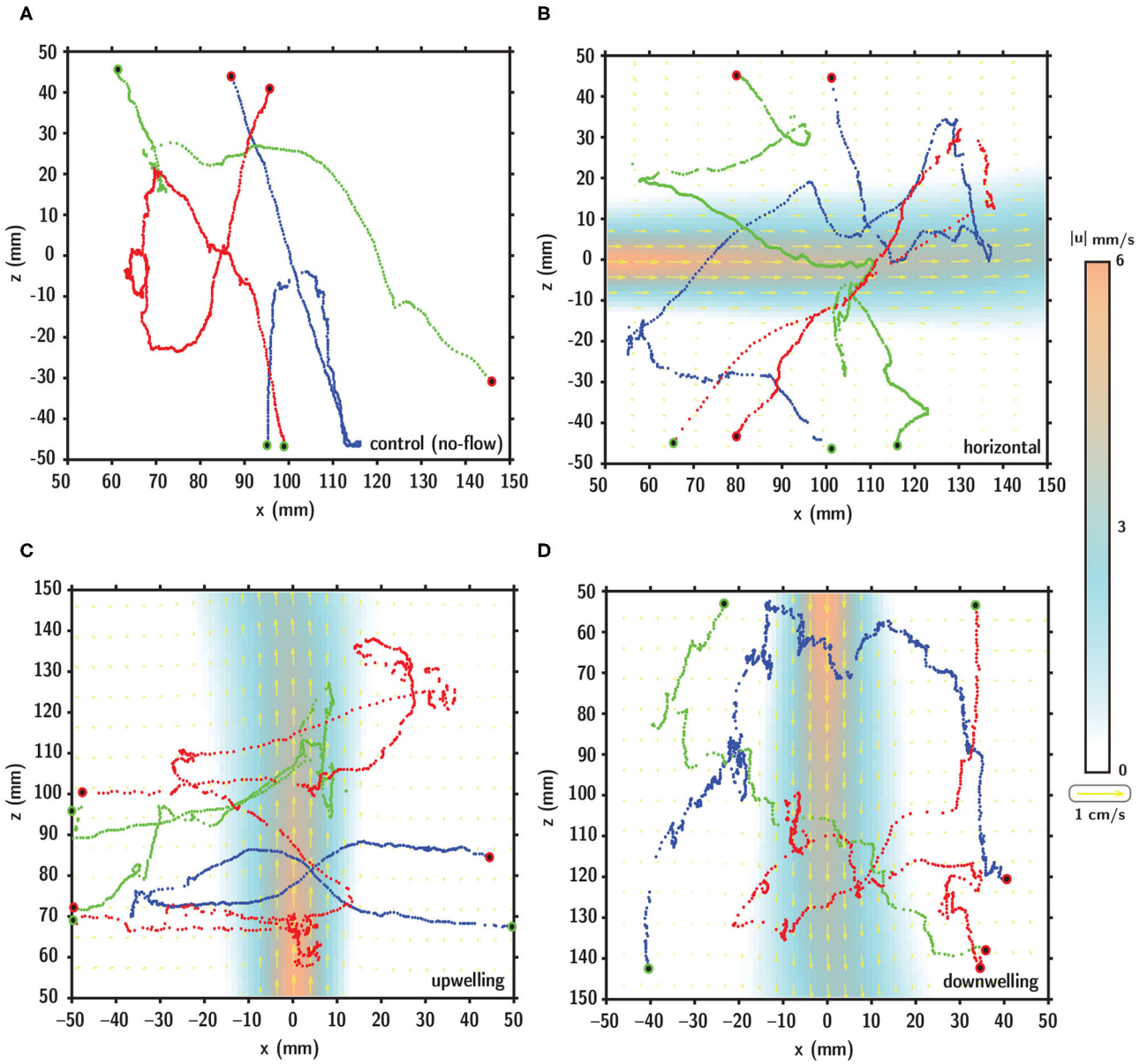

FIGURE 7 | Digitized larval swimming trajectories in **(A)** no-flow (control), **(B)** horizontal, **(C)** upwelling, and **(D)** downwelling shear flow configurations. In **(B–D)**, the shear layer is denoted by the velocity vectors (yellow) and velocity magnitude contours (orange to blue). In each panel, the starting and ending points of the trajectory are indicated by the green and red dots, respectively.

A more detailed view of a single larval swimming trajectory in the horizontally-oriented shear flow in **Figure 8A** shows a nuanced interplay between the instantaneous larval swimming behaviors and local hydrodynamic cues associated with the shear layer (**Figure 8B**). In **Figure 8B**, the orange time series is the instantaneous fluid vorticity experienced by the larva as it interacts with the fluid shear layer while progressing along its swimming trajectory. The blue curve is the corresponding instantaneous relative swimming acceleration of the larva, normalized by its maximum value. The vorticity time series clearly shows the larva entering the shear layer from below (experiencing rapidly increasing vorticity) and then exiting the layer (experiencing rapidly decreasing vorticity) before turning around, proceeding through the layer (two distinct peaks in vorticity with a local minimum between), and exiting out the top (experiencing rapidly decreasing vorticity). The acceleration time series (blue curve) shows multiple rapid corresponding changes of significant magnitude with complex temporal characteristics (rapid on/off, phase lag relative to the hydrodynamic cue, switching between acceleration and deceleration).

Probability density functions (pdfs) of swimming kinematics provide population-scale information about larval behavioral

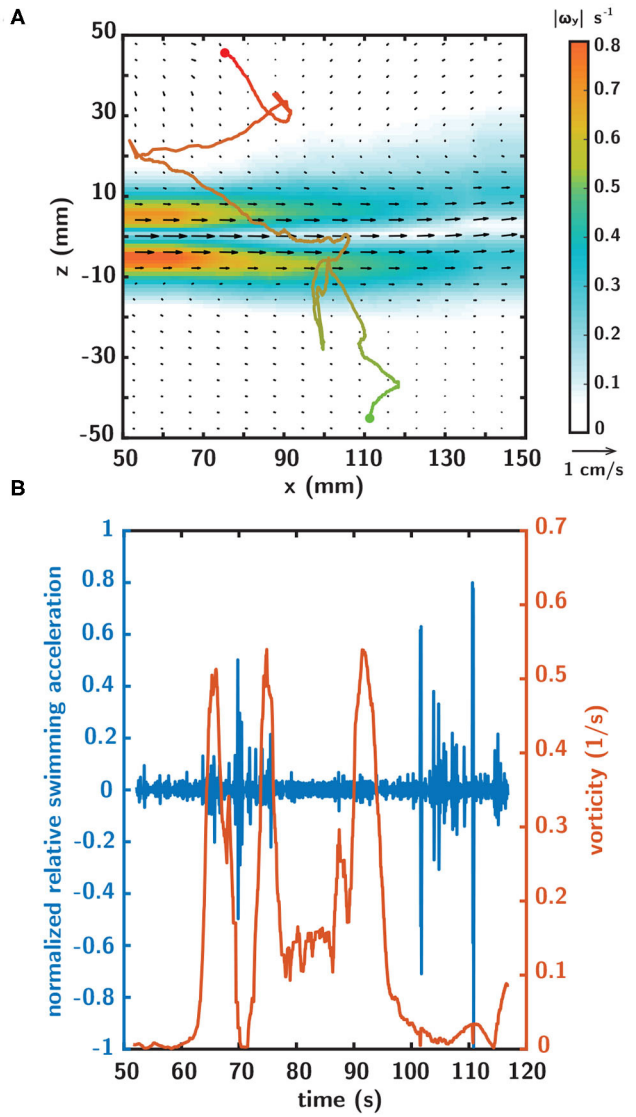

FIGURE 8 | (A) A representative larval swimming trajectory in the horizontally-oriented shear flow as denoted by the velocity vectors (black) and vorticity magnitude contours. The starting and ending points of the trajectory are indicated by the green and red dots, respectively, and the corresponding color gradient indicates the temporal progression of the trajectory. **(B)** Corresponding timeseries of normalized relative swimming acceleration (blue) and fluid vorticity (orange) over the trajectory duration.

responses to shear flow. In **Figure 9**, empirical pdfs (**Figures 9A,C**) and corresponding cumulative distribution functions (cdfs–**Figures 9B,D**) of relative swimming acceleration and change in directional heading reveal marked differences among shear flow configurations. Each distribution function is a population ensemble of each timepoint for all larvae (trajectories) in a given flow configuration and each kinematic parameter was normalized within a given trajectory by that trajectory's maximum value, effectively rescaling the abscissa from −1 to 1. To improve intuition about changes in directional heading, the raw data were reoriented such that a negative value corresponds to a heading change that yields a new heading that is more against the flow whereas a positive value corresponds to one producing a new heading more aligned with the bulk flow direction. To clarify, the raw directional heading change data (i.e., the difference in successive directional heading vectors which range from 0 to 360 degrees and where 0 degrees corresponds to the bulk flow direction, **Figure 5**) correspond to clockwise and counterclockwise heading changes that land in the four quadrants of the Cartesian grid. The reorientation effectively compresses the data into two regions, such that one corresponds to changes in directional heading that are more aligned with the bulk flow direction (assigned to positive values) and the other more against the bulk flow direction (assigned to negative values). Since there is no flow direction for the control (no-flow) case (black curve), a hypothetical horizontal flow direction is assumed for data reorientation to ensure consistency with shear flow data reorientations; this was necessary since the raw directional heading data were also computed under this assumption, which arbitrarily assigned a directional heading of 0 degrees to the horizontal bulk flow direction for the no-flow case.

Pdfs of relative swimming acceleration (**Figure 9A**) show that all shear flow orientations increase the kurtosis of the distributions relative to the no-flow case (black). The most significant changes were seen in the upwelling (red) and horizontal (blue) shear flow orientations, followed by downwelling (green). This compresses the values of relative swimming acceleration away from more extreme values and into a narrower band nearer to the mean. There are no clear impacts on the skewness of the distributions toward more or less acceleration relative to deceleration. The effects in the pdf are reflected in the corresponding cdfs (**Figure 9B**). In contrast, pdfs of heading change (**Figure 9C**) show that all shear flow orientations decrease the kurtosis of the distributions relative to the no-flow case (black). The most significant effects were seen in the downwelling (green) shear flow orientation, followed by horizontal (blue) and upwelling (red). This has the effect of shifting heading values away from the mean and toward more extreme values. In contrast to the relative swimming acceleration distributions, the heading change distributions do show a change in skewness associated with all shear flow orientations. The effect for all flow orientations is to shift the distributions toward heading changes that yield new directional headings that are more against the flow direction and also to focus heading changes in the flow direction into a narrower band (smaller peak). The changes are again reflected in the corresponding cdfs (**Figure 9D**).

To investigate corresponding differences in the hydrodynamic cue (fluid vorticity) associated with larval behavioral responses, a "consequential" behavioral response is defined as an instantaneous larval behavioral state in which both relative swimming acceleration and heading change are more than one standard deviation away from their respective mean values. In **Figure 10**, the statistical distributions of both the ensemble of all vorticity values encountered by larvae and the vorticity values that specifically elicit consequential behavioral responses are

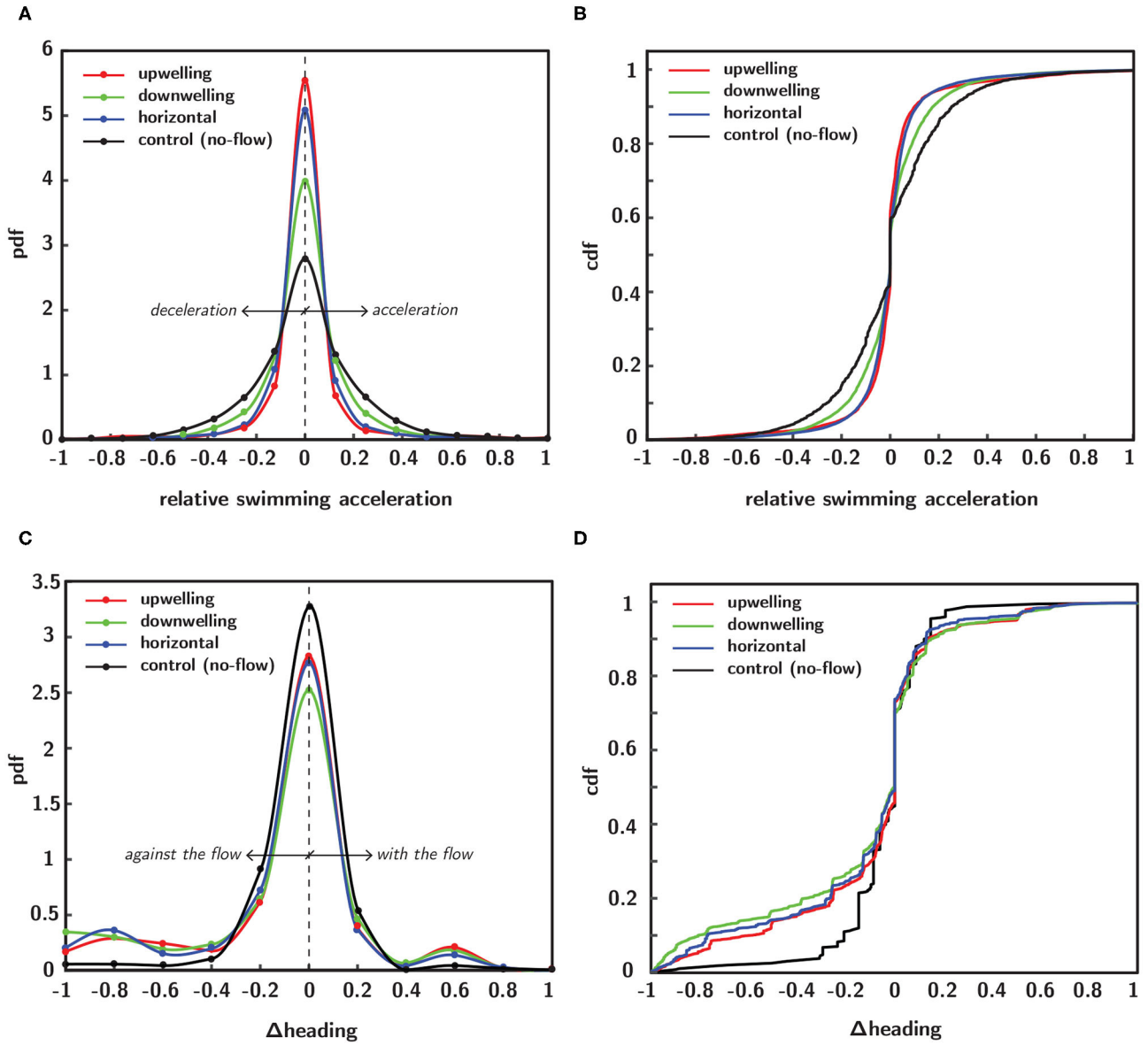

FIGURE 9 | Empirical probability (pdf) and cumulative (cdf) distribution functions of normalized swimming kinematics in different flow configurations, including no-flow (black), upwelling (red), downwelling (green) and horizontal (blue) shear flows. Pdfs of normalized relative swimming acceleration **(A)** and corresponding cdfs **(B)**. Pdfs of normalized change in directional heading **(C)** and corresponding cdfs **(D)**.

shown. The ensemble pdfs of all vorticity values encountered by larvae in each flow orientation are shown in **Figure 10A** and the corresponding cdfs in **Figure 10B**. The ensemble vorticity pdfs in **Figure 10A** resemble exponential distributions for all shear flow orientations, being weighted toward lower values but with long tails that extend to larger values. The commonality of the exponential-like distribution shapes reflect the spatiotemporal flow structure and vorticity magnitudes that larvae were exposed to in the shear flows, which are effectively identical, with the exception of the direction of the bulk flow relative to gravity (**Figure 6**). However, the differences in the statistical moments among different shear flow orientations (**Table 1**) suggest that active larval behavioral responses differ among shear flow orientations. To further explore these differences among shear flow orientations, in **Figure 10C** the pdfs of vorticity values that elicit consequential behavioral responses (dashed lines) are shown in addition to the ensemble vorticity pdfs from **Figure 10A** (solid lines). For all shear flow orientations, the consequential vorticity distributions (dashed lines) become more focused into a given vorticity range (more peaky), reminiscent of a threshold-type phenomena in which specific fluid vorticity values elicit consequential larval behavioral responses. This

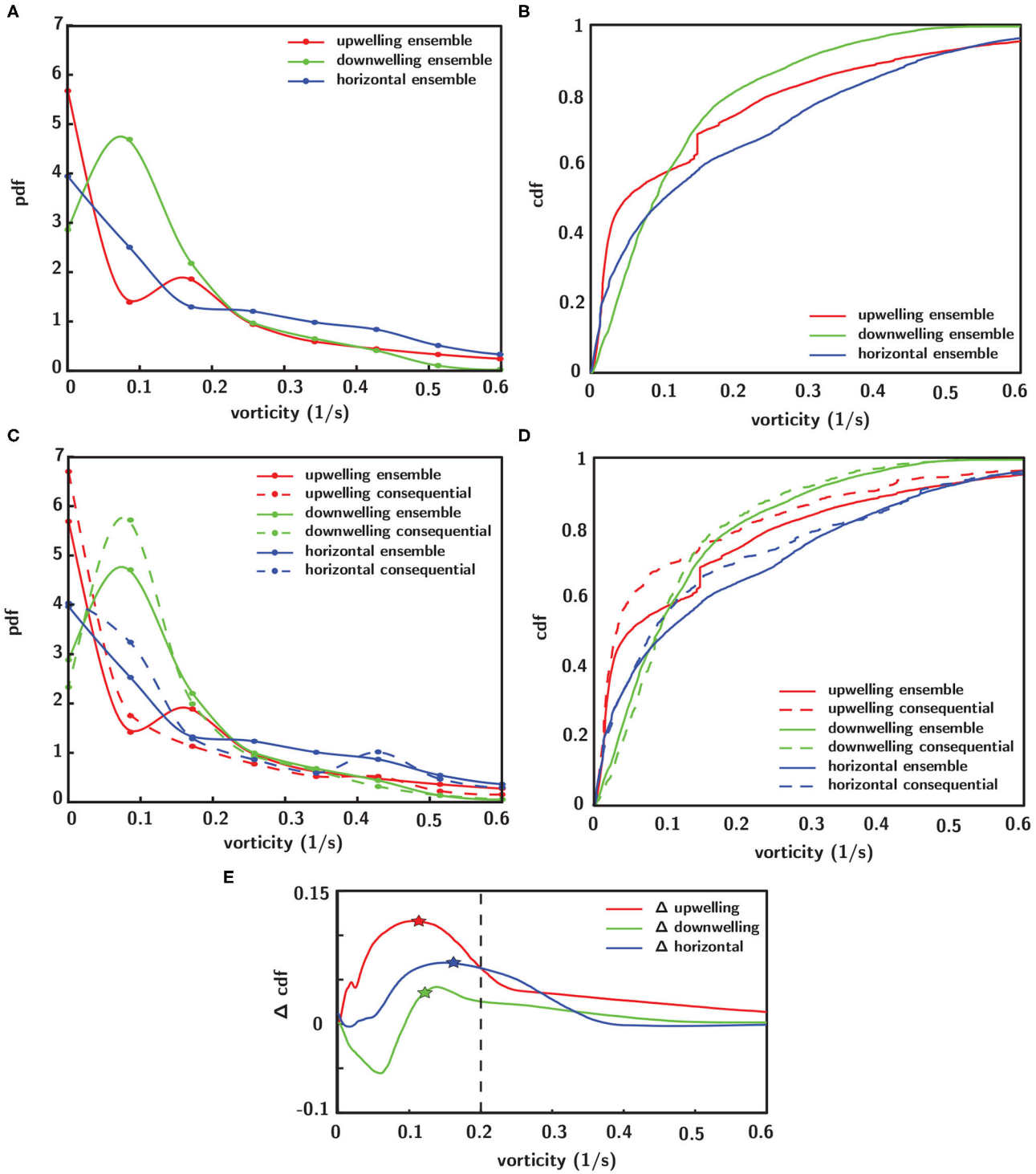

FIGURE 10 | Empirical probability (pdf, **A**) and cumulative (cdf, **B**) distribution functions of the ensemble of all vorticity values encountered by larvae in each shear flow orientation. **(C)** Pdfs of fluid vorticity magnitudes eliciting consequential behavioral responses (see text for definition of "consequential") in each shear flow orientation (dashed lines) in addition to ensemble distributions (solid lines). **(D)** Corresponding cdfs of consequential (dashed lines) and ensemble (solid lines) vorticity. **(E)** Difference in cumulative probabilities of consequential and ensemble vorticity cdfs (dashed–solid lines from **D**), where stars indicate the average values of the consequential behavior vorticity pdfs (dashed lines in **C**, **Table 1**) and the black dashed line at 0.2 s^{-1} corresponds to the common vorticity value chosen to delineate in-layer vs. out-of-layer regions for the ANOVAs.

TABLE 1 | Statistics for the probability distributions of fluid vorticity eliciting consequential larval behavioral responses in different shear flow orientations.

Flow orientation	Mean (1/s)	Standard deviation (1/s)	Skewness (1/s)	Kurtosis (1/s)
Upwelling	0.11	0.16	1.97	6.34
Downwelling	0.12	0.10	1.58	5.38
Horizontal	0.16	0.19	1.35	3.94

is reflected in the corresponding ensemble (solid lines) and consequential (dashed line) vorticity cdfs in **Figure 10D**. Relative to the ensemble vorticity cdfs, the consequential vorticity cdfs for all shear flow orientations are shifted upwards over a range of vorticity values, with only the downwelling shear flow showing an initial shift down at low vorticity values. The vertical shift upwards over specific vorticity ranges signifies that there is a higher cumulative probability of observing a consequential behavioral response. The differences between the consequential and ensemble vorticity cdfs (i.e. dashed minus solid lines in **Figure 10D**) are shown in **Figure 10E**. The cdf differences in **Figure 10E** show that the enhanced cumulative probability of a consequential behavioral response peaks at different vorticity values for each shear flow orientation. Interestingly, the vorticity peaks for all shear flow orientations correspond well with the average values of the consequential behavior vorticity pdfs (dashed lines in **Figure 10C**, **Table 1**) as signified by the stars in **Figure 10E**. In this light, the average fluid vorticity values that elicit consequential larval behavioral responses are good proxies for shear flow orientation-specific, threshold vorticity values. The black dashed line in **Figure 10E** at a vorticity of 0.2 s^{-1} corresponds to the common vorticity value chosen to delineate in-layer vs. out-of-layer regions for ANOVAs (described in detail above), which is sufficient to encompass the enhanced cumulative probability peaks for all shear flow orientations. Thus, not only are larval behavioral responses dependent on the directional orientation of shear flows (**Figure 9**), but the fluid vorticity values eliciting consequential larval behavioral responses are also orientation-specific (**Figure 10**, **Table 1**).

3.3. Larval Behavior by Shear Flow Orientation, Location, and Exposure

The evidence above suggests that larval behavioral responses to shear flow and the associated hydrodynamic cues (vorticity) for these responses depend on shear flow orientation. To evaluate potential ecological implications of these findings, the statistical significances of differences in swimming kinematics (relative swimming speed, turn frequency) and gross path parameters (*ngdr*, *vngdr*, *prt*) among shear flow orientations and relative to the no-flow condition are evaluated. Recall that statistical analyses of swimming kinematics are conducted by location (in-layer vs. out-of-layer) and exposure (pre-contact vs. post-contact) based on a hydrodynamic delineation of the shear layer region. The common definition used here for all layer orientations is a vorticity contour of 0.2 s^{-1} on the outer edges of the jet, visually corresponding to the light blue edges of the layer in **Figures 5**, **6**. This vorticity value is of the same order of magnitude as the mean vorticity eliciting consequential larval responses in all shear flow orientations (**Figure 10**, **Table 1**), but slightly larger to ensure that the defined in-layer region is readily sensed and responded to by larvae.

Relative swimming speed and turn frequency computed by location and exposure for all shear flow orientations are shown in **Figure 11** and the results of the corresponding repeated measures ANOVA are summarized in **Table 2**. The first *p*-value ("Location" or "Exposure") reports the significance of behavioral differences due to an individual larva's presence in the shear layer vs. outside of it or pre-contacting the shear layer vs. post-contact. The second *p*-value ("Orientation") reports the significance of behavioral differences due to shear layer orientation (upwelling vs. downwelling vs. horizontal). Finally, the third *p*-value ("Location × Orientation" or "Exposure × Orientation") is the interaction effect and evaluates whether or not behavioral differences by location or exposure are contingent upon shear layer orientation.

The lack of a significant interaction effect for both relative swimming speed and turn frequency signifies that differences in these parameters by location and exposure were not dependent on the orientation of the shear flow (**Table 2**). However, relative swimming speeds were on average significantly lower for the horizontal shear flow vs. both vertical orientations (significant orientation effect) and were slightly lower than control values (∼ 9.5 mm/s). Swimming speeds in the vertical layers (∼11.5 mm/s) were significantly larger. Turn frequency was on average significantly larger for the horizontal shear flow vs. both vertical orientations (significant orientation effect). Turn frequency in the horizontal shear flow (∼9.25 turns/ind/s) is significantly elevated compared to control (no-flow) values (∼7.5 turns/ind/s) whereas those in both vertical orientations are only slightly larger than control values (∼7.75–8.25 turns/ind/s). For all shear flow orientations, relative swimming speeds were smaller post-contact (significant exposure effect) and out-of-layer (significant location effect) and turn frequency increased out-of-layer (significant location effect). Exposure and location effects in both kinematic parameters were more pronounced for the vertical shear flow orientations (orientation effects; **Table 2**).

Gross path parameters (*ngdr*, *vngdr*, and *prt*) are shown for all shear flow orientations in addition to the no-flow condition in **Figure 12**, and the results of the corresponding ANOVA and *post-hoc* Dunnett's control tests are summarized in **Table 3**. The first *p*-value reports the significance of differences in flow configuration (shear flow and no-flow) on the given gross path parameter, and the final trio of *p*-values indicates the significance of each shear flow orientation relative to the no-flow condition.

Reduced *ngdr* for all shear flow orientations (**Figure 12**, **Table 3**) is consistent with the observed increased turn frequencies, causing trajectories to become more sinuous and diffuse (i.e., smaller *ngdr* values). Reduced *vngdr* for

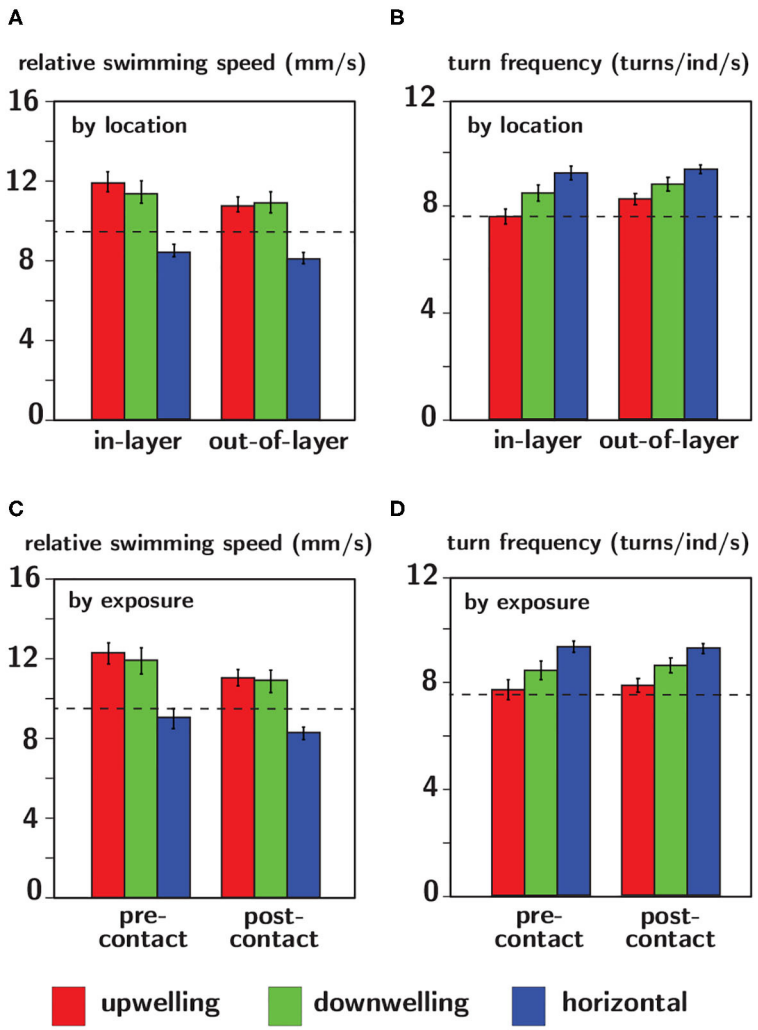

FIGURE 11 | Relative swimming speed **(A,C)** and turn frequency **(B,D)** analyzed by location **(A,B)** and exposure **(C,D)** for upwelling (red), downwelling (green), and horizontal (blue) shear flow orientations. The dashed black lines indicate average values of each respective parameter in no-flow (control) conditions. Error bars span ± one standard error.

TABLE 2 | Repeated measures analysis of variance model results for path kinematic parameters by location (in-layer vs. out-of-layer) and exposure (pre- vs. post-layer contact).

Parameter	***n***	**Error DF**	**Location (F_{ratio}, *p*)**	**Orientation (F_{ratio}, *p*)**	**Location × Orientation (F_{ratio}, *p*)**
Relative swimming speed	240	237	8.743, 0.0034*	17.995, <0.0001*	1.160, 0.32
Turn frequency	240	237	8.028, 0.005*	9.973, <0.0001*	1.069, 0.35
Parameter	***n***	**Error DF**	**Exposure (F_{ratio}, *p*)**	**Orientation (F_{ratio}, *p*)**	**Exposure × Orientation (F_{ratio}, *p*)**
Relative swimming speed	200	197	3.958, 0.048*	16.667, <0.0001*	0.190, 0.83
Turn frequency	200	197	0.334, 0.56	11.175, <0.0001*	0.093, 0.91

**Indicates statistical significance at $p < 0.05$.*

all shear flow orientations (**Figure 12**, **Table 3**) signifies that larvae are resisting sinking and/or vertical advection through depth-keeping behaviors (i.e., smaller *vngdr* values). Finally, significantly reduced residence time (*prt*) in both vertical shear flows (**Figure 12**, **Table 3**) signifies explicit avoidance of the shear layer region, potentially as a way of resisting vertical advection for improved depth-keeping. The lack of a significant change in residence time in the horizontal shear layer indicates that the in-layer region is neither explicitly avoided nor sought out.

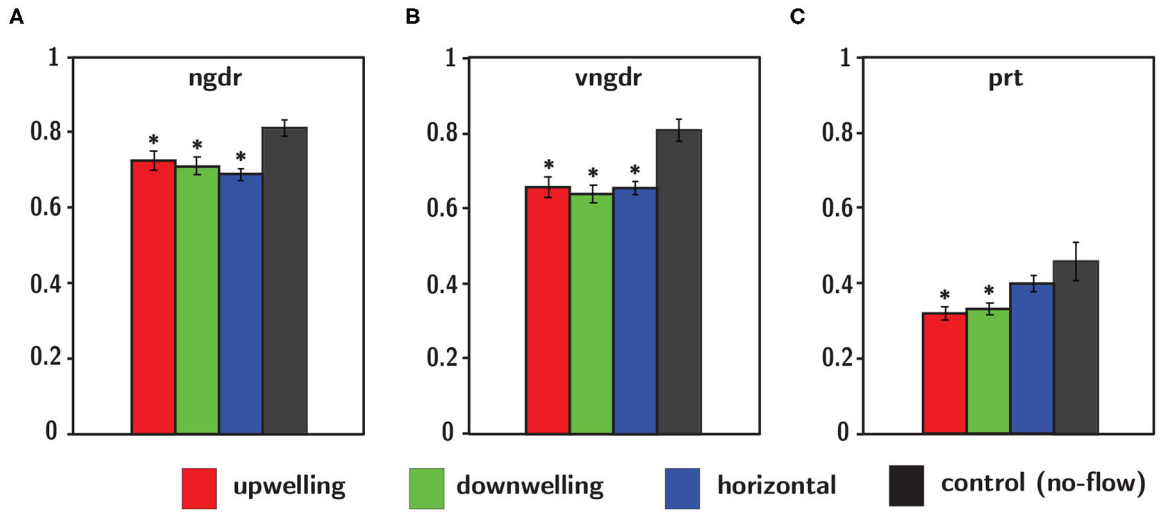

FIGURE 12 | Gross path parameters including **(A)** net-to-gross-displacement ratio *ngdr*, **(B)** vertical net-to-gross-displacement ratio *vngdr*, and **(C)** proportional residence time *prt* for upwelling (red), downwelling (green), and horizontal (blue) shear flow orientations in addition to the no-flow condition (black). Error bars span ± one standard error. *Indicates statistical significance ($p < 0.05$) of shear flow values relative to the no-flow condition.

TABLE 3 | Analysis of variance model results for gross path parameters and *post-hoc* Dunnett's control test results.

Parameter	*n*	Model SS	Model DF	Model MS	Error SS	Error DF	Error MS	F_{ratio}	*p*	DC Test, *p* (upwelling, downwelling, horizontal)
prt	280	0.919	3	0.306	16.670	276	0.060	5.072	0.002*	0.0018*, 0.0046*, 0.20
ngdr	280	0.807	3	0.269	14.427	276	0.052	5.146	0.0018*	0.039*, 0.012*, 0.0003*
vngdr	280	1.950	3	0.650	20.503	276	0.074	8.750	<0.0001*	0.0001*, <0.0001*, <0.0001*

**Indicates statistical significance ($p \leq 0.05$) of shear flow values relative to the control (no-flow) condition.*

4. DISCUSSION

4.1. Larval Behavior vs. Flow Forcing

It is useful to consider whether the results presented here support larval behavior or shear flow-induced forcing (advection and rotation) as the primary driver of observed swimming trajectory characteristics. Brachyuran crab larvae are some of the strongest swimmers among crustacean zooplankton and are capable of sustained swimming speeds from 0.2 to 8.3 cm/s, with typical values ranging from 0.5 to 2 cm/s (Mileikovsky, 1973; Sulkin et al., 1979; Forward, 1989a,b). Megalopae are well-equipped to sense hydrodynamic cues associated with velocity gradients through mechanosensitive setae (sensillae) distributed along appendages that are sensitive to fluid deformations and statocysts at the base of the antenna that function as accelerometers sensitive to angular accelerations induced by fluid rotation (Anger, 2001). Considering their exceptional swimming and mechanosensing capabilities relative to the weak bulk flow (6 mm/s maximum, 3 mm/s typical in-layer) and spatiotemporally persistent (predictable) vorticity structure presented in the shear layers (**Figure 6**), strong-swimming larvae can most likely sense and actively respond to local flow conditions everywhere without substantial shear flow-induced modifications to their swimming kinematics.

While the effects of flow-induced changes on swimming kinematics were accounted for when possible (e.g., subtracting local fluid velocity to analyze the relative swimming speed), unaccounted for advection and rotation effects may influence other observed trajectory parameters. In contrast to turbulence, with its characteristic unsteadiness and rapidly fluctuating hydrodynamic cues with differing magnitudes and spatial orientations, the flow-induced effects of steady shear flow on measured larval swimming trajectory characteristics in the present study are relatively straightforward to anticipate and evaluate. These consist of advection due to the bulk flow and rotation due to torque arising from velocity gradients (vorticity), and the anticipated effects of each on swimming kinematic parameters (relative swimming speed, turn frequency) and gross path parameters (*ngdr*, *vngdr*, *prt*) are discussed below. The results strongly and consistently suggest that larval behavioral processes, as opposed to flow forcing, are likely the predominant driver of observed swimming trajectory characteristics.

Comparing observed changes in swimming kinematics (relative swimming speed, turn frequency) by location (in-layer vs. out-of-layer) to expected kinematic effects of shear flow-induced advection and rotation provides a basis for evaluating the relative importance of larval behavior vs. flow forcing in observed swimming trajectories. If advective effects were

significant, relative swimming speed would decrease in-layer vs. out-of-layer since the advective velocity component would dominate the active swimming velocity in the measured (raw) swimming speeds in-layer where fluid velocities are non-zero. Similarly, if rotation effects were significant, turn frequency would likely increase in-layer vs. out-of layer since a torque of sufficient strength applied to an actively swimming larva would modify the trajectory heading, increasing turn frequency in-layer relative to out-of-layer where the torque is effectively zero. The magnitude of the rotation effects will depend on the strength of the torque (vorticity) and the larva's swimming capabilities, in particular the swimming speed relative to the fluid velocity (relative swimming speed) and the ability to resist rotation (further discussion below). For both swimming kinematic parameters, the ANOVAs detected a significant location effect (in-layer vs out-of-layer) in which relative swimming speeds were higher and turn frequencies were lower in-layer (**Table 2**, **Figure 11**), opposite of what would be expected if advection and rotation effects significantly modified larvae swimming kinematics. Additionally, both kinematic parameters had significant orientation effects, but no significant interaction effects (**Table 2**, **Figure 11**). The significant orientation effect indicates that, on average, swimming kinematics depend on the spatial orientation of the shear layers, while the lack of an interaction effect indicates that in-layer vs. out-of-layer trends in swimming kinematics do not depend on layer orientation. Furthermore, the hydrodynamic conditions in shear flows of differing spatial orientation are effectively identical, with the exception of the bulk flow direction relative to gravity (**Figure 6**). Accordingly, the differences in overall swimming kinematics between shear flows (orientation effect) and the identical in-layer vs. out-of-layer trends (opposite of the expected shear flow-induced kinematic modifications discussed above) among different layer orientations (no interaction effect) further support the conclusion that active larval behavior, as opposed to flow forcing, is the predominant driver of observed swimming trajectory characteristics.

A similar exercise for the gross path parameters (*ngdr*, *vngdr*, *prt*), comparing observed changes detected in the ANOVA to expected shear flow-induced modifications to these parameters from advection and rotation, yields the same conclusion as for the swimming kinematic parameters discussed above. That is, the results strongly suggest that active larval behavior, as opposed to flow forcing, is the predominant driver of observed swimming trajectory characteristics. If advective effects were significant, swimming trajectories would become more ballistic and linear due to an additional displacement component along the parallel fluid streamlines, corresponding to an increase in *ngdr* (and *vndgr*), assuming that larvae at least resist sinking since they are negatively buoyant (Queiroga and Blanton, 2005). Similarly, if rotation effects were significant, a variety of effects could manifest in swimming trajectory *ngdr* (and *vndgr*) values, depending on the larva's swimming speed relative to the flow speed and its directional stability (i.e., ability to resist rotation) relative to the strength of the vorticity (applied torque) in the shear layer (Durham et al., 2011). Some examples spanning different regimes of rotation effects include the following: (i) pure rotations about the larva's center of mass under extremely strong torque and/or little to no directional stability, (ii) helical trajectories of varying orbital radii depending on the strength of torque and the larva's directional stability, and (iii) no significant alteration to trajectory characteristics when the torque is simply not strong enough, relative to the larva's swimming ability and directional stability, to significantly alter its directional heading. When superposed on unidirectional advection along parallel streamlines in shear flow, the first example would manifest as pure linear advection (increased *ngdr*) under the spatial resolution limits of our system. The second case, which was rarely, if ever, observed (e.g., **Figure 7**), would manifest as increasingly orbital and loopy trajectories (reduced *ngdr*). The results suggest that the last case is most likely, which is consistent with the swimming kinematic results and preceding discussion here. In summary, the most likely manifestation of the effects of both advection and rotation on *ngdr* (and *vngdr*) in simple shear flow would be to create more linear, ballistic trajectories, increasing the observed *ngdr*. The results of the ANOVA show the exact opposite: significantly reduced *ngdr* (and *vngdr*) in all shear flow orientations relative to no-flow conditions (**Table 3**, **Figure 12**). Similarly derived arguments for layer residence time (*prt*) would suggest that both advection (non-zero and uniform in the layer, zero out-of-layer) and rotation (non-zero in the layer, zero out-of-layer) will cause increased residence time (again assuming larvae at least resist sinking). Again, the results of the ANOVA show the exact opposite: reduced residence time in all shear flows relative to no-flow conditions (reduction in the horizontal layer is the only nonsignificant case, **Table 3**, **Figure 12**). Collectively, the results again strongly support the conclusion that active larval behavior, as opposed to flow forcing, is the predominant driver of observed swimming trajectory characteristics.

4.2. Larval Responses in Ecological Context

Considering the stage-specific ecology of decapod crab megalopae and hydrodynamic conditions *in situ*, what types of behaviors might one expect to observe in response to steady shear flows lacking any other environmental cue? *P. herbstii* inhabits estuarine waters throughout dispersal (Dittel and Epifanio, 1982) and exhibits diel, endongenous (tidal), and ontogenetic (life-stage dependent) vertical migrations (Cronin and Forward, 1979; Garrison, 1999; Miller and Morgan, 2013). Postlarval megalopae are in the dispersed larval phase directly preceding benthic settlement and they typically aggregate near the surface at night, particularly during flood tide, to enhance flood tide transport (FTT) toward favorable settlement habitats (Queiroga and Blanton, 2005). Estuarine hydrodynamics in Wassaw Sound are ideal for FTT (Forward et al., 2001, 2003b), being tidally driven (tidal range ∼2–3 m) with extended periods of unidirectional flow and low wave action under normal conditions (Wilson et al., 2013). Moderate current speeds (∼0.5 m/s) and relatively shallow depths (∼10–15 m) yield spatiotemporally persistent, tidally-modulated vertical shear structure, while persistent horizontal shear structure is likely associated with boundary layers along the channel margins (oyster reefs, salt marsh

boundaries) and complex three-dimensional circulation around weakly-stratified estuarine fronts due to relatively low freshwater input. Both fronts (elevated horizontal shear structure) and clines (elevated vertical shear structure) are typically regions of enhanced biological productivity (Largier, 1993; O'Donnell, 1993; Durham and Stocker, 2012; Woodson et al., 2012), and competent megalopae can locate and exploit these resource patches during foraging and sampling behaviors to improve fitness throughout dispersed larval stages. Thus, for imminently-settling megalopae presented with persistent hydrodynamic cues often associated with nearby resource patches, one might expect to see depth-keeping behaviors for enhanced FTT (in darkness), combined with sampling or foraging behaviors elicited by ecologically-relevant hydrodynamic cues.

Depth-regulatory behaviors are primarily driven by combined geotaxis, phototaxis, and barokinesis (Forward, 1974; Sulkin, 1975, 1984; Sulkin et al., 1980), while foraging and sampling behaviors necessarily depend on successful detection and exploitation of finescale chemical and hydrodynamic cues (Anger, 2001; Queiroga and Blanton, 2005). During the shear layer behavioral assays here, larvae experience strong rotation and deformation cues associated with steep gradients of fluid velocity along the edges of the shear layer (**Figures 2**, **6**). As the flow is steady, effectively unidirectional, and characterized by one-dimensional velocity gradients, the local (unsteady) acceleration is identically zero and most convective acceleration terms, originating from the dot product of the velocity vector and velocity gradient tensor, are negligibly small, with the exception of those associated with in-plane shear deformation and rotation. Due to the spatial structure of the shear layers, the non-zero rotation (in-plane vorticity) and deformation (shear strain rate) cues experienced by free-swimming larvae are structurally identical and related in magnitude by a factor of two (vorticity is twice as large). Importantly, larvae are well-equipped to sense and respond to both fluid rotation and deformation. Mechanosensitive setae (sensillae) distributed along larval appendages are sensitive to fluid deformations, and statocysts as the base of the antenna function as accelerometers sensitive to angular accelerations induced by fluid rotation (Anger, 2001). While the specific hydrodynamic cue (rotation, deformation, or some combination) potentially driving larval behavioral responses to persistent shear flows is of interest ecologically (Fuchs et al., 2015; Wheeler et al., 2015), it is beyond the scope of the present study to disentangle the two. For this reason, the focus was simply on fluid rotation (vorticity) as a morphologically- and ecologically-relevant hydrodynamic cue that larvae may be responding to (**Figure 10**, **Table 1**). Clear differences in population swimming kinematics between shear flow and no-flow conditions (**Figure 9**) confirm that larvae readily sense and respond to the persistent rotation (vorticity) and/or deformation (shear strain rate) cues presented during shear layer behavioral assays.

What is the macro effect of larval behavioral responses to shear flows, and is it consistent with megalopal ecology? The effect of larval swimming kinematic responses to all shear flow orientations was to increase trajectory sinuosity and diffusivity (↓ *ngdr*) and enhance depth-keeping (↓ *vngdr*, ↓ *prt* in vertical shear layers) (**Figure 12**, **Table 3**). Increased trajectory diffusivity is consistent with observed changes in larval swimming kinematics (↓ speed post-contact and ↑ turn frequency out-of-layer, **Figure 11**, **Table 2**) and could enable larvae to remain in the vicinity of all shear layers through area-restricted search behaviors. Area-restricted searching through reduced speed and increased turning frequency is a common strategy that foraging organisms employ to locate and exploit discrete resource patches (Knell and Codling, 2012). Employing this strategy to remain in the vicinity of the shear layers, though not in the layers themselves, could provide larvae with an energetically-favorable means of simultaneously maintaining depth while also exploiting resource patches often associated with fronts and clines *in situ*. These behaviors would be consistent with the larval stage-specific goals of imminently-settling megalopae and suggest that hydrodynamic cues associated with spatiotemporally persistent flow features play an important, and perhaps fundamental, role in larval behavior throughout dispersal.

4.3. Orientation-Specific Responses Relative to *in situ* Hydrodynamics

As noted above, changes in kinematics by shear layer location and exposure were similar in all shear flow orientations (**Figure 11**, **Table 2**) and produced similar macro effects on trajectory characteristics (**Figure 12**, **Table 3**). Here, the emphasis is to highlight the significance of nuanced differences in swimming kinematics as a function of shear flow orientation, reflected in the orientation-specific kinematics pdfs and cdfs in **Figure 9**. The focus is specifically on why orientation-specific sensitivities to hydrodynamic cues make sense ecologically and would be advantageous to dispersed larvae.

In many relatively wide and shallow, weakly-stratified estuaries, persistent vertical shear structure (i.e., horizontally-oriented shear flows) associated with oscillating tidal flows and bottom boundary layer dynamics is characteristically stronger than persistent horizontal shear structure (i.e. vertically-oriented shear flows) around weakly-stratified estuarine fronts and along channel margins. The orientation-specific behavioral sensitivities to hydrodynamic cues (vorticity) associated with persistent shear flows seen here (**Figure 10**, **Table 1**) may be reflective of these predominant hydrodynamic realities. Larvae are most sensitive to vertically-oriented shear flows (mean consequential vorticity of 0.11–0.12 s^{-1}), suggesting an evolutionary basis for sensing and responding to typically weaker hydrodynamic cues associated with horizontal shear (vertical bulk flow) *in situ*. In contrast, larvae are significantly less sensitive to fluid vorticity associated with vertical shear structure (horizontal bulk flow, mean consequential vorticity of 0.16 s^{-1}), suggesting historical exposure and adaptation to more intense vertical shear structure. The higher behavioral sensitivities of larvae to hydrodynamic cues associated with horizontal shear structure may also be reflected in nuanced differences in average swimming kinematics among different shear flow orientations. For example, path kinematic responses show area-restricted search behaviors in the vicinity of all shear flows, but the response is only excited in vertically-oriented shear layers: swimming faster on average

(compared to control), swimming slower post-contact and out-of-layer, and greater turn frequency out-of-layer (**Figure 11**, **Table 2**). In contrast, the area-restricted search behavior in the horizontally-oriented shear layer features slower swimming speeds on average (compared to control), swimming slower post-contact and out-of-layer, and greater turn frequency out-of-layer (**Figure 11**, **Table 2**). While all shear flow orientations elicit area-restricted search behaviors in the vicinity of the layers, the *excited* search behavior seen in both vertically-oriented shear layers may be reflective of larvae explicitly resisting vertical advection (↓ *prt* and ↓ *vngdr*) while also remaining in the vicinity of the layer for sampling and foraging purposes. This example highlights how orientation specificity of both behavioral sensitivity to hydrodynamic cues associated with persistent flow features and swimming kinematic responses can be advantageous for dispersed larvae. For example, they can exploit ecologically-relevant hydrodynamic cues to forage and sample for nearby resource patches (e.g., fronts and clines), while also maintaining depth to reduce predation risk or enhance tidal transport toward favorable settlement habitats.

4.4. Persistent Hydrodynamic Cues as a Potential Driver of Larval Patchiness

The area-restricted search behaviors larvae exhibit in the vicinity of all shear flow orientations offer a potential behavioral basis for finescale spatiotemporal patchiness in larval populations *in situ*. Observed patchiness around fronts and clines has been attributed to both physical forcing and larval behavior (Natunewicz and Epifanio, 2001). For example, Eggleston et al. (1998) found that hydrodynamic forcing significantly enhanced megalopae densities around a large-scale frontal flow feature, while Garrison (1999) attributed finescale patchiness in Brachyuran crab larva populations to interactions with small-scale hydrodynamic features. Larval responses to other environmental cues such as changing stratification and food patch dynamics in the water column were also shown to disrupt vertical migratory behaviors and produce larval patches that were depth-segregated by larval stage (Lindley et al., 1994). Collectively, it is clear that (i) planktonic decapod larva populations exhibit considerable spatiotemporal patchiness, (ii) larval patches are often found near regions of enhanced productivity and resources, including around fronts and clines, and (iii) both larval behavior and physical forcing play important roles in influencing patch dynamics. Our findings corroborate these views and quantitatively establish that hydrodynamic cues associated with spatiotemporally persistent flow features are likely fundamental drivers of decapod larval behavior and may act as a potential driver of larval patchiness by directly influencing spatiotemporal population distributions.

Area-restricted searching and increased residence time in the vicinity of persistent flow features associated with fronts and clines would offer larvae the opportunity to improve fitness by exploiting coincident high-density resources patches. Fronts (e.g., in the estuarine transition zone) and clines (e.g., in thin plankton layers) are known ecological "hot spots" in which biomass can be several orders of magnitude greater than the surrounding waters (Haury and Wiebe, 1982; Largier, 1993; O'Donnell, 1993; Yoder et al., 1994; McManus et al., 2003; Durham and Stocker, 2012). The distinct hydrodynamic signature associated with persistent flow features around fronts and clines may incentivize mechanosensitive larvae to restrict search volume in hopes of exploiting a coincident chemical cue or resource patch (a cue hierarchy, Woodson et al., 2007). The findings, highlighting the fundamental importance of hydrodynamic cues associated with persistent flow features in affecting individual larval behaviors, further suggest that fronts and clines are intimately linked to larval foraging and sampling behaviors and behavior-driven patchiness *in situ* (Franks, 1992; Tiselius, 1992; Epstein and Beardsley, 2001; Simons et al., 2006; Benoit-Bird et al., 2009; Woodson et al., 2012).

The need to forage and sample may also cause larvae to depart from predominant behavioral modes such as diel and endogenous (tidally-modulated) vertical migrations (Lindley et al., 1994; Woodson and McManus, 2007). Disruptions to vertical migratory behaviors have the potential to significantly influence horizontal transport and dispersal of larval populations in the context of selective tidal stream transport phenomena (Cronin and Forward, 1986; Garrison, 1999; Queiroga et al., 2002; Miller and Morgan, 2013). While there is significant variability in vertical migratory behaviors among decapod crab species and by larval stage (Sulkin, 1984), there are also many environmental cues known to modify depth-regulation and disrupt vertical migrations (i.e., light, gravity, hydrostatic pressure, turbulence). The results here show another potential source of variability in vertical-migratory behaviors in the form of enhanced depth-keeping behaviors and larval patchiness around spatiotemporally persistent hydrodynamic features. As modifiers of depth-regulation and vertical migratory behaviors, hydrodynamic cues associated with persistent flow features have the potential to significantly alter dispersal trajectories and larval population connectivity (Olmi, 1994; Marta-Almeida et al., 2006).

5. CONCLUSION

This study has shown conclusively that hydrodynamic cues associated with spatiotemporally persistent flow features play an important, and perhaps fundamental, role in dispersed decapod crab larval behavior. When presented with a flow feature often associated with regions of enhanced productivity around fronts and clines *in situ* (steady shear flow), megalopae of the Atlantic mud crab *P. herbstii* significantly modified swimming kinematics. Larval behavioral responses depended strongly on the directional orientation of the persistent flow feature. Furthermore, larvae exhibited orientation-specific behavioral sensitivity to a relevant hydrodynamic cue presented (vorticity), and the kinematic changes triggered in response to shear flows in all spatial orientations yielded enhanced depth-keeping and area-restricted search behaviors. These area-restricted search behaviors may be reflective of foraging and sampling initiated by an ecologically-relevant hydrodynamic cue that is potentially indicative of nearby resources patches. In this regard, hydrodynamic cues

associated with spatiotemporally persistent flow features are likely fundamental drivers of decapod larval behavior and may act as another cause of larval patchiness by directly influencing spatiotemporal population distributions. This, in turn, can significantly affect larval dispersal trajectories and population connectivity in the larger ecological context of selective tidal stream transport toward favorable benthic settlement habitats.

DATA AVAILABILITY STATEMENT

The datasets generated for this study are available on request to the corresponding author.

AUTHOR CONTRIBUTIONS

AT, DW, MW, and JY conceived and designed the experiments. AT conducted the experiments and analysis. AT, DW, and MW conceived the analysis. AT and DW wrote the paper. Some aspects of this study were reported in AT's Ph.D. thesis (True, 2014). All authors approved the final manuscript.

FUNDING

Financial support was provided by a US National Science Foundation grant (OCE-0728238). Additional funding was provided by the Karen and John Huff Chair endowed funds.

ACKNOWLEDGMENTS

We thank REU researcher Allison Bergen for assistance with collection and identification of crab larvae in Wassaw Sound and digitization of larval swimming trajectories.

REFERENCES

Andrade, E. C. (1939). The velocity distribution in a liquid-into-liquid jet. Part 2: The plane jet. *Proc. Phys. Soc.* 51, 784–793.

Andrews, W. R., Targett, N. M., and Epifanio, C. E. (2001). Isolation and characterization of the metamorphic inducer of the common mud crab, *Panopeus herbstii*. *J. Exp. Mar. Biol. Ecol.* 261, 121–134. doi: 10.1016/S0022-0981(01)00268-4

Anger, K. (2001). *The Biology of Decapod Crustacean Larvae, Vol. 14*. Lisse: AA Balkema Publishers.

Benoit-Bird, K. J., Cowles, T. J., and Wingard, C. E. (2009). Edge gradients provide evidence of ecological interactions in planktonic thin layers. *Limnol. Oceanogr.* 54, 1382–1392. doi: 10.4319/lo.2009.54.4.1382

Bickley, W. G. (1937). The plane jet. *Philos. Mag.* 23, 727–731. doi: 10.1080/14786443708561847

Criales, M. M., Zink, I. C., Haus, B. K., Wylie, J., and Browder, J. A. (2013). Effect of turbulence on the behavior of pink shrimp post larvae and implications for selective total stream transport behavior. *Mar. Ecol. Prog. Ser.* 477, 161–176. doi: 10.3354/meps10141

Cronin, T. W., and Forward, R. B., Jr. (1979). Tidal vertical migration: an endogenous rhythm in estuarine crab larvae. *Science* 205, 1020–1022. doi: 10.1126/science.205.4410.1020

Cronin, T. W., and Forward, R. B., Jr. (1986). Vertical migration cycles of crab larvae and their role in larval dispersal. *Bull. Mar. Sci.* 39, 192–201.

Dekshenieks, M. M., Donaghay, P. L., Sullivan, J. M., Rines, J. E. B., Osborn, T. R., and Twardowski, M. S. (2001). Temporal and spatial occurrence of thin phytoplankton layers in relation to physical processes. *Mar. Ecol. Prog. Ser.* 223, 61–71. doi: 10.3354/meps223061

Dittel, A. I., and Epifanio, C. E. (1982). Seasonal abundance and vertical distribution of crab larvae in Delaware Bay. *Estuaries* 5, 197–202. doi: 10.2307/1351835

Durham, W. M., Climent, E., and Stocker, R. (2011). Gyrotaxis in a steady vortical flow. *Phys. Rev. Lett.* 106:238102. doi: 10.1103/PhysRevLett.106.238102

Durham, W. M., and Stocker, R. (2012). Thin phytoplankton layers: characteristics, mechanisms, and consequences. *Annu. Rev. Mar. Sci.* 4, 177–207. doi: 10.1146/annurev-marine-120710-100957

Eggleston, D. B., Armstrong, D. A., Elis, W. E., and Patton, W. S. (1998). Estuarine fronts as conduits for larval transport: hydrodynamics and spatial distribution of dungeness crab postlarvae. *Mar. Ecol. Prog. Ser.* 164, 73–82. doi: 10.3354/meps164073

Epstein, A. W., and Beardsley, R. C. (2001). Flow-induced aggregation of plankton at a front: a 2-d Eulerian model study. *Deep Sea Res. II* 48, 395–418. doi: 10.1016/S0967-0645(00)00086-2

Forward, R. B. Jr. (1974). Negative phototaxis in crustacean larvae: possible functional significance. *J. Exp. Mar. Biol. Ecol.* 16, 11–17. doi: 10.1016/0022-0981(74)90069-0

Forward, R. B. Jr. (1989a). Behavioural responses of crustacean larvae to rates of salinity change. *Biol. Bull.* 176, 229–238. doi: 10.2307/1541981

Forward, R. B. Jr. (1989b). Depth regulation of larval marine decapod crustaceans: test of an hypothesis. *Mar. Biol.* 176, 229–238.

Forward, R. B. Jr. (1990). Responses of crustacean larvae to hydrostatic pressure: behavioral basis of high barokinesis. *Mar. Behav. Physiol.* 17, 223–232. doi: 10.1080/10236249009378773

Forward, R. B. Jr., Reyns, N. B., Diaz, H., Cohen, J. H., and Eggleston, D. B. (2004). Endogenous swimming rhythms of juvenile blue crabs, *Callinectes sapidus*, as related to horizontal transport. *J. Exp. Mar. Biol. Ecol.* 229, 63–76. doi: 10.1016/j.jembe.2003.09.002

Forward, R. B. Jr., Tankersley, R. A., and Rittschof, D. (2001). Cues for metamorphosis of brachyuran crabs: an overview. *Am. Zool.* 41, 1108–1122. doi: 10.1093/icb/41.5.1108

Forward, R. B. Jr., Tankersley, R. A., Smith, K. A., and Welch, J. M. (2003a). Effects of chemical cues on orientation of blue crab, *Callinectes sapidus*, megalopae in flow: implications for location of nursery areas. *Mar. Biol.* 142, 747–756. doi: 10.1007/s00227-002-0966-7

Forward, R. B. Jr., Tankersley, R. A., and Welch, J. M. (2003b). Selective tidal-stream transport of the blue crab *Callinectes sapidus*: an overview. *Bull. Mar. Sci.* 72, 347–365.

Franks, P. J. S. (1992). Sink or swim: accumulation of biomass at fronts. *Mar. Ecol. Prog. Ser.* 82, 1–12. doi: 10.3354/meps082001

Fuchs, H. L., Christman, A. J., Gerbi, G. P., Hunter, E. J., and Diez, F. J. (2015). Directional flow sensing by passively stable larvae. *J. Exp. Biol.* 218, 2782–2792. doi: 10.1242/jeb.125096

Garrison, L. P. (1999). Vertical migration behavior and larval transport in brachyuran crabs. *Mar. Ecol. Prog. Ser.* 176, 103–113. doi: 10.3354/meps176103

Haury, L. R., and Wiebe, P. H. (1982). Fine-scale multi-species aggregations of oceanic zooplankton. *Deep Sea Res.* 29, 915–921. doi: 10.1016/0198-0149(82)90055-3

Hobbs, R. C., and Botsford, L. W. (1992). Diel vertical migration and timing of metamorphosis of larvae of the dungeness crab *Cancer magister*. *Mar. Biol.* 112, 417–428. doi: 10.1007/BF00356287

Houser, L. T., and Epifanio, C. E. (2009). Impacts of biochemical cues on horizontal swimming behavior of individual crab larvae. *Mar. Freshw. Behav. Physiol.* 42, 249–264. doi: 10.1080/10236240903165980

Hussein, H. J. (1994). Evidence of local axisymmetry in the small scales of a turbulent planar jet. *Phys. Fluids* 6, 2058–2070. doi: 10.1063/1.868212

Jamieson, G. S. and Phillips, A. C. (1988). Occurrence of *Cancer* spp. crab megalopae off the west coast of Vancouver Island, British Columbia. *US Fish. Bull.* 86, 525–542.

Knell, A. S., and Codling, E. A. (2012). Classifying area-restricted search (ars) using a partial sum approach. *Theor. Ecol.* 5, 325–339. doi: 10.1007/s12080-011-0130-4

Kundu, P., Cohen, I., and Dowling, D. (2011). *Fluid Mechanics, 5th Edn*. Cambridge, MA: Academic Press.

Largier, J. (1993). Estuarine fronts: how important are they? *Estuaries* 16, 1–11. doi: 10.2307/1352760

Lecchini, D., Mills, S. C., Brie, C., Maurin, R., and Banaigs, B. (2010). Ecological determinants and sensory mechanisms in habitat selection of crustacean postlarvae. *Behav. Ecol.* 17, 599–607. doi: 10.1093/beheco/arq029

Lindley, J. A., Williams, R., and Conway, D. V. P. (1994). Variability in dry weight and vertical distributions of decapod larvae in the Irish Sea and North Sea during the spring. *Mar. Biol.* 120, 385–395. doi: 10.1007/BF00680212

Marta-Almeida, M., Dubert, J., Peliz, A., and Queiroga, H. (2006). Influence of vertical migration pattern on retention of crab larvae in a seasonal upwelling system. *MEPS* 307, 1–19. doi: 10.3354/meps307001

McManus, M. A., Alldredge, A. L., Barnard, A. H., Boss, E., Case, J. F., Cowles, T. J., et al. (2003). Characteristics, distribution and persistence of thin layers over a 48 hour period. *Mar. Ecol. Prog. Ser.* 261, 1–19. doi: 10.3354/meps261001

McManus, M. A., and Woodson, C. B. (2012). Plankton distribution and ocean dispersal. *J. Exp. Biol.* 215, 1008–1016. doi: 10.1242/jeb.059014

Mehta, R. D., and Bradshaw, P. (1979). Design rules for small low speed wind tunnels. *Aeronaut. J.* 83, 443–449.

Mileikovsky, S. A. (1973). Speed of active movement of pelagic larvae of marine bottom invertebrates and their ability to regulate their vertical position. *Mar. Biol.* 23, 11–17. doi: 10.1007/BF00394107

Miller, S. H., and Morgan, S. G. (2013). Interspecific differences in depth preference: regulation of larval transport in an upwelling system. *Mar. Ecol. Prog. Ser.* 476, 301–306. doi: 10.3354/meps10150

Natunewicz, C. C., and Epifanio, C. E. (2001). Spatial and temporal scales of patches of crab larvae in coastal waters. *Mar. Ecol. Prog. Ser.* 212, 217–222. doi: 10.3354/meps212217

O'Donnell, J. (1993). Surface fronts in estuaries: a review. *Estuaries* 16, 12–39. doi: 10.2307/1352761

Olmi, E. J. (1994). Vertical migration of blue crab *Callinectes sapidus* megalopae: implications for transport in estuaries. *Mar. Ecol. Prog. Ser.* 113, 39–54. doi: 10.3354/meps113039

Ott, F. S., and Forward, R. B. Jr. (1976). The effect of temperature on phototaxis and geotaxis by larvae of the crab *Rhithropanopeus harrisii* (gould). *J. Exp. Mar. Biol.* 23, 97–107. doi: 10.1016/0022-0981(76)90134-9

Peacock, T., Bradley, E., Hertzberg, J., and Lee, Y. (2004). Forcing a planar jet flow using mems. *Exp. Fluids* 37, 22–28. doi: 10.1007/s00348-004-0780-8

Queiroga, H., and Blanton, J. (2005). Interactions between behaviour and physical forcing in the control of horizontal transport of decapod crustacean larvae. *Adv. Mar. Biol.* 47, 107–214. doi: 10.1016/S0065-2881(04)47002-3

Queiroga, H., Moksnes, P., and Meireles, S. (2002). Vertical migration behaviour in the larvae of the shore crab *Carcinus maenas* from a microtidal system (Gullmarsfjord, Sweden). *Mar. Ecol. Prog. Ser.* 237, 195–207. doi: 10.3354/meps237195

Raffel, M., Willert, C. E., Scarano, F., Kähler, C. J., Wereley, S. T., and Kompenhans, J. (2018). *Particle Image Velocimetry: A Practical Guide*. New York, NY: Springer.

Revuelta, A., Sanchez, A. L., and Linan, A. (2002). The virtual origin as a first-order correction for the far-field description of laminar jets. *Phys. Fluids* 14, 1821–1824. doi: 10.1063/1.1473650

Rodriguez, R. A., and Epifanio, C. E. (2000). Multiple cues for induction of metamorphosis in larvae of the common mud crab *Panopeus herbstii*. *Mar. Ecol. Prog. Ser.* 195, 221–229. doi: 10.3354/meps195221

Sato, H. (1960). The stability and transition of a two-dimensional jet. *J. Fluid Mech.* 7, 53–80. doi: 10.1017/S0022112060000049

Sato, H., and Sakao, F. (1964). An experimental investigation of the instability of a two-dimensional jet at low Reynolds numbers. *J. Fluid Mech.* 20, 337–352. doi: 10.1017/S0022112064001264

Schlichting, H. (1933). Laminare strahlausbreitung. *ZAMM* 8, 260–263.

Shanks, A. L. (1986). Vertical migration and cross-shelf dispersal of larval *Cancer spp.* and *Randallia ornata* (crustacea:brachyura) off the coast of southern California. *Mar. Biol.* 92, 189–199. doi: 10.1007/BF00392836

Simons, R. D., Monismith, S. G., Johnson, L. E., Winkler, G., and Saucier, F. J. (2006). Zooplankton retention in the estuarine transition zone of the St. Lawrence Estuary. *Limnol. Oceanogr.* 51, 2621–2631. doi: 10.4319/lo.2006.51.6.2621

Sulkin, S. D. (1975). The influence of light in the depth regulation of crab larvae. *Biol. Bull.* 148, 33–343. doi: 10.2307/1540551

Sulkin, S. D. (1984). Behavioral basis of depth regulation in the larvae of brachyuran crabs. *Mar. Ecol. Prog. Ser.* 15, 181–205. doi: 10.3354/meps015181

Sulkin, S. D., Phillips, I., and van Heukelem, W. (1979). On the locomotory rhythm of brachyuran crab larvae and its significance in vertical migration. *Mar. Ecol. Prog. Ser.* 1, 331–335. doi: 10.3354/meps001331

Sulkin, S. D., van Heukelem, W., Kelly, P., and van Heukelem, L. (1980). The behavioral basis of larval recruitment in the crab *Callinectes sapidus* Rathbun: a laboratory investigation of ontogenetic changes in geotaxis and barokinesis. *Biol. Bull.* 159, 402–417. doi: 10.2307/1541103

Tankersley, R. A., McKelvey, L. M., and Forward, R. B., Jr. (1995). Responses of estuarine crab megalopae to pressure, salinity and light: implications for flood-tide transport. *Mar. Biol.* 122, 391–400. doi: 10.1007/BF00350871

Tapia-Lewin, S., and Pardo, L. M. (2014). Field assessment of the predation risk - food availability trade-off in crab megalopae settlement. *PLoS ONE* 9:e95335. doi: 10.1371/journal.pone.0095335

Tiselius, P. (1992). Behavior of *Acartia tonsa* in patchy food environments. *Limnol. Oceanogr.* 37, 1640–1651. doi: 10.4319/lo.1992.37.8.1640

True, A., Webster, D., Weissburg, M., Yen, J., and Genin, A. (2015). Patchiness and depth-keeping of copepods in response to simulated frontal flows. *Mar. Ecol. Prog. Ser.* 539, 65–76. doi: 10.3354/meps11472

True, A. C. (2014). *Ecological engines: finescale hydrodynamic and chemical cues, zooplankton behavior, and implications for nearshore marine ecosystems* (Ph.D. thesis). Georgia Institute of Technology, Atlanta, GA, United States.

Warton, D. I. and Hui, F. K. (2011). The arcsine is asinine: the analysis of proportions in ecology. *Ecology* 92, 3–10. doi: 10.1890/10-0340.1

Welch, J. M., Forward, R. B., Jr. and Howd, P. A. (1999). Behavioural responses of blue crab *Callinectes sapidus* larvae to turbulence: implications for selective tidal stream transport. *Mar. Ecol. Prog. Ser.* 179, 135–143. doi: 10.3354/meps179135

Wheeler, J. D., Helfrich, K. R., Anderson, E. J., and Mullineaux, L. S. (2015). Isolating the hydrodynamic triggers of the dive response in eastern oyster larvae. *Limnol. Oceanogr.* 60, 1332–1343. doi: 10.1002/lno.10098

Whitney, M. M., Codiga, D. L., Ullman, D. S., McManus, P. M., and Jiorle, R. (2012). Tidal cycles in stratification and shear and their relationship to gradient richardson number and eddy viscosity variations in estuaries. *J. Phys. Oceanogr.* 42, 1124–1133. doi: 10.1175/JPO-D-11-0172.1

Wilson, M. L., Webster, D. R., and Weissburg, M. J. (2013). Spatial and temporal variation in the hydrodynamic landscape in intertidal salt marsh systems. *Limnol. Oceanogr.* 3, 156–172. doi: 10.1215/21573689-2373360

Woodson, C. B., and McManus, M. A. (2007). Foraging behavior can influence dispersal of marine organisms. *Limnol. Oceanogr.* 52, 2701–2709. doi: 10.4319/lo.2007.52.6.2701

Woodson, C. B., McManus, M. A., Tyburczy, J. A., Barth, J. A., Washburn, L., Caselle, J. E., et al. (2012). Coastal fronts set recruitment and connectivity patterns across multiple taxa. *Limnol. Oceanogr.* 57, 582–596. doi: 10.4319/lo.2012.57.2.0582

Woodson, C. B., Webster, D. R., Weissburg, M. J., and Yen, J. (2005). Response of copepods to physical gradients associated with structure in

the ocean. *Limnol. Oceanogr.* 50, 1552–1564. doi: 10.4319/lo.2005.50.5.1552

Woodson, C. B., Webster, D. R., Weissburg, M. J., and Yen, J. (2007). Cue hierarchy and foraging in calanoid copepods: ecological implications of oceanographic structure. *Mar. Ecol. Prog. Ser.* 330, 163–177. doi: 10.3354/meps330163

Yoder, J. A., Ackleson, S. G., Barber, R. T., Flament, P., and Balch, W. M. (1994). A line in the sea. *Nature* 371, 689–692. doi: 10.1038/371689a0

Zar, J. H. (1999). *Biostatistical Analysis, 4th Edn*. Upper Saddle Hall, NJ: Prentice Hall.

Conflict of Interest: The authors declare that the research was conducted in the absence of any commercial or financial relationships that could be construed as a potential conflict of interest.

Copyright © 2020 True, Webster, Weissburg and Yen. This is an open-access article distributed under the terms of the Creative Commons Attribution License (CC BY). The use, distribution or reproduction in other forums is permitted, provided the original author(s) and the copyright owner(s) are credited and that the original publication in this journal is cited, in accordance with accepted academic practice. No use, distribution or reproduction is permitted which does not comply with these terms.

frontiers in Marine Science

ORIGINAL RESEARCH
published: 11 August 2020
doi: 10.3389/fmars.2020.00648

Monsoonal Influence and Variability of Water Quality, Phytoplankton Biomass in the Tropical Coastal Waters – A Multivariate Statistical Approach

Subrat Naik[1,2], Rajani Kanta Mishra[3], K. C. Sahu[1], Aneesh A. Lotliker[4], U. S. Panda[2] and Pravakar Mishra[1]*

[1] Department of Marine Sciences, Berhampur University, Berhampur, India, [2] National Centre for Coastal Research, Ministry of Earth Sciences, Chennai, India, [3] National Centre for Polar and Ocean Research, Ministry of Earth Sciences, Goa, India, [4] Indian National Centre for Ocean Information Services, Ministry of Earth Sciences, Hyderabad, India

OPEN ACCESS

Edited by:
Malcolm McFarland, Florida Atlantic University, United States

Reviewed by:
Dipnarayan Ganguly, National Centre for Sustainable Coastal Management, India
Punyasloke Bhadury, Indian Institute of Science Education and Research Kolkata, India
Pradipta Ranjan Muduli, Wetland Research and Training Centre (WRTC), Chilika Development Authority, India

***Correspondence:**
Rajani Kanta Mishra
rajanimishra@yahoo.com

Specialty section:
This article was submitted to Marine Ecosystem Ecology, a section of the journal Frontiers in Marine Science

Received: *23 December 2019*
Accepted: *14 July 2020*
Published: *11 August 2020*

Citation:
Naik S, Mishra RK, Sahu KC, Lotliker AA, Panda US and Mishra P (2020) Monsoonal Influence and Variability of Water Quality, Phytoplankton Biomass in the Tropical Coastal Waters – A Multivariate Statistical Approach. Front. Mar. Sci. 7:648. doi: 10.3389/fmars.2020.00648

Rushikulya Estuary is rich in biodiversity facing significant changes in recent periods due to pollution/anthropogenic impacts from the industries and growing urbanization along the banks of the river. This estuary caters mass nesting of Olive Ridley sea turtles and one of the world's largest rookery in India. In view of the above, the present study examined the seasonal variability of water quality parameters [water temperature, pH, salinity, dissolved oxygen (DO), total suspended matter (TSM), inorganic nutrients (NO_2-N, NO_3-N, NH_4-N, PO_4-P, and SiO_4-Si), and the phytopigment, i.e., Chlorophyll-*a* (chl-*a*)] from the seawater samples of three different seasons pre-monsoon, monsoon, and post-monsoon. Time series observations were made at five locations off Rushikulya Estuary, Bay of Bengal, from March 2011 to February 2013. A wide range of nutrient concentrations except for NO_2-N, varied from 0.89–3.62 μmol/l in the NO_3-N, from 1.36–6.81 μmol/l in the NH_4-N, from 0.66–3.45 μmol/l in the PO_4-P and from 0.89–7.97 μmol/l in the SiO_4-Si. The highest chl-*a* (3.72 mg/m^3) was recorded during pre-monsoon than monsoon and post-monsoon. Factor analysis (FA) showed that three underlying factors, each during pre-monsoon, monsoon, and post-monsoon, influenced the water quality to the extent of 75.02, 67.33, and 66.37%, respectively. The significant result from a statistical view of non-metric multidimensional scaling (nm-MDS) and cluster analysis (CA) revealed that the chl-*a* variability was due to the direct influence of nutrients than the physical parameters. Correlation analysis revealed that chl-*a* has positive correlation with DO, NO_2, NO_3, PO_4, and SiO_4, while negative with salinity in pre-monsoon and monsoon. The composite results indicated that the study area is well oxygenated and rich in nutrients, and chl-*a* distribution represents typical upper ocean dynamics and food chain linked to the pristine coastal and ecologically rich ecosystem.

Keywords: water quality, phytopigment, multivariate analyses, tropical waters, Rushikulya Estuary

INTRODUCTION

The east coast of India experiences a tropical monsoon kind of climate like other parts of the country (Mishra et al., 2009). Two monsoon seasons *viz*. summer (June–September) and winter (November–March) monsoons are prevailing in the Indian subcontinent. Winds that are southwesterly during June–September and northeasterly during November–March are predominant. April–May and October are transition periods during which the wind and currents get reversed. The summer monsoon winds are moisture-laden and cause maximum rain (more than 70% of annual rainfall) over the subcontinent (India Metrological Department [IMD], 2006). The Bay of Bengal (BoB) is a semi-enclosed tropical ocean basin, which is significantly influenced by monsoon and gets enormous volume of fresh water from both waterway discharges and precipitation (Emmel and Curray, 1983). The annual freshwater release into the BoB surpasses 1.5×10^{12} m^3, which decreases the mean salinity enormously in the northernmost bay (Laviolette, 1967). The estuaries, therefore, show marked differences in physical parameters like salinity during the wet and dry seasons. This is apparent from the seasonal variation in the vertical salinity structure in the estuaries. The estuarine ecosystem and associated natural habitat have been adapted to this seasonality. Water quality is considered as the essential factor controlling the health and state of the marine condition. It means the water quality depends on natural processes, weathering, and soil disintegration and on anthropogenic inputs, metropolitan and industrial wastewater discharge, etc. The anthropogenic releases comprise a consistent contaminating source, though surface spillover is a seasonal phenomenon, to a great extent influenced by the atmosphere within the basin (Singh et al., 2004). The nutrient input to the beachfront waters has been significantly expanding in the most recent decades because of the intensification of human activities and urbanization along the coastal waters (Newton et al., 2003; Newton and Mudge, 2005). The spreading of nutrient concentrations in beachfront waters causes a few natural alterations like an increase in productivity and stock enhancements (Menon et al., 2000; Srinivasan et al., 2010). However, anthropogenic inputs cause eutrophication, especially in the shadow regions of estuaries and bays where circulation is restricted by geomorphological graduations. A swift change in chemical characteristics of water bodies due to shifting waterways and discharges leads to diverse ecological consequences like changes in species composition, proliferation of phytoplankton, and depletion of oxygen concentrations (Welsh and Eller, 1991; Zhang et al., 2009; Zhao et al., 2009; Barik et al., 2017). Nearshore and estuarine waters show noteworthy variability with respect to precipitation, tidal prism, abiotic and biotic interactions, their quantum impacting the nutrient cycle of the coastal environments (Mishra et al., 2003; Naik et al., 2014). The estimation of physicochemical parameters in the marine condition comprehends the oceanic biological system; however, it is complicated to extract inferences from a large set of spatiotemporal observations. The monsoonal influence and seasonal variation in the phytoplankton biomass, water quality, and the status of the ecosystem in the BoB region have been studied extensively (Mishra et al., 2009; Baliarsing et al., 2013). However, the estuarine effects on the coastal water quality with relation to productivity in this region are meager. Hence, the present study was carried out with various statistical analyses to understand the water quality and productivity to assess the ecosystem in the region. The multivariate statistical techniques are suitable tools for the reduction of multi-constituent chemical and physical observed data to a small number of inherent factors retaining substantial meaningful information for interpretation (Massart et al., 1988). The significant phytoplankton pigment [Chlorophyll-*a* (chl-*a*)] has been utilized broadly as an intermediary for biomass and a gauge of maritime essential profitability (Behrenfeld et al., 2005; Westberry et al., 2008). The spatial and temporal distribution of chl-*a* depends in a general sense upon physical procedures along with the availability of light, nutrients, and oxygen. In the tropics, shallow coastal water is commonly well mixed and oxygen rich and phytoplankton production is not light limited. The principal source of nutrients in coastal waters is from river discharge; consequently, the influx of river water associated with rainfall plays an important role in tropical coastal primary productivity often promoting phytoplankton bloom (Mishra et al., 2009; Sarma et al., 2009; Baliarsingh et al., 2015). The multivariate statistical techniques, for example, cluster analysis (CA) and factor analysis (FA), have been broadly used as unbiased techniques in the examination of water quality datasets for extracting meaningful information (Vega et al., 1998; Singh et al., 2004). Thus, the present study of seasonal variability of phytoplankton biomass, the environmental variables, and river discharge containing anthropogenic influence facilitates us to understand the dynamics of the estuarine ecosystem.

MATERIALS AND METHODS

Study Area

The present study was carried out off Rushikulya Estuary at five selected time series stations, southern coast of Odisha (**Figure 1**). Rushikulya is a perennial river, one of the major rivers that drains into the BoB. The river flows from the Daringbadi hill station in Kandhamal district flows through the Ganjam district for a distance of 165 km with a total catchment area of 7,700 km^2. As the catchment is rich in mineral wealth, there are about 3,360 numbers of small-scale industries of different categories, mainly food and allied, forest and wood-based, rubber, plastic products, glass, and ceramics. Domestic sewage also contributes a significant component of pollutant reaching the river. These industries and untreated sewage have directly or indirectly affected the river water quality. The estuary accommodates and accounts for mass nesting of Olive Ridley sea turtles and known as one of the world's major rookeries (*arribada*) in India (Pandav et al., 1994). The study area forms a complex ecosystem with highly variable primary production results mainly due to the concentration of nutrients, especially silicate and nitrate (Gouda and Panigrahy, 1992). The ecosystem received a high quantity of dissolved chemical inputs from several sources as runoff through the course of river and sea (Mohapatra and Padhy,

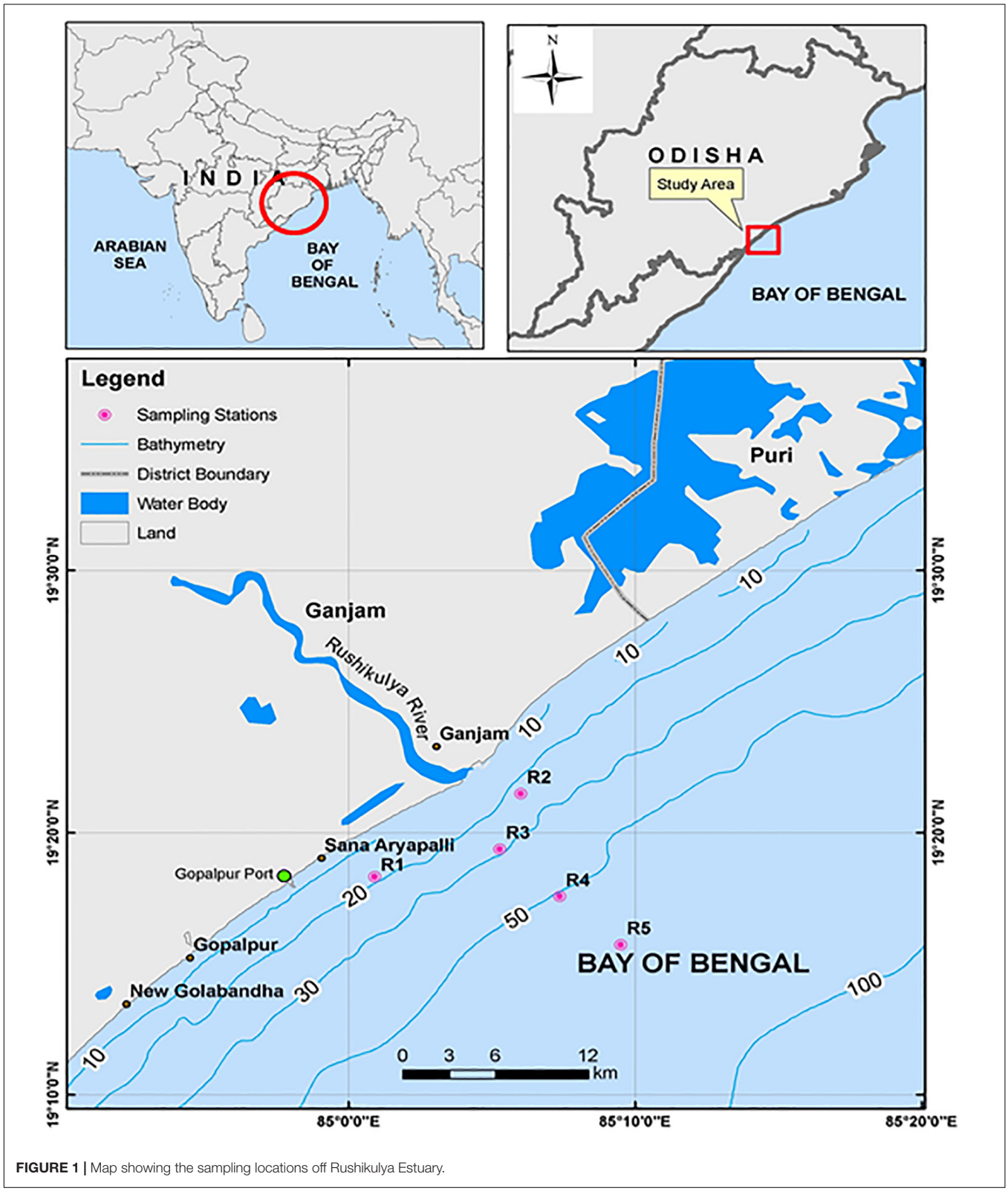

FIGURE 1 | Map showing the sampling locations off Rushikulya Estuary.

2001). The increasing activity of Gopalpur as well as weather port, fishing, coastal aquaculture, effluent discharge by heavy mineral exploration by Indian Rare Earth, Ltd., and growing urbanization has an influence on the coastal water quality off Rushikulya Estuary (Bramha et al., 2011). The circulation pattern of the study area is governed by the impacts of seasonal East India

Coastal Current (EICC), surface current driven by monsoon winds, cyclonic motion (Shetye et al., 1991). The tides along the coast of India are predominantly semi-diurnal but mixed. The important tidal constituents are M_2 (12.42 h), S_2 (with the period of 12.00 h), and K_1 (23.93 h). Tidal amplitudes along the coast of India increases from south to north (Pradhan et al., 2018). As the variation of flow, water quality and estuarine dynamics is apparent on seasonality induced by the Indian summer monsoon, Rushikulya Estuary is considered the monsoonal estuary.

Sampling and Analytical Methods

Physicochemical Parameters

Field surveys were carried out from March 2011 to February 2013 on boarding by a fishing trawler. The water samples were collected using the Niskin water sampler (5 l) from five selected time series stations at different depths of stations R1 (0, 5, and 10 m), R2 (0, 5, 10, and 15 m), R3 (0, 5, 10, 15, and 20 m), R4 and R5 (0, 5, 10, 15, 20, 25, and 30 m) along the coastal waters (**Figure 1**). The sampling stations were fixed according to bathymetry off Rushikulya Estuary. Though the samples were collected monthly, the datasets are taken for interpretation on a seasonal basis, i.e., pre-monsoon (March–May), monsoon (June–September), and post-monsoon (October–November; IMD). The *in situ* measurement of pH and water temperature (WT) used EUTECH pH meter (accuracy ± 0.01) and mercury-filled centigrade thermometer, respectively. Dissolved oxygen (DO) was fixed immediately using Winkler's A and B solutions. DO was measured by adopting Winkler's titration method (Grasshoff et al., 1999). For the analysis of nutrients, water samples were collected in clean polyethylene bottles, kept immediately in an ice box, and transported to the laboratory. The collected water samples were filtered by Millipore filtering system and analyzed for parameters such as nitrite (NO_2-N), nitrate (NO_3-N), ammonium (NH_4-N), inorganic phosphate (PO_4-P), silicate (SiO_4-Si), and total suspended matter (TSM). The analytical precision of each nutrient parameter (nitrate + nitrite ± 0.02 μmol/l, ammonium ± 0.02 μmol/l, phosphate ± 0.01 μmol/l, and silicate ± 0.02 μmol/l) was adopted by following standard protocols (Grasshoff et al., 1999). Each analysis was done in duplicate, and the mean value was taken. Millipore cellulose nitrate membrane, 47 mm diameter filter (porosity 0.45 μm) was used for gravimetric determination of TSM. Salinity was measured following Knudsen's argentometric titration method.

Phytopigment (Chlorophyll-*a*)

One liter of water sample was filtered through Whatman GF/F, 47-mm-diameter filter (porosity 0.7 μm) for the determination of chl-*a*. After filtration, the filter papers were stored securely at -4°C in freezing condition. Prior to spectrophotometric measurements, the filtrates were submerged in an individual centrifuge tube with 10 ml of 90% acetone and kept in a freezing condition for 24 h to facilitate complete extraction of pigments. The extracts were shaken vigorously in the dark and centrifuged at 4,000 rpm for about 10 min. The optical density of the supernatant solution was measured using a UV-visible double beam spectrophotometer [JASCO (V-650)] at 750, 665, 645, 630 NM with calibration of standard chl-*a* pigment (Sigma-Aldrich; C6144-1MG). Concentrations of chl-*a* were estimated following Strickland and Parsons (1972).

Data Treatment and Multivariate Statistical Method

In order to recognize the patterns that are inherent in water quality parameters as a whole, we considered the 11 parameters *viz.* WT, pH, salinity, DO, TSM, nutrients (NO_2-N, NO_3-N, NH_4-N, PO_4-P, and SiO_4-Si) and chl-*a* of five selected time series stations as a multivariate dataset. At the outset, we normalized the dataset as they were from different measurement scales. For each measured parameter, the mean is set at 0 and standard deviation at 1. Each value scaled in the range between −2 and + 2. This normalized the range of values for each parameter and assigned them equal values in the multivariate analysis (Clarke and Gorley, 2006). Equivalent matrix for these normalized values was evaluated using euclidean distance (difference between the clusters of parameters as a distance in multivariate space). The greater the euclidean distance, the lower the similarity between the clusters containing the water quality parameters. Differences in euclidean distances were applied to hierarchical CA, non-metric multidimensional scaling (nm-MDS). CA was applied to the water quality datasets with a view to group the parameter wise spread over the stretch and in the resulted dendrogram. FA was performed for three seasonal datasets. The variance/covariance and factor loadings of the variables with eigenvalues were computed. Besides considerable data reduction, entire dataset variability is described through few varifactors/principal components (VFs/PCs) without losing much information. Further, grouping of the studied variables according to their common features by VFs helps in data interpretation (Vega et al., 1998; Singh et al., 2004). Statistical software (Statistical Package for the Social Sciences-SPSS 17) was used for computation of correlation matrix and FA (Plymouth Routines in Multivariate Ecological Research-PRIMER-6), and CA was used in the present study. The varimax rotated factor loadings were calculated using eigenvalues greater than 1 and sorted by the results having values greater than 0.4 based on the significant influence of the geochemical processes (Rath et al., 2000). For the meaningful graphical representation of seasonal and vertical variation of physicochemical parameters and chl-*a*, Ocean Data View is used.

RESULTS AND DISCUSSION

The descriptive statistics of physicochemical parameters and chl-*a* are presented in **Supplementary Table S1**. The water temperature fluctuated between 25.25°C and 28.9°C throughout the study period. Spatial plots show that the highest temperature (28.9°C) was recorded at station R5 surface water during pre-monsoon season, and the lowest temperature (25.25°C) was recorded at 10 m depth of station R1 during post-monsoon season as shown in **Figures 2i,iii**. The water temperature hardly followed any particular trend of variability. Pearson's correlation coefficient indicates that the water temperature

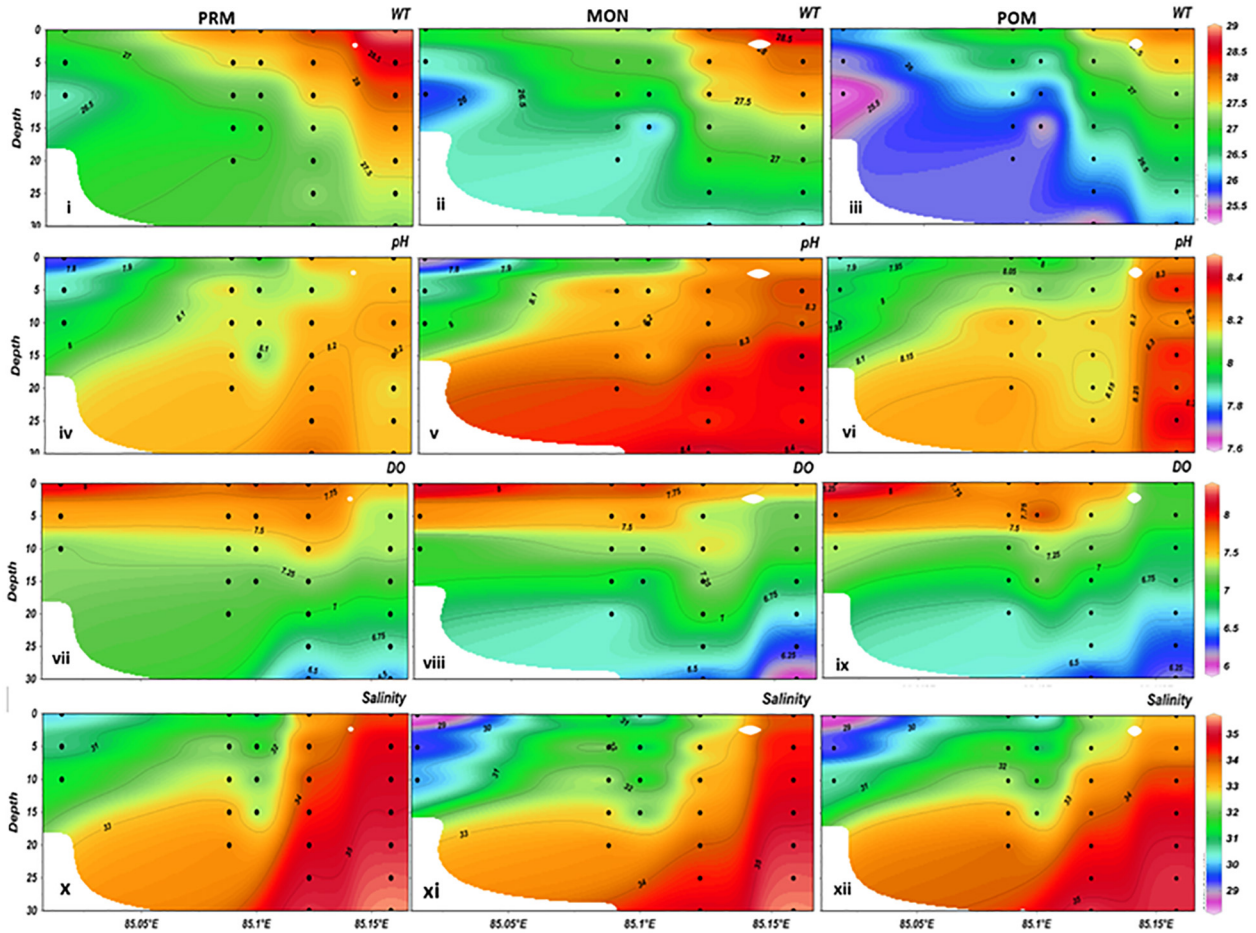

FIGURE 2 | (i–xii)/Vertical distribution of water temperature (WT), pH, dissolved oxygen (DO), and salinity off Rushikulya Estuary (Black dots represents stations in sequence R1 > R2 > R3 > R4 > R5; PRM, pre-monsoon; MON, monsoon, POM, post-monsoon).

exhibited a negative relation with nutrients throughout all seasons (**Supplementary Table S2**). The pH varied between 7.68 and 8.43 (**Supplementary Table S1**). The highest pH at 30 m water depth of station R5 was noticed during monsoon season, and the lowest value at the surface was observed at station R1 during the same season (**Figure 2v**). Observed pH values showed an increasing trend toward the bottom and offshore region of the study area. The highest pH value 8.43 was noticed during monsoon season at station R4 from 30 m depth, indicating an alkaline environment which is consistent with the value for tropical ocean water and values obtained from similar environmental offshore studies in Nigeria (STAR, 2003; Conoco, 2004). Such variations were also reported from many for Indian coastal waters (Chandran and Ramamurthy, 1984; Upadhyay, 1988). The DO content ranged between 5.96 and 8.3 mg/l during the study period (**Supplementary Table S1**). The maximum DO at surface was recorded at station R1 during post-monsoon season, and a minimum was noticed at 30 m depth of station R5 (**Figure 2ix**). DO values followed a vertically decreasing trend toward bottom and offshore stations. The high DO level in the surface water could be due to photosynthetic release by phytoplankton and air-sea interaction (Carignan et al., 2000). Correlation analysis revealed that the DO exhibited a positive correlation with chl-*a* and nutrients during all the seasons. The inverse relationship between DO and temperature is a natural process as warm water easily saturated with oxygen and, thus, can hold less DO. The negative correlation of DO with water temperature (**Supplementary Table S2**) can be addressed as solubility of oxygen in water diminishes with increasing temperature. The vertical profile of salinity along the five stations from various depths demonstrated wide variation of mean salinity ranging between 28.24 and 35.63 (**Supplementary Table S1**). The highest value of salinity was noticed at station R5 from 30 m depth during pre-monsoon, while the lowest was observed at station R1 from surface water during monsoon (**Figures 2x,xi**). Salinity followed an increasing trend toward bottom and offshore during all seasons. The most minimal salinity was recorded during monsoon season which may be ascribed because of precipitation brought by southwest monsoonal rains and a huge amount of fresh water inundation into the sea by means of estuary and terrestrial

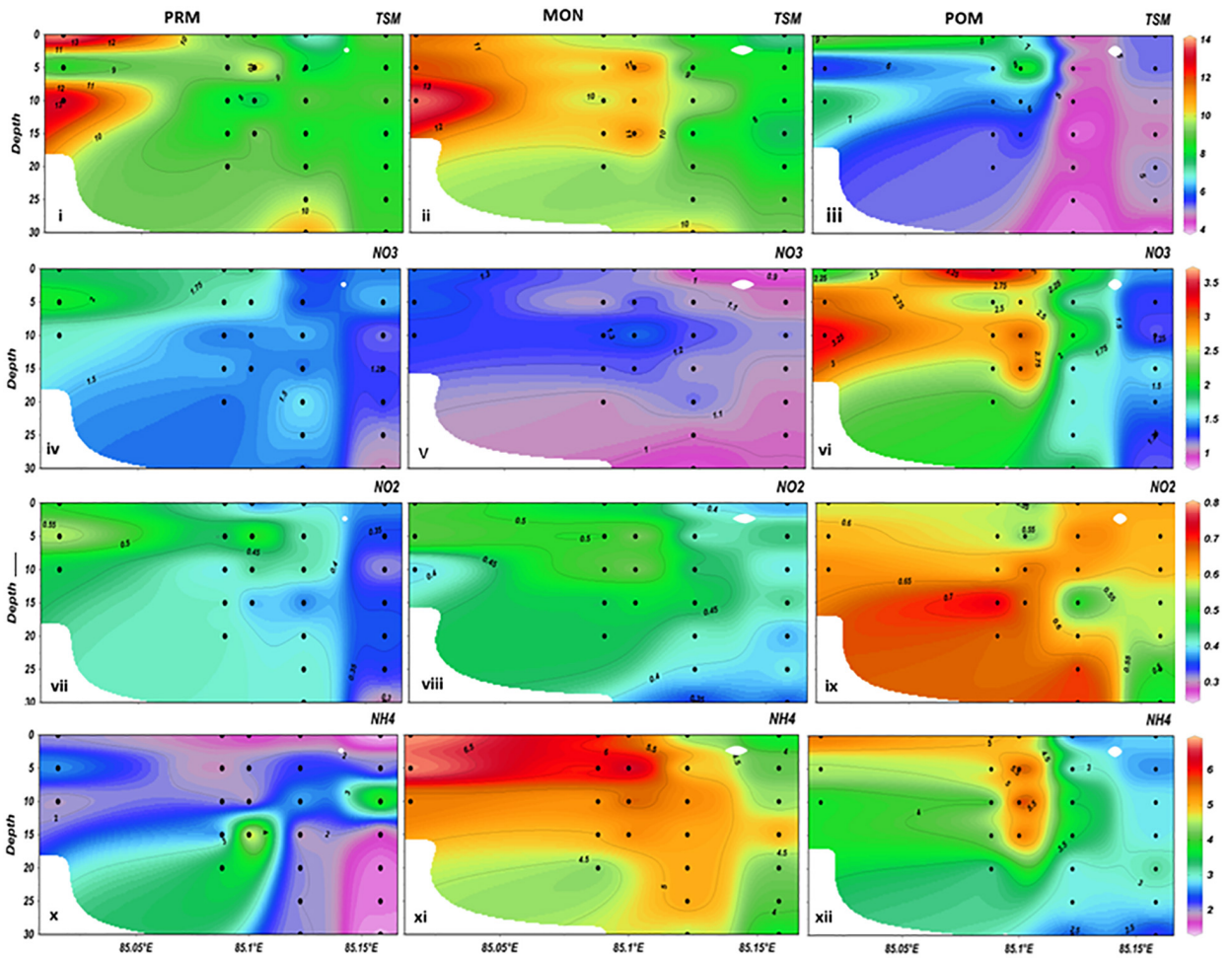

FIGURE 3 | (i–xii)/Vertical distribution pf total suspended matter (TSM), NO_3, NO_2, and NH_4 off Rushikulya Estuary (Black dots represents stations in sequence R1 > R2 > R3 > R4 > R5; PRM, pre-monsoon; MON, monsoon; POM, post-monsoon).

runoff. Salinity exhibited a negative correlation with nutrients (**Supplementary Table S2**). TSM ranged from 3.92 to 14.03 mg/l (**Supplementary Table S1**). The highest TSM was recorded during pre-monsoon at station R1 from 10 m depth and lowest at R3 from 20 m depth during the post-monsoon as shown in **Figures 3i,iii**. Relatively higher concentrations of TSM were observed in coastal stations which can be attributed to the turbulent waters and hence resuspension of bottom sediments. A pocket of increased TSM was noticed in subsurface during pre-monsoon, whereas this feature was persistent in surface as well as in subsurface during monsoon. The highest TSM was recorded during pre-monsoon season at station R1 (14.03 mg/l) which might be due to the addition of TSM from sediment resuspension and eroded sediments from beaches. This beach is highly eroding beach during pre-monsoon (Pradhan et al., 2018). Nearshore stations (R1 and R2) shows higher TSM as due to its shallowness and mostly laden with the riverine waters which carries a huge amount of sediments. It clearly shows the signature of resuspension of sediments which can be attributed to the tidal mixing and river influx observed during pre-monsoon and monsoon, respectively.

Nutrients and Phytopigment

The concentration of NO_3-N ranged from 0.89 to 3.62 μmol/l (**Supplementary Table S1**). The highest value of NO_3-N was observed at station R2 from 15 m depth in post-monsoon season, and lowest value was noticed in monsoon season at station R4 from 30 m depth as depicted in **Figures 3v,vi**. Lower values of NO_3-N were noticed in the vertical profile of all the stations during pre-monsoon and monsoon, whereas in post-monsoon, a subsurface flushing of NO_3-N was observed up to station R3. Natural sources of nitrate in surface water include igneous rock, land drains, and plant and animal debris. The anthropogenic contribution may be enhanced by municipal and industrial wastewater during post-monsoon season. The NO_2-N concentration in the study area showed well-marked spatiotemporal variations. Average NO_2-N varied from 0.28 to 0.77 μmol/l (**Supplementary Table S1**). The highest concentration of NO_2-N was observed at station R4 from 25 m

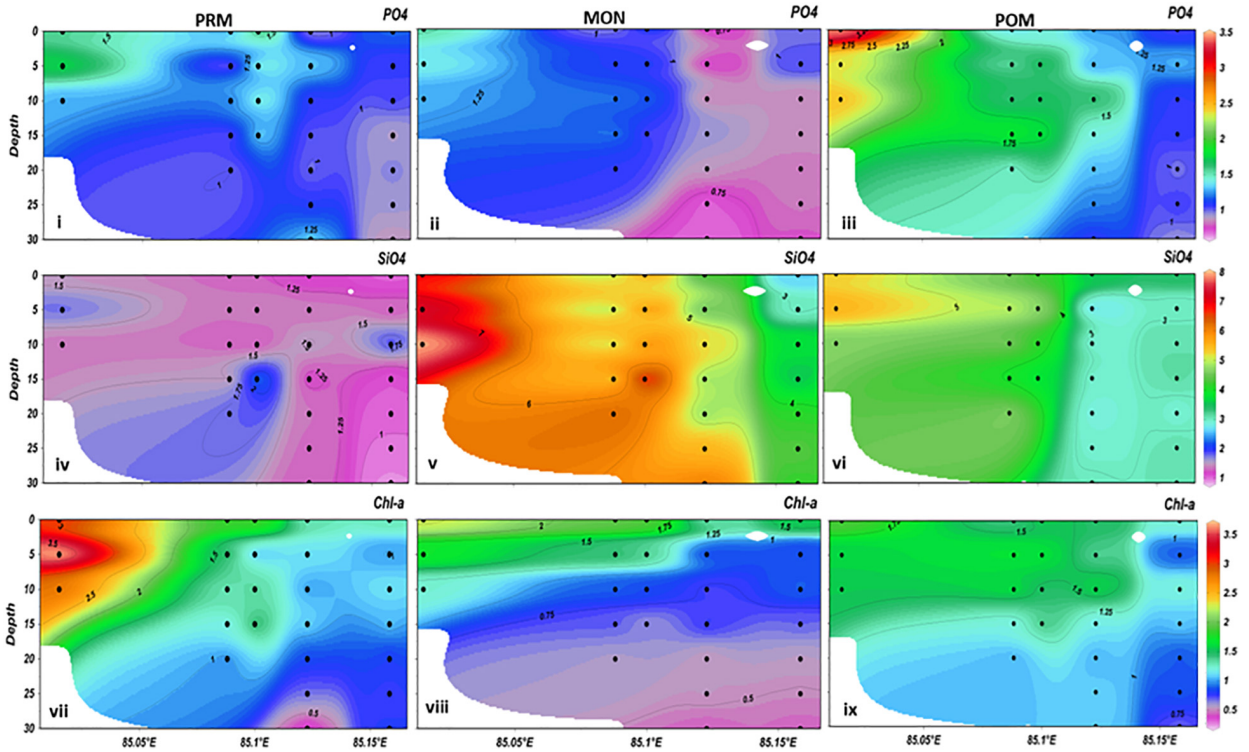

FIGURE 4 | (i–ix)/Vertical distribution pf PO_4, SiO_4, and Chl-*a* off Rushikulya Estuary (Black dots represents stations in sequence R1 > R2 > R3 > R4 > R5; PRM, pre-monsoon; MON, monsoon; POM, post-monsoon).

depth during post-monsoon season and lowest concentration at station R5 from surface water during pre-monsoon season (**Figures 3vii,ix**). A horizontal increasing trend of NO_2-N was noticed during pre-monsoon and monsoon, whereas in post-monsoon, higher values were noticed in the subsurface layer of all the stations. The highest concentration of NO_2-N was observed during post-monsoon and lowest concentration during pre-monsoon season. It is difficult to ascertain its causes, but it might be due to the addition of nitrite from exogenous sources or denitrification processes occurring at the sediment water interface (Sharp et al., 1982; Bianchi et al., 2004). Higher concentrations of subsurface nitrite and nitrate values during post-monsoon season were observed which might be due to their release from bottom sediments and land drainage. The similar observation was also reported by Shirodkar et al. (2009). During the study period, NH_4-N varied from 1.36 to 6.81 μmol/l (**Supplementary Table S1**). The peak value was noticed at station R1 from surface water during monsoon season and lowest was recorded at station R5 from 30 m depth during pre-monsoon season (**Figures 3x,xi**). The peak value of NH_4-N was recorded during monsoon season at station R1 from surface water. A similar observation was also reported off Rushikulya Estuary by Baliarsing et al. (2013). No natural sources have been noticed to increase the concentration of ammonia in the coastal waters. All the available information indicates anthropogenic releases and breaking down the organic matter as a source of ammonia to the coastal waters (Panigrahi et al., 2007; Smith et al., 2007). The phosphate concentration varied from 0.66 to 3.45 μmol/l (**Supplementary Table S1**). The maximum concentration of PO_4-P was noticed at the surface water of R1 during post-monsoon season and lowest concentration was recorded at station R5 from 30 m depth during monsoon season as shown in **Figures 4ii,iii**. The highest concentration of PO_4-P was noticed during post-monsoon season at station R1 from surface sample (0 m depth). The present results suggest that the main features of PO_4-P distribution with high values during the post-monsoon season were possibly caused by the intrusion of sewage and/or industrial effluents. The SiO_4-Si concentrations ranged from 0.89 to 7.97 μmol/l (**Supplementary Table S1**). The silicate concentration was found to be higher during monsoon season at station R2 from 5 m depth and the lowest value was found at station R5 from surface water during pre-monsoon season (**Figures 4iv,v**). The SiO_4-Si concentration was found to be higher during monsoon season. Comparatively lower concentrations of silicate in the offshore stations than nearshore stations might be related to high biological productivity and a biological removal of dissolved silicate by absorption onto suspended sediments (De Souza et al., 1981).

The vertical distribution of chl-*a* showed high concentrations in the surface and subsurface layers of all the stations and low concentrations in the bottom waters. There was no spatial uniformity in the seasonal cycle of chl-*a* across the study area. The chl-*a* concentration was recorded from 0.25 to 3.72 mg/m^3 during the study period (**Supplementary Table S1**). The highest

chl-*a* concentration was observed at station R1 from 5 m depth during pre-monsoon season and the lowest value was recorded at station R4 from 30 m depth. Both horizontal and vertical distributions of chl-*a* are depicted in **Figure 4vii**. During the study period, the highest chl-*a* concentration was observed during pre-monsoon season from subsurface water (5 m depth) at station R1. The results clearly featured the frequency of high chl-*a* due to the period of spring efficiency in the coastal waters off Rushikulya Estuary. The pre-monsoon convection (overturning) process which brings nutrient-rich subsurface waters to the photic zone found responsible for this enhanced biological production. The relationship considers that

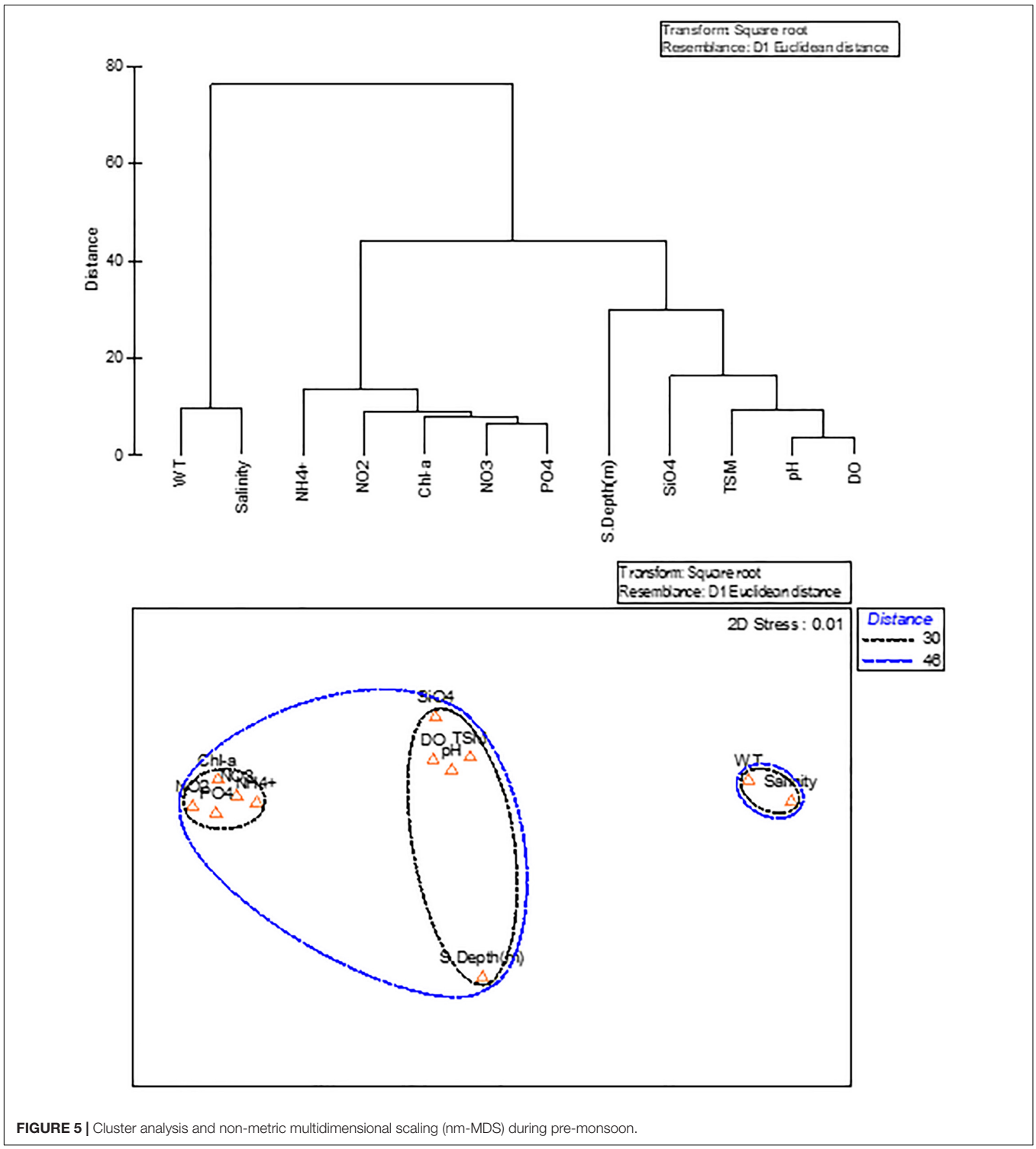

FIGURE 5 | Cluster analysis and non-metric multidimensional scaling (nm-MDS) during pre-monsoon.

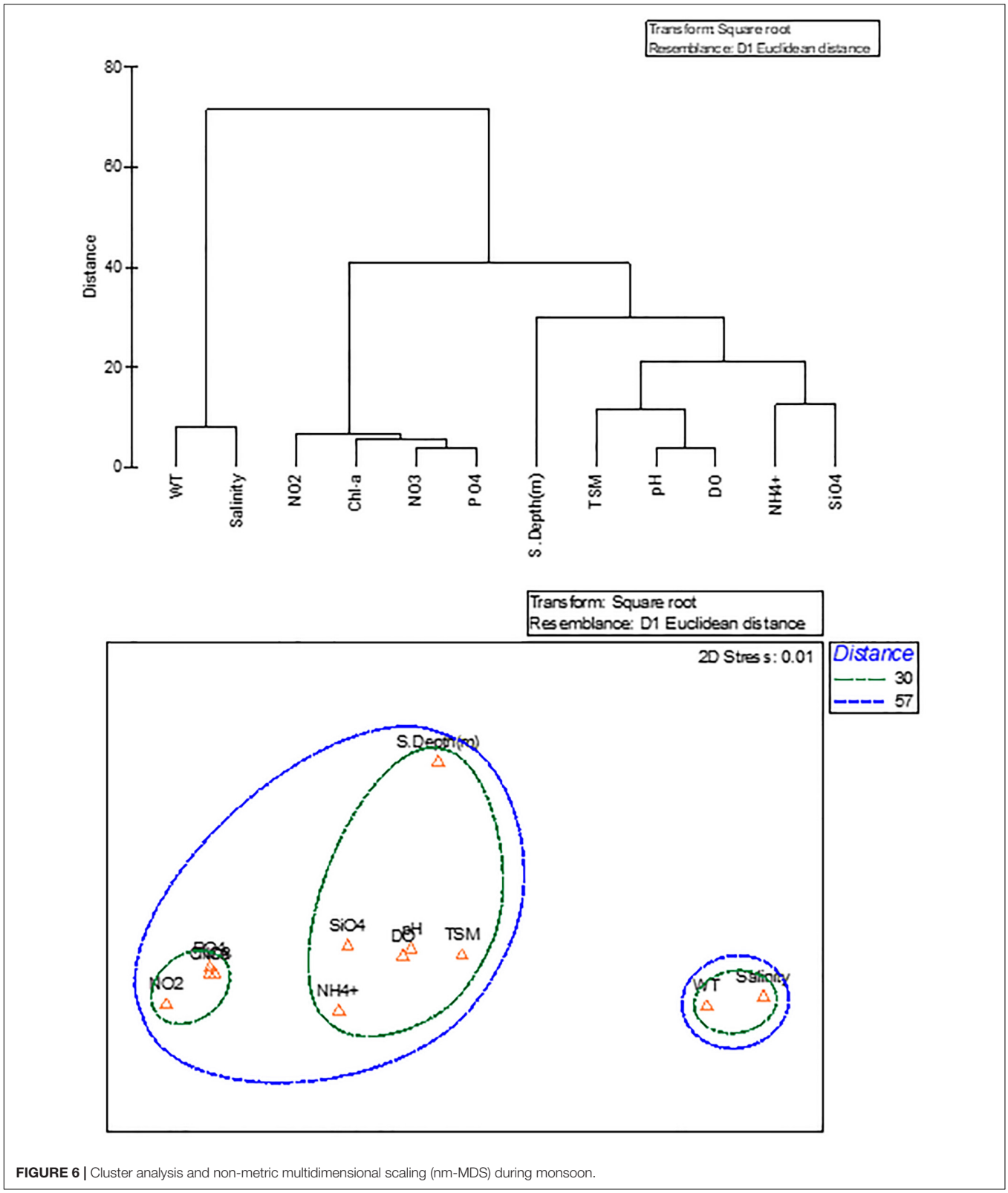

FIGURE 6 | Cluster analysis and non-metric multidimensional scaling (nm-MDS) during monsoon.

the chl-*a* exhibited a strong positive correlation with nutrients, which are shown in **Supplementary Table S2**. The seasonal transition of monsoon circulation was also affected by the wind direction and SST in Odisha coast. During the transition period from northeast to southwest monsoon, chl-*a* distribution was observed high in nearshore station off Rushikulya Estuary.

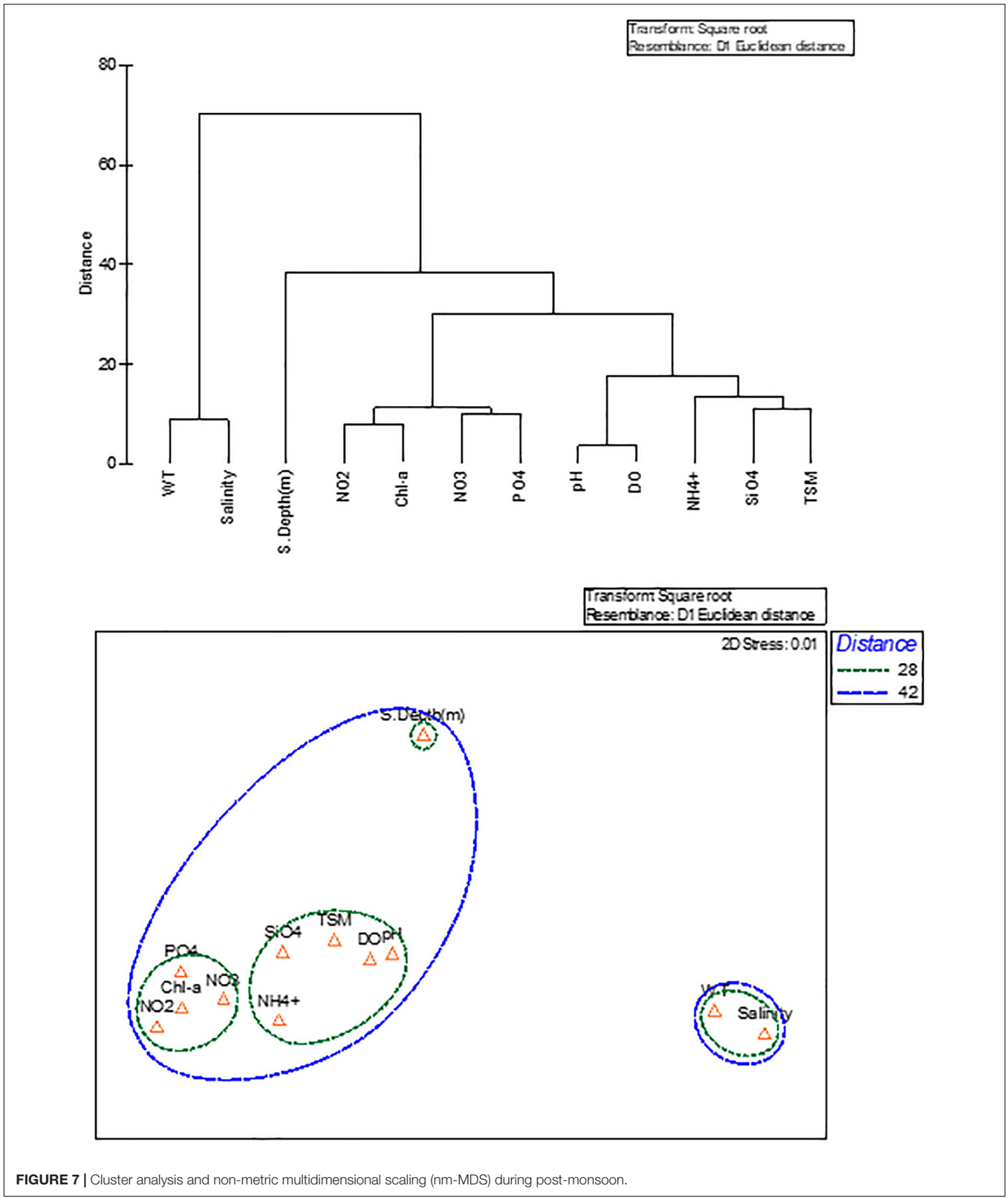

FIGURE 7 | Cluster analysis and non-metric multidimensional scaling (nm-MDS) during post-monsoon.

A similar observation was also reported in Pahang coastal waters (Sumadri et al., 2012).

Statistical Analyses

Factor Analysis

The three steps of FA, such as (i) generation of correlation matrix, (ii) extraction of underlying factors, and (iii) rotation of factors to extract maximum possible information from the datasets as explained by Gupta et al. (2005), were implemented for the datasets. The sorted rotated FA results along with eigenvalues and the percentage of total variance are given in **Supplementary Table S3**. For interpretation of associateships between different environmental variables, the factor loadings are termed as "strong," "moderate," and "weak" corresponding to absolute loading values of >0.75, 0.75–0.50, and 0.50–0.40, respectively (Liu et al., 2003). Factor loadings are correlations between the original variables and each factor. During pre-monsoon, three factors explained 67.27% of the total variance. F-1 explained about 35.67% of the total variance, which was strong loaded with DO and chl-*a* and moderate loaded with NO_2 and NO_3 and weak loaded with PO_4, whereas negative loaded with pH and salinity. F-2 contributed 19.85% of the total variance, which was strong loaded with TSM and negative loaded with water temperature. F-3 explained about 11.76% of the total variance found to be strongly associated with NH_4 and PO_4 moderate negative loaded with SiO_4 (**Supplementary Table S3**). The higher DO and chl-*a* values at the nearshore stations were due to the incursion of less saline riverine water when contrasted with high saline seaward waters. Moreover, increasing chl-*a* and decreasing salinity were also contributed by the riverine source. However, the moderate and weak relation of chl-*a* and DO suggests that the chl-*a* was not much influenced by other loadings but remained independent under the existing environmental conditions in this coastal environment. So, these factors can, therefore, be termed as productivity factors. In monsoon, three factors explained 73.95% of the total variance. F-1 contributed 37.55% of the total variance, which was strong loaded with TSM and SiO_4 and moderate loaded with NH_4 while negative and strong loaded with WT. F-2 explained about 24.82% of the total variance, which was strong loaded with PO_4 and NO_3 and moderate with chl-*a* and NO_2. F-3 accounted for 11.58% of the total variance. It was strong loaded with DO and weak loaded with WT and chl-*a* and negative loaded with pH and salinity (**Supplementary Table S3**). Whereas in case of post-monsoon, four factors explained about 71.60% of the total variance. F-1 contributed 30.20% of the total variance, which was strong loaded with DO and moderate with TSM while negative loaded with salinity and pH. F-2 accounted for about 18.75% of the total variance, which was strong loaded with NO_2 and moderate with NO_3 and NH_4. F-3 explained 12.25% of the total variance, which was strong loaded with WT and PO_4. F-4 explained about 10.40% of the total variance, which was strong loaded with chl-*a* and moderate loaded with SiO_4 (**Supplementary Table S3**). Results show that the nearshore water contains high nutrient values as compared to the offshore waters. These above factors signify that negative loading of pH with positive loading of nutrients can be termed as the terrigenous factors.

Cluster Analysis

The relationships among the environmental variables were obtained through cluster analyses using Ward's method (linkage between groups). In this method, an analysis of variance approach is used to evaluate the euclidean distance between the clusters as similarity measure and synthesized in dendrograms and nm-MDS (**Figures 5–7**). The dendrogram indicated that the

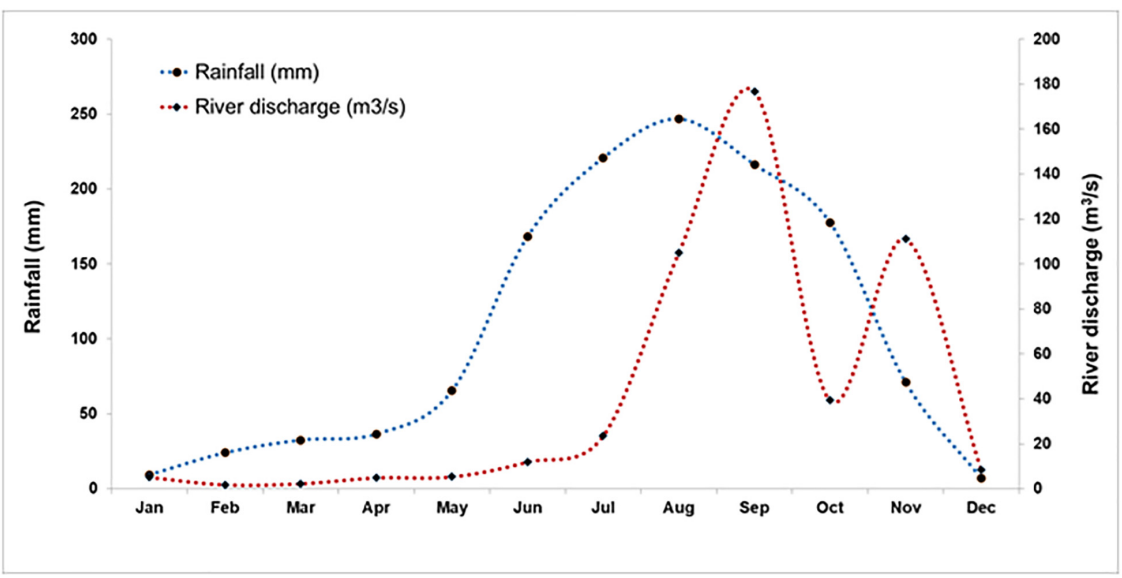

FIGURE 8 | Monthly average of rainfall and river discharge at Ganjam Rain Gauge station during 2011–2013 (Source: Department of Water Resources, Government of Odisha).

distance between the parameters was less significantly correlated. The physicochemical and biological parameters WT, pH, DO, salinity, TSM, NO_2-N, NO_3-N, NH_4-N, PO_4-P, SiO_4-Si, and chl-*a* were used as variables. During pre-monsoon, three major clusters were observed. In the first, WT and salinity were included, whereas NH_4-N, NO_2-N, chl-*a*, NO_3-N, and PO_4-P fall in the second group. In the third group, the DO, pH, TSM, SiO_4-Si, and depth were included. From the nm-MDS group, it was observed that the chl-*a* was the least influenced by WT and salinity. However, chl-*a* showed a very close proximity to NO_3, NH_4, NO_2, and PO_4. The intermediate group contains the parameters such as SiO_4, DO, TSM, and pH where depth remained constant (**Figure 5**). However, a moderate linkage was observed with SiO_4 and TSM to that of chl-*a*. It can be hypothesized that during pre-monsoon, the necessary nutrients for chl-*a* appeared as NO_3, NH_4, NO_2, and PO_4, whereas SiO_4 is an accessory nutrient. Depth remained homogeneous from the entire group, which is attributed as a non-linkage parameter having an insignificant contribution to the observation attained. During monsoon, there were three groups parallel out from CA. **Figure 5** shows that the chl-*a* was highly influenced by PO_4, NO_3, and NO_2. NH_4 was grouped in the second cluster, which was previously in close proximity to chl-*a* (**Figure 6**). It might be due to the ingress of fresh water because of riverine runoff and precipitation. Depth remained constant as per the previous condition. However, DO and pH were closely related, showing good saturation condition of DO in the study area. The TSM exhibited a distant relation with chl-*a*, which probably was due to the ingress of silt-borne fresh water from the nearby river discharge. During post-monsoon, the previous condition was maintained and no great variation was observed (**Figure 7**). In the tropical estuarine and coastal environment, the monsoon plays a major role in the variability of physicochemical parameters that can directly impact the dissemination of chl-*a* (Pednekar et al., 2012). As reflected from the rainfall and river discharge over the study area (**Figure 8**), the analysis of monthly average rainfall and river discharge over the study area shows that 80% of the annual rainfall is received during monsoon months *viz*. June–October, and the river discharge follows accordingly. Maximum river discharge is recorded during September (35%) followed by November (22%) and August (21%) (**Figure 8**). The major finding obtained from nm-MDS and CA is that a direct influence of nutrients rather than the physical parameters was a major cause of concern for chl-*a* distribution. Ammonia was linked with chl-*a* in pre-monsoon which has not maintained the same trend during monsoon and post-monsoon.

CONCLUSION

The present study established the ecological conditions of coastal waters off Rushikulya Estuary, BoB, from time series observations at five locations. The hydrography was noticed inconsistent, and significant spatiotemporal variability of nutrients in the water column was apparent. Nutrient-rich bottom water was found to act as a significant pool in reloading the water column under sediment resuspension. The dominant parameters affecting the water quality over different seasons is deciphered using factor analyses. This would help in understanding the contaminants which influence the water quality and assimilative capacity of the estuary, as the external loading of contaminants that reduces the assimilative capacity. The study concludes that the nutrients and TSM were of terrigenous origin. We noticed lower DO in the surface and water column during monsoon compared to the post-monsoon and pre-monsoon. The study indicates that water influx at the coastal waters with different physicochemical properties, nearshore and offshore of the 30 m isobath, due to different estuarine and terrestrial runoff strongly linked to the seasonal tropical monsoon. This possibly resulted in the variability of physicochemical parameters and regulated the chl-*a* (phytoplankton biomass) in the study region with respect to the monsoonal influence that supplies the nutrients and the biomass. However, the study further needs to be monitored for a longer period for supplementary data in the study region to understand the impact of monsoonal influence/river discharges, anthropogenic influence and its significant effect on the phytoplankton biomass, productivity, and ecosystem. In addition, the higher resolution *in situ* data would be a baseline information to validate models and satellite retrieval data in the extensive coastal water ecosystem.

DATA AVAILABILITY STATEMENT

All datasets generated for this study are included in the article/**Supplementary Material**.

AUTHOR CONTRIBUTIONS

SN, KS, AL, RM, UP, and PM conceived the study and conducted the data analyses. SN and KS conducted the sample collection. SN carried out the lab analyses. SN, RM, and UP drafted the manuscript. All authors revised and edited the manuscript.

ACKNOWLEDGMENTS

We would like to thank the vice-chancellor of Berhampur University for providing laboratory facilities and invaluable help and support for this study. We would also like to thank the Indian National Centre for Ocean Information Services, MoES, Government of India, for funding support during the study period. RM would like to thank the Director of NCPOR for encouraging to study the oceanographic parameters and biology extensively including the coastal waters and publications.

SUPPLEMENTARY MATERIAL

The Supplementary Material for this article can be found online at: https://www.frontiersin.org/articles/10.3389/fmars.2020.00648/full#supplementary-material

REFERENCES

Baliarsing, S. K., Srichandan, S., Naik, S., Sahu, K. C., Lotliker, A., and Kumar, T. S. (2013). Distribution of Hydro-biological Parameters in Coastal Waters off Rushikulya Estuary, East Coast of India: A Premonsoon Case Study. *Pakistan J. Biol. Sci.* 16, 779–787. doi: 10.3923/pjbs.2013.779.787

Baliarsingh, S. K., Lotliker, A. A., Sahu, K. C., and Sinivasa Kumar, T. (2015). Spatio-temporal distribution of chlorophyll-a in relation to physico-chemical parameters in coastal waters of the northwestern Bay of Bengal. *Environ. Monit. Assess.* 187:481. doi: 10.1007/s10661-015-4660-x

Barik, S. K., Muduli, P. R., Mohanty, B., Behera, A. T., Mallick, S., Das, A., et al. (2017). Spatio-temporal variability and the impact of Phailin on water quality of Chilika lagoon. *Cont. Shelf Res.* 136, 39–56. doi: 10.1016/j.csr.2017.01.019

Behrenfeld, M. J., Bose, E., Siegel, D. A., and Shea, D. M. (2005). Carbon based ocean productivity and phytoplankton physiology from space. *Glob. Biogeochem. Cy.* 19, 1–14. doi: 10.1029/2004GB002299

Bianchi, F., Ravagnan, E., Acri, F., Bernardi-Aubry, F., Boldrin, A., Camatti, E., et al. (2004). Variability and fluxes of hydrology, nutrients and particulate matter between the Venice Lagoon and the Adriatic Sea. Preliminary results (years 2001–2002). *J. Mar. Syst.* 51, 49–64. doi: 10.1016/j.jmarsys.2004.05.007

Bramha, S., Panda, U., Rath, P., Mohanty, P., and Satpathy, K. K. (2011). Anthropological influence in coastal water and and its impact on olive ridley turtle: A case study at Rushikulya mass nesting site. *J. Ecol. Nat. Environ.* 3, 268–272.

Carignan, R., Planas, D., and Vis, C. (2000). Planktonic production and respiration in oligotrophic Shield lakes. *Limnol. Oceanogr.* 45, 189–199. doi: 10.4319/lo.2000.45.1.0189

Chandran, R., and Ramamurthy, K. (1984). Hydrobiological studies in the gradient zone of Vellar estuary-I: physico-chemical parameters. *Mahasagar. Bull.* 17, 69–77.

Clarke, K. R., and Gorley, R. N. (2006). *PRIMER v6: User Manual/Tutorial (Plymouth Routines in Multivariate Ecological Research)*. Albany: PRIMER-E. Plymouth.

Conoco (2004). *Oil prospecting lease 248:Environmental Baseline Survey, Report No. CO/EIA*/011/04. Texas: Conoco.

De Souza, S. N. R., Gupta, S., Sanzgiri, S., and Rajgopal, M. D. (1981). Studies on nutrients of Mandovi and Zuari River systems. *Indian J.Mar. Sci.* 10, 314–321.

Emmel, F. J., and Curray, J. R. (1983). The Bengal Submarine Fan, Northeastern Indian ocean. *Geo Mar. Lett.* 3, 119–124. doi: 10.1007/bf02462456

Gouda, R., and Panigrahy, R. C. (1992). Seasonal distribution and behaviour of silicate in the Rushikulya estuary, east coast of India. *Indian J. Mar. Sci.* 24, 11–115.

Grasshoff, K., Ehrhardt, M., Kremling, K., and Anderson, L. G. (1999). *Methods of Seawater Analysis*. Wiley-VCH.

Gupta, A. K., Gupta, S. K., and Patil, R. S. (2005). Statistical analyses of coastal water quality for a port and harbour region in India. *Environ. Monit. Assess.* 102, 179–200. doi: 10.1007/s10661-005-6021-6027

India Metrological Department [IMD] (2006). *Ministry of Earth Sciences, Government of India, New Delhi, www.imd.gov.in*. New Delhi: IMD.

Laviolette, P. E. (1967). *Temperature, salinity and density of the worlds sea: Bay of Bengal and Andaman Sea*. Washington, DC: Naval Oceanographic Office.

Liu, C.-W., Lin, K.-H., and Kuo, Y.-M. (2003). Application of factor analysis in the assessment of groundwater quality in a blackfoot disease area in Taiwan. *Sci. Total Environ.* 313, 77–89. doi: 10.1016/s0048-9697(02)00683-686

Massart, D. L., Vandeginste, B. G. M., Deming, S. N., Michotte, Y., and Kaufman, L. (1988). Chemometrics: a textbook. D. L. Massart. B. G. M. Vandeginste, S. N. Deming, Y. Michotte, and L. Kaufman, Elsevier, Amsterdam, 1988. ISBN 0-444-42660-4. Price Dfl 175.00. *J. Chemom.* 2, 298–300. doi: 10.1002/cem.1180020409

Menon, N. N., Balchand, A. N., and Menon, N. R. (2000). Hydrobiology of the Cochin backwater system – A review. *Hydrobiologia* 430, 149–183. doi: 10.1023/a:1004033400255

Mishra, R. K., Shaw, B. P., Das, S. K., Rao, K. S., Choudhary, S. B., and Rao, K. H. (2003). Spatio-temporal variation of optically active substances in the coastal water off Orissa from Rushikulya to Dharma (east coast of India). *Indian J. Mar. Sci.* 32, 133–140.

Mishra, R. K., Shaw, B. P., Sahu, B. K., Mishra, S., and Senga, Y. (2009). Seasonal appearance of Chlorophyceae phytoplankton bloom by river discharge off Paradeep at Orissa Coast in the Bay of Bengal. *Environ. Monit. Assess.* 149, 261–273. doi: 10.1007/s10661-008-0200-2

Mohapatra, T. R., and Padhy, S. N. (2001). Seasonal fluctuations of physico-chemical parameters of Rushikulya estuary, Bay of Bengal. *Indian J. Environ. Ecoplann.* 5, 35–40.

Naik, S., Mishra, R. K., Mahapatro, D., and Panigrahy, R. C. (2014). Impact of water quality on phytoplankton community and biomass in Dhamara Eastury, East coast of India. *J. Environ. Biol.* 35, 229–235.

Newton, A., Icely, J. D., Falcao, M., Nobre, A., Nunes, J. P., Ferreira, J. G., et al. (2003). Evaluation of eutrophication in the Ria Formosa coastal lagoon, Portugal. *Cont. Shelf Res.* 23, 1945–1961. doi: 10.1016/j.csr.2003.06.008

Newton, A., and Mudge, S. (2005). Lagoon-sea exchanges, nutrient dynamics and water quality management of the Ria Formosa (Portugal). *Estuar. Coast. Shelf Sci.* 62, 405–414. doi: 10.1016/j.ecss.2004.09.005

Pandav, B., Choudhury, B. C., and Kar, C. S. (1994).). Discovery of a new sea turtle rookery in Orissa, India. *Mar. Turt. Newsl.* 67, 15–16.

Panigrahi, S., Acharya, B. C., Panigrahy, R. C., Nayak, B. K., Banarjee, K., and Sarkar, S. K. (2007). Anthropogenic impact on water quality of Chilika lagoon RAMSAR site: A statistical approach. *Wetl. Ecol. Manag.* 15, 113–126. doi: 10.1007/s11273-006-9017-3

Pednekar, S. M., Prabhu Matondkar, S. G., and Kerkar, V. (2012). Spatiotemporal distribution of harmful algal flora in the tropical estuarine complex of Goa, India. *Sci. World J.* 2012:596276. doi: 10.1100/2012/596276

Pradhan, U. K., Mishra, P., Mohanty, P. K., Panda, U. S., and Murthy, M. V. R. (2018). "Nearshore hydrodynamics near an open coast harbour at gopalpur, central east coast of India," in *Lecture Notes in Civil Engineering*, eds M. di Prisco, S.-H. Chen, I. Vayas, S. K. Shukla, A. Sharma, N. Kumar, et al. (Singapore: Springer), 219–237. doi: 10.1007/978-981-13-3134-3_17

Rath, P., Bhatta, D., Sahoo, B. N., and Panda, U. C. (2000). Multivariate Statistical Approach to Study Physico-Chemical Characteristics in Nandira - Brahmani River, Angul-Talcher Belt, Orissa. *Pollut. Res.* 19, 701–710.

Sarma, V. V. S. S., Gupta, S. N. M., Babu, P. V. R., Acharya, T., Harikrishnachari, N., Vishnuvardhan, K., et al. (2009). Influence of river discharge on plankton metabolic rates in the tropical monsoon driven Godavari estuary. India. *Estuar. Coast. Shelf Sci.* 85, 515–524. doi: 10.1016/j.ecss.2009.09.003

Sharp, J. H., Culberson, C. H., and Church, T. M. (1982). The chemistry of the Delaware estuary. General considerations1. *Limnol. Oceanogr.* 27, 1015–1028. doi: 10.4319/lo.1982.27.6.1015

Shetye, S. R., Shenoi, S. S. C., Gouveia, A. D., Michael, G. S., Sundar, D., and Nampoothiri, G. (1991). Wind-driven coastal upwelling along the western boundary of the Bay of Bengal during the southwest monsoon. *Cont. Shelf Res.* 11, 1397–1408. doi: 10.1016/0278-4343(91)90042-90045

Shirodkar, P. V., Mesquita, A., Pradhan, U. K., Verlekar, X. N., Babu, M. T., and Vethamony, P. (2009). Factors controlling physico-chemical characteristics in the coastal waters off Mangalore—A multivariate approach. *Environ. Res.* 109, 245–257. doi: 10.1016/j.envres.2008.11.011

Singh, K. P., Malik, A., Mohan, D., and Sinha, S. (2004). Multivariate statistical techniques for the evaluation of spatial and temporal variations in water quality of Gomti River (India)—a case study. *Water Res.* 38, 3980–3992. doi: 10.1016/j.watres.2004.06.011

Smith, A. M., Keene, W. C., Maben, J. R., Pszenny, A. A. P., Fischer, E., and Stohl, A. (2007). Ammonia sources, transport, transformation, and deposition incoastal New England during summer. *J. Geophys. Res.* 112, D10S08. doi: 10.1029/2006JD007574

Srinivasan, V., Gorelick, S. M., and Goulder, L. (2010). Factors determining informal tanker water markets in Chennai. *India. Water Int.* 35, 254–269. doi: 10.1080/02508060.2010.487931

STAR (2003). *Environmental Baseline survey of Agbami Field in OPL 216, Final Report. No. S0307C*. Nigeria: Nigerian Agip Oil Company.

Strickland, J. D. H., and Parsons, T. R. (1972). A practical handbook of seawater analysis, Bulletin. *Fish. Res. Board Canada* 167:293.

Sumadri, M., Lihan, T., and Mustapha, M. (2012). *N, and of Chlorophyll-a Distribution off Pahang Coastal Waters Using Satellite Images*. Putrajaya: Malaysia Geospatial Melaka.

Upadhyay, S. (1988). Physico-chemical characteristics of the Mahanadi estuarine eco-system. East coast of India. *Indian J. Mar. Sci.* 17, 19–23.

Vega, M., Pardo, R., Barrado, E., and Debán, L. (1998). Assessment of seasonal and polluting effects on the quality of river water by exploratory data analysis. *Water Res.* 32, 3581–3592. doi: 10.1016/S0043-1354(98)00138-9

Welsh, B. L., and Eller, F. C. (1991). Mechanisms controlling summertime oxygen depletion in western Long Island Sound. *Estuaries* 14, 265–278. doi: 10.2307/1351661

Westberry, T., Behrenfeld, M. J., Siegel, E., and Boss, E. (2008). Carbon-based primary productivity modeling with vertically resolved photoacclimation. *Glob. Biogeochem. Cy.* 22:GB2024. doi: 10.1029/2007GB003078

Zhang, J. Z., Kelble, C. R., Fischer, C. J., and Moore, L. (2009). Hurricane Katrina-inducednutrient runoff from an agricultural area to coastal waters in Biscayne Bay. Florida. *Estuar. Coast. Shelf Sci.* 84, 209–218. doi: 10.1016/j.ecss.2009.06.026

Zhao, H., Tang, D. L., and Wang, D. X. (2009). Phytoplankton blooms near the Pearl River Estuary induced by Typhoon Nuri. *J. Geophys. Res.* 114:C12027. doi: 10.1029/2009JC005384

Conflict of Interest: The authors declare that the research was conducted in the absence of any commercial or financial relationships that could be construed as a potential conflict of interest.

Frontiers Media SA remains neutral with regard to jurisdictional claims in published maps and institutional affiliations.

Copyright © 2020 Naik, Mishra, Sahu, Lotliker, Panda and Mishra. This is an open-access article distributed under the terms of the Creative Commons Attribution License (CC BY). The use, distribution or reproduction in other forums is permitted, provided the original author(s) and the copyright owner(s) are credited and that the original publication in this journal is cited, in accordance with accepted academic practice. No use, distribution or reproduction is permitted which does not comply with these terms.

frontiers in Marine Science

ORIGINAL RESEARCH
published: 21 August 2020
doi: 10.3389/fmars.2020.00667

Drivers of Plankton Distribution Across Mesoscale Eddies at Submesoscale Range

Nauzet Hernández-Hernández[1], Javier Arístegui[1], María F. Montero[1], Esther Velasco-Senovilla[1], Federico Baltar[2], Ángeles Marrero-Díaz[3], Antonio Martínez-Marrero[1] and Ángel Rodríguez-Santana[3]*

[1] Instituto de Oceanografía y Cambio Global, IOCAG, Universidad de Las Palmas de Gran Canaria, Las Palmas, Spain, [2] Department of Limnology and Bio-Oceanography, University of Vienna, Vienna, Austria, [3] Departamento de Física, Universidad de Las Palmas de Gran Canaria, Las Palmas, Spain

Cyclonic and anticyclonic eddies are common mesoscale features in the flow past the Canary Islands throughout the year. While drifting southward, eddy pairs interact among them but also with upwelling filaments and eddies generated at the coastal jet of the nearby African upwelling system. These interactions force the generation of frontal zones where ageostrophic secondary circulation (ASC) may occur. With the aim of contributing to understand how meso-submesoscale interactions modulate plankton distribution, we carried out an interdisciplinary cruise across a mesoscale eddy field. The sampled region was characterized by the presence of a cyclonic eddy interacting with two anticyclonic eddies and an upwelling filament. High-resolution sampling allowed us to assess the upwelling/downwelling processes associated with eddy pumping and ASC, the injection of nutrients into the euphotic zone, and the subduction of particles related to these processes. The planktonic community, which included heterotrophic bacteria, cyanobacteria-like *Prochlorococcus* and *Synechococcus*, pico and nanoautotrophic eukaryotes, and heterotrophic nanoflagellates, showed a heterogeneous distribution in response to meso-submesoscale processes. Redundancy analysis and plankton distribution suggest that while the distribution of small organisms (picoplankton) is modulated by a combination of physical and biogeochemical drivers, the distribution of larger autotrophic and heterotrophic nanoflagellates is modulated by nutrient inputs and grazing, respectively. These observational results provide new insights in the study of the impact of mesoscale structures in the dynamics of nutrients, chlorophyll and planktonic communities, and valuable to validate theoretical and modeling studies.

Keywords: plankton community structure, mesoscale-submesoscale interactions, eddies, upwelling filaments, eddy pumping, frontogenesis, Canary Islands, NW Africa upwelling

OPEN ACCESS

Edited by:
Malcolm McFarland, Florida Atlantic University, United States

Reviewed by:
Peter Strutton, University of Tasmania, Australia
Nestor Arandia-Gorostidi, Stanford University, United States

****Correspondence:***
Javier Arístegui
javier.aristegui@ulpgc.es

Specialty section:
This article was submitted to Marine Ecosystem Ecology, a section of the journal Frontiers in Marine Science

Received: *08 January 2020*
Accepted: *22 July 2020*
Published: *21 August 2020*

Citation:
Hernández-Hernández N, Arístegui J, Montero MF, Velasco-Senovilla E, Baltar F, Marrero-Díaz Á, Martínez-Marrero A and Rodríguez-Santana Á (2020) Drivers of Plankton Distribution Across Mesoscale Eddies at Submesoscale Range. Front. Mar. Sci. 7:667. doi: 10.3389/fmars.2020.00667

INTRODUCTION

Mesoscale eddies may originate nearly everywhere in the World Ocean (Chelton et al., 2007, 2011), being one of the key processes driving nutrient supply into the euphotic zone of the oceans (McGillicuddy et al., 2003; Klein and Lapeyre, 2009), and consequently affecting phytoplankton growth and its distribution at global scale (Mcgillicuddy et al., 2007; Lévy et al., 2018). Several

processes, known as the "Oceanic Vertical Pump," have been proposed as responsible of eddy-related nutrient fluxes (Klein and Lapeyre, 2009). Of particular interest are two mechanisms: "eddy pumping" at the core of the eddies (McGillicuddy, 2016 and reference therein), and frontogenesis, resulting from eddy-eddy interaction (Mahadevan and Tandon, 2006; Capet et al., 2008b; McWilliams, 2016).

Eddy pumping is used to define the upwelling and downwelling generated during eddy intensification. When cyclonic (anticyclonic) eddies intensify, isopycnals are uplifted (depressed) inducing to upwelling (downwelling) at the eddy center, with associated vertical velocities up to 1 $m{\cdot}d^{-1}$ (Gaube et al., 2014). This may lead to a surface enhancement of chlorophyll in cyclones and a depression and downward transport of chlorophyll in anticyclones (Falkowski et al., 1991; McGillicuddy et al., 1998; Siegel et al., 2008, 2011). On the other hand, eddy-eddy interactions may lead to frontogenesis, resulting in convergent strain fields that will act by destroying the thermal wind balance, establishing an ageostrophic secondary circulation (ASC) in order to restore geostrophy (Mahadevan, 2016; McWilliams, 2016). Vertical velocities originated by frontogenesis may be as high as 100 $m{\cdot}d^{-1}$ (Mahadevan and Tandon, 2006). Nagai et al. (2008) modeled the distribution of chlorophyll related to frontal ASC predicting a subduction in the cold (cyclonic) side (Fielding et al., 2001; Omand et al., 2015) and chlorophyll enhancement in the warm (anticyclonic) side (Hosegood et al., 2017).

Past studies reporting the effect of the "Oceanic Vertical Pump" over phytoplankton communities point out that the whole phytoplankton community does not respond in the same way against the same stressor (Benitez-Nelson et al., 2007; Nencioli et al., 2008; Bibby and Moore, 2011; Chenillat et al., 2015). Rodriguez et al. (2001) showed that the size structure of the phytoplankton community is controlled by the strength of vertical velocities. Their observations indicate that the relative proportion of large cells increases with the magnitude of the upward velocity. Sangrà et al. (2014) also observed in a not nutrient-limited environment that phytoplankton size spectra strongly correlate with turbulence, being the larger phytoplankton size classes more abundant in high-turbulence environments. In a study along the Kuroshio Front, Clayton et al. (2014) described the complexity of the phytoplankton community structure, shaped by a combination of the large-scale biogeographical variability of the region, mesoscale mixing of populations, and finer scale modification of the light and nutrient environment. However, none of these studies addresses the variability of the phytoplankton community composition at submesoscale levels, in spite of the generally accepted view that processes at small scales govern carbon fluxes in the ocean (Lévy et al., 2001; McGillicuddy, 2016).

With the aim of contributing to understand the impact of meso-submesoscale processes over plankton communities, we conducted an interdisciplinary survey across a highly variable mesoscale field south of Gran Canaria Island (Canary Island). The main goal of the study was to understand how physical and biological factors, resolved at a resolution close to submesoscale (∼1 km) could affect the distribution of pico- and nanoplankton, the main components of planktonic communities in the Canary Islands waters (Arístegui et al., 2004). This region spans the coastal transition zone between the rich eutrophic waters of the NW Africa upwelling system and the poor oligotrophic waters of the North Atlantic Subtropical Gyre (Arístegui et al., 2009). It is almost unique in terms of the high mesoscale and submesoscale variability resulting both from the topographic perturbation of the prevailing winds and currents by the islands of the archipelago and from baroclinic instabilities developed along the offshore boundary region of the NW African coastal upwelling system. Mesoscale eddies are continuously shed downstream off the islands (Arístegui et al., 1994, 1997; Piedeleu et al., 2009; Barceló-Llull et al., 2017a), being the origin of the main pathway of long-lived eddies of the northeast subtropical Atlantic, coined as the "Canary Eddy Corridor" by Sangrà et al. (2009). On the other hand, upwelling filaments and eddies, resulting from instabilities along the coastal upwelling jet, may exchange chemical and biological properties between the shelf waters and the open ocean, contributing largely to the coastal-ocean export of organic matter (García-Muñoz et al., 2004, 2005; Pelegrí et al., 2005; Álvarez-Salgado et al., 2007; Santana-Falcón et al., 2017). Eventually, upwelling filaments may interact with island-generated eddies, leading to a complex hydrographic environment that shapes the distribution and activity of planktonic communities (Barton et al., 2004; Arístegui and Montero, 2005; Sangrà et al., 2005). The almost permanent occurrence of several kind of meso-submesoscale features, as well as the interaction among them, makes the Canary region a perfect natural oceanographic laboratory to study the coupling between physical and biogeochemical processes.

MATERIALS AND METHODS

Sampling and Hydrographic Data

The data for this study were collected during the cruise "RODA I" (August 11, 2006 through September 7, 2006) on board of the *BIO Hespérides*. In order to map the hydrographic field to search for mesoscale features (**Figure 1a**), a 70 × 80-nm grid was first surveyed downstream of Gran Canaria (August 11–14), by means of 62 expendable bathythermographers (XBTs) casts down to 1,000 m (**Figure 1b**). After locating the eddies' emplacement, a high-resolution physical biogeochemical section was sampled (August 14–16) crossing a cyclonic eddy interacting with two anticyclonic eddies and an upwelling filament. The section consisted in 20 stations (named 64–83) separated 4 nautical miles from each other (**Figure 1b**).

At each station, hydrographic casts were performed down to 1,000 m using a SeaBird 911 Plus CTD system mounted on a General Oceanics rosette sampler equipped with 24 Niskin bottles of 12 L. A Wet Lab ECO-AFL/FL fluorescence sensor and a Sea Tech transmissometer were additionally equipped in the rosette and connected to the CTD probe. All CTD sensors were previously calibrated in the factory. Chlorophyll *a* (Chl *a*) was also inferred from the fluorescence sensor calibrated with chlorophyll reference patterns in the factory. Water samples were collected for inorganic nutrients and planktonic organisms at 5,

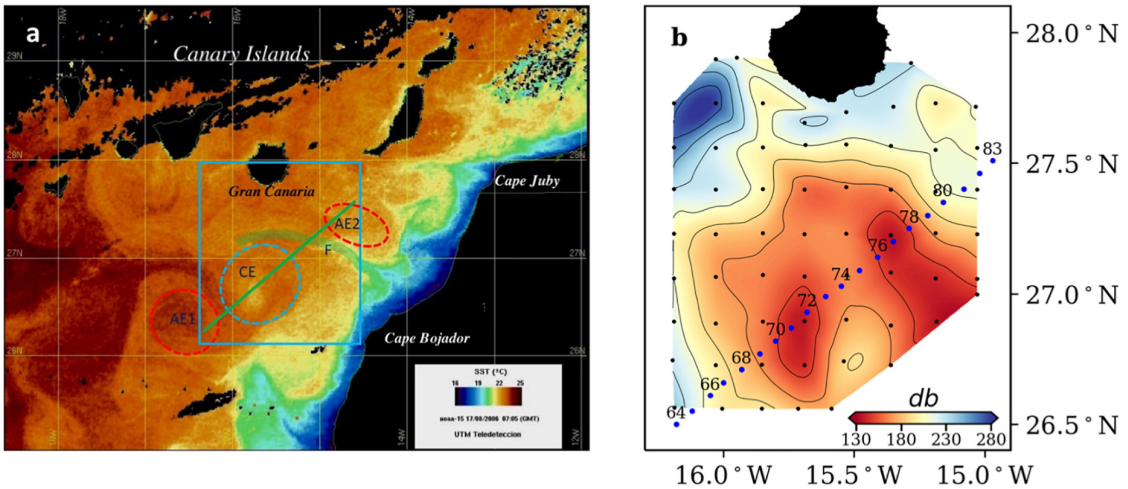

FIGURE 1 | (a) Sea surface temperature (SST) image from NOAA-15 for 15 August 2006. Study area (blue box), showing mesoscale and submesoscale features sampled during the cruise: upwelling filament (F), cyclonic eddy (CE) and anticyclonic eddies (AE1 and AE2). **(b)** Topography of the 16°C isotherm obtained from the XBT grid. Black dots indicate XBT stations; blue dots indicate CTD stations along the studied section. Labels are only included in the even stations.

25, 50, 75, 100, 150, and 200 m, plus an additional sample at the depth of the deep chlorophyll maximum (DCM).

The geostrophic velocity (V_g) field, relative to 1,000 dbar, was estimated from potential temperature (T_θ) and practical salinity (S). Potential temperature anomaly (ΔT_θ) was calculated using as reference values the T_θ profile at station 83 (outside eddy AE2), and then subtracted from each of the temperature profiles. The mixed layer depth (MLD) was inferred by means of the de Boyer Montégut et al. (2004) approximation.

Inorganic Nutrients

Triplicate samples for nitrate and nitrite determination were poured directly from the Niskin bottles into 15-mL polyethylene tubes (Van Waters and Rogers Co., VWR) and preserved frozen at −20°C until their analysis. Nitrate + nitrite (NO_x) were colorimetrically measured using a Bran + Luebbe Autoanalyzer AA3 model following the Hansen and Grasshoff (1983) protocol for automated seawater nutrients analysis. Detection limit for NO_x was 0.02 μM. Instrument precision (0.008 μM for NO_x) was calculated from the standard deviation of replicate samples.

Cell Abundance and Biomass Conversion

Picoplankton (0.2–2 μm) was enumerated by flow cytometry (Becton–Dickinson FACScalibur with 488 nm argon ion laser). Duplicate samples were collected in sterile cryovials (2 mL), immediately fixed with paraformaldehyde (2% final concentration), refrigerated at 4°C for half an hour, and quickly frozen in liquid nitrogen (−196°C) until their analysis on board. For the enumeration of total heterotrophic bacterioplankton (HB; which includes also Archaea), as well as the proportion of high DNA (HNA) and low DNA (LNA) bacteria (Gasol et al., 1999), the samples were stained with SYTO-13 (Molecular Probes Inc.), using a dilution of the stock solution (1:10) to a final concentration of 2.5 μM; and their signature was identified in a plot of side scatter vs. green fluorescence. The identification and enumeration of autotrophic picoplankton – the cyanobacteria *Prochlorococcus* (Pro) and *Synechococcus* (Syn), and picoeukaryotes (PEuk) – in unstained samples was based on the analysis of multiple bivariate scatter plots of side scatter, and red and orange fluorescence. The analyses were run at low speed for the HB and at medium or high speed for the autotrophic picoplankton, until 10,000 events were acquired. A suspension of yellow-green 1 μm latex beads (10^5 and 10^6 mL beads mL^{-1} for autotrophs and bacterioplankton, respectively) was added as an internal standard (Polyscience Inc.). The flow rate was determined volumetrically after every 10 samples run.

Autotrophic (NEuk) and heterotrophic (HNF) nanoplankton (2–20 μm) were analyzed by epifluorescence with an inverted microscope (ZEISS AXIOVERT 35) with 1000× resolution. Samples (100 ml) were preserved with glutaraldehyde (1% final concentration) and stored under cold (4°C) and dark conditions during few days. Subsamples (45 ml) were then filtered through 0.6-μm black polycarbonate filters and stained with DAPI (4,6-diamidino-2-phenylindole; Porter and Feig, 1980) at a final concentration of 5 $\mu g \cdot L^{-1}$ (Sieracki and Johnson, 1985). To differentiate between HNF and NEuk, the samples were analyzed under UV, green, and blue light filters. The enumeration included at least 100 cells of each group per sample.

Plankton abundances were transformed to biomass following the conversion factors obtained by Montero et al. (unpublished) for coastal and oceanic waters of the Canary Islands region. To estimate picoplankton cell biovolumes, more than 60 experiments of sequential filtration (through seven polycarbonate filters from 0.2 to 3 μm) were performed, with water from the surface and the deep chlorophyll maximum around Gran Canaria. Average biovolumes from cell counts obtained by flow cytometry were calculated from sigmoidal fits assuming a spherical shape. For nanoplankton, 140 samples were counted

and measured by epifluorescence microscopy from three size classes (2–6, 6–11, and 11–20 μm). Average biovolumes were derived from mathematical equations, according to the shape of the cell. The following conversion factors were applied: 18 fg C·cell^{-1} for HB, 43 fg C·cell^{-1} for Pro, 120 fg C·cell^{-1} for Syn, 500 fg C·cell^{-1} for PEuk, and 3,100 fg C·cell^{-1} for average NEuk and HNF.

Data Analysis

In order to elucidate the influence of the physical and biogeochemical variables (V_g, T_θ, MLD, NO_3, and HNF; environmental variables hereafter) on the distribution of the planktonic groups (Pro, Syn, PEuk, NEuk, HB, and HNF), a correlation analysis was performance following Legendre and Legendre (2012). Note that HNF is included in both environmental variables and planktonic groups since grazing by HNF may modulate other planktonic groups distribution. For statistical analysis, all plankton biomasses and nutrient concentrations were depth-integrated from 0 to 200 m at every station (**Tables 1**, **2**). Since both T_θ and V_g are not accumulative magnitudes, they were depth-averaged instead (**Table 2**). To select the suitable correlation analysis, data gradient linearity was first tested by means of a detrended correspondence analysis (DCA). Since all DCA values were below 3 (in fact, <0.4), which indicates linear gradient of the data set, a distance-based redundancy analysis (db-RDA) was computed. Plankton data matrix was transformed using the Hellinger's method, while environmental variables remained untransformed. Absence of multicollinearity was inferred by means of variance inflation factors. Monte Carlo permutation significance test was conducted to obtain the *p*-value and the adjusted correlation coefficient (R^2_{adj}) was calculated. RDA results were graphically represented in non-scaled correlation triplots. All statistical analyses were conducted in R software using vegan package[1].

TABLE 1 | Integrated (0–200 m) biomass concentrations (μg C·m^{-2}; ×10^3) for *Prochlorococcus* (Pro), *Synechococcus* (Syn), picoeukaryotes (PEuk), nanoeukaryotes (NEuk), heterotrophic bacteria (HB), and heterotrophic nanoeukaryotes (HNF) at every station.

Station	Pro	Syn	PEuk	NEuk	HB	HNF
64	334.830	34.3830	49.892	736.046	661.519	593.482
65	574.230	56.333	73.374	785.963	1358.828	604.955
66	424.76	39.652	167.522	1068.997	2525.680	786.170
67	241.890	39.862	110.502	901.381	686.436	702.452
68	176.116	43.465	142.390	918.386	591.305	740.412
69	92.503	11.328	57.641	684.336	506.492	579.007
70	98.385	11.416	72.033	1147.113	475.885	950.370
71	48.799	27.638	16.407	1146.802	636.875	963.380
72	154.056	29.138	84.533	1250.464	698.072	1050.256
73	314.795	42.327	136.298	1005.244	995.558	819.515
74	406.545	66.544	122.003	1255.191	1121.546	998.722
75	244.266	33.667	58.610	785.925	1095.068	754.185
76	309.070	40.824	88.703	1307.702	1701.209	1005.162
77	467.478	68.324	70.142	1270.363	1071.691	833.153
78	232.152	32.571	23.191	870.417	989.976	677.854
79	165.025	40.034	27.779	740.150	1147.866	652.270
80	191.887	56.646	43.179	662.869	1140.080	517.792
81	222.625	63.377	92.168	664.548	1218.129	556.902
82	381.959	53.109	67.812	966.238	1073.152	776.010
83	390.556	70.626	82.070	824.713	1103.313	641.420

TABLE 2 | Integrated (0–200 m) and averaged values for nitrate + nitrite (NO_x), and average values for across-section geostrophic velocities (V_g) and potential temperature (T_θ) at every station.

Station	NO_x (μM)	V_g (m·s^{-1})	T_θ (°C)	MLD (m)
64	2.00	0.09	20.62	16.61
65	1.60	0.19	20.45	15.1
66	3.40	0.47	19.92	26.17
67	8.43	0.14	18.59	22.65
68	1.76	0.09	18.01	18.63
69	10.06	0.18	17.59	9.06
70	10.19	0.17	17.80	11.58
71	10.32	0.02	17.70	8.05
72	8.39	0.12	17.94	14.09
73	10.32	0.18	18.33	16.61
74	1.88	0.23	18.24	15.01
75	7.76	0.04	17.86	22.65
76	5.14	0.20	17.93	20.64
77	8.49	0.20	18.50	22.65
78	2.60	0.15	18.66	15.1
79	1.85	0.39	19.25	16.61
80	1.08	0.04	19.01	14.09
81	0.88	0.33	19.38	31.21
82	2.59	0.03	19.30	18.63
83	6.12	0.02	18.84	19.13

MLD, Mixed Layer Depth.

RESULTS

Signature of Meso-Submesoscale Features in the Hydrographic Field

Figure 1a shows a satellite image of sea surface temperature (SST) at the time of the study, where the eddy field south of the Canary Islands and several offshore filaments stretching from the NW African upwelling region are observed. Four different mesoscale-submesoscale features were sampled during our cruise (blue box in **Figure 1a**): A cyclonic eddy (CE) in the center of the box, the margins of two anticyclonic eddies (AE1, AE2) at the southwest and northeast position of the CE, respectively, and the offshore extension of an upwelling filament (F) between CE and AE2. **Figure 1b** represents the 16°C isotherm topography as obtained from the XBT grid, and shows the position of the high-resolution biogeochemical section (stations 64–83) crossing all the mentioned features, with the isotherms' topography in AE1 being deeper than in AE2. In **Figure 2**, the CE is clearly identified by the doming of isotherms and isopycnals at stations 67–75, being the eddy center located at station 70. Although the XBT grid did not cover the whole extension of the two AE, the downwelling of surface warm and high salinity water at stations

[1]http://www.r-project.org

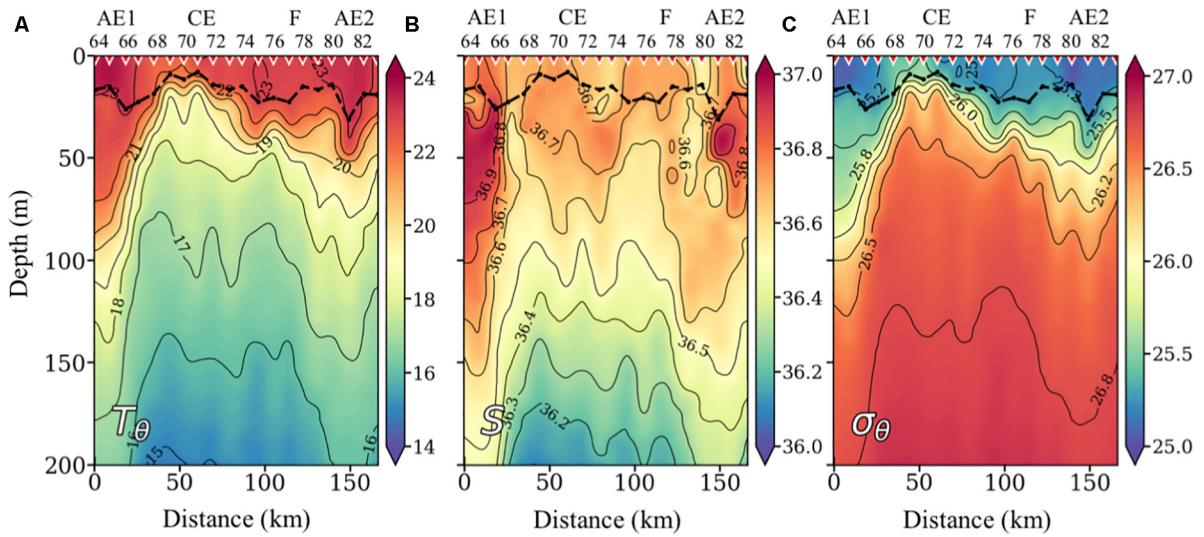

FIGURE 2 | Vertical sections of potential temperature (T_θ) in°C **(A)**, potential density (σ_θ) in kg·m^{-3} **(B)**, and practical salinity (S) **(C)**. Inverted red triangles on the top axis indicate stations position. The locations of the anticyclonic eddies (AE), the cyclonic eddy (CE), and the filament (F) are also indicated on the top axis. The bold black line shows the depth of the mixed layer (MLD).

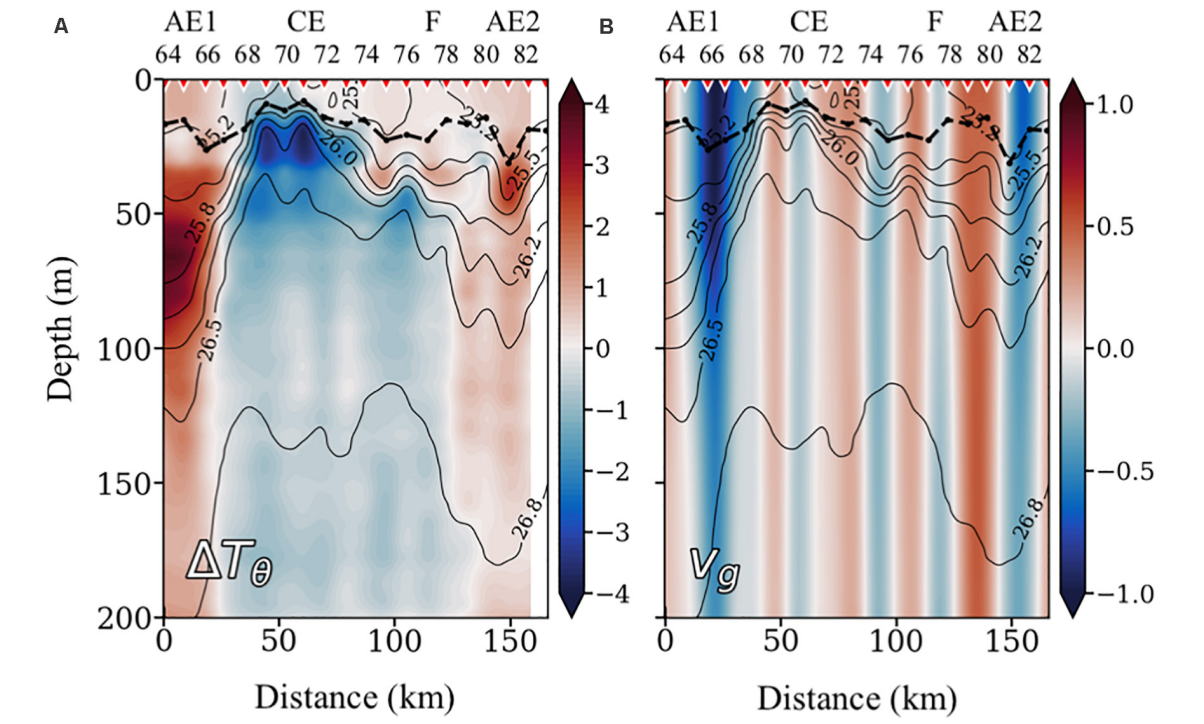

FIGURE 3 | Vertical sections of potential temperature anomaly (ΔT_θ) in°C **(A)** and across section geostrophic velocity (V_g), relative to 1,000 dbar, in m·s^{-1} **(B)**, both with the isopycnals superimposed. Inverted red triangles on the top axis indicate stations position. The locations of the anticyclonic eddies (AE), the cyclonic eddy (CE), and the filament (F) are also indicated on the top axis. The bold black line shows the depth of the mixed layer (MLD). In the V_g plot, positive values indicate north-westward currents, while negative values indicate south-eastward currents.

64–67 and 81–83, as well as other signatures (see below), indicate the presence of AE1 and AE2, respectively.

The representation of the potential temperature anomaly (ΔT_θ) shows that the CE introduces colder waters (about −4°C) in the upper layers (**Figure 3A**). The CE radius, as calculated from the vertical anomaly section, is about 40 km, which is of the order of the climatological first baroclinic radius of deformation (R_d) for the region (Chelton et al., 1998), being

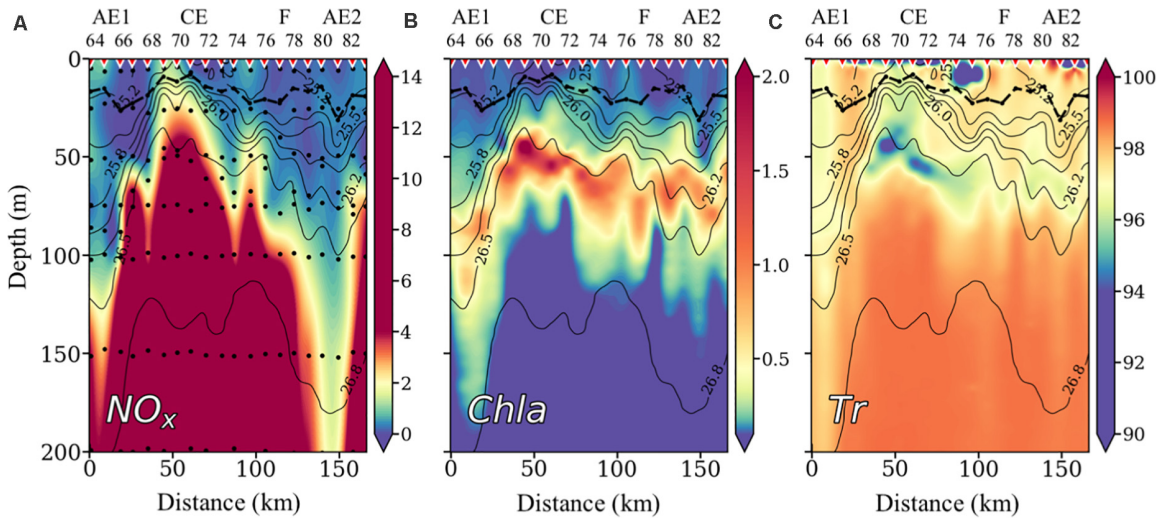

FIGURE 4 | Vertical distribution of nitrate + nitrite concentrations (NO_x) in μM **(A)**, chlorophyll *a* (Chl *a*) in $\mu g \cdot L^{-1}$ **(B)**, and Transmittance (T) in % **(C)**, with isopycnals superimposed. Inverted red triangles on the top axis indicate stations position. The locations of the anticyclonic eddies (AE), the cyclonic eddy (CE), and the filament (F) are also indicated on the top axis. The bold black line shows the depth of the mixed layer (MLD). Black dots indicate sampled depths.

thus a mesoscale structure. At the northern part of the section, the 21–23°C isotherms define a bowl-shape structure centered at station 81 (**Figure 2A**), introducing positive ΔT_θ of about +2°C (**Figure 3A**). This relatively shallow warm core structure is associated with the above-mentioned submesoscale anticyclonic eddy (AE2) of 20-km radius. Between the CE and AE2, the offshore branch of an upwelling filament is observed centered at station 77. The width of the filament is about 20 km, well below the R_d, being thus a submesoscale structure. Finally, at the southern end of the section, there is a strong frontal region between station 65 and 68 resulting from the interaction of the CE with AE1, as observed in the SST field (**Figure 1a**), with a positive ΔT_θ of about +3–4°C in the 50–100-m depth range (**Figure 3A**). The width of this frontal structure is about 35 km, well below R_d, being also a submesoscale structure. AE1 shows signatures of an intrathermocline eddy, characterized by a biconvex shape of the isopycnals and by a homogeneous layer of subtropical mode water embedded within (36.9 psu in 64–69 stations, **Figure 2B**) similar to the PUMP eddy described by Barceló-Llull et al. (2017a) in the same region. Along the south-north (left-right) section (**Figure 3B**) the frontal region between AE1 and CE (stations 65 and 68) originates a strong jet, with south-eastward V_g of up to 1 $m \cdot s^{-1}$. The subsurface maximum of the velocity field can be associated with the biconvex shape of the isopycnals in AE1. The estimated Rossby number (R_o) for this feature is 0.48, which represents a typical value for submesoscale processes (Mahadevan, 2016). On the other hand, relatively high positive and negative V_g regions are found at the boundaries of AE2, between stations 79 and 80 and 81 and 82, respectively; both reaching values up to 0.5 $m \cdot s^{-1}$.

Biogeochemistry

The NO_x (nitrate + nitrite) distribution (**Figure 4A**) presents low values (<1 μM) in the upper 50 m at all stations, except in the core of the cyclonic eddy (stations 69–73), where the uplifting of colder deep waters brings NO_x concentrations of about to 2–μM to the upper 50 m. The lowest NO_x concentrations in the upper 100-m layer are found at the CE boundaries (stations 68 and 74) and in the convergence regions of AE1 and AE2, due to downwelling of surface water.

Chlorophyll *a* (Chl *a*) (**Figure 4B**) presents the typical subtropical ocean distribution, with low values in surface waters and a maximum at depth (DCM). The DCM is closely related to the physical structure of the water column, being shallower and more intense in the center of the cyclonic eddy (where NO_x concentrations are higher) and deeper and weaker at stations associated with downwelling of surface water (AE1, AE2). In general, the DCM is placed below the seasonal thermocline along the section, between 50 and 80-m depth.

Transmittance (Tr), as a proxy of accumulation of organic and mineral particles (**Figure 4C**), is higher (less particles) in deep waters below the DCM. Lower Tr values (more particles) are found in surface waters and coinciding with the DCM (**Figure 4B**). The low Tr at surface waters between stations 74 and 76 is probably due to the accumulation of mineral and organic (low chlorophyll) particles at the intense frontal region between the CE and the F.

Plankton Community Distribution

The biomass concentrations of Pro and Syn are shown in **Figures 5A,B**, respectively. Both cyanobacteria groups present a rather similar distribution pattern with higher concentrations between stations 64 and 67, 72 and 77, and 81 and 83. However, maximum values of Pro are found below the MLD, while Syn highest concentrations are found above it. Cyanobacteria concentrations are lowest in the core of the CE (stations 69–71). PEuk biomass matches the pattern of distribution of the DCM (**Figure 5C**). High concentrations are observed below the

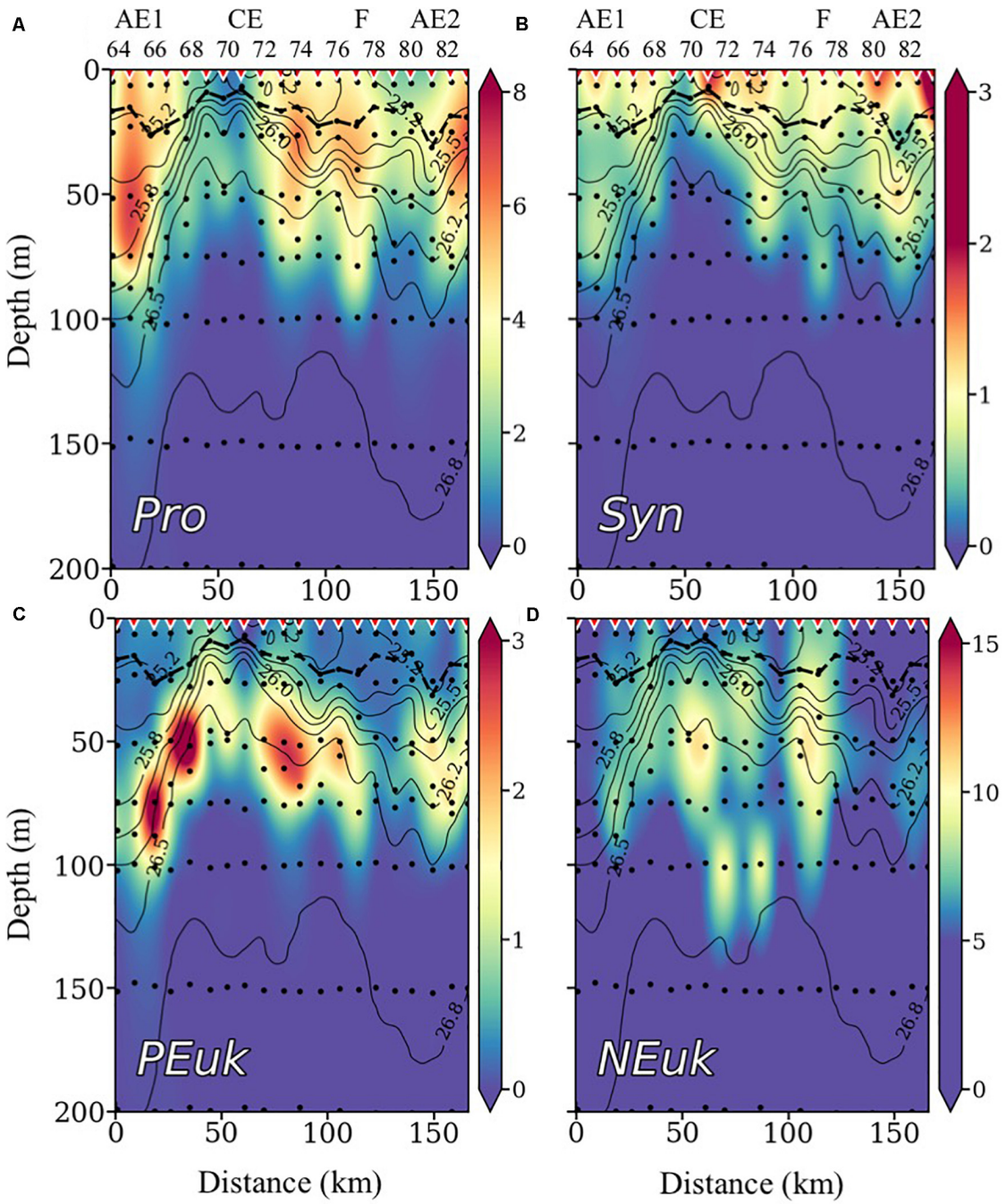

FIGURE 5 | Vertical distribution of cyanobacteria-like *Prochlorococcus* (Pro) **(A)**, *Synechococcus* (Syn) **(B)**, autotrophic picoeukaryotes (PEuk) **(C)**, and nanoeukaryotes (NEuk) **(D)** biomass concentrations in $\mu g\ C{\cdot}m^{-3}$, with isopycnals superimposed. Inverted red triangles on the top axis indicate stations position. The locations of the anticyclonic eddies (AE), the cyclonic eddy (CE), and the filament (F) are also indicated on the top axis. The bold black line shows the depth of the mixed layer (MLD). Black dots indicate sampled depths. Note the different scales for the plots.

seasonal thermocline with highest biomass at the margins of the CE. At the core of the CE and in the F region, where the isopycnals rise and NO_x concentrations are higher, PEuk drops in biomass, being replaced by larger autotrophic eukaryotes (NEuk; **Figure 5D**), which are the main contributors to the DCM in these areas (**Figure 4B**).

The highest bacteria accumulations (**Figure 6A**) are found at the frontal regions of CE, where isopycnals depress (**Figures 3**, **4**). The ratio of HNA/LNA bacteria (**Figure 6B**) is lower outside the CE region, and particularly low (<0.5) in the whole water column (down to 1,000 m; data not shown) at the frontal region between the CE and AE1, where water transmittance is

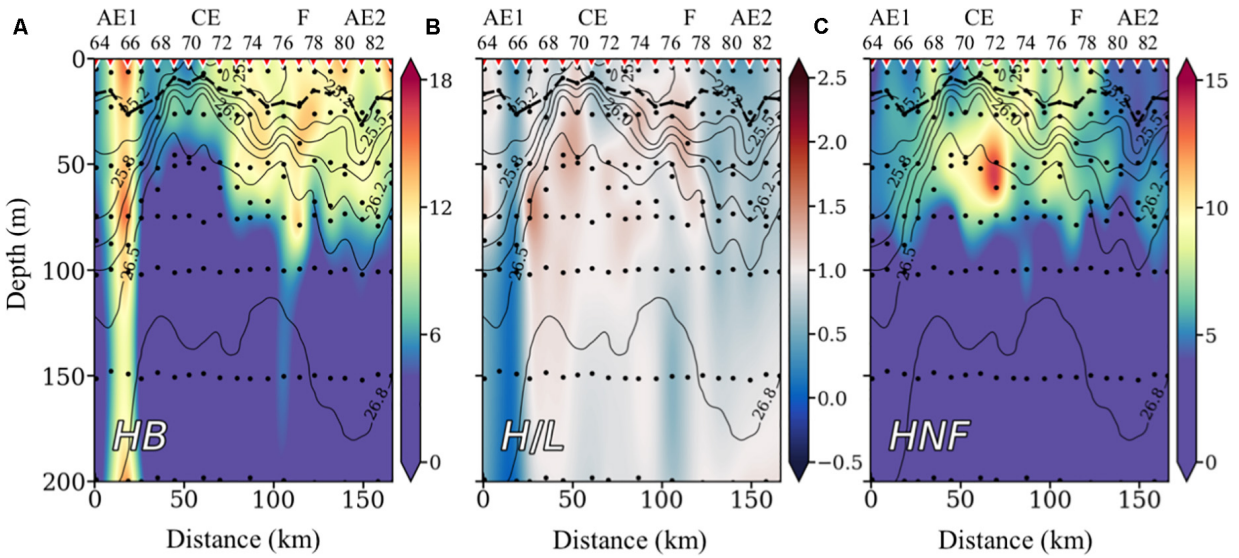

FIGURE 6 | Vertical distribution of heterotrophic bacteria (HB) biomass concentration in μg C·m^{-3} **(A)**, the ratio HNA/LNA **(B)**, and heterotrophic nanoeukaryotes (HNF) biomass concentration in μg C·m^{-3} **(C)**; all with isopycnals superimposed. Inverted red triangles on the top axis indicate stations position. The locations of the anticyclonic eddies (AE), the cyclonic eddy (CE), and the filament (F) are also indicated on the top axis. The bold black line shows the depth of the mixed layer (MLD). Black dots indicate sampled depths. Note that scales are different for the HB and NEuk plots.

lower (**Figure 4C**). The lowest HB biomasses, but with highest HNA/LNA ratios, are observed at the core of the CE, where HNF distribution are highest (**Figure 6C**), suggesting a prey-predator relationship (see below).

Distance-based redundancy analysis correlates phytoplankton groups with physical and biogeochemical variables. These correlations are presented in ordination triplots (**Figure 7**), where angles between vectors reflect the correlations (**Table 3**). Specifically, the correlation (R^2) is equal to the cosine of the angle between vectors. This means that vector pairs describing an angle of 90° are uncorrelated since the cosine of 90° is equal to 0, while vector pairs angles of 50° (or lower) would be highly correlated as cosine of 50° is 0.65 (>0.65).

In our case, phytoplankton groups and the physical and biogeochemical variables present statistically significant correlation ($R^2_{adj} = 0.41$, $p = 0.006$) being a significant percentage (55.7%) of the plankton variability explained by these variables. Positive correlations (angles lower than 50°, i.e., >0.65) are observed between (i) NEuk, HNF, and NO_x concentrations; (ii) total HB, HNA, LNA, T_θ, and MLD; and (iii) PEuk, V_g, and MLD. Conversely, there are negative correlations between (i) all prokaryotic groups (HB, Syn, and Pro) and HNF; and (ii) nanoplankton (NEuk and HNF) with T_θ and MLD.

DISCUSSION

Mesoscale-Submesoscale Interactions and Their Effects on Biogeochemistry

Our results show the presence of four different meso-submesoscale structures interacting among them. The main structure is a mesoscale CE characterized by a shoaling of the isopycnals and the nitracline in its core and the consequently increase in Chl *a*. The doming of the seasonal pycnocline produces the upwelling of nutrients into the euphotic zone, hence increasing Chl *a* in the core of the eddy at about 50-m depth. This process, referred as "eddy pumping" (Sangrà et al., 2007; McGillicuddy, 2016), is characteristic of young eddies south of the Canary Islands in their early stages of generation (Arístegui et al., 1997; Sangrà et al., 2009).

At stations 65–68, the CE interacts with AE1 in its south-western boundary, resulting in a strong submesoscale frontal zone. The convergence of two water masses with different densities in a mesoscale flow field, as observed in this frontal zone, may lead to a loss of the geostrophic balance and the subsequently ASC (Hoskins, 1982; Capet et al., 2008a; McWilliams, 2016). Despite vertical velocities not being measured, several observations give evidence of the presence of ASC in this frontal zone. The high R_o (0.48) associated with the front is an indicator of high relative vorticity, which generates losses in the geostrophic balance (Mahadevan and Tandon, 2006; Mahadevan, 2016). Moreover, Barceló-Llull et al. (2017b) obtained, in an intrathermocline eddy similar to AE1, maximum values of vertical velocity (w) of −6.4 m day^{-1} (downwelling) in the western edge of the eddy and 3.4 m day^{-1} (upwelling) in the eastern edge, between 160 and 185 m depth, showing a dipolar shape, with gradual changes with depth. **Figure 4A** shows that the upward vertical advection of nitrate into the euphotic zone crosses the isopycnals at the frontal regions of CE, suggesting diapycnal mixing (Mahadevan and Archer, 2000; Spall and Richards, 2000; Lévy et al., 2001; Klein and Lapeyre, 2009). To conserve potential vorticity, the implied ASC provides downwelling on the cyclonic (dense) side of the front and

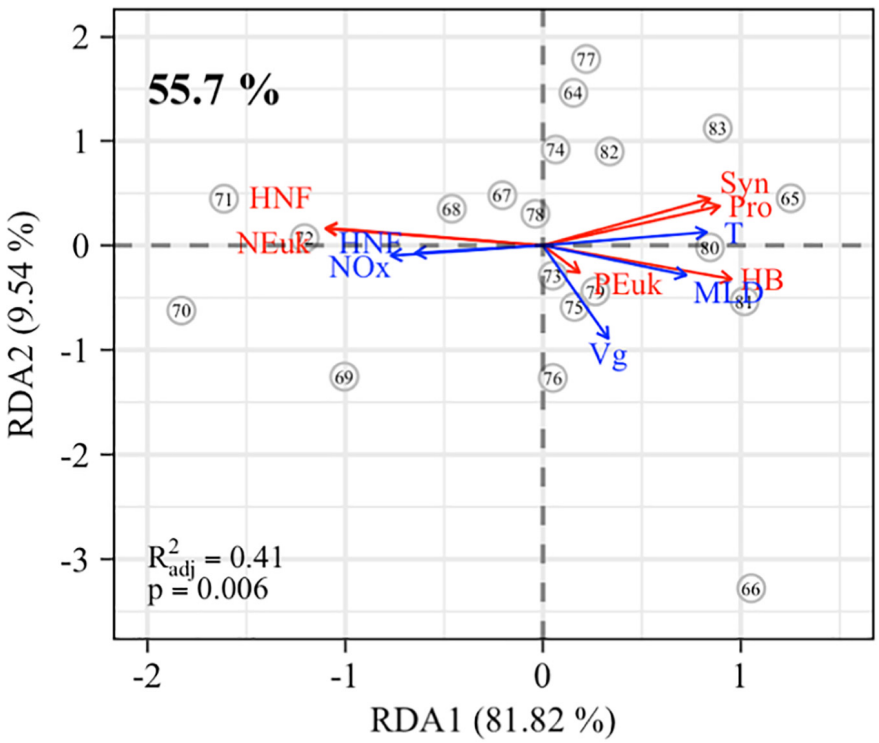

FIGURE 7 | Results of the correlation plot of db-RDA, for the integrated biomasses of the different plankton groups (red arrows: Pro, *Prochlorococcus*; Syn, *Synechococcus*; PEuk, picoeukaryotes; NEuk, nanoeukaryotes; HB, heterotrophic bacteria; HNF, heterotrophic nanoflagellates) and the physical-biogeochemical variables (blue arrows: T, potential temperature; MLD, mixed layer depth; Vg, geostrophic velocity; NO_x, nitrate + nitrite; HNF, heterotrophic nano flagellates). Stations are indicated by open dots. Note that distances among stations are not approximated to ecological distances. The explained variance for canonical axes RDA1 and RD2 is given on the axis. The percentage on the upper left corner refers to the explained constrained variance by all canonical axes. The adjusted correlation coefficient (R^2_{adj}) and the Monte Carlo permutation test *p*-value are also shown in the lower left corner.

upwelling on the anticyclonic (less dense) side (Nagai et al., 2008), as suggested from the nitrate field (**Figure 4A**). This leads to a patchy distribution of Chl *a* (**Figure 4B**), as well as of the PEuk and NEuk organisms responsible of the DCM along the front (**Figures 5C,D**).

One prominent characteristic of the AE1-CE frontal zone is the high horizontal V_g, which reaches up to 1 m·s^{-1}, a value five times higher than the average V_g (0.2 m·s^{-1}) reported for the Canary Current (Sangrà, 1995; Pelegrí et al., 2005), and of the same order of magnitude of the highest ones registered in the ocean. Strong horizontal velocities (up to ±0.5 m·s^{-1}) are also observed at the frontal regions of AE2, giving evidence of the anticyclonic nature of the eddy. These strong horizontal velocities associated with frontal zones would transport and redistribute small particles and organisms around the eddy field south of the islands, being responsible for the patchy distribution of organic matter and plankton observed in the Canary region (Arístegui et al., 2003; Arístegui and Montero, 2005; Baltar et al., 2009).

The filament (F) crossing our sampling region (**Figure 1a**) stems from the coastal jet of the upwelling system. It recirculates around the cyclonic eddy, although its signature is rather weak along our grid of study. In fact, although there are clear evidences of its presence from the T_θ, S, and σ_θ fields, there is no evidence of a larger transport of Chl *a*, in spite that NEuk present relatively higher biomasses down to 50 m near the core of F (station 77), coinciding with relatively higher nitrate concentrations close to the uplifted pycnocline (**Figures 4A**, **5D**). This agrees with

TABLE 3 | Correlation coefficients (R^2) and angles (α) between phytoplankton groups – *Prochlorococcus* (Pro), *Synechococcus* (Syn), picoeukaryotes (PEuk), nanoeukaryotes (NEuk), heterotrophic bacteria (HB), and heterotrophic nanoeukaryotes (HNF) – and variables –nitrate + nitrite (NO_x), geostrophic velocity (V_g), potential temperature (T_θ), mixed layer depth (MLD), and heterotrophic nanoeukaryotes (HNF).

		NO_x (μM)	V_g (m·s^{-1})	T_θ (°C)	MLD (m)	HNF
Pro	R^2	−0.96	−0.05	0.97	0.71	−0.96
	α	164°	93°	14°	44°	164°
Syn	R^2	−0.94	−0.13	0.94	0.65	−0.93
	α	159°	98°	19°	49°	159°
PEuk	R^2	−0.47	0.97	0.45	0.84	−0.49
	α	118°	15°	63°	33°	119°
NEuk	R^2	0.96	−0.49	−0.95	−0.98	0.97
	α	16°	119°	163°	167°	15°
HB	R^2	−0.90	0.63	0.89	0.99	−0.91
	α	154°	51°	27°	3°	155°
HNF	R^2	0.96	−0.48	−0.96	−0.97	–
	α	16°	119°	163°	167°	–

previous studies of filaments in this region that show a sharp demise in planktonic biomass along the offshore extension of the filaments (Arístegui et al., 2004; Baltar et al., 2009).

Drivers of Plankton Distribution and Community Structure

Although Syn and Pro share similar patterns of distribution, with higher concentrations in AE1 and AE2 and lower in the core of CE, Syn presents maximum concentrations in shallower waters than Pro, each one dominating different niche. This has been previously attributed to differences in light harvesting between the two groups (Bouman et al., 2006; Mackey et al., 2013; Biller et al., 2015; Grébert et al., 2018). RDA analysis shows a strong negative correlation between the two cyanobacteria groups and NO_x, indicating that either they are outcompeted by eukaryotes when nutrient concentrations are higher, or that picocyanobacteria rely mainly on dissolved organic matter for their growth (Berman and Bronk, 2003; Mulholland and Lee, 2009; Znachor and Nedoma, 2010; Duhamel et al., 2018). Strong vertical velocities associated with eddy pumping and ASC in CE could have contributed to displace the smaller picoplanktonic cells (Pro, Syn, and HB) to the frontal regions of the eddy, where they accumulate (McGillicuddy et al., 2003; Guidi et al., 2012; Omand et al., 2015). In particular, HB present high biomasses in the water column (down to at least 1,000 m; data not shown) at the strong frontal zone between AE1 and CE, presumably due to aggregation to sinking particles. Past studies in the Canary region have shown that HB accumulate in frontal zones between eddies, where dissolved and particulate organic matter are concentrated (Arístegui et al., 2003; Arístegui and Montero, 2005; Baltar et al., 2009). However, there is not a clear explanation of why LNA bacteria prevail over HNA bacteria in this frontal region, except that there could be preferential grazing pressure over HNA bacteria. Syn, Pro, and HB also present strong negative relationship with HNF, suggesting that grazing of bacteria and cyanobacteria by HNF, commonly reported in the literature (e.g., Massana et al., 2009; Baltar et al., 2016; Yang et al., 2018; Livanou et al., 2019), could have also contributed to determine their distribution across the eddy field.

Like in other oceanic regions (Zubkov et al., 2000), PEuk accumulate below the thermocline, close to the nitracline, being the principal contributor to the DCM across the section. Painter et al. (2014) observed that nitrate uptake rates by PEuk are 10-fold higher in the DCM than in surface waters, contributing to higher growth rates. They argued that PEuk are well adapted to low light regimes, granting them the benefit to thrive at deeper layers than other phytoplankton groups. RDA shows a strong inverse correlation between PEuk and the MLD, indicating that the deeper the mixed layer is (and hence the DCM) the greater the contribution of PEuk to the DCM.

There are two exceptions where PEuk dominance at the DCM is replaced by NEuk: the cores of the CE and the F, where the uplifting of isotherms brings high nutrient concentrations to the upper 50 m, with higher irradiances benefiting the growth of larger eukaryotic cells. Indeed, larger cells of micro- and nanoplankton have an advantage over smaller cells in utilizing nutrient pulses (Marañón et al., 2013; Marañón, 2015). Moreover, the greater motility of larger flagellate cells allows NEuk to withstand at some extent physical forcing, maintaining their position in the core of these features, in spite of advection. The strong positive relationship with NO_x and negative relationship with T_θ, obtained by RDA, support the notion that upwelling of cold nutrient-rich water drives NEuk distribution.

HNF display biomass maxima at the same stations than NEuk, also presenting strong positive correlations with NO_X and negative with T_θ and all prokaryotic groups (Pro, Syn, and HB). It is well-known that nanoflagellates prey over small picoplankton (Christaki et al., 2005; Tsai et al., 2018). However, the fact that HNF correlates inversely with nutrients could also indicate that a large part of these organisms may behave as mixotrophs (Stoecker et al., 2017 and references therein).

Collectively, the distribution of small prokaryotic picoplankton would be modulated by physical forcing, displacing the organisms away from highly advective regions (like the core of CE and F), but also by grazing of HNF and the availability of organic matter at the frontal regions between mesoscale features. The PEuk distribution would depend mainly on the competition with NEuk on light availability and nutrients, but also on grazing by HNF. Conversely, the distribution of larger flagellate organisms, with a moderate capacity to withstand water advection, would be driven by their metabolic requirements: nutrient concentration (NEuk) and prey availability (HNF).

CONCLUSION

The small-scale resolution of our sampling provides new insights into the study of the impact of mesoscale and submesoscale features in the dynamics of nutrients, chlorophyll, and planktonic communities. We were able to assess the upwelling/downwelling processes at submesoscale resolution, associated with eddy pumping and with the ageostrophic secondary circulation, which dominates small-scale circulation patterns at the frontal regions between adjacent structures.

We found that autotrophic and heterotrophic pico- and nanoplanktonic organisms presented a heterogeneous distribution in response to nutrient inputs caused by meso- and submesoscale processes, but also due to potential motility and grazing pressure. Redundancy analysis suggests that the distribution of motile organisms like the nanoplanktonic NEuk and HNF are driven by nutrient supply and prey availability, respectively. Due to their mobility, these organisms may maintain their position at the core of the eddy. On the contrary, the distribution of small picoplanktonic organisms is modulated by physical (vertical and horizontal velocities) and biogeochemical (nutrient/organic matter availability or grazing pressure) drivers, or a combination of both.

We are aware that this study is limited to a single section, and therefore, our conclusions may be interpreted with caution. However, our results strongly suggest that the structure of the planktonic community; hence, its contribution to primary

productivity and flux of carbon to the deep ocean will be modified along the life cycle of eddies through their interaction with other mesoscale and submesoscale features, from their generation state to their final fading, as the relative impact of physical and biogeochemical processes vary.

DATA AVAILABILITY STATEMENT

The datasets generated for this study are available on request to the corresponding author.

AUTHOR CONTRIBUTIONS

JA conceived and designed the cruise. JA and FB carried out sampling. NH-H, JA, MM, EV-S, ÁM-D, AM-M, and ÁR-S analyzed the data. NH-H performed the statistics. JA and NH-H wrote the manuscript with inputs from all co-authors. All authors contributed to the article and approved the submitted version.

FUNDING

This work was a contribution to projects RODA (CTM2004-06842-C03/MAR), PUMP (CTM2012-33355), FLUXES (CTM2015-69392-C3-1-R), and e-IMPACT (PID2019-109084RB-C2), funded by the Spanish "Plan Nacional de I + D," CEI2019-01, funded by the ULPGC, and to project TRIATLAS (AMD-817578-5) financed by the European Commission (H2020). NH-H was supported by a grant (TESIS2015010036) of the Agencia Canaria de Investigación, Innovación y Sociedad de la Información (ACIISI).

ACKNOWLEDGMENTS

We thank to the officers and crew of the *BIO Hespérides*, Minerva Espino, and the staff of the Unit of Marine Technology (UTM) of the Spanish Research Council (CSIC) for their invaluable help at sea. This manuscript is in memoriam of Dr. Pablo Sangrà, who passed away when we were working together on a preliminary draft of the manuscript.

REFERENCES

Álvarez-Salgado, X. A., Arístegui, J., Barton, E. D., and Hansell, D. A. (2007). Contribution of upwelling filaments to offshore carbon export in the subtropical Northeast Atlantic Ocean. *Limnol. Oceanogr.* 52, 1287–1292. doi: 10.4319/lo.2007.52.3.1287

Arístegui, J., Barton, E. D., Álvarez-Salgado, X. A., Santos, A. M. P., Figueiras, F. G., Kifani, S., et al. (2009). Sub-regional ecosystem variability in the canary current upwelling. *Prog. Oceanogr.* 83, 33–48. doi: 10.1016/j.pocean.2009.07.031

Arístegui, J., Barton, E. D., Montero, M. F., García-Muñoz, M., and Escánez, J. (2003). Organic carbon distribution and water column respiration in the NW Africa-Canaries coastal transition zone. *Aquat. Microb. Ecol.* 33, 289–301. doi: 10.3354/ame033289

Arístegui, J., Barton, E. D., Tett, P., Montero, M. F., García-Muñoz, M., Basterretxea, G., et al. (2004). Variability in plankton community structure, metabolism, and vertical carbon fluxes along an upwelling filament (Cape Juby, NW Africa). *Prog. Oceanogr.* 62, 95–113. doi: 10.1016/j.pocean.2004.07.004

Arístegui, J., and Montero, M. F. (2005). Temporal and spatial changes in plankton respiration and biomass in the Canary islands region: the effect of mesoscale variability. *J. Mar. Syst.* 54, 65–82. doi: 10.1016/j.jmarsys.2004.07.004

Arístegui, J., Sangrá, P., Hernández-León, S., Cantón, M., Hernández-Guerra, A., and Kerling, J. L. (1994). Island-induced eddies in the Canary islands. *Deep. Res. Part I Oceanogr. Res. Pap.*41, 1509–1525. doi: 10.1016/0967-0637(94)90058-90052

Arístegui, J., Tett, P., Hernández-Guerra, A., Basterretxea, G., Montero, M. F., Wild, K., et al. (1997). The influence of island-generated eddies on chlorophyll distribution: a study of mesoscale variation around Gran Canaria. *Deep. Res. Part I Oceanogr. Res. Pap.* 44, 71–96. doi: 10.1016/S0967-0637(96)00093-93

Baltar, F., Arístegui, J., Montero, M. F., Espino, M., Gasol, J. M., and Herndl, G. J. (2009). Mesoscale variability modulates seasonal changes in the trophic structure of nano- and picoplankton communities across the NW Africa-Canary Islands transition zone. *Prog. Oceanogr.* 83, 180–188. doi: 10.1016/j.pocean.2009.07.016

Baltar, F., Palovaara, J., Unrein, F., Catala, P., Hornák, K., Csimek, K., et al. (2016). Marine bacterial community structure resilience to changes in protist predation under phytoplnakton bloom conditions. *ISME J.* 10, 568–581. doi: 10.1038/ismej.2015.135

Barceló-Llull, B., Pallàs-Sanz, E., Sangrà, P., Martínez-Marrero, A., Estrada-Allis, S. N., and Arístegui, J. (2017a). Ageostrophic secondary circulation in a subtropical intrathermocline eddy. *J. Phys. Oceanogr.* 47, 1107–1123. doi: 10.1175/JPO-D-16-0235.1

Barceló-Llull, B., Sangrà, P., Pallàs-Sanz, E., Barton, E. D., Estrada-Allis, S. N., Martínez-Marrero, A., et al. (2017b). Anatomy of a subtropical intrathermocline eddy. *Deep Sea Res. Part I* 124, 126–139. doi: 10.1016/j.dsr.2017.03.012

Barton, E. D., Arístegui, J., Tett, P., and Navarro-Pérez, E. (2004). Variability in the Canary Islands area of filament-eddy exchanges. *Prog. Oceanogr.* 62, 71–94. doi: 10.1016/j.pocean.2004.07.003

Benitez-Nelson, C. R., Bidigare, R. R., Dickey, T. D., Landry, M. R., Leonard, C. L., Brown, S. L., et al. (2007). Mesoscale eddies drive increased silica export in the subtropical pacific ocean. *Science* 316, 1017–1022.

Berman, T., and Bronk, D. A. (2003). Dissolved organic nitrogen: a dynamic participant in aquatic ecosystems. *Aquat. Microb. Ecol.* 31, 279–305. doi: 10.3354/ame031279

Bibby, T. S., and Moore, C. M. (2011). Silicate:nitrate ratios of upwelled waters control the phytoplankton community sustained by mesoscale eddies in subtropical North Atlantic and Pacific. *Biogeosciences* 8, 657–666. doi: 10.5194/bg-8-657-2011

Biller, S. J., Berube, P. M., Lindell, D., and Chisholm, S. W. (2015). Prochlorococcus: the structure and function of collective diversity. *Nat. Rev. Microbiol.* 13, 13–27. doi: 10.1038/nrmicro3378

Bouman, H. A., Ulloa, O., Scanlan, D. J., Zwirglmaier, K., Li, W. K. W., Platt, T., et al. (2006). Oceanographic basis of the global surface distribution of *Prochlorococcus* ecotypes. *Science* 312, 918–921. doi: 10.1126/science.1122692

Capet, X., McWilliams, J. C., Molemaker, M. J., and Shchepetkin, A. F. (2008a). Mesoscale to submesoscale transition in the california current system. Part I: flow structure, eddy flux, and observational tests. *J. Phys. Oceanogr.* 38, 44–64. doi: 10.1175/2007JPO3672.1

Capet, X., McWilliams, J. C., Molemaker, M. J., and Shchepetkin, A. F. (2008b). Mesoscale to submesoscale transition in the california current system. Part II: frontal processes. *J. Phys. Oceanogr.* 38, 2256–2269. doi: 10.1175/2008JPO3810.1

Chelton, D. B., DeSzoeke, R. A., Schlax, M. G., El Naggar, K., and Siwertz, N. (1998). Geographical variability of the first baroclinic rossby radius of deformation. *J. Phys. Oceanogr.* 28, 433–460. doi: 10.1175/1520-0485(1998)028<0433:gvotfb>2.0.co;2

Chelton, D. B., Schlax, M. G., and Samelson, R. M. (2011). Global observations of nonlinear mesoscale eddies. *Prog. Oceanogr.* 91, 167–216. doi: 10.1016/j.pocean.2011.01.002

Chelton, D. B., Schlax, M. G., Samelson, R. M., and de Szoeke, R. A. (2007). Global observations of large oceanic eddies. *Geophys. Res. Lett.* 34, 1–5. doi: 10.1029/2007GL030812

Chenillat, F., Franks, P. J. S., Rivière, P., Capet, X., Grima, N., and Blanke, B. (2015). Plankton dynamics in a cyclonic eddy in the Southern California current system. *J. Geophys. Res. Ocean.* 120, 5566–5588. doi: 10.1002/2015JC010826. Received

Christaki, U., Vázquez-Domínguez, E., Courties, C., and Lebaron, P. (2005). Grazing impact of different heterotrophic nanoflagellates on eukaryotic (*Ostreococcus tauri*) and prokaryotic picoautotrophs (*Prochlorococcus* and *Synechococcus*). *Environ. Microbiol.* 7, 1200–1210. doi: 10.1111/j.1462-2920.2005.00800.x

Clayton, S., Nagai, T., and Follows, M. J. (2014). Fine scale phytoplankton community structure across the Kuroshio Front. *J. Plankton Res.* 36, 1017–1030. doi: 10.1093/plankt/fbu020

de Boyer Montégut, C., Madec, G., Fischer, A. S., Lazar, A., and Iudicone, D. (2004). Mixed layer depth over the global ocean: an examination of profile data and a profile-based climatology. *J. Geophys. Res. C Ocean.* 109, 1–20. doi: 10.1029/2004JC002378

Duhamel, S., Van Wambeke, F., Lefevre, D., Benavides, M., and Bonnet, S. (2018). Mixotrophic metabolism by natural communities of unicellular cyanobacteria in the western tropical South Pacific Ocean. *Environ. Microbiol.* 20, 2743–2756. doi: 10.1111/1462-2920.14111

Falkowski, P. G., Ziemann, D., Kolber, Z., and Bienfang, P. K. (1991). Role of eddy pumping in enhancing primary production in the ocean. *Nature* 352, 55–58. doi: 10.1038/352055a0

Fielding, S., Crisp, N., Allen, J. T., Hartman, M. C., Rabe, B., and Roe, H. S. J. (2001). Mesoscale subduction at the Almeria-Oran front Part 2. biophysical interactions. *J. Mar. Syst.* 30, 287–304. doi: 10.1016/S0924-7963(01)00063-X

García-Muñoz, M., Arístegui, J., Montero, M. F., and Barton, E. D. (2004). Distribution and transport of organic matter along a filament-eddy system in the Canaries – NW Africa coastal transition zone region. *Prog. Oceanogr.* 62, 115–129. doi: 10.1016/j.pocean.2004.07.005

García-Muñoz, M., Arístegui, J., Pelegrí, J. L., Antoranz, A., Ojeda, A., and Torres, M. (2005). Exchange of carbon by an upwelling filament off Cape Ghir (NW Africa). *J. Mar. Syst.* 54, 83–95. doi: 10.1016/j.jmarsys.2004.07.005

Gasol, J. M., Li Zweifel, U., Peters, F., Fuhrman, J. A., and Hagström, Å (1999). Significance of size and nucleic acid content heterogeneity as measured by flow cytometry in natural planktonic bacteria. *Appl. Environ. Microbiol.* 65, 4475–4483. doi: 10.13039/501100000780

Gaube, P., McGillicuddy, D. J. J., Chelton, D. B., Behrenfeld, J., and Strutton, P. G. (2014). Regional variations in the influence of mesoscale eddies on near-surface chlorophyll. *J. Geophys. Res. Ocean.* 119, 8195–8220. doi: 10.1002/2014JC010111.Received

Grébert, T., Doré, H., Partensky, F., Farrant, G. K., Boss, E. S., Picheral, M., et al. (2018). Light color acclimation is a key process in the global ocean distribution of *Synechococcus* cyanobacteria. *Proc. Natl. Acad. Sci. U.S.A.* 115, E2010–E2019. doi: 10.1073/pnas.1717069115

Guidi, L., Calil, P. H. R., Duhamel, S., Björkman, K. M., Doney, S. C., Jackson, G. A., et al. (2012). Does eddy-eddy interaction control surface phytoplankton distribution and carbon export in the North Pacific Subtropical Gyre? *J. Geophys. Res.* 117, 1–12. doi: 10.1029/2012JG001984

Hansen, H. P., and Grasshoff, K. (1983). "Automated chemical analysis," in *Methods of Seawater Analysis*, ed. K. Grashoff M. Ehrhardt and K. Kremling (Weinheim: Verlag Chemie) 347–379. doi: 10.1016/0304-4203(78)90045-2

Hosegood, P. J., Nightingale, P. D., Rees, A. P., Widdicombe, C. E., Woodward, E. M. S., Clark, D. R., et al. (2017). Nutrient pumping by submesoscale circulations in the mauritanian upwelling system. *Prog. Oceanogr.* 159, 223–236. doi: 10.1016/j.pocean.2017.10.004

Hoskins, B. J. (1982). The mathematical theory of frontogenesis. *Annu. Rev. Fluid Mech.* 14, 131–151. doi: 10.1146/annurev.fl.14.010182.001023

Klein, P., and Lapeyre, G. (2009). The oceanic vertical pump induced by mesoscale and submesoscale turbulence. *Ann. Rev. Mar. Sci.* 1, 351–375. doi: 10.1146/annurev.marine.010908.163704

Legendre, P., and Legendre, L. (eds) (2012). *Numerical Ecology*, 3rd Edn, Amsterdam: Elsevier, doi: 10.1016/B978-0-444-53868-0.50016-2

Lévy, M., Franks, P. J. S., and Smith, K. S. (2018). The role of submesoscale currents in structuring marine ecosystems. *Nat. Commun.* 9:4758. doi: 10.1038/s41467-018-07059-7053

Lévy, M., Klein, P., and Treguier, A.-M. (2001). Impact of sub-mesoscale physics on production and subduction of phytoplankton in an oligotrophic regime. *J. Mar. Res.* 59, 535–565. doi: 10.1357/002224001762842181

Livanou, E., Lagaria, A., Santi, I., Mandalakis, M., Pavlidou, A., Lika, K., et al. (2019). Pigmented and heterotrophic nanoflagellates: abundance and grazing on prokaryotic picoplankton in the ultra-oligotrophic Eastern Mediterranean Sea. *Deep. Res. Part II Top. Stud. Oceanogr.* 164, 100–111. doi: 10.1016/j.dsr2.2019.04.007

Mackey, K. R. M., Paytan, A., Caldeira, K., Grossman, A. R., Moran, D., McIlvin, M., et al. (2013). Effect of temperature on photosynthesis and growth in marine *Synechococcus* spp. *Plant Physiol.* 163, 815–829. doi: 10.1104/pp.113.221937

Mahadevan, A. (2016). The Impact of submesoscale physics on primary productivity of plankton. *Ann. Rev. Mar. Sci.* 8, 161–184. doi: 10.1146/annurev-marine-010814-015912

Mahadevan, A., and Archer, D. (2000). Modeling the impact of fronts and mesoscale circulation on the nutrient supply and biogeochemistry of the upper ocean. *J. Geophys. Res. Ocean.* 105, 1209–1225. doi: 10.1029/1999JC900216

Mahadevan, A., and Tandon, A. (2006). An analysis of mechanisms for submesoscale vertical motion at ocean fronts. *Ocean Model.* 14, 241–256. doi: 10.1016/j.ocemod.2006.05.006

Marañón, E. (2015). Cell size as a key determinant of phytoplankton metabolism and community structure. *Ann. Rev. Mar. Sci.* 7, 241–264. doi: 10.1146/annurev-marine-010814-015955

Marañón, E., Cermeño, P., López-Sandoval, D. C., Rodríguez-Ramos, T., Sobrino, C., Huete-Ortega, M., et al. (2013). Unimodal size scaling of phytoplankton growth and the size dependence of nutrient uptake and use. *Ecol. Lett.* 16, 371–379. doi: 10.1111/ele.12052

Massana, R., Unrein, F., Rodríguez-Martínez, R., Forn, I., Lefort, T., Pinhassi, J., et al. (2009). Grazing rates and functional diversity of uncultured heterotrophic flagellates. *ISME J.* 3, 588–595. doi: 10.1038/ismej.2008.130

McGillicuddy, D. J. (2016). Mechanisms of physical-biological-biogeochemical interaction at the oceanic mesoscale. *Ann Rev Mar Sci.* 8, 125–159. doi: 10.1146/annurev-marine-010814-015606

Mcgillicuddy, D. J., Anderson, L. A., Bates, N. R., Buesseler, K. O., Carlson, C. A., Davis, C. S., et al. (2007). Eddy/Wind interactions stimulate extraordinary mid-ocean blooms. *Science* 316, 1021–1026. doi: 10.1126/science.1136256

McGillicuddy, D. J., Anderson, L. A., Doney, S. C., and Maltrud, M. E. (2003). Eddy-driven sources and sinks of nutrients in the upper ocean: results from a 0.1° resolution model of the North Atlantic. *Global. Biogeochem. Cycles* 17:1035. doi: 10.1029/2002gb001987

McGillicuddy, D. J. J., Robinson, A. R., Siegel, D. A., Jannasch, H. W., Johnson, R., Dickey, T. D., et al. (1998). Influence of mesoscale eddies on new production in the Sargasso Sea. *Nature* 285, 263–266. doi: 10.1038/28367

McWilliams, J. C. (2016). Submesoscale currents in the ocean. *Proc. R. Soc. A Math. Phys. Eng. Sci.* 472:20160117. doi: 10.1098/rspa.2016.0117

Mulholland, M. R., and Lee, C. (2009). Peptide hydrolysis and the uptake of dipeptides by phytoplankton. *Limnol. Oceanogr.* 54, 856–868. doi: 10.4319/lo.2009.54.3.0856

Nagai, T., Tandon, A., Gruber, N., and McWilliams, J. C. (2008). Biological and physical impacts of ageostrophic frontal circulations driven by confluent flow and vertical mixing. *Dyn. Atmos. Ocean.* 45, 229–251. doi: 10.1016/j.dynatmoce.2007.12.001

Nencioli, F., Kuwahara, V. S., Dickey, T. D., Rii, Y. M., and Bidigare, R. R. (2008). Physical dynamics and biological implications of a mesoscale eddy in the lee of Hawai'i: cyclone opal observations during E-Flux III. *Deep. Res. Part II Top. Stud. Oceanogr.* 55, 1252–1274. doi: 10.1016/j.dsr2.2008.02.003

Omand, M. M., D'Asaro, E. A., Lee, C. M., Perry, M. J., Briggs, N., Cetini, I., et al. (2015). Eddy-driven subduction exports particulate organic carbon from the spring bloom. *Science* 348, 22–225. doi: 10.1126/science.1260062

Painter, S. C., Patey, M. D., Tarran, G. A., and Torres-Valdés, S. (2014). Picoeukaryote distribution in relation to nitrate uptake in the oceanic nitracline. *Aquat. Microb. Ecol.* 72, 195–213. doi: 10.3354/ame01695

Pelegrí, J. L., Arístegui, J., Cana, L., González-Dávila, M., Hernández-Guerra, A., Hernández-León, S., et al. (2005). Coupling between the open ocean and the coastal upwelling region off northwest Africa: water recirculation and offshore pumping of organic matter. *J. Mar. Syst.* 54, 3–37. doi: 10.1016/j.jmarsys.2004.07.003

Piedeleu, M., Sangra, P., Sánchez-Vidal, A., Fabrés, J., Gordo, C., and Calafat, A. (2009). An observational study of oceanic eddy generation mechanisms by tall deep-water islands (Gran Canaria). *Geophys. Res. Lett.* 36, 1–5. doi: 10.1029/2008GL037010

Porter, K. G., and Feig, Y. S. (1980). The use of DAPI for identifying and counting aquatic microflora. *Limnol. Oceanogr.* 25, 943–948. doi: 10.4319/Lo.1980.25.5.0943

Rodriguez, J., Tintore, J., Allen, J. T., Blanco, J. M., Gomis, D., Reul, A., et al. (2001). Mesoscale vertical motion and the size structure of phytoplakton in the ocean. *Nature* 410, 360–362.

Sangrà, P. (1995). *Perturbación de un Flujo Geofísico Por un Obstáculo: Aplicación a la isla de Gran Canaria*. Doctoral dissesrtation, University Of Las Palmas De Gran Canaria, Spain.

Sangrà, P., Auladell, M., Marrero-Díaz, A., Pelegrí, J. L., Fraile-Nuez, E., Rodríguez-Santana, A., et al. (2007). On the nature of oceanic eddies shed by the Island of Gran Canaria. *Deep. Res. Part I Oceanogr. Res. Pap.* 54, 687–709. doi: 10.1016/j.dsr.2007.02.004

Sangrà, P., García-Muñoz, C., García, C. M., Marrero-Díaz, Á, Sobrino, C., Mouriño-Carballido, B., et al. (2014). Coupling between upper ocean layer variability and size-fractionated phytoplankton in a non-nutrient-limited environment. *Mar. Ecol. Prog. Ser.* 499, 35–46. doi: 10.3354/meps10668

Sangrà, P., Pascual, A., Rodríguez-Santana, Á, Machín, F., Mason, E., McWilliams, J. C., et al. (2009). The canary eddy corridor: a major pathway for long-lived eddies in the subtropical North Atlantic. *Deep. Res. Part I Oceanogr. Res. Pap.* 56, 2100–2114. doi: 10.1016/j.dsr.2009.08.008

Sangrà, P., Pelegrí, J. L., Hernández-Guerra, A., Arregui, I., Martín, J. M., Marrero-Díaz, A., et al. (2005). Life history of an anticyclonic eddy. *J. Geophys. Res. C Ocean.* 110, 1–19. doi: 10.1029/2004JC002526

Santana-Falcón, Y., Álvarez-Salgado, X. A., Pérez-Hernández, M. D., Hernández-Guerra, A., Mason, E., and Arístegui, J. (2017). Organic carbon budget for the eastern boundary of the North Atlantic subtropical gyre: major role of DOC in mesopelagic respiration. *Sci. Rep.* 7, 1–12. doi: 10.1038/s41598-017-10974-y

Siegel, D. A., Court, D. B., Menzies, D. W., Peterson, P., Maritorena, S., and Nelson, N. B. (2008). Satellite and in situ observations of the bio-optical signatures of two mesoscale eddies in the Sargasso Sea. *Deep. Res. Part II Top. Stud. Oceanogr.* 55, 1218–1230. doi: 10.1016/j.dsr2.2008.01.012

Siegel, D. A., Peterson, P., McGillicuddy, D. J., Maritorena, S., and Nelson, N. B. (2011). Bio-optical footprints created by mesoscale eddies in the Sargasso Sea. *Geophys. Res. Lett.* 38, 1–6. doi: 10.1029/2011GL047660

Sieracki, M. E., and Johnson, P. W. (1985). Detection, enumeration, and sizing of planktonic bacteria by image-analyzed epifluorescence microscopy downloaded from. *Appl. Environ. Microbiol.* 49, 799–810.

Spall, S. A., and Richards, K. J. (2000). A numerical model of mesoscale frontal instabilities and plankton dynamics – I. model formulation and initial experiments. *Deep. Res. Part I Oceanogr. Res. Pap.* 47, 1261–1301. doi: 10.1016/S0967-0637(99)00081-83

Stoecker, D. K., Hansen, P. J., Caron, D. A., and Mitra, A. (2017). Mixotrophy in the marine Plankton. *Ann. Rev. Mar. Sci.* 9, 311–335. doi: 10.1146/annurev-marine-010816-060617

Tsai, A. Y., Gong, G. C., Chung, C. C., and Huang, Y. T. (2018). Different impact of nanoflagellate grazing and viral lysis on *Synechococcus* spp. and picoeukaryotic mortality in coastal waters. *Estuar. Coast. Shelf Sci.* 209, 1–6. doi: 10.1016/j.ecss.2018.05.012

Yang, J. W., Wu, W., Chung, C. C., Chiang, K. P., Gong, G. C., and Hsieh, C. H. (2018). Predator and prey biodiversity relationship and its consequences on marine ecosystem functioning – Interplay between nanoflagellates and bacterioplankton. *ISME J.* 12, 1532–1542. doi: 10.1038/s41396-018-0111-113

Znachor, P., and Nedoma, J. (2010). Importance of dissolved organic carbon for phytoplankton nutrition in a eutrophic reservoir. *J. Plankton Res.* 32, 367–376. doi: 10.1093/plankt/fbp129

Zubkov, M. V., Sleigh, M. A., Burkill, P. H., and Leakey, R. J. G. (2000). Picoplankton community structure on the atlantic meridional transect: a comparison between seasons. *Prog. Oceanogr.* 45, 369–386. doi: 10.1016/S0079-6611(00)00008-2

Conflict of Interest: The authors declare that the research was conducted in the absence of any commercial or financial relationships that could be construed as a potential conflict of interest.

Copyright © 2020 Hernández-Hernández, Arístegui, Montero, Velasco-Senovilla, Baltar, Marrero-Díaz, Martínez-Marrero and Rodríguez-Santana. This is an open-access article distributed under the terms of the Creative Commons Attribution License (CC BY). The use, distribution or reproduction in other forums is permitted, provided the original author(s) and the copyright owner(s) are credited and that the original publication in this journal is cited, in accordance with accepted academic practice. No use, distribution or reproduction is permitted which does not comply with these terms.

frontiers in Marine Science

ORIGINAL RESEARCH
published: 27 August 2020
doi: 10.3389/fmars.2020.00654

Stirring, Mixing, Growing: Microscale Processes Change Larger Scale Phytoplankton Dynamics

Francesco Paparella[1]* *and Marcello Vichi*[2]

[1] Division of Science and Center on Stability, Instability and Turbulence and Center for Astro, Particle, and Planetary Physics, New York University Abu Dhabi, Abu Dhabi, United Arab Emirates, [2] Department of Oceanography and Marine Research Institute, University of Cape Town, Cape Town, South Africa

The quantitative description of marine systems is constrained by a major issue of scale separation: phytoplankton production processes occur at sub-centimeter scales, while the contribution to the Earth's biogeochemical cycles is expressed at much larger scales, up to the planetary one. In spite of vastly improved computing power and observational capabilities, the modeling approach has remained anchored to an old view that sees the microscales as unable to substantially affect larger ones. The lack of a widespread theoretical appreciation of the interactions between vastly different scales has led to the proliferation of numerical models with uncertain predictive capabilities. In this paper, we use the phenology of phytoplankton blooms as one example of a macroscopic ecosystem feature affected by microscale interactions. We describe two distinct mechanisms that produce patchiness within a productive water column: turbulent entrainment of less-productive water at the base of the mixed layer, and stirring by slow turbulence of a vertical phytoplankton gradient sustained by depth-dependent light availability. In current eddy-diffusive models, patchiness produced in this way is wiped out very rapidly, because the time scales of irreversible mixing largely overlap those of mechanical stirring. We propose a novel Lagrangian modeling framework that allows for the existence of microscale patchiness, even when that is not fully resolved. We show, with a mixture of theoretical arguments and numerical simulations of increasing realism, how the presence of patchiness, in turn, affects larger-scale properties, demonstrating that the timing of phytoplankton blooms and vertical variability of chlorophyll in the oceanic upper layers is determined by the mutual interplay between the stirring, mixing and growing processes.

Keywords: biogeochemistry, plankton modeling, lagrangian particle, Bio-Geo-Chemical Argo (BGC-Argo), model bias and bias correction, phytoplankton bloom, aquacosms, irreversible mixing

OPEN ACCESS

Edited by:
Margaret Byron, Pennsylvania State University (PSU), United States

Reviewed by:
Evan Variano, University of California, Berkeley, United States
Jennifer Prairie, University of San Diego, United States

***Correspondence:**
Francesco Paparella
francesco.paparella@nyu.edu

Specialty section:
This article was submitted to Marine Ecosystem Ecology, a section of the journal Frontiers in Marine Science

Received: *11 December 2019*
Accepted: *17 July 2020*
Published: *27 August 2020*

Citation:
Paparella F and Vichi M (2020) Stirring, Mixing, Growing: Microscale Processes Change Larger Scale Phytoplankton Dynamics. Front. Mar. Sci. 7:654. doi: 10.3389/fmars.2020.00654

1. INTRODUCTION

Marine phytoplankton are involved in several biogeochemical processess at the microbial ocean scale that affect entire ecosystems (Azam and Worden, 2004; Legendre et al., 2018). Predictive models of phytoplanktonic processes are thus fundamental to many applications. In climate projections, the "biological pump" is a fundamental component of the carbon cycle (Gruber et al., 2009; Bopp et al., 2013), described by modeling phytoplankton primary production and

the net export of organic matter through the marine food web and the water column. Models of biogeochemical and phytoplankton processes are also employed in operational oceanography and coastal management (Hyder et al., 2015; Piroddi et al., 2015). Predictive models of coastal and near-shore transport are coupled with water quality and biogeochemical models to provide forecasts of undesirable disturbances such as eutrophication, hypoxia, or harmful algal blooms. Ultimately, the outputs of these models are used for fishery management, end-to-end ecosystem models, and indicators of ocean health (Travers et al., 2007; Fu et al., 2018).

There is, however, a fundamental difficulty in the modeling process: namely, the chasm between the scales where the biogeochemical processes occur and are being observed [by probes deployed in the ocean, laboratory experiments or metagenomics studies (Azam and Worden, 2004; Stec et al., 2017; Legendre et al., 2018)] and the scales where the system response is sought, observed and interpreted (by remote sensing, data aggregation and models). Laboratory experiments using cultures and mesocosms allow the empirical estimation of a model's biological terms, upon the assumption of homogeneous distribution of all the biochemical fields (Denman, 2003; Tian, 2006), while neglecting the physical terms. The interactions between these terms are ultimately mandated to the numerical solution of coupled physical-biogeochemical models (Nihoul, 1975; Nihoul and Djenidi, 1998), which cannot include all the spatial and temporal scales necessary to close the chasm.

In this paper, we address the theory behind marine physical-biogeochemical models, we expose some limits of the current models, and we propose a new approach. To make our point, we focus on the open ocean mixed layer and phytoplankton dynamics, which is at the base of the water column biogeochemistry (Legendre et al., 2018).

The distribution of plankton shows variability from the global scale down to the microscale (centimetric lengths) (Pinel-Alloul and Ghadouani, 2007; Prairie et al., 2012). Plankton patchiness at the mesoscale and sub-mesoscale is shaped by the interaction between biological growth processes and turbulent lateral stirring linked to upper ocean frontal eddies and currents (Martin, 2003; Mahadevan, 2016; Lévy et al., 2018). Lateral stirring and mixing alone cannot generate patchiness (Martin, 2003). A triggering mechanism is needed, and physics-driven processes affecting the vertical structure of the mixed layer (that is, on scales smaller than 100 m) may easily fulfill this role. This variability, in turn, is enhanced by biological processes such as the interplay between light and nutrient gradients, cell buoyancy adjustments, gyrotaxis, convergent swimming, and light-dependent grazing (Huisman et al., 2006; Durham and Stocker, 2011; Cullen, 2015; Moeller et al., 2019). The emerging very-high-resolution sampling techniques suggest that plankton remain patchy at the scales of one meter both in the vertical and in the horizontal (Foloni-Neto et al., 2016), and that homogeneity might not be reached even at the centimeter scales (Currie and Roff, 2006; Doubell et al., 2009; Foloni-Neto et al., 2016). As we shall illustrate in section 3, models assuming that biological scalars are homogeneously distributed at the fine and micro scales may easily incur serious biases.

Three classes of processes should be included to model marine biogeochemical processes: turbulent stirring, caused by fluid eddies, which displaces, stretches, and folds water volumes, increasing the gradients of the transported fields; irreversible mixing, caused by sub-microscale processes, which decreases these gradients; and growth (or decay) which changes the concentration of a field or a group of interacting fields by chemical or biological means. Even phenomena such as swimming/motility, grazing by zooplankton, and aggregate formation, are generally described as a combination of suitable transport, mixing and reaction processes. In principle, these processes must correspond to distinct terms in the equations resolved by numerical models.

In practice, when the model equations are solved on a digital computer, two broadly-defined formulations may be used to build a numerical model: the Eulerian and the Lagrangian. Each formulation binds the modeler to a set of approximations, briefly discussed below, which either blur the distinction between transport and irreversible mixing terms, or skip the latter altogether. As we shall illustrate throughout the rest of the paper, these approximations engender biases in the growth terms.

The majority of model applications mentioned above are Eulerian (Denman, 2003; Le Quéré et al., 2005; Vichi et al., 2007; Aumont et al., 2015). In this formulation, all three processes occur at the nodes of a fixed spatial grid, where all the relevant fields are located (**Figure 1A**). The biological variables are approximated as smoothly varying mean fields whose values at the grid nodes are representative of the average values in the grid cell (Vichi et al., 2007). An important feature of Eulerian models is that the unresolved turbulent stirring processes are assimilated to irreversible mixing. While this practice may achieve satisfactory results for non-reacting, passively transported tracers, it yields questionable, if not flawed, results for biological and chemical tracers, because it hopes that the biological response to the simulated Eulerian mean field is the same as the average response to the real, unresolved, patchy environment (Baudry et al., 2018; Paparella and Popolizio, 2018).

Other models use the Lagrangian formulation, which singles out either small portions of the fluid or individual biological agents, and follows them along their motion (**Figure 1B**). Despite their approximations (e.g., number of parcels insufficient to resolve all the fluid structures and use of stochastic processes to mimic turbulence), Lagrangian models describe stirring processes as such, rather than assimilating their effect to irreversible mixing. In plankton modeling, the Lagrangian formulation, originally identified with the term Lagrangian ensemble (Woods and Onken, 1982; Wolf and Woods, 1988; Woods et al., 1994; Woods, 2005), is often referred to as individual-based modeling (Cianelli et al., 2012). We argue that a clear distinction should be made between single cell Lagrangian models (Yamazaki and Kamykowski, 1991; Kamykowski et al., 1994), or agent-based models, in which the movement of a single individual is followed, but growth/death processes and cell division are not included, and Lagrangian ensembles (**Figure 1B**), where the super-individual concept (Scheffer et al., 1995) is used to describe the plankton population dynamics,

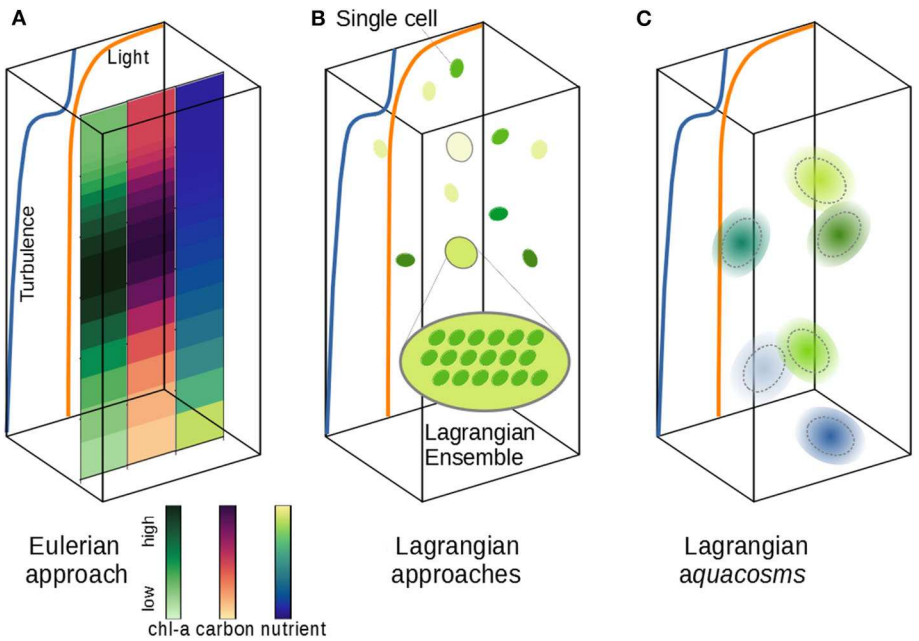

FIGURE 1 | Schematic of different phytoplankton modeling approaches. **(A)** The vertical distribution of phytoplankton carbon and chlorophyll can be simulated according to vertical nutrient and light gradients and a turbulent field. The Eulerian approach samples all active fields at the nodes of a fixed grid; fine and microscale stirring (turbulence) is modeled as irreversible mixing, wiping out fine, and microscale patchiness. **(B)** The Lagrangian Ensemble approach bundles individual cells into Lagrangian parcels; the number of organisms per parcel is modified by infra-parcel ecological interactions; unresolved turbulence is modeled as a stochastic motion of the parcels, which don't interact with each other. **(C)** The Lagrangian aquacosm approach tracks tiny Lagrangian water masses (*aquacosms*) moving as in **(B)**; biogeochemical interactions occur within aquacosms, which are permeable, thus allowing for mass exchanges between nearby aquacosms.

falling back to a description of biogeochemical processes based on interacting concentration fields.

Some authors have stated the superiority of the Lagrangian approach in describing plankton dynamics (Woods, 2005; Hellweger and Kianirad, 2007; Hellweger and Bucci, 2009; Baudry et al., 2018), because they allow the reconstruction of the life history of individual water parcels, and thus, ideally, of individual cells, tracking how they adapt to the local environment as the fluid moves. However, there are intrinsic limitations to applying the super-individual concept to the modeling of phytoplankton communities, because a Lagrangian ensemble is not conceived to exchange with surrounding ensembles any of the active agents that it carries (**Figure 1B**). Therefore, nearly all Lagrangian models (but see Dippner, 1998) neglect to include irreversible mixing processes. In the sporadic cases where Lagrangian and Eulerian formulations have been compared, this issue appears to have been overlooked (Wolf and Woods, 1988; Lande and Lewis, 1989; McGillicuddy, 1995; Kida and Ito, 2017; Baudry et al., 2018), even though it may lead to unrealistic, even paradoxical outcomes.

Consider a region of ocean with steady conditions, favorable for a phytoplankton bloom. Assume an initial random distribution dividing the fluid in very small patches, half devoid of phytoplankton, and the others at carrying capacity, which is the maximum phytoplankton biomass allowed by the system at those conditions. The ensembles of a Lagrangian model would mimic these patches, but, lacking any mutual interaction, plankton in those already at carrying capacity would never reach the nearby empty ones and trigger growth. The ensembles lacking phytoplankton would remain devoid of it, and the others would stay at the carrying capacity. The bulk concentration, computed as an average over all the Lagrangian ensembles, would indefinitely remain at one half of the carrying capacity: a baffling outcome given the favorable conditions! In an Eulerian model, irreversible mixing would quickly offset from zero the concentration of the empty nodes, triggering growth, so that the bulk concentration will eventually reach the carrying capacity. However, if the initial subdivision of empty and full patches were too fine to be resolved, then the amount of irreversible mixing computed by the Eulerian model would be a gross overestimation of the real one, which begs the question whether the modeled growth rate of the bulk concentration is realistic (Baudry et al., 2018).

Turbulent stirring, irreversible mixing, and growth are each associated to their own distinct time scales. For example, the celebrated Sverdrup model (Sverdrup, 1953) for the onset of phytoplanktonic blooms stems from the assumption that the growth time scale is slower than the stirring time scale. It is of extreme historical importance, and is the founding stone that all later bloom models have confronted, either to build on it, or to overthrow it (Fischer et al., 2014; Sathyendranath et al., 2015). It also has a peculiar feature: owing to its linearity, substituting stirring with irreversible mixing (if characterized by the same time scales as the stirring) leaves the results unchanged. As we

shall illustrate in the following, in the presence of non-linear biological terms, this equivalence is lost: in Sverdrup-like non-linear models, the separation between the time scales of stirring and of irreversible mixing determines the tempo and mode of the bulk phytoplankton growth. The proliferation of explanations for the occurrence of blooms, often distinct from each other by subtle details, may be a symptom of the lack of appreciation for a key theoretical issue: phytoplankton patchiness affects the bulk growth.

Occasionally, some attempts have been made to parameterize patchiness effects into Eulerian biogeochemical models. Realizing that the biological response is greatly affected by the treatment of the unresolved scales, authors like Fennel (Fennel and Neumann, 1996) have long proposed to use "effective" biological parameters. A time-delay parameterization was suggested for the case where patchiness is the result of oscillatory population dynamics occurring with different phases in different places (Wallhead et al., 2006). More recently, a closure parameterization was introduced, reminiscent of those used for turbulence (Mandal et al., 2016, 2019). Because the approach requires a truncated Taylor expansion of the non-linearities, it is formally valid only when the fluctuations are small, which high resolution chlorophyll profiles suggest is not the case (Doubell et al., 2014). Furthermore, it requires one additional equation for each pair of tracer variables, in order to track the evolution of their covariance, which may result in a substantial increase of the computational cost for some applications.

Overall, the bulk of the literature appears to overlook the issue, treating biogeochemical tracers in the same way as non-reacting ones.

We argue that the strategy of replacing unresolved transport with irreversible mixing, and then compensating the resulting biases by means of some parameterization, will face overwhelming difficulties. For example, different initial conditions, keeping everything else the same, may yield different bulk growth rates (Paparella and Popolizio, 2018) (an issue also noted in the early work on the plankton patchiness theory; Martin, 2003).

If turbulent stirring, irreversible mixing, and growth processes are modeled separately and independently from each other, then reproducing realistic phytoplankton dynamics in predictive models should become much easier. A class of Lagrangian methods recently proposed (Paparella and Popolizio, 2018) achieves this goal by depicting Lagrangian parcels as representing microscale-sized, homogeneous control volumes of water, rather than individual organisms or ensembles. In this framework, irreversible mixing processes are represented by exchanging small mass fluxes between nearby parcels. We call *aquacosms* such Lagrangian parcels subject to coupling fluxes (**Figure 1C**, section 2). The coupling is regulated by a parameter, p, whose value is proportional to the intensity of the fluxes. As we shall demonstrate, p sets the time scale associated with the irreversible destruction of biogeochemical variance at the microscales, which, in this approach, remains independent of the time scales of mechanical stirring. Results analogous to those of Lagrangian ensemble models are recovered for uncoupled parcels ($p = 0$). In the opposite limit, high values of p produce an excessive irreversible mixing, and yield results strongly resembling Eulerian simulations.

In the rest of the paper we shall build a hierarchy of models, from simple, idealized ones up to moderately realistic ones, to illustrate in detail the biases that Eulerian and Lagrangian ensemble models may generate in the presence of plankton patchiness, and the benefits of the aquacosm approach. Through the idealized models we identify two distinct mechanisms that generate and sustain patchiness in the biology, provided that transport and irreversible mixing are modeled as distinct processes. These findings reveal that irreversible mixing shapes the interaction between biogeochemical processes occurring at the microscales and larger scale transport processes. Building on these results, we use two simulations of an open ocean phytoplankton bloom, with parameters and forcings appropriate for the North East Pacific (PAPA station), and for the Southern Ocean sub-Antarctic Zone (SAZ), to illustrate that the same mechanisms are at work in the open ocean, affecting important parameters such as plankton patchiness, primary productivity and phenology of the bloom.

2. METHODS

Here we present all of the models that we shall use in the next section. In all cases, they describe a column of fluid in turbulent motion, where the only spatial dimension is the vertical (denoted by z). The complexity of the biological reaction term is progressively augmented although kept to a minimum level to better highlight the interplay between physics and biology.

We first present the Eulerian, eddy-diffusive formulation of each model, where turbulent transport is not explicitly resolved, and is instead parameterized as an eddy diffusivity term. At the end of the section we describe the aquacosm Lagrangian formulation, which represents turbulence as a stochastic vertical transport of fluid parcels, and explicitly allows for additional irreversible mixing of tunable intensity. When the intensity of irreversible mixing is reduced to zero, one recovers a standard Lagrangian ensemble model. In the paper we will use the term aquacosm to refer to interacting Lagrangian fluid parcels as shown in **Figure 1C**.

2.1. Idealized Eulerian Models

We begin with a simple turbulent dispersion model with no reaction term. Assuming homogeneity throughout the water column, the Eulerian, eddy-diffusive formulation describes the flow with the following diffusion equation

$$\frac{\partial C}{\partial t} = \frac{\partial^2 C}{\partial z^2} \tag{1}$$

where C is the concentration of a non-reactive substance dissolved in the fluid. The model is already written in non-dimensional units [see below, before Equation (5) for details]. We impose no-flux boundary conditions at the ends of the

water column $0 < z < 1$. We choose as initial condition the step function

$$C(z,0) = \begin{cases} 0, & z < 1/2 \\ 1, & z \geq 1/2 \end{cases}. \quad (2)$$

Next we consider a homogeneously turbulent water column carrying an idealized phytoplankton population subject to a logistic growth limited by the availability of light, whose intensity decreases as a function of depth. This is a generalization of the celebrated Sverdrup model of the onset of open-ocean blooms (Sverdrup, 1953). In dimensional units, the Eulerian, eddy-diffusive model is

$$\frac{\partial C}{\partial t} = \kappa \frac{\partial^2 C}{\partial z^2} + rf(z)C\left(1 - \frac{C}{K}\right) \quad (3)$$

where κ is the eddy diffusivity, assumed to be constant, and r is the maximum growth rate of phytoplankton, having concentration C and carrying capacity K. Zero-flux boundary conditions are imposed at both ends of the water column, that is at $z = 0$ and $z = \ell$. The non-dimensional function f quantifies the balance between light-stimulated growth, and loss of biomass due to respiration. Sverdrup defined it as

$$f(z) = e^{-\lambda z} - \frac{\mu}{r}, \quad (4)$$

where μ is a constant respiration rate, and λ is a measure of water transparency. Choosing ℓ as the unit of length, ℓ^2/κ as the unit of time, and K as the unit of concentration, Equation (3) takes the non-dimensional form:

$$\frac{\partial C}{\partial t} = \varepsilon f(z)C(1 - C) + \frac{\partial^2 C}{\partial z^2}. \quad (5)$$

The parameter $\varepsilon = r\ell^2/\kappa$ expresses the ratio of the turbulent and of the biological time scales (the former quantified through the eddy diffusivity as ℓ^2/κ). For $\varepsilon \ll 1$ the linearized version of this model reduces to the Sverdrup model.

2.2. The SAZ and PAPA Eulerian Models

We simulate open-ocean phytoplankton blooms at two distinct stations, intended to represent the North East Pacific and the Atlantic sector of the Southern Ocean. The chosen station locations are representative of two typical stratification regimes in the open ocean. Since we focus on the relationship between turbulence and light, the key distinguishing feature is the time evolution of the vertical water column structure. Weather station PAPA is located in the North-East Pacific (50°N, 145°W), and is characterized by mixing confined to less than 100 m with maximum cooling in March-April and the development of summer stratification between June and October. The PAPA station has been used in the literature to develop and analyze turbulence closure models (Burchard and Bolding, 2001; Reffray et al., 2015). We use a 1-D version of the NEMO physical ocean model with the parameterizations described in Reffray et al. (2015), implementing the generic length scale turbulence closure. The model is run with 75 vertical levels extending from the surface to the ocean floor and is forced by ECMWF ERA-interim reanalyses (Dee et al., 2011), to obtain hourly values of the eddy diffusivity required by the Eulerian and Lagrangian biogeochemical models. A similar model is used for the Sub-Antarctic zone of the Southern Ocean (SAZ), with the same vertical grid and same type of atmospheric forcing as in PAPA. This model site is ideally located in the Atlantic sector at 45°S 8°E, in similar light conditions as for PAPA. This region features deep mixing beyond 100 m between May and August and weak stratification during the Austral summer months.

To move forward from the logistic growth model used as an idealized case, we adopt a more realistic but still simplified version of the Biogeochemical Flux Model (Vichi et al., 2007). The chosen formulation tracks phytoplankton carbon concentration C, measured in mg m^{-3}, for a generic functional type of mid-sized diatoms, in which growth is only limited by light availability and an implicit temperature dependence is included in the parameter choice to account for the different oceanic regions.

The photosynthetic available radiation E_{PAR} is propagated according to the Lambert-Beer formulation

$$E_{PAR}(z) = \varepsilon_{PAR}\ Q_S\ e^{\lambda_w z + \int_z^0 \lambda_{bio}(z')dz'} \quad (6)$$

where Q_s is the net broadband solar radiation at the surface from ERA-interim (W m^{-2}), $\varepsilon_{PAR} = 0.4/0.217$ is the coefficient determining the fraction of photosynthetically-available radiation (converted to μE m^{-2}s^{-1} using the constant 0.217). Light propagation takes into account the extinction due to pure water λ_w (0.0435 m^{-1}) and to phytoplankton concentration λ_{bio}. The broadband biological light extinction is approximated to a linear function of the phytoplankton chlorophyll concentration L

$$\lambda_{bio} = cL \quad (7)$$

regulated by the specific absorption coefficient ($c = 0.03$ m^2 mg chl^{-1}). To be more comparable with the non-dimensional idealized experiments, the model neglects photoacclimation phenomena, therefore we assume

$$L = \theta_{chl}C \quad (8)$$

where the chlorophyll to carbon ratio θ_{chl} was taken to be 0.017 mg *chl* mg C^{-1} for PAPA and 0.013 for SAZ (Behrenfeld et al., 2005; Thomalla et al., 2017). The same results (not shown) were confirmed using the BFM acclimation model with variable chlorophyll, based on the Geider et al. formulation (Geider et al., 1997; Vichi et al., 2007). The carbon concentration rate of change is controlled by gross primary production, respiration and a crowding mortality term that parameterizes unresolved loss terms such as zooplankton grazing:

$$\dot{C} = rf^E C - bC - \frac{aC^2}{C_h + C} \quad (9)$$

where r is the maximum specific photosynthetic rate, b is the basal specific respiration rate, a is the specific crowding

mortality rate and C_h is the crowding half-saturation. Owing to the difference in the seasonal cycle of nutrients and water temperature, we use $r = 2$, $b = 0.16$, $a = 1$ days^{-1} for PAPA and $r = 0.5$, $b = 0.04$, $a = 0.25$ days^{-1} for SAZ. The lower realized growth rate in SAZ is due to the different mean temperature during the bloom period (see Equation (7) and (16) in Vichi et al., 2007). The other parameters are tuned to yield realistic values of chlorophyll at the study sites. In all cases we set $C_h = 12.5$ mg m^{-3}. The light regulating factor is defined as

$$f^E = 1 - \exp\left(-\frac{\alpha E_{PAR}}{r}\theta_{chl}\right) \tag{10}$$

where $\alpha = 1.38\,10^{-5}\ \mu\text{E}^{-1}\text{m}^2$ (Vichi et al., 2007).

The eddy-diffusive Eulerian version of this model is

$$\frac{\partial C}{\partial t} = \frac{\partial}{\partial z}\left(\kappa(z,t)\frac{\partial C}{\partial z}\right) + \dot{C}. \tag{11}$$

Starting from initial conditions having a small constant concentration, the runs extend for 4 years (each year repeats the same eddy diffusivity and radiation data). Except for the first year, in all models the results have negligible differences between the years.

2.3. Numerical Eulerian Scheme

All the Eulerian models in this paper are solved with an explicit, second-order finite differences scheme, with C and κ evaluated on staggered uniform grids. The depth of the simulated water column is one non-dimensional length unit for the idealized cases, and 200 m deep for the PAPA and SAZ simulations. In all cases the distance between consecutive grid nodes is 1/200 of the domain length. No-flux boundary conditions are imposed at the top and bottom of the water column. The eddy diffusivity κ is interpolated onto the uniform grid with the same B-spline interpolator used for the Lagrangian simulations (see below).

2.4. Lagrangian Aquacosm Simulations

A generic Lagrangian-ensemble water-column model is embodied by the following equations

$$dz_i = \frac{\partial}{\partial z}\kappa(z_i,t)\,dt + \sqrt{2\kappa(z_i,t)}\,dW_i \tag{12}$$

$$\begin{cases} \dot{c}_i^{(1)} &= f_1(c_i^{(1)},\ldots,c_i^{(m)},z_i,t) \\ &\vdots \\ \dot{c}_i^{(m)} &= f_m(c_i^{(1)},\ldots,c_i^{(m)},z_i,t) \end{cases} \tag{13}$$

where the index $i = 1,\ldots,N$ identifies the parcel having depth z_i, that performs a Brownian motion characterized by an eddy diffusivity κ, which may depend on depth and time t; W_i is a realization of the standard Wiener process. See Gräwe (2011) and Van Sebille et al. (2018) for a derivation of Equation (12). The quantities $c_i^{(1)},\ldots,c_i^{(m)}$ are the concentrations of the m scalar quantities describing the planktonic ecosystem (e.g., in the model of section 2.2, it would be $m = 2$, if we had modeled separately the dynamics of the concentration of phytoplankton carbon and chlorophyll) and the overlying dot denotes the time derivative. The functions $f_1,\ldots,f_m$ describe the reaction kinetics, where the dependence on depth and time accounts for the effect of light and its daily and seasonal variations, and for any other external forcing.

In the aquacosm approach we interpret the Lagrangian parcels as tiny control volumes. They should be thought of as minuscule aquatic mesocosms, which are carried by the ocean dynamics, and are homogeneous in their scalar content. This interpretation is shared with the Lagrangian-ensemble models, but, to avoid the issues discussed in the introduction, they are not isolated and exchange mass between nearby aquacosms (see **Figures 1B,C**). Following Paparella and Popolizio (2018), we define the mass fraction q_{ij} that the $i-$th aquacosm gives to the $j-$th aquacosm as

$$q_{ij} = \begin{cases} p\left(4\pi K_{ij}\Delta t\right)^{-1/2}\exp\left(-\frac{|z_i - z_j|^2}{4K_{ij}\Delta t}\right), & |z_i - z_j| < R \\ 0, & |z_i - z_j| \geq R \end{cases} \tag{14}$$

where R is an interaction radius, and the parameters p and the symmetric matrix K are defined below. At intervals of time Δt, we update the concentrations carried by each parcel as

$$c_i^{(l)} \longleftarrow c_i^{(l)} - \sum_{j=1}^{N} q_{ij}c_i^{(l)} + \sum_{j=1}^{N} q_{ji}c_j^{(l)}, \quad l = 1,\ldots,m \tag{15}$$

for all the scalars $l = 1,\ldots,m$. The first sum represents the mass fraction that leaves the $i-$th aquacosm and is redistributed to all the other aquacosms, and the second sum, conversely, represents an equal mass fraction received by the $i-$th aquacosm from all the others (note that $q_{ij} = q_{ji}$). The received mass fraction is composed of many distinct parts, each carrying the concentration of the scalars contained in the acquacosm of provenance. These parts immediately and irreversibly homogenize with the remaining content of the $i-$th aquacosm in order to determine its new concentration values. The constant p is a free parameter, which in this one-dimensional formulation has the dimensions of a length, but in three dimensions would be a volume, that can be used to tune the coupling strength between the aquacosms (choosing $p = 0$ is equivalent to isolating the parcels as in a Lagrangian ensemble model). The variance K_{ij} of the Gaussian kernel coupling the $i-$th and $j-$th aquacosms is chosen on the basis of the eddy diffusion coefficient as

$$K_{ij} = \min\left\{\kappa(z_i,t),\ \kappa(z_j,t)\right\}. \tag{16}$$

The choice of the minimum is dictated by the observation that there is very little flux across a region where the eddy diffusivity jumps from very small to very high values, e.g., at the base of the mixed layer. In order to allow for an efficient numerical implementation, the coupling between aquacosms further apart than the interaction radius R must be zero. This algorithm conserves mass and avoids the creation of spurious maxima

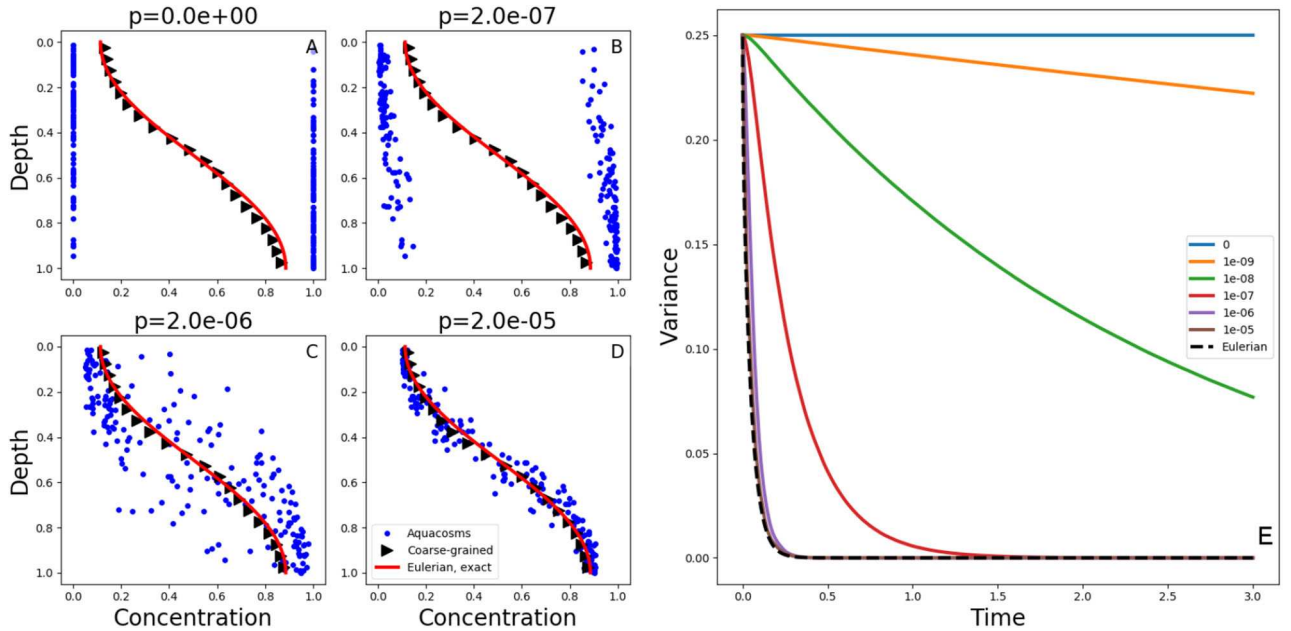

FIGURE 2 | (A–D) Exact solutions at time $t = 0.05$ of the diffusion Equation (1) with the initial condition (2) and no-flux boundary conditions (red lines). The blue dots show the position and the concentration of the aquacosm simulations with the same diffusivity and varying coupling strength p. The black triangles are a coarse-grained version of the same data, obtained with a Gaussian kernel estimator with standard deviation 0.1 (see section 2). **(E)** variance, as a function of time, in Lagrangian aquacosm simulations with varying coupling strength p (solid lines) and variance of the exact solution of the Eulerian problem (1) (dashed line).

and minima (Paparella and Popolizio, 2018), provided that the parameters are chosen so that, for all $i = 1, \ldots, N$, it is

$$\sum_{j=1}^{N} q_{ij} \leq 1. \tag{17}$$

Roughly speaking, one may think the aquacosms as oozing out part of their content into Gaussian clouds spreading at a rate specified by the eddy diffusion coefficient (**Figure 1C**). Then, at regular intervals of time Δt, all the material within a control volume (both what was left inside the volume, and what came from the overlapping clouds) is instantaneously and irreversibly homogenized, thus determining the concentrations which will evolve according to (13) for the next interval of time Δt. A conceptually similar technique describing advection-diffusion processes as the interleaving of short time intervals of pure transport alternated with instantaneous irreversible mixing events has already been successfully used to model mixed layer dynamics (Ferrari and Young, 1997). These sort of modeling procedures have their justification rooted in the fractional step method for the numerical solution of differential equations. From a different point of view, we should note the similarity between the aquacosm approach and the so-called tanks-in-series model, popular in chemical and environmental engineering (see e.g., Levenspiel, 2011, Chapter 8). The main difference is that, in that case, the topology of the interconnections between tanks does not change in time, while here the existence of a flux connecting two aquacosms depends on their relative position.

All Lagrangian results presented in this paper use 200 aquacosms. Equations (12) and (13) were integrated using, respectively, Milstein's and the midpoint methods (Gräwe, 2011; Van Sebille et al., 2018), with a time step $\Delta t = 10^{-5}$ non-dimensional time units for the idealized cases of **Figures 2–4** and $\Delta t = 5$ s for the PAPA and SAZ cases. The eddy diffusivity κ used in Equations (12) and (16) is the same as that of the corresponding Eulerian model. In particular, the eddy diffusivity for the PAPA and SAZ simulations are generated by the NEMO ocean model as described in section 2.2, and are interpolated at the position of the aquacosms with monotone B-splines (Ross and Sharples, 2004). In these two simulations the reaction terms (13) reduce to (9). Reflecting boundary conditions are imposed at both ends of the water column on all Lagrangian simulations. The interaction radius in Equation (14) is $R = 0.05$ non-dimensional units for the idealized cases and $R = 10$ m for the PAPA and SAZ simulations.

In the following, the amount of patchiness present in the various models is evaluated and visualized by showing the fluctuations around local averages, which we call coarse-grained profiles, and are obtained by smoothing the concentrations with a Gaussian kernel estimator (Gräwe, 2011) having a standard deviation of 1/20 of the domain for the idealized cases and 2.5 m for PAPA and SAZ, or as otherwise specified in the figure caption. As it is customary for fields transported by turbulence, we also quantify such fluctuations by evaluating the variance of the concentration field (see e.g., Warhaft, 2000 for more

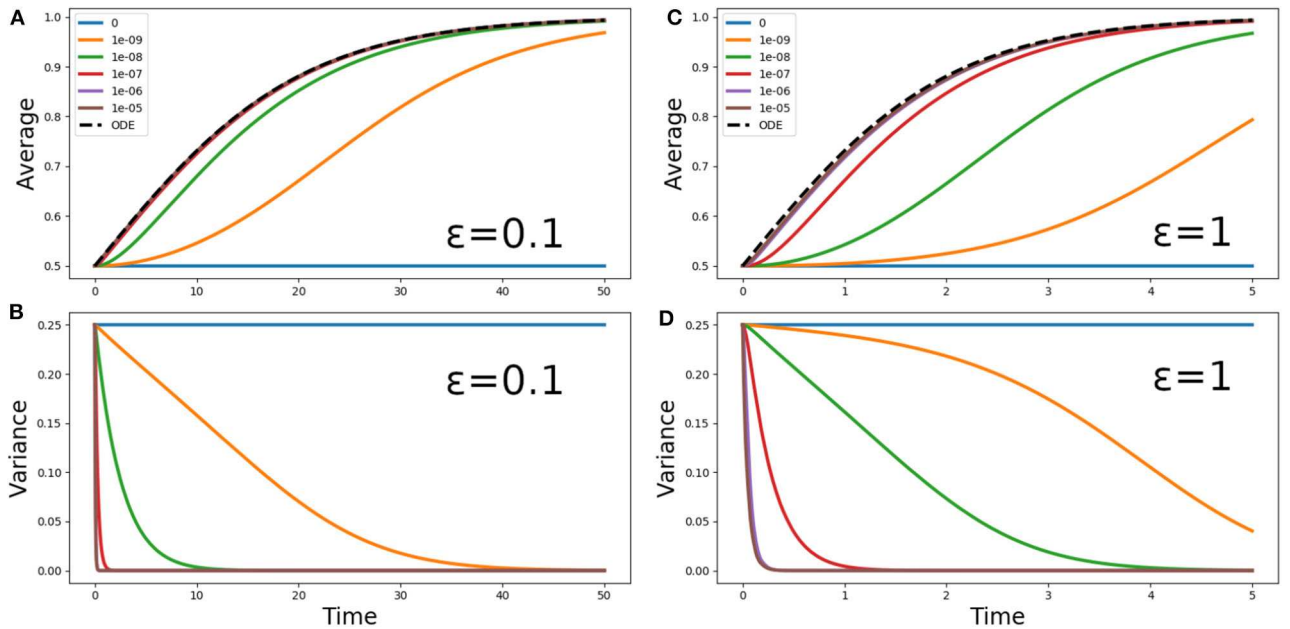

FIGURE 3 | (A,C) Average phytoplankton concentration and **(B,D)** variance, as a function of time, for the problem (5) with $f(z) = 1$, $\varepsilon = 0.1$ **(A,B)** or $\varepsilon = 1$ **(C,D)** and the step initial condition (2). The solid lines refer to Lagrangian aquacosm simulations with varying strength of the coupling parameter p. The dashed line is the solution of the Sverdrup's approximation (18). Note the different ranges of the time axes.

details). In the Eulerian formulation the variance is defined as $\langle (C - \langle C \rangle)^2 \rangle$, where the angular brackets denote an average over the whole water column. In Lagrangian models, the variance of the concentration field is estimated just by computing the variance of the concentration values carried by each parcel.

3. RESULTS

3.1. Pure Stirring and Mixing

First, we shall consider the case of turbulent stirring and mixing of a substance not subject to any reaction (section 2.1). The Eulerian formulation of this problem is given by Equation (1). The aquacosm formulation uses $\kappa = 1$ in Equations (12) and (16), and no reaction terms.

Figures 2A–D show the concentration and position of the aquacosms for different values of the coupling parameter p, together with the analytical solution of Equation (1). The Brownian motion scrambles the order of fluid parcels initially arranged as to produce the step-like initial condition (2), and this produces patchiness: a random alternation of parcels with high and low concentration values. Irreversible mixing equalizes the concentration of nearby parcels, thus removing patchiness, more and more effectively as the coupling strength p increases. Local weighted averages of the Lagrangian result (black triangles, see section 2), are essentially identical to the analytic solution of the Eulerian model. This coincidence might suggest that the Eulerian and all of the Lagrangian models are equivalent. The coarse-graining process of taking local averages, however, gives only a partial picture. **Figures 2A–D** do not depict equivalent microphysics. The concentration carried by the individual parcels (which, ultimately, is all that matters for the reaction terms when they are present) is vastly different in the four cases. The amount of irreversible mixing, set by the parameter p, determines how quickly the fluctuations around the local averages are dissipated, that is, p sets the time scale associated to irreversible mixing processes. We note that, on rearranging the position of the parcels without changing their concentration, the variance shown in **Figure 2E** remains the same (variance is invariant with respect to permutations). Therefore, in the special case $p = 0$, that is, when aquacosms are uncoupled and each maintains its initial concentration, the variance remains constant in time, and equal to the variance of the initial condition, even though the local averages still tend to uniformity, as prescribed by (1). The reason is that the Brownian motion (or the turbulent stirring in an actual turbulent water column) eventually produces such a fine interleaving of nearby parcels with vastly different concentrations, that upon averaging those fluctuations cancel out (**Figure 2A**). When $p > 0$ then the irreversible mixing [in the present model represented by mass exchanges between nearby aquacosms as in Equations (14) and (15)] damps the difference in concentration between nearby regions of the fluid, and thus reduces the variance, which becomes a decreasing function of time (**Figure 2E**). As the amount of irreversible mixing increases (that is, for increasing values of p) the decrease of fluctuations, and thus of the variance, becomes quicker. For sufficiently large values of p the variance decays just as quickly as in the Eulerian, eddy-diffusive case, where stirring is all assimilated to irreversible mixing.

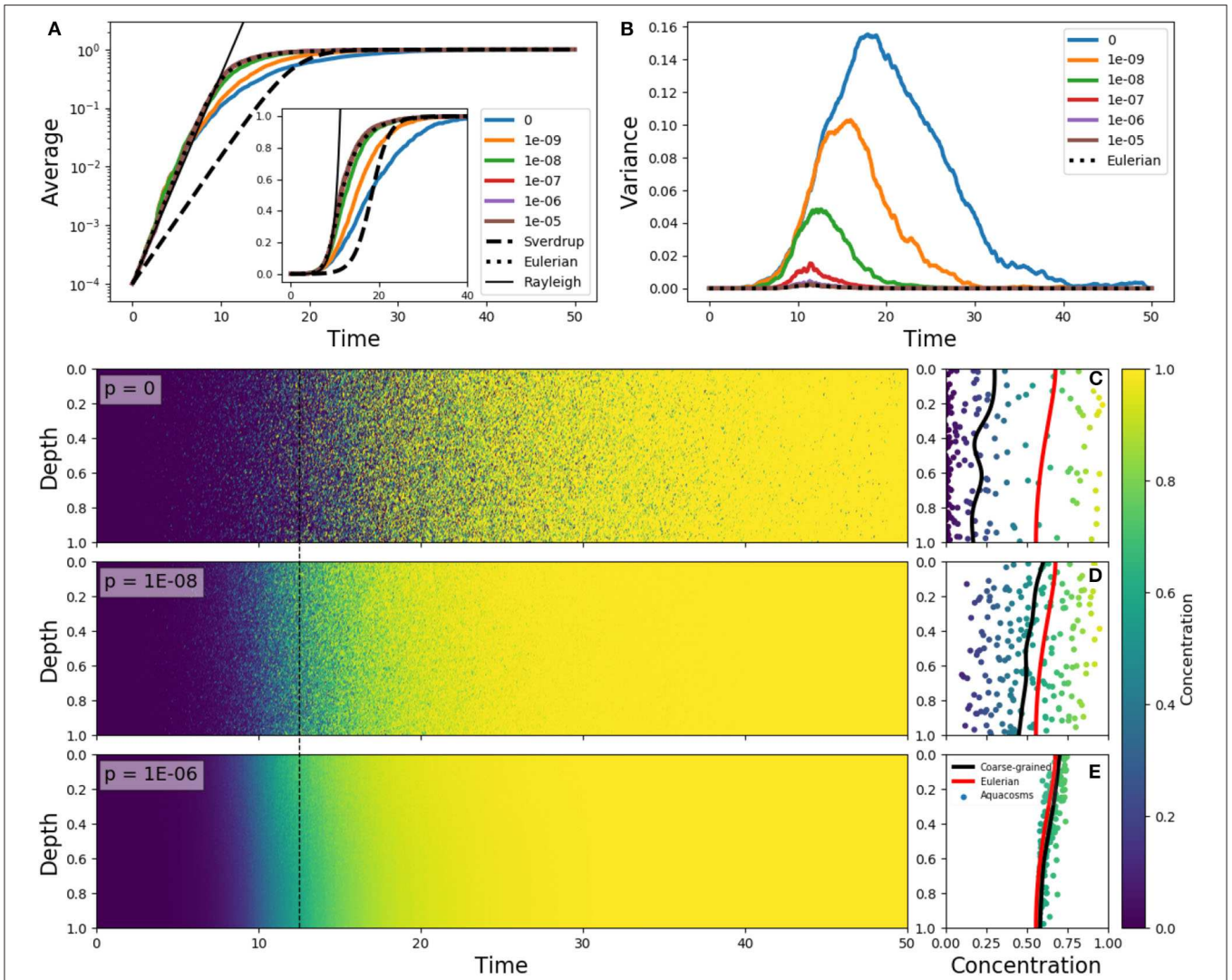

FIGURE 4 | (A) Average phytoplankton concentration and **(B)** variance as a function of time, for the Eulerian problem (5) with $f(z) = e^{-z/0.15} - 0.1$, $\varepsilon = 10$ and constant-in-space initial condition $C(z) = 10^{-4}$ (dotted lines). The solid lines in color refer to Lagrangian aquacosm simulations with the same parameters, with varying coupling strength p. The dashed line is the solution of Sverdrup's approximation (18). The thin black line is an exponential growth with a rate estimated by means of the Rayleigh quotient (section S2 in Supplementary Material) associated to Equation (5). The inset shows the same data as **(A)** but with a linear, rather than logarithmic, vertical axis. (Lower panels) Plankton concentration as a function of depth and time for Lagrangian simulations with $p = 0, 10^{-8}, 10^{-6}$. **(C–E)** concentration and depth of the aquacosms (dots), coarse-grained concentration of the aquacosms (black line) and numerical solution of the Eulerian model (red line) at the time marked by the dashed black line in the left panels.

3.2. Sverdrup's Model Expanded

3.2.1. Fast Turbulence, Homogeneous Light

Next we shall consider Equation (5), which is a very simple model of light-limited growth. If the time scale of turbulent overturning is much faster than the time scale of biological growth, that is for $\varepsilon \ll 1$, following Sverdrup (Sverdrup, 1953), one can argue that physics and biology disentangle: first turbulence makes the initial condition vertically homogeneous, in a coarse-grained sense, within a transient no longer than $O(1)$, and keeps the concentration C independent of depth at all later times. Then, on $O(\varepsilon^{-1})$ time scales, the vertically constant concentration changes in time according to the ODE

$$\dot{C} = \varepsilon I\, C(1 - C) \tag{18}$$

where I is the integral over the water column of the function f that appears in Equation (5) (see **Supplementary Material S1**), and the dot denotes a derivative with respect to time. Sverdrup's approximation does not require a specific form of the function f, but holds for any integrable f sandwiched between $O(1)$ bounds. The comparison with eddy-diffusive, Eulerian numerical simulations shows that in practice this approximation gives good results up to $\varepsilon \approx 1$.

The aquacosm formulation of this problem uses $\kappa = 1$ in Equations (12) and (16). The only reaction term in Equation (13) coincides with the reaction term of Equation (5).

As it should be clear from the previous subsection, reaching coarse-grained homogeneity implies having reached homogeneity at all scales in an eddy-diffusive Eulerian model, but not necessarily in a Lagrangian one (nor in the real world). This discrepancy leads to question the equivalence of the eddy-diffusive Eulerian and of the Lagrangian formulations (Lande and Lewis, 1989; McGillicuddy, 1995). We show here, and demonstrate analytically in section S1 of the Supplementary Materials, that for the linear Sverdrup model the two approaches yield the same averages, but non-linear reaction terms break down the equivalence.

Figure 3 shows the phytoplankton concentration mean and variance as a function of time for Equation (5) and its aquacosm counterpart, with $f(z) = 1$, the initial condition (2), and two values of the ratio $\varepsilon = 0.1$ and $\varepsilon = 1$. As sketched in the introduction, because all fluid parcels are initially set at a fixed point of the reaction terms (namely, half of them at $C = 0$ and the other half at $C = 1$, the value of the carrying capacity), with uncoupled aquacosms ($p = 0$) the mean unrealistically remains at one half of the carrying capacity despite the positive growth rate. When the coupling between the aquacosms is switched on, the mean gradually tends to the carrying capacity ($C = 1$) and the variance tends to zero. The rapidity with which the asymptotic values are approached depends on the strength of the coupling parameter p: high values produce results that behave just as predicted by Sverdrup's theory, but small ones produce growth curves that are nothing like the solution of the ODE associated with the reaction term.

3.2.2. Slow Turbulence, Inhomogeneous Light

The examples so far show that the fast stirring of a step-like initial condition produces patchiness, which then affects the bulk growth rate. Much attention has been given to the case of non-homogeneous biological growth [e.g., using the form (4) for $f(z)$] when growth is faster than stirring. Then, according to the critical turbulence theory (Huisman et al., 1999; Taylor and Ferrari, 2011; Ferrari et al., 2015), phytoplankton closer to the surface contributes to the overall growth more than Sverdrup's theory would provide for, so that a bloom may initiate even when the average light would not allow for that. Differences in light history and acclimation have also been affirmed to produce growth when Sverdrup's theory would predict decay (Lande and Lewis, 1989; Woods et al., 1994; Esposito et al., 2009). What has not been stressed is that these conditions would also naturally lead to the creation of patchiness if irreversible mixing processes are not fast enough to remove it. When growth is faster than turbulent stirring, then the phytoplankton in water parcels at shallow depth will have time to grow substantially more than that in the deeper parcels spending some time in darkness. As stirring makes some of the shallow parcels sink and replaces them with some of those that were at depth, then microscale patchiness ensues. Just as in the case of a step-like initial condition, patchiness affects growth. As the bloom progresses, water parcels having spent the most time close to the surface reach the carrying capacity before the others, and the rapidity of the bulk growth becomes regulated by the intensity of the irreversible mixing, which transfers the phytoplankton from high to low concentration parcels.

This process is illustrated in **Figure 4** for different degrees of the coupling between aquacosms. In the initial linear regime, when phytoplankton concentration is much smaller than the carrying capacity, the Eulerian model (5) and all the Lagrangian models show the same growth rate of the bulk concentration (**Figure 4A**), which is in excess of what Sverdrup's theory would dictate. This is in agreement with the critical turbulence prescriptions as long as the process is linear (see section S2 of Supplementary Materials for a demonstration). In the non-linear regime, the Lagrangian models yield distinct results: with small coupling strength, variance grows with time (**Figure 4B**), and this leads to bulk growth significantly slower than in the eddy-diffusive Eulerian model, due to the patchy environment. Once again, destroying the variance by using a strong enough coupling parameter recovers the results of the Eulerian model. **Figures 4C–E** shows that variance genuinely corresponds to patchiness: with low p, aquacosms of starkly different concentration are found next to each other, and the coarse-grained equivalence of Lagrangian and Eulerian models is lost. Depending on the degree of irreversible mixing, the non-linear reaction terms lead to small-scale patchiness and substantially different time evolution of the mean phytoplankton concentration in a vertically non-uniform, slow turbulence environment.

3.3. Microscales and Phytoplankton Phenology

To demonstrate in a realistic setting how phytoplankton growth and phenology are affected by patchiness arising from the mechanisms identified in sections 3.2.1 and 3.2.2, we run the PAPA and SAZ models defined in section 2.2, using both the eddy-diffusive Eulerian and the aquacosm Lagrangian formulations.

Figure 5 shows the simulated average chlorophyll content at PAPA station over the first 50 m of water column in the weeks when the bloom starts. We define the onset of the bloom as the first day of the year when the chlorophyll content exceeds the median plus 5% of the daily chlorophyll concentration tracked over 1 year (Racault et al., 2012). Reductions of the coupling strength p delay the onset by over 2 weeks. The results diverge from each other before the onset of stratification, from mid April until the beginning of May, when the mixed layer depth is $\ell \approx 100$ m (**Figure S1**) and the typical mixed layer eddy diffusivity is $\kappa \approx 0.05\ \mathrm{m^2 s^{-1}}$, yielding a value of $\varepsilon \approx 5$ with the growth rate $r = 2\ \mathrm{days^{-1}}$. This suggests that we are witnessing the same process illustrated in **Figure 4**, where slow turbulence, a vertical light gradient, and low irreversible mixing lead to the formation of high microscale patchiness, reducing bulk growth and delaying the bloom. The Lagrangian model without any coupling ($p = 0$) shows the slowest growth, but this limit case is unrealistic, as demonstrated above. In the following 15 days the mixed layer becomes much shallower (**Figure S1**), with typical eddy diffusivity values of $\kappa \approx 0.025\ \mathrm{m^2 s^{-1}}$. The time scales of

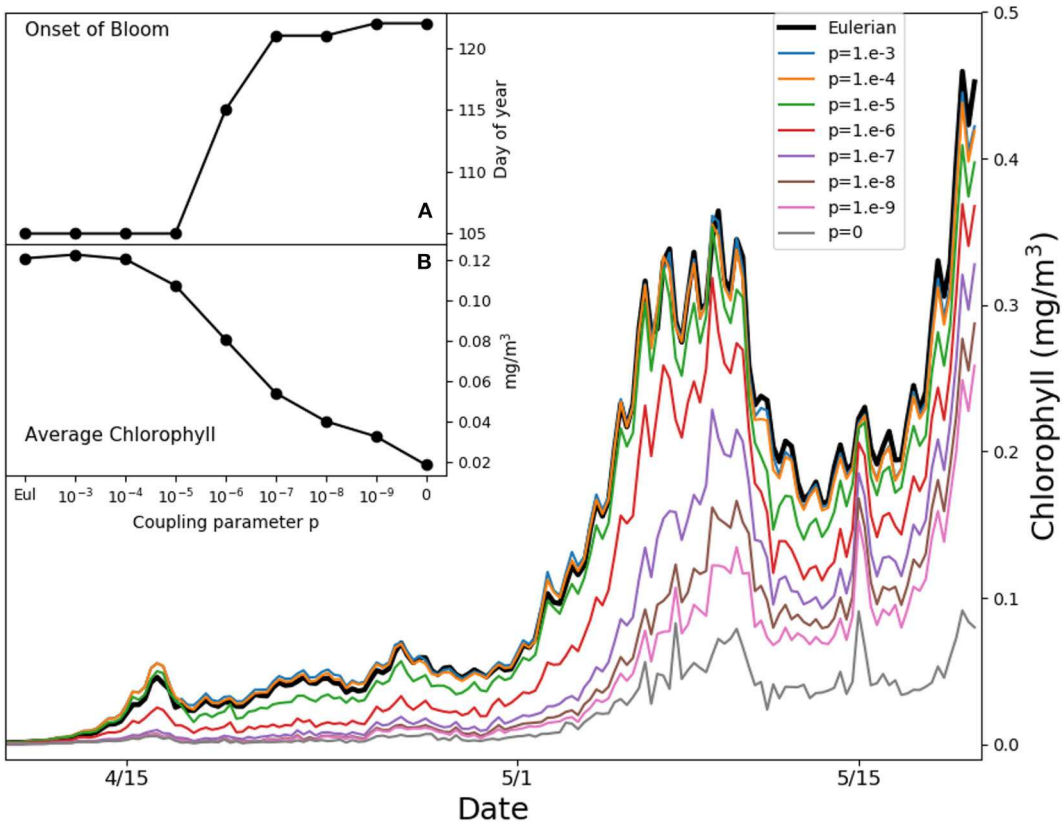

FIGURE 5 | Average chlorophyll in the first 50 m of water column for the simulated Ocean Station PAPA in the North-West Pacific. Thin colored lines refer to aquacosm simulations coupled with varying strength p. The thick back line refers to the eddy-diffusive Eulerian model. Inset **(A)** shows the day of the onset of the bloom (see main text); inset **(B)** shows the average chlorophyll in the period April 15th to May 15th, both of them plotted as functions of the coupling parameter.

growth and stirring become comparable, and the vertical light gradient ceases to be a source of patchiness. Only the entrainment of phytoplankton-poor aquacosms at the base of the mixed layer continues to be a source of patchiness. Overall, the chlorophyll content averaged over the month of the bloom initiation changes by as much as a factor 6 depending on the coupling strengths (inset B in **Figure 5**).

Next, we simulate the open ocean of the sub-Antarctic zone (SAZ), characterized by a mixed layer deeper than 100 m from July to October (**Figure S2**). Throughout the year, typical simulated eddy diffusivity values in the mixed layer are $\kappa \approx 0.06$ m^2s^{-1}, corresponding to $\varepsilon \approx 1$. Here, growth is never faster than stirring, and Sverdrup's approximation holds. Therefore, only the intermittent deepening of the mixed layer, which scoops phytoplankton-free aquacosms from the depths, contributes to the creation of patchiness in the mixed layer. In the days immediately after a sudden deepening of the mixed layer, the dynamics is reminiscent of that shown in **Figures 2**, **3**, whereby a step-like initial condition first breaks down into patchiness and then is brought to vertical homogeneity with a speed determined by the intensity of the irreversible mixing. The smaller is the mixing, the slower is the destruction of variance, and the slower is the bulk growth of phytoplankton (**Figure S2**). The phenological and productivity differences are not as marked as in the PAPA simulations, but we note that coarser resolution climate models with a larger impact of irreversible mixing are likely to generate greater differences and discrepancies in the bloom phenology (Hague and Vichi, 2018).

3.3.1. Comparison With BGC-Argo Float Observations

Recent bio-optical measurements using BGC-Argo floats from sub Antarctic zones (Carranza et al., 2018) reported the presence of substantial chlorophyll variance within the hydrographic mixed layer. This was interpreted as the signature of vertical gradients of chlorophyll at the fine scales (tens of meters), which called for some mechanism incompatible with the presence of strong turbulence. In particular, it was argued that periods of storm quiescence associated with slacking turbulence would occasionally leave the mixed layer homogeneous in density, but stirred only in its uppermost part, thus allowing for light-modulated growth below the turbocline (the base of the uppermost layer), generating a vertical gradient of chlorophyll.

In our models, slacking turbulence and vertical gradients of light definitely produce vertical gradients of chlorophyll, even when stirring is modeled as irreversible mixing (see e.g., the Eulerian simulation profiles in mid April and end of May in

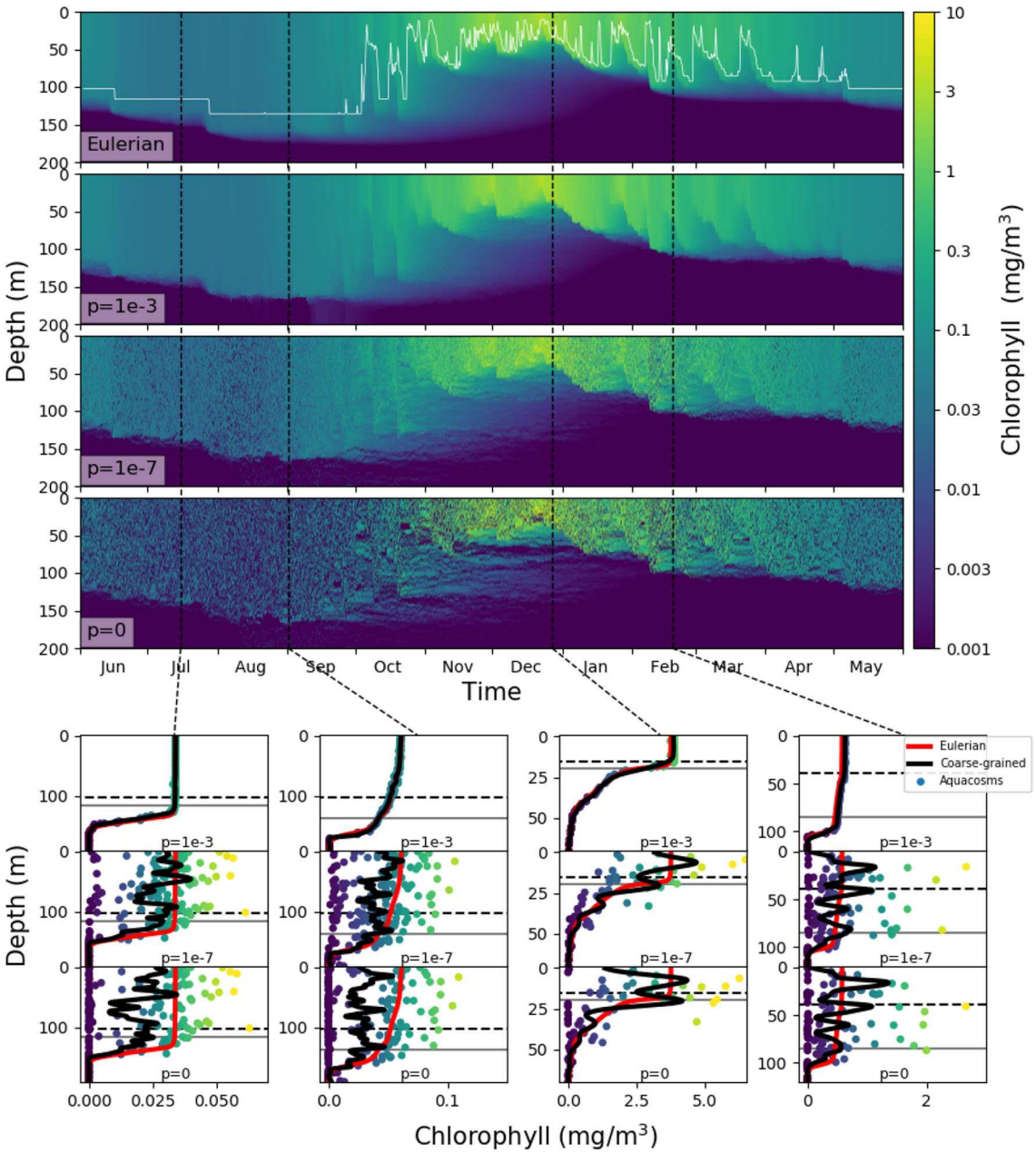

FIGURE 6 | Top four panels: chlorophyll in the SAZ simulation in logarithmic units. The top panel shows the eddy-diffusive Eulerian model, and the thin white line marks the mixed layer depth; the next three show the aquacosm simulations for $p = 10^{-3}, 10^{-7}, 0$. The lower panels show, as a function of depth, the chlorophyll content in mg/m^3 of the aquacosms (dots) for different values of p, their coarse-grained version (black line, see section 2), the mixed layer depth (horizontal gray line) and the turbocline depth (horizontal black dashed line) at the date marked in the upper panels by the vertical black dashed lines. For comparison, the chlorophyll concentration as a function of depth computed with the Eulerian simulation (red line) is repeated in all the panels corresponding to the same date.

Figure S1), and effects which our models neglect, such as light-dependent grazing, may greatly enhance these gradients (Moeller et al., 2019). However, in the models where irreversible mixing is weak, patchiness, rather than these vertical gradients, is the dominant source of variance in the mixed layer. Patchiness is visually evident in the bottom panels of **Figure 6**. At lower values of p, very large relative differences in the chlorophyll content of nearby aquacosms are normal even above the turbocline. This extreme variability is quantified in **Figure 7A** (see **Figure S3A** for the PAPA simulations), showing the monthly average of the coefficient of variation of chlorophyll (ratio of the standard deviation and the mean) computed above the turbocline depth, thus excluding the effects of slacking turbulence. In simulations with moderate and low irreversible mixing, the coefficient of

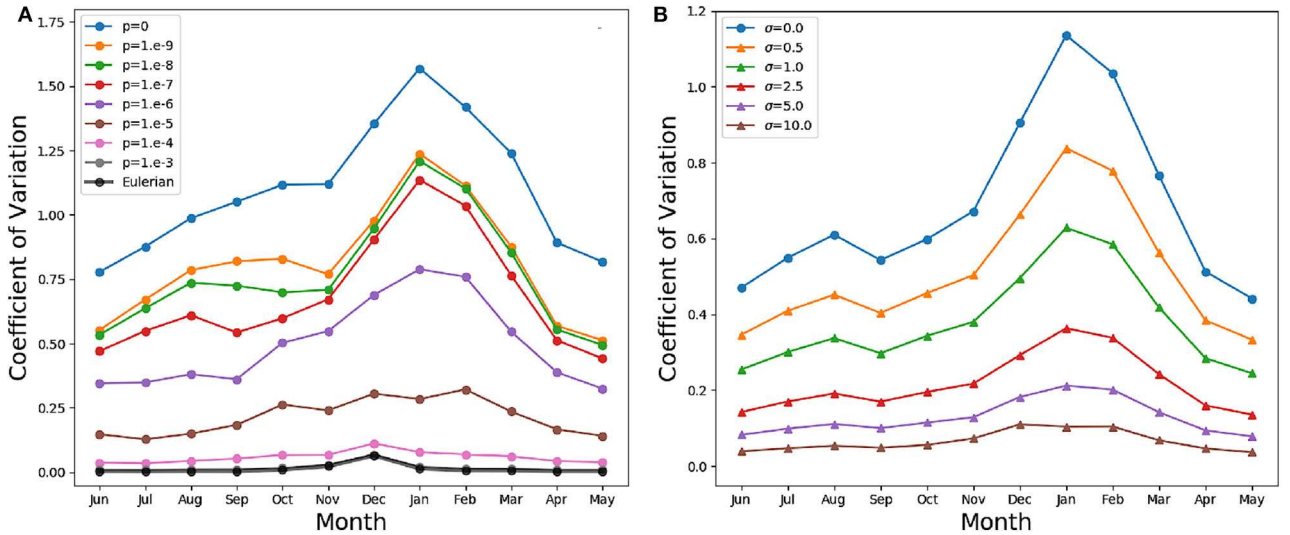

FIGURE 7 | (A) Monthly average coefficient of variation (standard deviation over mean) of the chlorophyll above the turbocline depth in the SAZ simulation. A value of 0 indicates homogeneity, while a value of 1 implies departures from the vertical mean that are as large as the mean itself. The thin lines in color refer to the Lagrangian aquacosms with different values of the coupling parameter p. The thick black line refers to the eddy-diffusive Eulerian simulation. **(B)** Monthly average coefficient of variation of the Lagrangian simulation with $p = 10^{-7}$, and the same quantity computed from profiles coarse-grained using a Gaussian kernel estimator with standard deviation $\sigma = 0.5, 1, 2.5, 5, 10$ m. The line $\sigma = 0$ refers to the results without coarsening.

variation is never negligibly small, and even when the mixed layer is deepest and the turbulence is strongest, it doesn't drop below about 0.5. As expected, the variability is larger during the Austral summer months, when turbulence is weaker than in other seasons, showing an extended peak from spring to autumn, in full agreement with the variability observed through autonomous observations in the SAZ (Little et al., 2018). In the Eulerian simulation, and in Lagrangian simulations with very strong irreversible mixing, the peak is small and occurs in December, when the mixed layer is the shallowest, while the coefficient of variation remains negligibly different from zero in other months.

These results, for $p = 10^{-6}$ or lower, bear a strong resemblance to the statistics of the BGC-Argo float observations in the Southern Ocean (Figure 6 in Carranza et al., 2018), but suggest that, rather than by external forcing, chlorophyll variability is mostly caused by differences in the Lagrangian histories of water parcels (Kida and Ito, 2017; Baudry et al., 2018) but modulated by irreversible mixing. We remark that BGC-Argo floats are not high-resolution chlorophyll profilers (Carranza et al., 2018), and can't accurately represent vertical fluctuations on scales smaller than a few meters. The black lines in the lower panels of **Figure 6** have been computed from the aquacosm concentration using a smoothing procedure yielding 5 m of resolution (see section 2), thus comparable with that of the floats. Chlorophyll fluctuations are damped, but not completely wiped out. The resolution length scale of observations affects variance estimations, as found when high-frequency sampling instruments are used (Little et al., 2018). In **Figure 7B** (**Figure S3B** for PAPA) we show the monthly average of the coefficient of variation of the simulation data relative to $p = 10^{-7}$, after they underwent this coarse-graining procedure at several resolutions. Extreme smoothing yields estimates of fluctuations not far from those of the Eulerian simulations, which progressively increase as the resolution increases. Thus, albeit the BGC-Argo data are surprising in the amount of variability that they show, we suspect that this is still an underestimation of the reality.

4. DISCUSSION AND CONCLUSION

When considering mesoscale, and, more recently, submesoscale dynamics, it has often been stressed that the joint effect of turbulent stirring and non-linear biochemical processes must produce an uneven, patchy distribution of active tracers, and this, in turn, may affect the bulk productivity and structure of oceanic ecosystems (see Martin, 2003; Levy and Martin, 2013; Mahadevan, 2016; Lévy et al., 2018 and references therein). Here we remark that the fundamental idea expressed in those studies should also be scrutinized at smaller scales, e.g., across the water column.

We do so by contrasting the results obtained with the eddy-diffusive, Eulerian formulation and the aquacosm Lagrangian formulation for water-column models of increasing physical and biological complexity. We demonstrate in sections 3.2 and 3.3 that, in the presence of non-linear reaction terms, a discrepancy between the Lagrangian and the Eulerian formulations arises because the latter postulates the equivalence of stirring and irreversible mixing, wrongly implying that the time scales of these two processes are the same. As a consequence, a water parcel devoid of plankton and one full of plankton would equalize their concentration within the stirring time scale. When stirring

and mixing are treated as separate processes, with the second allowed to be slower than the first, parcels lacking plankton are constantly seeded by the full ones, and the overall rate of growth is determined by a delicate interplay of biological processes, turbulent stirring and irreversible mixing. These findings lead to an important conclusion: in a generic non-homogeneous environment with concurrent stirring, mixing and growing, there is no reason to expect that the bulk phytoplankton concentration is described solely by the ODE associated with the reaction terms.

In order to illustrate how this delicate interplay occurs in a realistic situation, we focused on the specific problem of the onset of open-ocean blooms. There exists a very large body of literature on this decades-old subject. Some of this literature tackles the problem of how different turbulence properties affect biological growth. Yet the distinction between the time scales of turbulent stirring and the time scales of irreversible mixing is never considered. In spite of mounting evidence of ubiquitous presence of patchiness in the vertical direction across the mixed layer (Currie and Roff, 2006; Doubell et al., 2009, 2014; Foloni-Neto et al., 2016), theories of the onset of the bloom freely interchange turbulent stirring and irreversible mixing as if they were one and the same thing (see the recent review Fischer et al., 2014 and references therein). On the other hand, most of the literature on mixed layer plankton patchiness (Huisman et al., 2006; Durham and Stocker, 2011; Cullen, 2015; Moeller et al., 2019) focuses on unveiling the underlying mechanisms but does not investigate how patchiness contributes to signal at larger scales and how it should be included in predictive models.

In the present work we identified two simple and distinct mechanisms that create patchiness vertically in the mixed layer. The first mechanism, and the dominant one at SAZ, is essentially physical: when deeper, phytoplankton-poor water is entrained by turbulence into the phytoplankton-rich mixed layer, rapid mechanical stirring produces a highly patchy water column. The second mechanism requires the existence of a depth-dependent growth/decay process (e.g., due to the vertical gradient of light) acting on time scales faster than the stirring time scales. When this occurs, such as during spring at PAPA, the uneven growth at different depths creates a vertical gradient of the active tracers, which breaks down into patchiness under the action of stirring.

Eulerian models that replace unresolved stirring with irreversible mixing can't generate any patchiness from either of these mechanisms. Lagrangian ensemble models produce patchiness through both mechanisms, but their inability to represent irreversible mixing processes may lead to paradoxical results. Our aquacosm modeling framework extends the Lagrangian approach and incorporates irreversible mixing by allowing for locally interacting parcels.

The aquacosm approach appears to be preferable because, by design, the reaction terms are representative of the biogeochemical dynamics occurring in a very small, homogeneous water mass, therefore, they can effectively include empirical reaction norms derived from laboratory experiments and can retain the relationship with the environmental drivers as they were originally measured (Boyd et al., 2018). In contrast, the biological rates present in Eulerian models should always be considered as "effective" values, representative of aggregate bulk dynamics, which is not immediately comparable with laboratory experiments, or *in-situ* samplings.

Obviously, our PAPA and SAZ simulations should not be taken as an operational model for those two stations. In order to allow for a direct, quantitative comparison with the observed data throughout the year, the biological formulation should be expanded to include grazing, nutrients, remineralization, and, possibly, multiple phytoplankton functional groups, as well as data assimilation and formal, station-specific, parameter optimization procedures (Friedrichs et al., 2007). A comparison between **Figure 5** and **Figure S2** and the satellite observation of surface chlorophyll at the corresponding locations (**Figure S4**, data from the Ocean Colour Climate Change Initiative dataset, Version 3.1, European Space Agency) shows that at PAPA all simulations catch the May-June growth burst, but the eddy-diffusive Eulerian model has a prominent early May onset of the bloom, and that at SAZ all simulations show an early growth with respect to the December peak, but those with high irreversible mixing more so than the others.

We should stress that most Earth-System models simulate open-ocean blooms occurring earlier than the observed ones (Hague and Vichi, 2018). For strengths of irreversible mixing that we consider realistic, we find a shift forward in the onset of the bloom (section 3.2) by an amount which would largely mitigate the problem. This stubborn bias, which is the same magnitude as the projected change in bloom onset due to climate change in the twenty-first century (Henson et al., 2018), has often been attributed to inadequacies of the physical or biological formulations (McKiver et al., 2015), but in the light of our results, it is likely to stem from mismodeling the interaction, across vastly different scales, of growth and stirring, mediated by irreversible mixing.

A second puzzling issue that our findings help to unravel is that of the chlorophyll variance observed by BGC-Argo floats in the southern oceans. The proposed mechanisms for generating vertical plankton inhomogeneity in the mixed layer (referred to above) require periods of moderate to no turbulence as they occur in seasonally stratified systems like the Northeast Pacific, and thus are unlikely to be dominant in the Southern Ocean. And yet BGC-Argo floats ubiquitously find high chlorophyll variance (Carranza et al., 2018). As we showed with **Figure 7**, and discussed in detail in section 3.3.1, if the irreversible mixing terms are not blown out of proportion, this high variance is readily reproduced in our aquacosm framework, even though we adopt an extremely simplified description of the biological processes. This interpretation of BGC-Argo data is further corroborated by the uncanny resemblance between the distribution of chlorophyll carried by the aquacosms shown in the lower panels of **Figure 6** an **Figure S1** and that of the high-resolution profiles shown in Mandal et al. (2019), Doubell et al. (2014), and Doubell et al. (2009).

In this study we have used the parameter p that determines the strength of irreversible mixing as a free parameter. We have shown that for high enough values of p our aquacosm models reproduce the results of the corresponding eddy-diffusive, Eulerian model. We have also given proof that the Lagrangian ensemble models that one obtains by setting $p = 0$ may yield

paradoxical results. For very low, but non-zero values of p, the aquacosm models appear to shed light on the problems of the bloom onset timing, and of the observed chlorophyll variance. This suggests that those low values might be physically correct, although this alone would not be sufficient for upholding such a conclusion. In the **Supplementary Material S3**, we develop a theoretical argument supporting it. In summary, we evaluate the mixing rule embodied by Equation (15) for a regular arrangement of aquacosms, which allows the computation of a simple formula associating p and other parameters (inter-parcel distance, time step, etc.) to a diffusion coefficient representative of the irreversible mixing processes. On identifying those processes with molecular diffusion we can match that diffusion coefficient with the known diffusivity of sea-water solutes. We find that for the simulations of section 3.3, a value of p in the range between 10^{-7} and 10^{-8} appears to be the most realistic. Obviously, the mixing processes deemed to be "irreversible" need not always be identified with molecular diffusion. For some applications other choices might be justifiable, but for modeling the mixed layer, given the recent observations of chlorophyll fluctuations below the centimeter scale mentioned in the introduction, that seems to be the most appropriate and least arbitrary choice. Because aquacosms are assumed to be homogeneous parcels of water, the identification with molecular diffusion clarifies that the size of an aquacosm should be taken as comparable with Batchelor's scale, which is the scale where the concentration of sea-water solutes is homogeneous, and which is usually no larger than a millimeter (Thorpe, 2005).

Finally, we remark that aquacosm simulations offer an ideal tool for exploring which biological features and the relative parameterizations are able to build up large-scale impacts, and which are negligible in terms of bulk properties. The aquacosm approach is not limited to the extremely simplified treatment of the growth/decay processes that we have used here to illustrate the potentialities of the method, and can be expanded to include an extreme variety of biogeochemical processes that may be deemed relevant for the specific problem at hand.

DATA AVAILABILITY STATEMENT

The datasets generated for this study are available on request to the corresponding author.

AUTHOR CONTRIBUTIONS

FP and MV ideated the aquacosm approach and wrote the paper. FP developed the aquacosm mathematical theory and wrote the water column codes. MV run the NEMO model and generated the turbulence profiles for the PAPA and SAZ simulations. All authors contributed to the article and approved the submitted version.

FUNDING

This research was funded by internal resources of New York University Abu Dhabi, the Center on Stability, Instability and Turbulence, MV received funding from the NRF through the South African National Antarctic Program.

ACKNOWLEDGMENTS

An earlier version of this manuscript was released as a Pre- Print at https://arxiv.org/abs/1909.04334. We thank the editor and the reviewers for their careful reading and thoughtful comments which greatly improved the clarity of our manuscript. The authors acknowledge the public availability of the NEMO (https://www.nemo-ocean.eu) and BFM (https://www.bfm-community.eu) models.

SUPPLEMENTARY MATERIAL

The Supplementary Material for this article can be found online at: https://www.frontiersin.org/articles/10.3389/fmars.2020.00654/full#supplementary-material

REFERENCES

Aumont, O., Ethé, C., Tagliabue, A., Bopp, L., and Gehlen, M. (2015). PISCES-v2: an ocean biogeochemical model for carbon and ecosystem studies. *Geosci. Model Dev*. 8, 2465–2513. doi: 10.5194/gmd-8-2465-2015

Azam, F., and Worden, A. Z. (2004). Microbes, molecules, and marine ecosystems. *Science* 303, 1622–1624. doi: 10.1126/science.1093892

Baudry, J., Dumont, D., and Schloss, I. R. (2018). Turbulent mixing and phytoplankton life history: a Lagrangian versus Eulerian model comparison. *Mar. Ecol. Prog. Ser*. 600, 55–70. doi: 10.3354/meps12634

Behrenfeld, M. J., Boss, E., Siegel, D. A., and Shea, D. M. (2005).Carbon-based ocean productivity and phytoplankton physiology from space. *Global Biogeochem. Cycles* 19:GB1006. doi: 10.1029/2004GB002299

Bopp, L., Resplandy, L., Orr, J. C., Doney, S. C., Dunne, J. P., Gehlen, M., et al. (2013). Multiple stressors of ocean ecosystems in the 21st century: projections with CMIP5 models. *Biogeosciences* 10, 6225–6245. doi: 10.5194/bg-10-6225-2013

Boyd, P. W., Collins, S., Dupont, S., Fabricius, K., Gattuso, J. P., Havenhand, J., et al. (2018). Experimental strategies to assess the biological ramifications of multiple drivers of global ocean change: a review. *Glob. Change Biol.* 24, 2239–2261. doi: 10.1111/gcb.14102

Burchard, H., and Bolding, K. (2001). Comparative analysis of four second-moment turbulence closure models for the oceanic mixed layer. *J. Phys. Oceanogr*. 31, 1943–1967. doi: 10.1175/1520-0485(2001)031<1943:CAOFSM>2.0.CO;2

Carranza, M. M., Gille, S. T., Franks, P. J. S., Johnson, K. S., Pinkel, R., and Girton, J. B. (2018). When mixed layers are not mixed. storm-driven mixing and bio-optical vertical gradients in mixed layers of the southern ocean. *J. Geophys. Res. Oceans* 123, 7264–7289. doi: 10.1029/2018JC014416

Cianelli, D., Uttieri, M., and Zambianchi, E. (2012). "Individual based modelling of planktonic organisms," in *Ecological Modeling*, ed W. J. Zhang (New York, NY: Nova Science Publishers, Inc.), 83–96.

Cullen, J. J. (2015). Subsurface chlorophyll maximum layers: enduring enigma or mystery solved? *Annu. Rev. Mar. Sci.* 7, 207–239. doi: 10.1146/annurev-marine-010213-135111

Currie, W. J. S., and Roff, J. C. (2006). Plankton are not passive tracers: plankton in a turbulent environment. *J. Geophys. Res.* 111:C05S07. doi: 10.1029/2005JC002967

Dee, D. P., Uppala, S. M., Simmons, A. J., Berrisford, P., Poli, P., Kobayashi, S., et al. (2011). The ERA-Interim reanalysis: Configuration and performance of the data assimilation system. *Q. J. R. Meteorol. Soc*. 137, 553–597. doi: 10.1002/qj.828

Denman, K. L. (2003). Modelling planktonic ecosystems: parameterizing complexity. *Prog. Oceanogr*. 57, 429–452. doi: 10.1016/S0079-6611(03)00109-5

Dippner, J. W. (1998). Competition between different groups of phytoplankton for nutrients in the southern North Sea. *J. Marine Syst*. 14, 181–198. doi: 10.1016/S0924-7963(97)00025-0

Doubell, M. J., Prairie, J. C., and Yamazaki, H. (2014). Millimeter scale profiles of chlorophyll fluorescence: deciphering the microscale spatial structure of phytoplankton. *Deep Sea Res. II Top. Stud. Oceanogr*. 101, 207–215. doi: 10.1016/j.dsr2.2012.12.009

Doubell, M. J., Yamazaki, H., Li, H., and Kokubu, Y. (2009). An advanced laser-based fluorescence microstructure profiler (TurboMAP-L) for measuring bio-physical coupling in aquatic systems. *J. Plankton Res*. 31, 1441–1452. doi: 10.1093/plankt/fbp092

Durham, W. M., and Stocker, R. (2011). Thin phytoplankton layers: characteristics, mechanisms, and consequences. *Annu. Rev. Mar. Sci*. 4, 177–207. doi: 10.1146/annurev-marine-120710-100957

Esposito, S., Botte, V., Iudicone, D., and Ribera d'Alcala, M. (2009). Numerical analysis of cumulative impact of phytoplankton photoresponses to light variation on carbon assimilation. *J. Theoret. Biol*. 261, 361–371. doi: 10.1016/j.jtbi.2009.07.032

Fennel, W., and Neumann, T. (1996). The mesoscale variability of nutrients and plankton as seen in a coupled model. Germ. *J. Hydrog*. 48, 49–71. doi: 10.1007/BF02794052

Ferrari, R., Merrifield, S. T., and Taylor, J. R. (2015). Shutdown of convection triggers increase of surface chlorophyll. *J. Mar. Syst*. 147, 116–122. doi: 10.1016/j.jmarsys.2014.02.009

Ferrari, R., and Young, W. (1997). On the development of thermohaline correlations as a result of nonlinear diffusive parameterizations. *J. Mar. Res*. 55, 1069–1101. doi: 10.1357/0022240973224094

Fischer, A., Moberg, E., Alexander, H., Brownlee, E., Hunter-Cevera, K., Pitz, K., et al. (2014). Sixty years of sverdrup: a retrospective of progress in the study of phytoplankton blooms. *Oceanography* 27, 222–235. doi: 10.5670/oceanog.2014.26

Foloni-Neto, H., Tanaka, M., Joshima, H., and Yamazaki, H. (2016). A comparison between quasi-horizontal and vertical observations of phytoplankton microstructure. *J. Plankton Res*. 38, 993–1005. doi: 10.1093/plankt/fbv075

Friedrichs, M. A. M., Dusenberry, J. A., Anderson, L. A., Armstrong, R. A., Chai, F., Christian, J. R., et al. (2007). Assessment of skill and portability in regional marine biogeochemical models: role of multiple planktonic groups. *J. Geophys. Res.* 112:C08001. doi: 10.1029/2006JC003852

Fu, C., Travers-Trolet, M., Velez, L., Grass, A., Bundy, A., Shannon, L. J., et al. (2018). Risky business: the combined effects of fishing and changes in primary productivity on fish communities. *Ecol. Modell*. 368, 265–276. doi: 10.1016/j.ecolmodel.2017.12.003

Geider, R. J., MacIntyre, H. L., and Kana, T. M. (1997). A dynamic model of phytoplankton growth and acclimation: responses of the balanced growth rate and chlorophyll a:carbon ratio to light, nutrient limitation and temperature. *Mar. Ecol. Prog. Ser*. 148, 187–200. doi: 10.3354/meps148187

Gräwe, U. (2011). Implementation of high-order particle-tracking schemes in a water column model. *Ocean Modell*. 36, 80–89. doi: 10.1016/j.ocemod.2010.10.002

Gruber, N., Gloor, M., Mikaloff Fletcher, S. E., Doney, S. C., Dutkiewicz, S., Follows, M. J., et al. (2009). Oceanic sources, sinks, and transport of atmospheric CO2. *Glob. Biogeochem. Cycles* 23:GB1005. doi: 10.1029/2008GB003349

Hague, M., and Vichi, M. (2018). A link between CMIP5 phytoplankton phenology and sea ice in the Atlantic Southern Ocean. *Geophys. Res. Lett*. 45, 6566–6575. doi: 10.1029/2018GL078061

Hellweger, F. L., and Bucci, V. (2009). A bunch of tiny individuals—Individual-based modeling for microbes. *Ecol. Modell*. 220, 8–22. doi: 10.1016/j.ecolmodel.2008.09.004

Hellweger, F. L., and Kianirad, E. (2007). Accounting for intrapopulation variability in biogeochemical models using agent-based methods. *Environ. Sci. Technol*. 41, 2855–2860. doi: 10.1021/es062046j

Henson, S. A., Cole, H. S., Hopkins, J., Martin, A. P., and Yool, A. (2018). Detection of climate change-driven trends in phytoplankton phenology. *Glob. Change Biol*. 24, e101-e111. doi: 10.1111/gcb.13886

Huisman, J., Pham Thi, N. N., Karl, D. M., and Sommeijer, B. (2006). Reduced mixing generates oscillations and chaos in the oceanic deep chlorophyll maximum. *Nature* 439, 322–325. doi: 10.1038/nature04245

Huisman, J., van Oostveen, P., and Weissing, F. J. (1999). Critical depth and critical turbulence: two different mechanisms for the development of phytoplankton blooms. *Limnol. Oceanogr*. 44, 1781–1787. doi: 10.4319/lo.1999.44.7.1781

Hyder, K., Rossberg, A. G., Allen, J. I., Austen, M. C., Barciela, R. M., Bannister, H. J., et al. (2015). Making modelling count - increasing the contribution of shelf-seas community and ecosystem models to policy development and management. *Mar. Policy* 61, 291–302. doi: 10.1016/j.marpol.2015.07.015

Kamykowski, D., Yamazaki, H., and Janowitz, G. S. (1994). A Lagrangian model of phytoplankton photosynthetic response in the upper mixed layer. *J. Plankton Res*. 16, 1059–1069. doi: 10.1093/plankt/16.8.1059

Kida, S., and Ito, T. (2017). A Lagrangian view of spring phytoplankton blooms. *J. Geophys. Res. Oceans* 122, 9160–9175. doi: 10.1002/2017JC013383

Lande, R., and Lewis, M. R. (1989). Models of photoadaptation and photosynthesis by algal cells in a turbulent mixed layer. *Deep Sea Res. A Oceanogr. Res. Pap*. 36, 1161–1175. doi: 10.1016/0198-0149(89)90098-8

Le Quéré, C., Harrison, S. P., Prentice, I. C., Buitenhuis, E. T., Aumont, O., Bopp, L., et al. (2005). Ecosystem dynamics based on plankton functional types for global ocean biogeochemistry models. *Glob. Change Biol*. 11, 2016–2040. doi: 10.1111/j.1365-2486.2005.1004.x

Legendre, L., Rivkin, R. B., and Jiao, N. (2018). Advanced experimental approaches to marine water-column biogeochemical processes. *ICES J. Mar. Sci*. 75, 30–42. doi: 10.1093/icesjms/fsx146

Levenspiel, O. (2011). *Tracer Technology: Modeling the Flow of Fluids. Fluid Mechanics and Its Applications*. New York, NY: Springer. doi: 10.1007/978-1-4419-8074-8

Lévy, M., Franks, P. J. S., and Smith, K. S. (2018). The role of submesoscale currents in structuring marine ecosystems. *Nat. Commun*. 9:4758. doi: 10.1038/s41467-018-07059-3

Levy, M., and Martin, A. P. (2013). The influence of mesoscale and submesoscale heterogeneity on ocean biogeochemical reactions. *Global Biogeochem. Cycles* 27, 1139–1150. doi: 10.1002/2012GB004518

Little, H. J., Vichi, M., Thomalla, S. J., and Swart, S. (2018). Spatial and temporal scales of chlorophyll variability using high-resolution glider data. *J. Mar. Syst*. 187, 1–12. doi: 10.1016/j.jmarsys.2018.06.011

Mahadevan, A. (2016). The impact of submesoscale physics on primary productivity of plankton. *Annu. Rev. Mar. Sci*. 8, 161–184. doi: 10.1146/annurev-marine-010814-015912

Mandal, S., Homma, H., Priyadarshi, A., Burchard, H., Smith, S. L., Wirtz, K. W., et al. (2016). A 1D physical-biological model of the impact of highly intermittent phytoplankton distributions. *J. Plankton Res*. 38, 964–976. doi: 10.1093/plankt/fbw019

Mandal, S., Smith, S. L., Priyadarshi, A., and Yamazaki, H. (2019). Micro-scale variability impacts the outcome of competition between different modeled size classes of phytoplankton. *Front. Mar. Sci*. 6:259. doi: 10.3389/fmars.2019.00259

Martin, A. P. (2003). Phytoplankton patchiness: the role of lateral stirring and mixing. *Prog. Oceanogr*. 57, 125–174. doi: 10.1016/S0079-6611(03)00085-5

McGillicuddy, D. J. (1995). One-dimensional numerical simulation of primary production: Lagrangian and Eulerian formulations. *J. Plankton Res*. 17, 405–412. doi: 10.1093/plankt/17.2.405

McKiver, W. J., Vichi, M., Lovato, T., Storto, A., and Masina, S. (2015). Impact of increased grid resolution on global marine biogeochemistry. *J. Mar. Syst*. 147, 153–168. doi: 10.1016/j.jmarsys.2014.10.003

Moeller, H. V., Laufkotter, C., Sweeney, E. M., and Johnson, M. D. (2019). light-dependent grazing can drive formation and deepening of deep chlorophyll maxima. *Nat. Commun*. 10:1978. doi: 10.1038/s41467-019-09591-2

Nihoul, J. C. (1975). *Modelling of Marine Systems*. Amsterdam; Oxford; New York, NY: Elsevier.

Nihoul, J. C. J., and Djenidi, S. (1998). "Coupled physical and biological models," in *The Sea, Vol. 10*, eds K. H. Brink and A. R. Robinson (New York, NY: John Wiley & Sons, Inc.), 483–506.

Paparella, F., and Popolizio, M. (2018). Lagrangian numerical methods for ocean biogeochemical simulations. *J. Comput. Phys*. 360, 229–246. doi: 10.1016/j.jcp.2018.01.031

Pinel-Alloul, B., and Ghadouani, A. (2007). "Spatial heterogeneity of planktonic microorganisms in aquatic systems," in *The Spatial Distribution of Microbes in the Environment*, eds R. B. Franklin and A. L. Mills (Dordrecht: Springer), 203–310. doi: 10.1007/978-1-4020-6216-2_8

Piroddi, C., Teixeira, H., Lynam, C. P., Smith, C., Alvarez, M. C., Mazik, K., et al. (2015). Using ecological models to assess ecosystem status in support of the European Marine Strategy Framework Directive. *Ecol. Indicat*. 58, 175–191. doi: 10.1016/j.ecolind.2015.05.037

Prairie, J. C., Sutherland, K. R., Nickols, K. J., and Kaltenberg, A. M. (2012). Biophysical interactions in the plankton: a cross-scale review. *Limnol. Oceanogr. Fluids Environ*. 2, 121–145. doi: 10.1215/21573689-1964713

Racault, M.-F., Le Quéré, C., Buitenhuis, E., Sathyendranath, S., and Platt, T. (2012). Phytoplankton phenology in the global ocean. *Ecol. Indicat*. 14, 152–163. doi: 10.1016/j.ecolind.2011.07.010

Reffray, G., Bourdalle-Badie, R., and Calone, C. (2015). Modelling turbulent vertical mixing sensitivity using a 1-D version of NEMO. *Geosci. Model Dev*. 8, 69–86. doi: 10.5194/gmd-8-69-2015

Ross, O. N., and Sharples, J. (2004). Recipe for 1-D Lagrangian particle tracking models in space-varying diffusivity. *Limnol. Oceanogr. Methods* 2, 289–302. doi: 10.4319/lom.2004.2.289

Sathyendranath, S., Ji, R., and Browman, H. I. (2015). Revisiting Sverdrup's critical depth hypothesis. *ICES J. Mar. Sci*. 72, 1892–1896. doi: 10.1093/icesjms/fsv110

Scheffer, M., Baveco, J. M., DeAngelis, D. L., Rose, K. A., and van Nes, E. H. (1995). Super-individuals a simple solution for modelling large populations on an individual basis. *Ecol. Modell*. 80, 161–170. doi: 10.1016/0304-3800(94)00055-M

Stec, K. F., Caputi, L., Buttigieg, P. L., D'Alelio, D., Ibarbalz, F. M., Sullivan, M. B., et al. (2017). Modelling plankton ecosystems in the meta-omics era. Are we ready? *Mar. Genomics* 32, 1–17. doi: 10.1016/j.margen.2017.02.006

Sverdrup, H. V. (1953). On conditions for the vernal blooming of phytoplankton. *J. Cons. Perm. Int. Exp. Mer*. 18, 287–295. doi: 10.1093/icesjms/18.3.287

Taylor, J. R., and Ferrari, R. (2011). Shutdown of turbulent convection as a new criterion for the onset of spring phytoplankton blooms. *Limnol. Oceanogr*. 56, 2293–2307. doi: 10.4319/lo.2011.56.6.2293

Thomalla, S. J., Ogunkoya, A. G., Vichi, M., and Swart, S. (2017). Using optical sensors on gliders to estimate phytoplankton carbon concentrations and chlorophyll-to-carbon ratios in the Southern Ocean. *Front. Mar. Sci*. 4:34. doi: 10.3389/fmars.2017.00034

Thorpe, S. (2005). *The Turbulent Ocean*. Cambridge, MA: Cambridge University Press. doi: 10.1017/CBO9780511819933

Tian, R. C. (2006). Toward standard parameterizations in marine biological modeling. *Ecol. Modell*. 193, 363–386. doi: 10.1016/j.ecolmodel.2005.09.003

Travers, M., Shin, Y. J., Jennings, S., and Cury, P. (2007). Towards end-to-end models for investigating the effects of climate and fishing in marine ecosystems. *Prog. Oceanogr*. 75, 751–770. doi: 10.1016/j.pocean.2007.08.001

Van Sebille, E., Griffies, S. M., Abernathey, R., Adams, T. P., Berloff, P., Biastoch, A., et al. (2018). Lagrangian ocean analysis: fundamentals and practices. *Ocean Modell*. 121, 49–75. doi: 10.1016/j.ocemod.2017.11.008

Vichi, M., Pinardi, N., and Masina, S. (2007). A generalized model of pelagic biogeochemistry for the global ocean ecosystem. Part I: theory. *J. Mar. Syst*. 64, 89–109. doi: 10.1016/j.jmarsys.2006.03.006

Wallhead, P. J., Martin, A. P., Srokosz, M. A., and Fasham, M. J. (2006). Accounting for unresolved spatial variability in marine ecosystems using time lags. *J. Mar. Res*. 64, 881–914. doi: 10.1357/002224006779698387

Warhaft, Z. (2000). Passive scalars in turbulent flows. *Annu. Rev. Fluid Mech*. 32, 203–240. doi: 10.1146/annurev.fluid.32.1.203

Wolf, K. U., and Woods, J. D. (1988). "Lagrangian simulation of primary production in the physical environment–The deep chlorophyll maximum and nutricline," in *Toward a Theory on Biological-Physical Interactions in the World Ocean*, ed B. J. Rothschild (Springer), 51–70. doi: 10.1007/978-94-009-3023-0_4

Woods, J. D. (2005). The Lagrangian ensemble metamodel for simulating plankton ecosystems. *Prog. Oceanogr*. 67, 84–159. doi: 10.1016/j.pocean.2005.04.003

Woods, J. D., Barkmann, J., Beddington, J. R., Cushing, D. H., May, R. M., and Steele, J. H. (1994). Simulating plankton ecosystems by the Lagrangian ensemble method. *Philos. Trans. R. Soc. Lond. Ser. B Biol. Sci*. 343, 27–31. doi: 10.1098/rstb.1994.0004

Woods, J. D., and Onken, R. (1982). Diurnal variation and primary production in the ocean preliminary results of a Lagrangian ensemble model. *J. Plankton Res*. 4, 735–756. doi: 10.1093/plankt/4.3.735

Yamazaki, H., and Kamykowski, D. (1991). The vertical trajectories of motile phytoplankton in a wind-mixed water column. *Deep Sea Res. A Oceanogr. Res. Pap*. 38, 219–241. doi: 10.1016/0198-0149(91)90081-P

Conflict of Interest: The authors declare that the research was conducted in the absence of any commercial or financial relationships that could be construed as a potential conflict of interest.

Copyright © 2020 Paparella and Vichi. This is an open-access article distributed under the terms of the Creative Commons Attribution License (CC BY). The use, distribution or reproduction in other forums is permitted, provided the original author(s) and the copyright owner(s) are credited and that the original publication in this journal is cited, in accordance with accepted academic practice. No use, distribution or reproduction is permitted which does not comply with these terms.

frontiers in Marine Science

BRIEF RESEARCH REPORT
published: 28 August 2020
doi: 10.3389/fmars.2020.00653

Monitoring of Plankton Spatial and Temporal Characteristics With the Use of a Submersible Digital Holographic Camera

Victor Dyomin[1], Alexandra Davydova[1,2], Sergey Morgalev[1], Nikolay Kirillov[1], Alexey Olshukov[1,2], Igor Polovtsev[1] and Sergey Davydov[1]*

[1] Laboratory of Radiophysical and Optical Methods of Environmental Studies, National Research Tomsk State University, Tomsk, Russia, [2] Environmental Remote Sensing Laboratory, V.E. Zuev Institute of Atmospheric Optics of the Siberian Branch of the Russian Academy of Sciences, Tomsk, Russia

This study shows that the use of a submersible digital holographic camera as part of a multifunctional hardware and software complex allows carrying out *in situ* measurements of plankton, automating the process of obtaining data on plankton, as well as classifying plankton species up to an order within the specified taxonomic groups. Such automation ensures monitoring expeditionary or stationary research of species diversity and spatial and temporal organization of zooplankton in conjunction with the hydrophysical parameters of the medium. This paper presents the full-scale results of vertical profiles and daily measurements of plankton made with the use of the submersible digital holographic camera as well as the classification of plankton in laboratory and field conditions in the automatic mode. It is shown that, within the accomplished version, the classification algorithm using the morphological parameter makes it possible to solve the problem quickly (the time required to obtain the result is less than 1 s and depends on the number of plankton particles and the frame size of a restored image); however, the classification accuracy by orders varies within 50–60%.

Keywords: plankton, biodiversity, digital holography, spatial characteristics, temporal characteristics, submersible camera

OPEN ACCESS

Edited by:
Malcolm McFarland, Florida Atlantic University, United States

Reviewed by:
Alexander Khmaladze, University at Albany, United States
Björn Kemper, University of Münster, Germany
Lee Karp-Boss, University of Maine, United States

***Correspondence:**
Alexandra Davydova
starinshikova@mail.ru

Specialty section:
This article was submitted to Marine Ecosystem Ecology, a section of the journal Frontiers in Marine Science

Received: *19 January 2020*
Accepted: *17 July 2020*
Published: *28 August 2020*

Citation:
Dyomin V, Davydova A, Morgalev S, Kirillov N, Olshukov A, Polovtsev I and Davydov S (2020) Monitoring of Plankton Spatial and Temporal Characteristics With the Use of a Submersible Digital Holographic Camera. Front. Mar. Sci. 7:653. doi: 10.3389/fmars.2020.00653

INTRODUCTION

The main objectives of environmental monitoring of any water area include regular analysis of environmental conditions and forecasting of ecosystem changes under the influence of technogenic and other factors. Such analysis is performed against the background of the natural variability of the water area conditions, daily and seasonal temperature fluctuations, illumination, etc. The conservation of biodiversity typical for this water area, especially for pelagic plankton, may indicate the habitat optimum factors.

The pessimal factor associated with anthropogenic activities may change the number of different plankton species due to the difference in their environmental tolerance and vulnerability to anthropogenic effects. Thus, the violation of alpha diversity parameters, such as the species richness and the evenness of species abundance, indicates some environmental hazards.

Hydrobiological research that traditionally involves the sampling of phytoplankton, zooplankton, zoobenthos, periphyton, and field ichthyological survey forms a crucial part of

environmental monitoring of aquatic environments (Chiba et al., 2018; Batten et al., 2019; Lombard et al., 2019). For instance, such research is mandatory in the survey of the territory of future construction and monitoring of water areas within hazardous facilities. Furthermore, field and laboratory works involve the following:

- study of species diversity and spatial and temporal organization of zooplankton,
- study of seasonal dynamics of species diversity and abundance indicators,
- determination of the ecosystem trophic status according to the ratio of eutrophic and oligotrophic zooplankton species (Hakkari, 1972). The standard monitoring includes water sampling and subsequent laboratory analysis of plankton content. This process is time-consuming and cannot be frequently repeated since the sampling itself perturbs the controlled volume.

Digital holography is a promising method for the *in situ* study of plankton (Sun et al., 2008; Watson, 2011; Talapatra et al., 2012; Bochdansky et al., 2013; Rotermund et al., 2016; Davies and Nepstad, 2017; Guo et al., 2018; Lombard et al., 2019).

The study describes the possibilities and the peculiarities of using a submersible digital holographic camera (DHC) (Dyomin et al., 2019d) for such monitoring tasks as part of the hardware and the software complex developed by the research team. The main advantage of using DHC is the possibility of studying plankton in its habitat without sampling and interference into the biocenosis. DHC is also characterized by a fairly representative medium volume recorded per exposure – up to 1 L, while in similar holographic cameras the analyzed medium volume does not exceed 40 cm^3 (Watson, 2011; Talapatra et al., 2012; Rotermund et al., 2016; Dyomin et al., 2019b; HoloSea, 2020; Lisst-Holo2, 2020). Unlike photographic methods of particle research (Olson and Sosik, 2007; Cowen and Guigand, 2008; Ohman et al., 2012), it is possible when reconstructing a digital hologram to obtain sharp images of all particles that were in a given medium volume during exposure. In addition to the digital holographic camera, the hardware and the software complex includes hydrophysical sensors (pressure gauge, temperature gauge, and microwave conductivity sensor) and an onboard computer. All components are integrated into the local network controlled by the onboard computer, and the communication channel ensures continuous real-time data transfer to a shipboard computer. DHC records digital holograms of the controlled medium volume in a given sequence. The shipboard computer performs the numerical processing of holograms and automatically extracts information on plankton from them. Unlike other plankton classification algorithms (Lumini and Nanni, 2015; Lombard et al., 2019), the proposed automatic classification algorithm using the morphological parameter provides for fast (<1 s) classification of plankton according to the chosen taxa. The automation of information acquisition provides monitoring research of species diversity and spatial and temporal organization of zooplankton in conjunction with hydrophysical parameters of the medium.

METHODS

The developed DHC used in this study (Dyomin et al., 2018a,b,c,d, 2019a,b,c,d) provides for an automatic registration of a digital hologram that contains information on the entire studied volume with plankton. DHC ensures the detailed study of particles ranging from 200 μm in size. The application of such camera is described in Dyomin et al. (2018a). The DHC optical scheme is shown in **Figure 1A**. The light from the laser source (4) passes through the collimator (5), then through the volume with the analyzed particles (3), reflecting on a mirror prism

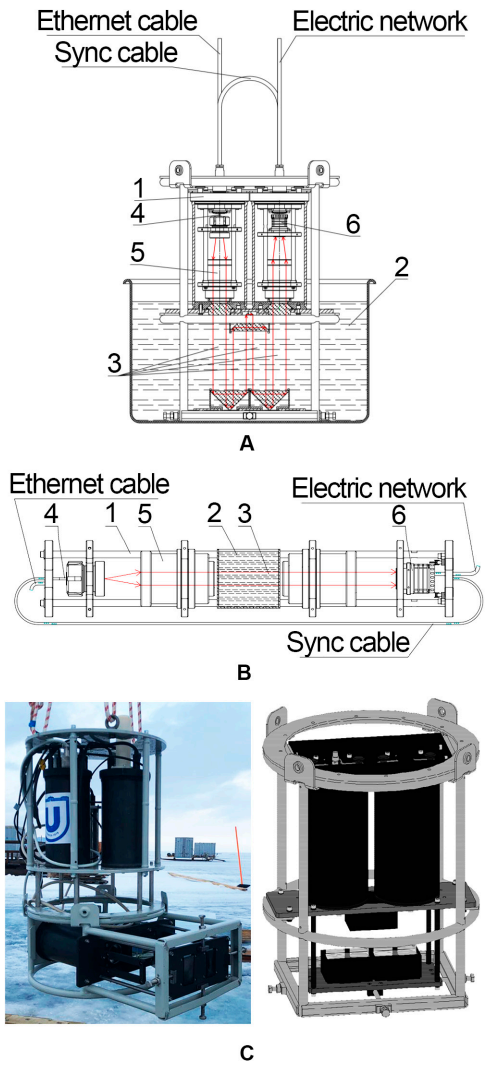

FIGURE 1 | (A) Digital hologram recording scheme using submersible digital holographic camera (DHC) (folded configuration) in laboratory conditions. **(B)** Digital hologram recording scheme using DHC (laboratory linear configuration) in laboratory conditions. 1 – DHC, 2 – laboratory water tank **(A)** or cuvette **(B)** with plankton, 3 – studied (recorded) volume, 4 – laser, 5 – beam expander, 6 – CMOS camera. **(C)** DHC horizontal layout as part of a hydrobiological probe in the study of vertical plankton distributions of Lake Baikal in February 2019 and DHC vertical layout for the study of plankton temporal characteristics.

system, and enters the camera (6) through the receiving lens. Thus, the camera (6) registers a digital hologram of the analyzed volume with the particles representing an interference pattern of two coherent waves – scattered on particles and passed without scattering. The design and the specifications of the camera are described in more detail in our previous studies (Dyomin et al., 2019a,c). **Figure 1C** shows the DHC layout.

The algorithm of numerical particle image restoration from the digital hologram is well known (Schnars and Juptner, 2002; Watson, 2018) and underlies the base software. The numerical processing of digital holograms and the algorithm of parameter determination and automatic classification of particles are described in our previous works (Dyomin and Olshukov, 2016; Dyomin et al., 2017; Dyomin et al., 2018b) and form the problem-oriented software. The entire software is commercial, so let us list its main components without describing them in detail.

The sequence of operations performed using DHC and registered digital holograms is called the DHC technology. In addition to digital hologram recording, the DHC technology includes a set of numerical operations on its special processing – hologram preprocessing to eliminate edge effects and to level the background noise (Dyomin and Olshukov, 2016; Dyomin et al., 2018b), restoration of holographic images of cross-sections of medium volume at various distances (Schnars and Juptner, 2002; Watson, 2018), and a 2D display of holographic volume with plankton (Dyomin et al., 2018b). The 2D display thus constructed consists of focused images of all plankton species in the studied medium volume at the time of hologram registration (Dyomin et al., 2018b). Besides that, the 3D coordinates of each species are known: the longitudinal coordinate is determined from the position of the best focus plane of a restored particle image; the coordinates of the image center of gravity are taken as transverse particle coordinates (Dyomin and Kamenev, 2016a,b).

This is followed by automatic binarization of the 2D display, identification of the image of each plankton species, and definition of its characteristics according to the parameters of a rectangle circumscribed around its restored image: size (width and length of a rectangle), tilt angle, boundary length, and area. Simultaneously, for each image of plankton species, we define the compactness (ratio of the boundary length square to the area of the image), morphological parameter M (ratio of the width and length H of the circumscribed rectangle), and the presence of antennas or other extremities (Dyomin et al., 2018b).

These parameters are used for the automatic classification of planktonic particles according to chosen taxonomic groups. The decision tree for automatic classification (**Figure 2A**) includes eight taxa: *Chaetognatha*, *Copepoda*, *Appendicularia*, *Cladocera*, *Rotifera*, colonies of phytoplankton, phytoplankton chains, and others (jellyfishes, meroplankton, and others) (Dyomin et al., 2017, 2018b).

The preliminary-formed database on plankton of this water area allows obtaining the species composition of particles (by orders) and the species distribution of particles by size as well as the species concentration of particles in the analyzed volume during monitoring.

Within the scope of the present work, the laboratory and the field studies of plankton were carried out using DHC and DHC technology to test and verify the features of the automatic classification of plankton as well as to confirm the possibilities of monitoring its temporal and spatial characteristics. The described results demonstrate only some capabilities of the developed equipment and software and make no pretense to comprehensive information on plankton species. The problem-oriented part of the software can be expanded or narrowed depending on the current task.

RESULTS AND DISCUSSION

Study of the Accuracy of Plankton Automatic Classification Algorithm

The laboratory studies using DHC were conducted to check the accuracy of the automatic classification algorithm. We used the camera that makes it possible to record a hologram with a water volume of 0.6 dm^3 per exposure. The camera was placed in a 90 dm^3 laboratory water tank filled with culture water. The entire optical part of the camera was submerged into the water (**Figure 1A**). We used *Daphnia pulex* and *Cyclops strenuus* sampled from a natural population in a freshwater reservoir near Tomsk. One hundred *C. strenuus* individuals were placed in the water tank, and then DHC was started in a mode of digital hologram recording every 4 s, with a total of 100 holograms recorded. Then, 100 *C. strenuus* individuals were additionally placed in the water tank and 100 holograms were recorded in the same mode. Furthermore, we continued adding individuals and registering digital holograms in the following order: 100 *C. strenuus* individuals, 100 *D. pulex* individuals, 100 *D. pulex* individuals, and 100 *D. pulex* individuals. During the last registration of digital holograms, there were 300 *C. strenuus* individuals and 300 *D. pulex* individuals. Thus, a total of 600 digital holograms were recorded throughout the experiment. The DHC software made it possible to obtain a database of particles recognized in the investigated volume from restored holographic images as well as to assess the parameters of their automatic classification algorithm. The classification was carried out using the decision tree (**Figure 2A**).

Supplementary Table S1 presents the confusion matrices compiled from laboratory studies of the automatic classification accuracy (Olson and Delen, 2008). The classification accuracy is understood here as the ratio of the number of accurately classified individuals to the total number of identified planktonic individuals of all taxa (the accuracy is indicated in the first cell for each confusion matrix in **Supplementary Table S1**).

The matrices summarize data on each group of 100 processed digital holograms. The rows of confusion matrices denote true taxa, while the columns define the classifier solutions (predictions). The confusion matrix is built by counting the number of times a classifier has identified a planktonic individual of a true taxon as a certain taxon. For example, for the case of recording 100 *C. strenuus* individuals in **Supplementary Table S1**, 22 *Copepoda* individuals were wrongly classified as *Cladocera* class, whereas 79 individuals were classified correctly as *Copepoda* taxon (diagonal element of the confusion matrix). The validity of automatic classification was verified manually by

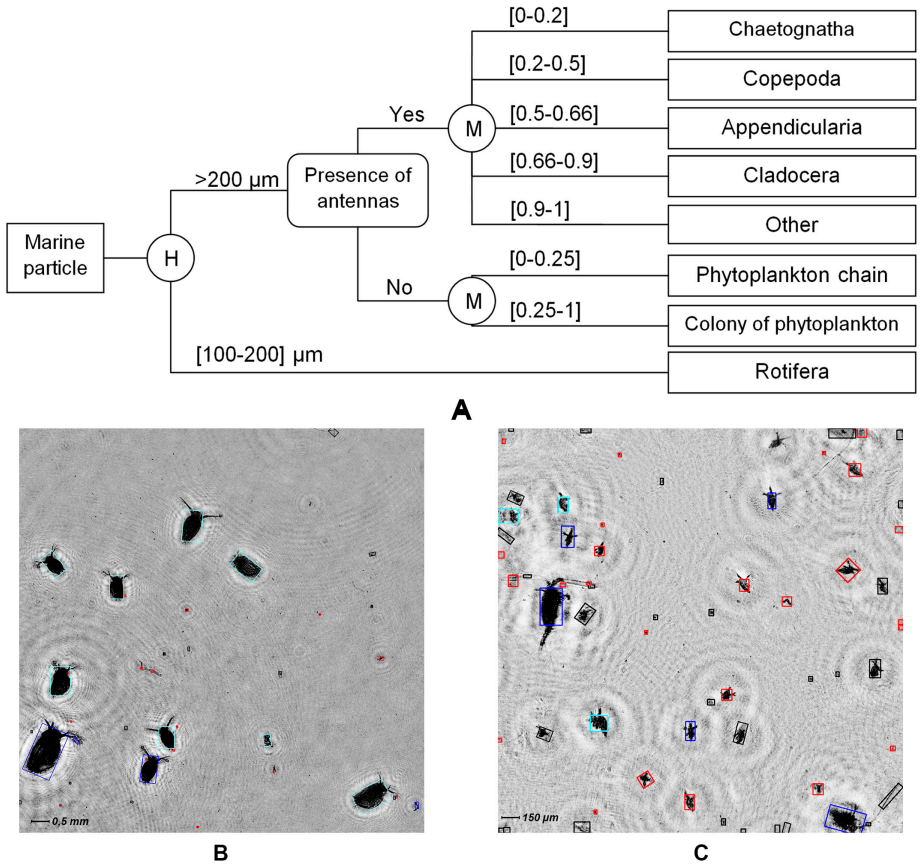

FIGURE 2 | (A) Decision tree of automatic classification of plankton individuals, where M – morphological parameter and H – rectangle length. 2D display of holographic image of the studied volume with **(B)** *Daphnia magna* and **(C)** *Epischura baikalensis* individuals (nauplii and adult specimen), where the result of automatic classification is marked with the color of the rectangle circumscribed around the particle: black – phytoplankton colonies, dark blue – *Copepoda*, blue – *Cladocera*, and red – other.

an operator. The precision and the recall (Olson and Delen, 2008) for each class are specified in the confusion matrices: precision equals the ratio of the corresponding diagonal element of the matrix to the sum of the entire column of the class; recall is the ratio of the diagonal element of the matrix to the sum of the entire row of the class. Precision determines the proportion of planktonic individuals classified as a certain taxon and indeed related to a given taxon (precision demonstrates the classifier's ability to distinguish a given taxon from others). Recall shows the share of plankton individuals of a certain taxon among all individuals of a given taxon found by the classifier (recall demonstrates the ability of the algorithm to detect a given taxon in general). The confusion matrices make it possible to visualize the result of the classification algorithm and to evaluate its quality numerically for each specific water area.

The laboratory studies with *D. pulex* (*Cladocera* taxon) and *C. strenuus* (*Copepoda* taxon) showed that the accuracy of the automatic classification of plankton was 61 ± 3%. The confusion matrices demonstrate that the classification accuracy for *Copepoda* taxon was 86 ± 9%, for *Cladocera* 77 ± 2%, and for others 76 ± 15%. The recall of the classification for the *Copepoda* taxon was 73 ± 7%, for *Cladocera* 52 ± 19%, and for others 45 ± 10%. The averaging was done for all relevant values from the confusion matrices (i.e., for 100 × 6 digital holograms) and given above in mean ± SD format. A low recall of *Cladocera* and others indicates a low automatic classification ability to detect these taxa. This is caused by a coherent noise in the recovered holographic images that make it difficult to detect the presence of antennas. It shall be noted that the classification accuracy in **Supplementary Table S1** for particles classified as *phytoplankton colony* and *other* is caused not only by the errors of the algorithm but also by the presence of feeds and by-products of plankton.

Examples of Application of DHC Technology and Automatic Classification Algorithm in Laboratory Experiments

Laboratory testing was carried out using a digital holographic camera model, the scheme of which is shown in **Figure 1B**. We used *Daphnia magna* sampled from a natural population in a freshwater reservoir near Tomsk. A cuvette filled with water containing plankton was placed between the camera and the laser (**Figure 1B**). The recorded volume was 0.11 dm^3. **Figure 2B** shows the example of an image of *D. magna*

individuals numerically reconstructed from a digital hologram and a 2D display of the studied volume with focused images of individuals. The figure also shows rectangles circumscribed around the particle images, with the color of the rectangle corresponding to a given kind of particles and planktonic individuals. **Supplementary Figure S1** shows the histograms of particle distribution by automatic classification taxa and by size. Here and on the following histograms, the particle size is understood as the length of a circumscribed rectangle. The classification time was about 0.9 s, with 45 particles detected in the recovered image and the frame size of the processed image amounting to 2,048 × 2,048 pixels. Hereinafter, the classification time is given without regard to the recovery time of the digital holograms, construction of the two-dimensional display of the holographic volume, and detection of particles. The classification accuracy was 63%. Out of nine *D. magna* individuals present in the frame, two are wrongly classified as *Copepoda*. Besides that, there are feeds and by-products of the culture in the aquarium, which the algorithm classifies as *other* and *colony of phytoplankton*. In turn, the last solution of the algorithm is erroneous and affects the accuracy of classification.

Figure 2C and **Supplementary Figure S2** demonstrate the performance of the DHC technology and automatic classification using another laboratory experiment – processing of digital holograms of a plankton sample obtained *via* the traditional Juday net in Lake Baikal in 2008. This sample in a cuvette was placed in a digital holographic camera model, as shown in **Figure 1B** (cuvette 3). The recorded volume amounted to 0.01 dm^3. The classification accuracy of *Epischura baikalensis* (*Copepoda* taxon) was 56%. The classification time also depends on the frame size of a processed image and on the number of particles in a frame. Thus, unlike the previous case, in this example, the frame size of the processed image was 1,024 × 1,024 pixels, so the classification time is less and only takes about 0.5 s, with 60 particles detected in the recovered image.

Examples of Application of DHC Technology and Automatic Classification Algorithm in Full-Scale Experiments

The next example of the DHC technology and classification algorithm involves DHC testing during the summer Arctic mission of the Institute of Oceanology RAS on the research ship Academician Mstislav Keldysh in the Kara Sea in 2016 (Dyomin et al., 2018a). During the mission, the DHC was submerged to a given depth on a winch to record digital holograms. The registered digital holograms were transmitted to a shipboard computer for further processing. The recorded volume per exposure was 1 dm^3. **Supplementary Figure S3** shows an example of the images of planktonic particles recovered through processing of one of the holograms recorded *in situ* during the mission in the Kara Sea. **Supplementary Figure S4** shows the histograms of particle distribution by automatic classification taxa and size. The classification accuracy is about 73%. The classification time is about 0.1 s, with the frame size of the processed image being 1,024 × 1,024 pixels and 16 particles were detected in the image.

Field studies of vertical distributions of various types of plankton were carried out in the Blue Bay of the Black Sea in 2019. The measurements were performed from the board of the research ship Ashamba. DHC, as part of the hardware and the software complex, was submerged *via* an onboard winch to a depth of up to 7 m. The sinking speed of the device was about 0.1 m/s, with data being recorded every second. Temperature and pressure were recorded simultaneously with the digital holograms of plankton. **Figure 3** shows the vertical distribution profile of plankton concentration by taxa (spp/m^3 is referred to individuals/m^3). As a result of automatic classification, no *Chaetognatha*, *Appendicularia*, *Rotifera*, and phytoplankton chains were found in the reconstructed holographic images, so they are not illustrated on the scheme. The time of obtaining one reference point of the scheme on the shipboard computer did not exceed 20 s; the full background profile to a depth of 7 m was formed within 2 min.

Discussion of Experimental Results on Plankton Classification Using the DHC Technology

The experiments showed that, within the accomplished version, the classification algorithm using the morphological parameter

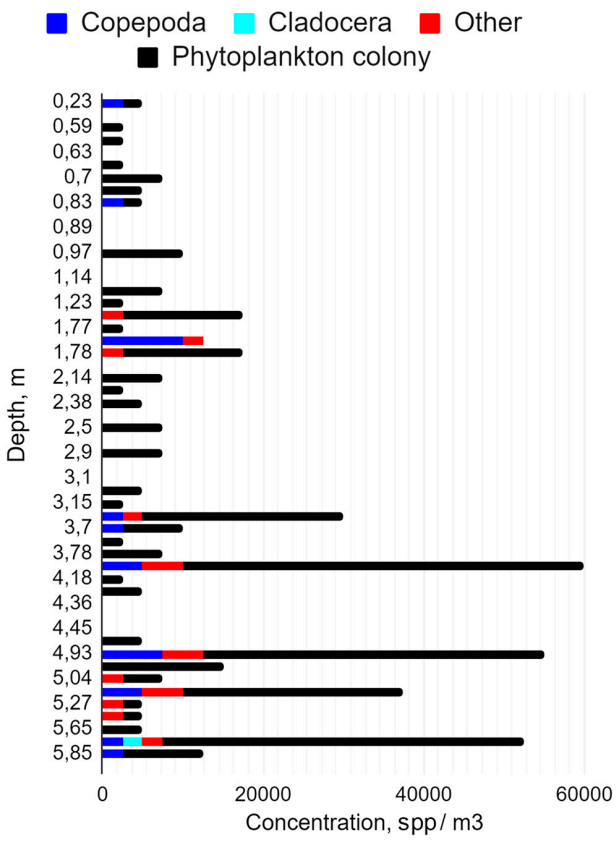

FIGURE 3 | Distribution profile of plankton concentrations of various taxa in depth up to 6 m. The following taxa are present: *Copepoda* (blue), *Cladocera* (turquoise), other (red), and phytoplankton colony (black).

makes it possible to solve the problem quickly (the time required to obtain the result is <1 s and depends on the number of plankton particles and the frame size of the restored image); however, the classification accuracy by orders varies within 50–60%. A relatively low accuracy is bound to both objective reasons (by-products, turbulence, and, as a result, noise of the restored particle images) and the software attempting to carry out a rapid preliminary classification. An increase in accuracy will require increasing the time for processing and recognition of images, i.e., depending on the task, here it is necessary to observe the "accuracy-computing speed" balance. Besides that, in order to classify such taxa as the *colonies of phytoplankton* and *other* with higher accuracy in the future, it is necessary to supplement the capabilities of hardware and problem-oriented software, in particular, to introduce the diagnostics of additional features such as "living" or "not living" and "phytoplankton" or "zooplankton."

EXPERIMENTAL MARINE STUDIES OF PLANKTON TEMPORAL CHARACTERISTICS

One of the experiments to study the temporal characteristics of plankton was conducted in the Kola Bay. The data were obtained in 2018, on the research ship *Dalnie Zelentsy* during its anchorage, using DHC. DHC as part of a hardware and a software complex including hydrophysical sensors (pressure gauge and microwave conductivity sensor) was fixed at a depth of 1.5 m from the bottom (6.5–8.5 m from the water surface, depending on the tidal processes). The conductivity and the pressure details were transmitted from the sensors of the hardware and the software complex to the shipboard computer simultaneously with the digital holograms of plankton. The data on plankton were acquired *via* the shipboard computer from digital holograms using DHC technology. One of the features of this experiment was the remote operation of the device – the device was connected and controlled remotely from Tomsk; simultaneously, the data (digital holograms and data on plankton, pressure, and conductivity) were transmitted *via* communication lines to Tomsk.

In order to obtain data on plankton concentration, the measurements were performed during the day with the frequency of one count per hour. The volume recorded per exposure was 1 dm^3. **Figure 4A** shows the daily range of the total concentration of all particles identified in images recovered from digital holograms as well as pressure and conductivity. Severe daily variations in the water level on the day of the

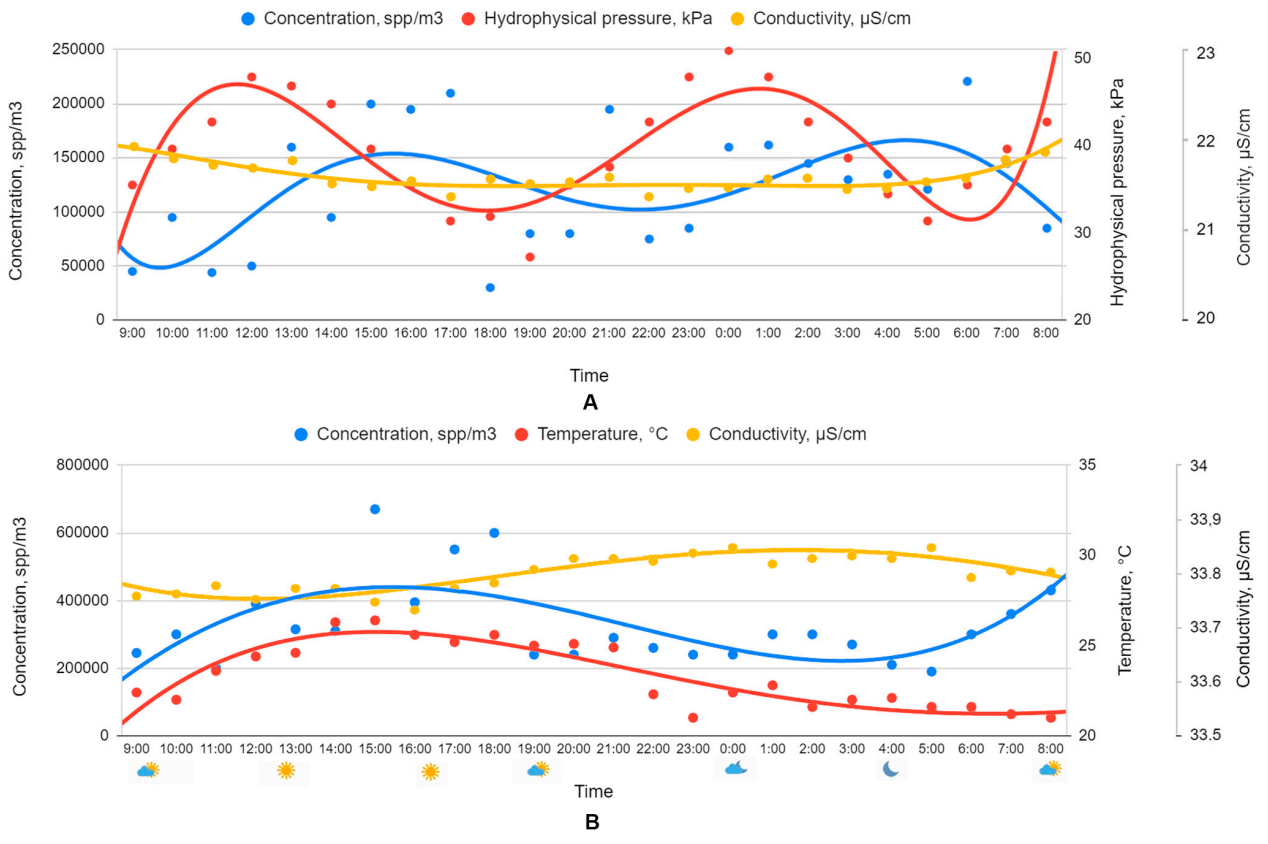

FIGURE 4 | Data obtained with the use of the digital holographic camera as part of the hardware and the software complex **(A)** in the Kola Bay at the stationary station, at a fixed depth of 1.5 m from the bottom (25.06.2018) and **(B)** in the Black Sea in the area of the stationary hydrophysical station (28.08.2018). The solid lines indicate **(A)** 6th- and **(B)** 4th-degree polynomial approximations.

measurements, caused by the tidal processes in the Kola Bay, resulted in significant changes in the depth of the coastal area from 8 to 10 m. This, in turn, led to changes in hydrostatic pressure in the anchorage area. The daily variations of coastal plankton concentration also strongly changed and were 20,000–220,000 spp/m^3. The given data (**Figure 4A**) show that the change in plankton concentration follows the tidal processes, with a delay of about 4 h. It can reasonably be assumed that this is caused by the horizontal advection of plankton toward the tidal movement of water masses since the device is fixed at a constant distance from the bottom (1.5 m). The results clearly illustrate the capabilities of the DHC technology; however, in this case, they are not sufficient for full interpretation, in particular, to explain the 4-h delay in the change in plankton concentration relative to the ebb and the flow.

Another type of plankton migration, vertical, is illustrated by the dependencies shown in **Figure 4B**, obtained during the mission to the Black Sea, near the Katsiveli village.

During the mission to the Black Sea, the DHC, as part of the hardware and the software complex, was operating from a stationary hydrophysical platform. The volume recorded per exposure, as in the previous case, was 1 dm^3. In order to study the temporal characteristics of plankton, the data were recorded every hour during the day at a depth of 10 m, fixed relative to the water surface, unlike in the previous case when the distance from the bottom was fixed. Conductivity and temperature details were transmitted from the sensors of the hardware and the software complex to the shipboard computer simultaneously with the digital holograms of plankton. The obtained results are graphically shown in **Figure 4B**. The concentration of plankton in the Black Sea is significantly higher than that in the waters of the Kola Bay in absolute magnitude, but the dynamics of these changes is slightly smaller. The daily variations of plankton concentration were 200,000–700,000 spp/m^3. It shall be noted that the daily variation of plankton concentration correlates reasonably well with the temperature change, thus indicating a vertical migration of plankton. At the same time, its noticeable deviation in pre-morning hours, which is most likely associated with sunrise, indicates the multifactority of processes.

Thus, the results given in this section demonstrate quite good DHC ability with respect to the study of plankton in a wide range of concentrations and in different weather conditions. Besides that, these clearly illustrate the need to register hydrophysical parameters simultaneously with plankton holographing to ensure a reliable interpretation of the processes.

CONCLUSION

These experimental results show that a submersible digital holographic camera based on the DHC technology as part of a hardware and a software complex allows carrying out *in situ* measurements of plankton, automating the process of obtaining data on its temporal and spatial distribution as well as classifying plankton species by classes within the specified taxonomic groups (*Chaetognatha*, *Copepoda*, *Appendicularia*, *Cladocera*, *Rotifera*, phytoplankton colonies, phytoplankton chains, and others).

The study presents the results of automatic classification of plankton in laboratory and field conditions together with depth profiles and daily variations of plankton concentration as measured by a submersible digital holographic camera in natural conditions (Kara Sea, Kola Bay, and Black Sea). The obtained results demonstrate quite good DHC ability with respect to the study of plankton in a wide range of concentrations and in different weather conditions. Besides that, these clearly illustrate the need to register hydrophysical parameters simultaneously with plankton holographing to ensure a reliable interpretation of the processes.

It is shown that, within the accomplished version, the classification algorithm using the morphological parameter makes it possible to solve the problem quickly (the time required to obtain the result is <1 s and depends on the number of plankton particles and the frame size of a restored image); however, the classification accuracy by orders varies within 50–60%.

The accuracy increase will require increasing the time for processing and recognition of images, i.e., depending on the task, here it is necessary to observe the "accuracy-computing speed" balance. Besides that, in order to classify such taxa as the *colonies of phytoplankton* and *other* with higher accuracy in the future, it is necessary to supplement the capabilities of hardware and problem-oriented software, in particular, to introduce the diagnostics of additional features such as "living" or "not living" and "phytoplankton" or "zooplankton."

DATA AVAILABILITY STATEMENT

The datasets generated for this study are available on request to the corresponding author.

AUTHOR CONTRIBUTIONS

VD and IP contributed to the concept and the design of the study and the results interpretation. AD developed and organized the soft database and performed the statistical analysis. SM performed the laboratory experiments and the validation of classification. NK, AO, and SD performed the field experiments. AD and IP wrote the first draft of the manuscript. VD contributed to revisions and corrections. All authors reviewed and approved the final version of the manuscript.

FUNDING

The research using DHC in laboratory and full-scale conditions was supported by the Tomsk State University Competitiveness Improvement Program under Academician D.I. Mendeleev Fund Program. The development of algorithms for particles classification based on the information extracted from digital holograms was funded by RFBR, project number 19-32-90233.

ACKNOWLEDGMENTS

We express our gratitude to the employees of the Center for Biosafety of Nanomaterials and Nanotechnologies of TSU for the laboratory experiment on the verification of classification capabilities and for the useful discussion.

SUPPLEMENTARY MATERIAL

The Supplementary Material for this article can be found online at: https://www.frontiersin.org/articles/10.3389/fmars.2020.00653/full#supplementary-material

FIGURE S1 | (A) Histogram of particle distribution by taxon (automatic classification). Taxon designation: 1 – phytoplankton colony, 2 – phytoplankton chain, 3 – *Copepoda*, 4 – *Appendicularia*, 5 – *Rotifera*, 6 – *Cladocera*, 7 – other. **(B)** Histogram of particle size distribution.

FIGURE S2 | (A) Histogram of particle distribution by taxon (automatic classification). Taxon designation: 1 – phytoplankton colony, 2 – phytoplankton chain, 3 – *Copepoda*, 4 – *Appendicularia*, 5 – *Rotifera*, 6 – *Cladocera*, 7 – other. **(B)** Histogram of particle size distribution.

FIGURE S3 | 2D display of holographic image obtained using digital holographic camera in the water area of the Kara Sea. The result of automatic classification – the color of the rectangle circumscribed around the particle: black, phytoplankton colony; gray, phytoplankton chain; dark blue, *Copepoda*; blue, *Cladocera*; red, other.

FIGURE S4 | (A) Histogram of particle distribution by taxon (automatic classification). Taxon designation: 1 – phytoplankton colony, 2 – phytoplankton chain, 3 – *Copepoda*, 4 – *Appendicularia*, 5 – *Rotifera*, 6 – *Cladocera*, 7 – other. **(B)** Histogram of particle size distribution.

TABLE S1 | Confusion matrices.

REFERENCES

Batten, S. D., Abu-Alhaija, R., Chiba, S., Edwards, M., Graham, G., Jyothibabu, R., et al. (2019). A global plankton diversity monitoring program. *Front. Mar. Sci.* 6:321. doi: 10.3389/fmars.2019.00321

Bochdansky, A. B., Jericho, M. H., and Herndl, G. J. (2013). Development and deployment of a point-source digital inline holographic microscope for the study of plankton and particles to a depth of 6000 m. *Limnol. Oceanogr. Methods* 11, 28–40. doi: 10.4319/lom.2013.11.28

Chiba, S., Batten, S., Martin, C. S., Ivory, S., Miloslavich, P., and Weatherdon, L. V. (2018). Zooplankton monitoring to contribute towards addressing global biodiversity conservation challenges. *J. Plankton Res.* 40, 509–518. doi: 10.1093/plankt/fby030

Cowen, R. K., and Guigand, C. M. (2008). In situ ichthyoplankton imaging system (ISIIS): system design and preliminary results. *Limnol. Oceanogr. Methods* 6, 126–132. doi: 10.4319/lom.2008.6.126

Davies, E. J., and Nepstad, R. (2017). In situ characterisation of complex suspended particulates surrounding an active submarine tailings placement site in a Norwegian fjord. *Reg. Stud. Mar. Sci.* 16, 198–207. doi: 10.1016/j.rsma.2017.09.008

Dyomin, V., Davydova, A., Davydov, S., Kirillov, N., Morgalev, Y., Olshukov, A., et al. (2019a). "Hydrobiological Probe for the in Situ Study and Monitoring of Zooplankton," in *2019 IEEE Underwater Technology (UT)*, Kaohsiung: IEEE, 1–6. doi: 10.1109/UT.2019.8734334

Dyomin, V., Davydova, A., Olshukov, A., and Polovtsev, I. (2019b). "Hardware means for monitoring research of plankton in the habitat: problems, state of the art, and prospects," in *OCEANS 2019 - Marseille*, Marseille: IEEE, 1–5. doi: 10.1109/OCEANSE.2019.8867512

Dyomin, V., Gribenyukov, A. I., Davydova, A. Y., Zinoviev, M. M., Olshukov, A. S., Podzyvalov, S. N., et al. (2019c). Holography of particles for diagnostic tasks. *Appl. Opt.* 58, G300–G310. doi: 10.1364/DH.2019.Th2A.1

Dyomin, V. V., Polovtsev, I. G., Davydova, A. Y., and Olshukov, A. S. (2019d). "Digital holographic camera for plankton monitoring," in *Practical Holography XXXIII: Displays, Materials, and Applications*, eds H. I. Bjelkhagen, and V. M. Bove, San Francisco, CA: SPIE, 109440L. doi: 10.1117/12.2512030

Dyomin, V. V., and Kamenev, D. V. (2016a). Evaluation of algorithms for automatic data extraction from digital holographic images of particles. *Russ. Phys. J.* 58, 1467–1474. doi: 10.1007/s11182-016-0669-z

Dyomin, V. V., and Kamenev, D. V. (2016b). "Information extraction from digital holograms of particles," in *Ocean. 2016 - Shanghai*, Shanghai, doi: 10.1109/OCEANSAP.2016.7485674

Dyomin, V. V., Olenin, A. L., Polovcev, I. G., Kamenev, D. V., Kozlova, A. S., and Olshukov, A. S. (2018a). Marine tests of a digital holographic module using a measuring technological platform. *Oceanology* 58, 749–759. doi: 10.1134/S0001437018050028

Dyomin, V. V., Olshukov, A., and Davydova, A. (2018b). "Data acquisition from digital holograms of particles," in *Unconventional Optical Imaging*, eds C. Fournier, M. P. Georges, and G. Popescu, Strasbourg: SPIE, 106773B. doi: 10.1117/12.2309868

Dyomin, V. V., Polovtsev, I. G., and Davydova, A. Y. (2018c). "Marine particles investigation by underwater digital holography," in *Unconventional Optical Imaging*, eds C. Fournier, M. P. Georges, and G. Popescu, Strasbourg: SPIE, 1067725. doi: 10.1117/12.2309871

Dyomin, V. V., Polovtsev, I. G., Olshukov, A. S., and Davydova, A. Y. (2018d). "DHC Sensor — a tool for monitoring the plankton biodiversity in a habitat," in *2018 OCEANS - MTS/IEEE Kobe Techno-Oceans (OTO)*, Kobe: IEEE, 1–5. doi: 10.1109/OCEANSKOBE.2018.8559131

Dyomin, V. V., and Olshukov, A. S. (2016). Improvement of the quality of reconstructed holographic images by extrapolation of digital holograms. *Russ. Phys. J.* 58, 1413–1419. doi: 10.1007/s11182-016-0663-5

Dyomin, V. V., Polovtsev, I. G., and Davydova, A. Y. (2017). "Fast recognition of marine particles in underwater digital holography," in *23rd International Symposium on Atmospheric and Ocean Optics: Atmospheric Physics*, eds O. A. Romanovskii, and G. G. Matvienko, Irkutsk: SPIE, 1046627. doi: 10.1117/12.2292019

Guo, B., Yu, J., Liu, H., Yuan, G., Xu, W., Hou, R., et al. (2018). "Miniaturized digital inline holographic camera for in-situ plankton detection," in *Advanced Sensor Systems and Applications VIII*, eds T. Liu, and S. Jiang, Beijing: SPIE, 32. doi: 10.1117/12.2500788

Hakkari, L. (1972). Zooplankton species as indicators of environment. *Aqua Fennica* 1, 46–54.

HoloSea (2020). *Submersible Holographic Microscope – 4Deep*. Available at: http://4-deep.com/products/submersible-microscope/ (accessed June 10, 2020).

Lisst-Holo2 (2020). - *Sequoia ScientificSequoia Scientific*. Available at: http://www.sequoiasci.com/product/lisst-holo/ (accessed June 10, 2020).

Lombard, F., Boss, E., Waite, A. M., Vogt, M., Uitz, J., Stemmann, L., et al. (2019). Globally consistent quantitative observations of planktonic ecosystems. *Front. Mar. Sci.* 6:196. doi: 10.3389/fmars.2019.00196

Lumini, A., and Nanni, L. (2015). Ocean ecosystems plankton classification: theories and applications. *Recent Adv. Comput. Eng. Ser.* 29, 257–263. doi: 10.1007/978-3-030-03000-1

Ohman, M. D., Powell, J. R., Picheral, M., and Jensen, D. W. (2012). Mesozooplankton and particulate matter responses to a deep-water frontal system in the southern California Current System. *J. Plankton Res.* 34, 815–827. doi: 10.1093/plankt/fbs028

Olson, D. L., and Delen, D. (2008). *Advanced Data Mining Techniques*. Berlin: Springer Berlin Heidelberg, doi: 10.1007/978-3-540-76917-0

Olson, R. J., and Sosik, H. M. (2007). A submersible imaging-in-flow instrument to analyze nano-and microplankton: imaging FlowCytobot. *Limnol. Oceanogr. Methods* 5, 195–203. doi: 10.4319/lom.2007.5.195

Rotermund, L. M., Samson, J., and Kreuzer, J. (2016). A submersible holographic microscope for 4-D in-situ studies of micro-organisms in the ocean with intensity and quantitative phase imaging. *J. Mar. Sci. Res. Dev.* 06, 1–5. doi: 10.4172/2155-9910.1000181

Schnars, U., and Juptner, W. P. O. (2002). Digital recording and numerical reconstruction of holograms. *Meas. Sci. Technol.* 13, R85–R101.

Sun, H., Benzie, P. W., Burns, N., Hendry, D. C., Player, M. A., and Watson, J. (2008). Underwater digital holography for studies of marine plankton. *Source Philos. Trans. Math. Phys. Eng. Sci.* 366, 1789–1806. doi: 10.1098/rsta.2007.2187

Talapatra, S., Sullivan, J., Katz, J., Twardowski, M., Czerski, H., Donaghay, P., et al. (2012). "Application of in-situ digital holography in the study of particles, organisms and bubbles within their natural environment," in *Proceedings of SPIE - The International Society for Optical Engineering*, eds W. W. Hou, and R. Arnone, Baltimore, MD, 837205. doi: 10.1117/12.920570

Watson, J. (2011). Submersible digital holographic cameras and their application to marine science. *Opt. Eng.* 50:091313. doi: 10.1117/1.3605678

Watson, J. (2018). "High-resolution underwater holographic imaging," in *Encyclopedia of Modern Optics*, eds D. G. Steel, and R. D. Guenther (Amsterdam: Elsevier), 106–112. doi: 10.1016/B978-0-12-803581-8.09612-0

Conflict of Interest: The authors declare that the research was conducted in the absence of any commercial or financial relationships that could be construed as a potential conflict of interest.

Copyright © 2020 Dyomin, Davydova, Morgalev, Kirillov, Olshukov, Polovtsev and Davydov. This is an open-access article distributed under the terms of the Creative Commons Attribution License (CC BY). The use, distribution or reproduction in other forums is permitted, provided the original author(s) and the copyright owner(s) are credited and that the original publication in this journal is cited, in accordance with accepted academic practice. No use, distribution or reproduction is permitted which does not comply with these terms.

frontiers in Marine Science

ORIGINAL RESEARCH
published: 07 September 2020
doi: 10.3389/fmars.2020.556239

Swimming and Sinking Behavior of Warm Water Pelagic Snails

*Ferhat Karakas[1], Jordan Wingate[2], Leocadio Blanco-Bercial[2], Amy E. Maas[2] and David W. Murphy[1]**

[1] Department of Mechanical Engineering, University of South Florida, Tampa, FL, United States, [2] Bermuda Institute of Ocean Sciences, St. Georges, Bermuda

Swimming and sinking behavior by pelagic snails is poorly studied but is important in their ecology, predator-prey interactions, and vertical distributions. We used a low magnification, high speed stereophotogrammetry system to study the swimming and sinking kinematics of nine warm water pelagic snail species (seven thecosomes, one gymnosome, and one heteropod). As different thecosomatous pteropod species may have coiled, elongated, or globular shell morphologies, we focused on how the shell shape, body geometry, and body size affect their swimming behavior from a fluid mechanics perspective. In addition, ZooScan image analysis and metabarcoding of archived vertically stratified MOCNESS samples were used to relate swimming behaviors to night time and daytime vertical distributions. While different large scale swimming patterns were observed, all species exhibited small scale sawtooth swimming trajectories caused by reciprocal appendage flapping. Thecosome swimming and sinking behavior corresponded strongly with shell morphology and size, with the tiny coiled shell pteropods swimming and sinking the slowest, the large globular shelled pteropods swimming and sinking the fastest, and the medium-sized elongated shell pteropods swimming and sinking at intermediate speeds. However, the coiled shell species had the highest normalized swimming and sinking speeds, reaching swimming speeds of up to 45 body lengths s^{-1}. The sinking trajectories of the coiled and elongated shell pteropods were nearly vertical, but globular shell pteropods use their hydrofoil-like shell to glide downwards at approximately 20° from the vertical, thus retarding their sinking rate. The swimming Reynolds number (*Re*) increased from the coiled shell species [$Re \sim O(10)$] to the elongated shell species [$Re \sim O(100)$] and again for the globular shell species [$Re \sim O(1000)$], suggesting that more recent lineages increased in size and altered shell morphology to access greater lift-to-drag ratios available at higher *Re*. Swimming speed does not correlate with the vertical extent of migration, emphasizing that other factors, likely including light, temperature, and predator and prey fields, influence this ecologically important trait. Size does play a role in structuring the vertical habitat, with larger individuals tending to live deeper in the water column, while within a species, larger individuals have deeper migrations.

Keywords: pteropod, zooplankton, heteropod, diel vertical migration, NGDR, Reynolds number, metabarcoding, ZooScan

OPEN ACCESS

Edited by:
Michelle Jillian Devlin, Centre for Environment, Fisheries and Aquaculture Science (CEFAS), United Kingdom

Reviewed by:
Jeannette Yen, Georgia Institute of Technology, United States
Clara Manno, British Antarctic Survey (BAS), United Kingdom

****Correspondence:***
David W. Murphy
davidmurphy@usf.edu

Specialty section:
This article was submitted to Marine Ecosystem Ecology, a section of the journal Frontiers in Marine Science

Received: *27 April 2020*
Accepted: *18 August 2020*
Published: *07 September 2020*

Citation:
Karakas F, Wingate J, Blanco-Bercial L, Maas AE and Murphy DW (2020) Swimming and Sinking Behavior of Warm Water Pelagic Snails. Front. Mar. Sci. 7:556239. doi: 10.3389/fmars.2020.556239

INTRODUCTION

Pteropods and heteropods are small (mm to cm scale) marine snails that may be found in mesopelagic to surface waters throughout the global ocean. Of the extant holoplanktonic mollusks, heteropods and pteropods are the most numerous and diverse, playing a role in food web structure and in carbon and carbonate export (Gilmer, 1972; Lalli and Gilmer, 1989; Hunt et al., 2008). Thecosomatous pteropods in particular maintain a large biomass in some regions and appear to have a substantial biogeochemical role in carbonate and carbon cycling (Bednaršek et al., 2012; Buitenhuis et al., 2019). Gymnosomes pteropods and heteropods are substantially less abundant but are ecologically important as they are active predators of other zooplankton, including the thecosomes.

Pteropods consist of two orders that include both the thecosomatous species, which are generally shelled as adults, and the gymnosomatous species, which lose their juvenile shell during development (Lalli and Gilmer, 1989; Peijnenburg et al., 2019). The shells of thecosomes vary dramatically by species, ranging from the basal spiral form, to conical, globular, and gelatinous forms. Two of the three families of heteropods have shells as adults, and although they are consistently spiral in shape, they are distinctly different in size and function. In the most numerous family, the Atlantidae, the adult individuals can retract completely into the dorsoventrally flattened shell, while in the larger more streamlined Carinariidae the dorsally oriented shell is substantially smaller than the body. Despite being from two distinct molluscan lineages, all three groups build shells composed of aragonite during some portion of their development, and use highly flexible appendages that are derived from the basal molluscan foot structure for locomotion (Lalli and Gilmer, 1989). In the pteropods the foot has evolved into a pair of muscular, wing-like appendages, while heteropods have a single muscular swimming appendage which, in Atlantidae, coordinates with the shell for swimming (Karakas et al., 2018).

These zooplanktonic marine snails are famously difficult to study, and most species currently cannot be cultured (Howes et al., 2014; Thabet et al., 2015). Thus, detailed study of much of their biology, ecology, and behavior has been limited. For instance, in most groups swimming, a key behavior for pelagic organisms, has not been assessed. In the zooplankton, swimming influences predator-prey dynamics, both moderating escape and hunting behavior, but also controlling the process of diel vertical migration. This migratory phenomenon is a common feature in pelagic ecosystems, whereby organisms actively congregate in the surface waters during the night to feed, and then descend to depth during the day. These daily migrations are thought to be energetically expensive, with pteropods and heteropods smaller than 1 cm traveling hundreds of meters per day (Wormuth, 1981; Maas et al., 2012; Wall-Palmer et al., 2018). Despite the costs, the process is believed to provide a number of advantages including niche partitioning, metabolic advantage due to colder temperatures at depth, avoidance of light or high temperatures, and, most importantly, predator avoidance (Hays, 2003; Antezana, 2009).

Even though it is challenging to study the pelagic marine snails, some previous research has been carried out on marine snail swimming, mostly on polar species with limited morphological or taxonomic diversity. In the gymnosomes, Satterlie et al. (1985) investigated *Clione limacina* swimming and noticed that this gymnosome flaps its wings back and forth in the dorsoventral plane with a high angle of attack and suggested that *C. limacina* may generate lift using the "clap-and-fling" mechanism described by Weis-Fogh (1973) in flying insects. Childress and Dudley (2004) investigated the critical flapping Reynolds number that enables *Clione antarctica* to propel itself by wing flapping. Borrell et al. (2005) studied the swimming kinematics of *Clione antarctica* and observed a sawtooth path during upward swimming. Szymik and Satterlie (2011) conducted experiments on *C. limacina* at slow and fast swimming speeds, and found that the wingbeat kinematics differ significantly between speeds. In the thecosomes, Chang and Yen (2012) found that *Limacina helicina* ascends along a sawtooth trajectory in mostly linear and sometimes helical swimming paths, but has straight sinking trajectories. *L. helicina* strokes its wings in a characteristic figure-of-eight pattern by extreme rotation of its body to produce lift (Murphy et al., 2016). Similar swimming characteristics such as sawtooth swimming trajectories and extreme body rotation were also observed in the closely related polar species *Limacina helicina antarctica* (Adhikari et al., 2016), and Mohaghar et al. (2019) performed a dimensional analysis of the swimming of this species. Morton (1954) described the swimming behavior of *Limacina retroversa* qualitatively, and more recently Bergan et al. (2017) conducted quantitative measurements of the swimming and sinking kinematics of the same species under the influence of elevated carbon dioxide, which alters shell properties. Karakas et al. (2020) showed that the tropical thecosome *Cuvierina atlantica* uses its highly flexible parapodia in a cylindrical overlap-and-fling mechanism twice during each stroke to generate lift. In the heteropods, Karakas et al. (2018) discovered that, contrary to previous accounts (Lalli and Gilmer, 1989), the atlantiid heteropod *Atlanta selvagensis* does not let its shell passively hang beneath it as it swims but instead flaps its shell in coordination with its swimming fin in order to swim. Finally, Zhou and Mittal (2017, 2018) used computational fluid dynamics simulations to examine the swimming behavior of the distantly related shell-less marine mollusks *Hexabranchus sanguineus* (the Spanish Dancer) and *Aplysia* (the sea hare), which are much larger than the pteropods and heteropods studied here.

Recent studies suggest that ocean acidification-induced changes to shell thickness or morphology may change pteropod swimming behavior, thus negatively affecting their ability to perform diel vertical migration. For example, Manno et al. (2012) claimed that a lower pH environment in combination with lower salinity negatively affected upward swimming ability of the pteropod *Limacina retroversa*. Ocean acidification may damage the pteropod shell, thus unbalancing the forces and torques involved in the animal swimming and thereby altering the swimming kinematics and fluid dynamics of swimming (Adhikari et al., 2016).

It has been posited that sinking may also be an important behavior for these pelagic marine snails in relation to their daily migration or predator avoidance. The aragonite shells of these animals make them extremely negatively buoyant, and for many species of shelled thecosomes or atlantid heteropods, disturbance causes retraction into the shell and rapid sinking behaviors (Gilmer and Harbison, 1986; Bergan et al., 2017). This negative buoyancy additionally strongly influences their role as important contributors to the active flux of carbon and carbonate from surface waters, as it increases the rate at which dead organisms are removed from the mixed layer and sequestered at depth. Importantly, the rapid sinking may allow shells to penetrate below the aragonite lysocline prior to dissolving, augmenting their export efficiency. Additionally, sinking can be energetically problematic as organisms must counteract their negative buoyancy to avoid sinking away from their desired vertical habitat.

Although thecosomes have been observed making large mucous webs that help them slow their sinking (Harbison and Gilmer, 1992), heteropods do not have this adaptation. However, Bergan et al. (2017) observed reduction in sinking speed when *L. retroversa* was filmed sinking with its wings extended compared to when a live animal sank with wings retracted. This suggests that pelagic snails can use their appendages to reduce their sinking speed.

Characterizing the behaviors associated with sinking and swimming in these groups thus has both ecological and biogeochemical significance. To date, however, most previous research has focused on high latitude species (e.g., *Limacina helicina*, *Limacina helicina antarctica*, *Limacina retroversa*, *Clione limacina*, and *Clione antarctica*). In polar regions, pteropods in particular are highly abundant, but there is little speciation and thus little variety in shell shape. In contrast, warm water regions are highly diverse, supporting a large variety or marine snails with distinct shell shapes and sizes (Burridge et al., 2017). Here we investigate the swimming and sinking kinematics of a large number of warm water thecosome species. We additionally investigate the swimming kinematics of a co-occurring gymnosome species and one atlantid heteropod species. The objective is to provide basic kinematic parameters across a range of species and to investigate the biomechanics of how swimming and sinking characteristics vary with shell shape and size. We then use imaging and metabarcoding techniques to detail the vertical habitat and migratory patterns of the pteropod species to explore how morphology and swimming biomechanics are related to distribution.

MATERIALS AND METHODS

Marine snails were collected offshore of Bermuda from a small boat using a Reeve net with 150 μm mesh size and a specialized 20 L cod end. Specimens were collected during nighttime cruises in May and September of 2017 and in May 2019. Animals were kept in the collected seawater for less than 1 h during the transit back to shore where they were quickly and gently isolated from the cod end. Individuals were visually checked for damage and species identification under a stereomicroscope, then stored in 1 L jars containing filtered seawater at an *in situ* temperature of 21°C and salinity of 36 psu. Data collection began immediately upon return from the cruise, and most experiments were completed within 1 day of collection.

A photogrammetry system comprising two synchronized high-speed monochrome Edgertronic cameras (Sanstreak Corp., San Jose, CA, United States) was used to measure the three-dimensional swimming trajectories of the organisms at low magnification (**Figure 1**). The cameras, lights, and aquarium were mounted on optical rails and a breadboard to rigidly support the system. Two 50 mm Nikon lenses at f/32 aperture and fiber optic illuminators with Fresnel lenses (focal length of 76.2 mm, part #32-593, Edmund Optics) were used to provide the field of view. A variety of pteropod and heteropod species were placed in an aquarium with 152.4 × 152.4 × 152.4 mm^3 inner dimensions and 6.35 mm wall thickness. This low magnification system provides a field of view at least 10 times larger than the largest animal of interest, thus allowing measurement of 15–20 full stroke cycles of upward swimming. The spatial resolution of the cameras was 98.4 μm $pixel^{-1}$ and the temporal resolution was 1.67 ms (corresponding to 600 frames per second). In a few videos, a frame rate of 300 frames per second was used. The low magnification stereophotogrammetric system was calibrated using the sparse bundle adjustment (SBA) method (Lourakis and Argyros, 2009) as implemented in Argus 3D (Jackson et al., 2016), in which a calibration wand was moved throughout the tank volume. The camera system was manually triggered when an animal swam into the field of view common to both cameras.

Ninety five videos of swimming marine snails ranging in length from 2 to 14 s were recorded. Videos were recorded of seven thecosome species (*Heliconoides inflatus*, *Limacina bulimoides*, *Cuvierina atlantica, Hyalocylis striata, Diacria trispinosa, Styliola subula, Creseis clava*), one gymnosome species *Pneumoderma atlantica*, and one unidentified atlantiid heteropod. Thecosome species which were captured but which could not be recorded swimming included *Diacria quadridentata*, *Diacavolinia longirostris, Limacina leuserii,* and *Creseis conica.* Recorded videos were divided into segments in which the animal was either sinking or swimming. Sinking was defined as when the animal completely ceased wing motion, resulting in downward motion. A video segment in which any wing motion was observed was classified as swimming, regardless of the resulting swimming direction. **Table 1** shows the number of swimming and sinking segments recorded for each species. Since many animals were added to the aquarium at once, it was not always possible to determine the individual identity of each animal. **Table 1** thus gives the estimated minimum number of individual animals of each species based on factors such as experiment date, animal length, and multiple animals of the same species simultaneously in the camera view. In order to measure swimming trajectories, one point in the center of the animal body was digitized in DLTdv software (versions 5, 7, and 8; Hedrick, 2008). Three dimensional swimming and sinking trajectories of the animal are thus reconstructed from the 2D camera coordinates. A global (XYZ) coordinate system is defined for trajectory analysis in which the XY plane is horizontal and the positive Z component

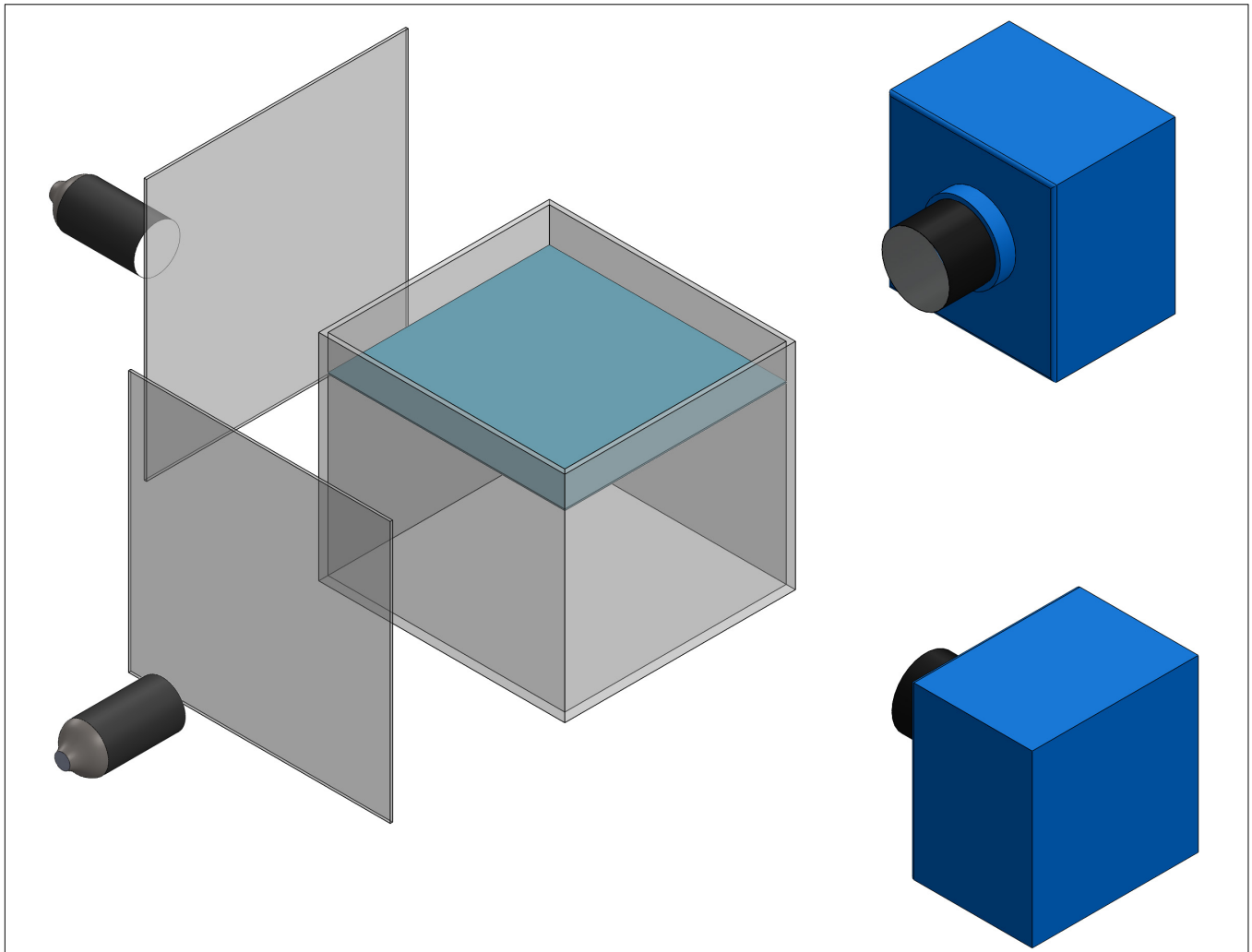

FIGURE 1 | Schematic of low magnification stereophotogrammetry system using to record swimming trajectories of various marine snails.

TABLE 1 | Number of individual animals, videos, and video segments analyzed for each marine snail species.

Order	Species	Minimum number of individual species	Number of videos	Number of video segments	Number of videos analyzed for swimming	Number of videos analyzed for sinking
Thecosome	*Heliconoides inflatus*	5	34	54	33	21
	Limacina bulimoides	2	4	7	4	3
	Cuvierina atlantica	3	28	34	21	13
	Hyalocylis striata	1	2	6	3	3
	Diacria trispinosa	3	8	11	8	3
	Creseis clava	1	4	4	4	0
	Styliola subula	2	7	15	10	5
Gymnosome	*Pneumoderma atlantica*	2	6	6	6	0
Heteropod	Atlantiid heteropod	2	2	2	2	0

is directed upward. **Figure 2** shows CAD models representing each of the recorded species and the measured body length L. In two species (e.g., *H. inflatus*, *L. bulimoides*), L represents the shell length, which corresponds to the longest dimension of the animal. In the other thecosome species, L includes the shell and the proximal portions of the parapodia. The length L was measured by digitizing the two corresponding points on the animal over at least 20 consecutive frames in DLTdv5 software

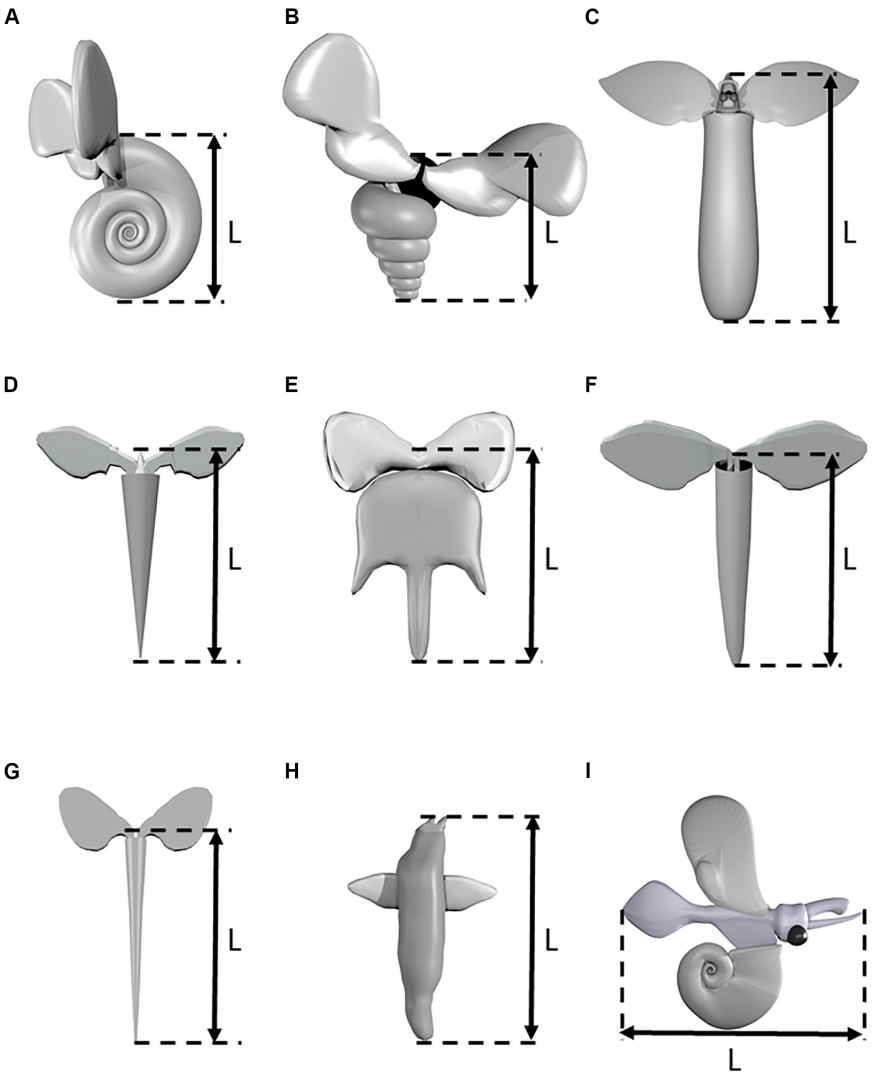

FIGURE 2 | Three-dimensional models of various marine snail species. **(A)** Heliconoides inflatus, **(B)** Limacina bulimoides, **(C)** Cuvierina atlantica, **(D)** Hyalocylis striata, **(E)** Diacria trispinosa, **(F)** Styliola subula, **(G)** Creseis clava, **(H)** Pneumoderma atlantica, **(I)** *Heteropod* sp. Models are not drawn to scale.

(Hedrick, 2008). The wingspan L_f (measured from wingtip to wingtip at the time point when the wings were fully extended) was similarly measured for *D. trispinosa*, *S. subula*, *C. clava*, *Pneumoderma atlantica*, and the heteropod species. Values of L_f for the other four species were similarly obtained from videos from the high magnification photogrammetry system described in Karakas et al. (2018).

Instantaneous swimming or sinking speed was calculated using the forward difference technique across consecutive time points. Mean swimming speed U and sinking speed U_{sink} for each trajectory were calculated by averaging the animal's speed over the entire extent of that trajectory. Species-specific swimming and sinking speeds $\bar{U}$ and $\bar{U}_{sink}$ were calculated by averaging the mean values of U and U_{sink} across all recorded trajectories for each species. Normalized swimming speeds U′ and sinking speeds U'_{sink} were calculated for each trajectory by dividing the U or U_{sink} by the corresponding animal's length L. Species-specific normalized swimming and sinking speeds $\bar{U}'$ and $\bar{U}'_{sink}$ were calculated by averaging the mean values of U′ and U'_{sink} across all recorded trajectories of each species in the same life stage. The vertical component of sinking speeds $\bar{U}_{sink}$ and $\bar{U}'_{sink}$ also were calculated. A mean body length $\bar{L}$ was calculated for each species by averaging L across all recorded trajectories. Mean beat frequency f for each trajectory was determined in ImageJ as the average beat frequency over at least 10 full wingbeat cycles. Videos from the high magnification photogrammetry system described in Karakas et al. (2018) also were used to acquire additional data on wingspan, and wingbeat frequency. In addition, the net-to-gross displacement ratio (NGDR), a measure of trajectory tortuosity, was determined for swimming behaviors. NGDR is defined as the ratio of the distance between the starting and ending points of the trajectory divided by the

total distance traveled between the starting and ending points. Because this metric is scale dependent, NGDR was calculated over a distance of five body lengths for each species. Thus, NGDR was calculated for five body length along each trajectory starting from the beginning of that trajectory. NGDR values could not be calculated for all recorded trajectories because some trajectories were less than five body lengths. Because many of the animals experienced some horizontal displacement as they sank, a glide angle α was also measured for the sinking trajectories, where α is the acute angle between the vertical axis and a line representing the total displacement. Finally, the body-based Reynolds number $Re = UL/\nu$ of each swimming animal was calculated, where the kinematic viscosity ν of seawater at 21°C is taken as 1.02×10^{-6} $m^2\ s^{-1}$. A sinking Reynolds number $Re_{sink} = U_{sink}L/\nu$ also was calculated.

One-way analysis of variance (ANOVA) was used to examine differences in the mean swimming speed, mean sinking speed, mean normalized swimming speed, mean normalized sinking speed, glide angle, and NGDR among the different thecosome shell groups (e.g., coiled, elongated, and globular), with a significance testing value of 0.05. Further, the Tukey-Kramer pair wise comparison test was used for multiple comparisons of these parameters among these groups. All statistical calculations and evaluations of data were performed in MATLAB (v9.6 R2019a, The MathWorks Inc., MA, United States).

To provide ecological context for our measurements we analyzed the vertical distribution of pteropods and heteropods using archived 1 m Multiple Opening/Closing Net and Environmental Sensing System (Wiebe et al., 1985) samples. These samples were collected with 150 μm nets that were deployed during the mid-day and mid-evening on cruises carried out in July of 2016, 2017, 2018, and 2019 as well as October 2018, from 0 to 1000 m in the vicinity of the Bermuda Atlantic Time Series (sampling details provided in **Supplementary File S1**). This resulted in six night time profiles and eight daytime profiles of the water column. Upon retrieval, the catch from each of the eight discrete nets was divided into splits and half was preserved in buffered 4% formalin in seawater. A subset of this sample was imaged and measured, and marine snails were taxonomically classified using a ZooSCAN ver. 3 at 4,800 dpi and the ZooProcess pipeline (Gorsky et al., 2010; Vandromme et al., 2012). All images representing pelagic snails were identified to species and only those that clearly had a body in the shell (more likely to represent a live individual) were enumerated. These were converted to abundances by applying the volume filtered and split counts to generate daytime and night time vertical distributions of adult individuals. The distribution was plotted as abundance per size bin (using major axis in mm) using the "violin plot" option of the ggplot2 packing in R.

Although the ZooSCAN method provides numerical counts and size class distributions for individuals, it is constrained by the fact that pteropods are relatively rare members of the zooplankton community. Additionally, it can be difficult to assign a species to some images, particularly for the smaller size classes. To augment our distributional analyses we additionally employed metabarcoding techniques on one MOCNESS tow pair. This tool provides species-specific identification and is more likely to sample rare individuals in the tows. Ethanol-preserved samples from July 2017 were analyzed following a metabarcoding protocol similar to Blanco-Bercial (2020) but interrogating the V1–V2 region of the 18S rDNA gene, using the primers described in Fonseca et al. (2010). Briefly, half of the ethanol sample was ground with a homogenizer, treated with proteinase K, and DNA was extracted using a SDS-chloroform protocol (OMEGA EZNA DNA Mollusk kit). Three PCR reactions were done for each sample with custom adapters and the resulting products were pooled by sample and sent to University of Rochester for sequencing using the MiSeq Reagent Kit v2 (500-cycles; 2 × 300) V2 chemistry.

Sequence data was processed as in Blanco-Bercial (2020), with initial cleaning and alignment with MOTHUR (Schloss et al., 2009). Relative counts for all samples were standardized to 20,000 reads $sample^{-1}$ and values below 1 discarded. Taxonomic units were built at 100% similarity after accounting for PCR error using Deblur (Amir et al., 2017) and a SILVA-derived custom 18S database was used to feed MOTHUR for the OTU assignment using the nr database from SILVA (see Blanco-Bercial, 2020). Pteropod taxonomy was confirmed by BLAST (March 22, 2020) and by phylogenetic placement using RAxML ver. 8 and mrBayes (Ronquist et al., 2012; Stamatakis, 2014 as in Maas et al., 2013), using an alignment created with sequences available from GenBank for "Pteropoda 18S" and adding some other Euopisthobranchia as outgroups. The sequence relative abundances were weighed against the measured total live biovolume (calculated from paired image dataset; see above), then calculated per square meter. This results in the proportional contribution of a particular sequence per mm^3 of living biovolume throughout the water column. The distribution of OTUs present in more than four samples were analyzed and plotted to assess diel vertical migratory patterns.

RESULTS

Figures 3, **4** show representative 3D upward swimming trajectories and **Figure 5** shows representative 3D sinking trajectories of the marine snails (i.e., 7 thecosomatous pteropods, 1 gymnosomatous pteropod, and 1 atlantiid heteropod) investigated in this study. These trajectories, along with data on shell length, swimming speed, wingbeat frequency, and *Re* presented in **Table 2**, will be used to describe the swimming kinematics of each species.

The thecosome *Heliconoides inflatus* (**Figure 2A**) has a flattened coiled shell with a thickened rib on the outer margin, and a body length of 0.9–1.2 mm and flaps it parapodia at 6.6–11.1 Hz, resulting in swimming speeds of 12–51 mm s^{-1} and *Re* = 12–66 (**Table 2**). As seen in **Figure 3**, small-scale trajectory oscillations are particularly evident in this species. These oscillations are due to individual power and recovery strokes by the swimming appendages which cause extreme pitching of the shell, resulting in a sawtooth swimming trajectory in which the animal may even sink at the end of each half stroke (Adhikari et al., 2016; Murphy et al., 2016; Karakas et al., 2018). At the large scale, *H. inflatus* exhibits a characteristic upwards helical

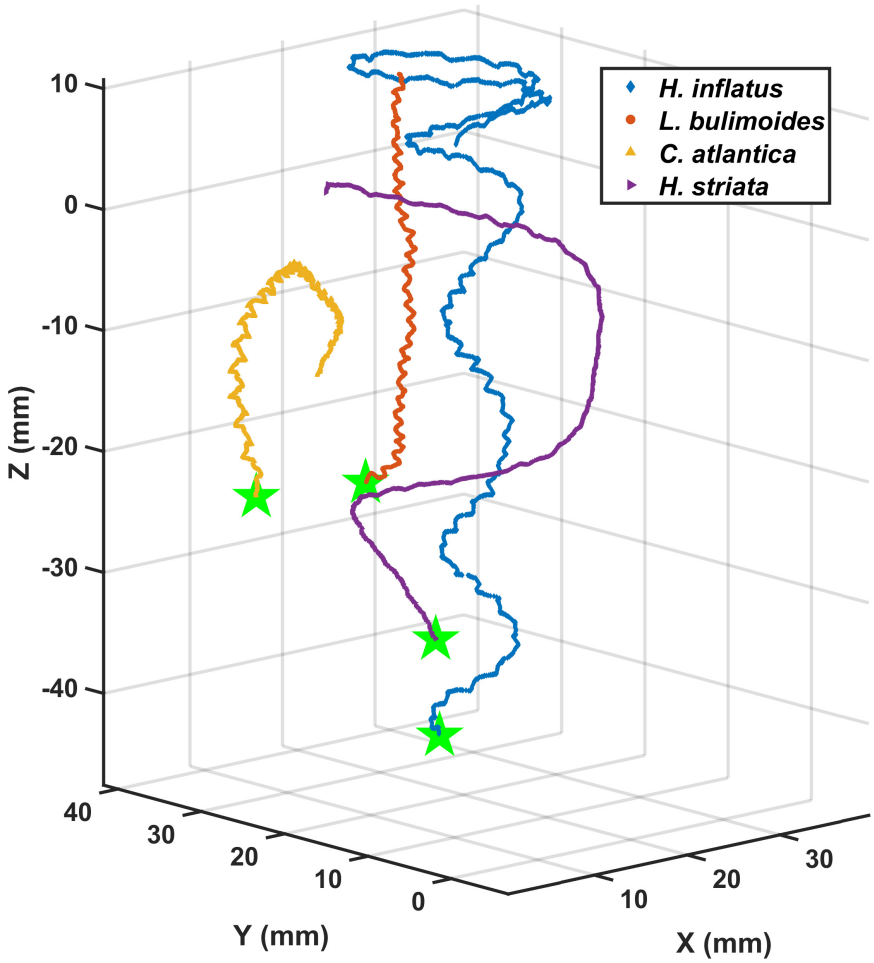

FIGURE 3 | Three-dimensional upward swimming trajectories of four thecosomatous pteropod species.

swimming trajectory and also often exhibits a circular swimming trajectory in the horizontal plane, features that are often seen in other swimming zooplankton such as copepods (Bianco et al., 2014). However, this species may also swim in a straight line, thus showing some behavioral variety in its swimming. **Figure 5** shows that *H. inflatus* has a fairly straight downward sinking trajectory, sinking at speeds of 13–22 mm s^{-1} and corresponding sinking Reynolds number of Re_{sink} = 12–29 (**Table 2**). While sinking, the wings of *H. inflatus* remain extended upwards, thus keeping this species largely in an upright posture.

The thecosome *Limacina bulimoides* (**Figure 2B**) has a high spiraled shell and a body length of 1.3–1.4 mm and flaps it parapodia at 8.8–12.9 Hz, resulting in swimming speeds of 18–40 mm s^{-1} and *Re* = 22–51 (**Table 2**). This species is similar in size and swimming speed to *H. inflatus* and, as seen in **Figure 3**, exhibits similar small-scale trajectory oscillations. However, at the large scale, *L. bulimoides* does not seem to exhibit the helical swimming patterns seen in *H. inflatus*. **Figure 5** shows that *H. inflatus* also has a straight sinking trajectory, sinking at speeds of 16–19 mm s^{-1} and corresponding sinking Reynolds number of Re_{sink} = 22–25 (**Table 2**). While sinking, the wings of *L. bulimoides* also remain extended upwards, but the shell is oriented horizontally.

The thecosome *Cuvierina atlantica* (**Figure 2C**) has an urn- or bottle-shaped shell and a body length of 8.5–10.6 mm and flaps it parapodia at 4.7–6.2 Hz, resulting in swimming speeds of 13–46 mm s^{-1} and *Re* = 124–434 (**Table 2**). As such, *C. atlantica* is much larger than the two previously described thecosomes but swims at a similar speed, thus operating in a Reynolds number regime that is an order of magnitude higher. In addition, *C. atlantica* flaps it parapodia at a slower rate than the two smaller thecosomes. Similar to the two previously described thecosomes, *C. atlantica* exhibits small-scale oscillations in its trajectory owing to individual power and recovery strokes. In addition, *Cuvierina atlantica* swims in a characteristic upright posture with its seemingly heavy shell hanging downwards and oscillating like a pendulum. At the large scale, *C. atlantica* also often exhibits a spiral upwards swimming trajectory (not shown). This species may also swim sideways, but when doing so, its elongated shell always hangs beneath it. *Cuvierina atlantica* rapidly sinks downwards when it stops flapping, at speeds of 19–53 mm s^{-1} and corresponding sinking Reynolds number of

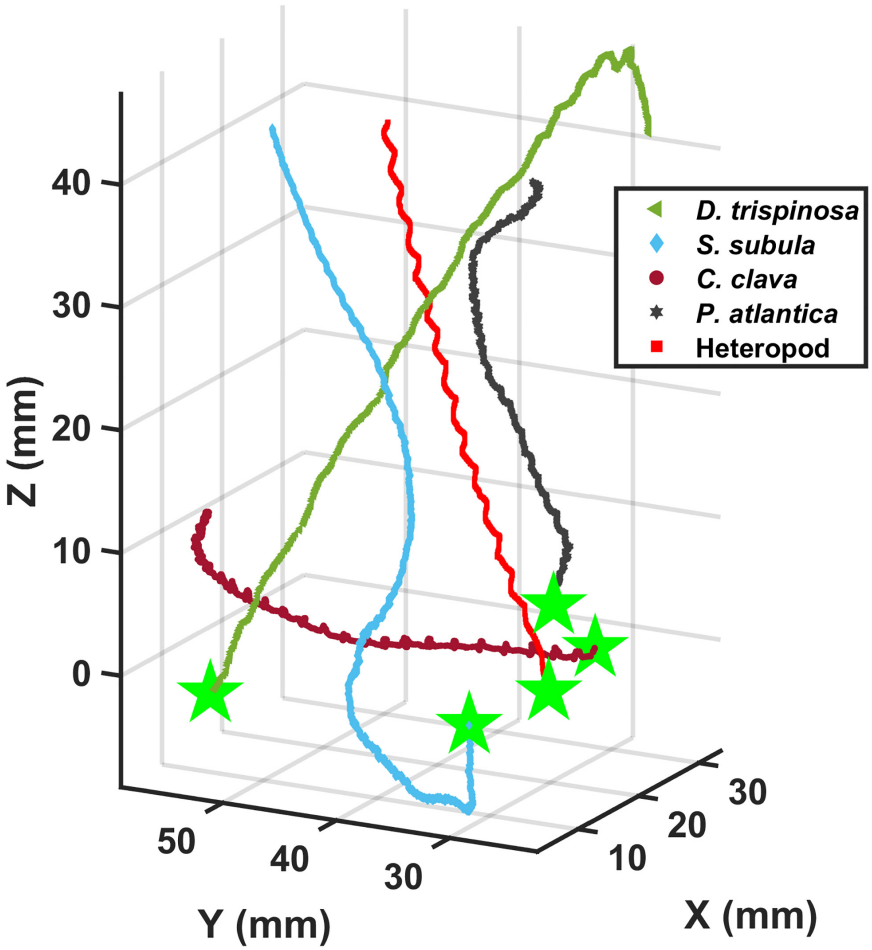

FIGURE 4 | Three-dimensional upward swimming trajectories of three thecosomatous pteropod species, one gymnosomatous pteropod species, and one atlantiid heteropod species.

Re_{sink} = 305–535 (**Table 2**). While sinking, the shell of *C. atlantica* usually reorients from a vertical to a horizontal orientation (with wings still extended), often resulting in a significant glide angle. In some cases, the downward sinking trajectory of *C. atlantica* forms a tight spiral (e.g., **Figure 5**).

The thecosome *Hyalocylis striata* (**Figure 2D**) has a very thin ribbed conical shell and a body length of 6.8–6.9 mm and flaps it parapodia at 7.6–8.1 Hz, resulting in swimming speeds of 18–28 mm s^{-1} and *Re* = 116–191 (**Table 2**). With its relatively large shell and high swimming speed, *H. striata* swims at a Reynolds number comparable to that of *C. atlantica*. The thecosome *H. striata* gives the impression of being a much stronger swimmer than the previously described thecosomes. For example, *H. striata*, though of comparable size, is much more maneuverable and agile than *C. atlantica* and does not seem to have a characteristic body position when swimming. Rather, it is capable of easily swimming in any direction and was often observed actively swimming downwards. Further, the small-scale oscillations seen in the previously described thecosomes are almost absent in *H. striata*, leading to a much smoother swimming trajectory (**Figure 3**). The sinking speed of *H. striata* is in the range of 24–26 mm s^{-1} with a corresponding sinking Reynolds number of Re_{sink} = 158–183, and this species largely exhibits a straight downwards sinking trajectory. While sinking, the shell of *H. striata* remains in a vertical position with no shell reorientation. The wings are initially held outwards but later turn upwards, acting to streamline the organism.

The thecosome *Diacria trispinosa* (**Figure 2E**) has a globular but dorsoventrally flattened shell with one posterior and two lateral spines. Further, *D. trispinosa* has a body length of 11.6–13.9 mm and flaps it parapodia at 4.9–6.8 Hz, resulting in swimming speeds of 58–114 mm s^{-1} and *Re* = 680–1567 (**Table 2**). With the largest body size and highest swimming speed of the marine snails tested, *D. trispinosa* also swims at the highest Reynolds number. *Diacria trispinosa* gives the impression of being a much stronger swimmer than the other thecosomes and may easily swim in any direction. This species characteristically swims upwards in a straight line at an average climbing angle of 47.5 ± 8.7° (mean ± standard deviation; n = 5) to the horizontal plane (**Figure 4**). The sinking behavior of *D. trispinosa* is unique

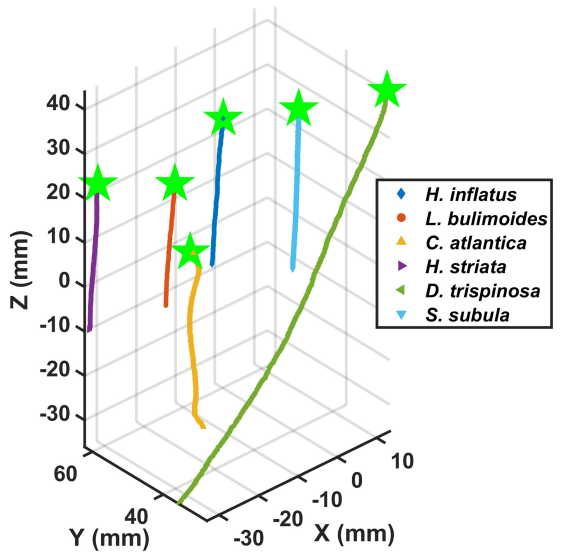

FIGURE 5 | Three-dimensional downward sinking trajectories of six thecosomatous pteropod species.

among the thecosomes. With its wings bending upwards, this species reorients from a vertical to a horizontal shell orientation when sinking, resulting in a trajectory that significantly deviates from the vertical. Thus, *D. trispinosa* sinks with a glide angle of 21.7 ± 10.1° (mean ± standard deviation; n = 3) from the vertical. This behavior seems to be enabled by the flattened shell of *D. trispinosa*, which acts as a hydrofoil to generate lift during the descent. The sinking speed of *D. trispinosa* is thus in the range of 60–105 mm s^{-1}, with a corresponding sinking Reynolds number of Re_{sink} = 830–1150 (**Table 2**), but would likely be higher in the absence of this gliding behavior.

The thecosome *Styliola subula* (**Figure 2F**) has a conical shell, with a thickened longitudinal spine running along the dorsal length. Further, *S. subula* has a body length of 3.6–8.7 mm and flaps it parapodia at 6.1–10.5 Hz, resulting in swimming speeds of 17–63 mm s^{-1} and Re = 60–505 (**Table 2**). The sinking speed of *S. subula* is 22–52 mm s^{-1} with a corresponding sinking Reynolds number of Re_{sink} = 348–417 (**Table 2**). The sinking behavior of *S. subula* was similar to that of *H. striata*, with a vertical orientation and the wings extended upwards. The large range of sizes and other parameters for this species reflects the fact that videos of a juvenile and an adult were captured. In general, the morphology and swimming style of *S. subula* are very similar to that of *H. striata* with the exception that the shell of *S. subula* seems bulkier and possibly heavier than that of *H. striata*. This difference is reflected in the larger sinking speed of *S. subula* and in the fact that *S. subula* seems less agile and maneuverable than *H. striata*.

The thecosome *Creseis clava* (**Figure 2G**) has an extremely elongated, needle-like shell and an extremely short wingspan relative to its body length. Further, *C. clava* has a body length of 6.8–7.2 mm and flaps it parapodia at 10.5–13.8 Hz, resulting in swimming speeds of 33–40 mm s^{-1} and Re = 238–278 (**Table 2**). It is worth noting that *C. clava* has the highest wingbeat frequency of all the studied thecosomes. With its elongated shell, *C. clava* has an upright swimming posture similar to that of *C. atlantica* and is not maneuverable. Further, *C. clava* exhibits high frequency small-scale oscillations in its trajectory similar to those of *C. atlantica* (**Figure 4**). No videos of *C. clava* sinking behavior were acquired.

The gymnosome *Pneumoderma atlantica* (**Figure 2H**) has an elongated soft body without the protection of a shell. *Pneumoderma atlantica* has a body length of 11.5–13.1 mm and flaps its wings at 3.5–4.5 Hz, resulting in swimming speed of 11–34 mm s^{-1} and Re = 134–438 (**Table 2**). Similar to many of the thecosome species, this gymnosome exhibited small-scale oscillations in its trajectory as a result of individual wing strokes. This agile species was often observed swimming upwards in a spiral but was also observed to hover in an upright posture at the same elevation for long periods of time and to actively swim downwards. No videos of sinking behavior were acquired for this species, but, due to its lack of shell, its sinking speed would presumably be much less than that of the shelled pteropods.

The heteropod species (**Figure 2I**) has a single swimming fin above the body and a downward hanging shell which functions as a second appendage that flaps synchronously with the fin to propel the animal (Karakas et al., 2018). The heteropod has a body length of 2.3–3.3 mm and flaps its parapodia at 9.3–9.6 Hz, resulting in swimming speeds of 22–35 mm s^{-1} and Re = 52–117 (**Table 2**). Small-scale side-to-side oscillations are observed in this animal's trajectory owing to individual strokes of its fin and shell. Though this heteropod species is negatively buoyant, no sinking behavior was observed in the current study.

Figures 6A,B show the mean and standard deviation of the swimming speeds U and U′, respectively, as a function of body length L for each recorded trajectory for all the marine snail species. **Figures 6C,D** show swimming speeds $\bar{U}$ and $\bar{U}'$ for each species as a function of $\bar{L}$. **Figure 6A** shows that L is tightly grouped into three classes corresponding to thecosome shell morphology. Coiled shell thecosomes (*H. inflatus* and *L. bulimoides*) have shell sizes ranging from 0.9 to 1.4 mm. Elongated shell thecosomes (*H. striata*, *C. atlantica*, *C. clava*, and *S. subula*) have shell sizes ranging from 6.8 to 10.6 mm (with the exception of a juvenile *S. subula* excluded from the calculation of $\bar{L}$). The single globular shell species (*D. trispinosa*) has shell sizes ranging from 11.6 to 14.0 mm. The mean of each of these groups also is shown in **Figures 6C,D**. Swimming speeds of individual species within these three classes do not differ much from each other. For example, no significant difference was found among the four species comprising the elongated shell group ($P > 0.05$, one−way ANOVA). However, swimming speed across the groups differs significantly as shown in **Supplementary Figure S1A** (F = 75.62, $P < 0.001$). The coiled shell, elongated shell, and globular shell pteropods have mean swimming speeds of 27.2, 33.5, and 83.7 mm s^{-1}, respectively, thus showing an increase with body length. A follow up Tukey-Kramer pairwise comparison test shows that all three shell groups are significantly different from the others (**Supplementary Table S1**). However, the normalized swimming speeds of the coiled shell pteropods are greatest, with $\bar{U}'$= 22.7 BL s^{-1} and a maximum U′ of

TABLE 2 | Comparison of morphological and swimming characteristics of various marine snail species from the current study and the literature.

Species	References	Body length L (mm)	Wing span L_f (mm)	Swimming speed U (mm s^{-1})	Wingbeat frequency f (Hz)	*Re*	Sinking speed U_{sink} (mm s^{-1})	Re_{sink}
Clione limacina	Satterlie et al. (1985)	Up to 20	>5 mm	100	1–3	Up to 1093	7–10	77–109
	Szymik and Satterlie (2011)	3–7	3.4–7.7	Tethered	1.1–3.2	NA	NA	NA
Clione antarctica	Borrell et al. (2005)	7–22	2.4–4.5	1–7	0.8–1.6	6–49	NA	NA
Limacina helicina	Chang and Yen (2012)	1–3.4	1–4	13–44	4.5–9.4	20–110	5–45	2–135
	Murphy et al. (2016)	1.6–2.0	2.1–2.9	15–26	4.3–4.7	19–42	NA	NA
Limacina helicina antarctica	Adhikari et al. (2016)	2.2	NA	21	2.9	29	NA	NA
	Mohaghar et al. (2019)	1.5–4.5	5.0–9.0	14–30	1.9–3.0	13–55	NA	NA
Heliconoides inflatus	Current study	1.1 (0.9–1.2)	2.4 (2.3–2.4)	26 (12–55)	8.8 (6.6–11.1)	27 (12–66)	17 (13–22)	18 (12–29)
Limacina bulimoides		1.3 (1.3–1.4)	2.3 (2.1–2.7)	29 (18–40)	10.8 (10.1–11.5)	38 (22–51)	17 (16–19)	23 (22–25)
Cuvierina atlantica		9.3 (8.5–10.6)	9.1 (8.5–9.5)	33 (13–46)	5.5 (4.7–6.2)	294 (124–434)	45 (19–53)	411 (303–535)
Hyalocylis striata		6.9 (6.8–6.9)	6.6 (6.5–6.7)	22 (18–28)	7.9 (7.6–8.1)	146 (116–191)	25 (24–26)	169 (158–183)
Diacria trispinosa		12.6 (11.6–13.9)	12.3 (11.6–12.9)	84 (58–114)	6.1 (4.9–6.8)	1051 (680–1567)	86 (60–105)	1016 (830–1150)
Styliola subula		8.3 (3.6–8.7)	3.7 (1.6–4.0)	42 (17–63)	8.4 (6.1–10.5)	338 (148–505)	39 (22–52)	375 (348–417)
Creseis clava		7.1 (6.8–7.2)	3.8 (3.6–4.0)	38 (33–40)	12.0 (10.5–13.8)	262 (238–278)	NA	NA
Pneumoderma atlantica		12.6 (11.5–13.1)	5.1 (5.0–5.2)	18 (11–34)	4.0 (3.7–4.3)	224 (134–438)	NA	NA
Heteropod		2.9 (2.3–3.3)	1.7 (1.6–1.8)	29 (22–35)	9.5 (9.3–9.6)	84 (52–117)	NA	NA
Atlanta selvagensis	Karakas et al. (2018)	2.2	2.1	27	9.1	59	NA	NA

Values indicate mean and range (in parentheses).

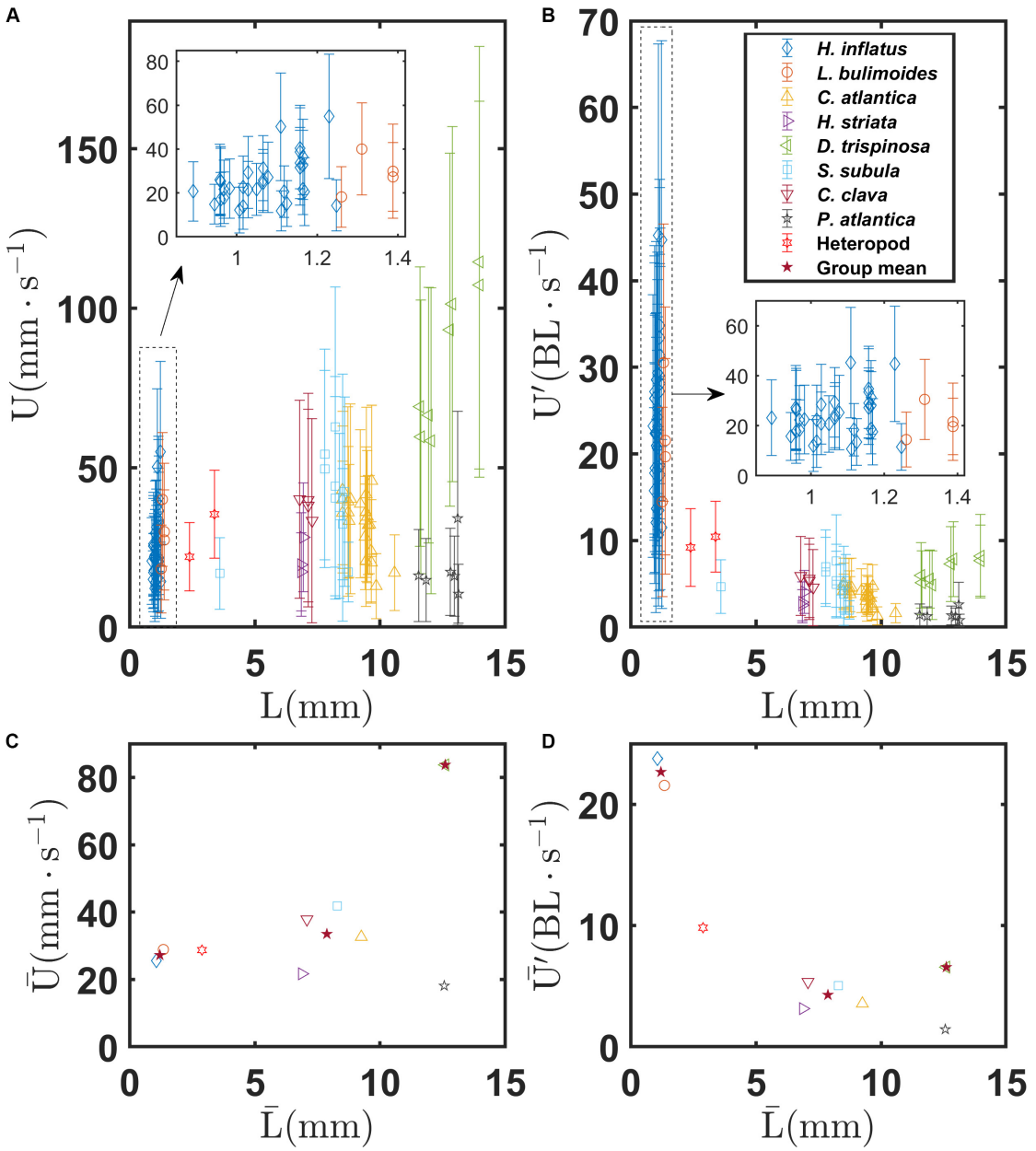

FIGURE 6 | (A) Mean and standard deviation of swimming speed U of individual marine snails as a function of body length L for various marine snail species. **(B)** Normalized mean and standard deviation of swimming speed U′ of individual marine snails as a function of body length L for various marine snail species. **(C)** Mean swimming speed $\bar{U}$ of various marine snail species as a function of mean body length $\bar{L}$. **(D)** Mean swimming speed $\bar{U}'$ of various marine snail species as a function of mean body length $\bar{L}$. Stars in **(C,D)** indicate group means of coiled, elongated, and globular shelled thecosome species.

45 BL s^{-1} for one individual of *H. inflatus*. In contrast, the normalized swimming speeds of the elongated shell pteropods are the least (4.3 BL s^{-1}), and the normalized swimming speeds of the globular shell pteropods are in between (6.6 BL s^{-1}). The coiled shell group has a significantly larger normalized mean swimming speed as confirmed by the one-way ANOVA ($F = 123.25$, $P < 0.001$, **Supplementary Figure S1B**), and the paired Tukey-Kramer test shows a significant difference between the coiled and elongated shell groups and between the coiled and globular shell groups ($P < 0.001$), but there is no statistically significant difference between the elongated and globular shell groups ($P = 0.495$, **Supplementary Table S1**). The heteropod has a coiled shell which is similar in size that of the coiled shell thecosomes and a mean swimming speed of 28.7 mm s^{-1}. However, owing to its completely different swimming style, the heteropod does not group with the coiled shell thecosomes in **Figure 6**. In addition, the gymnosome, though shell-less and of similar size to *D. trispinosa*, swims much slower (18.1 mm s^{-1}).

As expected, swimming speed generally increases with increasing beat frequency for all species, as shown in **Supplementary Figure S2** (though this trend is not seen for *D. trispinosa*).

Figures 7A,B show the mean and standard deviation of the sinking speeds U_{sink} and U', respectively, as a function of body length L for each recorded trajectory for all the marine snail species. **Figures 7C,D** show sinking speeds $\bar{U}$ and $\bar{U}'$ for each species as a function of $\bar{L}$. In each panel, the hollow symbols represent the sinking speed and the filled symbols represent the vertical component of sinking speed. As seen in **Figure 7A**, sinking speeds generally fall into three classes corresponding to coiled, elongated, and globular shell morphologies. However, in contrast to swimming speed, sinking speed clearly increases with body size. Mean sinking speed across the groups differs significantly as shown in **Supplementary Figure S1C** ($F = 129.56$, $P < 0.001$) as the globular shell pteropod has a higher sinking speed (86.2 mm s^{-1}) than the elongated (40.9 mm s^{-1}) and coiled (17.1 mm s^{-1}) shell groups. Similar to the mean swimming speed, the mean sinking speed between each pair is also significantly different from each other ($P < 0.001$ for each pair, **Supplementary Table S1**). For both the coiled and elongated shell pteropods, minimal differences are seen between the sinking speed and the vertical component of the sinking speed (vertical components are 96 and 87% of the sinking speed, respectively). These minor differences are possibly due to drag and lift forces on the shells and outstretched wings as the animals sink. These unbalanced forces may cause, for example, the helical sinking trajectories observed for *C. atlantica*. In contrast, the globular species *D. trispinosa* has a much larger difference between its sinking speed and the vertical component of its sinking speed (83%) due to the gliding behavior described earlier. A similar pattern

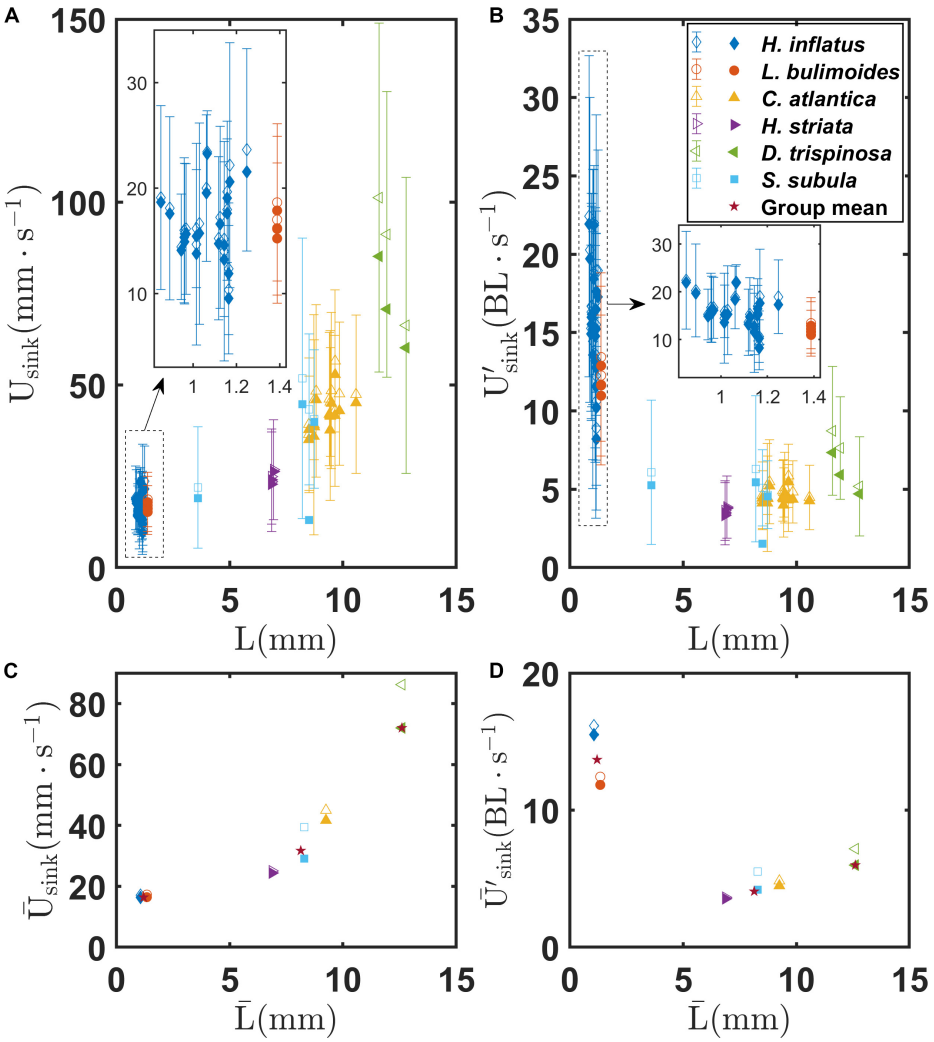

FIGURE 7 | (A) Mean and standard deviation of sinking speed U_{sink} of individual marine snails as a function of body length L for various marine snail species. **(B)** Normalized mean and standard deviation of sinking speed U'_{sink} of individual marine snails as a function of body length L for various marine snail species. **(C)** Mean sinking speed $\bar{U}_{sink}$ of various marine snail species as a function of mean body length $\bar{L}$. **(D)** Mean sinking speed $\bar{U}'_{sink}$ of various marine snail species as a function of mean body length $\bar{L}$. Stars in **(C,D)** indicate group means of coiled, elongated, and globular shelled thecosome species.

for normalized swimming speed among the three groups is also seen for the normalized sinking speed. The coiled shell species have the largest normalized sinking speed (13.7 BL s^{-1}) whereas the elongated shell group has the smallest (4.1 BL s^{-1}), and the globular shell species falls between (6.0 BL s^{-1}). Similar to the normalized mean swimming speed, there are also significant difference in the normalized mean sinking speed between different groups ($F = 105.79$, $P < 0.001$, **Supplementary Figure S1D**). Again, the normalized mean sinking speeds of the coiled shell and elongated shell pair and the coiled shell and globular shell pair are significantly different ($P < 0.001$ for both pairs), whereas that of the elongated shell and globular shell pair are not significantly different ($P = 0.393$, **Supplementary Table S1**).

Figure 8A shows the glide angle α measured from each recording as a function of L. **Figure 8b** shows the mean glide angle for each species and each shell morphology as a function of $\bar{L}$. The coiled shell species *H. inflatus* and *L. bulimoides* have $\alpha < 10°$, reflecting the fact that they sink almost vertically. As a group, the coiled shell pteropods have a mean glide angle of 4.1° (**Supplementary Figure S3A**). Values of α for the elongated species are slightly greater, with most falling in the range of $1° < \alpha < 15°$ and a few outliers with values up to almost 30° (**Supplementary Figure S3A**). The mean glide angle for the elongated shell pteropods is 7.7°. The globular shell species *D. trispinosa* sinks at glide angles up to 31.6° and has a mean glide angle value of 21.7° (**Supplementary Figure S3A**). This large glide angle is due to lift generated by the unique shell shape of *D. trispinosa* and by its partially outstretched wings. The one-way ANOVA test shows that a significant difference exists in the glide angles of the coiled, elongated, and globular shell groups ($F = 14.57$, $P < 0.001$, **Supplementary Figure S3A**). Further, the Tukey-Kramer pairwise tests showed significant differences between each pair (**Supplementary Table S1**).

Figure 9 shows mean values of NGDR over a distance of five body lengths for each species as a function of $\bar{L}$. Values of NGDR for all thecosome species except for *D. trispinosa* are fairly similar and fall within the range of 0.6–0.7. The one-way ANOVA test showed a significant difference among the three shell groups for the mean NGDR values ($F = 6.23$, $P = 0.003$, **Supplementary Figure S3B**). A follow up pairwise comparison showed there is no significant difference between the coiled shell and elongated shell groups ($P = 0.636$, **Supplementary Table S1**) but that there is a significant difference between the globular shell group and the other two groups. These relatively low values for the coiled and elongated shell species represent the tortuous "sawtooth" trajectories induced by individual power and recovery strokes. In contrast, *D. trispinosa* has a much higher NGDR of 0.89. This species is a much stronger swimmer, operating at an order of magnitude higher Reynolds number (**Table 2**), and its dorsoventrally flattened shell may help damp out the small-scale pitching oscillations observed in smaller pteropods. The heteropod had an elevated NGDR value of 0.81, whereas *P. atlantica* had a NGDR value (0.65) that was more similar to the thecosomes. Because NGDR was calculated over only five body lengths, these values represent the small-scale oscillations in their swimming trajectories and not large-scale swimming patterns. Values of NGDR at larger spatial scales would be useful but could not be calculated here because recorded swimming trajectories varied in length. Using all recorded trajectories regardless of length would have introduced a bias since NGDR is a scale-dependent parameter (Seuront et al., 2004). Bergan et al. (2017) calculated tortuosity, which is the inverse of NGDR, for the coiled shell species *Limacina retroversa*

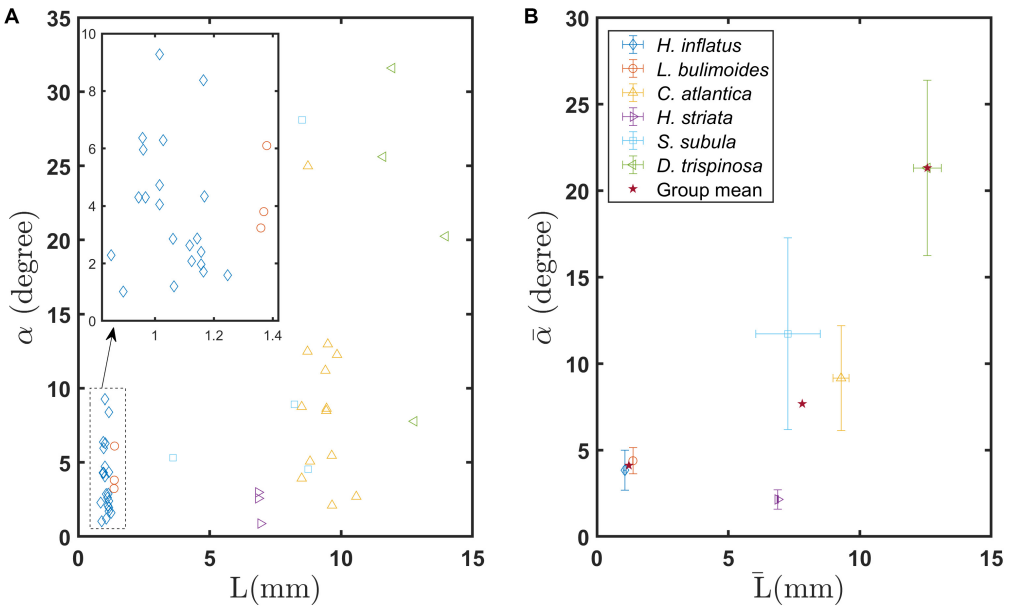

FIGURE 8 | (A) Gliding angle of individual marine snails as a function of body length L, **(B)** Mean gliding angles of various marine snail species as a function of mean body length $\bar{L}$. Stars in **(B)** indicate group means of coiled, elongated, and globular shelled thecosome species.

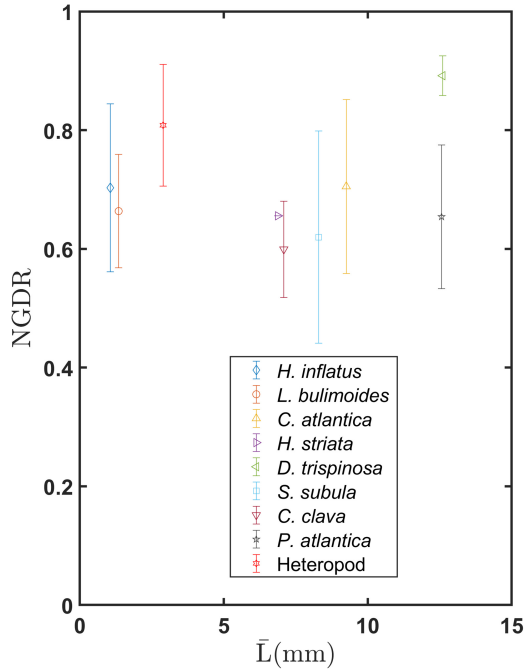

FIGURE 9 | Mean and standard deviation of NGDR measured over five body lengths for various marine snail species as a function of mean body length $\bar{L}$.

which is morphologically similar to *L. bulimoides* and *H. inflatus*. These authors found corresponding mean NGDR values of 0.49–0.79. While these values are similar to those of the coiled shell pteropods, it is difficult to make a direct comparison because these authors do not report the trajectory lengths over which NGDR was calculated.

Only four of the species we filmed were sufficiently abundant in the MOCNESS samples to allow for statistically meaningful assessment of their size-based distributions (**Figure 10**). Of the remainder of the groups they could either not be identified to species via the images (gymnosomes and atlantid heteropods), or were sampled too infrequently to reliably determine size-based day and night distributions. For some species there was a clear difference in depth habitat based on size with longer individuals found at deeper depths, including *H. inflatus*, *C. clava*, and *S. subula*.

Metabarcoding analyses confirmed the species identification made by the ZooSCAN and additionally allowed for better discrimination between taxa that are morphologically similar, providing a better context for the vertical distribution of the various species. Despite the fact that metabarcoding analyses were conducted on only one of the day and night pairs of MOCNESS tows that were analyzed for images, the patterns in distribution were similar overall and were consistent with findings in the previous literature (**Table 3** and **Supplementary Figure S4**). Discrepancies between molecular methods and previous findings appear to be more common in the larger species that are rare and therefore more poorly sampled. The use of paired image and barcoding allowed for greater understanding of the dataset, suggesting, for example, two gymnosome species with non-overlapping vertical distributions. The first, identified as *Pneumoderma atlantica*, was likely the species captured and used for our video analysis. Adults of this group appear to migrate from a daytime depth of 50–200 m to a night time habitat of 0–200 m. The other, an unidentified gymnosome, has a midwater habitat from 300 to 700 m. An uncertain problem is that metabarcoding did not detect *Limacina bulimoides*, despite its documented presence in the samples. The most plausible explanation would be a highly divergent sequence for this species, which might have affected its amplification efficiency during the PCR protocols due to mutations in the primer regions.

Of the species filmed in this study, there were a range of migratory patterns. The species with the widest vertical distribution (found abundantly from 50 to 400 m, but as deep as 550–700 m) was *D. trispinosa*. Similarly, *C. atlantica* (barcoded as *C. columnella*) was found from 0 to 400 m, although it was found most abundantly at 300–400 m. These two larger species were rarely captured in images, and both were under sampled at night (particularly in the metabarcoding analysis) making definitive characterization of diel migration patterns difficult. Our data suggests that all species used in this study are migratory, traveling 50–300 m per day. The extent of migration was not correlated with average species length, the swimming speed, or sinking speed.

DISCUSSION

Planktonic marine snails in warm waters have diverse shell and body geometries and sizes which affect their swimming abilities and sinking characteristics. Indeed, within a shell group (i.e., coiled, elongated, or globular), the various thecosome species studied here had similar sinking and swimming characteristics. Coiled shell species are the smallest thecosomes and swim and sink the slowest but have the highest normalized swimming and sinking speeds. These species thus also operate in a highly viscous regime at Reynolds numbers less than 100. These species thus experience both high frictional drag as well as pressure drag. Indeed, Vogel (2013) showed that the flow begins to separate around a circular cylinder (which is a good model of the shell shape of *H. inflatus*) at Reynolds numbers as low as 40. In addition, these species have a high pitching amplitude when swimming, a pattern which is facilitated by the coiled shell shape, which has low moment of inertia and low rotational drag (Murphy et al., 2016). This combination of translation and rotation used by coiled shell species may move the stagnation point on the shell to a different position (similar to the Magnus effect), thus increasing the lift to drag ratio. Coiled shell species that are sinking will presumably have a drag coefficient different from when they are swimming. At the sinking Reynolds numbers observed here, the wake behind an object in oncoming flow is symmetric, lacking the Karman vortex street in an object's wake which would be present at higher *Re*. This presumably symmetric wake thus explains why the sinking trajectories of

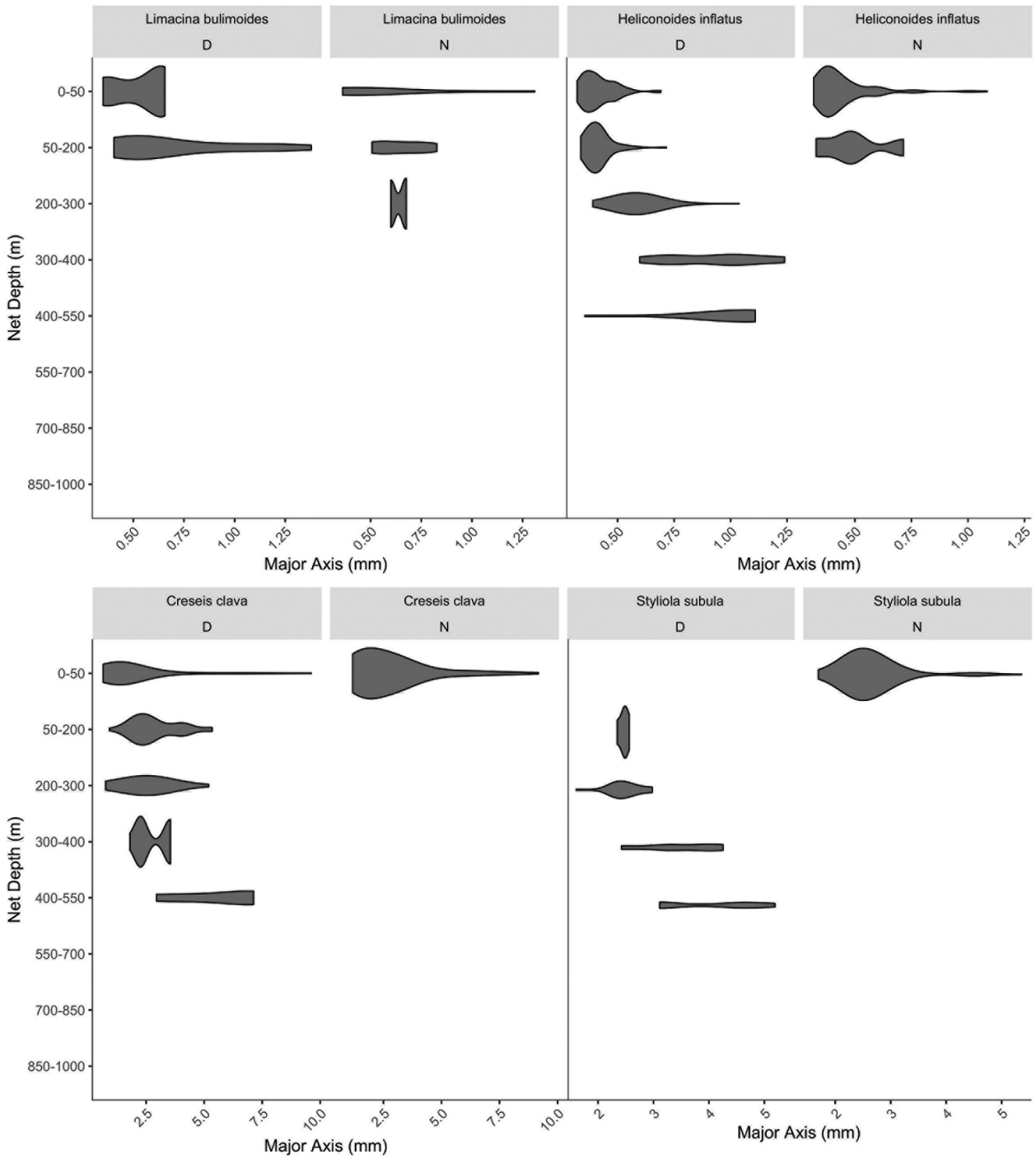

FIGURE 10 | Day and Night vertical distribution of species from MOCNESS net image data. The length of the organisms (*x*-axis) is plotted versus the median depth of the net of collection (*y*-axis) to demonstrate size-based differences in habitat selection. The width of the bar corresponds to relative abundance of individuals in that size bin.

the coiled shell species are straight. It should be noted that the sinking pteropods recorded here sank with extended wings. Pteropods escaping with retracted wings would sink faster and at a higher *Re* (Gilmer and Harbison, 1986). For example, Bergan et al. (2017) found that the coiled shell species *Limacina retroversa* in the size range of 0.56–2.37 mm sank at speeds of 16–19 mm s^{-1} with wings withdrawn and speeds of 13–16 mm s^{-1} with wings extended. These sinking values are similar those of the coiled shell thecosome species studied here (**Table 2**).

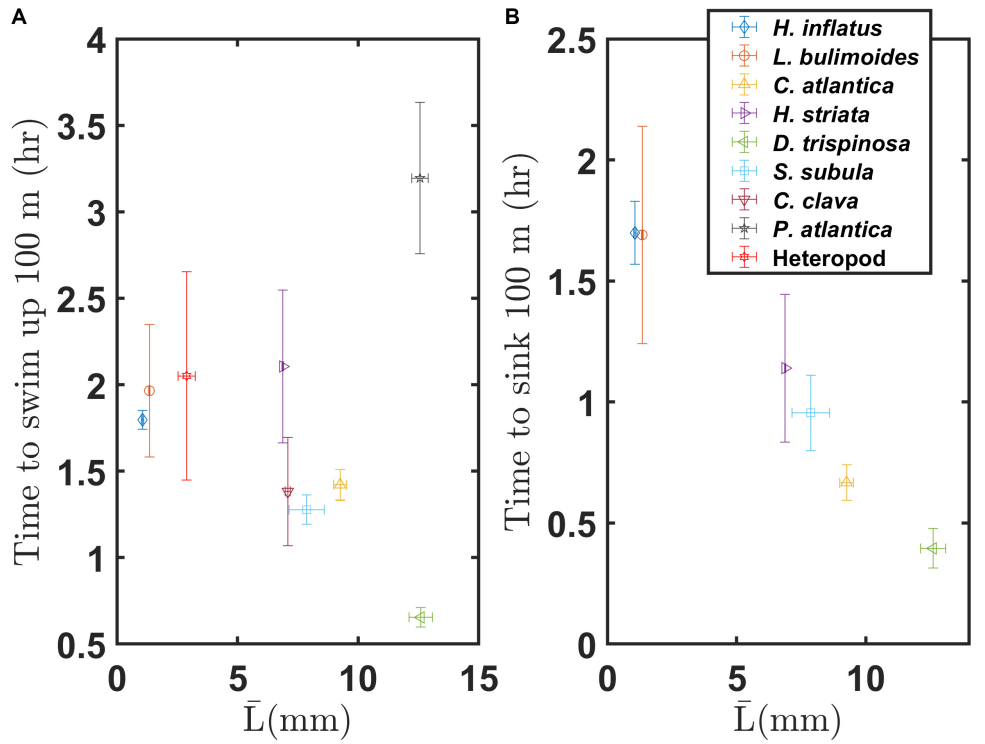

FIGURE 11 | (A) Upward and **(B)** downward migration times over a distance of 100 m for various marine snail species, based on the mean swimming and sinking speeds measured here.

TABLE 3 | MOCNESS distributions of species used in this study.

Species	Filmed	Image min	Image max	Molecular min	Molecular max	DVM extent	Literature source
Heliconoides inflatus	Y	0–50	250–400	Not identified in barcoding		~200 m	Wormuth, 1981
Limacina bulimoides	Y	0–50	150–250	Not identified in barcoding		~100 m	Wormuth, 1981
Cuvierina atlantica+	Y	0–50	300–400	0–50	300–400	~300 m	Wormelle, 1962
Hyalocylis striata	Y	50–200	50–200	0–50	50–200	~200 m	Maas et al., 2012
Diacria trispinosa	Y	50–200	300–400	50–200	300–400	~100 m	Wormelle, 1962
Styliola subula	Y	0–50	400–500	Not identified in barcoding		~250 m	Wormuth, 1981
Creseis clava	Y	0–50	50–200	0–50	50–200	~50	Wormuth, 1981
*Pneumoderma atlantica**	Y*	0–50*	0–50*	0–50	200–300	~100 m	
Gymnosomata sp.*	N	500–700*	500–700*	300–400	550–700	None	
Heteropoda	Y	0–50	400–500			Multiple species	
Clio pyramidata	N	50–200	550–700	50–200	50–200	~400 m	Wormuth, 1981
Creseis conica+	N	0–50	50–200	Not identified in barcoding		~100 m	Wormuth, 1981
Diacria quadridentata	N	Not identified in MOCNESS		50–200	50–200	None	Bé and Gilmer, 1977
Limacina leuseruii	N	Not identified in MOCNESS		0–50	300–400	~200 m	Wormuth, 1981

*The minimum (min) and maximum (max) depth (m) in which a large number of individuals of each group was observed in our image and molecular datasets. The depth of DVM was estimated from our data as well as from prior literature. Where inferred species names deviate from the molecular database due to recent changes in nomenclature are noted with a +. Information that was inferred from molecular datasets and applied to image or filming datasets are demarcated with a *.*

The elongated shell pteropods have larger shells and swim at speeds slightly faster than the coiled shell species, thus resulting in normalized swimming speeds an order of magnitude lower than the coiled shell species. The elongated shell species thus operate at a Reynolds number an order of magnitude higher (100–600) than that of the coiled shell species. Pressure drag is thus more important for the elongated shell pteropods at this *Re* as compared to the coiled shell species. Similar to the coiled shell species, the elongated shell species also exhibit forward-backwards body pitching with every wing stroke, but the pitching amplitude seems to be less for the elongated shell species. For example, Karakas et al. (2020) showed that *C. atlantica* has a pitching angle of 25°, which is much less than pitching amplitudes previously measured for the coiled shell species

L. helicina (up to 60°) and *L. helicina antarctica* (up to 110°; Adhikari et al., 2016; Murphy et al., 2016). The lower pitching amplitude of the elongated shell species makes sense because these shells have greater rotational drag and rotational inertia as compared to coiled shells. The elongated shell thecosomes are larger and weigh more and are generally less maneuverable than the coiled shell thecosomes, likely because rotational and translational acceleration theoretically can be scaled as mass$^{-2/3}$ and mass$^{-1/3}$, respectively (Vogel, 1988; Dudley, 2002). Inside the elongated shell group, there are also large differences in maneuverability. For example, though *H. striata* and *S. subula* have similarly shaped shells, the shell of *H. striata* seems more delicate, corresponding with its greater swimming over *S. subula*. Similarly, *C. atlantica*, with its large shell, is the least maneuverable of the elongated shell thecosomes. The higher swimming speeds and maneuverability of some species could be one reason why they are less sampled in net tows.

The sinking behavior (e.g. glide angle, trajectory, stability) of the various species depends on factors including size, shell shape, and the relative locations of the center of mass (center of gravity) and the geometric center (center of buoyancy). Indeed, in a study of the sinking behavior of simple cylindrical shapes, Chu et al. (2005) found that the relative locations of the center of mass and center of geometry largely controlled sinking trajectory and orientation and that a larger offset between these two points resulted in less lateral travel while sinking. However, in general, the descent angle cannot be predicted from this offset because instantaneous hydrodynamic forces (e.g., lift, drag, vortices created by flow past the object) could impact the trajectory (Chu et al., 2005), and the relative importance of these fluid forces increase with the Reynolds number. In considering pteropod shells, non-uniform mass distributions (e.g., differences in shell thickness) and complex geometries (e.g., changing wing positions) make knowledge of the locations of the center of mass and the geometric center extremely difficult. Nonetheless, we suspect that the coiled species, which sink at a low Re, always have their center of mass located below their geometric center (which includes the wings), and this may explain their stability and steep angle of descent while sinking. In contrast, elongated shell species may either rotate toward a horizontal orientation with the wings outstretched (e.g., *C. atlantica*) or may sink in a vertical position with the wings held upwards in a streamlined position (e.g., *H. striata* and *S. subula*). These different orientations will differentially affect the coefficient of drag. The species *C. atlantica* is larger than the other elongated species and thus may energetically benefit from a larger coefficient of drag resulting from its more horizontal sinking position, which slows its sinking (Field et al., 1997; Amin et al., 2019). For those elongated species that tend to rotate to a horizontal position while sinking, we suspect that their center of mass is located close to or above their geometric center. In addition, an order of magnitude increase in sinking *Re* from the coiled shell species to the elongated shell species also plays an important role in shell reorientation as the boundary layer separation starts to occur in this *Re* (10^2) regime and the resulting drag and lift forces introduce a non-negligible deflecting moment which alters the animal's trajectory, thus corresponding to the higher glide angles found for these species as a group. Further, Chamberlain and Weaver (1978) theoretically showed that sinking behavior is largely controlled by shell geometry. This finding also is observed in our study as the sinking behavior of these pteropod species naturally grouped by shell geometry.

The globular shell shape species *D. trispinosa* has the largest shell size among the thecosome groups studied here. It also appears to be a strong swimmer as well. This globular shell species operates at a Reynolds number an order of magnitude higher (700–1600) than that of the elongated shell species and two orders of magnitude greater than coiled ones. These *Re* numbers represent the upper limit of the intermediate *Re* regime, where both inertia and viscosity are important, and the lower end of the *Re* regime where inertia effects dominate. The pressure drag is thus dominant for the globular shell pteropods at this *Re* as compared to the coiled shell species and elongated shell species. Distinct from the coiled shell and elongated shell species, this globular shell species does not exhibit forward-backwards body pitching with each half wing stroke. Instead, the dorso-ventrally flattened shell of *D. trispinosa* appears to be adapted for lift generation as it has a large planform and the cross-sectional profile of a cambered airfoil. Indeed, unlike most of the coiled and elongated shell species, which swim almost vertically upwards with their shell hanging downwards like a pendulum, *D. trispinosa* species swims upward with an average climbing angle of 47.5 ± 8.7°. This characteristic shell orientation thus likely allows the shell to generate lift which would aid its ascent. With its high lift generation capability *D. trispinosa* has a high maneuverability compared to other thecosome groups. When sinking, this globular shell species glides with its wings partially folded. Considering the relatively high Reynolds number regime at which *D. trispinosa* sinks, it likely benefits from the large flat surface area that the shell provides, thus slowing down the sinking rate in the water column. The lift force on the flat shell and wings of the globular species may also cause greater horizontal deviation in their downward trajectories, a pattern which matches the higher glide angles observed for the *D. trispinosa,* since the shell shape is more aerodynamically streamlined and is always observed to orient in a horizontal position which maximizes the projected area in the sinking direction. Finally, it should be noted that there is only one globular species analyzed here which may not be fully representative of the globular shell shaped group which are often less dorsoventrally compressed. More species need to be studied to reach more representative results.

As seen in **Table 2**, *Pneumoderma atlantica* studied here is larger than its co-occurring thecosome species except for *D. trispinosa*, which is the same size. Further, the swimming speed of *P. atlantica* is less than the swimming speeds of these thecosomes. These low swimming speeds reflect the fact that *P. atlantica*, without external disturbance in the lab environment, spent most of its time hovering or slowly translating in a small area. *Pneumoderma atlantica* can hover for an extended amount of time partly because the lack of heavy calcareous shells, which make these animal less negatively buoyant. Though fast-swimming escape or hunting behaviors were not observed here, it has been reported that some gymnosome species can swim as fast as 1000 mm s^{-1} for short time intervals (Hamner

et al., 1975; Lalli and Gilmer, 1989), resulting in high Reynolds numbers comparable to that of fast-swimming fishes and some flying birds (Re = 10,000). Thus, their streamlined body shape, which is more efficient because of the low drag coefficient this body geometry provides in this Re regime, is advantageous for gymnosomes. Further, all gymnosomes studied to date have wings with short wingspans and low aspect ratios as compared to the thecosome pteropods. These low aspect ratio wings are useful for generating high levels of thrust and acceleration, which are useful for the quick maneuvers necessary for these predators to capture thecosomes. Interestingly, though of comparable body length with the temperate gymnosome species *C. limacina* and the polar species *C. antarctica* (Satterlie et al., 1985; Borrell et al., 2005; Szymik and Satterlie, 2011), the warm water species *P. atlantica* studied here has larger wingbeat frequency than its cold water counterparts. Other researchers have found that flies reared at high temperatures have lower body mass and smaller wings and exhibit higher beat frequencies than those reared at low temperatures, a trend related to the decreased wing loading and resonance and increased wing moment of inertia and induced power requirements to move larger wings (Barnes and Laurie-Ahlberg, 1986; Pétavy et al., 1997; Lehmann, 1999; Dillon and Dudley, 2004; Frazier et al., 2008). It is not known how the wing surface area compares among polar and tropical gymnosome species. In addition, water viscosity likely plays an important role in modulating flapping frequency since the kinematic viscosity of seawater changes greatly between polar and tropical temperatures.

The atlantiid heteropods studied here are larger than the coiled shell thecosomes but smaller than the elongated and globular shell thecosomes. Further, though they have a distinct body geometry and swimming style (Karakas et al., 2018), these heteropods have comparable swimming speeds to all but the fastest swimming thecosomes. It is known that atlantiid heteropods are visual predators and have large, complex eyes with a narrow retina and narrow field of view which they may actively rotate up and down through a 90° arc to scan the surrounding environment for prey (Seapy, 1980; Land, 1982, 1999). However, there is disagreement in the literature regarding their prey, with Thiriot-Quiévreux (1973) and Lalli and Gilmer (1989) suggesting that thecosomes are primary prey and Wall-Palmer et al. (2016) suggesting otherwise using fossil evidence. Based on the swimming speeds and body sizes measured here, it seems possible that this small atlantiid heteropod would be capable of preying on small thecosomes in the coiled shell group such as *H. inflatus* and *L. bulimoides*. Larger thecosomes from the elongated and globular shell groups may be susceptible as prey to correspondingly larger atlantiid heteropods. Indeed, one such large unidentified atlantiid heteropod species (likely *Oxygyrus inflatus*) was observed preying on a *Clio pyramidata* while both were lying on the floor of an aquarium (**Supplementary Movie S1**).

The swimming and sinking characteristics described here will significantly bear on the diel vertical migration and vertical distributions of these marine snails. **Figure 11** shows representative times needed to swim up or sink down 100 m in the water column. Upward swimming times and downward sinking times are based on the vertical component of the average swimming speed and the vertical component of the average sinking speed, respectively. Both plots assume continuous sinking or swimming (i.e., no breaks in that behavior). The thecosome groups roughly follow a negative correlation of swimming time versus average body length, with the large globular species swimming that distance in about 40 min and small coiled species taking about 2 h. In contrast, the sinking time has a strong negative relation with the average body length, with the large globular species sinking 100 m over about 20 min and the small coiled shell species taking 1.7 h. Although this figure does not necessarily represent the real distance across which these marine snails migrate or the time required for that migration, it gives insight into their vertical distribution in the water column and into the energy required for diel vertical migration. Larger species sink down and swim up much faster and thus can be active at much greater depths whereas the slower and smaller species are limited to shallower depths.

Besides its relevance to maintenance of vertical habitat, predator/prey interactions and migratory behavior, the rate of thecosome pteropod sinking is biogeochemically important as shells from dead thecosome sink to the deep ocean and dissolve in high pressure, contributing an estimated 12–13% of the carbonate flux globally (Berner and Honjo, 1981; Tsurumi et al., 2005) and greater than 50% of the carbonate flux in the Southern Ocean (Hunt et al., 2008). The sinking rates measured here, although likely slower than that of dead or empty shells, give insight into how shell size may affect carbon flux rate. These findings may be important as we seek to understand changes to flux due to anthropogenic forcings. Using time series observations, shifts in planktonic community composition, including poleward movement of centers of abundance have been demonstrated (Southward et al., 1995; Oviatt, 2004; Mackas et al., 2007) including in pteropods (Beaugrand et al., 2012). Due to basic thermodynamic principles, warmer conditions tend to be more favorable for smaller species and smaller individuals within a species (Berger, 1978; Berner and Honjo, 1981; Almogi-Labin et al., 1988; Fabry, 1990; Fabry and Deuser, 1991; Daufresne et al., 2009). Not only do smaller individuals carry less carbonate to depth, but our results demonstrate that they also sink slower, providing a greater window of time for dissolution effects to reduce the vertical extent of their carbonate export. Thus, changes in the species or size class composition could reduce both the amount and depth of calcium carbonate export. Ocean acidification, which degrades fragile aragonite shells and reduces calcification, may additionally alter these sinking rates, as well as pteropod swimming and sinking behavior, in the future (Sabine et al., 2004; Manno et al., 2010; Orr, 2011; Chang and Yen, 2012; Comeau et al., 2012; Adhikari et al., 2016; Murphy et al., 2016; Bergan et al., 2017; Bednaršek et al., 2019).

Body length has previously been analyzed as a predictor for vertical migration extent based on the idea that migration is a balance between the energetics of swimming and the ability of an individual to hide from visual predators. These constraints both scale with size, but in opposite directions. Consequently, it has been demonstrated that there is a U-shaped curve to the extent of vertical migration for copepods in the California

current (Ohman and Romagnan, 2016), with both longer and shorter individuals having small migrations, and intermediate sized organisms migrating the most. Longer individuals in the study by Ohman and Romagnan (2016) had a deeper overall habitat, while shorter individuals were present higher in the water column. Our dataset has substantially less sampling, however, the preferred depth habitat patterns are consistent with these previous findings. Longer species > 7 mm tended to have deeper distributions (*C. atlantica*, *D. trispinosa*, *Pneumoderma atlantica*), while smaller species < 3 mm (*H. inflatus, L. bulimoides*) are found abundantly in the upper water column (**Supplementary Figure S4A**). However, the vertical extent of migration patterns of the pteropods analyzed here do not have the same U-shaped curve, with some of the smaller species having long migrations (*H. inflatus;* 200 m) and one of the larger species having the shortest migration (*C. clava*; 50 m). This suggests that for pteropods there are factors other than length driving migratory behavior. It is very likely that for the negatively buoyant pteropods shell morphology and mass play a bigger role than for the neutrally buoyant copepods. For example, *Creseis clava*, although quite long, is substantially less heavy than similarly sized individuals of other species owing to its needle like morphology, while *H. inflatus* is known to have a thinner and lighter shell than similarly sized Creseis species (Lalli and Gilmer, 1989).

Size does, however, play a strong role in the extent of migration within a species in our dataset, with longer individuals of *S. subula*, *C. clava*, *C. pyramidata*, and *H. inflatus* having substantially deeper distributions than smaller individuals of the same species. Ontogenetic partitioning of the water column has been observed previously in cephalopods, fish and crustaceans (i.e., Hunt and Seibel, 2000; Titelman and Fiksen, 2004; Maas et al., 2014), but has not previously been quantified in pteropods. The interplay between the energetics of vertical migration, the threat of visual predation and the size of an individual clearly strongly structure the habitat of pelagic species. Understanding these evolutionary constraints will only be possible with further analyses that interrogate migratory patterns by considering all of these factors with the addition of additional environmental parameters including prey availability, temperature and midwater oxygen.

CONCLUSION

In this paper, we studied the swimming and sinking kinematics, biomechanics, and depth distributions of a variety of warm water marine snail species, with a particular focus on how the shell shape, body geometry, and body size affect their locomotion from a fluid mechanics perspective. Among the thecosomes, the tiny coiled species, intermediate elongated species, and large globular shell species have distinct locomotion characteristics which correspond strongly with shell morphology and size. Swimming speeds, sinking speeds, and glide angles are positively correlated with shell size and thus also strongly depend on shell morphology, whereas small-scale oscillations in swimming trajectories are lower in the largest, globular species. These changes in locomotion characteristics tightly correspond to changes in the *Re* and the governing fluid dynamics, with *Re* increasing by an order of magnitude from the coiled shell species to the elongated shell species and again by another order of magnitude from the elongated shell species to the globular shell species. These differences in *Re* strongly affect the flow fields around the animal's wings and body and may point toward more recent lineages evolving shell shapes and swimming styles to produce better swimming performance by maximizing lift and minimizing drag. Speed of swimming does not, however, equate to the vertical extent of migration, emphasizing that other factors, likely including light, temperature, and predator and prey fields, have a strong influence on this ecologically important trait. Size does play a role in structuring the vertical habitat, with larger individuals tending to live deeper in the water column, while within a species, the extent of migration is greater in larger individuals.

DATA AVAILABILITY STATEMENT

The datasets presented in this study can be found in online repositories. The names of the repository/repositories and accession number(s) can be found below: Reference sequences were downloaded from GenBank (https://www.ncbi.nlm.nih.gov/genbank/) under the accession numbers DQ237959 to DQ237970, DQ246443, DQ279946, GU969166, GU969171, MF049019, and MF049021 to MK749673.

AUTHOR CONTRIBUTIONS

FK, DM, and AM conceived and designed the experiment and wrote the manuscript. FK and DM carried out experimental work and data analysis. AM procured and identified the animals. JW helped digitize the videos. AM and LB-B analyzed depth distributions. All authors approved the final manuscript.

FUNDING

Funding was provided by the National Science Foundation CAREER grant to DM (CBET #1846925), a grant from the National Academies of Science Keck Futures Initiative (NAKFI) to AM and DM, the University of South Florida (USF) New Researcher Grant to DM, the USF Nexus Grant to DM, and the Bermuda Institute of Ocean Sciences Grant in Aid to DM. Distributional studies were funded through Simons Foundation International's BIOSSCOPE project (AM and LB-B).

ACKNOWLEDGMENTS

We gratefully acknowledge Kuvvat Garayev, Joseph Bello, and Josh Arandia for assistance in collecting the animals and in conducting experiments, Paola Rossi Bruttini, Tristen Mee, and Muhammad Shaikh for assistance with digitization, and Daniel D'Oliveira for assistance with creating 3D models.

We appreciate the expertise and efforts of Hannah Gossner who assisted in the creation of the distributional plots.

SUPPLEMENTARY MATERIAL

The Supplementary Material for this article can be found online at: https://www.frontiersin.org/articles/10.3389/fmars.2020.556239/full#supplementary-material

FIGURE S1 | Box plots of mean swimming speed, normalized mean swimming speed, sinking speed, and normalized mean sinking speed for three different shell shape groups. **(A)** Mean swimming speed. **(B)** Normalized mean swimming speed. **(C)** Mean sinking speed. **(D)** Normalized mean swimming speed plot. Groups which do not share a letter are statistically different from each other ($p < 0.05$) as determined by a one way ANOVA test and Tukey-Kramer pairwise comparisons. Outliers are demarcated as a plus sign (+).

FIGURE S2 | Swimming speed U of individual marine snails as a function of wing flapping frequency f for various marine snail species.

FIGURE S3 | Box plots of glide angle and swimming NGDR results for three different shell shape groups. **(A)** Glide angle. **(B)** NGDR. Groups which do not share a letter are statistically different from each other ($p < 0.05$) as determined by a one way ANOVA test and Tukey-Kramer pairwise comparisons. Outliers are demarcated as a plus sign (+).

FIGURE S4 | Vertical distributions based on image data and molecular data. **(A)** Day and Night vertical distribution based on the relative proportion of the population within a particular size bin (mm). **(B)** Average day and night biomass profiles based on imaging. **(C)** Average day and night biomass profiles based on molecular barcoding.

TABLE S1 | Tukey-Kramer pairwise comparison test between the three pteropod shell shape groups. C – coiled shell, E – elongated shell, G – globular shell groups. Bold values show $P < 0.05$.

FILE S1 | MOCNESS net sampling methods.

MOVIE S1 | Video of a large unidentified atlantiid heteropod species (likely *Oxygyrus inflatus*) preying on the pteropod *Clio pyramidata* while both were lying on the floor of an aquarium. Video shakiness was removed by using Warp Stabilizer effect in Adobe Premiere Pro CC 2018.

REFERENCES

Adhikari, D., Webster, D. R., and Yen, J. (2016). Portable tomographic PIV measurements of swimming shelled Antarctic pteropods. *Exp. Fluids* 57:180.

Almogi-Labin, A., Hemleben, C., and Deuser, W. G. (1988). Seasonal variation in the flux of euthecosomatous pteropods collected in a deep sediment trap in the Sargasso Sea. *Deep Sea Res. A Oceanogr. Res. Pap.* 35, 441–464.

Amin, K., Huang, J. M., Hu, K. J., Zhang, J., and Ristroph, L. (2019). The role of shape-dependent flight stability in the origin of oriented meteorites. *Proc. Natl. Acad. Sci. U.S.A.* 116, 16180–16185. doi: 10.1073/pnas.1815133116

Amir, A., Daniel, M., Navas-Molina, J., Kopylova, E., Morton, J., Xu, Z. Z., et al. (2017). Deblur rapidly resolves single-nucleotide community sequence patterns. *mSystems* 2:e00191-16.

Antezana, T. (2009). Species-specific patterns of diel migration into the Oxygen Minimum Zone by euphausiids in the Humboldt current ecosystem. *Prog. Oceanogr.* 83, 228–236. doi: 10.1016/j.pocean.2009.07.039

Barnes, P. T., and Laurie-Ahlberg, C. C. (1986). Genetic variability of flight metabolism in *Drosophila melanogaster*. III. Effects of GPDH allozymes and environmental temperature on power output. *Genetics* 112, 267–294.

Bé, A. W. H., and Gilmer, R. W. (1977). A zoogeographic and taxonomic review of euthecosomatous Pteropoda. *Ocean. Micropaleontol.* 1, 773–808.

Beaugrand, G., Mcquatters-Gollop, A., Edwards, M., and Goberville, E. (2012). Long-term responses of North Atlantic calcifying plankton to climate change. *Nat. Clim. Change* 3, 263–267. doi: 10.1038/nclimate1753

Bednaršek, N., Feely, R. A., Howes, E. L., Hunt, B., Kessouri, F., León, P., et al. (2019). Systematic review and meta-analysis towards synthesis of thresholds of ocean acidification impacts on calcifying pteropods and interactions with warming. *Front. Mar. Sci.* 6:227. doi: 10.3389/fmars.2019.00227

Bednaršek, N., Možina, J., Vogt, M., O'Brien, C., and Tarling, G. A. (2012). The global distribution of pteropods and their contribution to carbonate and carbon biomass in the modern ocean. *Earth Syst. Sci. Data* 5, 167–186. doi: 10.5194/essd-4-167-2012

Bergan, A. J., Lawson, G. L., Maas, A. E., and Wang, Z. A. (2017). The effect of elevated carbon dioxide on the sinking and swimming of the shelled pteropod *Limacina retroversa*. *ICES J. Mar. Sci.* 74, 1893–1905. doi: 10.1093/icesjms/fsx008

Berger, W. H. (1978). Deep-sea carbonate: pteropod distribution and the aragonite compensation depth. *Deep Sea Res.* 25, 447–452. doi: 10.1016/0146-6291(78)90552-0

Berner, R. A., and Honjo, S. (1981). Pelagic sedimentation of aragonite: its geochemical significance. *Science* 211, 940–942. doi: 10.1126/science.211.4485.940

Bianco, G., Mariani, P., Visser, A. W., Mazzocchi, M. G., and Pigolotti, S. (2014). Analysis of self-overlap reveals trade-offs in plankton swimming trajectories. *J. R. Soc. Interface* 11:20140164. doi: 10.1098/rsif.2014.0164

Blanco-Bercial, L. (2020). Metabarcoding analyses and seasonality of the zooplankton community at BATS. *Front. Mar. Sci.* 7:173. doi: 10.3389/fmars.2020.00173

Borrell, B. J., Goldbogen, J. A., and Dudley, R. (2005). Aquatic wing flapping at low Reynolds numbers: swimming kinematics of the Antarctic pteropod, *Clione antarctica*. *J. Exp. Biol.* 208, 2939–2949. doi: 10.1242/jeb.01733

Buitenhuis, E. T., Le Quéré, C., Bednaršek, N., and Schiebel, R. (2019). Large contribution of pteropods to shallow CaCO3 export. *Glob. Biogeochem. Cycles* 33, 458–468. doi: 10.1029/2018GB006110

Burridge, A. K., Goetze, E., Wall-Palmer, D., Le Double, S. L., Huisman, J., and Peijnenburg, K. T. C. A. (2017). Diversity and abundance of pteropods and heteropods along a latitudinal gradient across the Atlantic Ocean. *Prog. Oceanogr.* 158, 213–223. doi: 10.1016/j.pocean.2016.10.001

Chamberlain, J. A., and Weaver, J. S. (1978). Equations of motion for post-mortem sinking of cephalopod shells. *J. Int. Assoc. Math. Geol.* 10, 673–689. doi: 10.1007/BF01031898

Chang, Y., and Yen, J. (2012). Swimming in the intermediate Reynolds range: kinematics of the pteropod *Limacina helicina*. *Integr. Comp. Biol.* 52, 597–615. doi: 10.1093/icb/ics113

Childress, S., and Dudley, R. (2004). Transition from ciliary to flapping mode in a swimming mollusc: flapping flight as a bifurcation in Re. *J. Fluid Mech.* 498, 257–288. doi: 10.1017/S002211200300689X

Chu, P. C., Gilles, A., and Fan, C. (2005). Experiment of falling cylinder through the water column. *Exp. Therm. Fluid Sci.* 29, 555–568. doi: 10.1016/j.expthermflusci.2004.08.001

Comeau, S., Gattuso, J. P., Nisumaa, A. M., and Orr, J. (2012). Impact of aragonite saturation state changes on migratory pteropods. *Proc. R. Soc. B Biol. Sci.* 279, 732–738. doi: 10.1098/rspb.2011.0910

Daufresne, M., Lengfellner, K., and Sommer, U. (2009). Global warming benefits the small in aquatic ecosystems. *Proc. Natl. Acad. Sci. U.S.A.* 106, 12788–12793. doi: 10.1073/pnas.0902080106

Dillon, M. E., and Dudley, R. (2004). Allometry of maximum vertical force production during hovering flight of neotropical orchid bees (Apidae: Euglossini). *J. Exp. Biol.* 207, 417–425. doi: 10.1242/jeb.00777

Dudley, R. (2002). Mechanisms and implications of animal flight maneuverability. *Integr. Comp. Biol.* 42, 135–140. doi: 10.1093/icb/42.1.135

Fabry, V. J. (1990). Shell growth rates of pteropod and heteropod molluscs and aragonite production in the open ocean: implications for the marine carbonate system. *J. Mar. Res.* 48, 209–222. doi: 10.1357/002224090784984614

Fabry, V. J., and Deuser, W. G. (1991). Aragonite and magnesian calcite fluxes to the deep Sargasso Sea. *Deep Sea Res. A Oceanogr. Res. Pap.* 38, 713–728. doi: 10.1016/0198-0149(91)90008-4

Field, S. B., Klaus, M., Moore, M. G., and Nori, F. (1997). Chaotic dynamics of falling disks. *Nature* 388, 252–254. doi: 10.1038/40817

Fonseca, V. G., Carvalho, G. R., Sung, W., Johnson, H. F., Power, D. M., Neill, S. P., et al. (2010). Second-generation environmental sequencing unmasks marine metazoan biodiversity. *Nat. Commun.* 1:98. doi: 10.1038/ncomms1095

Frazier, M. R., Harrison, J. F., Kirkton, S. D., and Roberts, S. P. (2008). Cold rearing improves cold-flight performance in *Drosophila via* changes in wing morphology. *J. Exp. Biol.* 211, 2116–2122. doi: 10.1242/jeb.019422

Gilmer, R. W. (1972). Free-floating mucus webs: a novel feeding adaptation for the open ocean. *Science* 176, 1239–1240. doi: 10.1126/science.176.4040.1239

Gilmer, R. W., and Harbison, G. R. (1986). Morphology and field behavior of pteropod molluscs: feeding methods in the families Cavoliniidae, Limacinidae and Peraclididae (Gastropoda: Thecosomata). *Mar. Biol.* 91, 47–57. doi: 10.1007/BF00397570

Gorsky, G., Ohman, M. D., Picheral, M., Gasparini, S., Stemmann, L., Romagnan, J. B., et al. (2010). Digital zooplankton image analysis using the ZooScan integrated system. *J. Plankton Res.* 32, 285–303. doi: 10.1093/plankt/fbp124

Hamner, W. M., Madin, L. P., Alldredge, A. L., Gilmer, R. W., and Hamner, P. P. (1975). Underwater observations of gelatinous zooplankton: sampling problems, feeding biology, and behavior. *Limnol. Oceanogr.* 20, 907–917. doi: 10.4319/lo.1975.20.6.0907

Harbison, G. R., and Gilmer, R. W. (1992). Swimming, buoyancy and feeding in shelled pteropods: a comparison of field and laboratory observations. *J. Molluscan Stud.* 58, 337–339. doi: 10.1093/mollus/58.3.337

Hays, G. C. (2003). A review of the adaptive significance and ecosystem consequences of zooplankton diel vertical migrations. *Hydrobiologia* 503, 163–170. doi: 10.1023/B:HYDR.0000008476.23617.b0

Hedrick, T. L. (2008). Software techniques for two- and three-dimensional kinematic measurements of biological and biomimetic systems. *Bioinspir. Biomim.* 3:034001. doi: 10.1088/1748-3182/3/3/034001

Howes, E. L., Bednaršek, N., Büdenbender, J., Comeau, S., Doubleday, A., Gallager, S. M., et al. (2014). Sink and swim: a status review of thecosome pteropod culture techniques. *J. Plankton Res.* 36, 299–315. doi: 10.1093/plankt/fbu002

Hunt, B. P. V., Pakhomov, E. A., Hosie, G. W., Siegel, V., Ward, P., and Bernard, K. (2008). Pteropods in Southern ocean ecosystems. *Prog. Oceanogr.* 78, 193–221. doi: 10.1016/j.pocean.2008.06.001

Hunt, J. C., and Seibel, B. A. (2000). Life history of *Gonatus onyx* (Cephalopoda: Teuthoidea): ontogenetic changes in habitat, behavior and physiology. *Mar. Biol.* 136, 543–552. doi: 10.1007/s002270050714

Jackson, B. E., Evangelista, D. J., Ray, D. D., and Hedrick, T. L. (2016). 3D for the people: multi-camera motion capture in the field with consumer-grade cameras and open source software. *Biol. Open* 5, 1334–1342. doi: 10.1242/bio.018713

Karakas, F., D'Oliveira, D., Maas, A. E., and Murphy, D. W. (2018). Using a shell as a wing: pairing of dissimilar appendages in atlantiid heteropod swimming. *J. Exp. Biol.* 221:jeb192062. doi: 10.1242/jeb.192062

Karakas, F., Maas, A. E., and Murphy, D. W. (2020). A novel cylindrical overlap-and-fling mechanism used by sea butterflies. *J. Exp. Biol.* 223:jeb221499. doi: 10.1242/jeb.221499

Lalli, C. M., and Gilmer, R. W. (1989). *Pelagic Snails: the Biology of Holoplanktonic Gastropod Mollusks*. Palo Alto, CA: Stanford University Press.

Land, M. F. (1982). Scanning eye movements in a heteropod mollusc. *J. Exp. Biol.* 96, 427–430.

Land, M. F. (1999). Motion and vision: why animals move their eyes. *J. Comp. Physiol. A Sens. Neural Behav. Physiol.* 185, 341–352. doi: 10.1007/s003590050393

Lehmann, F. O. (1999). Ambient temperature affects free-flight performance in the fruit fly *Drosophila melanogaster*. *J. Comp. Physiol. B Biochem. Syst. Environ. Physiol.* 169, 165–171. doi: 10.1007/s003600050207

Lourakis, M. I., and Argyros, A. A. (2009). SBA: a software package for generic sparse bundle adjustment. *ACM Trans. Math. Softw.* 36:2. doi: 10.1145/1486525.1486527

Maas, A. E., Blanco-Bercial, L., and Lawson, G. L. (2013). Reexamination of the species assignment of *Diacavolinia* pteropods using DNA barcoding. *PLoS One* 8:e53889. doi: 10.1371/journal.pone.0053889

Maas, A. E., Frazar, S. L., Outram, D. M., Seibel, B. A., and Wishner, K. F. (2014). Fine-scale vertical distribution of macroplankton and micronekton in the Eastern Tropical North Pacific in association with an oxygen minimum zone. *J. Plankton Res.* 36, 1557–1575. doi: 10.1093/plankt/fbu077

Maas, A. E., Wishner, K. F., and Seibel, B. A. (2012). Metabolic suppression in thecosomatous pteropods as an effect of low temperature and hypoxia in the eastern tropical North Pacific. *Mar. Biol.* 159, 1955–1967. doi: 10.1007/s00227-012-1982-x

Mackas, D. L., Batten, S., and Trudel, M. (2007). Effects on zooplankton of a warmer ocean: recent evidence from the Northeast Pacific. *Prog. Oceanogr.* 75, 223–252. doi: 10.1016/j.pocean.2007.08.010

Manno, C., Morata, N., and Primicerio, R. (2012). *Limacina retroversa*'s response to combined effects of ocean acidification and sea water freshening. *Estuar. Coast. Shelf Sci.* 113, 163–171. doi: 10.1016/j.ecss.2012.07.019

Manno, C., Tirelli, V., Accornero, A., and Fonda Umani, S. (2010). Importance of the contribution of *Limacina helicina* faecal pellets to the carbon pump in terra nova bay (Antarctica). *J. Plankton Res.* 32, 145–152. doi: 10.1093/plankt/fbp108

Mohaghar, M., Adhikari, D., and Webster, D. R. (2019). Characteristics of swimming shelled Antarctic pteropods (*Limacina helicina antarctica*) at intermediate Reynolds number regime. *Phys. Rev. Fluids* 4:111101. doi: 10.1103/PhysRevFluids.4.111101

Morton, J. E. (1954). The biology of *Limacina retroversa*. *J. Mar. Assess. U.K.* 3, 297–312. doi: 10.1017/S002531540000833X

Murphy, D. W., Adhikari, D., Webster, D. R., and Yen, J. (2016). Underwater flight by the planktonic sea butterfly. *J. Exp. Biol.* 219, 535–543. doi: 10.1242/jeb.129205

Ohman, M. D., and Romagnan, J. B. (2016). Nonlinear effects of body size and optical attenuation on Diel Vertical Migration by zooplankton. *Limnol. Oceanogr.* 61, 765–770. doi: 10.1002/lno.10251

Orr, J. C. (2011). Recent and future changes in ocean carbonate chemistry. *Ocean Acidification* 2, 41–66.

Oviatt, C. A. (2004). The changing ecology of temperate coastal waters during a warming trend. *Estuaries* 27, 895–904. doi: 10.1007/bf02803416

Peijnenburg, K. T., Janssen, A. W., Wall-Palmer, D., Goetze, E., Maas, A., Todd, J. A., et al. (2019). The origin and diversification of pteropods predate past perturbations in the Earth's carbon cycle. *bioRxiv [Preprint]* doi: 10.1101/813386

Pétavy, G., Morin, J. P., Moreteau, B., and David, J. R. (1997). Growth temperature and phenotypic plasticity in two *Drosophila* sibling species: probable adaptive changes in flight capacities. *J. Evol. Biol.* 10, 875–887. doi: 10.1007/s000360050059

Ronquist, F., Teslenko, M., Van Der Mark, P., Ayres, D. L., Darling, A., Höhna, S., et al. (2012). Mrbayes 3.2: efficient bayesian phylogenetic inference and model choice across a large model space. *Syst. Biol.* 61, 539–542. doi: 10.1093/sysbio/sys029

Sabine, C. C. L., Feely, R. R. A., Gruber, N., Key, R. M. R., Lee, K., Bullister, J. L., et al. (2004). The oceanic sink for anthropogenic CO2. *Science* 305, 367–371. doi: 10.1126/science.1097403

Satterlie, R. A., Labarbera, M., and Spencer, A. N. (1985). Swimming in the pteropod mollusk, *Clione limacina* 1. Behavior and morphology. *J. Exp. Biol.* 116, 189–204.

Schloss, P. D., Westcott, S. L., Ryabin, T., Hall, J. R., Hartmann, M., Hollister, E. B., et al. (2009). Introducing mothur: open-source, platform-independent, community-supported software for describing and comparing microbial communities. *Appl. Environ. Microbiol.* 75, 7537–7541. doi: 10.1128/aem.01541-09

Seapy, R. R. (1980). Predation by the epipelagic heteropod mollusk *Carinaria cristata* forma japonica. *Mar. Biol.* 60, 137–146. doi: 10.1007/BF00389157

Seuront, L., Brewer, M. C., and Strickler, J. R. (eds). (2004). "Quantifying zooplankton swimming behavior: the question of scale," in *Handbook of Scaling Methods in Aquatic Ecology: Measurement, Analysis, Simulation*, (Boca Raton, FL: CRC Press), 333–360. doi: 10.1201/9780203489550.ch22

Southward, A. J., Hawkins, S. J., and Burrows, M. T. (1995). Seventy years' observations of changes in distribution and abundance of zooplankton and intertidal organisms in the western English Channel in relation to rising sea temperature. *J. Therm. Biol.* 20, 127–155. doi: 10.1016/0306-4565(94)00043-I

Stamatakis, A. (2014). RAxML version 8: a tool for phylogenetic analysis and post-analysis of large phylogenies. *Bioinformatics* 30, 1312–1313. doi: 10.1093/bioinformatics/btu033

Szymik, B. G., and Satterlie, R. A. (2011). Changes in wingstroke kinematics associated with a change in swimming speed in a pteropod mollusk, *Clione limacina*. *J. Exp. Biol.* 214, 3935–3947. doi: 10.1242/jeb.058461

Thabet, A. A., Maas, A. E., Lawson, G. L., and Tarrant, A. M. (2015). Life cycle and early development of the thecosomatous pteropod *Limacina retroversa* in the Gulf of Maine, including the effect of elevated CO2 levels. *Mar. Biol.* 162, 2235–2249. doi: 10.1007/s00227-015-2754-1

Thiriot-Quiévreux, C. (1973). *Heteropoda. Ocean. Mar. Biol. Ann. Rev.* 11, 237–261.

Titelman, J., and Fiksen, Ø. (2004). Ontogenetic vertical distribution patterns in small copepods: field observations and model predictions. *Mar. Ecol. Prog. Ser.* 284, 49–63. doi: 10.3354/meps284049

Tsurumi, M., Mackas, D. L., Whitney, F. A., Dibacco, C., Galbraith, M. D., and Wong, C. S. (2005). Pteropods, eddies, carbon flux, and climate variability in the Alaska Gyre. *Deep Sea Res. Part II Top. Stud. Oceanogr.* 52, 1037–1053. doi: 10.1016/j.dsr2.2005.02.005

Vandromme, P., Lars, S., Garcìa-Comas, C., Berline, L., Sun, X., and Gorsky, G. (2012). Assessing biases in computing size spectra of automatically classified zooplankton from imaging systems: a case study with the ZooScan integrated system. *Methods Oceanogr.* 1–2, 3–21. doi: 10.1016/j.mio.2012.06.001

Vogel, S. (1988). *Life's Devices: the Physical World of Animals and Plants*. Princeton, NJ: Princeton University Press.

Vogel, S. (2013). *Comparative Biomechanics: Life's Physical World*. Princeton, NJ: Princeton University Press.

Wall-Palmer, D., Metcalfe, B., Leng, M. J., Sloane, H. J., Ganssen, G., Vinayachandran, P. N., et al. (2018). Vertical distribution and diurnal migration of atlantid heteropods. *Mar. Ecol. Prog. Ser.* 587, 1–15. doi: 10.3354/meps12464

Wall-Palmer, D., Smart, C. W., Kirby, R., Hart, M. B., Peijnenburg, K. T. C. A., and Janssen, A. W. (2016). A review of the ecology, palaeontology and distribution of atlantid heteropods (Caenogastropoda: Pterotracheoidea: Atlantidae). *J. Molluscan Stud.* 82, 221–234. doi: 10.1093/mollus/eyv063

Weis-Fogh, T. (1973). Quick estimates of flight fitness in hovering animals, including novel mechanisms for lift production. *J. Exp. Biol.* 59, 169–230.

Wiebe, P. H., Morton, A. W., Bradley, A. M., Backus, R. H., Craddock, J. E., Barber, V., et al. (1985). New development in the MOCNESS, an apparatus for sampling zooplankton and micronekton. *Mar. Biol.* 87, 313–323. doi: 10.1007/BF00397811

Wormelle, R. L. (1962). A survey of the standing crop of plankton of the Florida current. VI. A study of the distribution of the pteropods of the Florida current. *Bull. Mar. Sci.* 12, 95–136.

Wormuth, J. H. (1981). Vertical distributions and diel migrations of *Euthecosomata* in the northwest Sargasso Sea. *Deep Sea Res. A Oceanogr. Res. Pap.* 28, 1493–1515.

Zhou, Z., and Mittal, R. (2017). Swimming without a Spine: computational modeling and analysis of the swimming hydrodynamics of the Spanish dancer. *Bioinspir. Biomim.* 13:015001. doi: 10.1088/1748-3190/aa9392

Zhou, Z., and Mittal, R. (2018). Swimming performance and unique wake topology of the sea hare (*Aplysia*). *Phys. Rev. Fluids* 3:33102. doi: 10.1103/PhysRevFluids.3.033102

Conflict of Interest: The authors declare that the research was conducted in the absence of any commercial or financial relationships that could be construed as a potential conflict of interest.

Copyright © 2020 Karakas, Wingate, Blanco-Bercial, Maas and Murphy. This is an open-access article distributed under the terms of the Creative Commons Attribution License (CC BY). The use, distribution or reproduction in other forums is permitted, provided the original author(s) and the copyright owner(s) are credited and that the original publication in this journal is cited, in accordance with accepted academic practice. No use, distribution or reproduction is permitted which does not comply with these terms.

frontiers in Marine Science

ORIGINAL RESEARCH
published: 14 December 2020
doi: 10.3389/fmars.2020.558745

Three-Dimensional Imaging Lidar for Characterizing Particle Fields and Organisms in the Mesopelagic Zone

Trevor McKenzie[1,2], Michael Twardowski[1,2], Nathan Briggs[3], Aditya R. Nayak[1,2], Kevin M. Boswell[4] and Fraser Dalgleish[1,2]*

[1] Harbor Branch Oceanographic Institute, Florida Atlantic University, Fort Pierce, FL, United States, [2] Department of Ocean and Mechanical Engineering, Florida Atlantic University, Boca Raton, FL, United States, [3] National Oceanography Centre, Southampton, United Kingdom, [4] Coastlines and Oceans Division of the Institute of Environment, Florida International University, North Miami, FL, United States

The ocean's mesopelagic zone is largely uncharacterized despite its vital role in sustaining ocean ecosystems. The composition, cycling, and fate of particle fields in the mesopelagic lacks an integrative multi-scale understanding of organism migration patterns, distribution, and diversity. This problem is addressed by combining complementary technologies with overlapping size spectra, including profiler mounted optical scattering sensors, profiler, and ship mounted acoustic devices, and a custom Unobtrusive Multi-Static Lidar Imager (UMSLI). This unique sensor suite can observe distributions of particles including organisms over a six order of magnitude dynamic size range, from microns to meters. Overlapping size ranges between different methods allows for cross-validation. This work focuses on the lidar imaging measurements and optical backscattering and attenuation, covering a combined particle size range of 0.1 mm to several cm. Particles at the small end of this range are sized using an existing backscattering time series inversion method after Briggs et al. (2013). Larger particles are resolved with UMSLI over an expanding volume using three-dimensional photo-realistic laser serial imaging. UMSLI's image rectifying ability over time allows for derivation of particle concentration, size, and spatial distribution. Technical details on the development and post-processing methods for the novel UMSLI system are provided. Image resolved particle size distributions (PSDs) revealed a size shift from smaller to larger particles (>0.5 mm) as indicated by flatter slopes from dawn (slope = 2.6) to dusk (slope = 3.0). PSD trends are supported by an optical backscatter and transmissometer time series inversion analysis. Size shifts in the particle field are largely attributed to aggregation effects. Images support evidence of temporal variation between dusk and dawn stations through statistical analysis of particle concentrations for particle sizes 0.50–5.41 mm. Spatial analysis of the particle field revealed a dominantly uniform distributed marine snow background. The importance and potential of integrated approaches to studying particle and organism dynamics in ocean environments are discussed.

Keywords: imaging lidar, mesopelagic, *in-situ* optics, image analysis, PSD, sound scattering layer

OPEN ACCESS

Edited by:
Alberto Basset, University of Salento, Italy

Reviewed by:
Enrique Nogueira, Spanish Institute of Oceanography (IEO), Spain
Sergio M. Vallina, Spanish Institute of Oceanography (IEO), Spain
Gianfranco D'Onghia, University of Bari Aldo Moro, Italy

****Correspondence:***
Trevor McKenzie
tmckenzie@fau.edu

Specialty section:
This article was submitted to Marine Ecosystem Ecology, a section of the journal Frontiers in Marine Science

Received: *04 May 2020*
Accepted: *03 November 2020*
Published: *14 December 2020*

Citation:
McKenzie T, Twardowski M, Briggs N, Nayak AR, Boswell KM and Dalgleish F (2020) Three-Dimensional Imaging Lidar for Characterizing Particle Fields and Organisms in the Mesopelagic Zone. Front. Mar. Sci. 7:558745. doi: 10.3389/fmars.2020.558745

INTRODUCTION

The Earth's oceans are a reservoir for an estimated 31% of anthropogenically produced CO_2. Of the 100 Gt of organic carbon taken up by ocean surface waters per year, up to 10% is transferred to the mesopelagic (similar magnitude as fossil fuel emissions) (Gardner et al., 2000; Giering et al., 2014, 2018). Without this carbon export mechanism, the concentration of CO_2 in the atmosphere would be an estimated 200 ppm higher than present day levels (McDonnell, 2011; Davison et al., 2013; Volk and Hoffert, 2013). This process, known as the "biological pump" is controlled by the productivity of primary producers in the surface ocean and active/passive downward transport of organic and inorganic composite material. Current estimates suggest, up to 90% of surface water detrital material is recycled, consumed, and respired before reaching 1,000 m (Stemmann et al., 2008; McDonnell, 2011; Davison et al., 2013; Hansen and Visser, 2016). Understanding the role of the mesopelagic zone (bottom of euphotic zone to 1,000 m) in mediating remineralization and transport to the deep ocean is currently a subject of intense research (Giering et al., 2019; Briggs et al., 2020).

Much of our knowledge of particle dynamics and transport through the water column has been gathered using sediment traps (Martin et al., 1987; Buesseler et al., 2007). Sediment traps function much like rain gauges, accumulating sinking particles over a period of days to weeks at predetermined depths. This allows for the collection and biological analysis of a wide size range of particles (Chester, 2000; Stemmann et al., 2008; Hung et al., 2010; Giering et al., 2018). While sediment traps have been used extensively, their spatial coverage is limited, thus decreasing the probability of capturing larger particles. Small sampling areas on the order of m^2 must also be extrapolated temporally and across large regional areas and wide depth ranges. This may be particularly problematic for resolving significant episodic, localized sinking events associated with bloom crashes (Briggs et al., 2020). Sediment traps also hydrodynamically disturb suspended particles, inhibiting their efficiency and making interpretation more complex (Yu et al., 2001).

To compensate for an imbalance between carbon export and metabolic demands in the mesopelagic, many processes such as mortality, defecation, fragmentation, and export from diel vertical migrators require further investigation to accurately gauge these contributions in carbon budget models (Burd et al., 2010; Kelly et al., 2019; Briggs et al., 2020). Many studies have shifted the view of the mesopelagic to a more dynamic transit zone of the ocean that harbors organisms participating in massive diel vertical migrations (DVM) (Passow and Alldredge, 1995; Hiaka et al., 2001; Steinberg et al., 2002; Kaartvedt et al., 2012; Taucher et al., 2018; Proud et al., 2019; Boswell et al., 2020). Some of these animal's form what is called the deep scattering layer (DSL), named for its strong acoustic reflection. This layer has long been observed to migrate upward to the surface at dusk and back downward at dawn as motivated by predation and feeding (Hays, 2003; Hansen and Visser, 2016; Calleja et al., 2018; Taucher et al., 2018). Migration by zooplankton and nekton are increasingly recognized as playing a significant role in transport of carbon through the mesopelagic (Steinberg et al., 2002; Burd et al., 2010; Kaartvedt et al., 2012; Klevjer et al., 2012; Hansen and Visser, 2016; Calleja et al., 2018; Kelly et al., 2019). Mesopelagic micronekton and zooplankton directly affect the distribution and size of suspended particles through feeding, migration and defecation. Similarly, gelatinous grazers also directly affect the repackaging and vertical fluctuation of sinking particles, through ingestion and release of larger fecal pellets. These processes affect the rates of fragmentation and remineralization of sinking particles and are often excluded from carbon export budgets. Studies of DVM and other active transport mechanisms in the mesopelagic suggest that these missing export processes could explain apparent imbalances between carbon supply and metabolic demands (Steinberg et al., 2002; Burd et al., 2010; Kelly et al., 2019). New technologies which feature *in situ* measurements using optical instrumentation and autonomous platforms create new potential for characterizing particle fields for size, shape, distribution, and concentration (Nayak and Twardowski, 2020).

To investigate this potential and to better understand particle dynamics in the mesopelagic ocean, acoustic, and optical techniques are used to characterize distributions of particle fields (including organisms) and spatial patchiness. The focus of this work is on using optical backscattering and beam attenuation instrumentation in combination with UMSLI to resolve particle size distributions (including organisms) from about 0.1 to 50 mm. UMSLI uses three-dimensional laser serial scanning to provide traceable volumetric images of particle and organism fields down to about 1 mm. Smaller particles are resolved from optical backscattering and attenuation with a time series inversion method (Briggs et al., 2013). Details of UMSLI data processing are discussed and particle distribution results compared between the two methods.

MATERIALS AND METHODS

Imaging Lidar

Lidar systems consist of two main components, a transmitter and receiver. The transmitter consists of a highly collimated laser, often directed by a mechanical mirror device. The receiver may take many forms, but generally consist of a light receptor that quantifies intensity per unit area. Just as a conventional camera measures the reflection of light off objects with dependency on source and receiver geometry, so does a lidar system. The basis of a lidar's function is to actively illuminate a volume of water with an intense pulse of optical energy from a laser transmitter and measure irradiance returned as a function of time with a receiver coupled with a high-speed digitizer. The range (R) of a target is described by McGill (2002):

$$R = \frac{c_l \times \Delta t}{2}, \tag{1}$$

where c_l is the speed of light. Time of arrival (TOA) is defined as the time it takes for a laser pulse to leave the transmitter, reflect from a specific volume of water, and return to the receiver. The sampling capability of the receiver defines the gate time (Δt) and

temporal resolution of the system. Lasers are capable of emitting light at very fast repetition rates with high energy levels and the collimated monochromatic nature of the beam makes it ideal for probing environments such as water. A complete physical characterization of laser transmission for lidar is well summarized in several studies (Mullen et al., 2009; Caimi and Dalgleish, 2013; Dalgleish F.R. et al., 2013; De Dominicis, 2013).

The method of laser imaging for UMSLI uses serially scanned pulsed lasers for extending imaging range in turbid seawater (Dalgleish F. et al., 2013; Dalgleish F.R. et al., 2013). Traditional optical cameras can be effective when significant ambient or artificial light is present in low turbidity conditions. When using artificial light in imaging, marine life can show a behavior response, i.e., attraction or avoidance, to light within their visual light frequency range (Zorn et al., 2000). Artificial light in conventional imaging also introduces backscatter path radiance effects that can obscure objects. However, unlike active acoustic solutions, the primary advantage of using optical approaches is high resolution contrasted scene descriptions essential for object classification and detailed observations.

Red lasers can be configured below the wavelength range that is visible to marine wildlife allowing for unobtrusive observation. UMSLI uses a 638 nm red diode laser which is beyond the photopic response for most marine organisms in the mesopelagic (Zorn et al., 2000). The UMSLI system was originally built with the intention of observing large marine species without affecting behavior (Dalgleish et al., 2017). It features an alternating field-of-view (FOV) that outputs time-resolved images capable of extracting three-dimensional features. The quasi-monostatic approach and dynamically expanding scan field make UMSLI suitable for resolving organisms across discrete size classes due to an adaptive resolution feature based on the angular control of the laser scan field during operation. For this study, capabilities are extended to observe relatively small particles, such as copepods, krill, and flocs of marine snow.

UMSLI Components

UMSLI's design concept was focused on surveying a large volume of water for the use of observation and identification of targets on a wide range of size scales (mm to m). Transmitters serially illuminate a volume of water by scanning a grid of pulses in a bi-directional raster pattern using an analog micromirror device (AMD) and a scan angle expansion lens. The scan field of the receiver can be instantly configured to operate in three different modes, i.e., sparse, dense, or densest. Each different scan mode features a different image resolution and scan volume as controlled by the transmitter. The resolution is adjusted by concentrating a lower density pulse grid through a wider range of angles (sparse). Once an object is detected, a higher pulse density scan can be conducted through a narrower range of angles (dense/denser) using a digital Micro-Electro-Mechanical-Systems (MEMS) scanning device. The volume scan field for each channel is maximized by an overlapping FOV region between the quasi-monostatic transmitters and receivers. The system consists of three transmitter housings (each with a different total scan field) and three receiver housings, the details of which are described below.

The UMSLI transmitter (**Figure 1A**), features a 638 nm red laser diode with a laser driver that controls the laser pulse output energy. A separate transmitter controller uses RS-232 communication protocol with the MEMS driver that adjusts the polar and azimuthal angle of a scanning two axis (tip-tilt) MEMS mirror (or "micromirror"). The MEMS mirror is mechanically responsible for the serial scan-like pattern of the system (Dalgleish et al., 2018). The reflected beam from the MEMS mirror is expanded using a small angle expansion lens that outputs a full beam divergence of 2.80 mrad in water. The beam radial intensity follows an azimuthally symmetric Gaussian profile.

The total scan angle of the volume, post beam expansion, emits over a polar angle of 0.9425 radians. For this setup, the geometry of the fully illuminated plane is consistent for both polar and azimuthal angles. The transmitter has a 4 ns Full-Width-at-Half-Maximum (FWHM) pulse duration with an average power of 185 mW at a pulse rate of 80 kHz. The transmitter emits each pulse in a raster-like fashion, such that the transmitter emits 200 lines consisting of 200 pulses each. Individual lines take the transmitter 2.50 ms to complete, which allows the system to scan a full 200 × 200 plane in 500 ms for a total of 40,000 pulses (**Supplementary Appendix A**). The UMSLI system's adaptive viewing mode emits the same number of pulses at a smaller angle of 0.3142 radians (dense) and 0.1047 radians (densest).

The receivers consist of a pair of bi-directional red sensitive high-speed photomultiplier modules with focusing optics and a spectral bandpass filter. Receivers are designed to collect backscatter returns from the emitted laser pulses (Dalgleish et al., 2018). To eliminate ambient light, the PMT is capped with a rectangular light shield that allows for a 30° acceptance angle; **Figure 1B** demonstrates a ray trace of the light shield rejection pattern. A high-speed digitizer and digital signal processor are used to reconstruct the illuminated volume and output imagery waveforms. These waveforms are transformed and processed as a volumetric scan, within a x–y spatial plane and a temporal z-plane. A single element Photo-Multiplier Tube (PMT) is used as a detector. The PMT used for this system is a Hamamatsu R11265U series, type H11934-20 with a spectral response from 300 to 920 nm, a quantum efficiency of 19% and radiant efficiency of 78 mA/W. The temporal response of the PMT is the dominant restriction for the system response time. **Figure 1C** shows the rise time of the impulse response to be 1.3 ns and the fall time 5.8 ns. The PMT and its components described above are housed in a Vitrovex glass sphere from Nautilus which are paired as two combined hemispheres. The 187 mm outside diameter glass housing has a total glass thickness of 14 mm and is pressure rated to a depth of 12,000 m.

Field Experiment

During March 25, 2018, the NOAA *Okeanos Explorer* navigated the Gulf of Mexico to explore the mesopelagic region and monitor biological migration patterns. A single deployment was carried out at each station. The first deployment was in the morning from 0430 to 0900 (local) at 28.66N, 87.86W and the second deployment was in the evening at 1,600–2,100 (local) at 28.66N, 87.46W (**Figure 2A**). The two sites were 57.92 km

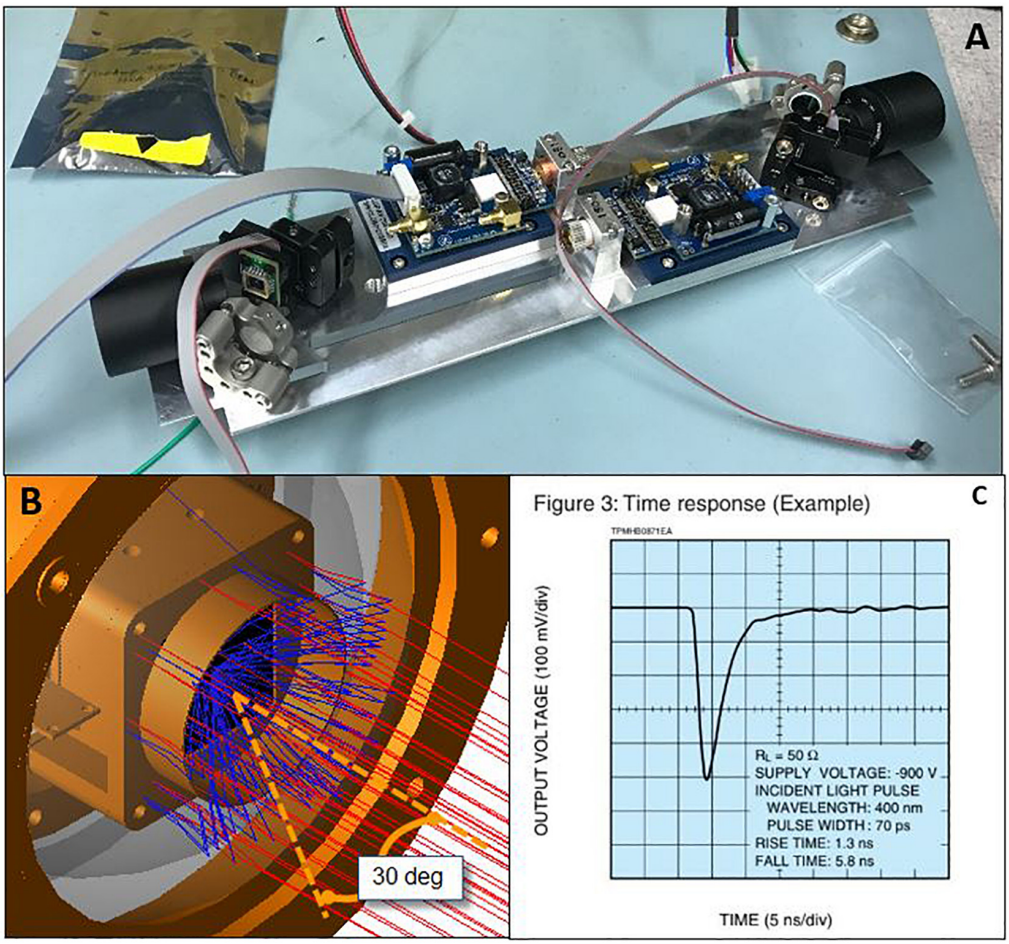

FIGURE 1 | (A) Inside components of the transmitter with DMD device for laser scanning array. **(B)** Represents a ray-trace of the PMT array with acceptance angle shield. **(C)** Rise and fall time of PMT.

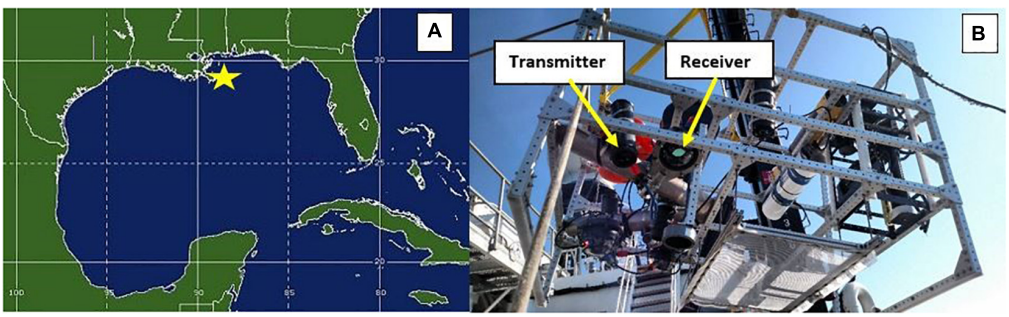

FIGURE 2 | (A) Map with yellow star showing locations of the two stations sampled. **(B)** Profiler set up with UMSLI transmitter and receiver configuration highlighted (yellow arrows).

apart. For each station, an instrument cage was profiled from the surface to 300 m. Immediately after reaching 300 m sampling began and lasted 3 h. Periods for time series were aligned with dusk ascents and dawn descents of the DSL. The dusk migration was sampled at the first site, the dawn migration at the second. Deployed instrumentation included UMSLI, Seabird Scientific ac-9 and ECO-VSF, and a hull mounted and calibrated Simrad EK-80 multifrequency echosounder. Deployment protocols and post-processing for ac-9 and ECO-VSF followed Twardowski et al. (2018) and Sullivan et al. (2013), respectively. These sensors (excluding the EK-80) were mounted onto an aluminum frame with dimensions of 1.8 × 1.2 × 1.7 (m^3) as shown in

Figure 2B. During deployment, the EK-80 measured profiles of acoustic water column backscatter at 18 and 38 kHz to monitor migration patterns from the surface to 600 m. The EK-80 was configured to transmit narrowband signals with pulse duration at 0.2 transmissions per second. Acoustic data were processed following procedures outlined in Boswell et al. (2020). UMSLI's sampling period was programmed before deployments; for the first station, it continuously sampled from 0515 to 0630 (local) and at the second station it sampled from 1,745 to 1,900 (local). UMSLI's scan modes were sequenced, following the scan order sparse, dense, densest (see **Supplementary Appendix A**).

RESULTS

Overview

Throughout this section, emphasis is on the dense and densest lidar scan modes, which have the highest resolution for particle sizes and the most overlap given their relatively close scan angles. The sparse scan mode, while still valuable, is better adapted toward identifying marine fish and larger organisms, which is beyond the size range focus of this analysis. Densest scans for the dawn station are unusable due to lack of quality.

EK-80

During deployments the EK-80 displayed the pattern of the sound scattering layers in real-time. A persistent DSL was observed between 300 and 400 m at both stations with migrating filaments linking the surface layers during the upward and downward migrations (**Figure 3**). Upward migration was observed as coherent vertical layers of backscatter ascending from 300 to 375 m to shallower surface layers $<$ 100 m at dusk. The layers detected in the 38 kHz data followed a similar pattern and revealed persistent less dense backscatter return at deeper depths ($\sim$600 m). At dawn, multiple downward migrating layers were detected beginning at 0600 (local) in both the 18 and 38 kHz data. In the 18 kHz data, the downward migration was comprised of two main layers, splitting and settling at 300 and 450 ms, respectively. Similarly, the downward migration recorded at 38 kHz displayed several coherent layers settling to form a high-density scattering layer between 350 and 450 ms.

Lidar Derived Particle Size Distributions (PSDs)

Particle size distributions (PSDs) include all particles, i.e., living organisms as well as detrital flocs and fecal pellets. Analyzing single image slices avoids alternating resolution capabilities (**Supplementary Appendix A**). PSDs are reported as equivalent spherical diameter D, derived from $\sqrt{4A/\pi}$ where A is the extracted filled particle area (**Supplementary Appendix B.7**). Note that A is a measure of the image pixel count for a particle and the calculated diameter was scaled in accordance with the resolution of the image slice. All extracted particles were then subcategorized into size bins based on calculated diameter. The concentration levels of each size bin were normalized by dividing the total number of particles counted per size bin, by the sample volume, resolution of the size bin and the fractional volume lost due to masking (**Supplementary Appendix B.6**). PSDs were modeled as a power law also known as a Junge distribution:

$$n(D) = n_o(D/D_o)^{-\gamma}, \quad (2)$$

where D_o is a reference diameter, n_o is the differential particle concentration at D_o (L^{-1} mm^{-1}) and γ is the slope of the distribution (Kitchen et al., 1982; Liley, 1992; Boss et al., 2001, 2009; Twardowski et al., 2001; Sullivan et al., 2005, 2013; Buonassissi and Dierssen, 2010; Nayak et al., 2018).

Due to the path attenuation of the transmitted and returned signals, an exponential loss was observed in extracted particles for slices with increasing distance from the sensor. As a result, only particle field data from the first slice, i.e., closest to the sensor, are presented. **Figure 4** shows resulting PSDs averaged over the entire dusk and dawn time series. After applying a correction for blurring (see **Supplementary Appendix A**), reasonable agreement was observed between sparse, dense, and densest scan modes. Power law slopes in corrected data were approximately 3.0 and 2.6 for the dusk and dawn time series, respectively, slopes were flatter at dawn for all scan modes.

For the dense scans, comparison of averaged PSDs revealed elevated particle concentrations for the dusk time series in comparison to the dawn time series below 5 mm (**Figure 5**), while for particles $>$ 5 mm higher concentrations were observed at dawn relative to dusk. Above 10 mm, the dawn station recorded much higher concentrations; these size bins most likely represent swimming organisms periodically entering the sample volume. A cumulative view of the particle concentrations for each size bin revealed a non-normal distribution, this led to outlier selection using nonparametric statistics, detailed in the next sub-section.

Outlier Scans With Enhanced Particle Concentrations

Outlier scans record anomalously high particle concentrations relative to the typical marine snow background and are labeled "particle enhancements." Outliers are identified as values greater than the upper quartile whisker of a box plot for a size bin. The upper whisker is calculated as $Q_3 + 2.5 \times (Q_3 - Q_1)$, where Q_1 is the lower quartile and Q_3 is the upper quartile (**Figure 6**). Particle enhancements were assessed for the first four size bins for the dense and densest scans; beyond the first four size bins particle abundance was too low to conduct statistical analysis. Images from the dusk and dawn stations revealed particle enhancements occurring for particle size bins 3.96 (**Figures 6A,B**) and 5.41 mm (**Figures 6C,D**), respectively. For the densest scans, particle enhancements were most observed for size bin 2.52 mm. This particle enhancement analysis can be used as a metric to identify images where organisms such as copepods may be entering image volumes. The increasing trend in particle size is consistent with trends found in **Figure 4**. The densest station had enhancement events relatively evenly distributed across all size classes. The most notable feature in many of the densest scans were long, ellipsoid shaped organisms with enhancements for size bins 0.5, 0.96, 1.43, and 2.5 mm (**Figure 6F**).

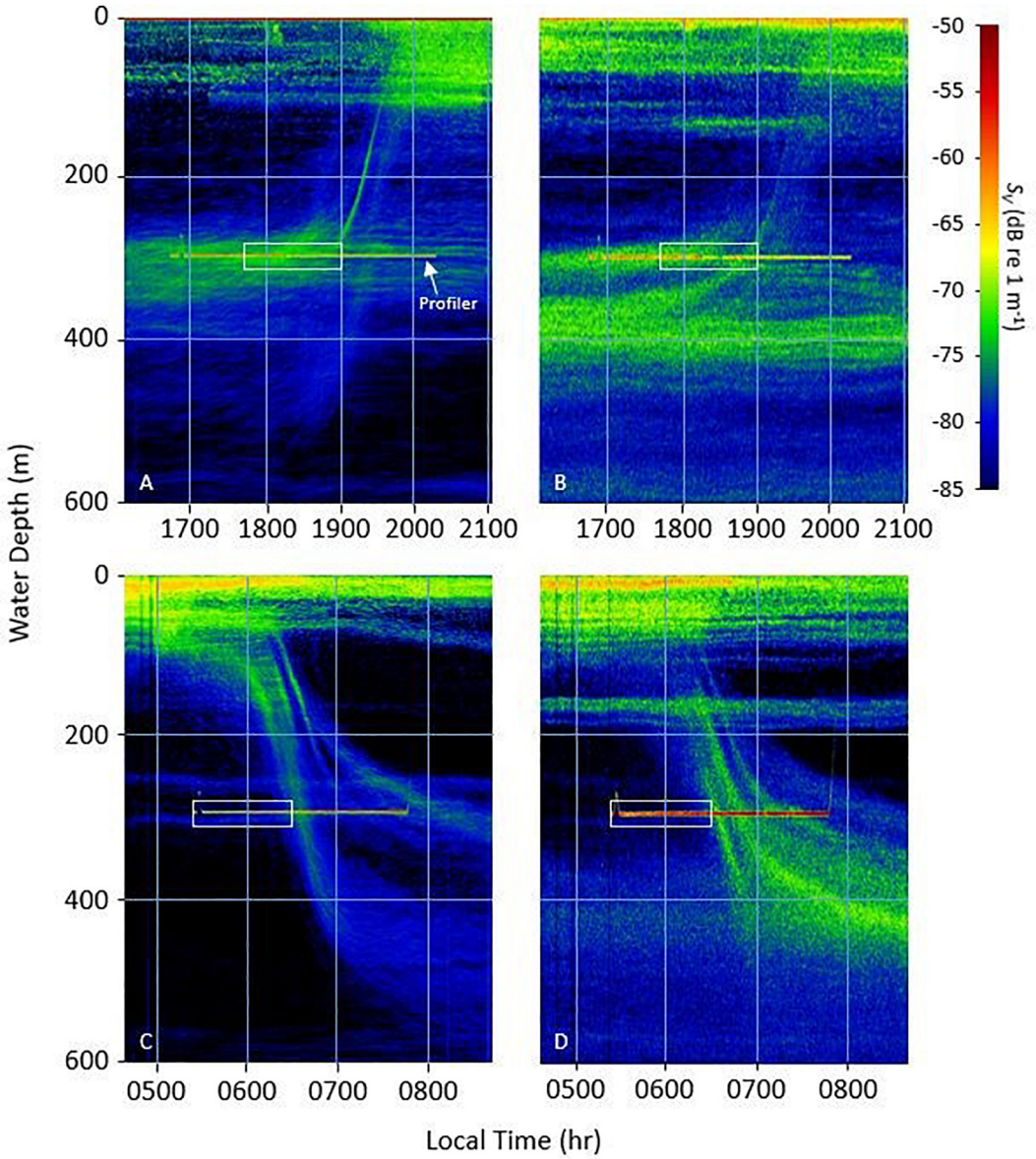

FIGURE 3 | Acoustic volume backscatter strength (S_V, dB re 1 m^{-1}) profiles derived from the shipboard EK-80 echosounder at 18 kHz **(A,C)** and 38 kHz **(B,D)**. Persistent backscatter at approximately 300 m is coincident with the position of the profiling package during full timeseries, while the white boxes represents the time period for which data with the lidar imager is presented.

Large organisms were imaged in the sparse, dense and densest scan modes for both dusk and dawn stations; these occurrences are too few to represent statistically but this is a notable result which indicates a population of larger organisms present among the marine snow background (**Figure 7**). Size and shape characteristics indicate these include siphonophores, various cnidarians, tunicates, and micronekton.

Lidar Derived Particle Patchiness

For every particle extracted from the volume, its Euclidian distance from all other particles was determined to assess relative clustering or dispersion of particles. A two-tail z-test was conducted for this distance metric (Malkiel et al., 2006). This form of hypothesis testing determines the likelihood that the sample distribution differs statistically from the population distribution mean ($\overline{X_p}$) and standard deviation (σ_p). Statistical significance for this hypothesis test was determined by the z-score, defined as,

$$z = \frac{\overline{X_s} - \overline{X_p}}{\sigma/\sqrt{n}}, \tag{3}$$

where $\overline{X_s}$ is the mean distance between particles in the scan slice and N is the combination of distances counted for each particle.

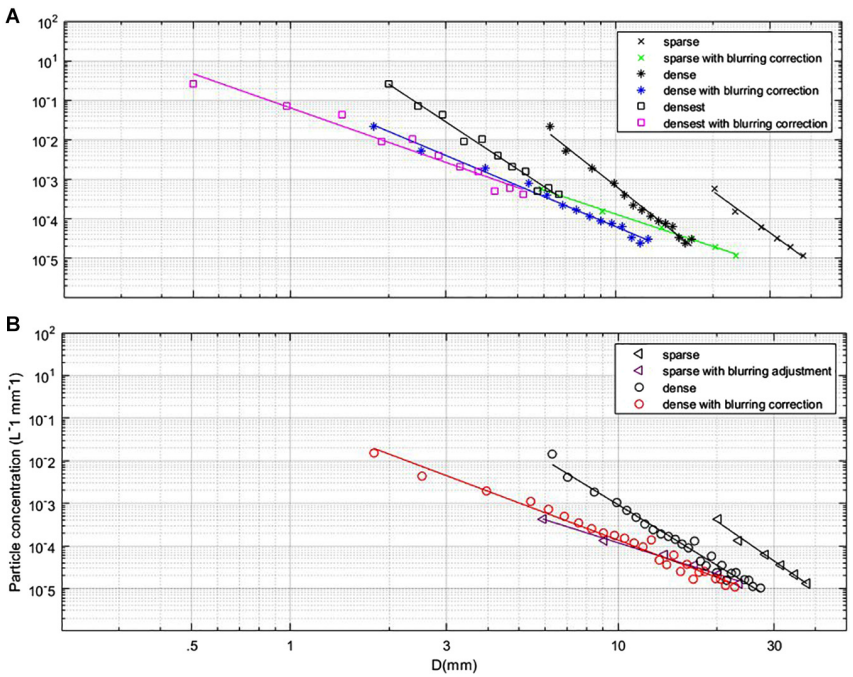

FIGURE 4 | (A) PSD averages from sparse, dense and densest scan modes with and without blurring correction for dusk time-series. **(B)** PSD averages for sparse and dense scan modes with and without blurring correction for dawn timeseries.

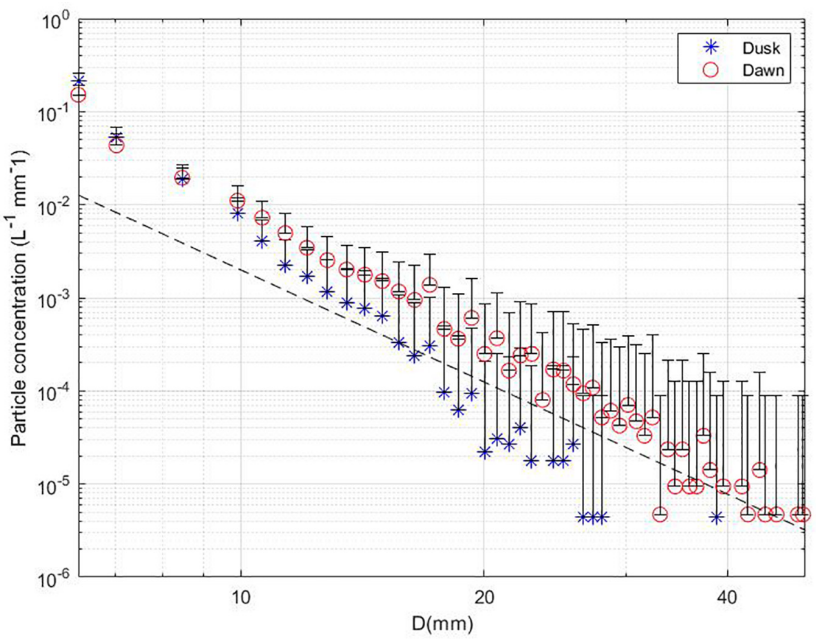

FIGURE 5 | Average particle concentrations for dense scan mode at dusk (blue stars) and dawn (red circles); error bars represent one positive standard deviation. Large particles (>50 mm) are not shown due to insufficient numbers sampled. Dotted line represents the steady state slope of −4.

Z-score is an indicator of significance, where $z < -3$ corresponds to significant ($p < 0.001$) particle clustering and $z > 3$ to significant dispersion. The spatial distribution of particles in each scan was compared to a random uniform distribution of particles. The random distribution was simulated with similar particle concentrations and the same geometric sample volume as all scans from the dusk and dawn timeseries. The simulated uniform distribution defined the population mean ($\overline{X_p}$) and standard

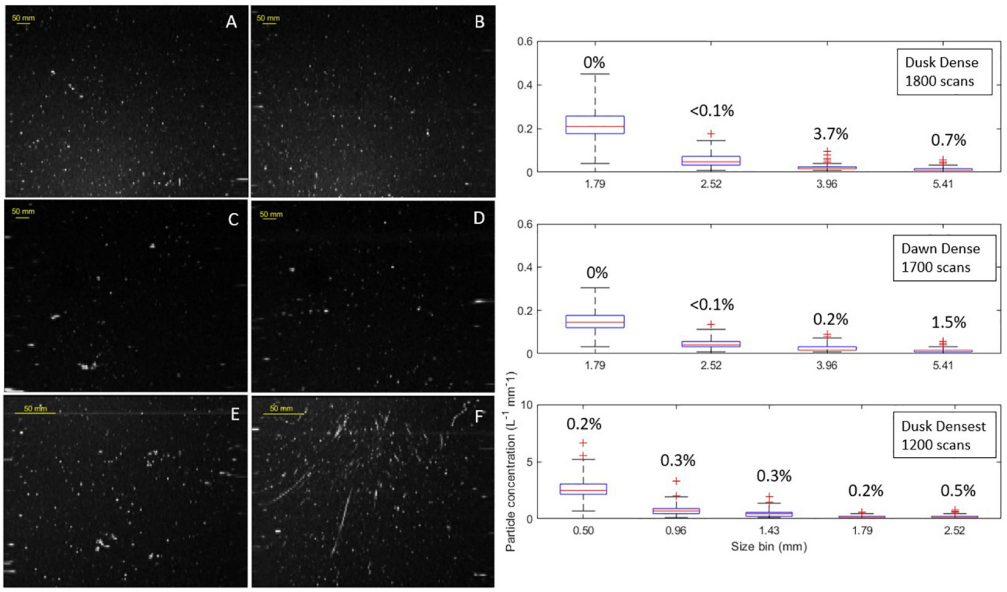

FIGURE 6 | Gray scale images containing anomalous particle enhancements taken in dense scan mode for dusk **(A,B)** and dawn **(C,D)** stations, similarly images taken in densest scan mode for dusk station **(E,F)**. Box and whisker plots per size bin for dense and densest scan modes on right with percentage of particle enhancement events provided above box and whiskers (see text for details).

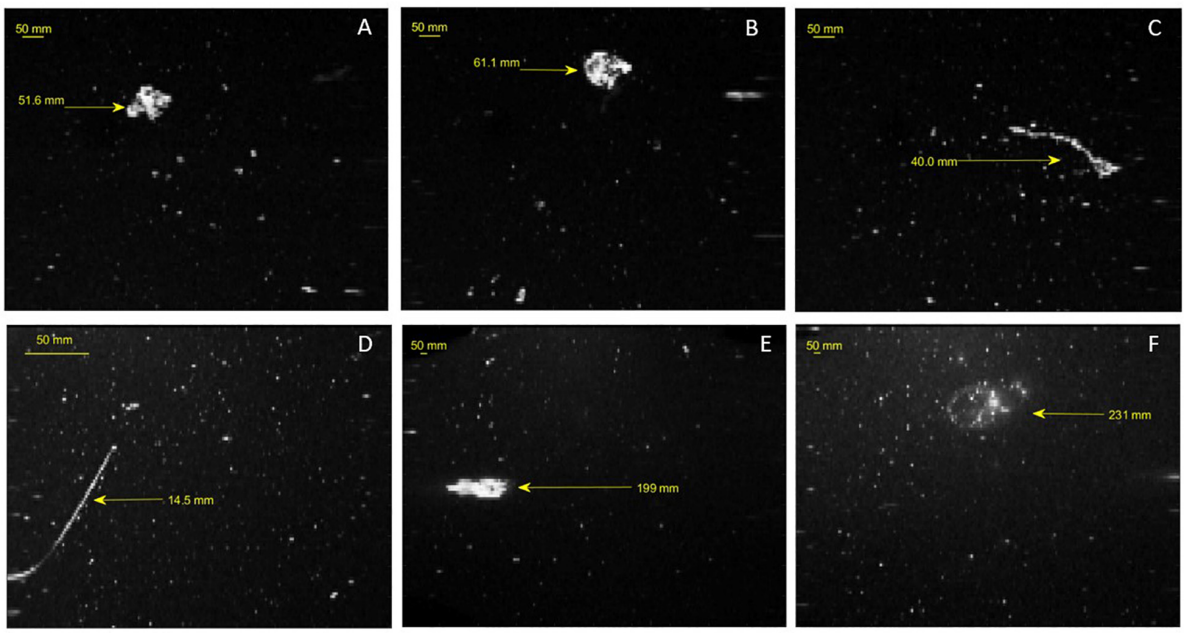

FIGURE 7 | Gray-scale images of large organisms with calculated spherical diameter in mm. Images **(A–C)** are imaged in dense mode, image **(D)** represents the densest scan mode **(E,F)** are imaged in sparse scan mode.

deviation (σ_p) to allow for an unbiased description of particle proximity when calculating the z-score. **Figure 8** provides a comparison of the particle spatial distribution of an image from the dawn station with a simulated uniform distribution. The z-score for the sample image (**Figure 8A**) was calculated as −0.53, indicating agreement with uniformly distributed particles. The rectangular (200 × 100) image skews the proximity of uniform particles as exemplified by the simulated data line in **Figure 8B**. Z-scores are calculated for every dense scan for each station to test for closer particle proximity (clustering) or more distant particle proximity (dispersion) than the average simulated distribution. Scans which feature mostly marine

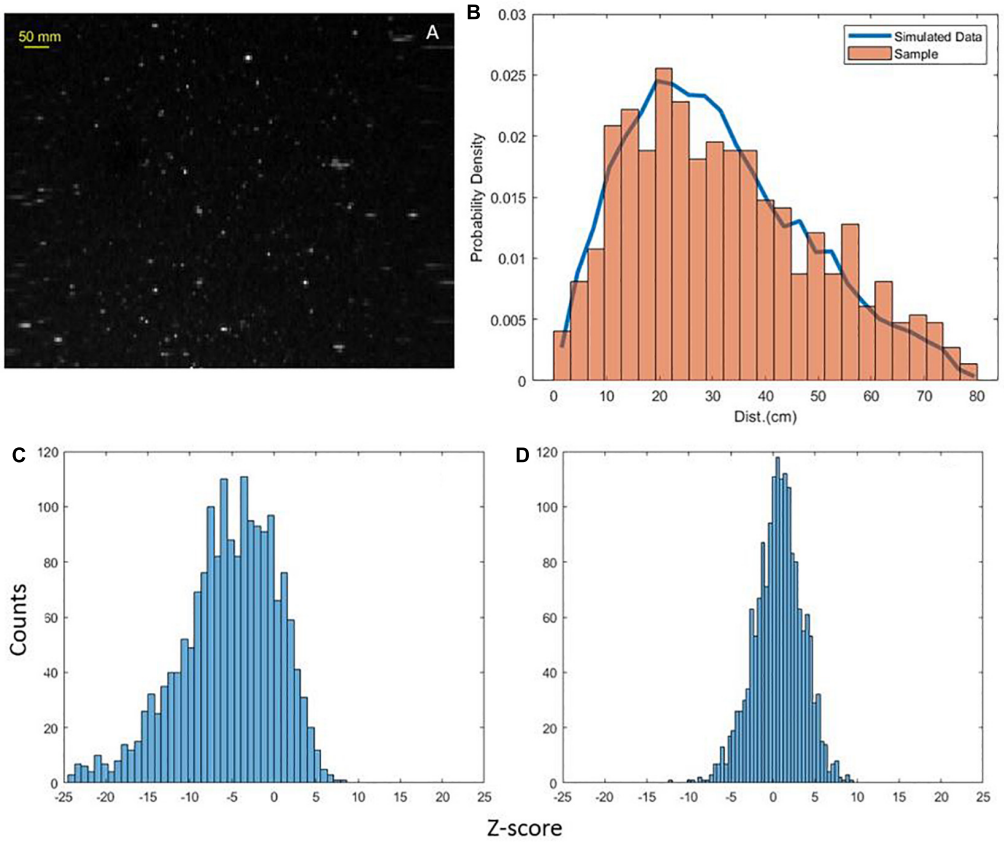

FIGURE 8 | Sample dense image from dawn station **(A)**. Probability density function of spatial distance of particles from sample image compared with simulated data **(B)**. Histogram of all calculated *z*-scores for dense scans at dusk **(C)** and dawn **(D)**.

snows background are expected to demonstrate a particle field with a uniform distribution. The dusk station scans strongly favored clustering as indicated by the extended lower limit tail and the peak in *z*-scores falling below 0 (**Figure 8C**). The cumulative *z*-scores of the dawn station were centered around 0 (**Figure 8D**), indicating the majority of scans had particles uniformly distributed in the scan volume. Visual inspection of the images such as those shown in **Figures 6**, **7** confirms the statistical interpretation of dusk and dawn differences in PSDs and spatial patchiness. Generally, the dusk scans featured a higher concentrations of particles less than 5 mm. The increased population of small particles (<5 mm) created a higher likelihood of clustering caused by smaller particles (**Figure 5**). At both dusk and dawn, less than 4% of all scans featured images with particle enhancements and clustering. There were select cases of images with large organisms > 50 mm and clustering; examples of these included **Figures 7A,D** with z-scores of −3.65 and −12.5, respectively. Excluding scans with particle enhancements and large organisms, the spatial distribution of the particle field followed a uniform distribution.

The scarcity of larger particles in the relatively small volumes sampled allows for interpretation of spiking in optical backscatter and transmissometer time series data to be classified as individual particles (Gardner et al., 2000; Briggs et al., 2013; Giering et al., 2019). Briggs et al. (2013) present an inversion method which uses the variance-to-mean ratio (VMR) of optical signal to estimate mean particle size. Briefly, Briggs et al. (2013) used the VMR of de-trended optical time series data to obtain a weighted mean signal per particle. This per particle optical proxy was then converted to a particle cross-sectional area using estimates of sample volume, scattering efficiency Q, particle residence time in the sample volume t_{res}, and sample integration time t_{samp}. This area was then converted to an equivalent circular diameter. Here, we follow the same method, but replace the VMR with the height of each optical parameter spike above a running median background of smaller particles, effectively deriving a diameter for each spike height, rather than a single mean diameter for the time series. The window for the running median was seven times either t_{res} or t_{samp}, whichever was greater. For attenuation, Q_c = 2 and t_{samp} = 0.003 s were used (Briggs et al., 2013). The sample volume was 12.5 ml, 2.5 times larger than Briggs et al. (2013) due to the 25 cm path length and t_{res} was estimated following Briggs et al. (2013) to be 0.39 s (dusk) and 0.61 s (dawn). Logarithmically spaced bins from 0.11 to 11 mm were derived for c_p and divided by bin width and the total volume sampled after correcting for water movement for each time series to yield c_p-derived PSDs for each station (Briggs et al., 2013). The c_p-derived PSD was calculated separately for

each of the nine ac-9 wavelengths and all the resulting PSDs were averaged. As in Briggs et al. (2013), the same method was used to calculate PSDs from the b_{bp} time series, substituting b_{bp} for c_p and Q_{bb} for Q_c. A Q_{bb} of 0.04 was chosen following Briggs et al. (2013) based on the mean b_{bp}/c_p ratio of ∼1/50 observed during this study. The sample volume was estimated at 0.62 ml, t_{samp} was 1 s, and t_{res} was estimated continuously from the estimated path length of a particle through the ECO-VSF sample volume (∼1 cm) divided by the vertical velocity of the sensor package calculated from the pressure sensor over a 3 s interval. A b_{bp}-derived PSD was estimated separately for each of the three angles of the ECO-VSF, and the three PSDs were averaged to create a final PSD. **Figure 9** presents b_{bp} measurements recorded during the time series for dusk and dawn, with the spikier dawn timeseries indicating enhanced concentrations of large particles. **Figure 10** shows combined PSDs from ECO-VSF backscattering, ac-9 attenuation, and all available lidar scan modes. PSD slopes from c_p and b_{bp} were about 4.7 and 4.5 from the dusk and dawn time series, respectively, both significantly steeper than the slopes observed from lidar (also see **Figure 5**). PSDs were also higher for the lidar measurements for overlapping size bins.

DISCUSSION

The marine particle field and its variability in relation to the mesopelagic ecosystem is of growing interest in the scientific community, but still lacks understanding as it is deeply connected through many processes which span a wide size spectra (Stemmann et al., 2000b, 2004; Baird and Suthers, 2007; Guidi et al., 2008; Boss et al., 2009; Burd and Jackson, 2009; Stemmann and Boss, 2012; Burd, 2013; Giering et al., 2014; St. John et al., 2016; Calleja et al., 2018; Cavan et al., 2019). Imaging lidar is presented as a new tool with a unique niche in capturing both non-living macroscopic aggregates (marine snow) and living macro-zooplankton, crustaceans, decapods, gelatinous taxon and other swimming fauna. Lidar allows *in situ* imaging of large delicate aggregates such as larvacean houses, mucous webs of pteropods, and other delicate organisms such as salps and siphonophores which are otherwise destroyed by nets, meshes and pumps. **Figure 7** exemplifies the imaging ability of UMSLI as it serves as a tool for observing a large array of organisms but also shows the limits of identification due to resolution. Image processing expands UMSLI's abilities beyond large organisms and into particle sizes down to 0.5 mm, allowing connectivity between intra-class organisms and processes affecting mesopelagic marine snow.

Particle abundance and size are useful metrics for biogeochemical models which describe the function of the mesopelagic zone in the biological pump process. PSDs presented here are consistent with other methods which use imaging techniques to derive PSDs for living and non-living particles ranging up to several mm (Jackson et al., 1997; Checkley et al., 2008; Picheral et al., 2010; Slade et al., 2011; Stemmann and Boss, 2012; Taucher et al., 2018). The PSD slopes presented in **Figure 5** were 3.0 for the dusk station and 2.6 for dawn, where a slope of 4 indicates equal particle volumes in equal logarithmic size intervals that are representative of oceanic environments without significant influence from active biogeochemical processes (Twardowski et al., 2001; Sullivan et al., 2005; Stemmann et al., 2008). Flatter slopes in this study are likely due to aggregation of particles into larger flocs of marine snow which has occurred through downward flux from upper waters (Stemmann et al., 2004; Taucher et al., 2018). For large aggregates, studies suggest that aggregation through particle–particle interaction occurs through shear and differential sedimentation, which greatly depend on collision

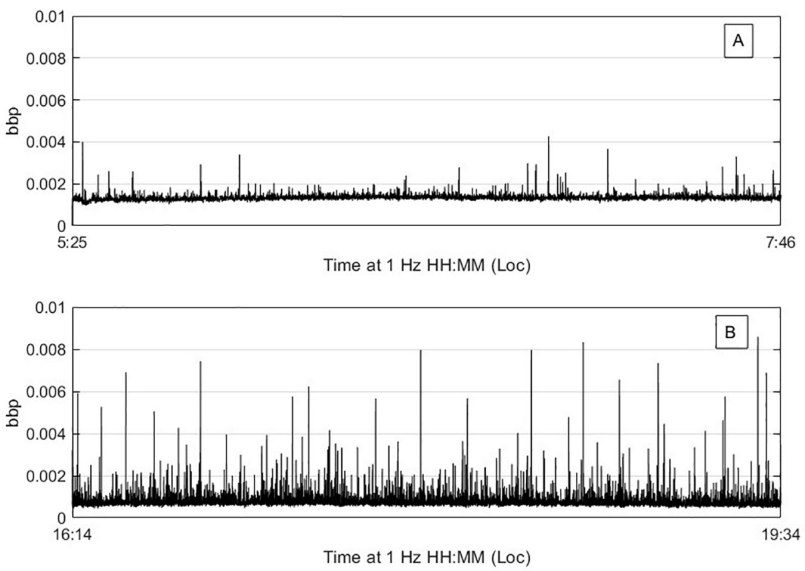

FIGURE 9 | Particle backscatter time series from the ECO-VSF for dusk **(A)** and dawn **(B)**.

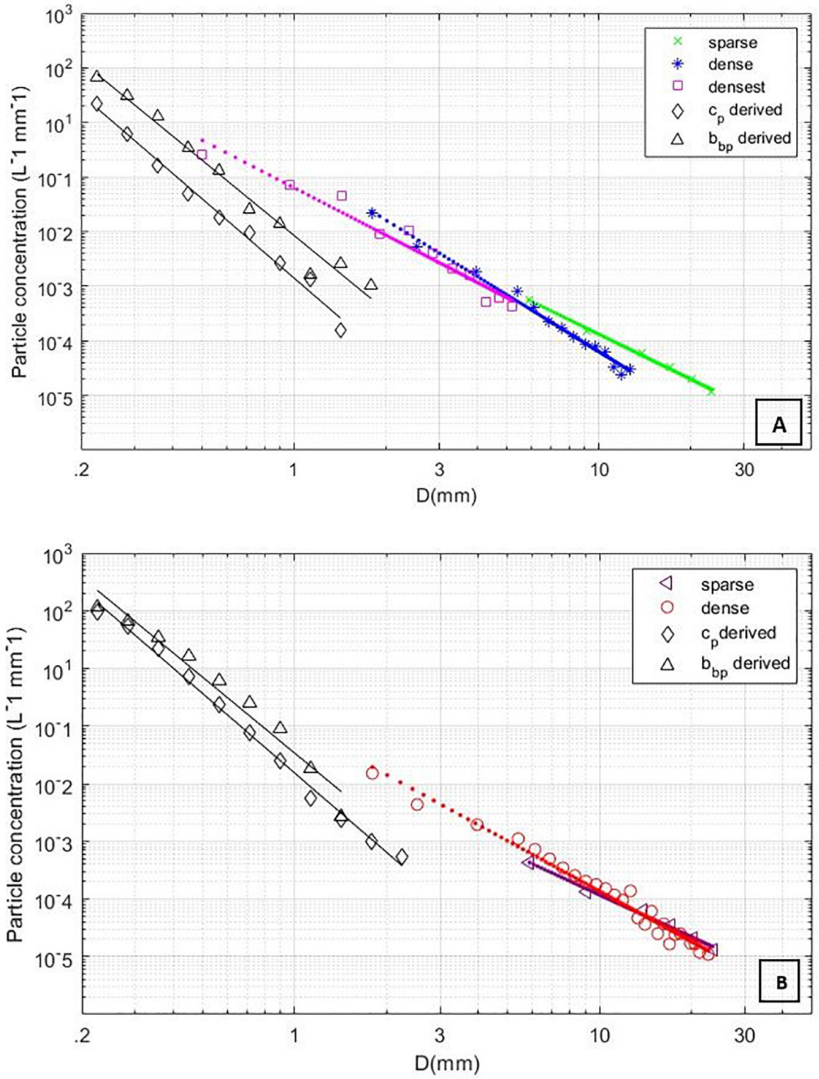

FIGURE 10 | (A) Sparse, dense, and densest lidar derived PSDs with b_{bp} and c_p derived PSDs for dusk time series. **(B)** Sparse and dense lidar derived PSDs with b_{bp} and c_p derived PSDs for dawn time series.

rates between particles, stickiness, and overall diffuse turbulence of the water column (Hunt, 1980; Jackson, 1995; Stemmann et al., 2004; Stemmann and Boss, 2012). The use of instrumentation which measure aggregate sequestration processes are vital to supplementing biogeochemical models. This study demonstrates the potential of using lidar imaging to record large aggregates within natural particle fields without causing particle breakup. UMSLI shows potential for making distinctions between living and non-living organisms based on target shape, size, and perspective information from imagery. UMSLI's high sampling rate captures identifiable targets across multiple images, allowing for multiple capture angles and positions. It is conceivable to use this information with machine learning algorithms for organism identification based on size and morphology if a representative library could be constructed for algorithm training. This is a current area of interest in our lab.

While our dataset includes only two stations, preventing statistical inferences, results from this study reveal differences between stations that were plausibly associated with temporal dynamics of mesopelagic activity. Further such deployments to verify patterns could therefore enable important insight. Night time activity in the mesopelagic has been reported to shift particles into larger size classes (Stemmann et al., 2000a,b). Stemmann et al. (2000a); reported size shifts of increasing particle abundance at night for particles > 0.5 mm and showed that this pattern was reversed during the day. In the northeast Atlantic, observations reported in Lampitt et al. (1993) using time-lapse camera recordings showed evidence for increasing concentrations of particulate matter at night, linked specifically to the abundance in large particles. These observations are consistent with results from the dawn station, which recorded larger concentrations of particles greater than

5 mm in comparison to the dusk station (**Figure 5**). Stemmann et al. (2000a) suggest that, "diel vertical migration is the best candidate to explain the diel transformation of PM (particulate matter)." As DVMs hold a diverse array of organisms with dynamic temporal migratory patterns, it is difficult to attribute particle field changes to a single cause. There has been evidence linking zooplankton including copepods with particulate matter fluxes and migration activity (Stemmann and Boss, 2012). However, it is difficult to discriminate particle flux contribution between migratory consumers and residential nightly feeder (Stemmann et al., 2000a,b, 2004; Guidi et al., 2008; Giering et al., 2014; Archibald et al., 2019).

Resident and migratory mesopelagic fish are responsible for up to 15% of the total export of carbon through the mesopelagic zone, and the passive and active transport of carbon is largely attributed to swimming organisms and their fecal matter production (Davison et al., 2013; Cavan et al., 2019). It is expected that if biological activity such as feeding was apparent then resulting PSDs would demonstrate a bump at specific size classes. Evidence of this type of activity was investigated through the evaluation of outlier scans and patchiness. Overall, the results showed limited cases of scans with particle concentration enhancements for specific size classes (**Figure 6**). While PSD slopes for all scan modes showed no major inconsistencies which would indicate biological activity, it is obvious that the dawn station featured a higher concentration of particles $>$ 20 mm (**Figure 5**). This is supported by images in **Figure 7** which feature evidence of nightly feeders or migratory species. During the time periods of measurement, most observations showed uniformly distributed particle fields largely composed of marine snow (**Figure 8**). As mentioned, clustering in the dawn time period resulted from increased particle concentrations, likely associated with the nighttime migration. Clustering may also be caused by groups of swimming organisms. Observations of both particle enhancements and spatial clustering provided an approach to identify swimming organisms moving through the scan field in smaller size bins. The dense scan data for dawn and dusk recorded limited association of particle enhancements with clustering ($<$4%), this was only for smaller size bins dominated by marine snow. For the dense scans, particle enhancements were most common for the 3.96 and 5.41 mm size bins. This may be evidence of macro-zooplankton such as copepods, or small fish larvae swimming through the scan volume. The combination of images with PSD calculation allows for observation across broad size scales further connecting detritus remineralization, fauna abundance, nightly migrators, and full-time residents of the mesopelagic. Further expansion with complementary instruments could supplement the goal of observing mesopelagic dynamics in greater detail.

Despite significant differences in measurement approaches for lidar, b_{bp}, and c_p, they all showed similar trends in particle abundance, increasing for the dawn timeseries. Increases in backscatter spiking for the dawn station associated with large particles was consistent with PSD results from the lidar imager. For overlapping size bins, b_{bp} and c_p approaches result in lower PSD abundances, and overall steeper PSD slopes. Moreover, the steeper slopes, much steeper than 4, may not be realistic (Sullivan et al., 2005). Differences in derived PSDs may have resulted from differences in sample volumes and the way the b_{bp} and c_p inversions were formulated. While the lidar scans a large undisturbed sample volume, the ECO-VSF has a sample volume that is $<$ 1 mL and only $\sim$1 cm away from the sensor face. The c_p measurement has an active pump rapidly flowing samples through a cuvette. There is thus the potential for turbulent disruption of relatively large, fragile aggregates for b_{bp} and c_p measurements, shifting particle abundance from larger to smaller particles (Slade et al., 2011). The greater turbulence associated with the c_p measurement may explain its lower PSD relative to the PSD obtained from b_{bp} inversion. Additionally, the larger the particle the more rare its occurrence, which may lead to an increasing level of under sampling with increasing particles size for the relatively small sample volumes associated with b_{bp} and c_p measurements. Indeed, this likely is the cause of apparent rollovers in the log-log representation of size distributions derived from b_{bp} and c_p that were clearly observed for the dawn station.

The inversion of b_{bp} and c_p measurements is also sensitive to the assumed efficiencies Q_c and Q_{bb}. While estimations used here are expected to approximate the bulk optical signal, Q_{bb} and Q_c differ with particle size and shape (Briggs et al., 2011, 2013). Briggs et al. (2013) showed an apparent decreasing bulk Q_c for clay aggregates measured using an ac-9 device leading to an estimated mean size decrease in the inversion. Despite these differences, results from all measurements showed similar trends and magnitudes were comparable, particularly for lidar and b_{bp} inversion results, where PSDs could be nearly seamlessly linked (**Figure 10**). Moreover, the comparison with c_p and b_{bp} spike method provided a valuable check. Relative agreement between independent approaches demonstrates the potential for extending the range over which PSDs can be resolved using multiple techniques, a key objective of this study.

In order to progress in the study of how organisms play a role in the transport of carbon through the mesopelagic zone, new technologies must be developed to both monitor particle fields while observing organisms without effecting behavior. UMSLI, as an instrument originally designed for imaging large marine fish and mammals, has shown extended capabilities for characterization of relatively small particles including marine snow in this field experiment. UMSLI's unobtrusive red laser creates opportunity for observing larger swimming organisms that otherwise practice avoidance behaviors from tow nets and ROVs (Peña, 2019; Urmy et al., 2019; Robison et al., 2020). With demonstrated capabilities of observing nekton *in situ* simultaneously with particulate organic matter fields, this technology shows potential for studying interactions of aggregates with organisms and resulting transformations through remote, undisturbed observation. The potential of UMSLI can also be further enhanced. The possibility of calibrating lidar returns in absolute units of backscattering would enable another approach for quantifying particle abundance while providing a measure of backscattering for a particle population that is not included in current measurements made by the oceanographic community with very small sample volumes. The contribution of this large particle size class on ocean color remote sensing

in surface waters is unknown. Coupling optical measurements with multi-frequency acoustics may also allow seamless remote monitoring of size distributions over the range of microns to meters (Gruber et al., 2016). This is the focus of future work.

DATA AVAILABILITY STATEMENT

The raw data supporting the conclusions of this article will be made available by the authors, without undue reservation, to any qualified researcher.

AUTHOR CONTRIBUTIONS

TM was responsible for the processing and analysis of data and manuscript preparations. MT conceived of the study, participated in the analysis of methods and results, and provided guidance in presentation and preparation of manuscript. NB assisted with the PSD inversion method from c_p and b_{bp} data with associated results and assisted in aspects of manuscript development. AN assisted with image processing methods and manuscript development. KB processed and analyzed the acoustic data presented. FD was the principal investigator for the design, fabrication, laboratory, and field testing of the UMSLI system, and provided guidance on interpretation of raw lidar waveform arrays, filtering, and noise reduction, processing protocols, and analysis. All authors contributed to the article and approved the submitted version.

FUNDING

This research was funded through an award to MST by the NOAA Office of Ocean Exploration and Research under grants NA09OAR4320073 and NA14OAR4320260 to the Cooperative Institute for Ocean Exploration, Research and Technology (CIOERT) at Florida Atlantic University's Harbor Branch Oceanographic Institute. This work was also supported by a HBOI Foundation award to MST. The development of UMSLI comes from a Marine Hydrokinetic project awarded to FD and funded by the Department of Energy under award DE-EE0006787.

ACKNOWLEDGMENTS

We thank the crew of the R/V *Okeanos Explorer*, and all correspondents with NOAA, CIOERT, and the DOE. We thank Brian Ramos, Bing Ouyang, David Windisch, Christopher Strait, and Nicole Stockley at HBOI for their contributions to the UMSLI development, field deployment, data collection, and helpful discussions in data analyses.

SUPPLEMENTARY MATERIAL

The Supplementary Material for this article can be found online at: https://www.frontiersin.org/articles/10.3389/fmars.2020.558745/full#supplementary-material

REFERENCES

Archibald, K. M., Siegel, D. A., and Doney, S. C. (2019). Modeling the impact of zooplankton diel vertical migration on the carbon export flux of the biological pump. *Global Biogeochem. Cycles* 33, 181–199. doi: 10.1029/2018GB005983

Baird, M. E., and Suthers, I. M. (2007). A size-resolved pelagic ecosystem model. *Ecol. Model.* 203, 185–203. doi: 10.1016/j.ecolmodel.2006.11.025

Boss, E., Slade, W., and Hill, P. (2009). Effect of particulate aggregation in aquatic environments on the beam attenuation and its utility as a proxy for particulate mass. *Opt. Express* 17:9408. doi: 10.1364/OE.17.009408

Boss, E., Twardowski, M. S., and Herring, S. (2001). Shape of the particulate beam attenuation spectrum and its inversion to obtain the shape of the particulate size distribution. *Appl. Opt.* 40:4885. doi: 10.1364/AO.40.004885

Boswell, K. M., D'Elia, M., Johnston, M. W., Mohan, J. A., Warren, J. D., Wells, R. J. D., et al. (2020). Oceanographic structure and light levels drive patterns of sound scattering layers in a low-latitude oceanic system. *Front. Mar. Sci.* 7:51. doi: 10.3389/fmars.2020.00051

Bradley, D., and Roth, G. (2007). Adaptive thresholding using the integral image. *J. Graph. Tools* 12, 13–21. doi: 10.1080/2151237X.2007.10129236

Briggs, N., Dall'Olmo, G., and Claustre, H. (2020). Major role of particle fragmentation in regulating biological sequestration of CO2 by the oceans. *Science* 367, 791–793. doi: 10.1126/science.aay1790

Briggs, N., Perry, M. J., Cetiniæ, I., Lee, C., D'Asaro, E., Gray, A. M., et al. (2011). High-resolution observations of aggregate flux during a sub-polar North Atlantic spring bloom. *Deep Sea Res. Part I* 58, 1031–1039. doi: 10.1016/j.dsr.2011.07.007

Briggs, N. T., Slade, W. H., Boss, E., and Perry, M. J. (2013). Method for estimating mean particle size from high-frequency fluctuations in beam attenuation or scattering measurements. *Appl. Opt.* 52:6710. doi: 10.1364/AO.52.006710

Buesseler, K. O., Antia, A. N., Chen, M., Fowler, S. W., Gardner, W. D., Gustafsson, O., et al. (2007). An assessment of the use of sediment traps for estimating upper ocean particle fluxes. *J Mar. Res.* 65, 345–416. doi: 10.1357/002224007781567621

Buonassissi, C. J., and Dierssen, H. M. (2010). A regional comparison of particle size distributions and the power law approximation in oceanic and estuarine surface waters. *J. Geophys. Res.* 115:C10028. doi: 10.1029/2010JC006256

Burd, A. B. (2013). Modeling particle aggregation using size class and size spectrum approaches: Modeling Particle Aggregation. *J. Geophys. Res. Oceans* 118, 3431–3443. doi: 10.1002/jgrc.20255

Burd, A. B., Hansell, D. A., Steinberg, D. K., Anderson, T. R., Arístegui, J., Baltar, F., et al. (2010). Assessing the apparent imbalance between geochemical and biochemical indicators of meso- and bathypelagic biological activity: what the @$#! is wrong with present calculations of carbon budgets? *Deep Sea Res. Part II* 57, 1557–1571. doi: 10.1016/j.dsr2.2010.02.022

Burd, A. B., and Jackson, G. A. (2009). Particle aggregation. *Annu. Rev. Mar. Sci.* 1, 65–90. doi: 10.1146/annurev.marine.010908.163904

Caimi, F. M., and Dalgleish, F. R. (2013). "Subsea laser scanning and imaging systems," in *Subsea Optics and Imaging* (Amsterdam: Elsevier), 327–352. doi: 10.1533/9780857093523.3.327

Calleja, M. L., Ansari, M. I, Røstad, A., Silva, L., Kaartvedt, S., Irigoien, X., et al. (2018). The mesopelagic scattering layer: a hotspot for heterotrophic prokaryotes in the red sea twilight zone. *Front. Mar. Sci.* 5:259. doi: 10.3389/fmars.2018.00259

Cavan, E. L., Laurenceau-Cornec, E. C., Bressac, M., and Boyd, P. W. (2019). Exploring the ecology of the mesopelagic biological pump. *Progr. Oceanogr.* 176:102125. doi: 10.1016/j.pocean.2019.102125

Checkley, D. M., Davis, R. E., Herman, A. W., Jackson, G. A., Beanlands, B., and Regier, L. A. (2008). Assessing plankton and other particles in situ with the SOLOPC. *Limnol. Oceanogr.* 53, 2123–2136. doi: 10.4319/lo.2008.53.5_part_2.2123

Chester, R. (2000). *Marine Geochemistry*. Second. Hoboken, NJ: Blackwell Science.

Choksi, B., Venkitaraman, A., and Mali, S. (2017). Finding best fit for hand-drawn curves using polynomial regression. *IJCA* 174, 20–23. doi: 10.5120/ijca2017915390

Dalgleish, F., Ouyang, B., Dalgleish, A., Ramos, B., Li, Y., Principe, J., et al. (2018). "MEMS-based serial LiDAR detection and imaging architecture for automated surveillance of undersea marine life," in *Proceedings of the SPIE 10677, Unconventional Optical Imaging, 1067726 (24 May 2018)*, Strasbourg. doi: 10.1117/12.2309997

Dalgleish, F., Ouyang, B., and Vuorenkoski, A. (2013). "A unified framework for image performance enhancement of extended range laser seabed survey sensors," in *Proceedings of the 2013 IEEE International Underwater Technology Symposium (UT)*, (Tokyo: IEEE), 1–7. doi: 10.1109/UT.2013.6519906

Dalgleish, F., Ouyang, B., Vuorenkoski, A., Ramos, B., Alsenas, G., Metzger, B., et al. (2017). "Undersea LiDAR imager for unobtrusive and eye safe marine wildlife detection and classification," in *Proceedings of the OCEANS 2017 – Aberdeen*, (Aberdeen: IEEE), 1–5. doi: 10.1109/OCEANSE.2017.8085029

Dalgleish, F. R., Vuorenkoski, A. K., and Ouyang, B. (2013). Extended-range undersea laser imaging: current research status and a glimpse at future technologies. *Mar. Technol. Soc. J.* 47, 128–147. doi: 10.4031/MTSJ.47.5.16

Davison, P. C., Checkley, D. M., Koslow, J. A., and Barlow, J. (2013). Carbon export mediated by mesopelagic fishes in the northeast Pacific Ocean. *Progr. Oceanogr.* 116, 14–30. doi: 10.1016/j.pocean.2013.05.013

De Dominicis, L. (2013). "Underwater 3D vision, ranging and range gating," in *Subsea Optics and Imaging*, (Amsterdam: Elsevier), 379–410. doi: 10.1533/9780857093523.3.379

Fang, H.-T., and Huang, D.-S. (2004). Noise reduction in lidar signal based on discrete wavelet transform. *Opt. Commun.* 233, 67–76. doi: 10.1016/j.optcom.2004.01.017

Foi, A., Trimeche, M., Katkovnik, V., and Egiazarian, K. (2008). Practical poissonian-gaussian noise modeling and fitting for single-image raw-data. *IEEE Trans. Image Process* 17, 1737–1754. doi: 10.1109/TIP.2008.2001399

Fournier, G. R. (1993). Range-gated underwater laser imaging system. *Opt. Eng.* 32:2185. doi: 10.1117/12.143954

Gardner, W. D., Richardson, M. J., and Smith, W. O. (2000). Seasonal patterns of water column particulate organic carbon and fluxes in the Ross Sea, Antarctica. *Deep Sea Res. Part II* 47, 3423–3449. doi: 10.1016/S0967-0645(00)00074-6

Giering, S. L. C., Cavan, E. L., Basedow, S. L., Briggs, N., Burd, A. B., Darroch, L., et al. (2019). Sinking organic particles in the ocean – Flux estimates from in situ optical devices. *Front. Mar. Sci.* 6:834. doi: 10.3389/fmars.2019.00834

Giering, S. L. C., Sanders, R., Lampitt, R. S., Anderson, T. R., Tamburini, C., Boutrif, M., et al. (2014). Reconciliation of the carbon budget in the ocean's twilight zone. *Nature* 507, 480–483. doi: 10.1038/nature13123

Giering, S. L. C., Yan, B., Sweet, J., Asper, V., Diercks, A., Chanton, J. P., et al. (2018). The ecosystem baseline for particle flux in the Northern Gulf of Mexico. *Elem. Sci. Anth.* 6:6. doi: 10.1525/elementa.264

Gonzalez, R., Woods, R., and Eddins, S. (2009). *Digital Image Processing Using MATLAB*, 2nd Edn. Knoxville, TN: Gatesmark Publishing.

Gruber, P., Felix, D., Storti, G., Lattuada, M., Fleckenstein, P., and Deschwanden, F. (2016). Acoustic measuring techniques for suspended sediment. *IOP Conf. Ser.* 49:122003. doi: 10.1088/1755-1315/49/12/122003

Guidi, L., Jackson, G. A., Stemmann, L., Miquel, J. C., Picheral, M., and Gorsky, G. (2008). Relationship between particle size distribution and flux in the mesopelagic zone. *Deep Sea Res. Part I* 55, 1364–1374. doi: 10.1016/j.dsr.2008.05.014

Hansen, A. N., and Visser, A. W. (2016). Carbon export by vertically migrating zooplankton: an optimal behavior model: optimal vertical migration and carbon export. *Limnol. Oceanogr.* 61, 701–710. doi: 10.1002/lno.10249

Hays, G. C. (2003). A review of the adaptive significance and ecosystem consequences of zooplankton diel vertical migrations. *Hydrobiologia* 503, 163–170. doi: 10.1023/B:HYDR.0000008476.23617.b0

Hiaka, K., Kawaguchi, K., and Murakami, M. (2001). *Downward Transport of Organic Carbon by diel Migratory Micronekton in the Western Equatorial Pacific: Its Quantitative and Qualitative Importance – ScienceDirect*. Available online at: https://www.sciencedirect.com/science/article/pii/S0967063701000036 (accessed December 5, 2019).

Hung, C.-C., Xu, C., Santschi, P. H., Zhang, S.-J., Schwehr, K. A., Quigg, A., et al. (2010). Comparative evaluation of sediment trap and 234Th-derived POC fluxes from the upper oligotrophic waters of the Gulf of Mexico and the subtropical northwestern Pacific Ocean. *Mar. Chem.* 121, 132–144. doi: 10.1016/j.marchem.2010.03.011

Hunt, J. R. (1980). "Prediction of oceanic particle size distributions from coagulation and sedimentation mechanisms," in *Particulates in Water Advances in Chemistry*, eds M. C. Kavanaugh and J. O. Leckie (Washington, DC: American Chemical Society), 243–257. doi: 10.1021/ba-1980-0189.ch011

Jackson, G. A. (1995). Comparing observed changes in particle size spectra with those predicted using coagulation theory. *Deep Sea Res. Part II* 42, 159–184. doi: 10.1016/0967-0645(95)00010-N

Jackson, G. A., Maffione, R., Costello, D. K., Alldredge, A. L., Logan, B. E., and Dam, H. G. (1997). Particle size spectra between 1 μm and 1 cm at Monterey Bay determined using multiple instruments. *Deep Sea Res. Part I* 44, 1739–1767. doi: 10.1016/S0967-0637(97)00029-0

Kaartvedt, S., Staby, A., and Aksnes, D. (2012). Efficient trawl avoidance by mesopelagic fishes causes large underestimation of their biomass. *Mar. Ecol. Prog. Ser.* 456, 1–6. doi: 10.3354/meps09785

Kelly, T. B., Davison, P. C., Goericke, R., Landry, M. R., Ohman, M. D., and Stukel, M. R. (2019). The importance of mesozooplankton diel vertical migration for sustaining a mesopelagic food web. *Ecology* 6, 2–14. doi: 10.1101/642975

Kitchen, J. C., Zaneveldan, J. R. V., and Pak, H. (1982). Effect of particle size distribution and chlorophyll content on beam attenuation spectra. *Appl. Opt.* 21:3913. doi: 10.1364/AO.21.003913

Klevjer, T. A., Torres, D. J., and Kaartvedt, S. (2012). Distribution and diel vertical movements of mesopelagic scattering layers in the Red Sea. *Mar. Biol.* 159, 1833–1841. doi: 10.1007/s00227-012-1973-y

Lampitt, R. S., Hillier, W. R., and Challenor, P. G. (1993). Seasonal and diel variation in the open ocean concentration of marine snow aggregates. *Nature* 362, 737–739. doi: 10.1038/362737a0

Liley, J. B. (1992). Fitting size distributions to optical particle counter data. *Aeros. Sci. Technol.* 17, 84–92. doi: 10.1080/02786829208959562

Liu, Z., Hunt, W., Vaughan, M., Hostetler, C., McGill, M., Powell, K., et al. (2006). Estimating random errors due to shot noise in backscatter lidar observations. *Appl. Opt.* 45:4437. doi: 10.1364/AO.45.004437

Malkiel, E., Abras, J. N., Widder, E. A., and Katz, J. (2006). On the spatial distribution and nearest neighbor distance between particles in the water column determined from in situ holographic measurements. *J. Plankton Res.* 28, 149–170. doi: 10.1093/plankt/fbi107

Martin, J. H., Knauer, G. A., Karl, D. M., and Broenkow, W. W. (1987). VERTEX: carbon cycling in the northeast Pacific. *Deep Sea Res. Part A* 34, 267–285. doi: 10.1016/0198-0149(87)90086-0

McDonnell, A. M. P. (2011). *Marine Particle Dynamics: Sinking Velocities, Size Distributions, Fluxes, and Microbial Degradation Rates*. Woods Hole, MA: Massachusetts Institute of Technology and Woods Hole Oceanographic Institution. doi: 10.1575/1912/4512

McGill, M. J. S. (2002). *Lidar Remote Sensing*. Available online at: https://ntrs.nasa.gov/search.jsp?R=20020070892 (accessed May 3, 2020).

Mullen, L., Laux, A., and Cochenour, B. (2009). Propagation of modulated light in water: implications for imaging and communications systems. *Appl. Opt.* 48:2607. doi: 10.1364/AO.48.002607

Mullen, L. J., Contarino, V. M., Laux, A., Concannon, B. M., Davis, J. P., Strand, M. P., et al. (1999). "Modulated laser line scanner for enhanced underwater imaging," in *SPIE 3761, Airborne and In-Water Underwater Imaging, (28 October 1999)*, ed. G. D. Gilbert (Denver, CO: SPIE), 2–9. doi: 10.1117/12.366470

Nayak, A. R., McFarland, M. N., Sullivan, J. M., and Twardowski, M. S. (2018). Evidence for ubiquitous preferential particle orientation in representative oceanic shear flows: nonrandom particle orientation in ocean. *Limnol. Oceanogr.* 63, 122–143. doi: 10.1002/lno.10618

Nayak, A. R., and Twardowski, M. S. (2020). "Breaking" news for the ocean's carbon budget. *Science* 367, 738–739. doi: 10.1126/science.aba7109

Otsu, N. (1979). A threshold selection method from gray-level histograms. *IEEE Trans. Syst. Man Cybern.* 9, 62–66. doi: 10.1109/TSMC.1979.4310076

Ouyang, B., Dalgleish, F., Vuorenkoski, A., Britton, W., Ramos, B., and Metzger, B. (2013). Visualization and image enhancement for multistatic underwater laser line scan system using image-based rendering. *IEEE J. Oceanic Eng.* 38, 566–580. doi: 10.1109/JOE.2012.2229066

Passow, U., and Alldredge, A. L. (1995). Aggregation of a diatom bloom in a mesocosm: the role of transparent exopolymer particles (TEP). *Deep Sea Res. Part II* 42, 99–109. doi: 10.1016/0967-0645(95)00006-C

Peña, M. (2019). Mesopelagic fish avoidance from the vessel dynamic positioning system. *ICES J. Mar. Sci.* 76, 734–742. doi: 10.1093/icesjms/fsy157

Picheral, M., Guidi, L., Stemmann, L., Karl, D. M., Iddaoud, G., and Gorsky, G. (2010). The Underwater Vision Profiler 5: an advanced instrument for high spatial resolution studies of particle size spectra and zooplankton. *Limnol. Oceanogr.* 8, 462–473. doi: 10.4319/lom.2010.8.462

Proud, R., Handegard, N. O., Kloser, R. J., Cox, M. J., and Brierley, A. S. (2019). From siphonophores to deep scattering layers: uncertainty ranges for the estimation of global mesopelagic fish biomass. *ICES J. Mar. Sci.* 76, 718–733. doi: 10.1093/icesjms/fsy037

Prucnal, P. R., and Saleh, B. E. A. (1981). Transformation of image-signal-dependent noise into image-signal-independent noise. *Opt. Lett.* 6:316. doi: 10.1364/OL.6.000316

Robison, B. H., Sherlock, R. E., Reisenbichler, K. R., and McGill, P. R. (2020). Running the gauntlet: assessing the threats to vertical migrators. *Front. Mar. Sci.* 7:64. doi: 10.3389/fmars.2020.00064

Slade, W. H., Boss, E., and Russo, C. (2011). Effects of particle aggregation and disaggregation on their inherent optical properties. *Opt. Express* 19:7945. doi: 10.1364/OE.19.007945

St. John, M. A., Borja, A., Chust, G., Heath, M., Grigorov, I., Mariani, P., et al. (2016). A Dark Hole in our understanding of marine ecosystems and their services: perspectives from the mesopelagic community. *Front. Mar. Sci.* 3:31. doi: 10.3389/fmars.2016.00031

Steinberg, D. K., Goldthwait, S. A., and Hansell, D. A. (2002). Zooplankton vertical migration and the active transport of dissolved organic and inorganic nitrogen in the Sargasso Sea. *Deep Sea Res.* 49, 1445–1461. doi: 10.1016/S0967-0637(02)00037-7

Stemmann, L., and Boss, E. (2012). Plankton and particle size and packaging: from determining optical properties to driving the biological pump. *Annu. Rev. Mar. Sci.* 4, 263–290. doi: 10.1146/annurev-marine-120710-100853

Stemmann, L., Eloire, D., Sciandra, A., Jackson, G. A., Guidi, L., Picheral, M., et al. (2008). Volume distribution for particles between 3.5 to 2000 μm in the upper 200 m region of the South Pacific Gyre. *Biogeosciences* 5, 299–310. . doi: 10.5194/bg-5-299-2008

Stemmann, L., Jackson, G. A., and Ianson, D. (2004). A vertical model of particle size distributions and fluxes in the midwater column that includes biological and physical processes—Part I: model formulation. *Deep Sea Res.* 51, 865–884. doi: 10.1016/j.dsr.2004.03.001

Stemmann, L., Picheral, M., and Gorsky, G. (2000a). Diel variation in the vertical distribution of particulate matter (>0.15mm) in the NW Mediterranean Sea investigated with the Underwater Video Profiler. *Deep Sea Res. Part I* 47, 505–531. doi: 10.1016/S0967-0637(99)00100-4

Stemmann, L., Picheral, M., and Gorsky, G. (2000b). Vertical distribution of suspended aggregates at station DYNAPROC_PVM33. In supplement to: Stemmann, L et al. (2000): diel variation in the vertical distribution of particulate matter (>0.15 mm) in the NW Mediterranean Sea investigated with the Underwater Video Profiler. *Deep Sea Res. Part I* 47, 505–531. doi: 10.1016/S0967-0637(99)00100-4

Sullivan, J. M., Twardowski, M. S., Donaghay, P. L., and Freeman, S. A. (2005). Use of optical scattering to discriminate particle types in coastal waters. *Appl. Opt.* 44, 1667–1680. doi: 10.1364/AO.44.001667

Sullivan, J. M., Twardowski, M. S., Ronald, J., Zaneveld, V., and Moore, C. C. (2013). "Measuring optical backscattering in water," in *Light Scattering Reviews 7*, (Berlin: Springer), 189–224. doi: 10.1007/978-3-642-21907-8_6

Taucher, J., Stange, P., Algueró-Muñiz, M., Bach, L. T., Nauendorf, A., Kolzenburg, R., et al. (2018). In situ camera observations reveal major role of zooplankton in modulating marine snow formation during an upwelling-induced plankton bloom. *Prog. Oceanogr.* 164, 75–88. doi: 10.1016/j.pocean.2018.01.004

Twardowski, M. S., Boss, E., Macdonald, J. B., Pegau, W. S., Barnard, A. H., and Zaneveld, J. R. V. (2001). A model for estimating bulk refractive index from the optical backscattering ratio and the implications for understanding particle composition in case I and case II waters. *J. Geophys. Res.* 106, 14129–14142. doi: 10.1029/2000JC000404

Twardowski, M. S., Dalgleish, F. R., Tonizzo, A., Vuorenkoski, D. A. K., and Strait, C. (2018). "Development and assessment of lidar modeling to retrieve IOPs," in *Ocean Sensing and Monitoring X*, eds W. Hou and R. A. Arnone (Orlando, FL: SPIE), 32. doi: 10.1117/12.2309998

Urmy, S. S., Benoit-Bird, K. J., Ryan, J. P., and Horne, J. K. (2019). Mesopelagic predator-prey interactions revealed by joint passive and active acoustic observations. *J. Acoust. Soc. Am.* 146, 2899–2899. doi: 10.1121/1.5137058

Volk, T., and Hoffert, M. I. (2013). "Ocean carbon pumps: analysis of relative strengths and efficiencies in ocean-driven atmospheric CO_2 changes," in *Geophysical Monograph Series*, eds E. T. Sundquist and W. S. Broecker (Washington, DC: American Geophysical Union), 99–110. doi: 10.1029/GM032p0099

Yu, E.-F., Francois, R., Bacon, M. P., Honjo, S., Fleer, A. P., Manganini, S. J., et al. (2001). Trapping efficiency of bottom-tethered sediment traps estimated from the intercepted fluxes of 230Th and 231Pa. *Deep Sea Res. Part I* 48, 865–889. doi: 10.1016/S0967-0637(00)00067-4

Zorn, H. M., Churnside, J. H., and Oliver, C. W. (2000). Laser safety thresholds for cetaceans and pinnipeds. *Mar. Mam. Sci.* 16, 186–200. doi: 10.1111/j.1748-7692.2000.tb00912.x doi: 10.1111/j.1748-7692.2000.tb00912.x

Conflict of Interest: The authors declare that the research was conducted in the absence of any commercial or financial relationships that could be construed as a potential conflict of interest.

Copyright © 2020 McKenzie, Twardowski, Briggs, Nayak, Boswell and Dalgleish. This is an open-access article distributed under the terms of the Creative Commons Attribution License (CC BY). The use, distribution or reproduction in other forums is permitted, provided the original author(s) and the copyright owner(s) are credited and that the original publication in this journal is cited, in accordance with accepted academic practice. No use, distribution or reproduction is permitted which does not comply with these terms.

frontiers in Marine Science

ORIGINAL RESEARCH
published: 22 December 2020
doi: 10.3389/fmars.2020.542701

High-Resolution Sampling of a Broad Marine Life Size Spectrum Reveals Differing Size- and Composition-Based Associations With Physical Oceanographic Structure

Adam T. Greer[1,2], John C. Lehrter[3], Benjamin M. Binder[4], Aditya R. Nayak[5,6], Ranjoy Barua[5,6], Ana E. Rice[7,8], Jonathan H. Cohen[9], Malcolm N. McFarland[6], Alexis Hagemeyer[3], Nicole D. Stockley[6], Kevin M. Boswell[4], Igor Shulman[7], Sergio deRada[7] and Bradley Penta[7]*

[1] Skidaway Institute of Oceanography, University of Georgia, Savannah, GA, United States, [2] Division of Marine Science, School of Ocean Science and Engineering, The University of Southern Mississippi, Stennis Space Center, MS, United States, [3] Dauphin Island Sea Lab, University of South Alabama, Dauphin Island, AL, United States, [4] Institute of Environment, Florida International University, Miami, FL, United States, [5] Department of Ocean & Mechanical Engineering, Florida Atlantic University, Boca Raton, FL, United States, [6] Harbor Branch Oceanographic Institute, Florida Atlantic University, Fort Pierce, FL, United States, [7] U.S. Naval Research Laboratory, Stennis Space Center, MS, United States, [8] Bureau of Ocean Energy Management, New Orleans, LA, United States, [9] School of Marine Science & Policy, University of Delaware, Lewes, DE, United States

OPEN ACCESS

Edited by:
Christian Grenz, UMR7294 Institut Méditerranéen d'Océanographie (MIO), France

Reviewed by:
Fabien Lombard, Sorbonne Universités, France
Anna Metaxas, Dalhousie University, Canada

***Correspondence:**
Adam T. Greer
atgreer@uga.edu

Specialty section:
This article was submitted to Marine Ecosystem Ecology, a section of the journal Frontiers in Marine Science

Received: 13 March 2020
Accepted: 27 November 2020
Published: 22 December 2020

Citation:
Greer AT, Lehrter JC, Binder BM, Nayak AR, Barua R, Rice AE, Cohen JH, McFarland MN, Hagemeyer A, Stockley ND, Boswell KM, Shulman I, deRada S and Penta B (2020) High-Resolution Sampling of a Broad Marine Life Size Spectrum Reveals Differing Size- and Composition-Based Associations With Physical Oceanographic Structure. Front. Mar. Sci. 7:542701. doi: 10.3389/fmars.2020.542701

Observing multiple size classes of organisms, along with oceanographic properties and water mass origins, can improve our understanding of the drivers of aggregations, yet acquiring these measurements remains a fundamental challenge in biological oceanography. By deploying multiple biological sampling systems, from conventional bottle and net sampling to *in situ* imaging and acoustics, we describe the spatial patterns of different size classes of marine organisms (several microns to ∼10 cm) in relation to local and regional (m to km) physical oceanographic conditions on the Delaware continental shelf. The imaging and acoustic systems deployed included (in ascending order of target organism size) an imaging flow cytometer (CytoSense), a digital holographic imaging system (HOLOCAM), an *In Situ* Ichthyoplankton Imaging System (ISIIS, 2 cameras with different pixel resolutions), and multi-frequency acoustics (SIMRAD, 18 and 38 kHz). Spatial patterns generated by the different systems showed size-dependent aggregations and differing connections to horizontal and vertical salinity and temperature gradients that would not have been detected with traditional station-based sampling (∼9-km resolution). A direct comparison of the two ISIIS cameras showed composition and spatial patchiness changes that depended on the organism size, morphology, and camera pixel resolution. Large zooplankton near the surface, primarily composed of appendicularians and gelatinous organisms, tended to be more abundant offshore near the shelf break. This region was also associated with high phytoplankton biomass and higher overall organism abundances in the ISIIS, acoustics,

and targeted net sampling. In contrast, the inshore region was dominated by hard-bodied zooplankton and had relatively low acoustic backscatter. The nets showed a community dominated by copepods, but they also showed high relative abundances of soft-bodied organisms in the offshore region where these organisms were quantified by the ISIIS. The HOLOCAM detected dense patches of ciliates that were too small to be captured in the nets or ISIIS imagery. This near-simultaneous deployment of different systems enables the description of the spatial patterns of different organism size classes, their spatial relation to potential prey and predators, and their association with specific oceanographic conditions. These datasets can also be used to evaluate the efficacy of sampling techniques, ultimately aiding in the design of efficient, hypothesis-driven sampling programs that incorporate these complementary technologies.

Keywords: *in situ* imaging, zooplankton, acoustics, size distribution, community composition, patchiness, phytoplankton, sampling systems

INTRODUCTION

Accurate measurements of size and abundance of organisms and particles are fundamental to process-oriented research in biological oceanography (Blanchard et al., 2017). Size correlates with many ecological properties of plankton and nekton and is a "taxa-transcending trait" that plays a fundamental role in ecosystem structure in both marine and terrestrial realms (Andersen et al., 2016; Kiørboe et al., 2018; Woodson et al., 2018). For example, size dictates which prey are available for consumption and influences metabolic rates. In general, marine prey are 0.1–1.0% of the mass of a predator (Jennings et al., 2001; Kiørboe, 2008); however, there are many exceptions where predators (or something to a similar effect, like parasites) are smaller (e.g., Wakabayashi et al., 2012; Peacock et al., 2014; Feunteun et al., 2018) or orders of magnitude larger (Sutherland et al., 2010; Henschke et al., 2016; Conley et al., 2018; Dadon-Pilosof et al., 2019) than their prey. Despite the widely accepted importance of size in affecting marine ecosystem functioning, measurement of size distributions from micro-organisms to nektonic animals is challenging due to limitations or taxonomic biases for various sampling gears (Cowen et al., 2013; Skjoldal et al., 2013; Wiebe et al., 2017). In addition, the data generated from coarse sampling gears, such as net tows, are not easily associated with the spatial scales of oceanographic variability from m to km that may structure the abundances of different organism sizes classes.

In situ imaging systems represent one method of assessing size distributions with high spatial resolution, while providing taxonomic identifications to family or genus level (in most cases). These systems, when compared to net-based or station-based sampling, have been demonstrated to mitigate biases related to organism fragility (Greer et al., 2014, 2018; Luo et al., 2014; Biard et al., 2016), patchiness or fine-scale changes in abundance (Davis and McGillicuddy, 2006; Greer et al., 2016), and size or swimming speed of the organisms of interest (Cowen et al., 2013; Parra et al., 2019). Some imaging systems have shown consistency in comparison to acoustically-derived abundances, particularly for more durable taxa, such as shrimps, chaetognaths, and copepods (Trevorrow et al., 2005; Whitmore et al., 2019). These comparisons are more uncertain when they include gelatinous organisms (Båmstedt et al., 2003).

Describing the degree of patchiness accurately for different biological constituents is key for assessing various biological rates (Letcher and Rice, 1997; Davis and McGillicuddy, 2006; Priyadarshi et al., 2019) and trophic interactions (Benoit-Bird and McManus, 2012; Greer et al., 2016; Schmid et al., 2020) that can also affect marine ecosystem structure, production, and biodiversity (Woodson and Litvin, 2015; Woodson et al., 2018; Priyadarshi et al., 2019). Often the high-resolution systems describing this patchiness, because of their technical complexity and various stages of instrument development, are used in isolation or with more conventional oceanographic sampling methods (CTD, plankton nets, Niskin bottle sampling, etc.). However, there has been a recent push to describe and integrate the observations from these different platforms into a cohesive framework that will enhance our understanding of plankton dynamics (Lombard et al., 2019).

Imaging systems use a variety of lighting techniques, such as strobes [e.g., Video Plankton Recorder (Davis et al., 2005) and the Underwater Vision Profiler (UVP, Picheral et al., 2010)] or back-lit shadowgraphs, such as the Shadowed Image Particle Profiling and Evaluation Recorder (SIPPER, Samson et al., 2001), the *In Situ* Ichthyoplankton Imaging System (ISIIS, Cowen and Guigand, 2008), and ZooGlider (Ohman et al., 2019). The shadowgraph imagers, and the ISIIS in particular, quantify the larger size range of planktonic organisms (Wiebe et al., 2017; Lombard et al., 2019). Two or more optical systems can be directly compared, such as the Pelagic *In Situ* Observing System (PELAGIOS) and the UVP (Hoving et al., 2019) or the Optical Plankton Counter to the SIPPER (Remsen et al., 2004), to reveal the size classes or taxa captured by each system. The sample volume (relative to organism abundance), camera resolution, tow speed, or method of deployment, however, are usually given minimal consideration when determining which sampling system is optimal to answer particular biological questions.

As automated sampling platforms are increasingly developed and deployed for describing biological patterns, it is apparent

that each system has its own tradeoffs for the kinds of organisms or patterns it can detect (Lombard et al., 2019). Deploying these different systems within similar water masses can be used to assess how their detected patterns compare to one another, generating improved understanding of plankton and nekton distributions in relation to physical and biogeochemical properties. While direct comparisons have been performed for a variety of net systems (Wiebe and Benfield, 2003; Broughton and Lough, 2006; Skjoldal et al., 2013), near simultaneous deployment of multiple imaging systems is less common, and these are also rarely deployed in conjunction with acoustics (Sevadjian et al., 2014; Whitmore et al., 2019). Sometimes a direct comparison can reveal tradeoffs among the systems that would otherwise be obscured if used in isolation (Skjoldal et al., 2013; Wiebe et al., 2017), while simultaneously providing a general understanding of the connection of different biological size classes to the oceanographic environment.

A unique combination of instrumentation was deployed on the continental shelf east of Delaware Bay (United States, western Atlantic) to address two main objectives: (1) To describe and evaluate imaging and acoustical methods in relation to each other and to traditional net-based sampling and (2) to measure biological patterns across a range of spatial scales in relation to variability in hydrographic characteristics and concentrations of nutrients and phytoplankton. For the first objective, we hypothesized that the different characteristics of the image, acoustic, and net based sampling methods would influence the detection of size classes and taxonomic composition. For the second objective, we hypothesized that dense aggregations observed by the multiple sampling methods across multiple size classes would occur at density gradients, but the community compositions would differ based on water mass nutrient concentrations and the biomass and size composition of the phytoplankton community. This approach using multiple imaging and acoustic systems allowed us to quantify the individuals that comprised specific size classes.

MATERIALS AND METHODS

General Field Sampling Plan

The sampling scheme combined station-based and transect sampling for the different systems (**Figure 1**), and each system was deployed to maximize spatial coverage (within each system's limitations). A grid was laid out with a pattern of lettered sampling lines approximately perpendicular to the coast of Delaware and southern New Jersey centered at the mouth of Delaware Bay. Station names are used throughout the text in reference to this grid. Numbered transects ran parallel to the coast starting at the coast. The intersections of these lines defined the sampling grid, with 9.26 km (5 nautical miles) between stations. The research cruise on the *RV Hugh R. Sharp* encompassed a time period between April 26 and May 09, 2018.

The multi-hour imaging and acoustical instrument deployments were bracketed by vertical water column profile sampling at fixed stations both prior and subsequent to the tows. At each station, we deployed a CTD rosette consisting of temperature, conductivity, pressure, oxygen, and fluorescence measurements (SBE 9plus, SBE 11plus V 5.2- SeaSoft processing software, SBE 43, WET Labs ECO-AFL/FL) and collected discrete samples in Niskin bottles in the surface layer and at targeted depths associated with gradients of density, dissolved oxygen, and fluorescence. At a subset of stations, we deployed an optical profiling package containing a holographic imaging system (HOLOCAM). The CytoSense was used to image water from the discrete samples from the CTD rosette collected near-surface, at the fluorescence maximum, below this maximum, and occasionally at other depths (e.g., oxygen minima or maxima).

The full suite of station-based samples and profiles was taken before and after towing an *In Situ* Ichthyoplankton Imaging System (Cowen and Guigand, 2008, ISIIS tow #1) at Station I5 on April 27, 2018 and, after the tow was completed, at Station I12 on April 28 (**Figure 1A**). ISIIS tow #3 was "U-shaped" – the first part of the tow, called transect 1, was initiated at Station I12 and moved westward to K9. A full suite of hydrographic measurements was taken at both I12 and I15 prior to transect 1 to characterize the offshore waters. At station K9, the ship turned with the ISIIS still in the water and began to transit toward station K13, thus initiating transect 2. Depth-stratified net samples (top and bottom halves of the water column) were collected at J13 after ISIIS tow #3 was completed. For details about the ISIIS and other imaging systems used in this study see **Table 1** and **Appendix I**.

To describe the larger-scale physical conditions influencing the sampled water masses, regional-scale surface current and wind velocities were obtained from various publicly available sources. Surface currents, downloaded from the Mid-Atlantic Regional Association Coastal Ocean Observing System[1], are derived from an observation network of SeaSonde-type Coastal Ocean Dynamics Applications Radars (CODAR) instruments deployed in the Delaware Bay region. SeaSonde-type HF radar instruments exploit information in the radiowave backscatter from the ocean surface to infer movement of the near surface water. Wind velocity data for the NDBC station 44009 (located to the south of the Delaware Bay entrance, **Figure 1**) were obtained the NOAA station website[2].

HOLOCAM Data Processing and Analysis

Imagery and oceanographic data were obtained from the HOLOCAM between 12:47 and 15:44 (EDT) on May 1, 2018 at station I15, which was located near the offshore end of the ISIIS tows (**Figure 1A**). The HOLOCAM package was profiled vertically from the surface to depths of 28–32 m across different profiles. Data were recorded continuously during the downcast profiles, which lasted 5–8.5 min, corresponding to 4,500–7,650 recorded holograms per profile. A total of five profiles were recorded at this station (referred to as profiles a-e hereafter), but profile d is not presented because of data quality concerns. Based on the package descent rate, only every other recorded hologram was processed for analysis to ensure individual particles were not duplicated (in case a particle is present in two successive holograms). Particle counts from each

[1]http://maracoos.org/download.shtml

[2]https://www.ndbc.noaa.gov/station_realtime.php?station=44009

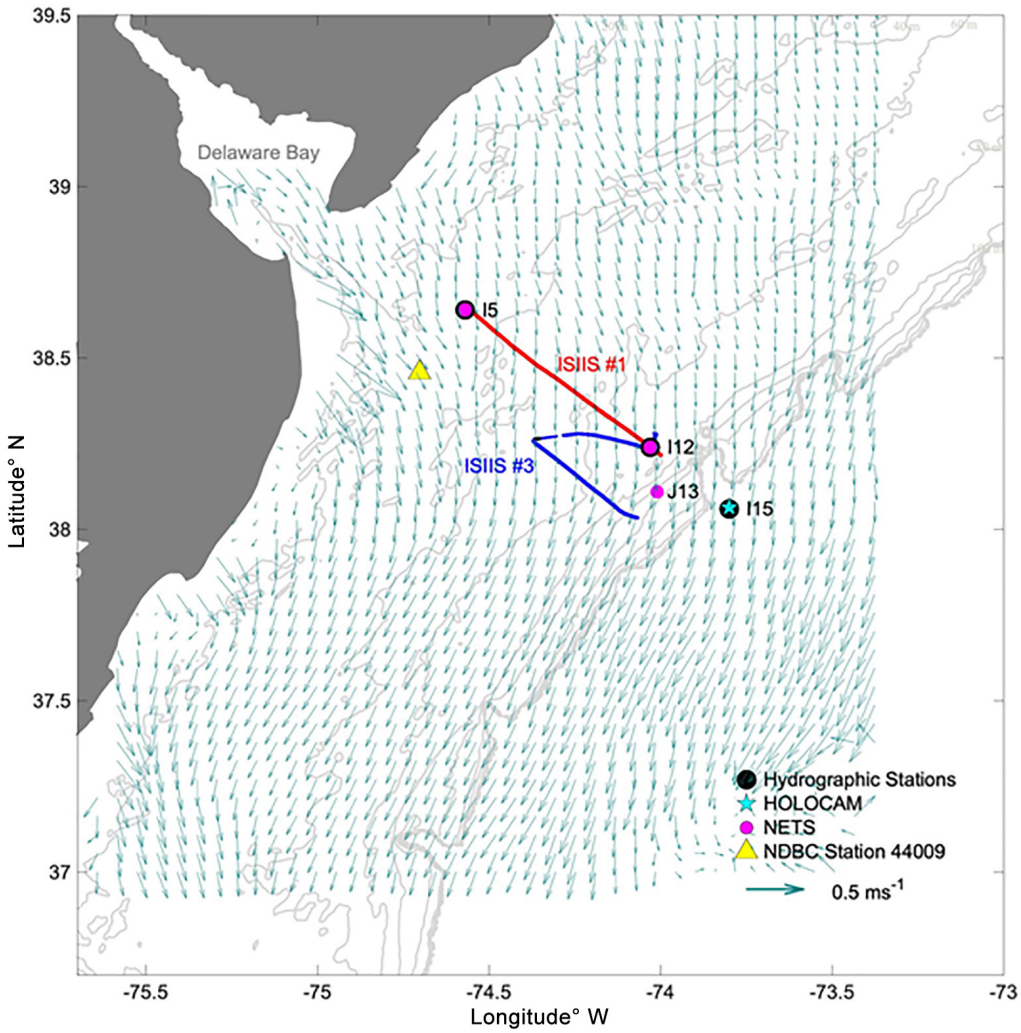

FIGURE 1 | Map of the sampling transects on April 28 and May 01, 2018. The points mark the locations of the hydrographic stations, net tows, HOLOCAM deployment, and wind velocity observations. Acoustic sampling occurred during ISIIS tow #1 but was not conducted during the U-shaped tow. Background arrows indicate the 25 h averaged currents derived from HF radar on April 29–30, 2018.

TABLE 1 | Method of deployment, optical resolution, and sampling rate for the different camera systems. The ISIIS small and large camera are the only two systems that are deployed in almost exactly the same water mass.

Imager	Method	Field of view	Depth of field	Image pixel resolution	Sampling rate
CytoSense	Discrete bottle samples from inside chl-a max and surface	Length of 10 mm	<850 μm	0.7 μm	0.0012 L s^{-1}
HOLOCAM	Profiling	9.6 mm × 9.6 mm^2	40 mm	4.68 μm	0.055 L s^{-1}
ISIIS Small Camera	Tow-yo	43 mm	89 mm	42 μm	9.57 L s^{-1}
ISIIS Large Camera	Tow-yo	120 mm	500 mm	59 μm	150 L s^{-1}

hologram over a 20 cm depth range were averaged to produce one particle concentration value per bin.

The equivalent spherical diameter (ESD) was used to represent the particle sizes and calculated as $ESD = \sqrt{4A_F/\pi}$, where A_F is the area of the particle including empty spaces within the particle perimeter. In cases where the image segmentation results in the loss of a few pixels within the particle bounds, the missing pixels are included to represent or obtain the "filled area." The same formula for ESD was used for all image data from other instruments where applicable. A subsurface peak was identified in the HOLOCAM profiles, and images from this area were manually examined to identify particles based on size and morphology. For each profile, a subset of ten holograms at three different depths within the peak were selected. In these subsets,

particles within the broad range of 60–100 μm were selected and enumerated. All particles within that size range were then visually identified to generate the percentage of ciliates.

ISIIS Data Processing and Analysis

The imagery data from the ISIIS underwent a series of processing steps to extract and size particles and plankton in the images. First, the images were transformed using a "flat-fielding" procedure that evened out background gray level and improved particle contrast relative to the background. The images were then segmented (i.e., regions of interest were extracted) using a binary image gray level threshold of 170. The choice of this threshold value was based on experimenting with different individual images from different regions of the tow, and the chosen value was similar to thresholds used in previous work (e.g., Greer et al., 2018). It is important to note, however, that any chosen threshold will result in features within an image that are detected or ignored, and an optimal threshold detects individual particles or organisms without being too sensitive to faint particles in the background. An overly sensitive threshold value or method can generate many large "particles" composed of several different organisms, prohibiting accurate classification. The choice of these thresholds has not been systematically evaluated for different plankton taxa but likely has a profound impact on the objects detected and how imagery data are interpreted (Giering et al., 2020). After applying the threshold, all black particles were extracted above a certain size limit, along with particle characteristics, including the area of the particle (including white space in the middle of particles, which is common for gelatinous organisms). For the small camera, the particle areas extracted ranged from 400 to 2,500 pixels (0.95–2.37 mm ESD). The particles from the large camera were 800 pixels (1.88 mm ESD) to over 13,000 pixels (7.59 mm ESD, upper limit was ∼40 mm ESD). The flat fielding and segmentation procedures were both implemented in ImageJ (v1.52a, Schneider et al., 2012).

Each extracted particle was merged to the corresponding physical data (depth, temperature, salinity, etc.) using the nearest timestamp. The particles were then binned into 20 m horizontal bins, the approximate distance for the large camera to sample 1 m^3 of water (assuming a 50 cm depth of field), and the mean oceanographic variables were calculated for each bin to generate a dataset of particle concentrations, oceanographic variables, and their locations along the transects. With the 0.2 m s^{-1} vertical movement of the vehicle, these 20 m horizontal bins corresponded to vertical bins of approximately 1.6 m (narrower near surface and bottom when the vehicle was turning). The counts from the small camera were multiplied by 15.67 to generate fine-scale concentrations because that camera system samples 0.0638 (1/15.67) of the volume of water compared the large camera when towed over the equivalent horizontal distance (field of view × depth of field × distance). To examine the abundances vs. particle size, the particles were assigned discrete size classes of roughly equal value (larger size ranges for rarer and larger particles) and were standardized by dividing the abundances in each size category by the bin width of the size category (producing units of individuals m^{-3} mm^{-1}). The bin width was calculated from the difference in ESD between the largest and smallest particles for that size class. The mean and standard deviations of the concentrations were calculated for each size class and plotted using the midpoint ESD for each size class (3rd quartile of 20,908 pixels or 9.63 mm ESD for the largest size class). These calculations and analyses were performed in R (v3.6.1) with extensive use of the packages 'plyr,' 'reshape2,' and 'ggplot2' (Wickham, 2016). The potential density anomaly was calculated using the R package 'gsw' (Kelley et al., 2017). The ISIIS sensor data and organism abundances were linearly interpolated using the R package 'akima' (Akima and Gebhardt, 2016).

To examine changes in composition among the different size classes detected in the small and large camera systems, 2,000 image segments were randomly extracted for each size class and categorized into one of 15 categories. These categories included appendicularian (animal), appendicularian house (no animal visible), chaetognath, copepod, ctenophore, diatom, echinoderm larva, fish larva, hydromedusa, pteropod veliger, marine snow aggregate, other (identifiable but too rare to influence proportions, data not shown), shrimp, siphonophore, and unknown (cannot be determined from the image). These image segments were classified using customized keyboard shortcuts in ImageJ. By multiplying the concentration of total particles by the composition across a particular size range, abundance estimates for different taxa could be obtained.

A series of steps and additional calculations were made to directly compare the two camera systems on the ISIIS. First, the particles from the small camera that were larger than 1.88 ESD and the particles less than 2.37 mm ESD from the large camera (overlapping size classes) were enumerated and interpolated across the length of ISIIS tow #3 for both cameras (2 transects). To quantify the degree of spatial aggregation, the Lloyd's patchiness index (Bez, 2000) was applied to evenly distributed size bins (based on pixel area) for particles $\leq$ 5.73 mm ESD.

Hydroacoustic System and Data Collection

A pair of split-beam echosounders were used in tandem with the ISIIS tow #1 operating at 18 and 38 kHz (SIMRAD ES18 and ES38-10). Split-beam echosounders have the advantage of remotely sampling large swaths of the full water-column, while underway or stationary, and can be integrated with traditional sampling methods (e.g., net or optical sampling) that are typically volume limited (i.e., taking snap-shots of discrete layers). Split-beam echosounders can detect a wide-range of size classes, from krill swarms to large mega-fauna; and with the correct combination of frequencies, can be used to remotely discriminate taxa observed in the water column (Korneliussen et al., 2008; Koslow, 2009). The beam angle and pulse duration for both instruments was 10° and 1.024 μs, respectively. The 18 kHz transducer was deployed to 2.5 m depth, with a rotating pole along the side of the ship. The 38 kHz transducer was deployed to 3.9 m depth, inside the keel of the ship. Technical drawings of the ship were used to measure the spatial offset between the two transducers, and post-processing techniques were used to synchronize the data in time and space. Transect data were

collected on April 27, 2018 from 20:00 to 06:00 (EDT) the following morning. The two echosounders were calibrated at sea according to the standard sphere calibration procedures described by Demer et al. (2015).

Hydroacoustic Data Processing and Analysis

Data were manually scrutinized and processed in Echoview (v10.0, Echoview Software Pty Ltd.). The upper 10 m of the water column was excluded due to nearfield-noise and bubble wash along the transducer faces. Data within 2 m from the bottom were also excluded. Noise artifacts were filtered and excluded following D'Elia et al. (2016). A threshold of −85 dB re 1 m^{-1} was applied to the filtered data to ensure detection of a mixed assemblage of zooplankton groups (e.g., pteropods, copepods, euphausiids, etc.). The full water column was then echo-integrated in 100 m horizontal by 5 m vertical cells to derive estimates of the Nautical Area Scattering Coefficient (NASC m^2 nmi^{-2}), which is considered to be proportional to "acoustic biomass" or energy density (Simmonds and MacLennan, 2005). NASC estimates from both the 18 and 38 kHz transducers were used as an index of scattering in the water column attributed to detritus, plankton, and fish along the transect (Simmonds and MacLennan, 2005).

To account for the separation between the ISIIS (towed) and echosounder (hull-mounted) data, telemetry information from the ISIIS was used to identify a narrow corridor of near-coincident data along the ISIIS sampling path. A 33.0 s time offset was applied to the acoustic data based on the average vessel speed (∼2.5 m s^{-1}) and length of the cable attached to the ISIIS (∼100 m) to obtain comparable datasets. In Echoview, acoustic data collected within >2.5 m from the ISIIS flight path (5 m corridor) were excluded, allowing for a paired comparison between NASC estimates and particle concentrations, as measured by the ISIIS, at discrete depths along the transect (accounting for errors in matching acoustics with the ISIIS positioning). Particle concentration data from the ISIIS was divided into three size classes (5.60–7.59, 7.6–9.4, and >9.41 mm ESD) to determine the degree of correlation between NASC and particle concentration at different sizes. Total particle concentration (>4.6 mm ESD) independent of size class, was also compared to NASC estimates by calculating Spearman's correlation coefficient (ρ).

Nutrient and Phytoplankton Concentrations

Nutrient samples were collected from Niskin bottles and stored at −20°C until analysis. Nutrient samples were analyzed for nitrate plus nitrite ($NO_3^- + NO_2^-$), nitrite (NO_2^-), phosphate (PO_4^{3-}), and silicate [$Si(OH)_4$] using fluorometric (N species) and spectrophotometric (PO_4^{3-}), and $Si(OH)_4$ methods on an Astoria-Pacific Astoria2 (A2) nutrient auto-analyzer (Method #A179, A027, A205, and A221; Astoria-Pacific International, OR, United States). Nitrate concentrations were subsequently calculated by difference of nitrate plus nitrite and nitrite concentrations.

Phytoplankton pigment samples were collected onto filters under a low light environment. Seawater samples for phytoplankton pigment analysis were vacuum filtered through 25-mm GF/F filters (Whatman, 0.7-μm pore size) until color appeared on the filter and the volume of seawater filtered was recorded. Filters were placed in cryo filter capsules and submerged in liquid nitrogen for storage until analysis. Pigments were analyzed by high performance liquid chromatography (HPLC) following the method of Hooker et al. (2005).

Chlorophyll *a* (chl-a) and a set of diagnostic pigments were used to assign taxonomic groups and size classes (Uitz et al., 2006). Specifically, the taxonomic biomarkers were: fucoxanthin (diatoms); peridinin (dinoflagellates); 19-hexanoyloxyfucoxanthin (chromophytes and nanoflagellates); 19-butanoyloxyfucoxanthin (chromophytes and nanoflagellates); alloxanthin (cryptophytes); chlorophyll *b* (green flagellates); and zeaxanthin (cyanobacteria). Pigment:chlorophyll *a* ratios compiled by Uitz et al. (2006) were used to normalize the measured pigment concentrations to total phytoplankton

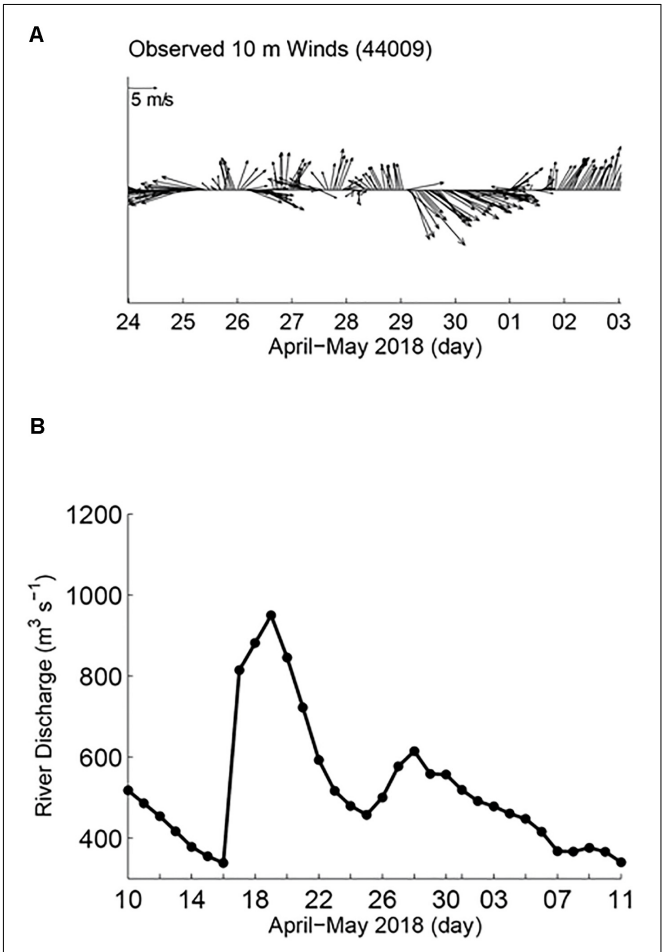

FIGURE 2 | Broader scale physical properties influencing the study area including, **(A)** time-series of wind direction and speed and **(B)** river discharge volume in the Delaware River.

biomass (chlorophyll *a*). The pigment data were further used to calculate the size fractions of microplankton (f_micro), nanoplankton (f_nano), and picoplankton (f_pico) where f_micro was comprised of fucoxanthin and peridin, f_nano was comprised of 19-hexanoyloxyfucoxanthin, 19-butanoyloxyfucoxanthin, and alloxanthin, and f_pico was comprised of chlorophyll *b* and zeaxanthin. Though these size groupings based on pigment concentrations do not strictly conform to specific size ranges, traditionally microplankton are defined to represent the >20 μm size range in equivalent spherical diameter, nanoplankton represent the 2–20 μm size range, and picoplankton represent the 0.2–2 μm size range.

Plankton Net Sampling

Mesozooplankton were sampled with vertical, depth-stratified ring net casts (0.75 m diameter net, 200 μm mesh) to obtain the zooplankton community composition at the beginning and end of each ISIIS tow. The net was fitted with a General Oceanics 2030R mechanical flowmeter to quantify volume sampled (5.95 m^3, mean ± 1.92 standard deviation), and a General Oceanics double trip mechanism to control net opening and closure. At a given station, the closed net was lowered to ∼1 m off bottom, where it was then opened and recovered at 0.5 m s^{-1} to mid-water column and closed. The net was then recovered, rinsed, and the sample fixed in 4% borax-buffered formaldehyde for later processing. Immediately following the first cast, the closed net was lowered to the mid-depth where the previous sample ended. The net was then opened and recovered to the surface for processing as with the first cast.

Fixed samples were digitally analyzed with a Hydroptic ZooScan optical scanner, with subsequent processing using ZooProcess and PkID software (Gorsky et al., 2010). Each sample was transferred to freshwater and sieved into three size fractions (>1,000, >500, and >200 μm) to minimize loss of larger taxa in the splitting process. Each size fraction was then split by Folsom splitter to obtain ∼1,000 individuals in the scan. Images were processed by normalizing their gray levels, then extracting and measuring individual objects (i.e., sections of image with individual zooplankters), including calculation of object equivalent size diameter. A "random forest" algorithm was used to automatically classify extracted objects into 17 predicted categories (i.e., zooplankton taxa) using a learning set developed for these samples. Each object's classification was manually validated before back-calculating abundance of each taxon based on count, volume sampled, and split fraction.

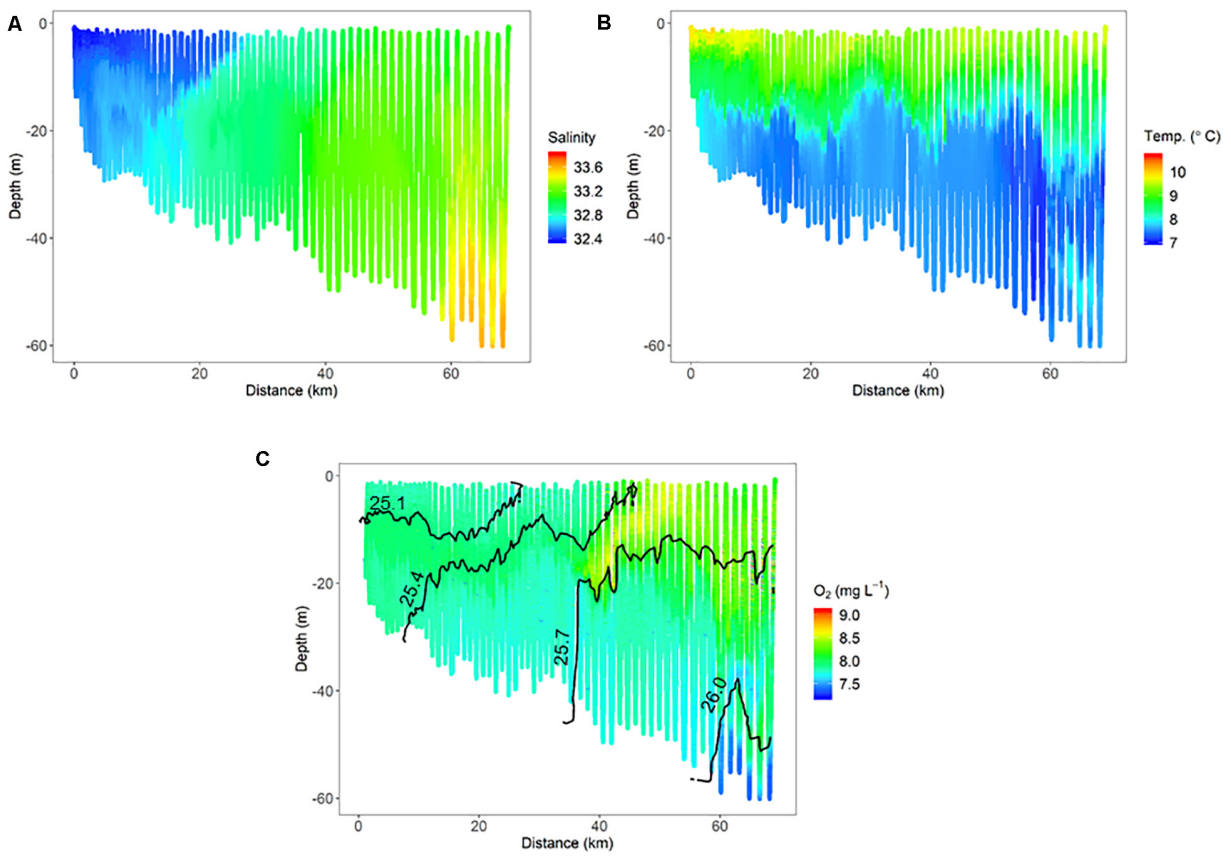

FIGURE 3 | Physical oceanographic conditions from ISIIS tow #1 including, **(A)** salinity, **(B)** temperature, and **(C)** dissolved oxygen. Isopycnals located in panel C (1025.1, 1025.4, 1025.7, and 1026.0 kg m^{-3}) are displayed as a reference to other figures.

RESULTS

Physical Oceanographic Properties

Larger-scale measurements indicated the influence of freshwater discharge in the study area during the time of sampling. The HF radar showed a generally offshore trajectory of surface currents from the mouth of the Bay, followed by a southward turn near the shelf break (**Figure 1**). Hourly averaged 10-m wind velocities from NDBC station 44009 (located to the south of the Delaware Bay, **Figure 1**) from April 30 to May 03 showed weak and variable direction winds until May 01, followed by upwelling favorable (northward) winds (**Figure 2A**). The USGS Delaware River daily discharge record at Trenton, NJ indicated high river discharge ∼1,000 m^3 s^{-1} around April 19, 2018 (**Figure 2B**, note that monthly climatology of the Delaware River discharge is around 630 m^3 s^{-1} for April and 401 m^3 s^{-1} for May). The discharge record at Trenton, NJ is proportional to outflow at the Bay mouth with about an 8-day time lag (Sanders and Garvine, 2001). Therefore, this elevated outflow of fresher water would reach the Delaware Bay mouth around April 27–30. It is known that during upwelling favorable winds, Delaware Bay outflow water masses are mixed with offshore saltier water, and they are advected offshore and to the north (Whitney and Garvine, 2006).

Finer-scale physical oceanographic data collected by the ISIIS also suggested influence from freshwater sources on the inner shelf. During ISIIS tow #1 on April 27–28, inner shelf surface waters were substantially warmer and lower in salinity (**Figures 3A,B**). Salinity became relatively uniform vertically around the middle of the tow, adjacent to deeper saltier waters offshore. The combination of temperature and salinity resulted in isopycnals sloping upward from the shelf toward deeper waters offshore. A tongue of high oxygen waters (∼8.7 mg L^{-1}) had a similar trajectory to the isopycnals at ∼40 km along the transect (**Figure 3C**). ISIIS tow #3 commenced on the evening of May 1 (2 transects, U-shaped tow). The salinity range for both transects combined was similar to ISIIS tow #1, but the low salinities were confined to a narrow vertical range on the inshore side. In deeper waters further offshore, salinity reached a peak of ∼33.7 (**Figure 4A**). Warmer waters were generally confined to the surface 5–10 m for both transects (**Figure 4B**). A peak in dissolved oxygen generally resided between the surface and 20 m throughout most of the tow as well (**Figure 4C**), and similar to ISIIS tow #1, dissolved oxygen tended to follow the trajectory of the isopycnals.

Vertical Distribution and Size vs. Abundance From Imaging Systems

Vertical particle concentration distributions from HOLOCAM profiles (a, b, c, and e) at one station (I15) showed a consistent peak in concentrations between 18 and 23 m depth (**Figure 5**),

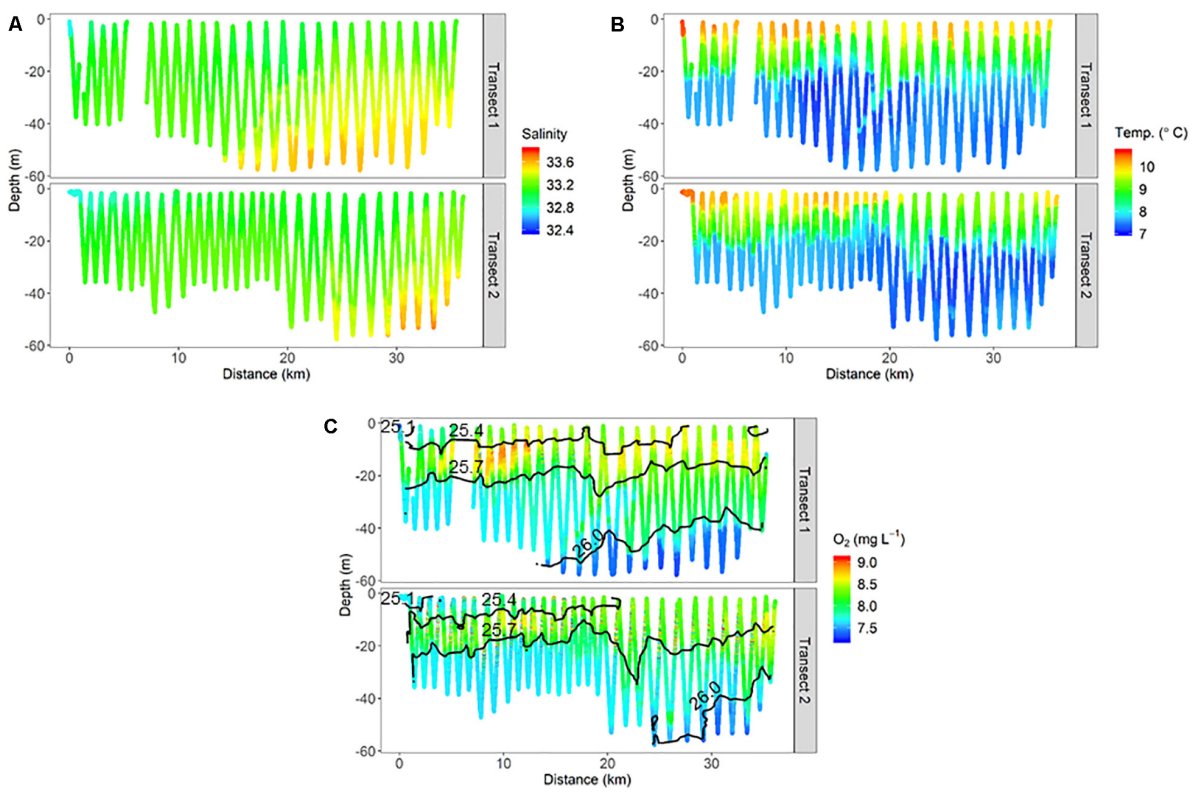

FIGURE 4 | Physical oceanographic conditions from ISIIS tow #3 including, **(A)** salinity, **(B)** temperature, and **(C)** dissolved oxygen. Isopycnals located in panel C (1025.1, 1025.4, 1025.7, and 1026.0 kg m^{-3}) are displayed as a reference.

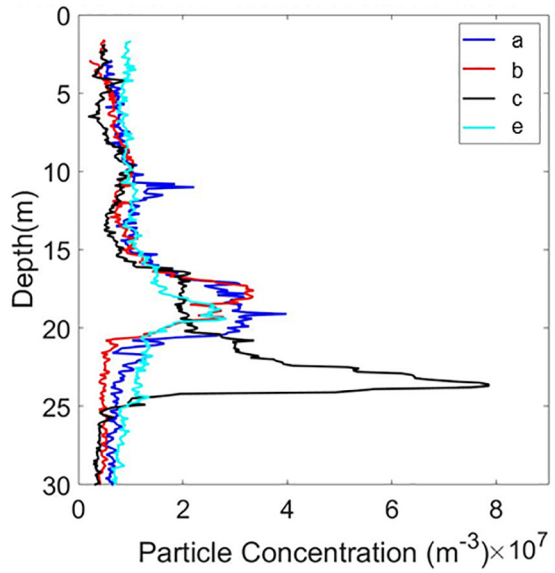

FIGURE 5 | Vertical distribution of particles detected from 4 profiles at the same station (I15) by the HOLOCAM.

with variations in the precise vertical location. The ciliate numbers varied between 76 and 83% of the manually identified particles in this size range, clearly indicating that the peak was driven by the enhanced ciliate concentrations at these depths (see **Figure 6E** for example of copepod with background full of ciliates).

The CytoSense analyzed small volumes of water from the Niskin bottle samples in a qualitative manner with regards to taxonomy but also enumerated and measured particle lengths. The CytoSense detected the smallest size class of organisms imaged (see **Figure 6** for examples). Data pooled from all hydrographic stations on May 01, 2018 and later showed a steady decline in abundance with increasing particle length, but the particle lengths above 0.5 mm were likely not being quantified based on the data missing in some larger size bins. The smallest bin showed a strong spike in abundance possibly due to break up of fragile detritus in the Niskin bottle (**Figure 7**).

The depth-averaged particle size spectra for the 4 HOLOCAM profiles showed a distinct peak in the ciliate size range (0.08–0.1 mm or −1.3 log10 mm ESD, **Figure 7**). The spike in this size abundance corresponded to depths associated with the peaks from **Figure 7**. From 0.1 to 0.4 mm, the particle size distribution spectra for each profile indicate that particle compositions did not change much over the duration of these profiles. Above 0.4 mm ESD, the data became more scattered as large particles/organisms (e.g., copepods) were much lower in concentration and less likely to be observed within the HOLOCAM sample volume. Slopes of the particle size vs. abundance plots between the HOLOCAM and CytoSense were similar (−3.05 and −2.97) despite the fact that they measured ESD and particle length, respectively.

Comparison of the small and large cameras on the ISIIS revealed similar patterns in size and abundance from the U-shaped tow on May 01 (**Figure 7**). From the small camera, a total of 1,001,264 particles were segmented between 0.95 and 2.37 mm ESD over a total imaged volume of water of 267.08 m^3 (mean concentration of 3748.97 ind. m^{-3} for this size class). The large camera, which sampled 15.67 times more water volume along the same transect distance, imaged 1,705,535 particles ranging between 1.88 mm and ∼40 mm ESD. (Note that the large camera did not collect images for the final ∼6 km of transect 2 due to a malfunction in the image acquisition software). For both camera systems, relatively larger particles and plankton were rarer and had less variability in their small scale abundances compared to the smaller size classes (**Figure 7**). Linear regressions between log10 transformed abundances and sizes revealed nearly identical slopes between the two camera systems (−4.64 and −4.59 for the large and small cameras, respectively). The abundance offset between the most comparable size class ∼1.99 mm ESD (the smallest for the large camera and the second largest for the small camera) was 887.42 ind. m^{-3} mm^{-1} for the large camera versus 689.20 ind. m^{-3} mm^{-1} for the small camera. In other words, the large camera detected 28.8% higher abundances relative to the small camera in this size class, which is potentially a consequence of imaging through a larger distance of water (depth of field 50 cm vs. 8.9 cm), organism avoidance of the small camera sampling tube in the middle of the vehicle, or a combination of both.

For ISIIS tow #1, 1,243,482 particles were segmented in the large camera system over the 69.1 km transect (4151.41 m^3 sampled, particles > 1.88 mm ESD). This corresponded to a mean particle concentration of 299.53 ind. m^{-3}, which was substantially less than the mean abundances on ISIIS tow #3 for particles of the same size class (>1.83 mm ESD were 445.63 ind. m^{-3}). Tow #1, however, transited through a large region of lower salinity water (**Figures 3**, **4**), while Tow #3 started and ended in more offshore waters.

Size-Dependent Composition of Plankton From the ISIIS Cameras

The relative abundance of different types of plankton was dependent on the particle size, and, in some cases, on the camera systems used to measure them (**Figure 8**). The ISIIS small camera (8.9 cm depth of field) was dominated by diatoms and copepods across most size classes. Among the size classes that overlapped between the small and large camera systems, some plankton types exhibited little difference between systems (e.g., appendicularians, chaetognaths, gelatinous organisms, and shrimp), while several groups had much higher proportions in the large camera (50 cm depth of field), such as copepods, pteropod veligers, and marine snow aggregates. Segments associated with appendicularian houses were present in low numbers across a wide range of size classes in both cameras, while appendicularians (animal visible in the segment) were more common in the larger size range. The diatoms were the only plankton group that substantially increased in relative abundance in the small camera, jumping from 3.8% in the large camera to 29.0% in the small camera for the identical size class (∼2.0 mm ESD, **Figure 8**). Echinoderm larvae were found in

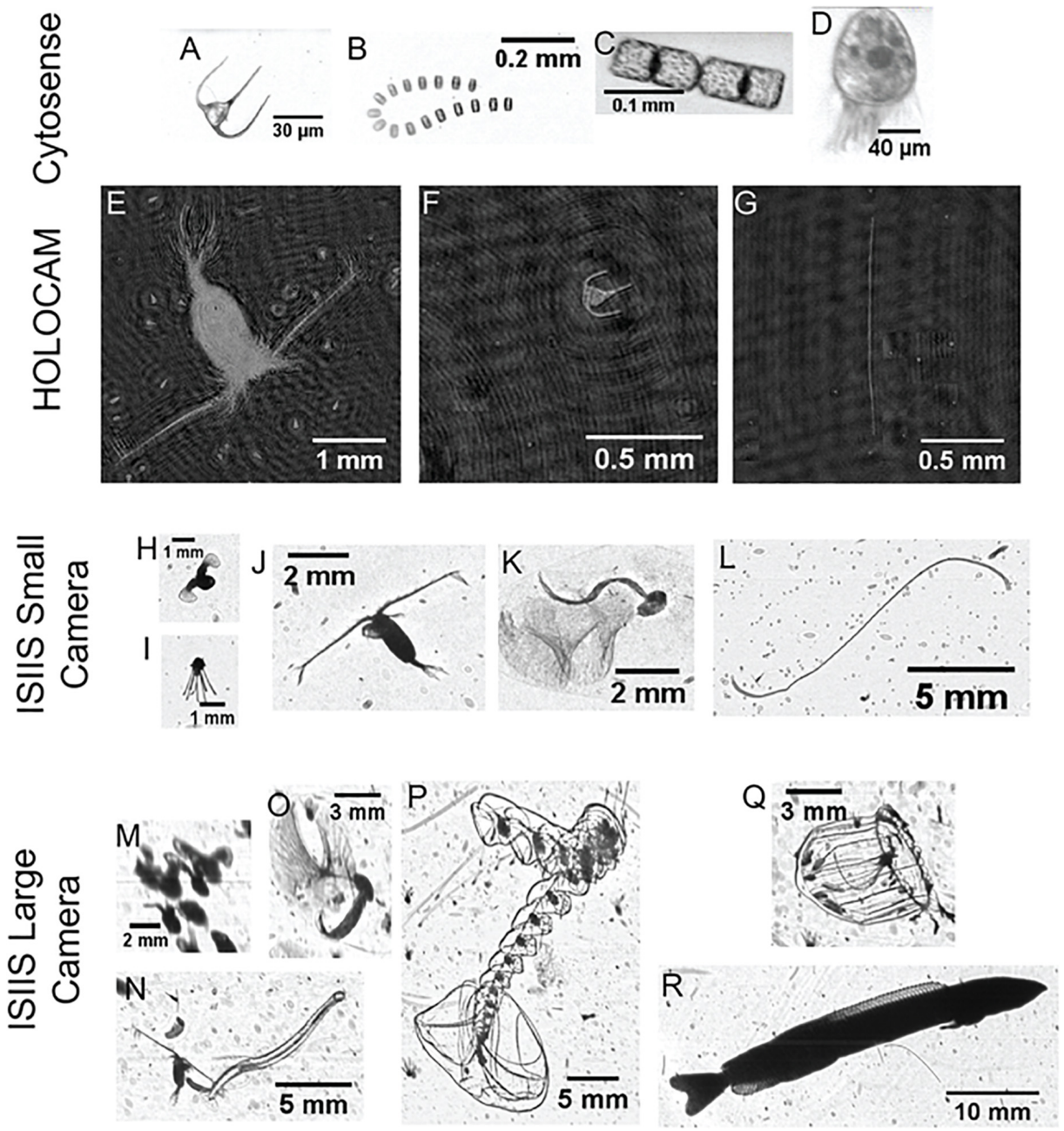

FIGURE 6 | Example organisms detected by different imaging systems. For the Cytosense, **(A)** *Ceratium* spp. dinoflagellate, **(B)** *Thalassiosira* spp. diatom and **(C)** *Cerataulina* spp. diatom and **(D)** a ciliate (likely *Strombidium* spp.). For the HOLOCAM, **(E)** calanoid copepod (with numerous ciliates in the background), **(F)** *Ceratium* spp., and **(G)** diatom chain (genus and species not resolvable). For the ISIIS small camera, **(H)** veliger (early stage pteropod), **(I)** echinoderm larva, **(J)** calanoid copepod, **(K)** appendicularian, **(L)** diatom chain with numerous unresolved particles in the background. For the ISIIS large camera, **(M)** multiple veligers that appear to be touching, generating a large 'particle' (imaged through the 50-cm depth of field), **(N)** chaetognath and copepod, **(O)** appendicularian, **(P)** siphonophore (*Sphaeronectes* spp.), **(Q)** hydromedusa (*Aglantha* spp.), **(R)** juvenile sand lance (*Ammodytes* spp.).

dense aggregations but were only segmented consistently in the smallest size category. These organisms also occasionally dominated the plankton abundances in the nets (**Table 2**). Both cameras showed an increasing proportion of gelatinous zooplankton with increasing particle size, and the largest size category was the only one to detect fish larvae/juveniles in any substantial number (1.6%, data not shown). The relative peaks in ctenophores, siphonophores, and hydromedusae all occurred within the largest size class as well (ESD > 5.6 mm, 57.4%), with siphonophores comprising 2.3%. The proportion of image segments that could not be identified by an expert was fairly consistent across the size classes for the large camera but made

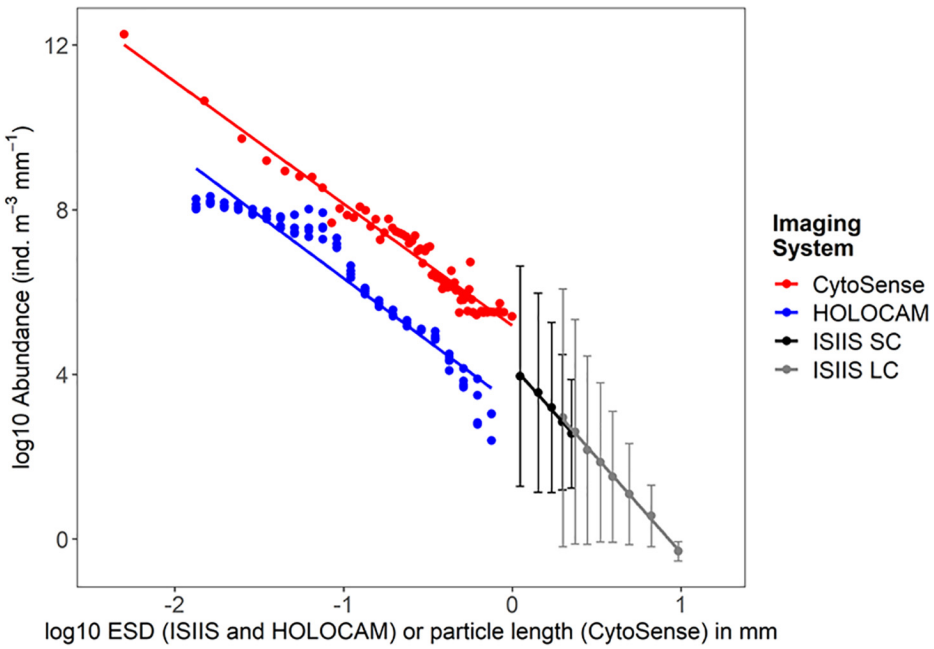

FIGURE 7 | Particle size vs. abundance as detected by the CytoSense (for hydrographic stations visited on May 01, 2018 and afterward), 4 vertical profiles from the HOLOCAM, and the two cameras (SC, small camera; LC, large camera) from the ISIIS. Errorbars on the ISIIS data indicate the standard deviation of the particle concentrations from the different size classes.

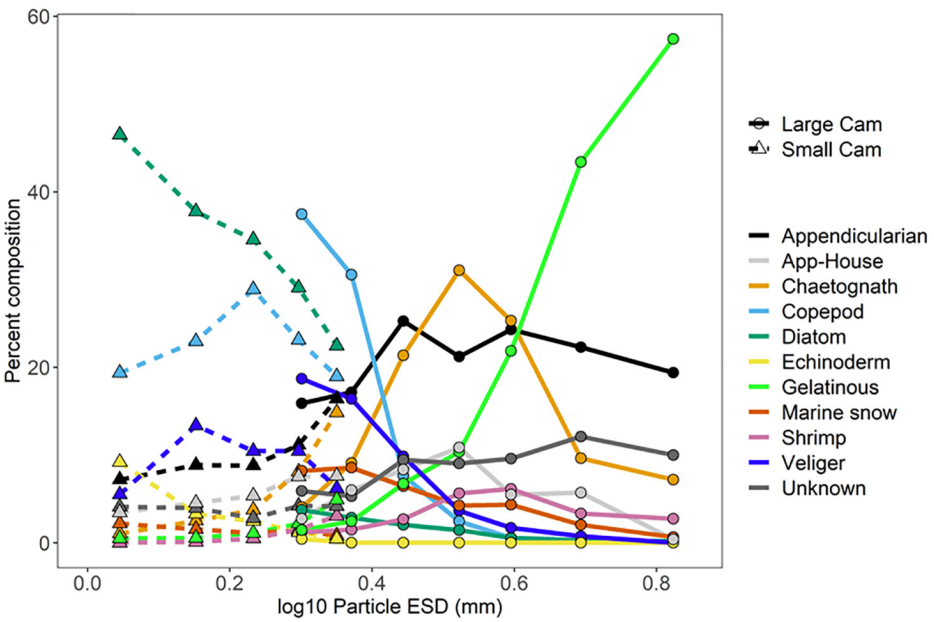

FIGURE 8 | Measured particle sizes (log10 ESD) vs. percent composition for the ISIIS small and large cameras.

up a slightly smaller proportion when transitioning to the data from the small camera.

Two size classes of plankton (1.88–2.82 mm and 2.83–7.59 mm ESD) from the ISIIS large camera, with the larger size class roughly corresponding to the shift toward increasing dominance of gelatinous organisms, had slightly differing spatial patterns for both tows (**Figure 9**). For ISIIS tow #1, there were two highly-concentrated patches in shallower water, but most individuals tended to be aggregated just above the 1025.7 kg m^{-3} isopycnal further offshore (near the offshore end of ISIIS tow #3). The larger plankton size class had high concentrations in a similar region of the aggregations for the smaller size class, but there was another

TABLE 2 | Detected concentrations for plankton collected in the vertical net samples (ind. m^{-3}) at the beginning and end of the ISIIS tows #1 and #3.

	ISIIS tow #1				ISIIS tow #3			
Taxa	**I5 (15–0 m)**	**I5 (27–15 m)**	**I12 (33–0 m)**	**I12 (67–33 m)**	**I12 (33–0 m)**	**I12 (65–33 m)**	**J13 (30–0 m)**	**J13 (60–30 m)**
Appendicularians	0	0	21	97	756	326	146	211
Chaetognaths	4	5	90	542	330	80	201	190
Copepods	1,187	1,809	4,318	9,256	2,457	2,069	6,128	3,409
Other crustaceans	0	1	4	91	26	12	45	225
Echinoderm larvae	0	0	4,632	4,952	2,423	2,872	1,149	419
Fish eggs	0	0	0	0	3	0	8	4
Veligers (pteropods)	4	0	20	207	30	1	3	7
Hydromedusae	7	2	1	190	3	6	13	21

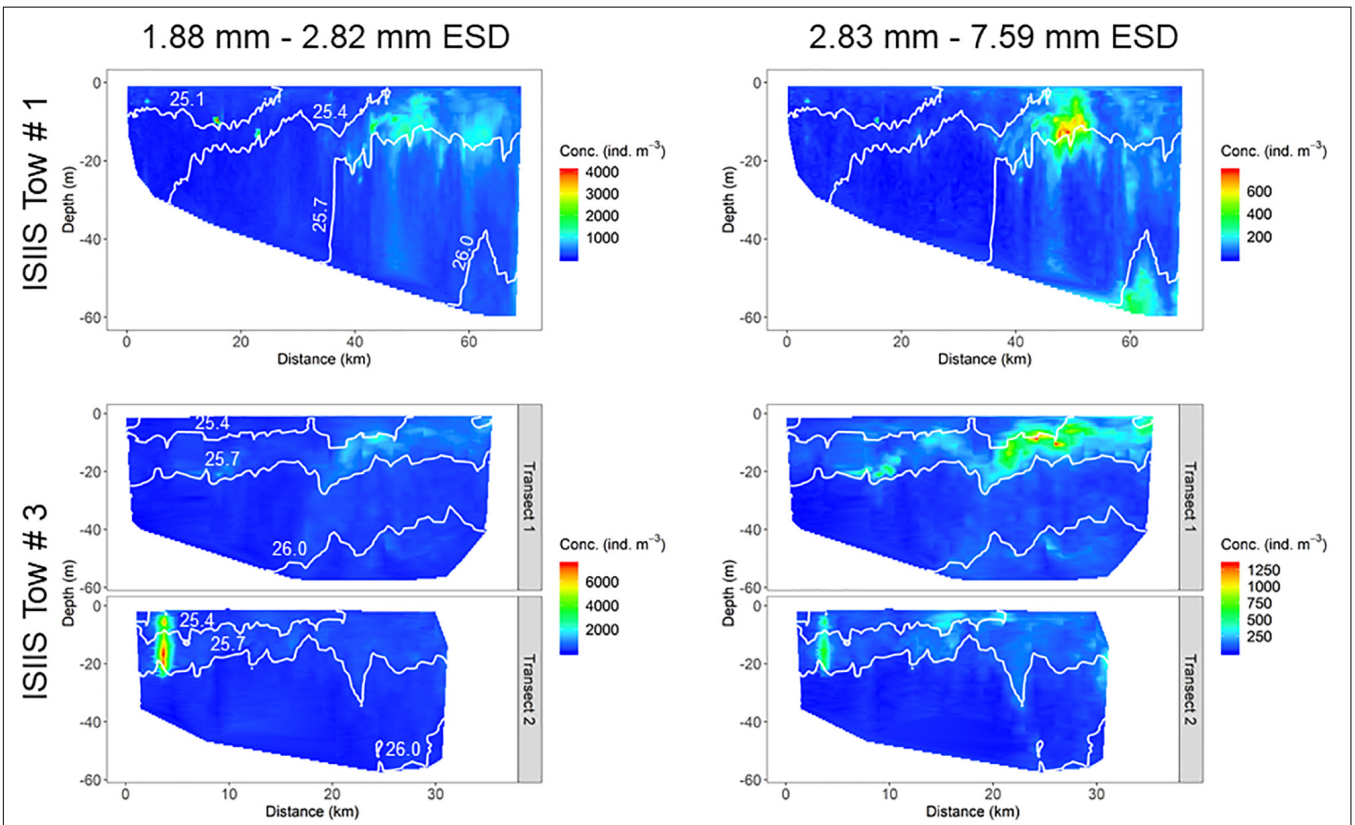

FIGURE 9 | Distribution of particles for two size classes from the ISIIS for both tows.

group of individuals in deeper waters that was absent in the smaller size class. ISIIS tow #3 abundances in the small size class were dominated by a patch of pteropod veligers in the inshore area of the tow on transect #2. The larger size class, although still represented in the dense patch on transect #2, tended to be abundant closer to the surface and further offshore compared to the smaller size class.

The physical conditions detected by the ISIIS instrumentation and the broader-scale observations suggested a biological response for different planktonic groups, as indicated by changes in abundances and distributions. Both ISIIS tows showed a predominance of organisms of all size classes residing within the shallowest 25 m of the water column, which also generally had higher concentrations of dissolved oxygen. For ISIIS tow #1, peak abundances formed around a distance of 40 km from the start of the transect (near I9), corresponding to an area where there was a transition from a water column with uniform salinity, to slightly higher salinities at depth (~33.3). Salinity peaked at ~60 km along the transect and corresponded spatially to a region with high abundances of large particles, including aggregations of juvenile sand lance (*Ammodytes* spp.) near the bottom (station I12). For ISIIS tow #3, aggregation of veligers occurred below a surface plume of fresher and warmer waters (transect #2), potentially originating from the mouth of Delaware

Bay. High concentrations of veligers were also detected near the surface during the "turn" between ISIIS transects #1 and #2 (data not shown), indicating their presence within the fresher surface waters. Another near surface zooplankton aggregation occurred from 20 to 30 km along transect #1, also associated with a surface plume of warmer and slightly fresher waters. This aggregation, however, contained a larger variety of planktonic organisms (mainly appendicularians and gelatinous organisms) and lower abundances of veligers. Similar to ISIIS tow #1, this patch was located just above the 1025.7 kg m^{-3} isopycnal.

Comparison of Imagery-Derived Abundances to Plankton Nets

The net samples captured similar broad-scale patterns in the plankton abundances relative to the imaging systems but with differing detected community compositions. Copepods were the most dominant taxa in all net samples, comprising 98.6–99.6% of the taxa in the inshore station (I5) and 47.5–60.4% of the offshore station (I12, **Table 2**) that bracketed ISIIS tow #1. The offshore net sample (I12) contained appendicularians, albeit in relatively low concentrations compared to the ISIIS where they composed 10-30% of all particles across size classes. All plankton taxa were most abundant in the deeper sample from the offshore station, with some groups, such as chaetognaths increasing by an order of magnitude or more. Net samples from ISIIS tow #3 showed more echinoderm larvae compared to the tow #1 samples. However, copepods were generally the most abundant group, comprising >75% of the taxa from the final station after ISIIS tow #3 was completed. The mean ESD of the individuals collected in the nets corresponded roughly to what was detected by the ISIIS small camera but also included sizes slightly smaller than the ISIIS can reliably identify (data not shown). The echinoderm larvae and pteropod veligers that were patchy (according to the ISIIS data) and common in this small size class were detected in variable abundances in the net samples, with patches in horizontal space possibly missed due to the lower station-based spatial resolution of the nets.

A direct comparison of the quantified size classes that overlapped between the two ISIIS cameras (1.88–2.37 mm ESD) on tow #3 revealed changes in detected abundances and degree of plankton aggregation (i.e., patchiness). Although fine-scale concentrations from both cameras were highly correlated (Spearman's $\rho = 0.767$), the large camera detected higher maximum concentrations compared to the small camera, and the aggregations qualitatively appeared to be more diffuse in the spatial distributions generated by the small camera (**Figures 10A,B**). The degree of spatial aggregation, described by the Lloyd's patchiness index (1 = random distribution of plankton) across different size classes, showed a steady increase in patchiness with increasing size. In the size ranges that overlapped between the two camera systems, the large camera tended to detect higher patchiness, although the small camera data did show a sharp increase in patchiness for the largest size class (2.27–2.37 mm ESD, **Figure 10C**). Patchiness tended to be more variable toward the less abundant larger sizes. These different spatial distributions and patchiness metrics may have been related to the detected plankton composition differences between the two cameras. For example, diatom chains were a much higher percentage of the composition in the small camera system (**Figure 8**).

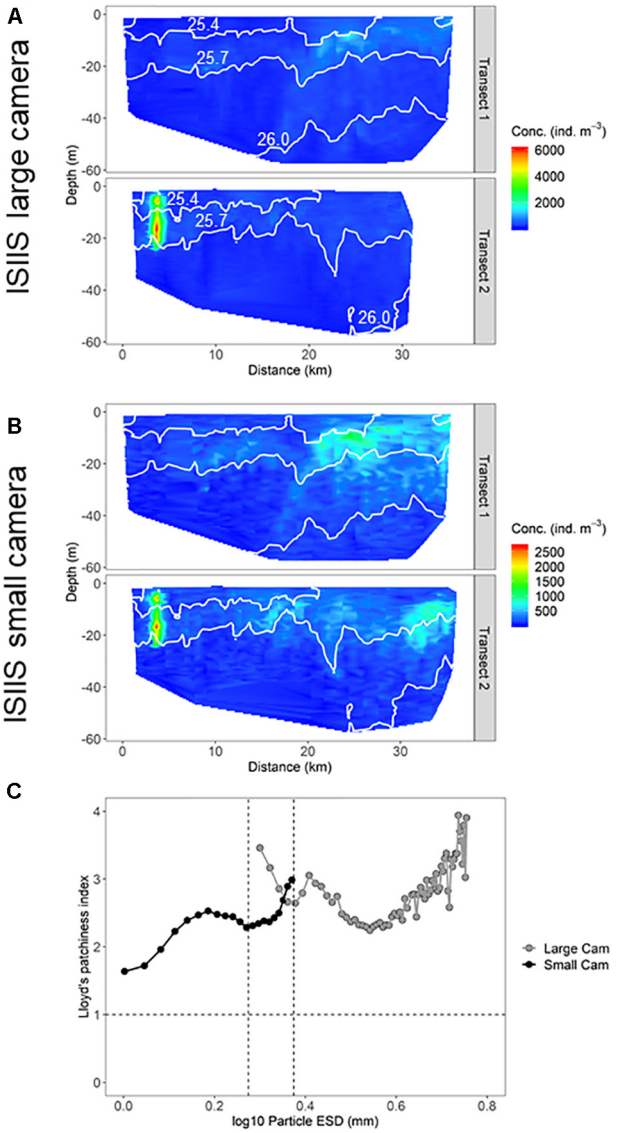

FIGURE 10 | Distribution of particles in the ISIIS **(A)** large and **(B)** small cameras that overlap in size (1.88–2.37 mm ESD). **(C)** Lloyd's patchiness index (random distribution = 1. Higher values indicate more patchiness.) for particles vs. size detected by the two cameras on the ISIIS. The two vertical dotted lines indicate the size range where the two cameras overlap.

Hydroacoustic Backscatter in Relation to Organisms Detected by the ISIIS

Acoustic data from the 18 and 38 kHz transducers indicated acoustic backscatter was relatively low inshore (<40 km along the transect, **Figure 11**). However, a thin scattering layer was consistently observed at 18 kHz between 10–15 m depth

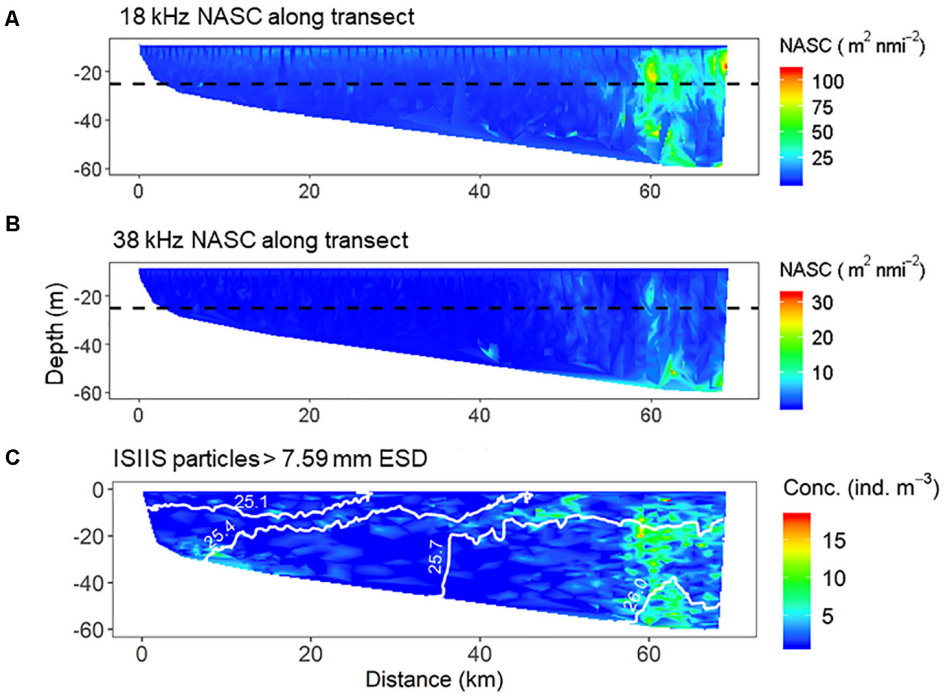

FIGURE 11 | Distribution of NASC (acoustic backscatter) for the **(A)** 18 kHz and **(B)** 38 kHz transducers. **(C)** Abundance of particles larger than 7.59 mm ESD as detected by the ISIIS along the same transect.

along the transect (ISIIS tow #1). Water column backscatter increased substantially beyond 50 km along the transect, and beyond 60 km, a strong scattering layer was observed at both 18 and 38 kHz extending from the seabed into the water column. These observations reflect the patterns observed in the ISIIS for the >7.59 mm ESD size class (dominated by gelatinous zooplankton), particularly the increased scattering in the 18 kHz echosounder and large particle abundance near the offshore end of the cross-shelf transect (**Figure 11C**). This high scattering region also corresponded to the highest detected zooplankton abundances in the nets (dominated by copepods). There was a significant positive correlation between the ISIIS particle abundance (>4.6 mm ESD) and NASC (Spearman's rank correlation coefficient, $\rho = 0.52$), but the relationship was weaker for the largest size organisms (>9.4 mm ESD) that were sampled more sporadically by the ISIIS (Spearman's $\rho = 0.37$).

Nutrient and Phytoplankton Concentration and Composition

Nitrate concentrations in surface waters from all 33 samples at stations examined during this study ranged from 0 to 4.6 mmol m^{-3}, with highest surface concentrations occurring at lowest salinity (28.6) near the coast. Generally, at intermediate salinities from 29.5 to 33, nitrate was near 0 in surface waters, whereas at surface salinity > 33, nitrate was approximately 2 mmol m^{-3}. Nitrate concentrations increased with depth. This pattern was observed at the stations at the beginning (station I5) and end (station I12) of ISIIS tow #1 (**Figure 12**). Nitrite concentrations (not shown) were, on average, about 10% of the nitrate and had a similar spatial pattern to the nitrate. Ammonium concentrations were also lower than nitrate and had similar spatial patterns (**Figure 12C**). Phosphate concentrations in surface waters ranged from 0.3 to 0.7 mmol m^{-3}, and silicate concentrations were between 0.4 and 4.3 mmol m^{-3}. At the beginning of ISIIS tow #1 at station I5, the surface layer chl-a concentration measured by HPLC was 0.8 mg m^{-3} (**Figure 12F**). At the end of ISIIS tow #1 at station I12, chl-a concentration was higher at 2.8 mg m^{-3}. Accompanying the increase in chl-a from I5 to I12, there was a shift in the dominant size fraction of the phytoplankton (**Figure 12**) as calculated from the HPLC pigment data and the size fraction equations of Uitz et al. (2006). Microplankton dominated at I5, comprising 52% of the chl-a but decreasing to 34% of the chl-a at I12. In contrast, nanoplankton comprised 36% of the chl-a at I5 but increased to 59% at I12. Picoplankton decreased from 13% of the chl-a at I5 to 7% at I12 (**Figure 12G**).

Taxonomically, phytoplankton biomass across the shelf was dominated by diatoms, representing, on average, 47% of the chl-a concentration (**Figure 12H**). Cryptophytes/nanoflagellates/chromophytes were the next most abundant group, representing an average of 35% of the chl-a concentration. The remainder of the phytoplankton biomass contained green flagellates/prochlorophytes (11%), dinoflagellates (6%), and cyanobacteria (1%).

DISCUSSION

By deploying several systems in the same shelf environment, and in some cases directly comparing the fine-scale spatial

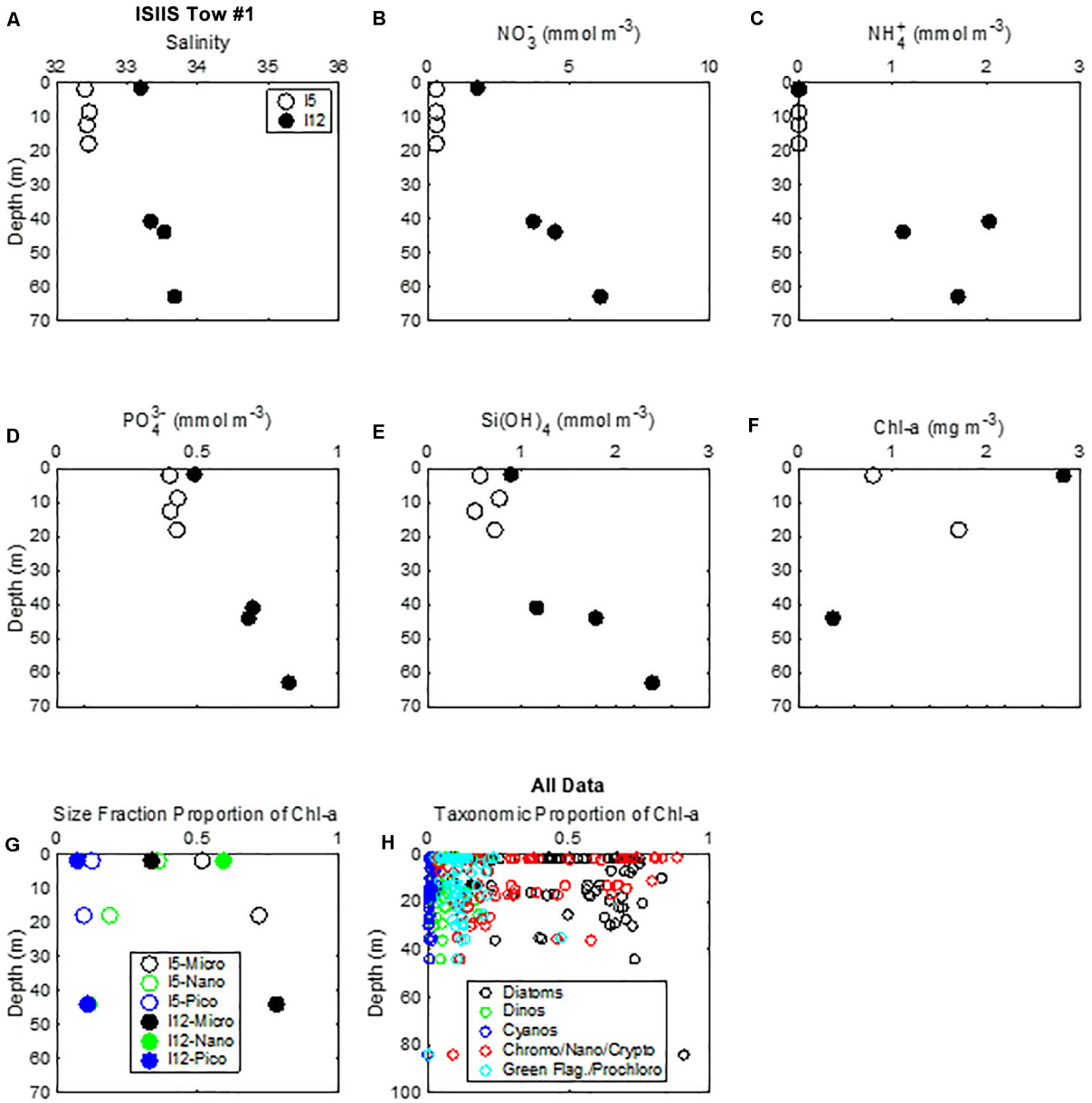

FIGURE 12 | Vertical distribution of **(A)** salinity, nutrients **(B)** nitrate, **(C)** ammonium, **(D)** phosphate, **(E)** silica), and **(F)** chlorophyll-a at the beginning and end of ISIIS tow #1. **(G)** Size fraction of chlorophyll-a for the same stations as the nutrients. **(H)** Total taxonomic proportion of chlorophyll-a determined by HPLC.

distribution and composition of similar size classes, we described detailed spatial patterns of an unprecedented size range of different organisms in connection to the physical oceanographic environment. The aggregations detected by the different systems were variable depending on organism size and composition. For the smallest size classes, aggregations of ciliates detected by the HOLOCAM were confined to a relatively narrow portion of the water column. For the smaller size classes captured by the ISIIS, dense aggregations were vertically dispersed, tended to cross isopycnals (e.g., pteropod veligers), and were associated with near surface fresher waters. Larger size classes tended to inhabit offshore water masses and were dominated by gelatinous zooplankton whose spatial distributions were tightly coupled to isopycnals. The acoustics detected a general trend toward higher backscatter further offshore where larger particles tended to reside in the ISIIS, and zooplankton abundances were generally higher in the net samples from this area. Although the samples encompass a relatively short time period, the instruments, combined, describe detailed environmental conditions for different taxa and size classes, while also providing new lessons for interpreting the size and composition data from imaging systems.

Influence of Sampling Method on Detected Abundances

Our evaluation of the imagery data demonstrated that, for systems that were directly comparable, the optical setup influenced the detected abundances, which supported our first hypothesis. Small changes in pixel resolution or sampling volume can also impact which organisms are detected, as demonstrated by the direct comparison between the ISIIS small and large cameras. The effect of pixel resolution was most apparent for the diatom chains imaged by the ISIIS; diatoms were quite rare in the large camera (59-μm pixel resolution) but became a majority of the segmented particles in the small camera (42-μm pixel resolution). These differences in diatom detection are likely related to their thin, chain-forming morphology – a trait that also influences their interactions with grazers (Kenitz et al., 2020). Diatom chains in the ISIIS images are typically only ∼1–3 pixels wide (50–150 μm) but can be >1 cm long. A slight increase in pixel resolution, therefore, effectively makes them double the number of pixels in area because their area is approximately equal to their perimeter. Such a dramatic increase in particle area from slight enhancement of pixel resolution would not occur with more round particles due to this simple fact of morphology. In other words, when particle thickness is a limiting factor for detection, small changes in pixel resolution can be the difference between particles being abundant or not detected at all. This should be considered for future studies utilizing automated image processing, as the perimeter to area ratio could indicate which particles may experience different detection rates under varied camera pixel resolutions and image processing settings. Diatoms were also relatively rare in the HOLOCAM imagery, probably due to relatively low abundances of diatoms at the particular station where the system was deployed (I15), as indicated by HPLC data from offshore sites, and the relatively small hologram volume relative to the ISIIS small camera images (∼3.7 mL per hologram and ∼165 mL per image, respectively).

The net samples served as a "ground-truth" for the imagery and showed copepods as the dominant zooplankton group for most stations (occasionally surpassed by echinoderm larvae), which appears to contrast strongly with the imagery data. The percent composition for copepods found at the stations greatly differed from that found in the ISIIS for the relevant size classes (maximum of 10 to 30% copepods). Although the trajectory of the ISIIS sampling differed from where the nets were deployed (in addition to the vast differences in spatial scale), a combination of the total particle abundance and the percent composition in the ISIIS compares favorably with the plankton nets. Because the copepods made up ∼30% of the organisms in the ISIIS from 1 mm to 3 mm ESD (**Figure 8**), and the mean concentration of organisms in that size range was ∼10,000 individuals m^{-3} mm^{-1} (**Figure 7**), that would correspond to ∼6,000 ind. m^{-3}, which is similar to copepod abundance found in the nets (water column average ranged from 1,000 to 9,000 ind. m^{-3}). Similar calculations for other taxa, however, would reveal stark differences, particularly for soft-bodied organisms. These discrepancies are likely due to biases of net systems toward robust zooplankton body compositions and against gelatinous organisms, which has been described previously using more thorough direct comparisons (e.g., Båmstedt et al., 2003; Remsen et al., 2004). The *relative* abundances of these fragile organisms in the net samples, however, did match the broad-scale patterns detected by the ISIIS (higher abundances offshore).

Even at relatively fast tow speeds (∼2.5 m s^{-1} for the ISIIS), avoidance behaviors likely explain some discrepancies in patchiness between the two cameras, as well as some consistencies in the percentage of unidentifiable organisms for different size classes. The composition of the plankton clearly shifted toward more gelatinous organisms for larger sizes. Surprisingly, the percentage of unknown organisms was relatively consistent across size classes for the large camera. With more pixels per object, larger particles should have a higher probability of identification to a "known" category. The reason for an "unknown" identification, however, appears to change with size. Larger particles, particularly shrimps and small fishes, have good swimming ability and sometimes attempt to avoid the imager (indicated by blurriness or an obvious startle response). Toward the larger end of the size spectrum, there is more avoidance, and toward the smaller size classes, the pixel resolution becomes the limiting factor, which generates a relatively consistent rate of unknowns across size classes. This hypothesis is further supported by the fact that the unknowns were less frequent in the smaller camera data (higher pixel resolution), particularly for the size classes that overlapped with the large camera. Along similar lines of thinking, organism avoidance could be one factor driving to the reduced patchiness detected by the small camera.

Persistent Hurdles for Assessing Size and Composition With Imagery

Organism body composition differences present a challenge for extraction (i.e., segmentation), identification, and sizing with imaging systems. Appendicularians were common across the size classes, and they are often surrounded by mucous "houses" that can collect marine snow aggregates on their surfaces. Because of the differences in pixel gray level between the organism body (dark) and the mucous house (faint), the body is often segmented alone. However, when the house contains marine snow aggregates, or the optical path goes through a particularly dark portion of the house, the mucous house may be segmented. We identified marine snow segments associated with a house and classified these as an "appendicularian house." This approach can artificially expand size range of "houses" because they are often detected after being discarded by the organism and in various stages of degradation. It is difficult to determine if segmentation was inaccurate when looking at individual segments, and it highlights the somewhat philosophical question of what constitutes the appropriate "size" of marine particles and organisms with complex morphologies. These "house" segments could also be classified as marine snow and, in fact, might be with automated image processing algorithms. The rate at which this error occurs, however, has not been systematically evaluated. One approach to mitigate the over-segmentation issue includes detecting and joining adjacent segments, which is effective for chains of diatom cells (e.g., Nayak et al., 2018),

yet in other contexts, this approach can introduce problems, such as determining the identification for a segment with more than one organism type present. More experimentation with segmentation algorithms and methods of classification is needed, particularly for closely associated organisms that are frequently detected when deploying *in situ* imaging systems (e.g., Möller et al., 2012; Takahashi et al., 2013; Greer et al., 2018).

Dense aggregations of organisms can also introduce errors with regards to measuring size and abundance [i.e., under-segmentation, see Greer et al. (2014) for an example regarding copepods]. Pteropod veligers were so highly concentrated that they were under-segmented within patches on ISIIS tow #3, but they were also abundant in other areas. This under-segmentation issue is directly related to the depth of field for the optical setup. For larger depths of field, which is necessary to have for quantifying rarer organisms, high concentrations of plankton will lead to increased probability of overlap in the images. Addressing the relationships between overlap probability, particle size, abundance, and depth of field should be examined through simulation, which would be useful for applying correction factors to size and abundance estimates (e.g., Luo et al., 2018). In some ecosystems, the overlap problem may not influence quantified abundances; however, evidence regarding this issue is elusive, as patchiness is only recently being described with the level of taxonomic and spatial detail needed to assess this kind of problem (Greer et al., 2016).

As automated algorithms continue to be applied to imagery datasets for examining taxonomic patterns (e.g., Faillettaz et al., 2016; Luo et al., 2018; Ellen et al., 2019), these hurdles for accurate analysis may be difficult to detect with typical validation workflows. The intensity of aggregations and rapid shifts in composition found in our study suggests that these issues with image processing deserve more attention. For the vast majority of studies utilizing plankton imagery, there is a size-detection threshold or specified size classes, and understanding general composition (i.e., dominance of diatom chains or appendicularians) is key for determining if these errors may influence detected patterns.

Relationships Between Biological and Physical Variables and Organism Distributions

There was a clear relationship between organism size and broad-scale (1–10 km) abundance that may have been related to the phytoplankton community structure. Chlorophyll-a and nutrients tended to be higher offshore near the shelf break, and the plankton community structure shifted between inshore and offshore stations. Other than fresher surface waters that were irregular and often connected to aggregations of zooplankton (e.g., pteropod veligers), temperature and salinity did not change dramatically across the shelf. The nearshore environment was dominated by microplankton, particularly diatoms (>50% of total composition), whereas the offshore zone was dominated by nanoplankton (non-diatom) size fraction (>50% of total composition). In relation to this pattern, there were substantial changes in the size classes of zooplankton represented in the imagery, which were related to the taxonomic composition (larger sizes tended to include more gelatinous organisms). The offshore region with more nanoplankton had large numbers of gelatinous zooplankton, including appendicularians, and the inshore region tended to have patches of hard-bodied zooplankton and generally smaller-sized organisms relative to offshore. The net samples, although few in number, reflected this broad-scale pattern in that more appendicularians and hydromedusae were captured offshore.

While the phytoplankton community may have influenced some of the larger scale patterns of zooplankton abundance, the *in situ* imagery showed that organism distributions had differing spatial relationships to physical oceanographic structure, depending on both size and body composition. Thus, the support for our second hypothesis, that organism aggregations would occur at density gradients, was mixed. Locally high abundances, particularly for the larger size classes of organisms, were often just above the 1025.7 kg m^{-3} isopycnal for both ISIIS tows (**Figure 9**). These results are consistent with other high-resolution observations of gelatinous organisms, which dominated the larger size classes and can display tight spatial correlation with certain isotherms or isopycnals (e.g., Jacobsen and Norrbin, 2009; Frost et al., 2010; Luo et al., 2014; Suzuki et al., 2018). Patches of hard-bodied zooplankton, on the other hand, can show similar coupling to isopycnals (Möller et al., 2012) or be relatively untethered to physical discontinuities in the water column (Baumgartner et al., 2013; Greer et al., 2014). Further inshore on May 1 (ISIIS tow #3), the large aggregation of pteropod veligers (most apparent in the smaller size classes) was perpendicular to the isopycnal trajectory, but was associated with the edge of a fresher water parcel near the surface. High abundances of veligers were also imaged within these fresher waters while turning the ISIIS near the surface (data not shown). Although few high-resolution observations of pteropods exist, Gallager et al. (1996) found that pteropods concentrated near the center of the water parcels, rather than near water parcel boundaries. This pattern is generally consistent with our findings: gelatinous organisms aggregated near the physical transitions, while the pteropod veligers did not appear to have the same affinities for water mass boundaries or isopycnals. Although the precise ecological interactions producing these distributions are not known, controlled experiments offer promise for resolving interactions between size- or taxon-specific zooplankton behavior and the entrained prey communities near density discontinuities (e.g., True et al., 2018).

Fine-scale acoustic backscatter showed strong spatial overlap with the abundances of large organisms detected by the ISIIS, especially beyond ∼50 m depth. However, the majority of organisms observed by the ISIIS in this size category (i.e., gelatinous) are not likely to be significant sources of backscatter at 18 and 38 kHz. Hydroacoustic surveys conducted with similar frequencies to the ones used in this study can detect small fishes and siphonophores, which have gas-filled body parts (Proud et al., 2019), and post-processing techniques can be used to classify distinct taxonomic groups (e.g., fishes with and without swim bladders, crustaceans, etc.) based on their unique frequency-dependent response (Jech and Michaels, 2006; De Robertis et al., 2010; McQuinn et al., 2013; D'Elia et al., 2016). According the subsample of the largest imaged organisms,

juvenile fishes (*Ammodytes* spp.) were confined to the deeper waters offshore and could have produced some portion of the acoustic backscatter. Approximately 2.3% of the organisms in the largest size class (>5.57 mm ESD) were siphonophores, including many from the genus *Nanomia*, which have pneumatophores that contribute to acoustic backscatter (Davison et al., 2015). The siphonophores were slightly more common than the fishes that comprised 1.6% of this size class. It seems likely, based on the concentration of the large particles offshore, that fishes and larger gelatinous organisms are spatially co-located, implying that more detailed analyses are required to determine the contribution of different taxa to the acoustic backscatter. In other instances, however, avoidance of the ISIIS by potential scatterers (e.g., fishes >5 cm) may prohibit robust identifications of the contributors to acoustic backscatter at the frequencies used in this study. Determining the identity of the scatters is particularly difficult when multiple target organisms are present (Stanton, 2012; Wiebe et al., 2017) and capable of movement throughout the water column with changing orientation depending on their ecology and environmental cues (Benfield et al., 2000; Parra et al., 2019; Boswell et al., 2020).

CONCLUSION

With the increasing use of high-frequency sampling systems to understand how organisms aggregate in the ocean, it is important to consider which organisms or patterns are sampled quantitatively with a particular sampling technology. Depending on the actual organism taxonomic composition, concentrations, and the tow speed or optical setup, a system can produce misleading results. Although imaging systems detect fine-scale patterns for fragile and hard-bodied zooplankton, there are many caveats with the relationship between detected size and organism morphology that are also influenced by the optical properties of the system. Deploying multiple high-resolution systems showed size-dependent patterns that differed in their associations with the physical oceanographic conditions. This intense patchiness likely has implications for the ecology of the planktonic groups examined here, but these relatively new technologies are just scraping the surface of what remains to be discovered. Our approach allowed us to better understand the strengths and weaknesses of each system in terms of what kinds of patterns they can detect, but more thorough evaluations of sampling tradeoffs among systems are still needed. Achieving this goal of understanding these quantitative samplers is critical for assimilating zooplankton data into ecological models (Everett et al., 2017).

Walter Munk referred to the state of oceanography in the 20th century as the "century of undersampling" (Munk, 2000). Although he was mostly referring to the lack of spatiotemporal resolution for various physical processes, the same or more extreme statements could be made about the previous century of sampling the ocean's biological constituents. High-resolution biological sampling in coastal, open ocean, and within the context of global surveys is now possible across a range of size classes, including both hard- and soft-bodied zooplankton (Lombard et al., 2019). Characterizing the distributions and properties of these organisms or particles has many implications for the functioning of trophic food webs (Heneghan et al., 2016; Everett et al., 2017) and the global biological pump (Guidi et al., 2016; Fender et al., 2019). Future deployments of these systems, along with a robust evaluation of the sampling trade-offs, will increase their utility for describing critical biological processes and understanding how these systems may operate together to "see" previously unresolvable phenomena.

DATA AVAILABILITY STATEMENT

The raw data supporting the conclusions of this manuscript will be made available by the authors, without undue reservation, to any qualified researcher.

AUTHOR CONTRIBUTIONS

AG collected the ISIIS data, analyzed the data, and wrote the manuscript. JL analyzed the Niskin bottle samples, wrote relevant sections, and edited the manuscript. BB collected and analyzed the acoustic backscatter data and wrote relevant sections. AN collected and analyzed the HOLOCAM data, wrote relevant sections, and edited the manuscript. RB analyzed HOLOCAM data and edited the manuscript. AR designed the field study, analyzed physical oceanographic data, and edited the manuscript. JC analyzed the plankton net data, wrote relevant sections, and edited the manuscript. MM collected the HOLOCAM data and edited the manuscript. AH collected the Niskin bottle samples, analyzed the phytoplankton and nutrient data, and edited the manuscript. NS collected the HOLOCAM data and edited the manuscript. KB analyzed the acoustic data and edited the manuscript. IS analyzed the HF radar data and physical oceanographic data and edited the manuscript. SR analyzed physical data and edited the manuscript. BP designed the field study, coordinated ship data collection efforts, analyzed CytoSense data, wrote relevant sections, and edited the manuscript. All authors contributed to the article and approved the submitted version.

FUNDING

This research was funded by the Naval Research Laboratory project InTro: Intermediate Trophic Levels - Interconnections with Fronts, Eddies and Primary Production (Program Element 61153N). The holographic data collection and processing efforts were also supported by NSF grants OCE-1634053 and OCE-1657332.

ACKNOWLEDGMENTS

We would like to thank the captain and crew of the *RV Hugh R. Sharp*. Stephanie Anderson assisted in generating some of the figures. Ian Martens supported all aspects of cruise

logistics and was instrumental in making for a successful field sampling expedition. Frank Hernandez provided guidance with the identification of the juvenile fish imaged by the ISIIS. We would also like to thank Laura Treible and two reviewers who provided thorough comments and edits that helped improve this manuscript.

REFERENCES

Akima, H., and Gebhardt, A. (2016). *Akima: Interpolation of Irregularly and Regularly Spaced Data*.

Andersen, K. H., Berge, T., Goncalves, R. J., Hartvig, M., Heuschele, J., Hylander, S., et al. (2016). Characteristic sizes of life in the oceans, from bacteria to whales. *Annu. Rev. Mar. Sci.* 8, 217–241. doi: 10.1146/annurev-marine-122414-034144

Båmstedt, U., Kaartvedt, S., and Youngbluth, M. (2003). An evaluation of acoustic and video methods to estimate the abundance and vertical distribution of jellyfish. *J. Plankton Res.* 25, 1307–1318. doi: 10.1093/plankt/fbg084

Baumgartner, M. F., Lysiak, N. S. J., Esch, H. C., Zerbini, A. N., Berchok, C. L., and Clapham, P. J. (2013). Associations between North Pacific right whales and their zooplanktonic prey in the southeastern Bering Sea. *Mar. Ecol. Prog. Ser.* 490, 267–284. doi: 10.3354/meps10457

Benfield, M. C., Davis, C. S., and Gallager, S. M. (2000). Estimating the in-situ orientation of *Calanus finmarchicus* on Georges Bank using the Video Plankton Recorder. *Plankton Biol. Ecol.* 47, 69–72.

Benoit-Bird, K. J., and McManus, M. A. (2012). Bottom-up regulation of a pelagic community through spatial aggregations. *Biol. Lett.* 8, 813–816. doi: 10.1098/rsbl.2012.0232

Bez, N. (2000). On the use of Lloyd's index of patchiness. *Fish. Oceanogr.* 9, 372–376. doi: 10.1046/j.1365-2419.2000.00148.x

Biard, T., Stemmann, L., Picheral, M., Mayot, N., Vandromme, P., Hauss, H., et al. (2016). In situ imaging reveals the biomass of giant protists in the global ocean. *Nature* 532, 504–507. doi: 10.1038/nature17652

Blanchard, J. L., Heneghan, R. F., Everett, J. D., Trebilco, R., and Richardson, A. J. (2017). From bacteria to whales: using functional size spectra to model marine ecosystems. *Trends Ecol. Evol.* 32, 174–186. doi: 10.1016/j.tree.2016.12.003

Boswell, K. M., D'Elia, M., Johnston, M. W., Mohan, J. A., Warren, J. D., Wells, R. J., et al. (2020). Oceanographic structure and light levels drive patterns of sound scattering layers in a low-latitude oceanic system. *Front. Mar. Sci* 7:51. doi: 10.3389/fmars.2020.00051

Broughton, E. A., and Lough, R. G. (2006). A direct comparison of MOCNESS and Video Plankton Recorder zooplankton abundance estimates: Possible applications for augmenting net sampling with video systems. *Deep Sea Res. II* 53, 2789–2807. doi: 10.1016/j.dsr2.2006.08.013

Buskey, E. J., Baker, K. S., Smith, R. C., and Swift, E. (1989). Photosensitivity of the oceanic copepods Pleuromamma gracilis and Pleuromamma xiphias and its relationship to light penetration and daytime depth distribution. *Mar. Ecol. Prog. Ser.* 55, 207–216. doi: 10.3354/meps055207

Conley, K. R., Lombard, F., and Sutherland, K. R. (2018). Mammoth grazers on the ocean's minuteness: a review of selective feeding using mucous meshes. *Proc. R. Soc. B-Biol. Sci.* 285:20180056. doi: 10.1098/rspb.2018.0056

Cowen, R. K., Greer, A. T., Guigand, C. M., Hare, J. A., Richardson, D. E., and Walsh, H. J. (2013). Evaluation of the *In Situ* Ichthyoplankton Imaging System (ISIIS): comparison with the traditional (bongo net) sampler. *Fish. Bull.* 111, 1–12. doi: 10.7755/FB.111.1.1

Cowen, R. K., and Guigand, C. M. (2008). *In situ* ichthyoplankton imaging system (ISIIS): system design and preliminary results. *Limnol. Oceanogr. Methods* 6, 126–132. doi: 10.4319/lom.2008.6.126

Dadon-Pilosof, A., Lombard, F., Genin, A., Sutherland, K. R., and Yahel, G. (2019). Prey taxonomy rather than size determines salp diets. *Limnol. Oceanogr.* 64, 1996–2010. doi: 10.1002/lno.11165

Davis, C. S., and McGillicuddy, D. J. Jr. (2006). Transatlantic abundance of the N2-fixing colonial cyanobacterium Trichodesmium. *Science* 312, 1517–1520. doi: 10.1126/science.1123570

Davis, C. S., Thwaites, F. T., Gallager, S. M., and Hu, Q. (2005). A three-axis fast-tow digital Video Plankton Recorder for rapid surveys of plankton taxa and hydrography. *Limnol. Oceanogr. Methods* 3, 59–74. doi: 10.4319/lom.2005.3.59

Davison, P. C., Koslow, J. A., and Kloser, R. J. (2015). Acoustic biomass estimation of mesopelagic fish: backscattering from individuals, populations, and communities. *ICES J. Mar. Sci.* 72, 1413–1424. doi: 10.1093/icesjms/fsv023

De Robertis, A., McKelvey, D. R., and Ressler, P. H. (2010). Development and application of an empirical multifrequency method for backscatter classification. *Can. J. Fish. Aquat. Sci.* 67, 1459–1474. doi: 10.1139/F10-075

D'Elia, M., Warren, J. D., Rodriguez-Pinto, I., Sutton, T. T., Cook, A., and Boswell, K. M. (2016). Diel variation in the vertical distribution of deep-water scattering layers in the Gulf of Mexico. *Deep-Sea Res. Part I-Oceanogr. Res. Pap* 115, 91–102. doi: 10.1016/j.dsr.2016.05.014

Demer, D. A., Berger, L., Bernasconi, M., Bethke, E., Boswell, K., Chu, D., et al. (2015). Calibration of acoustic instruments. *ICES Cooperat. Res. Rep.* 326:133.

Ellen, J. S., Graff, C. A., and Ohman, M. D. (2019). Improving plankton image classification using context metadata. *Limnol. Ocenogr. Methods* 17, 439–461. doi: 10.1002/lom3.10324

Everett, J. D., Baird, M. E., Buchanan, P., Bulman, C., Davies, C., Downie, R., et al. (2017). Modeling what we sample and sampling what we model: challenges for zooplankton model assessment. *Front. Mar. Sci* 4:77. doi: 10.3389/fmars.2017.00077

Faillettaz, R., Picheral, M., Luo, J. Y., Guigand, C., Cowen, R. K., and Irisson, J. (2016). Imperfect automatic image classification successfully describes plankton distribution patterns. *Methods Oceanogr.* 15-16, 60–77. doi: 10.1016/j.mio.2016.04.003

Fender, C. K., Kelly, T. B., Guidi, L., Ohman, M. D., Smith, M. C., and Stukel, M. R. (2019). Investigating particle size-flux relationships and the biological pump across a range of plankton ecosystem states from coastal to oligotrophic. *Front. Mar. Sci.* 6:603. doi: 10.3389/fmars.2019.00603

Feunteun, A., de Schrevel, C., Verhaegen, M., Chevallier, D., Duchemin, M., Ziani, N., et al. (2018). First evaluation of the cookie-cutter sharks (Isistius sp.) predation pattern on different cetacean species in Martinique. *Environ. Biol. Fishes* 101, 749–759. doi: 10.1007/s10641-018-0735-1

Frost, J. R., Jacoby, C. A., and Youngbluth, M. J. (2010). Behavior of *Nemopsis bachei* L. Agassiz, 1849 medusae in the presence of physical gradients and biological thin layers. *Hydrobiologia* 645, 97–111. doi: 10.1007/s10750-010-0213-z

Gallager, S. M., Davis, C. S., Epstein, A. W., Solow, A., and Beardsley, R. C. (1996). High-resolution observations of plankton spatial distributions correlated with hydrography in the Great South Channel. Georges Bank. *Deep Sea Res. Part II Top. Stud. Oceanogr.* 43, 1627–1663. doi: 10.1016/s0967-0645(96)00058-6

Giering, S. L. C., Hosking, B., Briggs, N., and Iversen, M. H. (2020). The interpretation of particle size, shape, and carbon flux of marine particle images is strongly affected by the choice of particle detection algorithm. *Front. Mar. Sci* 7:564. doi: 10.3389/fmars.2020.00564

Gorsky, G., Ohman, M. D., Picheral, M., Gasparini, S., Stemmann, L., and Romagnan, J. B. (2010). Digital zooplankton image analysis using the ZooScan integrated system. *J. Plankton Res.* 32, 285–303. doi: 10.1093/plankt/fbp124

Greer, A. T., Chiaverano, L. M., Luo, J. Y., Cowen, R. K., and Graham, W. M. (2018). Ecology and behaviour of holoplanktonic scyphomedusae and their interactions with larval and juvenile fishes in the northern Gulf of Mexico. *ICES J. Mar. Sci.* 75, 751–763. doi: 10.1093/icesjms/fsx168

Greer, A. T., Cowen, R. K., Guigand, C. M., Hare, J. A., and Tang, D. (2014). The role of internal waves in larval fish interactions with potential predators and prey. *Prog. Oceanogr.* 127, 47–61. doi: 10.1016/j.pocean.2014.05.010

Greer, A. T., Woodson, C. B., Smith, C. E., Guigand, C. M., and Cowen, R. K. (2016). Examining mesozooplankton patch structure and its implications for trophic interactions in the northern Gulf of Mexico. *J. Plankton Res.* 38, 1115–1134. doi: 10.1093/plankt/fbw033

Guidi, L., Chaffron, S., Bittner, L., Eveillard, D., Larhlimi, A., Roux, S., et al. (2016). Plankton networks driving carbon export in the oligotrophic ocean. *Nature* 532:465. doi: 10.1038/nature16942

Heneghan, R. F., Everett, J. D., Blanchard, J. L., and Richardson, A. J. (2016). Zooplankton are not fish: improving zooplankton realism in size-spectrum models mediates energy transfer in food webs. *Front. Mar. Sci* 3:201. doi: 10.3389/fmars.2016.00201

Henschke, N., Everett, J. D., Richardson, A. J., and Suthers, I. M. (2016). Rethinking the role of salps in the ocean. *Trends Ecol. Evol.* 31, 720–733. doi: 10.1016/j.tree.2016.06.007

Hooker, S. B., Heukelem, L., Thomas, C., Claustre, H., Ras, J., Barlow, R., et al. (2005). The second SeaWiFS HPLC analysis round-robin experiment (SeaHARRE-2). *NASA Tech. Mem.* 1–112.

Hoving, H., Christiansen, S., Fabrizius, E., Hauss, H., Kiko, R., Linke, P., et al. (2019). The pelagic in situ observation system (PELAGIOS) to reveal biodiversity, behavior, and ecology of elusive oceanic fauna. *Ocean Sci.* 15, 1327–1340. doi: 10.5194/os-15-1327-2019

Jacobsen, H. P., and Norrbin, M. F. (2009). Fine-scale layer of hydromedusae is revealed by Video Plankton Recorder (VPR) in a semi-enclosed bay in northern Norway. *Mar. Ecol. Prog. Ser.* 380, 129–135. doi: 10.3354/meps07954

Jech, J. M., and Michaels, W. L. (2006). A multifrequency method to classify and evaluate fisheries acoustics data. *Can. J. Fish. Aquat. Sci.* 63, 2225–2235. doi: 10.1139/F06-126

Jennings, S., Pinnegar, J., Polunin, N., and Boon, T. (2001). Weak cross-species relationships between body size and trophic level belie powerful size-based trophic structuring in fish communities. *J. Anim. Ecol.* 70, 934–944. doi: 10.1046/j.0021-8790.2001.00552.x

Katz, J., and Sheng, J. (2010). Applications of holography in fluid mechanics and particle dynamics. *Annu. Rev. Fluid Mech.* 42, 531–555. doi: 10.1146/annurev-fluid-121108-145508

Kelley, D., Richards, C., and WG127 S. (2017). *gsw: Gibbs Sea Water Functions*. Available online at: https://CRAN.R-project.org/package=gsw.

Kenitz, K. M., Orenstein, E. C., Roberts, P. L. D., Franks, P. J. S., Jaffe, J. S., Carter, M. L., et al. (2020). Environmental drivers of population variability in colony-forming marine diatoms. *Limnol. Oceanogr.* 65, 2515-2528. doi: 10.1002/lno.11468

Kiørboe, T. (2008). *A Mechanistic Approach to Plankton Ecology*. Princeton: Princeton University Press.

Kiørboe, T., Visser, A. P., and Andersen, K. H. (2018). A trait-based approach to ocean ecology. *ICES J. Mar. Sci.* 75, 1849–1863. doi: 10.1093/icesjms/fsy090

Korneliussen, R. J., Diner, N., Ona, E., Berger, L., and Fernandes, P. G. (2008). Proposals for the collection of multifrequency acoustic data. *ICES J. Mar. Sci* 65, 982–994. doi: 10.1093/icesjms/fsn052

Koslow, J. A. (2009). The role of acoustics in ecosystem-based fishery management. *ICES J. Mar. Sci.* 66, 966–973. doi: 10.1093/icesjms/fsp082

Letcher, B. H., and Rice, J. A. (1997). Prey patchiness and larval fish growth and survival: inferences from an individual-based model. *Ecol. Model.* 95, 29–43. doi: 10.1016/s0304-3800(96)00015-4

Lombard, F., Boss, E., Waite, A. M., Vogt, M., Uitz, J., Stemmann, L., et al. (2019). Globally consistent quantitative observations of planktonic ecosystems. *Front. Mar. Sci.* 6:196. doi: 10.3119/fmars.2019.00196

Luo, J. Y., Grassian, B., Tang, D., Irisson, J. O., Greer, A. T., Guigand, C. M., et al. (2014). Environmental drivers of the fine-scale distribution of a gelatinous zooplankton community across a mesoscale front. *Mar. Ecol. Prog. Ser.* 510, 129–149. doi: 10.3354/meps10908

Luo, J. Y., Irisson, J. O., Graham, B., Guigand, C., Sarafraz, A., Mader, C., et al. (2018). Automated plankton image analysis using convolutional neural networks. *Limnol. Oceanogr. Methods.* 16, 814–827. doi: 10.1002/lom3.10285

McQuinn, I. H., Dion, M., and St Pierre, J. F. (2013). The acoustic multifrequency classification of two sympatric euphausiid species (*Meganyctiphanes norvegica* and *Thysanoessa raschii*), with empirical and SDWBA model validation. *ICES J. Mar. Sci.* 70, 636–649. doi: 10.1093/icesjms/fst004

Möller, K. O., St John, M., Temming, A., Floeter, J., Sell, A. F., Herrmann, J., et al. (2012). Marine snow, zooplankton and thin layers: indications of a trophic link from small-scale sampling with the Video Plankton Recorder. *Mar. Ecol. Prog. Ser.* 468, 57–69. doi: 10.3354/meps09984

Moore, T. S., Churnside, J. H., Sullivan, J. M., Twardowski, M. S., Nayak, A. R., McFarland, M. N., et al. (2019). Vertical distributions of blooming cyanobacteria populations in a freshwater lake from LIDAR observations. *Remote Sens. Environ.* 225, 347–367. doi: 10.1016/j.rse.2019.02.025

Munk, W. (2000). Oceanography before, and after, the advent of satellites. *Elsevier Oceanogr. Ser.* 63, 1–4. doi: 10.1016/S0422-9894(00)80002-1

Nayak, A. R., McFarland, M. N., Sullivan, J. M., and Twardowski, M. S. (2018). Evidence for ubiquitous preferential particle orientation in representative oceanic shear flows. *Limnol. Oceanogr.* 63, 122–143. doi: 10.1002/lno.10618

Ohman, M. D., Davis, R. E., Sherman, J. T., Grindley, K. R., Whitmore, B. M., Nickels, C. F., et al. (2019). Zooglider: an autonomous vehicle for optical and acoustic sensing of zooplankton. *Limnol. Oceanogr. Methods* 17, 69–86. doi: 10.1002/lom3.10301

Parra, S. M., Greer, A. T., Book, J. W., Deary, A. L., Soto, I. M., Culpepper, C., et al. (2019). Acoustic detection of zooplankton diel vertical migration behaviors on the northern Gulf of Mexico shelf. *Limnol. Oceanogr.* 64, 2092–2113. doi: 10.1002/lno.11171

Peacock, E. E., Olson, R. J., and Sosik, H. M. (2014). Parasitic infection of the diatom Guinardia delicatula, a recurrent and ecologically important phenomenon on the New England Shelf. *Mar. Ecol. Prog. Ser.* 503, 1–10. doi: 10.3354/meps10784

Picheral, M., Guidi, L., Stemmann, L., Karl, D. M., Iddaoud, G., and Gorsky, G. (2010). The Underwater Vision Profiler 5: an advanced instrument for high spatial resolution studies of particle size spectra and zooplankton. *Limnol. Oceanogr. Methods* 8, 462–473. doi: 10.4319/lom.2010.8.462

Priyadarshi, A., Smith, S. L., Mandal, S., Tanaka, M., and Yamazaki, H. (2019). Micro-scale patchiness enhances trophic transfer efficiency and potential plankton biodiversity. *Sci. Rep.* 9:17243. doi: 10.1038/s41598-019-53592-6

Proud R., Handegard, N. O., Kloser, R. J., Cox, M. J., and Brierley, A. S. (2019). From siphonophores to deep scattering layers: uncertainty ranges for the estimation of global mesopelagic fish biomass. *ICES J. Mar. Sci.* 76, 718–733. doi: 10.1093/icesjms/fsy037

Remsen, A., Hopkins, T. L., and Samson, S. (2004). What you see is not what you catch: a comparison of concurrently collected net, Optical Plankton Counter, and Shadowed Image Particle Profiling Evaluation Recorder data from the northeast Gulf of Mexico. *Deep-Sea Res. Part I-Oceanogr. Res. Pap.* 51, 129–151. doi: 10.1016/j.dsr.2003.09.008

Samson, S., Hopkins, T., Remsen, A., Langebrake, L., Sutton, T., and Patten, J. (2001). A system for high-resolution zooplankton imaging. *IEEE J. Ocean. Eng.* 26, 671–676. doi: 10.1109/48.972110

Sanders, T., and Garvine, R. (2001). Fresh water delivery to the continental shelf and subsequent mixing: an observational study. *J. Geophys. Res. Oceans* 106, 27087–27101. doi: 10.1029/2001JC000802

Schmid, M. S., Cowen, R. K., Robinson, K., Luo, J. Y., Briseño-Avena, C., and Sponaugle, S. (2020). Prey and predator overlap at the edge of a mesoscale eddy: fine-scale, in-situ distributions to inform our understanding of oceanographic processes. *Sci. Rep.* 10:921. doi: 10.1038/s41598-020-57879-x

Schnars, U., and Jueptner, W. (2005). *Digital Holography*, 1st edn. New York, NY: Springer.

Schneider, C. A., Rasband, W. S., and Eliceiri, K. W. (2012). NIH Image to ImageJ: 25 years of image analysis. *Nat. Methods* 9, 671–675. doi: 10.1038/nmeth.2089

Sevadjian, J. C., McManus, M. A., Ryan, J., Greer, A. T., Cowen, R. K., and Woodson, C. B. (2014). Across-shore variability in plankton layering and abundance associated with physical forcing in Monterey Bay, California. *Cont. Shelf Res.* 72, 138–151. doi: 10.1016/j.csr.2013.09.018

Simmonds, J., and MacLennan, D. (2005). *Observation and Measurement of Fish: Fisheries Acoustics: Theory and Practice*. Hoboken, NJ: Wiley.

Skjoldal, H. R., Wiebe, P. H., Postel, L., Knutsen, T., Kaartvedt, S., and Sameoto, D. D. (2013). Intercomparison of zooplankton (net) sampling systems: results from the ICES/GLOBEC sea-going workshop. *Prog. Oceanogr.* 108, 1–42. doi: 10.1016/j.pocean.2012.10.006

Stanton, T. K. (2012). 30 years of advances in active bioacoustics: a personal perspective. *Methods Oceanogr.* 1-2, 49–77. doi: 10.1016/j.mio.2012.07.002

Sutherland, K. R., Madin, L. P., and Stocker, R. (2010). Filtration of submicrometer particles by pelagic tunicates. *Proc. Natl. Acad. Sci. U.S.A.* 107, 15129–15134. doi: 10.1073/pnas.1003599107

Suzuki, K. S., Niida, Y., Tsubono, T., Takimoto, H., Kumakura, E., Ishii, H., et al. (2018). Mechanisms underlying heterogeneous distribution of moon jellyfish *Aurelia aurita* s.l. across a sharp pycnocline. *Mar. Ecol. Prog. Ser.* 591, 229–239. doi: 10.3354/meps12357

Takahashi, K., Ichikawa, T., Saito, H., Kakehi, S., Sugimoto, Y., Hidaka, K., et al. (2013). Sapphirinid copepods as predators of doliolids: their role in doliolid mortality and sinking flux. *Limnol. Oceanogr.* 58, 1972–1984. doi: 10.4319/lo.2013.58.6.1972

Trevorrow, M. V., Mackas, D. L., and Benfield, M. C. (2005). Comparison of multifrequency acoustic and in situ measurements of zooplankton abundances

in Knight Inlet, British Columbia. *J. Acoust. Soc. Am.* 117, 3574–3588. doi: 10.1121/1.1920087

True, A. C., Webster, D. R., Weissburg, M. J., and Yen, J. (2018). Copepod avoidance of thin chemical layers of harmful algal compounds. *Limnol. Oceanogr.* 63, 1041–1055. doi: 10.1002/lno.10752

Uitz, J., Claustre, H., Morel, A., and Hooker, S. B. (2006). Vertical distribution of phytoplankton communities in open ocean: an assessment based on surface chlorophyll. *J. Geophys. Res. -Oceans* 111:C08005. doi: 10.1029/2005JC003207

Vikram, C. (1992). *Particle Field Holography*, 1st edn. Cambridge: Cambridge University Press.

Wakabayashi, K., Sato, R., Hirai, A., Ishii, H., Akiba, T., and Tanaka, Y. (2012). Predation by the phyllosoma larva of *Ibacus novemdentatus* on various kinds of venomous jellyfish. *Biol. Bull.* 222, 1–5. doi: 10.1086/bblv222n1p1

Whitmore, B. M., Nickels, C. E., and Ohman, M. D. (2019). A comparison between Zooglider and shipboard net and acoustic mesozooplankton sensing systems. *J. Plankton Res.* 41, 521–533. doi: 10.1093/plankt/fbz033

Whitney, M., and Garvine, R. (2006). Simulating the Delaware Bay buoyant outflow: comparison with observations. *J. Phys. Oceanogr.* 36, 3–21. doi: 10.1175/JPO2805.1

Wickham, H. (2016). *ggplot2: Elegant graphics for data analysis*. New York, NY: Springer-Verlag.

Wiebe, P. H., and Benfield, M. C. (2003). From the Hensen net toward four-dimensional biological oceanography. *Prog. Oceanogr.* 56, 7–136. doi: 10.1016/s0079-6611(02)00140-4

Wiebe, P. H., Bucklin, A., and Benfield, M. C. (2017). "Sampling, preservation and counting of samples II: Zooplankton," in *Marine Plankton*, eds C. Castellani and M. Edwards (Oxford: Oxford University Press), 104–135.

Woodson, C. B., and Litvin, S. Y. (2015). Ocean fronts drive marine fishery production and biogeochemical cycling. *Proc. Natl. Acad. Sci. U.S.A.* 112, 1710–1715. doi: 10.1073/pnas.1417143112

Woodson, C. B., Schramski, J. R., and Joye, S. B. (2018). A unifying theory for top-heavy ecosystem structure in the ocean. *Nat. Commun.* 9:23. doi: 10.1038/s41467-017-02450-y

Conflict of Interest: The authors declare that the research was conducted in the absence of any commercial or financial relationships that could be construed as a potential conflict of interest.

Copyright © 2020 Greer, Lehrter, Binder, Nayak, Barua, Rice, Cohen, McFarland, Hagemeyer, Stockley, Boswell, Shulman, deRada and Penta. This is an open-access article distributed under the terms of the Creative Commons Attribution License (CC BY). The use, distribution or reproduction in other forums is permitted, provided the original author(s) and the copyright owner(s) are credited and that the original publication in this journal is cited, in accordance with accepted academic practice. No use, distribution or reproduction is permitted which does not comply with these terms.

APPENDIX I: DESCRIPTION OF IMAGING SYSTEMS

CytoSense

The CytoSense (CytoBuoy, b.v., NL) scanning flow cytometer uses a 75 mW, 488 nm laser to enumerate and characterize individual particles in whole seawater (∼0.2 to 700 μm diameter and up to 10 mm in length). Sample water is injected into the center of a sheath fluid stream at a rate that allows single particles to be resolved individually. The sheath fluid is obtained by filtering 2 L of seawater (0.2-μm pore size) from the same location as the sample from the same Niskin bottle. An auto-ranging sample dosing pump and programmable detection thresholds allow a range of particle concentrations from 10^2 to 10^{10} to be analyzed. During the entire passage of the particles across the laser beam, photodiodes detect near-forward and sideward scattering of the laser (and depolarization of a second, 20 mW red laser), and photomultipliers detect fluorescence in 3 spectral bands (red, yellow-green, and orange). The amplitude, duration, and shape of the resulting 'pulse' signals of the various detectors provide information about the particles. Targeted imaging-in-flow allows select particles to be photographed with an in-line 1,280 pixel × 1,024 pixel CMOS camera (Pixelink PL-A741-BL).

HOLOCAM

The digital holographic imaging technique involves illuminating a sample volume with a coherent light source (i.e., laser beam). A portion of the light passing through the volume gets scattered by particles in its path, while the remaining fraction passes through undisturbed. The hologram represents the recording of the interference pattern of the scattered and undisturbed light fields (Katz and Sheng, 2010). Subsequently, numerical reconstruction techniques can be used to get in-focus 2-D planes or sections within the 3-D sample volume, thus enabling accurate characterization of 3-D spatial distributions of particles at different depths. Further details on holography and applications can be found elsewhere (Vikram, 1992; Schnars and Jueptner, 2005; Katz and Sheng, 2010).

The HOLOCAM uses a 660 nm Nd-YAG laser as the source of illumination. Most aquatic organisms are minimally sensitive to this portion of the visible light spectrum, thus helping us record their behavior in the least obtrusive manner (Buskey et al., 1989). The unit images a sample volume of 3.69 mL per hologram at a frequency of 15 Hz. Further details about the HOLOCAM and methods of deployment can be found in Nayak et al. (2018). (See **Table 1** for a comparison to other imaging systems). A Seabird Electronics 49 Fastcat CTD, strapped to the HOLOCAM, facilitated recording of co-located salinity, temperature and depth profiles during deployment. The timestamps of the CTD and HOLOCAM data were matched, and the CTD data were resampled at the HOLOCAM sampling frequency, thus providing depth information for each recorded hologram. Numerical reconstruction of holograms obtained in-focus particles at different depths using the Fresnel diffraction formula (Katz and Sheng, 2010). Post-processing steps, using established algorithms, have been described elsewhere (Nayak et al., 2018; Moore et al., 2019). The steps include image segmentation and binarization to isolate all particles in each hologram, thus populating a data table with relevant parameters for each particle, including major and minor axis length, aspect ratio, and equivalent size diameter, among others.

In situ Ichthyoplankton Imaging System

The *In Situ* Ichthyoplankton Imaging System (ISIIS) is a towed instrument that generates a continuous image of planktonic organisms while simultaneously collecting measurements of water column properties (Cowen and Guigand, 2008). The current version of the ISIIS has two cameras designed to sample different volumes of water (**Table 1**). The large camera has field of view of 12 cm (2,048 pixels) and uses a collimated light source projected across a 50 cm depth of field into a line scan camera (Dalsa Piranha 2 P2-22-02k40). The large camera is set toward the front of the vehicle near torpedo-shaped pods that minimize water disturbance. The small camera has a similar optical setup but a smaller field of view (4.3 cm, 1,024 pixels) with an 8.9 cm depth of field. This camera is set further toward the middle of the vehicle and about 50 cm higher (shallower). For both of these line scan cameras, a continuous "strip" of non-overlapping imagery is collected, but the image acquisition software breaks up the continuous image into roughly square images based on the field of view. For this reason, the constant speed of the ship (2.5 m s^{-1}) and relatively stationary particles are key for obtaining accurate size measurements. Under high particle concentrations, multiple overlapping particles that can lead to erroneously low abundance calculations and inflated particle sizes (Greer et al., 2014) are less of an issue with the smaller camera setup due to the shorter optical path through the sampled water. Thin features on different organisms will also appear thicker (due to higher camera resolution in the small camera), which can affect the organisms' detectability after image processing to extract regions of interest (i.e., image segmentation).

The ISIIS (including both cameras and oceanographic sensors) vertical position is controlled by motor-actuated wings that move the vehicle up and down throughout the water column from near-surface to 2–5 m from the bottom at a target vertical speed (0.2 m s^{-1}). While collecting images from the two cameras, the ISIIS also measures salinity, temperature, depth (SBE 49 CTD, Seabird Electronics, Inc.), and dissolved oxygen (SBE 43, Seabird Electronics, Inc.) at a rate of 6 Hz, which, along with the image data, are transmitted via a fiber optic cable onto the shipboard computer.

frontiers in Marine Science

REVIEW
published: 22 January 2021
doi: 10.3389/fmars.2020.572147

A Review of Holography in the Aquatic Sciences: *In situ* Characterization of Particles, Plankton, and Small Scale Biophysical Interactions

Aditya R. Nayak[1,2], Ed Malkiel[2], Malcolm N. McFarland[2], Michael S. Twardowski[1,2] and James M. Sullivan[2]*

[1] Department of Ocean and Mechanical Engineering, Florida Atlantic University, Boca Raton, FL, United States, [2] Harbor Branch Oceanographic Institute, Florida Atlantic University, Fort Pierce, FL, United States

The characterization of particle and plankton populations, as well as microscale biophysical interactions, is critical to several important research areas in oceanography and limnology. A growing number of aquatic researchers are turning to holography as a tool of choice to quantify particle fields in diverse environments, including but not limited to, studies on particle orientation, thin layers, phytoplankton blooms, and zooplankton distributions and behavior. Holography provides a non-intrusive, free-stream approach to imaging and characterizing aquatic particles, organisms, and behavior *in situ* at high resolution through a 3-D sampling volume. Compared to other imaging techniques, e.g., flow cytometry, much larger volumes of water can be processed over the same duration, resolving particle sizes ranging from a few microns to a few centimeters. Modern holographic imaging systems are compact enough to be deployed through various modes, including profiling/towed platforms, buoys, gliders, long-term observatories, or benthic landers. Limitations of the technique include the data-intensive hologram acquisition process, computationally expensive image reconstruction, and coherent noise associated with the holograms that can make post-processing challenging. However, continued processing refinements, rapid advancements in computing power, and development of powerful machine learning algorithms for particle/organism classification are paving the way for holography to be used ubiquitously across different disciplines in the aquatic sciences. This review aims to provide a comprehensive overview of holography in the context of aquatic studies, including historical developments, prior research applications, as well as advantages and limitations of the technique. Ongoing technological developments that can facilitate larger employment of this technique toward *in situ* measurements in the future, as well as potential applications in emerging research areas in the aquatic sciences are also discussed.

Keywords: holography, underwater imaging, particle interactions, plankton distributions, plankton imaging, biophysical interactions, particle patchiness

OPEN ACCESS

Edited by:
Alberto Basset, University of Salento, Italy

Reviewed by:
Pietro Ferraro, National Research Council (CNR), Italy
Alexander B. Bochdansky, Old Dominion University, United States

****Correspondence:***
Aditya R. Nayak
anayak@fau.edu

Specialty section:
This article was submitted to Marine Ecosystem Ecology, a section of the journal Frontiers in Marine Science

Received: *12 June 2020*
Accepted: *30 December 2020*
Published: *22 January 2021*

Citation:
Nayak AR, Malkiel E, McFarland MN, Twardowski MS and Sullivan JM (2021) A Review of Holography in the Aquatic Sciences: In situ Characterization of Particles, Plankton, and Small Scale Biophysical Interactions. Front. Mar. Sci. 7:572147. doi: 10.3389/fmars.2020.572147

INTRODUCTION

Since the introduction of holography to the scientific community in a pair of seminal papers more than seven decades ago (Gabor, 1948, 1949), it has become an indispensable technique used across a range of disciplines, including but not limited to, environmental and applied fluid mechanics, interferometric studies, metrology, and medical imaging. While the utility of holography in oceanographic and limnological field research has been evident since the 1970s, the last decade and a half has brought significant technological advances and an increase in off-the-shelf availability of holographic imaging systems, leading to a surge in its use by the aquatic sciences community.

This review endeavors to provide a brief background on the history of *in situ* holographic instrumentation in the aquatic sciences, predominantly focusing on the advances made since the advent of digital holography at the turn of the millennium. While a brief introduction to the technique and processing methods is provided, an exhaustive discussion is beyond the scope of this review and can be found elsewhere (Schnars and Jüptner, 2002, 2005; Katz and Sheng, 2010). An overview of the diverse applications of *in situ* holography that demonstrate its versatility is provided. Finally, existing limitations, scope for further development of the technique to enable widespread utility in the aquatic sciences community, and future avenues of applications in emerging research areas are discussed. For additional information about the development of holography, the readers are referred to other publications (Watson, 2005, 2011), where an overview of the technique, with a focus on different systems developed at the University of Aberdeen over the decades is provided. While these reviews highlight developments in holography for aquatic applications prior to 2011, their main focus is on the system design and processing approaches. Furthermore, marked improvements in the technology and the development of several commercial holographic systems have led to its increased use in the last decade for a variety of scientific applications, which will be covered here. Lab-based studies (e.g., Sheng et al., 2007; Hong et al., 2012) as well as flow through based approaches (e.g., Yourassowsky and Dubois, 2014; Zetsche et al., 2014) characterizing aquatic particles/plankton find a fleeting mention but are generally out of the purview of this article. Hologrammetry used as a tool for underwater inspections of offshore installations (e.g., Foster and Watson, 1997) is also not covered here. Historically speaking, holography in the aquatic sciences has been predominantly used for marine applications, and this fact is reflected in the material covered in the review. While all these applications are easily transferable to limnological research, prior field studies in lake environments have been scarce and are only touched upon briefly.

AQUATIC PARTICLES AND *IN SITU* MEASUREMENT TECHNIQUES

A diverse range of planktonic species, marine snow, detrital matter, sediments, microplastics, and fecal pellets constitute the particle population in the world's water bodies (Lal, 1977; Turner, 2015). Together, these particles and their interactions with the local environment, affect a range of processes across vast spatial and temporal scales, with consequence to marine ecology, human health, climate change, coastal engineering, ocean optics, acoustics, and remote sensing. For example, healthy phytoplankton and zooplankton populations are critical to sustaining aquatic ecosystems (Tett et al., 2008); conversely, abnormal and drastic increases in plankton abundance can lead to massive harmful algal blooms (HABs), which can severely impact aquatic ecosystems, human health and local economies (Anderson et al., 2002; Carmichael and Boyer, 2016; Glibert et al., 2018). Under favorable conditions, plankton can accumulate in enhanced concentrations to form "thin layers," which can enhance foraging success rates for fish and other species (Sullivan et al., 2010a). The presence (or absence) of particles, and their composition, concentration and orientation, can alter optical and acoustic propagation through the ocean (Sullivan et al., 2005; Holliday et al., 2009; Basterretxea et al., 2020). Sinking particles are major pathways of carbon transport into the ocean's interior and important to understanding the ocean carbon budget, and consequently, climate change research (Turner, 2015; Briggs et al., 2020). Sediment suspension and transport influence key coastal processes (Conley et al., 2012). Thus, developing and utilizing methods and instrumentation to quantify particle composition, distribution and particle-flow interactions have been an important focus of the aquatic sciences community for decades.

Among these methods, *in situ* imaging provides a direct way to record particle characteristics in their natural environment. A more comprehensive review on the field of underwater optical imaging can be found elsewhere (Dahms and Hwang, 2010; Jaffe, 2014). To date, different imaging techniques used by aquatic scientists include, but are not limited to, lidar imaging (Churnside and Wilson, 2004; Busck, 2005; McKenzie et al., 2020), bulk and planar laser-induced fluorescence (Prairie et al., 2011; Jaffe et al., 2013), laser sheet reflective imaging, e.g., Laser Optical Plankton Recorder (Herman et al., 2004; Checkley et al., 2008), underwater light microscopy (Mullen et al., 2016), imaging-in-flow cytometry (Olson and Sosik, 2007), silhouette photography (Milligan, 1996), and holography (Katz et al., 1999; Watson, 2011). Among these, holography can provide 3-D spatial distributions of particles in the micron to centimeter range, within a freestream sample volume, thus enabling mapping of particle characteristics at high resolution without fragmenting them. Furthermore, as opposed to methods like flow cytometry, much larger volumes can be sampled.

Broadly speaking, the applications of holography toward particle characterization can provide the following information: (a) Particle counts and size distributions; (b) Particle shape metrics, including cross-sectional area, major and minor axis lengths, and aspect ratio; (c) 3-D spatial structure of the particle field, e.g., nearest neighbor distances (NNDs) and particle orientation; (d) Particle identification and classification; (e) Particle interactions, including aggregation, settling speed, predator-prey behavior, and organism swimming trajectories; and (f) 3-D velocity distributions by integrating particle image velocimetry with holography (HPIV).

HOLOGRAPHY

Briefly, holography involves the recording of an interference pattern (hologram) of the diffracted light field from particles in a given volume illuminated by a coherent light source (e.g., laser) and the reference beam (Schnars and Jüptner, 2002; Katz and Sheng, 2010). The hologram encapsulates the information about the phase and intensity of the diffracted light field. Direct visual observations of a recorded hologram would typically not produce any useful information, unless a particle is very close to the hologram plane; rather, optical or numerical reconstruction techniques are required to elicit information about in-focus particles in different 2-D cross-sections within the 3-D sample volume. Based on the geometric configuration of the object and reference beams, holography can be further classified as inline and off-axis holography. In the inline configuration, the reference and object beams are parallel to each other. Here, the sample volume is illuminated by a coherent beam of light, and the interference pattern recorded is caused by the portion of the beam scattered by the particles and the undisturbed part of the same beam. In the off-axis configuration, the object and reference beams are at an angle to each other. Inline geometric configurations are relatively simple, especially in the context of field instrumentation design; thus, most (but not all) *in situ* holographic systems have opted to use the inline setup. Readers are referred to other review articles or texts on holography for a more detailed explanation on different geometrical configurations (Vikram, 1992; Murata and Yasuda, 2000; Pan and Meng, 2003; Katz and Sheng, 2010; Picart and Montresor, 2020).

History of Development of Holography for *in situ* Aquatic Applications

The history of holographic development and *in situ* applications for marine sciences can be broadly divided into the pre-digital (e.g., recording on photographic plates) and the digital eras (**Figure 1**). Two related technological developments (lasers and digital cameras) have led to separate inflection points four decades apart, each leading to a subsequent surge in diversifying scientific applications of holography. While holography was introduced in 1948, it was only in the 1960s, that the emergence of lasers as a source of coherent light led to significant progress and expansion of the scope of holography. To the best of our knowledge, the potential of holography toward oceanographic applications was first demonstrated by Knox (1966), wherein a lab-based inline setup was used to image planktonic organisms (also see Beers et al., 1970). This was later extended to recording high-speed holographic movies of plankton (70 frames per second), where all particles >10 μm were resolved (Knox and Brooks, 1969). Stewart et al. (1973) developed and deployed the first known submersible *in situ* holographic imaging system, which weighed ∼1000 kg and could sample approximately 100 L of water per hologram. Further modifications to this system followed, with an off-axis configuration developed by Heflinger et al. (1978). Over the next decade and a half, several groups led other early efforts toward developing holographic imaging systems for diverse applications, including plankton characterization, studying cavitation nuclei and particle size, and settling rates in the ocean (Carder, 1979, Carder et al., 1982; Katz et al., 1984; O'Hern et al., 1988; Costello et al., 1989). A remotely operable inline submersible holocamera with an adaptable optical configuration (i.e., capability to switch between in-line and off-axis modes) was developed by Katz et al. (1999), with multiple deployments of the same instrument reported in other studies (Malkiel et al., 1999, 2006). Submersible holocameras which recorded both inline and off-axis holograms simultaneously were reported by Watson et al. (2001) and Hobson and Watson (2002). The readers are also referred to Watson (2005) and Hobson and Watson (2002) for further details on historical film-based holographic imaging systems. While film-based holographic systems used powerful, pulsed lasers that could sample very large volumes of water at high resolution, the systems themselves were bulky, physically unwieldy and challenging to deploy (e.g., Katz et al., 1999). Also, hologram processing was done manually, which is exceedingly cumbersome; for reference, processing one hologram could take several days, an unimaginable scenario in today's big data world. Malkiel et al. (2004) reported improvements in processing methods with the development of an automated approach; however, this still required 5 h to process a 500 mL sample volume over one hologram. Furthermore, film-based approaches severely constrained the number of holograms that could be recorded, with these data limitations oftentimes leading to a paucity of data to draw conclusions from. For example, Katz et al. (1999) reported the recording of 300 holograms during each deployment of the submersible system. To put this in context of typical sampling rates of 15 Hz in digital holographic systems today, 300 holograms correspond to data recorded across a 20 s time interval. An instrument can record 9,000 holograms over a 10 min vertical profile, albeit with much smaller sample volumes for each hologram as opposed to film-based systems (between 1–10%).

Around the turn of the century, with the development of digital cameras as well as increasing miniaturization of lasers, the second burst in advancement in underwater holographic imaging systems occurred. The first known digital *in situ* holographic system was developed by Owen and Zozulya (2000), where they employed a 10 mW diode laser to image over a ∼25 cm deep depth of field, resolving particulate sizes down to 5 μm. Jericho et al. (2006) developed a holographic microscope that used point source illumination to record marine organisms *in situ*. Bochdansky et al. (2013) developed the first deep-sea holographic microscope rated to 6000 m water depth. Other successfully deployed *in situ* holographic sensors with different optical setups and varying sampling parameters include those by Pfitsch et al. (2005, 2007), Sun et al. (2008), Graham et al. (2012), Talapatra et al. (2012, 2013), Dyomin et al. (2019, 2020), and Nayak et al. (2020). **Table 1** provides further details on some selected systems. The last decade has also seen the development of a handful of commercial holographic imaging systems, including Sequoia Scientific's LISST-HOLO (Davies and Nepstad, 2017; Ouillon, 2018), 4Deep Imaging's holographic microscope (Rotermund et al., 2016) and the WET Labs

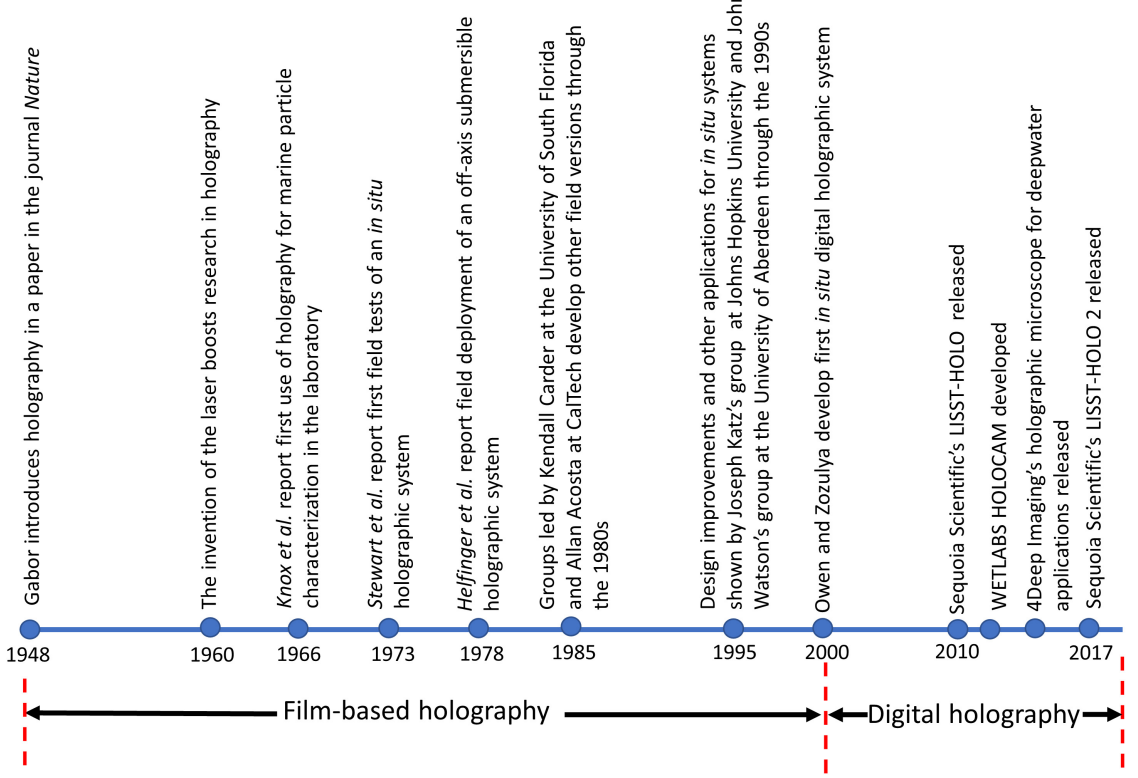

FIGURE 1 | A timeline of the historical developments in holography in the context of *in situ* aquatic applications.

TABLE 1 | Sampling characteristics of selected free-stream, digital holographic imaging systems reported in literature since 2000.

Digital holographic imaging systems	Wavelength (nm)	Sampling frequency (Hz)	Sample volume (mL)	Resolution (μm/pixel)	Min. resolved particle[a] (μm)	Field of view (mm)
Owen and Zozulya (2000)	680/780	30	Variable	5	8	?
Pfitsch et al. (2007)	660	15	40.5	7.48	11.9	15.3 × 15.3
Jericho et al. (2006)	532/630	7	0.009	?	1.5	?
Sun et al. (2008)	532	25	36.5	3.5	5.6	10.5 × 7.7
Graham and Nimmo Smith (2010)	532	25	1.653[b]	7.4	11.8	7.4 × 7.4
Bochdansky et al. (2013)	640	7	1.8	Variable	Variable	N/A[d]
Nayak et al. (2018a)	660	15	3.73	4.59	7.4	9.4 × 9.4
Dyomin et al. (2019)	660	?	880[b]	5.5	8.8	11.3 × 11.3
Nayak et al. (2020)	532	3.2	72[b]	5.5	8.8	27 × 18

[a] *To standardize this value across different systems, any particle of at least two pixels in size is considered as the smallest resolvable value. Particle size is reported in "Equivalent Spherical Diameter,"* ESD $= \sqrt{4A/\pi}$, *where A is the area of the particle. The "?" symbol refers to parameters of the instruments that are not directly or indirectly interpretable from the relevant literature.*

[b] *These systems have variable sampling volume, achieved by increasing or decreasing the spacing between the windows, i.e., increasing the depth of field. Only relevant parameters for a single configuration are reported here.*

[c] *These systems were of dual resolution, only the low-resolution parameters are shown here.*

[d] *Bochdansky et al. (2013) used a cone-shaped sample volume, so the field of view does not apply.*

HOLOCAM (Moore et al., 2017, 2019; Nayak et al., 2018a,b). These developments leave the scientific community poised to take further advantage of the holographic technique in the near future.

Holographic Data Processing

Digital holographic data processing can be a computationally expensive process, which is a function of several parameters. Briefly, the image processing steps for each hologram can be sub-divided as follows: (a) Image pre-processing; (b) Hologram reconstruction; (c) 3-D segmentation and/or image plane consolidation; and (d) Particle feature extraction. Pre-processing of raw holograms is required to eliminate any nonuniformities associated with uneven laser beam illumination and dust or other unwanted particles on the windows. Typically, this is achieved

by computing the average background intensity calculated from a sequence of holograms and subtracting this from each single one (Talapatra et al., 2013; Nayak et al., 2018a). Alternately, a reference background hologram can be recorded just prior to data acquisition and then subtracted from each of the holograms to generate a "contrast hologram" (Bochdansky et al., 2013). A further pre-processing step could include grayscale histogram equalization (Toloui and Hong, 2015). After suitable pre-processing, the hologram reconstruction is carried out using numerical techniques, usually the Kirchoff-Fresnel transform, which is mathematically described elsewhere (Owen and Zozulya, 2000; Katz and Sheng, 2010). Reconstruction at different depths (or planes) brings all particles in each particular plane in focus over the entire 3-D sample volume. Typically, hologram reconstruction is the most memory intensive step in the entire processing routine. After reconstruction, the task is to isolate and label in-focus particles. 3-D segmentation can be directly implemented on the reconstructed stack to achieve this, providing in-focus locations of particles (Katz and Sheng, 2010). In cases where the particle field is sparse and the objects are compact, the stack can first be consolidated into a single composite image, because the in-focus images do not overlap one another, thus expediting processing. Further operations could include median filtering, image thresholding and segmentation and defining regions of interest (Jericho et al., 2006; Graham and Nimmo Smith, 2010; Bochdansky et al., 2013; Talapatra et al., 2013; Nayak et al., 2018a). All these steps are then repeated for each hologram in the dataset to generate a distribution of particles for further analysis. **Figure 2** shows the steps involved in the holographic processing routine. **Figure 3** shows a collage of planktonic images from processed holograms collected in diverse environments using the WET Labs HOLOCAM.

SAMPLE APPLICATIONS OF HOLOGRAPHY IN AQUATIC RESEARCH

Aquatic Particle Characterization

Particle Size Distributions

The characterization of spatial and temporal particle size distributions (PSDs) is vital to many oceanographic research topics. For example, PSDs are an important parameter in sediment transport studies (Mikkelsen and Pejrup, 2001; Conley et al., 2012). Physical processes such as molecular diffusion, turbulence, and settling, lead to aggregation and fragmentation of particles which are reflected in variations in the PSDs; this is important in the quantification of particle fluxes in the ocean (Jackson et al., 1997; Sullivan et al., 2005). PSDs can also affect light absorption and scattering in the ocean (Ulloa et al., 1994; Jonasz and Fournier, 2007). Phytoplankton functional type variability, of relevance to global biogeochemical models, are assessed using modeled PSDs (Kostadinov et al., 2010; Stemmann and Boss, 2012). While some of the seminal work on oceanic PSDs have employed an *in situ* imaging system (Underwater Video Profiler), sometimes in conjunction with a shipboard particle counter, to resolve a broad size spectrum (Stemmann et al., 2000, 2002, 2008), PSDs are usually estimated from direct samples collected and processed in the laboratory using instruments such as Coulter counters and flow cytometers (Jackson et al., 1997; Boss et al., 2001; McFarland et al., 2015). Inherent biases exist in inferring PSDs from discrete samples, primarily because particles get fragmented during the collection, sampling, and analysis process, potentially leading to an enhanced concentration of smaller particles. Indirect methods focus on employing models to invert acoustic or optical scattering to infer PSDs (e.g., Sequoia Scientific's LISST series of instruments), and may require some *a priori* knowledge of particle shape and scattering properties. Thus, validation by direct imaging is recommended to ensure fidelity in measurements (Graham et al., 2012).

Aquatic PSDs are most commonly described using a simple power law, also referred to as a "Junge type" distribution, because such a relationship is generally representative in diverse environments for smaller particles <100 μm that are important for aquatic optical properties (Kitchen et al., 1982; Buonassissi and Dierssen, 2010). Here, the PSD shape is embodied in a single parameter, i.e., the exponent, which is convenient for modeling and inversions (Fournier and Forand, 1994; Boss et al., 2001; Twardowski et al., 2001). While particles <100 μm control optical properties such as scattering and absorption, larger particles can affect diffraction at very near-forward angles. More complex models such as the two-component gamma (Risović, 1993) have also been developed to describe oceanic PSDs. The wide particle size range that can be mapped by holography (few microns to cm) makes it an attractive technique for direct *in situ* PSD measurements.

A few studies have compared PSDs obtained from holographic systems and other instruments. For example, O'Hern et al. (1988) evaluated PSDs using holographic and Coulter counter measurements. It was reported that the Coulter counter consistently under-estimated the PSDs, with the authors concluding that this most likely occurred due to assumptions inherent in the Coulter counter calibration procedures. Kumar et al. (2020) compared PSDs estimated using a laser diffraction based approach and holography, with a lab-based setup to characterize spray droplets. Here, it was found that the PSDs were under-estimated in the laser diffraction based approach for droplet sizes higher than 1 mm. Graham et al. (2012) co-deployed a LISST-100X alongside a holographic system, where they reported that in the overlapping size ranges, the LISST-100X showed higher particle concentrations, especially in smaller size bins. They suggest that in particle fields dominated by non-spherical particles, the LISST-100X might report a single large particle as several individual particles, thus skewing the PSD. While the above studies use holography as a standard to compare other instrumentation, a study by Walcutt et al. (2020) is also pertinent to this discussion. Here, a 4Deep holographic microscope was simultaneously used along with a FlowCam, Imaging Flow Cytobot (IFCB), and standard microscope, to compare PSDs. Ocean water samples, lab-grown cultures and microspheres provided diverse datasets to characterize PSDs across these methods. After appropriate post processing

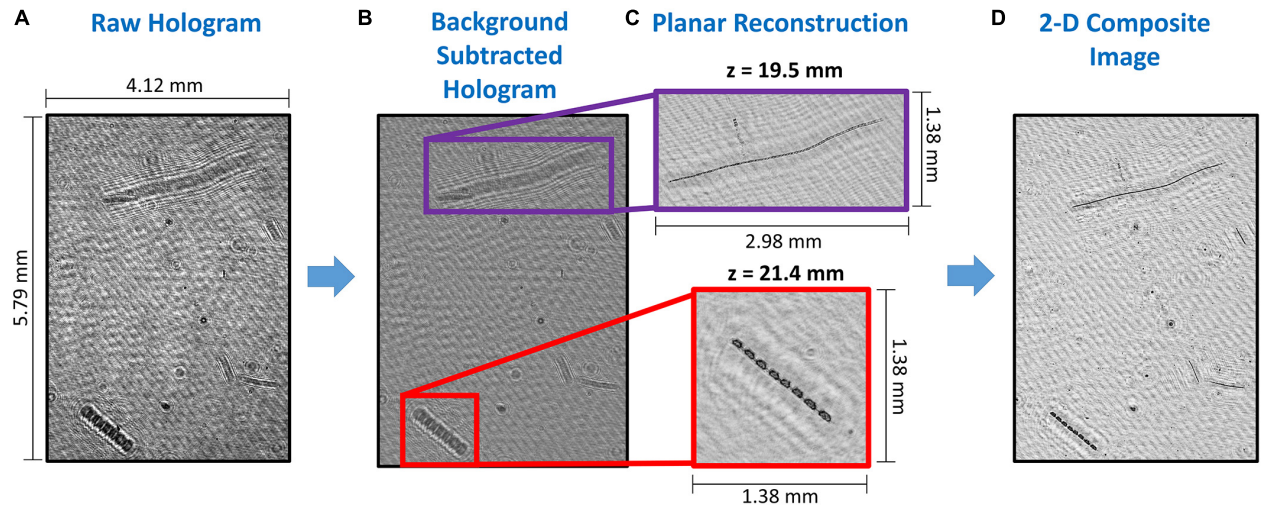

FIGURE 2 | An illustrative example showing the different steps in holographic data processing: **(A)** A sample raw unprocessed hologram; **(B)** The same image after background subtraction, with regions of interest highlighted, and showing only interference patterns; **(C)** The in-focus diatom chains at different reconstruction depths (*z*) within the sample volume in the highlighted region; and **(D)** The 2-D composite image, where all in-focus particles are collapsed onto the same plane for further analysis.

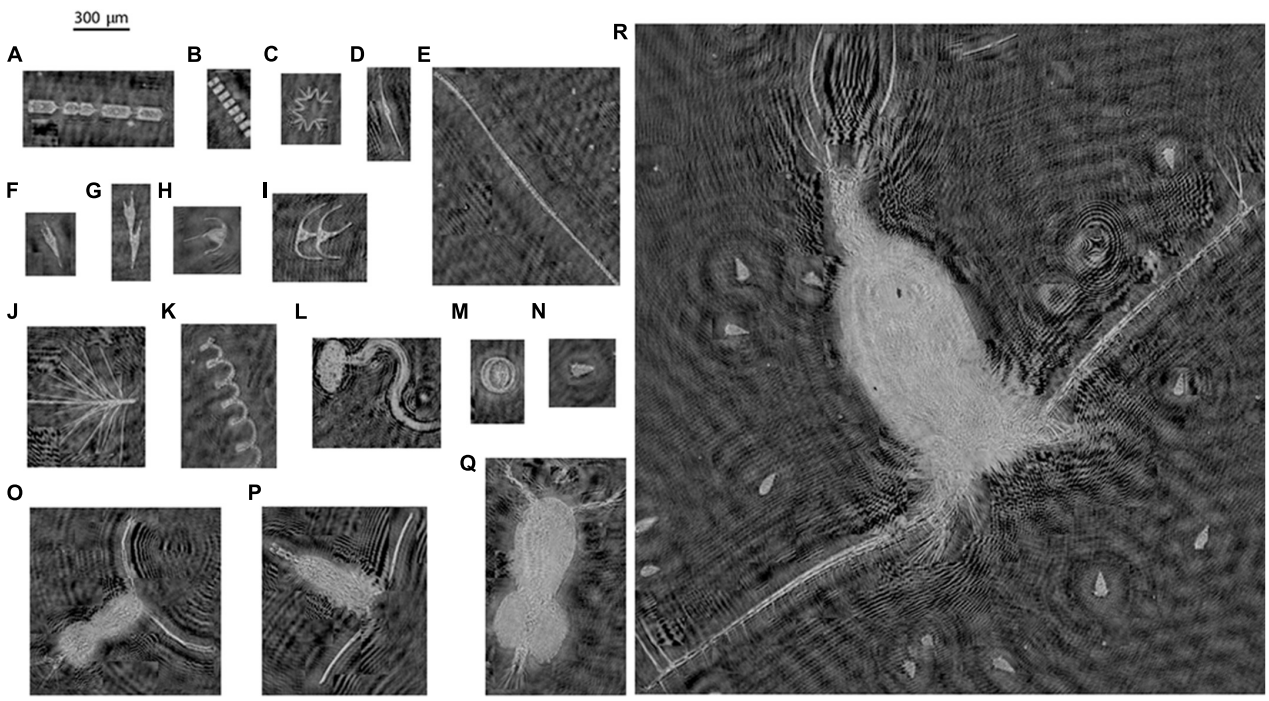

FIGURE 3 | A collage of different plankton recorded from diverse environments on field cruises in the Atlantic Ocean (Delaware shelf), the Gulf of Mexico and East Sound, Washington, a coastal fjord in the Pacific Northwest. **(A)** *Ditylum brightwelli*; **(B)** *Thalassiosira* sp.; **(C)***Thalassionema* sp.; **(D)** *Tripos* cf. *fusus*; **(E)** Unidentified colony; **(F)** *Tripos* cf. *furca*; **(G)** *Tripos* cf. *furca*, dividing cell; **(H)** *Tripos muelleri*; **(I)** *Tripos* sp. dividing; **(J)** *Chaetoceros* sp.; **(K)** *Chaetoceros* cf. *debilis*; **(L)** Appendicularian; **(M)** *Coscinodiscus* sp.; **(N)** cf. *Strombidium* sp.; **(O)** Calanoid copepod with egg sac; **(P)** Calanoid copepod; **(Q)** Cyclopoid copepod with paired egg sacs; and **(R)** Unidentified large copepod, potentially feeding on cf. *Strombidium* sp.

corrections, it was found that holographic measurements under-estimated the PSD by about 3–10%. However, the slopes of the distributions remained comparable. The authors list several potential factors, e.g., nonuniform illumination of the sample volume, which might possibly need to be accounted for to gain higher statistical confidence in inferring particle concentrations and distributions from holographic data.

Bochdansky et al. (2016) reported the particle distributions in bathy- and abyssopelagic waters (up to 5,500 m depth) at several stations in the North Atlantic Ocean, using a digital

inline holographic microscope. A majority of the particles seen in the holograms consisted of marine snow, fecal pellets, phytoplankton, and other detrital matter. When all other particles excluding marine snow were considered, they fit a typical oceanic PSD, with a systematic decrease in particle counts in the larger size bins. However, when only marine snow was considered, the particle counts across the size bins did not exhibit any specific trends, such as a skew toward the smaller sizes. For all particles, including marine snow, the PSD slope deviated significantly from an expected Junge distribution above a certain size threshold (∼380 μm). The authors termed particles that were significantly more frequent than expected from the frequency distribution of smaller particles as "dragon kings." Aggregation is an important process that can skew PSDs and cause deviations from a simple power law (Boss et al., 2009; Hill et al., 2011).

Similar trends in deviations of the PSDs from expected profiles have been reported by other studies in diverse aquatic environments. Nayak et al. (2018a) analyzed the small-scale PSD variations with depth in a coastal fjord, where a holographic system was slowly profiled through a ∼25 m deep water column. Here, the particle field was dominated by diatoms, and size was represented by considering the equivalent size diameter (ESD $= \sqrt{4A/\pi}$, where A represents the measured area of the particle). At shallow depths, a broad peak in the PSD was observed, centered around 300 μm, which corresponded to an enhanced abundance in diatom chains in that size range (**Figure 4A**). Across stations and depths, PSD slopes presented two linear ranges, with a shallower slope (−1.7 to −1.9) fitting the 50–250 μm range. For particles above 250 μm, slopes were much steeper (−5.7 to −6.1). Moore et al. (2017) reported the deployment of a holographic system to characterize PSDs across different stations in western Lake Erie during a cyanobacterial bloom. In locations dominated by detrital particles, the mean PSD slopes were ∼−3.45 across depths. At stations where the particle field was dominated by the cyanobacteria *Microcystis aeruginosa* which forms amorphous colonies, the PSDs show a pronounced bump, broadly between 200 and 500 μm, with overall mean slope ∼−2.3 (**Figure 4B**). Modeling studies characterizing colony size and associated vertical migrations have previously shown that a colony ∼250 μm in size corresponded to the highest migration ranges (Visser et al., 1997). Finally, at stations dominated by a second, morphologically distinct (elongate) cyanobacteria, *Planktothrix aghardii*, similar PSD slopes to the *M. aeruginosa* dominant waters were observed, albeit with the absence of the bumps (**Figure 4C**). These different studies in diverse conditions demonstrate the feasibility of using holography to characterize fine-scale PSDs in the water column and highlight trends which other methods might miss. It should be noted that while oceanic bubbles do not fall under the general ambit of particles being discussed in most of this paper, there is a substantial community focusing research efforts in this direction. Acoustics and optics remain the preferred method of characterization for large and small bubbles, respectively (Czerski et al., 2011; Twardowski et al., 2012). Holography has been successfully demonstrated to be applicable to *in situ* bubble research by at least two previous studies (O'Hern et al., 1988; Talapatra et al., 2012).

Particle Settling Velocities

Particle size and density directly affects sinking rates and transport in the water column (McDonnell and Buesseler, 2010; Bach et al., 2012). In the open ocean, particle sinking is an important pathway for carbon sequestration to the ocean's interior (Trull et al., 2008; Fischer and Karakas, 2009; Nayak and Twardowski, 2020), while settling rates are critical to inform coastal studies involving sediment suspension and transport (Agrawal and Pottsmith, 2000). Carder et al. (1982) integrated a holographic setup into a free-floating sediment trap to quantify settling rates of individual particles in the water column, with holograms recorded at discrete intervals. The processed data provided size distributions of particles >15 μm. Some of the faster sinking particles were segregated to compute attributes: observed particle densities ranged from 1370–5100 kg/m^3, with associated settling velocities corresponding to daily excursions of 16–199 m across the particle spectrum. This was the first demonstration of holography for oceanic particle settling analysis, with results corroborated from microscopic analysis of the particles collected in the sediment trap. Graham and Nimmo Smith (2010) demonstrated the applicability of holography to study suspended sediment size distributions and settling velocities in the coastal ocean. Automated tracking software, incorporating parameters such as particle area and major and minor axis lengths was used to identify a particle across different frames, thus facilitating computation of trajectories and consequently velocities. Cross et al. (2013) studied particle resuspension in the context of the relation between turbulence and particle size. Holographic data was used to identify suspended particle matter and characterize variations in their size distribution over different tidal cycles. These data were compared to turbulence measurements obtained from a microstructure profiler; based on their observations, the authors postulated that the growth and size of flocs are dependent not only on turbulence, but also biological controls.

Particle Orientation

In atmospheric studies, preferential (or non-random) orientation of particles and ice crystals in clouds has been relatively well-documented (Ono, 1969; Sassen and Takano, 2000; Noel and Chepfer, 2004). Only fairly recently has this area of research gained traction in oceanography. The consequences of particle orientation are significant to optical oceanographers as most models assume that particles are randomly oriented in the ocean (Bohren and Huffman, 1983; Jonasz and Fournier, 2007). In aquatic ecology, preferential horizontal orientation of phytoplankton chains could potentially increase light capture and thus enhance primary productivity (Sun et al., 2016; McFarland et al., 2020). Several laboratory and modeling studies have shown that particle and plankton orientation is a function of the small-scale flow physics (Karp-Boss and Jumars, 1998; Karp-Boss et al., 2000; Marcos et al., 2011) and influences light propagation (Marcos et al., 2011; McFarland et al., 2020). Basterretxea et al. (2020) provide a useful overview of phytoplankton orientation in the ocean, laying it in the context of microscale plankton-flow interactions. While recent innovative approaches at inferring *in situ* particle orientation from indirect scattering measurements

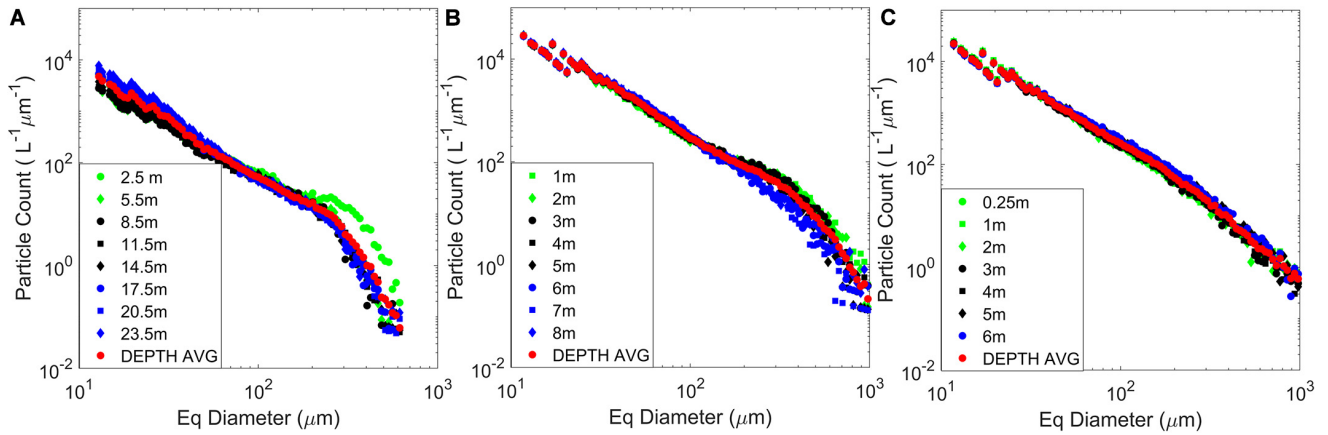

FIGURE 4 | Depth-binned and depth-averaged particle size distributions (PSDs) obtained from vertical profiles of a holographic imaging system during two field experiments at East Sound, Washington, in September 2015 and at Lake Erie in August 2014. Figure adapted from data presented in Moore et al. (2017) and Nayak et al. (2018a; 2018b). **(A)** The East Sound profile was recorded during the presence of a "thin layer" of diatoms, dominated by *Ditylum brightwelli*; **(B)** Data recorded during a *Microcystis aeruginosa* bloom in western Lake Erie; and **(C)** PSDs at Lake Erie in a water mass dominated by the cyanobacteria *Planktothrix aghardii*.

have been reported (Font-Muñoz et al., 2019, 2020), direct imaging still provides the best means to do so.

Most reports to date on particle orientation in aquatic environments have used holographic systems. To the best of our knowledge, the first, albeit limited, direct observations on non-random particle orientation in the ocean were reported by Malkiel et al. (1999). From a sample of 300 holograms recorded during a vertical scan of the water column, the majority of diatom chains present (*Chaetoceros* spp. and *Ditylum* sp.) at a certain depth (15.3 m) were found to be preferentially oriented within $\pm 15°$ to the horizontal. Talapatra et al. (2013) documented the occurrence of enhanced preferential horizontal orientation of colonial diatom species (primarily *Chaetoceros debilis* and *Chaetoceros radicans*) at several distinct depths in two vertical profiles. A pulsed laser acting as the illumination source allowed for particles to be tracked over successive frames, enabling co-located small-scale flow and turbulence measurements, which indicated that regions of enhanced preferential particle concentrations coincided with regions of low turbulent kinetic energy (TKE) dissipation. A comprehensive set of measurements of oceanic particle orientation were later provided by Nayak et al. (2018a). A bio-optical profiling package consisting of a holographic system, an acoustic Doppler velocimeter, and a CTD, among other instruments, was gently profiled through the water column at several stations to simultaneously quantify particle orientation, small-scale shear, and TKE dissipation rates with depth. Across all stations, preferential horizontal orientation was observed at several depths, each time corresponding to regions of low shear and TKE dissipation rates. Further analysis highlighted the relation between instantaneous orientation of a particle and its aspect ratio (ratio of the major axis length to the minor axis length of a particle). In simple 2-D laminar shear flow, Jeffrey (1922) derived a set of relations for spheroidal particles, showing that they exhibit periodic flipping motions, where higher aspect ratio particles spend more time oriented in the horizontal direction; *in situ* data presented in Nayak et al. (2018a) were in reasonable agreement with Jeffrey's theory.

Plankton Distributions and Patchiness

In situ observations of plankton distributions, behavior and interactions with the natural environment provide valuable insights into the functioning of aquatic ecosystems. It has been well-established that plankton distributions in aquatic systems tend to be incredibly "patchy," i.e., non-homogeneous (Durham and Stocker, 2012; McManus and Woodson, 2012; Prairie et al., 2012; Graff and Menden-Deuer, 2016). There exists a plethora of possible mechanisms for the formation of these patches across different spatial scales, including small-scale shear, horizontal and vertical mixing, and enhanced nutrient availability (Powell and Okubo, 1994; Abraham, 1998; Sullivan et al., 2010a; Breier et al., 2018). Examples of plankton patchiness include algal blooms (harmful or otherwise) and phytoplankton and zooplankton "thin layers," which are discussed further below.

Phytoplankton Blooms and Vertical Distributions

Large phytoplankton blooms covering several hundreds of kilometers occur annually in different gyres, sometimes tied with the formation and transport of mesoscale eddies (Guidi et al., 2012). Anderson et al. (2018) deployed Sequoia Scientific's LISST-HOLO on a neutrally buoyant towed body from an autonomous vehicle to characterize a summer phytoplankton bloom in the North Pacific subtropical gyre, which was dominated by several species of colonial diatoms. Holographic images were processed to obtain cell and aggregate counts of *Hemiaulus* and *Rhizosolenia sp.* over the course of the campaign. These observations showed that the overall bloom was comprized of two distinct phases, where either species dominated; simultaneous large abundances of both taxa seldom occurred. Similarly, Bochdansky et al. (2017) reported the particle composition in the Ross Sea in Antarctica, where massive phytoplankton blooms occur seasonally, connecting the distribution of important

phytoplankton species to carbon export. In particular, large scale sinking of *Phaeocystis antarctica* colonies from the surface to the deep layer below the pycnocline was noted. These observations were made during the weakening of the pycnocline, thus establishing the significant contribution of *Phaeocystis* colonies to total carbon export, even during the non-bloom season.

In a limnological study, Moore et al. (2017, 2019) used holography to characterize phytoplankton community composition during a HAB event in western Lake Erie, where the particle field was dominated by two cyanobacterial species, *M. aeruginosa* and *P. aghardii*. The profiling system enabled characterization of vertical distributions of colony and cell counts of either species. A majority of *Microcystis* colonies were found to be located near the surface, while *Planktothrix* tended to be located in larger numbers deeper in the water column, and the vertical variability was correlated to the light availability and tolerance of either species. All these studies further highlight the ability of *in situ* holography (and direct imaging in general) to tease out small-scale patterns and variations between distinct particle and plankton populations which could help scientists to better understand ecosystem dynamics as well as inform robust modeling efforts.

Thin Layers and Phytoplankton in Turbulence

The term "thin layers" refers to vertically limited (few cm to meters) dense aggregations of plankton which are temporally coherent, i.e., last for several hours to days (Sullivan et al., 2010a; Durham and Stocker, 2012). Manual sample collections at discrete depths oftentimes miss these finescale structures in the water column; high frequency *in situ* observations provide the best means to characterize them (Donaghay et al., 1992; Twardowski et al., 1999; Rines et al., 2002). Previous field studies have shown that thin layers are frequently present in coastal waters, with their vertical location controlled by the physical structure and/or vertical migration of the organisms (Sullivan et al., 2010a). For a comprehensive study of thin layers, the readers are directed to Sullivan et al. (2010b) and articles within that special issue.

In a constrained coastal fjord at East Sound, Washington, where thin layers have been previously well-documented (Dekshenieks et al., 2001; McManus et al., 2003), Talapatra et al. (2013) deployed a holographic system to characterize the small-scale biophysical interactions and particle populations. A thin layer comprising of small, non-motile particles as well as larger colonies of the diatom *Chaetoceros socialis* were observed. Associated CTD profiles indicated that this layer was present at the base of a strong pycnocline. Zooplankton distributions showed that they seemed to avoid the thin layer. At the same geographical location, other studies reported the presence of a strong thin layer, predominantly containing the diatom *Ditylum brightwellii*, again coincident with the location of a near-surface pycnocline (**Figure 5**; Nayak et al., 2018a,b; McFarland et al., 2020). In all these reports, the water column was stably stratified, and the presence of the thin layer was associated with regions of low shear and TKE dissipation.

Turbulence has long been known to play an important role in predator-prey encounters, enhancing phytoplankton nutrient uptake, as well as affecting growth rates (Karp-Boss et al., 1996; Sullivan and Swift, 2003; Durham et al., 2013); thus, there is a lot of interest in simultaneously quantifying plankton populations and turbulence *in situ*. Cross et al. (2014) used integrated holographic imaging and microstructure turbulence profiler measurements to study the effect of episodic and enhanced turbulent mixing on vertical distributions of colonial diatoms. Although limited to a single set of observations over a tidal cycle, enhanced mixing seemed to correlate with shorter chain lengths, with diatoms being transported to lower depths, where they were found to aggregate with other suspended matter. Nayak et al. (2018a; 2018b), albeit qualitatively, also report similar observations with chain lengths, demonstrating the importance of slowly profiling the water column with large instrument packages used in particle characterization studies. Vigorous mixing during fast profiles can lead to bias in observations, with enhanced concentrations of particles at lower sizes, possibly due to breakage of chains due to enhanced turbulence.

Nearest Neighbor Distances

Yet another interesting application of holography is the ability to characterize instantaneous 3-D spatial distributions across each individual hologram in a time series, thus allowing computation of vital statistics such as NNDs. These parameters allow for quantification of predator-prey interactions and population dynamics in the local community, which is of great interest to biological oceanographers and ecological modelers.

Malkiel et al. (1999, 2006) computed NNDs between particles detected in holograms by employing two-tailed hypothesis testing (Freedman et al., 2007). Qualitatively, differences were represented by looking at the histogram of NNDs of the sample and a random distribution. Quantitatively, a "z-score" was computed as $z = \frac{\bar{x}-\bar{x}_R}{\sigma_R/N^{1/2}}$, where $\bar{x}$ and N are the mean NND and the size of the sample, respectively, while $\bar{x}_R$ and σ_R represent the mean and standard deviation of the NND obtained by a random distribution. If $|z| > 2$, the sample data are deemed different from a random distribution. Using this method, statistics were computed to study NNDs between individual particles (or plankton) within the same class, as well as different classes, to come up with the following observations: (a) Detrital particles exhibited clustering at certain depths below the pycnocline, while appearing to be randomly distributed elsewhere; (b) No significant clustering was found among dinoflagellates; and (c) No significant correlation between the location of copepods with respect to small particle clusters were detected. To the best of our knowledge, these are the only *in situ* holographic studies characterizing NNDs to date; further observations in different environments to better understand population dynamics are warranted.

Bacterial and Zooplankton Behavioral Studies

Holographic cinematography provides a way to visualize 3-D trajectories of multiple motile organisms, including zooplankton, simultaneously, as well as observe their natural behavior *in situ*. While this ability has been leveraged by several laboratory studies, far too many to list here in detail (e.g., Sheng et al., 2007; Hong et al., 2012), very few studies report this in the field. During

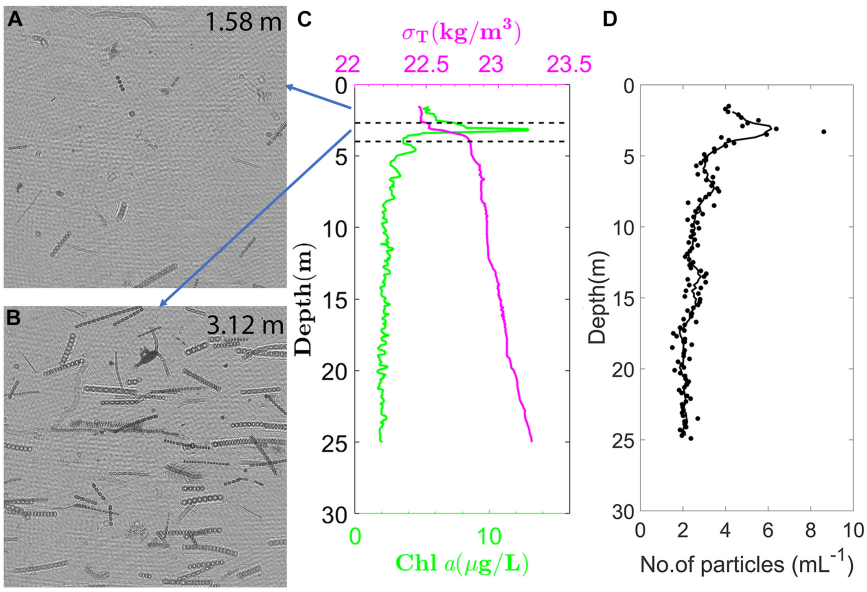

FIGURE 5 | Holographic data acquired on September 22, 2015 during a vertical profile through a diatom thin layer at East Sound, Washington. Background subtracted holograms showing the representative particle fields **(A)** above the thin layer at 1.58 m depth; and **(B)** within the thin layer at 3.12 m depth; **(C)** Chl *a* and density profiles acquired during the same profile, showing the thin layer occurred in a stably stratified region within the pycnocline; and **(D)** Particle distribution with depth, where only particles >200 μm in length and aspect ratio >5 are considered, consisting of different elongate diatom species, and dominated primarily by *Ditylum brightwelli*. Figure generated from a dataset presented in Nayak et al. (2018a; 2018b).

deployment in a Lagrangian, drifting mode, Pfitsch et al. (2005) observed the behavior of swimming medusa jellyfish *in situ*, in the Ria de Pontevedra in coastal Spain. The same authors also recorded the swimming behavior of an appendicularian (Pfitsch et al., 2007). Appendicularians (or larvaceans) are filter feeders that generate a mucous "house" around them to trap particles. The long tail, flapping at a particular frequency, helps pump water through the house and facilitates their feeding (Alldredge, 1981; Selander and Tiselius, 2003). In this instance, the flapping frequency of the tail was found to be in the range of those observed in controlled laboratory measurements (Pfitsch et al., 2007). Other observations with the same instrument included interactions between copepods and dinoflagellates, which can provide pertinent data to modelers such as perception distances by predator/prey species in the turbulent environment. These observations include instances of copepods initiating jumps and orienting their feeding currents after prey and dinoflagellate behavioral changes (jumps and quick spiraling) to avoid a cyclopoid copepod that was cruising through their neighborhood (Malkiel et al., 2007). Jericho et al. (2006) also reported observations of the trajectory of organisms during a field deployment; however, the organisms were not clearly identifiable as they were at the edge of the detection limit of the instrument.

While not a free stream approach, Lindensmith et al. (2016) developed a flow-through based off-axis submersible holographic microscope, geared toward studying microbial motility in extreme, icy environments. During a deployment in Greenland over winter, brine samples were collected and inserted into the sampling chamber of the microscope, to characterize microbial motility. Analyzed samples recorded both prokaryotes and eukaryotes; motility was observed in only a few instances in either case. Swimming trajectories clearly recorded the motion of organisms, at swimming rates varying from 5–50 μm/s between different individuals. This highlights the ability of holographic microscopy for use in extreme environments, including in potential future extraterrestrial missions (Bedrossian et al., 2017).

DISCUSSION

The previous sections have shown the applicability of holography toward diverse research areas in the aquatic sciences. Here, existing limitations, future potential applications and advancements of holographic technology in emergent aquatic research areas are outlined.

Limitations

The main limitation associated with holography is the depth-of-focus (DOF) problem, which refers to the depth over which a particle in the image tends to appear in focus in the axial direction (Vikram, 1992; Katz et al., 1999; Katz and Sheng, 2010). The DOF can be approximated based on the smallest particle diameter (d) resolvable and the wavelength of light used (λ), being proportional to d^2/λ (Yang et al., 2005; Katz and Sheng, 2010). For example, an optical system capable of resolving particles sized 10 and 50 μm and above, will have a depth of focus of ∼0.16 and 4.17 mm, respectively, assuming the illumination source is red light (660 nm). Thus, while the particle location in the image plane can be detected fairly accurately, there is a certain degree of uncertainty associated with detecting the axial location (Gao et al., 2013).

The quality of recorded holograms (as with other optical methods) also depends, to a certain extent, on the turbidity and particle size and abundance within the water column. In-line systems in particular are susceptible to loss of image quality for particle concentrations beyond certain thresholds (Katz et al., 1999). Furthermore, the presence of a large number of sub-micron particles below the resolution limit of typical holographic systems can lead to loss of coherency in the reference laser beam, thus leading to bad quality recordings. A related and important problem in holography is the inherent coherent noise, which includes (a) parasitic interference fringes, caused by multiple reflections or scattering (Pan et al., 2017); and (b) speckle noise, resulting from scattering by particles larger than the wavelength of the laser in dense particle fields (Meng et al., 1993; Garcia-Sucerquia, 2013). This can lead to serious degradation in image quality and holographic reconstructions. Typically, these noise reduction techniques involve engineering the coherent source (Garcia-Sucerquia, 2013; Pan et al., 2017), or optimizing numerical reconstruction schemes (e.g., Kosmeier et al., 2012; Leo et al., 2014). While a detailed discussion is beyond the scope, readers are also referred to Bianco et al. (2018), where different approaches to tackle the speckle noise problem in digital holography are reviewed.

The data-intensive nature of hologram acquisition and the extensive processing routines involved have so far limited the use of *in situ* holographic systems in long-term and/or real-time monitoring networks. For near real-time observations, data transmission is one of the main bottlenecks due to the large file sizes; rapid onboard processing to provide simplified data (e.g., organism presence and counts) in a compressed format, instead of transmitting entire images could help alleviate this problem. For this to work, is it key to develop not only fast and efficient automated classification algorithms, but also those feasible to be developed in a light-weight architecture (Guo et al., 2021). Previous and ongoing efforts toward automated classification of detected particles using various machine learning techniques, including convolutional neural networks, still need holograms to be reconstructed and processed (Davies et al., 2015; Bianco et al., 2020). Recent work has focused on the application of deep learning techniques to extract features from the interference patterns recorded on the raw holograms (Shao et al., 2020; Guo et al., 2021). Successful translation to *in situ* applications would help revolutionize the field, as this would enable skipping the holographic reconstruction step, greatly reducing processing times and facilitating near real-time data dissemination. To continue improving these algorithms, building enormous labeled datasets of hundreds of different particle and plankton types and morphologies from *in situ* deployments is critical.

Current Research and Future Frontiers

Holographic Particle Image Velocimetry (HPIV)

Different methods of particle tracking as well as 2-D and stereo PIV have been used to characterize small-scale 2-D and 3-D velocity distributions in aquatic environments (Nimmo Smith, 2008; Steinbuck et al., 2010; Nayak et al., 2015). Talapatra et al. (2013) used holographic data from in-focus particles at a particular plane to perform PIV and calculate the 2-D velocity fields (not 3-D measurements). The ability to simultaneously quantify particles and flow distributions within the same volume holds enormous appeal and would greatly help elucidate particle-flow interaction studies. In laboratory studies, HPIV has been successfully established as a valuable tool to characterize three-dimensional velocity measurements within a sample volume (e.g., Barnhart et al., 1994; Hinsch, 2002; Katz and Sheng, 2010). Translating this to field applications, while challenging, would be the next step.

Other potential directions include integrating holography with other methodologies to develop new techniques that could significantly enhance particle or plankton characterization capabilities. For example, the ability to quantify the refractive index (RI) of individual particles is valuable to optical oceanographers. Typically, the particle of interest is immersed in fluids of varying RIs and studied under a microscope (Hodgson and Newkirk, 1975). When the RI of the particle is the same as the fluid in which it is immersed, the particle becomes nearly invisible (or least opaque). This is a highly tedious process; thus, previous efforts have estimated the bulk RI of a water sample from scattering measurements (Carder et al., 1972; Twardowski et al., 2001). Holotomography has recently emerged as a tool to map high-resolution 3-D refractive indices of cells, including diatoms, in laboratory measurements (Charrière et al., 2006; Merola et al., 2017; Umemura et al., 2020), and has high potential to be transformed to *in situ* aquatic applications (Poulin and Zhang, 2020).

Microplastics

Microplastics have emerged as a primary source of pollutants in aquatic systems in recent times, leading to an increasing number of studies focusing on their presence, fate and transport in aquatic environments, and effects on aquatic ecosystems (Cózar et al., 2014; Zhao et al., 2018; Granek et al., 2020). Early estimates have shown that only a fraction of the known anthropogenic microplastic inputs into the oceans have been accounted for, leading to questions about the fate of the remaining portion. Consequently, improvements in monitoring and detection techniques of microplastics have become crucial to understanding this issue (Garaba and Dierssen, 2018; Mai et al., 2018). Recent laboratory studies have shown that holography can be a valuable tool in the detection of microplastics in the ocean (Merola et al., 2018; Bianco et al., 2020). Future efforts geared toward testing these in field environments are needed.

Long-Term and Real-Time Observation Networks

The democratization of oceanographic data access has received significant attention in the past decade; consequently, data collected from networks of floats, gliders, buoys, and other observation and monitoring platforms are freely available to scientists and the public. Examples include National Oceanic

and Atmospheric Administration's Integrated Ocean Observing System (IOOS) and Marine Biodiversity Observation Networks (MBONs), National Science Foundation's Ocean Observatories Initiative (OOI), the Argo global network of profiling floats, etc. Other *in situ* imaging systems, such as the IFCB, are now being routinely used for real-time monitoring of plankton community composition as well as HAB events (Kudela et al., 2015). The versatile nature of holography allows for enough flexibility to be used in a variety of purposes, with appropriate modifications or trade-offs in resolution and image quality. For example, efforts to develop holographic imaging systems for long-term aquatic deployments with a wide particle resolution range (Nayak et al., 2020) can be complemented with low-cost robotic holographic samplers for environmental monitoring (Mallery et al., 2019). Future work should be geared toward integrating holographic systems into aquatic monitoring networks, e.g., MBONs and/or Argo floats. Continuing improvements in image processing methods, technological improvements in data transmission and storage, and an increasing focus on machine learning for automated particle and plankton classification are promising indicators of the aquatic sciences community being poised to embrace holographic systems on a large scale in the near future.

AUTHOR CONTRIBUTIONS

AN conceived the manuscript and compiled the literature survey. AN, EM, MM, MT, and JS prepared the manuscript. All authors contributed to the article and approved the submitted version.

FUNDING

AN, MM, and JS were primarily supported through United States National Science Foundation awards OCE-1634053 and OCE-1657332. AN and MT were partially supported by the Harbor Branch Oceanographic Institute Foundation (HBOIF). AN was also supported by an Early Career Research Fellowship from the Gulf Research Program of the National Academies of Sciences, Engineering, and Medicine.

ACKNOWLEDGMENTS

The authors are grateful to Lisa Nyman for her help in generating some of the figures used in this manuscript and Ranjoy Barua for useful inputs.

REFERENCES

Abraham, E. R. (1998). The generation of plankton patchiness by turbulent stirring. *Nature* 391, 577–580. doi: 10.1038/35361

Agrawal, Y., and Pottsmith, H. (2000). Instruments for particle size and settling velocity observations in sediment transport. *Mar. Geol.* 168, 89–114. doi: 10.1016/s0025-3227(00)00044-x

Alldredge, A. L. (1981). The impact of appendicularian grazing on natural food concentrations in situ. *Limnol. and Oceanogr.* 26, 247–257. doi: 10.4319/lo.1981.26.2.0247

Anderson, D. M., Glibert, P. M., and Burkholder, J. M. (2002). Harmful algal blooms and eutrophication: nutrient sources, composition, and consequences. *Estuaries* 25, 704–726. doi: 10.1007/bf02804901

Anderson, E. E., Wilson, C., Knap, A. H., and Villareal, T. A. (2018). Summer diatom blooms in the eastern north pacific gyre investigated with a long-endurance autonomous surface vehicle. *PeerJ* 6:e5387. doi: 10.7717/peerj.5387

Bach, L. T., Riebesell, U., Sett, S., Febiri, S., Rzepka, P., and Schulz, K. G. (2012). An approach for particle sinking velocity measurements in the 3–400 μm size range and considerations on the effect of temperature on sinking rates. *Mar. Biol.* 159, 1853–1864. doi: 10.1007/s00227-012-1945-2

Barnhart, D. H., Adrian, R. J., and Papen, G. C. (1994). Phase-conjugate holographic system for high-resolution particle-image velocimetry. *Appl. Opt.* 33, 7159–7170. doi: 10.1364/ao.33.007159

Basterretxea, G., Font-Munoz, J. S., and Tuval, I. (2020). Phytoplankton orientation in a turbulent ocean: a microscale perspective. *Front. Mar. Sci.* 7:185. doi: 10.3389/fmars.2020.00185

Bedrossian, M., Lindensmith, C., and Nadeau, J. L. (2017). Digital holographic microscopy, a method for detection of microorganisms in plume samples from enceladus and other icy worlds. *Astrobio* 17, 913–925. doi: 10.1089/ast.2016.1616

Beers, J. R., Knox, C., and Strickland, J. D. (1970). A permanent record of plankton samples using holography. *Limnol. Oceanogr.* 15, 967–970. doi: 10.4319/lo.1970.15.6.0967

Bianco, V., Memmolo, P., Carcagnì, P., Merola, F., Paturzo, M., Distante, C., et al. (2020). Microplastic identification via holographic imaging and machine learning. *Adv. Int. Sys.* 2:1900153. doi: 10.1002/aisy.201900153

Bianco, V., Memmolo, P., Leo, M., Montresor, S., Distante, C., Paturzo, M., et al. (2018). Strategies for reducing speckle noise in digital holography. *Light Sci. Appl.* 7, 1–16.

Bochdansky, A. B., Clouse, M. A., and Hansell, D. A. (2017). Mesoscale and high-frequency variability of macroscopic particles (> 100 μm) in the Ross Sea and its relevance for late-season particulate carbon export. *J. Mar. Syst.* 166, 120–131. doi: 10.1016/j.jmarsys.2016.08.010

Bochdansky, A. B., Clouse, M. A., and Herndl, G. J. (2016). Dragon kings of the deep sea: marine particles deviate markedly from the common number-size spectrum. *Sci. Rep.* 6, 1–7.

Bochdansky, A. B., Jericho, M. H., and Herndl, G. J. (2013). Development and deployment of a point-source digital inline holographic microscope for the study of plankton and particles to a depth of 6000 m. *Limnol. Oceanogr. Methods* 11, 28–40. doi: 10.4319/lom.2013.11.28

Bohren, C., and Huffman, D. (1983). *Light Scattering and Absorption by Small Particles*. New York, NY: Wiley.

Boss, E., Slade, W., and Hill, P. (2009). Effect of particulate aggregation in aquatic environments on the beam attenuation and its utility as a proxy for particulate mass. *Opt. Express* 17, 9408–9420. doi: 10.1364/oe.17.009408

Boss, E., Twardowski, M. S., and Herring, S. (2001). Shape of the particulate beam attenuation spectrum and its inversion to obtain the shape of the particulate size distribution. *Appl. Opt.* 40, 4885–4893. doi: 10.1364/ao.40.004885

Breier, R. E., Lalescu, C. C., Waas, D., Wilczek, M., and Mazza, M. G. (2018). Emergence of phytoplankton patchiness at small scales in mild turbulence. *Proc. Nat. Acad. Sci. U.S.A.* 115, 12112–12117. doi: 10.1073/pnas.1808711115

Briggs, N., Dall'Olmo, G., and Claustre, H. (2020). Major role of particle fragmentation in regulating biological sequestration of co2 by the oceans. *Science* 367, 791–793. doi: 10.1126/science.aay1790

Buonassissi, C., and Dierssen, H. (2010). A regional comparison of particle size distributions and the power law approximation in oceanic and estuarine surface waters. *J. Geophys. Res. Oceans* 115:C10028.

Busck, J. (2005). Underwater 3-d optical imaging with a gated viewing laser radar. *Opt. Eng.* 44:116001. doi: 10.1117/1.2127895

Carder, K. L. (1979). Holographic microvelocimeter for use in studying ocean particle dynamics. *Opt. Eng.* 18:185524.

Carder, K. L., Steward, R. G., and Betzer, P. R. (1982). *In situ* holographic measurements of the sizes and settling rates of oceanic particulates. *J. Geophys. Res. Oceans* 87, 5681–5685. doi: 10.1029/jc087ic08p05681

Carder, K. L., Tomlinson, R. D., and Beardsley, G. F. Jr. (1972). A technique for the estimation of indices of refraction of marine phytoplankters. *Limnol. Oceanogr.* 17, 833–839. doi: 10.4319/lo.1972.17.6.0833

Carmichael, W. W., and Boyer, G. L. (2016). Health impacts from cyanobacteria harmful algae blooms: implications for the north american great lakes. *Harmful Algae* 54, 194–212. doi: 10.1016/j.hal.2016.02.002

Charrière, F., Marian, A., Montfort, F., Kuehn, J., Colomb, T., Cuche, E., et al. (2006). Cell refractive index tomography by digital holographic microscopy. *Opt. Lett.* 31, 178–180. doi: 10.1364/ol.31.000178

Checkley, D. Jr., Davis, R., Herman, A., Jackson, G., Beanlands, B., and Regier, L. (2008). Assessing plankton and other particles *in situ* with the solopc. *Limnol. Oceanogr.* 53(5, Pt 2), 2123–2136. doi: 10.4319/lo.2008.53.5_part_2.2123

Churnside, J. H., and Wilson, J. J. (2004). Airborne lidar imaging of salmon. *Appl. Opt.* 43, 1416–1424. doi: 10.1364/ao.43.001416

Conley, D., Buscombe, D., and Nimmo Smith, A. (2012). Use of digital holographic cameras to examine the measurement and understanding of sediment suspension in the nearshore. *Coast. Eng. Proc.* 1, 73. doi: 10.9753/icce.v33.sediment.73

Costello, D., Carder, K., Betzer, P., and Young, R. (1989). *In situ* holographic imaging of settling particles: applications for individual particle dynamics and oceanic flux measurements. *Deep Sea Res. Part A* 36, 1595–1605. doi: 10.1016/0198-0149(89)90060-5

Cózar, A., Echevarría, F., González-Gordillo, J. I., Irigoien, X., Úbeda, B., Hernández-León, S., et al. (2014). Plastic debris in the open ocean. *Proc. Nat. Acad. Sci. U.S.A.* 111, 10239–10244.

Cross, J., Nimmo Smith, W. A. M., Hosegood, P. J., and Torres, R. (2014). The dispersal of phytoplankton populations by enhanced turbulent mixing in a shallow coastal sea. *J. Mar. Syst.* 136, 55–64. doi: 10.1016/j.jmarsys.2014.03.009

Cross, J., Nimmo Smith, W. A. M., Torres, R., and Hosegood, P. J. (2013). Biological controls on resuspension and the relationship between particle size and the kolmogorov length scale in a shallow coastal sea. *Mar. Geol.* 343, 29–38. doi: 10.1016/j.margeo.2013.06.014

Czerski, H., Vagle, S., Farmer, D. M., and Hall-Patch, N. (2011). Improvements to the methods used to measure bubble attenuation using an underwater acoustical resonator. *J. Acoust. Soc. Am.* 130, 3421–3430. doi: 10.1121/1.3569723

Dahms, H.-U., and Hwang, J.-S. (2010). Perspectives of underwater optics in biological oceanography and plankton ecology studies. *J. Mar. Sci. Technol.* 18, 112–121.

Davies, E. J., Buscombe, D., Graham, G. W., and Nimmo Smith, W. A. M. (2015). Evaluating unsupervised methods to size and classify suspended particles using digital in-line holography. *J. Atmos. Oceanic Technol.* 32, 1241–1256. doi: 10.1175/jtech-d-14-00157.1

Davies, E. J., and Nepstad, R. (2017). *In situ* characterisation of complex suspended particulates surrounding an active submarine tailings placement site in a norwegian fjord. *Reg. Stud. Mar. Sci.* 16, 198–207. doi: 10.1016/j.rsma.2017.09.008

Dekshenieks, M. M., Donaghay, P. L., Sullivan, J. M., Rines, J. E., Osborn, T. R., and Twardowski, M. S. (2001). Temporal and spatial occurrence of thin phytoplankton layers in relation to physical processes. *Mar. Ecol. Prog. Ser.* 223, 61–71. doi: 10.3354/meps223061

Donaghay, P., Rines, H. M., and Sieburth, J. M. (1992). Simultaneous sampling of fine-scale biological, chemical, and physical structure in stratified waters. *Arch. Hydrobiol.* 36, 1–14.

Durham, W. M., Climent, E., Barry, M., De Lillo, F., Boffetta, G., Cencini, M., et al. (2013). Turbulence drives microscale patches of motile phytoplankton. *Nat. Commun.* 4, 1–7.

Durham, W. M., and Stocker, R. (2012). Thin phytoplankton layers: characteristics, mechanisms, and consequences. *Annu. Rev. Mar. Sci.* 4, 177–207. doi: 10.1146/annurev-marine-120710-100957

Dyomin, V., Davydova, A., Morgalev, S., Kirillov, N., Olshukov, A., Polovtsev, I., et al. (2020). Monitoring of plankton spatial and temporal characteristics with the use of a submersible digital holographic camera. *Front. Mar. Sci.* 7:653. doi: 10.3389/fmars.2020.00653

Dyomin, V., Gribenyukov, A., Davydova, A., Zinoviev, M., Olshukov, A., Podzyvalov, S., et al. (2019). Holography of particles for diagnostics tasks. *Appl. Opt.* 58, G300–G310.

Fischer, G., and Karakas, G. (2009). Sinking rates and ballast composition of particles in the atlantic ocean: implications for the organic carbon fluxes to the deep ocean. *Biogeosciences* 6, 85–102. doi: 10.5194/bg-6-85-2009

Font-Muñoz, J. S., Jeanneret, R., Arrieta, J., Anglès, S., Jordi, A., Tuval, I., et al. (2019). Collective sinking promotes. selective cell pairing in planktonic pennate diatoms. *Proc. Nat. Acad. Sci. U.S.A.* 116, 15997–16002

Font-Muñoz, J. S., Jeanneret, R., Tuval, I., and Basterretxea, G. (2020). Method for the determination of preferential orientation of marine particles from laser diffraction measurements. *Opt. Express* 28, 14085–14099.

Foster, E., and Watson, J. (1997). Holography for underwater inspection and measurement: an overview of current work. *Opt. Laser Technol.* 29, 17–23.

Fournier, G. R., and Forand, J. L. (1994). "Analytic phase function for ocean water," in *Ocean Optics XII*, ed. J. S. Jaffe (Bellingham, WA: International Society for Optics and Photonics), 194–201.

Freedman, D., Pisani, R., and Purves, R. (2007). *Statistics*. New York, NY: W.W. Norton & Company, Inc.

Gabor, D. (1948). A new microscopic principle. *Nature* 161, 777–778.

Gabor, D. (1949). Microscopy by reconstructed wave-fronts. *Proc. R. Soc. London, Ser. A* 197, 454–487.

Gao, J., Guildenbecher, D. R., Reu, P. L., and Chen, J. (2013). Uncertainty characterization of particle depth measurement using digital in-line holography and the hybrid method. *Opt. Express* 21, 26432–26449.

Garaba, S. P., and Dierssen, H. M. (2018). An airborne remote sensing case study of synthetic hydrocarbon detection using short wave infrared absorption features identified from marine-harvested macro-and microplastics. *Remote Sens. Environ.* 205, 224–235.

Garcia-Sucerquia, J. (2013). Noise reduction in digital lensless holographic microscopy by engineering the light from a light-emitting diode. *Appl. Opt.* 52, A232–A239.

Glibert, P. M., Berdalet, E., Burford, M. A., Pitcher, G. C., and Zhou, M. (2018). *Global Ecology and Oceanography of Harmful Algal Blooms*. Berlin: Springer.

Graff, J. R., and Menden-Deuer, S. (2016). Physical and optical properties of phytoplankton-rich layers in a coastal fjord: a step toward prediction and strategic sampling of plankton patchiness. *Mar. Ecol. Prog. Ser.* 544, 1–14.

Graham, G., Davies, E., Nimmo Smith, W., Bowers, D., and Braithwaite, K. (2012). Interpreting LISST-100X measurements of particles with complex shape using digital in-line holography. *J. Geophys. Res. Oceans* 117:C05034.

Graham, G. W., and Nimmo Smith, W. A. M. (2010). The application of holography to the analysis of size and settling velocity of suspended cohesive sediments. *Limnol. Oceanogr. Methods* 8, 1–15.

Granek, E. F., Brander, S., and Holland, E. (2020). Microplastics in aquatic organisms: improving understanding and identifying research directions for the next decade. *Limnol. Oceanogr. Lett.* 5, 1–4.

Guidi, L., Calil, P. H., Duhamel, S., Björkman, K. M., Doney, S. C., Jackson, G. A., et al. (2012). Does eddy-eddy interaction control surface phytoplankton distribution and carbon export in the north pacific subtropical gyre? *J. Geophys. Res. Biogeosci.* 117:G02024.

Guo, B., Nyman, L., Nayak, A. R., Milmore, D., McFarland, M., Twardowski, M., et al. (2021). Automated plankton classification from holographic imagery with deep convolutional neural networks. *Limnol. Oceanogr. Methods* 19, 21–36. doi: 10.1002/lom3.10402

Heflinger, L., Stewart, G., and Booth, C. (1978). Holographic motion pictures of microscopic plankton. *Appl. Opt.* 17, 951–954.

Herman, A., Beanlands, B., and Phillips, E. (2004). The next generation of optical plankton counter: the laser-opc. *J. Plankton Res.* 26, 1135–1145.

Hill, P., Boss, E., Newgard, J., Law, B., and Milligan, T. (2011). Observations of the sensitivity of beam attenuation to particle size in a coastal bottom boundary layer. *J. Geophys. Res. Oceans* 116:C02023.

Hinsch, K. D. (2002). Holographic particle image velocimetry. *Meas. Sci. Technol.* 13:R61.

Hobson, P. R., and Watson, J. (2002). The principles and practice of holographic recording of plankton. *J. Opt. A Pure Appl. Opt.* 4:S34.

Hodgson, R. T., and Newkirk, D. D. (1975). "Pyridine immersion: a technique for measuring the refractive index of marine particles," in *Ocean Optics IV*, (Bellingham, WA: International Society for Optics and Photonics), 62–65.

Holliday, D., Donaghay, P., Greenlaw, C., Napp, J., and Sullivan, J. (2009). High-frequency acoustics and bio-optics in ecosystems research. *ICES J. Mar. Sci.* 66, 974–980.

Hong, J., Talapatra, S., Katz, J., Tester, P. A., Waggett, R. J., and Place, A. R. (2012). Algal toxins alter copepod feeding behavior. *PLoS One* 7:e36845. doi: 10.1371/journal.pone.0036845

Jackson, G., Maffione, R., Costello, D., Alldredge, A. L. B., and Dam, H. (1997). Particle size spectra between 1 um and 1 cm at monterey bay determined using multiple instruments. *Deep Sea Res. Part I* 44, 1739–1767.

Jaffe, J., Franks, P., Briseño-Avena, C., Roberts, P., and Laxton, B. (2013). "Advances in underwater fluorometry: from bulk fluorescence to planar laser imaging," in *Subsea Optics and Imaging*, eds J. Watson and O. Zielinski (Amsterdam: Elsevier), 536–549.

Jaffe, J. S. (2014). Underwater optical imaging: the past, the present, and the prospects. *IEEE J. Oceanic Eng.* 40, 683–700.

Jeffrey, G. (1922). The motion of ellipsoidal particles immersed in a viscous fluid. *Proc. R. Soc. London, Ser. A* 102, 161–179.

Jericho, S., Garcia-Sucerquia, J., Xu, W., Jericho, M., and Kreuzer, H. (2006). Submersible digital in-line holographic microscope. *Rev. Sci. Instrum.* 77:043706.

Jonasz, M., and Fournier, G. (2007). *Light Scattering by Particles in Water: Theoretical and Experimental Constraints*. Cambridge, MA: Academic Press.

Karp-Boss, L., Boss, E., and Jumars, P. (1996). Nutrient fluxes to planktonic osmotrophs in the presence of fluid motion. *Oceanogr. Mar. Biol.* 34, 71–108.

Karp-Boss, L., Boss, E., and Jumars, P. A. (2000). Motion of dinoflagellates in a simple shear flow. *Limnol. Oceanogr.* 45, 1594–1602. doi: 10.4319/lo.2000.45.7.1594

Karp-Boss, L., and Jumars, P. A. (1998). Motion of diatom chains in steady shear flow. *Limnol. Oceanogr.* 43, 1767–1773. doi: 10.4319/lo.1998.43.8.1767

Katz, J., Donaghay, P., Zhang, J., King, S., and Russell, K. (1999). Submersible holocamera for detection of particle characteristics and motions in the ocean. *Deep Sea Res. Part A* 46, 1455–1481. doi: 10.1016/S0967-0637(99)00011-4

Katz, J., O'Hern, T., and Acosta, A. (1984). "An underwater holographic camera system for detection of microparticulates," in *Proceedings of the ASME Cavitation and Multiphase Flow Forum*, New Orleans.

Katz, J., and Sheng, J. (2010). Applications of holography in fluid mechanics and particle dynamics. *Annu. Rev. Flu. Mech.* 42, 531–555. doi: 10.1146/annurev-fluid-121108-145508

Kitchen, J., Zaneveldan, J., and Pak, H. (1982). Effect of particle size distribution and chlorophyll content on beam attenuation spectra. *Appl. Opt.* 21, 3913–3918. doi: 10.1364/AO.21.003913

Knox, C. (1966). Holographic microscopy as a technique for recording dynamic microscopic subjects. *Science* 153, 989–990. doi: 10.1126/science.153.3739.989

Knox, C., and Brooks, R. (1969). Holographic motion picture microscopy. *Proc. R. Soc. London, Ser. B* 174, 115–121. doi: 10.1098/rspb.1969.0083

Kosmeier, S., Langehanenberg, P., Von Bally, G., and Kemper, B. (2012). Reduction of parasitic interferences in digital holographic microscopy by numerically decreased coherence length. *Appl. Phys. B* 106, 107–115. doi: 10.1007/s00340-011-4667-0

Kostadinov, T., Siegel, D., and Maritorena, S. (2010). Global variability of phytoplankton functional types from space: assessment via the particle size distribution. *Biogeosci. Discuss.* 7, 4295–4340. doi: 10.5194/bgd-7-4295-2010

Kudela, R. M., Bickel, A., Carter, M. L., Howard, M. D., and Rosenfeld, L. (2015). "The monitoring of harmful algal blooms through ocean observing: the development of the california harmful algal bloom monitoring and alert program," in *Coastal Ocean Observing Systems*, eds Y. Liu, H. Kerkering, and R. Weisberg (Amsterdam: Elsevier), 58–75. Available online at: https://www.elsevier.com/books/coastal-ocean-observing-systems/liu/978-0-12-802022-7

Kumar, S. S., He, Z., Hogan, C. J., Fredericks, S. A., and Hong, J. (2020). Evaluation of laser diffraction-based particle size measurements using digital inline holography. *Meas. Sci. Technol.* 31:125201. doi: 10.1088/1361-6501/aba78b

Lal, D. (1977). The oceanic microcosm of particles. *Science* 198, 997–1009. doi: 10.1126/science.198.4321.997

Leo, M., Piccolo, R., Distante, C., Memmolo, P., Paturzo, M., and Ferraro, P. (2014). Multilevel bidimensional empirical mode decomposition: a new speckle reduction method in digital holography. *Opt. Eng.* 53:112314. doi: 10.1117/1.OE.53.11.112314

Lindensmith, C. A., Rider, S., Bedrossian, M., Wallace, J. K., Serabyn, E., Showalter, G. M., et al. (2016). A submersible, off-axis holographic microscope for detection of microbial motility and morphology in aqueous and icy environments. *PLoS One* 11:e0147700. doi: 10.1371/journal.pone.0147700

Mai, L., Bao, L.-J., Shi, L., Wong, C. S., and Zeng, E. Y. (2018). A review of methods for measuring microplastics in aquatic environments. *Environ. Sci. Pollut. Res.* 25, 11319–11332. doi: 10.1007/s11356-018-1692-0

Malkiel, E., Abras, J., Widder, E., and Katz, J. (2006). On the spatial distribution and nearest neighbor distance between particles in the water column determined from *in situ* holographic measurements. *J. Plankton Res.* 28, 149–170. doi: 10.1093/plankt/fbi107

Malkiel, E., Abras, J. N., and Katz, J. (2004). Automated scanning and measurements of particle distributions within a holographic reconstructed volume. *Meas. Sci. Technol.* 15:601. doi: 10.1088/0957-0233/15/4/001

Malkiel, E., Alquaddoomi, O., and Katz, J. (1999). Measurements of plankton distribution in the ocean using submersible holography. *Meas. Sci. Technol.* 10:1142. doi: 10.1088/0957-0233/10/12/305

Malkiel, E., Pfitsch, D. W., Sheng, J., and Katz, J. (2007). "Observing the 3-dimensional zooplankton world with holography," in *ASLO Aquatic Sciences Meeting*, Santa Fe, MX.

Mallery, K., Canelon, D., Hong, J., and Papanikolopoulos, N. (2019). Design and experiments with a robot-driven underwater holographic microscope for low-cost *in situ* particle measurements. *arXiv* [preprint], Avaliable at: https://arxiv.org/abs/1911.10231 (accessed May 15, 2020).

Marcos, J. R., Seymour, J. R., Luhar, M., Durham, W. M., Mitchell, J. G., Macke, A., et al. (2011). Microbial alignment in flow changes ocean light climate. *Proc. Nat. Acad. Sci. U.S.A.* 108, 3860–3864. doi: 10.1073/pnas.1014576108

McDonnell, A. M., and Buesseler, K. O. (2010). Variability in the average sinking velocity of marine particles. *Limnol. Oceanogr.* 55, 2085–2096. doi: 10.4319/lo.2010.55.5.2085

McFarland, M., Nayak, A. R., Stockley, N., Twardowski, M., and Sullivan, J. (2020). Enhanced light absorption by horizontally oriented diatom colonies. *Front. Mar. Sci.* 7:494. doi: 10.3389/fmars.2020.00494

McFarland, M. N., Rines, J., Sullivan, J., and Donaghay, P. (2015). Impact of phytoplankton size and physiology on particulate optical properties determined with scanning flow cytometry. *Mar. Ecol. Prog. Ser.* 531, 43–61. doi: 10.3354/meps11325

McKenzie, T. L., Twardowski, M., Briggs, N., Nayak, A. R., Boswell, K. M., and Dalgleish, F. (2020). Three-dimensional imaging lidar for characterizing particle fields and organisms in the mesopelagic zone. *Front. Mar. Sci.* 7:1021.

McManus, M., Alldredge, A., Barnard, A., Boss, E., Case, J., Cowles, T., et al. (2003). Characteristics, distribution and persistence of thin layers over a 48 hour period. *Mar. Ecol. Prog. Ser.* 261, 1–19. doi: 10.3354/meps261001

McManus, M. A., and Woodson, C. B. (2012). Plankton distribution and ocean dispersal. *J. Exp. Biol.* 215, 1008–1016. doi: 10.1242/jeb.059014

Meng, H., Anderson, W., Hussain, F., and Liu, D. D. (1993). Intrinsic speckle noise in in-line particle holography. *J. Opt. Soc. Am. A* 10, 2046–2058. doi: 10.1364/JOSAA.10.002046

Merola, F., Memmolo, P., Bianco, V., Paturzo, M., Mazzocchi, M., and Ferraro, P. (2018). Searching and identifying microplastics in marine environment by digital holography⋆. *Eur. Phys. J. Plus* 133:350. doi: 10.1140/epjp/i2018-12190-y

Merola, F., Memmolo, P., Miccio, L., Savoia, R., Mugnano, M., Fontana, A., et al. (2017). Tomographic flow cytometry by digital holography. *Light Sci. Appl.* 6:e16241. doi: 10.1038/lsa.2016.241

Mikkelsen, O., and Pejrup, M. (2001). The use of a LISST-100 laser particle sizer for in-situ estimates of floc size, density and settling velocity. *Geo Mar. Lett.* 20, 187–195. doi: 10.1007/s003670100064

Milligan, T. (1996). *In situ* particle (floc) size measurements with the benthos 373 plankton silhouette camera. *J. Sea Res.* 36, 93–100. doi: 10.1016/S1385-1101(96)90777-7

Moore, T. S., Churnside, J. H., Sullivan, J. M., Twardowski, M. S., Nayak, A. R., McFarland, M. N., et al. (2019). Vertical distributions of blooming cyanobacteria populations in a freshwater lake from lidar observations. *Remote Sens. Environ.* 225, 347–367. doi: 10.1016/j.rse.2019.02.025

Moore, T. S., Mouw, C. B., Sullivan, J. M., Twardowski, M. S., Burtner, A. M., Ciochetto, A. B., et al. (2017). Bio-optical properties of cyanobacteria blooms in western lake erie. *Front. Mar. Sci.* 4:300. doi: 10.3389/fmars.2017.00300

Mullen, A. D., Treibitz, T., Roberts, P. L., Kelly, E. L., Horwitz, R., Smith, J. E., et al. (2016). Underwater microscopy for *in situ* studies of benthic ecosystems. *Nat. Commun.* 7, 1–9. doi: 10.1038/ncomms12093

Murata, S., and Yasuda, N. (2000). Potential of digital holography in particle measurement. *Opt. Laser Technol.* 32, 567–574. doi: 10.1016/S0030-3992(00)00088-8

Nayak, A. R., Li, C., Kiani, B. T., and Katz, J. (2015). On the wave and current interaction with a rippled seabed in the coastal ocean bottom boundary layer. *J. Geophys. Res. Oceans* 120, 4595–4624. doi: 10.1002/2014JC010606

Nayak, A. R., McFarland, M., Sullivan, J. M., Dalgleish, F., and Garavelli, L. (2020). "AUTOHOLO: A novel, *in situ*, autonomous holographic imaging system for long-term particle and plankton characterization studies in diverse marine environments," in *Ocean Sciences Meeting 2020*, San Diego, CA.

Nayak, A. R., McFarland, M. N., Sullivan, J. M., and Twardowski, M. S. (2018a). Evidence for ubiquitous preferential particle orientation in representative oceanic shear flows. *Limnol. Oceanogr.* 63, 122–143. doi: 10.1002/lno.10618

Nayak, A. R., McFarland, M. N., Twardowski, M. S., and Sullivan, J. M. (2018b). "On plankton distributions and biophysical interactions in diverse coastal and limnological environments," in *Ocean Sensing and Monitoring X*, Bellingham, WA: International Society for Optics and Photonics, 106310. doi: 10.1117/12.2309798

Nayak, A. R., and Twardowski, M. S. (2020). "Breaking" news for the ocean's carbon budget. *Science* 367, 738–739. doi: 10.1126/science.aba7109

Nimmo Smith, W. A. (2008). A submersible three-dimensional particle tracking velocimetry system for flow visualization in the coastal ocean. *Limnol. Oceanogr. Methods* 6, 96–104. doi: 10.4319/lom.2008.6.96

Noel, V., and Chepfer, H. (2004). Study of ice crystal orientation in cirrus clouds based on satellite polarized radiance measurements. *J. Atmos. Sci.* 61, 2073–2081. doi: 10.1175/1520-0469(2004)061<2073:SOICOI>2.0.CO;2

O'Hern, T., d'Agostino, L., and Acosta, A. (1988). Comparison of holographic and coulter counter measurements of cavitation nuclei in the ocean. *J. Fluids Eng.* 110, 200–207. doi: 10.1115/1.3243535

Olson, R. J., and Sosik, H. M. (2007). A submersible imaging-in-flow instrument to analyze nano-and microplankton: imaging flowcytobot. *Limnol. Oceanogr. Methods* 5, 195–203. doi: 10.4319/lom.2007.5.195

Ono, A. (1969). The shape and riming properties of ice crystals in natural clouds. *J. Atmos. Sci.* 26, 138–147. doi: 10.1175/1520-0469(1969)026<0138:TSARPO>2.0.CO;2

Ouillon, S. (2018). Why and how do we study sediment transport? Focus on coastal zones and ongoing methods. *Water* 10:390. doi: 10.3390/w10040390

Owen, R. B., and Zozulya, A. A. (2000). In-line digital holographic sensor for monitoring and characterizing marine particulates. *Opt. Eng.* 39, 2187–2197. doi: 10.1117/1.1305542

Pan, F., Yang, L., and Xiao, W. (2017). Coherent noise reduction in digital holographic microscopy by averaging multiple holograms recorded with a multimode laser. *Optics Express* 25, 21815–21825. doi: 10.1364/OE.25.021815

Pan, G., and Meng, H. (2003). Digital holography of particle fields: reconstruction by use of complex amplitude. *Appl. Opt.* 42, 827–833. doi: 10.1364/AO.42.000827

Pfitsch, D., Malkiel, E., Ronzhes, Y., King, S., Sheng, J., and Katz, J. (2005). "Development of a free-drifting submersible digital holographic imaging system," in *Proceedings of OCEANS 2005 MTS/IEEE*, Washington, DC, 690–696. doi: 10.1109/OCEANS.2005.1639833

Pfitsch, D., Malkiel, E., Takagi, M., Ronzhes, Y., King, S., and Sheng, J. (2007). Analysis of in-situ microscopic organism behavior in data acquired using a free-drifting submersible holographic imaging system. *OCEANS* 2007, 1–8. doi: 10.1109/OCEANS.2007.4449197

Picart, P., and Montresor, S. (2020). "Digital holography," in *Optical Holography-Materials, Theory and Applications*, ed. P.-A. Blanche (Amsterdam: Elsevier), 83–120. doi: 10.1016/B978-0-12-815467-0.00005-0

Poulin, C., and Zhang, X. (2020). "Evaluating holotomography as a new way to measure the refractive index of phytoplankton," in *Ocean Sciences Meeting 2020*, San Diego, CA.

Powell, T. M., and Okubo, A. (1994). Turbulence, diffusion and patchiness in the sea. *Phil. Trans. R. Soc. London. Ser. B* 343, 11–18. doi: 10.1098/rstb.1994.0002

Prairie, J. C., Franks, P. J., Jaffe, J. S., Doubell, M. J., and Yamazaki, H. (2011). Physical and biological controls of vertical gradients in phytoplankton. *Limnol. Oceanogr. Fluids Environ.* 1, 75–90. doi: 10.1215/21573698-1267403

Prairie, J. C., Sutherland, K. R., Nickols, K. J., and Kaltenberg, A. M. (2012). Biophysical interactions in the plankton: a cross-scale review. *Limnol. Oceanogr. Fluids Environ.* 2, 121–145. doi: 10.1215/21573689-1964713

Rines, J., Donaghay, P. L., Dekshenieks, M., Sullivan, J., and Twardowski, M. (2002). Thin layers and camouflage: hidden *Pseudo-nitzschia* spp.(*Bacillariophyceae*) populations in a fjord in the San Juan Islands. Washington, USA. *Mar. Ecol. Prog. Ser.* 225, 123–137. doi: 10.3354/meps225123

Risović, D. (1993). Two-component model of sea particle size distribution. *Deep Sea Res. Part I* 40, 1459–1473. doi: 10.1016/0967-0637(93)90123-K

Rotermund, L., Samson, J., and Kreuzer, H. (2016). A submersible holographic microscope for 4-d in-situ studies of micro-organisms in the ocean with intensity and quantitative phase imaging. *J. Mar. Sci. Res. Dev.* 6:181. doi: 10.4172/2155-9910.1000181

Sassen, K., and Takano, Y. (2000). Parry arc: a polarization lidar, ray-tracing, and aircraft case study. *Appl. Opt.* 39, 6738–6745. doi: 10.1364/AO.39.006738

Schnars, U., and Jüptner, W. (2005). *Digital Holography*. Berlin: Springer.

Schnars, U., and Jüptner, W. P. (2002). Digital recording and numerical reconstruction of holograms. *Meas. Sci. Technol.* 13:R85. doi: 10.1088/0957-0233/13/9/201

Selander, E., and Tiselius, P. (2003). Effects of food concentration on the behaviour of oikopleuradioica. *Mar. Biol.* 142, 263–270. doi: 10.1007/s00227-002-0949-8

Shao, S., Mallery, K., Kumar, S. S., and Hong, J. (2020). Machine learning holography for 3D particle field imaging. *Opt. Express* 28, 2987–2999. doi: 10.1364/OE.379480

Sheng, J., Malkiel, E., Katz, J., Adolf, J., Belas, R., and Place, A. R. (2007). Digital holographic microscopy reveals prey-induced changes in swimming behavior of predatory dinoflagellates. *Proc. Nat. Acad. Sci. U.S.A.* 104, 17512–17517. doi: 10.1073/pnas.0704658104

Steinbuck, J. V., Roberts, P. L., Troy, C. D., Horner-Devine, A. R., Simonet, F., Uhlman, A. H., et al. (2010). An autonomous open-ocean stereoscopic PIV profiler. *J. Atmos. Oceanic Technol.* 27, 1362–1380. doi: 10.1175/2010JTECHO694.1

Stemmann, L., and Boss, E. (2012). Plankton and particle size and packaging: from determining optical properties to driving the biological pump. *Annu. Rev. Mar. Sci.* 4, 263–290. doi: 10.1146/annurev-marine-120710-100853

Stemmann, L., Eloire, D., Sciandra, A., Jackson, G., Guidi, L., Picheral, M., et al. (2008). Volume distribution for particles between 3.5 to 2000 μm in the upper 200 m region of the south pacific gyre. *Biogeosciences* 5, 299–310. doi: 10.5194/bg-5-299-2008

Stemmann, L., Gorsky, G., Marty, J.-C., Picheral, M., and Miquel, J.-C. (2002). Four-year study of large-particle vertical distribution (0–1000 m) in the NW Mediterranean in relation to hydrology, phytoplankton, and vertical flux. *Deep Sea Res. Part II* 49, 2143–2162. doi: 10.1016/S0967-0645(02)00032-2

Stemmann, L., Picheral, M., and Gorsky, G. (2000). Diel variation in the vertical distribution of particulate matter (> 0.15 mm) in the nw mediterranean sea investigated with the underwater video profiler. *Deep Sea Res Part I* 47, 505–531. doi: 10.1016/S0967-0637(99)00100-4

Stewart, G. L., Beers, J. R., and Knox, C. (1973). "Application of holographic techniques to the study of marine plankton in the field and in the laboratory," in *Developments in Laser Technology II*, (Bellingham, WA: International Society for Optics and Photonics), 183–188. doi: 10.1117/12.953852

Sullivan, J. M., Donaghay, P. L., and Rines, J. E. (2010a). Coastal thin layer dynamics: consequences to biology and optics. *Cont. Shelf Res.* 30, 50–65. doi: 10.1016/j.csr.2009.07.009

Sullivan, J. M., Van Holliday, D., McFarland, M., McManus, M. A., Cheriton, O. M., Benoit-Bird, K. J., et al. (2010b). Layered organization in the coastal ocean: an introduction to planktonic thin layers and the loco project. *Cont. Shelf Res.* 30, 50–65. doi: 10.1016/j.csr.2009.09.001

Sullivan, J. M., and Swift, E. (2003). Effects of small-scale turbulence on net growth rate and size of ten species of marine dinoflagellates 1. *J. Phycol.* 39, 83–94. doi: 10.1046/j.1529-8817.2003.02094.x

Sullivan, J. M., Twardowski, M. S., Donaghay, P. L., and Freeman, S. A. (2005). Use of optical scattering to discriminate particle types in coastal waters. *Appl. Opt.* 44, 1667–1680. doi: 10.1364/AO.44.001667

Sun, B., Kattawar, G. W., Yang, P., Twardowski, M. S., and Sullivan, J. M. (2016). Simulation of the scattering properties of a chain-forming triangular prism oceanic diatom. *J. Quant. Spec. Rad. Trans.* 178, 390–399. doi: 10.1016/j.jqsrt.2016.02.035

Sun, H., Benzie, P. W., Burns, N., Hendry, D. C., Player, M. A., and Watson, J. (2008). Underwater digital holography for studies of marine plankton. *Phil. Trans. R. Soc. A* 366, 1789–1806. doi: 10.1098/rsta.2007.2187

Talapatra, S., Hong, J., McFarland, M., Nayak, A. R., Zhang, C., Katz, J., et al. (2013). Characterization of biophysical interactions in the water column using *in situ* digital holography. *Mar. Ecol. Prog. Ser.* 473, 29–51. doi: 10.3354/meps10049

Talapatra, S., Sullivan, J., Katz, J., Twardowski, M., Czerski, H., Donaghay, P., et al. (2012). "Application of in-situ digital holography in the study of particles, organisms and bubbles within their natural environment," in *Ocean Sensing and Monitoring IV*, (Bellingham, WA: International Society for Optics and Photonics), 837205. doi: 10.1117/12.920570

Tett, P., Carreira, C., Mills, D., Van Leeuwen, S., Foden, J., Bresnan, E., et al. (2008). Use of a phytoplankton community index to assess the health of coastal waters. *ICES J. Mar. Sci.* 65, 1475–1482. doi: 10.1093/icesjms/fsn161

Toloui, M., and Hong, J. (2015). High fidelity digital inline holographic method for 3d flow measurements. *Opt. Express* 23, 27159–27173. doi: 10.1364/OE.23.027159

Trull, T., Bray, S., Buesseler, K., Lamborg, C., Manganini, S., Moy, C., et al. (2008). *In situ* measurement of mesopelagic particle sinking rates and the control of carbon transfer to the ocean interior during the vertical flux in the global ocean (vertigo) voyages in the north pacific. *Deep Sea Res. Part II* 55, 1684–1695. doi: 10.1016/j.dsr2.2008.04.021

Turner, J. T. (2015). Zooplankton fecal pellets, marine snow, phytodetritus and the ocean's biological pump. *Prog. Oceanogr.* 130, 205–248. doi: 10.1016/j.pocean.2014.08.005

Twardowski, M., Zhang, X., Vagle, S., Sullivan, J., Freeman, S., Czerski, H., et al. (2012). The optical volume scattering function in a surf zone inverted to derive sediment and bubble particle subpopulations. *J. Geophys. Res. Oceans* 117:C00H17. doi: 10.1029/2011JC007347

Twardowski, M. S., Boss, E., Macdonald, J. B., Pegau, W. S., Barnard, A. H., and Zaneveld, J. R. V. (2001). A model for estimating bulk refractive index from the optical backscattering ratio and the implications for understanding particle composition in Case I and Case II waters. *J. Geophys. Res. Oceans* 106, 14129–14142. doi: 10.1029/2000JC000404

Twardowski, M. S., Sullivan, J. M., Donaghay, P. L., and Zaneveld, J. R. V. (1999). Microscale quantification of the absorption by dissolved and particulate material in coastal waters with an ac-9. *J. Atmos. Oceanic Technol.* 16, 691–707. doi: 10.1175/1520-0426(1999)016<0691:MQOTAB>2.0.CO;2

Ulloa, O., Sathyendranath, S., and Platt, T. (1994). Effect of the particle-size distribution on the backscattering ratio in seawater. *Appl. Opt.* 33, 7070–7077. doi: 10.1364/AO.33.007070

Umemura, K., Matsukawa, Y., Ide, Y., and Mayama, S. (2020). Corrigendum to "label-free imaging and analysis of subcellular parts of a living diatom cylindrotheca sp. using optical diffraction tomography" [methodsx: 7 (2020) 100889]. *MethodsX* 7:100923. doi: 10.1016/j.mex.2020.100889

Vikram, C. (1992). *Particle Field Holography*, 1st Edit Edn. Cambridge: Cambridge University Press. doi: 10.1017/CBO9780511524196

Visser, P. M., Passarge, J., and Mur, L. R. (1997). Modelling vertical migration of the cyanobacterium *Microcystis*. *Hydrobiologia* 349, 99–109. doi: 10.1023/A:1003001713560

Walcutt, N. L., Knörlein, B., Cetinić, I., Ljubesic, Z., Bosak, S., and Sgouros, T. (2020). Assessment of holographic microscopy for quantifying marine particle size and concentration. *Limnol. Oceanogr. Methods* 18, 516–530. doi: 10.1002/lom3.10379

Watson, J. (2005). "Underwater holography: past and future," in *Holography 2005: International Conference on Holography, Optical Recording, and Processing of Information*, (Bellingham, WA: International Society for Optics and Photonics), 62521T.

Watson, J. (2011). Submersible digital holographic cameras and their application to marine science. *Opt. Eng.* 50:091313. doi: 10.1117/1.3605678

Watson, J., Alexander, S., Craig, G., Hendry, D. C., Hobson, P., Lampitt, R., et al. (2001). Simultaneous in-line and off-axis subsea holographic recording of plankton and other marine particles. *Meas. Sci. Technol.* 12:L9. doi: 10.1088/0957-0233/12/8/101

Yang, W., Kostinski, A. B., and Shaw, R. A. (2005). Depth-of-focus reduction for digital in-line holography of particle fields. *Opt. Lett.* 30, 1303–1305. doi: 10.1364/OL.30.001303

Yourassowsky, C., and Dubois, F. (2014). High throughput holographic imaging-in-flow for the analysis of a wide plankton size range. *Opt. Express* 22, 6661–6673. doi: 10.1364/OE.22.006661

Zetsche, E. M., El Mallahi, A., Dubois, F., Yourassowsky, C., Kromkamp, J. C., and Meysman, F. J. (2014). Imaging-in-flow: digital holographic microscopy as a novel tool to detect and classify nanoplanktonic organisms. *Limnol. Oceanogr. Methods* 12, 757–775. doi: 10.4319/lom.2014.12.757

Zhao, S., Ward, J. E., Danley, M., and Mincer, T. J. (2018). Field-based evidence for microplastic in marine aggregates and mussels: implications for trophic transfer. *Environ. Sci. Technol.* 52, 11038–11048. doi: 10.1021/acs.est.8b03467

Disclaimer: The content is solely the responsibility of the authors and does not necessarily represent the official views of the Gulf Research Program of the National Academies of Sciences, Engineering, and Medicine.

Conflict of Interest: The authors declare that the research was conducted in the absence of any commercial or financial relationships that could be construed as a potential conflict of interest.

Copyright © 2021 Nayak, Malkiel, McFarland, Twardowski and Sullivan. This is an open-access article distributed under the terms of the Creative Commons Attribution License (CC BY). The use, distribution or reproduction in other forums is permitted, provided the original author(s) and the copyright owner(s) are credited and that the original publication in this journal is cited, in accordance with accepted academic practice. No use, distribution or reproduction is permitted which does not comply with these terms.

Advantages of publishing in Frontiers

OPEN ACCESS
Articles are free to read for greatest visibility and readership

FAST PUBLICATION
Around 90 days from submission to decision

HIGH QUALITY PEER-REVIEW
Rigorous, collaborative, and constructive peer-review

TRANSPARENT PEER-REVIEW
Editors and reviewers acknowledged by name on published articles

Frontiers
Avenue du Tribunal-Fédéral 34
1005 Lausanne | Switzerland

Visit us: www.frontiersin.org
Contact us: frontiersin.org/about/contact

REPRODUCIBILITY OF RESEARCH
Support open data and methods to enhance research reproducibility

DIGITAL PUBLISHING
Articles designed for optimal readership across devices

FOLLOW US
@frontiersin

IMPACT METRICS
Advanced article metrics track visibility across digital media

EXTENSIVE PROMOTION
Marketing and promotion of impactful research

LOOP RESEARCH NETWORK
Our network increases your article's readership